CHARLES PANKOW FOUNDATION

Building Innovation through Research

Seismic Design Methodology Document for Precast Concrete Diaphragms

Project Deliverable to the Charles Pankow Foundation from The University of Arizona for Revised CPF 08-07 Grant "Development and Design of Untopped Precast Concrete Diaphragm Systems for High Seismic Zones",

Robert B. Fleischman

2/16/2014

Seismic Design Methodology for Precast Concrete Floor Diaphragms

Developed by the DSDM Consortium

Robert B. Fleischman, Principal Investigator

<u>**DSDM Research Sponsors**</u>

The Precast/Prestressed Concrete Institute (*PCI*)
The Charles Pankow Foundation (*CPF*)
The National Science Foundation (*NSF*)
The George E. Brown Network for Earthquake Engineering Simulation (*NEES*)

PART 1: Seismic Design Procedure and Commentary for Precast Concrete Diaphragms
PART 2: Qualification Protocol for Precast Concrete Diaphragm Reinforcement
PART 3: Analysis Techniques and Design Aids for Precast Diaphragm Design
PART 4: Design Examples
PART 5: Background on the Precast Concrete Diaphragm Seismic Design Methodology
PART 5: Background Appendices

CHARLES PANKOW FOUNDATION

Building Innovation through Research

Seismic Design Methodology Document for Precast Concrete Diaphragms

PART 1: SEISMIC DESIGN PROCEDURE
and Commentary
for Precast Concrete Diaphragms

2/16/2014

PART 1:

SEISMIC DESIGN PROCEDURE

and Commentary

for Precast Concrete Diaphragms

Table of Contents:

Executive Summary

This design procedure in PART 1 is part of a new seismic design methodology for precast concrete diaphragms. The design methodology and procedure are the product of a large multi-university research project initiated and guided by the Precast/Prestressed Concrete Institute (PCI) can co-funded by PCI, the National Science Foundation (NSF) and the Charles Pankow Foundation (CPF), termed the Diaphragm Seismic Design Methodology (DSDM) project.

The primary objectives of the DSDM project, as laid out in the PCI RFP are to develop an industry-endorsed design procedure, including:

1. The forces to which precast diaphragms are to be designed
2. The deformations to which precast diaphragms are to be designed.
3. The precast diaphragm reinforcing details that can provide this behavior.

A further objective of the DSDM project, added as a deliverable as part of supplemental funding by the Charles Pankow Foundation, was the demonstration of viable systems for high seismic zones.

The research project, led by the University of Arizona, accomplished these goals through an integrated experimental-analytical research program using the NSF Network for Earthquake Engineering Simulation (NEES) Sites at Lehigh University and University of California- San Diego (UCSD).

The key outcomes of the research are:

1. The diaphragm design force levels required to keep diaphragms elastic in the design earthquake.
2. The relationship between precast diaphragm strength and anticipated diaphragm reinforcement[1] deformation demands[2] for different diaphragm geometries and seismic hazard levels.
3. The required increase in diaphragm shear strength, with respect to diaphragm flexure strength, to prevent undesirable high inelastic shear deformations in precast diaphragms.
4. The key characteristics of several typical precast diaphragm reinforcements under cyclic tension and shear, including stiffness, strength and reliable deformation capacity.
5. New precast diaphragm reinforcement concepts providing improved cyclic performance.

The research also provided new information on: (1) The response of precast diaphragm connectors under combined tension and shear; (2) The seismic diaphragm force profiles that occur in multi-story structures; (3) The force paths that develop in precast floor systems, including parking structures and office buildings; (4) The inelastic deformation patterns that develop in the diaphragm reinforcement, including concentrated demands at columns lines. This information informed the design methodology.

The key research outcomes listed above are embodied in the design procedure as follows:

1. Diaphragm design force levels that are calibrated to different performance targets for precast diaphragms via a diaphragm design force reduction factor, R_s, applied to newly proposed (higher) diaphragm forces[3].
2. Diaphragm reinforcement and connector classifications (*Low, Moderate and High Deformability Elements or LDE, MDE, HDE*) based on inelastic deformation capacity.
3. Diaphragm shear overstrength factors (Ω_v) to protect the diaphragm from undesirable shear mechanisms.

---

[1] The term *diaphragm reinforcement* is used to refer generically to reinforcing bars or mesh in topped diaphragms, and precast connectors in topped/untopped diaphragms.

[2] Deformation demands occur at joints between precast units.

[3] BSSC proposal IT06-001for the ASCE7-14 Provisions.

The new diaphragm design forces, diaphragm design factors (R_s, Ω_v) and diaphragm reinforcement classifications (*LDE, MDE, HDE*) are used within a performance based design framework for precast diaphragms, developed jointly by researchers and industry, which allows the designer three options:

1. An *Elastic Design Option*, where the diaphragm is designed to the highest force levels, calibrated to keep the diaphragm elastic, not only for the design earthquake, but also in a rare maximum event, but, in exchange for the higher design force, permits the designer to detail the diaphragm with the ordinary (*LDE*) reinforcement that need not meet any deformation requirements.

    This option is limited in its use through the introduction of *Diaphragm Seismic Demand Levels*, which are based on building height, diaphragm geometry and seismic hazard level, and preclude the use of the Elastic Design Option for *High* Diaphragm Seismic Demand.

2. A *Basic Design Option*, in which the diaphragm is designed to a force level calibrated to keep the diaphragm elastic in the design earthquake, thus lower than the Elastic Design Option strength, but requires *MDE* diaphragm reinforcement, specified to provide an inelastic deformation capacity sufficient to survive the anticipated deformation demands in a rare maximum event.

    This option, and the next, requires the use of a diaphragm shear overstrength factor to assure that a non-ductile shear failure does not occur prior to the reinforcement reaching its intended inelastic target deformation. Note that *inelastic deformation* is associated with joint *opening* due to diaphragm flexure, not joint sliding deformation due to shear.

3. A *Reduced Design Option*, in which the diaphragm is designed for the lowest design force level. Because these levels are lower than in the Basic Design Option, some yielding in the diaphragm is anticipated in the design earthquake. The force levels have been calibrated to keep diaphragm inelastic deformation demands in a rare maximum event within the allowable deformation capacity for the highest classification of precast diaphragm reinforcement, termed *HDE* details.

The design methodology permits the designer to calculate the internal forces in the diaphragm using the simple horizontal beam methods commonly used today. Alternatively, the internal forces (in plane shear, moment, and in cases axial force) can be determined using free-body methods developed for common configurations, or using the semi-rigid diaphragm option available in most design office computer structural analysis packages. For the latter case, an estimate of diaphragm stiffness is required. The design methodology provides approximate values of effective elastic and shear moduli (E_{eff}, G_{eff}) for this purpose, as well as an alternative method to directly calculate these values. Guidance for these methods appears in PART 3 of the *Seismic Design Methodology Document*.

Diaphragm reinforcement must conform to the required classification of the selected design option. Existing diaphragm reinforcement is prequalified for different classifications (*LDE, MDE and HDE*) and tables of connector nominal strength and stiffness values are provided in an Appendix. A qualification protocol is provided for classifying and determining properties of new diaphragm reinforcement. The qualification protocol appears in PART 2 of the *Seismic Design Methodology Document*. Recommendations are also given for connections in the precast floor system that are not part of the primary diaphragm reinforcement, including connections between precast units and gravity beams.

Diaphragm reinforcement is to be provided in sufficient quantities to meet the required strength established by the calculated internal forces. The methodology promotes a strength design for the precast reinforcement at the joint level. In this approach, all the reinforcement across the joint is accounted together to carry the design forces. A general interaction equation is provided to design joints under combinations of shear, flexure, or collector actions. Many diaphragm joints are dominated by a single force component where the equation simplifies to a direct comparison to the capacity of the connections.

In rare cases, the precast diaphragm flexibility must be evaluated to ensure that gravity system columns remote to primary lateral force resisting elements (shear walls, moment frames) are not susceptible to excessive inter-story drifts due to the added deflection of the diaphragm.

Design Methodology Summary:

- Applicability
  - Seismic design of precast concrete diaphragms with and without topping slabs in general precast concrete building construction
- Objective
  - Provide adequate strength and deformability of connectors between precast floor units
- Method
  - Calculate diaphragm force F_{px} based on *proposal IT06-001* for the *2014 ASCE 7 provisions*, applying the appropriate diaphragm design force reduction factor R_s aligned to the desired performance targets
  - Amplify the diaphragm shear forces additionally by an overstrength factor Ω to avoid diaphragm nonductile failure modes
  - Select appropriate diaphragm reinforcing based on required deformation capacity
  - Check gravity system drifts as amplified by diaphragm flexibility if applicable.

Design Step Summary:

Step 1: Determine *diaphragm seismic demand level* (**Low, Moderate,** or **High**) based on seismic design category (SDC), number of stories and diaphragm span.

Step 2: Select *diaphragm design option* (**Elastic, Basic** or **Reduced**) based on diaphragm seismic demand level, in conjunction with a *diaphragm reinforcement classification* (Low, Moderate, or High deformability element - **LDE**, **MDE**, **HDE**).

Step 3: (a) Determine the *diaphragm design forces,* $\mathbf{F_{px}}$ *using ASCE 7 proposal IT06-001* with *diaphragm design force reduction factors* R_s based on the *diaphragm design option*;

   (b) Determine the corresponding *diaphragm required strength* ($\mathbf{V_u, M_u}$ and in cases $\mathbf{N_u}$) based on the internal design forces at the precast joints

Step 4: Design diaphragm connections for the required strength, including special provisions for shear reinforcement overstrength (Ω_v) and collectors, <u>using diaphragm reinforcement types meeting the required *diaphragm reinforcement classification (See Step B below)*</u> to provide adequate nominal strength ($\mathbf{\phi V_n,\ \phi M_n}$ and in cases $\mathbf{\phi N_n}$).

Step 5: Determine *diaphragm stiffness,* if needed, via an *effective elastic modulus* (E_{eff}) and *shear modulus* (G_{eff}), and check *diaphragm-amplified gravity column drift*, when applicable.

Design Step Summary – Preferred Connector Set for Diaphragm Reinforcement:

Step A: Select specific diaphragm reinforcement types based on a preferred connector set.

Step B: If connectors are prequalified, look up diaphragm reinforcement classification (LDE, MDE, HDE) and properties in PART 1: Appendix 1; If not prequalified connectors, perform qualification testing following protocols in PART 2.

Step C: Select diaphragm design option (*Elastic, Basic, or Reduced*) based on *diaphragm seismic demand level* and *diaphragm reinforcement classification* for the selected connectors.

Step D: Check applicability of selected diaphragm design option and diaphragm connector set with corresponding diaphragm seismic demand level (*Low, Moderate, or High*).

Steps 3-5: As above.

Seismic Design Procedure for Precast Concrete Diaphragms

Step 1: Determine diaphragm seismic demand level
   (1) Three diaphragm seismic demand levels are defined: **Low**, **Moderate**, and **High**
   (2) Diaphragm seismic demand level is based on seismic design category (*SDC*), number of stories *n*, diaphragm span *L* and aspect ratio *AR*:
   - Determine *SDC* from structure risk category and SDS, SD1 at the site per ASCE Section 11.6
       - Diaphragm seismic demand level is:
            For SDC B and C: **Low**
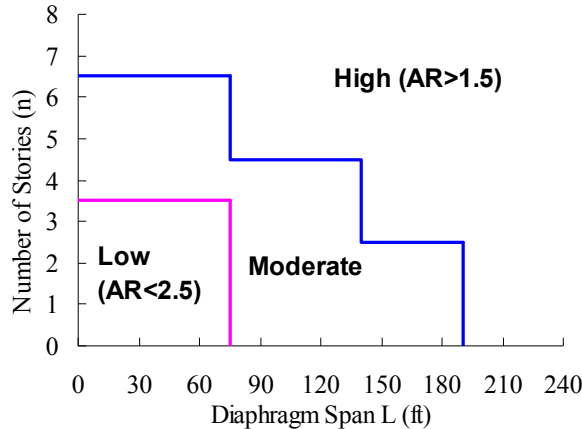   For SDC D and E: See Fig. 1

Fig. 1. Diaphragm seismic demand level.

   Notes on Figure 1:
            If AR>2.5 and the diaphragm seismic demand falls in *Low*,
                it shall be moved from *Low* to **Moderate**.

            If AR<1.5 and the diaphragm seismic demand falls in *High*,
                it can be moved from *High* to **Moderate**.

   (3) Diaphragm span on a floor level is defined as the larger value of:
   - maximum interior distance between two LFRS elements
   - twice the exterior distance between the outer LFRS element and the building free edge
   (4) Diaphragm span for the structure is selected as the maximum diaphragm span on any floor in the structure in any direction.
   (5) Diaphragm aspect ratio (AR) is defined as the diaphragm span-to-depth ratio, using the diaphragm span determined in steps (3), (4) above. Depth is defined as the floor diaphragm dimension perpendicular to diaphragm span associated with the pair of adjacent chord lines for the diaphragm or sub-diaphragm (See *Commentary* Fig. C-1).

Step 2: Select diaphragm design option and appropriate diaphragm reinforcement classification
  (1) Three diaphragm design options are defined: **Elastic**, **Basic** and **Reduced**
  (2) Diaphragm design option applicability is based on diaphragm seismic demand level, see Table 1
  (3) Three diaphragm reinforcement classifications are defined: **High, Moderate** and **Low deformability elements**
  (4) Diaphragm reinforcement applicability is based on diaphragm design option, see Table 2.
  (5) The applicable Diaphragm Reinforcement Classification is based on the lowest classified reinforcement used in the diaphragm.

Table 1. Diaphragm design option

Design Option	Diaphragm Seismic Demand level		
	Low	Moderate	High
Elastic	**Recommended**	With Penalty*	Not Allowed
Basic	Alternative	**Recommended**	With Penalty*
Reduced	Alternative	Alternative	**Recommended**

* Diaphragm design force shall be increased by 15%.

Table 2. Required diaphragm reinforcement classification

Design Option	Diaphragm Reinforcement Classification		
	Low	Moderate	High
Elastic	**Recommended**	Allowable	Allowable
Basic	Not allowed	**Recommended**	Allowable
Reduced	Not allowed	Not allowed	**Recommended**

Comments:
- An **Elastic Design Option (EDO):**
    - The EDO targets elastic diaphragm behavior in the maximum considered earthquake (MCE).
    - The diaphragm force reduction factor, R_s, is less than unity for the EDO, reflecting a greater strength than the BDO.
    - The EDO allows the use of low deformability connections or better.
- The **Basic Design Option (BDO):**
    - The BDO targets elastic diaphragm design in the design basis earthquake (DBE).
    - The diaphragm force reduction factor, R_s, for the BDO is unity, as its design intent aligns directly with the diaphragm design forces provided in *ASCE 7 proposal IT06-001*.
    - The BDO requires the use of moderate deformability connections or better.
- A **Reduced** (Force) **Design Option** (**RDO**)**:**
    - The RDO permits diaphragm yielding in the DBE
    - The diaphragm force reduction factor, R_s, is greater than unity for the RDO, reflecting a lower strength than the BDO..
    - The RDO requires the use of high deformability connections.

- **High deformability element** (**HDE**): An element that demonstrates a reliable and stable maximum joint opening deformation capacity of greater than 0.6"
- **Moderate deformability element** (**MDE**): An element that demonstrates a reliable and stable maximum joint opening capacity of between 0.3" and 0.6"
- **Low deformability element** (**LDE**): An element that does not meet moderate or high deformability element requirements

- Classification of a given diaphragm reinforcement element or connection is determined through testing of individual elements following the cyclic testing protocols of the *Precast Diaphragm Reinforcement Qualification Procedure* in PART 2 of the *Seismic Design Methodology Document.*

Step 3: Determine the diaphragm design forces and the corresponding diaphragm joint required strengths:

(3a) The diaphragm design forces are calculated according to the ASCE 7 using proposal IT06-001 for the 2014 provision, herein, termed as IT06-001:

(1) Determine the diaphragm design acceleration coefficient at level x (C_{px}) according to 12.11.2.1 and Figure 12.11.1 of IT06-001

(2) Determine the flexible diaphragm acceleration amplification factor at level x (α_{fx}) according to Eqn.12.11-12[4] of IT06-001

(3) Determine the diaphragm design force at each level according to Eqn. 12.11-1, Eqn. 12.11-2, 12.11.2.2 and Table 12.11.5-1 of IT06-001, and simplified as follow:

$$F_{px} = \alpha_{fx}\, C_{px}\, w_{px} / R_s \qquad\qquad \text{(Eqn. 1a)}$$

but not less than:

$$F_{px} = 0.2\, \alpha_{fx}\, S_{DS}\, I_e\, w_{px} \qquad\qquad \text{(Eqn.1b)}$$

where:

w_{px} is the tributary weight of floor at level x

F_{px} is the diaphragm design force at level x

R_s (Table 12.11.5-1 of IT06-001)   = 0.7 for EDO

        = 1.0 for BDO

        = 1.4 for RDO

For cast-in-place equivalent diaphragms (defined in Comments below), R_s is the same as for cast-in-place diaphragms (*See Table 12.11.5-1, IT06-001*).

(4) For design of collectors in SDC C through F, amplify the design force by 1.5 according to 12.11.4 of IT06-001.

(5) Determine diaphragm shear overstrength factor: $\Omega_V = 1.4\, R_s$

Comments:
- R_s is a lower bound (conservative) diaphragm design force reduction factor based on analytical research whose values are:
    - Calibrated to produce elastic diaphragm response in the MCE for the **EDO**.
    - Calibrated to produce elastic diaphragm response in the DBE for the **BDO**, and
        - το produce maximum inelastic opening deformation demand in the MCE not exceeding the allowable value for a Moderate Deformability Element, 0.2″
    - Calibrated to produce the maximum inelastic opening deformation demand in MCE not exceeding the allowable value for a High Deformability Element, 0.4″ for the **RDO**.
- A cast-in-place equivalent diaphragm is a topped precast diaphragm with the topping designed to act as the diaphragm according to ACI 318-11 section 21.11.5 or a pretopped precast diaphragm where all chords, collectors, and joints between precast elements are constructed of field-cast reinforced concrete with details consistent with the requirements of ACI 318.
- Ω_v is applied to the *required* shear force in Step 4
- For the purposes of determining C_{px}, a ramp element will be associated with the top-most level to which it is attached.
- See *Appendix 4* for alternate design force procedure based on ASCE 7-10 diaphragm forces.

---

[4] Eliminated (i.e. set to unity) in a subsequent version of IT06-001, See Commentary for α_{fx} expression.

(3b) Determine diaphragm internal forces

Determine the diaphragm required strength (V_u, M_u and/or N_u,) for all potential critical diaphragm joints by applying the diaphragm design force F_{px} from Eqn. 1 to each floor/roof diaphragm. The diaphragm is to be evaluated for the effects of seismic loading in each orthogonal direction individually, with the critical set of diaphragm internal forces at a joint used to design the diaphragm reinforcement in Step 4.

Determination of diaphragm in-plane design moments, shears, and axial forces shall be consistent with requirements of equilibrium and design boundary conditions. It shall be permitted to determine design moments, shears, and axial forces in accordance with one of (1) through (4), as appropriate:

(1) <u>Analysis using free-body diagrams</u>: Internal forces at all potential critical sections in the diaphragm can be determined by taking the applied diaphragm forces (F_{px}) and reactions on the diaphragm and evaluating appropriate free-bodies around each critical section using the principles of statics. Among these methods is the commonly-used horizontal beam analogy (*See Comments below*). Diaphragm reactions can be determined based on a rigid diaphragm assumption, flexible diaphragm assumption or bounding analyses as applicable.

(2) <u>Semi-rigid diaphragm model</u>: If the structural analysis model for the building includes semi-rigid modeling of the floor and roof diaphragms, the internal forces at critical sections can be extracted directly from the analysis model subjected to the diaphragm forces (F_{px}).

(3) <u>Design aids</u>: Diaphragm free-body diagrams and internal force expressions developed for common precast structure floor configurations are provided in PART 3 of the *Seismic Design Methodology Document*.

(4) <u>Strut-and-Tie models</u>: A strut-and-tie approach can be used to determine diaphragm internal actions in accordance with the provisions of ACI 318 Section 18.5.

Comments:
- The horizontal beam analogy is an equilibrium-based simplified analysis method. This method permits a simple calculation of moments and shears by idealizing the diaphragm or segments of the diaphragm as a beam with spans between the vertical elements of the lateral force-resisting system (LFRS).
  - The beam analogy does not include the development of diaphragm tension forces that may occur in semi-rigid models. (i.e. $N_u = 0$ for joints not associated with collector action)
  - The beam analogy does not consider deep beam effects, and will produce conservative estimates of the lateral force actions on the diaphragm.
- The diaphragm reactions at the LFRS vertical elements for free-body analysis methods are typically determined by considering the diaphragm rigid or flexible:
  - The rigid diaphragm assumption distributes diaphragm reactions in proportion to the relative stiffness of each LFRS vertical element. This assumption has historically been applied to precast concrete diaphragms with aspect ratios less than 3.
  - The flexible diaphragm assumption distributes diaphragm reactions in proportion to the tributary mass of each LFRS vertical element. This assumption has historically been applied to precast concrete diaphragms with aspect ratios greater than 3.
  - A bounding analyses can be performed in which the design values are the envelope of values obtained by assuming upper and lower bound in-plane stiffness for the diaphragm in two, or more, separate analyses. (See *PCI Seismic Design Manual*)
- For semi-rigid diaphragms, the diaphragm effective elastic moduli, E_{eff} and G_{eff}, can be estimated as 25%~35% of the uncracked concrete E and G for the structural analysis model. These estimated values should be verified in Step 5 after sizing the diaphragm reinforcement.
- Further guidance on modeling the diaphragm appears in PART 3 of the *Seismic Design Methodology Document*. The designer is also directed to the new ACI 318-14 diaphragm chapter.

Step 4: Design diaphragm connections for required strength.
(1) Select diaphragm connections based on required Diaphragm Reinforcement Classification.
   – Diaphragm connections shall be classified using the cyclic testing protocols in the *Precast Diaphragm Reinforcement Qualification Procedure*.
   – See *Appendix 1*: *Prequalified Precast Diaphragm Reinforcement* to determine the classification of <u>commonly-used existing diaphragm reinforcement</u>.

(2) Establish diaphragm reinforcement properties required for design including:
   (a) Elastic stiffness in tension and shear: k_t, k_v
   (b) Yield strength in tension and shear: t_n , v_n
   – Diaphragm connection properties shall be determined using the qualification backbones in the *Precast Diaphragm Reinforcement Qualification Procedure*.
   – See *Appendix 1*: *Prequalified Precast Diaphragm Reinforcement* to look up the properties of <u>commonly-used existing diaphragm reinforcement</u>.

(3) Diaphragm connections at each joint between precast elements must possess sufficient total strength (N_n, V_n, M_n) to resist the diaphragm internal forces. The following general interaction formula is permitted to be used for diaphragm joint design:

$$\sqrt{\left(\frac{|M_u|}{\phi_f M_n} + \frac{N_u}{\phi_f N_n}\right)^2 + \left(\frac{\Omega_v V_u}{\phi_v V_n}\right)^2} \leq 1.0 \qquad \text{(Eqn. 2)}$$

where the strength reduction factors ϕ_f and ϕ_v are given in the relative material standard.

   • **Note**: For the design of collectors and connections to the LFRS, use Eqn. 2 calculating the required strength (V_u, M_u , *and* N_u) based on note (4) of Step 3a, and use Ω_v =1.0.

(4) The nominal strength of the joint for Eqn. 2 can be calculated as follows:

$$N_n = \sum t_n \qquad \text{(Eqn. 3a)}$$

$$V_n = \sum v_n \qquad \text{(Eqn. 3b)}$$

where t_n and v_n are the nominal tension and shear strengths of individual reinforcement elements crossing the joint. The appropriate nominal *flexural* strength M_n of the joint depends on the diaphragm design option:

   • For **elastic design option**: $\qquad\qquad M_n = M_y \qquad$ (Eqn. 4a)

   • For **basic design option**: $\qquad\qquad M_n = \dfrac{1+\Omega_d}{2} M_y \qquad$ (Eqn. 4b)

   – For **reduced design option**: $\qquad\qquad M_n = \Omega_d M_y \qquad$ (Eqn. 4c)

where:
   M_y is the yield moment of the precast diaphragm joint, and
   Ω_d is the diaphragm flexural overstrength factor

   – M_y can be taken conservatively as $t_n^{chrd} d'$ where t_n^{chrd} is the chord yield force ($A_s f_y$ for typical chord reinforcement and connectors) and d' is the depth between chords (See *Commentary* Fig. C-1).
   – Ω_d is defined as the ratio of the diaphragm plastic moment to the diaphragm yield moment, M_p/M_y, conservatively taken as *1.0* for a *pretopped* diaphragm, and *1.25* for a *topped* diaphragm.
   – Alternately, M_y and Ω_d can be determined from a strain curvature or pushover analysis.

Comments:

- The *Precast Diaphragm Reinforcement Qualification Procedure* appears in **PART 2** of the *Seismic Design Methodology Document.*
- Equation 2 pertains to the primary joints in the diaphragm, including those between precast floor units, diaphragm-to-LFRS joints in both orthogonal direction, and internal beam joints residing between chord lines. So-called "*secondary*" connections in the floor system, including diaphragm-to-spandrel connections, spandrel-to-column connections, internal beams outside the chord lines and ramp-to-lite wall non-diaphragm connections, DO NOT require a seismic strength design.
- Note that for diaphragm joints without significant combined forces, Eqn. 2 simplifies considerably:
  - In most diaphragms, there are areas strongly dominated by either shear or bending where the interaction of the structural effects is not significant and the dominant action can be compared directly to the capacity of the connections in the joints ($\phi_f M_n > M_u$ or $\phi_v V_n > \Omega_v V_u$).
  - When the rigid diaphragm assumption is used, the application of the connection interaction Eqn. 2 can be simplified by removing the axial force term as the beam analogy does not produce separate tension in the diaphragm:

$$\sqrt{\left(\frac{|M_u|}{\phi_f M_n}\right)^2 + \left(\frac{\Omega_v V_u}{\phi_v V_n}\right)^2} \leq 1.0 \qquad \text{Eqn. 2 - alt}$$

  - Collectors and diaphragm-to-LFRS connection can be designed directly for the diaphragm reaction based on note (4), Step 3a and $\Omega_v=1.0$, unless a rational load path method is used.
- A rational method is provided for calculating the diaphragm flexural strengths M_y and M_p and been embedded in a design aid program. See "Diaphragm Joint Strength Calculation" and "Design Aids for Diaphragm Design: Spreadsheet Program" in **PART 3** of the *Seismic Design Methodology Document.*
- Deformation capacity of primary reinforcement is directly accounted in the design through the diaphragm classification. However, deformation capacity should be considered for other connections and reinforcement in the floor system including:
  - diaphragm-to-LFRS connections, which require a different set of required deformation characteristics than those defined by the diaphragm reinforcement classification
  - diaphragm-to-spandrel connections, spandrel-to-column connections, and internal beam connections not included in the strength design.
  - Recommendations for the deformation capacity of these connections appear in *Appendix 1*.
- The determination of diaphragm nominal strength and the use of Equation 2 are further discussed in the Step 4 *Commentary.*

Step 5: Determine diaphragm stiffness and check gravity system drifts if applicable.
1. A diaphragm stiffness calculation is required if:
   - a semi-rigid diaphragm computer structural analysis model is used, or
   - a gravity system drift check is required.
2. For a semi-rigid diaphragm model, determine a diaphragm effective elastic modulus (E_{eff}) and shear modulus (G_{eff}). The calculated E_{eff} and G_{eff} shall be checked with respect to the estimated values in Step 3, and the analysis repeated if necessary.
3. A check for the gravity system drift is required for certain design cases as specified in Table 3. If required, the procedure for the gravity system drift check is provided in Appendix 3.

Table 3. Design cases requiring drift check.

Design Option	Cases Requiring Drift Check		
	n ≤ 3	3 < n ≤ 5	n>5
EDO	-	-	AR>3.5
BDO	AR>3.8	AR>3.5	AR>3.2
RDO	AR>3.6	AR>3.4	AR>3.1

Comment: A rational method has been developed for the diaphragm E_{eff} and G_{eff} calculations. This method is embedded in a design aid program. See "Diaphragm Joint Stiffness Calculation" and "Design Aids for Diaphragm Design: Spreadsheet Program" in PART 3 of the *Seismic Design Methodology Document for Precast Concrete Diaphragms.*

Appendix to Precast Concrete Diaphragm Design Procedure

APPENDICES:

APPENDIX 1: **Prequalified Diaphragm Connections**

Table A-1 provides the prequalified diaphragm reinforcement including:
  (1) Diaphragm Reinforcement Classification: Low Deformability Element (LDE); Moderate Deformability Element (MDE), High Deformability Element (HDE).
  (2) Pertinent reinforcement properties for use in the design procedure: elastic tension stiffness k_t , nominal tension strength t_n, elastic shear stiffness k_v and nominal shear strength v_n

The connector identification (ID) in the first column refers to the connector labels shown in Table 2A-3 (PART 2 of the *Diaphragm Seismic Design Methodology Document*). Table 2A-3 in PART 2 provides a photo and schematic of each tested connector, including the prequalified connectors. The schematic provides the major details of the connectors; however, the designer must refer to the Lehigh testing reports (Naito et al. 2006) (Naito et al. 2007) for the full description of the connector detailing.

Table A-1. Prequalified Diaphragm Reinforcement Table

ID	2A-1a. Reinforcing bars	Classification	Tension				Shear		
			k_t/A	t_n/A	δ_{ty}	δ_{tu}	k_v/A	v_n/A	δ_{vy}
			[k/in/in^2]	[ksi]	[in]	[in]	[k/in/in^2]	[ksi]	[in]
B-1, B-2, B-3	Dry chord Gr.60	LDE	1018	60	0.071	0.1	382	24.2	0.090
D	Dry chord w/ flat plate Gr. 60	MDE	1018	60	0.071	0.3	382	24.2	0.090
E	Pour strip chord Gr.60	HDE	1234	60	0.057	0.7	382	24.2	0.090
G	Ductile ladder Gr.1018	HDE	1260	54	0.043	0.6	217	21.7	0.100
F	Standard ASTM A185 wwr	LDE	1414*	65*	0.035*	0.1*	709	39.7	0.056

* based on testing of wwr with 10″ gage spacing perpendicular to joint

ID	2A-1b. Connectors	Classification	Tension				Shear		
			k_t	t_n	δ_{ty}	δ_{tu}	k_v	v_n	δ_{vy}
			[k/in]	[kips]	[in]	[in]	[k/in]	[kips]	[in]
A-1, A-2	JVI	HDE	55	3.1	0.066	0.6	226	18.1	0.082
C-2	Hairpin (#4)	HDE	209	9.0	0.043	0.6	181	18.1	0.100
-	Angled bar (#3)	MDE	300	10.2	0.059	0.3	372	17.1	0.045

k_t	= Elastic tension stiffness	k_v	= Elastic shear stiffness
t_n	= Nominal Tension strength	v_n	= Nominal Shear strength
δ_{ty}	= Yield tension deformation	δ_{vy}	= Yield shear deformation
δ_{tu}	= Tension deformation capacity	A	= Bar cross-sectional area

APPENDIX 2: Connector Deformation Capacity

Primary Diaphragm Reinforcement: Shear and Flexural Reinforcement

Table A-2.1 lists the tension (joint opening) capacity associated with each of the Connector Deformability Classifications used in the design methodology.

Table A-2.1 Diaphragm Reinforcement Classification

Deformability Category	Tension deformation capacity
LDE	$\delta_t < 0.3"$
MDE	$0.3 \leq \delta_t < 0.6"$
HDE	$0.6" \leq \delta_t$

Primary Diaphragm Reinforcement: Diaphragm –to-LFRS Connections

The deformation capacity (δ_c) for reinforcement or connectors comprising the diaphragm-to-LFRS connection shall satisfy the following condition:

$$\delta_c \geq C_2 \delta_{cb}$$

where C_2 is a coefficient multiplier for diaphragm seismic demand level (See Table A-2.2), and δ_{cb} is a reference deformation capacity for diaphragm-to-LFRS connection (See Table A-2.3). Deformation capacity is to be reliable and stable at the deformation capacity under cyclic loading.

Table A-2.2 Diaphragm-to-LFRS connection Coefficient multiplier C_2.

Seismic Demand Level	C_2
Low	1.0
Moderate	1.5
High	2.0

Table A-2.3 Diaphragm-to-LFRS connections reference deformation capacity δ_{cb}.

δ_{cb}	Exterior wall	Interior wall	Lite wall	Moment frame
Opening	0.05"	0.15"	0.05"	0.1"
Sliding	0.1"	0.05"	0.15"	0.1"

Diaphragm Secondary Connections Deformation Recommendations

Recommended deformation capacity for diaphragm secondary connections are the product of the reference deformation capacities listed in Table A-2.4 multiplied by the appropriate C_2 factor.

Table A-2.4 Deformation capacity recommendations for diaphragm secondary connections .

Deformation	Parking Structure		Regular building	
	Internal beam	Spandrel	Internal beam	Spandrel
Opening	0.125"	0.05"	0.125"	0.075"
Sliding	0.075"	0.075"	0.05"	0.05"

APPENDIX 3: Diaphragm Contribution to Drift

Procedure to calculate the diaphragm contribution to gravity column interstory drift:

(1) Determine the diaphragm elastic deformation ($\delta_{dia,\,el}$) under design force (F_{Dia}):
  - If using a free-body diagram method, obtain the maximum diaphragm deformation based on the moment and shear diagrams obtained in Step 3b, and using the calculated E_{eff} and G_{eff}.
  - If using a semi-rigid diaphragm model, extract the maximum diaphragm deformation from the static analysis performed in Step 3b using the calculated E_{eff} and G_{eff}

(2) Determine the diaphragm inelastic deformation by applying the deformation amplifier ($C_{d,dia}$) to elastic diaphragm deformation ($\delta_{dia,\,el}$):

$$\delta_{dia} = C_{d,dia}\, \delta_{dia,\,el} \qquad \text{(Eqn. A3-1)}$$

  where for EDO: $C_{d,dia} = 1.0\ C_\Delta$
  for BDO: $C_{d,dia} = 1.5\ C_\Delta$
  for RDO: $C_{d,dia} = 2.9\ C_\Delta$

  and C_Δ is the diaphragm drift P-Δ multiplier, $C_\Delta = 1 + C_1 (L/240)(AR/4)$ where C_1 is a the design option factor equal to 0.06 for EDO, 0.08 for BDO and 0.10 for RDO.

(3) Determine the diaphragm induced gravity column drift by introducing a diaphragm drift reduction factor ($C_{r,dia}$) to the diaphragm inelastic deformation (δ_{dia})

$$\theta_{dia} = \delta_{dia} C_{r,dia}\, /h \qquad \text{(Eqn. A3-2)}$$

  where h is the floor-to-floor height and $C_{r,dia}$ is calculated from:

  For EDO: $0.4 \leq C_{r,dia} = 1.11 - 0.13 AR \leq 1.0$ (Eqn. A3-3)

  For BDO: $0.4 \leq C_{r,dia} = 1.08 - 0.11 AR \leq 1.0$ (Eqn. A3-4)

  For RDO: $0.4 \leq C_{r,dia} = 1.00 - 0.11 AR \leq 1.0$ (Eqn. A3-5)

  and AR is diaphragm aspect ratio as limited in Appendix 4.

(4) Check the diaphragm induced gravity column drift with design limit:

  - If $\theta_{dia} \leq 0.01$ OK

  - If $\theta_{dia} > 0.01$ then check $\theta_{dia} + \theta_{LFRS}$
    where θ_{LFRS} is 1.5 times the LFRS story drift determined per ASCE 7, 12.8.6:

    If $\theta_{dia} + \theta_{LFRS} \leq 0.04$ OK

    If $\theta_{dia} + \theta_{LFRS} > 0.04$, then redesign the diaphragm to increase diaphragm stiffness (via diaphragm reinforcement or span)

Comments:
  - The C_r factor is intended to account for the fact that diaphragm deformation is not directly related to the column inter-story drift due to higher mode effects & deformation of adjacent floor diaphragms (except for the lowest diaphragm which typically has low deformation demand compared to upper floors).
  - The C_Δ factor is intended to account for added gravity system drift due to P-Δ effects.
  - The diaphragm induced drift limit 0.01 is set as the difference of the estimated allowable gravity column drift ($\theta_{col} = 0.04$) and the expected LFRS drift ($\theta_{LFRS} = 0.03$) in the MCE.
  - The 1.5 factor for θ_{LFRS} is to scale the code (DBE) drift to the MCE level.
  - Further guidance on performing the diaphragm deformation calculation for substep 1 above appears in PART 3 of the *Seismic Design Methodology Document.*

APPENDIX 4: **Alternate Diaphragm Design Force Procedure Based on ASCE 7-10**

To use the diaphragm design methodology with current ASCE7-10 diaphragm procedures, use alternate Step 3a below in lieu of current PART 1: Step 3a, using the $F_{dia,x}$ calculated in Eqn. A4-5 for F_{px}.

Step 3a - Alternate:

(1) Determine diaphragm force amplification factor (Ψ)
- For **elastic design option, $\Psi = \Psi_E$**:
$$\Psi_E = 1.75\Omega n^{0.35}[1 - 0.04(3.0 - AR)^2], \ 1.0 \leq \Psi_E \qquad \text{(Eqn. A4-1a)}$$
- For **basic design option, $\Psi = \Psi_D$**:
$$\Psi_D = 1.75\Omega n^{0.2}[1 - 0.03(3.0 - AR)^2], \ 1.0 \leq \Psi_D \qquad \text{(Eqn. A4-1b)}$$
- For **reduced design option, $\Psi = \Psi_R$**:
$$\Psi_R = 1.10\Omega n^{0.3}[1 - 0.03(2.5 - AR)^2], \ 1.0 \leq \Psi_R \qquad \text{(Eqn. A4-1c)}$$

where:

n is building total number of stories

AR is diaphragm aspect ratio ($0.25 \leq AR \leq 4.0$)

Ω is a multiplier to consider the effect of LFRS overstrength: $\Omega = 1 + 2.5 \log \Omega_0 / n^{0.4}$

based on the structure system overstrength factor (Ω_0) defined in ASCE7-10.

(2) Determine diaphragm shear overstrength factor (Ω_v)
- For **elastic design option, $\Omega_v = \Omega_{vE}$**:
$$\Omega_{vE} = 1.0 \qquad \text{(Eqn. A4-2a)}$$
- For **basic design option, $\Omega_v = \Omega_{vD}$**:
$$\Omega_{vD} = 1.42 / AR^{0.13} \leq 1.70 \qquad \text{(Eqn. A4-2b)}$$
- For **reduced design option, $\Omega_v = \Omega_{vR}$**:
$$\Omega_{vR} = 1.92 / AR^{0.18} \leq 2.46 \qquad \text{(Eqn. A4-2c)}$$

where AR is diaphragm aspect ratio:
$0.25 \leq AR \leq 4.0$, use 4.0 if AR >4.0 and use 0.25 if AR < 0.25

(3) Determine Diaphragm Force Vertical Distribution (α_x) Factor

The diaphragm force vertical distribution factor α_x, for use in Eqn. A4-4 is calculated as follows:

Parking garage with ramp: $\alpha_x = 1.0$ for top floor , $\alpha_x = 0.68$ for other floors
Other types of buildings: α_x as determined in Table A4-1.

(4) Calculate the lateral seismic design force F_x at each floor level as per ASCE 7-10 using equation Eqn. 12.8-11 as per ASCE 7 Sections 12.8.1-12.8.3.
- **Note**: *The approximate structure fundamental period T_a in ASCE 7 Section 12.8.2 shall be used to calculate the controlling seismic response coefficient C_s.*

(5) Calculate the top level diaphragm force F_{pn} using Eqn. 12.10-1 as per ASCE 7 Section 12.10.1.1.
- **Note**: *The lower bound diaphragm design force $0.2S_{DS}Iw_{px}$ shall apply in the calculation of F_{pn} (ASCE 7 Section 12.10.1.1), where terms S_{DS}, I, w_{px} are defined in ASCE7-05.*

(6) Calculate diaphragm design acceleration at the uppermost level n, $C_{dia,n}$

$$C_{dia,n} = F_{pn} / w_{pn}$$ (Eqn. A4-3)

(7) Calculate baseline diaphragm force at each level x, F_{Dx}

$$F_{Dx} = \alpha_x \ C_{dia,n} \ w_{px}$$ (Eqn. A4-4)

where α_x is a *diaphragm force vertical distribution factor,* which can be taken as 1.0, or alternatively calculated using Appendix 4 of PART 1.

(8) Amplify the baseline diaphragm force obtained from Eqn. A4-4 by the diaphragm force amplification factor obtained from Eqns. A4-1a-c:

$$F_{Dia,x} = \Psi F_{Dx}$$ (Eqn. 43-5)

Comments:
- Design equations are greater than or equal to 90% of mean data of the maximum response from 5 ground motions.
- Ψ_E – Diaphragm force amplification factor used in the **EDO**.
  - Calibrated to produce elastic diaphragm response in the MCE.
- Ψ_D – Diaphragm force amplification factor used in the **BDO**.
  - Calibrated to produce elastic diaphragm response in the DBE.
  - Ψ_D produces maximum inelastic opening deformation demand in MCE not exceeding the allowable value for a Moderate Deformability Element, $0.2''$
- Ψ_R – Diaphragm force amplification factor used in the **RDO**.
  - Calibrated to produce the maximum inelastic opening deformation demand in MCE not exceeding the allowable value for a High Deformability Element, $0.4''$
- An estimate of actual LFRS overstrength can be substituted for Ω_0 in determining Ω (See *Commentary Appendix 4*).
- Ω_v is applied to the *required* shear force in Step 4
- For this method, collectors should be designed for axial force equivalent to the diaphragm-to-LFRS connection design shear, given by the maximum of ($\Omega_v V_u$, $\Omega_o V_u/\Psi$), unless a rational load path method (*Step 5 Comm*entary) is used.
- Uppermost floor level for buildings with vertical appendages (e.g. penthouses) is level containing 95% of total building weight as measured from ground. Design appendage for C_{dia} at its level.
- The upper bound diaphragm design force in ASCE 7 does not apply.
- A ramp element will be associated with the top-most level to which it is attached.

Table A4-1. Diaphragm design force distribution factor (α_x)

Story Number	Total Number of Story									
	1	2	3	4	5	6	7	8	9	10
1	1.00	1.00	1.00	0.90	0.90	0.90	0.90	0.90	0.90	0.90
2		1.00	1.00	0.90	0.90	0.90	0.90	0.90	0.90	0.90
3			1.00	0.70	0.80	0.83	0.80	0.83	0.84	0.85
4				1.00	0.70	0.77	0.70	0.75	0.78	0.80
5					1.00	0.70	0.60	0.68	0.72	0.75
6						1.00	0.80	0.60	0.66	0.70
7							1.00	0.80	0.60	0.65
8								1.00	0.80	0.60
9									1.00	0.80
10										1.00

Table A4.1 provides the α_x values calculated for 1 to 10 story structures (See *Appendix 4 Commentary* for general equation).

APPENDIX 5: Capacity Design Considerations for Precast Diaphragms

A capacity design check should be performed in an effort to achieve the desired diaphragm ultimate mechanism, i.e., an inelastic flexural mechanism with elastic shear response. This check enforces that the diaphragm joint nominal shear capacity is not less than the expected shear demand based on the maximum diaphragm flexural strength:

$$V_n \geq 4\beta(M_n^- + M_n^+)/L' \qquad \text{(Eqn. A5-1)}$$

where M_n^+ and M_n^- are the diaphragm joint nominal flexural strength at the support and midspan respectively, and L' is the diaphragm span between the LFRS inelastic flexure (See Commentary Appendix 5). β is a factor to account for possible strain hardening in diaphragm reinforcement, recommended as 1.2.

Commentary to Precast Concrete Diaphragm Design Procedure

Terminology and Notation

Note: Terms in **bold** represent new terminology and notation developed for the procedure. Normal font is used for accepted or code terminology.

Terminology:

AR:	Aspect Ratio
BDO:	Basic Design Option
DBE:	Design Basis Earthquake
DSDM:	Diaphragm Seismic Design Methodology
EDO:	Elastic Design Option
ELF:	Equivalent Lateral Force
HDE:	High Deformability Element
LDE:	Low Deformability Element
LFRS:	Lateral Force Resisting System
MCE:	Maximum Considered Earthquake
MDE:	Moderate Deformability Element
RDO:	Reduced Design Option
SDC:	Seismic Design Category

Notation:

$C_{d,dia}$	Diaphragm Drift Reduction Factor
$C_{r,dia}$	Diaphragm Inelastic Deformation Amplifier
E_{eff}	Diaphragm Effective Young's Modulus
F_x	Seismic Design Force
G_{eff}	Diaphragm Effective Shear Modulus
h	Floor to Floor Height
k_t, k_v	Connector Tension, Shear Stiffness
L	Diaphragm Span
N_u, V_u, M_u	Diaphragm Design Internal Forces: Axial, Shear and Moment
n	Number of Stories
t_n, v_n	Connector Tension, Shear Strength
w_{px}	Tributary Floor Mass
δ_{dia}	Diaphragm Inelastic Deformation
$\delta_{dia, el}$	Diaphragm Elastic Deformation
ϕ_f	Flexural Strength Reduction Factor
ϕ_v	Shear Strength Reduction Factor
θ_{col}	Allowable Gravity Column Drift
θ_{dia}	Diaphragm Induced Gravity Column Drift
θ_{LFRS}	Allowable LFRS Drift
Ω_V	Diaphragm Shear Overstrength Factor

Notation for Alternate (ASCE7 10) Diaphragm Design Force Procedure:

$C_{dia,max}$	Maximum Diaphragm Design Acceleration
C_{vc}	Vertical Distribution Factor
$F_{Dia,x}$	Amplified Diaphragm Design Force
F_{Dx}	Diaphragm Baseline Design Force
α_x	Diaphragm Force Vertical Distribution Factor
Ω_0	System Overstrength Factor
Ω	Diaphragm Force LFRS Overstrength Factor
Ψ	Diaphragm Force Amplification Factor

Preface to Commentary on the Seismic Design Procedure for Precast Concrete Diaphragms

This preface to the Commentary summarizes the main points of the design methodology and design factor calibration. A reader unfamiliar with the design approach adopted for the design methodology is encouraged to first read PART 5 Section 5.2: *Background on the Seismic Design Methodology*. The design factor calibration involved analytical research using models developed and calibrated on the basis of extensive large scale physical testing, as described in PART 5: *Appendix C*.

Design Methodology Summary

The design methodology allows the designer three options (See Figure C-I):

1. An *Elastic Design Option* (EDO) in which the diaphragm is designed to remain elastic up to the *Maximum Considered Earthquake* (MCE). This objective is realized through the use of a Diaphragm Design Force Reduction Factor R_s less than unity, in conjunction with newly proposed diaphragm forces aligned to elastic response in the DBE. In exchange for a higher diaphragm design force, the designer can detail the diaphragm with reinforcement classified as *Low Deformability Elements* (LDE), i.e. reinforcement without any deformation requirements.

2. A *Basic Design Option* (BDO) in which the diaphragm is designed to remain elastic up to the *Design Basis Earthquake* (DBE). This objective is realized through the use of R_s equal to unity, in conjunction with the newly proposed diaphragm forces aligned to elastic response in the DBE. The design requires reinforcement classified as *Moderate Deformability Elements* (MDE), whose classification provide an inelastic deformation capacity sufficient to survive the anticipated deformation demands for a BDO design in the MCE.

3. A *Reduced Design Option* (RDO) in which the diaphragm is designed with R_s greater than unity, in conjunction with the newly proposed diaphragm forces. At these design force levels, some yielding in the diaphragm is anticipated in the DBE. In exchange for the lowest diaphragm design force, the designer must use the highest classification of precast diaphragm reinforcement, termed *High Deformability Elements* (HDE). The R_s value is calibrated such that the diaphragm inelastic deformation demands in the MCE are targeted within the HDE allowable deformation capacity.

A diaphragm shear overstrength factor (Ω_V) is used to assure that non-ductile shear failure does not occur prior to the diaphragm reaching its intended inelastic target deformation. Note that *inelastic deformation* is associated with joint *opening* due to diaphragm flexure, not joint sliding deformation due to shear.
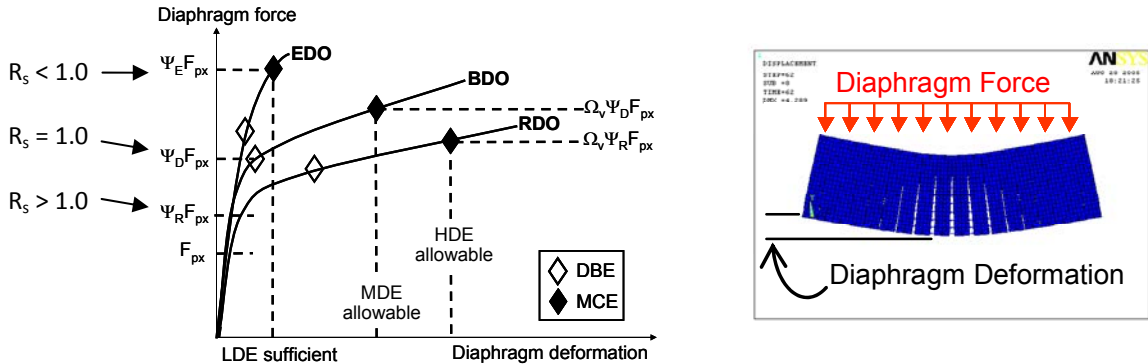

Figure C-I. Schematic of Diaphragm Response indicating Diaphragm Design Options.

It is noted that prior to the introduction of the new diaphragm force proposal, these same design intents were realized through the application of diaphragm design force amplification factors (Ψ_E ,

Ψ_D , Ψ_R) to the current (ASCE 7-10) diaphragm forces. The original notation is also indicated in Fig. C-I, and is maintained as an alternate design approach in Appendix 3 of the design procedure. Table C-1 below summarizes the design options available and how ASCE7-10 maps to (the proposed) ASCE7-14.

Table C-I. Diaphragm Design Options

Diaphragm Design Option	Design Factors		Diaphragm Strength Performance Target			
	ASCE7-10 (Appendix 3)	ASCE7-14* (PART 1)	Flexure		Shear	
			DBE	MCE	DBE	MCE
EDO	Ψ_E	$R_s = 0.7$	Elastic	Elastic	Elastic	Elastic
BDO	Ψ_D	$R_s = 1.0$	Elastic	Inelastic	Elastic	Elastic
RDO	Ψ_R	$R_s = 1.4$	Inelastic	Inelastic	Elastic	Elastic

* Proposed through IT06-001

Calibration of Design Factors

The design factors were calibrated through analytical parameter studies. These studies involved earthquake simulations of a precast evaluation structure to determine diaphragm seismic demands, as described in PART 5: *Appendix A1*. Where these analytical results support a step in the design procedure, they will be presented in the corresponding commentary section. Unless otherwise indicated, analytical results shown are the mean of maximum from a suite of 5 spectrum compatible ground motions. It is noted that the analytical research was limited to SDC C to E; no analyses were performed for SDC B.

In general, two performance targets are used to determine the factors for the design methodology (See Table C-II): (1) elastic diaphragm response, measured in terms of the maximum diaphragm inertial forces anticipated for a given seismic hazard; and, (b) inelastic diaphragm deformation demands, measured in terms of the maximum expected opening of joints between precast units at the chord lines.

The performance targets are illustrated schematically using the monotonic backbones in Figure C-II: (a) a global pushover curve of diaphragm force (F_{dia}) vs. deformation (Δ_{dia}); and, (b) a plot of local demand on the critical flexure (midspan) joint, in terms of chord connector tension force (T) vs. joint opening (δ). These actions are graphically displayed in the Fig. C-IIa inset.

The force-based diaphragm performance targets pertain to elastic diaphragm response, and are indicated in Fig. C-II as grey solid circles. The deformation-based diaphragm performance targets pertain to aligning the chord reinforcement joint opening demands to the allowable connector deformations δ_a^{MDE} or δ_a^{HDE} , as indicated by vertical trend lines in Fig. C-IIb. These allowable deformations are defined in the Commentary for Step 2. Note that the design force amplification factors (Ψ_E , Ψ_D , Ψ_R) are replaced by diaphragm design force reduction factors R_s in the current version of the design methodology.
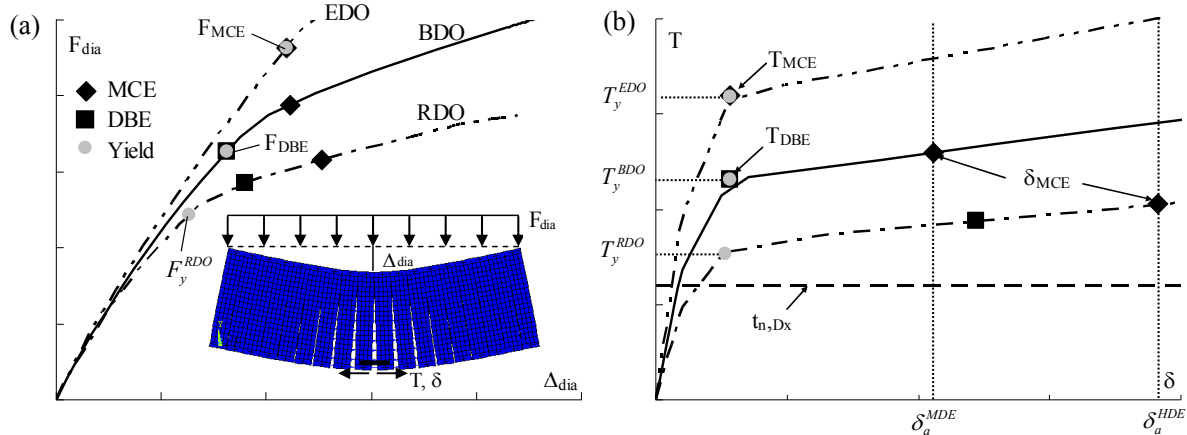

Figure C-II. Performance targets on: (a) Pushover curves; (b) Chord tension vs. opening..

Table C-II. Performance Targets and Metrics in Analytical Study

Design Option	Diaphragm Performance Target		Target Metric in Analysis		Force Amplification Factor
	Force	Deformation	Force	Deformation	
EDO	Elastic in MCE	-	$T_{MCE} = T_y^{EDO}$		$\Psi_E = T_{MCE}/t_{n,Dx}$
BDO	Elastic in DBE	MDE allowable in MCE	$T_{DBE} = T_y^{BDO}$	$\delta_{MCE} = \delta_a^{MDE}$	$\Psi_D = T_{DBE}/t_{n,Dx}$
RDO	-	HDE allowable in MCE		$\delta_{MCE} = \delta_a^{HDE}$	$\Psi_R = T_y^{RDO}/t_{n,Dx}$

Gray text boxes are used throughout the Commentary to provide background information in the form of analytical results that support the design methodology. It should be recognized that the analytical research was performed using analytical models built, calibrated and verified through an extensive experimental research program including isolated tests of diaphragm connectors, hybrid testing of critical precast diaphragm joints, and a shake table test of a half-scale diaphragm sensitive precast structure. The figures in the text box are labeled with a small "*c*".

Figure c-i shows analytical results from three selected earthquake simulations from the extensive analytical parameter study. These results are shown for the same 4-story structure with a 3.0 aspect ratio floor plan under the same MCE level ground motion with three different diaphragm strengths: 1.39, 1.93 and 2.66 times the current (ASCE7 10) diaphragm force. *Figure c-i a* shows the global diaphragm force (F_{top}) vs. diaphragm deformation (Δ) at the top level diaphragm of the structure (See schematic in inset Figure *c-i b* for the definition of these terms). *Figure c-i b* shows the local demands on the diaphragm reinforcement in the top level diaphragm midspan (critical flexure) joint for these same analyses in terms of chord force *T* vs. joint opening (δ) (See schematic in inset Figure *c-i b*). As seen, the chord response for the strongest design (2.66 times current code F_{px}) is essentially elastic (dark black lines in Figure *c-i b*); the chord response for the intermediate strength design (1.93 times current code F_{px}) of these earthquakes has a maximum opening deformation demand of 0.2″ (dark gray lines in Figure *c-i b*); and, the chord response for the weakest design (1.39 times current code F_{px}) has a maximum opening deformation demand of 0.4″ (light gray lines in Figure *c-i b*); These openings represent the allowable deformation demands for the Low, Moderate and High Deformability (LDE, MDE, and HDE) Classifications in the Design Methodology. As these demands are in the Maximum Considered Earthquake (MCE), these design strengths therefore represent, from strongest to weakest, the Elastic, Basic and Reduced Design Options (EDO, BDO, and RDO), as defined by the performance targets in Table C-II. Thus, the values 1.39, 1.93 and 2.66 approximate the Ψ_E, Ψ_D, and Ψ_R, factors for this design case (they only approximate since the factors are based on the 90% confidence interval of the average over the suites of ground motions). Finally, these equations were converted into Rs factors for the ASCE7-14 diaphragm force proposal as described in the commentary for Step 3a.
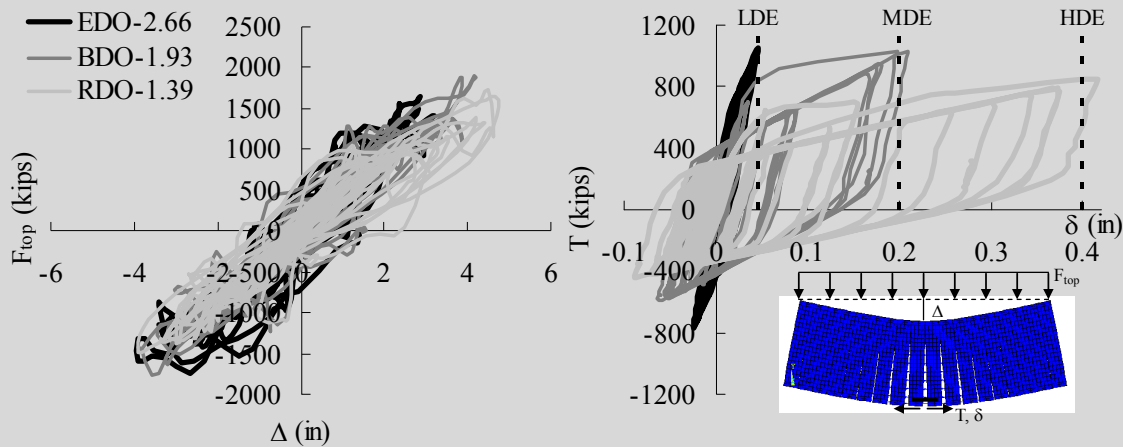

Figure c-i. Analytical Results: (a) Diaphragm pushover curves; (b) Chord tension vs. opening.

Verification of Design Factors

The design factors were verified through a limited set of analyses of realistic precast prototype structures, including a 4-story precast parking structure (*Fig. C-IIIa*) and an 8-story precast shear wall or moment frame office building (*Fig. C-IIIb*), as described in PART 5: *Appendix A2*. Prototype structure analytical results are used to demonstrate certain design aspects in gray text boxes in the *Commentary*.
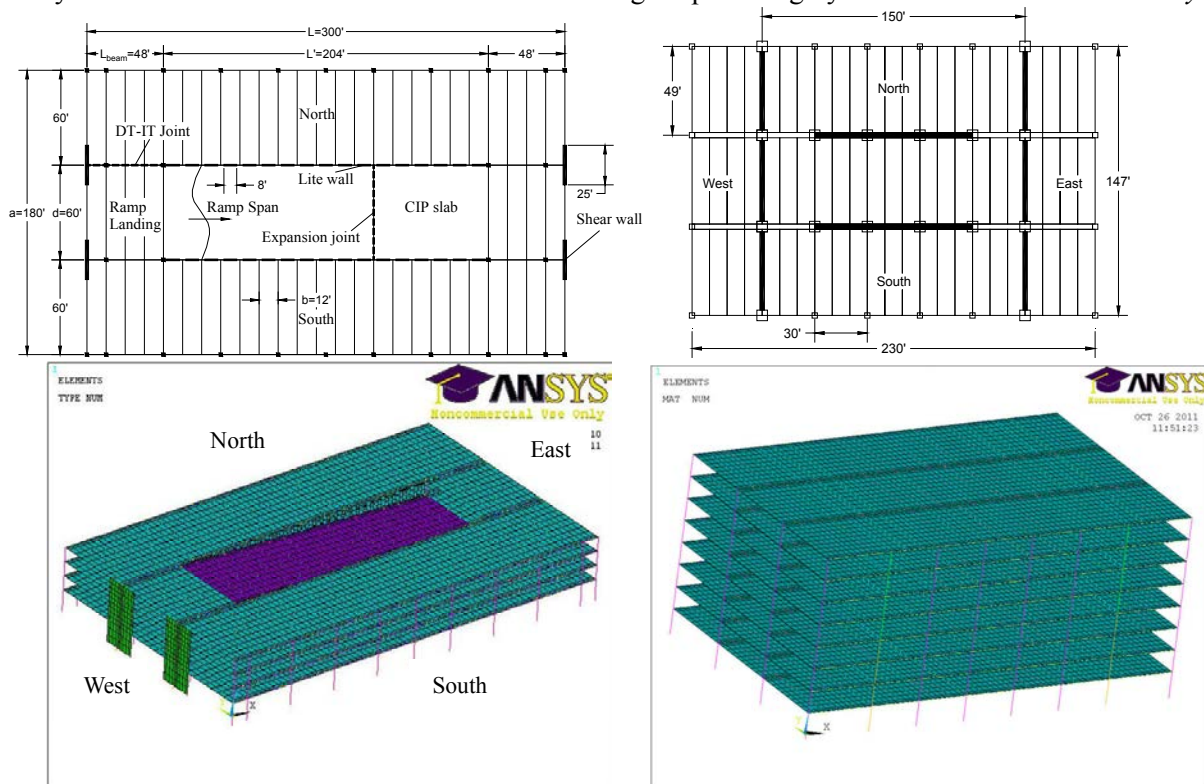

Figure C-III. Precast Prototype Structures Plan and Models: (a) Parking Structure; (b) Office Building.

Figure c-ii shows an example of how the prototype structures were used to verify the design factors developed in the analytical parameter study. Figure *c-ii* a shows the total maximum diaphragm force at each level of the prototype parking structure in the MCE. The red lines represent the maximum envelope of the forces; the blue line is the instantaneous profile and maximum diaphragm force. The green line is the design strength produced in the design methodology, indicated a reasonable and conservative prediction of the diaphragm force demands. Figure *c-ii* b shows this same information for the forces in each sub-diaphragm (outer flats and ramp), indicating an accurate and conservative design.
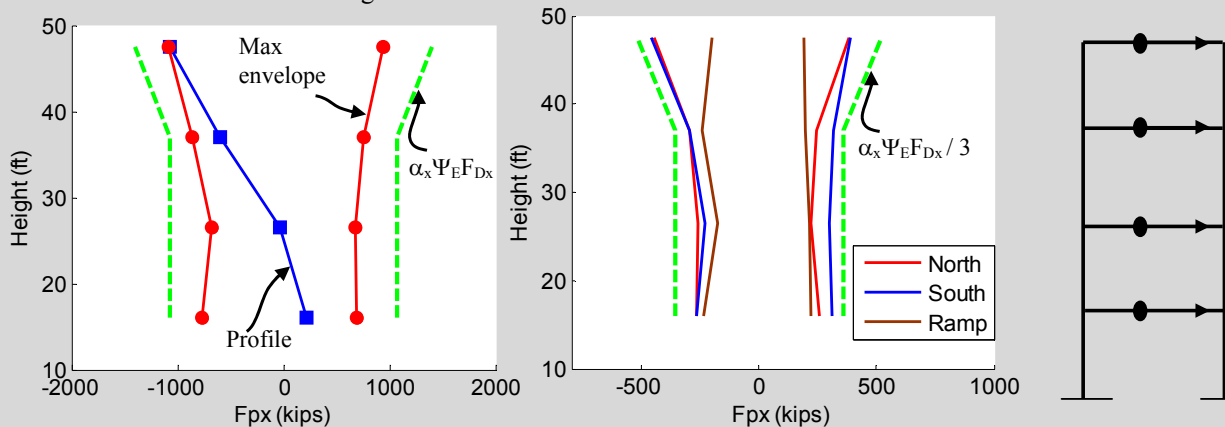

Figure c-ii. Diaphragm inertia force in transverse direction: (a) floor total; (b) sub-diaphragm.

Commentary on the Seismic Design Procedure for Precast Concrete Diaphragms

This section provides a commentary for the **PART 1 Design Procedure**. The design procedure involves 5 sequential steps. The commentary section is organized in the same format to provide a one-to-one correspondence between design step and commentary. Figures in the commentary use the notation *C* to distinguish them from the PART 1 design procedure figures being discussed, which are denoted in **bold**. The commentary text focuses on background for the use of the design procedure. Gray text boxes within pertinent steps of the Commentary explain how the PART 1 design factors were established based on the analytical results from the research program, with figures labeled using a small italicized "*c*".

Step 1: Determine diaphragm seismic demand level (*Low, Moderate, and High*).

Step 1 Description. In the first design step, the diaphragm seismic design level is established. Three levels (*Low, Moderate, and High*) are defined and depend on seismic design category (SDC), number of stories in the structure, and diaphragm geometry (span and aspect ratio).

Based on the consensus of the DSDM Task Group Design Development Team (listed in PART 5: *Sec 5.1*), all diaphragm designs in SDC B and C are considered to be in the *Low* Seismic Demand Level. For designs in SDC D and E, the chart in **Figure 1** of PART 1 is used to determine the diaphragm seismic demand level. The chart relates Seismic Demand Level Classification to combinations of diaphragm span, aspect ratio, and number of building stories.

A diaphragm that would be considered in the:
1. *Low* Seismic Demand Level based on diaphragm length and building stories, but which possesses an aspect ratio > 2.5, is to be moved (up) to the *Moderate* Seismic Demand Level.
2. *High* Seismic Demand Level based on diaphragm length and building stories, but which possesses an aspect ratio < 1.5, is permitted be moved down to *Moderate* Seismic Demand Level.

Step 1 Commentary. The intent of the design procedure is to provide the diaphragm the proper combination of strength and deformation capacity in order to survive anticipated seismic events. Three different design options are provided to the designer to accomplish this objective, ranging from a fully elastic diaphragm design to designs that permit significant inelastic deformation in the diaphragm. The motivation for this approach is the recognition that under certain conditions, a fully elastic diaphragm design may not be economical or reliable for precast diaphragms. Under other conditions, however, an elastic diaphragm design will be satisfactory and may be most desirable.

The *diaphragm seismic demand levels* are introduced into the design procedure to help distinguish between these different conditions, so as to guide selection of the appropriate diaphragm design option. Thus, this classification permits enforcement of the deformation capacity measures where needed, for instance long span diaphragms subjected to high seismic hazard, while permitting the design to avoid such measures for cases where significant inelastic deformation capacity is unnecessary, for instance short-span diaphragms subjected to low seismic hazard.

> **Diaphragm Seismic Demand Level Chart, Design Procedure Step 1:** The construction of the **Figure 1** chart in Step 1 of PART1 is guided by analytical results for the *Basic Design Option* (BDO) as follows:
>
> The primary design target for the BDO is elastic diaphragm behavior in the *Design Basis Earthquake* (DBE). This target is established by the newly proposed diaphragm forces (or using the current code forces, by the diaphragm force amplification factor Ψ_D). The second design target for the BDO is limiting diaphragm inelastic deformation demands within allowable values in the *Maximum Considered Earthquake* (MCE). The *moderate deformability element* (*MDE*) diaphragm reinforcement specified in the BDO design possesses an allowable deformation of $0.2''$ (*See Commentary, Step 2*). Accordingly, in the analytical research, inelastic joint opening demands for BDO diaphragms under MCE level hazard were evaluated with respect to this *MDE reinforcement* allowable deformation. The success in achieving this second target is plotted in *Figure c-1*:

Figure c-1a reproduces the **Figure 1** chart with markers denoting the maximum diaphragm joint opening demand measured in the analyses for BDO designs under the MCE. Three ranges are denoted by the markers: *Triangle*- demands between 0.1″- 0.2″, representing *efficient and safe* designs for MDE reinforcement; *Square*- demands greater than 0.2″, representing *unsafe* designs in which the MDE allowable deformation is exceeded; *Circle*- demands less than 0.1″, representing *inefficient* designs where the MDE allowable deformation limit is not closely approached. The results shown in Figure c-1a imply that a set of BDO designs that *equally* meet the DBE target of elastic diaphragm behavior may have quite different MCE performance in terms of inelastic deformation demands. The outcomes (*unsafe*, *safe* and *efficient*, *inefficient*) are well-predicted by the building configuration parameters of number of stories and diaphragm length. The transitions between these outcomes are used to designate the boundaries between *High*, *Moderate* and *Low* Diaphragm Seismic Demand Levels. These classifications trigger different requirements in the Diaphragm Design Option selection of Step 2.

Though the primary parameters controlling diaphragm joint opening demand are diaphragm span and number of stories, diaphragm aspect ratio was found to have a secondary but non-negligible effect. As seen in *Figure c-1b*, a longer diaphragm (in this case L=180′) with a sufficiently stocky aspect ratio (in this case *AR=1.0*) can have its opening demand drop from *high* to *moderate*; likewise, a shorter diaphragm (in this case L=60′) with a sufficiently slender aspect ratio (in this case, *AR=3.0*), can have its opening demand rise from *low* to *moderate*. These diaphragm geometries could occur for a floor plan three 60′ double tees deep with tributary reinforcement across the internal beam lines (e.g. shown in Fig. C-1a) and a 20′ hollowcore diaphragm, respectively. Therefore the exceptions based on AR are provided for the **Figure 1** Chart in **PART 1**.

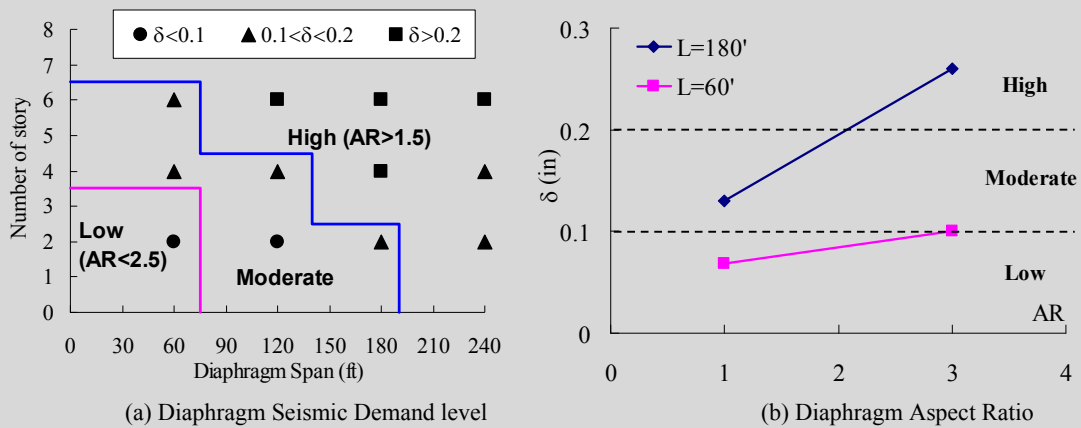(a) Diaphragm Seismic Demand level   (b) Diaphragm Aspect Ratio

Figure c-1. Diaphragm maximum joint opening for BDO designs under the MCE.

While number of stories and SDC are straightforward determinations, assigning a diaphragm span, and consequently diaphragm aspect ratio, is more complicated, and engineering judgment may be required, particularly for more complicated floor plans.

Diaphragm span for the structure is selected as the maximum diaphragm span on a floor in either orthogonal direction. Most precast diaphragms contain precast units running in only one direction, and typically the maximum span will be oriented perpendicular to the joints between the primary precast floor units. The design methodology factors are calibrated relative to joint opening demand between the precast floor-units, and thus based on the more typical orientation. For the procedure:

1. Diaphragm span is defined as the larger value of the maximum interior distance between two LFRS elements and twice the exterior distance between the outer LFRS element and the building free edge (See Fig. C-1).
2. Diaphragm aspect ratio (AR) is defined as the diaphragm span-to-depth ratio using the maximum span calculated above. Depth is defined as the floor diaphragm dimension perpendicular to the diaphragm span that is associated with the pair of adjacent chord lines for the diaphragm or sub-diaphragm. This dimension is also illustrated in Fig. C-1.
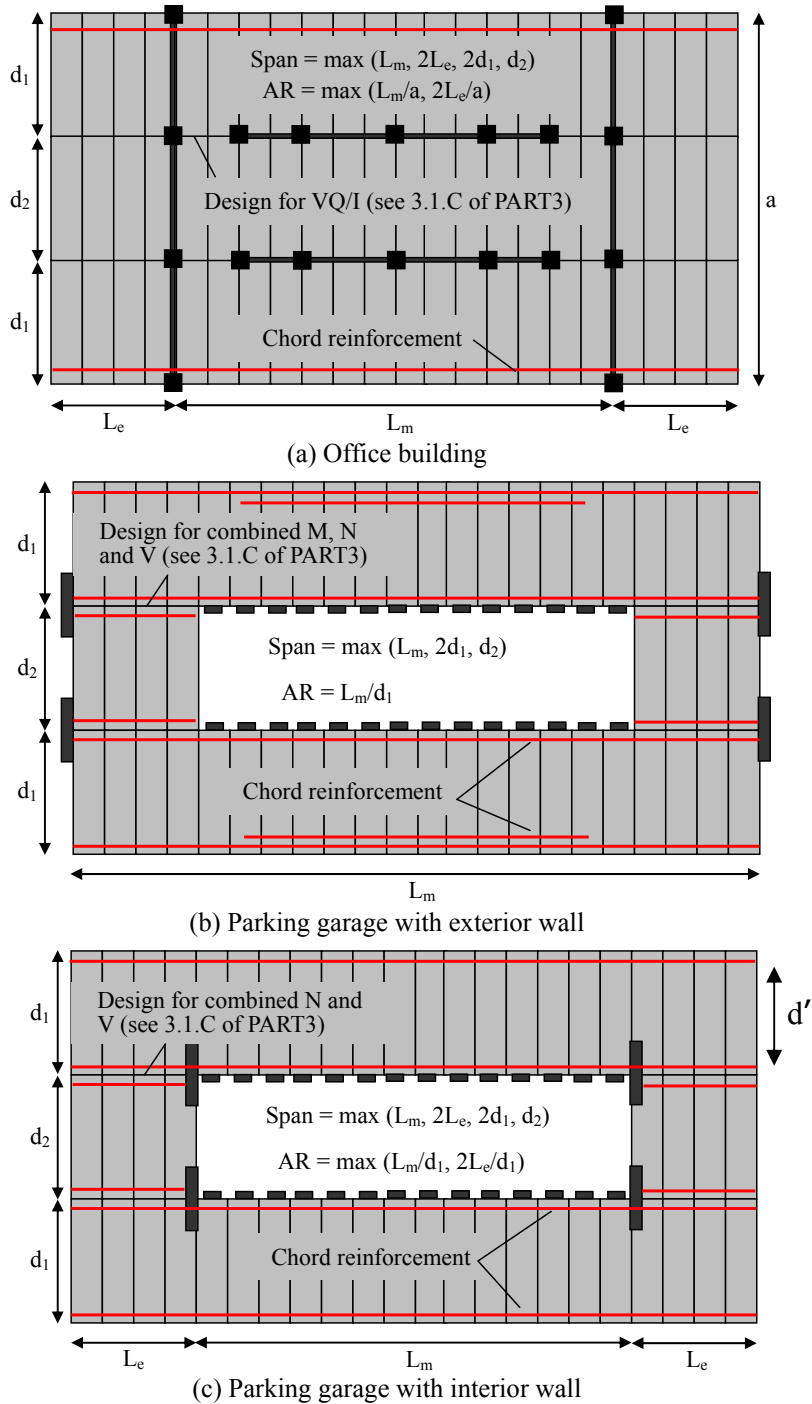
(a) Office building

Span = max (L_m, $2L_e$, $2d_1$, d_2)
AR = max (L_m/a, $2L_e/a$)

Design for VQ/I (see 3.1.C of PART3)

Chord reinforcement

(b) Parking garage with exterior wall

Design for combined M, N and V (see 3.1.C of PART3)

Span = max (L_m, $2d_1$, d_2)

AR = L_m/d_1

Chord reinforcement

(c) Parking garage with interior wall

Design for combined N and V (see 3.1.C of PART3)

Span = max (L_m, $2L_e$, $2d_1$, d_2)

AR = max (L_m/d_1, $2L_e/d_1$)

Chord reinforcement

Figure C-1. Diaphragm span and aspect ratio.

The intent of the design procedure is to have a single classification for a given floor level. There are cases where it is possible to assign multiple classifications within a floor (a diaphragm with short and long diaphragm spans, e.g. the overhangs vs. the main spans in Fig. C-1a,c). However, this practice is not encouraged. Likewise, the classification procedure is based on maximum diaphragm span and maximum aspect ratio occurring at the same location in a floor. Floor configurations that do not conform to this are considered rare and the secondary location is likely a non-controlling case.

Likewise, the procedure intends a single classification to be assigned for the structure based on the maximum diaphragm span/aspect ratio on any floor. This will be the typical procedure for structures with similar floor plans up the building. However, it is recognized that for certain cases, it may be advantageous for the designer to distinguish between conditions on different floors (podiums, shear wall vertical cut-offs, etc.). Thus, for structures with highly variable floor plans, it is permissible to divide floor levels in a structure into two or more distinct regions for the purposes of determining diaphragm seismic demand classifications.

Step 2: Select diaphragm design option and associated diaphragm reinforcement classification.

Step 2 Description. In this step, one of three diaphragm design options (*Elastic, Basic and Reduced*) is selected based on the Diaphragm Seismic Demand Classification determined in Step 1. The performance targets for each design option were shown in Table C-I. The classes of diaphragm reinforcement available in the design are then determined based on the selected diaphragm design option.

Step 2 Commentary. The ***Diaphragm Design Option*** is selected using **Table 1** of PART 1. As seen in **Table 1**, there is a recommended pairing between a Diaphragm Seismic Demand Classification and a Diaphragm Design Option: *Low* Diaphragm Seismic demand with the EDO; *Moderate* Diaphragm Seismic demand with the BDO; and, *High* Diaphragm Seismic demand with the RDO. As also shown in **Table 1**, the designer is permitted to deviate from the recommended pairings as follows:
1. A design option involving a greater targeted deformation capacity than recommended can be selected. Thus, both the BDO and the RDO are alternatives for the *Low Seismic Demand Level*; and the RDO is an alternative for the *Moderate Seismic Demand Level*.
2. A design option involving less targeted deformation capacity than recommended is permitted in certain cases, but with an added requirement. These cases include the use of EDO for the *Moderate Seismic Demand Level* and BDO for the *High Seismic Demand Level*. For these cases, the calculated design force must be further increased with a penalty multiplier of 15%.
3. The use of the EDO is not permitted for the *High Seismic Demand Level*.

The ***Diaphragm Reinforcement Classification*** is selected in Step 2 using **Table 2**, PART 1. As seen in **Table 2**, there is a recommended pairing between the diaphragm reinforcement classifications and a diaphragm design option: *low deformability element* (LDE) for the EDO; *moderate deformability element* (MDE) for the BDO; and *high deformability element* (HDE) with the RDO. It is always allowable to use diaphragm reinforcement with *greater* deformation capability than required, i.e., MDE or HDE for the EDO; or HDE for the BDO. However, it is never permitted to use diaphragm reinforcement with *lower* deformation capability than required, i.e., LDE or MDE for the RDO; or LDE for the BDO.

Diaphragm Design Option
As described above, there are recommended pairings between Diaphragm Seismic Demand Classification and a Diaphragm Design Option. However, these are only recommendations and the other options listed above are available. These options are discussed further here.
1. Using a design option with a greater targeted deformation capacity than the recommended design option allows the designer to use the lower forces associated with the alternate option. Thus, the designer may prefer to insert better connectors into the design. Likewise, there may be reasons unrelated to the seismic design that lead to the use of better connectors, and this improved toughness should be recognized in the design. In general, the use a better class of connectors leads to improved structural integrity and is therefore encouraged.
2. Using a design option with a lower targeted deformation capacity than the recommended design option is also allowed, though not strongly encouraged since it moves the design away from higher structural integrity. This approach permits the designer the option of using a preferred set of diaphragm reinforcement with less deformation capacity than the class associated with the recommended option. The tradeoff is a higher diaphragm design force, not only that inherent in a

design option with less targeted deformation capacity, but also a further penalty increase of 15%. The justification for the value of this penalty is discussed in the text box below.

3. Calibrated EDO diaphragm design strength values for *High Seismic Demand Level* were produced in the research. However, it was viewed as unwise to allow diaphragm designs with no structural integrity requirements in cases of high diaphragm demand, regardless of how large the diaphragm forces are. Thus, this design case was prohibited in the design methodology.

Diaphragm Force Penalty Justification, Design Procedure Step 2:

The original intent was to allow *MDE reinforcement* for any BDO design. However, as described in the previous text box, no a priori assurance for the adequacy of this condition existed since the primary BDO design target is *elastic diaphragm response in the DBE*, and therefore the calibration of the BDO force level does not directly establish limits on the diaphragm deformation demands in the *MCE*. This outcome was evidences in the *Figure c-1a* chart, and confirms that a modification is required in the original intent because the maximum opening demands in the MCE for certain BDO design cases do indeed exceed the MDE allowable limit of 0.2″.

A choice existed in how to modify the design methodology to resolve this non-conformance to the design targets: (a) The allowable deformation ranges for the diaphragm reinforcement could be modified (i.e., a more stringent deformation requirement for MDE reinforcement); (b) the diaphragm force levels could be increased across the board (i.e., change the DBE performance target from the diaphragm yield point itself to a lower value within the diaphragm elastic range); or (c) increment diaphragm forces only for non-conforming cases. The first choice did not align well with the typical deformation capacities of existing connectors, and would not produce evenly-sized deformation ranges for the *LDE, MDE and HDE* reinforcement classifications. The second choice not only produces overly conservative designs for many cases, but also blurs the clean BDO performance target of elastic diaphragm response in the DBE. For these reasons, the third choice was considered as most desirable and realized through the design force penalty in **Table 1** of PART 1.

The magnitude of the design force penalty is 15%. *Figure c-2* shows the manner in which this value is selected. The solid markers indicate the maximum opening demand for BDO designs without any force penalty, i.e., the same data from the *Figure c-1a* chart plotted directly along the vertical axis. As expected, a number of data points corresponding to BDO designs in *High Diaphragm Seismic Demand* have MCE joint opening demands greater than the 0.2″ allowable value for *Moderate Deformability Elements*. The hollow markers indicate MCE joint opening demands for the same BDO designs *with the 15% force increase*. This force increment is seen in to lower the opening demand to within the allowable limit. The same penalty is enforced in Table 1 for use of the EDO in the *Moderate Seismic Demand Level*, though this provision was not based on any quantitative analytical results.
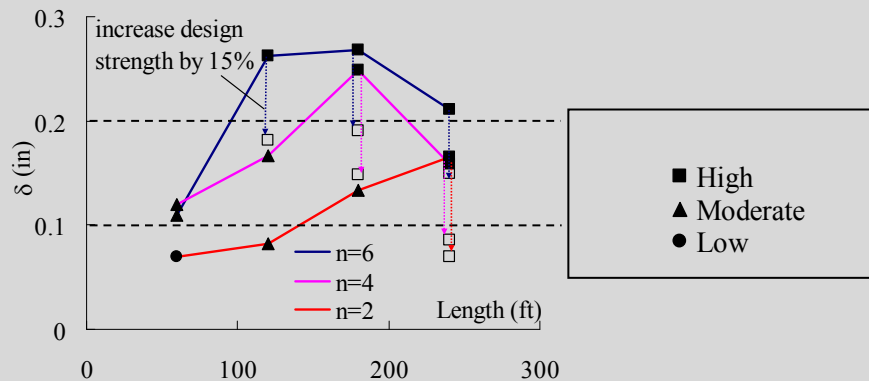

Figure c-2 Diaphragm maximum joint opening for BDO designs under the MCE.

Diaphragm Reinforcement Classification

Classification of a given diaphragm reinforcement type is determined through testing of individual elements following the cyclic testing protocols of the *Precast Diaphragm Reinforcement Qualification Procedure* (See PART 2 of the *Seismic Design Methodology Document for Precast Concrete Diaphragms*). The connector's "reliable and stable maximum joint opening deformation capacity" as defined in the evaluation criteria of the *Precast Diaphragm Reinforcement Qualification Procedure,* must be demonstrated in testing to exceed the qualification deformation of a certain classification.

The diaphragm reinforcement classifications are *high deformability elements* (HDE), *moderate deformability elements* (MDE), and *low deformability elements* (LDE). The qualification deformation values for each diaphragm reinforcement class were selected by considering the range of the ultimate (cyclic tension opening) deformations exhibited by the various precast diaphragm connectors examined in the experimental program (Naito et al. 2006) (Naito et al. 2007). Based on these results, a qualification deformation of 0.6″ was assigned for *HDE reinforcement* and 0.3″ for *MDE reinforcement*. There is no deformation requirement for *LDE reinforcement*.

A factor of safety of 1.5 was introduced into the design procedure by establishing the allowable maximum joint opening value at 2/3 of the connector's reliable and stable maximum joint opening deformation capacity. The 2/3 factor produces maximum allowable deformations of 0.4″ and 0.2″ for the *high deformability element* (HDE) and *moderate deformability element* (MDE) respectively. No deformation capacity requirement is needed for the *low deformability* element (LDE) since this classification of reinforcement is used with fully elastic designs.

The allowable maximum joint openings are used as performance targets in the analytical parameter studies to calibrate the design factors.

A few further comments are given about the reinforcement classification:
1. The diaphragm reinforcement classification is based on *inelastic deformation* associated with joint *opening* due to diaphragm flexure, not joint sliding deformation due to shear.
2. The diaphragm reinforcement classification applies to the chord reinforcement and shear reinforcement. Other reinforcement (collector/anchorages, tributary shear, and secondary connections to spandrels) have different requirements or recommended characteristics (See *Appendix 1*).
3. In meeting the required maximum deformation capacity using the testing protocols in the *Qualification Procedure*, the required cumulative inelastic deformation capacity is also met.

Diaphragm Reinforcement Classification, Design Procedure Step 2:

1. The condition that the required *cumulative* inelastic deformation capacity is also satisfied in meeting the required *maximum* deformation capacity using the testing protocols in the *Qualification Procedure* is evidenced in *Figure c-3*. The figure shows the diaphragm *cumulative* joint opening demand under MCE analyses corresponding to the design factors that produced the *maximum* allowable joint opening demand. As seen, the cumulative demands are significantly lower than the cumulative deformation capacity achieved in the cyclic tension tests, as indicated by the horizontal trend line (Naito et al. 2006) for both the BDO and RDO.

2. It also may asked how the diaphragm classifications can be tied to allowable deformations based on *absolute deformations* (0.2″, 0.4″), rather than a non-dimensional value, for instance joint rotation (e.g. deformation divided by joint depth). To show the adequacy of this assumption, consider *Figure c-4*, showing the analytical results (shown as profiles along the height of the structure) for two different diaphragm depths (32′ and 60′).

As seen, these different diaphragm depths produce significantly different joint inelastic rotation demands (See *Figure c-4a*), but these translate to essentially the same chord opening demand (See *Figure c-4b*), with a slightly larger demand for the deeper diaphragm. Since most of the analyses in the parameter study were conducted at this deeper dimension, and the difference in chord opening is small, the calibration of the design factors based on an absolute opening deformation is considered sufficiently accurate and slightly conservative for diaphragms with precast units of lower depths.
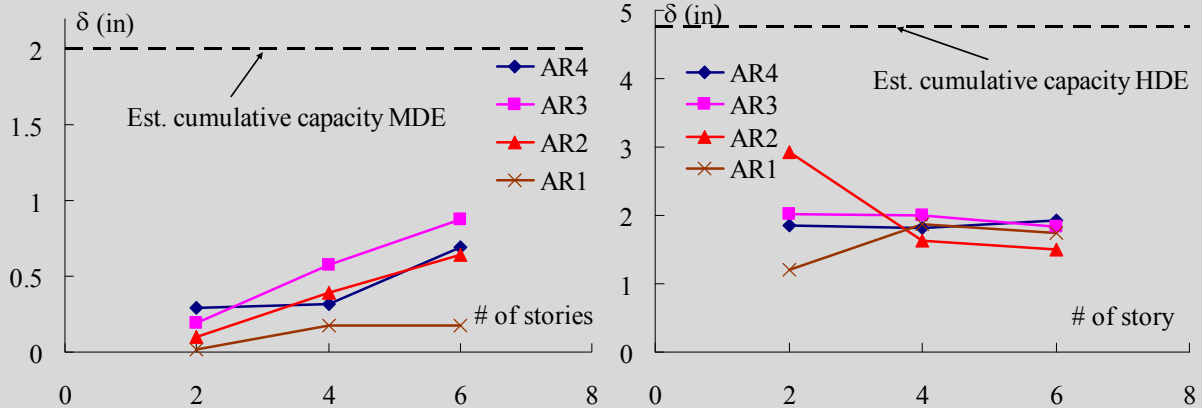
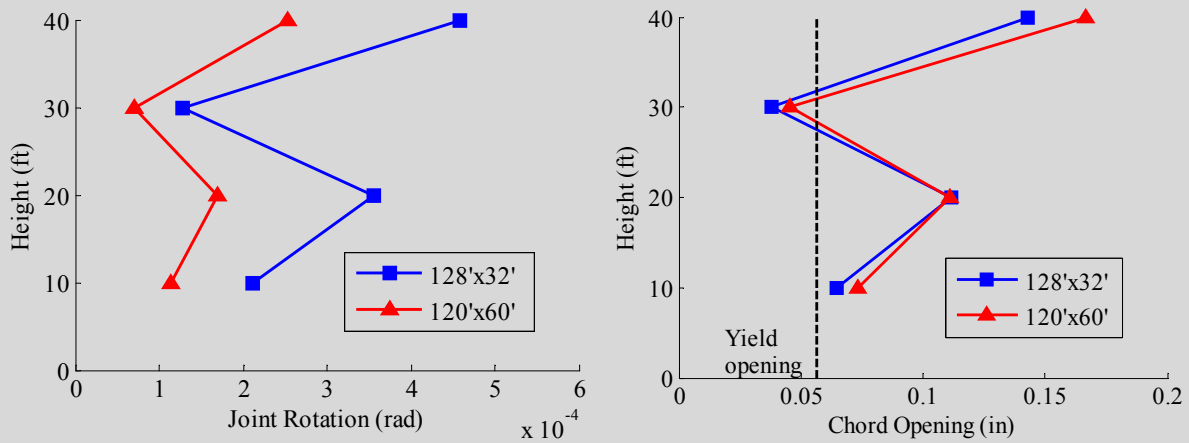**Figure c-3.** Diaphragm cumulative joint opening demand under MCE analysis: (a) BDO design; (b) RDO design.

Figure c-4. Effect of diaphragm depth on critical flexure joint MCE demands: (a) joint rotation; (b) chord opening.

30

Step 3: Determine the diaphragm design forces and the corresponding diaphragm joint required strengths.

Step 3a: The diaphragm design forces (F_{px}) are calculated according to using proposal IT06-001 for the ASCE 7 2014 provisions. The IT06-001 procedure uses a *diaphragm force reduction factor*, R_s in order to realize the different force levels required for the EDO, BDO and RDO diaphragm design options.

Step 3a Commentary. The need for an increase in diaphragm design forces was recognized from the outset of the research effort to develop the precast diaphragm seismic design methodology. It was initially decided to determine these design force increases relative to current code diaphragm design forces (initially IBC 2003 and subsequently ASCE 7-10). As such, diaphragm force amplification factors (Ψ_E, Ψ_D, Ψ_R) were developed for the EDO, BDO and RDO respectively to be applied to current code forces (*See Appendix 3*). During the codification process, the limitations of scaling to the current code values became apparent:

1. Current code diaphragm forces are based on the fundamental mode, however the large diaphragm forces identified during earthquake excitation (Fleischman et al 2002) are attributable to higher mode effects (Rodriguez et al 2002). Thus, first and foremost, the use of current code forces as a baseline produces inconsistent results since different designs will have a varying relationship of the spectral acceleration for periods of the fundamental and higher modes.

2. Further, the "self-contained" nature of the original design procedure developed by the DSDM research project, i.e. tying the diaphragm force amplification factors directly to the construction material (that is, the Ψ_E, Ψ_D, Ψ_R factors of the original procedure are directly calibrated to the available deformation capacity of precast diaphragm reinforcement) presents some difficulties in the codification process as in current codes, seismic design forces are controlled by one document (ASCE 7), while material design is covered in another code (e.g. ACI 318).

3. Finally, the underestimation of diaphragm forces in current code is a material-independent issue (*See PART 5: Sec. 5.4*), and thus it is conceptually inconsistent and economically punitive to have a procedure that singles out precast construction for higher diaphragm forces.

For the reasons listed above, the BSSC IT 6 committee charged with developing a white paper on diaphragm seismic design (Ghosh, 2012) promoted a rationally-based method for predicting diaphragm seismic forces for all construction types for use in the ASCE-7 loading standard. This method, based on the First Mode Reduced (FMR) method, proposed by DSDM project co-PI Restrepo (2007), is being balloted under proposal IT06-001 for the ASCE 7 2014 provisions.

The FMR method provides a more realistic estimation of the elastic diaphragm forces in the design basis earthquake (DBE) than current code provisions (Rodriguez et. al, 2002). With regard to its performance target, the FMR method is nominally equivalent to the BDO design, since both target elastic diaphragm response in the DBE. The diaphragm forces produced by the FMR method were checked relative to the Ψ_D factors and indeed found to be consistent for most design cases. For limited cases where discrepancy was observed, the underlying reasons were readily identified and rectified (*See Comm., Apdx. 3*). The result is DSDM BDO forces and FMR forces that are essentially aligned (*See text box below*).

The alignment of the DSDM BDO design forces with the FMR method allowed the original DSDM procedure to be revised to work with ASCE 7-14 proposal IT06-001. In the revised procedure, the different diaphragm force levels associated with the different design options (EDO, BDO, RDO) are realized through the introduction of diaphragm force reduction factors R_s, as discussed subsequently in the commentary. It is noted that while diaphragm flexibility has an effect on diaphragm forces, it was considered more straightforward to use an upper bound value in the final ASCE 7-14 proposal IT06-001, and thus eliminate (set to unity) the flexible diaphragm acceleration amplification factor at level x (α_{fx}), The expression for α_{fx}, originally in IT06-001 Eqn.12.11-12, is: $\alpha_{fx}=1.0\leq0.3\delta_{MDD}/\Delta_{ADVE}+0.4\leq1.3$.

The *revised procedure aligned to the based on the FMR method is the design procedure contained in PART 1, in anticipation of the future code revisions; the original DSDM procedure is preserved in Appendix 3 for use with current code.*

Diaphragm Design Forces, Design Procedure Step 3a:

Figure c-5 compares the diaphragm force amplification factor (Ψ) equations to the FMR design equations. The Ψ factors (*found in Appendix 4*) were developed in the DSDM Research and are applied to ASCE7-10 design forces. The figure compares the FMR to the equations for Ψ_E Ψ_D and Ψ_R factors for the EDO, BDO and RDO respectively. The vertical dimension for each design expression represents the range of diaphragm force variation due to diaphragm flexibility. Four different seismic sites are examined for structures up to 12 stories.

The FMR expressions are aligned to required elastic diaphragm strength for the DBE, and thus the appropriate comparison group for the FMR is Ψ_D (*APPENDIX 4:* **Eqn. A4-1b**), since the BDO and FMR method share the same performance target. The potential for mapping the Ψ equations to the FMR method is seen to be possible, given the good agreement between Ψ_D and FMR over most of the ranges shown in Figure C-6. As such, the design procedure was revised to use the FMR forces in place of Ψ_D, and use diaphragm force reduction factors R_s to realize the three performance-based design options of the BDO, EDO and RDO.
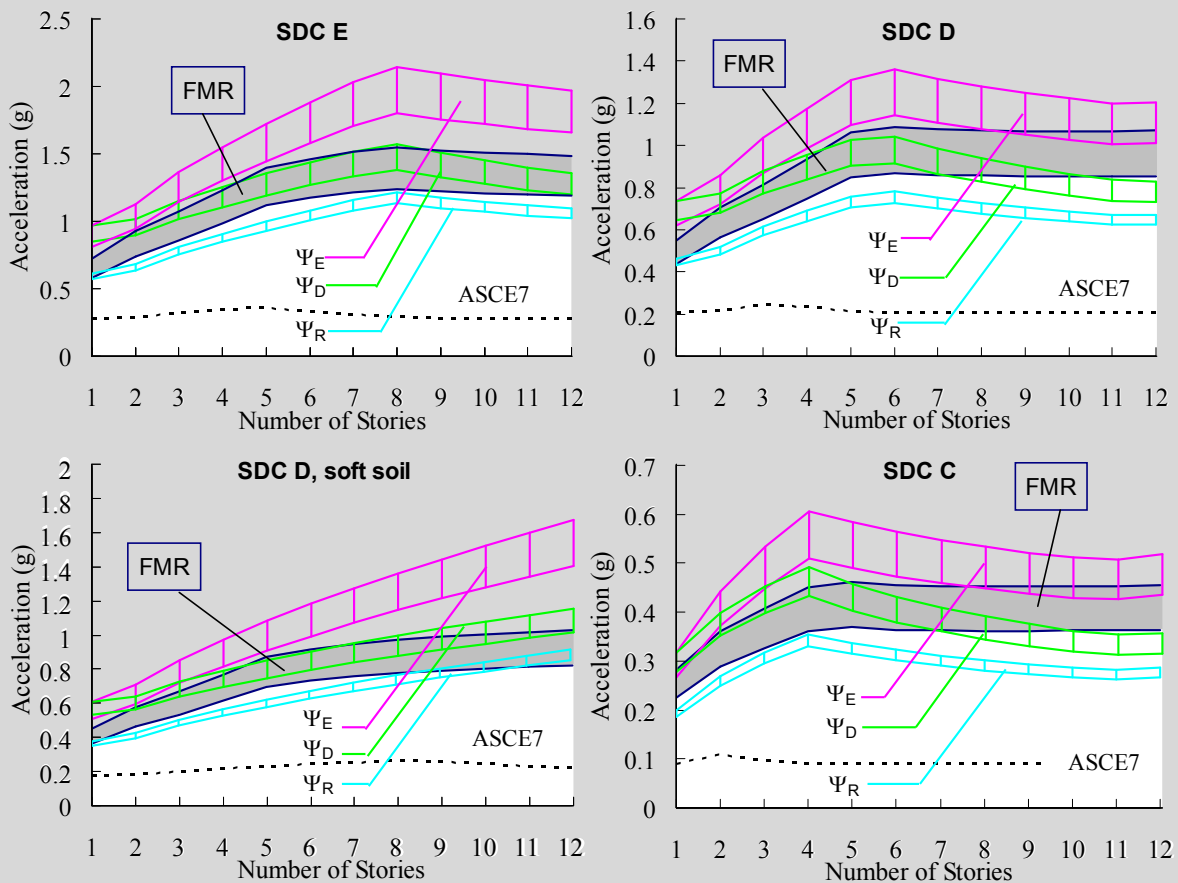

Figure c-5. Diaphragm design acceleration comparison for different sites: Ψ vs. FMR.

Diaphragm Force Reduction Factors (R_s)

The proposed IT06-001 diaphragm design force procedure implemented in Step 3(a) of PART1 is based on the FMR method, which estimates the elastic diaphragm forces in the DBE. The IT06-001 procedure introduces a *diaphragm force reduction factor*, R_s in order to allow for other design conditions (or intent) than strictly elastic diaphragm response in the DBE. This approach is similar to the conceptual framework proposed by Maffei (2005) which separated the diaphragm force into factors pertaining to dynamic amplification, force reduction based on available ductility, and overstrength (*See PART 5: Sec.*

5.3). Diaphragm force reduction factors for floor diaphragms of various construction materials are found in ***Table 12.11.5-1*** of proposal IT06-001.

The R_s factor modifies the diaphragm forces produced in an elastic diaphragm in recognition of the ductility in the diaphragm. For certain constructions types, the factor is based on the inherent ductility in the diaphragm. For precast diaphragms, the R_s factor is aligned to the detailing requirements of the selected design option: EDO, BDO, RDO. The R_s factors for precast concrete diaphragms provided in ***Table 12.11.5-1*** are reproduced in Step 3(a). It is noted that these factors address precast concrete diaphragms designed in accordance with ACI 318 (ACI, 2011).

The R_s factors for precast concrete diaphragms were established based on the results of the analytical earthquake simulation studies of experimentally-supported models conducted within the DSDM Project. The diaphragm design force levels are aligned with the diaphragm deformation capacities specifically for precast concrete diaphragms for the three different design options (EDO, BDO, RDO) and corresponding design performance targets (as indicated in Tables C-I and C-II).

The diaphragm design force amplification factors Ψ originally developed were dependent on the deformation capacity of the precast diaphragm reinforcement, calibrated directly to the deformation patterns of precast diaphragms. These factors were a function of several design parameters including diaphragm and building geometry (See *Commentary for Appendix 3*). The subsequent R_s factors developed are single value (for each design option) conservative upper bounds of the forces produced by the Ψ equations over the range of practical designs.

In the research used to produce the Ψ factors, the relationships were developed on the basis of diaphragm *local* ductility demand, that is, the deformation capacity of the diaphragm connectors or reinforcement crossing the joints between the precast units. However, to make the ASCE 7 2014 proposal IT06-001 procedure useful across construction materials, it was preferable to relate diaphragm force levels to diaphragm *global* ductility capacity, as the localized demands and deformation capacities for precast diaphragm are quite specific to this construction form. For this reason, the diaphragm force relationships were first transformed from local to global ductility, where global ductility is defined as maximum diaphragm deformation divided by diaphragm yield deformation (*Refer to Fig. C-II*).

The relationship between diaphragm design force levels and diaphragm local ductility demands established in the DSDM research project, and the transformation of these relationships from local to global diaphragm ductility are summarized in the next text box. These relationships were used to derive the R_s for precast concrete diaphragms in Table 12.11.5-1 of the ASCE 7 2014 proposal IT06-001:

In the DSDM research, precast diaphragm connectors have been extensively tested (Fleischman et al. 2012) and have been qualified into three categories: High-deformability elements (HDE), moderate-deformability elements (MDE) and low-deformability elements (LDE) which are required as a minimum for designs employing the reduced design objective (RDO), the basic design objective (BDO), and the elastic design objective (EDO), respectively.

The local deformation and ductility capacities for diaphragm connector categories are summarized in Table C-1. Considering that the proposed diaphragm design force level (Eq. 12.11-1) targets elastic diaphragm response at the design earthquake, which is equivalent to design employing BDO where $\mu_{local} = 3.5$ at MCE

Options	Diaphragm Connector Category	δ_{local} (in)	μ_{local}	μ_{global}	$\mu_{global, red}$	R_s
EDO	LDE	0.06	1.0	1.0	0.58	0.7
BDO	MDE	0.2"	3.5	1.4	1.0	1.0
RDO	HDE	0.4"	7.0	2.0	1.6	1.4

Table C-1. Diaphragm Force Reduction Factors

(See Table C-1), the available diaphragm global ductility capacity has to be reduced from Fig. 1a, acknowledging more severe demands in the MCE,

$$\mu_{global, red} = 0.17(\mu_{local} - 3.5) + 1 \qquad \text{(Eqn. C-1)}$$

Accordingly, the R_s factor can be modified from *Figure c-7(b)* (See Table C-1):

$$R_s = 0.67 \mu_{global, red} + 0.33 \qquad \text{(Eqn. C-2)}$$

Diaphragm Force Reduction Factors R_s, Design Procedure Step 3a:

The transformation of the diaphragm design force procedure from the original DSDM force amplification factors to the proposed procedure was a two-step process: First, the diaphragm force amplification factors Ψ were related to the local ductility; then the local ductility was related to the diaphragm global ductility demand μ_{global} to develop the final expressions.

Diaphragm R_{dia}- μ_{local} Relationships: The diaphragm force amplification factors were first mapped to the FMR equations by developing a relationship between a diaphragm design force reduction factor (R_{dia}) and the diaphragm (local) reinforcement ductility demand (μ). Extensive analytical studies were performed (Fleischman et al. 2012) to develop the relationship between R_{dia} and μ_{local}. R_{dia} is the diaphragm force reduction factor (similar to the R_s in Table 12.11.5-1) measured from the required elastic diaphragm design force at MCE level. μ_{local} is the diaphragm local connector ductility demand measured at MCE level.

The R_{dia}- μ_{local} relationship is obtained by plotting this relationship for all the analytical results in the design factor parameter study (See Section X). *Figure c-6* plots the data for every design point analyzed for a given case (Berkeley SDC E Shear Wall structures). Each marker on the plot is the mean of maximum values from a suite of 5 ground motions for a given design *that met the performance targets*. Note that these markers represent designs that met the performance targets at any of the design options, including the EDO, BDO and the RDO.

Figure c-6 is divided into four plots; each for a different diaphragm aspect ratio. The markers differentiate between the number of stories, as well as the DBE (hollow marker) and MCE (solid marker) analyses. As seen, a fairly linear relationship exists for each diaphragm aspect ratio. A linear curve fit was applied to these results, shown in *Figure c-6* as a dashed black line, and can be expressed as:

$$R_{dia} = 1 + [0.11 + 0.015(AR-3)^2] \ (\mu - 1) \qquad \text{(Eqn. C-4)}$$
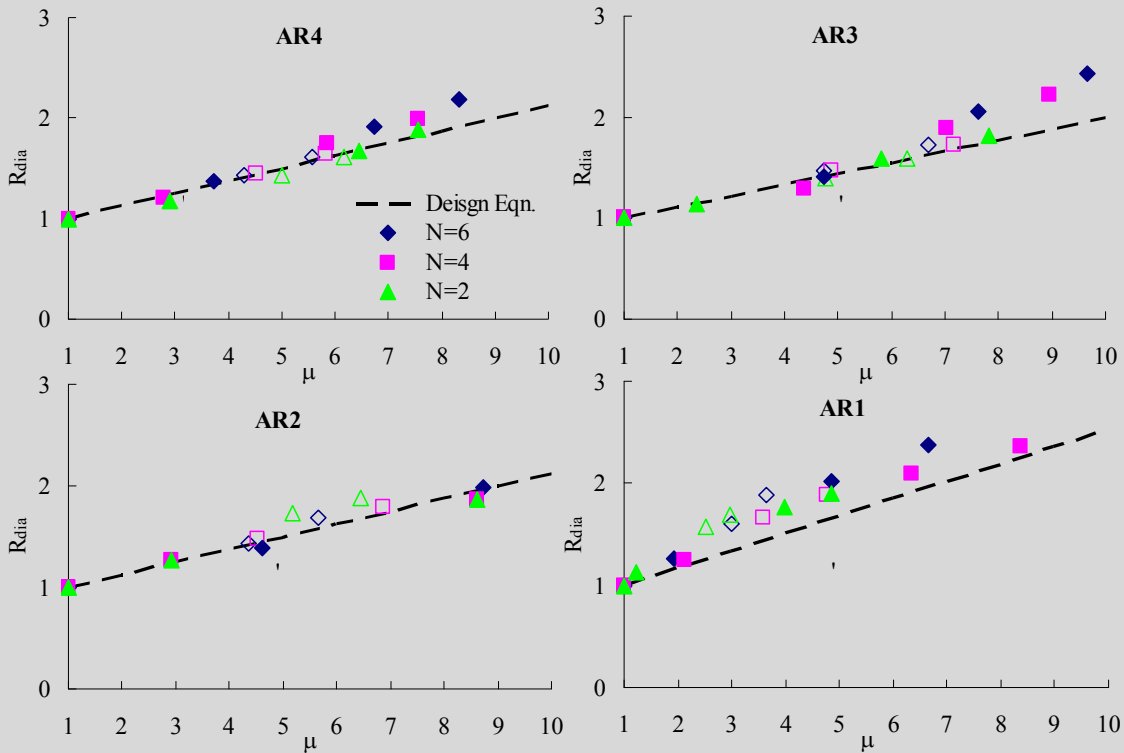

Figure c-6. Diaphragm force reduction (R_{dia}) vs. precast diaphragm connector local ductility demand μ.

The data points in *Figure c-6* are calculated as follows:

- For each successful design point, the diaphragm design force reduction factor (R_{dia}) is calculated as the design force amplification factor associated with elastic diaphragm response at the given level of seismic hazard divided by the diaphragm force amplification factor for the given design option, so R_{dia} is Ψ_E/Ψ for the MCE and is Ψ_D/Ψ for the DBE
  - Thus for MCE level hazard:
    - **EDO:** $R_{dia} = \Psi_E/\Psi_E = 1.0$
    - **BDO:** $R_{dia} = \Psi_E/\Psi_D$
    - **RDO:** $R_{dia} = \Psi_E/\Psi_R$
  - and for DBE level hazard:
    - **BDO:** $R_{dia} = \Psi_D/\Psi_D = 1.0$
    - **RDO:** $R_{dia} = \Psi_D/\Psi_R$
  - Note that with this definition, for all cases $R \geq 1.0$.

- Likewise, for each successful design point, the diaphragm reinforcement ductility demand (μ) is calculated as the mean of maximum of the maximum chord opening deformation demand in the analyses divided by the yield deformation of the chord.
  - Thus for MCE level hazard:
    - **EDO:** $\mu = 1.0$.
  - and for DBE level hazard:
    - **BDO:** $\mu = 1.0$.
  - Note that with this definition, for all cases $\mu \geq 1.0$.

Diaphragm μ_{global} - μ_{local} Relationships:

      With the relationship between diaphragm force reduction (relative to elastic response) and local ductility (inelastic deformation demand on the precast diaphragm connectors or reinforcement) established (as shown in Figure c-6), the diaphragm forces can now be related to diaphragm global ductility. *Figure c-7* shows these relationships as scatter plots for all the analyses performed in the analytical study (analytical results for different diaphragm aspect ratios, *AR*), first as: (a) the relationship between the local ductility, measured at the diaphragm reinforcement under maximum deformation demand, and the corresponding global ductility, $\mu_{global} - \mu_{local}$. Then, by relating the results in *Figure c-6* and *Figure c-7a*, (b) the resulting relationship between the diaphragm force reduction (relative to elastic response) to diaphragm global ductility, R_{dia}-μ_{global}, as shown in *Figure c-7a*. Each plot includes the proposed linear equations derived from the data.
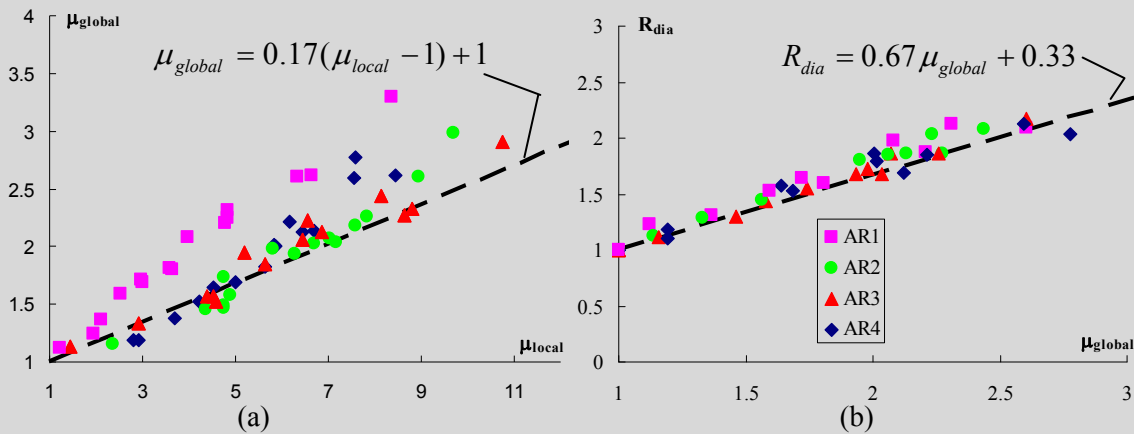

Figure c-7. Precast diaphragm global ductility relationships: (a) $\mu_{global} - \mu_{local}$ (b) R_{dia}-μ_{global}

Using the equations shown in *Figure c-7*, the R_s factor is calculated for different diaphragm design options provided the diaphragm local reinforcement ductility capacity is known.

Figure C-2 shows the comparison of the three design option with current code for various structures, including both a 4-story parking structure and a 8 story office building for SDC C and D.
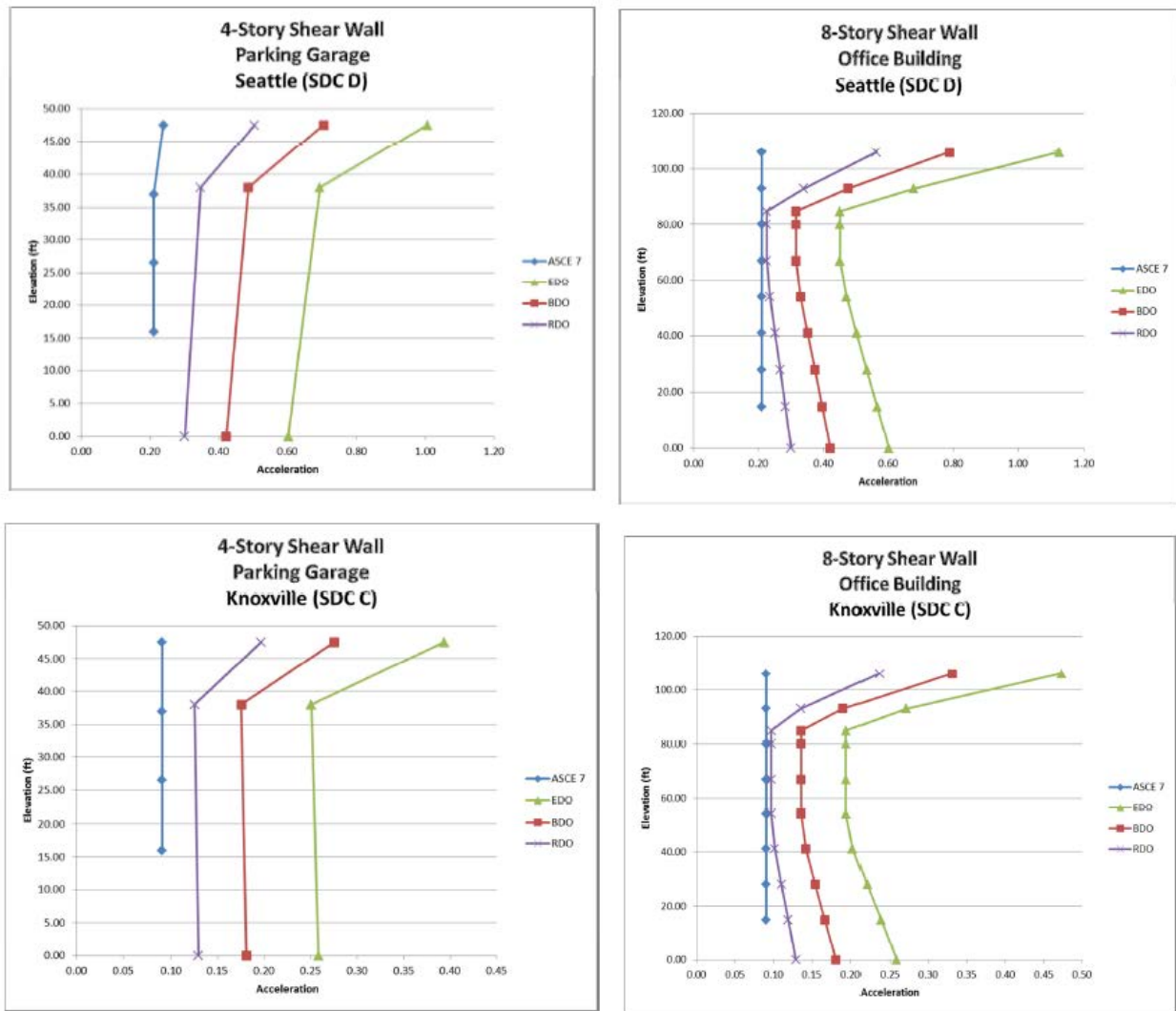

Figure C-2. Diaphragm Design Force Comparisons between ASCE 7-10 and proposed ASCE 7-14.

Diaphragm Shear Overstrength Factor (Ω$_v$)

Precast diaphragms typically exhibit ductile flexural response but brittle shear response. In order to avoid brittle shear failure, elastic shear response targets are required for both flexure-controlled and shear-controlled systems at design earthquake and MCE levels. Thus, a capacity design factor, shear overstrength factor (Ω$_v$), is required for the diaphragm shear design. For EDO design, since the diaphragm is expected to remain elastic under the MCE, no shear overstrength is needed. Figure C-9 shows the analytical results for required shear overstrength factors for BDO and RDO (Shown as marks). A simplified conservative equation is proposed as (see black lines in Fig. C-9):

$$\Omega_v = 1.4 R_s \qquad\qquad \text{(Eqn. C-3)}$$

The shear overstrength factor Ω$_v$ is scaled relative to the amplified diaphragm force, i.e. a diaphragm designed with the appropriate diaphragm amplification Ψ. Thus the Ω$_v$ factor is stacked on top of the Ψ factor. In the design, the Ω$_v$ factor is applied directly to the required shear force (See

Commentary Step 6). It should be noted that the Ω_v factor is independent of the shear strength reduction factor ϕ_v as it is applied to the demand side, while the ϕ_v factor is applied to the material capacity side. Thus, both are applied together to provide reliable elastic shear strength under MCE demand.

Diaphragm Shear Overstrength Factors (Ω_v), Design Procedure Step 3a:

The Ω_v values for the design procedure were determined in the analytical parameter study. The required magnitude of Ω_v was calibrated to design targets through MCE analyses. Please see PART 5: *Appendix A1* for full details of analytical research to determine these factors.

The shear overstrength factor values were obtained by bounding the maximum shear force V_{max} occurring in the diaphragm at the critical shear joint at MCE-level hazard as the diaphragm develops a flexural mechanism (in other regions of the floor), and scaling it by the design shear V_u. Accordingly:

- Ω_E, the diaphragm shear overstrength factor for the EDO, is taken as unity ($\Omega_E = 1.0$) since the Ψ_E factor is calibrated to the elastic force demand in the MCE.

- Ω_D, the diaphragm shear overstrength factor for the BDO, is taken as an upper bound on the V_{max}/V_u ratio for the BDO design under MCE level hazard.

- Ω_R, the diaphragm shear overstrength factor for the RDO, is taken as an upper bound on the V_{max}/V_u ratio for the RDO design under MCE level hazard. Ω_R is larger than Ω_D due to the larger expected diaphragm strain-hardening in the RDO.

Figure c-8 shows a scatter plot of the V_{max}/V_u ratios from the analytical research. The data is the mean of the maximum response from 5 ground motions. The expression used for Ω_v in the design methodology, $\Omega_v = 1.4R_s$, is plotted as a horizontal green line in each plot, indicating conservatism relative to all design cases. Also shown on the plot is the alternate design equations for $\Omega_v = \Omega_E, \Omega_D, \Omega_R$ used in the original procedure for use with ASCE7-10 (See Appendix: **Eqns. A4-2a-c**), superimposed as solid black lines in *Fig. c-8 (See Commentary, Appendix 4)*.
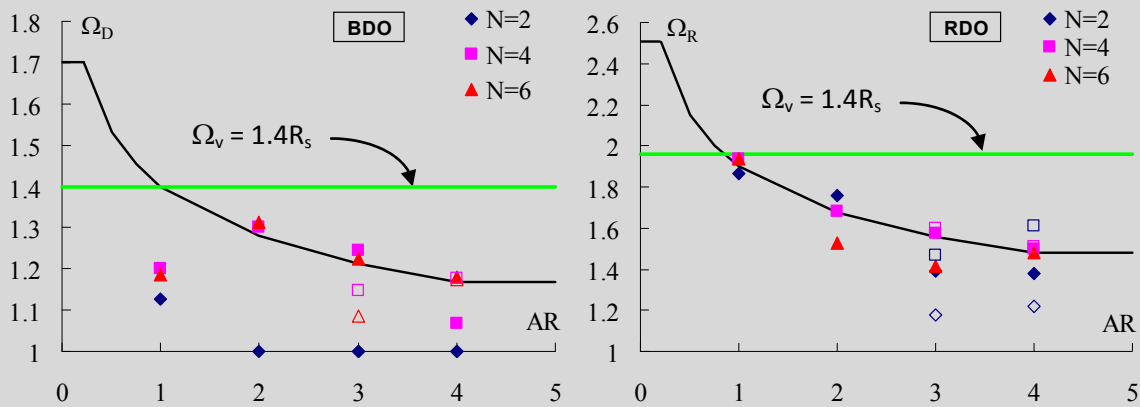

Figure c-8. Diaphragm shear overstrength factor equations: (a) BDO; (b) RDO.

The analyses used to develop Ω_v made use of a simple evaluation structure with well-defined shear-critical regions and flexure-critical regions. The shear overstrength, as obtained, provides an estimate of the maximum required shear force. However, in itself it does not directly address the impact of in-plane axial force (due to flexure or collector actions) on the precast diaphragm shear response. The effect of axial force is directly included in the design procedure through the interaction equation (See *Commentary Step 4*) to determine required diaphragm reinforcement at a joint based on internal force combinations determined in Step 3(b). It should be further noted that while the Ω_v factor has been calibrated in the analytical research to provide elastic shear response of the diaphragm in the MCE, care must be taken in ensuring the anticipated M/V ratio occurs in the diaphragm (See *"Capacity Design Considerations for Precast Diaphragms", Commentary to Appendix 5*).

Step 3b: Determine the diaphragm internal forces.

       Step 3b Description. In this step, the diaphragm internal force demands (N_u, V_u, M_u) are calculated at all potential critical joints between precast elements. The designer can select from one of four approaches to determine these internal force demands: (1) <u>Analysis using free-body diagrams</u>; (2) <u>Semi-rigid diaphragm model</u>; (3) <u>Design aids</u>; and (4) <u>Strut-and-Tie models</u>.

       Step 3b Commentary. The transformation of the story-level diaphragm force F_{diax} into internal forces within the diaphragm is viewed as a key step in diaphragm design (Clough 1982). Several methods are available to the designer as listed above and discussed below:

       Horizontal Beam Analogy
       Current practice (PCI Design Handbook 2004) employs a horizontal beam analogy (Gates 1981). The horizontal beam analogy permits a simple calculation of moments and shears as if the diaphragm were a beam. The method permits the diaphragm, or segments of the diaphragm, to be idealized as an equivalent beam with spans between the vertical elements of the lateral force-resisting system.
       For perimeter configurations (perimeter frames or walls), the diaphragm is treated as a simple beam in calculating a maximum moment ($w_uL^2/8 = F_{px}L/8$), shear and beam reactions ($w_uL/2 = F_{px}/2$). For more complex configurations, the designer typically must consider whether the diaphragm is rigid or flexible in determining how to apportion "beam" reactions at each wall or frame (*discussed later in this Commentary step*), in order to calculate diaphragm shear and moment, or resort to semi-rigid diaphragm models available with most commercial software packages (*also discussed later in this Commentary step*). The reactions to the lateral force resisting elements are also used to determine the collector steel requirements, which can be placed in the slab or the precast unit.
       Once diaphragm shear and moment are established, the chord reinforcement (near each edge of the diaphragm) is designed for the tension component of the couple due to in-plane diaphragm moment and the shear reinforcement (along the joints between precast units) is designed for the shear. The designer may often design the chord and shear reinforcement for the maximum moment and shear; the designer can also use the moment and shear diagrams to determine bar cutoffs and different shear connector spacing to create a more economical design.
       While straightforward, the horizontal beam approach has certain limitations or assumptions that should be understood by the designer. These include:

1. an internal force distribution assumed in the horizontal beam analogy that implicitly relies upon elements with plastic redistribution qualities, without enforcing this characteristic.
2. the horizontal beam analogy is unable to capture complex force paths that can exist in the precast floor system, including force combinations involving simultaneous axial, shear and moment.
3. the horizontal beam analogy does not produce an accurate force path for squat diaphragms, in which the internal forces more closely resemble that of a deep beam.

       Comments on these limitations and assumptions follow:

- The precast diaphragm design methodology enforces the same tension deformation requirement for the shear reinforcement as it does for the chord reinforcement (*See Comments for Step 4 in PART 1*) in order to ensure sufficient plastic redistribution in the diaphragm, thereby addressing the first limitation.
- The horizontal beam method does not include the development of diaphragm tension forces that may occur in semi-rigid diaphragm models (e.g., in computer structural analysis); while at first consideration this may seem unconservative, the use of the simple beam moment ($w_uL^2/8$) will produce conservative (or incases equivalent) chord demands than a semi-rigid diaphragm model; thus relegating the second limitation to acceptable for most design cases. However care should be taken at reentrant corners, regions of the floor under restraint, or at locations where collector actions in one direction act together with bending actions in the other (*See Commentary Step 4*).

- The horizontal beam method does not consider deep beam effects, which also can be represented in computer structural analysis models or strut and tie models.

Thus, the horizontal beam analogy can be considered an approximate and typically conservative method for calculating the internal force diagrams in the precast diaphragm design methodology. Regardless, in the absence of a computer structural analysis with semi-rigid diaphragm modeling, internal forces at all potential critical sections in the diaphragm should be determined by taking the diaphragm forces (F_{px}) and reactions on the diaphragm and evaluating appropriate free-bodies around each critical section using the principles of statics.

Alternate methods that provide more accurate results, but may be potentially more time-consuming, and may be considered a departure from current practice, are made available to the designer in the design methodology. These methods are discussed subsequently in this Commentary step.

Regardless of the approach, the designer has the choice in determining the internal design forces, either: (1) calculated for their maximum values at the critical joints, and design all the joints in the floor to this level; or (2) calculated at each diaphragm joint, for a more economical but more time-intensive design with more variance of details in the construction procedure. It is noted that critical joints include joints between precast units, diaphragm-to-LFRS joints in both orthogonal direction, and, depending on the design, internal beam joints. The diaphragm internal forces are to be calculated for the effects of seismic loading in each orthogonal direction individually. Each joint is to be designed for the set of coinciding diaphragm internal force components from the direction that produces the more critical condition in Equation 2 of PART 1, Step 4.

The effect of gravity load on diaphragm connector performance is considered secondary (as most connectors are located between floor units acting as one-way slab elements, and thus vertical force components are not expected to be significant), and thus was not considered in the experimental or analytical research, nor included in the design procedures. These actions can be considered in cases where important.

Rigid vs. Flexible Diaphragms

NOTE: Rigid vs. flexible diaphragms were considered in Step 3a with respect to the diaphragm forces developed at a given level (*vertical* profile) of the structure. This section pertains to rigid vs. flexible diaphragms as it affects the *horizontal* distribution of diaphragm forces at a given level among the individual walls and frames that make up the lateral force resisting system.

For a diaphragm associated with by a pair of primary (vertical plane) lateral force resisting system (LFRS) elements, for instance perimeter walls or frames, or a pair of interior walls and frames, the calculation of diaphragm reactions is statically determinate (e.g. $F_{px}/2$ for a symmetric system).

For layouts with multiple or asymmetric layouts, care must be taken in determining the internal forces using free-bodies since the relative magnitudes of the reactions depend on the relative flexibility of the diaphragm to the LFRS elements. For these more complex configurations, the designer typically must consider whether the diaphragm is rigid or flexible in determining how to apportion the "beam" reactions at each wall or frame, in order to calculate the diaphragm shears and moments, or resort to semi-rigid diaphragm models available with most commercial software packages (*discussed later in this Commentary step*).

- The rigid diaphragm assumption has historically been applied to precast concrete diaphragms with aspect ratios less than 3. The support elements are not taken as rigid supports, but instead distributes diaphragm reactions in proportion to the relative stiffness of each LFRS vertical element at the diaphragm level with respect to the base of the structure. In this case, the sum of the forces for the beam supports is equal to the total force at the level, but an imbalance in moment that may occur is resolved by resistance provided by the vertical elements in the orthogonal direction taking the actual and accidental torsion moments.

- The flexible diaphragm assumption distributes diaphragm reactions in proportion to the tributary mass of each LFRS vertical element. This assumption has historically been applied to precast concrete diaphragms with aspect ratios greater than 3.

- Common practice is to create an envelope of force diagrams, one for a rigid diaphragm (reactions proportional to the LFRS stiffness due to displacement compatibility), and one for a flexible diaphragm where the reaction is distributed based on tributary area (PCI Design Handbook 2004).

- An alternate procedure is presented in the PCI Seismic Design Manual (Cleland and Ghosh 2007) that attempts to optimize the design by tuning the LFRS stiffness to the diaphragm layout. Bounding analyses can be performed in which the design values are the envelope of values obtained by assuming upper and lower bound in-plane stiffness for the diaphragm in two, or more, separate analyses. (See *PCI Seismic Design Manual*)

Semi-Rigid Diaphragm Model

In this approach, the designer will rely upon the computer structural analysis software model of the building structure to determine diaphragm internal forces. Most structural analysis software provides the option for semi-rigid modeling of the floor and roof diaphragms, thereby permitting the internal forces at critical sections to be extracted from the analysis model.

Currently, most software packages provide a diaphragm modeling option for three-dimensional models: (1) no diaphragm, i.e., LFRS elements act independently; (2) rigid diaphragm, i.e., all LFRS elements at a story are subjected to a rigid body translation: $u_i = u_o + \phi\, y_i$, where u_o is the translation of the floor plate centroid, u_i is the resulting translation of a point on the floor a distance y_i from the centroid, and ϕ is the in-plane twist of the floor (all points on the floor translate the same in the absence of torsion); and (3) semi-rigid diaphragm, where the elastic stiffness of the floor system is modeled.

For the semi-rigid diaphragm model, design office software packages typically offer two basic options: (1) membrane action, in which only the in-plane elastic stiffness of the floor system is modeled; and (2) plate or shell action, in which the out-of-plane two-way bending and shear stiffness of the floor system is modeled in addition to the membrane action. Note that in either case, the diaphragm is modeled in two-dimensions (2D), i.e. the horizontal plane of the floor slab. For precast systems, the in-plane stiffness should be based on the floor plate (e.g., ignore the stiffness associated with the stems of double tees, etc.).

In employing the semi-rigid modeling option, most structural analysis programs request as input a slab thickness and an elastic modulus (E). If shear deformations are available, which typically is a standard feature in modern structural analysis programs, a shear modulus (G) can also be entered. Many design office structural analysis programs now also include an option to enter orthotropic stiffness properties S_{11}, S_{22}, S_{12} to account for different floor stiffness in each direction. This option is useful in modeling precast diaphragms, which have dissimilar stiffness properties in the precast floor unit spanning direction, and the direction perpendicular to the precast floor unit span.

In order to perform a computer structural analysis using the semi-rigid diaphragm option for precast diaphragms, a membrane stiffness has to be assigned to the diaphragm. This property is intorduced in Step 5 of the PART 1 design procedure once the diaphragm reinforcement has been designed. A rational method has been provided in PART 3 (and also described in the commentary for Steps 4 and 5) whose calculations produce diaphragm effective elastic and shear moduli, E_{eff} and G_{eff}. For the purposes of determining the internal forces in this step, E_{eff} and G_{eff} can be estimated as 25%~35% of the uncracked concrete E and G. These estimated values are to be verified in Step 5 after sizing of the diaphragm reinforcement. Note that the concrete *cracked* or *uncracked* elastic moduli (E_c and G_c) can be used as the properties for the semi-rigid diaphragm in the direction of the precast flooring units (i.e. S_{11}), depending on the assumed effects of the prestressing in the floor plate. In this case it may be reasonable to assign cracked modulus ($0.5E_c$) for double tee units and uncracked (E_c) for hollowcore units, as the effects of prestress are minor in the former and more effective in the latter.

If the structural analysis model for the building includes semi-rigid modeling of the floor and roof diaphragms, the internal forces at critical sections can be extracted directly from an analysis model subjected to the diaphragm forces (F_{px}). Currently designers rely on full 3D structure models for reinforced concrete diaphragms in high-rise structures for cases involving transfer diaphragms (Meyer 2012). For these analyses, free-body cuts can be made at diaphragm sections along the lines of the precast joints to determine internal forces.

There has been some debate as to how to apply the diaphragm forces, particularly in cases of a transfer diaphragm, where the forces in the floor system at one level are dependent on the lateral loading at each level. There is challenges in selecting the loading to apply to the structure, since the ELF pattern F_i is an instantaneous pattern, which is appropriate to apply but does not capture floor maxima, while the diaphragm force pattern F_{px} is a profile of maximums, and thus is not a rationale pattern to apply to the structure. Useful methods for applying this load in design are proposed in (Sabelli et. al. 2011).

Further guidance on modeling the diaphragm and discussion of analysis techniques is found in PART 3.

Analysis using Design Aids

Diaphragm free-body diagrams and internal force expressions developed for common precast structure floor configurations are provided in PART 3 of the *Seismic Design Methodology Document*. Design examples demonstrating the use of the Free Body Diagrams appear in PART 4.

Many precast structures share similar layouts, particularly those with challenging diaphragm conditions (e.g. parking structures) and so it may be useful for the designers to determine free-body diagrams for those common configurations and create spreadsheet tools to automatically calculate the internal forces. A set of free bodies for common configurations are found in PART 3, along with a description of spreadsheet methods to calculate the internal force diagrams from these free bodies.

It is noted that the set of free body diagrams in PART 3 involve symmetric LFRS layouts involving pairs of primary LFRS elements (walls or frames) and thus essentially a statically determinate system regarding the diaphragm reaction being carried by these elements (50% of the total load to each). For more complex LFRS layouts, the designer is referred to the PCI Seismic Design Manual (Cleland and Ghosh 2007)

Analysis using Rational Methods

Many floor layouts create diaphragms that act more similarly to a deep beam (Bull 1997) than the Bernoulli flexural member implied in the horizontal beam assumption. Irregular floor plan configurations (Paulay and Priestley 1992) and openings in floor systems (Moehle et al. 2010) require care in diaphragm design. For these cases, diaphragm design may benefit from the use of rational force path methods to determine the internal force design and reinforcement layouts. Such methods include the strut and tie method (Schlaich et al. 1987) and the panel-stringer method (Blaauwendraad and Hoogenboom 1996). These rational methods, effective for deep squat diaphragms, collectors, or more complex floor configurations, can also be applied to regular floor plans (McSaveny 1997). The strut-and-tie approach can be used to determine diaphragm internal actions in accordance with the provisions of ACI 318 Section 18.5.

Transfer diaphragms, for instance occurring over podiums or in dual systems, are not directly covered in the design methodology. Care must be taken in carrying the large transfer forces with precast diaphragms, including assessing the effectiveness of bond between the precast units and topping slab (Bull 1997). These transfer conditions have led to failures in recent earthquakes (EERI 2011). See fib (2003) and (Moehle et al, 2010) for more information.

For more information on rational methods, the reader is referred to (fib 2003), (Schlaich et al 1987), and (Blaauwendraad and Hoogenboom 1996).

Diaphragm Internal Forces, Design Procedure Step 3b:

Figure c-9 shows the internal diaphragm force results for the top level diaphragm of the prototype parking structure in *Figure C-IIIa*. The results are from the dynamic time-history analysis (earthquake simulation) under the MCE ground motion (bi-directional components). The figure shows the force diagrams for: (a) Diaphragm axial thrust; (b) Diaphragm in-plane Shear; and (c) Diaphragm in-plane moment, along the north diaphragm flat (from 0 to L as described in *Fig. C-IIIa*). The red lines indicate the envelope of maximum forces that occurred during the earthquake; the blue line indicates the instantaneous force in the diaphragm at maximum force. The green line represents the design values (N_u, V_u and M_u) determined in Step 3b and used to design the prototype parking structure for the analysis (for an EDO design). The method selected to determine internal forces inthis case was the design aids provided in PART 3 of the *Design Methodology*. As seen, these methods produced accurate and for the most part conservative results. Note: (1) the large axial forces (-300k) observed at the bottom of the Fig. c-9a chart that exceed the design values (225k) are compressive and thus do not violate the design (the N_u term in the interaction equation 2 is sign sensitive and thus compression lowers demand); (2) the maximum moment predicted is accurate but the moment diagram is offset due to the asymmetry caused by the ramp in the parking structure.
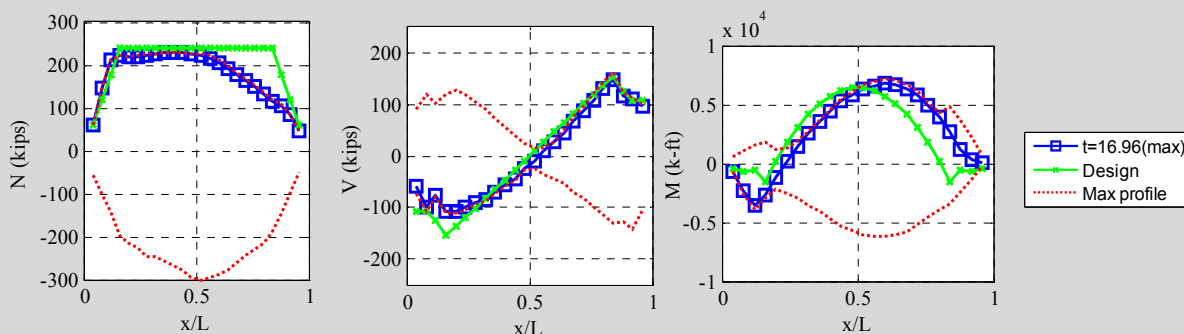

Fig. c-9. Diaphragm joint internal force comparison, Design vs. Analysis: (a) axial; (b) shear and (c) moment.

Figure c-10 reproduces the maximum response (blue line) and the design value used (green lines) for the case depicted in Fig. 9. The red lines on the plot indicate the forces that would be produced if the horizontal beam analogy was used in Step 3(a) instead of the design aid method (also shown for comparison as a black line is the horizontal beam method applied with current (unamplified) code forces). As seen, the horizontal beam method does not accurately predict the diaphragm N, V, and M. However the simple beam conditions in the horizontal beam method are seen to significantly overestimate the diaphragm moment (*Fig. c-10a*). This overestimation is sufficient to overcome the fact that the horizontal beam method does not produce any diaphragm axial thrusts (*Fig. c-10b*). For this reason, the horizontal beam method can be considered typically conservative, provided the diaphragm can redistribute the forces to the assumed equilibrium pattern, which is enforced in the design methodology by providing deformation capacity for both the chord and shear reinforcement (*See Commentary Step 4*).
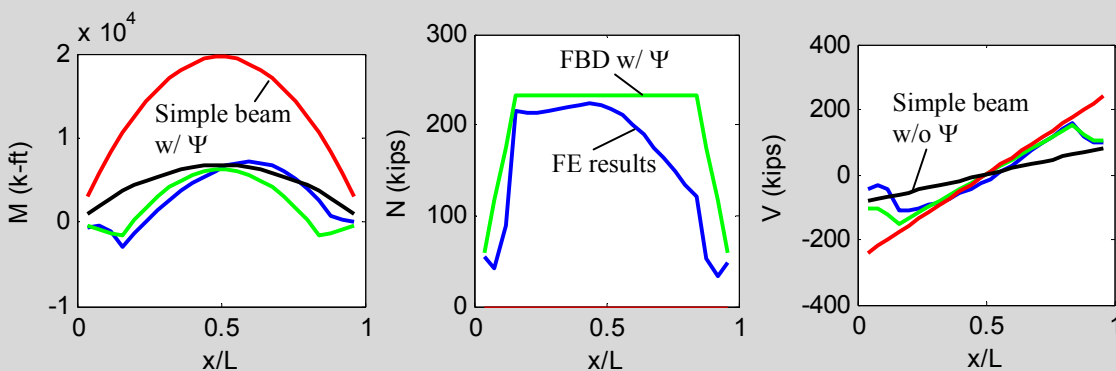

Fig. c-10. Diaphragm joint internal force comparison, Design Aid vs. Horizontal Beam: (a) moment; (b) axial and (c) shear.

Step 4: Design diaphragm reinforcement for required strength.

Step 4 Description. In this step, diaphragm reinforcement is designed for the required strength. This step involves: (1) selecting diaphragm reinforcement types from the appropriate classification; (2) looking up or testing the reinforcement to determine properties; and (3) designing the diaphragm for sufficient strength. An interaction formula is provided for the diaphragm strength design. Recommendations are provided for deformation capacity of secondary connections in the floor system.

Step 4 Commentary:

Selecting Diaphragm Reinforcement: The diaphragm reinforcement is selected based on the Diaphragm Reinforcement Classification determined in Step 2 of PART 1. Thus, the diaphragm reinforcement types allowable in this step are dependent on choices made earlier in the design. In cases, designs will involve a preferred set of precast connectors to use as diaphragm reinforcement, whether due to availability, local practices of the precast producer, etc. In this case, the designer should begin with this step first; bring this information to Steps 2 and 3, and perform a check on Step 1, prior to starting the design procedure with Step 3.

Diaphragm reinforcement types that meet the Diaphragm Reinforcement Classifications are determined using PART 2 of the *Seismic Design Methodology Document for Precast Concrete Diaphragms*. In PART 2, a *Precast Diaphragm Reinforcement Qualification Procedure* (Naito and Ren 2011) developed in parallel with the design procedure is used to determine the diaphragm reinforcement classification. A distinction is made in PART 2 between existing connections *that have been prequalified* and connections *that have not been prequalified*, whether new connections under development or existing connections that have yet to be prequalified. For the former, the *Qualification Procedure* has already been applied to some commonly-used existing diaphragm reinforcement. The Diaphragm Reinforcement Classification for these connectors appears in Table A-1 of Appendix 1 of the PART 1 Design Procedure. For the latter, the *Qualification Procedure* provides specific step-by-step guidance on the testing procedures, cyclic loading protocols, measurements and performance metrics required to determine the different diaphragm reinforcement classifications.

Each connection group in the diaphragm has a different set of design requirements in terms of strength and deformation as summarized in Table C-2. The PART 2 *Qualification Procedure* and Appendix 1 *Prequalified Connections* apply to chord and shear reinforcement only. Thus, the Diaphragm Reinforcement Classifications do not apply to diaphragm-to-LFRS connections, diaphragm-to-IT beam connections, and the so-called diaphragm *secondary* connections, which include diaphragm-to-spandrel, spandrel-to-column, and ramp-to-lite wall (non-LFRS) connections. Each of these connections are governed by a different set of deformation requirements (See Appendix 2).

Table C-2. Design requirement for diaphragm reinforcement.

Design Requirement	Diaphragm reinforcement		Diaphragm to LFRS	Collector	Internal beam Connection		Spandrel connection
	Chord	Shear			Within chord	Outside chord	
Force Determination	X	X	X	X	X[1]	X	
Interaction Equation	X	X	X		X	X	
Connector Classification	X	X					
Addtl. Defo. Reqs.[2]			X		X	X	X

[1] Tributary shear (VQ/I)　　　　[2] Allowable or Recommended: See Appendix 2

The Diaphragm Reinforcement Classifications are based on connector inelastic deformation capacity. It should be understood that the intent of the BDO and RDO is to provide the precast diaphragm with inelastic deformation capability related to a *flexural* mechanism. Thus the desired inelastic deformation capacity is a *tension deformation*, related to the precast diaphragm floor joint opening associated with in-plane flexure (and to a lesser extent in-plane axial thrust). For this reason, the key reinforcement group with respect to the deformation requirements is the chord reinforcement, as the chord

steel provides the primary flexure transfer in the diaphragm, and at a location along the joint in which the maximum opening occurs due to flexure.

The *tension* deformability requirements are also applicable to the *shear* reinforcement. Thus, the shear reinforcement used in the design must also meet the required Diaphragm Reinforcement Classification. The reason for this requirement is three-fold: (1) the shear reinforcement can also contribute to the flexural transfer, as permitted by ACI 318 (2005); (2) the shear reinforcement must be able to undergo the compatible displacements associated with the joint opening (See Fig. C-3) and still maintain shear load-carrying capacity (Wood et al. 2000), even in cases where it is not providing significant flexural resistance, and (3) analytical research (Fleischman and Wan 2007) has indicated that precast diaphragms

Figure C-3. Flexural Deformation Demands on Precast Joint.

with shear reinforcement with limited tension deformation capacity tend to have inelastic deformation concentrate at a single joint rather than be spread out among the diaphragm joints (See *text box*).
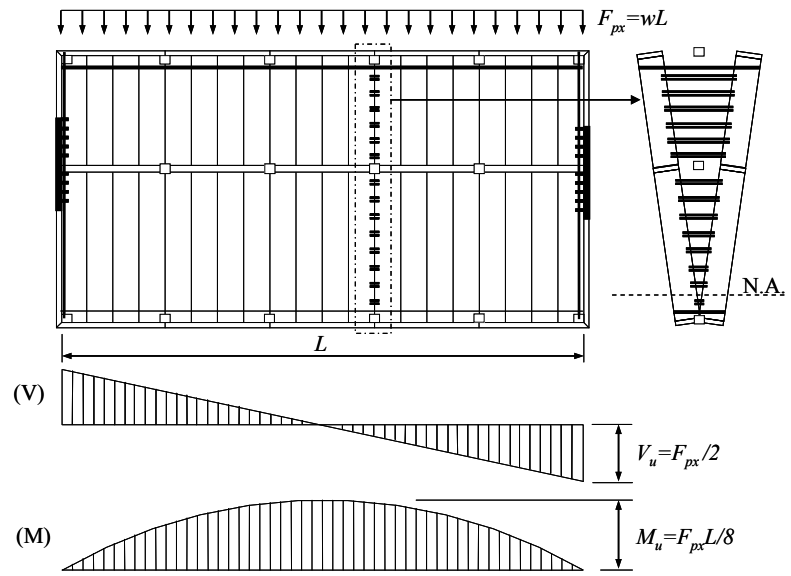

Diaphragm Reinforcement Classification, Design Procedure Step 4:

Figure c-11 shows the pushover curves (diaphragm force vs. deformation) for two otherwise identical precast diaphragms (same dimensions, reinforcement strength, etc.), except one possesses shear reinforcement with *tension* inelastic deformation capacity; the other shear reinforcement that is nonductile in *tension*. The chord reinforcement is identical. As seen by comparing PO curves A and D the global ductility of the diaphragm is significantly affected by the tension deformation capacity of the shear reinforcement (ductility reduction from ~6 to ~ 1.5). The insets A and D show the reason: the loss of the non-ductile shear reinforcement causes the midspan joint strength to drop below the surrounding joints, leading to a "necking" of the diaphragm deformation demands at the midspan joint, and thus a concentration of ductility demands leading to a failure of the chord at midspan; while the ductile shear reinforcement permits spread of the inelastic deformation demands to surrounding joints, which share the inelastic deformation demand, leading to greater global ductility.
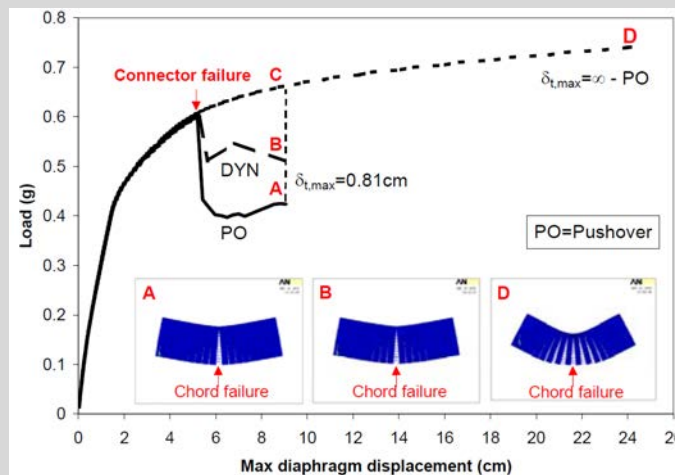

Fig. c-11. Effect of shear reinforcement tension deformation on diaphragm ductility.

Diaphragm Reinforcement Properties: The diaphragm reinforcement properties required for the design procedure are determined in conjunction with the selection of the diaphragm reinforcement types based on the Diaphragm Reinforcement Classification. For the prequalified connections, the pertinent connector properties are given in Table A-1 of Appendix 1 of the PART 1 Design Procedure. For new connections, the *Qualification Procedure* provides specific procedures for measuring and characterizing the appropriate connector properties through the use of a qualification backbone. Note that these properties pertain to chord and shear reinforcement.

The diaphragm reinforcement properties that are required for design (in addition to the deformation capacity used to determine the Diaphragm Reinforcement Classification) include:

- Yield strength in tension t_n
- Yield strength in shear v_n

In addition, these properties may be needed depending on the design approach or conditions:

- Elastic stiffness in tension k_t
- Elastic stiffness in shear k_v

The first pair of properties is used in this Step 4 to determine the diaphragm strength design. The second pair of properties is used in Step 5 to determine the diaphragm stiffness, if needed. The manner in which these properties are defined for response in tension and shear are shown in Figure C-4.

The strength properties (t_n, v_n) are also required for the diaphragm-to-LFRS connections.

Fig. C-4. Diaphragm Connector Properties: (a) Tension; (b) Shear.

Note at this time these values must be estimated using rational methods as they were not tested as part of the research program. No strength or stiffness properties are required for secondary connections in the floor system (See discussion after "Diaphragm Reinforcement Strength Design").
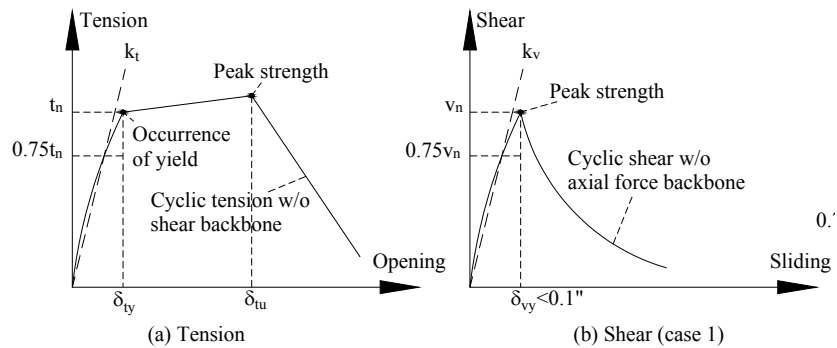

Diaphragm Reinforcement Properties, Design Procedure Step 4:

Figure c-12 shows examples of experimental data from the Lehigh testing program on diaphragm connectors. Fig. c-12a shows the cyclic axial loading of chord reinforcement in a topped precast diaphragm; Fig. c-12b shows the cyclic shear loading of a shear connector in an untopped precast diaphragm. As seen, the definitions of stiffness and strength described in Figure C-4 are applied to the cyclic backbone to determine the design properties of the precast diaphragm reinforcement.
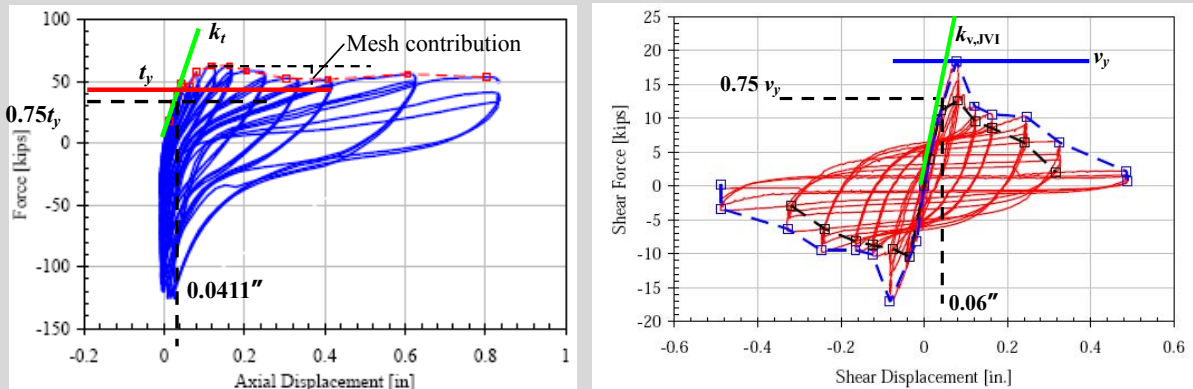
Fig. c-12. Diaphragm Connector Cyclic Tests: (a) Chord reinforcement under tension; (b) Shear connector under shear.

Diaphragm Reinforcement Strength Design: The diaphragm reinforcement is designed using the interaction formula given in PART 1 Eqn. 2 and repeated below:

$$\sqrt{\left(\frac{|M_u|}{\phi_f M_n} + \frac{N_u}{\phi_f N_n}\right)^2 + \left(\frac{\Omega_v V_u}{\phi_v V_n}\right)^2} \leq 1.0 \qquad\qquad (Eqn.\ 2\ from\ PART\ I)$$

The interaction equation is to be applied collectively to all the diaphragm reinforcement along the diaphragm joint being evaluated. Using this equation, diaphragm reinforcement *at a given joint* must possess sufficient nominal strength to resist the diaphragm internal design forces. In this expression, the nominal strength (N_n, V_n, M_n) is expressed as the collective axial, shear and flexural strength of all reinforcement across the joint. Likewise, the diaphragm internal design forces are expressed as the set of internal axial thrust, in-plane shear and in-plane moment acting at the diaphragm joint. These demands represent the required strength and are therefore expressed with the customary notation (N_u, V_u, M_u).

Eqn. 2 pertains to the primary joints in the diaphragm, including those between precast floor units, diaphragm-to-LFRS joints in both orthogonal direction, and internal beam joints. A distinction is made between internal beam connections within and outside of chord lines (Refer to Table C-2), as the latter are not governed by tributary shear requirements. Diaphragm connections in secondary joints in the floor system, including diaphragm-to-spandrel and spandrel-to-column connections, internal beams outside chord lines and ramp-to-lite wall non-LFRS connections, DO NOT require a seismic strength design using Eqn. 2, but may be required to provide deformation capacity (discussed later in this step).

It should be recognized that Eqn. 2 is a general equation intended to cover the significant force combinations that can arise in certain regions of the diaphragm, particularly when analyzing the diaphragm as semi-rigid using computer analysis software. While these combined force conditions should be addressed in the design (*See text box*), there are many cases where Eqn. 2 will simplify considerably:

- In most diaphragms, there are areas strongly dominated by either shear or bending where the interaction of the structural effects is not significant and the dominant action can be compared directly to the capacity of the connections in the joints ($\phi_f M_n > M_u$ or $\phi_v V_n > \Omega_v V_u$).
- When the rigid diaphragm assumption is used, the application of the connection interaction Eqn. 2 can be simplified by removing the axial force term as the beam analogy does not produce separate tension in the diaphragm:

$$\sqrt{\left(\frac{|M_u|}{\phi_f M_n}\right)^2 + \left(\frac{\Omega_v V_u}{\phi_v V_n}\right)^2} \leq 1.0 \qquad\qquad \text{Eqn. 2 - alt}$$

- Collectors and diaphragm-to-LFRS connection can be designed directly for the diaphragm reaction based on note (4), Step 3a and Ω_v=1.0, unless a rational load path method is used.

Diaphragm Strength Interaction Equation, Design Procedure Step 4:

Figure c-13 shows analytical results diaphragm connectors for a joint under significant force combinations, in this case high moment and shear force. The joint is in the outer flat of a precast parking structure with interior shear walls flanking the interior ramp where the ramp meets the ramp landing (See schematic in *Fig. c-13*). This joint is under high shear and bending due to the interior layout of the wall; as well as some (axial) collector action due to the lite walls (*not shown*) along the ramp cavity. The top plots are the *tension* force vs. deformation demands on the connectors; the bottom plots are the *shear* force vs. deformation demands on the connectors. The left hand plots are for a shear connectors; the right hand plots are for the chord connector (See inset in *Fig. c-13*). The blue lines are the hysteretic response measured in the analyses; the red dashed line is the monotonic backbone representing the response of the connector under a single load component (i.e. only tension or only shear).

As can be seen, the combination of forces acting on this joint lead to: (1) significant reduction in both the effective shear and tension force that the shear connector can transfer; and (2) a smaller but still noticeable reduction in the effective tension and shear force that the chord connector can transfer. These results imply the need for the force interaction equation in the design of diaphragm reinforcement in certain regions of the floor.
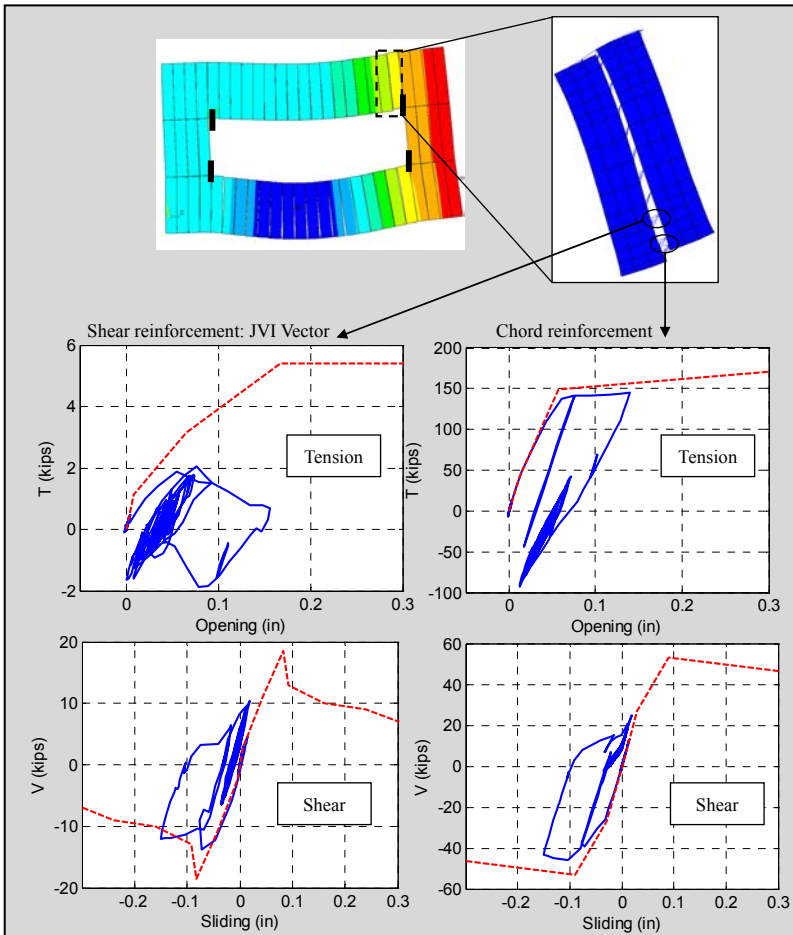

Fig. c-13. Diaphragm reinforcement hysteretic response under combined forces.

Figure c-14 shows the effectiveness of the design procedure with respect to the interaction equation for elastic diaphragm performance, i.e., designing to the EDO force level. The plot shows the maximum internal force demands in a MCE hazard earthquake simulation of the prototype Parking Structure with EDO diaphragm designs.

The forces are expressed as a design unity ratio, i.e. the ratio of demand to strength, by replacing the required strength (M_u, N_u and V_u) in the interaction equation (Eqn. 2) with the maximum value produced by the simultaneous values from the force time histories $M(t)$, $N(t)$ and $V(t)$ measured during the earthquake analysis. These values are plotted along the diaphragm (each marker represents a joint between precast units) for each of the four floor levels for the prototype structure. The north, south and ramp sub-diaphragms are plotted separately (refer to schematic in Fig. c-14). Also shown on the plot as a dashed line is the unity ratio produced in the EDO design (showing values less than unity where the design produced an overstrength).

As seen in Fig. c-14, the interaction equation predicts well the force demands for the majority of joints in the structure, with some joints at lower unity ratios (0.5-0.7), and a small number of joints close to or just exceeding unity. Note that a design based on *maximum* moment and shear will be less efficient at many joints.
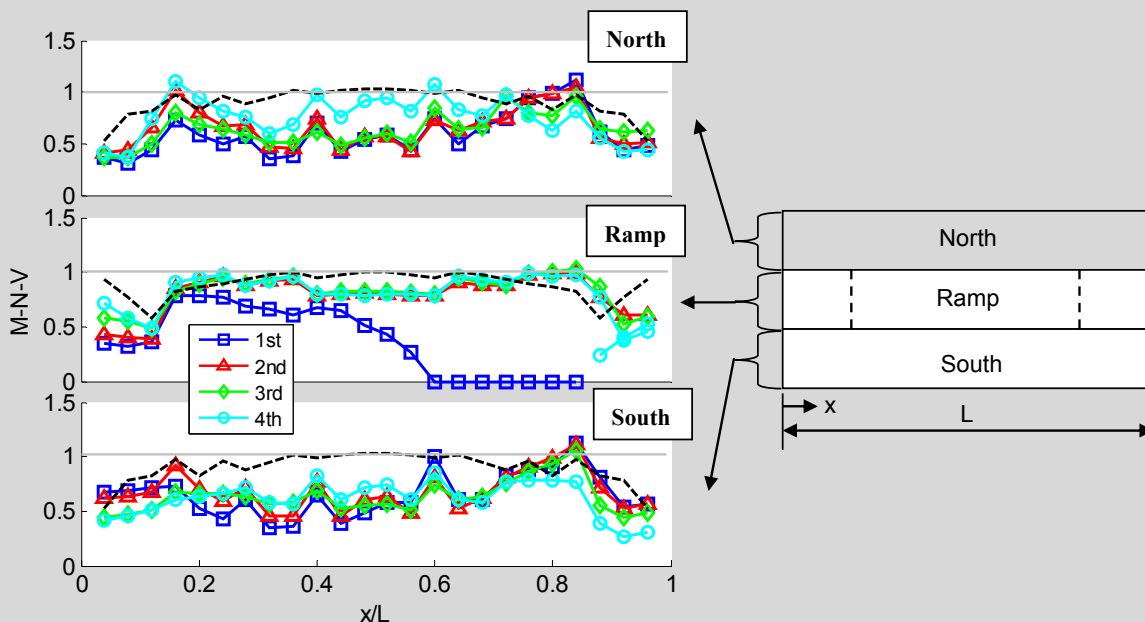

Fig. c-14. Prototype Parking Structure, EDO Design, MCE Hazard: Diaphragm joint (M-N-V) demand ratio.

Figure c-15 shows the effectiveness of the interaction equation (Eqn. 2, PART 1) for *inelastic* diaphragm performance, demonstrated here for an RDO design for the prototype precast parking structure. In this case, the interaction equation, used with the RDO R_s and Ω_v factors, is intended to provide sufficient strength to the diaphragm that will translate into: (a) diaphragm inelastic flexural deformations under MCE level hazard that remain below the High Deformability Element (HDE) allowable deformation of 0.4″ joint opening; and (b) diaphragm shear forces under MCE level hazard that are carried elastically. Note the distinction with the previous example involving the EDO design (*Fig. c-14*), where the interaction equation in intended to directly provide the strength required to keep the diaphragm *elastic* under MCE level hazard.

The *Figure c-15* plot shows the maximum deformation demands on the diaphragm reinforcement for every joint in the prototype structure: (a) the top set of plots shows the joint opening acting on the diaphragm chord reinforcement; (b) the lower set of plots shows the relative shear deformation of the panels at each joint ("sliding"), acting on the diaphragm shear reinforcement. Note that each set of plots shows results for each of the parking structure sub-diaphragms (north flat, ramp and south flat) As seen in *Fig. c-15a*, the RDO design produces inelastic chord deformation (opening) demands below the HDE allowable value of 0.4″ at all joints in the structure. Likewise, as seen in *Fig. c-15b*, the RDO design produces elastic shear response (sliding deformation demands below the yield value) for all joints in the structure. Together, these outcomes describe successful achievement of the RDO performance requirements. Further comment on this performance is found later in this commentary on step 4 in the subsection pertaining to Capacity Design Considerations.
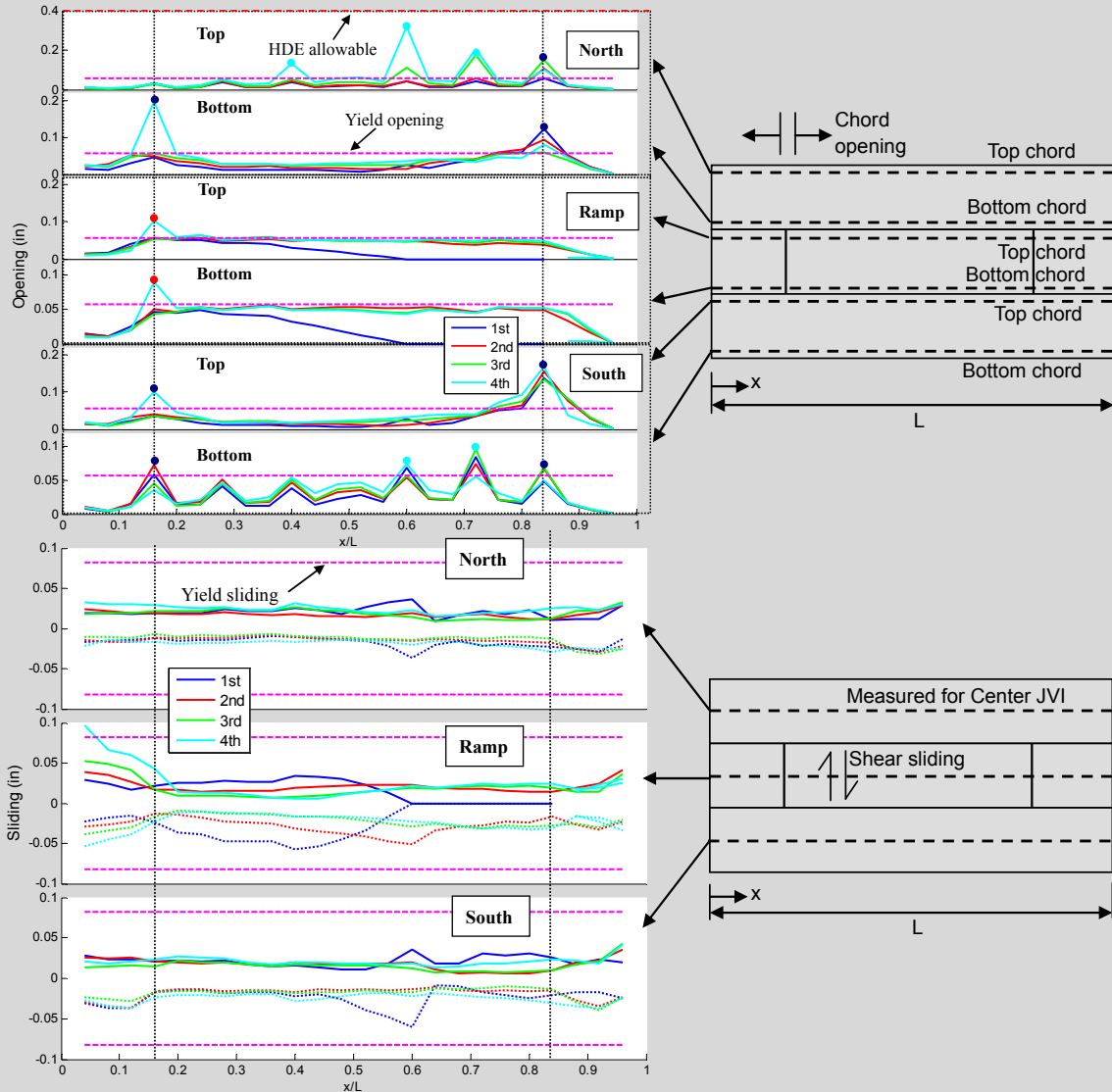

Fig. c-15. Diaphragm reinforcement deformation demands, RDO Design, MCE Hazard: (a) chord opening; (b) shear sliding.

48

Diaphragm Nominal Strength: An estimation of the diaphragm nominal shear and flexural strength, V_n and M_n, must be calculated, whether using a simplified approach like the horizontal beam method or a more involved procedure. If using the general (unreduced) interaction equation (PART 1 Eqn. 2) associated with a semi-rigid diaphragm analysis, an estimation of the diaphragm nominal axial strength N_n is also needed.

The diaphragm joint design moment strength (M_n) is calculated based on the design option (EDO, BDO, RDO), to align the diaphragm strength with the performance target (e.g. elastic or inelastic response). In the design procedure, M_n is determined using the following equations:

For Elastic Design Option (EDO): $M_n = M_y$ (*Eqn. 4a from PART 1*)

For Basic Design Option (BDO): $M_n = \dfrac{1+\Omega_d}{2} M_y$ (*Eqn. 4b from PART 1*)

For Reduced Design Option (RDO): $M_n = \Omega_d M_y$ (*Eqn. 4c from PART 1*)

where M_y is the nominal yield moment strength of the precast diaphragm joint and Ω_d is diaphragm flexural overstrength factor. The diaphragm nominal flexural strength is considered further below:

Two diaphragm flexural limit states are illustrated in the internal force schematics of a precast joint in Figure C-5: (a) the yield moment M_y; and (b) the plastic moment M_p. The former represents the moment when the chord reinforcement, located at the end of the joint (analogous to the extreme fiber in a beam cross-section), reaches its yield stress (and strain). Note that the reinforcement along the remainder of the diaphragm joint will still be in the elastic range, unless the shear reinforcement yield deformation is significantly lower than that of the chord reinforcement (See Fig. C-5a). The latter represents the moment at which all the reinforcement along the joint has yielded (See Fig. C-5b), and thus occurs at a higher moment, and after the joint has undergone some plastic rotation.
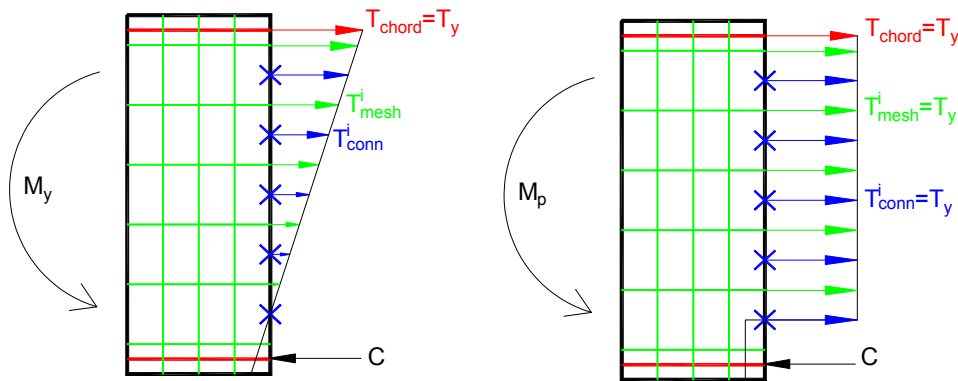

Figure C-5. Joint force distribution at: (a) yield moment; (b) plastic moment.

The ratio of M_p/M_y, that is how much larger the moment at full joint yielding is to when the diaphragm joint reaches initial yielding (See text box), is termed the diaphragm overstrength, and represented by the term Ω_d. Since the yield moment M_y represents the limit of the elastic range of diaphragm response, it is associated with the EDO (Eqn. 4a). The plastic moment, associated with developing inelastic deformation capacity in the diaphragm, is associated with the RDO, as expressed by $M_p=\Omega_d M_y$ (Eqn. 4c). The BDO employs an average value of the two limit values (Eqn. 4b).

As is typically done in current practice, the nominal yield moment M_y can be taken conservatively as $t_n^{chrd} d'$ where the chord yield force $t_n^{chrd} = A_s f_y$ and d' is the depth between chords. However, depending on the tension stiffness characteristics and the depth of the diaphragm joint, the contribution of the shear reinforcement to the diaphragm flexural strength may be significant. Thus, it may be economically advantageous to calculate the diaphragm joint flexural strength based on all reinforcement crossing the joint, i.e. as shown in Fig. C-5a, though this involves a more involved calculation. This calculation can be accomplished through a strain curvature analysis or pushover analyses as described subsequently.

Likewise, the overstrength of the diaphragm can be ignored ($\Omega_d = 1.0$) or estimated using approximate but conservative values. The approximate values proposed in the diaphragm seismic design methodology are *1.0* for a *pretopped* diaphragm, and *1.25* for a *topped* diaphragm. The distinction between diaphragm construction types is made because the topped system, typically consisting of shear reinforcement (web connectors, wire mesh or bars) that is stiffer and stronger in tension than the pretopped system, typically has a larger flexural overstrength than the pretopped system (See text box). Ω_d can be alternately determined from a strain curvature analysis or pushover analyses as described next.

Diaphragm Nominal Strength, Design Procedure Step 4:

Figure c-16 compares the response of typical topped and pretopped diaphragms of the same nominal yield strength, M_y. *Figure c-16a* shows the global pushover response curve (refer to inset Fig. C-I): diaphragm force (expressed as the inertial force acceleration as a percentage of g) vs. midspan diaphragm deformation. Figure c-16b shows the corresponding local response of the critical midspan joint: in-plane diaphragm moment vs. rotation of the joint, indirectly expressed as the joint opening deformation at the chord.

As can be seen in *Fig. c-16b*, the topped and pretopped systems share the same yield moment. However, the post-yield response of the systems is significantly different: the topped system develops significant overstrength (a M_p higher than M_y), while the pretopped system develops almost no overstrength ($M_p \approx M_y$). This result is due entirely to the characteristics of the *shear reinforcement* used in these two systems, with the typical pretopped diaphragm using tension-compliant shear connectors (e.g. JVI Vector), whose contribution to flexure is negligible when compared to the chord reinforcement strength; while the topped system possesses distributed mesh reinforcement that possesses sufficient tension strength to provide a significant increment of moment strength as the diaphragm joint moves from yield (Fig. C-5a) to plastic or ultimate flexural strength (Fig. C-5b).

As seen in *Figure c-16a*, the overstrength in flexural strength provided by the shear reinforcement contribution to the critical midspan flexure joint in the typical topped diaphragm, translates directly to increased diaphragm strength for the (flexure-contolled) topped diaphragm. It is noted that the larger overstrength observed for the topped vs. pretopped diaphragm is due to the typical shear reinforcement used in construction; thus it is at least theoretically possible to design a pretopped diaphragm with large overstrength, and a topped diaphragm with lower overstrength.

It is additionally noted that the shear reinforcement will also contribute to the yield moment itself (Fig. C-5a), with a more significant contribution in the topped case; thus the same yield moment can be achieved with less chord reinforcement if the nominal flexural strength calculation includes the shear reinforcement (as described in the next section).

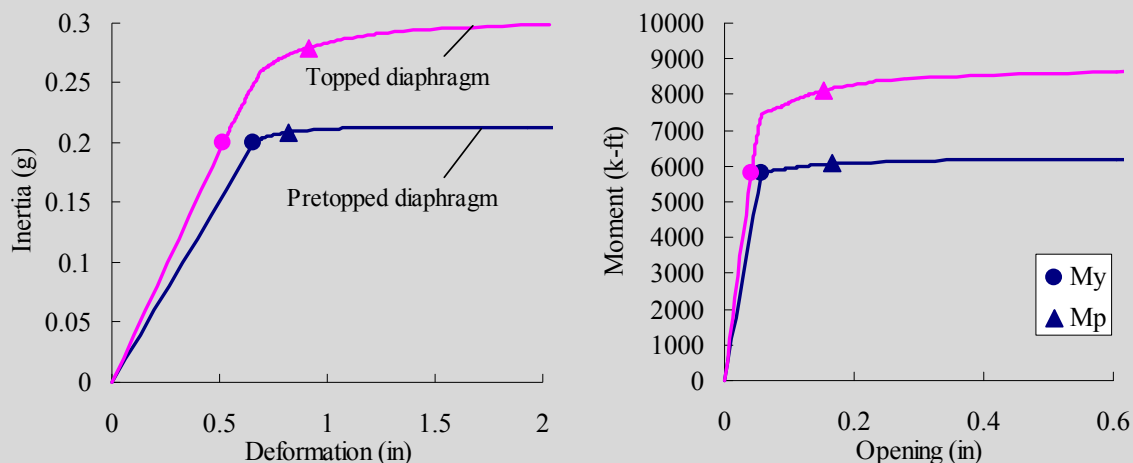**Figure c-16.** Pushover analyses: (a) Diaphragm global response; (b) Midspan flexural response.

The approach to designing the precast diaphragm reinforcement as a group along the joint, based on all reinforcement crossing the joint, though consistent with recent code modifications that permit the contribution of the shear reinforcement to the diaphragm flexural strength (ACI, 2008), is substantially

different than the procedures used in current practice The following can be included for the reinforcing elements (connectors, bars or mesh) across the precast diaphragm joint when calculating the nominal diaphragm strength: (a) shear reinforcement contribution to flexure; (b) chord reinforcement contribution to shear; and (c) diaphragm reinforcement contribution to axial force. Note that these do not need to be considered, but are available to the designer to make the design more economical.

Diaphragm Strength and Stiffness Calculations: If a designer decides to take advantage of all the reinforcement crossing the joint in determining the diaphragm nominal flexural strength, the procedure is more involved than the simple calculations of the horizontal beam method. As such, a rational method has been developed to determine the diaphragm joint flexural strength (and stiffness). The method, originally appearing in (BSSC 2009), makes a reasonable estimation of the neutral axis (NA) and employs Bernoulli principles to estimate the flexural stiffness and strength of the diaphragm.

The derivation of the method appears in "*3.3 DIAPHRAGM JOINT STIFFNESS AND STRENGTH CALCULATION"* in PART 3 of the *Seismic Design Methodology*. The method has also been embedded in a computer spreadsheet utility for ease of use, as described in "3.4 DESIGN AIDS FOR DIAPHRAGM DESIGN: SPREADSHEET PROGRAM" in PART 3 of the *Seismic Design Methodology*. The *Design Aid Spreadsheet* is available for download with the *Design Methodology* Documents.

The expressions used in the rational method are summarized here in the commentary. *Please refer to PART 3* of the *Seismic Design Methodology for full details of the method and spreadsheet.*

Rational Method Summary: The procedure uses the panel geometry, concrete properties, connector layout and connector stiffness and strength properties to approximate: (A) the diaphragm stiffness; (B) the diaphragm yield moment M_y and (C) the diaphragm plastic moment M_p. The diaphragm axial and shear strength can also be calculated.

Rational Method Terminology: Figure C-6 shows a schematic of the panel joint and flexural actions indicating the notation used for dimensions and forces. The connector properties required are those described in Table A-1 in the PART 1, Design Procedure APPENDIX 1, and labeled here in Table C-3 to distinguish between the chord reinforcement, the shear reinforcement and a distributed topping reinforcement, if present. The modulus of concrete E_c, can be taken as the full ACI 318 (2005) value.
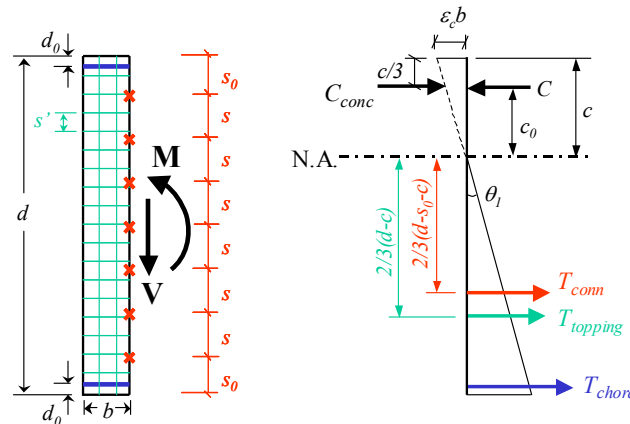
Figure C-6. FBD of diaphragm joint used to determine initial stiffness.

Table C-3. Design requirement for diaphragm reinforcement.

Reinforcement	Elastic stiffness		Yield strength		Yield deformation	Secant stiffness
	Tension (k_t)	Shear (k_v)	Tension (t_n)	Shear (v_n)	Tension (δ_{ty})	Tension (t_n/δ_{ty})
Chord	$K_{t,chord}$	$K_{v,chord}$	$T_{y,chord}$	$V_{y,chord}$	$\delta_{y,chord}$	$K'_{t,chord}$
Shear	$K_{t,conn}$	$K_{v,conn}$	$T_{y,conn}$	$V_{y,conn}$	$\delta_{y,conn}$	$K'_{t,conn}$
Topping	$K_{t,topping}$	$K_{v,topping}$	$T_{y,topping}$	$V_{y,topping}$	$\delta_{y,topping}$	$K'_{t,topping}$

51

A. Diaphragm Stiffness

Step 1: Determine Neutral Axis Location, c

$$c = \frac{-A_2 + \sqrt{A_2^2 - 4A_1 A_3}}{2A_1} \qquad \text{(Eqn C-4)}$$

where, $A_1 = \frac{1}{2}(E_c t / b - K_{t,conn} / s - K_{t,topping} / s')$,

$\qquad A_2 = K_{t,chord} + K_{t,conn} / s \cdot (d - s_0) + K_{t,topping} / s' \cdot (d - 2d_0)$,

and $\quad A_3 = -[K_{tc}(d - d_0) + \frac{1}{2} K_{t,conn} / s \cdot (d - s_0)^2 + \frac{1}{2} K_{t,topping} / s' \cdot (d - 2d_0)^2]$

Step 2: Determine Center of Compression, c_0

Topped diaphragm:
$$c_0 = 2/3 \cdot c \qquad \text{(Eqn C-5a)}$$

Untopped diaphragm (dry system):
$$c_0 = \frac{K_{c,chord}(c - d_0)^2 + 1/3 \cdot K_{c,conn} / s \cdot (c - s_0)^3}{K_{c,chord}(c - d_0) + 1/2 \cdot K_{c,conn} / s \cdot (c - s_0)^2} \qquad \text{(Eqn C-5b)}$$

Untopped system (pour strip):
$$c_0 = c - d_0 \qquad \text{(Eqn C-5c)}$$

Step 3: Determine Diaphragm Joint Initial Rotational Stiffness, K_Θ

$$K_\Theta = \frac{1}{2b} E_c t c^2 c_0 + K_{t,chord}(d - d_0 - c)^2 + \frac{K_{t,conn}}{3s}(d - s_0 - c)^3 + \frac{K_{t,topping}}{3s'}(d - c - 2d_0)^3 \qquad \text{(Eqn C-6)}$$

Step 4: Determine Diaphragm Joint Shear Stiffness, K_γ

$$K_\gamma = 2K_{v,chord} + \left(\frac{d - 2s_0}{s} + 1\right) K_{v,conn} + d / s' K_{v,topping} \qquad \text{(Eqn C-7)}$$

Step 5: Determine Diaphragm Effective Elastic Modulus, E_{eff}

$$E_{eff} = \frac{E_c b K_\Theta}{b K_\Theta + E_c I} \qquad \text{(Eqn C-8)}$$

Step 6: Determine Diaphragm Effective Shear Modulus, G_{eff}

$$G_{eff} = \frac{1.2 b G_c K_\gamma}{1.2 b K_\gamma + A G_c} \qquad \text{(Eqn C-9)}$$

Note that the E_{eff} and G_{eff} values represent the stiffness of one panel and joint region. If the reinforcement varies in the diaphragm (bar cut-offs, more shear connectors at diaphragm end, etc.), the values of E_{eff} and G_{eff} will be dependent on the particular joint these calculations are made. See Step 5 Commentary for acceptable techniques for approximating the overall diaphragm stiffness in these cases.

B. Diaphragm Yield Moment

Step 1: Determine Diaphragm Yield Rotation, θ_y

$$\theta_y = \min\left[\delta_{y,chord}/(d-d_0-c), \delta_{y,conn}/(d-s_0-c), \delta_{y,topping}/(d-2d_0-c)\right] \qquad \text{(Eqn C-10)}$$

Step 2: Determine Diaphragm Joint Secant Rotational Stiffness, K'_{Θ}

Repeat Equations C-4 to C-6 in Steps 1 to 3 of the diaphragm Stiffness Calculation using secant stiffness (See Table C-3) rather than elastic stiffness of connectors to calculate K'_{Θ} in Eqn. C-6.

Step 3: Diaphragm Yield Moment, M_y

$$M_y = K'_{\Theta} \cdot \theta_y \qquad \text{(Eqn C-11)}$$

C. Diaphragm Plastic Moment, M_p

Step 1: Assume location of plastic neutral axis (20% of diaphragm depth):

$$c = d / 5 \qquad \text{(Eqn C-12)}$$

Step 2: Determine Center of Compression, c_0

Calculate value by selecting appropriate Eqn. C-5a to C-5c.

Step 3: Calculate diaphragm plastic moment strength:

$$M_p = T_{y,chord}(d - d_0 - c + c_0) + T_{y,conn}\frac{d-c-s_0}{s}\left(\frac{d-c-s_0}{2}+c_0\right) + T_{y,topping}\frac{d-c-2d_0}{s'}\left(\frac{d-c-2d_0}{2}+c_0\right) \qquad \text{(Eqn C-13)}$$

Step 4: Calculate diaphragm overstrength, Ω_d :

$$\Omega_d = M_p / M_y \qquad \text{(Eqn C-14)}$$

Diaphragm Joint Shear Strength Calculation:
The diaphragm joint shear strength is given in the design procedure are:

$$V_n = \sum v_n \qquad \textit{(Eqn. 3b from PART 1)}$$

This diaphragm joint shear strength can be calculated as the sum of the yield shear strengths of all the reinforcement across the joint:

$$V_n = 2V_{y,chord} + \left(\frac{d-2s_0}{s}+1\right)V_{y,conn} + \left(\frac{d-2d_0}{s'}+1\right)V_{y,topping} \qquad \text{(Eqn. C-15)}$$

Note that the chord connections can contribute to both moment and shear strength. The shear strength of the chord may be limited by the strength of the welds or by the strength of the chord reinforcement, as determined in testing. The values for chord shear strength in Appendix 1 are based on the qualification testing of these details. It is acceptable to determine the shear strength for the chord reinforcement in a topping either by shear friction, $\varphi f_y A_s \mu$, or by the direct shear strength of the reinforcement as dowels, $\varphi 0.6 f_y A_s$.

The shear strength at the joint, then, can be taken as the sum of the shear strength of the chord connectors and the summed shear strength of the shear connectors between the chords. The shear connections can be proportioned to carry the total shear demand in the joint, but the chord connection may still attract a portion of the shear and must be checked to ensure that chord design satisfies the combined forces by applying Eqn. 2 from PART 1.

Diaphragm Joint Axial Strength Calculation:

If using the general (unreduced) interaction equation (PART 1 Eqn. 2) associated with a semi-rigid diaphragm analysis, an estimation of the diaphragm nominal axial strength N_n is also needed.

The diaphragm joint shear strength is given in the design procedure are:

$$N_n = \sum t_n \qquad \text{(Eqn. 3a from PART 1)}$$

This diaphragm joint axial strength can be calculated as the sum of yield tension strength of all the reinforcement across the joint:

$$N_n = 2T_{y,chord} + \left(\frac{d - 2s_0}{s} + 1\right)T_{y,conn} + \left(\frac{d - 2d_0}{s'} + 1\right)T_{y,topping} \qquad \text{(Eqn. C-16)}$$

Diaphragm Strength and Stiffness Calculation, Design Procedure Step 4:

Figure c-17 shows pretopped diaphragm stiffness and strength values for a wide variety of diaphragm aspect ratios and lengths. The figures compare the response of a nonlinear pushover analysis of using a finite element model of the diaphragm that models the reinforcement at the joint discretely with values obtained from a design calculation using the results of the rational method described in Eqns. C-4 to C-11.

In Figure c-17a a comparison of the displacement at midspan under the diaphragm design load is given for the computer analysis versus a design calculation using the effective moduli E_{eff} and G_{eff} (Eqns. C-8, C-9). As seen, the method produces a reasonably accurate match to the analysis across a range of aspect ratios, diaphragm lengths, and diaphragm reinforcement details. In particular, the method can accurately predict stiffness for both shear dominated (low aspect ratio) and flexure dominated (large aspect ratio) diaphragms.

Figure c-17b compares the moment strength for the diaphragm, (expressed in terms of the inertial force acceleration that produces the nominal moment strength) produced by computer analysis to the value calculated with Eqn. C-11 . As seen, the method again produces a reasonably accurate match to the analysis across a range of aspect ratios, diaphragm lengths, and diaphragm reinforcement details, with slight underestimation for shear critical diaphragms (shorter aspect ratios).
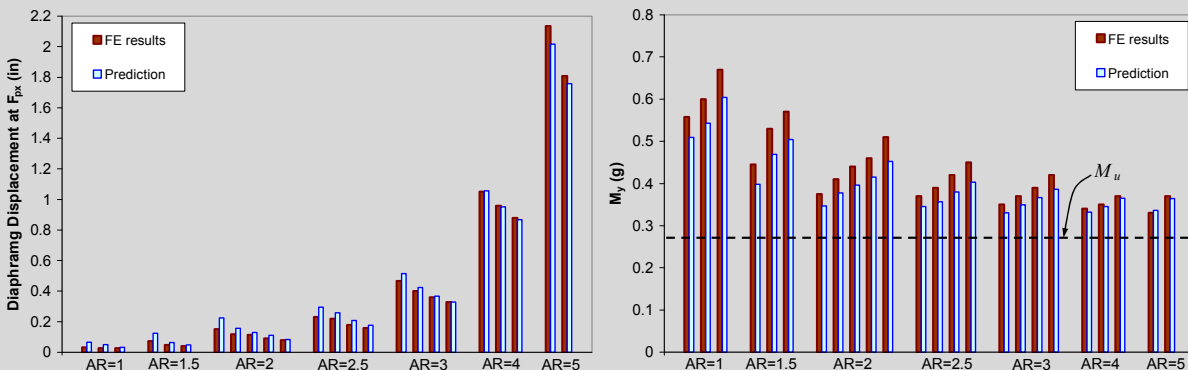

Figure c-17. Comparison with FE analysis: (a) Diaphragm stiffness; (b) Yield strength.

Step 5: Determine diaphragm stiffness and check gravity system drifts

      Step 5 Description. In this step, diaphragm stiffness is calculated, if necessary, for: (1) semi-rigid diaphragm models used in computer structural analysis and/or (2) to check gravity system column inter-story drifts amplified by diaphragm flexibility. The diaphragm stiffness is expressed in the form of an effective elastic modulus (E_{eff}) and effective shear modulus (G_{eff}), for ease of insertion into computer structural analysis programs. The need for a drift calculation is determined by a check using Table 3 of PART 1. If a drift check calculation is necessary, the procedure is found in Appendix 3.

      Step 5 Commentary:

      An estimation of the precast floor diaphragm elastic stiffness is required in the design procedure when one of the following conditions exist: (1) semi-rigid diaphragm models used in computer structural analysis, in particular those with redundant lateral force resisting layouts where diaphragm stiffness is required in determining diaphragm internal force distributions; and (2) in long span diaphragms, where diaphragm stiffness is required to perform a drift check on gravity system columns.

      Discussion on Diaphragm Stiffness

      A diaphragm stiffness calculation has not typically been part of current design. For precast construction, the combination of higher inherent flexibility of paneled systems with the effective use of these systems for structures with long floor spans can create a highly flexible diaphragm. Diaphragm flexibility can impact diaphragm response in several ways, including modifying: (1) Structure Period; (2) Diaphragm Force Magnitude; (3) Diaphragm Internal Force Path; and, (4) Gravity System Drift. Each of these is discussed in more detail below.

      Structure Period: The period of the structure will lengthen due to diaphragm flexibility. It was the consensus of the development team that the design factors be calibrated relative to current design forces, i.e. on the forces based on the period calculated in current design, which is based on a rigid diaphragm. In fact, as the diaphragm maximum forces are related strongly to the higher modes, the need to tie it to the fundamental period adjusted for diaphragm flexibility is less important than other measures. Thus the diaphragm design force factors, though based on analyses incorporating diaphragm flexibility, are mapped onto the response of a rigid diaphragm design. For this reason, a special calculation of period, different than what is already done, is not required. It should be noted that for long span precast diaphragms, the structure period including the effect of diaphragm flexibility is typically longer than the maximum design period permitted in current code, C_uT_a (ASCE 7 2010). Therefore it was deemed unnecessary to recalculate the structure period including the effect of diaphragm flexibility.

      Diaphragm Force Magnitude: The magnitude of diaphragm force is affected by diaphragm flexibility (Farrow and Fleischman 2003). The effect of diaphragm flexibility (on both diaphragm force and drift) is a complex combination of the floor's absolute stiffness and its relative stiffness with respect to the LFRS (Fleischman and Farrow 2001). The effect of diaphragm flexibility on diaphragm force is handled indirectly in the design procedure as the original diaphragm force amplification factor equations for ASCE 7-10 include diaphragm length L and aspect ratio AR (See Appendix 4). This effect is realized in the updated design force equations (Step 3a, PART 1) through flexible diaphragm acceleration amplification factors (α_{fx}) according to Eqn.12.11-12 of proposal IT06-001 for the ASCE 7-14 provisions. Since the diaphragm flexibility is more significantly affected by geometry, the effect the magnitude of the diaphragm inertial force due to the variation of stiffness caused by different diaphragm reinforcement details is not required in determining the diaphragm amplification factor (Schoettler, 2010). It is further noted that the most significant effect on diaphragm force is due to higher order modes (Rodriguez et al. 2002), as realized in Eqns. 3-5 through the number of stories (*n*) parameter and the total effect of diaphragm flexibility (geometry and rigidity) is secondary (Fleischman and Farrow 2001) to this larger effect (See *Background* Appendices *A1)*.

      Diaphragm Internal Force Path: The internal force paths that develop within the floor system can depend on the relative shear and elastic in-plane stiffness of the floor system relative to each other, and

the LFRS elements. (including tributary reactions to the LFRS elements) for diaphragms with redundancy in LFRS layout, displacement compatibility conditions (dual system) or inter-story elements (e.g. ramps). The difference in diaphragm stiffness is not critical for diaphragm internal force paths for determinate LFRS layouts (See *Background* Appendices A2.4.6). However, when using the semi-rigid diaphragm option (See *Commentary Step 4*) for indeterminate LFRS layouts, it is important to insert the proper stiffness values for the diaphragm to get the proper proportion (See discussion in *Commentary Step 4*).
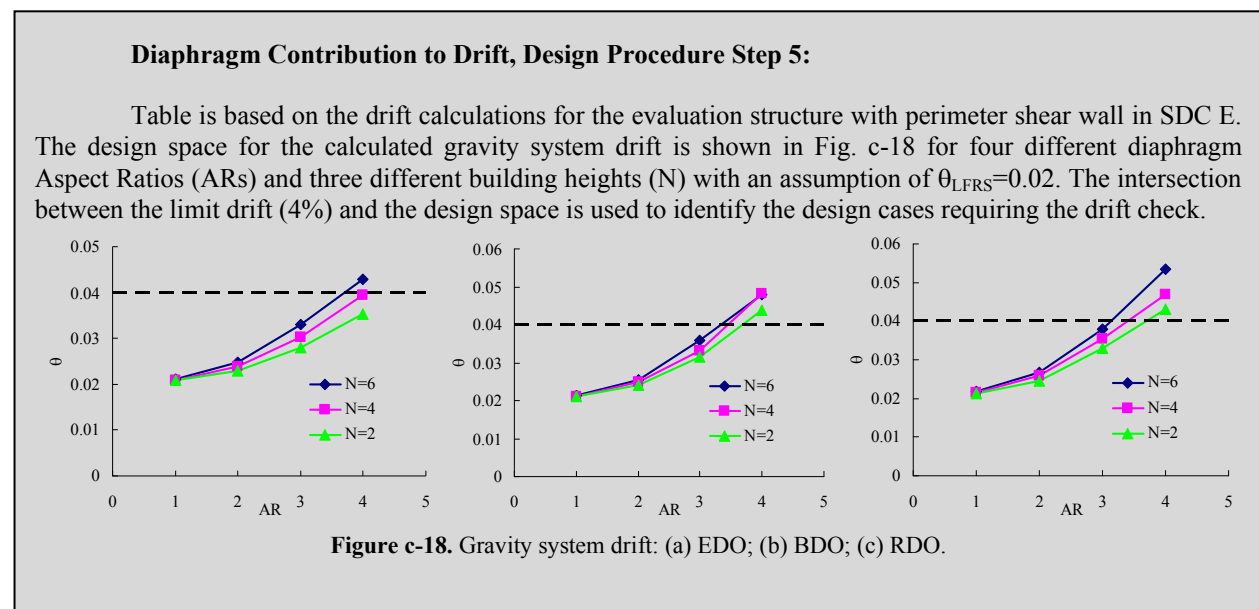
Gravity System Drift: Diaphragm stiffness is required in performing a drift check for gravity system columns remote to LFRS elements. Most diaphragm configurations and building geometries are such that the diaphragm does not contribute significantly to gravity system columns drifts due to compatible displacement. However, for highly flexible diaphragms (due mostly to geometry, but also to inherent flexibility in the precast floor system construction), gravity system columns remote to the primary (vertical) elements of the LFRS may undergo too large of a lateral drift (Fleischman et al. 1998) (Rhodes et al. 1997). This design check is performed in Step 5.

For precast concrete structures with long floor spans, e.g. parking structures, unacceptable gravity column inter-story drift at regions remote to the primary LFRS might occur during a seismic event due to the drift increment from diaphragm deformation (Fleischman et al. 1998) (Fleischman and Farrow 2001). Therefore the gravity column inter-story drift is checked explicitly in the design procedure

Drift Check Determination

The need for a drift calculation is determined by checking the design conditions relative to the values in Table 3 of PART 1. Table 3 provides the critical diaphragm aspect ratio where a drift check is required, and is a function of building height and diaphragm design option (taller buildings can have more significant gravity system drifts, and an inelastic diaphragm has a reduced stiffness after yielding, which can contribute more to drift due to diaphragm deformation).

The relationship between diaphragm flexibility and amplified gravity system drift was determined through analytical research, and approximated using design equations in Appendix 3. In order to simplify the design procedure, Table 3 provides a first check to determine if that amplification is significant. Thus, the intent of the design procedure is to only perform a drift check for cases where the diaphragm flexibility may have an effect on the design drift. The values in the table are chosen such that the conditions result in the gravity system drifts passing the threshold of 4% drift in the MCE for a 2% drift of the lateral force resisting system (See text box).

Diaphragm Contribution to Drift, Design Procedure Step 5:

Table is based on the drift calculations for the evaluation structure with perimeter shear wall in SDC E. The design space for the calculated gravity system drift is shown in Fig. c-18 for four different diaphragm Aspect Ratios (ARs) and three different building heights (N) with an assumption of θ_{LFRS}=0.02. The intersection between the limit drift (4%) and the design space is used to identify the design cases requiring the drift check.

Figure c-18. Gravity system drift: (a) EDO; (b) BDO; (c) RDO.

Precast Diaphragm Effective Stiffness

Equations C-8 and C-9, introduced in the commentary for Step 4 on rational methods, produce effective moduli, an effective elastic modulus E_{eff} and an effective shear modulus G_{eff}. The need for both properties arises from the non-negligible contribution of shear deformation in precast concrete floor diaprhagms, due to aspect ratio geometry, and shear flexibility at the joints between precast units. Note that the effective modulus values represent the combined stiffness of one panel and joint region.

Note that if the reinforcement varies in the diaphragm (bar cut-offs, more shear connectors at diaphragm end, etc.), the values of E_{eff} and G_{eff} will be dependent on the particular joint these calculations are made. The designer can attempt to analyze the diaphragm with the changing stiffness, however it maybe more expedient to calculate an average value to use across the diaphragm.

Approximate methods to produce an average E_{eff} and G_{eff} for the diaphragm, include:

1. Use the E_{eff} calculated at midspan, and the G_{eff} calculated at the end span. Reasonable and quick, but will tend to underestimate diaphragm deformations for typical varying diaphragm reinforcement layouts.

2. Use the average of the E_{eff} and G_{eff} values calculated at midspan and end span. This is typically a better estimate, and relaltively quick, but will tend to overestimate diaphragm deformations for typical varying diaphragm reinforcement layouts.

3. Use a weighted average of the E_{eff} and G_{eff} values calculated at midspan and end span (suggest 0.75, 0.25 for flexure; 0.25, 0.75 for shear where the first number of the pair is the weighted value for midspan). This approach will provide a good estimate, and is still relatively simple.

See the Commentary to Appendix 3 for different methods to calculate diaphragm deformation, either by using the changing diaphragm stiffness, or by calculating an average value to use across the diaphragm. It is noted that the design aid spreadsheet provided with the design methodology is capable of producing deflection calculations based on varied stiffness at each diaphragm joint.

Effective Moduli, Design Procedure Step 5:

Figure c-19 shows the ratio of effective moduli to the gross section moduli (E_c, G_c) for a three story precast structure using different diaphragm details. The effective Moduli (E_{eff} and G_{eff}) are calculated at top floor using Equation C-8 and C-9.

As seen, the effective elastic modulus ranges from 30%~45% of the gross section elastic modulus while the effective shear modulus ranges from 15%~45% of the gross section shear modulus.

The accuracy of these values, relative to nonlinear finite element analysis of precast diaphragms of different geometry, was demonstrated in *Figure c-17*.
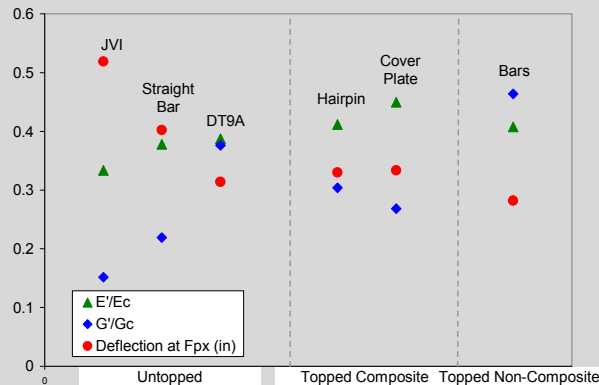

Figure c-19. Effective precast diaphragm moduli for different design details.

Commentary to Appendix 1: Prequalified Diaphragm Connections.

Table A-1 provides the classifications and connector properties for the precast diaphragm reinforcement that was "pre-qualified" through testing in the DSDM project and other conforming testing programs.

The classification of the particular reinforcement or connector (HDE, MDE or LDE) can be read directly from the table.

The properties provided in Table A-1 can be directly input into Equations C-4 to C-16 to calculate diaphragm strength and stiffness for diaphragms using the prequalified diaphragm connections. These properties are determined based experimental data from the Lehigh testing program on diaphragm reinforcement and connector.

Table A-1a provides the values for precast diaphragm reinforcement comprised of bars, while Table A-1b provides the same for precast diaphragm connectors. Note that while for the latter, values are read directly (per connector), for the former the strength and stiffness properties are normalized by the reinforcement bar area. This permits a designer to use the table for different sized bars, by multiplying the stiffness and strength value in Table A-1a by the nominal area of the reinforcement bar being used (as well as the number of bars) before inserting into Equations C-4 to C-16.

It is anticipated that new reinforcement, once tested through the qualification protocols described in PART 2 of the Diaphragm Seismic Design Methodology, will be added to this Appendix.

Please consult in PART 2 of the Diaphragm Seismic Design Methodology for more detailed explanations of the prequalification and qualification protocols, and acceptance criteria.

Commentary to Appendix 2: Connector Deformation Capacity.

The shear and chord reinforcement are subjected to the diaphragm reinforcement classification and thus have prescriptive deformation capacity requirements (See Table A2, Appendix 2). As indicated in Table C-2 (*Commentary for Step 4*), and reproduced below in Table C-A2.1, additional deformation requirements or recommendations exist for the connections in the floor system that are not covered by the diaphragm reinforcement classification. Appendix 2 provides these deformation requirements - for the diaprhragm to lateral force resisting system (LFRS) connections, and recommendations – for the so-called "secondary" connections in the floor system: spandrel and IT beam connections; non-LFRS lite wall connections, etc.

Table C-A2.1 Design requirement for diaphragm reinforcement.

Design Requirement	Diaphragm reinforcement		Diaphragm to LFRS	Collector	Internal beam Connection		Spandrel connection
	Chord	Shear			Within chord	Outside chord	
Force Determination	X	X	X	X	X[1]	X	
Interaction Equation	X	X	X		X	X	
Connector Classification	X	X					
Addtl. Defo. Reqs.[2]			X		X	X	X

[1] Tributary shear (VQ/I)   [2] Allowable or Recommended: See Appendix 2

Deformation Requirements for Diaphragm-to-LFRS Connections:

The tension deformability requirements associated with the Diaphragm Reinforcement Classification are not applicable to the diaphragm-to-LFRS connection. Thus, the diaphragm-to-LFRS connection has a separate set of deformation capacity requirements.

The joint between the diaphragm and the LFRS does undergo deformation demands in an earthquake, but they do not resemble the demands occurring within the floor system. This outcome is partially due to dominance of shear force in the total diaphragm reaction to the LFRS, which creates a largely force-controlled design due to shear overstrength factor Ω, and partially due to LFRS layout within the floor plan geometry which in most cases has limited moment demand at this joint.

In particular, the diaphragm-to-LFRS connection deformation demands are not as directly related the design option selected, as is the case for the chord and shear reinforcement. Analytical results for prototype structures using the design methodology indicate that most connectors within a diaphragm-to-LFRS connection, remain elastic under MCE demand regardless of design option (EDO, BDO, RDO), except for localized small inelastic deformation for a portion of the connectors due to non-uniform distribution along the joint between diaphragm and LFRS (*See text box*).

In essence, the connectors in the diaphragm-to-LFRS connection require a measure of inelastic deformation capacity to allow the anchorage forces to redistribute along the LRFS. This condition occurs primarily because while typically considered a pure shear reaction, the diaphragm "reaction" forces observed in the analytical models tend to have a non-negligible in-plane bending component. Thus, connectors near the end of the LFRS tend to attract larger stresses. Non-ductile diaphragm-to-LFRS connectors would tend to "unzip" under these actions.

Thus to avoid such behavior, the diaphragm-to-LFRS reinforcement has its own set of deformation requirements, given in *Appendix 2, Table A-2.3*. It was considered prudent to relate the deformation requirements to the diaphragm seismic demand level (See *Commentary Step 2*). For this reason, the analytically obtained values are multiplied by a C_2 factor given in *Appendix 2, Table A-2.2*. The C_2 factor values are (1.0, 1.5, 2.0) for the low, medium and high diaphragm seismic demand levels respectively. These values are considered conservative, and the topic require further research to better determine the needed deformation capacity, and ability for diaphragm to LFRS connections to achieve these opening and sliding deformations for different wall to floor connection configurations, in particular bearing conditions, and under the out-of the-floor plane action at this interface during seismic response.

Diaphragm –to LFRS Connection Deformation Capacity, Appendix 2:

Figure c-20 shows the LFRS deformation demands for various layouts of the Prototype Precast Office Building (refer to *Verification of Design Factors* in Preface to Commentary). The values obtained in these analyses were used to establish the reference deformation capacities for Table *A-2.3* It can also be seen that the diaphragm-to-LFRS demands were not greatly different among different design options (See Fig. c-20), and thus by the C_2 factors in Table *A-2.2* are a factor of safety, not a result directly obtained from the analytical research.
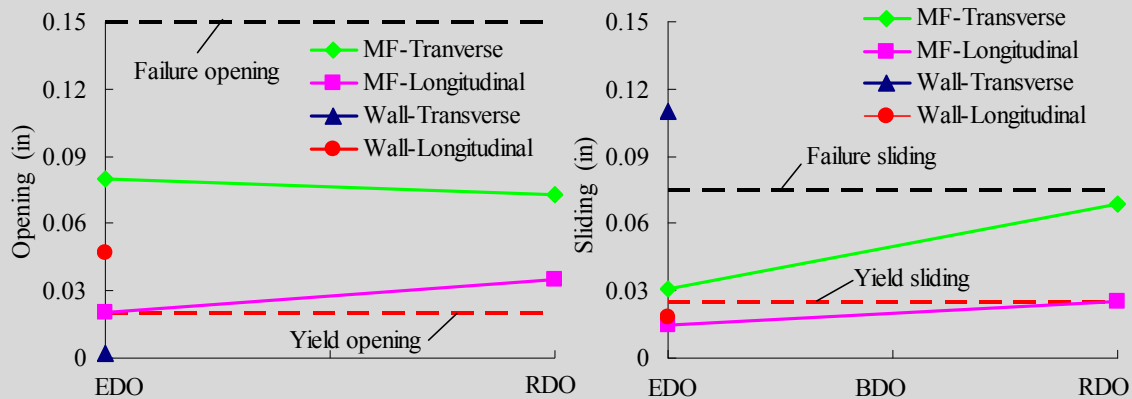
Figure c-20. Diaphragm-to-LFRS deformation demand in the prototype office building: (a) opening; (b) sliding.

Deformation Requirements for Non-Primary Diaphragm Reinforcement:

Deformation capacity should to be considered for other reinforcement in the floor system, including diaphragm-to-spandrel connections, spandrel-to-column connections, and internal beam connections not included in the design. These so called "secondary" connections are not formally part of the diaphragm design, but nonetheless will have an effect on the diaphragm response, particularly for an inelastic diaphragm (Wan et al. 2012). The secondary connections were outside the testing scope for the prequalified connections provided in PART 2. Thus, secondary connection deformation capacities were estimated in the research, and could be verified in a future testing program.

The estimated deformation demands on the secondary connections were determined in the DSDM research by introducing the secondary elements directly into the analytical models. In this way, the analyses performed on the evaluation and prototype structures (*See Preface to Commentary*), primarily for determining diaphragm design factors and reinforcement classification limits, also provide information toward design recommendations for the diaphragm secondary connections. The secondary connection deformation demands measured directly in the analytical research (*See text box*) established deformation recommendations for connectors of nominal strength typical of standard industry connectors.

The reason that the deformation capacities are *recommended* rather than required at this point is that it is unclear the ramifications of the loss of secondary connections. The loss of these connections may change load path, modify deformation patterns on the primary diaphragm reinforcement, and decrease diaphragm stiffness. However, since the secondary elements (spandrels, IT beams) are typically secured directly to columns or walls, it is unclear if the loss of their connections to the floor diaphragm would lead to collapse or global failure of the diaphragm. The key consideration may be to avoid unseating of the precast floor units after connection failure. The impact of the loss of the secondary connections requires further consideration, e.g. the ramifications of loss of these connections with regard to load path, seating requirements, etc. It should be re-emphasized, however, that a LDE secondary connector (e.g. the one-sided bar-plate) will not survive the imposed compatible diaphragm deformations witnessed in the research, e.g. for high seismic demand cases and BDO or RDO designs (*See text box*).

Figure C-7 shows the assumed diaphragm design reaction force flows of outer sub-diaphragms for: (a) perimeter wall parking structure; and (b) interior wall parking structure. As seen, for the perimeter wall structure, a part of diaphragm reactions is assumed to be transferred through the internal beam joint. However for the exterior wall structure, all of diaphragm reactions are assumed to be transferred directly to the interior shear wall. Therefore the internal beam joint in the perimeter wall structure is designed to resist an axial force for transferring the diaphragm reactions which results in a "strong" connector while the internal beam joint in the interior wall structure is selected as an industry standard connector. These design assumptions result in a higher opening demand in the internal beam joint for the interior wall structure compared to the perimeter wall structure in the earthquake simulations (*See text box, Fig c-21a*).
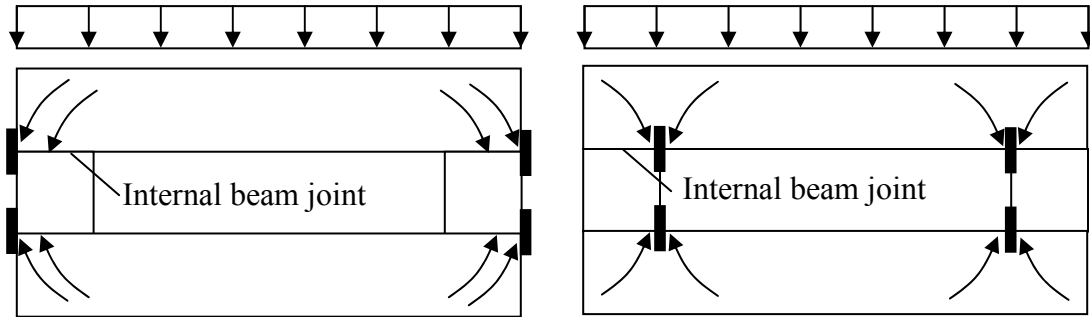
Figure C-7. Diaphragm reaction force flow: (a) perimeter shear wall structure; (b) interior shear wall structure.

Secondary Diaphragm Reinforcement Effect on Primary Reinforcement Demands:

Figure C-8 shows the effect of the spandrels on the join sliding and opening in the precast diaphragm. It is important to note that the inclusion of secondary elements in the analytical models is also central to achieving the analytical research primary goals, since the secondary elements have a non-negligible effect on global diaphragm response and diaphragm primary reinforcement demands (Wan et al. 2012), as evidenced in the analytical and test results shown in Fig C-9. In the absence of test results, the secondary connection characteristics had to be estimated. The characteristics were approximated as one-sided versions of the plate-bar flange-to-flange connector tested by Pincheira et al. (1998). Thus, these connections were given the nominal stiffness and strength expected of standard industry hardware.

(a) Diaphragm high shear region   (b) Diaphragm high flexure region
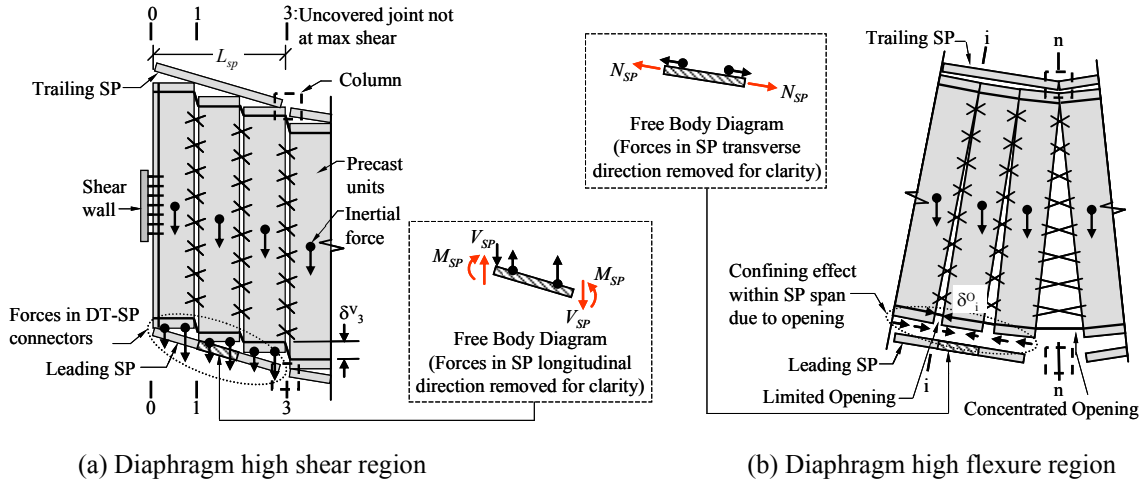
Figure C-8. Schematics of interaction between spandrels and precast floor units after (Wan et al. 2012).

(a) Joint shear displacement   (b) Joint opening
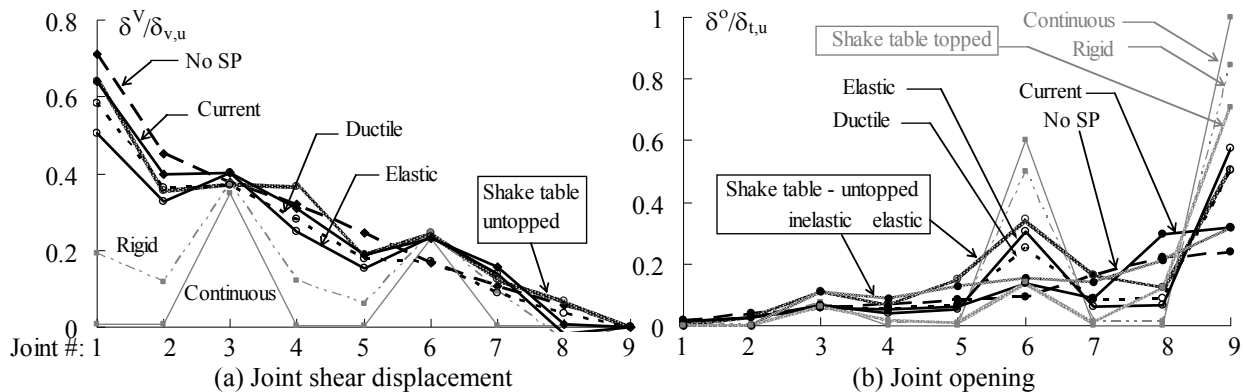
Figure C-9. Joint deformation profiles (Δ_{dia}=3.15cm) after (Wan et al. 2012).

62

Commentary to Appendix 3: Diaphragm Drift.

Diaphragm Elastic Deformation Calculation:

Diaphragm elastic deformation can be calculated using the following methods:

(1) Simply beam analogy:

$$\delta_{dia,\,el} = 5F_{px}L^3/384E_{eff}I + F_{px}/A_eG_{eff}$$

(2) Computer Analysis Method

The same structure model and static analysis used for the diaphragm internal force calculation are applied to obtain the diaphragm elastic deformation. The diaphragm elastic deformation measurement is taken as the difference between the diaphragm displacement and the LFRS displacement at each floor level. Please refer to *Semi-Rigid Diaphragm Model*, Commentary for Step 3b.

(3) Integration Method

This method is to integrate the shear and flexure deformation of each precast panel with the previous calculated design shear/moment diagram and diaphragm effective moduli. The diaphragm elastic deformation is calculated as the sum of shear and flexure deformation ($\delta_{el} = \delta_v + \delta_f$).
The shear deformation (δ_v) is calculated by sum of the shear deformation of each precast panel:

$$\delta_v = \sum_{i=1}^{n} 1.2V_i / AG_{effi}$$

where, V_i is the average shear force with the ith panel; A is the gross cross-section area of precast panel; G_{effi} is the effective elastic shear modulus for i^{th} panel (refer to Diaphragm Joint Stiffness Calculation" section); and n is number of precast panels.

The flexure deformation (δ_f) can be calculated by any accepted method, including virtual work, moment area, conjugate beam method, etc. With the latter method, the diaphragm moment diagram is scaled by the $1/E_{eff}I$ (E_{eff} is the effective elastic Young's modulus and I is gross section secondary moment of inertia for preast panel) and applied as the distributed load (w') on the conjugated beam as seen in Fig. C-10. The diaphragm flexure deformation is the resulting moment diagram for the conjugate beam.
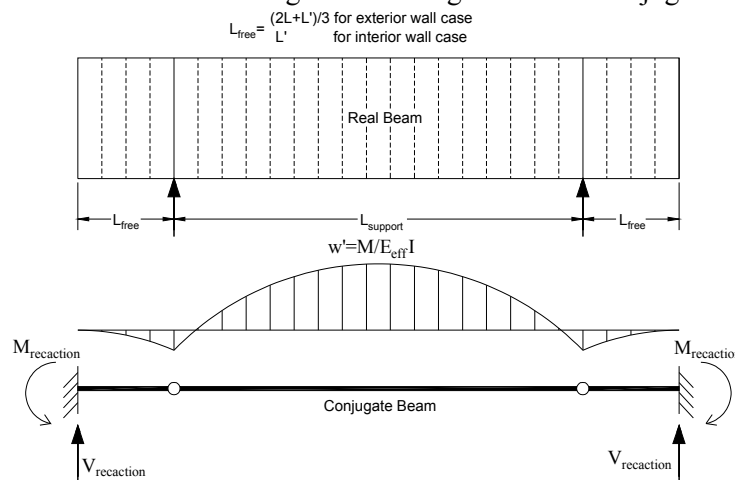
Figure C-10. FBD of conjugate beam.

For methods (1) and (2), an average E_{eff} and G_{eff} for the diaphragm is needed. Please refer to *Precast Diaphragm Effective Stiffness*, Commentary on Step 5.

Diaphragm Deformation Contribution on Drift:

For the cases requiring the diaphragm drift check, the diaphragm contribution to gravity column inter-story drift (θ_{dia}) can be calculated as ($\delta_{dia,\,i}$ - $\delta_{dia,\,i-1}$)/h, where $\delta_{dia,\,i}$ and $\delta_{dia,\,i-1}$ are the expected diaphragm deformation at consecutive stories i and $i-1$, where diaphragm deformation is measured relative to the LFRS drift (See Fig. C-11); and h is the floor-to-floor height. Thus, θ_{dia} is not directly related to diaphragm deformation at a given floor level except for the 1st floor, which typically has non-critical diaphragm deformation demand (*See PART 5: Background*).
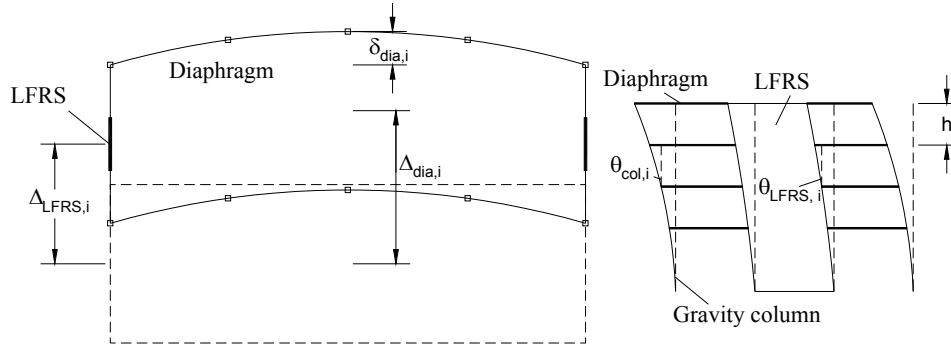
Figure C-11. Diaphragm deformed shape: (a) plan; (b) elevation.

The drift check is performed on both diaphragm deformation alone and also on total drift of the LFRS and diaphragm together. The calculated maximum diaphragm-induced gravity column drift (θ_{dia}) is compared to an allowable design value. The allowable value is set as 0.01 which considers a 0.04 limit for total gravity column inter-story drift (θ_{col}) in the MCE, and a 0.03 limit for LFRS inter-story drift (θ_{LFRS}). When θ_{dia} is larger than 0.01, an additional check is performed for the total gravity column inter-story drift using the 0.04 drift limit, before requiring a redesign for the diaphragm. This last check reflects consideration of cases where the expected LFRS inter-story MCE drift may be less than its allowable limit of 0.03.

Design Option	C_1
EDO	0.06
BDO	0.08
RDO	0.10

Commentary Appendix 3: Diaphragm Contribution to Drift

Figure C-23 shows structural inter-story drift profiles contributed by LFRS, diaphragm and total (gravity column) for a 4-story parking structure under MCE obtained from an earthquake simulation. As seen, the inter-drift of gravity column is amplified by the diaphragm flexibility especially at top floor. However the total column and diaphragm induced inter-story drifts are under the design limit proposed in the design procedure.
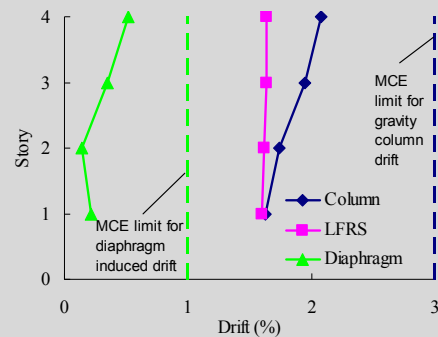
Fig. c-23. Maximum inter-story drift profile.

Maximum diaphragm deformation on a given floor may not occur simultaneously with maximum diaphragm deformation on an adjacent floor, which could occur at a different time during the earthquake; nor necessarily the maximum LFRS drift, which tends to be slightly out of phase with the diaphragm. For this reason, a diaphragm drift reduction factor $C_{r,dia}$ is introduced into the maximum (added) inter-story drift due to the diaphragm:

$$\theta_{dia} = \delta_{dia}\,C_{r,dia}\,/\,h \qquad (Eqn.\ A2\text{-}2)$$

The factor $C_{r,dia}$, always less than unity, provides the approximate reduction in value between maximum diaphragm deformation δ_{dia} and the associated drift due to diaphragm deformation θ_{dia}. The equations for this factor are linear curve-fits, shown as black solid lines in Fig. c-24 (See Text box)

The maximum diaphragm deformation (δ_{dia}) in Eqn. A3-2 is the expected diaphragm maximum deformation under MCE, which will include inelastic deformation. To allow this code check to be made on the basis of an elastic structural analysis, the drift check follows a procedure similar to provisions in current design codes. Accordingly, the maximum diaphragm deformation δ_{dia} is calculated by multiplying the diaphragm deformation from an elastic analysis ($\delta_{dia, el}$) with an inelastic deformation amplifier ($C_{d,dia}$) to account for inelastic diaphragm deformation in the MCE. The $C_{d,dia}$ factor is a different constant for different design options is established based on analysis results (*See text box*). For the EDO, $C_{d,dia} = 1.0$ since no inelastic diaphragm deformation is expected. The diaphragm elastic deformation ($\delta_{dia, el}$) used in Eqn. A3-1 is to be calculated using the methods described in this commentary step (See also PART 3). $C_{d,dia}$ also has a C_Δ factor, a P-Δ multiplier for the gravity columns due to diaphragm-amplified drift.

Diaphragm Contribution to Drift, Appendix 3:
The equations for this factor are linear curve-fits, shown as black solid lines in Fig. c-24 which reproduces the analysis results from the trial design factor parametric study (See *Commentary Preface*). The $C_{d,dia}$ factor for different design options is established as a constant upper bound factor based on the BDO and RDO analysis results (See Fig. c-25), and is unity for the EDO. Data used to create the C_Δ multiplier is shown in Fig. c-26.
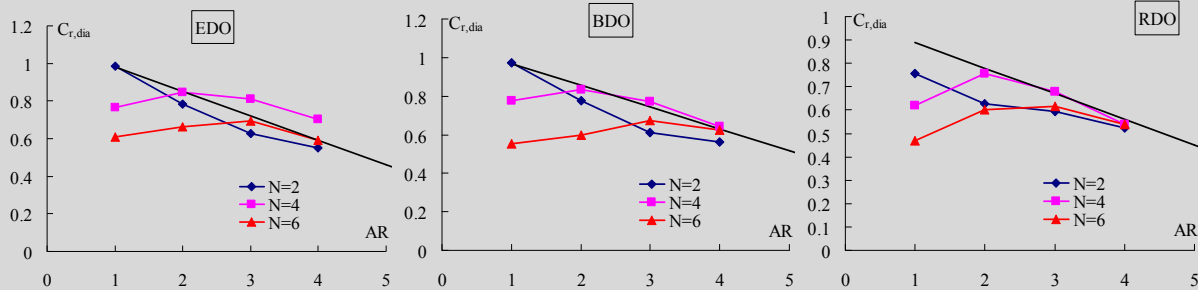
Figure c-24. Diaphragm drift reduction factor.
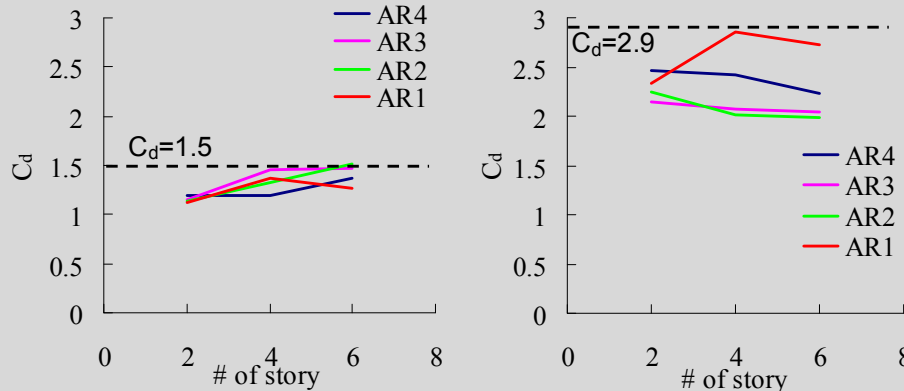
Figure c-25. Diaphragm inelastic deformation amplification factor: (a) BDO; (b) RDO.
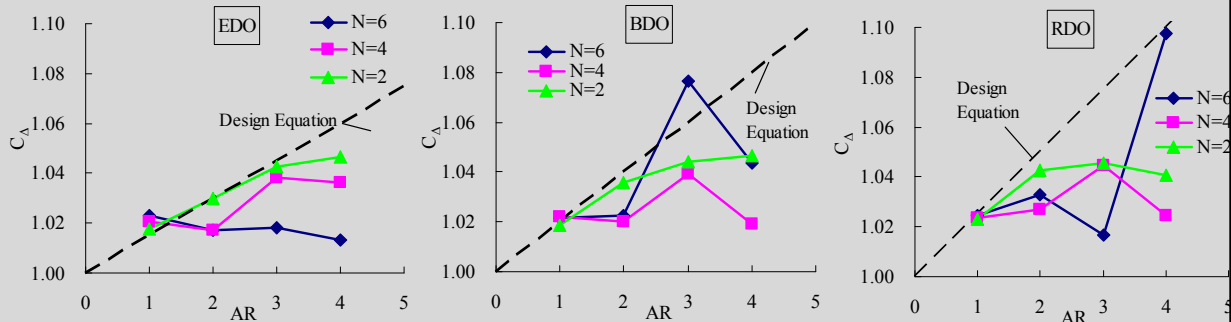
Figure c-26. P-Δ multiplier for the gravity columns: (a) EDO; (b) BDO; and (c) RDO.

Commentary to Appendix 4: Alternate Diaphragm Design Force Procedure for ASCE 7-10.

Appendix 4 is an alternate procedure to PART 1: Step 3a for using the diaphragm design methodology with the current ASCE 7-10 diaphragm forces. The alternate procedure has 8 substeps.

Appendix 4: Step 3a-Alt., Substep 1: Determine diaphragm force amplification factor (Ψ).

Description. The diaphragm force amplification factor (Ψ) is determined. The Ψ factors are applied to *baseline* diaphragm forces determined using the ASCE 7-10 code. Subscripts E, D and R differentiate between the different amplification factor magnitudes required for the EDO, BDO and RDO respectively. The equations for Ψ_E, Ψ_D, and Ψ_R, (Appendix 4: **Eqns.** A4-1a-c) take as input the following design parameters defined in the design procedure: number of stories n, diaphragm span length L (in feet), and diaphragm aspect ratio AR. It is noted that AR is limited by ($0.25 \leq AR \leq 4.0$). The contribution of LFRS overstrength is included via the ASCE 7-10 structure system overstrength factor (Ω_0).

The following is noted about the use of PART 1 Equation 2 with the alternate procedure: (1) strength reduction factors of ϕ_f is 0.9 and ϕ_v is 0.85 are used; the former is the typical value used in the current codes; the latter values was selected as per Appendix C of ACI 318 (2005); (2) N_u, V_u, M_u contain the diaphragm amplification factor Ψ internally; (3) the shear overstrength factor Ω_v is included directly in Eqn. 2, and (4) to ensure designs are not unconservative in relation to current code, a check is performed for collectors and diaphragm-to-LFRS connections relative to the System Overstrength Factor Ω_o per ASCE 7-10.

Commentary. The magnitude of Ψ used in the design procedure was calibrated to design targets through analysis at DBE and MCE levels (Refer to Table C-I):

- Ψ_E, the diaphragm force amplification factor for the **EDO**, is calibrated in the analytical research to produce elastic diaphragm response in the *MCE*.

- Ψ_D, the diaphragm force amplification factor for the **BDO**, is calibrated in the analytical research to produce elastic diaphragm response in the *DBE*.

- Ψ_R, the diaphragm force amplification factor for the **RDO**, is calibrated to produce a maximum joint opening demand in *MCE* equivalent to the maximum allowable inelastic opening deformation of *high deformability element* (*HDE*) reinforcement of $0.4''$.

The Appendix 4: **Eqns.**. A4-1a-c are simplified versions of expressions developed during the research involving combinations of power, polynomial and exponential terms. The original expressions are reproduced below, followed by the modifications used to arrive at the current expressions:

Original Expressions:

$$1.0 \leq \Psi_E = 1.7 n^{0.38}[1 - 0.04(3 - AR)^2]1.05^{(L/60 - AR)} \leq 3.9 \qquad \text{(Eqn. C-A4-1)}$$

$$1.0 \leq \Psi_D = 1.65 n^{0.21}[1 - 0.03(3 - AR)^2]1.05^{(L/60 - AR)} \leq 2.9 \qquad \text{(Eqn. C-A4-2)}$$

$$1.0 \leq \Psi_R = 1.05 n^{0.3}[1 - 0.03(2.5 - AR)^2]1.05^{(L/60 - AR)} \leq 2.2 \qquad \text{(Eqn. C-A4-3)}$$

> where
> > n is the total number of stories in building,
> > L is the diaphragm span in ft and
> > AR is diaphragm aspect ratio ($0.25 \leq AR \leq 4.0$).
> > ($L/60$-AR) not to be taken larger than 1.0 nor less than -1.0.

Diaphragm Force Amplification Factor Calibration wrt ASCE 7-10 Procedures, APPENDIX 4

Figure c-27 shows scatter plots of the results of the analytical parameter study to determine the diaphragm design force factors (See PART 5: *Appendix A1*), corresponding to the diaphragm force when the associated performance target is met for: (a) the EDO; (b) the BDO; and (c) the RDO. Also shown on the plots are the solid line curve-fits of the analytical results *that produced* Eqns. C-A4-1 to C-A4-3 The data used in the curve-fit is the mean of the maximum response from 5 ground motions applied to 24 design configuration of a simple evaluation structure (See *Calibration of Design Factors* in the *Preface to the Commentary*). The design equations produce values greater than or equal to 90% of mean data.
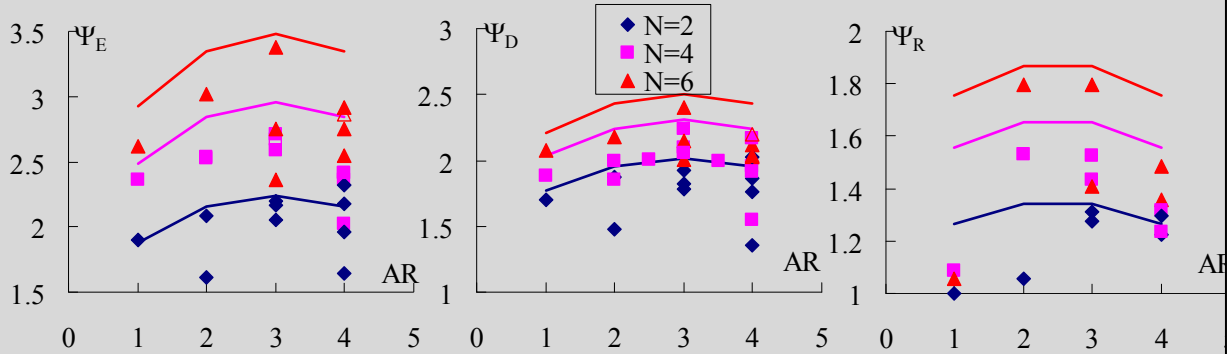
Figure c-27. Diaphragm force amplification factor equations: (a) EDO; (b) BDO; (c) RDO.

Simpler linear (blue solid lines in Fig. c-28) and power (black solid line in Fig. c-28) curve fits were also produced as simpler, but more conservative, alternatives to the equations in the main procedure. These expressions, based on number of stories only, can be used in lieu of the equations in Appendix 4.
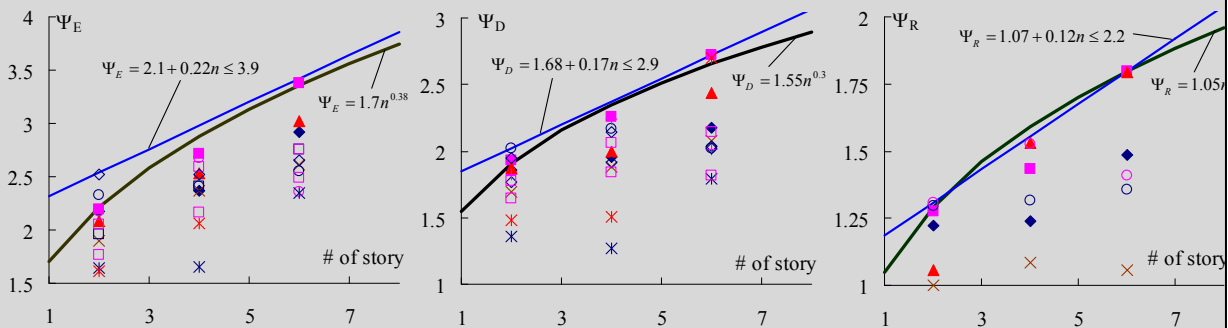
Figure c-28. Simplified diaphragm force amplification factor equations: (a) EDO; (b) BDO; (c) RDO.

Eqns.. A4-1a - c in Appendix 4 were created by modifying the original expressions as follows:

(1) The term $[1.05^{(L/60-AR)}]$ which captured the effect of diaphragm span was removed, and simply replaced by the constant value 1.05. This modification was taken in order to simplify the design equations. Note that the effect of aspect ratio is still included in the expressions.

(2) As seen in Eqns. C-A4-1 to C- A4-3, a lower limit of unity and upper limits existed in the original expressions. The upper limit has since been removed. There was no physical justification for the upper limit on the diaphragm force, and better agreement is obtained between these diaphragm design forces and the diaphragm forces in ASCE 7-14 proposal IT06-001.

67

(3) The final modification to the original expressions is the inclusion of a Lateral Force Resisting System (LFRS) Overstrength factor Ω. The Ω factor is a multiplier to capture the effect of LFRS overstrength in the diaphragm design force: $\Omega = 1 + 2.5 \log \Omega_0 / n^{0.4}$ where Ω_0 is the structure system overstrength factor defined in ASCE7-10. The Ω factor is further discussed below.

LFRS Overstrength Factor (Ω): Based on DSDM TG consensus, the original studies were conducted using designs with low LFRS overstrength (shear wall or moment frames designed with M_n/M_u close to unity), with the effect of LFRS overstrength relegated to subsequent study. Based on results of parallel research in the project showing the importance of the LFRS overstrength (Rodriguez et al. 2007), a subsequent study was performed to examine this factor (*See text box*).

LFRS Overstrength Factor for Alternate (ASCE 7-10) Procedure, APPENDIX 4

The study on LFRS overstrength was performed using a subset of the analytical design space of the overall design factor parameter study described in the *Preface to the Commentary*, and in more detail in PART 5: *Appendix A1*. The overstrength study included the 2-, 4- and 6-story shear wall evaluation structures possessing a rectangular 180′ x 60′ diaphragm. The structures are designed for SDC E, Berkeley, using the BDO for diaphragm design. The analytical results shown are mean results from a suite of 5 spectrum compatible ground motions scaled to the *Design Basis Earthquake* (DBE). Figure c-29 shows these results for LFRS overstrength ranging from 1.0 to 2.5. As seen, the required diaphragm force amplification factors increase with the increase of the LFRS overstrength. The expressions for the Ω multiplier are developed using a curve fit of the data points. The Ψ_D values based on the current design equations that include the Ω factor are shown as dashed lines in Figure c-29.
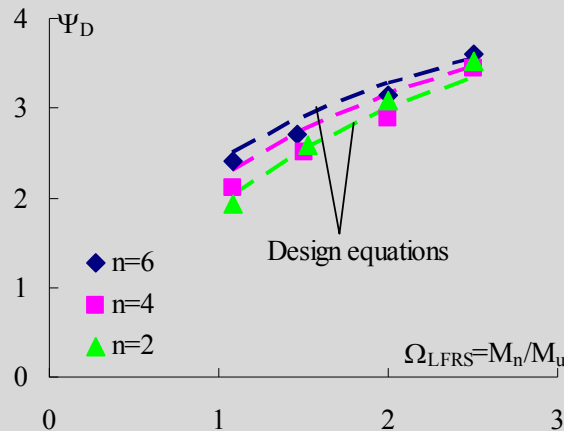
Figure c-29. Effect of LFRS overstrength of Diaphragm Force.

Diaphragm Force for Long Period Structures:

The analytical studies used to determine the diaphragm design force amplification factors were limited to buildings of 2, 4, and 6 story structures. This scope decision, based on DSDM TG consensus, covered typical heights of many precast structures. Later in the project, interest arose in evaluating the applicability of the diaphragm equations to taller structures. Accordingly, supplemental analytical studies were performed on taller structures to examine the applicability of the design force equations (*See text box*). These analyses indicated that the original DSDM Ψ factors were unconservative for tall structures.

Accordingly, two modifications were introduced into the Appendix 4 alternate diaphragm design force procedure in the calculation of the baseline diaphragm design force: (1) the diaphragm baseline design force is to be calculated on the basis of the code approximate structure fundamental period T_a (determined per ASCE 7 Section 12.8.2), not T; and (2) in calculating the baseline force, the current code diaphragm lower bound design force, *$0.2S_{DS}Iw_{px}$* from ASCE 7 Section 12.10.1.1, is to be enforced.

Adjustment for Long Period Structures, ASCE 7-10 Diaphragm Procedure, APPENDIX 4

The study on diaphragm forces for tall buildings followed the same approach as the original study (See PART 5: *Appendix A1*), but was conducted on 8, 10 and 12 story structures. The structure had perimeter RC shear walls designed for SDC E, Berkeley, with a rectangular plan of 180′ x 60′ and a BDO diaphragm design.

Figure c-30a shows the 5%-damped design acceleration spectrum for SDC E, Berkeley. Also shown on the plot are the design periods for the structures of different number of stories, determined using ASCE 7-10: (1) the approximate fundamental period (T_a) and (2) the calculated fundamental period as limited by the code maximum (T). Also shown is the structural second mode (T_2), as measured through modal analysis. It is noted for all these structures, the actual fundamental period T_1 based on modal analysis is longer than he code maximum, and thus T for all these cases is limited by the code value.

As seen in Fig. c-30a, for shorter structures (e.g. n=4), the spectral ordinates corresponding to the first two modes are similar; however, notice that taller structures (e.g. n=12), the spectral ordinate corresponding to the second mode is significantly higher. This outcome implies that diaphragm design forces scaled to the design spectrum will not have a consistent relationship to the anticipated diaphragm demand, and that Ψ factors calibrated on shorter structures will be unconservative for taller structures, since the relative effect of the higher modes is more significant. This last point is important as this is how the Ψ factors were developed. Note also that for these same cases, the corresponding design spectral ordinates are: (1) similar for T_a and T for the short structure; and (2). different for T_a and T for the taller structure, with the design spectral ordinate for T_a higher. Thus, the relationship between T_a and T follows similar trends as T_2 and T, and will be used in adjusting the ASCE 7-10 baseline forces to render the Appendix 4 diaphragm design procedure accurate, as will be shown.

Figure c-30b shows the analytical results for maximum diaphragm force plotted as an apparent diaphragm overstrength factor, $\Psi_D = F_{max}/F_{pn}$, where F_{max} is the mean maximum diaphragm force measured in DBE level analyses, and F_{pn} is calculated two ways: based on T and based on T_a. The a maximum diaphragm force are the mean results from a suite of 5 ground motions. The green dashed line is the Ψ_D value from the design equations. As seen, for shorter structures (n=2-6), the design equation accurately represents the required diaphragm force amplification factors applied to the baseline design force calculated, regardless of the design period chosen, T_a or T. However, for taller structures (n=8-12), the design equations only accurately represent the required diaphragm force amplification factors applied to a baseline design force calculated using T_a (blue diamonds), while those calculated using T would require a higher Ψ_D value than produced in the design equations, and are thus unconservative. This outcome reflects the fact that T_a better captures the spectral ordinates of the higher modes than T. It was further noted in comparison to other methods (Restrepo and Rodriguez, 2012), that for high-rise structures, the calculated diaphragm design force can be slightly unconservative, even when using T_a. These cases occur when the diaphragm baseline design force is less than the current code diaphragm lower bound design force. These two observations led to the changes listed above.
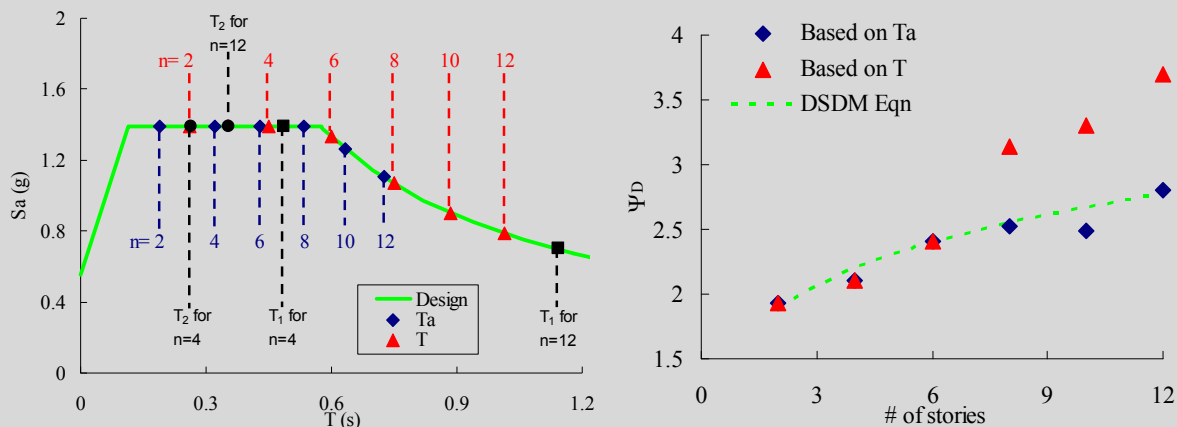
Figure c-30. (a) Design spectrum with structure periods; (b) Effect of Period used in Ψ expressions.

The need for "fixes" to the procedure based on scaling existing diaphragm design forces represents one of the major reasons that the original diaphragm design force procedure based on ASCE 7-10 has been relegated to the Appendix, and replaced by the rational approach of proposal IT06-001, ASCE 7-14.

Appendix 4: Step 3a-Alt., Substep 2: Determine Diaphragm Shear Overstrength factor (Ω_v).

Description. A diaphragm shear overstrength factor (Ω_v) is determined.

Commentary: *Diaphragm Shear Overstrength Factors (Ω_v):*

The Ω_v values for the design procedure were determined in the same study used to establish the Ψ factors. The required magnitude of Ω_v was calibrated to design targets through MCE analyses. Please see PART 5: *Appendix A1* for full details of analytical research to determine these factors.

The shear overstrength factor values were obtained by measuring the maximum shear force V_{max} occurring in the diaphragm at the critical shear joint at MCE-level hazard as the diaphragm develops a flexural mechanism (in other regions of the floor), and scaling it by the design shear V_u. Accordingly:

- Ω_E, the diaphragm shear overstrength factor for the EDO, is taken as unity ($\Omega_E = 1.0$) since the Ψ_E factor is calibrated to the elastic force demand in the MCE.
- Ω_D, the diaphragm shear overstrength factor for the BDO, is the V_{max}/V_u ratio for the BDO design under MCE level hazard.
- Ω_R, the diaphragm shear overstrength factor for the RDO, is the V_{max}/V_u ratio for the RDO design under MCE level hazard. Ω_R is somewhat larger than Ω_D due to the larger expected diaphragm strain-hardening in the RDO.

Note that the use of the system overstrength factor Ω_0: 2.5 for RC shear wall; 3.0 for moment frame (ASCE 7 2010) in the Ω expression will tend to be conservative for most of the data shown in Figure c-31. Thus, while the use of this factor is straightforward, a designer may choose to calculate an LFRS overstrength value directly via analytical pushover methods using expected strengths, and use it in place of the system overstrength factor Ω_0 in the Ω multiplier expression.

Diaphragm Shear Force Overstrength Factors, Design Procedure Step 3a Alt (APPENDIX 4):

Also shown on the plot is the alternate design equations for $\Omega_v = \Omega_E, \Omega_D, \Omega_R$ used in the original procedure for use with ASCE7-10 (See Appendix: **Eqns. A4-2a-c**), superimposed as solid black lines in *Fig. c-31 (See Commentary, Appendix 4)*. The design equations are power curve fits of the analytical results based on values greater than or equal to 90% of mean data. A detailed description of the development of these design factor equations is presented in PART 5: *Appendix A1*.

Figure c-31. Diaphragm shear overstrength factor equations: (a) BDO; (b) RDO.

The analyses used to generate the data in Fig. c-31 made use of a simple evaluation structure with well-defined shear-critical regions and flexure-critical regions (See *Commentary Preface* and *Part 5: Background*). The shear overstrength, as obtained, provides an estimate of the maximum required shear

force. However, in itself it does not directly address the impact of in-plane axial force (due to flexure or collector actions) on the precast diaphragm shear response. The effect of axial force is directly included in the design procedure through the interaction equation (See *Commentary Step 4*) to determine required diaphragm reinforcement at a joint based on internal force combinations determined in Step 3b. It should be further noted that while the Ω_v factor has been calibrated in the analytical research to provide elastic shear response of the diaphragm in the MCE, care must be taken in ensuring the anticipated M/V ratio occurs in the diaphragm (See *Appendix 5, Capacity Design Considerations*).

The shear overstrength factor Ω_v is scaled relative to the amplified diaphragm force, i.e. a diaphragm designed with the appropriate diaphragm amplification Ψ. Thus the Ω_v factor is stacked on top of the Ψ factor. In the design, the Ω_v factor is applied directly to the *required* shear force. It should be noted that the Ω_v factor is independent of the shear strength reduction factor ϕ_v as it is applied to the demand side, while the ϕ_v factor is applied to the material capacity side. Thus, both are applied together to provide reliable elastic shear strength under MCE demand.

Appendix 4: Step 3a-Alt., Substep 3: Determine Diaphragm Force Vertical Distribution Factor (α_x).

Description. The vertical distribution of diaphragm forces is controlled by the diaphragm vertical force distribution factor, α_x.

$n \leq 3$:

$$\alpha_x = 1.0 \quad \text{for all floors}$$

$3 < n \leq 6$:

$$\alpha_x = 1.0 \quad \text{for top floor and} \quad \alpha_x = 0.9 \quad \text{for 1}^{\text{st}} \text{ floor}$$

$$\alpha_x = 0.7 + 0.2(n-1-x)/(n-3) \quad \text{for other floors (i.e. } x = n\text{-1, } n\text{-2, ... 2)}$$

$n > 6$:

$$\alpha_x = 1.0 \quad \text{for the top and 1}^{\text{st}} \text{ floor}$$

$$\alpha_x = 1 - 0.2(n-x) \quad \text{for two floors directly below the top floor (} x = n\text{-1, } n\text{-2)}$$

$$\alpha_x = 0.6 + 0.3(n-2-x)/(n-4) \quad \text{for other floors (i.e. } x = n\text{-3, } n\text{-4, ... 2)}$$

where is n the total number of stories, x is the story number and α_x is the diaphragm force vertical distribution factor.

Commentary. The story-based α_x factor is intended to provide a reasonable distribution of the diaphragm forces along the height of the structure. It is noted that the α_x factor provides a different vertical distribution that that produced by F_{px} in current code ELF procedures.

It is also noted that in the past, researchers endorsed a constant design force distribution along the height of the structure (Fleischman et al. 2002). The introduction of the α_x factor is in recognition of the results of earthquake simulations using more improved analytical models that incorporate certain features into the structural models not present previously, e.g. gravity system columns.

In general, a simple but potentially overly conservative alternate approach is to use a value of $\alpha_x = 1.0$ at each floor. However, in order to provide a more economical design option, α_x values have been determined on the basis of results from three-dimensional nonlinear transient dynamic analysis (Zhang and Fleischman 2012a). It is noted that the α values are based on a fairly limited sample of analyses as described next and could benefit from a more comprehensive examination.

A distinction is made between the distribution of general building structures and parking structures as a different distribution was obtained for each. The α_x values for general building structures are found in **Appendix 4: Table A4-1**.

It is suggested that a structure with significant vertical irregularity be assigned a constant vertical force distribution (α_x = 1.0), though this suggestion is not based on any analytical research. Note also that in using the α_x factor for a parking structure, it is necessary to assign a level for a ramp sub-diaphragm. In this procedure, such an element is considered part of the uppermost level to which it connects.

Finally, note that consistent with certain other codes and guidelines (Standards New Zealand 2004) (ASCE/SEI 41 2006), the designer is permitted to perform nonlinear time history analysis on the particular structure under design to obtain the diaphragm forces directly. Such an approach requires realistic models and a carefully selected suite of ground motions, as described in PART 3 of the Design Methodology. The design procedure has been developed to avoid the need for such models and analyses.

Diaphragm Force Vertical Distribution Factor, Design Procedure Step 3a Alt (APPENDIX 4?):

Commentary Appendix 4: Diaphragm Force Vertical Distribution (α_x) Factor

The α_x factors were determined from the average distribution of 5 earthquake simulations for 24 separate design cases using a simple evaluation structure (See *Preface to Commentary*, and PART 5 Appendix A1), and verified by a single earthquake simulation of a realistic 8-story office building under a bi-directional ground motion (See *Preface to Commentary* and PART 5: *Appendix A2*). As an example, Fig. C-32a shows analytical results for an 8-story shear wall and moment frame structure.

For mid-rise parking structures, the diaphragm force is maximum at the roof, and reasonably bounded by a constant reduced value for the remainder of the lower floors (See Fig.C-32b). The α_x factors for the parking structure were established based on the results of five total analyses of realistic 4-story parking structures under bidirectional earthquake ground motions: three with exterior transverse shear walls and lite walls (along the ramp); one with interior transverse shear walls and lite-walls; and one with perimeter shear walls in both directions (See PART 5: *Appendix A2*).
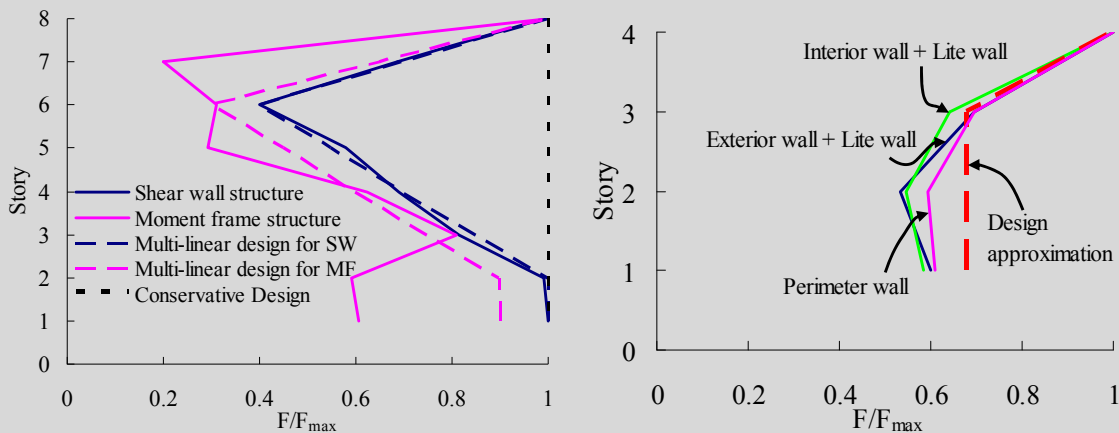
Figure c-32. Max diaphragm force profile: (a) 8-story office building; (b) 4-story parking garage.

Appendix 4: Step 3a-Alt., Substeps 4-7: Calculate baseline diaphragm force based on ASCE 7-10.

Description. In this step, the diaphragm seismic design force is calculated by first determining a baseline design force based on current code, and then applying the diaphragm force amplification factor. Summarizing the steps in Appendix 4 - Step 3a, Substeps 4-7:

- The code diaphragm force F_{px} at top level *n*, termed F_{pn}, is calculated according to current code (ASCE 7-10) provisions: Eqn. 12.10-1 {*Sec. 12.10.1.1*}. To do this requires first calculating the lateral seismic design force F_x at each floor using Eqn. 12.8-11 {*Sec. 12.8.1-12.8.3*}.
- This top level diaphragm design force is converted into a maximum design *acceleration* coefficient $C_{dia,n}$ (PART 1: **Eqn. A4-3**) by dividing by the top level floor weight w_{pn}.

- Then the baseline diaphragm force at each level x, F_{Dx}, is calculated (PART 1: **Eqn. A4-4**) applying this maximum design *acceleration* to the floor at each level, and further modifying the value using a *diaphragm force vertical distribution factor,* α_x, which accounts for typical maximum inertial force profiles in multi-story structures. Tables for α_x are given in **Appendix 4, Table A4-1**.

The following notes are provided about the PART 1, Step 3a diaphragm design force calculation steps:

1. *Substep (4)*: In determining the seismic design force F_x per ASCE 7-10, the *seismic response coefficient C_s {Sec. 12.8.3}* is to be calculated using the *approximate structure fundamental period T_a* from ASCE 7 Section 12.8.2. This practice was explained above in the *text box associated with Fig. c-30*.

2. *Substep (5)*: In determining the top level diaphragm force per ASCE 7-10, the *lower bound diaphragm design force $0.2S_{DS}Iw_{px}$ {Sec. 12.10.1.1}* shall apply in the calculation of F_{px}. This practice is explained below in the *Commentary*.

   - The ASCE 7-10 upper bound diaphragm design force $0.4S_{DS}Iw_{px}$ *{Sec. 12.10.1.1}* does not apply in the diaphragm design procedure.

3. *Substep (6)*: The intent of the procedure is to define the amplification factors relative to the current code maximum diaphragm seismic design force. The maximum equivalent lateral force F_x typically occurs at the roof, however is not assured in cases of variable floor mass distribution. Accordingly:
   - A design acceleration coefficient $C_{dia,n}$ is used instead of the design force for ease of applying to structures with non-uniform floor masses.
   - A special case involves a building with a penthouses or other vertical appendage. For the purpose of calculating the diaphragm forces in these cases, the uppermost floor level for buildings is defined as the level containing 95% of total building weight, as measured up from the ground floor. The appendage itself can be designed for the C_{dia} at its own level.
   - In parking structures, a ramp element is to be associated with the top-most level to which it is attached, for the purpose of floor weights and the design of the ramp itself.

   Appendix 4: Step 3a-Alt., Substep 8: Calculate the amplified diaphragm force (relative to ASCE 7-10).The diaphragm design force amplification factor is applied to a baseline design force based on the current code diaphragm design force (ASCE 7-10). Thus, the amplified diaphragm design forces are scaled relative to the current code design forces. This approach was discussed during DSDM TG meetings at the onset of the research program, and deemed effective since it would be useful for codification to build the new design methodology relative to existing provisions. However, it was noted that a force amplification approach defined relative to the current code value may not be fully rational, since the current code diaphragm design force is proportional to the seismic force reduction factor R, and the actual diaphragm inertial force is due from a combination of modes, of which only the fundamental mode has this direct relationship to the R factor (Rodriguez et al. 2002). The ramifications of scaling to current code are as follows:

   Current code forces are based on the first mode while maximum diaphragm forces are related to higher mode effects, primarily the second mode (Restrepo and Rodriguez, 2012). One issue with scaling the diaphragm design forces to current code is that the relationship between the first and second mode design spectrum ordinates changes with building period. This fact is particularly apparent when considering tall structures (*Refer to text box Fig. c-30*). Accordingly, two considerations were introduced into the calculation of the baseline diaphragm design force in Steps 4-7: (1) the diaphragm baseline design force is to be calculated on the basis of the code approximate structure fundamental period T_a (determined per ASCE 7 Section 12.8.2), not T; and (2) in calculating the baseline force, the current code diaphragm lower bound design force, $0.2S_{DS}Iw_{px}$ from ASCE 7 Section 12.10.1.1, is to be enforced.

For the reasons stated above, an alternative diaphragm design force equation to scaling to the existing ASCE 7-10 diaphragm forces has been proposed. This alternate method, described below, was used to permit the precast diaphragm seismic design procedure to be used with the First Mode Reduction (FMR) equation, developed by Restrepo and Rodriguez (2012), and proposed for the ASCE 7-14 Code Provisions in IT06-001. A simplified version of this procedure is now included in the (main) PART 1 Design Procedure Step 3a, and described in detail in the commentary for Step 3a.

Alternate Diaphragm Design Force Procedure (basis for PART 1 procedure for IT06-001*)*

The FMR design equation was developed for a design target of elastic diaphragm response under DBE. Using the design methodology design targets, as supported by the analytical results, this design is anticipated to produce a diaphragm reinforcement maximum inelastic deformation equal to the MDE allowable deformation capacity (0.2″) under MCE hazard. This value is equivalent to a ductility demand of 3.5, given the yield deformation $\delta_y=0.0568″$ of the pour strip chord element measured in testing (Naito et al. 2006). Defining the MDE ductility demand as $\mu_{MDE}=3.5$, the R_{dia} equation can be modified as:

$$R_{dia} = 1 + [0.11 + 0.015(AR-3)^2]\ (\mu - \mu_{MDE})$$

where *AR* is the floor aspect ratio and is limited between 0.25 to 4.0; μ_{LDE} μ_{MDE} and μ_{HDE} are the allowable ductility capacity of the LDE, MDE and HDE reinforcement respectively: Recognize that the allowable deformation values and the resulting ductility associated with each design option are then:

EDO:	$\delta_a = \delta_y$	$\mu=1.0$
BDO:	$\delta_a = 0.2″$	$\mu=3.5$
RDO:	$\delta_a = 0.4″$	$\mu=7.0$

Thus R_{dia} factor can then be directly applied to the FMR equations to obtain diaphragm design forces using the following expression:

$$F_{dia,x} = A_x w_x / R_{dia}$$

where w_x is the weight of floor at level *x*;
and A_x is the FMR diaphragm design acceleration

Diaphragm Nominal Strength, Design Procedure Step 4:
Figure c-33 shows the comparison between the diaphragm design forces (expressed as floor accelerations) for Berkeley SDC E. Shown on the plot are: (1) markers indicating the mean of the maximums from the analytical research results; (2) dashed lines representing the design equations from Appendix 4 (Eqns. A4-1a-c); and (3) solid lines representing the FMR mapped design equations, the basis of IT06-001 (PART 1).
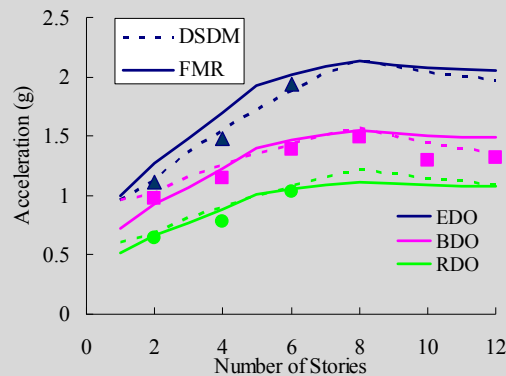
Figure c-33. Diaphragm design acceleration comparison between Appendix 4 and PART 1 Equations.

Commentary to Appendix 5: Capacity Design Considerations for Precast Diaphragms

The shear overstrength factor, Ω_v, is associated with capacity design concepts in that it is included to protect the diaphragm from undergoing a non-ductile shear failure. However, the Ω_v factor cannot truly be considered a capacity design factor given the difficulty in clearly defining needed relative strengths due to the complex internal force patterns that develop in the precast diaphragm during a seismic event. Thus, while the Ω factor has been calibrated in the analytical research to provide elastic shear response of the diaphragm in the MCE, care must be taken in ensuring the anticipated *M/V* ratio occurs in the diaphragm (See PART 5: *Background*).

Figure C-12 shows an example where the longitudinal walls, not part of the transverse LFRS, actually suppress transverse bending, developing large shears. This action lowers the moment, which would be fine in an elastic design. However, in a design procedure where lower design forces are being allowed in return for inelastic deformation capacity, such action may redirect the inelastic action elsewhere, including as into a shear failure. Thus for these interior LFRS elements, care must be taken to assure a proper mechanism in the diaphragm.
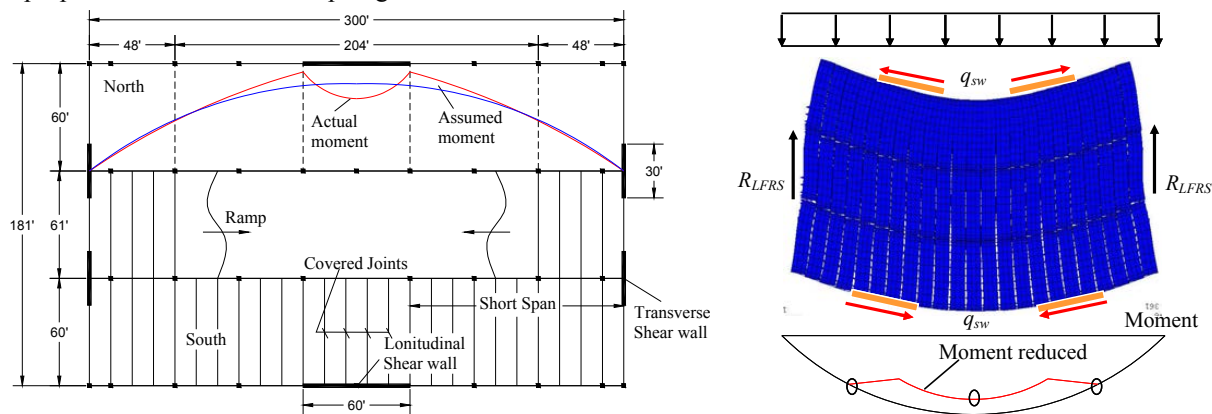
Figure C-12. Plan for a 4-story parking garage with perimeter shear walls.

A capacity design check can be performed in an effort to achieve the desired diaphragm ultimate mechanism, i.e., an inelastic flexural mechanism with elastic shear response. This check requires that the diaphragm joint nominal shear capacity is not less than the expected shear demand based on the maximum diaphragm flexural strength:

$$V_n \geq 4\beta(M_n^- + M_n^+)/L'$$

where M_n^+ and M_n^- are the diaphragm joint nominal flexural strength at the support and midspan respectively, and L' is the diaphragm span between the LFRS inelastic flexure (See Fig. C-13). β is a factor to account for possible strain hardening in diaphragm reinforcement, recommended as 1.2.
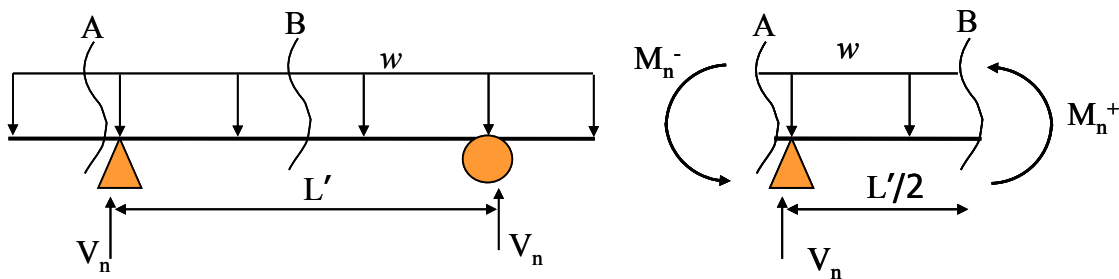
Figure C-13. FBD illustration for a capacity design check on shear.

Collectors and Diaphragm to LFRS Connections. The interaction equation is also applied for the design of the diaphragm-to-LFRS connections (i.e. connections between the floor and shear walls, moment frames, etc.). Thus, shear, axial and flexural reactions are calculated for these connections, but the overstrength factor, Ω_v, is applied only to the shear component. This approach is conceptually similar to current procedures in which an overstrength factor (Ω_o) is applied to the diaphragm-to-LFRS reaction force, because: (1) in current code typically only the shear force is considered for the diaphragm reaction; (2) the shear component dominates the diaphragm reaction total force. Thus, the diaphragm-to-LFRS designs produced by this procedure are similar to current practice. Regardless, a check relative to current code is performed to ensure that the new design procedure does not produce lower strengths than current code (which is possible for the RDO design). With regard to collectors, if a rational strut-and-tie model is not used, the collector should be designed for the shear force required to be transferred from diaphragm to the LFRS using Eqn. 2 with N_u and M_u input as zero.

Diaphragm Capacity Design, Appendix 5:

Figures c-34 and c-35 show two cases where a sufficiently strong design may force an undesirable mechanism in the diaphragm. In each plot, the required design strength in shown as a red line; the MCE seismic demands observed in the analysis are dark blue lines, and the actual nominal flexural strength produced is shown as a light blue line. Both are interior wall structures with inelastic diaphragm designs (e.g., BDO or RDO), where the contribution of shear reinforcement supplements the flexural strength sufficiently that the diaphragm remains elastic due to a large flexural overstrength, and approaches a shear overload failure condition.
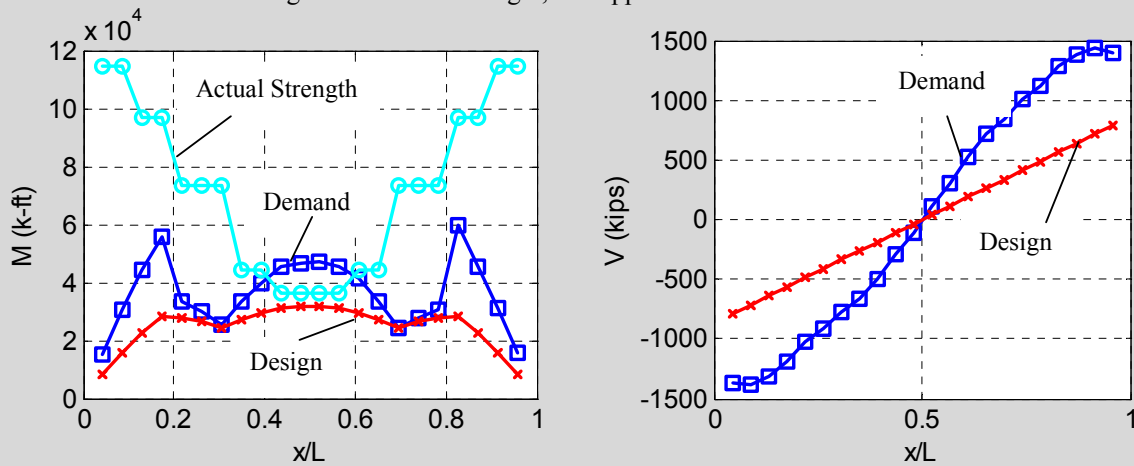
Figure c-34. Diaphragm internal force diagram at 2nd floor: (a) Moment; (b) Shear.
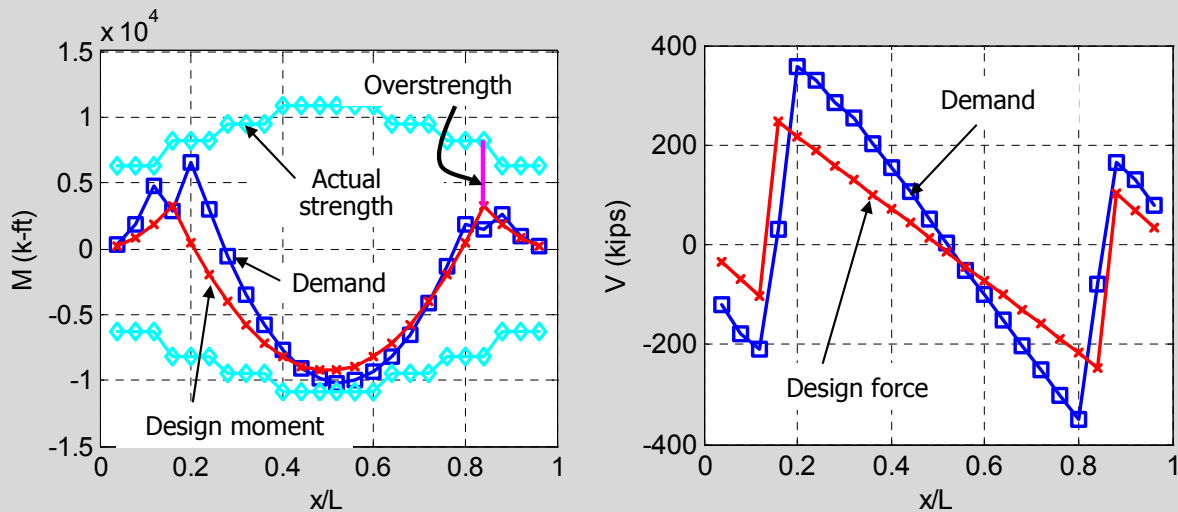
Fig. c-35. Diaphragm internal force diagram: (a) Moment; (b) Shear.

76

References

ACI 318-05. (2005). Building Code Requirements for Structural Concrete (ACI 318-05) and Commentary (ACI 318-05), American Concrete Institution committee 318.

ASCE 7-05. "Minimum Design Loads for Buildings and Other Structures". American Society of Civil Engineering 2005.

American Society of Civil Engineers, Seismic Rehabilitation of Existing Buildings, ASCE Standard No.7 ASCE/SEI 41-06, 2007.

Bull, D.K. (1997). "Diaphragms". Seismic Design of Reinforced Concrete Structures, Technical Report No.20, New Zealand Concrete Society.

Building Seismic Safety Council, Committee TS-4. (2009). "Seismic design methodlgy for precast concrete floor diaphragms," Part III, 2009 NEHRP Recommended Sesimic Provisions, Federal Emergency Management Agency, Washington, D.C.

Blaauwendraad, J. and Hoogenboom, P.C.J. (1996). "Stringer panel model for structural concrete design". ACI Structural Journal V93 (3): 295-305.

Clough D.P. (1982). "Considerations in the design and construction of precast concrete diaphragms for earthquake loads". PCI Journal. March-April: 78-93.

Cleland N. and Ghosh S.K. (2007). "Seismic design of precast/prestressed concrete structures". PCI Seismic Design Manual, 1st Edition.

EERI (2011). Learning from Earthquakes: The M 6.3 Christchurch, New Zealand, Earthquake of February 22, 2011. Special Earthquake Report, Earthquake Engineering Research Institute, K. Elwood, Editor, May.

Fib. (2003). "Seismic design of precast concrete building structures". fib State-of-art report No.27.

Farrow, K. T. and Fleischman, R. B. (2003). "Effect of dimension and detail on the capacity of precast concrete parking structure diaphragms" PCI Journal 48(5): 46-61.

Fleischman, R. B., and Farrow, K. T. (2001) "Dynamic response of perimeter lateral-system structures with flexible diaphragms", Journal of Earthquake Engineering & Structural Dynamics, V.30, No. 5, May, pp. 745-763.

Fleischman, R.B. Farrow, K.T. Eastman, K. (2002) "Seismic response of perimeter lateral-system structures with highly flexible diaphragms" Earthquake Spectra, 18 (2) May: 251-286.

Fleischman, R.B., Naito C.J., Restrepo J., Sause R., Ghosh S.K., Wan G., Schoettler M., and Cao L. (2005b). "Seismic design methodology for precast concrete diaphragms, Part 2: research program." PCI Journal, 51(6), 2-19.

Fleischman, R.B., Sause, R., Pessiki, S., and Rhodes, A.B. (1998). "Seismic behavior of precast parking structure diaphragms." PCI Journal, 43 (1), Jan-Feb: 38-53.

Fleischman, R.B. and Wan, G. (2007). "Appropriate overstrength of shear reinforcement in precast concrete diaphragms", ASCE J. Structure Eng. 133(11), 1616-1626.

Gates W.E. (1981). "Seismic design considering for untopped precast concrete floor and roof diaphragm". Proceedings, Workshop on Design of Prefabricated Concrete Buildings for Earthquake Loads, Applied Technology Council.

Maffei, J.R. (2005). DSDM Task Group Research Meeting #5, Napa CA, August.

McSaveney, L.G. (1997). "Precast concrete flooring system design and detailing for seismic purpose". Conference Technical Papers (TR19), New Zealand Concrete Society, August: 14-26.

Meyer, T. Magnusson Klemencic Associates, , BSSC IT 6 discussions, San Francisco, February 2012.

Moehle, J.P., Hooper, J.D., Kelly, D.J. and Meyer, T.R. (2010) "Seismic Design of Cast-in-Place Concrete Diaphragms, Chords, and Collections" NEHRP Seismic Design Technical Brief No.3.

NZS (2004). Standards New Zealand, 2004 Edition, Wellington New Zealand.

Naito, C., Jones, C., Cullen T. and Ren, R. (2007). "Development of a seismic design methodology for precast diaphragms - phase 1b summary report". ATLSS Report. ATLSS Center, Lehigh University, PA.

Naito, C., Peter, W. and Cao, L. (2006). "Development of a seismic design methodology for precast diaphragms - phase 1 summary report". ATLSS Report No.06-01, ATLSS Center, Lehigh University, PA.

Precast/Prestressed Concrete Institution. (2004). "PCI design handbook: precast and prestressed concrete." Sixth Edition, Chicago IL.

Pincheira, J. A., Oliva, M. G., and Kusumo-rahardjo, F. I. (1998). "Tests on double tee flange connectors subjected to monotonic and cyclic loading." PCI Journal, 43 (3): 82-96.

Paulay, T. and Priestley, M.J.N. (1992). "Seismic design of reinforced concrete and masonry buildings". John Wiley and Sons.

Restrepo, J.I. and Rodriguez, M. (2007) "Proposal to Revise the 2005 Edition of ASCE7". Task Committee Action on Proposal: Revise Section 12.10 of ASCE 7 Standard.

Restrepo, J.I. and Rodriguez, M. (2012) "Proposal to Revise the Diaphragm Design Force". BSSC IT6 Internal Document.

Rodriguez, M., Restrepo, JI, and Blandon, J.J. (2007) "Seismic design forces of rigid floor diaphragms in precast concrete building structures". ASCE Journal of Structural Engineering 133(11): 1604-1615.

Rodriguez, M., Restrepo, JI, and Carr, A.J. (2002) "Earthquake induced floor horizontal accelerations in buildings". Earthquake Eng. & Structural Dynamics, 31(3): 693-718.

Rhodes, A.B., Sause, R., Pessiki, S. and Fleischman, R.B. (1997). "Seismic performance of precast parking structures: transverse direction". Earthquake Engineering Research Report No. EQ-97-03, Department of Civil and Environmental Engineering, Lehigh University, Bethlehem, PA, 1997.

Sabelli, R., Sabol, T. and Easterling, S.W. (2011). "Seismic design of composite steel deck and concrete-filled diaphragms". NEHRP Seismic Design Technical Brief No.5, NIST GCR 11-917-10.

Schoettler, M.J. (2010) "Seismic demands in precast concrete diaphragms" Ph.D. Dissertation. University of California, San Diego, CA.

Schoettler, M.J., Belleri, A., Zhang, D., Restrepo, J., and Fleischman, R.B., (2009). "Preliminary results of the shake-table testing for development of a diaphragm seismic design methodology." PCI Journal, 54 (1), 100-124.

Schlaich, J. Schaefer, K. and Jennewein, M. (1987). "Towards a consistent design of structural concrete". PCI Journal V32 (3): 74-150.

Wan, G., Fleischman, R.B. and Zhang, D. (2012). "Effect of spandrel beam to double tee connection characteristic of flexure-controlled precast diaphragms", J. of Structural Eng. ASCE. Scheduled published in Feb. 2012.

Wood, S. L., Stanton, J. F., and Hawkins, N. M. (1995), "Performance of precast parking garages during the 1994 Northridge earthquake", Proceedings, XIII ASCE Structures Congress, Restructuring: America and Beyond, 1, New York, NY, pp. 563-566.

Zhang, D. and Fleischman, R.B. (2012a). "Establishment of Seismic Design Force Factors for Precast Concrete Diaphragms". under preparation.

Seismic Design Methodology Document for Precast Concrete Diaphragms

PART 2: QUALIFICATION PROTOCOL

for Precast Concrete Diaphragm Reinforcement

2/16/2014

PART 2: Precast Concrete Diaphragm Reinforcement Qualification Protocol

PART 2A. *Prequalified Precast Diaphragm Reinforcement*

Table 2A-1 provides the prequalified diaphragm reinforcement including:

      (1) Diaphragm Reinforcement Classification: Low Deformability Element (LDE); Moderate
           Deformability Element (MDE), High Deformability Element (HDE).

      (2) Pertinent reinforcement properties for use in the design procedure: elastic tension stiffness k_t ,
           nominal tension strength t_n, elastic shear stiffness k_v and nominal shear strength v_n

        The connector identification (ID) in the first column refers to the connector labels shown in Table 2A-3. Table 2A-3 provides a photo and schematic of each tested connector, including the prequalified connectors. The schematic provides the major details of the connectors; however, the designer must refer to the Lehigh testing reports (Naito et al. 2006) (Naito et al. 2007) for the full description of the connector detailing.

Table 2A-1. Prequalified Diaphragm Reinforcement Table

ID	2A-1a. Reinforcing bars	Classification	Tension				Shear		
			k_t/A	t_n/A	δ_{ty}	δ_{tu}	k_v/A	v_n/A	δ_{vy}
			[k/in/in^2]	[ksi]	[in]	[in]	[k/in/in^2]	[ksi]	[in]
B-1, B-2, B-3	Dry chord Gr.60	LDE	1018	60	0.071	0.1	382	24.2	0.090
D	Dry chord w/ flat plate Gr. 60	MDE	1018	60	0.071	0.3	382	24.2	0.090
E	Pour strip chord Gr.60	HDE	1234	60	0.057	0.7	382	24.2	0.090
G	Ductile ladder Gr.1018	HDE	1260	54	0.043	0.6	217	21.7	0.100
F	Standard ASTM A185 wwr	LDE	1414*	65*	0.035*	0.1*	709	39.7	0.056

* based on testing of wwr with 10″ gage spacing perpendicular to joint

ID	2A-1b. Connectors	Classification	Tension				Shear		
			k_t	t_n	δ_{ty}	δ_{tu}	k_v	v_n	δ_{vy}
			[k/in]	[kips]	[in]	[in]	[k/in]	[kips]	[in]
A-1, A-2	JVI	HDE	55	3.1	0.066	0.6	226	18.1	0.082
C-2	Hairpin (#4)	HDE	209	9.0	0.043	0.6	181	18.1	0.100
-	Angled bar (#3)	MDE	300	10.2	0.059	0.3	372	17.1	0.045

k_t	= Elastic tension stiffness	k_v	= Elastic shear stiffness
t_n	= Nominal Tension strength	v_n	= Nominal Shear strength
δ_{ty}	= Yield tension deformation	δ_{vy}	= Yield shear deformation
δ_{tu}	= Tension deformation capacity	A	= Bar cross-sectional area

Table 2A-2 Diaphragm Reinforcement Classification

Deformability Category	Tension deformation capacity
LDE	$\delta_t < 0.3"$
MDE	$0.3 \leq \delta_t < 0.6"$
HDE	$0.6" \leq \delta_t$

Table 2A-3 Connector Property Database

A-1. Stainless 304 JVI
A-2. A36 JVI

B-1. Bonded chord

B-2. Unbonded carbon chord; B-3. Unbonded stainless chord

C-1. Pretopped hairpin
C-2. Topped hairpin

D. Cover plate

E. Pour strip

F. Topping

G Ductile Ladder

G&C. Topped Hairpin & Ductile Mesh

Tyep A: A to B(single weld) Type B: B to A(2 welds)
a. Uniform 102mm panel
b. Stepped panel
c. ALTUS panel (83mm thickness)
H-1. B-A w/ a; H-2. A-B w/ a; H-3. A-B w/ b;
H-4. A-B w/ c; H-5. A-A w/ b; H-6. B-A w/ b;
H-7. A w/b; H-8. B w/ b; H-9. B w/ a;
H-10. A w/ c; H-11. B w/ c
H. Meadow Burke Connector

I-1. Stainless 304 steel w/ 51mm panel

I-2. A36 steel w/ 102mm panel
I. Twister Connector

J-1. 1008 steel w/ 102mm panel
J-2. 10B38 steel w/ 102mm panel
J-3. A36 steel w/ 51mm panel
J. Metromont Corporation Flange Connector

L-1. 1018 S   L-2. 1018 L   L-3. 304 S
L-4. 304 L   L-5. Rebar S   L-6. Rebar L
L-7. A36 L   L-8. A36 S
Note: S (Small), L (Large); Small connectors go w/ 51mm panel; large connectors go w/ 102mm panel.
L. Universal Building Products Edge Connector

K-1. Large size w/ 102mm panel
K-2. Small size w/ 51mm panel
K. Next Gen Twister Connector by Universal Form Clamp Company

Diaphragm-to-LFRS Connection Deformation Requirements

The diaphragm-to-LFRS connection has a separate set of deformation capacity requirements. The reinforcement or connectors comprising the diaphragm-to-LFRS connection deformation capacity (δ_c) shall satisfy the following condition:

$$\delta_c \geq C_2 \delta_{cb}$$

where C_2 is a coefficient for diaphragm seismic demand level (See Table 2A-4), and δ_{cb} is a reference deformation capacity for diaphragm-to-LFRS connection (See Table 2A-5).

Table 2A-4. C_2 coefficient for diaphragm-to-LFRS connections.

Seismic Demand Level	C_2
Low	1.0
Moderate	2.0
High	3.0

Table 2A-5. Reference deformation capacity for diaphragm-to-LFRS connections.

δ_{cb}	Exterior wall	Interior wall	Lite wall	Moment frame
Opening	0.05"	0.15"	0.05"	0.1"
Sliding	0.1"	0.05"	0.15"	0.1"

Diaphragm Secondary Connection Deformation Requirements

The recommendations for diaphragm for diaphragm secondary connections are listed in Table 2A-6

Table 2A-6. Deformation capacity recommendations for diaphragm secondary connections.

Deformation	Parking Structure		Regular building	
	Internal beam	Spandrel	Internal beam	Spandrel
Opening	0.25"	0.10"	0.25"	0.15"
Sliding	0.15"	0.15"	0.10"	0.10"

PART 2B. *Precast Diaphragm Reinforcement Qualification Procedure*

This section provides a qualification procedure using experimental methods to assess the in-plane strength, stiffness, and deformation capacity of precast concrete diaphragm connections. The methodology is developed specifically for diaphragm flange-to-flange connections, and is intended to provide the required properties and classification for use in the seismic design procedure in PART 1 of the *Seismic Design Methodology Document for Precast Concrete Diaphragms*.

EXPERIMENTAL SETUP

Test Modules

To evaluate the performance of a precast concrete connection a test module representing the connection and the precast concrete element it is embedded in shall be fabricated and tested. A separate test module shall be used for each characteristic of interest. At a minimum, one in-plane shear test module, and one in-plane tension test module shall be evaluated. It is strongly recommended to conduct multiple tests to assess repeatability and consistency.

Modules shall be fabricated at full scale for qualification. Reduced scale connectors with appropriate reductions in maximum aggregate size and following laws of similitude can be used as research tools to gain knowledge but are not to be used for connector qualification. Full scale modules shall include a tributary concrete section of at least 2 ft (0.61 m). Since the test module represents only a small portion of a precast concrete panel, potential confinement effects are not provided and the panel may be subjected to premature cracking. Additional reinforcement shall be used to prevent premature failure of the test module. The additional reinforcement shall not be placed in a way that would alter the performance of the connector. Example reinforcing strategies for the 2 ft by 4 ft (600 mm by 1200 mm) ½ test module is illustrated in **Figure** 1. The connections should be installed and welded in the test module in accordance with the intended guidelines.
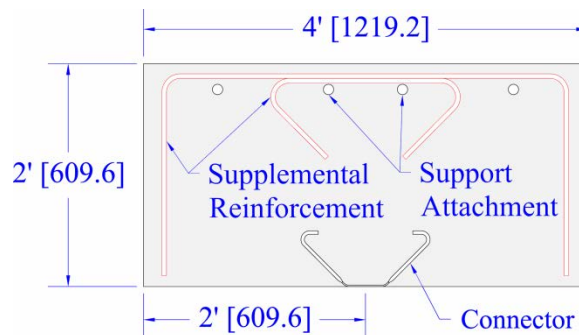
Figure 1. Test module: plan view of half specimen.

Test Setup

For each connection test a multi-directional test fixture shall be used to allow for the simultaneous control of shear, axial, and potential bending deformations at the panel joint. A possible setup is illustrated in **Figure** 2. The fixture is composed of three independently controlled actuators, two providing axial displacement and one providing shear displacement to the connection. Demand shall be

applied through displacement control of each of the three actuators. The test specimen shall be connected to restraint beams on either end of the panel, slip between the test module and beams shall be minimized. One support beam shall be fastened to the laboratory floor, providing a fixed end, while the other beam rests on a low friction movable support. Vertical movement of the panel shall be restricted by providing support under the center of each panel.
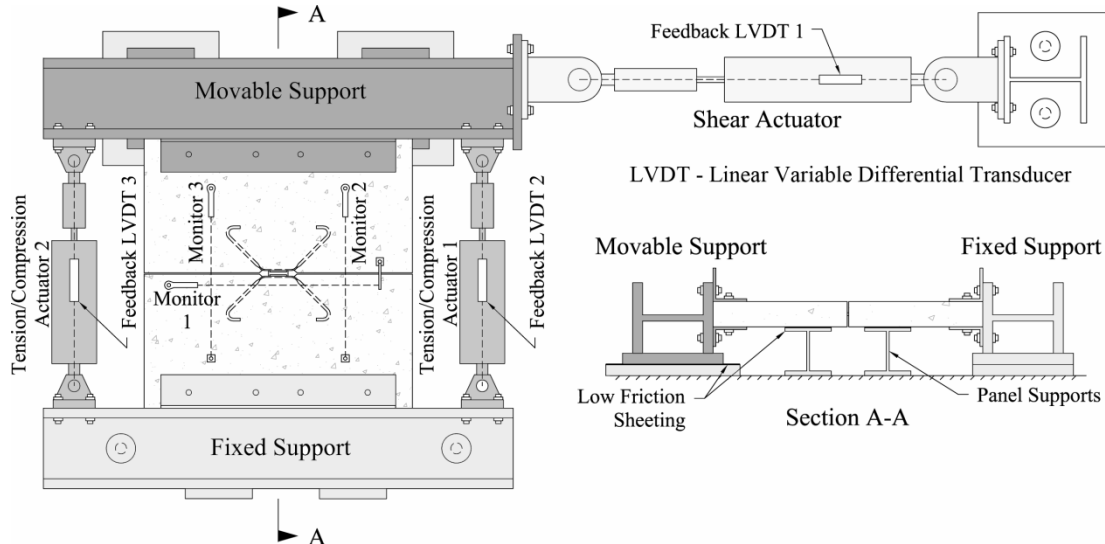
Figure 2: Multi-directional test fixture

Instrumentation

At a minimum instrumentation shall consist of displacement and force transducers. Force shall be measured in line with each actuator to quantify shear and axial demands on the connection. To accommodate displacement control of the actuators feedback transducers shall be incorporated into each actuator. Connection deformation shall be measured directly on the test module (use of actuator transducers is not recommended due to potential slip in the test fixture). A minimum of two axial transducers shall be used to determine the average axial opening and closing at the connection. Shear deformation shall be determined from measurements taken at the location of the connection. Placement of the transducers on the test module shall be at an adequate distance from the connection to minimize damage to the transducer supports during the test history. A possible arrangement of transducers is illustrated in **Figure** 2.

LOADING PROTOCOLS

Connections shall be evaluated for in-plane shear, tension, and combinations of shear with tension.

Load Control and Loading Rate

Tests shall be conducted under displacement control using quasi-static rates less than 0.05 in. / sec (1.25 mm /sec) or through an enhanced mixed displacement and force control. All test modules shall be tested until the specimen capacity approaches zero.

Monotonic Load Test

A monotonic test shall be performed to determine the reference deformation of the connection if a reference is not available. The reference deformation represents the effective yield of the test module.

The monotonic shear and tension loading protocol consists of three preliminary cycles to 0.01 in. (0.25 mm) to verify control and instrumentation operation. Following verification of the system the test module shall be loaded under a monotonically increasing displacement until failure.

Cyclic Shear Protocol

Cyclic shear protocol consists of three preliminary cycles to 0.01 in. (0.25 mm) to verify control and instrumentation operation. Following verification of the system the test module shall be loaded in increasing sets of shear deformation as illustrated as in **Figure** 3. The tension deformation across the joint shall be maintained at a constant level during the shear history through adjustment of the tension/compression actuators 1 and 2. The axial deformation shall be maintained at zero or at a tension opening of 0.1 in. (2.5 mm).

- In-plane cyclic shear tests (with a constant 0.1 in. axial opening) shall be conducted to failure to determine stiffness and strength capacity of connection under shear loading. .
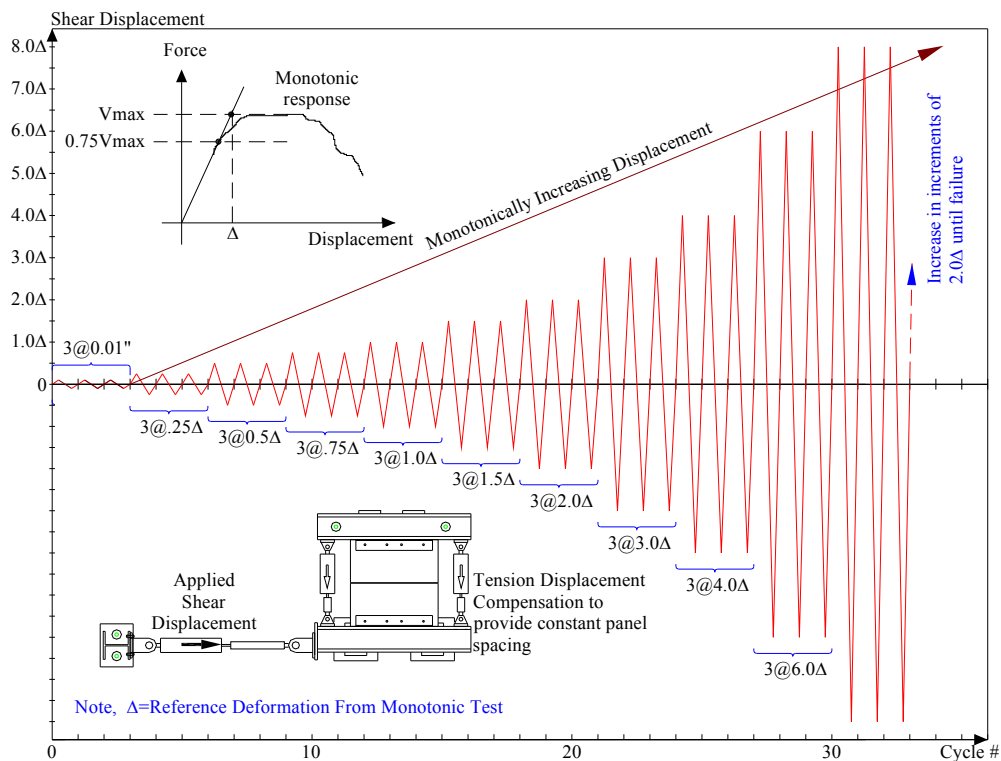
Figure 3: Shear loading protocol

Cyclic Tension / Compression Protocol

Cyclic tension / compression protocol consists of three preliminary cycles to 0.01 in. (0.25 mm) to verify control and instrumentation operation. Following verification of the system, the test module shall be loaded in increasing sets of tension deformation as illustrated as in **Figure** 4. Due to the high compression stiffness of connections the compression portion of each cycle shall be force limited. Each compression half cycle shall consist of an increasing compression deformation until a force limit is reached. The force limit for each cycle shall be equal to the max force of the preceding tension half cycle.

8

The shear deformation shall be maintained at zero through adjustment of the shear actuator. As an alternate, the shear actuator may be disconnected from the setup prior to loading allowing for zero shear force during the cyclic tension/compression history.

- In-plane cyclic tension tests shall be conducted to failure to determine stiffness, strength capacity and deformation capacity of connection under tension loading. The measured tension deformation capacity shall be used to establish the performance category of the connection.
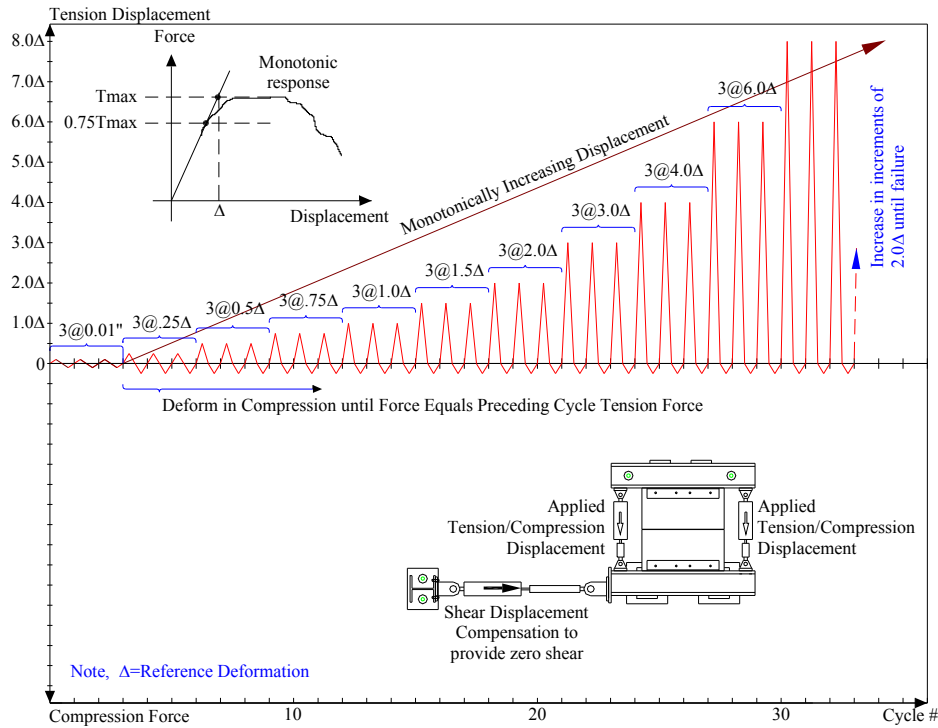
Figure 4: Tension/Compression loading protocol.

MEASUREMENT INDICES

Test Observations and Acquisition of Data

Quantitative data shall be recorded from the test such that interpretation can be made of the performance of the test module. A continuous record shall be made of the force versus deformation. For in-plane tests the axial and shear force, and deformations should be recorded. Data shall be recorded at a minimum rate of 1.0 cycle/second. Photographs shall be taken to illustrate the condition of the test module at the initiation and completion of testing as well as points through the testing history. Ideally photos should be taken at the end of each group of cycles. Test history photos taken at points of interest, such as cracking, yield, ultimate load and post-test, are adequate for most evaluations.

Reference Deformation

Experimental determination of the reference deformation, $\varDelta$, shall be based on a monotonic test of a connection test module. The reference deformation represents the effective yield deformation of the connector. It shall be computed by taking the intercept of a horizontal line at the maximum tension force (T_{max}) or shear force (V_{max}) and a secant stiffness line at 75% of the maximum measured load (**Figure** 4 inset). As an alternate to the monotonic test, analytical determination of the reference deformation is allowed in accordance with section 6 and 7.

9

Backbone Qualification Envelope

The measured cyclic response shall be processed in accordance with the procedures outlined in ASCE/SEI 41-06 Seismic Rehabilitation of Existing Buildings.[18] Each connection shall be classified as deformation-controlled (ductile) or force-controlled (non-ductile). This assessment shall be determined based on the backbone curve of the response.

An envelope of the cyclic force deformation response shall be constructed from the points making up the peak displacement applied during the first cycle of each increment of loading (or deformation) as indicated in ASCE/SEI 41-06.[18] This method provides a higher estimate of strength than alternate methods outlined in FEMA 356, in which the envelope is defined by drawing through the intersection of the first cycle curve for all the ith deformation step with the second cycle curve of $(i-1)^{th}$ deformation step.[19] The difference between the two methods is illustrated in **Figure** 5 for a ladder connection[20].
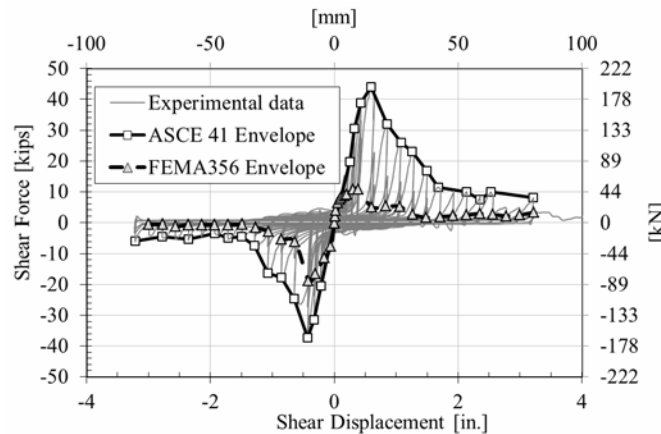
Figure 5: Cyclic envelope determination

The cyclic envelope shall be further simplified to a multi-segment backbone curve. The backbone curve shall consist of a four point (Point '1', '2', '2a', '3') multi-linear curve as illustrated in **Figure** 6.
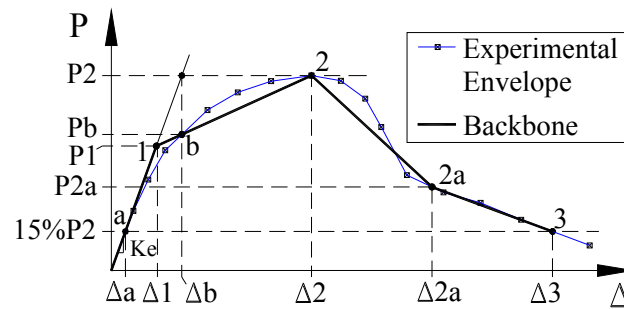
Figure 6: Backbone Qualification curve

The backbone curve is adopted to represent a simplistic approximation of the load-deformation response of the connection. Point 2 represents the peak envelope load. Point 'a' is defined as the point where the strength first achieves 15% of peak load. Initial elastic stiffness is calculated as the secant of strength-displacement relationship from origin to point 'a'. Point 'b' is the point on the envelope curve at a displacement Δ_b. The deformation Δ_b is the intersection of a horizontal line from the max envelope load and the initial elastic stiffness line at 15% of the max load. Point '1' represents the occurrence of yield, which is defined by drawing a line between point '2' and 'b' and extending back to intersect the initial elastic stiffness line at 15% of the max load. Point '3' is defined as the point where the strength is less than 15% of the peak load. Point '2a' is defined as the point where the deformation is 50% of the summation of deformations at point '2' and '3'. The points are defined in terms of the resistance P_a, P_1, P_b, P_2, P_{2a}, and P_3, and the displacements Δ_a, Δ_1, Δ_b, Δ_2, Δ_{2a} and Δ_3. The initial elastic stiffness K_e is the secant at point a. The procedure of determination of these points is shown as follows:

1. Determine the force at point 2, $P_2 = P_{max}$

2. Determine the force at point a, $P_a = 15\% \times P_{max}$

   Determine the deformation at point a, Δ_a from original data.
3. Determine the initial elastic stiffness, $K_e = P_a/\Delta_a$; Determine the deformation at point b, $\Delta_b = P_2/K_e$

   Determine the force at point b, P_b from the original data.
5. Determine the deformation, Δ_1, and force, P_1 at point 1 using:

$$\Delta_1 = \frac{(P_b\Delta_2 - P_2\Delta_b)}{K_e(\Delta_2 - \Delta_b) - (P_b - P_2)} \qquad P_1 = K_e\Delta_1$$

6. Determine the force at point 3, $P_3 = 15\% \times P_{max}$ The deformation, Δ_3 can be found from original data.
7. Determine the deformation at point 2a, $\Delta_{2a} = (\Delta_2 + \Delta_3)/2$ Determine the force at point 2a, P_{2a}, from the original data.

The backbone curve shall be classified as one of the types indicated in **Figure** 7. As depicted in **Figure** 7, the type 1 curve is representative of ductile behavior where there is an elastic range (point 0 to point 1 on the curve) and an inelastic range (point 1 to point 3 on the curve), followed by loss of force-resisting capacity. The type 2 curve is representative of ductile behavior where there is an elastic range (point 0 to point 1) and an inelastic range (point 1 to point 2 on the curve), followed by substantial loss of force-resisting capacity. Some connections may exhibit a small peak strength with limited ductility. For these cases the alternate type 2 curve is recommended. The type 3 curve is representative of a brittle or non-ductile behavior where there is an elastic range (point 0 to point 1) followed by loss of strength. Deformation controlled elements shall conform to type 1 or type 2 response with $\Delta_2 \geq 2\Delta_1$. All other responses shall be classified as force-controlled.
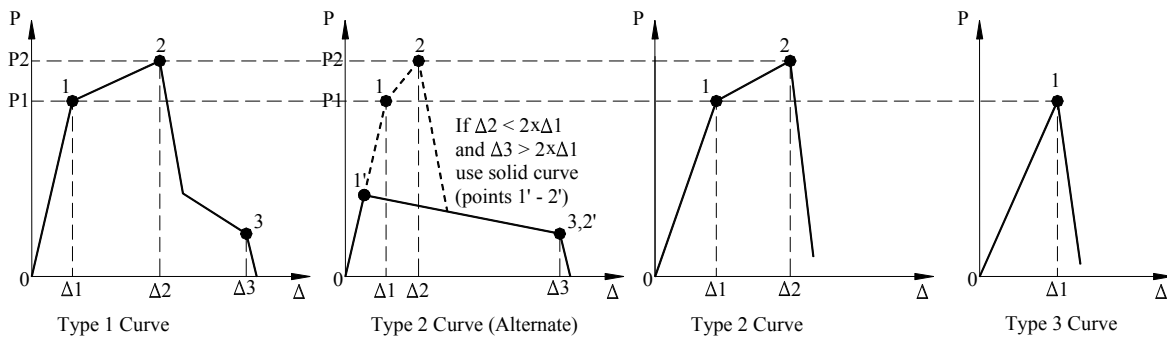
Figure 7: Deformation curve types

Response Properties

The performance characteristics of the connector shall be quantified from the backbone response. The following values shall be quantified.

Stiffness

The initial elastic stiffness of the connection shall be determined from the secant to yield point 1. The previous formulation for K_e shall be used.

Deformation Capacity

The reliable and stable maximum deformation capacity is defined for design code purposes as the connector deformation at peak load, point Δ_2 on the backbone curve, obtained in testing following the loading protocols defined here. It is noted that the analytical calibrations were performed for a reliable and stable maximum deformation capacity corresponding to a deformation where the strength reduces to 80% of P_2 , which is similar to the beam-column connection deformation capacity definition for steel structures (AISC Seismic Provisions 2005). Thus, an added degree of conservatism is provided in the definition proposed for the design code. When multiple tests are conducted for repeatability, the deformation capacity for each connection test shall be used as follows. The connection deformation capacity shall be determined as the mean value of each test deformation capacity for deformation-controlled elements and the mean minus one standard deviation for force-controlled connections.

Deformation Category

The connection shall be classified as a low-deformability element (LDE), a moderate-deformability element (MDE), or a high-deformability element (HDE) based on its deformation capacity in tension. The deformation capacity as defined in 8.2.2 shall be used to classify the deformability category of the connector in accordance **Table** 2A-2. The category ranges were determined from finite element analysis of a database of diaphragm systems under a range of seismic demands[5]. Alternate deformation limits can be used if supportive data is provided.

Tension Force Capacity

The tension force capacity of the connection is defined as the maximum force, P_2 for deformation controlled connections and as P_1 for force controlled connections.

Shear Force Capacity

The intention is for the diaphragm system to remain elastic under shear demands. Consequently the inelastic shear force capacity of connections shall not be considered. The shear force capacity shall be computed at force level P_1 for all connections. Due to the existence of low stiffness connections limits are placed on the allowable deformation at which the force capacity, P_1, can be determined.
- If the shear deformation Δ_1 is less than 0.25 in. (6.4 mm), the shear force capacity shall be taken as the yield force P_1.
- If the shear deformation Δ_1 is greater than 0.25 in. (6.4 mm), the shear force capacity shall be taken as the force value at 0.25 in. This shear force capacity can be computed as the stiffness, K_e, multiplied by 0.25 in.

Test Report

The test report must be sufficiently complete and self-contained for a qualified expert to be satisfied that the tests have been designed and carried out in accordance with the criteria previously described, and that the results satisfy the intent of these provisions. The test report shall contain sufficient evidence for an independent evaluation of the performance of the test module. As a minimum, all of the following information shall be provided:
- Details of test module design and construction, including engineering drawings.
- Specified materials properties used for design, and actual material properties obtained by testing.
- Description of test setup, including diagrams and photographs.
- Description of instrumentation, location, and purpose.
- Description and graphical presentation of applied loading protocol.

- Material properties of the concrete measured in accordance with ASTM C39[21]. The average of a minimum of three tests shall be used. The compression tests shall be conducted within 7 days of the connection tests or shall be interpolated from compression tests conducted before and after the connection test series.
- Material properties of the connector, slug, and weld metal based on material testing or mill certification. As a minimum the yield stress, tensile stress, and the ultimate strain shall be reported.
- Description of observed performance, including photographic documentation, of test module condition at key loading cycles.
- Graphical presentation of force versus deformation response.
- The envelope and backbone of the load-deformation response.
- Yield strength, peak strength, and deformation capacity and connection category.
- Test data, report data, name of testing agency, report author(s), supervising professional engineer, and test sponsor.

Note: All the connections should be installed and welded in accordance with the manufacturer's published installation instructions. The results of the data generated shall be limited to connections built to the specified requirements.

PART 2C. *Commentary on Precast Diaphragm Reinforcement Qualification Protocol*

This commentary is based on *An Evaluation Method for Precast Concrete Diaphragm Connectors Based on Structural Testing* (Naito and Ren, 2011).

INTRODUCTION

The precast diaphragm seismic design methodology, unlike conventional force-based diaphragm design, uses a performance-based approach that requires knowledge of the diaphragm connector stiffness, deformation capacity, and strength to effectively and efficiently design the diaphragm system for seismic forces. To meet this need it is critical that the connector properties be determined in a repeatable, reproducible, and consistent manner so that existing and new connections can be utilized effectively in the diaphragm system. The qualification protocol provides an experimental evaluation approach for assessing the mechanical properties of embedded connections used in conventional precast concrete panel systems. The measured responses are tied to performance levels which are used to categorize connectors in accordance with the procedure in PART 1 of the the *Seismic Design Methodology Document for Precast Concrete Diaphragms*.

Scope

This recommendation is intended to meet American Concrete Institute's (ACI's) *Building Code Requirements for Structural Concrete (ACI 318-08) and Commentary (ACI 318R-08)* for precast concrete connections[15]. As defined in Section 16.6.1.1 the *adequacy of connections to transfer forces between members shall be determined by analysis or by test*. This recommendation provides test procedures for assessing both strength and deformation capacity.

Under seismic demands connections between adjacent precast concrete diaphragms elements are subject to combinations of shear, tension and compression. The relative combinations of these deformation or force components are dependent on the location within the diaphragm and the presence of discontinuities. The testing method independently determines the shear and tension performance of connections. Alternate procedures are also provided for determination of combined interactions of shear and tension.

Background

Precast concrete floor diaphragms are composed of large precast concrete panels connected to each other through discrete embedded connections. These connections act to transfer vertical and in-plane demands between panels. Vertical force demands are limited to 3 kips (13.3 kN) in accordance with ASCE 7 [2010][1]. Assurance of connector vertical capacity can be achieved through standard strength testing. Under seismic events the floor system is subject to in-plane inertial demands which subject the discrete connections to combinations of in-plane shear, tension and compression [Fleischman et. al. 1998][2].

Using traditional diaphragm design approaches, adequate in-plane force capacity is required for each connection to safely support the expected earthquake demands. Simplified diaphragm modeling methods are provided in the *PCI Design Handbook: Precast and Prestressed Concrete*[3] to determine the required shear and tension demand in each connection. Subsequent force-based connection design approaches such as those outlined in the *PCI Connection Manual for Precast and Prestressed Concrete Construction*[4] can be followed to size the connection required.

To provide enhanced safety and economy in design, a new performance-based formulation for precast diaphragms has been outlined in the *Building Seismic Safety Committee TS4* [2009][5]. This method relies not only on the strength of the connections used but also on the stiffness and deformation capacities. Under the proposed design methodology the choice of connection type is tied to the flexure and shear over-strength factors needed by the diaphragm to meet the required level of seismic performance. While the methodology is complex, in essence the use of connections with limited deformation capacity could result in higher required design forces while ductile connections could allow for lower design forces. To choose the appropriate over-strength factor thus requires knowledge on the deformation capacity of each connection type used in the diaphragm.

Due to the variety of connections in use, analytical determination of the expected deformability is not trivial. Connection deformation capacity under in-plane tension and shear is contingent on a series of inelastic failure modes. These include concrete breakout, yield of the anchorage bars, flexure or torsion of the faceplate, yield of the slug or jumper plate, fracture of the welds, or fracture of the faceplate or anchorage as illustrated in **Figure 1**. The occurrence of each of these conditions is difficult to accurately predict even with finite element methods. Furthermore each connection type exhibits variations in these modes of failure. Consequently proper determination of the deformation capacity of connections is best determined through experimental evaluation.
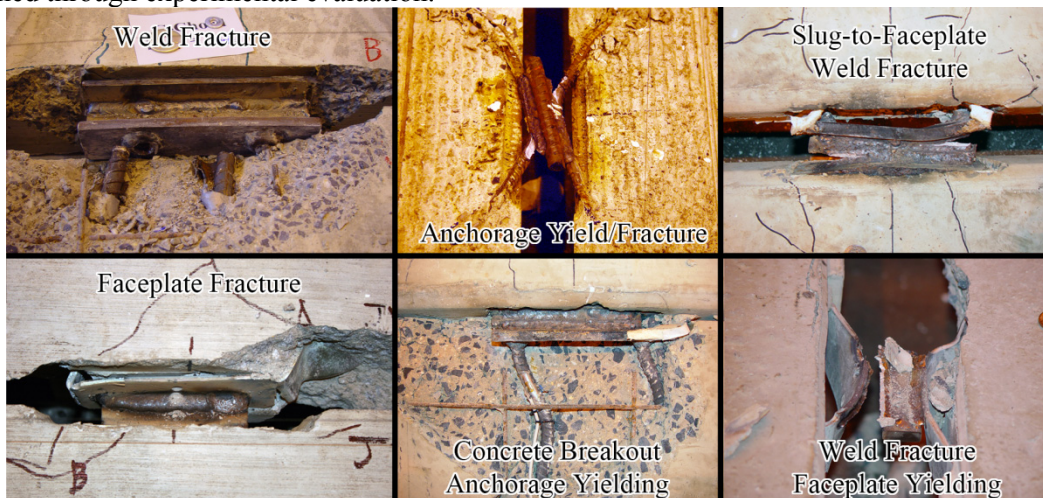
Figure 1: Potential in-plane failure modes in diaphragm connections

Existing Experimental Methods

A significant amount of experimental research has been conducted on evaluating response of diaphragm connectors under in-plane demands. Initial experiments on shear mechanical connector were conducted in 1968 when Venuti (1970)[6] examined 68 rebar connections. Since then many studies have been conducted to qualify the performance of flange to flange connectors[7-13]. Connections were evaluated under in-plane shear loading, in-plane tension loading, and combined in-plane shear and tension demands. Studies were conducted both monotonically and cyclically. Most test fixtures from 1970 to 1980 were developed to examine the connector performance under monotonic in-plane shear strength through force control. This approach is unable to capture post-peak behavior and deformation capacity. In addition, most studies utilized half the connection to ease installation and lower testing cost. Research has shown that the level of axial restraint significantly affects the measured shear capacity[14]. These systems were connected to a stiff loading beam to artificially restrain the connector; unfortunately for most cases the axial restraint provided by the loading beam was not measured. With these shortcomings, the previous experimental approaches have limited ability to correctly quantify both the strength and deformation properties of diaphragm connections under in-plane demands.

Loading Protocols

Under seismic demands a floor diaphragm system is subjected to a spectrum of relative motions. Analytical studies on the precast concrete diaphragm response to seismic demands[16] have shown that the connection displacement history is dependent on the location within the diaphragm. Connections located at the mid-span of the diaphragm are subjected to high flexural demands while connections located at the boundaries are subjected to high shear demands with minimal tensile opening. Connections located in intermediate diaphragm regions are subjected to combined shear and tensile deformation demands with a common shear-to-tension deformation ratio of 2.0. To encompass these possible motions, six displacement protocols are possible to assess the performance of diaphragm connectors subjected to seismic demands. These protocols include:

- *Monotonic Shear* – For determination of connection shear yield and associated reference deformation for use in the cyclic loading protocol. Monotonic tests shall be eliminated if connection yield deformation can be estimated.
- *Cyclic Shear* – For determination of connector shear stiffness, strength, deformation limits, and modes of failure.
- *Monotonic Tension* – For determination of connection tension yield and associated reference deformation for use in the cyclic loading protocol. Monotonic tests shall be eliminated if connection yield deformation can be estimated.
- *Cyclic Tension and Compression* – For determination of connector tension stiffness, strength, deformation limits, and modes of failure.
- *Monotonic Shear with Proportional Tension* – Alternate protocol to assess influence of combined tension and shear.
- *Cyclic Shear with Axial Force Control* – Alternate protocol to assess influence of axial confinement on shear performance.

Cyclic Protocols

To assess the performance of diaphragm connections for use in seismic applications, evaluation shall be conducted with cyclically increasing demands. The cyclic demand shall be applied relative to the reference deformation of the connection to ensure that an appropriate number of elastic and inelastic cycles are applied.

Cyclic loading protocols in accordance with Precast Seismic Structural Systems (PRESSS) program are recommended[17]. Testing with three preliminary cycles to 0.01 in. (0.25 mm) shall be conducted to evaluate control and acquisition accuracy. The remaining protocol consists of groups of three symmetric cycles at increasing deformation levels. Each level is based on a percentage of a reference deformation computed from the corresponding monotonic tests.

Alternate Protocols

For cases where additional connector performance is needed, two alternative loading protocols can be used.

Monotonic Shear with Proportional Tension

Diaphragm connections may be subject to combinations of shear and tension due to their location in the diaphragm. A shear to tensile deformation ratio of 2.0 is recommended for web connections used in shear dominated regions of the diaphragm. A ratio of 0.5 is recommended for chord connections in tension dominated regions of the diaphragm. The monotonic shear with tension test consists of three cycles of 0.01 in. (0.25 mm) in shear and a proportional tension/compression deformation (**Error! Reference source not found.**). The shear and tension deformations are increased proportionally using the

chosen constant shear-to-tension deformation ratio. The test shall be paused at each 0.1 in. (2.5 mm) of shear deformation for observations.

- In-plane monotonic shear with proportional tension tests may also be conducted for the connections used in intermediate diaphragm regions. In-plane cyclic shear with a target axial load tests could be conducted if needed.

Cyclic Shear with Axial Force Control

Enhanced displacement based control protocols may be used to evaluate the connections under in-plane shear. Standard shear displacement based protocols hold the joint opening at a fixed opening which may result in the build-up of large axial forces. The enhanced protocols are developed to examine the shear performance of connections under fixed levels of axial force. These test protocols provide information that can be used to model the shear resistance of connections at various locations in the floor diaphragm. This includes regions of high compression, tension or areas where zero axial loads are present.

All tests shall be conducted at quasi-static rates under mixed displacement and force control. The control shall be achieved using an inner control loop and an outer control loop. The outer loop conforms to the deformation based shear protocols shown in **Figure** 3. Each displacement step shall be divided into small sub-steps of approximately 0.001 in. (0.025 mm). Each sub-step shall be applied in the inner control loop. The inner loop is controlled in a mixed load and displacement manner. After the application of each inner loop shear sub-step, the force in the axial actuators shall be measured. If the sum of the forces is greater than the target axial load, the actuators shall be extended an equal amount until the axial force equals the target. If the axial force is less than the target axial load, the actuators shall be retracted until the axial force equals the target. An error tolerance of 500 lbf (2.2 kN) to 1000 lbf (4.5 kN) shall be used for acceptance. Following this procedure the next sub-step shall be applied and the axial inner loop shall be repeated. This process shall be continued until the full outer shear step is applied. Then next shear step would be applied and the process would be repeated.

The algorithm of applying shear deformation with zero axial load is as follows:

1. Apply shear deformation step to shear actuator;

2. Read force in compression/tension actuators 1 and 2, F_1 and F_2;

3. Compute Total force, $F_t = F_1 + F_2$;

   a. If, $F_t > 0$, Extend actuators 1 and 2 until $F_t = 0$

   b. If, $F_t < 0$, Retract actuators 1 and 2 until $F_t = 0$

4. Go to Step 1 until target shear displacement is reached.

Reference Deformation

- A monotonic tension test shall be conducted to determine the initial reference deformation for use in the cyclic tension tests. Two alternative (non-experimental) methods may be used for determination of the reference deformation. (1) The reference deformation may be based on an analytical estimate of the yield deformation of the connection. (2) The reference deformation may be based on a desired deformation capacity for the connection. For this method, the deformation category of the connection may be used as the reference deformation.

- A monotonic shear test shall be conducted to determine the initial reference deformation for use in the cyclic shear tests. Two alternative (non-experimental) methods may be used for determination of the reference deformation. (1) The reference deformation may be based on an analytical estimate of the shear yield deformation of the connection. (2) The reference deformation may be based on a desired deformation capacity for the connection.

Multiple Tests Approach

To provide accurate stiffness, strength, and deformation capacity multiple tests for shear and tension are recommended. The connection performance shall be tied to the number of tests conducted. The performance of the connector shall be based on the average of the tests if: a minimum of five tests are conducted, or at least three tests are conducted with none of the results varying more than 15 percent from the average of the three. Otherwise the lowest measured values shall be used. Additional requirements are recommended for determination of deformation capacity (see section 8.2.2).

Conclusions

An evaluation method for precast concrete diaphragm connectors based on structural testing is provided. The recommendation provides a detailed procedure for determination of stiffness, deformation capacity, and force capacity. Details on developing a test module, loading setup, load histories, instrumentation, data reduction, reporting and performance categorization is given. Adherence to the test method allows connection properties to be determined in a repeatable, reproducible, and consistent manner so that existing and new connections can be quantified and utilized effectively in the diaphragm system.

Notation

All the symbols are defined in this section.

LVDT = linear variable differential transformer

Δ = reference deformation, in

T_{max} = maximum tension force, kip

V_{max} = maximum shear force, kip

F_1 = axial force read from actuator 1, kip

F_2 = axial force read from actuator 2, kip

F_t = axial force resisted by connections, kip

P_{max} = force at yield point on multi-segment backbone curve, kip

P_a = force at point 'a' on the multi-segment backbone curve, kip

P_b = force at point 'b' on the multi-segment backbone curve, kip

P_1 = force at point '1' on multi-segment backbone curve, kip

P_2 = force at point '2' on multi-segment backbone curve, kip

P_{2a} = force at point '2a' on multi-segment backbone curve, kip

P_3 = force at point '3' on multi-segment backbone curve, kip

Δ_a = deformation at point 'a' on the multi-segment backbone curve, in

Δ_1 = deformation at point '1' on the multi-segment backbone curve, in

Δ_b = deformation at point 'b' on the multi-segment backbone curve, in

Δ_2 = deformation at point '2' on the multi-segment backbone curve, in

Δ_{2a} = deformation at point '2a' on the multi-segment backbone curve, in

Δ_3 = deformation at point '3' on the multi-segment backbone curve, in

K_e = initial elastic stiffness of the multi-segment backbone curve, kip/in

LDE = low-deformability element

MDE = moderate-deformability element

HDE = high-deformability element

ΔT = tension deformation measured across the connectors, in

PART 2D. *Lehigh Test Database*

		See Table 2A-3 for connector ID			Table 3 DT/DT Web Connector Performance							
ID	Test Type	Testing Notation	Δa (mm)	P1 (kN)	P2 (kN)	Δ2 (mm)	P2a (kN)	P3 (kN)	Δ3 (mm)	Initial Stiffness Ke (kN/mm)	Category	Ultimate Force (kN)
A-1	Tension	MT	0.248	21.0	45.2	32.00	41.2	6.6	51.02	28	HDE	45.2*
		CT	0.343	11.9	26.6	12.65	25.3	4.0	20.10	12		26.6*
	Shear	MV(ΔT= 0)	0.580	47.5	157.0	19.30	98.3	23.5	50.77	41	LDE	157.0*
		MTV(ΔT/ΔV = 0.5)	0.330	58.2	126.0	5.08	113.1	18.7	63.73	57		126.0*
A-2	Tension	MT	0.208	23.3	56.2	53.34	19.5	8.6	127.67	41	HDE	56.2*
		CT	0.135	9.6	32.7	14.61	31.5	4.8	25.93	37		32.7*
	Shear	MV_LC(Ft=0)	0.152	44.7	95.2	28.19	28.1	14.1	116.45	94	LDE	95.2*
		CV(ΔT= 0)*3	0.354	36.4	127.9	7.31	94.0	19.2	14.98	54		127.9
		CV_LC(Ft=0)	0.171	36.4	82.2	1.91	52.8	12.3	8.80	72		82.2*
		CV_LC(Ft=10kip)	0.197	61.0	122.6	3.14	43.7	18.9	12.38	96		122.6*
B-1	Tension	MT	0.109	79.3	166.5	8.38	123.8	25.0	24.19	229	MDE	166.5*
		MTV(ΔT/ΔV = 0.5)	0.159	59.7	150.8	9.53	28.9	22.5	28.04	143		150.8*
	Shear	MTV(ΔT/ΔV = 0.5)	0.302	70.1	141.5	7.11	69.3	21.2	23.28	70	LDE	141.5*
		MV(ΔT= 0)	0.213	64.0	241.9	3.05	52.6	37.3	22.84	175		241.9*
		CV(ΔT= 0.1)	0.341	122.2	283.9	5.98	202.6	42.6	12.54	125		283.9*
B-2	Tension	MT	0.177	117.4	245.5	22.35	186.0	36.9	121.73	208	MDE	245.5*
		CT	0.185	100.1	206.9	6.99	145.6	31.1	10.37	168		206.9*
	Shear	MV(ΔT= 0)	1.562	21.2	139.0	19.05	72.0	21.1	83.74	14	MDE	139.0*
		MV_LC(Ft=0)	1.715	18.5	122.2	17.53	83.4	18.4	89.19	11		122.2*
		CV(ΔT= 0)	1.969	20.0	133.7	16.51	38.4	20.0	51.78	10		133.7*
B-3	Tension	MT	0.237	138.3	311.5	12.19	277.0	46.7	12.62	197	MDE	311.5*
		CT	0.199	111.4	232.5	6.20	105.4	35.0	50.64	175		232.5*
	Shear	MV(ΔT= 0)	0.876	18.4	122.7	19.05	71.5	18.4	100.03	21	MDE	122.7*
		CV(ΔT= 0)	1.562	16.9	112.6	14.61	37.7	16.9	54.83	11		112.6*
		CV_LC(Ft=0)	3.073	123.0	129.0	20.32	44.1	18.6	41.45	6		129.0*
C-1	Tension	MT	0.419	11.9	34.3	36.58	29.8	5.1	47.04	12	HDE	34.3*
	Shear	MV(ΔT= 0)*2	0.297	16.8	38.6	32.51	10.2	5.8	58.15	20	HDE	38.6
C-2	Tension	MT	0.069	18.4	111.3	1.14	102.5	16.8	4.17	244	LDE	111.3*
		MTV(ΔT/ΔV = 0.5)	0.075	24.4	100.8	1.14	97.9	15.1	3.75	201		100.8*
	Shear	MV(ΔT= 0.1)*2	0.379	99.2	228.2	7.11	112.6	34.2	58.89	95	LDE	228.2
		MTV(ΔT/ΔV = 0.5)	0.201	32.1	132.6	5.08	104.0	19.9	19.10	99		132.6*

Table 3 DT/DT Web Connector Performance												

Table 3 DT/DT Web Connector Performance

Group	Mode	Test									Class	Max
		CV(ΔT= 0.1)	0.364	89.3	239.4	12.10	137.1	36.6	17.65	100		239.4*
D	Tension	MT	0.080	55.2	193.2	3.81	114.9	28.9	14.56	363	LDE	193.2*
		MTV(ΔT/ΔV = 0.5)	0.066	19.0	125.4	3.05	63.5	18.8	25.91	285		125.4*
	Shear	MV(ΔT= 0.1)	0.428	94.2	239.8	8.13	81.1	35.9	72.14	84		239.8*
		MTV(ΔT/ΔV = 0.5)	0.228	50.0	151.8	4.06	37.3	22.8	23.62	100	LDE	151.8*
		CV(ΔT= 0.1)	0.284	55.5	117.8	4.12	77.2	17.7	17.61	62		117.8*
E	Tension	MT	0.122	130.0	277.3	3.43	207.0	41.6	56.66	341		277.3*
		MTV(ΔT/ΔV = 2.0)	0.129	111.1	271.8	3.05	247.7	40.8	55.15	316	LDE	271.8*
		CT	0.240	57.7	278.5	2.54	247.4	41.7	31.75	174		278.5*
	Shear	MV(ΔT= 0.1)	0.327	71.8	154.0	9.14	57.3	23.1	88.95	71		154.0*
		MTV(ΔT/ΔV = 2.0)	0.152	6.3	41.8	1.02	17.9	6.1	27.55	41	LDE	41.8*
		CV(ΔT= 0.1)	0.187	21.4	75.9	2.30	32.4	11.4	66.10	61		75.9*
F	Tension	MT	0.107	51.7	110.6	2.29	101.7	16.6	4.82	155	LDE	110.6*
		MTV(ΔT/ΔV = 0.5)	0.107	45.3	97.4	1.91	93.4	14.6	3.71	137		97.4*
	Shear	MV(ΔT= 0.1)	0.447	16.9	48.9	9.14	8.5	7.5	83.62	17		48.9*
		MV(ΔT= 0)	0.268	84.2	194.8	6.10	63.8	29.2	40.13	109	LDE	194.8*
		CV(ΔT= 0)	0.164	15.5	84.7	1.78	70.9	12.7	17.75	78		84.7*
G	Tension	MT	0.092	23.0	131.1	27.94	93.6	19.7	41.86	215	MDE	131.1*
		CT	0.109	18.1	119.3	10.11	34.3	17.9	31.03	165		119.3*
	Shear	MV(ΔT= 0)	0.823	144.3	328.7	12.19	300.6	49.3	16.53	60		328.7*
		MV_LC(Ft=0)	0.511	86.6	155.7	8.38	63.4	23.4	51.27	46	MDE	155.7*
		CV(ΔT= 0)	1.156	74.3	195.6	15.02	57.2	29.3	65.80	25		195.6*
		CV_LC(Ft=0)	1.124	17.8	118.6	19.47	22.8	17.8	67.67	16		118.6*
C& G	Tension	CT	0.104	25.9	170.7	9.53	34.3	25.7	26.42	248	MDE	170.7*
	Shear	CV(ΔT= 0.1)	0.314	86.1	232.0	13.81	228.5	34.7	21.56	111		232.0*
		CV_LC(Ft=10)*2	0.241	75.6	170.3	8.42	113.6	25.5	20.77	107	LDE	170.3
		CV(ΔT/ΔV=0.5(p) ΔT = 0.10(n)	0.145	56.4	164.7	5.72	65.6	24.7	49.30	171		164.7*
H-1	Tension	MT	2.179	15.6	16.1	29.97	12.8	2.5	56.27	1	HDE	16.1*
		MTV(ΔT/ΔV = 0.5)	0.508	7.6	50.1	17.27	42.3	7.5	51.36	15		50.1*
	Shear	MV(ΔT= 0)	0.305	43.4	104.2	30.10	29.1	15.6	76.28	51		104.2*
		MTV(ΔT/ΔV = 0.5)	0.191	28.2	67.6	33.53	40.3	10.2	91.10	54	HDE	67.6*
		CV(ΔT= 0)	0.197	36.6	74.6	17.78	51.1	11.3	40.17	58		74.6*
H-2	Shear	MV(ΔT= 0)	1.905	36.8	95.4	21.34	27.3	14.4	107.58	8	HDE	95.4*
		CV(ΔT= 0)	2.604	74.4	85.4	18.42	71.6	13.0	28.92	5		85.4*

Table 3 DT/DT Web Connector Performance												
H-3	Shear	MV	1.880	57.7	60.4	15.88	39.0	8.9	44.77	5	MDE	60.4*
		CV(ΔT= 0)*4	1.332	34.7	52.5	12.82	27.5	7.9	43.81	7		52.5
H-4	Shear	MV	3.937	10.6	70.6	20.96	29.9	10.4	108.06	3	MDE	70.6*
		CV(ΔT= 0)*4	1.214	28.1	70.1	16.41	24.5	10.5	43.06	12		70.1
		CVT(ΔT/ΔV = 0.5)*4	1.434	37.3	41.2	12.73	30.9	6.2	39.82	5		41.2
H-5	Tension	MT	11.163	4.4	28.9	47.63	25.6	4.4	48.65	0.4	HDE	28.9*
		CT*3	17.526	4.4	29.2	50.74	21.9	4.3	64.10	0.4		29.2
	Shear	MV	6.464	7.2	47.8	33.66	26.3	7.2	105.92	1.1	HDE	47.8*
		CV(ΔT= 0)*4	6.436	14.7	42.4	38.94	15.8	6.3	101.69	1.1		42.4
H-6	Tension	MT	0.141	8.2	18.1	17.91	8.9	2.7	39.59	20	MDE	18.1*
		CT*4	0.167	6.2	14.9	10.83	6.6	2.2	19.49	14		14.9
	Shear	MV	0.187	36.8	75.4	54.61	38.9	11.3	101.52	61	LDE	75.4*
		CV(ΔT= 0)*4	0.132	10.9	40.4	2.98	24.9	6.1	12.54	46		40.4
		CVT(ΔT/ΔV = 0.5)*3	0.117	8.1	37.2	2.12	21.1	5.5	26.02	49		37.2
H-7	Out of Plane Shear	OV*4	0.244	3.7	9.1	12.19	8.0	1.4	18.99	8	LDE	9.1
H-8	Out of Plane Shear	OV*4	0.483	7.2	12.6	21.34	12.1	1.9	26.03	8	LDE	12.6
H-9	Out of Plane Shear	OV*4	0.483	20.0	30.3	8.13	28.2	4.5	11.36	16	LDE	30.3
H-10	Out of Plane Shear	OV*5	1.155	8.5	20.2	10.77	13.6	3.0	20.78	7	LDE	20.2
H-11	Out of Plane Shear	OV*5	0.446	11.3	21.5	7.32	19.9	3.2	13.34	9	LDE	21.5
I-1	Tension	MT	0.229	11.9	33.6	37.72	11.7	5.0	89.52	22	HDE	33.6*
	Shear	MV	0.126	10.9	44.4	1.91	11.0	6.6	66.54	53	LDE	44.4*
		CV(ΔT= 0)	0.133	12.1	43.8	1.79	41.5	6.7	6.55	50		43.8*
I-2	Tension	MT	0.152	15.6	37.3	8.38	8.4	5.6	57.03	37	MDE	37.3*
	Shear	MV	0.245	79.2	178.8	6.35	35.5	26.8	88.88	110	LDE	178.8*
		MTV(ΔT/ΔV = 0.5)	0.119	26.3	131.8	1.91	64.6	19.8	19.73	167		131.8*
		CV(ΔT= 0)	0.174	72.1	158.9	3.81	37.7	23.8	25.99	137		158.9*
J-1	Tension	MT	0.457	7.7	51.1	49.91	18.2	7.5	77.05	17	HDE	51.1*
		CT	0.400	9.7	36.5	30.48	27.4	5.5	33.46	14		36.5*
	Shear	MV	0.110	11.9	78.5	1.91	62.9	11.7	74.90	107	LDE	78.5*
		CV(ΔT= 0)	0.100	11.4	74.6	1.64	65.8	11.2	7.55	113		74.6*
	Out of Plane Shear	OV*2	0.569	13.2	20.3	12.45	7.6	3.0	24.71	6	LDE	20.3
J-2	Tension	MT	0.175	16.0	40.8	13.34	32.1	6.2	34.17	36	MDE	40.8*
		CT	0.248	18.9	44.1	10.07	8.7	6.7	20.10	27		44.1*
	Shear	MV	0.217	64.5	133.0	8.26	96.6	20.0	61.46	92	LDE	133.0*
		CV(ΔT= 0)	0.222	49.3	102.4	5.72	46.2	15.4	14.25	69		102.4*

PART 2E. *References*

1. American Society of Civil Engineers (ASCE) 2010. *Minimum Design Loads for Buildings and Other Structures*. ASCE/SEI 7-10., Reston, VA.

2. Fleischman, R. B., R. Sause, S. Pessiki, and A. B. Rhodes. 1998. Seismic Behavior of Precast Parking Structure Diaphragms. *PCI Journal*, 43(1), 38–53.

3. PCI Industry Handbook Committee. 2004. *PCI Design Handbook: Precast and Prestressed Concrete*. 6th ed. Chicago, IL: PCI.

4. PCI Connection Details Committee. 2008. *PCI Connection Manual for Precast and Prestressed Concrete Construction.*1st ed. Chicago, IL: PCI.

5. Building Seismic Safety Council, Committee TS4. 2009. Seismic Design Methodology for Precast Concrete Floor Diaphragms, Part III. 2009 NEHRP Recommended Seismic Provisions, Federal Emergency Management Agency, Washington, D.C.

6. Venuti, W. J. 1970. Diaphragm Shear Connectors between Flanges of Prestressed Concrete T-Beams. *PCI Journal*, 15(1), 67-78.

7. Concrete Technology Corporation. 1974. Tests of Shear Connectors Report. CTA-74-B8/9, 55-62.

8. Spencer, R. A., and Neille, D.S. 1976, Cyclic Tests of Welded Headed Stud Connectors, *PCI Journal*, 21(3), 70-83.

9. Aswad, A. 1977. Comprehensive Report on Precast and Prestressed Connectors Testing Program. *Research Report*, Stanley Structures, Inc, Denver, Colorado.

10. Pincheira, J. A., Oliva, M.G., and Kusumo-Rahardjo, F. I. 1998. Tests on Double Flange Connectors Subjected to Monotonic and Cyclic Loading. *PCI Journal*, 43(3) 82-96.

11. Pincheira, J.A., Oliva, M.G., and Zheng, W. 2005. "Behavior of Double-Tee Flange Connectors Subjected to In-Plane Monotonic and Reversed Cyclic Loads" *PCI Journal*, 50(6), 32-54.

12. Naito, C., Cao, L., Peter, W., 2009. Precast Double-Tee Floor Connectors Part I: Tension Performance. *PCI Journal*, 54(1), 49-66.

13. Cao, L., Naito, C., 2009. Precast Double-Tee Floor Connectors Part II: Shear Performance. *PCI Journal*, 54(2), 97-115.

14. Naito, C., W. Peter, L. Cao. 2006.   Development of a Seismic Design Methodology for Precast Diaphragms - PHASE 1 SUMMARY REPORT. Advanced Technology for Large Structural Systems (ATLSS) Report No.06-03, ATLSS Center, Lehigh University.

15. American Concrete Institute (ACI) Committee 318. 2008. *Building Code Requirements for Structural Concrete (ACI 318-08) and Commentary (ACI 318R-08)*. Farmington Hills, MI: ACI.

16. Cao, L. (2006). "Effective Design of Precast Concrete Diaphragm Connections Subjected to In-Plane

Demands", PhD dissertation, Lehigh University, Bethlehem, PA

17. Priestley, M. J. N. 1992. The U.S.–PRESSS Program Progress Report. Third Meeting of the U.S. – Japan Joint Technical Coordinating Committee on Precast Seismic Structural Systems (JTCC-PRESSS), San Diego, CA, November 18-20.

18. American Society of Civil Engineers (ASCE). 2007. *Seismic Rehabilitation of Existing Buildings*. ASCE/SEI 41-06. ASCE, Reston, VA.

19. Federal Emergency Management Agency (FEMA). 2000. *NEHRP Commentary on the Guidelines for the Seismic Rehabilitation of Buildings*. FEMA 356, Washington, DC.

20. Naito, C., Ren, R., Jones, C., Cullen, T., 2007, "Development of a Seismic Design Methodology for Precast Diaphragms – Connector Performance PHASE 1B," Advanced Technology for Large Structural Systems (ATLSS) Report No.07-04, ATLSS Center, Lehigh University.

21. ASTM Standard C39, 2005, "Standard Test Method for Compressive Strength of Cylindrical Concrete Specimens," ASTM International, West Conshohocken, PA, 2005, DOI: 10.1520/C0039_C0039M-05E01, www.astm.org.

Seismic Design Methodology Document for Precast Concrete Diaphragms

PART 3:
ANALYSIS TECHNIQUES AND DESIGN AIDS

for Precast Diaphragm Design

2/16/2014

TABLE OF CONTENTS

INTRODUCTION

PART 3 provides guidance on the analysis techniques that can be used for the diaphragm seismic design methodology. These analysis techniques include computer methods using standard design office structural analysis software and calculation-based methods that can be readily inserted into spreadsheet programs.

PART 3 is divided into five sections: (1) Computer Structural Analysis Methods for Diaphragm Design; (2) Diaphragm Internal Force Calculations; (3) Diaphragm Joint Stiffness and Strength Calculations; (4) Diaphragm Elastic Deformation Calculations; and, (5) Spreadsheet-based Design Aids for Diaphragm Design.

In the first section, the manner in which design office structural analysis software can be used in the design methodology is discussed.

To use the design methodology, the designer must be able to calculate: (1) the diaphragm internal force demand; (2) the diaphragm joint strength and stiffness; and (3) the diaphragm induced gravity column drift. Techniques to perform these calculations are covered in the next three sections.

In the final section, a spreadsheet program developed as a design aid for the diaphragm seismic design methodology is described. Section 3.4 provides step-by-step instruction on how to use the design aid spreadsheet program for the diaphragm seismic design procedure. The software is to be made available at the PCI website.

3.1 COMPUTER STRUCTURAL ANALYSIS METHODS FOR DIAPHRAGM DESIGN

In this section, the role design office computer structural analysis can play in facilitating the design of diaphragms using the seismic design methodology in PART 1 is discussed. It is noted that computer structural analysis methods is *not required* for using the design methodology, but can be used if desired or if a three-dimensional structural model is being created in the normal process of the design.

A. Design Office Computer Structural Analysis

Computer structural analysis has become a mainstream method for structural design in recent years. Originally the computer structural analysis was typically limited to analysis of the lateral force resisting system (LFRS), while the gravity load takedown was relegated to spreadsheet methods. However, with advances in graphical interfaces, design optimization, and BIM (Building Information Modeling), these analyses have extended to the gravity load resisting system, including the floor system. In this section, current approaches to spatial representation (2D vs. 3D) and modeling (elastic/inelastic, static/dynamic) are briefly summarized.

A.1 Three-Dimensional Structural Analysis

In the recent past, design office computer structural analysis might be limited to a two-dimensional (2D) model of the primary LFRS elements (moment frame, braced frame, etc.). In cases where the LFRS elements are at isolated locations in the floor, the tributary load from the surrounding floors and gravity system could be added as a fictitious P-Δ column in the plane of the frame. In recent years, however, it is not uncommon to create a fully-realized three-dimensional (3D) model of the structure using commercially available structural analysis packages such as ETABS[1], SAP2000[1], PERFORM-3D[1], RAM[2], RISA-3D[3], etc. This approach should become more prevalent in the coming years as software further facilitates the use of three-dimensional modeling, in particular with the advent of BIM, where there is a further incentive to have a fully-realized 3D building model beyond the three-dimensional structural behavior captured. Three-dimensional BIM modeling is being used to an advantage at certain precast companies, e.g. (Harman 2012), where clearances, tolerances and fit-up are crucial to the success of construction of prefabricated components.

A.2 Structural Analysis Methods for Seismic Effects

Design office structural analysis has typically involved static linear analysis. For gravity load or wind lateral load analysis this approach is natural since the structure is to remain in the elastic range under service loads and respond to them pseudo-statically. For earthquake lateral loads, where neither of these conditions typically occurs under the design earthquake, the dynamic effects are captured in the equivalent lateral forces through a response spectrum, while the effects of nonlinear action are approximated through the introduction of response modification coefficient R, system overstrength factor Ω and deflection amplification factor C_d (ASCE 7 2005).

For assessment and retrofit of existing structures, where it may not be as straightforward to use the code prescriptive approach used for new buildings, four analysis procedure options of increasing sophistication are typically provided (ASCE/SEI 41 2006): (1) linear static procedure; (2) nonlinear static (pushover) procedure; (3) linear dynamic (modal superposition) procedure; and (4) nonlinear dynamic (time history) procedure.

The minimum level of analysis required is driven by the characteristics of the structure, including irregularity and site conditions. Analysis levels greater than what is legally required are rarely performed,

---

[1] Computers and Structures, Inc. Berkeley, CA 94704
[2] Bentley Systems, Inc. Exton, PA 19341
[3] RISA Technologies, LLC. Foothill Ranch, CA 92610

unless a client has requested added performance information or retrofit alternatives (e.g. supplemental damping, etc.) in which a more advanced analysis would facilitate the performance based design.

Each analysis option is briefly described below. The applicability of these approaches for precast diaphragm design is considered next in Section A.3.

Linear Static Analysis: In this method, an elastic model of the structure is subjected to equivalent lateral forces intended to represent the effects of the earthquake. This analysis level captures neither inelastic behavior nor dynamic response, actions both of which that are anticipated in a structure. Thus, linear static analysis relies on measures that implicitly include the dynamic effects (pseudo-acceleration response spectra based on an inherent amount of damping) factors, in conjunction with factors that account for the inelastic behavior (R, Ω, C_d) as discussed above for new construction(ASCE 7 2005); and C_1, C_2, J, m and κ factors for retrofit (ASCE/SEI 41 2006). The use of these factors, while approximate, is justified given the straightforward and similar nature of the linear static analysis to wind/gravity load analysis for design.

Linear Dynamic Analysis: This analysis level includes dynamic response through modal analysis of an elastic model. Thus, analysis level captures dynamic effects but not inelastic behavior. The modal analysis uses the response spectrum to determine input excitation. It is important to note that the maximum dynamic actions are represented approximately through modal superposition (e.g. SSRS or CQC methods). The, linear static method relies on similar factors to account for the inelastic behavior as in the linear static analysis. This analysis method is desirable over the linear static method for structures where higher mode effects are important (since typical ELF patterns are based on first mode response), or for building irregularity in plan or profile such that a prescribed ELF pattern may not capture the mode shapes properly. This method is often used in lieu of the linear static analysis because modern computer tools have rendered the time and effort commitment for the two methods nearly equal.

Nonlinear Static Analysis: In this method, an *inelastic* model of the structure is subjected to equivalent lateral forces intended to represent the effects of the earthquake. This method therefore attempts to directly capture the damage and limit states that may occur in an earthquake. The method, often termed a pushover analysis, does not attempt to directly capture dynamic effects. Instead, the model is steppe through incremental increases in loading until it reaches a failure mechanism. Thus, the pushover analysis provides capacity, and not demand. Demand is estimated using approximate methods such as target displacements (ASCE/SEI 41 2006) or capacity spectrum methods (NZSEE 2006). Except for special adaptive techniques for pushovers (Antoniou and Pinho 2004), the nonlinear static analysis is typically based on a first-mode ELF. This method is popular because of the ability to directly consider the failure mechanism.

Nonlinear Dynamic Analysis: This analysis attempts to directly capture the response of the structure to a seismic event by using a nonlinear model of the structure time-stepped through the earthquake using nonlinear transient dynamic analysis (NLTDA). While this method is the most direct, it is rarely used in design or even assessment due to the level of involvement in the analysis: (1) it takes a significant amount of time to build the models, perform the analyses and post-process the results; (2) the amount of data produced in these analyses is significant (time stepping typically involves discretizing the earthquake into thousands of time steps); (3) the level of expertise required to successfully build a model and perform an analysis is quite high; and (4) a suite of ground motions is typically required to provide equivalence to the smooth averaged design spectrum. Such analyses are typically only warranted for designs or assessments with complicated dynamic or inelastic mechanisms or designs employing special seismic devices, performance based design targets, etc.

A.3 Structural Analysis Methods: Options for Diaphragm Seismic Design

For the reasons given in the previous section, while the latter two approaches (nonlinear static or dynamic) were used heavily in the diaphragm *research*, the design methodology has been constructed such that the diaphragm *design* can be performed using the first method (linear static analysis), or if desired, the second method (linear dynamic analysis). It is important to remember that for projects where a computer structural analysis model *is not* being created as part of the normal process, the diaphragm design can be carried out simply with hand or spreadsheet-based calculations.

Linear Static Analysis (Suggested Method for Diaphragm Design)

The design methodology adopts factors which are similar in spirit to the factors mentioned above (for instance the Ψ factor considers both dynamic amplification and inelastic response of the diaphragm). For this reason, linear static analysis is the approach promoted in the design methodology.

This method is <u>is promoted for use</u> with the diaphragm design methodology, if computer structural analysis is desired.

Linear Dynamic Analysis

For design offices with proficiency with modal superposition methods, the upgrade from linear static to linear dynamic analysis does not involve a significant time or effort penalty. Such techniques are readily available and facilitated in current structural analysis software packages.

This method is <u>suggested as an alternative</u> for use with the diaphragm design methodology, if computer structural analysis is desired.

Nonlinear Static Analysis

This method was an essential *research* tool in developing knowledge of the *capacity* of precast diaphragms. Findings based on these analyses are built into the design methodology.

This method is <u>not necessary</u> for the design of precast diaphragms using the design methodology.

Nonlinear Dynamic Analysis

This method was an essential *research* tool in developing knowledge of the *seismic demands* of precast diaphragms. Findings based on these analyses are built into the design methodology.

This method is <u>not necessary</u> for the design of precast diaphragms using the design methodology.

B. Diaphragm Action in Computer Structural Analysis

Computer structural analysis is not typically involved in the current design of precast diaphragms. Typically current diaphragm design involves calculating the equivalent lateral force (ELF), using this pattern to determine the diaphragm design forces F_{px}, using the horizontal beam method to determine maximum diaphragm moment and shear $M_{max} = (F_{px}L/8)$ and $V_{max} = F_{px}/2$ then sizing the chord and shear reinforcement, $\phi_b A_s F_y > M_{max}/d$ and $n_v = V_{max}/\phi_v V_{n..}$ Thus, precast diaphragm design often involves single page in the current design of precast structures. In this section, the use of computer structural analysis for diaphragm design in discussed.

B.1 Methods Available for Modeling Diaphragms

B.1.1 Rigid vs. Semi-rigid Diaphragm Models

Currently, most software packages provide a diaphragm modeling option for three-dimensional models: (1) no diaphragm, i.e., LFRS elements act independently; (2) rigid diaphragm, i.e., all LFRS elements at a story are subjected to a rigid body translation: $u_i = u_o + \phi\, y_i$, where u_o is the translation of the floor plate centroid, u_i is the resulting translation of a point on the floor a distance y_i from the centroid, and ϕ is the in-plane twist of the floor (all points on the floor translate the same in the absence of torsion); and (3) semi-rigid diaphragm, where the elastic stiffness of the floor system is modeled.

For the semi-rigid diaphragm model, design office software packages typically offer two basic options: (1) membrane action, in which only the in-plane elastic stiffness of the floor system is modeled; and (2) plate or shell action, in which the out-of-plane two-way bending and shear stiffness of the floor system is modeled in addition to the membrane action. Note that in either case, the diaphragm is modeled in two-dimensions (2D), i.e. the horizontal plane of the floor slab.

In employing the semi-rigid modeling option, most structural analysis programs request as input a slab thickness and an elastic modulus (E). If shear deformations are available, a shear modulus (G) can also be entered. Many design office structural analysis programs now include an option to enter orthotropic stiffness properties S_{11}, S_{22}, S_{12} to account for different floor stiffness in each direction. This option could be useful in modeling precast diaphragms, which have dissimilar stiffness properties in the precast floor unit spanning direction, and the direction perpendicular to the precast floor unit span.

B.1.2   Isolated Diaphragm vs. Structural Models

Computer structural analysis to determine diaphragm internal design forces can be performed either by: (a) considering each floor plate individually, i.e. 2D analysis of isolated diaphragms; or, (b) examining the floor diaphragms in the context of the overall structure in a 3D structural model. In the DSDM research, both of these approaches were used extensively. There are advantages and disadvantages of each approach. The approach recommended for the design methodology, if structural analysis is to be used, is to <u>evaluate the diaphragms in the full structural model</u>.

Isolated Diaphragm Model: The advantage of using an isolated model is that the model is easier to build, analyze and post-process. However, since the use of computer structural analysis is not required for the design methodology, it is considered likely that it will only be used when there is an existing model of the structure. Thus, what might be a time saver in a research setting, is likely extra work in the design office setting. Further, the handling of boundary conditions is somewhat challenging for the isolated diaphragm model. Lateral force resisting elements are typically modeled as idealized boundary conditions (pins and rollers). This does not allow for accounting for differences in stiffness between the various LFRS elements or due to the level above the ground without the introduction of "foundation springs" between the diaphragm and the fixed boundaries. These are somewhat cumbersome to introduce and it may be more straightforward to simply model the structure so as to include the vertical spatial and stiffness relationships directly. For these reasons, the full structural model is promoted.

Full Structural Model: The internal forces and deformations for a precast diaphragm can be modified by the presence of vertical elements (walls, frames, columns), including in their out of plane direction. In cases, these actions can be impacted by the relative stiffness of the various vertical elements, or can be sensitive to the conditions on different floors or how far the floor level is from the foundation. Thus, the full 3D structural model is recommended if computer structural analysis is used.

It is important to note that there are some remaining shortcomings with the static analysis, even with the full 3D structural model. For instance, there are inter-floor actions that can only truly be accurately captured through nonlinear transient analysis. These could include restraining forces from columns, in particular due to higher mode effects where the floors get out of phase, or the effect of ramps in parking garages. Further, there is challenges in selecting the loading to apply to the structure, since the ELF pattern F_i is an instantaneous pattern, which is appropriate to apply but does not capture floor

maxima, while the diaphragm force pattern F_{px} is a profile of maximums, and thus is not a rationale pattern to apply to the structure. Methods for applying this load are proposed in (Sabelli et al. 2011)

B.1.3 Monolithic vs. Discrete Diaphragm Models

As discussed in Appendix B of Section 5, the research was performed using models termed "discrete" diaphragm models. In these models, the individual connectors in the precast floor system are discretely modeled at their locations along the joint between precast units. Such models were essential to the research, but were used to determine design procedures, classifications and factors such that the designer would not have to use these discrete diaphragm models. Thus, while some designers have attempted such modeling approaches (Cleland 2012), discrete diaphragm models are not necessary in the use of the design methodology procedures. It is noted for completeness that the use of idealized boundary conditions used in 2D isolated diaphragm representations are somewhat problematic with discrete diaphragm models, which require joint opening for diaphragm deformation. Likewise, the discrete diaphragm models are also difficult to use for modal analysis, for instance to determine the structural fundamental period, since the discrete diaphragm models depend on contact elements whose initial status (open or closed, stuck or sliding) is unknown.

B.2 Structural Analysis Methods for Precast Diaphragm Design

As mentioned, computer structural analysis is not currently common for precast diaphragm design. For distributed lateral force resisting systems, designers have used line-type beam elements with idealized boundary conditions (rollers and pins), and the diaphragm force F_{px} applied as a distributed load, to determine shears and moments at different locations in the floor.

For more complicated floor configurations, precast floor systems can be modeled using structural analysis software, as described in Section A3. Such analyses are not currently common. Currently designers rely on full 3D structure models for reinforced concrete diaphragms in high-rise structures for cases involving transfer diaphragms (Meyer 2012). For these analyses, free-body cuts can be made at diaphragm sections along the lines of the precast joints to determine internal forces.

C. Guidelines for Computer Structural Analysis of Precast Diaphragms

C.1 Diaphragm Modeling

The design methodology can be performed using hand calculations or spreadsheet methods (See Section 3.2). If computer structural analysis is desired, the approach recommended for the design methodology is a full 3D structural model. The diaphragm internal forces can be calculated through computer analysis by using the following procedure:

(a) 3D Structure Model
- ◆ The floor system can be modeled as a planar semi-rigid diaphragm through membrane action
  - ✓ input thickness as flange thickness for pretopped system
  - ✓ sum of flange thickness and topping slab thickness for topped system
  - ✓ effective density to produce the proper total mass of the floor system (tee stems, internal beams, etc).
  - ✓ prestressing effects do not need to be modeled as they are not typically significant in the floor slab.

- ◆ The floor system stiffness is calculated using effective moduli (E_{eff}, G_{eff})

✓ In preliminary design, the effective moduli can be estimated as 20% - 40% of E_c and 10% - 30% of G_c, where E_c and G_c are concrete uncracked elastic and shear modulus.

✓ In final design, the effective moduli are obtained based on the actual reinforcement layout using the procedure given in "Diaphragm Joint Stiffness and Strength Calculation" of PART 3.

✓ For diaphragms with varying reinforcement, it is suggested to apply the average E_{eff} and G_{eff} over all the joints in the floor. E_{eff} can be applied in both directions. It can be increased in the precast floor span direction, with a recommended value of $2E_{eff}$.

◆ The lateral force resistant system (LFRS) can be modeled as elastic planar (shell element for shear wall) or elastic beam (beam element for frame) elements using cracked section properties to provide boundary supports to diaphragm in the LFRS out-of-plane direction.

◆ The interfaces between the LFRS to diaphragm, the internal beam to diaphragm and the spandrel to diaphragm are modeled as continuous elements.

◆ It is recommended to model the vertical gravity system (e.g. gravity column) as elastic beam elements with pinned connection to the floor system and an appropriate base condition.

C.2 Structural Analysis

If computer structural analysis is desired to perform the diaphragm design using the design methodology, the linear static method is recommended. Linear dynamic analysis can be used as an alternative method.

(a) Linear Static Analysis
◆ Apply the appropriate amplified diaphragm force (F_{dia} obtained in step 7 of PART 1) to the 3D structure model as body loads at each floor level

◆ Apply the loads individually in each orthogonal direction

◆ Perform static analysis to obtain the moment, shear and axial forces at diaphragm joints and interfaces between diaphragms to secondary elements: LFRS, internal beam and spandrel etc. for each loading direction

(b) Linear Dynamic Analysis
◆ Construct the design acceleration spectrum base on Chapter 11 of ASCE 7 (2005) at DBE level and 5% damping.

◆ Perform model superposition analysis using SRSS or CQC method

◆ Measure the diaphragm inertia force (F_i) at each floor

◆ Measure the moment, shear and axial forces at diaphragm joints and interfaces between diaphragms to secondary elements: LFRS, internal beam and spandrel etc. for each loading direction.

◆ Scale the measured diaphragm internal forces (obtained in previous step) by $\Psi F_{Dx}/F_i$

C.3 Internal Force Measurements

- ◆ Cut free body diagram at each precast diaphragm joints and interfaces between diaphragms to secondary elements: LFRS, internal beam and spandrel etc.

- ◆ Measure the moment, shear and axial (including directionality for tension and compression) by sum of all the node forces at the cut section

C.4 Diaphragm Deformation Measurements

- ◆ Measure the maximum diaphragm displacement (Δ_{dia}) at a given floor level

- ◆ Measure the displacements at the two LFRS (Δ_{LFRS1} and Δ_{LFRS2}) which are furthest to the location of diaphragm maximum displacement on each side at the same floor level

- ◆ Calculated the diaphragm deformation as $\delta_{dia} = \Delta_{dia} - (\Delta_{LFRS1} + \Delta_{LFRS2})/2$

3.2 INTERNAL FORCE CALCULATIONS: FREE BODY METHOD

The diaphragm internal force (in-plane moment, shear and axial force at each joint) is to be calculated by applying the amplified diaphragm design force (obtained in Step 7 of PART 1) to the diaphragm. Free Body Method (FBD) is introduced in this section to determine these internal forces.

A. Free Body Method

The free body method to calculate the diaphragm internal forces can be performed as follows:

- ◆ Cut a free body for the diaphragm or sub-diaphragm (typically at the interfaces between diaphragm-to-LFRS and internal beam, etc.)
- ◆ Apply the appropriate amplified diaphragm force (F_{dia} obtained in PART 1: Step 7) to the 3D structure model as body loads at each floor level
- ◆ Calculate the reaction forces at boundary of the diaphragm free body to satisfy the global equilibrium for static determinate free body. For indeterminate free body, assumption has to be made based on mechanics (See Examples in 3.2.B)
- ◆ Determine the diaphragm internal forces using local equilibrium with section cut at diaphragm joints
- ◆ Consider the loading in each orthogonal direction individually; use the maximum case of combined (M,N,V) forces

B. Free Body Diagrams for Common Precast Diaphragm Configurations

In this section, free body diagrams (FBDs) for common precast structure diaphragm configurations are provided. These configurations correspond to the examples in PART 4.

B.1 Structure Configuration 1: 4-story perimeter wall parking garage (Example 1 in PART4)

The first precast diaphragm configuration is shown in Figure 1. A distinction is made between the flat parking region (at the top or bottom of the figure) and the ramp. Each of these regions is treated as a sub-diaphragm and will be provided with a separate FBD.
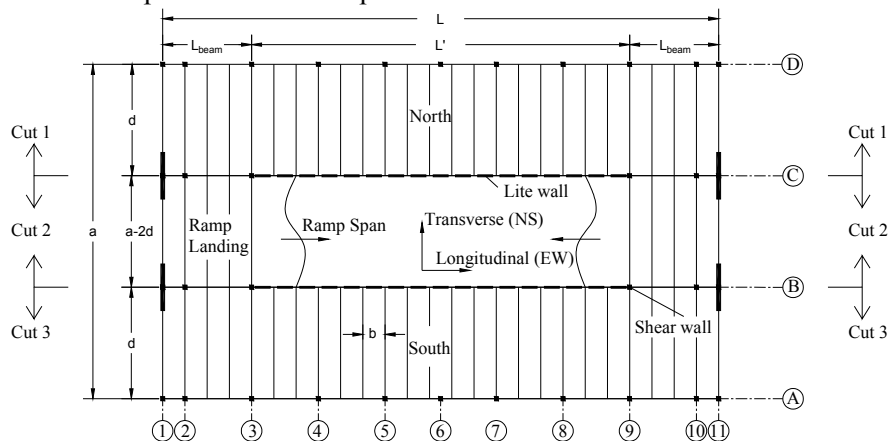
Fig.1. Plan view of structure 1.

The figures in the following pages are the free body diagrams for each case: (a) flat and (b) ramp under (a) transverse and (b) longitudinal loading. The assumptions involved in the free body diagrams shown are presented after each free body table. These assumptions were developed based on basic mechanics and verified through the nonlinear dynamic transient analysis using three dimensional models in Appendix A2 Section A2.3.1. The diaphragm internal force diagrams are shown in Design Example 1 in Appendix A of PART 4.

Table 3.1 Configuration 1

(a) North/south flat sub-diaphragm under transverse loading (Cut 1 or 3)

Distributed Load:

$$w = \Psi F_{Dx}\,/(3L - L'/2)\text{ for top floor;}\qquad w = \Psi F_{Dx}\,/3L\text{ for other floors}$$

Reactions at Boundary:

$$N_{lw} = 0.15w;\quad N_{Beam} = V_{SW} = 0.5(wL - N_{lw}L')/2$$

$$V_{beam} = VQL_{beam}\,/\,I\ \text{ where } V = 3w(L_{beam} + L')/2\text{, and } Q/I = 4/9d$$

Diaphragm Joints:

$0 \le x \le L_{beam}$:

$$N_u = xV_{beam}\,/\,L_{beam};$$
$$V_u = V_{sw} - wx - xN_{beam}\,/\,L_{beam};$$
$$M_u = xV_{sw} - wx^2\,/\,2 - x^2N_{beam}\,/\,3L_{beam}$$

$L_{beam} < x \le L/2$:

$$N_u = V_{beam};$$
$$V_u = V_{sw} - wx - N_{beam} + N_{lw}(x - L_{beam});$$
$$M_u = xV_{sw} - wx^2\,/\,2 - N_{beam}(x - 2L_{beam}\,/\,3) + N_{lw}(x - L_{beam})^2\,/\,2$$

$L/2 < x \le L$:

   Internal forces are symmetrical

Assumptions:
1. The total sub-diaphragm end reactions shared 50-50 between the end shear wall projecting past the IT beam and the IT beam itself.
2. The internal beam joint must be designed to carry 50% of the sub-diaphragm end reaction.
3. The litewall provides restraint such that the axial force (N_{lw}) as 15% of w.
4. Shear reaction (V_{beam}) at the internal beam joint is uniformly distributed.
5. Due to bending, a triangular distribution is assumed for the axial force at the IT interface.

Table 3.1 Configuration 1 (con't)

(b) Ramp sub-diaphragm under transverse loading (Cut 2)

Distributed Load:

$$w = \Psi F_{Dx} / (3L - L'/2) \text{ for top floor;} \qquad w = \Psi F_{Dx} / 3L \text{ for other floors}$$

Reactions at Boundary:

$$N_{lw} = 0.15w \,; \quad N_{Beam} = (wL - N_{lw}L') / 4 \,;$$

$$V_{SW,ramp} = (wL - N_{lw}L') / 2 + 2N_{beam}$$

$$V_{lw} = 0.2wL / L' \,; \quad V_{beam} = VQL_{beam} / I$$

$$\text{where } V = 3W(L_{beam} + L') / 2 \,, \text{ and } Q/I = 4/9d$$

Diaphragm Joint:

$0 \le x \le L_{beam}$:

$$N_u = 0 \,;$$

$$V_u = V_{SW,ramp} - wx - 2xN_{beam} / L_{beam} \,;$$

$$M_u = xV_{sw} - wx^2 / 2 - x^2 N_{beam} / L_{beam}$$

$L_{beam} < x \le L/2$

$$N_u = 0 \,;$$

$$V_u = V_{sw} - wx - 2N_{beam} + N_{lw}(x - L_{beam}) \,;$$

$$M_u = xV_{sw} - wx^2 / 2 - 2N_{beam}(x - L_{beam} / 2) + N_{lw}(x - L_{beam})^2 / 2 - (x - L_{beam})V_{lw}d$$

$L/2 < x \le L$:

Internal forces are symmetrical

Assumptions:
1. Load (shear, V_{beam} and axial, N_{beam}) are transferred from N/S flat through internal beam joint.
2. The litewall provides restraint such that the axial force (N_{lw}) as 15% of w.
3. The Litewall provides restraint such that the shear force (V_{lw}) as 20% of total diaphragm inertia force.
4. Shear reaction (V_{beam}) and axial reaction (N_{beam}) at internal beam joint are uniformly distributed.

Table 3.1 Configuration 1 (con't)

North/south flat under longitudinal loading (Cut 1 or 3)

Distributed Load:

$$n = \Psi F_{Dx}/(3L - L'/2) \text{ for top floor}; \quad n = \Psi F_{Dx}/3L \text{ for other floors}$$

$$n_1 = 1.6n; \quad n_2 = (nL - n_1 L_{beam})/(L - L_{beam})$$

Reactions at Boundary:

$$q_1 = 0.5n; \quad q_2 = 1.75n; \quad q_{lw} = [nL - (q_2 - q_1)L_{beam}]/L'$$

$$N_t = nd/L_{beam}; \quad N_c = nd/(L - L_{beam})$$

Diaphragm Joint:

$0 \le x \le L_{beam}$:

$$N_u = x(q_2 - n_2); \qquad V_u = xN_t; \qquad M_u = N_t x^2/2 - dxq_2/2$$

$L_{beam} < x \le L - L_{beam}$:

$$N_u = q_2 L_{beam} + q_{lw}(x - L_{beam}) - xn_2; \quad V_u = L_{beam}N_t - N_c(x - L_{beam})$$

$$M_u = N_t L_{beam}(x - L_{beam}/2) - dL_{beam}q_2/2 - d(x - L_{beam})q_{lw}/2 - N_c(x - L_{beam})^2/2$$

$L - L_{beam} < x \le L$:

$$N_u = q_2 L_{beam} + q_{lw}L' - q_1(x - L_{beam} - L'); \quad V_u = L_{beam}N_t - N_c(x - L_{beam})$$

$$M_u = N_t L_{beam}(x - L_{beam}/2) - dL_{beam}q_2/2 - dL'q_{lw}/2 - N_c(x - L_{beam})^2/2$$

$$+ d(x - L_{bean} - L')q_1/2$$

Assumptions:

1. Two different -uniform distributed loads (n_1 and n_2) are used due to twisting effect.
2. Twist moment caused by eccentricity of shear reaction (q_1 and q_2) is balanced by the axial restraint (N_t and N_c) from internal beam joint and litewall joint.

Table 3.1 Configuration 1 (con't)

Ramp under longitudinal loading (Cut 2)

Distributed Load:

$$n = \Psi F_{Dx} /(3L - L'/2) \text{ for top floor;} \qquad n = \Psi F_{Dx} / 3L \text{ for other floors}$$

Reactions at Boundary:

$$q_{lw,ramp} = 0.2nL / L'$$

$$V'_{beam} = nL_{beam}$$

Diaphragm Joint:

$0 \le x \le L_{beam}$:

$$N_u = (2V'_{beam} / L + n)x; \quad V_u = 0; \quad M_u = 0$$

$L_{beam} < x \le L/2$

$$N_u = 2V'_{beam} + nx - 2q_{lw,ramp}(x - L_{beam}); \quad V_u = 0; \quad M_u = 0$$

$L/2 < x \le L$:

Internal forces are symmetrical

Assumptions:

1. Considering half of ramp is loaded in one direction with upper floor and half of ramp is loaded in other direction with lower floor.
2. The loading is in self-equilibrium.
3. The Litewall provides restraint such that the shear force (V_{lw}) as 20% of total diaphragm inertia force.
4. Shear force (V_{beam}) at internal beam joint is transferred from N/S flat and is uniformly distributed.

Interface Joints (Critical Loading direction only)
Diaphragm-to-Shear Wall Connection (per Wall):
$\qquad N_u = 0; \quad V_u = \Psi F_{px} / 4; \quad M_u = 0$
Diaphragm-to-Litewall Joint Connection (per Wall):
$\qquad N_u = N_c b; \quad V_u = q_{lw} b; \quad M_u = 0$
Internal Beam Joint along B1 to B3 in Fig. 1:
$\qquad N_u = N_{beam}; \quad V_u = V_{beam}; \quad M_u = N_{beam} L_{beam} / 6 \ ^{\#}$

[#] based on triangular force distribution

B.2 Structure Configuration 2: 4-story interior wall parking garage (Example 2 in PART4)

Precast diaphragm configuration 2 is shown in Figure 2. The configuration is identical to Structure Configuration 1 except the perimeter transverse shear walls are now moved inbound to the interior column line at the termination of the ramp. A distinction is made between the flat parking region (at the top or bottom of the figure) and the ramp. Each of these regions is treated as a su-bdiaphragm and has separate Free Body Diagram.
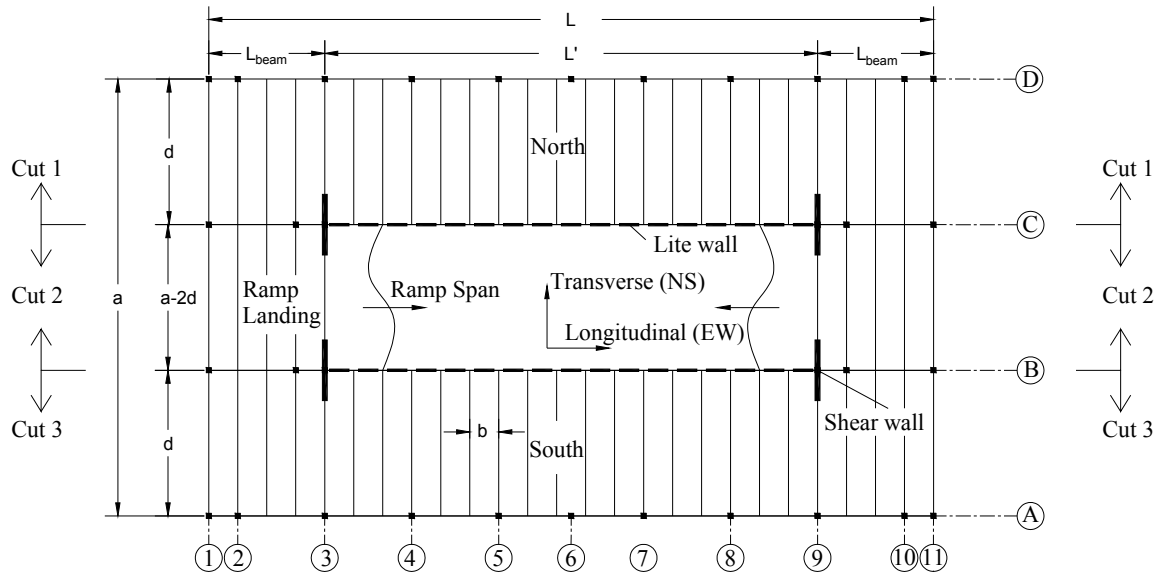
Fig.2. Plan view of structure 2.

The figures in the following pages are the free body diagrams for each case: (a) flat and (b) ramp under (a) transverse and (b) longitudinal loading. The assumptions involved in the free body diagrams shown are presented after each free body table. These assumptions were developed based on basic mechanics and verified through the nonlinear dynamic transient analysis using three dimensional models in Appendix A2 Section A2.3.4. The diaphragm internal force diagrams are shown in Design Example 2 in Appendix A of PART 4.

Table 3.2 Configuration 2

North/south flat under transverse loading (Cut 1 and 2)

Distributed Load:

$$w = \Psi F_{Dx} /(3L - L'/2) \text{ for top floor}; \qquad w = \Psi F_{Dx} /3L \text{ for other floors}$$

Reactions at Boundary:

$$N_{lw} = 0.15w; \quad V_{SW} = (wL - N_{lw}L')/2$$

Diaphragm Joint:

$0 \leq x \leq L_{beam}$:

$$N_u = 0;$$
$$V_u = -wx;$$
$$M_u = -wx^2/2$$

$L_{beam} < x \leq L/2$:

$$N_u = 0;$$
$$V_u = V_{sw} - wx + N_{lw}(x - L_{beam});$$
$$M_u = (x - L_{beam})V_{sw} - wx^2/2 + N_{lw}(x - L_{beam})^2/2$$

$L/2 < x \leq L$:

Internal forces are symmetrical

Assumptions:
1. The reactions at internal beam joint are ignored.
2. The litewall provides restraint such that the axial force (N_{lw}) as 15% of w.

Table 3.2 Configuration 2 (con't)

Ramp under transverse loading (Cut 2)

Distributed Load:

$$w = \Psi F_{Dx} / (3L - L'/2) \text{ for top floor;} \qquad w = \Psi F_{Dx} / 3L \text{ for other floors}$$

Reactions at Boundary:

$$N_{lw} = 0.15w$$

For top floor:

$$V_{SW,ramp} = (wL + N_{lw}L')/2 \,; \quad V_{lw} = 0.2wL / L'$$

For other floors:

$$V_{SW,ramp} = (wL + 3N_{lw}L')/2 \,; \quad V_{lw} = 0.4wL / L'$$

Diaphragm Joint:

$0 \le x \le L_{beam}$:

$$N_u = 0 \,;$$
$$V_u = -wx \,;$$
$$M_u = -wx^2 / 2$$

$L_{beam} < x \le L/2$

$$N_u = 0 \,;$$
$$V_u = V_{sw} - wx - N_{lw}(x - L_{beam}) \,;$$
$$M_u = (x - L_{beam})V_{sw} - wx^2 / 2 - N_{lw}(x - L_{beam})^2 / 2 - (x - L_{beam})V_{lw}d$$

$L/2 < x \le L$:

Internal forces are symmetrical

Assumptions:
1. The Litewall provides restraint such the axial force as 8% of w and the shear as 20% of w at top floor.
2. The Litewall provides restraint such the axial force as 23% of w and the shear as 40% of w at other floors.

Table 3.2 Configuration 2 (con't)

North/south flat under longitudinal loading (Cut 1 and 3)

Distributed Load:

$$n = \Psi F_{Dx} / (3L - L'/2) \text{ for top floor}; \quad n = \Psi F_{Dx} / 3L \text{ for other floors}$$

$$n_1 = 1.6n; \quad n_2 = (nL - n_1 L_{beam}) / (L - L_{beam})$$

Reactions at Boundary:

$$q_1 = 0.5n; \quad q_2 = 1.75n; \quad q_{lw} = [nL - (q_2 - q_1)L_{beam}] / L'$$

$$N_t = nd / L_{beam}; \quad N_c = nd / (L - L_{beam})$$

Diaphragm Joint:

$0 \le x \le L_{beam}$:

$$N_u = x(q_2 - n_2); \quad V_u = xN_t; \quad M_u = N_t x^2 / 2 - dxq_2 / 2$$

$L_{beam} < x \le L - L_{beam}$:

$$N_u = q_2 L_{beam} + q_{lw}(x - L_{beam}) - xn_2; \quad V_u = L_{beam}N_t - N_c(x - L_{beam})$$

$$M_u = N_t L_{beam}(x - L_{beam} / 2) - dL_{beam}q_2 / 2 - d(x - L_{beam})q_{lw} / 2 - N_c(x - L_{beam})^2 / 2$$

$L - L_{beam} < x \le L$:

$$N_u = q_2 L_{beam} + q_{lw}L' - q_1(x - L_{beam} - L'); \quad V_u = L_{beam}N_t - N_c(x - L_{beam})$$

$$M_u = N_t L_{beam}(x - L_{beam} / 2) - dL_{beam}q_2 / 2 - dL'q_{lw} / 2 - N_c(x - L_{beam})^2 / 2$$

$$+ d(x - L_{bean} - L')q_1 / 2$$

Assumptions:

1. Two different -uniform distributed loads (n_1 and n_2) are used due to twisting effect.
2. Twist moment caused by eccentricity of shear reaction (q_1 and q_2) is balanced by the axial restraint (N_t and N_c) from internal beam joint and litewall joint.

Table 3.2 Configuration 2 (con't)

Ramp under longitudinal loading (Cut 2)

Distributed Load:

$$n = \Psi F_{Dx} / (3L - L'/2) \text{ for top floor}; \qquad n = \Psi F_{Dx} / 3L \text{ for other floors}$$

Reactions at Boundary:

$$q_{lw,ramp} = 0.3nL / L'$$

$$V'_{beam} = nL_{beam}$$

Diaphragm Joint:

$0 \le x \le L_{beam}$:

$$N_u = (2V'_{beam} / L + n)x; \quad V_u = 0; \quad M_u = 0$$

$L_{beam} < x \le L/2$

$$N_u = 2V'_{beam} + nx - 2q_{lw,ramp}(x - L_{beam}); \quad V_u = 0; \quad M_u = 0$$

$L/2 < x \le L$:

Internal forces are symmetrical

Assumptions:
1. Considering half of ramp is loaded in one direction with upper floor and half of ramp is loaded in other direction with lower floor.
2. The loading is in self-equilibrium.
3. The Litewall provides restraint such that the shear force (V_{lw}) as 30% of total diaphragm inertia force.
4. Shear force (V_{beam}) at internal beam joint is transferred from N/S flat and is uniformly distributed.

Other Joints under Critical Loading
Diaphragm to Shear Wall Joint per Wall: $$N_u = 0; \quad V_u = 1.5(V_{sw} - wL_{beam}); \quad M_u = 1.5wL_{beam}^2 / 2$$
Diaphragm to Litewall Joint per Wall: $$N_u = N_c b; \quad V_u = q_{lw} b; \quad M_u = 0$$
Internal Beam Joint along B1 to B3 in Fig. 2: $$N_u = N_t L_{beam}; \quad V_u = 1.75nL_{beam}; \quad M_u = 0$$

B.3 Structure Configuration 3: 8-story moment frame office building (Example 3 in PART 4)

Precast diaphragm configuration 3 is shown in Figure 3. The whole diaphragm is treated as a single Free Body Diagram. The internal beam line (B and C) is designed for the tributary shear VQ/I.
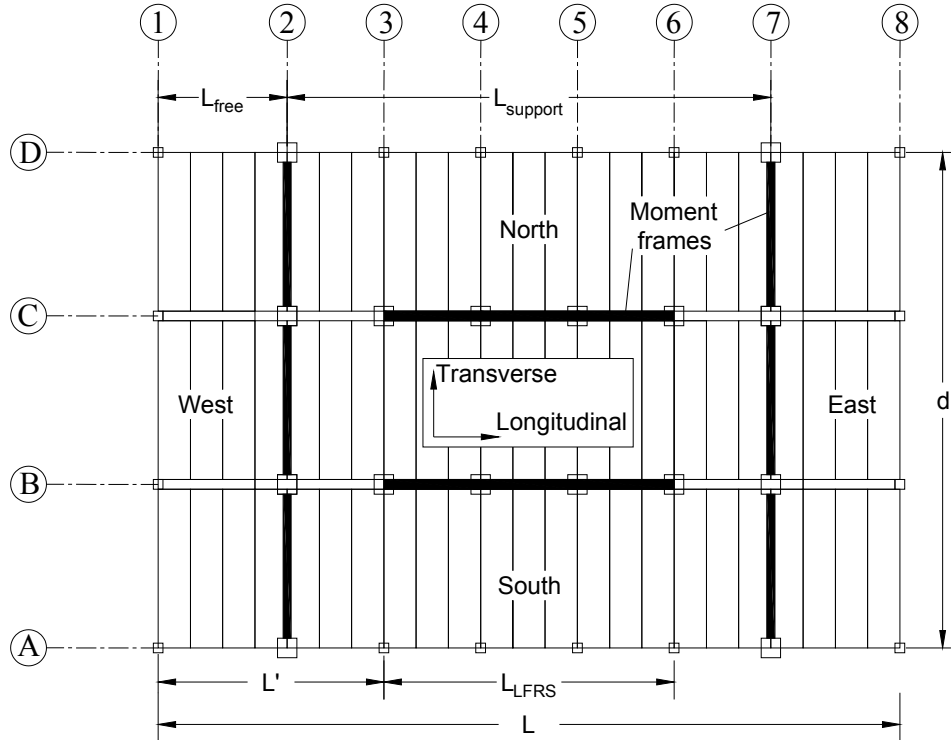
Fig.3. Plan view of structure 3.

The figures in the following pages are the free body diagrams under (a) transverse and (b) longitudinal loading. The assumptions involved in the free body diagrams shown are presented after each free body table. These assumptions were developed based on basic mechanics and verified through the nonlinear dynamic transient analysis using three dimensional models in Appendix A2 Section A2.3.6. The diaphragm internal force diagrams are shown in Design Example 3 in Appendix A of PART 4.

Table 3.3 Configuration 3

Transverse Loading

Distributed Load:

$$w = \Psi F_{Dx} / L$$

Reactions at Boundary:

$$R_{LFRS} = wL / 2 \,;$$

Diaphragm Joint:

$0 \le x \le L_{free}$:

$$N_u = 0 \,; \ \ V_u = -wx \,; \ \ M_u = -wx^2 / 2$$

$L_{free} < x \le L/2$:

$$N_u = 0 \,; \ \ V_u = R_{LFRS} - wx \,;$$
$$M_u = (x - L_{beam})R_{LFRS} - wx^2 / 2$$

$L/2 < x \le L$:

    Internal forces are symmetrical

Internal Beam Joint:

$$V_{int} = V_u Qb / I \ \text{ where } b \text{ is the panel width and } Q/I = 4/3d$$

Diaphragm to Transverse Frame Joint:

$$N_u = 0 \,; \ \ \ V_u = (R_{LFRS} - wL_{free}) \,; \ \ \ M_u = wL_{free}^2 / 2$$

Assumptions:
1. The internal beam joint is designed for the shear flow (VQ/I)

22

Table 3.3 Configuration 3 (con't)

Longitudinal Loading

Distributed Load:

$$n = \Psi F_{px} / L$$

Reactions at Boundary:

$$q = nL / 2L_{LFRS};$$

Diaphragm Joint:

$0 \le x \le L'$:

$$N_u = nx; \ V_u = 0; \ M_u = 0$$

$L' < x \le L/2$:

$$N_u = nx - 2q(x - L');$$
$$V_u = 0; \ M_u = 0$$

$L/2 < x \le L$:

Internal forces are symmetrical

Diaphragm to Longitudinal Frame Joint:

$$N_u = 0; \quad V_u = nL/3; \quad M_u = nLd/18$$

B.4 Structure Configuration 4: 8-story perimeter wall office building (Example 4 in PART 4)

Precast diaphragm configuration 3 is shown in Figure 3. The whole diaphragm is treated as a single Free Body Diagram. The internal beam line (B and C) is designed for the tributary shear VQ/I.
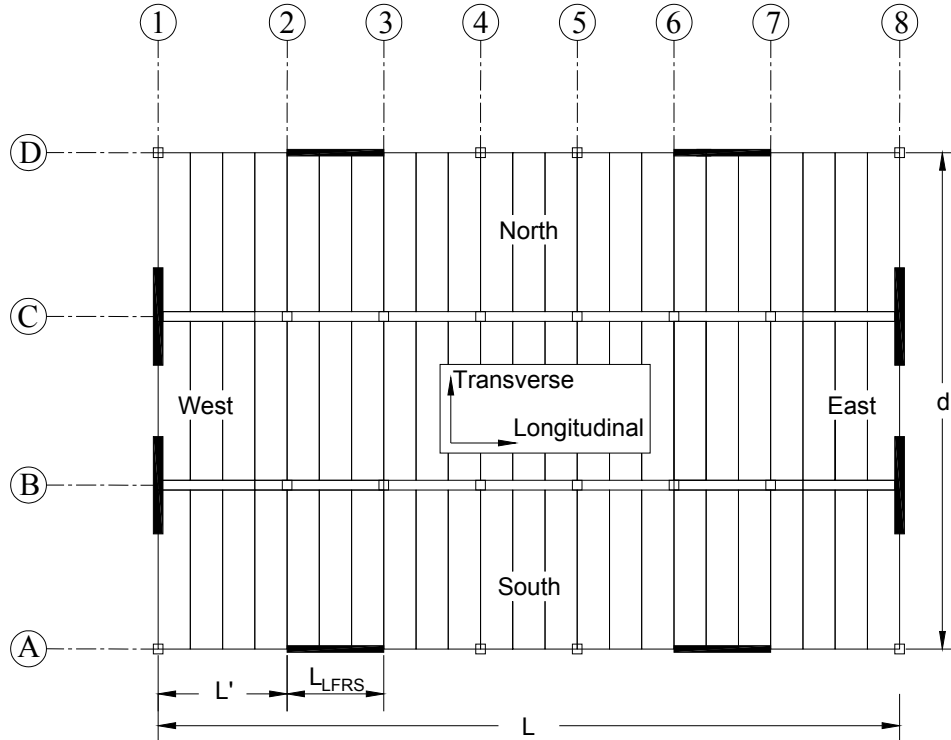
Fig.4. Plan view of structure 4.

The figures in the following pages are the free body diagrams under (a) transverse and (b) longitudinal loading. The assumptions involved in the free body diagrams shown are presented after each free body table. These assumptions were developed based on basic mechanics and verified through the nonlinear dynamic transient analysis using three dimensional models in Appendix A2 Section A2.3.8. The diaphragm internal force diagrams are shown in Design Example 4 in Appendix A of PART 4.
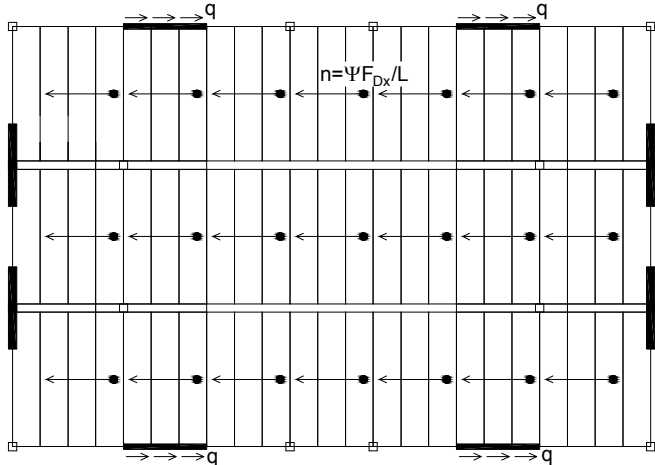
Table 3.4 Configuration 4

Transverse Loading

Distributed Load:
$$w = \Psi F_{Dx} / L$$

Reactions at Boundary:
$$R_{LFRS} = wL/2 \; ; \quad q_{SW} = 0.05 wL / L_{LFRS}$$

Primary Diaphragm Joint:

$0 \le x \le L'$:
$$N_u = 0 \; ; \quad V_u = R_{LFRS} - wx \; ; \quad M_u = R_{LFRS}x - wx^2/2$$

$L' < x \le L' + L_{LFRS}$:
$$N_u = 0 \; ; \quad V_u = R_{LFRS} - wx \; ;$$
$$M_u = (x - L_{beam})R_{LFRS} - wx^2/2 - q_{sw}(x - L')d$$

$L' + L_{LFRS} < x \le L/2$:
$$N_u = 0 \; ; \quad V_u = R_{LFRS} - wx \; ;$$
$$M_u = (x - L_{beam})R_{LFRS} - wx^2/2 - q_{sw}L_{LFRS}d$$

$L/2 < x \le L$:
    Internal forces are symmetrical

Internal Beam Joint:
$$V_{int} = V_u Q b / I \text{ where } b \text{ is the panel width and } Q/I = 4/3d$$

Diaphragm to Transverse Wall Joint per Wall:
$$N_u = 0 \; ; \quad V_u = R_{LFRS}/2 \; ; \quad M_u = 0$$

Assumptions:
1. The perimeter wall provides restraint such that the shear flow (q_{sw}) as 5% of total diaphragm inertia force.
2. The shear restraints from perimeter walls form a force couple to reduce diaphragm moment between the perimeter wall span.

25

Table 3.4 Configuration 4 (con't)

Longitudinal Loading
Distributed Load: $$n = \Psi F_{Dx} / L$$ Reactions at Boundary: $$q = nL / 4L_{LFRS};$$
Primary Diaphragm Joint: $0 \le x \le L'$: $$N_u = nx;\ \ V_u = 0;\ \ M_u = 0$$ $L' < x \le L' + L_{LFRS}$: $$N_u = nx - 2q(x - L');$$ $$V_u = 0;\ M_u = 0$$ $L' + L_{LFRS} < x \le L/2$: $$N_u = nx - 2qL_{LFRS};$$ $$V_u = 0;\ M_u = 0$$ $L/2 < x \le L$: Internal forces are symmetrical Diaphragm to Longitudinal Wall Joint per Wall: $$N_u = 0;\qquad V_u = qL_{LFRS};\qquad M_u = 0$$

3.3 DIAPHRAGM JOINT STIFFNESS AND STRENGTH CALCULATION

An analytical based procedure is used for calculating diaphragm joint stiffness and strength. This method is similar to that presented in (Zheng and Oliva 2005) with the exception that the diaphragm joint neutral axis calculation is based on the stiffness difference between the tension stiffness of the precast reinforcement in tension and the high compression stiffness of the joint coming into contact.

The following assumption is used for this procedure:
- ◆ Plane sections remain plane at the joint between precast units for stiffness and yield moment calculation
- ◆ Concrete in the precast unit is linear elastic and un-cracked
- ◆ Precast unit thickness is constant ignoring the contribution of washes or curbs
- ◆ Reinforcement in the diaphragm compression zone is ignored in determine compression stiffness (i.e. deformation based on precast concrete unit only)

The following diaphragm geometry is required for the procedure:
- ◆ d = Diaphragm Depth
- ◆ b = Panel width
- ◆ t = Flange thickness of precast units (plus topping if applicable)
- ◆ Layout of diaphragm reinforcing:
  - d_0 = Distance from center of chord reinforcement to diaphragm edge
  - n = Number of shear connectors
  - s_0 = Distance of the first shear connector to diaphragm edge
  - s = Spacing of shear connectors
  - s' = Spacing of topping reinforcement (bars or wires)
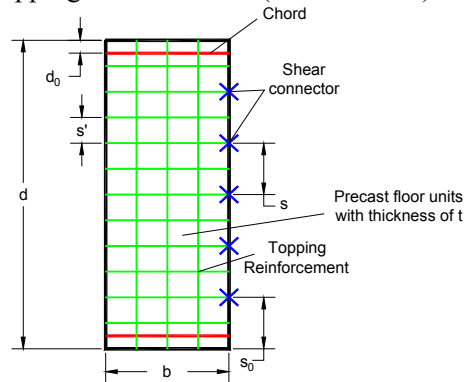
Fig.5. Required diaphragm geometry.

The following diaphragm reinforcement properties are required as shown in Table 1. These reinforcement properties can be obtained from Table 2A-1 in PART 2:

Table 1. Diaphragm reinforcement properties

Reinforcement	Elastic stiffness		Yield strength		Yield deformation	Secant stiffness
	Tension (k_t)	Shear (k_v)	Tension (t_n)	Shear (v_n)	Tension (t_n/δ_{ty})	Tension (v_n/δ_{vy})
Chord	$K_{t,chord}$	$K_{v,chord}$	$T_{y,chord}$	$V_{y,chord}$	$d_{y,chord}$	$K'_{t,chord}$
Shear	$K_{t,conn}$	$K_{v,conn}$	$T_{y,conn}$	$V_{y,conn}$	$d_{y,conn}$	$K'_{t,conn}$
Topping	$K_{t,topping}$	$K_{v,topping}$	$T_{y,topping}$	$V_{y,topping}$	$d_{y,topping}$	$K'_{t,topping}$

Note: the symbols in parenthesis are the same as those listed in Table A2-1 in PART 2.

A. Diaphragm Joint Stiffness

(a) Determine location of neutral axis

As indicated in Figure 6, the joint rotation is given as θ_l and the diaphragm compression zone depth is given as c. Ignoring the contribution of reinforcement in the diaphragm compression zone, the compression resultant on the concrete panel is expressed as

$$C_{conc} = \frac{1}{2} E_c \varepsilon_c t \cdot c \tag{1}$$

where $\varepsilon_c = c\theta_l/b$. Substituting ε_c to Eqn. (1),

$$C_{conc} = \frac{1}{2} E_c t / b \cdot c^2 \cdot \theta_1 \tag{2}$$

The total compression force acting on the joint, C, is

$$C = C_{conc} \tag{3}$$

The tension force developed in chord reinforcement is:

$$T_{chord} = K_{tc}(d - d_0 - c)\theta_1 \tag{4}$$

The tension force developed in shear reinforcement (summed over all connectors in tension) is

$$T_{conn} = \frac{1}{2} K_{t,conn} / s(d - s_0 - c)^2 \theta_1 \tag{5}$$

The tension force developed in topping reinforcement (similarly summed) is

$$T_{topping} = \frac{1}{2} K_{t,topping} / s'(d - c - 2d_0)^2 \theta_1 \tag{6}$$

Thus, the total tension force acting on the joint, T, is

$$T = T_{chord} + T_{conn} + T_{topping} \tag{7}$$

The force equilibrium of the joint requires $C=T$, which can be expressed as a function of c:

$$A_1 c^2 + A_2 c + A_3 = 0 \tag{8}$$

where, $A_1 = \frac{1}{2}(E_c t / b - K_{t,conn} / s - K_{t,topping} / s')$,

$A_2 = K_{t,chord} + K_{t,conn} / s \cdot (d - s_0) + K_{t,topping} / s' \cdot (d - 2d_0)$,

and $A_3 = -[K_{tc}(d - d_0) + \frac{1}{2} K_{t,conn} / s \cdot (d - s_0)^2 + \frac{1}{2} K_{t,topping} / s' \cdot (d - 2d_0)^2]$

Solving Eqn. (8)

$$c = \frac{-A_2 + \sqrt{A_2^2 - 4A_1 A_3}}{2A_1} \tag{9}$$
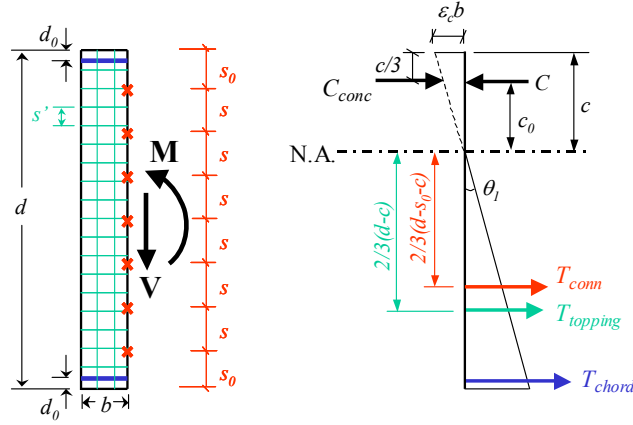
Fig.6. FBD of diaphragm joint.

(b) Determine location of center of compression

The center of compression, c_0, is calculated differently for topped and untopped systems. For topped diaphragm systems, the compression distribution is assumed linear, since concrete-to-concrete contact will occur along the entire compression zone and the compression stiffness can be assumed to be constant in this region, i.e. the compression resultant, C, acting at:

$$c_0 = 2/3 \cdot c \tag{10}$$

For untopped diaphragm systems with a dry chord, the center of force c_o is estimated by the relative compressive stiffness of the shear connectors to the chord:

$$c_0 = \frac{K_{c,chord}(c - d_0)^2 + 1/3 \cdot K_{c,conn}/s \cdot (c - s_0)^3}{K_{c,chord}(c - d_0) + 1/2 \cdot K_{c,conn}/s \cdot (c - s_0)^2} \tag{11}$$

For untopped systems with chord reinforcement in a pour strip, $K_{c,chord} >> K_{c,conn}$, thus, the compression force center is assumed to be at compression chord reinforcement, i.e.

$$c_0 = c - d_0 \tag{12}$$

(c) Determine diaphragm joint stiffness

The service stiffness of the diaphragm is comprised of a flexural component and a shear component. The stiffness is calculated using gross section properties by determining an effective Young's modulus E_{eff} and shear modulus G_{eff}.

Flexure Stiffness:
The rotational stiffness of the joint will be termed, K_Θ, i.e.

$$K_\Theta = M/\theta_l \tag{13}$$

The moment acting on the joint can be expressed as:

$$M = C \cdot c_0 + T_{chord}(d - d_0 - c) + T_{conn} \cdot 2/3(d - s_0 - c) + T_{topping} \cdot 2/3(d - c - 2d_0) \tag{14}$$

Substitute Eqns (3), (4), (5) and (6) into (14), the rotational stiffness becomes:

$$K_\Theta = \frac{1}{2b} E_c t c^2 c_0 + K_{t,chord}(d - d_0 - c)^2 + \frac{K_{t,conn}}{3s}(d - s_0 - c)^3 + \frac{K_{t,topping}}{3s'}(d - c - 2d_0)^3 \quad (15)$$

Considering now a panel segment (1 panel and 1 joint), the total flexural rotation of this substructure can be represented as

$$\theta_t = \theta_1 + \theta_2 \tag{16}$$

where θ_1 is, as before, the rotation within the joint and θ_2 is the rotation attributed to the precast floor unit,

$$\theta_2 = Mb/(E_cI) \tag{17}$$

An equivalent Young's modulus E_{eff} can now be defined:

$$\theta_t = \frac{Mb}{E_{eff}I} \tag{18}$$

where E_{eff} is smeared across the panel segment and can be equated to the individual stiffness of the panel and joint by substituting Eqn. (13), (17) and (18) into Eqn. (16):

$$\frac{Mb}{E_{eff}I} = \frac{Mb}{E_cI} + \frac{M}{K_\Theta} \tag{19}$$

Simplifying Eqn. (19) produces

$$E_{eff} = \frac{E_c b K_\Theta}{bK_\Theta + E_cI} \tag{20}$$

Shear Stiffness:

Defining K_Ψ as the shear stiffness of the joint, the shear displacement of a joint, δ_1 is then given as:

$$\delta_1 = V / K_\Psi \tag{21}$$

where V is the shear acting on the shear critical joint, and summing individual stiffness:

$$K_\Psi = 2K_{v,chord} + nK_{v,conn} + d / s' K_{v,topping} \tag{22}$$

Considering now in addition the precast unit, the total shear displacement of the panel segment, δ_t, is:

$$\delta_t = \delta_1 + \delta_2 \tag{23}$$

where δ_2 is the shear deformation over the precast panel and can be expressed:

$$\delta_2 = \frac{1.2V}{G_cA} \tag{24}$$

An equivalent shear modulus G_{eff} can now be defined:

$$\delta_t = \frac{1.2V}{G_{eff}A} \tag{25}$$

where G_{eff} is smeared across the panel segment and can be equated to the individual stiffness of the panel and joint by substituting Eqn. (21), (24) and (25) into Eqn. (23),

$$\frac{1.2V}{G_{eff}A} = \frac{1.2V}{G_cA} + \frac{V}{K_\Psi} \tag{26}$$

Simplifying Eqn. (26) produces

$$G_{eff} = \frac{1.2bG_cK_\Psi}{1.2bK_\Psi + AG_c}$$

(27)

B. Diaphragm Joint Strength

B.1 Strength in the Joints between Precast Floor Units

Diaphragm joint strength is calculated in this section as uncoupled axial, shear and moment strength. The axial-shear-moment coupling effect is considered in sizing the diaphragm reinforcement (refer to Eqn. 10 in PART 1).

(a) Diaphragm joint axial strength

Diaphragm joint axial strength is calculated as the sum of yield tension strength of all the reinforcement across the joint:

$$N_n = 2T_{y,chord} + \left(\frac{d - 2s_0}{s} + 1\right)T_{y,conn} + \left(\frac{d - 2d_0}{s'} + 1\right)T_{y,topping}$$

(28)

(b) Diaphragm joint shear strength

Diaphragm joint shear strength is calculated as the sum of yield shear strength of all the reinforcement across the joint:

$$V_n = 2V_{y,chord} + \left(\frac{d - 2s_0}{s} + 1\right)V_{y,conn} + \left(\frac{d - 2d_0}{s'} + 1\right)V_{y,topping}$$

(29)

(c) Diaphragm joint flexural strength

Two types of diaphragm flexural strength are considered: yield moment strength and plastic moment strength.

Yield moment strength (M_y):

Yield moment strength is defined as the point when any of reinforcement first reaches yield tension strength. The rotation at the critical joint θ_{ly} at diaphragm yield can be expressed through strain-compatibility as:

$$\theta_{ly} = \min\left[\delta_{y,chord}/(d-d_0-c),\ \delta_{y,conn}/(d-s_0-c),\ \delta_{y,topping}/(d-2d_0-c)\right]$$

(30)

The corresponding flexural stiffness of the critical joint, K'_Θ, at diaphragm yield can be calculated following the same procedure as for diaphragm elastic stiffness (see previous section), with the following modifications:
- Replace the reinforcement elastic stiffness in Eqn. (9) by secant stiffness for the calculation of c for neutral axis at yield.
- Determine c_0 from this new c, based on Eqn. (10), (11) or (12)

◆ Replace the reinforcement elastic stiffness in Eqn. (15) by secant stiffness for calculating K'_Θ, the diaphragm (secant) yield stiffness.

Once K'_Θ, is known, the diaphragm yield moment capacity is simply:

$$M_y = K'_\Theta \cdot \theta_{1y} \tag{31}$$

Plastic moment strength (M_p):

The plastic moment strength is defined as the point when all the tension reinforcement yields. Neutral axis and compression center cannot be calculated using the procedure for stiffness and yield strength since the plane section remaining plane is not valid. The following approximate procedure is used to calculate the plastic moment strength:

Assume the location of natural axis is 20% of diaphragm depth from the compression edge, which gives:

$$c = d/5 \tag{32}$$

For untopped system using Eqn. (10) or for topped system using Eqn. (11) calculate the compression center (c_0).

Then the diaphragm plastic moment strength is calculated as:

$$M_p = T_{y,chord}(d - d_0 - c + c_0) + T_{y,conn}\frac{d - c - s_0}{s}(\frac{d - c - s_0}{2} + c_0) + T_{y,topping}\frac{d - c - 2d_0}{s'}(\frac{d - c - 2d_0}{2} + c_0) \tag{33}$$

Design moment strength (M_n):

Diaphragm joint design moment strength (M_n) is determined based on yield moment strength and a diaphragm flexural overstregnth factor (Ω_d) for different design option:

For Elastic Design Option (EDO): $\qquad M_n = M_y$ $\qquad\qquad$ (34a)

For Basic Design Option (BDO): $\qquad M_n = \frac{1 + \Omega_d}{2}M_y$ $\qquad$ (34b)

For Reduced Design Option (RDO): $\qquad M_n = \Omega_d M_y$ $\qquad\qquad$ (34c)

where:

M_y is the yield moment of the precast diaphragm joint;

Ω_d is the diaphragm flexural overstrength factor, defined as the ratio of the diaphragm plastic moment to the diaphragm yield moment, M_p/M_y , conservatively taken as *1.0* for a *pretopped* diaphragm, and *1.25* for a *topped* diaphragm. Ω_d can be alternately determined from a strain curvature analysis or pushover analyses.

B.2 Strength in Other Joints

The strength for other joints including diaphragm-to-LFRS joint and diaphragm-to-internal beam joint is calculated using the following equations:

$$N_n = nt_n \tag{35a}$$

$$V_n = n v_n \tag{35b}$$

$$M_n = \frac{n t_n}{2} \frac{2L_J}{3} \tag{35c}$$

where t_n and v_n is the nominal tension and shear strength of connector across the joint; n is the number of connector across the joint; L_j is the length of joint. The moment strength calculated in Eqn. 35c is based on a triangle normal force distribution across the joint.

C. Diaphragm Elastic Deformation

Diaphragm elastic deformation is used in the diaphragm induced gravity column drift check (step 12 in PART 1). Two alternative methods are used for obtaining the elastic diaphragm deformation: (1) computer analysis method; and (2) integration method.

C.1 Computer Analysis Method

The same structure model and static analysis used for the diaphragm internal force calculation (refer to "Diaphragm Internal Force Calculation" section) are applied to obtain the diaphragm elastic deformation. The diaphragm elastic deformation measurement is taken as the difference between the diaphragm displacement and the LFRS displacement at each floor level.

C.2 Integration Method

This method is to integrate the shear and flexure deformation of each precast panel with the previous calculated design shear/moment diagram and diaphragm effective moduli (step 8 in PART 1). The diaphragm elastic deformation is calculated as the sum of shear and flexure deformation ($\delta_{el} = \delta_v + \delta_f$). The shear deformation (δ_v) is calculated by sum of the shear deformation of each precast panel:

$$\delta_v = \sum_{i=1}^{n} 1.2 V_i / A G_{effi}$$

where, V_i is the average shear force with the ith panel; A is the gross cross-section area of precast panel; G_{effi} is the effective elastic shear modulus for i^{th} panel (refer to Diaphragm Joint Stiffness Calculation" section); and n is number of precast panels.

The flexure deformation (δ_f) is calculated by conjugate beam method. With this method, the diaphragm moment diagram is scaled by the $1/E_{eff}I$ (E_{eff} is the effective elastic Young's modulus and I is gross section secondary moment of inertia for preast panel) and applied as the distributed load (w') on the conjugated beam as seen in Fig. 7. The diaphragm flexure deformation is the resulting moment diagram for the conjugate beam.
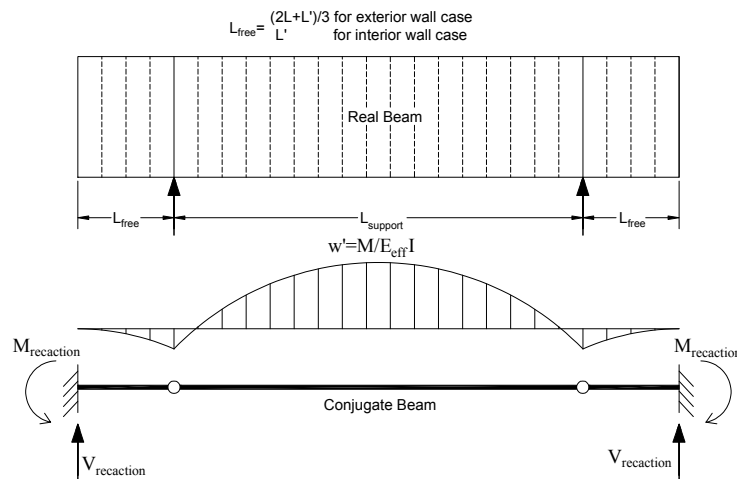
Fig.7. FBD of conjugate beam.

3.4 DESIGN AIDS FOR DIAPHRAGM DESIGN: SPREADSHEET PROGRAM

The techniques discussed in Sections 2 and 3 can easily be implemented in a spreadsheet. As an example, a spreadsheet based design program is developed for the diaphragm seismic design as part of the research program, and is available with the design methodology. This program translates the step-by-step design procedure (refer to PART 1) and the design analysis techniques as discussed in previous sections into Excel spreadsheets. In this section, the instruction on how to use the program is provided.

General notes for the spreadsheet program:
- Cells with blue text require user input
- Cells with black text are calculated automatically
- All cells with black text are locked and are not allowed to modify
- Green push button is used for automatic calculation (e.g. generate story and diaphragm joint locations, etc.)
- Program is created in Excel-VBA which requires the macro security level to be "medium" or "low" (go to "Tool"- "Macro"- " Security" to modify the security level)

A. Diaphragm Seismic Baseline Design Force

This sheet calculates the diaphragm seismic baseline design force (refer to step 1 in PART 1) as follows:
(1) Input seismic design parameters (Cell A2 to Cell B14)

	A	B
2	Design Code:	ASCE 2005
3	Site:	Knoxville
4	$S_s =$	0.58
5	$S_1 =$	0.147
6	Site Class =	C
7	$F_a =$	1.17
8	$F_v =$	1.65
9	$S_{ms} = F_v \times S_s =$	0.68
10	$S_{m1} = F_v \times S_1 =$	0.24
11	$S_{DS} = 2/3 \times S_{ms} =$	0.45
12	$S_{D1} = 2/3 \times S_{m1} =$	0.16
13	Seismic Design Category =	E
14	Long period T_L (sec)=	6

(2) Input building geometry (Cell D2 to Cell F10)

	D	E	F
2	Building Geometry		
3	# of story	4	
4	Building height	47.5	[ft]
5	Floor span	300	[ft]
6	Floor depth	181	[ft]
7	Floor area	54300	[ft^2]
8	Typ. story height	10.5	[ft]
9	1st story height	16	[ft]
10	Total weight	24262	[kips]

(3) Input LFRS seismic coefficient (Cell H2 to Cell O4)

	H	I	J	K	L	M	N	O
2	LFRS System	R	Ω_o	C_d	Importance factor	Type		
3	Transverse (NS)	5	2.5	4.5	1	Intermidate precast shear wall		
4	Longitudinal (EW)	4	2.5	4	1	Intermidate precast bearing wall		

(4) Calculate approximate building period (Cell H6 to Cell J13)

	H	I	J
6	Building Period		
7	x=	0.75	
8	$C_t =$	0.02	
9	$C_u =$	1.58	
10	$T_a =$	0.362	sec
11	T =	0.571	sec
12	Manual input period		sec
13	Design Period	0.571	sec

Program automatically calculates base shear (Cell L6 to Cell O11)

	L	M	N	O
6	Base shear	Transverse (NS)	Longitudinal (EW)	
7	$C_s =$	0.090	0.113	
8	$C_{s,min} =$	0.01	0.01	
9	$C_{s,max} =$	0.057	0.071	
10	$V_u=C_sW=$	1375	1719	kips
11	k=	1.04		

(5) Calculate diaphragm design acceleration (Cell C20 to Cell K72)

	B	C	D	E	F	G	H	I	J	K
								Transverse (NS)		Longitudinal (NS)	
		Story	h_x (ft)	W_x (kips)	$W_x h_x^k$	C_{vx}	F_x (kips)	C_{diax}	F_x (kips)	C_{diax}
	Generate Stories	4	47.5	5529	300926	0.350	482	0.087	602	0.109
		3	37	6245	262419	0.305	420	0.077	525	0.084
		2	26.5	6245	185750	0.216	297	0.067	372	0.060
		1	16	6245	110173	0.128	176	0.057	220	0.035

Click to generate column C and D automatically

Note: Maximum 50 stories is allowed in this program

Program automatically calculates diaphragm baseline forces

	D	E	F	G	H	I
15	Diaphragm baseline design				Top floor	Other floor
16	force		$C_{diax,max}$	α	F_{px} (kips)	F_{px} (kips)
17	Transverse (NS) direction		0.087	0.68	482	370
18	Longitudinal (EW) direction		0.109	0.68	602	462

B. Amplified Diaphragm Seismic Design Force

This sheet is to calculate the amplified diaphragm seismic design force (refer to step 2 to step 7 in PART 1) as follows:

(1) Input diaphragm geometry (Cell D20 to Cell N6)

	D	E	F	G	H	I	J	K	L	M	N
4											
5	L (ft)	d (ft)	a (ft)	L_{seam} (ft)	# of Story	L' (ft)	Wall Location	AR	b (ft)	Floor Area (ft²)	Ramp Area (ft²)
6	300	60	181	48	4	204	Exterior	5	12	54300	12444

(2) Diaphragm baseline design force imported from previous sheet (Cell D8 to Cell G10)

	D	E	F	G
8	Transverse (NS) direction		Longitudinal (EW) direction	
9	Top floor	Other floors	Top floor	Other floors
10	482	370	602	462

(3) Program automatically calculates the diaphragm design factors (Cell D12 to Cell G15)

	A	B	C	D	E	F	G
12	Diaphragm Design Factors			Ψ	Ω	$C_{d,dia}$	$C_{r,dia}$
13	EDO			2.90	1.0	1.0	0.59
14	BDO			2.25	1.19	1.5	0.64
15	RDO			1.56	1.50	2.9	0.56

(4) Amplified diaphragm seismic design force (Cell D17 to Cell H23)

36

	A	B	C	D	E	F	G	H
17					Transverse (NS) direction		Longitudinal (EW) direction	
18	Factored Design Forces			Design option	Top floor	Other floors	Top floor	Other floors
19	ΨF_{px} (kips)			EDO	1398	1073	1747	1342
20								
21	Distributed load for sub-diaphragm			Top floor	Other floors			
22	EW direction		w (k/ft)	1.74	1.19			
23	NS direction		n (k/ft)	2.18	1.49			

Designer selects design option

C. Diaphragm Internal Forces

With the information input/calculated in previous two sheets, diaphragm internal force is automatically generated using free body method by the program for exterior wall case in "Internal force-exterior wall" sheet and for interior wall case in "Internal force-interior wall" (refer to step 8 in PART 1). An illustration given here is for exterior wall case.

(1) Loading and reactions for the FBD (Cell C2 to Cell T5)

Loading and reactions on FBDs

	w	N_{lw}	V_{beam}	N_{beam}	V_{sw}	$V_{sw,ramp}$	V_{lw}	n	q_1	q_{lw}	q_2	N_t	N_c	n_1	n_2	$q_{lw,ramp}$	V_{beam}
	[k/ft]	[k/ft]	[kips]	[kips]	[kips]	[kips]	[k/ft]	[k/ft]	[k/ft]	[k/ft]	[k/ft]	[k/ft]	[k/ft]	[k/ft]	[k/ft]	[k/ft]	[kips]
Top floor	1.74	0.26	232	117	117	470	0.513	2.18	1.09	2.57	3.82	2.73	0.52	3.49	1.93	0.64	105
Other floor	1.19	0.18	159	80	80	321	0.351	1.49	0.75	1.75	2.61	1.86	0.35	2.39	1.32	0.44	72

(2) Diaphragm force for each joint under different loading cases (Cell D8 to Cell Y198)

Diaphragm Joint Internal Forces

Transverse (NS) Direction

x	N/S Flat-Top floor			Ramp-Top floor			N/S Flat-Other floors			Ramp-Other floors		
	N	V	M	N	V	M	N	V	M	N	V	M
[ft]	[kips]	[kips]	[k-ft]	[kips]	[kips]	[k-ft]	[kips]	[kips]	[k-ft]	[kips]	[kips]	[k-ft]
0	0	117	0	0	470	0	0	80	0	0	321	0
12	58	104	-430	0	390	1674	40	71	-294	0	267	114
24	116	105	-935	0	311	2391	79	72	-640	0	212	163
36	174	121	-1339	0	231	2153	119	83	-916	0	158	147
48	232	151	-1466	0	151	958	159	103	-1002	0	103	65
60	232	133	242	0	133	2666	159	91	166	0	91	182
72	232	116	1737	0	116	4161	159	79	1188	0	79	284
84	232	98	3018	0	98	5442	159	67	2064	0	67	372
96	232	80	4086	0	80	6509	159	55	2794	0	55	445
108	232	62	4940	0	62	7363	159	43	3378	0	43	503
120	232	44	5580	0	44	8004	159	30	3816	0	30	547
132	232	27	6007	0	27	8431	159	18	4107	0	18	576
144	232	9	6221	0	9	8644	159	6	4253	0	6	591
156	232	-9	6221	0	-9	8644	159	-6	4253	0	-6	591

Generate Joints

Generates diaphragm joint locations in column D based on span and panel width

Note: Maximum 185 joints are allowed in the program.

(3) Diaphragm FBD and N, V, M diagram are displayed in (Cell AE1 to Cell AW156)
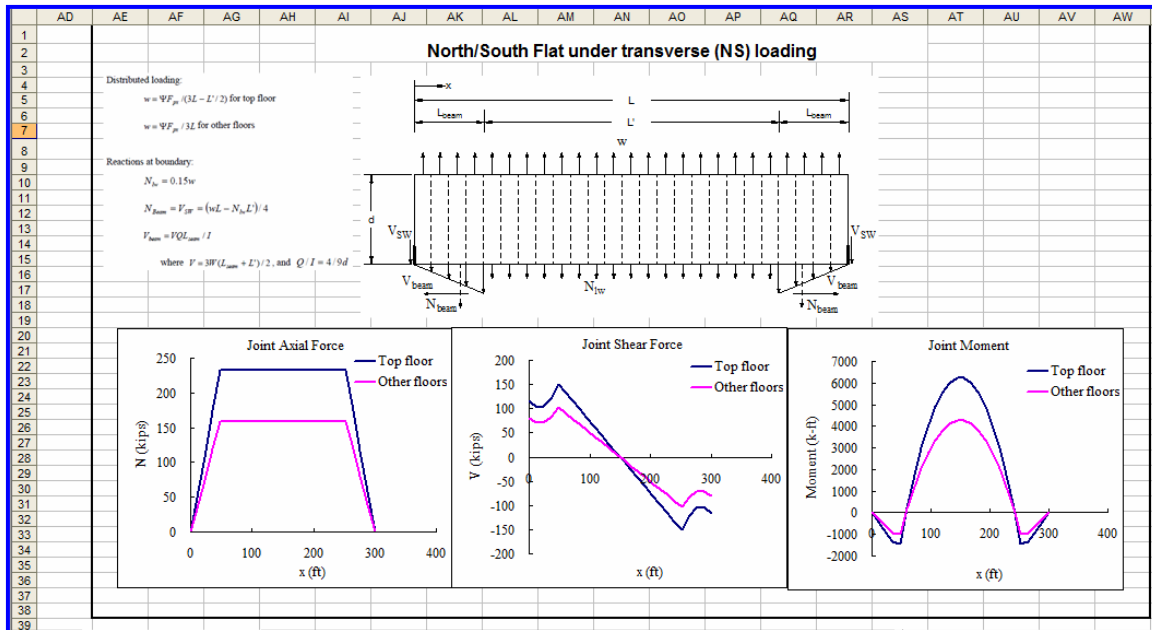
D. Diaphragm Reinforcement Design

This sheet is to calculate the diaphragm joint stiffness and strength and size the diaphragm primary reinforcement (refer to step 9 to step 11 in PART 1) using the analytical based procedure as discussed in "Diaphragm Joint Stiffness/Strength Calculation" section). The sizing of diaphragm reinforcement is a trial and error design check process using interaction design equation (refer to Eqn. 10 of PART 1)

(1) Select parameters for importing diaphragm joint force (Cell A1 to Cell D4) including: "Sub-diaphragm", "loading direction" and "floor level"

(2) Input diaphragm reinforcement properties (Cell F1 to Cell M6)

	F	G	H	I	J	K	L	M
1				**Diaphragm reinforcement properties**				
2	Diaphragm reinforcemnt			K_t	K_v	t_n	v_n	δ_{yt}
3				k/in	k/in	k	k	in
4	Chord (per in^2)			1234	382	60	24.2	0.0568
5	Web connector			55	226	3.1	18.1	0.06
6	Topping mesh (per in^2)							

(3) Input precast panel section properties (Cell Q1 to Cell V4)

	O	P	Q	R	S	T	U	V
1	**Diaphragm Section Properties**							
2	d	b	t	fc'	A	I	E_c	G_c
3	[ft]	[ft]	[in]	[ksi]	[in^2]	[in^4]	[ksi]	[ksi]
4	60	12	4	5	2880	124416000	4031	1679

(4) Input design factors (Cell X1 to Cell Z4)

	X	Y	Z
1	**Design Factors**		
2	ϕ_f	ϕ_v	Ω_v
3	0.9	0.85	1.00

(5) Import diaphragm joint forces from FBD calculation in previous sheet or manually input diaphragm joint forces obtained from computer analysis (Cell D13 to Cell G198)

Note: Automatically imported diaphragm joint forces is corresponding to parameter selected in (1)

	A	B	C	D	E	F	G
8							
9				x	Joint force demand		
10							
11			Import		N	V	M
12				[ft]	[kips]	[kips]	[k-ft]
13			Import the diaphragm joint forces from FBD methods by click "Import" or input manually	0	0	0	0
14				12	0	15	-693
15				24	0	29	-1213
16				36	0	41	-1575
17				48	0	53	-1793
18				60	0	63	-1884
19				72	0	72	-1861
20			Chord	84	0	79	-1741
21				96	0	85	-1537
22				108	0	90	-1266
23			Web connector	120	0	94	-942
24				132	0	97	-580
25				144	0	98	-196
26				156	0	98	196
27				168	0	97	580
28				180	0	94	942
29				192	0	90	1266
30				204	0	85	1537
31				216	0	79	1741
32			Topping mesh	228	0	72	1861
33				240	0	63	1884
34				252	0	53	1793
35				264	0	41	1575
36				276	0	29	1213
37				288	0	15	693
38				300	0	0	0
39							

(6) Input trial diaphragm reinforcement (Cell H8 to Cell Q198)

	H	I	J	K	L	M	N	O	P	Q
8	Design Check									
9-10	Chord Bars					Web connector			Topping mesh	
11	d_0	Bar size	# of bars	Manual, A_s	A_s	s_0	# of Connector	s	s'	Area
12	[in]			[in²]	[in²]	[in]		[ft]	[ft]	[in²]
13					0			0		
14	18	6	5		2.2	45	12	4.8		
15	18	6	5		2.2	45	12	4.8		
16	18	6	5		2.2	45	12	4.8		
17	18	6	6		2.64	45	16	3.5		
18	18	6	6		2.64	45	16	3.5		
19	18	6	6		2.64	45	16	3.5		
20	18	6	8		3.52	45	13	4.4		
21	18	6	8		3.52	45	13	4.4		
22	18	6	8		3.52	45	13	4.4		
23	18	6	9		3.96	45	7	8.8		
24	18	6	9		3.96	45	7	8.8		
25	18	6	9		3.96	45	7	8.8		
26	18	6	9		3.96	45	7	8.8		
27	18	6	9		3.96	45	7	8.8		
28	18	6	9		3.96	45	7	8.8		
29	18	6	8		3.52	45	13	4.4		
30	18	6	8		3.52	45	13	4.4		
31	18	6	8		3.52	45	13	4.4		
32	18	6	6		2.64	45	16	3.5		
33	18	6	6		2.64	45	16	3.5		

(7) Check the selected reinforcement with M-N-V interaction (Cell X8 to Cell Y198)

	R	S	T	U	V	W	X	Y
9		Joint Design Strength			Effective Joint Stiffness		Design Check	
10	Axial	Shear	Moment					
11	Nn	Vn	N.A. (c)	Mn	E_{eff}	G_{eff}	M-N-V	Check
12	[kips]	[kips]	[in]	[k-ft]	[ksi]	[ksi]		
13	0	0	0	0	0	0	#DIV/0!	#DIV/0!
14	301	324	157	8033	935	228	0.47	OK
15	301	324	157	8033	935	228	0.68	OK
16	301	324	157	8033	935	228	0.94	OK
17	366	417	171	9710	1057	281	0.97	OK
18	366	417	171	9710	1057	281	0.82	OK
19	366	417	171	9710	1057	281	0.96	OK
20	463	406	190	12568	1238	281	0.87	OK
21	463	406	190	12568	1238	281	0.95	OK
22	463	406	190	12568	1238	281	1.01	NG
23	497	318	197	13805	1308	237	0.98	OK
24	497	318	197	13805	1308	237	1.01	NG
25	497	318	197	13805	1308	237	1.02	NG
26	497	318	197	13805	1308	237	1.02	NG
27	497	318	197	13805	1308	237	1.01	NG

- ◆ Redo (6) to make the M-N-V to close "1.0"

- ◆ Check the selected reinforcement with the joint design force in two orthogonal directions respectively

ragm	Loading direction	F
uth	Longitudinal (EW) ▼	
	Transverse (NS)	
	Longitudinal (EW)	
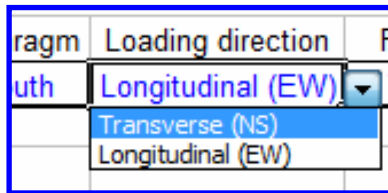
(8) Save the diaphragm designs: reinforcement and E_{eff}/G_{eff} (Cell AB8 to Cell BO198)

	Z	AA	AB	AC	AD	AE	AF	AG	AH	AI	AJ	AK	AL
8													
9							North/South Flat- Top floor						
10		Save design		Chord Bars			Web connector			Topping mesh		Effective Stiffness	
11			d_0	Bar size	# of bars	s_0	# of	s	s'	Area	E_{eff}	G_{eff}	d_0
12		Save the diaphragm	[in]			[in]	Connector	[ft]	[ft]	[in^2]	[ksi]	[ksi]	[in]
13		design in	18	6	4	45	12	4.77			715	213	
14		North/South flat and	18	6	4	45	12	4.77			715	213	18
15		ramp at top or other	18	6	4	45	12	4.77			715	213	18
16		floors by clicking	18	6	6	45	12	4.77			930	243	18
17		"Save design" after	18	6	6	45	16	3.50			942	281	18
18		checking the design	18	6	6	45	16	3.50			942	281	18
19		in two directions (NS	18	6	6	45	16	3.50			942	281	18
20		and EW)	18	6	8	45					1109	281	18
21			18	6	8	45					1109	281	18
22			18	6	8	45					1109	281	18
23			18	6	9	45					1174	237	18
24			18	6	9	45					1174	237	18
25			18	6	9	45					1174	237	18
26			18	6	9	45					1174	237	18
27			18	6	9	45					1174	237	18
28			18	6	9	45					1174	237	18
29			18	6	8	45	13	4.38			1109	281	18

Note: Design for North/South-top floor is saved [OK]
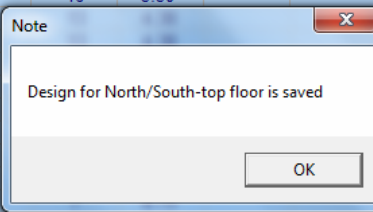
E. Secondary Reinforcement Design

This sheet is to size the secondary diaphragm reinforcement including LFRS anchorage and internal beam joint connector (refer to step 11 of PART 1). Two alternatives are available for the design forces: (1) import the design forces from the FBD calculation in previous sheet and (2) manually input the design forces obtained from computer analysis.

(1) Alternative 1: import design forces from FBD (Cell F2 to Cell O17)

	F	G	H	I	J	K	L	M	N	O
2										
3					Import design forces from FBD method automatically					
4	Anchorage design		Wall length	V_u	N_u	M_u	v_n per conn.	t_n per conn.	Req'd conn	Provide
5			[ft]	[kips]	[kips]	[k-ft]	[kips]	[kips]	Per wall	#4 angled bar
6	NS shear wal	Top	25	349	0	0	31.1	18.6	13.2	14
7		Others	25	268	0	0	31.1	18.6	10.2	11
8	EW lite wall-	Top	8	523	106	0	31.1	18.6	1.2	2
9	S/N Flat	Others	8	358	72	0	31.1	18.6	0.8	2
10	EW lite wall -	All floors	Provide flexible connector: 4"x3"x1/2"-5" angle plate with C-shape weld per wall							
11	Ramp									
12										
13										
14	Internal beam	Q	I	V_u	N_u	M_u	v_n per conn.	t_n per conn.	Req'd conn	Provide
15	joint design	[ft³]	[ft⁴]	[kips]	[kips]	[k-ft]	[kips]	[kips]	Per DT	#4 angled bar
16	Top floor	1210	164715	232	117	940	31.1	18.6	3.4	4
17	Other floors	1210	164715	159	80	643	31.1	18.6	2.3	3

(2) Alternative 2: input design forces from manually (Cell F20 to Cell O35)

	F	G	H	I	J	K	L	M	N	O	
	P37		f_x								
20					Import design forces manually						
21											
22	Wall anchorage design		Wall length	V_u	N_u	M_u	v_n per conn.	t_n per conn.	Req'd conn	Provide	
23			[ft]	[kips]	[kips]	[k-ft]	[kips]	[kips]	Per wall	#4 angled bar	
24	NS shear wal	Top floor	25	349	0	0	31.1	18.6	13.2	14	
25		Other floors	25	268	0	0	31.1	18.6	10.2	11	
26	EW lite wall-	Top floor	8	523	106	0	31.1	18.6	1.2	2	
27	S/N Flat	Other floors	8	358	72	0	31.1	18.6	0.8	2	
28	EW lite wall -	All floors	Provide flexible connector: 4"x3"x1/2"-5" angle plate with C-shape weld per wall								
29	Ramp										
30											
31											
32	Internal beam	Q	I	V_u	N_u	M_u	v_n per conn.	t_n per conn.	Req'd conn	Provide	
33	joint design	[ft³]	[ft⁴]	[kips]	[kips]	[k-ft]	[kips]	[kips]	Per DT	#4 angled bar	
34	Top floor	1210	164715	232	117	940	31.1	18.6	3.4	4	
35	Other floors	1210	164715	159	80	643	31.1	18.6	2.3	3	
36											

F. Diaphragm Induced Drift Check

This sheet automatically calculates the diaphragm deformation and diaphragm induced column drift using the integration method discussed in previous section. A drift check is also provided.

(1) Parameters for calculation (Cell B1 to Cell P4)

	B	C	D	E	F	G	H	I	J	K	L	M	N	O	P
1		Subdiaphragm				Section properties			Conjugate beam parameters				Drift check factors		
2	Wall location	Sub-diaphragm	Loading direction	Floor	A	I	b	$L_{support}$	L_{free}	$V_{reaction}$	$M_{reaction}$	$C_{d,dia}$	$C_{r,dia}$	H	θ_{LFRS}
3					[in²]	[in⁴]	[in]	[in]	[in]	[rad]	[in]			[in]	[rad]
4	Exterior	North/South	Transverse (NS)	Top	2880	124416000	144	3216	192	0.000322546	-0.062330016	1.00	0.59	126	0.02

Note: the LFRS drift (θ_{LFRS}) in "cell O4" can be input as the LFRS drift check calculation

(2) Diaphragm deformation calculation and drift check (Cell D9 to Cell Q198)

42

	D	E	F	G	H	I	J	K	L	M	N	O	P	Q
9							Drift Check							
10														
11	x	V	M	E_{eff}	G_{eff}	δ_v	w'=Mb/EI	"Shear" from w'	"Moment" from w'	δ_f	$\delta_{dia,el}$	δ_{dia}	θ_{dia}	Check
12	[in]	[kips]	[k-in]	[ksi]	[ksi]	[in]	[rad]	[rad]	[in]	[in]	[in]	[in]	[rad]	
13	0	117	0	715	213	0.000	0	0	0	-0.062	-0.062	-0.062	-0.0003	OK
14	144	104	-5162	715	213	0.031	-8.4E-06	-8.35762E-06	0	-0.016	0.015	0.015	0.0001	OK
15	288	105	-11224	715	213	0.061	-1.8E-05	-2.65293E-05	-0.001203497	0.032	0.092	0.092	0.0004	OK
16	432	121	-16070	930	243	0.090	-2E-05	-4.65391E-05	-0.005023716	0.082	0.172	0.172	0.0008	OK
17	576	151	-17587	942	281	0.122	-2.2E-05	-6.81566E-05	-0.011725342	0.135	0.257	0.257	0.0012	OK
18	720	133	2910	942	281	0.152	3.58E-06	-6.45799E-05	-0.021539897	0.191	0.343	0.343	0.0016	OK
19	864	116	20844	942	281	0.179	2.56E-05	-3.89581E-05	-0.030839398	0.247	0.426	0.426	0.0020	OK
20	1008	98	36217	1109	281	0.201	3.78E-05	-1.17471E-06	-0.036449363	0.299	0.501	0.501	0.0023	OK
21	1152	80	49027	1109	281	0.220	5.11E-05	4.99731E-05	-0.036618521	0.346	0.566	0.566	0.0027	OK
22	1296	62	59276	1109	281	0.235	6.18E-05	0.000111813	-0.029422388	0.385	0.621	0.621	0.0029	OK
23	1440	44	66962	1174	237	0.248	6.6E-05	0.000177846	-0.013321374	0.415	0.663	0.663	0.0031	OK
24	1584	27	72086	1174	237	0.257	7.11E-05	0.000248933	0.012288473	0.436	0.693	0.693	0.0032	OK
25	1728	9	74648	1174	237	0.261	7.36E-05	0.000322546	0.048134802	0.447	0.708	0.708	0.0033	OK
26	1872	-9	74648	1174	237	0.261	7.36E-05	0.000396159	0.09458144	0.447	0.708	0.708	0.0033	OK
27	2016	-27	72086	1174	237	0.257	7.11E-05	0.000467246	0.151628386	0.436	0.693	0.693	0.0032	OK
28	2160	-44	66962	1174	237	0.248	6.6E-05	0.00053328	0.218911814	0.415	0.663	0.663	0.0031	OK
29	2304	-62	59276	1109	281	0.235	6.18E-05	0.000595119	0.295704076	0.385	0.621	0.621	0.0029	OK
30	2448	-80	49027	1109	281	0.220	5.11E-05	0.000646267	0.381401218	0.346	0.566	0.566	0.0027	OK
31	2592	-98	36217	1109	281	0.201	3.78E-05	0.00068405	0.474463652	0.299	0.501	0.501	0.0023	OK
32	2736	-116	20844	942	281	0.179	2.56E-05	0.000709672	0.572966892	0.247	0.426	0.426	0.0020	OK
33	2880	-133	2910	942	281	0.152	3.58E-06	0.000713249	0.675159669	0.191	0.343	0.343	0.0016	OK
34	3024	-151	-17587	942	281	0.122	-2.2E-05	0.000691631	0.777867499	0.135	0.257	0.257	0.0012	OK
35	3168	-121	-16070	930	243	0.090	-2E-05	0.000671621	0.877462401	0.082	0.172	0.172	0.0008	OK
36	3312	-105	-11224	715	213	0.061	-1.8E-05	0.00065345	0.974175895	0.032	0.092	0.092	0.0004	OK
37	3456	-104	-5162	715	213	0.031	-8.4E-06	0.000645092	1.068272667	-0.016	0.015	0.015	0.0001	OK
38	3600	-117	0	715	213	0.000	0	0.000645092	1.161165943	-0.062	-0.062	-0.062	-0.0003	OK
39														

3.5 REFERENCES

ASCE 7 (2005). "Minimum Design Loads for Buildings and Other Structures". ASCE, Reston, VA.

ASCE/SEI 41 (2006). "Seismic Rehabilitation of Existing Buildings". ASCE, Reston, VA.

Antoniou S. and Pinho R. (2004). "Development and verification of a displacement-based adaptive pushover procedure". Journal of Earthquake Engineering, 8(5):643-661.

Cleland, N. BSSC IT 6 discussions, San Francisco, February 2012.

Harman, R. Coreslab Structures Plant Site Visit, University of Arizona ASCE Student Chapter, March 2012.

Meyer, T. BSSC IT 6 discussions, San Francisco, February 2012.

NZSEE (2006). "Assessment and improvement of the structure performance of buildings in earthquakes". New Zealand Society for Earthquake Engineering.

Sabelli, R., Sabol, T. and Easterling, S.W. (2011). "Seismic design of composite steel deck and concrete-filled diaphragms". NEHRP Seismic Design Technical Brief No.5, NIST GCR 11-917-10.

Zheng, W. and Oliva, M.G. (2005). "A practical method to estimate elastic deformation of precast pretopped Double-Tee diaphragms". PCI Journal. March-April: 44-55.

Seismic Design Methodology Document for Precast Concrete Diaphragms

PART 4:
DESIGN EXAMPLES

2/16/2014

PART 4: Diaphragm Examples

INTRODUCTION

This section provides diaphragm design examples using the new seismic design methodology created from the PCI/CPF/NSF diaphragm research project. This design methodology is aligned with ASCE 7 diaphragm IT06-001 proposal for the 2014 provision, herein termed IT06-001. Design examples are provided for two common precast structures: a four-story precast parking structure and an eight story precast office building. Each structure has two lateral force-resisting system (LFRS) configurations: an exterior shear wall and interior shear wall configuration for the parking garage; and a moment frame and shear wall design for the office building. Designs are provided for two Seismic Design Categories (SDCs): C and D. The diaphragm designs are executed following the step by step procedure described in PART 1. Equation numbers indicated in the examples follow the numbering given in PART 1. Where appropriate, the design examples references diaphragm reinforcement information from PART 2 and diaphragm design analytical techniques and design aids from PART 3.

Example 1: 4-Story Perimeter Wall Parking Garage

The structure for example 1 is a 4-story perimeter shear wall parking garage. As seen in plan view of Figure1a, the parking structure has three bays with a central ramp. The structural plan has a footprint of $300' \times 180'$, resulting in $300' \times 60'$ for each sub-diaphragm. The floor-to-floor height is $10.5'$ for the typical floor and $16'$ at the 1st story. The lateral force resisting system (LFRS) in the transverse direction is composed of four $25'$ perimeter precast walls at each end of structure. The LFRS in longitudinal direction are 34 interior lite walls flanking the central ramp (See elevation in Figure 1b).
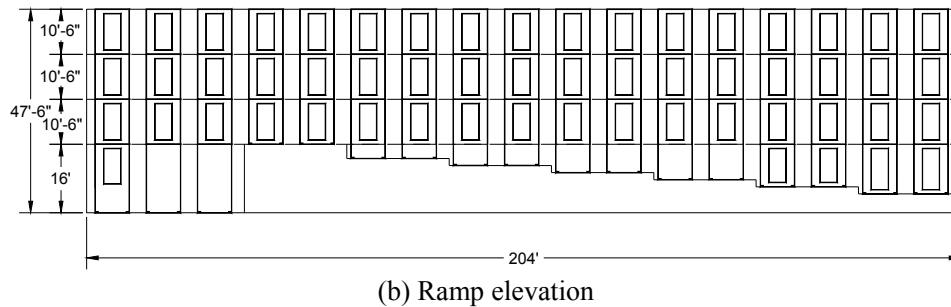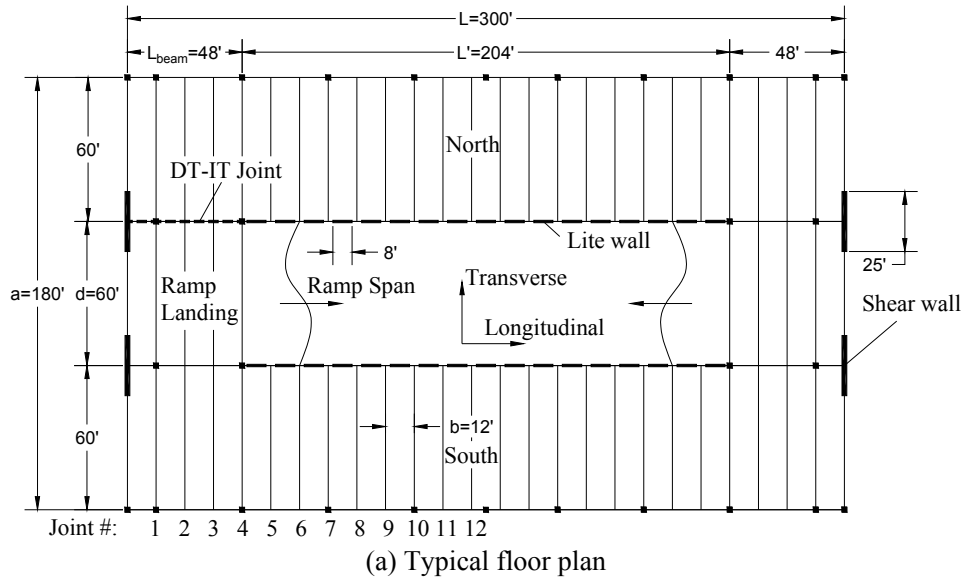

(a) Typical floor plan

(b) Ramp elevation

Fig. 1. Example 1 Structure: 4-story perimeter wall parking garage.

Example Structure 1 is located in a Seismic Design Category (SDC) C Site in Knoxville TN. The diaphragm design will be completed for three different diaphragm design options:

Design Example 1A.   Elastic Design Option (EDO Design)
Design Example 1B.   Basic Design Option (BDO Design)
Design Example 1C.   Reduced Design Option (RDO Design)

Because many design steps are shared among the different diaphragm design options, the design examples are arranged to follow the step by step procedure in part 1, with the different calculations for Examples 1A, 1B and 1C appearing as sequential sub-sections within each design step.

DESIGN STEPS:

Step 1: *Determine the Diaphragm Seismic Demand Level*

    This step is the same for all three design examples, 1A, 1B, and 1C.

        For SDC C: **Low**

           Note: All buildings in SDC C are assigned "Low" Seismic Demand

Step 2: *Select Diaphragm Design Option and Appropriate Diaphragm Reinforcement Classification*

<u>Diaphragm Design Option</u>
    Design example 1A: (EDO)

        For low seismic demand: **Elastic design option (EDO)**   is recommended

    Design example 1B: (BDO)

        For low seismic demand: **Basic design option (BDO)**   is an alternative

    Design example 1C: (RDO)

        For low seismic demand: **Reduced design option (RDO)**   is an alternative

<u>Diaphragm Reinforcement Classification</u>
    Design example 1A: (EDO)

        For elastic design option: **Low deformability element (LDE)**   is permitted.

    Design example 1B: (BDO)

        For basic design option: **Moderate deformability element (MDE)**   is permitted.

    Design example 1C: (RDO)

        For reduced design option: **High deformability element (HDE)**   is required.

Step 3: *Determine Diaphragm Design Force*

    (1) Determine the diaphragm design acceleration coefficient at level *x* (C_{px}) :

        <u>From ASCE 7 (2010):</u>

Design site:	**Knoxville, TN**
SDC	**C**
S_s	**0.58**
S_1	**0.147**
Soil site class	**C**
F_a	1.17
F_v	1.65
$S_{ms} = F_a \times S_s$	0.68
$S_{m1} = F_v \times S_1$	0.24

$S_{DS} = 2/3 \times S_{ms}$ 0.45

$S_{D1} = 2/3 \times S_{m1}$ 0.16

N-S/Intermediate precast wall   **R=5, Ω_0=2.5, C_d=4.5**

E-W/Intermediate precast bearing wall   **R=4, Ω_0=2.5, C_d=4**

$$T_a = C_t H_n^{3/4} = 0.02 \times 47.5^{3/4} = 0.362 \sec; \quad T = C_u T_a = 1.58 \times 0.362 = 0.571 \sec$$

From IT06-001:

$\Gamma_{m1} = 1 + z_s(1 - 1/n)/2 = 1 + 1.0 \times (1 - 1/4)/2 = 1.38$ (Eqn. 12.11-10)

$\Gamma_{m2} = 0.9 z_s(1 - 1/n)^2 = 0.9 \times 1.0 \times (1 - 1/4)^2 = 0.51$ (Eqn. 12.11-11)

$C_{s2} = (0.15n + 0.25)I_e S_{DS} = 0.38$ **controls**   (Eqn. 12.11-7)

$C_{s2} = I_e S_{DS} = 0.45$;   (Eqn. 12.11-8)

$C_{s2} = I_e S_{DS} / 0.03 / (n - 1) = 5$ (Eqn. 12.11-9a)

$C_{p0} = 0.4 I_e S_{DS} = 0.18$ (Eqn. 12.11-3)

N-S direction:

From ASCE 7 (2010):

$$C_S = \frac{S_{DS}}{R/I_E} = 0.09, \; C_{S,min} = 0.01, \; C_{S,max} = \frac{S_{D1}}{(R/I_E)T} = \frac{0.16}{5 \times 0.571} = 0.057 \; \textbf{controls}$$

From IT06-001:

$C_{pi} = 0.3 S_{DS} I_e = 0.3 \times 0.45 \times 1.0 = 0.135$ (Eqn. 12.11-5)

$C_{pi} = 0.9 \Gamma_{m1} \Omega_0 C_S = 0.9 \times 1.38 \times 2.5 \times 0.057 = 0.177$ **controls**   (Eqn. 12.11-6)

$C_{pn} = \sqrt{(\Gamma_{m1}\Omega_0 C_S)^2 + (\Gamma_{m2} C_{s2})^2} = 0.276$ (Eqn. 12.11-4)

Table 1. C_{px} in N-S direction.   (Figure 12.11-1)

Level	h_i [ft]	C_{px}
4	47.5	0.276
i@0.8h_n	38	0.177
3	37	0.177
2	26.5	0.178
1	16	0.179
0	0	0.180

E-W direction:

From ASCE 7 (2010):

$$C_S = \frac{S_{DS}}{R/I_E} = 0.11, \; C_{S,min} = 0.01, \; C_{S,max} = \frac{S_{D1}}{(R/I_E)T} = \frac{0.16}{4 \times 0.571} = 0.071 \; \textbf{controls}$$

From IT06-001:

$C_{pi} = 0.3 S_{DS} I_e = 0.3 \times 0.45 \times 1.0 = 0.135$ (Eqn. 12.11-5)

$$C_{pi} = 0.9\Gamma_{m1}\Omega_0 C_S = 0.9 \times 1.38 \times 2.5 \times 0.071 = 0.22 \textbf{ \underline{controls}} \qquad \text{(Eqn. 12.11-6)}$$

$$C_{pn} = \sqrt{(\Gamma_{m1}\Omega_0 C_S)^2 + (\Gamma_{m2}C_{s2})^2} = 0.312 \qquad \text{(Eqn. 12.11-4)}$$

Table 2. C_{px} in E-W direction.   (Figure 12.11-1)

Level	h_i [ft]	C_{px}
4	47.5	0.312
i@0.8h_n	38	0.220
3	37	0.219
2	26.5	0.208
1	16	0.197
0	0	0.180

(2) Determine the flexible diaphragm acceleration amplification factor at level x (α_{fx}) :

From IT06-001:
$$\alpha_{fx} = 0.3\delta_{MDD} / \Delta_{ADVE} + 0.14 \leq 1.3 \qquad \text{(Eqn. 12.11-12)}$$

Table 3. α_{fx} calculation (Figure 12.3-1)

Story	Δ_{ADVE} * [in]	δ_{MDD} ** [in]	$\delta_{MDD} / \Delta_{ADVE}$	α_f
4	0.12	0.65	5.5	1.3
3	0.12	0.57	4.9	1.3
2	0.10	0.40	4.0	1.3
1	0.08	0.24	2.9	1.3

* Using cracked section for shear wall: I_{cr}=0.35I_g and A_{cr}=0.4A_g.
** Using approximate effective properties for diaphragm: E_{eff}=0.2E_c and G_{eff}=0.2G_c.

(3) Determine diaphragm design force at each level

From New Design Procedure:
$$F_{px} = \alpha_{fx} C_{px} w_{px} / R_s \qquad \text{(Eqn 1a)}$$

but not less than

$$F_{px} = 0.2\alpha_{fx} S_{DS} I_e w_{px} \qquad \text{(Eqn 1b)}$$

Controlled values of F_{px} are bold in the Table 4 to 9.

From IT06-001 (Table 12.11.5-1):
R_s = 0.7 for **Example 1A (EDO)**
= 1.0 for **Example 1B (BDO)**
= 1.4 for **Example 1C (RDO)**

Design example 1A: (EDO)

Table 4. F_{px} in N-S direction (EDO).

Story	α_{fx}	C_{px}	w_{px} [kips]	R_s	F_{px} (1a) [kips]	F_{px} (1b) [kips]
4	1.3	0.276	5529	0.7	**2834**	647
3	1.3	0.177	6245	0.7	**2054**	731
2	1.3	0.178	6245	0.7	**2063**	731
1	1.3	0.179	6245	0.7	**2073**	731

Table 5. F_{px} in E-W direction (EDO).

Story	α_{fx}	C_{px}	w_{px} [kips]	R_s	F_{px} (1a) [kips]	F_{px} (1b) [kips]
4	1.3	0.312	5529	0.7	**3204**	647
3	1.3	0.219	6245	0.7	**2539**	731
2	1.3	0.208	6245	0.7	**2411**	731
1	1.3	0.197	6245	0.7	**2283**	731

Design example 1B: (BDO)

Table 6. F_{px} in N-S direction (BDO).

Story	α_{fx}	C_{px}	w_{px} [kips]	R_s	F_{px} (1a) [kips]	F_{px} (1b) [kips]
4	1.3	0.276	5529	1.0	**1984**	647
3	1.3	0.177	6245	1.0	**1438**	731
2	1.3	0.178	6245	1.0	**1444**	731
1	1.3	0.179	6245	1.0	**1451**	731

Table 7. F_{px} in E-W direction (BDO).

Story	α_{fx}	C_{px}	w_{px} [kips]	R_s	F_{px} (1a) [kips]	F_{px} (1b) [kips]
4	1.3	0.312	5529	1.0	**2243**	647
3	1.3	0.219	6245	1.0	**1778**	731
2	1.3	0.208	6245	1.0	**1688**	731
1	1.3	0.197	6245	1.0	**1598**	731

Design example 1C: (RDO)

Table 8. F_{px} in N-S direction (RDO).

Story	α_{fx}	C_{px}	w_{px} [kips]	R_s	F_{px} (1a) [kips]	F_{px} (1b) [kips]
4	1.3	0.276	5529	1.4	**1417**	647
3	1.3	0.177	6245	1.4	**1027**	731
2	1.3	0.178	6245	1.4	**1032**	731
1	1.3	0.179	6245	1.4	**1036**	731

Table 9. F_{px} in E-W direction (RDO).

Story	α_{fx}	C_{px}	w_{px} [kips]	R_s	F_{px} (1a) [kips]	F_{px} (1b) [kips]
4	1.3	0.312	5529	1.4	**1602**	647
3	1.3	0.219	6245	1.4	**1270**	731
2	1.3	0.208	6245	1.4	**1206**	731
1	1.3	0.197	6245	1.4	**1141**	731

(4) For design of collectors, amplify the design force by 1.5 (IT06-001: 12.11.4)

(5) Determine diaphragm shear overstrength factor, $\Omega_V = 1.4\ R_s$ (New design procedure)

Table 10. Diaphragm shear overstrength factor.

Design example/option	R_s	Ω_v
Design example 1A (EDO)	0.7	1.0
Design example 1B (BDO)	1.0	1.4
Design example 1C (RDO)	1.4	2.0

Step 4: *Determine Diaphragm Internal Forces*

The free-body diagram method (*Option 8b*) is selected to obtain the diaphragm internal forces. Use is made of existing free body diagrams created for common precast diaphragm configurations (See PART 3: *Free Body Diagrams for Typical Precast Parking Structures*). The associate calculations have been embedded in a design spreadsheet program (See PART 3: *Design Aids for Diaphragm Design: Spreadsheet Program*).

The tables below show the resulting required strength (maximum diaphragm internal forces) at each diaphragm joint (Refer to Fig. 1a for joint numbering) and joints between diaphragm to other members (LFRS and internal beam) under transverse and longitudinal directions. Although the effect of two orthogonal direction loadings (transverse and longitudinal) is considered independently, at this step the critical loading direction in the diaphragm joint cannot be explicitly determined because the diaphragm reinforcement selection at step 5 is based on an M-N-V interaction equation (Eqn. 2).

As noticed in Table 4-9, diaphragm design forces are similar in the floors other than top floor. Therefore the lower three floors will all be designed for the maximum design forces among these floors.

Design example 1A (EDO):

Table 11: Joint between precast floor units: Transverse (N-S) Loading

Joint	x	Top floor						Other floors					
		N/S Flat			Ramp			N/S Flat			Ramp		
		N_u	V_u	M_u	N_u	V_u	M_u	N_u	V_u	M_u	N_u	V_u	M_u
	[ft]	[kips]	[kips]	[k-ft]	[kips]	[kips]	[k-ft]	[kips]	[kips]	[k-ft]	[kips]	[kips]	[k-ft]
1	12	118	211	-872	0	791	3393	77	137	-568	0	515	2210
2	24	236	213	-1896	0	630	4848	154	139	-1235	0	410	3157
3	36	354	245	-2715	0	468	4365	230	159	-1768	0	305	2842
4	48	471	307	-2972	0	307	1942	307	200	-1935	0	200	1265
5	60	471	271	492	0	271	4657	307	176	320	0	176	3033
6	72	471	234	3522	0	234	6938	307	153	2294	0	153	4518
7	84	471	198	6119	0	198	8786	307	129	3985	0	129	5722
8	96	471	162	8284	0	162	10202	307	106	5395	0	106	6644
9	108	471	126	10015	0	126	11185	307	82	6523	0	82	7284
10	120	471	90	11314	0	90	11734	307	59	7368	0	59	7642
11	132	471	54	12180	0	54	11851	307	35	7932	0	35	7718
12	144	471	18	12613	0	18	11535	307	12	8214	0	12	7512

Table 12: Joint between precast floor units: Longitudinal (E-W) Loading

Joint	x	Top floor						Other floors					
		N/S Flat*			Ramp			N/S Flat*			Ramp		
		N_u	V_u	M_u	N_u	V_u	M_u	N_u	V_u	M_u	N_u	V_u	M_u
	[ft]	[kips]	[kips]	[k-ft]	[kips]	[kips]	[k-ft]	[kips]	[kips]	[k-ft]	[kips]	[kips]	[k-ft]
1	12	101	11	-788	144	0	0	64	7	-500	91	0	0
2	24	202	23	-1714	288	0	0	128	14	-1087	183	0	0
3	36	302	34	-2776	432	0	0	192	22	-1761	274	0	0
4	48	403	46	-3976	576	0	0	256	29	-2522	365	0	0
5	60	389	57	-2899	596	0	0	247	36	-1839	378	0	0
6	72	375	69	-1960	615	0	0	238	43	-1243	390	0	0
7	84	361	80	-1157	635	0	0	229	51	-734	403	0	0
8	96	347	91	-492	655	0	0	220	58	-312	415	0	0
9	108	333	103	36	675	0	0	211	65	23	428	0	0
10	120	319	114	427	694	0	0	203	72	271	440	0	0
11	132	305	126	681	714	0	0	194	80	432	453	0	0
12	144	291	137	798	734	0	0	185	87	506	466	0	0

* *Symmetric design will be applied although loading is not symmetric. The most critical diaphragm internal forces are shown in the table for each symmetric joint.*

Table 13: Other Joints (Diaphragm-to-LFRS and Diaphragm-to-internal beam):

Joint	Top Floor						Other Floors					
	Transverse (N-S)			Longitudinal (E-W)			Transverse (N-S)			Longitudinal (E-W)		
	N_u	V_u	M_u	N_u	V_u	M_u	N_u	V_u	M_u	N_u	V_u	M_u
	[kips]	[kips]	[k-ft]	[kips]	[kips]	[k-ft]	[kips]	[kips]	[k-ft]	[kips]	[kips]	[k-ft]
DT-to-SW	**0**	**709**	**0**	-	-	-	**0**	**518**	**0**	-	-	-
DT-to-LW	6.4	12.5	0	**11.4**	**56**	**0**	4.1	8.1	0	**7.2**	**36**	**0**
DT-to-IT	**238**	**471**	**1906**	240	336	**0**	**155**	**307**	**1241**	152	213	0

Note: Critical force demand is marked as bond.

Design example 1B (BDO):

Table 14: Joint between precast floor units: Transverse (N-S) Loading

Joint	x	Top floor						Other floors					
		N/S Flat			Ramp			N/S Flat			Ramp		
		N_u	V_u	M_u	N_u	V_u	M_u	N_u	V_u	M_u	N_u	V_u	M_u
	[ft]	[kips]	[kips]	[k-ft]	[kips]	[kips]	[k-ft]	[kips]	[kips]	[k-ft]	[kips]	[kips]	[k-ft]
1	12	83	147	-611	0	554	2376	54	96	-398	0	361	1547
2	24	165	149	-1328	0	441	3394	107	97	-864	0	287	2210
3	36	248	171	-1901	0	328	3056	161	112	-1238	0	213	1990
4	48	330	215	-2080	0	215	1360	215	140	-1355	0	140	885
5	60	330	189	344	0	189	3260	215	123	224	0	123	2123
6	72	330	164	2466	0	164	4857	215	107	1605	0	107	3163
7	84	330	139	4284	0	139	6151	215	90	2789	0	90	4005
8	96	330	114	5799	0	114	7142	215	74	3776	0	74	4651
9	108	330	88	7012	0	88	7830	215	58	4566	0	58	5098
10	120	330	63	7921	0	63	8215	215	41	5158	0	41	5349
11	132	330	38	8527	0	38	8297	215	25	5552	0	25	5402
12	144	330	13	8830	0	13	8075	215	8	5750	0	8	5258

Table 15: Joint between precast floor units: Longitudinal (E-W) Loading

Joint	x	Top floor						Other floors					
		N/S Flat*			Ramp			N/S Flat*			Ramp		
		N_u	V_u	M_u	N_u	V_u	M_u	N_u	V_u	M_u	N_u	V_u	M_u
	[ft]	[kips]	[kips]	[k-ft]	[kips]	[kips]	[k-ft]	[kips]	[kips]	[k-ft]	[kips]	[kips]	[k-ft]
1	12	71	8	-552	101	0	0	50	6	-389	71	0	0
2	24	141	16	-1200	202	0	0	100	11	-847	142	0	0
3	36	212	24	-1943	302	0	0	149	17	-1372	213	0	0
4	48	282	32	-2783	403	0	0	199	23	-1964	284	0	0
5	60	272	40	-2030	417	0	0	192	28	-1432	294	0	0
6	72	263	48	-1372	431	0	0	185	34	-968	304	0	0
7	84	253	56	-810	445	0	0	178	40	-572	314	0	0
8	96	243	64	-344	458	0	0	172	45	-243	324	0	0
9	108	233	72	25	472	0	0	165	51	18	333	0	0
10	120	224	80	299	486	0	0	158	56	211	343	0	0
11	132	214	88	477	500	0	0	151	62	337	353	0	0
12	144	204	96	559	514	0	0	144	68	394	363	0	0

Symmetric design will be applied although loading is not symmetric. The most critical diaphragm internal forces are shown in the table for each symmetric joint.

Table 16: Other Joints (Diaphragm-to-LFRS and Diaphragm-to-internal beam):

Joint	Top Floor						Other Floors					
	Transverse (N-S)			Longitudinal (E-W)			Transverse (N-S)			Longitudinal (E-W)		
	N_u	V_u	M_u	N_u	V_u	M_u	N_u	V_u	M_u	N_u	V_u	M_u
	[kips]	[kips]	[k-ft]	[kips]	[kips]	[k-ft]	[kips]	[kips]	[k-ft]	[kips]	[kips]	[k-ft]
DT-to-SW	**0**	**496**	**0**	-	-	-	**0**	**363**	**0**	-	-	-
DT-to-LW	4.5	8.7	0	**8.0**	**40**	**0**	2.9	5.7	0	**5.6**	**28**	**0**
DT-to-IT	**167**	**330**	**1334**	168	235	**0**	**109**	**215**	**869**	119	166	0

Note: Critical force demand is marked as bond.

Design example 1C (RDO):

Table 17: Joint between precast floor units: Transverse (N-S) Loading

Joint	x	Top floor						Other floors					
		N/S Flat			Ramp			N/S Flat			Ramp		
		N_u	V_u	M_u	N_u	V_u	M_u	N_u	V_u	M_u	N_u	V_u	M_u
	[ft]	[kips]	[kips]	[k-ft]	[kips]	[kips]	[k-ft]	[kips]	[kips]	[k-ft]	[kips]	[kips]	[k-ft]
1	12	59	105	-436	0	396	1697	38	69	-284	0	258	1104
2	24	118	106	-948	0	315	2424	77	69	-617	0	205	1578
3	36	177	122	-1358	0	234	2182	115	80	-884	0	152	1421
4	48	236	153	-1486	0	153	971	153	100	-967	0	100	632
5	60	236	135	246	0	135	2328	153	88	160	0	88	1516
6	72	236	117	1761	0	117	3469	153	76	1146	0	76	2258
7	84	236	99	3060	0	99	4393	153	65	1992	0	65	2860
8	96	236	81	4142	0	81	5101	153	53	2696	0	53	3320
9	108	236	63	5008	0	63	5592	153	41	3260	0	41	3640
10	120	236	45	5657	0	45	5867	153	29	3682	0	29	3819
11	132	236	27	6090	0	27	5926	153	18	3964	0	18	3857
12	144	236	9	6306	0	9	5768	153	6	4105	0	6	3754

Table 18: Joint between precast floor units: Longitudinal (E-W) Loading

Joint	x	Top floor						Other floors					
		N/S Flat*			Ramp			N/S Flat*			Ramp		
		N_u	V_u	M_u	N_u	V_u	M_u	N_u	V_u	M_u	N_u	V_u	M_u
	[ft]	[kips]	[kips]	[k-ft]	[kips]	[kips]	[k-ft]	[kips]	[kips]	[k-ft]	[kips]	[kips]	[k-ft]
1	12	50	6	-394	72	0	0	36	4	-278	51	0	0
2	24	101	11	-857	144	0	0	71	8	-605	102	0	0
3	36	151	17	-1388	216	0	0	107	12	-980	152	0	0
4	48	202	23	-1988	288	0	0	142	16	-1403	203	0	0
5	60	195	29	-1450	298	0	0	137	20	-1023	210	0	0
6	72	188	34	-980	308	0	0	132	24	-692	217	0	0
7	84	181	40	-579	318	0	0	127	28	-408	224	0	0
8	96	174	46	-246	327	0	0	123	32	-174	231	0	0
9	108	167	51	18	337	0	0	118	36	13	238	0	0
10	120	160	57	214	347	0	0	113	40	151	245	0	0
11	132	153	63	341	357	0	0	108	44	240	252	0	0
12	144	146	69	399	367	0	0	103	48	282	259	0	0

* *Symmetric design will be applied although loading is not symmetric. The most critical diaphragm internal forces are shown in the table for each symmetric joint.*

Table 19: Other Joints (Diaphragm-to-LFRS and Diaphragm-to-internal beam):

Joint	Top Floor						Other Floors					
	Transverse (N-S)			Longitudinal (E-W)			Transverse (N-S)			Longitudinal (E-W)		
	N_u	V_u	M_u	N_u	V_u	M_u	N_u	V_u	M_u	N_u	V_u	M_u
	[kips]	[kips]	[k-ft]	[kips]	[kips]	[k-ft]	[kips]	[kips]	[k-ft]	[kips]	[kips]	[k-ft]
DT-to-SW	**0**	**354**	**0**	-	-	-	**0**	**259**	**0**	-	-	-
DT-to-LW	3.2	6.2	0	**5.7**	**28**	**0**	2.1	4.1	0	**4.0**	**20**	**0**
DT-to-IT	**119**	**236**	**953**	120	168	**0**	**78**	**153**	**620**	85	119	0

Note: Critical force demand is marked as bond.

Step 5: *Design diaphragm reinforcement for required strength.*

(1) Select Diaphragm Reinforcement

Diaphragm reinforcement type selected to meet Required Diaphragm Reinforcement Classification (*See Step 2*). Prequalified connectors will be used in this example. Select appropriate diaphragm reinforcement types from PART 2: Table 2A-1.

Design example 1A: (EDO)

Chord Reinforcement:	**Dry chord connector**
Shear Reinforcement:	**JVI Vector**
Secondary Reinforcement:	**#4 angled bar**

Design example 1B: (BDO)

Chord Reinforcement:	**Dry chord with flat plate connector**
Shear Reinforcement:	**JVI Vector**
Secondary Reinforcement:	**#4 angled bar**

Design example 1C: (RDO)

Chord Reinforcement:	**Pour strip bars**
Shear Reinforcement:	**JVI Vector**
Secondary Reinforcement:	**Pour strip bars**

(2) Determine Diaphragm Reinforcement Properties:

As the diaphragm reinforcement selected is prequalified, the diaphragm reinforcement properties can also be looked up in PART 2: Table 2A-1.

Table 20: Design example 1A: (EDO)

Reinforcing bars	k_t / A k/in/in^2	k_v / A k/in/in^2	t_n / A k/in^2	v_n / A k/in^2	δ_{ty} in
Dry chord Gr.60	1018	382	60	24.2	0.071
Connectors	k_t k/in	k_v k/in	t_n k	v_n k	δ_{ty} in
JVI Vector	55	226	3.1	18.1	0.066
Angled bar #4	545	676	18.5	31.1	-

Table 21: Design example 1B: (BDO)

Reinforcing bars	k_t / A k/in/in^2	k_v / A k/in/in^2	t_n / A k/in^2	v_n / A k/in^2	δ_{ty} in
Dry chord w/ flat plate Gr.60	1018	382	60	24.2	0.071
Connectors	k_t k/in	k_v k/in	t_n k	v_n k	δ_{ty} in
JVI Vector	55	226	3.1	18.1	0.066
Angled bar #4	545	676	18.5	31.1	-

12

Table 23: Design example 1C: (RDO)

Reinforcing bars	k_t / A k/in/in^2	k_v / A k/in/in^2	t_n / A k/in^2	v_n / A k/in^2	δ_{ty} in
Pour strip chord Gr.60	1234	382	60	24.2	0.057

Connectors	k_t k/in	k_v k/in	t_n k	v_n k	δ_{ty} in
JVI Vector	55	226	3.1	18.1	0.066

(3) Design the Diaphragm Reinforcement at Joints

Use the interaction equation (Eqn. 2) to determine the required diaphragm reinforcement:

$$M - N - V = \sqrt{\left(\frac{|M_u|}{\phi_f M_n} + \frac{N_u}{\phi_f N_n} \right)^2 + \left(\frac{\Omega V_u}{\phi_v V_n} \right)^2} \le 1.0$$

Insert the diaphragm joint required strength values (M_u, N_u and V_u) from Step 4.

The diaphragm joint nominal design strength (M_n, N_n and V_n) is based on v_n and t_n in Table 21-23.

- An analytically-based procedure from PART 3 is used for determining the moment strength at precast floor unit to precast floor unit joint. Triangle force distribution is used for determining the moment strength at other joints (diaphragm-to-LFRS joint and diaphragm-to-internal beam joint) (See PART 3).

- Using Eqn. 28, 29, 34 for the joint between precast floor units and Eqn. 35 for the joint between LFRS/beam and precast floor unit in Sec. 3.3 of PART 3 to determine the diaphragm joint strength.

- Selection of a trial design is greatly facilitated through the use of spreadsheet methods (See PART 3).

Primary diaphragm reinforcement:

(a) Chord and shear reinforcement design

Diaphragm chord and shear reinforcement final design is shown below for each Design Option. The M-N-V for each direction is shown in the table with the critical value marked as bold.

Design example 1A: (EDO)

Table 24: Top Floor

Joint	North/South flat						Ramp					
	Chord		JVI		M-N-V		Chord		JVI		M-N-V	
	Size	#	#	s (ft)	Tran.	Long.	Size	#	#	s (ft)	Tran.	Long.
1	#9	6	7	8.75	**0.64**	0.25	#9	12	18	3.09	**1.03**	0.11
2	#9	6	7	8.75	**0.76**	0.47	#9	12	18	3.09	**0.83**	0.21
3	#9	6	7	8.75	**0.97**	0.66	#9	12	18	3.09	**0.62**	0.32
4	#9	7	13	4.38	**0.97**	0.70	#9	6	13	4.38	0.69	**0.84**
5	#9	7	13	4.38	**0.83**	0.64	#9	6	13	4.38	0.66	**0.87**
6	#9	7	13	4.38	**0.90**	0.58	#9	6	13	4.38	0.65	**0.90**
7	#9	8	13	4.38	**0.86**	0.48	#9	6	13	4.38	0.66	**0.93**
8	#9	8	13	4.38	**0.92**	0.46	#9	6	13	4.38	0.67	**0.96**
9	#9	8	13	4.38	**0.97**	0.44	#9	6	13	4.38	0.68	**0.99**
10	#9	9	7	8.75	**0.92**	0.45	#9	7	7	8.75	0.61	**0.90**
11	#9	9	7	8.75	**0.94**	0.44	#9	7	7	8.75	0.59	**0.92**
12	#9	9	7	8.75	**0.95**	0.44	#9	7	7	8.75	0.56	**0.95**

Table 25: Other Floors

Joint	North/South flat						Ramp					
	Chord		JVI		M-N-V		Chord		JVI		M-N-V	
	Size	#	#	s (ft)	Tran.	Long.	Size	#	#	s (ft)	Tran.	Long.
1	#7	6	7	8.75	**0.59**	0.24	#7	10	18	3.09	**0.99**	0.13
2	#7	6	7	8.75	**0.73**	0.45	#7	10	18	3.09	**0.80**	0.26
3	#7	6	7	8.75	**0.96**	0.64	#7	10	18	3.09	**0.60**	0.39
4	#7	7	13	4.38	**0.94**	0.72	#7	6	13	4.38	0.58	**0.86**
5	#7	7	13	4.38	**0.81**	0.65	#7	6	13	4.38	0.58	**0.89**
6	#7	7	13	4.38	**0.90**	0.59	#7	6	13	4.38	0.60	**0.92**
7	#7	8	13	4.38	**0.89**	0.48	#7	6	13	4.38	0.64	**0.95**
8	#7	8	13	4.38	**0.96**	0.44	#7	6	13	4.38	0.67	**0.98**
9	#7	8	13	4.38	**1.02**	0.42	#7	6	13	4.38	0.70	**1.01**
10	#7	9	7	8.75	**0.98**	0.43	#7	7	7	8.75	0.64	**0.93**
11	#7	9	7	8.75	**1.01**	0.43	#7	7	7	8.75	0.63	**0.96**
12	#7	9	7	8.75	**1.02**	0.43	#7	7	7	8.75	0.60	**0.98**

Note: Symmetric design is applied. The chord bar cut-off and shear reinforcement space varying are conducted at every three joint. Therefore not all joints are designed against the required diaphragm joint strength, i.e. M-N-V = 1.0

Design example 1B: (BDO)

Table 26: Top Floor

Joint	North/South flat						Ramp					
	Chord		JVI		M-N-V		Chord		JVI		M-N-V	
	Size	#	#	s (ft)	Tran.	Long.	Size	#	#	s (ft)	Tran.	Long.
1	#8	5	11	5.25	**0.66**	0.25	#9	12	18	3.09	**1.01**	0.07
2	#8	5	11	5.25	**0.78**	0.48	#9	12	18	3.09	**0.81**	0.15
3	#8	5	11	5.25	**1.00**	0.68	#9	12	18	3.09	**0.60**	0.22
4	#8	6	15	3.75	**1.02**	0.70	#7	6	13	4.38	0.87	**0.95**
5	#8	6	15	3.75	**0.88**	0.65	#7	6	13	4.38	0.81	**0.98**
6	#8	6	15	3.75	**0.93**	0.61	#7	6	13	4.38	0.78	**1.01**
7	#8	7	13	4.38	**0.89**	0.55	#7	7	13	4.38	0.69	**0.91**
8	#8	7	13	4.38	**0.93**	0.52	#7	7	13	4.38	0.68	**0.94**
9	#8	7	13	4.38	**0.96**	0.50	#7	7	13	4.38	0.67	**0.96**
10	#8	8	7	8.75	**0.91**	0.53	#7	8	7	8.75	0.62	**0.90**
11	#8	8	7	8.75	**0.92**	0.51	#7	8	7	8.75	0.58	**0.93**
12	#8	8	7	8.75	**0.92**	0.50	#7	8	7	8.75	0.54	**0.96**

Table 27: Other Floors

Joint	North/South flat						Ramp					
	Chord		JVI		M-N-V		Chord		JVI		M-N-V	
	Size	#	#	s (ft)	Tran.	Long.	Size	#	#	s (ft)	Tran.	Long.
1	#6	5	9	6.56	**0.64**	0.29	#7	9	18	3.09	**1.02**	0.11
2	#6	5	9	6.56	**0.80**	0.54	#7	9	18	3.09	**0.82**	0.22
3	#6	5	9	6.56	**1.04**	0.77	#7	9	18	3.09	**0.61**	0.34
4	#6	6	13	4.38	**1.04**	0.85	#6	6	13	4.38	0.64	**0.89**
5	#6	6	13	4.38	**0.89**	0.77	#6	6	13	4.38	0.61	**0.92**
6	#6	6	13	4.38	**0.98**	0.70	#6	6	13	4.38	0.60	**0.95**
7	#6	7	13	4.38	**0.94**	0.57	#6	7	13	4.38	0.55	**0.85**
8	#6	7	13	4.38	**1.01**	0.53	#6	7	13	4.38	0.56	**0.88**
9	#6	7	13	4.38	**1.06**	0.50	#6	7	13	4.38	0.56	**0.90**
10	#6	8	7	8.75	**1.03**	0.57	#6	7	7	8.75	0.60	**0.97**
11	#6	8	7	8.75	**1.05**	0.56	#6	7	7	8.75	0.57	**1.00**
12	#6	8	7	8.75	**1.06**	0.56	#6	7	7	8.75	0.54	**1.03**

Note: Symmetric design is applied. The chord bar cut-off and shear reinforcement space varying are conducted at every three joint. Therefore not all joints are designed against the required diaphragm joint strength, i.e. M-N-V = 1.0

Design example 1C: (RDO)

Table 28: Top Floor

Joint	North/South flat						Ramp					
	Chord		JVI		M-N-V		Chord		JVI		M-N-V	
	Size	#	#	s (ft)	Tran.	Long.	Size	#	#	s (ft)	Tran.	Long.
1	#7	5	13	4.38	**0.67**	0.24	#9	12	18	3.09	**1.01**	0.05
2	#7	5	13	4.38	**0.77**	0.47	#9	12	18	3.09	**0.80**	0.11
3	#7	5	13	4.38	**0.97**	0.67	#9	12	18	3.09	**0.60**	0.16
4	#7	6	16	3.50	**1.01**	0.70	#7	4	13	4.38	**1.01**	0.97
5	#7	6	16	3.50	**0.88**	0.66	#7	4	13	4.38	0.93	**1.01**
6	#7	6	16	3.50	**0.90**	0.62	#7	4	13	4.38	0.88	**1.04**
7	#7	6	13	4.38	**0.98**	0.65	#7	5	13	4.38	0.74	**0.88**
8	#7	6	13	4.38	**1.01**	0.62	#7	5	13	4.38	0.70	**0.91**
9	#7	6	13	4.38	**1.04**	0.59	#7	5	13	4.38	0.67	**0.94**
10	#7	7	7	8.75	**0.97**	0.66	#7	5	7	8.75	0.72	**1.01**
11	#7	7	7	8.75	**0.97**	0.64	#7	5	7	8.75	0.65	**1.04**
12	#7	7	7	8.75	**0.97**	0.61	#7	5	7	8.75	0.60	**1.07**

Table 29: Other Floors

Joint	North/South flat						Ramp					
	Chord		JVI		M-N-V		Chord		JVI		M-N-V	
	Size	#	#	s (ft)	Tran.	Long.	Size	#	#	s (ft)	Tran.	Long.
1	#6	3	13	4.38	**0.77**	0.29	#7	10	18	3.09	**0.97**	0.07
2	#6	3	13	4.38	**1.03**	0.53	#7	10	18	3.09	**0.77**	0.15
3	#6	3	13	4.38	**1.01**	0.80	#7	10	18	3.09	**0.57**	0.22
4	#6	4	16	3.50	**0.87**	0.83	#6	4	13	4.38	0.72	**0.90**
5	#6	4	16	3.50	**0.95**	0.75	#6	4	13	4.38	0.68	**0.93**
6	#6	4	16	3.50	**0.93**	0.69	#6	4	13	4.38	0.65	**0.96**
7	#6	5	13	4.38	**0.98**	0.59	#6	4	13	4.38	0.65	**0.99**
8	#6	5	13	4.38	**1.02**	0.56	#6	4	13	4.38	0.65	**1.02**
9	#6	5	13	4.38	**0.97**	0.53	#6	4	13	4.38	0.65	**1.05**
10	#6	6	7	8.75	**0.98**	0.63	#6	5	7	8.75	0.60	**0.95**
11	#6	6	7	8.75	**0.98**	0.61	#6	5	7	8.75	0.56	**0.98**
12	#6	6	7	8.75	**0.77**	0.59	#6	5	7	8.75	0.52	**1.01**

Note: Symmetric design is applied. The chord bar cut-off and shear reinforcement space varying are conducted at every three joint. Therefore not all joints are designed against the required diaphragm joint strength, i.e. M-N-V = 1.0

(b) LFRS-to-diaphragm connection and collector design

Design example 1A: (EDO)

Anchorage design		Wall length [ft]	V_u kips	N_u [kips]	M_u [k-ft]	v_n* [kips]	t_n* [kips]	Req'd # Per wall	Provide #4 angled bar
NS shear wall	Top	25	709	0	0	31.1	18.6	26.8	27
	Others	25	518	0	0	31.1	18.6	19.6	20
EW lite wall - S/N Flat	Top	8	56	11.4	0	31.1	18.6	2.2	3
	Others	8	36	7.2	0	31.1	18.6	1.4	2
EW lite wall - Ramp	All floors	Provide flexible connector: 4"x3"x1/2"-5" angle plate with C-shape weld per wall							

* Tension and shear nominal strength of #4 angled bar connector.

Diaphragm collector reinforcement:
Collector reinforcement is designed to resistant the portion of diaphragm forces not transferred from the DT-IT joints ($V_u/2$).
$$A_s = 1.5 V_u / 2\phi f_y = 1.5 \times 709 / 0.9 / 60 / 2 = 10 \text{ in}^2$$
Choose 10#9 (10 in^2) at each end of structure

Design example 1B: (BDO)

Anchorage design		Wall length [ft]	V_u kips	N_u [kips]	M_u [k-ft]	v_n* [kips]	t_n* [kips]	Req'd # Per wall	Provide #4 angled bar
NS shear wall	Top	25	496	0	0	31.1	18.6	26.3	26
	Others	25	363	0	0	31.1	18.6	19.2	20
EW lite wall - S/N Flat	Top	8	40	8.0	0	31.1	18.6	2.1	2
	Others	8	28	5.6	0	31.1	18.6	1.5	2
EW lite wall - Ramp	All floors	Provide flexible connector: 4"x3"x1/2"-5" angle plate with C-shape weld per wall							

* Tension and shear nominal strength of #4 angled bar connector.

Diaphragm collector reinforcement:
Collector reinforcement is designed to resistant the portion of diaphragm forces not transferred from the DT-IT joints ($V_u/2$).
$$A_s = 1.5 V_u / 2\phi f_y = 1.5 \times 496 / 0.9 / 60 / 2 = 6.9 \text{ in}^2$$
Choose 7#9 (7 in^2) at each end of structure

Design example 1C: (RDO)

Anchorage design		Wall length [ft]	V_u kips	N_u [kips]	M_u [k-ft]	v_n * [kips]	t_n * [kips]	Req'd # Per wall	Provide #9 rebar
NS shear wall	Top	25	354	0	0	24.2	60	33.8	34
	Others	25	259	0	0	24.2	60	24.7	25
EW lite wall - S/N Flat	Top	8	28	5.7	0	24.2	60	2.7	3
	Others	8	20	4.0	0	24.2	60	1.9	2
EW lite wall - Ramp	All floors	Provide flexible connector: 4"x3"x1/2"-5" angle plate with C-shape weld per wall							

* Tension and shear nominal strength of #9 rebar.

Diaphragm collector reinforcement:
Collector reinforcement is designed to resistant the portion of diaphragm forces not transferred from the DT-IT joints ($V_u/2$).

$$A_s = 1.5 V_u / 2\phi f_y = 1.5 \times 354 / 0.9 / 60 / 2 = 4.9 \text{ in}^2$$

Choose 5#9 (5.0 in^2) at each end of structure

Secondary diaphragm reinforcement:

Design example 1A: (EDO)

(1) Internal beam joint design

Beam joint design	Q [ft^3]	I [ft^4]	V_u [kips]	N_u [kips]	M_u [k-ft]	v_n * [kips]	t_n * [kips]	Req'd # Per DT	Provide #4 angled bar
Top floor	1210	164715	471	238	1906	31.1	18.6	7.0	7
Other floors	1210	164715	307	155	1241	31.1	18.6	4.5	5

* Tension and shear nominal strength of #4 angled bar connector.

(2) Spandrel to diaphragm connector

Use 2#4 angled bar connector per precast floor unit.

Design example 1B: (BDO)

(1) Internal beam joint design

Beam joint design	Q [ft^3]	I [ft^4]	V_u [kips]	N_u [kips]	M_u [k-ft]	v_n * [kips]	t_n * [kips]	Req'd # Per DT	Provide #4 angled bar
Top floor	1210	164715	330	167	1334	31.1	18.6	5.7	6
Other floors	1210	164715	215	109	869	31.1	18.6	3.7	4

* Tension and shear nominal strength of #4 angled bar connector.

(2) Spandrel to diaphragm connector

Use 2#4 angled bar connector per precast floor unit.

Design example 1C: (RDO)

(1) Internal beam joint design

Beam joint design	Q	I	V_u	N_u	M_u	v_n *	t_n *	Req'd #	Provide
	[ft³]	[ft⁴]	[kips]	[kips]	[k-ft]	[kips]	[kips]	Per DT	#9 rebar
Top floor	1210	164715	236	119	953	24.2	60	5.7	6
Other floors	1210	164715	153	78	620	24.2	60	3.7	4

* Tension and shear nominal strength of #9 rebar.

(2) Spandrel to diaphragm connector
Use 2#5 rebar per precast floor unit.

Step 6: *Determine diaphragm stiffness and check gravity system drifts if applicable*

L   =   300 ft
L'   =   204 ft
AR   =   204/60 = 3.4
n   =   4

According to **Table 3** of New Design Procedure, no gravity system drift check is required. Since the design presented here using a free body method, diaphragm stiffness calculation is not required.

EDO Diaphragm Design (Example 1A)
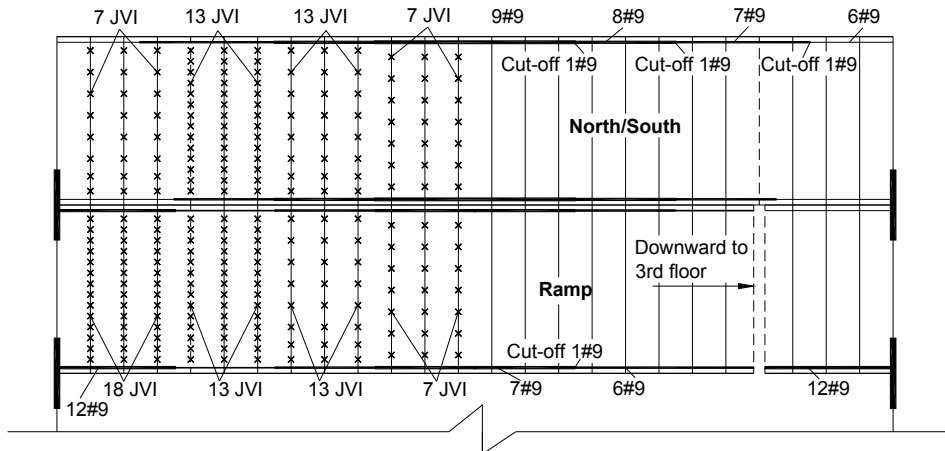
Fig. 2. Diaphragm reinforcement at top floor for example 1A.
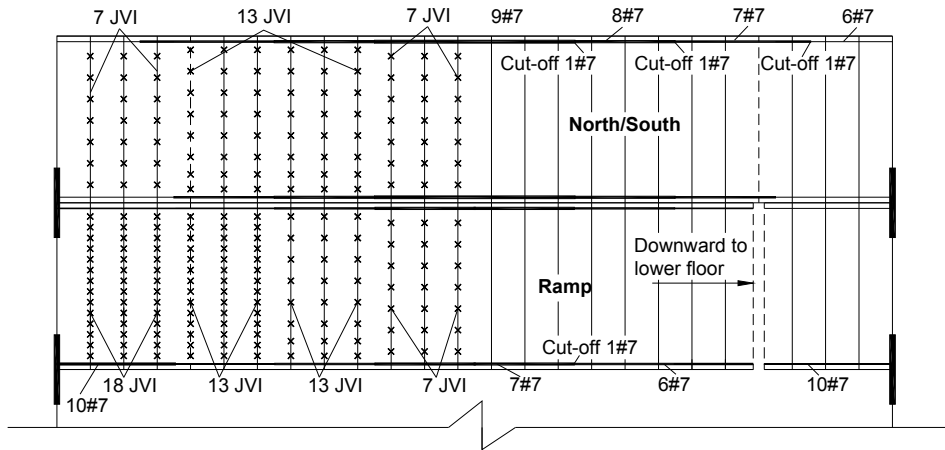
Fig. 3. Diaphragm reinforcement at other floors for example 1A.
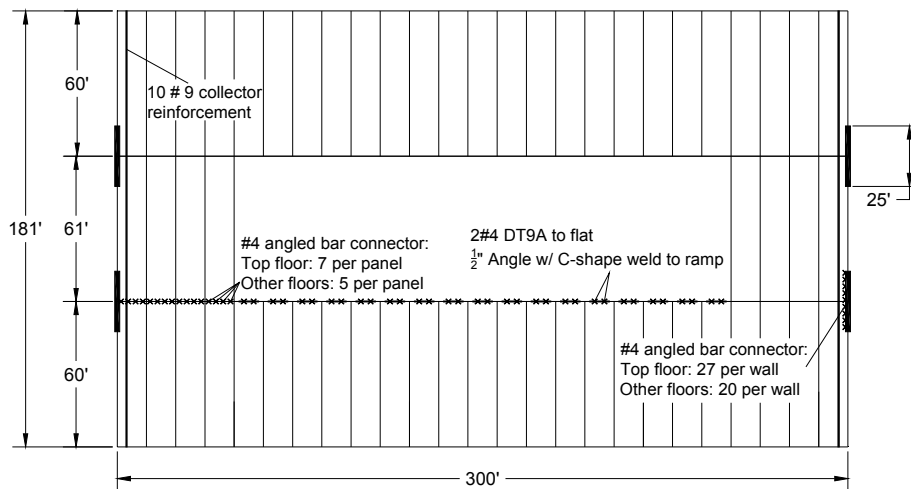
Fig. 4. Secondary reinforcement for example 1A.

BDO Diaphragm Design (Example 1B)
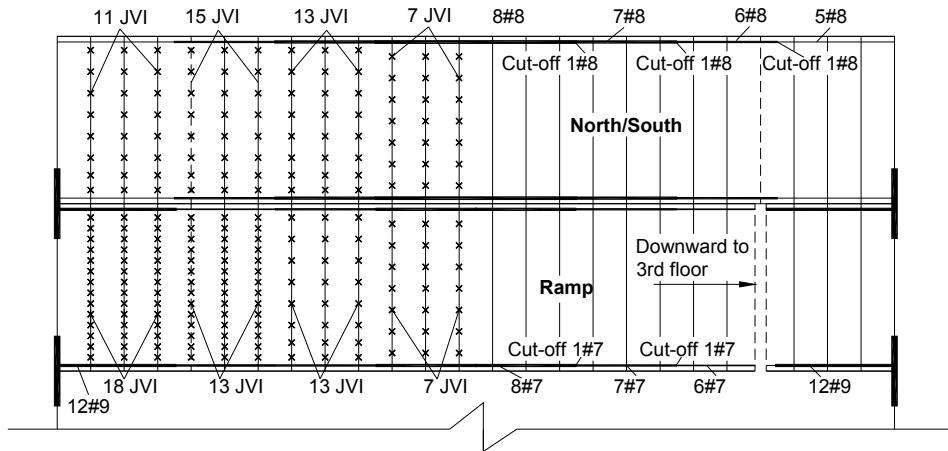
Fig. 5. Diaphragm reinforcement at top floor for example 1B.
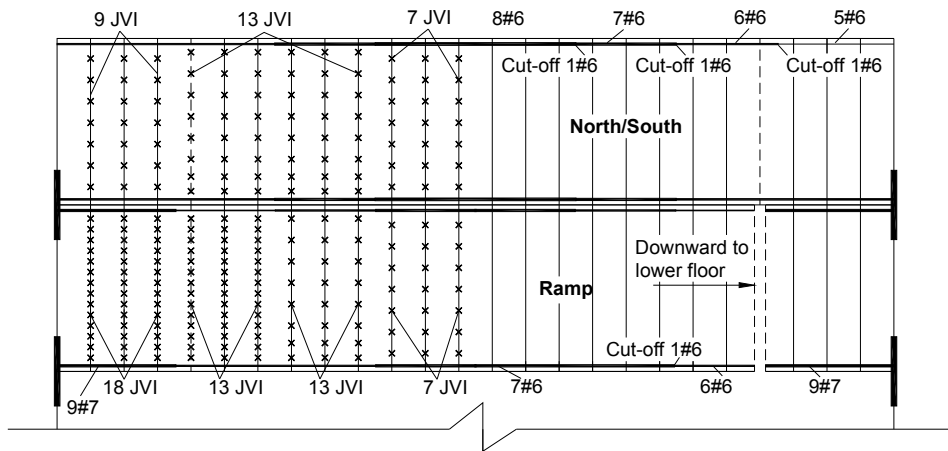
Fig. 6. Diaphragm reinforcement at other floors for example 1B.
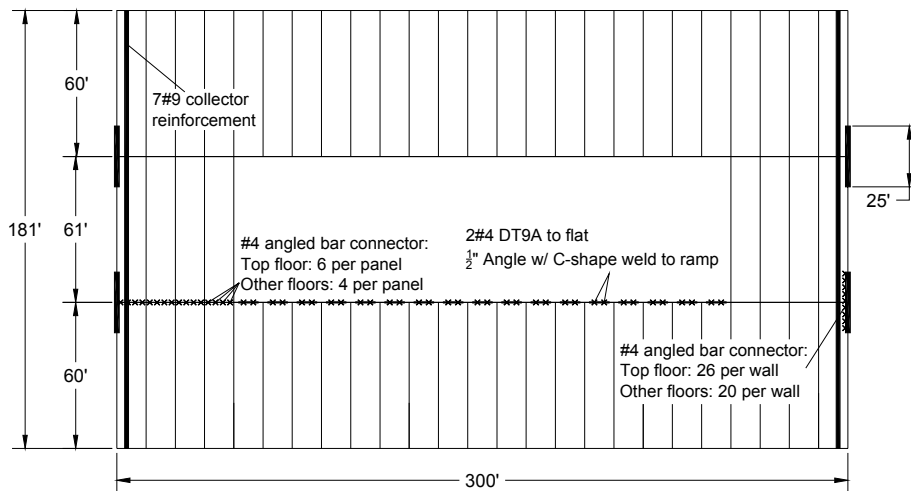
Fig. 7. Secondary reinforcement for example 1B.

RDO Diaphragm Design (Example 1C)
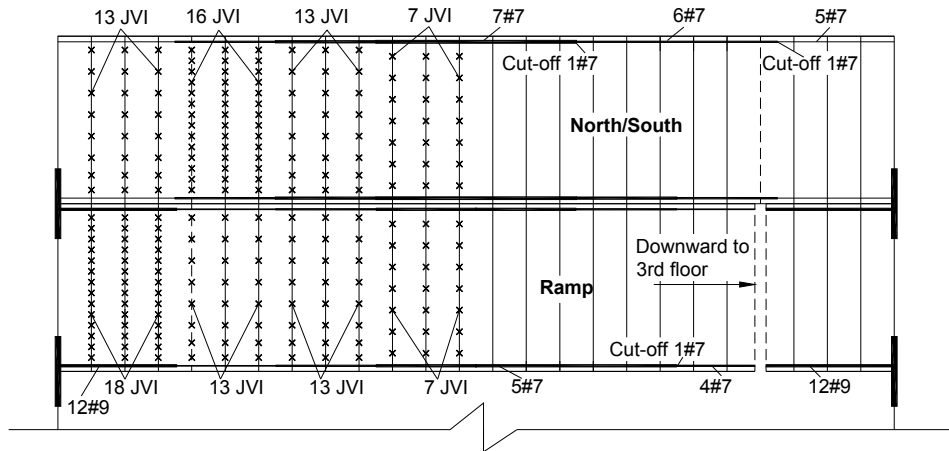
Fig. 8. Diaphragm reinforcement at top floor for example 1C.
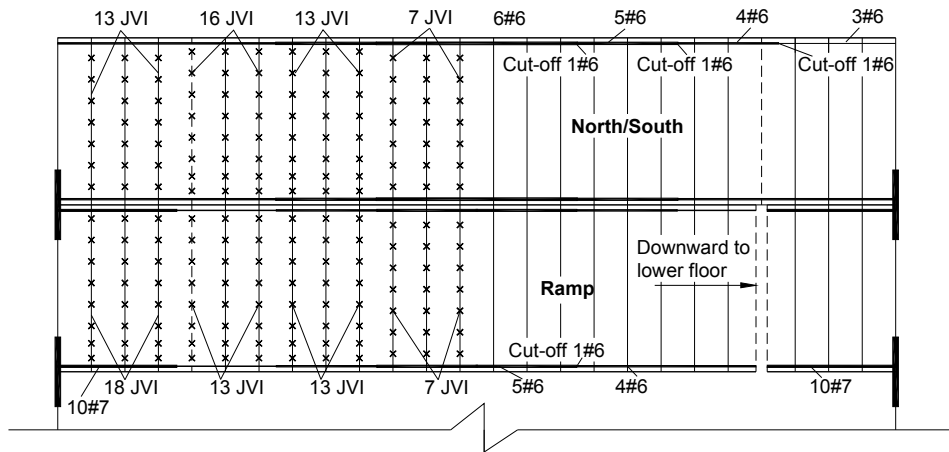
Fig. 9. Diaphragm reinforcement at other floors for example 1C.
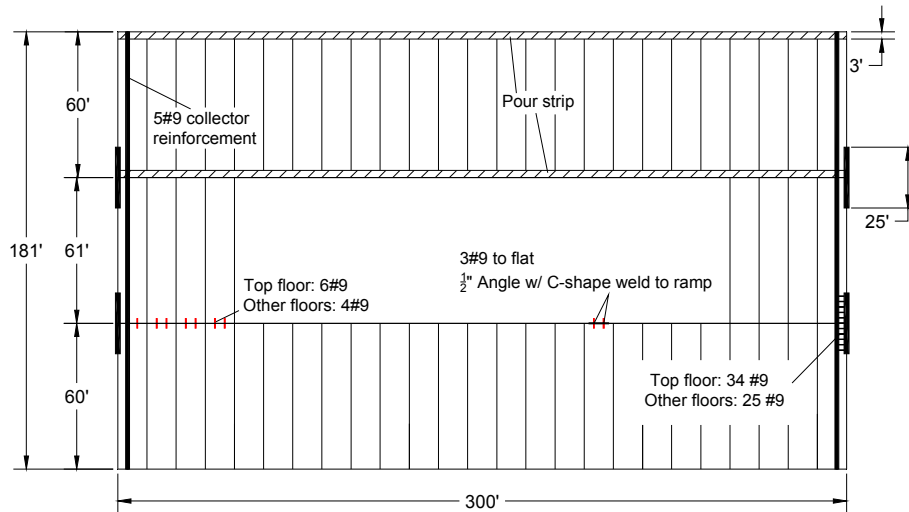
Fig. 10. Secondary reinforcement for example 1C.

22

APPENDIX A: Design Examples According to Alternate Diaphragm Design Force Procedure Based on ASCE 7-10

Example 1: 4-Story Perimeter Wall Parking Garage

The structure for example 1 is a 4-story perimeter shear wall parking garage. As seen in plan view of Figure1a, the parking structure has three bays with a central ramp. The structural plan has a footprint of $300' \times 180'$, resulting in $300' \times 60'$ for each sub-diaphragm. The floor-to-floor height is $10.5'$ for the typical floor and $16'$ at the 1st story. The lateral force resisting system (LFRS) in the transverse direction is composed of four $25'$ perimeter precast walls at each end of structure. The LFRS in longitudinal direction are 34 interior lite walls flanking the central ramp (See elevation in Figure 1b).

(a) Typical floor plan

(b) Ramp elevation

Fig. A- 1. Example 1 Structure: 4-story perimeter wall parking garage.

Example Structure 1 is located in a Seismic Design Category (SDC) C Site in Knoxville TN. The diaphragm design will be completed for three different diaphragm design options:

Design Example 1A.   Elastic Design Option (EDO Design)
Design Example 1B.   Basic Design Option (BDO Design)
Design Example 1C.   Reduced Design Option (RDO Design)

Because many design steps are shared among the different diaphragm design options, the design examples are arranged to follow the step by step procedure in part 1, with the different calculations for Examples 1A, 1B and 1C appearing as sequential sub-sections within each design step.

DESIGN STEPS:

Step 1: *Determine the Diaphragm Seismic Baseline Design Forces as per ASCE 7-05*

This step is the same for all three design examples, 1A, 1B, and 1C.

(1) and (2): Seismic design parameters

Design site:	**Knoxville, TN**
SDC	**C**
S_s	**0.58**
S_1	**0.147**
Soil site class	**C**
F_a	1.17
F_v	1.65
$S_{ms} = F_a \times S_s$	0.68
$S_{m1} = F_v \times S_1$	0.24
$S_{DS} = 2/3 \times S_{ms}$	0.45
$S_{D1} = 2/3 \times S_{m1}$	0.16
N-S/Intermediate precast wall	**R=5, Ω_0=2.5, C_d=4.5**
E-W/Intermediate precast bearing wall	**R=4, Ω_0=2.5, C_d=4**

(3): Seismic response coefficient C_s

$$T_a = C_t H_n^{3/4} = 0.02 \times 47.5^{3/4} = 0.362 \text{ sec}; \quad T = C_u T_a = 1.58 \times 0.362 = 0.571 \text{ sec}$$

N-S direction:

$$C_S = \frac{S_{DS}}{R/I_E} = 0.09, \ C_{S,min} = 0.01, \ C_{S,max} = \frac{S_{D1}}{(R/I_E)T} = \frac{0.16}{5 \times 0.571} = 0.057 \ \underline{\textbf{controls}}$$

E-W direction:

$$C_S = \frac{S_{DS}}{R/I_E} = 0.11, \ C_{S,min} = 0.01, \ C_{S,max} = \frac{S_{D1}}{(R/I_E)T} = \frac{0.16}{4 \times 0.571} = 0.071 \ \underline{\textbf{controls}}$$

(4), (5), (6) and (7):

Diaphragm maximum design acceleration $C_{dia, \, max}$=max (F_x/w_x) (Eqn.1)

Diaphragm baseline design force $F_{Dx} = \alpha_x C_{dia, \, max} w_x$ (Eqn.2)

Note: α_x =1.0 at top floor and α_x =0.68 at lower floors for parking structure.

N-S direction:

	h_x (ft)	W_x (kips)	$W_x h_x^k$	C_{vx}	F_x (kips)	$C_{dia, \, max}$ (1)	α_x	F_{Dx} (kips) (2)
Roof	47.5	5529*	300926	0.35	482	0.087	1.0	482
4th	37	6245	262419	0.31	420	0.087	0.68	370
3rd	26.5	6245	185750	0.22	297	0.087	0.68	370
2nd	16	6245	110173	0.13	176	0.087	0.68	370
Sum	0	24262	859267	1	1375			

Note: * The top floor has less seismic mass due to ramp.

24

E-W direction:

	h_x (ft)	W_x (kips)	$W_x h_x^k$	C_{vx}	F_x (kips)	$C_{dia, max}$ (1)	α_x	F_{Dx} (kips) (2)
Roof	47.5	5529*	300926	0.35	602	0.109	1.0	602
4th	37	6245	262419	0.31	525	0.109	0.68	462
3rd	26.5	6245	185750	0.22	372	0.109	0.68	462
2nd	16	6245	110173	0.13	220	0.109	0.68	462
Sum	0	24262	859267	1	1719			

Note: * The top floor has less seismic mass due to ramp.

Step 2: *Determine the Diaphragm Seismic Demand Level*

This step is the same for all three design examples, 1A, 1B, and 1C.

For SDC C: **Low**

Note: All buildings in SDC C are assigned "Low" Seismic Demand

Step 3: *Select Diaphragm Design Option*

Design example 1A: (EDO)

For low seismic demand: **Elastic design option (EDO)** is an alternative

Design example 1B: (BDO)

For low seismic demand: **Basic design option (BDO)** is recommended

Design example 1C: (RDO)

For low seismic demand: **Reduced design option (RDO)** is an alternative

Step 4: *Determine Required Diaphragm Reinforcement Classification*

Design example 1A: (EDO)

For elastic design option: **Low deformability element (LDE)** is permitted.

Design example 1B: (BDO)

For basic design option: **Moderate deformability element (MDE)** is permitted.

Design example 1C: (RDO)

For reduced design option: **High deformability element (HDE)** is required.

Step 5: *Determine Diaphragm Force Amplification Factor*

The entire diaphragm is treated as three individual sub-diaphragms for the diaphragm design as shown in PART 3: North, South and Ramp sub-diaphragm.

L	=	300 ft
AR	=	300/60 = 5
		$(0.25 \le AR \le 4.0)$ Use AR = 4 in Eqns. 3-8
n	=	4
L/60-AR	=	1

Design example 1A: (EDO)

Eqn. 3: $\Psi_E = 1.7 \times 4^{0.38}[1 - 0.04(3-4)^2] \times 1.05^{(300/60-4)} = 2.9$

Design example 1B: (BDO)

Eqn.4: $\Psi_D = 1.65 \times 4^{0.21}[1 - 0.03(3-4)^2] \times 1.05^{(300/60-4)} = 2.25$

Design example 1C: (RDO)

Eqn. 5: $\Psi_R = 1.05 \times 4^{0.3}[1 - 0.03(2.5-4)^2] \times 1.05^{(300/60-4)} = 1.56$

Step 6: *Determine Diaphragm Shear Overstrength Factor*

Design example 1A: (EDO)

Eqn. 6: $\Omega_{vE} = 1.0$

Design example 1B: (BDO)

Eqn. 7: $\Omega_{vB} = 1.42 AR^{-0.13} = 1.42 \times 4^{-0.13} = 1.19$

Design example 1C: (RDO)

Eqn. 8: $\Omega_{vR} = 1.92 AR^{-0.18} = 1.92 \times 4^{-0.18} = 1.5$

Step 7: *Determine Diaphragm Design Force*
Inserting the baseline diaphragm forces from Step 1 and the diaphragm amplification factor from Step 5 into Equation 9:

Design example 1A: (EDO)

N-S direction:
   Top Floor:
      $F_{dia} = \Psi_E F_{Dx} = 2.9 \times 482 = 1398$ kips $> 0.2 S_{DS} I w_x = 498$ kips
   Other Floors
      $F_{dia} = \Psi_E F_{Dx} = 2.9 \times 370 = 1073$ kips $> 0.2 S_{DS} I w_x = 562$ kips

E-W direction:
   Top Floor
      $F_{dia} = \Psi_E F_{Dx} = 2.9 \times 602 = 1747$ kips $> 0.2 S_{DS} I w_x = 498$ kips
   Other Floors
      $F_{dia} = \Psi_E F_{Dx} = 2.9 \times 462 = 1342$ kips $> 0.2 S_{DS} I w_x = 562$ kips

Design example 1B: (BDO)

26

N-S direction:
>   Top Floor
$$F_{dia} = \Psi_D F_{Dx} = 2.25 \times 482 = 1083 \text{ kips} > 0.2 S_{DS} I w_x = 498 \text{ kips}$$
>   Other Floors
$$F_{dia} = \Psi_D F_{Dx} = 2.25 \times 370 = 832 \text{ kips} > 0.2 S_{DS} I w_x = 562 \text{ kips}$$

E-W direction:
>   Top Floor
$$F_{dia} = \Psi_D F_{Dx} = 2.25 \times 602 = 1354 \text{ kips} > 0.2 S_{DS} I w_x = 498 \text{ kips}$$
>   Other Floors
$$F_{dia} = \Psi_D F_{Dx} = 2.25 \times 462 = 1040 \text{ kips} > 0.2 S_{DS} I w_x = 562 \text{ kips}$$

Design example 1C: (RDO)

N-S direction:
>   Top Floor
$$F_{dia} = \Psi_R F_{Dx} = 1.56 \times 482 = 751 \text{ kips} > 0.2 S_{DS} I w_x = 498 \text{ kips}$$
>   Other Floors
$$F_{dia} = \Psi_R F_{Dx} = 1.56 \times 370 = 576 \text{ kips} > 0.2 S_{DS} I w_x = 562 \text{ kips}$$

E-W direction:
>   Top Floor
$$F_{dia} = \Psi_R F_{Dx} = 1.56 \times 602 = 938 \text{ kips} > 0.2 S_{DS} I w_x = 498 \text{ kips}$$
>   Other Floors
$$F_{dia} = \Psi_R F_{Dx} = 1.56 \times 462 = 721 \text{ kips} > 0.2 S_{DS} I w_x = 562 \text{ kips}$$

Step 8: *Determine Diaphragm Internal Forces*

The free-body diagram method (*Option 8b*) is selected to obtain the diaphragm internal forces. Use is made of existing free body diagrams created for common precast diaphragm configurations (See PART 3: *Free Body Diagrams for Typical Precast Parking Structures*). The associate calculations have been embedded in a design spreadsheet program (See PART 3: *Design Aids for Diaphragm Design: Spreadsheet Program*).

The tables below show the resulting required strength (maximum diaphragm internal forces) at each diaphragm joint (Refer to Fig. A- 1a for joint numbering) and joints between diaphragm to other members (LFRS and internal beam) under transverse and longitudinal directions. Although the effect of two orthogonal direction loadings (transverse and longitudinal) is considered independently, at this step the critical loading direction in the diaphragm joint cannot be explicitly determined because the diaphragm reinforcement selection at step 10 is based on an M-N-V interaction equation (Eqn. 10).

Design example 1A (EDO):

Joint between precast floor units: Transverse (N-S) Loading

Joint	x	Top floor						Other floors					
		N/S Flat			Ramp			N/S Flat			Ramp		
		N_u	V_u	M_u	N_u	V_u	M_u	N_u	V_u	M_u	N_u	V_u	M_u
	[ft]	[kips]	[kips]	[k-ft]	[kips]	[kips]	[k-ft]	[kips]	[kips]	[k-ft]	[kips]	[kips]	[k-ft]
1	12	58	104	-430	0	390	1674	40	71	-294	0	267	1144
2	24	116	105	-935	0	311	2391	79	72	-640	0	212	1635
3	36	174	121	-1339	0	231	2153	119	83	-916	0	158	1472
4	48	232	151	-1466	0	151	958	159	103	-1002	0	103	655
5	60	232	133	242	0	133	2297	159	91	166	0	91	1570
6	72	232	116	1737	0	116	3422	159	79	1188	0	79	2340
7	84	232	98	3018	0	98	4334	159	67	2064	0	67	2963
8	96	232	80	4086	0	80	5032	159	55	2794	0	55	3441
9	108	232	62	4940	0	62	5516	159	43	3378	0	43	3772
10	120	232	44	5580	0	44	5787	159	30	3816	0	30	3957
11	132	232	27	6007	0	27	5845	159	18	4108	0	18	3997
12	144	232	9	6221	0	9	5689	159	6	4254	0	6	3890

Joint between precast floor units: Longitudinal (E-W) Loading

Joint	x	Top floor						Other floors					
		N/S Flat*			Ramp			N/S Flat*			Ramp		
		N_u	V_u	M_u	N_u	V_u	M_u	N_u	V_u	M_u	N_u	V_u	M_u
	[ft]	[kips]	[kips]	[k-ft]	[kips]	[kips]	[k-ft]	[kips]	[kips]	[k-ft]	[kips]	[kips]	[k-ft]
1	12	55	6	-430	78	0	0	38	4	-294	54	0	0
2	24	110	12	-934	157	0	0	75	9	-639	107	0	0
3	36	165	19	-1514	235	0	0	113	13	-1035	161	0	0
4	48	220	25	-2168	314	0	0	150	17	-1482	215	0	0
5	60	212	31	-1581	325	0	0	145	21	-1081	222	0	0
6	72	205	37	-1069	336	0	0	140	26	-731	229	0	0
7	84	197	44	-631	346	0	0	135	30	-431	237	0	0
8	96	189	50	-268	357	0	0	129	34	-183	244	0	0
9	108	182	56	20	368	0	0	124	38	14	252	0	0
10	120	174	62	233	379	0	0	119	43	159	259	0	0
11	132	167	69	372	389	0	0	114	47	254	266	0	0
12	144	159	75	435	400	0	0	109	51	298	274	0	0

* Symmetric design will be applied although loading is not symmetric. The most critical diaphragm internal forces are shown in the table for each symmetric joint.

Other Joints (Diaphragm-to-LFRS and Diaphragm-to-internal beam):

Joint	Top Floor						Other Floors					
	Transverse (N-S)			Longitudinal (E-W)			Transverse (N-S)			Longitudinal (E-W)		
	N_u	V_u	M_u	N_u	V_u	M_u	N_u	V_u	M_u	N_u	V_u	M_u
	[kips]	[kips]	[k-ft]	[kips]	[kips]	[k-ft]	[kips]	[kips]	[k-ft]	[kips]	[kips]	[k-ft]
DT-to-SW	**0**	**349**	**0**	-	-	-	**0**	**268**	**0**	-	-	-
DT-to-LW	3.1	6.2	0	**6.2**	**31**	**0**	2.2	4.2	0	**4.3**	**21**	**0**
DT-to-IT	**117**	**232**	**940**	131	183	**0**	**80**	**159**	**643**	89	125	0

Note: Critical force demand is marked as bond.

Design example 1B (BDO):

Joint between precast floor units: Transverse (N-S) Loading

Joint	x	Top floor						Other floors					
		N/S Flat			Ramp			N/S Flat			Ramp		
		N_u	V_u	M_u	N_u	V_u	M_u	N_u	V_u	M_u	N_u	V_u	M_u
	[ft]	[kips]	[kips]	[k-ft]	[kips]	[kips]	[k-ft]	[kips]	[kips]	[k-ft]	[kips]	[kips]	[k-ft]
1	12	45	80	-333	0	302	1297	31	55	-228	0	207	887
2	24	90	81	-725	0	241	1853	62	56	-496	0	165	1267
3	36	135	94	-1038	0	179	1668	92	64	-709	0	122	1140
4	48	180	117	-1136	0	117	742	123	80	-776	0	80	508
5	60	180	103	188	0	103	1779	123	71	128	0	71	1217
6	72	180	90	1346	0	90	2651	123	61	920	0	61	1813
7	84	180	76	2338	0	76	3358	123	52	1599	0	52	2296
8	96	180	62	3166	0	62	3898	123	42	2165	0	42	2666
9	108	180	48	3827	0	48	4274	123	33	2617	0	33	2922
10	120	180	34	4323	0	34	4484	123	24	2956	0	24	3066
11	132	180	21	4654	0	21	4529	123	14	3183	0	14	3097
12	144	180	7	4820	0	7	4408	123	5	3296	0	5	3014

Joint between precast floor units: Longitudinal (E-W) Loading

Joint	x	Top floor						Other floors					
		N/S Flat*			Ramp			N/S Flat*			Ramp		
		N_u	V_u	M_u	N_u	V_u	M_u	N_u	V_u	M_u	N_u	V_u	M_u
	[ft]	[kips]	[kips]	[k-ft]	[kips]	[kips]	[k-ft]	[kips]	[kips]	[k-ft]	[kips]	[kips]	[k-ft]
1	12	43	5	-333	61	0	0	29	3	-228	42	0	0
2	24	85	10	-724	122	0	0	58	7	-495	83	0	0
3	36	128	14	-1173	182	0	0	87	10	-802	125	0	0
4	48	170	19	-1680	243	0	0	116	13	-1149	166	0	0
5	60	164	24	-1225	252	0	0	112	17	-838	172	0	0
6	72	159	29	-828	260	0	0	108	20	-566	178	0	0
7	84	153	34	-489	268	0	0	104	23	-334	183	0	0
8	96	147	39	-208	277	0	0	100	26	-142	189	0	0
9	108	141	43	15	285	0	0	96	30	10	195	0	0
10	120	135	48	181	293	0	0	92	33	123	201	0	0
11	132	129	53	288	302	0	0	88	36	197	206	0	0
12	144	123	58	337	310	0	0	84	40	231	212	0	0

* Symmetric design will be applied although loading is not symmetric. The most critical diaphragm internal forces are shown in the table for each symmetric joint.

Other Joints (Diaphragm-to-LFRS and Diaphragm-to-internal beam):

Joint	Top Floor						Other Floors					
	Transverse (N-S)			Longitudinal (E-W)			Transverse (N-S)			Longitudinal (E-W)		
	N_u	V_u	M_u	N_u	V_u	M_u	N_u	V_u	M_u	N_u	V_u	M_u
	[kips]	[kips]	[k-ft]	[kips]	[kips]	[k-ft]	[kips]	[kips]	[k-ft]	[kips]	[kips]	[k-ft]
DT-to-SW	**0**	**271**	**0**	-	-	-	**0**	**208**	**0**	-	-	-
DT-to-LW	2.4	4.8	0	**4.8**	**24**	**0**	1.7	3.3	0	**3.3**	**16**	**0**
DT-to-IT	**91**	**180**	**728**	101	142	**0**	**62**	**123**	**498**	69	97	0

Note: Critical force demand is marked as bond.

Design example 1C (RDO):

Joint between precast floor units: Transverse (N-S) Loading

Joint	x	Top floor						Other floors					
		N/S Flat			Ramp			N/S Flat			Ramp		
		N_u	V_u	M_u	N_u	V_u	M_u	N_u	V_u	M_u	N_u	V_u	M_u
	[ft]	[kips]	[kips]	[k-ft]	[kips]	[kips]	[k-ft]	[kips]	[kips]	[k-ft]	[kips]	[kips]	[k-ft]
1	12	31	56	-231	0	210	899	21	38	-158	0	143	615
2	24	62	56	-502	0	167	1284	43	39	-343	0	114	878
3	36	94	65	-719	0	124	1156	64	44	-492	0	85	790
4	48	125	81	-787	0	81	514	85	56	-538	0	56	352
5	60	125	72	130	0	72	1233	85	49	89	0	49	843
6	72	125	62	933	0	62	1837	85	42	638	0	42	1256
7	84	125	53	1621	0	53	2327	85	36	1108	0	36	1591
8	96	125	43	2194	0	43	2702	85	29	1500	0	29	1847
9	108	125	33	2652	0	33	2962	85	23	1814	0	23	2025
10	120	125	24	2996	0	24	3108	85	16	2049	0	16	2125
11	132	125	14	3226	0	14	3139	85	10	2206	0	10	2146
12	144	125	5	3340	0	5	3055	85	3	2284	0	3	2089

Joint between precast floor units: Longitudinal (E-W) Loading

Joint	x	Top floor						Other floors					
		N/S Flat*			Ramp			N/S Flat*			Ramp		
		N_u	V_u	M_u	N_u	V_u	M_u	N_u	V_u	M_u	N_u	V_u	M_u
	[ft]	[kips]	[kips]	[k-ft]	[kips]	[kips]	[k-ft]	[kips]	[kips]	[k-ft]	[kips]	[kips]	[k-ft]
1	12	30	3	-231	42	0	0	20	2	-158	29	0	0
2	24	59	7	-502	84	0	0	40	5	-343	58	0	0
3	36	89	10	-813	126	0	0	61	7	-556	86	0	0
4	48	118	13	-1164	169	0	0	81	9	-796	115	0	0
5	60	114	17	-849	174	0	0	78	11	-580	119	0	0
6	72	110	20	-574	180	0	0	75	14	-392	123	0	0
7	84	106	23	-339	186	0	0	72	16	-232	127	0	0
8	96	102	27	-144	192	0	0	70	18	-98	131	0	0
9	108	98	30	11	198	0	0	67	21	7	135	0	0
10	120	94	33	125	203	0	0	64	23	86	139	0	0
11	132	89	37	200	209	0	0	61	25	136	143	0	0
12	144	85	40	234	215	0	0	58	27	160	147	0	0

* Symmetric design will be applied although loading is not symmetric. The most critical diaphragm internal forces are shown in the table for each symmetric joint.

Other Joints (Diaphragm-to-LFRS and Diaphragm-to-internal beam):

Joint	Top Floor						Other Floors					
	Transverse (N-S)			Longitudinal (E-W)			Transverse (N-S)			Longitudinal (E-W)		
	N_u	V_u	M_u	N_u	V_u	M_u	N_u	V_u	M_u	N_u	V_u	M_u
	[kips]	[kips]	[k-ft]	[kips]	[kips]	[k-ft]	[kips]	[kips]	[k-ft]	[kips]	[kips]	[k-ft]
DT-to-SW	**0**	**188**	**0**	-	-	-	**0**	**144**	**0**	-	-	-
DT-to-LW	3.1	6.2	0	**3.3**	**17**	**0**	2.2	4.2	0	**2.3**	**11**	**0**
DT-to-IT	**63**	**125**	**505**	70	98	**0**	**43**	**85**	**345**	48	67	0

Note: Critical force demand is marked as bond.

Step 9: *Select Diaphragm Reinforcement*

Diaphragm reinforcement type selected to meet Required Diaphragm Reinforcement Classification (*See Step 4*). Prequalified connectors will be used in this example. Select appropriate diaphragm reinforcement types from PART 2: Table 2A-1.

Design example 1A: (EDO)

Chord Reinforcement:	**Dry chord connector**
Shear Reinforcement:	**JVI Vector**
Secondary Reinforcement:	**#4 angled bar**

Design example 1B: (BDO)

Chord Reinforcement:	**Dry chord with flat plate connector**
Shear Reinforcement:	**JVI Vector**
Secondary Reinforcement:	**#4 angled bar**

Design example 1C: (RDO)

Chord Reinforcement:	**Pour strip bars**
Shear Reinforcement:	**JVI Vector**
Secondary Reinforcement:	**Pour strip bars**

Determine Diaphragm Reinforcement Properties: As the diaphragm reinforcement selected is prequalified, the diaphragm reinforcement properties can also be looked up in PART 2: Table 2A-1.

Design example 1A: (EDO)

Reinforcing bars	k_t / A k/in/in^2	k_v / A k/in/in^2	t_n / A k/in^2	v_n / A k/in^2	δ_{ty} in
Dry chord Gr.60	1018	382	60	24.2	0.071
Connectors	k_t k/in	k_v k/in	t_n k	v_n k	δ_{ty} in
JVI Vector	55	226	3.1	18.1	0.066
Angled bar #4	545	676	18.5	31.1	-

Design example 1B: (BDO)

Reinforcing bars	k_t / A k/in/in^2	k_v / A k/in/in^2	t_n / A k/in^2	v_n / A k/in^2	δ_{ty} in
Dry chord w/ flat plate Gr.60	1018	382	60	24.2	0.071
Connectors	k_t k/in	k_v k/in	t_n k	v_n k	δ_{ty} in
JVI Vector	55	226	3.1	18.1	0.066
Angled bar #4	545	676	18.5	31.1	-

Design example 1C: (RDO)

Reinforcing bars	k_t / A k/in/in^2	k_v / A k/in/in^2	t_n / A k/in^2	v_n / A k/in^2	δ_{ty} in
Pour strip chord Gr.60	1234	382	60	24.2	0.057

Connectors	k_t k/in	k_v k/in	t_n k	v_n k	δ_{ty} in
JVI Vector	55	226	3.1	18.1	0.066

Step 10: *Design the Diaphragm Reinforcement at Joints*

Use the interaction equation (Eqn. 10) to determine the required diaphragm reinforcement:

$$M - N - V = \sqrt{\left(\frac{|M_u|}{\phi_f M_n} + \frac{N_u}{\phi_f N_n} \right)^2 + \left(\frac{\Omega V_u}{\phi_v V_n} \right)^2} \leq 1.0$$

Insert the diaphragm joint required strength values (M_u, N_u and V_u) from Step 8.

The diaphragm joint nominal design strength (M_n, N_n and V_n) is based on v_n and t_n from Step 9.

- An analytically-based procedure from PART 3 is used for determining the moment strength at precast floor unit to precast floor unit joint. Triangle force distribution is used for determining the moment strength at other joints (diaphragm-to-LFRS joint and diaphragm-to-internal beam joint) (See PART 3).

- Using Eqn. 28, 29, 34 for the joint between precast floor units and Eqn. 35 for the joint between LFRS/beam and precast floor unit in Sec. 3.3 of PART 3 to determine the diaphragm joint strength.

- Selection of a trial design is greatly facilitated through the use of spreadsheet methods (See PART 3).

Primary diaphragm reinforcement

(c) Chord and shear reinforcement design

Diaphragm chord and shear reinforcement final design is shown below for each Design Option. The M-N-V for each direction is shown in the table with the critical value marked as bold.

Design example 1A: (EDO)

Top Floor

Joint	North/South flat						Ramp					
	Chord		JVI		M-N-V		Chord		JVI		M-N-V	
	Size	#	#	s (ft)	Transverse	Longitudinal	Size	#	#	s (ft)	Transverse	Longitudinal
1	#6	4	12	4.8	**0.52**	0.32	#6	8	18	3.1	**0.94**	0.18
2	#6	4	12	4.8	**0.79**	0.65	#6	8	18	3.1	**0.77**	0.36
3	#6	6	12	4.8	**0.82**	0.70	#6	8	18	3.1	**0.58**	0.55
4	#6	6	16	3.5	**0.97**	0.92	#6	7	16	3.5	0.42	**0.83**
5	#6	6	16	3.5	0.82	**0.83**	#6	7	16	3.5	0.43	**0.86**
6	#6	6	16	3.5	**0.96**	0.75	#6	7	16	3.5	0.46	**0.89**
7	#6	8	13	4.4	**0.88**	0.54	#6	7	13	4.4	0.53	**0.94**
8	#6	8	13	4.4	**0.95**	0.50	#6	7	13	4.4	0.57	**0.97**
9	#6	8	13	4.4	**1.02**	0.47	#6	7	13	4.4	0.59	**1.00**
10	#6	9	7	8.8	**0.99**	0.47	#6	8	7	8.8	0.56	**0.95**
11	#6	9	7	8.8	**1.02**	0.48	#6	8	7	8.8	0.55	**0.97**
12	#6	9	7	8.8	**1.03**	0.48	#6	8	7	8.8	0.52	**1.00**

Other Floors

Joint	North/South flat						Ramp					
	Chord		JVI		M-N-V		Chord		JVI		M-N-V	
	Size	#	#	s (ft)	Transverse	Longitudinal	Size	#	#	s (ft)	Transverse	Longitudinal
1	#6	3	7	8.8	**0.54**	0.19	#6	5	16	4.8	**0.81**	0.19
2	#6	3	7	8.8	**0.63**	0.62	#6	5	16	4.8	**0.67**	0.38
3	#6	4	7	8.8	0.86	**0.94**	#6	5	16	4.8	0.51	**0.57**
4	#6	4	13	4.4	**0.95**	0.92	#6	5	16	3.5	0.32	**0.76**
5	#6	4	13	4.4	0.80	**0.83**	#6	5	16	3.5	0.35	**0.79**
6	#6	4	13	4.4	**0.79**	0.75	#6	5	16	3.5	0.40	**0.81**
7	#6	5	13	4.4	**0.90**	0.68	#6	6	13	4.4	0.41	**0.74**
8	#6	5	13	4.4	**0.99**	0.51	#6	6	13	4.4	0.44	**0.76**
9	#6	5	13	4.4	**0.90**	0.47	#6	6	13	4.4	0.47	**0.78**
10	#6	6	7	8.8	**1.00**	0.53	#6	6	7	9.0	0.50	**0.85**
11	#6	6	7	8.8	**1.03**	0.46	#6	6	7	9.0	0.49	**0.87**
12	#6	6	7	8.8	**1.04**	0.46	#6	6	7	9.0	0.47	**0.90**

Note: Symmetric design is applied. The chord bar cut-off and shear reinforcement space varying are conducted at every three joint. Therefore not all joints are designed against the required diaphragm joint strength, i.e. M-N-V = 1.0

For the purpose of comparing the proposed FBD design method to the simple beam method used in current design practice, the diaphragm design for Example 1A has been performed using the simple beam method as shown below.

Diaphragm design forces:

Top floor

$$V_u = F_{dia}/3/2 = 1398/3/2 = 233 \text{ kips}$$

$$M_u = F_{dia}/3 \times L/8 = 1398/3 \times 300/8 = 17475 \text{ k-ft}$$

Other floors

$$V_u = F_{dia}/3/2 = 1073/3/2 = 179 \text{ kips}$$

$$M_u = F_{dia}/3 \times L/8 = 1073/3 \times 300/8 = 13413 \text{ k-ft}$$

Select the # of JVI based on shear demand and the # of chord based on moment demand including the chord contribution to joint shear strength and the JVI contribution to joint moment strength:

Top floor: select 13#6 and 7 JVI Vector @ 8.8′ without bar "cut-off" or JVI Vector spacing variation

$$V_n = 404 \text{ kips} > V_u/\phi = 233/0.85 = 274 \text{kips OK}$$

$$M_n = 19510 \text{ k-ft} > M_u/\phi = 17475/0.9 = 19417 \text{ k-ft OK}$$

Other floors: select 10#6 and 7 JVI Vector @ 8.8′ without bar "cut-off" or JVI Vector spacing variation

$$V_n = 340 \text{ kips} > V_u/\phi = 179/0.85 = 211 \text{kips OK}$$

$$M_n = 15048 \text{ k-ft} > M_u/\phi = 13413/0.9 = 14903 \text{ k-ft OK}$$

An cost comparison between the simple beam method and FBD method in the following Figure for weight of chord steel and total number of JVI Vectors. As seen, the simple beam method requires about twice of chord steel than the FBD method while the FBD method requires about 50% more number of JVI Vectors than the simpe beam method.
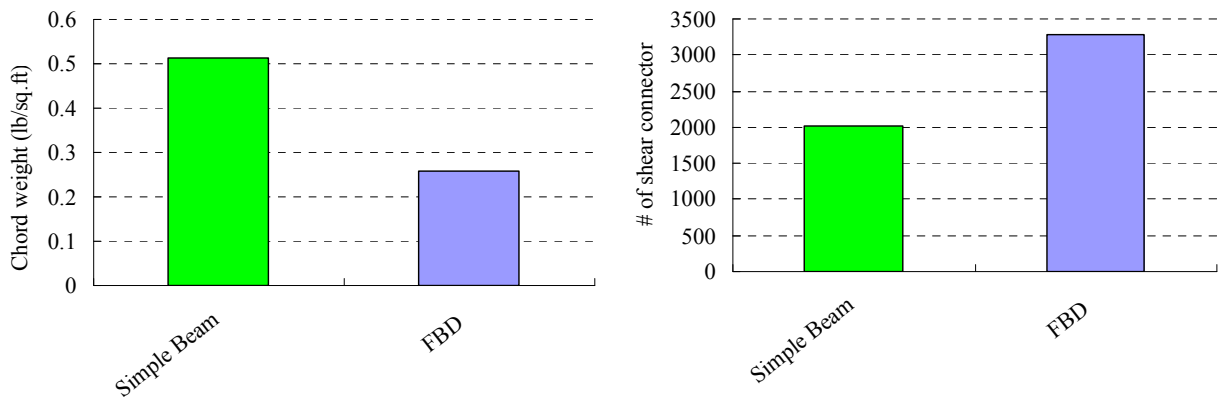
Figure: cost comparison: (a) chord weight; (b) # of JVI Vectors.

Design example 1B: (BDO)

Top Floor

Joint	North/South flat						Ramp					
	Chord		JVI		M-N-V		Chord		JVI		M-N-V	
	Size	#	#	s (ft)	Transverse	Longitudinal	Size	#	#	s (ft)	Transverse	Longitudinal
1	#6	4	10	5.8	**0.50**	0.25	#6	4	19	2.9	**1.00**	0.25
2	#6	4	10	5.8	**0.68**	0.52	#6	4	19	2.9	**0.83**	0.50
3	#6	4	10	5.8	**0.93**	0.79	#6	4	19	2.9	0.64	**0.75**
4	#6	5	13	4.4	**0.94**	0.85	#6	5	16	3.5	0.42	**0.86**
5	#6	5	13	4.4	**0.80**	0.77	#6	5	16	3.5	0.43	**0.89**
6	#6	5	13	4.4	**0.92**	0.70	#6	5	16	3.5	0.47	**0.92**
7	#6	6	13	4.4	**0.88**	0.55	#6	5	13	4.4	0.55	**0.98**
8	#6	6	13	4.4	**0.95**	0.50	#6	5	13	4.4	0.58	**1.01**
9	#6	6	13	4.4	**1.01**	0.47	#6	5	13	4.4	0.61	**1.04**
10	#6	7	7	8.8	**0.97**	0.47	#6	6	7	8.8	0.57	**0.96**
11	#6	7	7	8.8	**0.99**	0.48	#6	6	7	8.8	0.55	**0.99**
12	#6	7	7	8.8	**1.01**	0.48	#6	6	7	8.8	0.53	**1.02**

Other Floors

Joint	North/South flat						Ramp					
	Chord		JVI		M-N-V		Chord		JVI		M-N-V	
	Size	#	#	s (ft)	Transverse	Longitudinal	Size	#	#	s (ft)	Transverse	Longitudinal
1	#6	3	10	5.8	**0.39**	0.22	#6	3	16	4.8	**0.84**	0.22
2	#6	3	10	5.8	**0.57**	0.45	#6	3	16	4.8	**0.70**	0.44
3	#6	3	10	5.8	**0.79**	0.69	#6	3	16	4.8	0.54	**0.67**
4	#6	3	13	4.4	**0.93**	0.89	#6	4	16	3.5	0.31	**0.71**
5	#6	3	13	4.4	0.79	**0.81**	#6	4	16	3.5	0.33	**0.73**
6	#6	3	13	4.4	**0.93**	0.73	#6	4	16	3.5	0.37	**0.76**
7	#6	4	13	4.4	**0.84**	0.53	#6	4	13	4.4	0.44	**0.81**
8	#6	4	13	4.4	**0.92**	0.48	#6	4	13	4.4	0.48	**0.84**
9	#6	4	13	4.4	**0.98**	0.45	#6	4	13	4.4	0.50	**0.86**
10	#6	5	7	8.8	**0.91**	0.42	#6	5	7	9.0	0.46	**0.78**
11	#6	5	7	8.8	**0.93**	0.43	#6	5	7	9.0	0.45	**0.80**
12	#6	5	7	8.8	**0.95**	0.43	#6	5	7	9.0	0.43	**0.82**

Note: Symmetric design is applied. The chord bar cut-off and shear reinforcement space varying are conducted at every three joint. Therefore not all joints are designed against the required diaphragm joint strength, i.e. M-N-V = 1.0

Design example 1C: (RDO)

Top Floor

Joint	North/South flat						Ramp					
	Chord		JVI		M-N-V		Chord		JVI		M-N-V	
	Size	#	#	s (ft)	Transverse	Longitudinal	Size	#	#	s (ft)	Transverse	Longitudinal
1	#5	3	13	4.4	**0.45**	0.28	#5	4	18	3.1	**0.97**	0.23
2	#5	3	13	4.4	**0.69**	0.57	#5	4	18	3.1	**0.80**	0.46
3	#5	3	13	4.4	**0.97**	0.87	#5	4	18	3.1	0.61	**0.69**
4	#5	4	16	3.5	**0.95**	0.90	#5	5	13	4.4	0.47	**0.83**
5	#5	4	16	3.5	0.81	**0.81**	#5	5	13	4.4	0.46	**0.86**
6	#5	4	16	3.5	**0.94**	0.74	#5	5	13	4.4	0.48	**0.88**
7	#5	6	13	4.4	**0.82**	0.51	#5	5	10	5.8	0.56	**0.95**
8	#5	6	13	4.4	**0.89**	0.47	#5	5	10	5.8	0.58	**0.98**
9	#5	6	13	4.4	**0.94**	0.44	#5	5	10	5.8	0.59	**1.01**
10	#5	7	7	8.8	**0.93**	0.46	#5	6	7	8.8	0.54	**0.92**
11	#5	7	7	8.8	**0.95**	0.47	#5	6	7	8.8	0.52	**0.95**
12	#5	7	7	8.8	**0.96**	0.48	#5	6	7	8.8	0.50	**0.97**

Other Floors

Joint	North/South flat						Ramp					
	Chord		JVI		M-N-V		Chord		JVI		M-N-V	
	Size	#	#	s (ft)	Transverse	Longitudinal	Size	#	#	s (ft)	Transverse	Longitudinal
1	#5	2	10	5.8	**0.43**	0.27	#5	3	13	4.4	**0.91**	0.21
2	#5	2	10	5.8	**0.67**	0.56	#5	3	13	4.4	**0.75**	0.42
3	#5	2	10	5.8	**0.94**	0.85	#5	3	13	4.4	0.57	**0.63**
4	#5	3	13	4.4	**0.84**	0.80	#5	4	13	4.4	0.34	**0.68**
5	#5	3	13	4.4	0.72	**0.73**	#5	4	13	4.4	0.34	**0.70**
6	#5	3	13	4.4	**0.84**	0.66	#5	4	13	4.4	0.37	**0.72**
7	#5	4	10	5.8	**0.82**	0.51	#5	4	10	5.8	0.44	**0.79**
8	#5	4	10	5.8	**0.89**	0.47	#5	4	10	5.8	0.46	**0.81**
9	#5	4	10	5.8	**0.95**	0.44	#5	4	10	5.8	0.48	**0.83**
10	#5	5	7	8.8	**0.86**	0.41	#5	5	7	8.8	0.43	**0.74**
11	#5	5	7	8.8	**0.88**	0.42	#5	5	7	8.8	0.42	**0.76**
12	#5	5	7	8.8	**0.89**	0.42	#5	5	7	8.8	0.40	**0.79**

Note: Symmetric design is applied. The chord bar cut-off and shear reinforcement space varying are conducted at every three joint. Therefore not all joints are designed against the required diaphragm joint strength, i.e. M-N-V = 1.0

(d) LFRS-to-diaphragm connection and collector design

Design example 1A: (EDO)

Check $\Psi_E \times \Omega_{vE} = 2.9 \times 1.0 = 2.9 > \Omega_o = 2.5$ **OK**

Anchorage design		Wall length [ft]	V_u kips	N_u [kips]	M_u [k-ft]	v_n * [kips]	t_n * [kips]	Req'd # Per wall	Provide #4 angled bar
NS shear wall	Top	25	349	0	0	31.1	18.6	13.2	14
	Others	25	268	0	0	31.1	18.6	10.2	11
EW lite wall - S/N Flat	Top	8	31	6.2	0	31.1	18.6	1.2	2
	Others	8	21	4.3	0	31.1	18.6	0.8	2
EW lite wall - Ramp	All floors	Provide flexible connector: 4"x3"x1/2"-5" angle plate with C-shape weld per wall							

* Tension and shear nominal strength of #4 angled bar connector.

Diaphragm collector reinforcement:
Collector reinforcement is designed to resistant the same shear demand as the anchorage of shear wall:
$$A_s = \Omega V_u / \phi f_y = 1.0 \times 349 / 0.9 / 60 = 6.5\ \text{in}^2$$
Choose 7#9 (7 in^2) at each end of structure

Design example 1B: (BDO)

Check $\Psi_D \times \Omega_{vB} = 2.25 \times 1.19 = 2.68 > \Omega_o = 2.5$ **OK**

Anchorage design		Wall length [ft]	V_u kips	N_u [kips]	M_u [k-ft]	v_n * [kips]	t_n * [kips]	Req'd # Per wall	Provide #4 angled bar
NS shear wall	Top	25	271	0	0	31.1	18.6	12.1	12
	Others	25	208	0	0	31.1	18.6	9.3	10
EW lite wall - S/N Flat	Top	8	24	4.8	0	31.1	18.6	1.1	2
	Others	8	16	3.3	0	31.1	18.6	0.8	2
EW lite wall - Ramp	All floors	Provide flexible connector: 4"x3"x1/2"-5" angle plate with C-shape weld per wall							

* Tension and shear nominal strength of #4 angled bar connector.

Diaphragm collector reinforcement:
Collector reinforcement is designed to resistant the same shear demand as the anchorage of shear wall:
$$A_s = \Omega V_u / \phi f_y = 1.19 \times 271 / 0.9 / 60 = 5.97\ \text{in}^2$$
Choose 6#9 (6 in^2) at each end of structure

Design example 1C: (RDO)

Check $\Psi_R \times \Omega_{vR} = 1.56 \times 1.5 = 2.34 < \Omega_o = 2.5$; Increase V_u from step 8 for walls by a factor of $2.5/2.34 = 1.07$

Anchorage design		Wall length [ft]	V_u kips	N_u [kips]	M_u [k-ft]	v_n* [kips]	t_n* [kips]	Req'd # Per wall	Provide #9 rebar
NS shear wall	Top	25	201	0	0	24.2	60	14.6	15
	Others	25	154	0	0	24.2	60	11.2	11
EW lite wall - S/N Flat	Top	8	18	3.3	0	24.2	60	1.3	2
	Others	8	12	2.3	0	24.2	60	0.9	2
EW lite wall - Ramp	All floors	Provide flexible connector: 4"x3"x1/2"-5" angle plate with C-shape weld per wall							

* Tension and shear nominal strength of #9 rebar.

Diaphragm collector reinforcement:

Collector reinforcement is designed to resistant the same shear demand as the anchorage of shear wall:

$$A_s = \Omega V_u / \phi f_y = 1.5 \times 201 / 0.9 / 60 = 5.58 \text{ in}^2$$

Choose 6#9 (6.0 in^2) at each end of structure

Secondary diaphragm reinforcement

Design example 1A: (EDO)

(3) Internal beam joint design

Beam joint design	Q [ft^3]	I [ft^4]	V_u [kips]	N_u [kips]	M_u [k-ft]	v_n* [kips]	t_n* [kips]	Req'd # Per DT	Provide #4 angled bar
Top floor	1210	164715	232	117	940	31.1	18.6	3.4	4
Other floors	1210	164715	159	80	643	31.1	18.6	2.3	3

* Tension and shear nominal strength of #4 angled bar connector.

(4) Spandrel to diaphragm connector

Use 2#4 angled bar connector per precast floor unit.

Design example 1B: (BDO)

(3) Internal beam joint design

Beam joint design	Q [ft^3]	I [ft^4]	V_u [kips]	N_u [kips]	M_u [k-ft]	v_n* [kips]	t_n* [kips]	Req'd # Per DT	Provide #4 angled bar
Top floor	1210	164715	180	91	728	31.1	18.6	2.9	3
Other floors	1210	164715	123	62	498	31.1	18.6	2.0	2

* Tension and shear nominal strength of #4 angled bar connector.

(4) Spandrel to diaphragm connector

Use 2#4 angled bar connector per precast floor unit.

Design example 1C: (RDO)

(3) Internal beam joint design

Beam joint design	Q [ft³]	I [ft⁴]	V_u [kips]	N_u [kips]	M_u [k-ft]	v_n * [kips]	t_n * [kips]	Req'd # Per DT	Provide #5 rebar
Top floor	1210	164715	125	63	505	7.502	18.6	7.5	8
Other floors	1210	164715	85	43	345	7.502	18.6	5.1	5

* Tension and shear nominal strength of #5 rebar.

(4) Spandrel to diaphragm connector
Use 2#5 rebar per precast floor unit.

Step 11: *Determine the diaphragm effective elastic modulus and shear modulus*

The diaphragm joint effective elastic Young's modulus (E_{eff}) and effective shear modulus (G_{eff}) are calculated using the analytical based procedure (see "Diaphragm Joint Stiffness Calculation" in PART 3). E_{eff} and G_{eff} will be used in step 12 for calculating the diaphragm induced drift. These values can be calculated in a spreadsheet at the same time as the diaphragm reinforcement is selected. An average of the maximum and minimum values at any joint is suggested in design as shown in the bottom row of tables below. (See Appendix for tables output per joint.)

Design example 1A: (EDO)

Joint	Top Floor				Other Floors			
	North/South flat		Ramp		North/South flat		Ramp	
	E_{eff} [ksi]	G_{eff} [ksi]	E_{eff} [ksi]	G_{eff} [ksi]	E_{eff} [ksi]	G_{eff} [ksi]	E_{eff} [ksi]	G_{eff} [ksi]
Min	715	213	1025	222	566	142	841	191
Max	1174	281	1122	327	914	238	933	267
Ave	1002.9	255.5	1068.8	277.8	768.3	199.9	882.3	244.5
Des	944.5	247	1073.5	274.5	740	190	887	229

Design example 1B: (BDO)

Joint	Top Floor				Other Floors			
	North/South flat		Ramp		North/South flat		Ramp	
	E_{eff} [ksi]	G_{eff} [ksi]	E_{eff} [ksi]	G_{eff} [ksi]	E_{eff} [ksi]	G_{eff} [ksi]	E_{eff} [ksi]	G_{eff} [ksi]
Min	707	192	742	191	580	175	607	175
Max	1008	253	914	282	810	223	810	253
Ave	869.8	222.5	832.0	244.5	675.5	195.5	716.5	222.3
Des	857.5	222.5	828	236.5	695	199	708.5	214

Design example 1C: (RDO)

Joint	Top Floor				Other Floors			
	North/South flat		Ramp		North/South flat		Ramp	
	E_{eff} [ksi]	G_{eff} [ksi]	E_{eff} [ksi]	G_{eff} [ksi]	E_{eff} [ksi]	G_{eff} [ksi]	E_{eff} [ksi]	G_{eff} [ksi]
Min	534	174	668	163	391	149	534	151
Max	912	235	824	255	727	194	727	205
Ave	737.5	207.3	745.3	204.5	571.8	166.8	635.8	180.8
Des	723	204.5	746	209	559	171.5	630.5	178

Step 12: *Check the diaphragm induced gravity column drift*

The following tables show the diaphragm induced gravity column drift at the midspan column j obtained from the spreadsheet design program in PART 3).

Design example 1A: (EDO)

Sub Diaphragm	Floor	C_Δ	$C_{d,dia}$	$C_{r,dia}$	$\delta_{dia,el}$ [in]	δ_{dia} [in]	θ_{dia} [rad]
N/S Flat	Top	1.09	1.09	0.59	0.708	0.775	0.0036
	Others	1.09	1.09	0.59	0.637	0.697	0.0033
Ramp	Top	1.09	1.09	0.59	0.934	1.021	0.0048
	Others	1.09	1.09	0.59	0.746	0.816	0.0038

Design example 1B: (BDO)

Sub Diaphragm	Floor	C_Δ	$C_{d,dia}$	$C_{r,dia}$	$\delta_{dia,el}$ [in]	δ_{dia} [in]	θ_{dia} [rad]
N/S Flat	Top	1.13	1.69	0.64	0.639	1.078	0.0055
	Others	1.13	1.69	0.64	0.531	0.895	0.0045
Ramp	Top	1.13	1.69	0.64	0.859	1.450	0.0074
	Others	1.13	1.69	0.64	0.669	1.129	0.0057

Design example 1C: (RDO)

Sub Diaphragm	Floor	C_Δ	$C_{d,dia}$	$C_{r,dia}$	$\delta_{dia,el}$ [in]	δ_{dia} [in]	θ_{dia} [rad]
N/S Flat	Top	1.16	3.35	0.56	0.479	1.605	0.0071
	Others	1.16	3.35	0.56	0.416	1.395	0.0062
Ramp	Top	1.16	3.35	0.56	0.675	2.262	0.0101
	Others	1.16	3.35	0.56	0.539	1.809	0.0080

For all design examples, the maximum diaphragm induced gravity column drift (θ_{dia}) is less than 0.01, **OK**

EDO Diaphragm Design (Example 1A)
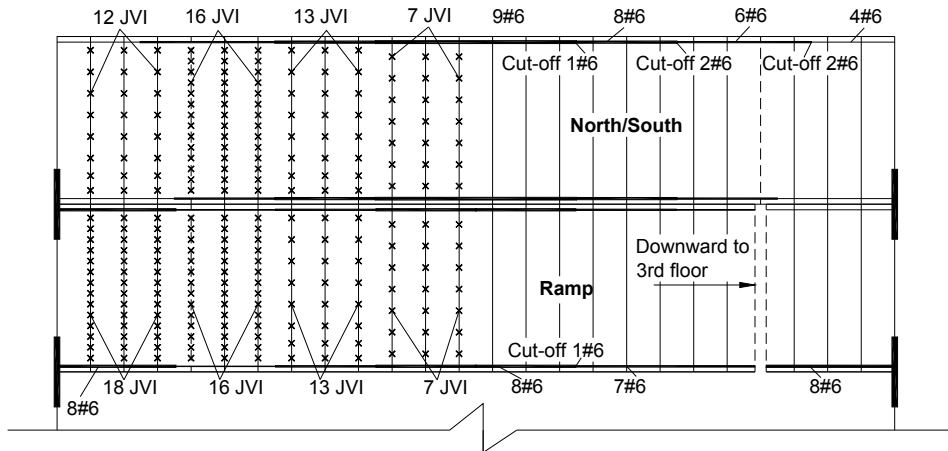
Fig. A- 2. Diaphragm reinforcement at top floor for example 1A.
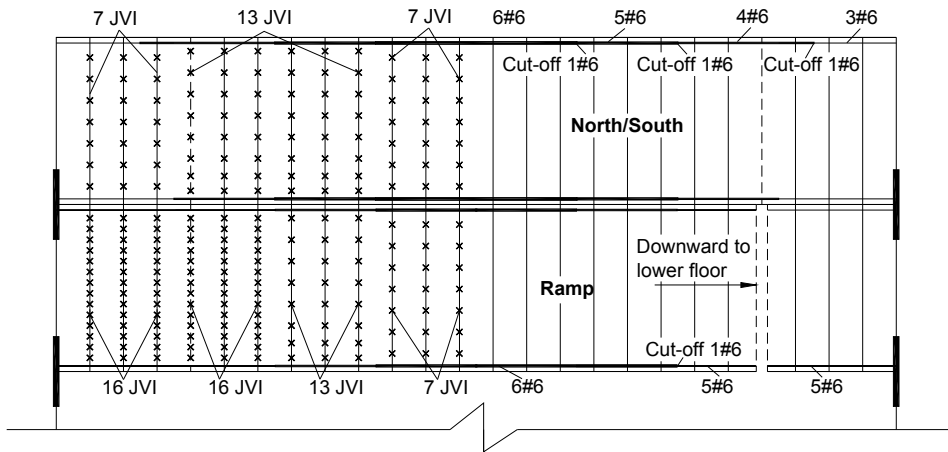
Fig. A- 3. Diaphragm reinforcement at other floors for example 1A.
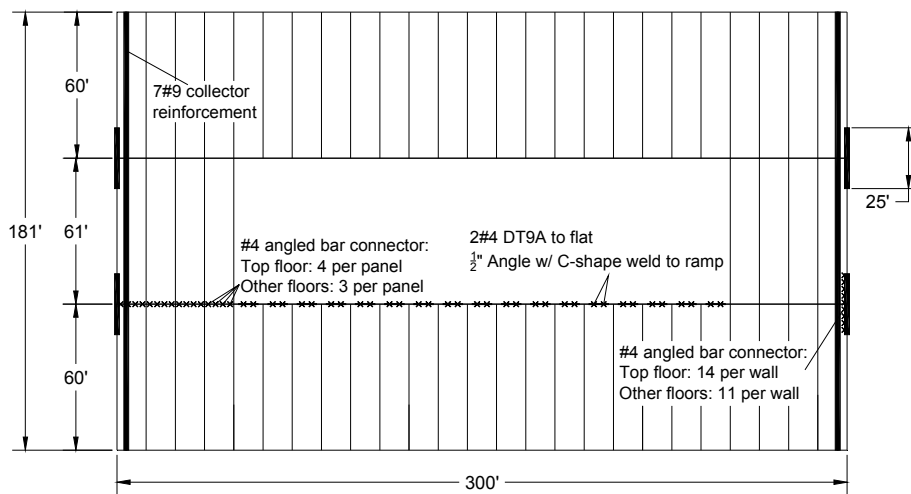
Fig. A- 4. Secondary reinforcement for example 1A.

BDO Diaphragm Design (Example 1B)
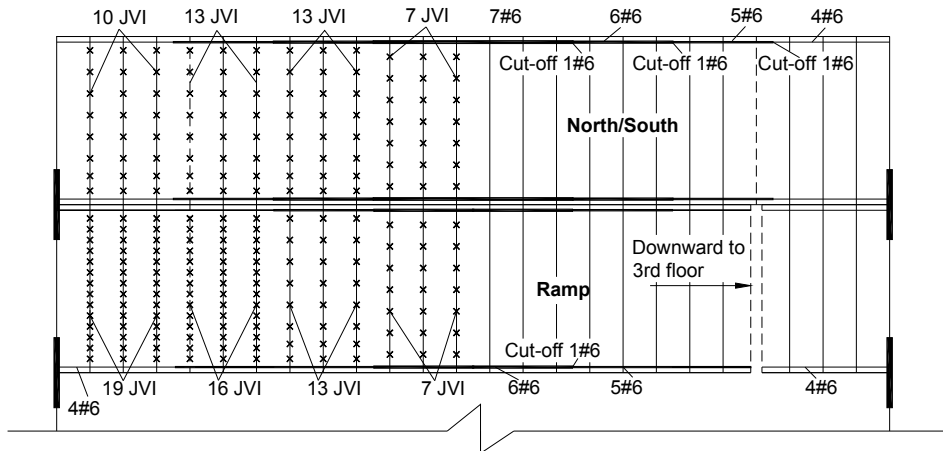
Fig. A- 5. Diaphragm reinforcement at top floor for example 1B.
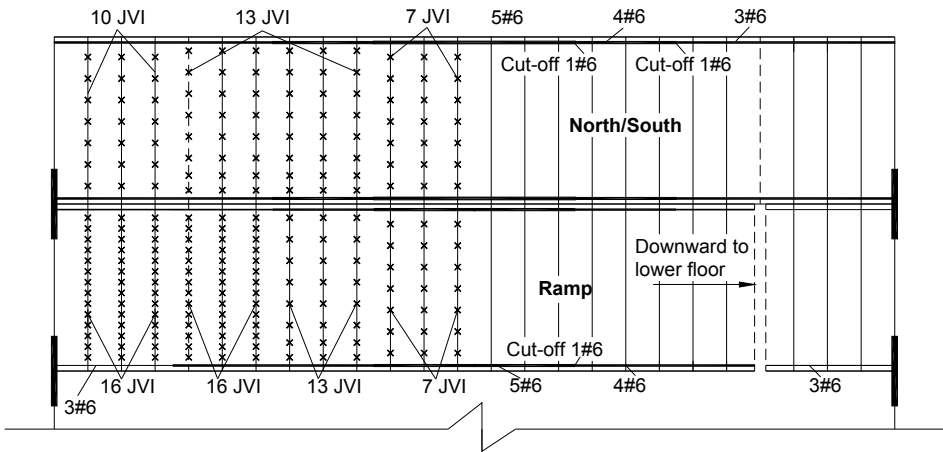
Fig. A- 6. Diaphragm reinforcement at other floors for example 1B.
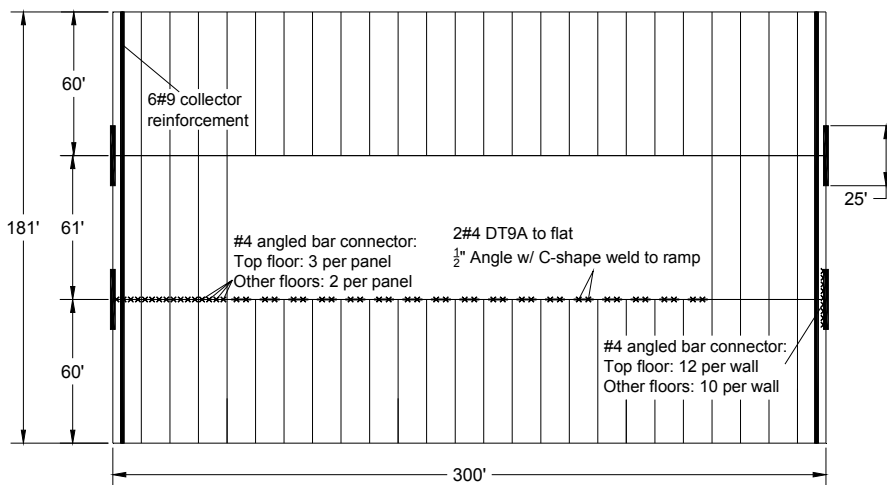
Fig. A- 7. Secondary reinforcement for example 1B.

RDO Diaphragm Design (Example 1C)
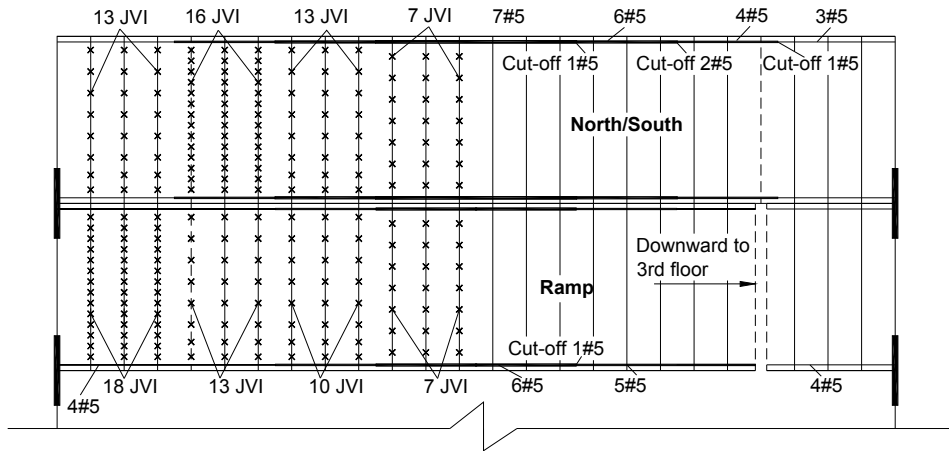
Fig. A- 8. Diaphragm reinforcement at top floor for example 1C.
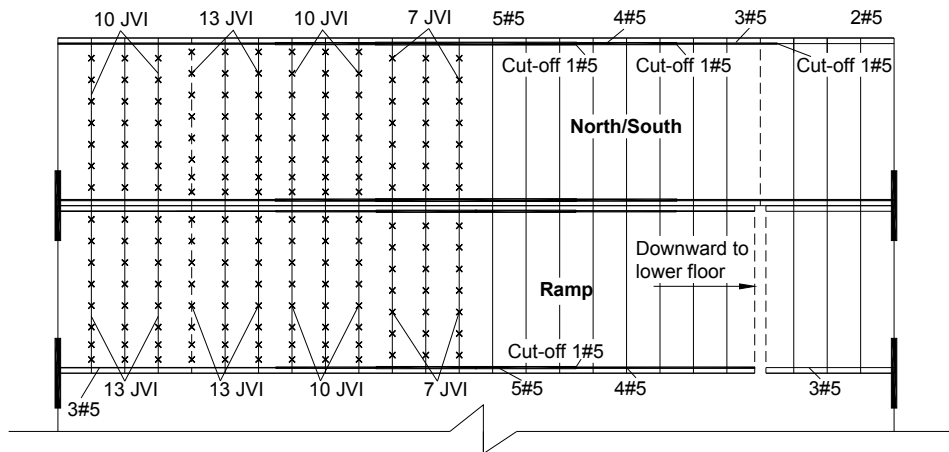
Fig. A- 9. Diaphragm reinforcement at other floors for example 1C.
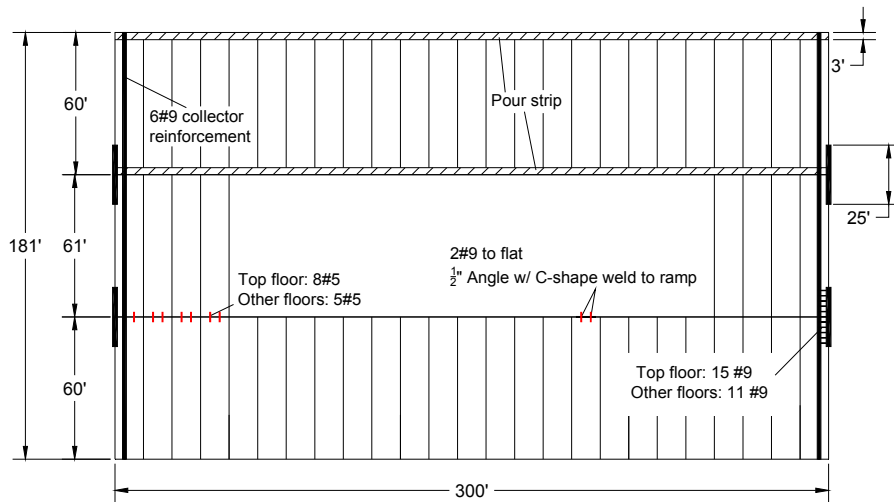
Fig. A- 10. Secondary reinforcement for example 1C.

Example 2: 4-Story Interior Wall Parking Garage

The structure for example 2 is a 4-story interior wall partaking garage. As seen in plan view of Figure 11a, the parking structure has three bays with a central ramp. The structural plan has a footprint of $300' \times 180'$, resulting in $300' \times 60'$ for each sub-diaphragm. The floor-to-floor height is 10.5' for the typical floor and 16' at the 1st story. LFRS in transverse direction is composed of four 25' interior precast wall for SDC C and RC walls for SDC D. The LFRS in longitudinal direction are 34 interior lite walls flanking the central ramp (See elevation in Figure 11b).
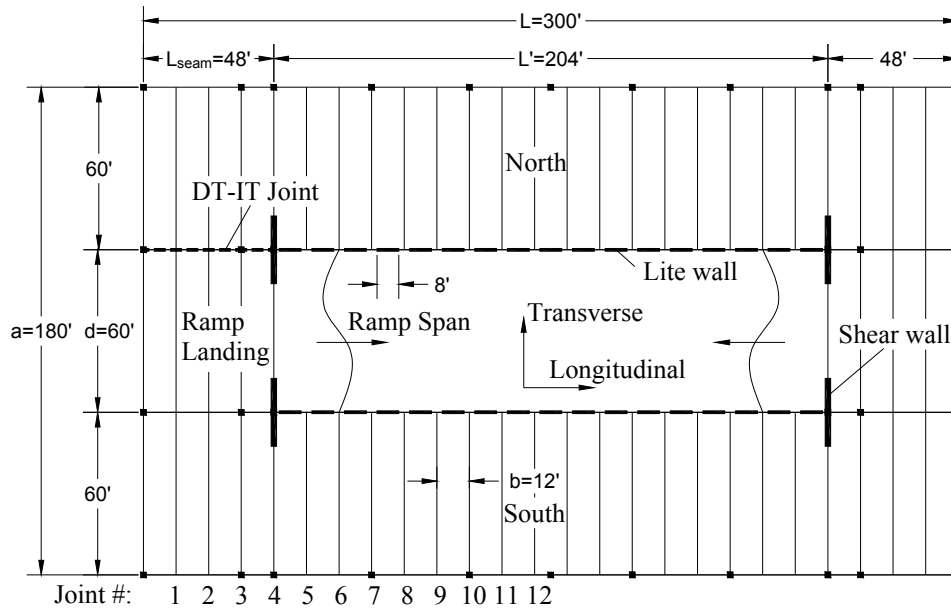
(a) Typical floor plan
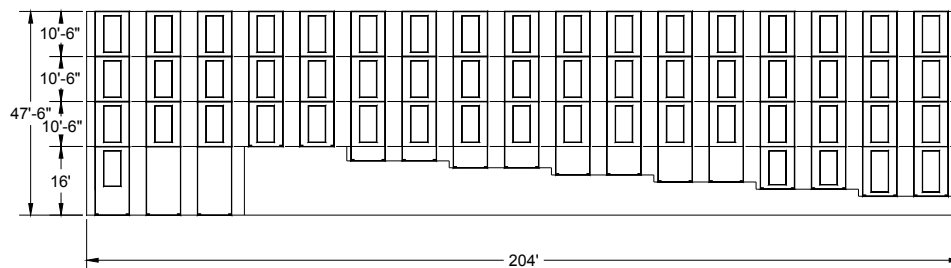
(b) Ramp elevation

Fig. A- 11. 4-story interior wall partaking garage.

Example Structure 2 is located in a Seismic Design Category (SDC) C Site in Knoxville TN and a SDC D Site in Seattle WA. The diaphragm design will be completed for two different diaphragm design options:

Design Example 2A: SDC C Elastic Design Option (EDO Design)
Design Example 2B: SDC D Reduced Design Option (RDO Design)

Because many design steps are shared among the different diaphragm design options, the design examples are arranged to follow the step by step procedure in PART 1, with the different calculations for Examples 2A and 2B appearing as sequential sub-sections within each design step.

DESIGN STEPS:

Step 1: *Determine the Diaphragm Seismic Baseline Design Forces as per ASCE 7-05*

Design example 2A: (SDC C EDO)

For SDC C EDO, this step is same as the design example 1. Refer to step 1 of example 1 to get the diaphragm seismic baseline design forces.

Design example 2B: (SDC D RDO)

(1) and (2): Seismic design parameters

Design site:	**Seattle, WA**
SDC	**D**
S_s	**1.58**
S_1	**0.55**
Soil site class	**C**
F_a	1.00
F_v	1.30
$S_{ms} = F_a \times S_s$	1.58
$S_{m1} = F_v \times S_1$	0.72
$S_{DS} = 2/3 \times S_{ms}$	1.05
$S_{D1} = 2/3 \times S_{m1}$	0.48
N-S/Special RC wall	**R=6, Ω_0=2.5, C_d=5**
E-W/ Special precast bearing wall	**R=5, Ω_0=2.5, C_d=5**

(3): Seismic response coefficient C_s

$$T_a = C_t H_n^{3/4} = 0.02 \times 47.5^{3/4} = 0.362 \sec; \quad T = C_u T_a = 1.40 \times 0.362 = 0.507 \sec$$

N-S direction:

$$C_S = \frac{S_{DS}}{R/I_E} = 0.18, \; C_{S,min} = 0.01, \; C_{S,max} = \frac{S_{D1}}{(R/I_E)T} = \frac{0.48}{6 \times 0.507} = 0.157 \; \underline{\textbf{controls}}$$

E-W direction:

$$C_S = \frac{S_{DS}}{R/I_E} = 0.21, \; C_{S,min} = 0.01, \; C_{S,max} = \frac{S_{D1}}{(R/I_E)T} = \frac{0.48}{5 \times 0.507} = 0.188 \; \underline{\textbf{controls}}$$

(4), (5), (6) and (7):

Diaphragm maximum design acceleration $C_{dia,\,max} = \max (F_x/w_x)$ (Eqn.1)
Diaphragm baseline design force $F_{Dx} = \alpha_x C_{dia,\,max} w_x$ (Eqn.2)

Note: $\alpha_x = 1.0$ at top floor and $\alpha_x = 0.68$ at lower floors for parking structure.

N-S direction:

	h_x (ft)	W_x (kips)	$W_x h_x^k$	C_{vx}	F_x (kips)	$C_{dia,\,max}$ (1)	α_x	F_{Dx} (kips) (2)
Roof	47.5	5560*	267494	0.347	1325	0.238	1.0	1325
4th	37	6276	235002	0.304	1164	0.238	0.68	1017
3rd	26.5	6276	168127	0.218	833	0.238	0.68	1017
2nd	16	6276	101341	0.131	502	0.238	0.68	1017
Sum	0	24388	771964	1	3824			

Note: * The top floor has less seismic mass due to ramp

E-W direction:

	h_x (ft)	W_x (kips)	$W_x h_x^k$	C_{vx}	F_x (kips)	$C_{dia,\,max}$ (1)	α_x	F_{Dx} (kips) (2)
Roof	47.5	5560*	267494	0.347	1590	0.286	1.0	1590
4th	37	6276	235002	0.304	1397	0.286	0.68	1221
3rd	26.5	6276	168127	0.218	999	0.286	0.68	1221
2nd	16	6276	101341	0.131	602	0.286	0.68	1221
Sum	0	24388	771964	1	4589			

Note: * The top floor has less seismic mass due to ramp

Step 2: *Determine the Diaphragm Seismic Demand Level*

Design example 2A: (SDC C EDO)

For SDC C: **Low**

Note: All buildings in SDC C are assigned "Low" Seismic Demand

Design example 2B: (SDC D RDO)

L=204 ft > 190 ft: **High**

Step 3: *Select Diaphragm Design Option*

Design example 2A: (SDC C EDO)

For low seismic demand: **Elastic design option (EDO)** is recommended

Design example 2B: (SDC D RDO)

For high seismic demand: **Reduced design option (RDO)** is recommended

Step 4: *Determine Required Diaphragm Reinforcement Classification*

Design example 2A: (SDC C EDO)

For elastic design option: **Low deformability element (LDE)**

Design example 2B: (SDC D RDO)

For reduced design option: **High deformability element (HDE)**

Step 5: *Determine Diaphragm Force Amplification Factor*

The entire diaphragm is treated as three individual sub-diaphragms for the diaphragm design as shown in PART 3: North, South and Ramp sub-diaphragm.

L	=	204 ft
AR	=	204/60 = 3.4
n	=	4
L/60-AR	=	0

Design example 2A: (SDC C EDO)

Eqn. 3: $$\Psi_E = 1.7 \times 4^{0.38}[1 - 0.04(3 - 3.4)^2] \times 1.05^{(204/60-3.4)} = 2.86$$

Design example 2B: (SDC D RDO)

Eqn. 5: $$\Psi_R = 1.05 \times 4^{0.3}[1 - 0.03(2.5 - 3.4)^2] \times 1.05^{(300/60-3.4)} = 1.55$$

Step 6: *Determine Diaphragm Shear/Anchorage Overstrength Factor*

Design example 2A: (SDC C EDO)

Eqn. 6: $$\Omega_{vE} = 1.0$$

Design example 2B: (SDC D RDO)

Eqn. 8: $$\Omega_{vR} = 1.92 AR^{-0.18} = 1.92 \times 3.4^{-0.18} = 1.54$$

Step 7: *Determine Diaphragm Design Force*

Inserting the baseline diaphragm forces from Step 1 and the diaphragm amplification factor from Step 5 into Equation 9:

Design example 2A: (SDC C EDO)

N-S direction:
Top Floor:
$$F_{dia} = \Psi_E F_{Dx} = 2.86 \times 482 = 1378 \text{ kips} > 0.2 S_{DS} I w_x = 500.4 \text{ kips}$$
Other Floors
$$F_{dia} = \Psi_E F_{Dx} = 2.86 \times 370 = 1058 \text{ kips} > 0.2 S_{DS} I w_x = 565 \text{ kips}$$

E-W direction:
Top Floor
$$F_{dia} = \Psi_E F_{Dx} = 2.86 \times 602 = 1722 \text{ kips} > 0.2 S_{DS} I w_x = 500.4 \text{ kips}$$
Other Floors
$$F_{dia} = \Psi_E F_{Dx} = 2.86 \times 462 = 1323 \text{ kips} > 0.2 S_{DS} I w_x = 565 \text{ kips}$$

Design example 2B: (SDC D RDO)

N-S direction:

Top Floor

$$F_{dia} = \Psi_R F_{Dx} = 1.55 \times 1325 = 2058 \text{ kips} > 0.2S_{DS}Iw_x = 1168 \text{ kips}$$

Other Floors

$$F_{dia} = \Psi_R F_{Dx} = 1.55 \times 1017 = 1579 \text{ kips} > 0.2S_{DS}Iw_x = 1318 \text{ kips}$$

E-W direction:
Top Floor

$$F_{dia} = \Psi_R F_{Dx} = 1.55 \times 1590 = 2469 \text{ kips} > 0.2S_{DS}Iw_x = 1168 \text{ kips}$$

Other Floors

$$F_{dia} = \Psi_R F_{Dx} = 1.55 \times 1221 = 1895 \text{ kips} > 0.2S_{DS}Iw_x = 1318 \text{ kips}$$

Step 8: *Determine Diaphragm Internal Forces*

The free-body diagram method (*Option 8b*) is selected to obtain the diaphragm internal forces. Use is made of existing free body diagrams created for common precast diaphragm configurations (See PART 3: *Free Body Diagrams for Typical Precast Parking Structures*). The associate calculations have been embedded in a design spreadsheet program (See PART 3: *Design Aids for Diaphragm Design: Spreadsheet Program*).

The tables below show the resulting required strength (maximum diaphragm internal forces) at each diaphragm joint (Refer to Fig. A- 23a for joint numbering) and joints between diaphragm to other members (LFRS and internal beam) under transverse and longitudinal directions. Although the effect of two orthogonal direction loadings (transverse and longitudinal) is considered independently, at this step the critical loading direction cannot be explicitly determined because the diaphragm reinforcement selection at step 10 is based on an M-N-V interaction equation (Eqn. 10).

Design example 2A: (SDC C EDO)

Joint between precast floor units: Transverse (N-S) Loading

Joint	x	Top floor						Other floors					
		N/S Flat			Ramp			N/S Flat			Ramp		
		N_u	V_u	M_u	N_u	V_u	M_u	N_u	V_u	M_u	N_u	V_u	M_u
	[ft]	[kips]	[kips]	[k-ft]	[kips]	[kips]	[k-ft]	[kips]	[kips]	[k-ft]	[kips]	[kips]	[k-ft]
1	12	0	-21	-124	0	-21	-124	0	-14	-85	0	-14	-85
2	24	0	-41	-495	0	-41	-495	0	-28	-339	0	-28	-339
3	36	0	-62	-1114	0	-62	-1114	0	-42	-762	0	-42	-762
4	48	0	149	-1981	0	202	-1981	0	102	-1354	0	174	-1354
5	60	0	132	-297	0	178	-67	0	90	-203	0	153	112
6	72	0	114	1176	0	154	1562	0	78	804	0	133	1332
7	84	0	96	2439	0	131	2906	0	66	1668	0	113	2307
8	96	0	79	3491	0	107	3966	0	54	2387	0	92	3036
9	108	0	61	4333	0	83	4741	0	42	2963	0	72	3520
10	120	0	44	4964	0	59	5231	0	30	3394	0	51	3759
11	132	0	26	5385	0	36	5436	0	18	3682	0	31	3752
12	144	0	9	5596	0	12	5357	0	6	3826	0	10	3500

Joint between precast floor units: Longitudinal (E-W) Loading

Joint	x	Top floor						Other floors					
		N/S Flat*			Ramp			N/S Flat*			Ramp		
		N_u	V_u	M_u	N_u	V_u	M_u	N_u	V_u	M_u	N_u	V_u	M_u
	[ft]	[kips]	[kips]	[k-ft]	[kips]	[kips]	[k-ft]	[kips]	[kips]	[k-ft]	[kips]	[kips]	[k-ft]
1	12	54	6	-424	77	0	0	37	4	-290	53	0	0
2	24	108	12	-921	155	0	0	74	8	-630	106	0	0
3	36	162	18	-1492	232	0	0	111	13	-1020	159	0	0
4	48	217	25	-2137	309	0	0	148	17	-1461	212	0	0
5	60	209	31	-1558	313	0	0	143	21	-1066	214	0	0
6	72	202	37	-1053	316	0	0	138	25	-720	216	0	0
7	84	194	43	-622	319	0	0	133	29	-425	218	0	0
8	96	187	49	-264	322	0	0	128	34	-181	220	0	0
9	108	179	55	20	325	0	0	123	38	13	222	0	0
10	120	172	61	230	328	0	0	117	42	157	224	0	0
11	132	164	68	366	331	0	0	112	46	250	226	0	0
12	144	157	74	429	334	0	0	107	50	293	228	0	0

* Symmetric design will be applied although loading is not symmetric. The most critical diaphragm internal forces are shown in the table for each symmetric joint.

Other Joints (Diaphragm-to-LFRS and Diaphragm-to-internal beam):

Joint	Top Floor						Other Floors					
	Transverse (N-S)			Longitudinal (E-W)			Transverse (N-S)			Longitudinal (E-W)		
	N_u	V_u	M_u	N_u	V_u	M_u	N_u	V_u	M_u	N_u	V_u	M_u
	[kips]	[kips]	[k-ft]	[kips]	[kips]	[k-ft]	[kips]	[kips]	[k-ft]	[kips]	[kips]	[k-ft]
DT-to-SW	**0**	**224**	**2971**	-	-	-	**0**	**153**	**2032**	-	-	-
DT-to-LW	3.1	6.1	0	**6.1**	**30**	**0**	2.2	8.3	0	**4.2**	**21**	**0**
DT-to-IT	-	-	-	**129**	**181**	**0**	-	-	-	**88**	**123**	**0**

Note: Critical force demand is marked as bond.

Design example 2B: (SDC D RDO)
Joint between precast floor units: Transverse (N-S) Loading

Joint	x	Top floor						Other floors					
		N/S Flat			Ramp			N/S Flat			Ramp		
		N_u	V_u	M_u	N_u	V_u	M_u	N_u	V_u	M_u	N_u	V_u	M_u
	[ft]	[kips]	[kips]	[k-ft]	[kips]	[kips]	[k-ft]	[kips]	[kips]	[k-ft]	[kips]	[kips]	[k-ft]
1	12	0	-31	-185	0	-31	-185	0	-21	-126	0	-21	-126
2	24	0	-62	-740	0	-62	-740	0	-42	-505	0	-42	-505
3	36	0	-92	-1664	0	-92	-1664	0	-63	-1137	0	-63	-1137
4	48	0	223	-2958	0	301	-2958	0	152	-2022	0	260	-2022
5	60	0	196	-444	0	266	-100	0	134	-303	0	229	166
6	72	0	170	1757	0	230	2333	0	116	1200	0	198	1988
7	84	0	144	3643	0	195	4341	0	98	2489	0	168	3444
8	96	0	118	5214	0	159	5923	0	81	3563	0	137	4533
9	108	0	92	6472	0	124	7081	0	63	4423	0	107	5255
10	120	0	65	7415	0	89	7813	0	45	5067	0	76	5611
11	132	0	39	8043	0	53	8119	0	27	5497	0	46	5601
12	144	0	13	8358	0	18	8001	0	9	5711	0	15	5224

Joint between precast floor units: Longitudinal (E-W) Loading

Joint	x	Top floor						Other floors					
		N/S Flat*			Ramp			N/S Flat*			Ramp		
		N_u	V_u	M_u	N_u	V_u	M_u	N_u	V_u	M_u	N_u	V_u	M_u
	[ft]	[kips]	[kips]	[k-ft]	[kips]	[kips]	[k-ft]	[kips]	[kips]	[k-ft]	[kips]	[kips]	[k-ft]
1	12	78	9	-608	111	0	0	53	6	-415	76	0	0
2	24	155	18	-1321	222	0	0	106	12	-903	152	0	0
3	36	233	26	-2140	333	0	0	159	18	-1462	227	0	0
4	48	311	35	-3064	444	0	0	212	24	-2094	303	0	0
5	60	300	44	-2234	448	0	0	205	30	-1527	306	0	0
6	72	289	53	-1510	452	0	0	198	36	-1032	309	0	0
7	84	278	62	-892	457	0	0	190	42	-610	312	0	0
8	96	268	70	-379	461	0	0	183	48	-259	315	0	0
9	108	257	79	28	466	0	0	176	54	19	318	0	0
10	120	246	88	329	470	0	0	168	60	225	321	0	0
11	132	235	97	525	474	0	0	161	66	359	324	0	0
12	144	225	106	615	479	0	0	154	72	420	327	0	0

* Symmetric design will be applied although loading is not symmetric. The most critical diaphragm internal forces are shown in the table for each symmetric joint.

Other Joints (Diaphragm-to-LFRS and Diaphragm-to-internal beam):

Joint	Top Floor						Other Floors					
	Transverse (N-S)			Longitudinal (E-W)			Transverse (N-S)			Longitudinal (E-W)		
	N_u	V_u	M_u	N_u	V_u	M_u	N_u	V_u	M_u	N_u	V_u	M_u
	[kips]	[kips]	[k-ft]	[kips]	[kips]	[k-ft]	[kips]	[kips]	[k-ft]	[kips]	[kips]	[k-ft]
DT-to-SW	**0**	**334**	**4438**	-	-	-	**0**	**229**	**3033**	-	-	-
DT-to-LW	4.7	9.1	0	**8.8**	**44**	**0**	3.1	12.4	0	**6.0**	**30**	**0**
DT-to-IT	-	-	-	**185**	**259**	**0**	-	-	-	**126**	**177**	**0**

Note: Critical force demand is marked as bond.

Step 9: *Select Diaphragm Reinforcement Type Based on DRC*

Diaphragm reinforcement type selected to meet Required Diaphragm Reinforcement Classification (*See Step 4*). Prequalified connectors will be used in this example. Select appropriate diaphragm reinforcement types from PART 2: Table 2A-1.

Design example 2A: (SDC C EDO)

Chord Reinforcement:	**Dry chord connector**
Shear Reinforcement:	**JVI Vector**
Secondary Reinforcement:	**#4 angled bar**

Design example 2B: (SDC D RDO)

Chord Reinforcement:	**Pour strip bars**
Shear Reinforcement:	**JVI Vector**
Secondary Reinforcement:	**Pour strip bars**

Determine Diaphragm Reinforcement Properties: As the diaphragm reinforcement selected is prequalified, the diaphragm reinforcement properties can also be looked up in PART 2: Table 2A-1:

Design example 2A: (SDC C EDO)

Reinforcing bars	k_t / A	k_v / A	t_n / A	v_n / A	δ_{ty}
	$k/in/in^2$	$k/in/in^2$	k/in^2	k/in^2	in
Dry chord Gr.60	1018	382	60	24.2	0.071
Connectors	k_t	k_v	t_n	v_n	δ_{ty}
	k/in	k/in	k	k	in
JVI Vector	55	226	3.1	18.1	0.066
Angled bar #4	545	676	18.5	31.1	-

Design example 2B: (SDC D RDO)

Reinforcing bars	k_t / A	k_v / A	t_n / A	v_n / A	δ_{ty}
	$k/in/in^2$	$k/in/in^2$	k/in^2	k/in^2	in
Pour strip chord Gr.60	1234	382	60	24.2	0.057
Connectors	k_t	k_v	t_n	v_n	δ_{ty}
	k/in	k/in	k	k	in
JVI Vector	55	226	3.1	18.1	0.066

Step 10: *Design the Diaphragm Reinforcement at Joints*

Use the interaction equation (Eqn. 10) to determine the required diaphragm reinforcement:

$$M - N - V = \sqrt{\left(\frac{|M_u|}{\phi_f M_n} + \frac{N_u}{\phi_f N_n} \right)^2 + \left(\frac{\Omega V_u}{\phi_v V_n} \right)^2} \leq 1.0$$

Insert the diaphragm joint required strength values (M_u, N_u and V_u) from Step 8.

The diaphragm joint nominal design strength (M_n, N_n and V_n) is based on v_n and t_n from Step 9.

– An analytically-based procedure from PART 3 is used for determining the moment strength at precast floor unit to precast floor unit joint. Triangle force distribution is used for determining the moment strength at other joints (diaphragm-to-LFRS joint and diaphragm-to-internal beam joint) (See PART 3).

– Using Eqn. 28, 29, 34 for the joint between precast floor units and Eqn. 35 for the joint between LFRS/beam and precast floor unit in Sec. 3.3 of PART 3 to determine the diaphragm joint strength.

– Selection of a trial design is greatly facilitated through the use of spreadsheet methods (See PART 3).

Primary diaphragm reinforcement design

(1) Chord and shear reinforcement design

Diaphragm chord and shear reinforcement final design is shown below for each Design Option. The M-N-V for each direction is shown in the table with the critical value marked as bold.

Design example 2A: (SDC C EDO)

Top Floor

Joint	North/South flat						Ramp					
	Chord		JVI		M-N-V		Chord		JVI		M-N-V	
	Size	#	#	s (ft)	Transverse	Longitudinal	Size	#	#	s (ft)	Transverse	Longitudinal
1	#5	7	7	8.8	0.11	**0.28**	#6	6	7	8.8	0.10	**0.25**
2	#5	7	7	8.8	0.22	**0.57**	#6	6	7	8.8	0.20	**0.51**
3	#5	7	7	8.8	0.35	**0.86**	#6	6	7	8.8	0.32	**0.76**
4	#5	7	16	3.5	0.52	**1.08**	#6	6	16	3.5	0.61	**0.94**
5	#5	7	16	3.5	0.39	**0.97**	#6	6	16	3.5	0.50	**0.95**
6	#5	7	16	3.5	0.38	**0.88**	#6	6	16	3.5	0.47	**0.96**
7	#5	7	11	5.3	0.51	**0.84**	#6	7	11	5.3	0.53	**0.88**
8	#5	7	11	5.3	0.59	**0.77**	#6	7	11	5.3	0.54	**0.89**
9	#5	7	11	5.3	0.66	**0.71**	#6	7	11	5.3	0.56	**0.89**
10	#5	7	7	8.8	0.76	**0.78**	#6	7	7	8.8	0.60	**0.93**
11	#5	7	7	8.8	**0.80**	0.78	#6	7	7	8.8	0.59	**0.94**
12	#5	7	7	8.8	**0.82**	0.78	#6	7	7	8.8	0.56	**0.95**

Other Floors

Joint	North/South flat						Ramp					
	Chord		JVI		M-N-V		Chord		JVI		M-N-V	
	Size	#	#	s (ft)	Transverse	Longitudinal	Size	#	#	s (ft)	Transverse	Longitudinal
1	#5	5	7	8.8	0.08	**0.26**	#5	6	7	8.8	0.08	**0.24**
2	#5	5	7	8.8	0.18	**0.53**	#5	6	7	8.8	0.16	**0.48**
3	#5	5	7	8.8	0.29	**0.80**	#5	6	7	8.8	0.26	**0.72**
4	#5	5	16	3.5	0.41	**0.97**	#5	6	16	3.5	0.58	**0.86**
5	#5	5	16	3.5	0.29	**0.88**	#5	6	16	3.5	0.48	**0.87**
6	#5	5	16	3.5	0.29	**0.79**	#5	6	16	3.5	0.46	**0.88**
7	#5	5	11	5.3	0.43	**0.76**	#5	6	11	5.3	0.60	**0.94**
8	#5	5	11	5.3	0.52	**0.69**	#5	6	11	5.3	0.63	**0.95**
9	#5	5	11	5.3	0.61	**0.64**	#5	6	11	5.3	0.65	**0.96**
10	#5	5	7	8.8	**0.71**	0.70	#5	6	7	8.8	0.70	**1.02**
11	#5	5	7	8.8	**0.75**	0.70	#5	6	7	8.8	0.66	**1.03**
12	#5	5	7	8.8	**0.78**	0.70	#5	6	7	8.8	0.60	**1.04**

Note: Symmetric design is applied. The shear reinforcement space varying are conducted at every three joint. Therefore not all joints are designed against the required diaphragm joint strength, i.e. M-N-V = 1.0

Design example 2B: (SDC D RDO)

Top Floor

Joint	North/South flat						Ramp					
	Chord		JVI		M-N-V		Chord		JVI		M-N-V	
	Size	#	#	s (ft)	Transverse	Longitudinal	Size	#	#	s (ft)	Transverse	Longitudinal
1	#6	8	12	4.8	0.14	**0.24**	#7	7	12	4.8	0.13	**0.23**
2	#6	8	12	4.8	0.30	**0.50**	#7	7	12	4.8	0.27	**0.46**
3	#6	8	12	4.8	0.46	**0.76**	#7	7	12	4.8	0.42	**0.68**
4	#6	8	19	2.9	0.82	**0.98**	#7	9	19	2.9	**0.92**	0.70
5	#6	8	19	2.9	0.69	**0.89**	#7	9	19	2.9	**0.80**	0.70
6	#6	8	19	2.9	0.62	**0.81**	#7	9	19	2.9	0.70	**0.71**
7	#6	8	15	3.8	0.67	**0.78**	#7	9	15	3.8	0.71	**0.73**
8	#6	8	15	3.8	0.65	**0.73**	#7	9	15	3.8	0.64	**0.74**
9	#6	8	15	3.8	0.66	**0.69**	#7	9	15	3.8	0.58	**0.74**
10	#5	8	12	4.8	0.94	**0.98**	#7	7	12	4.8	0.68	**0.96**
11	#5	8	12	4.8	0.97	**0.99**	#7	7	12	4.8	0.63	**0.97**
12	#5	8	12	4.8	0.99	**1.00**	#7	7	12	4.8	0.59	**0.98**

Other Floors

Joint	North/South flat						Ramp					
	Chord		JVI		M-N-V		Chord		JVI		M-N-V	
	Size	#	#	s (ft)	Transverse	Longitudinal	Size	#	#	s (ft)	Transverse	Longitudinal
1	#5	6	12	4.8	0.13	**0.29**	#7	5	12	4.8	0.11	**0.21**
2	#5	6	12	4.8	0.26	**0.59**	#7	5	12	4.8	0.22	**0.42**
3	#5	6	12	4.8	0.41	**0.91**	#7	5	12	4.8	0.34	**0.64**
4	#5	8	19	2.9	0.64	**0.90**	#7	7	19	2.9	**0.87**	0.60
5	#5	8	19	2.9	0.53	**0.82**	#7	7	19	2.9	**0.76**	0.60
6	#5	8	19	2.9	0.47	**0.74**	#7	7	19	2.9	**0.67**	0.61
7	#5	6	15	3.8	0.61	**0.71**	#7	7	15	3.8	**0.69**	0.63
8	#5	6	15	3.8	0.66	**0.83**	#7	7	15	3.8	0.62	**0.64**
9	#5	6	15	3.8	0.72	**0.78**	#7	7	15	3.8	0.55	**0.64**
10	#5	6	12	4.8	0.82	**0.83**	#7	5	12	4.8	0.68	**0.90**
11	#5	6	12	4.8	**0.85**	0.84	#7	5	12	4.8	0.60	**0.91**
12	#5	6	12	4.8	**0.87**	0.84	#7	5	12	4.8	0.52	**0.91**

Note: Symmetric design is applied. The shear reinforcement space varying are conducted at every three joint. Therefore not all joints are designed against the required diaphragm joint strength, i.e. M-N-V = 1.0

(2) LFRS-to-diaphragm connection and collector design

Design example 2A: (SDC C EDO)

Check $\Psi_E \times \Omega_{vE} = 2.86 \times 1.0 = 2.86 > \Omega_o = 2.5$ **OK**

Anchorage design		Wall length [ft]	V_u kips	N_u kips	M_u [k-ft]	v_n * [kips]	t_n * [kips]	Req'd # Per wall	Provide #4 angled bar
NS shear wall	Top	25	224	0	2971	31.1	18.6	22.9	23
	Others	25	153	0	2032	31.1	18.6	15.7	16
EW lite wall - S/N Flat	Top	8	30	6.1	0	31.1	18.6	1.2	2
	Others	8	21	4.2	0	31.1	18.6	0.8	2
EW lite wall - Ramp	All floors	Provide flexible connector: 4"x3"x1/2"-5" angle plate with C-shape weld per wall							

* Tension and shear nominal strength of #4 angled bar connector.

Diaphragm collector reinforcement:

Collector reinforcement is designed to resistant the same shear demand as the anchorage of shear wall:

$$A_s = \Omega V_u / \phi f_y = 1.0 \times 224 / 0.9 / 60 = 4.2 \text{ in}^2$$

Choose 10#6 (4.4 in^2) at each face of interior wall

Design example 2B: (SDC D RDO)

Check $\Psi_R \times \Omega_{vR} = 1.55 \times 1.54 = 2.387 < \Omega_o = 2.5$; Increase V_u from Step 8 for walls by a factor of 2.5/2.387=1.05

Anchorage design		Wall length [ft]	V_u kips	N_u kips	M_u [k-ft]	v_n * [kips]	t_n * [kips]	Req'd # Per wall	Provide #9 rebar
NS shear wall	Top	30	351	0	4438	24.2	60	27.5	28
	Others	30	240	0	3033	24.2	60	18.8	19
EW lite wall - S/N Flat	Top	8	46	8.8	0	24.2	60	3.4	4
	Others	8	31	6.0	0	24.2	60	2.3	3
EW lite wall - Ramp	All floors	Provide flexible connector: 4"x3"x1/2"-5" angle plate with C-shape weld per wall							

* Tension and shear nominal strength of #9 rebar.

Diaphragm collector reinforcement:

Collector reinforcement is designed to resistant the same shear demand as the anchorage of shear wall:

$$A_s = \Omega V_u / \phi f_y = 1.54 \times 351 / 0.9 / 60 = 10 \text{ in}^2$$

Choose 10#9 (10.0 in^2) at each face of interior wall

Secondary diaphragm reinforcement

Design example 2A: (SDC C EDO)

(1) Internal beam joint design

Beam joint design	Q [ft^3]	I [ft^4]	V_u [kips]	N_u [kips]	M_u [k-ft]	v_n * [kips]	t_n * [kips]	Req'd # Per DT	Provide #4 angled bar
Top floor	1210	164715	181	129	0	31.1	18.6	2.6	3
Other floors	1210	164715	123	88	0	31.1	18.6	1.8	2

* Tension and shear nominal strength of #4 angled bar connector.

(2) Spandrel to diaphragm connector

Use 2#4 angled bar connector per precast floor unit.

Design example 2B: (SDC D RDO)

(1) Internal beam joint design

Beam joint design	Q [ft³]	I [ft⁴]	V_u [kips]	N_u [kips]	M_u [k-ft]	v_n * [kips]	t_n * [kips]	Req'd # Per DT	Provide #9 rebar
Top floor	1210	164715	259	185	0	24.2	60	4.9	5
Other floors	1210	164715	177	126	0	24.2	60	3.4	4

* Tension and shear nominal strength of #9 rebar.

(2) Spandrel to diaphragm connector

Use 2#5 rebar per precast floor unit.

Step 11: *Determine the diaphragm effective elastic modulus and shear modulus*

The diaphragm joint effective elastic Young's modulus (E_{eff}) and effective shear modulus (G_{eff}) are calculated using the analytical based procedure (see "Diaphragm Joint Stiffness Calculation" in PART 3). E_{eff} and G_{eff} will be used in step 12 for calculating the diaphragm induced drift. These values can be calculated in a spreadsheet at the same time as the diaphragm reinforcement is selected. An average of the maximum and minimum values at any joint is suggested in design as shown in the bottom row of tables below. (See Appendix for tables output per joint.)

Design example 2A: (SDC C EDO)

Joint	Top Floor				Other Floors			
	North/South flat		Ramp		North/South flat		Ramp	
	E_{eff} [ksi]	G_{eff} [ksi]	E_{eff} [ksi]	G_{eff} [ksi]	E_{eff} [ksi]	G_{eff} [ksi]	E_{eff} [ksi]	G_{eff} [ksi]
Min	803	174	914	191	636	151	722	163
Max	834	266	1019	281	673	246	757	256
Ave	814	208	971	232	649	186	735	197
Des	818	220	967	236	654	198	739	209

Design example 2B: (SDC D RDO)

Joint	Top Floor				Other Floors			
	North/South flat		Ramp		North/South flat		Ramp	
	E_{eff} [ksi]	G_{eff} [ksi]	E_{eff} [ksi]	G_{eff} [ksi]	E_{eff} [ksi]	G_{eff} [ksi]	E_{eff} [ksi]	G_{eff} [ksi]
Min	1007	237	1360	293	841	216	1128	255
Max	1250	335	1552	388	1026	304	1372	355
Ave	1184	286	1455	333	890	246	1248	296
Des	1129	286	1456	341	934	260	1250	305

Step 12: *Check the diaphragm induced gravity column drift*

   The following tables show the diaphragm induced gravity column drift at the midspan column j obtained from the spreadsheet design program in PART 3).

Design example 2A: (SDC C EDO)

Sub Diaphragm	Floor	C_Δ	$C_{d,dia}$	$C_{r,dia}$	$\delta_{dia,el}$ [in]	δ_{dia} [in]	θ_{dia} [rad]
N/S Flat	Top	1.04	1.04	0.67	0.443	0.462	0.0025
	Others	1.04	1.04	0.67	0.419	0.437	0.0023
Ramp	Top	1.04	1.04	0.67	0.476	0.497	0.0026
	Others	1.04	1.04	0.67	0.482	0.503	0.0027

Design example 2B: (SDC D RDO)

Sub Diaphragm	Floor	C_Δ	$C_{d,dia}$	$C_{r,dia}$	$\delta_{dia,el}$ [in]	δ_{dia} [in]	θ_{dia} [rad]
N/S Flat	Top	1.07	3.11	0.63	0.574	1.784	0.0089
	Others	1.07	3.11	0.63	0.477	1.483	0.0074
Ramp	Top	1.07	3.11	0.63	0.510	1.586	0.0079
	Others	1.07	3.11	0.63	0.455	1.414	0.0070

For all design examples, the maximum diaphragm induced gravity column drift (θ_{dia}) is less than 0.01, **OK**

Resulting Designs: Example 2A: (SDC C EDO)
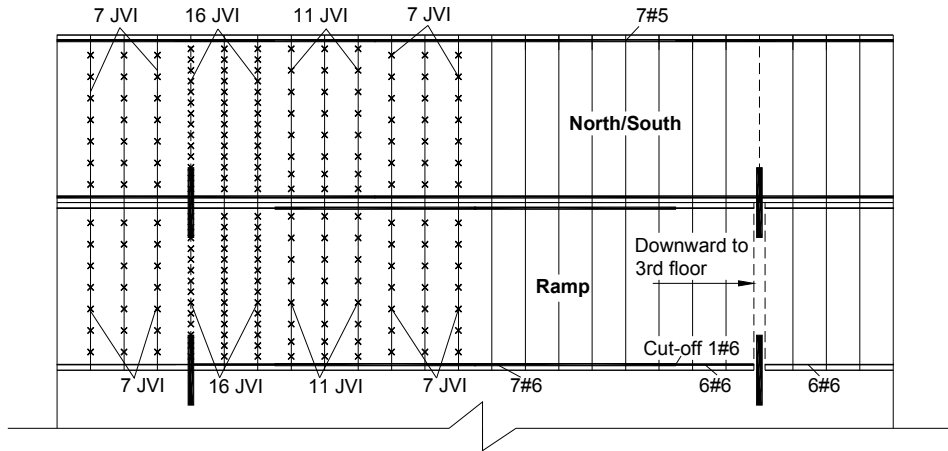
Fig. A- 12. Diaphragm reinforcement at top floor for example 2A.
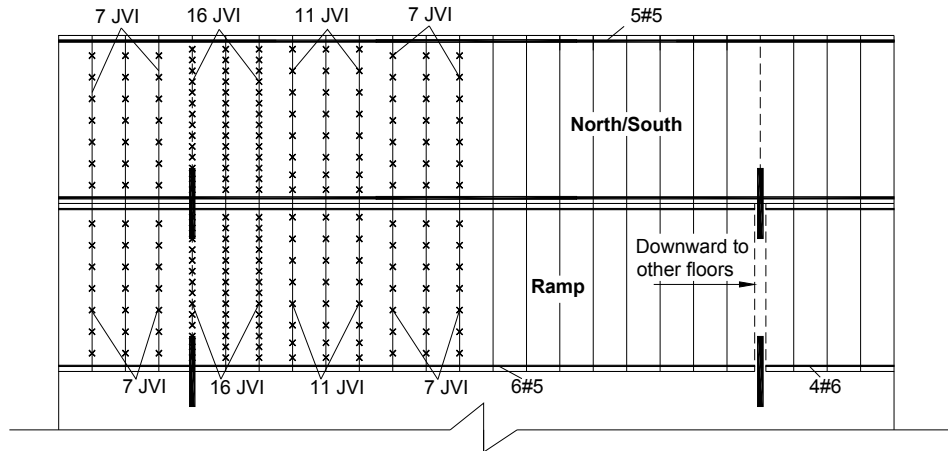
Fig. A- 13. Diaphragm reinforcement at other floors for example 2A.
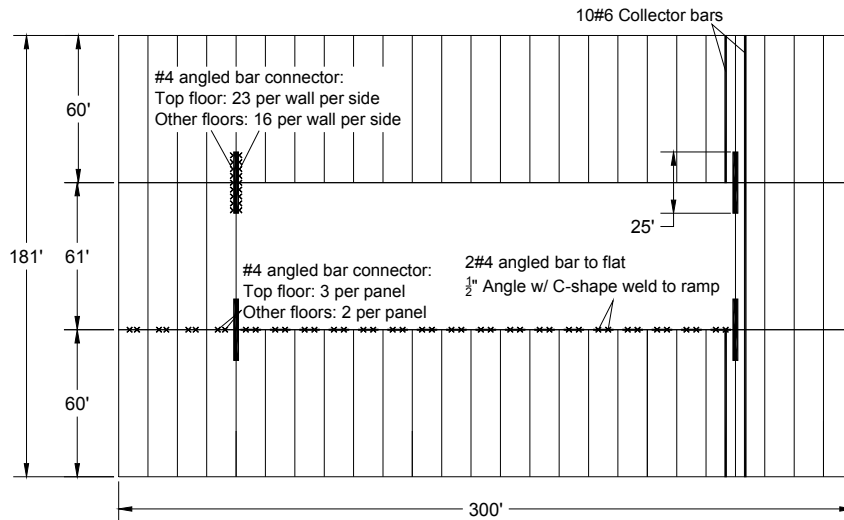
Fig. A- 14. Secondary reinforcement for example 2A.

Resulting Designs: Example 2B: (SDC D RDO)
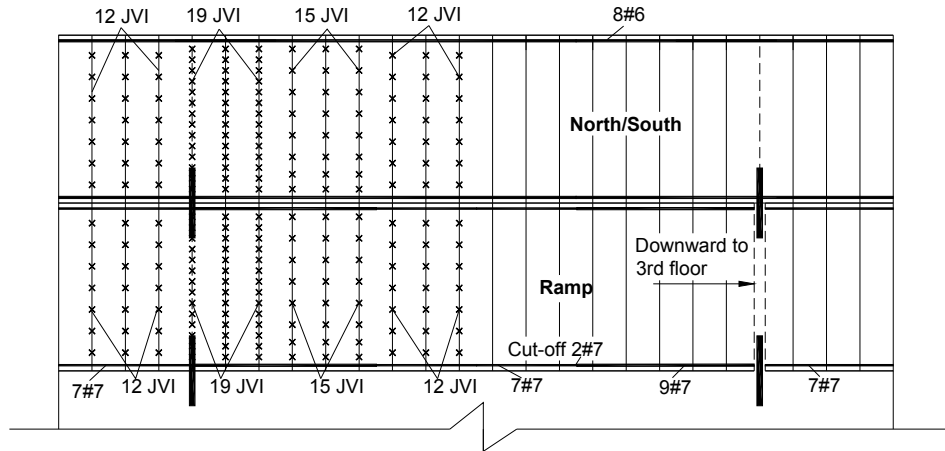
Fig. A- 15. Diaphragm reinforcement at top floor for example 2B.
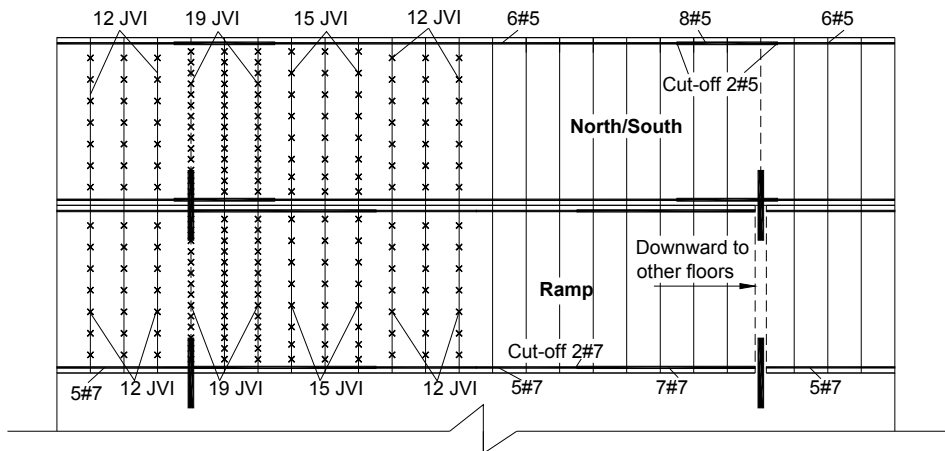
Fig. A- 16. Diaphragm reinforcement at other floors for example 2B.
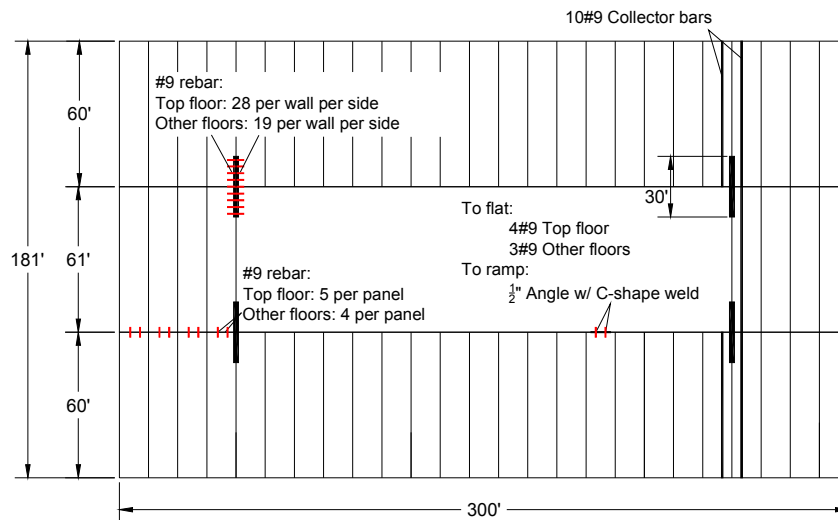
Fig. A- 17. Secondary reinforcement for example 2B.

Example 3: 8-Story Moment Frame Office Building

The structure for example 3 is an 8-story moment frame office building. As seen in Fig. A-18 and Fig. A-19, the structure has three bays with a footprint of $230' \times 147'$. The story to story height is $13'$ for typical floor and $15'$ for 1st floor. LFRS in transverse and longitudinal direction is composed of intermediate moment frames for SDC C and special moment frames for SDC D. The precast floor system is topped double Tee with $3''$ toping.

(a) SDC C   (b) SDC D
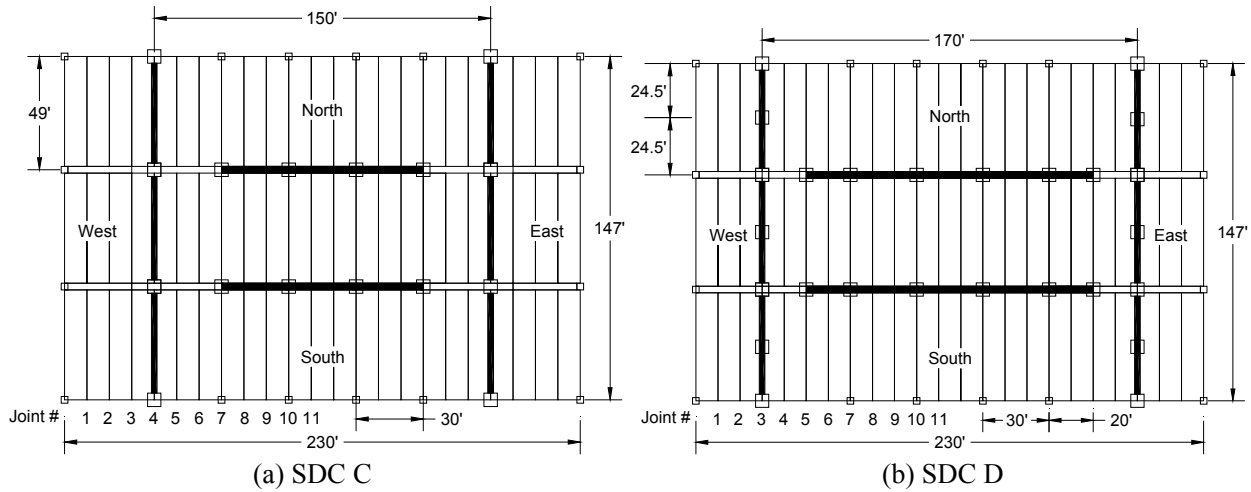
Fig. A- 18. Plan of 8-story moment frame office building.

(a) SDC C   (b) SDC D
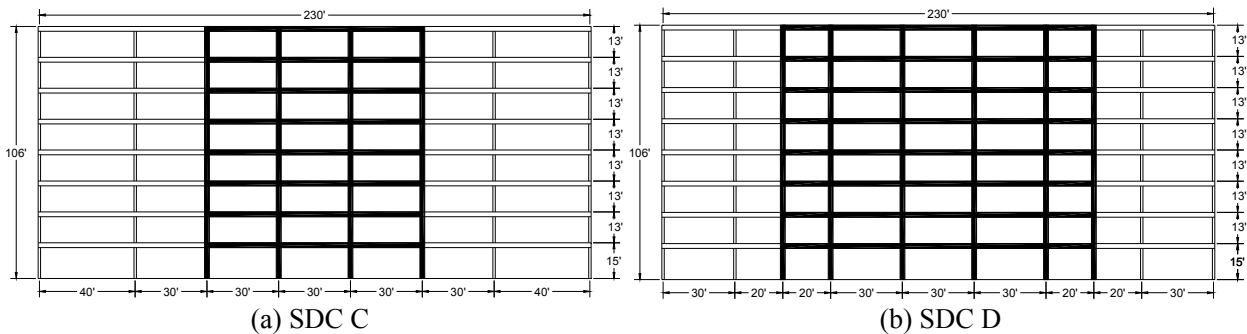
Fig. A- 19. Elevation of 8-story moment frame office building.

Example Structure 3 is located in a Seismic Design Category (SDC) C Site in Knoxville TN and a SDC D Site in Seattle WA. The diaphragm design will be completed for two different diaphragm design options:

            Design Example 3A: SDC C Elastic Design Option (EDO Design)
            Design Example 3B: SDC D Reduced Design Option (RDO Design)

Because many design steps are shared among the different diaphragm design options, the design examples are arranged to follow the step by step procedure in PART 1, with the different calculations for Examples 3A and 3B appearing as sequential sub-sections within each design step.

DESIGN STEPS:

Step 1: *Determine the Diaphragm Seismic Baseline Design Forces as per ASCE 7-05*

Design example 3A: (SDC C EDO)

(1) and (2): Seismic design parameters

Design site:	**Knoxville, TN**
SDC	**C**
S_s	**0.58**
S_1	**0.147**
Soil site class	**C**
F_a	1.17
F_v	1.65
$S_{ms} = F_a \times S_s$	0.68
$S_{m1} = F_v \times S_1$	0.24
$S_{DS} = 2/3 \times S_{ms}$	0.45
$S_{D1} = 2/3 \times S_{m1}$	0.16
N-S/Intermediate moment frame	**R=5, Ω_0=2.5, C_d=4.5**
E-W/Intermediate moment frame	**R=5, Ω_0=2.5, C_d=4.5**

(3): Seismic response coefficient C_s

$$T_a = C_t H_n^{3/4} = 0.016 \times 106^{0.9} = 1.06 \sec; \quad T = C_u T_a = 1.58 \times 1.06 = 1.68 \sec$$

$$C_S = \frac{S_{DS}}{R/I_E} = 0.09, \ C_{S,min} = 0.01, \ C_{S,max} = \frac{S_{D1}}{(R/I_E)T} = \frac{0.16}{5 \times 1.68} = 0.019 \ \underline{\textbf{controls}}$$

(4), (5), (6) and (7):

Diaphragm maximum design acceleration $C_{dia,\ max}$=max (F_x/w_x) (Eqn.1)

Diaphragm baseline design force $F_{Dx} = \alpha_x \ C_{dia,\ max} \ w_x$ (Eqn.2)

Note: conservatively α_x =1.0 for all floors.

In N-S and E-W directions:

	h_x (ft)	W_x (kips)	$W_x h_x^k$	C_{vx}	F_x (kips)	$C_{dia,\ max}$ (1)	α_x	F_{Dx} (kips) (2)
Roof	106	5101	8417461	0.273	215	0.042	1.0	215
7th	93	5101	6837679	0.222	174	0.042	1.0	215
6th	80	5101	5382963	0.175	137	0.042	1.0	215
5th	67	5101	4061349	0.132	104	0.042	1.0	215
4th	54	5101	2882988	0.093	74	0.042	1.0	215
3rd	41	5101	1861329	0.060	47	0.042	1.0	215
2nd	28	5101	1015546	0.033	26	0.042	1.0	215
1st	15	5101	376761	0.012	10	0.042	1.0	215
Sum		40808	30836078	1	787			

Design example 3B: (SDC D RDO)

(1) and (2): Seismic design parameters

Design site:	**Seattle, WA**
SDC	**D**
S_s	**1.58**
S_1	**0.55**
Soil site class	**C**
F_a	1.00
F_v	1.30
$S_{ms} = F_a \times S_s$	1.58
$S_{m1} = F_v \times S_1$	0.72
$S_{DS} = 2/3 \times S_{ms}$	1.05
$S_{D1} = 2/3 \times S_{m1}$	0.48
N-S/Special moment frame	**R=8, Ω_0=3.0, C_d=5.5**
E-W/ Special moment frame	**R=8, Ω_0=3.0, C_d=5.5**

(3): Seismic response coefficient C_s

$$T_a = C_t H_n^{3/4} = 0.016 \times 106^{0.9} = 1.06 \text{ sec}; \quad T = C_u T_a = 1.4 \times 1.06 = 1.49 \text{ sec}$$

$$C_S = \frac{S_{DS}}{R/I_E} = 0.132, \quad C_{S,\min} = 0.01, \quad C_{S,\max} = \frac{S_{D1}}{(R/I_E)T} = \frac{0.48}{8 \times 1.49} = 0.04 \text{ \underline{\textbf{controls}}}$$

(4), (5), (6) and (7):

Diaphragm maximum design acceleration $C_{dia,\ max} = \max (F_x/w_x)$ (Eqn.1)

Diaphragm baseline design force $F_{Dx} = \alpha_x C_{dia,\ max} w_x$ (Eqn.2)

Note: conservatively α_x =1.0 for all floors.

In N-S and E-W directions:

	h_x (ft)	W_x (kips)	$W_x h_x^k$	C_{vx}	F_x (kips)	$C_{dia,\ max}$ (1)	α_x	F_{Dx} (kips) (2)
Roof	106	5392	5741377	0.265	457	0.085	1.0	457
7th	93	5392	4721518	0.218	375	0.085	1.0	457
6th	80	5392	3769966	0.174	300	0.085	1.0	457
5th	67	5392	2892153	0.133	230	0.085	1.0	457
4th	54	5392	2095050	0.097	167	0.085	1.0	457
3rd	41	5392	1388069	0.064	110	0.085	1.0	457
2nd	28	5392	784958	0.036	62	0.085	1.0	457
1st	15	5392	308800	0.014	25	0.085	1.0	457
Sum		43136	21701892	1	1726			

Step 2: *Determine the Diaphragm Seismic Demand Level*

  Design example 3A: (SDC C EDO)

    For SDC C: **Low**

         Note: All buildings in SDC C are assigned "Low" Seismic Demand

  Design example 3B: (SDC D RDO)

    n=8>7.5:   **High**

Step 3: *Select Diaphragm Design Option*

  Design example 3A: (SDC C EDO)

    For low seismic demand: **Elastic design option (EDO)** is recommended

  Design example 3B: (SDC D RDO)

    For high seismic demand: **Reduced design option (RDO)** is recommended

Step 4: *Determine Required Diaphragm Reinforcement Classification*

  Design example 3A: (SDC C EDO)

    For elastic design option: **Low deformability element (LDE)**

  Design example 3B: (SDC D RDO)

    For reduced design option: **High deformability element (HDE)**

Step 5: *Determine Diaphragm Force Amplification Factor*

  The whole diaphragm is treated as one free-body for diaphragm design as shown in PART 3.

  Design example 3A: (SDC C EDO)

L	=	150 ft
AR	=	150/147= 1.02
n	=	8
L/60-AR	=	1.48
Eqn. 3:		$\Psi_E = 1.7 \times 8^{0.38}[1 - 0.04(3 - 1.02)^2] \times 1.05^{(150/60 - 1.02)} = 3.4$

  Design example 3B: (SDC D RDO)

L	=	170 ft
AR	=	170/147= 1.16

$$n \quad = \quad 8$$
$$L/60\text{-}AR \quad = \quad 1.67$$
$$\text{Eqn. 5:} \quad \Psi_R = 1.05 \times 8^{0.3}[1 - 0.03(2.5 - 1.16)^2] \times 1.05^{(170/60-1.16)} = 2.01$$

Step 6: *Determine Diaphragm Shear/Anchorage Overstrength Factor*

Design example 3A: (SDC C EDO) (Eqn. 6)

Eqn. 6: $\quad \Omega_{vE} = 1.0$

Design example 3B: (SDC D RDO) (Eqn. 8)

Eqn. 8: $\quad \Omega_{vR} = 1.92 AR^{-0.18} = 1.92 \times 1.16^{-0.18} = 1.87$

Step 7: *Determine Diaphragm Design Force*

Inserting the baseline diaphragm forces from Step 1 and the diaphragm amplification factor from Step 5 into Equation 9:

Design example 3A: (SDC C EDO)

$F_{dia} = \Psi_E F_{Dx} = 3.4 \times 215 = 729$ kips $> 0.2 S_{DS} I w_x = 459$ kips

Design example 3B: (SDC D RDO)

$F_{dia} = \Psi_R F_{Dx} = 2.01 \times 457 = 918$ kips $< 0.2 S_{DS} I w_x = 1132$ kips, So $F_{dia} = 1132$ kips

Step 8: *Determine Diaphragm Internal Forces*

The free-body diagram method (*Option 8b*) is selected to obtain the diaphragm internal forces. Use is made of existing free body diagrams created for common precast diaphragm configurations (See PART 3: *Free Body Diagrams for Typical Precast Parking Structures*). The associate calculations have been embedded in a design spreadsheet program (See PART 3: *Design Aids for Diaphragm Design: Spreadsheet Program*).

The tables below show the resulting required strength (maximum diaphragm internal forces) at each diaphragm joint (Refer to Fig. A- 23a for joint numbering) and joints between diaphragm to other members (LFRS and internal beam) under transverse and longitudinal directions. Although the effect of two orthogonal direction loadings (transverse and longitudinal) is considered independently, at this step the critical loading direction cannot be explicitly determined because the diaphragm reinforcement selection at step 10 is based on an M-N-V interaction equation (Eqn. 10).

Design example 3A: (SDC C EDO)

Joint between precast floor units

Joint	x	Transverse (N-S) loading			Longitudinal (E-W) loading		
		N_u	V_u	M_u	N_u	V_u	M_u
	[ft]	[kips]	[kips]	[k-ft]	[kips]	[kips]	[k-ft]
1	10	0	-32	-159	32	0	0
2	20	0	-63	-634	63	0	0
3	30	0	-95	-1427	95	0	0
4	40	0	238	-2537	127	0	0
5	50	0	206	-317	159	0	0
6	60	0	174	1585	190	0	0
7	70	0	143	3171	222	0	0
8	80	0	111	4439	173	0	0
9	90	0	79	5391	123	0	0
10	100	0	48	6025	74	0	0
11	110	0	16	6342	25	0	0

Other Joints (Diaphragm-to-LFRS and Diaphragm-to-internal beam):

Joint	Top Floor					
	Transverse			Longitudinal		
	N_u	V_u	M_u	N_u	V_u	M_u
	[kips]	[kips]	[k-ft]	[kips]	[kips]	[k-ft]
DT-to-N/S Frame	**0**	**238**	**2537**	-	-	-
DT-to-E/W Fram	-	-	-	**0**	**243**	**5956**
DT-to-IT per DT	**23**	**22**	**-**	-	-	**-**

Note: Critical force demand is marked as bond.

Design example 3B: (SDC D RDO)

Joint between precast floor units

Joint	x	Transverse (N-S) loading			Longitudinal (E-W) loading		
		N_u	V_u	M_u	N_u	V_u	M_u
	[ft]	[kips]	[kips]	[k-ft]	[kips]	[kips]	[k-ft]
1	10	0	-49	-247	49	0	0
2	20	0	-99	-988	99	0	0
3	30	0	420	-2222	148	0	0
4	40	0	370	1729	198	0	0
5	50	0	321	5186	247	0	0
6	60	0	272	8149	209	0	0
7	70	0	222	10618	171	0	0
8	80	0	173	12594	133	0	0
9	90	0	123	14075	95	0	0
10	100	0	74	15063	57	0	0
11	110	0	25	15557	19	0	0

Other Joints (Diaphragm-to-LFRS and Diaphragm-to-internal beam):

Joint	Top Floor					
	Transverse			Longitudinal		
	N_u	V_u	M_u	N_u	V_u	M_u
	[kips]	[kips]	[k-ft]	[kips]	[kips]	[k-ft]
DT-to-N/S Frame	**0**	**420**	**2222**	-	-	-
DT-to-E/W Fram	-	-	-	**0**	**379**	**9277**
DT-to-IT per DT	**37**	**38**	**-**	-	-	**-**

Note: Critical force demand is marked as bond.

Step 9: *Select Diaphragm Reinforcement Type Based on DRC*

Diaphragm reinforcement type selected to meet Required Diaphragm Reinforcement Classification (*See Step 4*). Prequalified connectors will be used in this example. Select appropriate diaphragm reinforcement types from PART 2: Table 2A-1.

Design example 3A: (SDC C EDO)

Chord Reinforcement: **Topped chord**
Shear Reinforcement: **Standard wwr and hairpin**
Secondary Reinforcement: **Topped chord**

Design example 3B: (SDC D RDO)

Chord Reinforcement: **Topped chord**
Shear Reinforcement: **Ductile ladder and hairpin**
Secondary Reinforcement: **Topped chord**

Determine Diaphragm Reinforcement Properties: As the diaphragm reinforcement selected is prequalified, the diaphragm reinforcement properties can also be looked up in PART 2: Table 2A-1:

Design example 3A: (SDC C EDO)

	k_t / A	k_v / A	t_n / A	v_n / A	δ_{ty}
	k/in/in²	k/in/in²	k/in²	k/in²	in
Topped chord Gr.60	1234	382	60	24.2	0.0568
Standard ASTM A185 wwr	1414	709	65	39.7	0.039
	k_t	k_v	t_n	v_n	δ_{ty}
	k/in	k/in	k	k	in
Hairpin connector	209	181	9	18.1	0.043

Design example 3B: (SDC D RDO)

	k_t / A	k_v / A	t_n / A	v_n / A	δ_{ty}
	k/in/in^2	k/in/in^2	k/in^2	k/in^2	in
Topped chord Gr.60	1234	382	60	24.2	0.0568
Ductile ladder Gr.1018	1260	216.8	54.2	21.68	0.043
	k_t	k_v	t_n	v_n	δ_{ty}
	k/in	k/in	k	k	in
Hairpin connector	209	181	9	18.1	0.043

Step 10: *Design the Diaphragm Reinforcement at Joints*

Use the interaction equation (Eqn. 10) to determine the required diaphragm reinforcement:

$$M - N - V = \sqrt{\left(\frac{|M_u|}{\phi_f M_n} + \frac{N_u}{\phi_f N_n} \right)^2 + \left(\frac{\Omega V_u}{\phi_v V_n} \right)^2} \leq 1.0$$

Insert the diaphragm joint required strength values (M_u, N_u and V_u) from Step 8.

The diaphragm joint nominal design strength (M_n, N_n and V_n) is based on v_n and t_n from Step 9.

- An analytically-based procedure from PART 3 is used for determining the moment strength at precast floor unit to precast floor unit joint. Triangle force distribution is used for determining the moment strength at other joints (diaphragm-to-LFRS joint and diaphragm-to-internal beam joint) (See PART 3).

- Using Eqn. 28, 29, 34 for the joint between precast floor units and Eqn. 35 for the joint between LFRS/beam and precast floor unit in Sec. 3.3 of PART 3 to determine the diaphragm joint strength.

- Selection of a trial design is greatly facilitated through the use of spreadsheet methods (See PART 3).

Primary diaphragm reinforcement design

(1) Chord and shear reinforcement design

Diaphragm chord and shear reinforcement final design is shown below for each Design Option. The M-N-V for each direction is shown in the table with the critical value marked as bold.

Design example 3A: (SDC C EDO)

| Joint | Chord | | | Hairpin | wwr W2.9 x W2.9 | | M-N-V | |
#	Size	#	#	Spacing (ft)	Area (in^2)	10″ x ″	N-S	E-W
1	#5	2	15	10.0	0.029	12	**0.10**	0.08
2	#5	2	15	10.0	0.029	12	**0.19**	0.16
3	#5	2	15	10.0	0.029	12	**0.30**	0.24
4	#5	2	15	10.0	0.029	12	**0.41**	0.32
5	#5	2	15	10.0	0.029	12	**0.73**	0.32
6	#5	2	15	10.0	0.029	12	**0.62**	0.40
7	#5	2	15	10.0	0.029	12	**0.53**	0.48
8	#5	2	15	10.0	0.029	12	0.47	**0.56**
9	#5	2	15	10.0	0.029	12	0.43	**0.44**
10	#5	2	15	10.0	0.029	12	**0.40**	0.31
11	#5	2	15	10.0	0.029	12	**0.39**	0.19

Design example 3B: (SDC D RDO)

| Joint | Chord | | | Hairpin | Ductile ladder W4.9 x W4.9 * | | M-N-V | |
#	Size	#	#	Spacing (ft)	Area (in^2)	10″ x ″	N-S	E-W
1	#5	3	15	10.0	0.049	12	**0.23**	0.09
2	#5	3	15	10.0	0.049	12	**0.46**	0.17
3	#5	3	32	4.5	0.049	6	**0.99**	0.14
4	#5	3	32	4.5	0.049	6	**0.87**	0.19
5	#5	3	32	4.5	0.049	6	0.76	0.23
6	#5	3	24	6.1	0.049	12	**0.96**	0.32
7	#5	3	24	6.1	0.049	12	**0.82**	0.26
8	#5	3	24	6.1	0.049	12	**0.68**	0.21
9	#5	3	15	10.0	0.049	12	**0.70**	0.17
10	#5	4	15	10.0	Not Provided		**1.00**	0.22
11	#5	4	15	10.0	Not Provided		**0.92**	0.07

* wwr W2.9xW2.9: 12″x12″ is provided within the projection of the panel for temperature and shrinkage.

(2) LFRS-to-diaphragm connection and collector design

Design example 3A: (SDC C EDO)

Check $\Psi_E \times \Omega_{vE} = 3.4 \times 1.0 = 3.4 > \Omega_o = 2.5$ **OK**

| Anchorage design | length | V_u | N_u | M_u | v_n * | t_n * | Req'd conn | Provide |
	[ft]	[kips]	[kips]	[k-ft]	[kips]	[kips]	Per LFRS	#7 bar
NS frame	147	238	0	2537	14.52	36	19.3	20
EW frame	90	243	0	5956	14.52	36	20.6	3 per panel

* Tension and shear nominal strength of #7 rebar.

No collector reinforcement is needed. Provide 2#5 at each face of E-W frames.

Design example 3B: (SDC D RDO)

Check $\Psi_R \times \Omega_{vR} = 2.01 \times 1.87 = 3.76 > \Omega_o = 3.0$ **OK**

Anchorage design	length [ft]	V_u [kips]	N_u [kips]	M_u [k-ft]	v_n* [kips]	t_n* [kips]	Req'd conn Per LFRS	Provide #9 bar
NS frame	147	420	0	2222	24.2	60	38.2	38
EW frame	130	379	0	9277	24.2	60	34.7	3 per panel

* Tension and shear nominal strength of #9 rebar.

No collector reinforcement is needed. Provide 2#5 at each face of E-W frames.

Secondary diaphragm reinforcement

Design example 3A: (SDC C EDO)

(1) Internal beam joint design

Internal beam joint design	V_u [kips]	N_u [kips]	M_u [k-ft]	v_n* [kips]	t_n* [kips]	Req'd conn Per DT panel	Provide #7 bar
Top floor	22	23	0	14.52	36	1.9	2 per panel

* Tension and shear nominal strength of #7 rebar.

(2) Spandrel to diaphragm connector

Use 2#5 rebar per precast floor unit.

Design example 3B: (SDC D RDO)

(1) Internal beam joint design

Internal beam joint design	V_u [kips]	N_u [kips]	M_u [k-ft]	v_n* [kips]	t_n* [kips]	Req'd conn Per DT panel	Provide #9 bar
Top floor	38	37	0	24.2	60	3.5	4 per panel

* Tension and shear nominal strength of #9 rebar.

(2) Spandrel to diaphragm connector

Use 2#5 rebar per precast floor unit.

Step 11: *Determine the diaphragm effective elastic modulus and shear modulus*

The diaphragm joint effective elastic Young's modulus (E_{eff}) and effective shear modulus (G_{eff}) are calculated using the analytical based procedure (see "Diaphragm Joint Stiffness Calculation" in PART 3). E_{eff} and G_{eff} will be used in step 12 for calculating the diaphragm induced drift. These values can be calculated in a spreadsheet at the same time as the diaphragm reinforcement is selected. An average of the maximum and minimum values at any joint is suggested in design as shown in the bottom row of tables below. (See Appendix for tables output per joint.)

Design example 3A: (SDC C EDO)

Joint	E_{eff} [ksi]	G_{eff} [ksi]
Min	541	78
Max	541	78
Ave	541	78
Des	541	78

Design example 3B: (SDC D RDO)

Joint	E_{eff} [ksi]	G_{eff} [ksi]
Min	574	82
Max	1392	267
Ave	1011	175
Des	983	174

Step 12: *Check the diaphragm induced gravity column drift*

The following tables show the diaphragm induced gravity column drift at the midspan column j obtained from the spreadsheet design program in PART 3).

Design example 3A: (SDC C EDO)

Floor	C_Δ	$C_{d,dia}$	$C_{r,dia}$	$\delta_{dia,el}$ [in]	δ_{dia} [in]	θ_{dia} [rad]
Top	1.01	1.01	0.98	0.151	0.152	0.0010

Design example 3B: (SDC D RDO)

Floor	C_Δ	$C_{d,dia}$	$C_{r,dia}$	$\delta_{dia,el}$ [in]	δ_{dia} [in]	θ_{dia} [rad]
Top	1.02	2.95	0.873	0.15	0.442	0.0025

For all design examples, the maximum diaphragm induced gravity column drift (θ_{dia}) is less than 0.01, **OK**

Resulting Designs: Example 3A: (SDC C EDO)
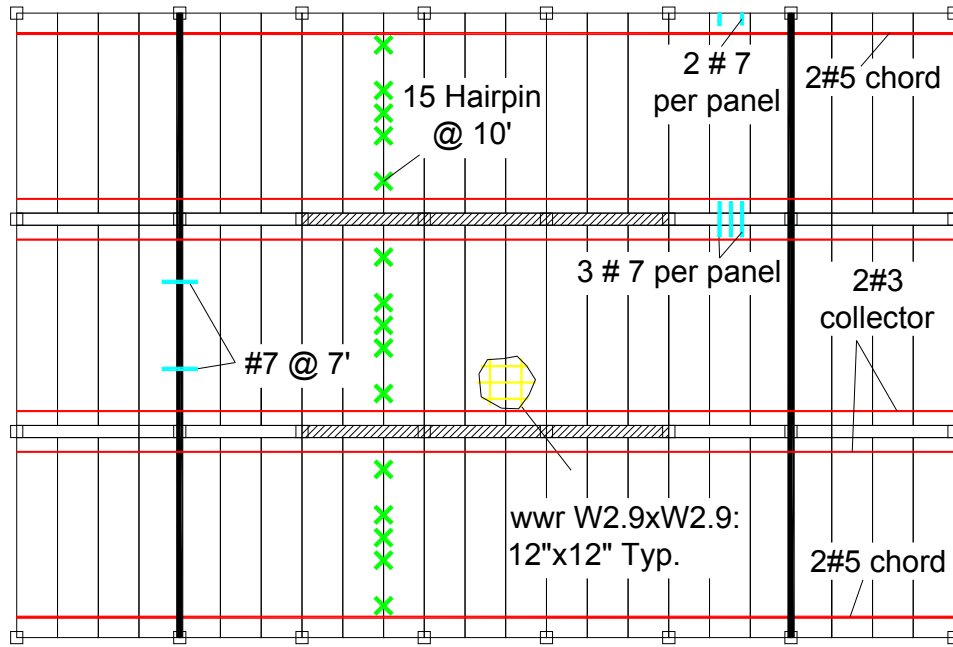
Fig. A-20. Diaphragm reinforcement for example 3A.

Resulting Designs: Example 3B: (SDC D RDO)
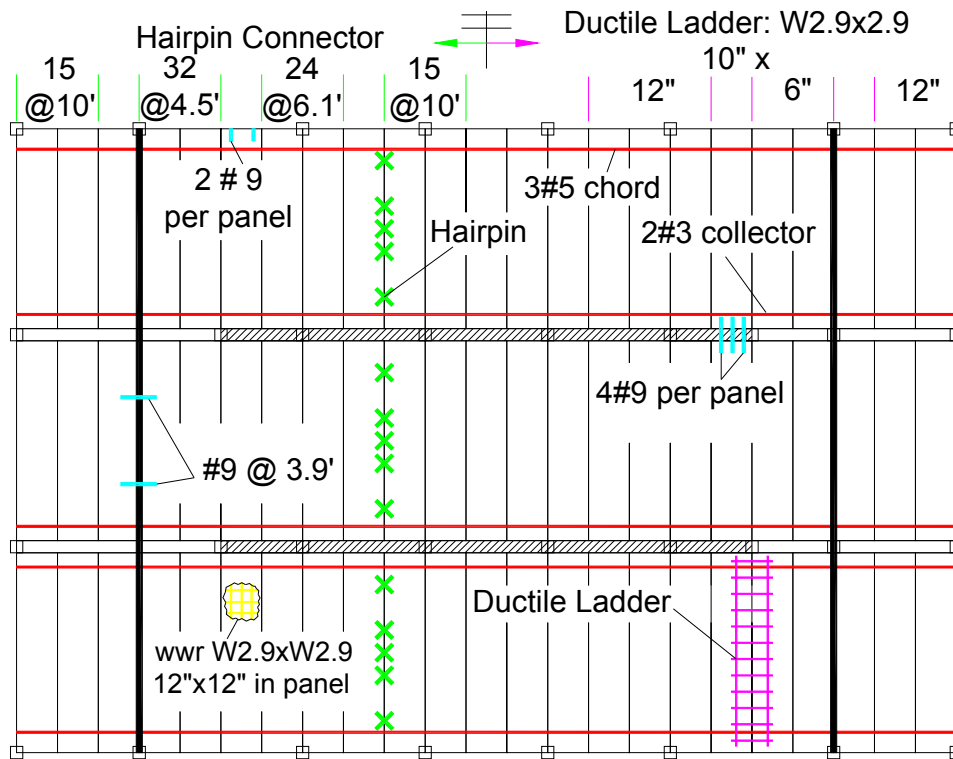
Fig. A-21. Diaphragm reinforcement for example 3B.

Example 4: 8-Story Shear Wall Office Building

The structure for example 4 is an 8-story perimeter shear wall office building. As seen in Fig. A- 22 and Fig. A- 23, the structure has three bays with a footprint of $230' \times 147'$. The story to story height is 13′ for typical floor and 15′ for 1st floor. LFRS in transverse is composed of 2 perimeter ordinary RC shear walls for SDC C and four perimeter special RC shear walls for SDCD. LFRS in longitudinal is composed of 4 perimeter ordinary RC bearing wall for SDC C and 4 perimeter special RC bearing wall for SDCD. The precast floor system is topped double Tee with 3″ toping.

(a) SDC C   (b) SDC D
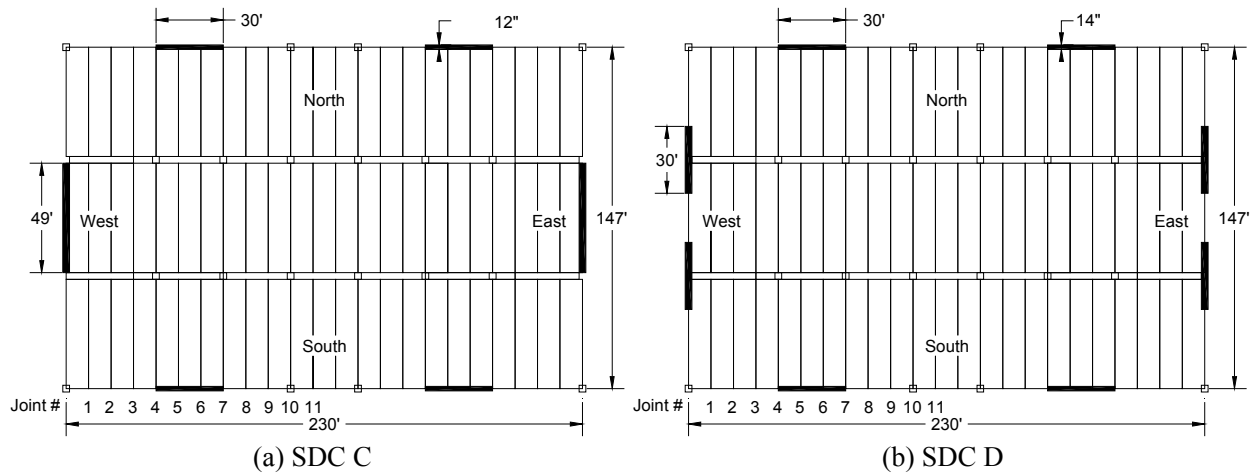
Fig. A- 22. Plan of 8-story shear wall office building.
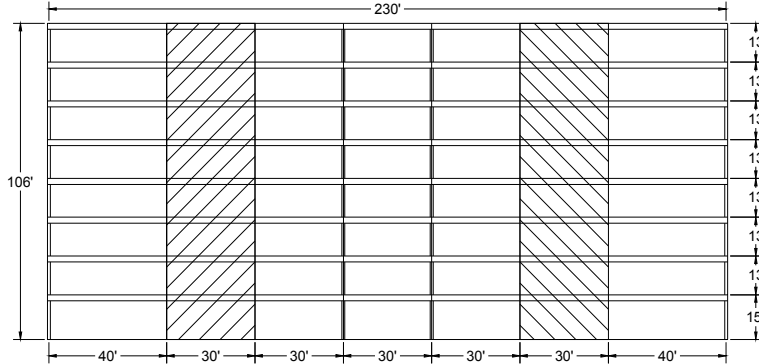
Fig. A- 23. Elevation of 8-story shear wall office building.

Example Structure 4 is located in a Seismic Design Category (SDC) C Site in Knoxville TN and a SDC D Site in Seattle WA. The diaphragm design will be completed for two different diaphragm design options:

Design Example 4A: SDC C Elastic Design Option (EDO Design)
Design Example 4B: SDC D Reduced Design Option (RDO Design)

Because many design steps are shared among the different diaphragm design options, the design examples are arranged to follow the step by step procedure in PART 1, with the different calculations for Examples 4A and 4B appearing as sequential sub-sections within each design step.

DESIGN STEPS:

Step 1: *Determine the Diaphragm Seismic Baseline Design Forces as per ASCE 7-05*

    Design example 4A: (SDC C EDO)

(1) and (2): Seismic design parameters

Design site:	**Knoxville, TN**
SDC	**C**
S_s	**0.58**
S_1	**0.147**
Soil site class	**C**
F_a	1.17
F_v	1.65
$S_{ms} = F_a \times S_s$	0.68
$S_{m1} = F_v \times S_1$	0.24
$S_{DS} = 2/3 \times S_{ms}$	0.45
$S_{D1} = 2/3 \times S_{m1}$	0.16
N-S/Ordinary RC wall	**R=5, Ω_0=2.5, C_d=4.5**
E-W/ Ordinary RC bearing wall	**R=4, Ω_0=2.5, C_d=4**

(3): Seismic response coefficient C_s

$$T_a = C_t H_n^{3/4} = 0.02 \times 106^{0.75} = 0.661 \sec; \quad T = C_u T_a = 1.58 \times 0.661 = 1.04 \sec$$

N-S direction:

$$C_S = \frac{S_{DS}}{R/I_E} = 0.09, \ C_{S,min} = 0.01, \ C_{S,max} = \frac{S_{D1}}{(R/I_E)T} = \frac{0.16}{5 \times 1.04} = 0.031 \ \underline{\textbf{controls}}$$

E-W direction:

$$C_S = \frac{S_{DS}}{R/I_E} = 0.11, \ C_{S,min} = 0.01, \ C_{S,max} = \frac{S_{D1}}{(R/I_E)T} = \frac{0.16}{4 \times 1.04} = 0.039 \ \underline{\textbf{controls}}$$

(4), (5), (6) and (7):

    Diaphragm maximum design acceleration $C_{dia, \ max}$=max (F_x/w_x) (Eqn.1)

    Diaphragm baseline design force $F_{Dx} = \alpha_x C_{dia, \ max} w_x$ (Eqn.2)

    Note: conservatively α_x =1.0 for all floors.

N-S direction:

	h_x (ft)	W_x (kips)	$W_x h_x^k$	C_{vx}	F_x (kips)	$C_{dia, max}$ (1)	α_x	F_{Dx} (kips) (2)
Roof	106	5000	1874137	0.244	303	0.061	1.0	303
7th	93	5000	1587043	0.207	257	0.061	1.0	303
6th	80	5000	1310645	0.171	212	0.061	1.0	303
5th	67	5000	1046192	0.136	169	0.061	1.0	303
4th	54	5000	795350	0.104	129	0.061	1.0	303
3rd	41	5000	560472	0.073	91	0.061	1.0	303
2nd	28	5000	345200	0.045	56	0.061	1.0	303
1st	15	5000	156167	0.020	25	0.061	1.0	303
Sum		40000	7675206	1	1242			

E-W direction:

	h_x (ft)	W_x (kips)	$W_x h_x^k$	C_{vx}	F_x (kips)	$C_{dia, max}$ (1)	α_x	F_{Dx} (kips) (2)
Roof	106	5000	1874137	0.244	379	0.076	1.0	379
7th	93	5000	1587043	0.207	321	0.076	1.0	379
6th	80	5000	1310645	0.171	265	0.076	1.0	379
5th	67	5000	1046192	0.136	212	0.076	1.0	379
4th	54	5000	795350	0.104	161	0.076	1.0	379
3rd	41	5000	560472	0.073	113	0.076	1.0	379
2nd	28	5000	345200	0.045	70	0.076	1.0	379
1st	15	5000	156167	0.020	32	0.076	1.0	379
Sum		40000	7675206	1	1552			

Design example 4B: (SDC D RDO)

(1) and (2): Seismic design parameters

Design site:	**Seattle, WA**
SDC	**D**
S_s	**1.58**
S_1	**0.55**
Soil site class	**C**
F_a	1.00
F_v	1.30
$S_{ms} = F_a \times S_s$	1.58
$S_{m1} = F_v \times S_1$	0.72
$S_{DS} = 2/3 \times S_{ms}$	1.05
$S_{D1} = 2/3 \times S_{m1}$	0.48
N-S/Special RC wall	**R=6, Ω_0=2.5, C_d=5**
E-W/ Special RC bearing wall	**R=5, Ω_0=2.5, C_d=5**

(3): Seismic response coefficient C_s

$$T_a = C_t H_n^{3/4} = 0.02 \times 106^{0.75} = 0.661 \sec; \quad T = C_u T_a = 1.4 \times 0.661 = 0.925 \sec$$

N-S direction:

$$C_S = \frac{S_{DS}}{R/I_E} = 0.176, \; C_{S,\min} = 0.01, \; C_{S,\max} = \frac{S_{D1}}{(R/I_E)T} = \frac{0.48}{6 \times 0.925} = 0.086 \; \underline{\textbf{controls}}$$

E-W direction:

$$C_S = \frac{S_{DS}}{R/I_E} = 0.211, \; C_{S,\min} = 0.01, \; C_{S,\max} = \frac{S_{D1}}{(R/I_E)T} = \frac{0.48}{5 \times 0.925} = 0.103 \; \underline{\textbf{controls}}$$

(4), (5), (6) and (7):

Diaphragm maximum design acceleration $C_{dia,\,\max}$=max (F_x/w_x) (Eqn.1)
Diaphragm baseline design force $F_{Dx} = \alpha_x C_{dia,\,\max} w_x$ (Eqn.2)

Note: conservatively α_x =1.0 for all floors.

N-S direction:

	h_x (ft)	W_x (kips)	$W_x h_x^k$	C_{vx}	F_x (kips)	$C_{dia,\,\max}$ (1)	α_x	F_{Dx} (kips) (2)
Roof	106	5000	1427723	0.239	820	0.164	1.0	820
7th	93	5000	1218278	0.204	700	0.164	1.0	820
6th	80	5000	1014981	0.170	583	0.164	1.0	820
5th	67	5000	818611	0.137	470	0.164	1.0	820
4th	54	5000	630216	0.105	362	0.164	1.0	820
3rd	41	5000	451298	0.075	259	0.164	1.0	820
2nd	28	5000	284212	0.048	163	0.164	1.0	820
1st	15	5000	133345	0.022	77	0.164	1.0	820
Sum		40000	5978664	1	3435			

E-W direction:

	h_x (ft)	W_x (kips)	$W_x h_x^k$	C_{vx}	F_x (kips)	$C_{dia,\,\max}$ (1)	α_x	F_{Dx} (kips) (2)
Roof	106	5000	1427723	0.239	984	0.197	1.0	984
7th	93	5000	1218278	0.204	840	0.197	1.0	984
6th	80	5000	1014981	0.170	700	0.197	1.0	984
5th	67	5000	818611	0.137	564	0.197	1.0	984
4th	54	5000	630216	0.105	435	0.197	1.0	984
3rd	41	5000	451298	0.075	311	0.197	1.0	984
2nd	28	5000	284212	0.048	196	0.197	1.0	984
1st	15	5000	133345	0.022	92	0.197	1.0	984
Sum		40000	5978664	1	4123			

Step 2: *Determine the Diaphragm Seismic Demand Level*

    Design example 4A: (SDC C EDO)

        For SDC C: **Low**

                      Note: All buildings in SDC C are assigned "Low" Seismic Demand

    Design example 4B: (SDC D RDO)

        n=8>7.5:   **High**

Step 3: *Select Diaphragm Design Option*

    Design example 4A: (SDC C EDO)

        For low seismic demand: **Elastic design option (EDO)**   is recommended

    Design example 4B: (SDC D RDO)

        For high seismic demand: **Reduced design option (RDO)**   is recommended

Step 4: *Determine Required Diaphragm Reinforcement Classification*

    Design example 4A: (SDC C EDO)

        For elastic design option: **Low deformability element (LDE)**

    Design example 4B: (SDC D RDO)

        For reduced design option: **High deformability element (HDE)**

Step 5: *Determine Diaphragm Force Amplification Factor*

    The whole diaphragm is treated as one free-body for diaphragm design as shown in PART 3.

L	=	230 ft
AR	=	230/147= 1.56
n	=	8
L/60-AR	=	2

    Design example 4A: (SDC C EDO)

        Eqn. 3: $\Psi_E = 1.7 \times 8^{0.38}[1 - 0.04(3 - 1.56)^2] \times 1.05^2 = 3.79$

    Design example 4B: (SDC D RDO)

        Eqn. 5: $\Psi_R = 1.05 \times 8^{0.3}[1 - 0.03(2.5 - 1.56)^2] \times 1.05^2 = 2.10$

Step 6: *Determine Diaphragm Shear/Anchorage Overstrength Factor*

    Design example 4A: (SDC C EDO)

        Eqn.6: $\Omega_{vE} = 1.0$

    Design example 4B: (SDC D RDO)

        Eqn.8: $\Omega_{vR} = 1.92\,AR^{-0.18} = 1.92 \times 1.56^{-0.18} = 1.77$

Step 7: *Determine Diaphragm Design Force*
        Inserting the baseline diaphragm forces from Step 1 and the diaphragm amplification factor from Step 5 into Equation 9:

    Design example 4A: (SDC C EDO)

        N-S direction:
            All Floors: $F_{dia} = \Psi_E F_{Dx} = 3.79 \times 303 = 1149$ kips $> 0.2 S_{DS} I w_x = 450$ kips

        E-W direction:
            All Floors: $F_{dia} = \Psi_E F_{Dx} = 3.79 \times 379 = 1437$ kips $> 0.2 S_{DS} I w_x = 450$ kips

    Design example 4B: (SDC D RDO)

        N-S direction:
            All Floors: $F_{dia} = \Psi_R F_{Dx} = 2.1 \times 820 = 1726$ kips $> 0.2 S_{DS} I w_x = 1050$ kips

        E-W direction:
             All Floors: $F_{dia} = \Psi_R F_{Dx} = 2.1 \times 984 = 2071$ kips $> 0.2 S_{DS} I w_x = 1050$ kips

Step 8: *Determine Diaphragm Internal Forces*

    The free-body diagram method (*Option 8b*) is selected to obtain the diaphragm internal forces. Use is made of existing free body diagrams created for common precast diaphragm configurations (See PART 3: *Free Body Diagrams for Typical Precast Parking Structures*). The associate calculations have been embedded in a design spreadsheet program (See PART 3: *Design Aids for Diaphragm Design: Spreadsheet Program*).
    The tables below show the resulting required strength (maximum diaphragm internal forces) at each diaphragm joint (Refer to Fig. A- 23a for joint numbering) and joints between diaphragm to other members (LFRS and internal beam) under transverse and longitudinal directions. Although the effect of two orthogonal direction loadings (transverse and longitudinal) is considered independently, at this step the critical loading direction cannot be explicitly determined because the diaphragm reinforcement selection at step 10 is based on an M-N-V interaction equation (Eqn. 10).

Design example 4A: (SDC C EDO)

Joint between precast floor units

Joint	x	Transverse (N-S) loading			Longitudinal (E-W) loading		
		N_u	V_u	M_u	N_u	V_u	M_u
	[ft]	[kips]	[kips]	[k-ft]	[kips]	[kips]	[k-ft]
1	10	0	525	5497	62	0	0
2	20	0	475	10494	125	0	0
3	30	0	425	14991	187	0	0
4	40	0	375	18988	250	0	0
5	50	0	325	19670	73	0	0
6	60	0	275	19853	-104	0	0
7	70	0	225	19535	-281	0	0
8	80	0	175	21534	-219	0	0
9	90	0	125	23033	-156	0	0
10	100	0	75	24033	-94	0	0
11	110	0	25	24532	-31	0	0

Other Joints (Diaphragm-to-LFRS and Diaphragm-to-internal beam):

Joint	Top Floor					
	Transverse			Longitudinal		
	N_u	V_u	M_u	N_u	V_u	M_u
	[kips]	[kips]	[k-ft]	[kips]	[kips]	[k-ft]
DT-to-N/S Frame	**0**	**575**	**0**	-	-	-
DT-to-E/W Fram	0	57	0	**0**	**359**	**0**
DT-to-IT per DT	**37**	**52**	**-**	-	-	**-**

Note: Critical force demand is marked as bond.

Design example 4B: (SDC D RDO)

Joint between precast floor units

Joint	x	Transverse (N-S) loading			Longitudinal (E-W) loading		
		N_u	V_u	M_u	N_u	V_u	M_u
	[ft]	[kips]	[kips]	[k-ft]	[kips]	[kips]	[k-ft]
1	10	0	788	8253	90	0	0
2	20	0	713	15757	180	0	0
3	30	0	638	22509	270	0	0
4	40	0	563	28512	360	0	0
5	50	0	488	29536	105	0	0
6	60	0	413	29810	-150	0	0
7	70	0	338	29333	-405	0	0
8	80	0	263	32335	-315	0	0
9	90	0	188	34586	-225	0	0
10	100	0	113	36086	-135	0	0
11	110	0	38	36837	-45	0	0

Other Joints (Diaphragm-to-LFRS and Diaphragm-to-internal beam):

Joint	Top Floor					
	Transverse			Longitudinal		
	N_u	V_u	M_u	N_u	V_u	M_u
	[kips]	[kips]	[k-ft]	[kips]	[kips]	[k-ft]
DT-to-N/S Frame	0	431	0	-	-	-
DT-to-E/W Fram	0	86	0	0	518	0
DT-to-IT per DT	56	78	-	-	-	-

Note: Critical force demand is marked as bond.

Step 9: *Select Diaphragm Reinforcement Type Based on DRC*

Diaphragm reinforcement type selected to meet Required Diaphragm Reinforcement Classification (*See Step 4*). Prequalified connectors will be used in this example. Select appropriate diaphragm reinforcement types from PART 2: Table 2A-1.

Design example 4A: (SDC C EDO)

Chord Reinforcement:	**Topped chord**
Shear Reinforcement:	**Standard wwr and hairpin**
Secondary Reinforcement:	**Topped chord**

Design example 4B: (SDC D RDO)

Chord Reinforcement:	**Topped chord**
Shear Reinforcement:	**Ductile ladder and hairpin**
Secondary Reinforcement:	**Topped chord**

Determine Diaphragm Reinforcement Properties: As the diaphragm reinforcement selected is prequalified, the diaphragm reinforcement properties can also be looked up in PART 2: Table 2A-1*:*

Design example 4A: (SDC C EDO)

	k_t / A	k_v / A	t_n / A	v_n / A	δ_{ty}
	k/in/in^2	k/in/in^2	k/in^2	k/in^2	in
Topped chord Gr.60	1234	382	60	24.2	0.0568
Standard ASTM A185 wwr	1414	709	65	39.7	0.039
	k_t	k_v	t_n	v_n	δ_{ty}
	k/in	k/in	k	k	in
Hairpin connector	209	181	9	18.1	0.043

Design example 4B: (SDC D RDO)

	k_t/A k/in/in^2	k_v/A k/in/in^2	t_n/A k/in^2	v_n/A k/in^2	δ_{ty} in
Topped chord Gr.60	1234	382	60	24.2	0.0568
Ductile ladder Gr.1018	1260	216.8	54.2	21.68	0.043
	k_t k/in	k_v k/in	t_n k	v_n k	δ_{ty} in
Hairpin connector	209	181	9	18.1	0.043

Step 10: *Design the Diaphragm Reinforcement at Joints*

Use the interaction equation (Eqn. 10) to determine the required diaphragm reinforcement:

$$M - N - V = \sqrt{\left(\frac{|M_u|}{\phi_f M_n} + \frac{N_u}{\phi_f N_n} \right)^2 + \left(\frac{\Omega V_u}{\phi_v V_n} \right)^2} \leq 1.0$$

Insert the diaphragm joint required strength values (M_u, N_u and V_u) from Step 8.

The diaphragm joint nominal design strength (M_n, N_n and V_n) is based on v_n and t_n from Step 9.

- An analytically-based procedure from PART 3 is used for determining the moment strength at precast floor unit to precast floor unit joint. Triangle force distribution is used for determining the moment strength at other joints (diaphragm-to-LFRS joint and diaphragm-to-internal beam joint) (See PART 3).

- Using Eqn. 28, 29, 34 for the joint between precast floor units and Eqn. 35 for the joint between LFRS/beam and precast floor unit in Sec. 3.3 of PART 3 to determine the diaphragm joint strength.

- Selection of a trial design is greatly facilitated through the use of spreadsheet methods (See PART 3).

Primary diaphragm reinforcement design

(1) Chord and shear reinforcement design

Diaphragm chord and shear reinforcement final design is shown below for each Design Option. The M-N-V for each direction is shown in the table with the critical value marked as bold.

Design example 4A: (SDC C EDO)

Joint	Chord		Hairpin		wwr W2.9 x W2.9		M-N-V	
#	Size	#	#	Spacing (ft)	Area (in^2)	10″ x ″	N-S	E-W
1	#6	5	27	5.4	0.029	12	**0.92**	0.09
2	#6	5	27	5.4	0.029	12	**0.89**	0.19
3	#6	5	27	5.4	0.029	12	**0.90**	0.28
4	#6	5	27	5.4	0.029	12	**0.92**	0.38
5	#6	5	27	5.4	0.029	12	**0.88**	0.11
6	#6	5	27	5.4	0.029	12	**0.84**	0.16
7	#6	5	27	5.4	0.029	12	**0.78**	0.42
8	#6	5	27	5.4	0.029	12	**0.81**	0.33
9	#6	5	27	5.4	0.029	12	**0.83**	0.24
10	#6	5	27	5.4	0.029	12	**0.85**	0.14
11	#6	5	27	5.4	0.029	12	**0.86**	0.05

Design example 4B: (SDC D RDO)

Joint	Chord		Hairpin		Ductile ladder W4.9 x W4.9 *		M-N-V	
#	Size	#	#	Spacing (ft)	Area (in^2)	10″ x ″	N-S	E-W
1	#8	12	48	3.0	0.049	0.5	**1.00**	0.04
2	#8	12	48	3.0	0.049	0.5	**0.91**	0.09
3	#8	10	39	3.7	0.049	0.5	**0.97**	0.14
4	#8	10	39	3.7	0.049	0.5	**0.87**	0.19
5	#8	10	39	3.7	0.049	0.5	**0.77**	0.06
6	#8	7	30	4.8	0.049	1	**0.97**	0.13
7	#8	7	30	4.8	0.049	1	**0.82**	0.34
8	#8	7	30	4.8	0.049	1	**0.71**	0.26
9	#8	5	15	10.0	0.049	1	**0.88**	0.25
10	#8	5	15	10.0	Not provided		**1.07**	0.25
11	#8	5	15	10.0	Not provided		**0.97**	0.08

* wwr W2.9xW2.9: 12″x12″ is provided within the projection of the panel for temperature and shrinkage.

(2) LFRS-to-diaphragm connection and collector design

Design example 4A: (SDC C EDO)

Check $\Psi_E \times \Omega_{vE} = 3.79 \times 1.0 = 3.79 > \Omega_o = 2.5$ **OK**

Anchorage design	length	V_u	N_u	M_u	v_n *	t_n *	Req'd conn	Provide
	[ft]	[kips]	[kips]	[k-ft]	[kips]	[kips]	Per LFRS	#7 bar
NS frame	49	575	0	0	14.52	36	46.6	47
EW frame	30	359	0	0	14.52	36	29.1	30

* Tension and shear nominal strength of #7 rebar.

Diaphragm collector reinforcement:
Collector reinforcement is designed to resistant the same shear demand as the anchorage of shear wall:

$$A_s = \Omega V_u / \phi f_y = 1.0 \times 575 / 2 / 0.9 / 60 = 5.32 \text{ in}^2$$

Choose 9#7 (5.4 in^2) at each face of exterior wall

Design example 4B: (SDC D RDO)

Check $\Psi_E \times \Omega_{vE} = 2.1 \times 1.77 = 3.72 > \Omega_o = 2.5$ **OK**

Anchorage design	length [ft]	V_u [kips]	N_u [kips]	M_u [k-ft]	v_n * [kips]	t_n * [kips]	Req'd conn Per LFRS	Provide #9 bar
NS frame	30	431	0	0	24.2	60	37.2	38
EW frame	30	518	0	0	24.2	60	44.6	45

* Tension and shear nominal strength of #9 rebar.

Diaphragm collector reinforcement:
Collector reinforcement is designed to resistant the same shear demand as the anchorage of shear wall:
$$A_s = \Omega V_u / \phi f_y = 1.77 \times 431 / 0.9 / 60 = 14.1 \text{ in}^2$$

Choose 14#9 (14.0 in^2) at each face of exterior wall

Secondary diaphragm reinforcement

Design example 4A: (SDC C EDO)

(1) Internal beam joint design

Internal beam joint design	V_u [kips]	N_u [kips]	M_u [k-ft]	v_n * [kips]	t_n * [kips]	Req'd conn Per DT panel	Provide #7 bar
Top floor	52	0	0	14.52	36	4.4	5 per panel

* Tension and shear nominal strength of #7 rebar.

(2) Spandrel to diaphragm connector

Use 2#5 rebar per precast floor unit.

Design example 4B: (SDC D RDO)

(3) Internal beam joint design

Internal beam joint design	V_u [kips]	N_u [kips]	M_u [k-ft]	v_n * [kips]	t_n * [kips]	Req'd conn Per DT panel	Provide #9 bar
Top floor	78	0	0	24.2	60	6.8	7 per panel

* Tension and shear nominal strength of #9 rebar.

(4) Spandrel to diaphragm connector

Use 2#5 rebar per precast floor unit.

Step 11: *Determine the diaphragm effective elastic modulus and shear modulus*

The diaphragm joint effective elastic Young's modulus (E_{eff}) and effective shear modulus (G_{eff}) are calculated using the analytical based procedure (see "Diaphragm Joint Stiffness Calculation" in PART 3). E_{eff} and G_{eff} will be used in step 12 for calculating the diaphragm induced drift. These values can be calculated in a spreadsheet at the same time as the diaphragm reinforcement is selected. An average of the maximum and minimum values at any joint is suggested in design as shown in the bottom row of tables below. (See Appendix for tables output per joint.)

Design example 4A: (SDC C EDO)

Joint	E_{eff} [ksi]	G_{eff} [ksi]
Min	1090	177
Max	1090	177
Ave	1090	177
Des	1090	177

Design example 4B: (SDC D RDO)

Joint	E_{eff} [ksi]	G_{eff} [ksi]
Min	1023	141
Max	2116	537
Ave	1482	301
Des	1569	339

Step 12: *Check the diaphragm induced gravity column drift*

The following tables show the diaphragm induced gravity column drift at the midspan column j obtained from the spreadsheet design program in PART 3).

Design example 4A: (SDC C EDO)

Floor	C_Δ	$C_{d,dia}$	$C_{r,dia}$	$\delta_{dia,el}$ [in]	δ_{dia} [in]	θ_{dia} [rad]
Top	1.02	1.02	0.91	0.401	0.410	0.0024

Design example 4B: (SDC D RDO)

Floor	C_Δ	$C_{d,dia}$	$C_{r,dia}$	$\delta_{dia,el}$ [in]	δ_{dia} [in]	θ_{dia} [rad]
Top	1.04	3.01	0.83	0.368	1.107	0.0059

For all design examples, the maximum diaphragm induced gravity column drift (θ_{dia}) is less than 0.01, **OK**

Resulting Designs: Example 4A: (SDC C EDO)

2 # 7 per panel

30 # 7

5#6 chord

27 Hairpin @ 5.4'

5 # 7 per panel

9#7 collector

47 # 7

2#3 collector

wwr W2.9xW2.9: 12"x12" Typ.
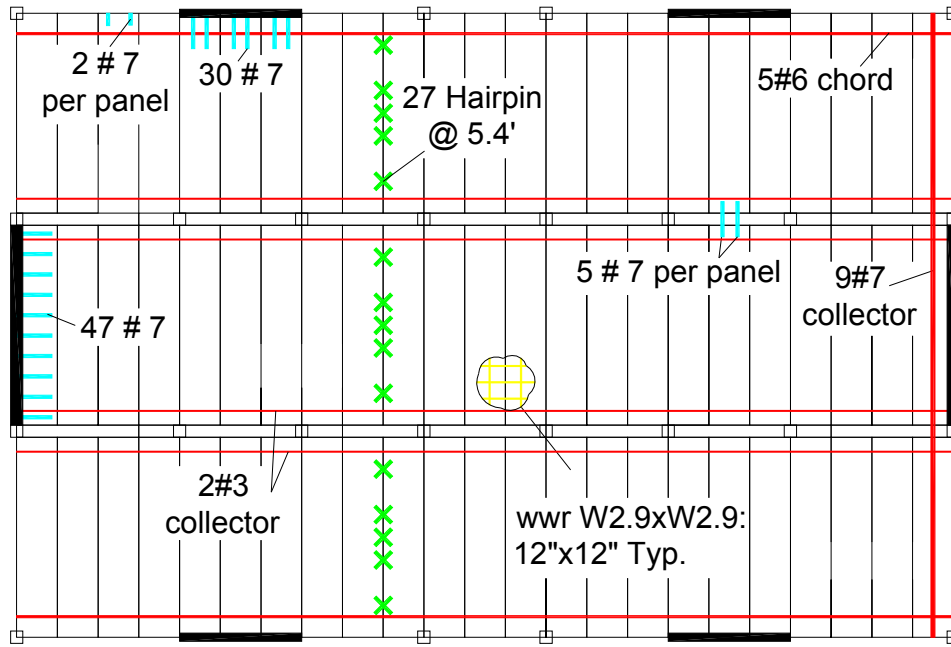
Fig. A-24. Diaphragm reinforcement for example 4A.

Resulting Designs: Example 4B: (SDC D RDO)

Hairpin Connector

Ductile Ladder: W4.9x4.9

48 @3'	39 @3.7'	30 @4.8'	15 @10'

10"x12" **10"x6"**

45 # 9

Chord: 5#8   7#8   10#8 12 #8

38 # 9

Ductile Ladder

7 # 9 per panel

14#9 collector

2#3 collector

wwr W2.9xW2.9 12"x12" in panel

2 # 9 per panel
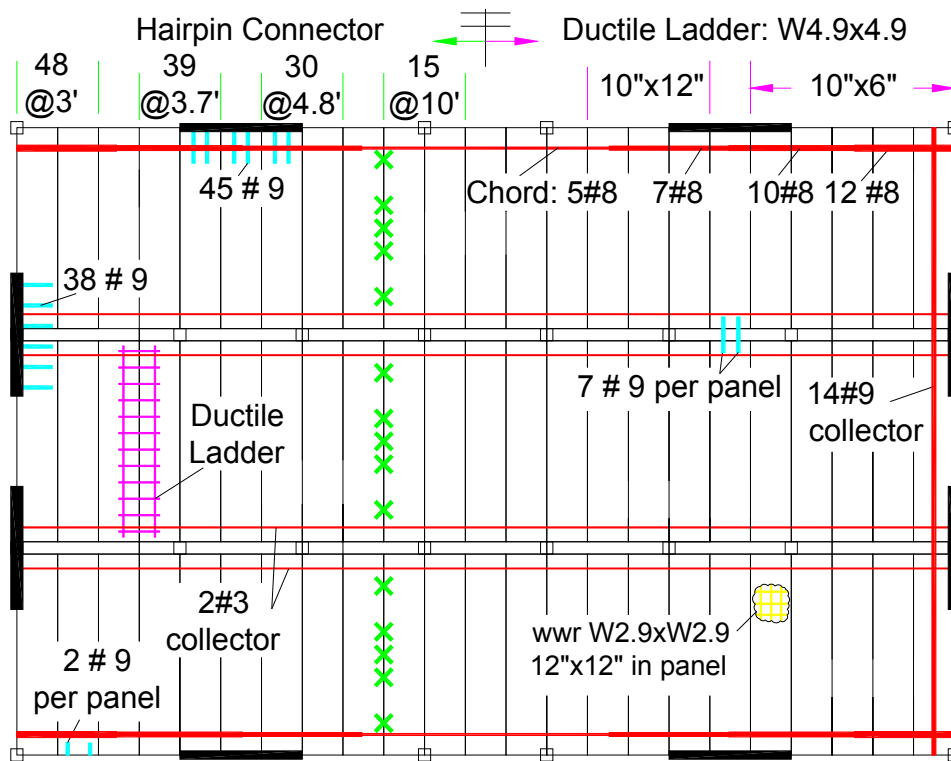
Fig. A-25. Diaphragm reinforcement for example 4B.

APPENDIX B: Diaphragm Internal Force Diagrams and Tables for APPENIX A

Using free-body diagram method to get the diaphragm internal forces (See "Free Body Diagrams for Typical Precast Parking Structures" in PART 3). The following diagrams and tables are obtained from the spreadsheet program (see "Design Aids for Diaphragm Design: Spreadsheet Program" in PART 3).

Design example 1A: (EDO)

North/South flat under transverse loading:
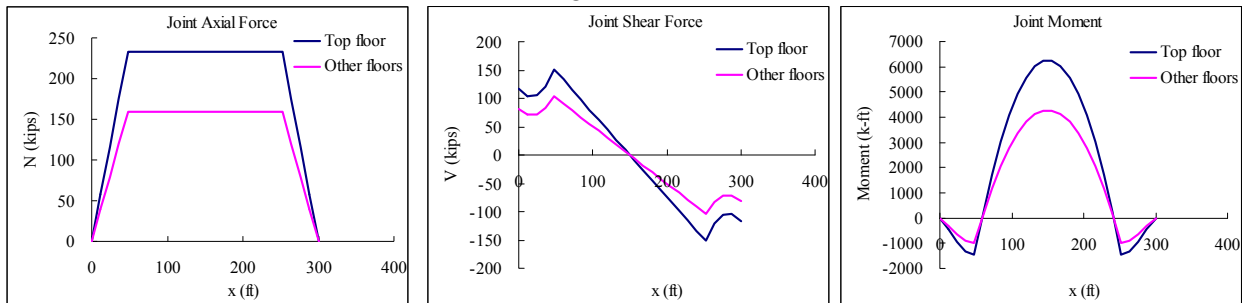
Fig. B-1. Diaphragm internal forces North/South flat under transverse loading for example 1A.

North/South flat under longitudinal loading:
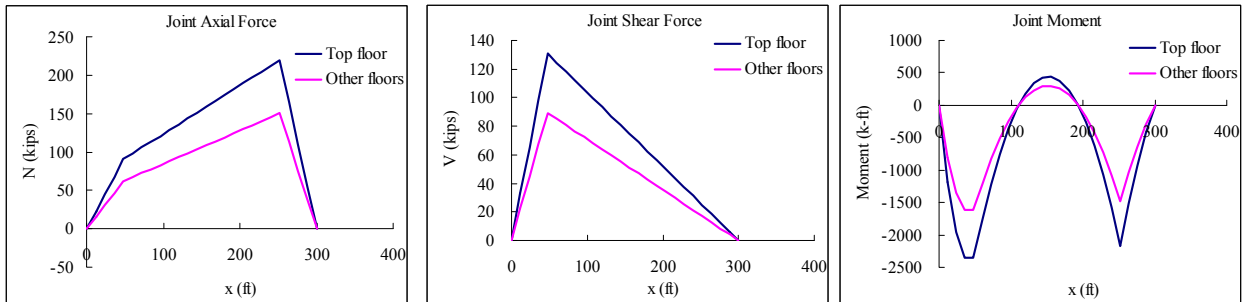
Fig. B-2. Diaphragm internal forces North/South flat under longitudinal loading for example 1A.

Ramp Loading: Axial force longitudinal loading; Shear and Moment under transverse loading:
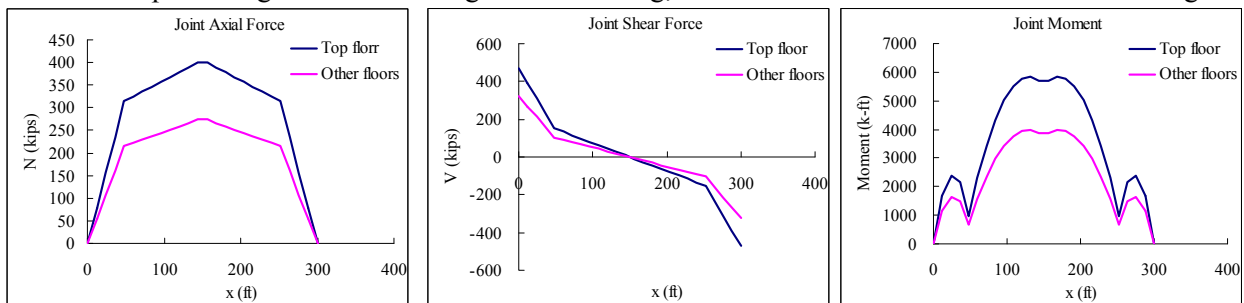
Fig. B-3. Diaphragm Ramp internal forces, example 1A: (a) axial under longitudinal loading; (b) shear under transverse loading; (c) moment under transverse loading.

Table B-1. Diaphragm internal forces for Example 1A.

x	Transverse (NS) Direction												Longitudinal (EW) Direction											
	N/S Flat-Top floor			Ramp-Top floor			N/S Flat-Other floors			Ramp-Other floors			Ramp-Top floor			Ramp-other floors			N/S Flat-Top floor			N/S Flat-Other floors		
	N	V	M	N	V	M	N	V	M	N	V	M	N	V	M	N	V	M	N	V	M	N	V	M
[ft]	[kips]	[kips]	[k-ft]	[kips]	[kips]	[k-ft]	[kips]	[kips]	[k-ft]	[kips]	[kips]	[k-ft]	[kips]	[kips]	[k-ft]	[kips]	[kips]	[k-ft]	[kips]	[kips]	[k-ft]	[kips]	[kips]	[k-ft]
12	58	104	-430	0	390	1674	40	71	-294	0	267	1144	78	0	0	54	0	0	23	33	-1177	15	22	-805
24	116	105	-935	0	311	2391	79	72	-640	0	212	1635	157	0	0	107	0	0	45	65	-1962	31	45	-1342
36	174	121	-1339	0	231	2153	119	83	-916	0	158	1472	235	0	0	161	0	0	68	98	-2355	46	67	-1610
48	232	151	-1466	0	151	958	159	103	-1002	0	103	655	314	0	0	215	0	0	90	131	-2355	62	89	-1610
60	232	133	242	0	133	2297	159	91	166	0	91	1570	325	0	0	222	0	0	98	125	-1746	67	85	-1194
72	232	116	1737	0	116	3422	159	79	1188	0	79	2340	336	0	0	229	0	0	106	118	-1212	72	81	-828
84	232	98	3018	0	98	4334	159	67	2064	0	67	2963	346	0	0	237	0	0	113	112	-752	77	77	-514
96	232	80	4086	0	80	5032	159	55	2794	0	55	3441	357	0	0	244	0	0	121	106	-367	83	72	-251
108	232	62	4940	0	62	5516	159	43	3378	0	43	3772	368	0	0	252	0	0	128	100	-57	88	68	-39
120	232	44	5580	0	44	5787	159	30	3816	0	30	3957	379	0	0	259	0	0	136	93	178	93	64	122
132	232	27	6007	0	27	5845	159	18	4108	0	18	3997	389	0	0	266	0	0	144	87	339	98	60	232
144	232	9	6221	0	9	5689	159	6	4254	0	6	3890	400	0	0	274	0	0	151	81	424	103	55	290
156	232	-9	6221	0	-9	5689	159	-6	4254	0	-6	3890	400	0	0	274	0	0	159	75	435	109	51	298
168	232	-27	6007	0	-27	5845	159	-18	4108	0	-18	3997	389	0	0	266	0	0	167	69	372	114	47	254
180	232	-44	5580	0	-44	5787	159	-30	3816	0	-30	3957	379	0	0	259	0	0	174	62	233	119	43	159
192	232	-62	4940	0	-62	5516	159	-43	3378	0	-43	3772	368	0	0	252	0	0	182	56	20	124	38	14
204	232	-80	4086	0	-80	5032	159	-55	2794	0	-55	3441	357	0	0	244	0	0	189	50	-268	129	34	-183
216	232	-98	3018	0	-98	4334	159	-67	2064	0	-67	2963	346	0	0	237	0	0	197	44	-631	135	30	-431
228	232	-116	1737	0	-116	3422	159	-79	1188	0	-79	2340	336	0	0	229	0	0	205	37	-1069	140	26	-731
240	232	-133	242	0	-133	2297	159	-91	166	0	-91	1570	325	0	0	222	0	0	212	31	-1581	145	21	-1081
252	232	-151	-1466	0	-151	958	159	-103	-1002	0	-103	655	314	0	0	215	0	0	220	25	-2168	150	17	-1482
264	174	-121	-1339	0	-231	2153	119	-83	-916	0	-158	1472	235	0	0	161	0	0	165	19	-1514	113	13	-1035
276	116	-105	-935	0	-311	2391	79	-72	-640	0	-212	1635	157	0	0	107	0	0	110	12	-934	75	9	-639
288	58	-104	-430	0	-390	1674	40	-71	-294	0	-267	1144	78	0	0	54	0	0	55	6	-430	38	4	-294

Design example 1B: (BDO)

North/South flat under transverse loading:
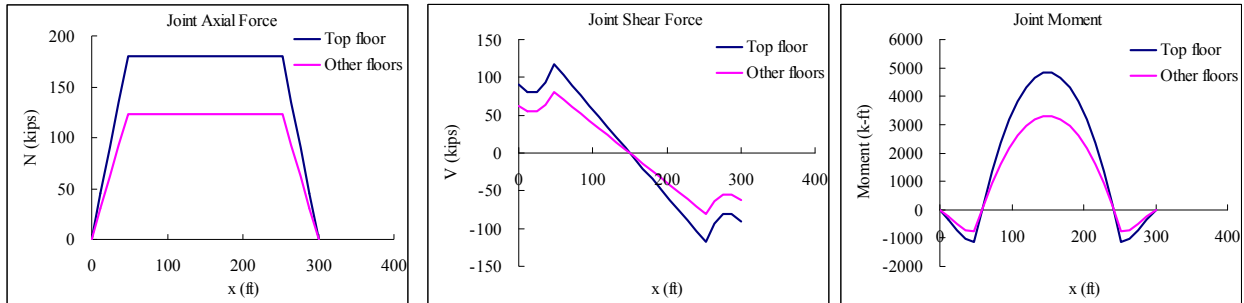
Fig. B-4. Diaphragm internal forces North/South flat under transverse loading for example 1B.

North/South flat under longitudinal loading:
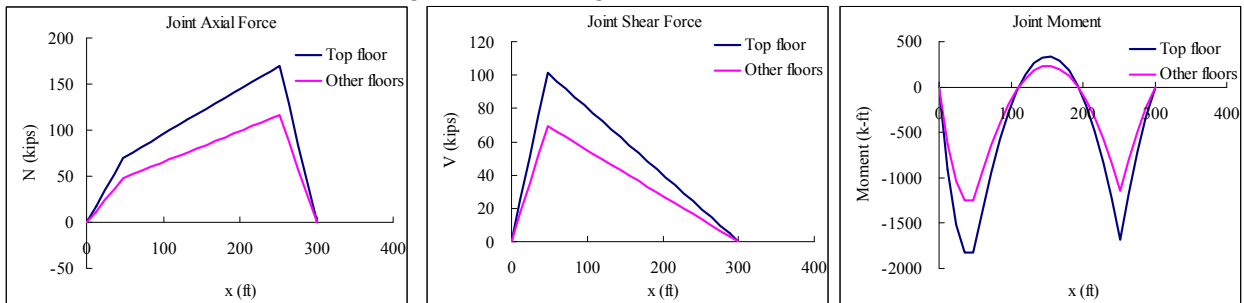
Fig. B-5. Diaphragm internal forces North/South flat under longitudinal loading for example 1B.

Ramp under transverse loading:
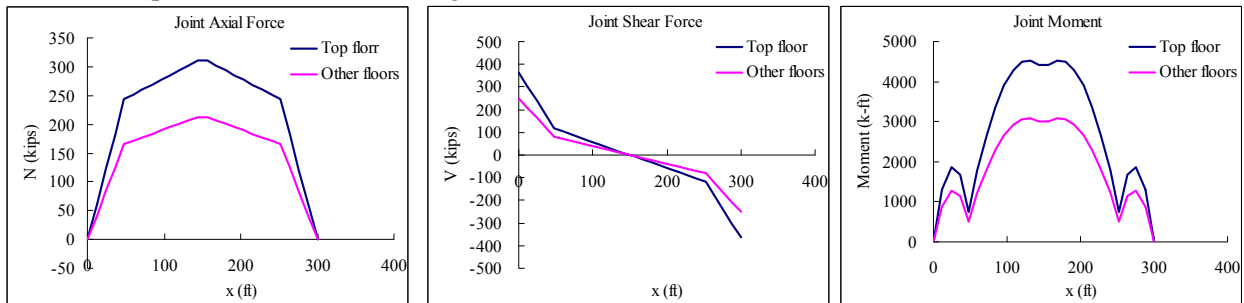
Fig. B-6. Diaphragm Ramp internal forces, example 1B: (a) axial under longitudinal loading; (b) shear under transverse loading; (c) moment under transverse loading.

Table B-2. Diaphragm internal forces for Example 1B.

x	Transverse (NS) Direction												Longitudinal (EW) Direction												
	N/S Flat-Top floor			Ramp-Top floor			N/S Flat-Other floors			Ramp-Other floors			Ramp-Top floor			Ramp-other floors			N/S Flat-Top floor			N/S Flat-Other floors		
	N	V	M	N	V	M	N	V	M	N	V	M	N	V	M	N	V	M	N	V	M	N	V	M
[ft]	[kips]	[kips]	[k-ft]	[kips]	[kips]	[k-ft]	[kips]	[kips]	[k-ft]	[kips]	[kips]	[k-ft]	[kips]	[kips]	[k-ft]	[kips]	[kips]	[k-ft]	[kips]	[kips]	[k-ft]	[kips]	[kips]	[k-ft]
12	0	91	0	0	364	0	0	62	0	0	249	0	0	0	0	0	0	0	0	0	0	0	0	0
24	45	80	-333	0	302	1297	31	55	-228	0	207	887	61	0	0	42	0	0	18	25	-912	12	17	-624
36	90	81	-725	0	241	1853	62	56	-496	0	165	1267	122	0	0	83	0	0	35	51	-1520	24	35	-1040
48	135	94	-1038	0	179	1668	92	64	-709	0	122	1140	182	0	0	125	0	0	53	76	-1825	36	52	-1248
60	180	117	-1136	0	117	742	123	80	-776	0	80	508	243	0	0	166	0	0	70	101	-1825	48	69	-1248
72	180	103	188	0	103	1779	123	71	128	0	71	1217	252	0	0	172	0	0	76	97	-1353	52	66	-925
84	180	90	1346	0	90	2651	123	61	920	0	61	1813	260	0	0	178	0	0	82	92	-939	56	63	-642
96	180	76	2338	0	76	3358	123	52	1599	0	52	2296	268	0	0	183	0	0	88	87	-583	60	59	-398
108	180	62	3166	0	62	3898	123	42	2165	0	42	2666	277	0	0	189	0	0	94	82	-284	64	56	-195
120	180	48	3827	0	48	4274	123	33	2617	0	33	2922	285	0	0	195	0	0	100	77	-44	68	53	-30
132	180	34	4323	0	34	4484	123	24	2956	0	24	3066	293	0	0	201	0	0	105	72	138	72	50	94
144	180	21	4654	0	21	4529	123	14	3183	0	14	3097	302	0	0	206	0	0	111	68	262	76	46	179
156	180	7	4820	0	7	4408	123	5	3296	0	5	3014	310	0	0	212	0	0	117	63	329	80	43	225
168	180	-7	4820	0	-7	4408	123	-5	3296	0	-5	3014	310	0	0	212	0	0	123	58	337	84	40	231
180	180	-21	4654	0	-21	4529	123	-14	3183	0	-14	3097	302	0	0	206	0	0	129	53	288	88	36	197
192	180	-34	4323	0	-34	4484	123	-24	2956	0	-24	3066	293	0	0	201	0	0	135	48	181	92	33	123
204	180	-48	3827	0	-48	4274	123	-33	2617	0	-33	2922	285	0	0	195	0	0	141	43	15	96	30	10
216	180	-62	3166	0	-62	3898	123	-42	2165	0	-42	2666	277	0	0	189	0	0	147	39	-208	100	26	-142
228	180	-76	2338	0	-76	3358	123	-52	1599	0	-52	2296	268	0	0	183	0	0	153	34	-489	104	23	-334
240	180	-90	1346	0	-90	2651	123	-61	920	0	-61	1813	260	0	0	178	0	0	159	29	-828	108	20	-566
252	180	-103	188	0	-103	1779	123	-71	128	0	-71	1217	252	0	0	172	0	0	164	24	-1225	112	17	-838
264	180	-117	-1136	0	-117	742	123	-80	-776	0	-80	508	243	0	0	166	0	0	170	19	-1680	116	13	-1149
276	135	-94	-1038	0	-179	1668	92	-64	-709	0	-122	1140	182	0	0	125	0	0	128	14	-1173	87	10	-802
288	90	-81	-725	0	-241	1853	62	-56	-496	0	-165	1267	122	0	0	83	0	0	85	10	-724	58	7	-495

Design example 1C: (RDO)

North/South flat under transverse loading:
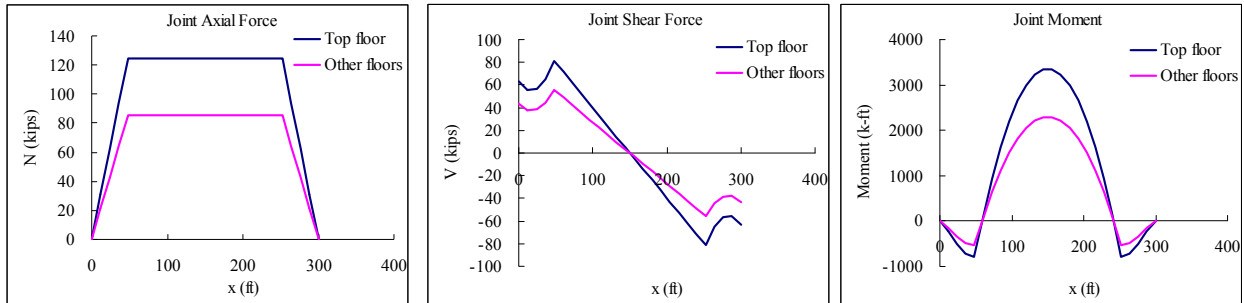
Fig. B-7. Diaphragm internal forces North/South flat under transverse loading for example 1C.

North/South flat under longitudinal loading:
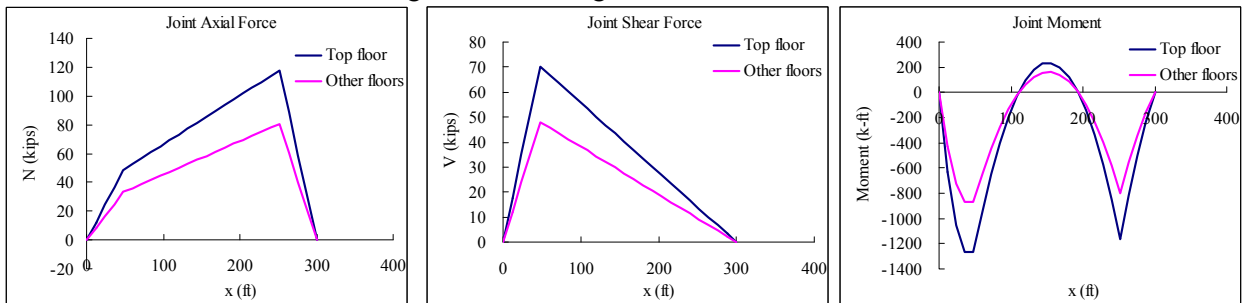
Fig. B-8. Diaphragm internal forces North/South flat under longitudinal loading for example 1C.

Ramp under transverse loading:
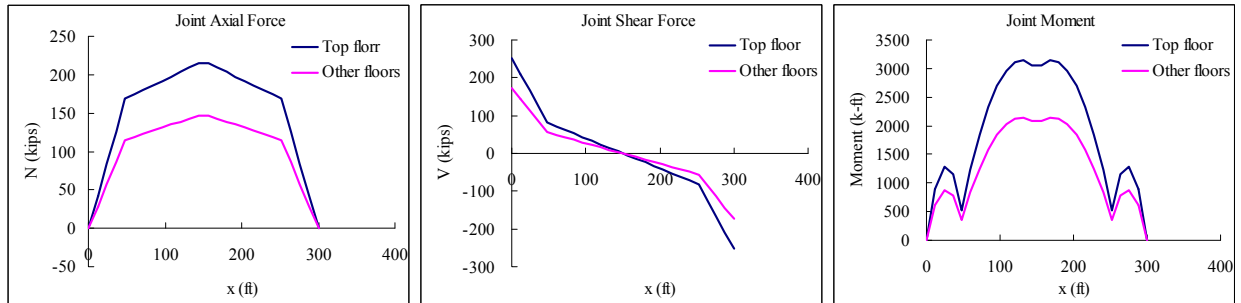
Fig. B-9. Diaphragm Ramp internal forces, example 1A: (a) axial under longitudinal loading; (b) shear under transverse loading; (c) moment under transverse loading.

Table B-3. Diaphragm internal forces for Example 1C.

x	Transverse (NS) Direction												Longitudinal (EW) Direction											
	N/S Flat-Top floor			Ramp-Top floor			N/S Flat-Other floors			Ramp-Other floors			Ramp-Top floor			Ramp-other floors			N/S Flat-Top floor			N/S Flat-Other floors		
	N	V	M	N	V	M	N	V	M	N	V	M	N	V	M	N	V	M	N	V	M	N	V	M
[ft]	[kips]	[kips]	[k-ft]	[kips]	[kips]	[k-ft]	[kips]	[kips]	[k-ft]	[kips]	[kips]	[k-ft]	[kips]	[kips]	[k-ft]	[kips]	[kips]	[k-ft]	[kips]	[kips]	[k-ft]	[kips]	[kips]	[k-ft]
12	0	63	0	0	252	0	0	43	0	0	173	0	0	0	0	0	0	0	0	0	0	0	0	0
24	31	56	-231	0	210	899	21	38	-158	0	143	615	42	0	0	29	0	0	12	18	-632	8	12	-432
36	62	56	-502	0	167	1284	43	39	-343	0	114	878	84	0	0	58	0	0	24	35	-1054	17	24	-721
48	94	65	-719	0	124	1156	64	44	-492	0	85	790	126	0	0	86	0	0	36	53	-1264	25	36	-865
60	125	81	-787	0	81	514	85	56	-538	0	56	352	169	0	0	115	0	0	49	70	-1264	33	48	-865
72	125	72	130	0	72	1233	85	49	89	0	49	843	174	0	0	119	0	0	53	67	-937	36	46	-641
84	125	62	933	0	62	1837	85	42	638	0	42	1256	180	0	0	123	0	0	57	64	-651	39	43	-445
96	125	53	1621	0	53	2327	85	36	1108	0	36	1591	186	0	0	127	0	0	61	60	-404	42	41	-276
108	125	43	2194	0	43	2702	85	29	1500	0	29	1847	192	0	0	131	0	0	65	57	-197	44	39	-135
120	125	33	2652	0	33	2962	85	23	1814	0	23	2025	198	0	0	135	0	0	69	54	-31	47	37	-21
132	125	24	2996	0	24	3108	85	16	2049	0	16	2125	203	0	0	139	0	0	73	50	96	50	34	65
144	125	14	3226	0	14	3139	85	10	2206	0	10	2146	209	0	0	143	0	0	77	47	182	53	32	124
156	125	5	3340	0	5	3055	85	3	2284	0	3	2089	215	0	0	147	0	0	81	43	228	56	30	156
168	125	-5	3340	0	-5	3055	85	-3	2284	0	-3	2089	215	0	0	147	0	0	85	40	234	58	27	160
180	125	-14	3226	0	-14	3139	85	-10	2206	0	-10	2146	209	0	0	143	0	0	89	37	200	61	25	136
192	125	-24	2996	0	-24	3108	85	-16	2049	0	-16	2125	203	0	0	139	0	0	94	33	125	64	23	86
204	125	-33	2652	0	-33	2962	85	-23	1814	0	-23	2025	198	0	0	135	0	0	98	30	11	67	21	7
216	125	-43	2194	0	-43	2702	85	-29	1500	0	-29	1847	192	0	0	131	0	0	102	27	-144	70	18	-98
228	125	-53	1621	0	-53	2327	85	-36	1108	0	-36	1591	186	0	0	127	0	0	106	23	-339	72	16	-232
240	125	-62	933	0	-62	1837	85	-42	638	0	-42	1256	180	0	0	123	0	0	110	20	-574	75	14	-392
252	125	-72	130	0	-72	1233	85	-49	89	0	-49	843	174	0	0	119	0	0	114	17	-849	78	11	-580
264	125	-81	-787	0	-81	514	85	-56	-538	0	-56	352	169	0	0	115	0	0	118	13	-1164	81	9	-796
276	94	-65	-719	0	-124	1156	64	-44	-492	0	-85	790	126	0	0	86	0	0	89	10	-813	61	7	-556
288	62	-56	-502	0	-167	1284	43	-39	-343	0	-114	878	84	0	0	58	0	0	59	7	-502	40	5	-343

Design example 2A: (EDO)

North/South flat under transverse loading:
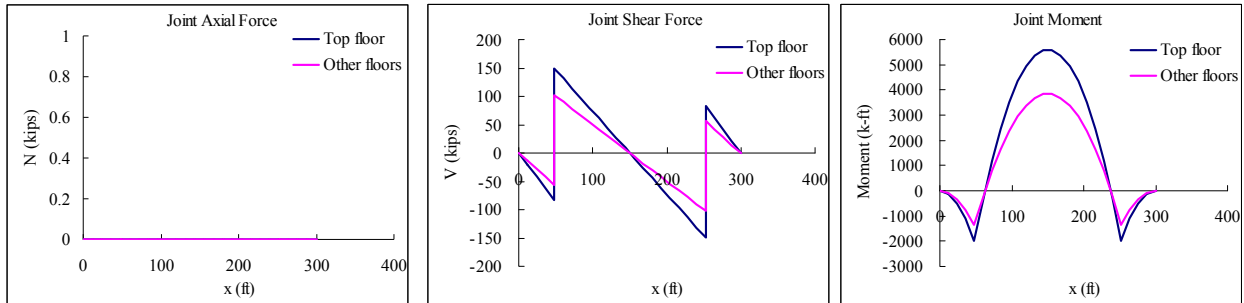
Fig. B-10. Diaphragm internal forces North/South flat under transverse loading for example 2A.

North/South flat under longitudinal loading:
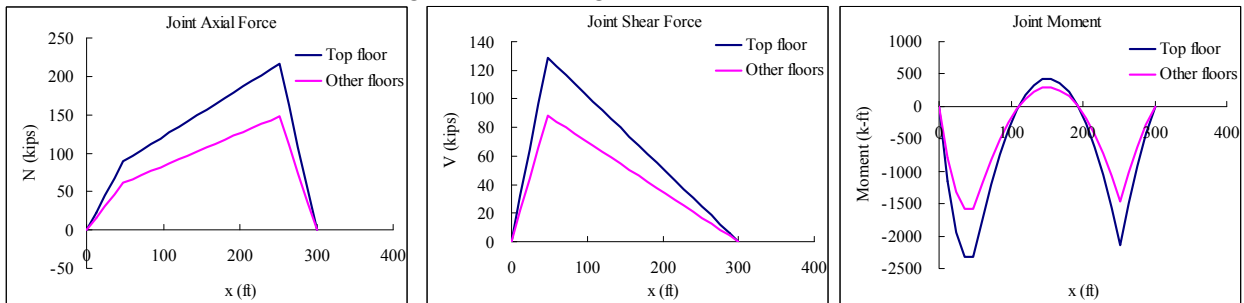
Fig. B-11. Diaphragm internal forces North/South flat under longitudinal loading for example 2A.

Ramp Loading: Axial force longitudinal loading; Shear and Moment under transverse loading:
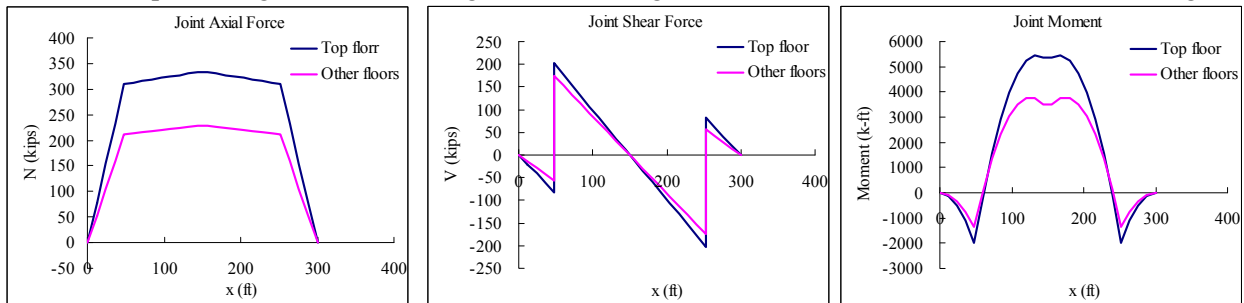
Fig. B-12. Diaphragm Ramp internal forces, example 2A: (a) axial under longitudinal loading; (b) shear under transverse loading; (c) moment under transverse loading.

Table B-4. Diaphragm internal forces for Example 2A.

x	Transverse (NS) Direction												Longitudinal (EW) Direction											
	N/S Flat-Top floor			Ramp-Top floor			N/S Flat-Other floors			Ramp-Other floors			Ramp-Top floor			Ramp-other floors			N/S Flat-Top floor			N/S Flat-Other floors		
	N	V	M	N	V	M	N	V	M	N	V	M	N	V	M	N	V	M	N	V	M	N	V	M
[ft]	[kips]	[kips]	[k-ft]	[kips]	[kips]	[k-ft]	[kips]	[kips]	[k-ft]	[kips]	[kips]	[k-ft]	[kips]	[kips]	[k-ft]	[kips]	[kips]	[k-ft]	[kips]	[kips]	[k-ft]	[kips]	[kips]	[k-ft]
12	0	-21	-124	0	-21	-124	0	-14	-85	0	-14	-85	77	0	0	53	0	0	22	32	-1161	15	22	-794
24	0	-41	-495	0	-41	-495	0	-28	-339	0	-28	-339	155	0	0	106	0	0	45	64	-1934	30	44	-1323
36	0	-62	-1114	0	-62	-1114	0	-42	-762	0	-42	-762	232	0	0	159	0	0	67	97	-2321	46	66	-1587
48	0	149	-1981	0	202	-1981	0	102	-1354	0	174	-1354	309	0	0	212	0	0	89	129	-2321	61	88	-1587
60	0	132	-297	0	178	-67	0	90	-203	0	153	112	313	0	0	214	0	0	97	123	-1721	66	84	-1177
72	0	114	1176	0	154	1562	0	78	804	0	133	1332	316	0	0	216	0	0	104	117	-1194	71	80	-817
84	0	96	2439	0	131	2906	0	66	1668	0	113	2307	319	0	0	218	0	0	112	111	-741	76	76	-507
96	0	79	3491	0	107	3966	0	54	2387	0	92	3036	322	0	0	220	0	0	119	104	-362	81	71	-247
108	0	61	4333	0	83	4741	0	42	2963	0	72	3520	325	0	0	222	0	0	127	98	-56	87	67	-39
120	0	44	4964	0	59	5231	0	30	3394	0	51	3759	328	0	0	224	0	0	134	92	176	92	63	120
132	0	26	5385	0	36	5436	0	18	3682	0	31	3752	331	0	0	226	0	0	142	86	334	97	59	228
144	0	9	5596	0	12	5357	0	6	3826	0	10	3500	334	0	0	228	0	0	149	80	418	102	55	286
156	0	-9	5596	0	-12	5357	0	-6	3826	0	-10	3500	334	0	0	228	0	0	157	74	429	107	50	293
168	0	-26	5385	0	-36	5436	0	-18	3682	0	-31	3752	331	0	0	226	0	0	164	68	366	112	46	250
180	0	-44	4964	0	-59	5231	0	-30	3394	0	-51	3759	328	0	0	224	0	0	172	61	230	117	42	157
192	0	-61	4333	0	-83	4741	0	-42	2963	0	-72	3520	325	0	0	222	0	0	179	55	20	123	38	13
204	0	-79	3491	0	-107	3966	0	-54	2387	0	-92	3036	322	0	0	220	0	0	187	49	-264	128	34	-181
216	0	-96	2439	0	-131	2906	0	-66	1668	0	-113	2307	319	0	0	218	0	0	194	43	-622	133	29	-425
228	0	-114	1176	0	-154	1562	0	-78	804	0	-133	1332	316	0	0	216	0	0	202	37	-1053	138	25	-720
240	0	-132	-297	0	-178	-67	0	-90	-203	0	-153	112	313	0	0	214	0	0	209	31	-1558	143	21	-1066
252	0	-149	-1981	0	-202	-1981	0	-102	-1354	0	-174	-1354	309	0	0	212	0	0	217	25	-2137	148	17	-1461
264	0	62	-1114	0	62	-1114	0	42	-762	0	42	-762	232	0	0	159	0	0	162	18	-1492	111	13	-1020
276	0	41	-495	0	41	-495	0	28	-339	0	28	-339	155	0	0	106	0	0	108	12	-921	74	8	-630
288	0	21	-124	0	21	-124	0	14	-85	0	14	-85	77	0	0	53	0	0	54	6	-424	37	4	-290

Design example 2B: (RDO)

North/South flat under transverse loading:
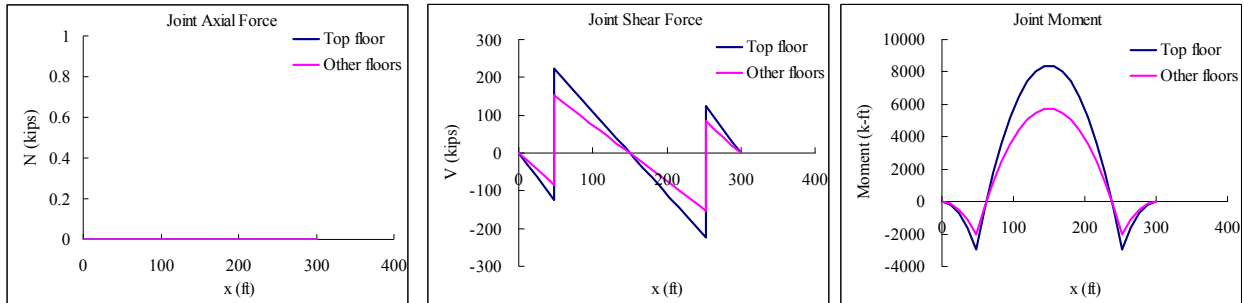
Fig. B-13. Diaphragm internal forces North/South flat under transverse loading for example 2B.

North/South flat under longitudinal loading:
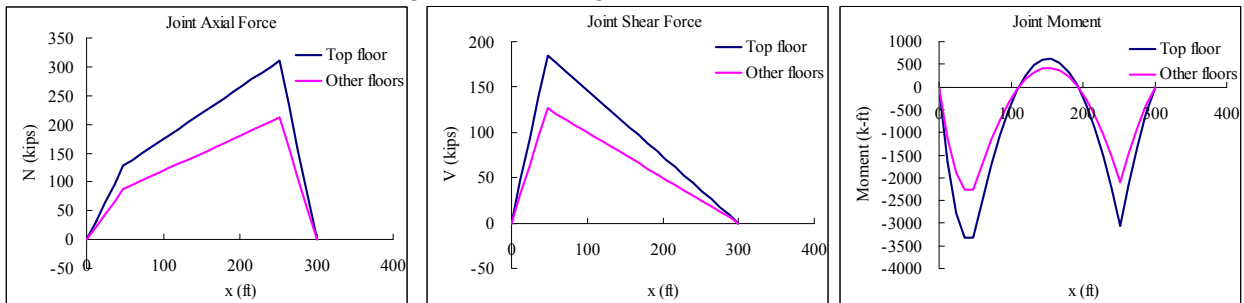
Fig. B-14. Diaphragm internal forces North/South flat under longitudinal loading for example 2B.

Ramp Loading: Axial force longitudinal loading; Shear and Moment under transverse loading:
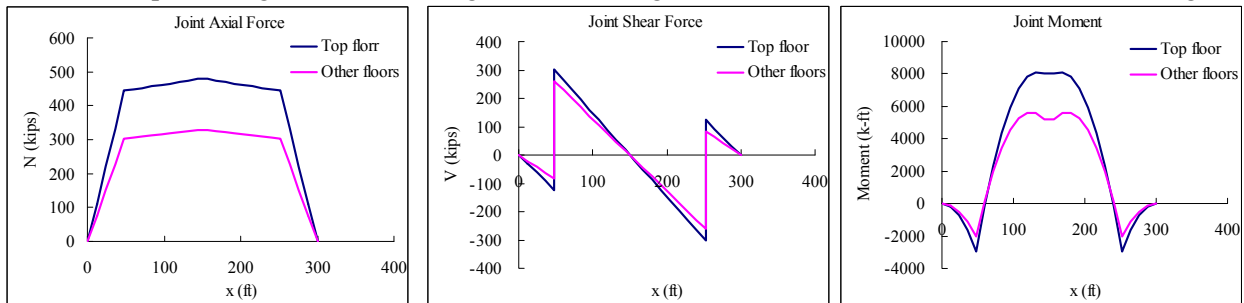
Fig. B-15. Diaphragm Ramp internal forces, example 2B: (a) axial under longitudinal loading; (b) shear under transverse loading; (c) moment under transverse loading.

Table B-5. Diaphragm internal forces for Example 2B.

x	Transverse (NS) Direction												Longitudinal (EW) Direction											
	N/S Flat-Top floor			Ramp-Top floor			N/S Flat-Other floors			Ramp-Other floors			Ramp-Top floor			Ramp-other floors			N/S Flat-Top floor			N/S Flat-Other floors		
	N	V	M	N	V	M	N	V	M	N	V	M	N	V	M	N	V	M	N	V	M	N	V	M
[ft]	[kips]	[kips]	[k-ft]	[kips]	[kips]	[k-ft]	[kips]	[kips]	[k-ft]	[kips]	[kips]	[k-ft]	[kips]	[kips]	[k-ft]	[kips]	[kips]	[k-ft]	[kips]	[kips]	[k-ft]	[kips]	[kips]	[k-ft]
12	0	-31	-185	0	-31	-185	0	-21	-126	0	-21	-126	111	0	0	76	0	0	32	46	-1664	22	32	-1137
24	0	-62	-740	0	-62	-740	0	-42	-505	0	-42	-505	222	0	0	152	0	0	64	92	-2774	44	63	-1895
36	0	-92	-1664	0	-92	-1664	0	-63	-1137	0	-63	-1137	333	0	0	227	0	0	96	139	-3328	66	95	-2274
48	0	223	-2958	0	301	-2958	0	152	-2022	0	260	-2022	444	0	0	303	0	0	128	185	-3328	87	126	-2274
60	0	196	-444	0	266	-100	0	134	-303	0	229	166	448	0	0	306	0	0	139	176	-2467	95	120	-1686
72	0	170	1757	0	230	2333	0	116	1200	0	198	1988	452	0	0	309	0	0	149	167	-1712	102	114	-1170
84	0	144	3643	0	195	4341	0	98	2489	0	168	3444	457	0	0	312	0	0	160	158	-1063	109	108	-726
96	0	118	5214	0	159	5923	0	81	3563	0	137	4533	461	0	0	315	0	0	171	150	-519	117	102	-355
108	0	92	6472	0	124	7081	0	63	4423	0	107	5255	466	0	0	318	0	0	182	141	-81	124	96	-55
120	0	65	7415	0	89	7813	0	45	5067	0	76	5611	470	0	0	321	0	0	192	132	252	131	90	172
132	0	39	8043	0	53	8119	0	27	5497	0	46	5601	474	0	0	324	0	0	203	123	479	139	84	327
144	0	13	8358	0	18	8001	0	9	5711	0	15	5224	479	0	0	327	0	0	214	114	600	146	78	410
156	0	-13	8358	0	-18	8001	0	-9	5711	0	-15	5224	479	0	0	327	0	0	225	106	615	154	72	420
168	0	-39	8043	0	-53	8119	0	-27	5497	0	-46	5601	474	0	0	324	0	0	235	97	525	161	66	359
180	0	-65	7415	0	-89	7813	0	-45	5067	0	-76	5611	470	0	0	321	0	0	246	88	329	168	60	225
192	0	-92	6472	0	-124	7081	0	-63	4423	0	-107	5255	466	0	0	318	0	0	257	79	28	176	54	19
204	0	-118	5214	0	-159	5923	0	-81	3563	0	-137	4533	461	0	0	315	0	0	268	70	-379	183	48	-259
216	0	-144	3643	0	-195	4341	0	-98	2489	0	-168	3444	457	0	0	312	0	0	278	62	-892	190	42	-610
228	0	-170	1757	0	-230	2333	0	-116	1200	0	-198	1988	452	0	0	309	0	0	289	53	-1510	198	36	-1032
240	0	-196	-444	0	-266	-100	0	-134	-303	0	-229	166	448	0	0	306	0	0	300	44	-2234	205	30	-1527
252	0	-223	-2958	0	-301	-2958	0	-152	-2022	0	-260	-2022	444	0	0	303	0	0	311	35	-3064	212	24	-2094
264	0	92	-1664	0	92	-1664	0	63	-1137	0	63	-1137	333	0	0	227	0	0	233	26	-2140	159	18	-1462
276	0	62	-740	0	62	-740	0	42	-505	0	42	-505	222	0	0	152	0	0	155	18	-1321	106	12	-903
288	0	31	-185	0	31	-185	0	21	-126	0	21	-126	111	0	0	76	0	0	78	9	-608	53	6	-415

Design example 3A: (EDO)
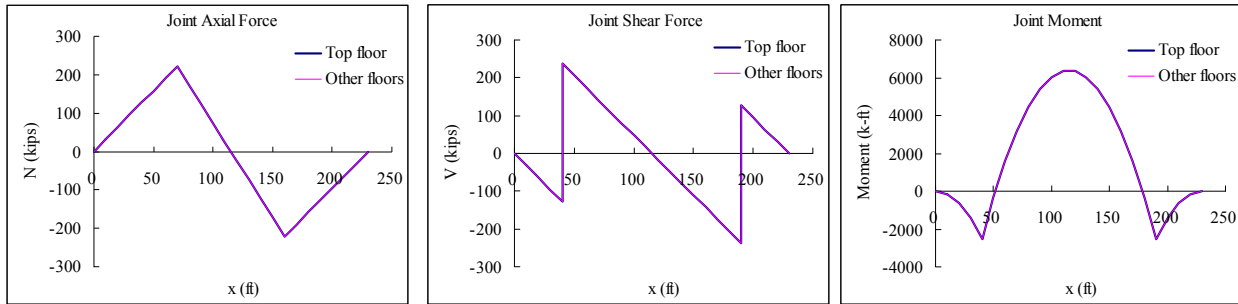
Fig. B-16. Diaphragm internal forces, example 3A: (a) axial under longitudinal loading; (b) shear under transverse loading; (c) moment under transverse loading.

Table B-6. Diaphragm internal forces for Example 3A.

x	Transverse Loading			Transverse Loading		
	N	V	M	N	V	M
[ft]	[kips]	[kips]	[k-ft]	[kips]	[kips]	[k-ft]
0	0	0	0	0	0	0
10	0	-32	-159	32	0	0
20	0	-63	-634	63	0	0
30	0	-95	-1427	95	0	0
40	0	-127	-2537	127	0	0
40	0	238	-2537	127	0	0
50	0	206	-317	159	0	0
60	0	174	1585	190	0	0
70	0	143	3171	222	0	0
80	0	111	4439	173	0	0
90	0	79	5391	123	0	0
100	0	48	6025	74	0	0
110	0	16	6342	25	0	0
120	0	-16	6342	-25	0	0
130	0	-48	6025	-74	0	0
140	0	-79	5391	-123	0	0
150	0	-111	4439	-173	0	0
160	0	-143	3171	-222	0	0
170	0	-174	1585	-190	0	0
180	0	-206	-317	-159	0	0
190	0	-238	-2537	-127	0	0
190	0	127	-2537	-127	0	0
200	0	95	-1427	-95	0	0
210	0	63	-634	-63	0	0
220	0	32	-159	-32	0	0
230	0	0	0	0	0	0

Design example 3B: (RDO)
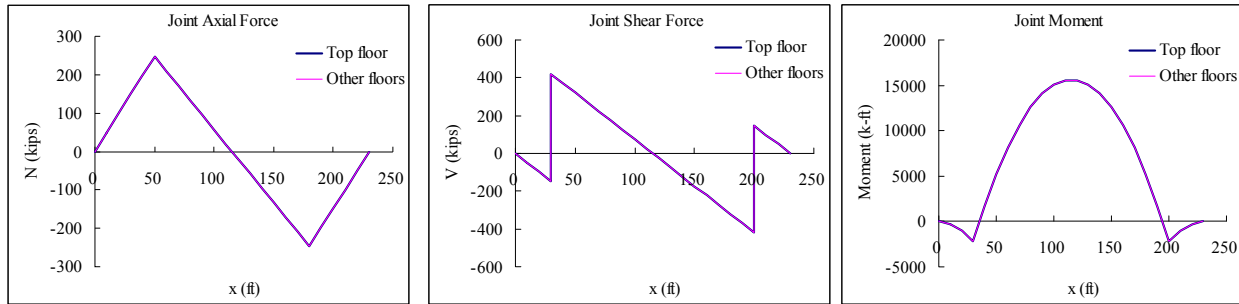
Fig. B-17. Diaphragm internal forces, example 3B: (a) axial under longitudinal loading; (b) shear under transverse loading; (c) moment under transverse loading.

Table B-7. Diaphragm internal forces for Example 3B.

x	Transverse Loading			Transverse Loading		
	N	V	M	N	V	M
[ft]	[kips]	[kips]	[k-ft]	[kips]	[kips]	[k-ft]
0	0	0	0	0	0	0
10	0	-49	-247	49	0	0
20	0	-99	-988	99	0	0
30	0	-148	-2222	148	0	0
40	0	420	-2222	148	0	0
40	0	370	1729	198	0	0
50	0	321	5186	247	0	0
60	0	272	8149	209	0	0
70	0	222	10618	171	0	0
80	0	173	12594	133	0	0
90	0	123	14075	95	0	0
100	0	74	15063	57	0	0
110	0	25	15557	19	0	0
120	0	-25	15557	-19	0	0
130	0	-74	15063	-57	0	0
140	0	-123	14075	-95	0	0
150	0	-173	12594	-133	0	0
160	0	-222	10618	-171	0	0
170	0	-272	8149	-209	0	0
180	0	-321	5186	-247	0	0
190	0	-370	1729	-198	0	0
190	0	-420	-2222	-148	0	0
200	0	148	-2222	-148	0	0
210	0	99	-988	-99	0	0
220	0	49	-247	-49	0	0
230	0	0	0	0	0	0

Design example 4A: (BDO)
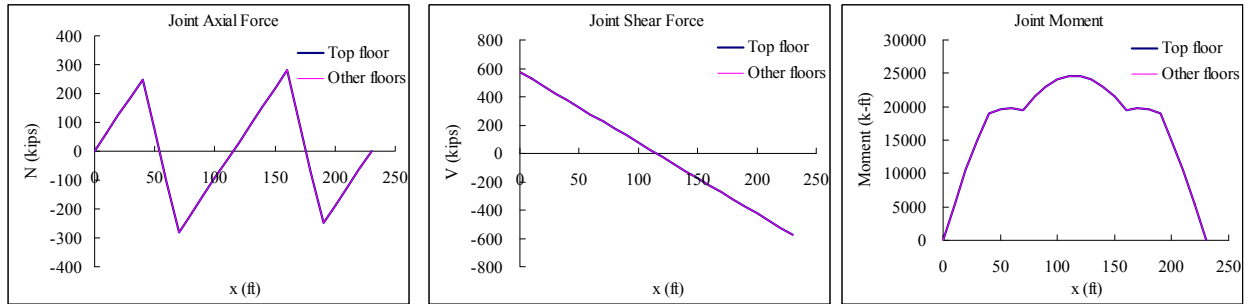
Fig. B-18. Diaphragm internal forces, example 4A: (a) axial under longitudinal loading; (b) shear under transverse loading; (c) moment under transverse loading.

Table B-8. Diaphragm internal forces for Example 4A.

x	Transverse Loading			Transverse Loading		
	N	V	M	N	V	M
[ft]	[kips]	[kips]	[k-ft]	[kips]	[kips]	[k-ft]
0	0	575	0	0	0	0
10	0	525	5497	62	0	0
20	0	475	10494	125	0	0
30	0	425	14991	187	0	0
40	0	375	18988	250	0	0
50	0	325	19670	73	0	0
60	0	275	19853	-104	0	0
70	0	225	19535	-281	0	0
80	0	175	21534	-219	0	0
90	0	125	23033	-156	0	0
100	0	75	24033	-94	0	0
110	0	25	24532	-31	0	0
120	0	-25	24532	31	0	0
130	0	-75	24033	94	0	0
140	0	-125	23033	156	0	0
150	0	-175	21534	219	0	0
160	0	-225	19535	281	0	0
170	0	-275	19853	104	0	0
180	0	-325	19670	-73	0	0
190	0	-375	18988	-250	0	0
200	0	-425	14991	-187	0	0
210	0	-475	10494	-125	0	0
220	0	-525	5497	-62	0	0
230	0	-575	0	0	0	0

Design example 4B: (RDO)
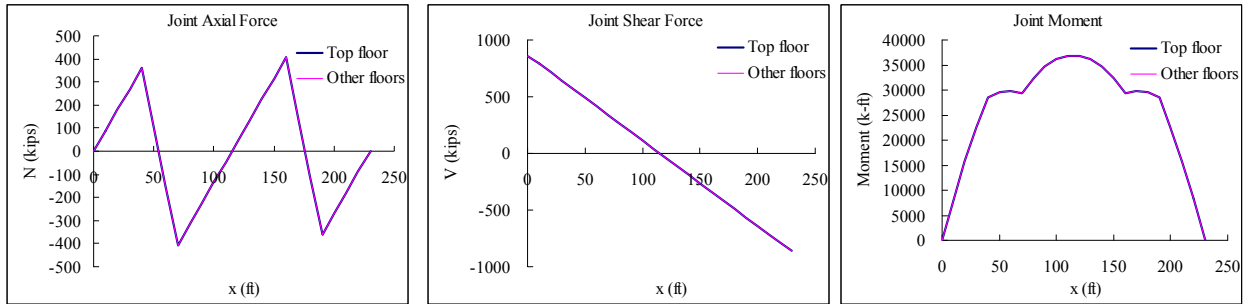
Fig. B-19. Diaphragm internal forces, example 4B: (a) axial under longitudinal loading; (b) shear under transverse loading; (c) moment under transverse loading.

Table B-9. Diaphragm internal forces for Example 4B.

x	Transverse Loading			Transverse Loading		
	N	V	M	N	V	M
[ft]	[kips]	[kips]	[k-ft]	[kips]	[kips]	[k-ft]
0	0	863	0	0	0	0
10	0	788	8253	90	0	0
20	0	713	15757	180	0	0
30	0	638	22509	270	0	0
40	0	563	28512	360	0	0
50	0	488	29536	105	0	0
60	0	413	29810	-150	0	0
70	0	338	29333	-405	0	0
80	0	263	32335	-315	0	0
90	0	188	34586	-225	0	0
100	0	113	36086	-135	0	0
110	0	38	36837	-45	0	0
120	0	-38	36837	45	0	0
130	0	-113	36086	135	0	0
140	0	-188	34586	225	0	0
150	0	-263	32335	315	0	0
160	0	-338	29333	405	0	0
170	0	-413	29810	150	0	0
180	0	-488	29536	-105	0	0
190	0	-563	28512	-360	0	0
200	0	-638	22509	-270	0	0
210	0	-713	15757	-180	0	0
220	0	-788	8253	-90	0	0
230	0	-863	0	0	0	0

Table B-10. Diaphragm Effective Moduli for example 1A.

Joint	Top Floor				Other Floors			
	North/South flat		Ramp		North/South flat		Ramp	
	E_{eff}	G_{eff}	E_{eff}	G_{eff}	E_{eff}	G_{eff}	E_{eff}	G_{eff}
	[ksi]	[ksi]	[ksi]	[ksi]	[ksi]	[ksi]	[ksi]	[ksi]
1	715	213	1122	327	566	142	841	267
2	715	213	1122	327	566	142	841	267
3	930	243	1122	327	695	159	841	267
4	942	281	1033	295	719	223	841	267
5	942	281	1033	295	719	223	841	267
6	942	281	1033	295	719	223	841	267
7	1109	281	1025	267	831	238	933	253
8	1109	281	1025	267	831	238	933	253
9	1109	281	1025	267	831	238	933	253
10	1174	237	1095	222	914	191	914	191
11	1174	237	1095	222	914	191	914	191
12	1174	237	1095	222	914	191	914	191

Table B-11. Diaphragm Effective Moduli for example 1B.

Joint	Top Floor				Other Floors			
	North/South flat		Ramp		North/South flat		Ramp	
	E_{eff}	G_{eff}	E_{eff}	G_{eff}	E_{eff}	G_{eff}	E_{eff}	G_{eff}
	[ksi]	[ksi]	[ksi]	[ksi]	[ksi]	[ksi]	[ksi]	[ksi]
1	707	192	742	282	580	176	607	238
2	707	192	742	282	580	176	607	238
3	707	192	742	282	580	176	607	238
4	831	238	841	267	593	208	730	253
5	831	238	841	267	593	208	730	253
6	831	238	841	267	593	208	730	253
7	933	253	831	238	719	223	719	223
8	933	253	831	238	719	223	719	223
9	933	253	831	238	719	223	719	223
10	1008	207	914	191	810	175	810	175
11	1008	207	914	191	810	175	810	175
12	1008	207	914	191	810	175	810	175

Table B-12. Diaphragm Effective Moduli for example 1C.

Joint	Top Floor				Other Floors			
	North/South flat		Ramp		North/South flat		Ramp	
	E_{eff} [ksi]	G_{eff} [ksi]	E_{eff} [ksi]	G_{eff} [ksi]	E_{eff} [ksi]	G_{eff} [ksi]	E_{eff} [ksi]	G_{eff} [ksi]
1	534	194	668	255	391	149	534	194
2	534	194	668	255	391	149	534	194
3	534	194	668	255	391	149	534	194
4	660	235	750	216	534	194	647	205
5	660	235	750	216	534	194	647	205
6	660	235	750	216	534	194	647	205
7	844	226	739	184	635	173	635	173
8	844	226	739	184	635	173	635	173
9	844	226	739	184	635	173	635	173
10	912	174	824	163	727	151	727	151
11	912	174	824	163	727	151	727	151
12	912	174	824	163	727	151	727	151

Table B-13. Diaphragm Effective Moduli for example 2A.

Joint	Top Floor				Other Floors			
	North/South flat		Ramp		North/South flat		Ramp	
	E_{eff} [ksi]	G_{eff} [ksi]	E_{eff} [ksi]	G_{eff} [ksi]	E_{eff} [ksi]	G_{eff} [ksi]	E_{eff} [ksi]	G_{eff} [ksi]
1	803	174	914	191	636	151	722	163
2	803	174	914	191	636	151	722	163
3	803	174	914	191	636	151	722	163
4	834	266	942	281	673	246	757	256
5	834	266	942	281	673	246	757	256
6	834	266	942	281	673	246	757	256
7	817	217	1019	248	652	195	738	206
8	817	217	1019	248	652	195	738	206
9	817	217	1019	248	652	195	738	206
10	803	174	1008	207	636	151	722	163
11	803	174	1008	207	636	151	722	163
12	803	174	1008	207	636	151	722	163

Table B-14. Diaphragm Effective Moduli for example 2B.

Joint	Top Floor				Other Floors			
	North/South flat		Ramp		North/South flat		Ramp	
	E_{eff} [ksi]	G_{eff} [ksi]	E_{eff} [ksi]	G_{eff} [ksi]	E_{eff} [ksi]	G_{eff} [ksi]	E_{eff} [ksi]	G_{eff} [ksi]
1	1236	272	1360	293	841	216	1128	255
2	1236	272	1360	293	841	216	1128	255
3	1236	272	1360	293	841	216	1128	255
4	1250	335	1552	388	1026	304	1372	355
5	1250	335	1552	388	1026	304	1372	355
6	1250	335	1552	388	1026	304	1372	355
7	1242	300	1547	355	851	246	1365	320
8	1242	300	1547	355	851	246	1365	320
9	1242	300	1547	355	851	246	1365	320
10	1007	237	1360	293	841	216	1128	255
11	1007	237	1360	293	841	216	1128	255
12	1007	237	1360	293	841	216	1128	255

Table B-15. Diaphragm Effective Moduli for example 3 and 4.

Joint	Example 3				Example 4			
	3A		3B		4A		4B	
	E_{eff} [ksi]	G_{eff} [ksi]	E_{eff} [ksi]	G_{eff} [ksi]	E_{eff} [ksi]	G_{eff} [ksi]	E_{eff} [ksi]	G_{eff} [ksi]
1	541	78	574	82	1090	177	2116	537
2	541	78	574	82	1090	177	2116	537
3	541	78	1392	267	1090	177	1616	341
4	541	78	1392	267	1090	177	1616	341
5	541	78	1392	267	1090	177	1594	307
6	541	78	1375	245	1090	177	1508	287
7	541	78	1375	245	1090	177	1508	287
8	541	78	859	151	1090	177	1089	198
9	541	78	809	116	1090	177	1089	198
10	541	78	809	116	1090	177	1023	141
11	541	78	574	82	1090	177	1023	141

APPENDIX C. Cost Comparisons, Economic Studies

The cost of diaphragm reinforcement in terms of weight of chord reinforcement and number of shear connector for the design examples is examined in this section. The diaphragm reinforcement cost using the DSDM design methodology according to Appendix A is compared to that from the current code design (ASCE 7 2005) (PCI Design Handbook 2004).

C1. Current Code Diaphragm Design

The diaphragm design force using the current code is determined based on ASCE 7 (2005) without amplification factor (See *Step 1 in Design Methodology PART 1*). The diaphragm design forces for the design examples are summarized in Table B-1. As seen, the diaphragm design force has an approximate constant profile along building height due to the minimum F_{px} is controlled at lower floors. Therefore all floors are designed using the same and most critical forces. The diaphragm reinforcement design is based on PCI Design Handbook (2004) using the horizontal beam analogy. The diaphragm design moment is only carried by chord reinforcement and the diaphragm design shear is only carried by shear connector. No bar cut-off or shear connector spacing varying are applied. The detail design for different design examples is shown in Table C-2.

Table C-1. Diaphragm design force in the 4-story parking garage using current code

SDC	Floor	W_x (kips)	F_x (kips)	F_{px} (kips)	$F_{px, min} = 0.2 S_{DS} W_x$
C	4	5529	482	482	**500**
	3	6245	420	478	**565**
	2	6245	297	416	**565**
	1	6245	176	354	**565**
D	4	5560	1325	**1325**	1171
	3	6276	1164	1320	**1322**
	2	6276	833	1151	**1322**
	1	6276	502	984	**1322**

Table C-2. Diaphragm reinforcement selection.

Structure	F_{px} (kips)		Moment	Shear	Chord		Shear connector (JVI)	
	Total	Sub-Dia	[k-ft]	[kips]	Req'd Area	Provide	Req'd #	Provide
SDC C Exterior Wall	565	188	5900	94	1.93	7#5	6.94	7
SDC C Interior Wall	565	188	2543	64	0.83	3#5	4.72	7*
SDC D Interior Wall	1325	442	5950	150	1.93	7#5	11.04	11

*Minimum spacing control

B2. Cost Comparison

The cost of diaphragm reinforcement is expressed in terms of the chord reinforcement weight per square foot and number of shear connector in the structure.

Figure B-1 shows the chord reinforcement weight and number of shear connector comparison for design example 1 (4-story exterior wall parking structure) and 2A (4-story interior wall parking structure) in SDC C. The following conclusions are made based on Figure C-1:

(1) EDO design requires more chord reinforcement than the current design for both exterior and interior wall parking structure.

(2) BDO and RDO design requires less chord reinforcement than the current design. This is because the design methodology uses a more complex and accurate free body method (See *Design Methodology PART 3*) and uses a lower diaphragm design force for lower floor.

(3) All design options requires more number of shear connector that the current design due to introduce of shear overstrength factor for the BDO and RDO options.
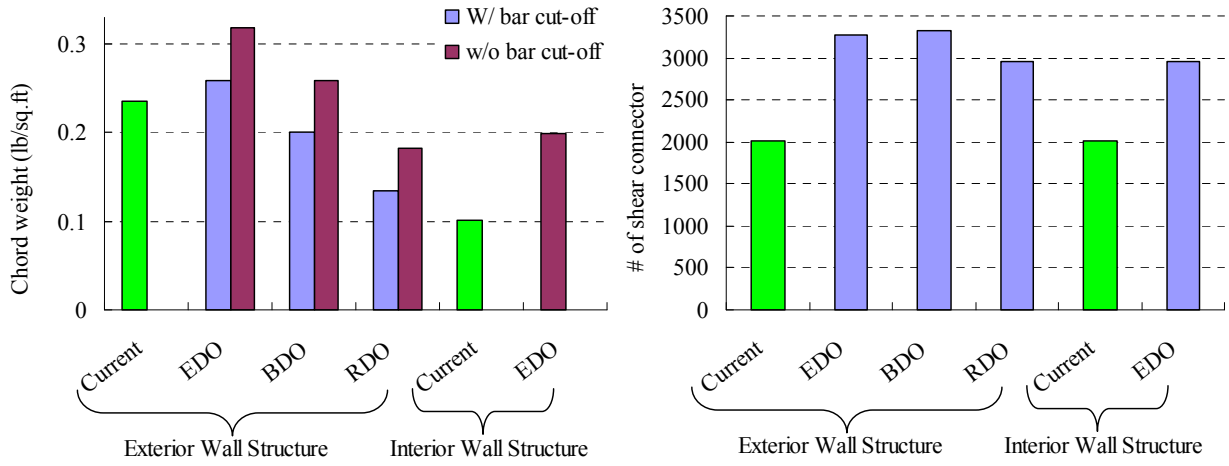
Fig.C-1. Diaphragm reinforcement cost comparison for parking structure in SDC C: (a) Chord; (b) Shear connector.

Figure C-2 shows the chord reinforcement weight and number of shear connector comparison for design 2B (4-story interior wall parking structure) in SDC D. As seen in Fig. C-2, The DSDM design methodology requires higher diaphragm chord reinforcement and number of shear connector than current design.
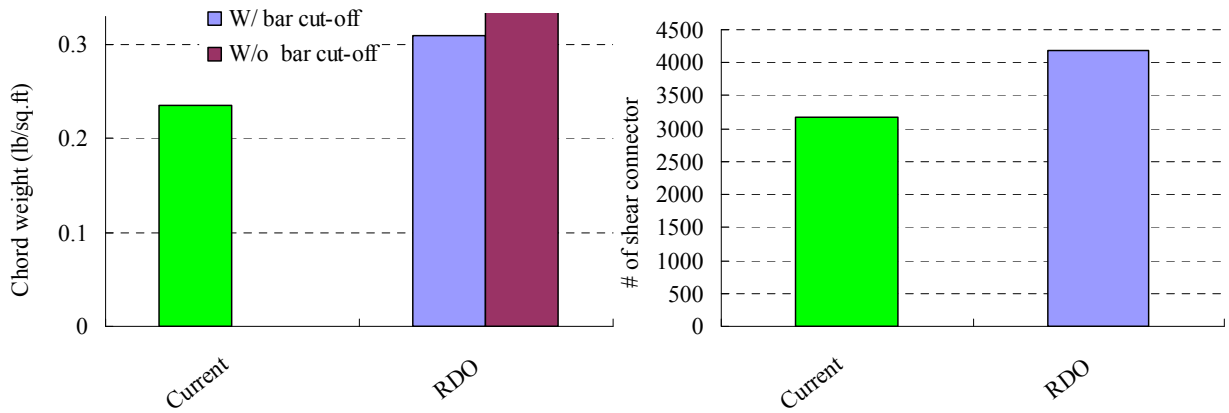
Fig.C-2. Diaphragm reinforcement cost comparison for parking structure in SDC D: (a) Chord; (b) Shear connector.

Seismic Design Methodology Document for Precast Concrete Diaphragms

PART 5: BACKGROUND

on the Precast Concrete Diaphragm Seismic Design Methodology

2/16/2014

Background on Design Methodology

TABLE OF CONTENTS

Appendices

5.1 DSDM Industry Task Group/Design Development Team

DSDM Design Development Team
- Roger Becker, Director, Research and Development, PCI.
- Dr. Ned Cleland, President, Blue Ridge Design, Inc., Winchester, VA.
- Tom D'Arcy, Founder, The Consulting Engineers Group, San Antonio, TX.
- David Dieter, President/General Manager, Mid State Precast, Inc., Cocoran, CA.
- Dr. Robert Fleischman*, Associate Professor, University of Arizona
- Dr. S.K. Ghosh, President, S.K. Ghosh Associates, Inc., Skokie, IL.
- Dr. Neil Hawkins, Professor Emeritus, University of Illinois, Urbana-Champaign, IL.
- Pavel Kravets, Principal, Vector Structures, LLC. Marietta, GA.
- Dr. Joseph Maffei, Principal, Rutherford & Chekene Engineers, Oakland, CA.
- Susie Nakaki, President, The Nakaki Bashaw Group, Inc., Irvine, CA.
- Karl Telleen, Engineer, Rutherford & Chekene Engineers, Oakland, CA.
- Dr. Dichuan Zhang*, Postdoctoral Researcher, University of Arizona

DSDM Industry Task Group Members

- Tom D'Arcy, DSDM Task Group Chair, PCI R&D Committee; founder, The Consulting Engineers Group, San Antonio, TX.
- Roger Becker, Vice President, Spancrete Industries, Inc., Waukesha, WI.
- Dr. Ned Cleland, President, Blue Ridge Design, Inc., Winchester, VA.
- David Dieter, President/General Manager, Mid State Precast, Inc., Cocoran, CA.
- Dr. S.K. Ghosh, DSDM Project Co-Principal Investigator, President, S.K. Ghosh Associates, Inc., Skokie, IL.
- Harry Gleich, Vice President-Engineering, Metromont Prestress, Greenville, NC.
- Dr. Neil Hawkins, Professor Emeritus, University of Illinois, Urbana-Champaign, IL.
- Paul Johal, PCI Research Director, Precast/Prestressed Concrete Institute, Chicago, IL.
- Dr. Joseph Maffei, Structural engineer, Rutherford & Chekene Engineers, Oakland, CA.
- Chuck Magnesio, Senior Vice President of Engineering & Technical Marketing, JVI Inc, Pittsfield, MA.
- Susie Nakaki, President, The Nakaki Bashaw Group, Inc., Irvine, CA.
- Dr. Douglas Sutton, Chair, PCI Research & Development Committee, and Professor, Purdue University, West Lafayette, IN.

University Researchers

- Dr. Robert Fleischman, University of Arizona, Principal Investigator
- Dr. Clay Naito and Dr. Richard Sause, Lehigh University
- Dr. Jose Restrepo, University of California, San Diego

Graduate and Post-Graduate Researchers

- Drs. Ge Wan and Dichuan Zhang, University of Arizona
- Drs. Liling Cao and Rui Ren, Lehigh University
- Dr. Matt Schoettler, University of California, San Diego
- Dr. Andrea Belleri, University of Bergamo, Italy

*Co-authors, DSDM Design Methodology Documents

5.2 <u>Background on the Design Methodology:</u>

The seismic design methodology for precast concrete floor diaphragms described in PARTS 1-5 was developed as part of a large multi-university research project termed the DSDM Project. The DSDM Project was co-funded by the Precast/Prestressed Concrete Institute (PCI), the Charles Pankow Foundation (CPF) and the National Science Foundations (NSF) and involved strong industry collaboration (Fleischman et al. 2005a).

The seismic design methodology is performance-based and possesses key features that address aspects of behavior not treated adequately in previous precast concrete diaphragm seismic design provisions, including: (1) Diaphragm seismic design forces that more accurately reflect the actual inertial forces that develop during strong shaking; (2) More rational methods of determining diaphragm internal forces; (3) Inelastic deformation capacity requirements for the diaphragm reinforcement; (4) Protection of potentially non-ductile elements in the precast concrete diaphragm through the use of capacity design concepts; and, (5) Explicit inclusion of diaphragm flexibility in drift limits checks.

The design methodology offers the designer different options associated with different performance targets, involving different required diaphragm design force and diaphragm deformation capacity requirements. A diaphragm reinforcement classification system is introduced to meet the deformation capacity requirements. In general, the diaphragm force levels that meet the performance targets require an increase in current diaphragm design force levels, and are therefore realized through the introduction of diaphragm design force amplification factors.

Design Methodology Main Features:

The design methodology is intended for precast concrete diaphragms with or w/out topping slabs. The design procedure attempts to provide adequate strength and deformability to the connectors between precast diaphragm units. The method employs the following main features (BSSC 2009):

1. Three design options (Elastic, Basic and Reduced) are available each with a distinct diaphragm performance targets.
2. The code forces F_p are amplified by a factor Ψ based on the selected diaphragm design option.
3. The diaphragm design shear forces, including the shear component of the diaphragm-to-LFRS connection forces, are amplified by an overstrength factor Ω.
4. Appropriate diaphragm reinforcing (HDE, MDE or LDE) is selected based on deformation capacity to meet the diaphragm performance targets associated by the selected design approach.
5. The diaphragm flexibility influence on inter-story drifts is calculated using factors $C_{d,dia}$ and $C_{r,dia}$ and compared to appropriate limits.

Design Methodology Concepts:

The conceptual framework of the design methodology is driven by the following considerations: (1) the maximum inertial forces that develop in a building structures during an actual earthquake can be significantly larger than those suggested by current code diaphragm forces; and (2) larger than anticipated diaphragm forces can have significant detrimental effect in a floor system with limited plastic redistribution qualities. A full treatment of these considerations appears in *Sections 5.3: Rationale for Design Approach* and *5.5: Background on Diaphragm Seismic Behavior*.

The design procedure accounts for the higher anticipated diaphragm forces through the use of diaphragm force amplification factors (Ψ). The Ψ factors have been calibrated through extensive computer earthquake simulation of precast structures using analytical models developed in conjunction with extensive large-scale physical experimentation. The Ψ factors are dependent on the design parameters (number of stories, diaphragm geometry, etc.) and are aligned to performance targets associated with three design options: (1) an Elastic Design Option (EDO) where the diaphragm is intended to remain elastic in the MCE; (2) a Basic Design Option (BDO) where the diaphragm is intended to remain elastic in the DBE and therefore requires a certain amount of inelastic deformation capacity in the MCE; and (3) a Reduced Design Option (RDO) in which diaphragm yielding is allowed in the DBE.

The EDO is presumably the most straightforward design option, but the results of the analytical research indicate that it is difficult in many situations to create reliable fully-elastic diaphragm designs economically. Hence the need for the BDO and RDO, as designers may find these the most desirable options in many cases. Each of these design options involves performance targets that translate into differing levels of inelastic deformation demand in the diaphragm reinforcement.

It should be noted that intent of the design options involving inelastic diaphragm response (i.e., the BDO and RDO) is not for the diaphragm to serve as the primary energy dissipation mechanism (special detail) for the structure, but rather that the floor system simply have sufficient inelastic deformation capacity (ductility) to allow it to remain intact during a strong earthquake event.

Recognizing the many existing precast diaphragm reinforcement types and wide variety of reinforcement response characteristics, a diaphragm reinforcement classification system is adopted in the design methodology (Naito and Ren 2011). The classification system is based entirely on the diaphragm reinforcement inelastic deformation capacity as it pertains to joint opening, and applies to both the chord reinforcement and the shear reinforcement. Diaphragm reinforcement is classified as *low deformability element* (LDE), *moderate deformability element* (MDE), *high deformability element* (HDE). The classification system approach also permits straightforward inclusion into the design procedure of any new diaphragm connectors or reinforcing details that the precast industry may be motivated to develop.

In order to obviate non-ductile failure modes, a shear overstrength factor, Ω, is applied in the design to the shear force component for joints in the diaphragm. This factor is "stacked" on top of the Ψ factors for the potentially non-ductile shear actions (serving in a role similar to capacity design factors) relative to the ductile chord reinforcement. The Ω factor cannot truly be considered a capacity design factor given the difficulty in clearly defining needed relative strengths due to the complex internal force patterns that develop in the precast diaphragm during a seismic event. Thus, while the Ω factor has been calibrated in the analytical research to provide elastic shear response of the diaphragm in the MCE, it is suggested that a check be performed to ensure the desired *M/V* ratio occurs in a more complex diaphragm.

The design occurs at the joint level; hence groups of precast diaphragm reinforcement crossing a joint is designed collectively to resist the total diaphragm internal forces acting at that joint (in-plane axial, shear and moment). An interaction formula is introduced to perform this design step. This approach represents a departure from the commonly used "horizontal beam" method in which the chord reinforcement and shear reinforcement are considered separately. The interaction formula also applies to the diaphragm-to-LFRS connection. However, this connection is subjected to a separate deformation requirement (i.e., from the chord) due to different deformation demands than joints throughout the floor.

It is noted that a flexural limit state has been selected as the desirable inelastic mechanism for the diaphragm, and thus the factors and detail classifications pertain to designs in which flexural mechanisms are promoted and shear mechanisms are prevented. While not included in the methodology presented here, an alternate approach embodying the same design philosophy could involve promoting shear mechanisms. In this case, diaphragm connectors would require *shear* deformation capacity. This approach may be desirable for: (1) squat diaphragms where it is difficult to develop a flexural mechanism; (2) complex diaphragms where a capacity design based on flexure may be difficult to accomplish. The design factors and classifications developed here do not apply to this alternate approach.

The design concepts underlying the methodology can be illustrated by considering diaphragm load-deflection monotonic response "pushover" curves. Figure C-1a shows a pushover schematic demonstrating the *Basic Design Option* (BDO). The Ψ factor for the BDO is termed Ψ_D and is calibrated for the performance target of elastic diaphragm behavior in the DBE. As implied in the schematic, the MDE classification for the diaphragm reinforcement has been calibrated to provide sufficient deformation capacity to meet the inelastic deformation demands expected of BDO designs in an MCE event. Likewise, the Ω factor has been calibrated to the maximum elastic force demand in the MCE event.

The *Elastic Design Option* (EDO) targets elastic diaphragm response *in the MCE* (See Fig. C-1b). This option will be uneconomical and, moreover, potentially unsafe in many cases and is reserved primarily for low aspect ratio (so called "squat") diaphragms in regions of lower seismic hazard. The

EDO requires a larger increase in diaphragm force as realized by the diaphragm force amplification factor Ψ_E. However, LDE reinforcing details can be used for the EDO since there is no significant inelastic response anticipated. Likewise, no shear overstrength (i.e., $\Omega = 1.0$) is required for the EDO.

Finally, a Reduced Design Option (RDO) is offered primarily for longer span diaphragms in high seismic hazard where the BDO does not produce economical designs. The RDO allows limited inelastic diaphragm response in the DBE as realized by a smaller diaphragm force amplification factor Ψ_R (See Fig. B-1c). HDE reinforcing details are required to accommodate the larger MCE deformation demand for the RDO. The RDO performance target is a MCE inelastic deformation demand equal to the allowable maximum HDE deformation capacity. The RDO-calibrated Ω_v values are higher than those in the BDO.
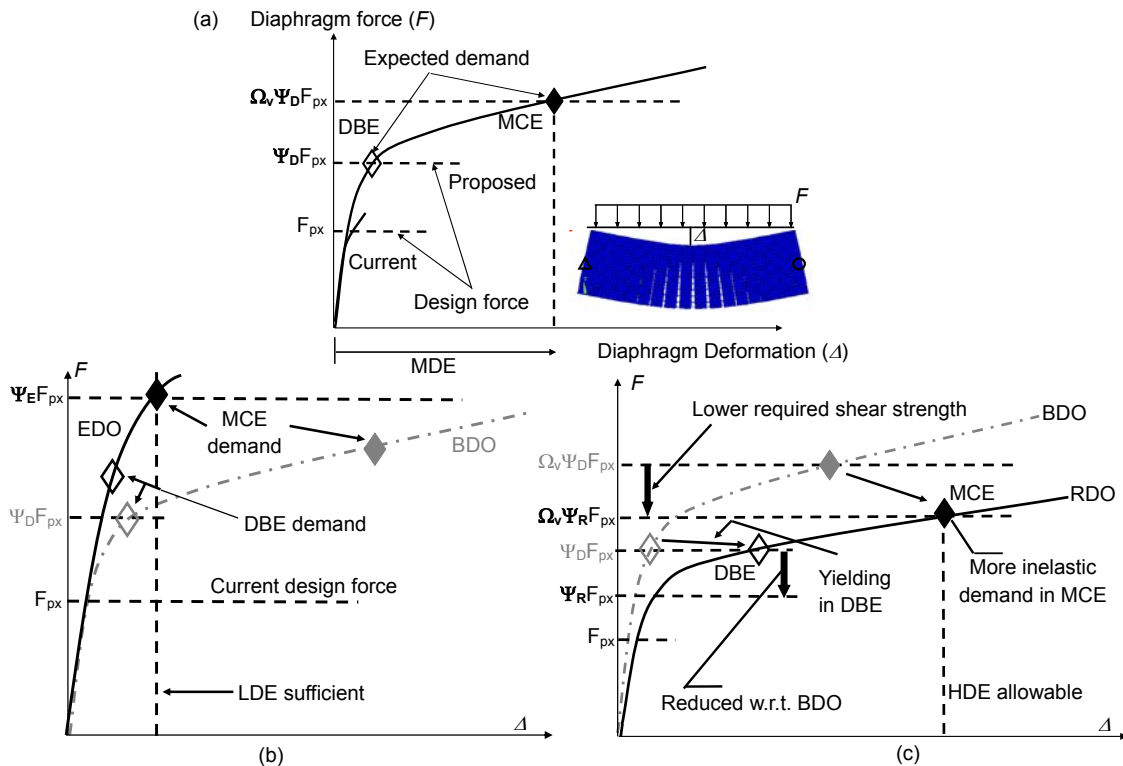
Figure B-1. Diaphragm design options: (a) BDO; (b) EDO; (c) RDO

Design Methodology Development and Calibration:

The DSDM project possessed a research stage and a design procedure development stage. The research stage involved an integrated analytical/experimental program performed in support of the design methodology development (See *Background Appendix C*). Major aspects included determining connector characteristics, and the development and calibration of analytical models (See *Background Appendix B*).

During the research stage, the framework of the design methodology and the steps of the design procedure were broadly established, as described in Part III of the National Earthquake Hazards Reduction Program (NEHRP) Recommended Seismic Provisions for New Buildings (BSSC 2009).

The design procedure development stage was performed largely to provide specific numbers to the concepts introduced in BSSC (2009). In this stage, two main analytical studies were performed, as described in *Background Appendix A*: (1) develop trial design factors, and (2) calibrate these factors on realistic structure designed with the new methodology. It is noted that the latter study was also used to "scrub" the design procedure and produce design examples.

These appendices are referenced throughout the *Background* as *Background-Appendix A1, A2, B* and *C*. These appendices should be distinguished from design procedure Appendices I and II in PART 1, which provide the force distribution factors α_x, and diaphragm-to-LFRS connection requirements.

5.3 Rationale for the Design Approach

In this section, the rationale for the performance-based approach adopted in the diaphragm seismic design methodology is provided. This rationale can best be understood with a thorough knowledge of the dynamic response of building structures, the deformation and force paths in floor diaphragms, and the issues associated with the paneled floor systems found in precast structures. The reader is encouraged to review background information on these topics provided in Section 5.4. This section focuses on design philosophies, code provisions, code changes, and design ramifications.

A key aspect of the diaphragm seismic design methodology is the use of a performance-based approach with design targets (Fleischman et al. 2005a), rather than a prescriptive elastic diaphragm design. Elastic response is desirable but is not always practically realized (BSSC 2009). The reasons for this condition and the code provisions relationship to elastic design is highlighted in this section.

The discussions provided here and in Section 5.4 are updated versions of previous commentary on the topic by the DSDM Project Principal Investigator, including as part of a State-of-the-art Report on the Seismic Design of Precast Concrete structures for The International Federation for Structural Concrete (fib 2003) and a white paper on precast concrete diaphragms approved by the Building Seismic Safety Council (BSSC) Provisions Update Committee (PUC) for the 2009 National Earthquake Hazards Reduction Program (NEHRP) Recommended Seismic Provisions (BSSC 2009).

Overview

There has been considerable discussion since the 1994 Northridge Earthquake regarding the appropriate approach to the seismic design of precast concrete floor diaphragms. While certain ad hoc codes changes were made in the interim, the precast industry recognized the need for a comprehensive industry-endorsed seismic design methodology for precast concrete floor diaphragms, and in 2003 issued the RFP that led to the DSDM project. The DSDM research team identified four major aspects of diaphragm response that are not adequately addressed in the seismic codes. These aspects include:

1. The underestimation in current code of the actual floor inertial forces that occur in earthquakes.
2. The inability of simple techniques such as the horizontal beam method to accurately capture the complex internal force patterns in floor diaphragms.
3. Insufficient consideration of the need for deformation capacity in diaphragm reinforcement.
4. Incomplete treatment of the role diaphragm flexibility plays in the response of the diaphragm.

This list pertains to design aspects of general building systems, and not necessarily any behavior specific to precast concrete. However, these aspects may all be present and prominent in precast concrete structures, and given that precast concrete construction is used effectively for long floor span structures where diaphragm demands are significant, and thus requires careful consideration, including identifying inadequacies in current codes pertaining to diaphragm design.

Recognition that these are building structure seismic design issues, and not necessarily precast concrete structure design issues is important due to the manner in which the building codes are written. The issues described above pertain both to the loading of diaphragms, controlled by a standard for general construction, i.e. ASCE-7 (2005); as well as material and detailing issues, controlled by a separate set of standards, i.e. ACI 318 (2008) as guided by the PCI Handbook (2004). Thus it is important to identify the separate conditions that combine to create the potential for a diaphragm-critical state in structures, and understand where these conditions exist in precast construction and in other construction types.

A BSSC PUC Issue Team has been tasked to summarize the key diaphragm issues across different construction types (BSSC IT6 2012). Diaphragm design, detailing, construction, configuration and ultimately seismic behavior are quite dissimilar for different building construction. A major objective of the BSSC effort is to determine the diaphragm-related behaviors that are common among the different construction techniques and those that are particular to a given material. Also planned is a comparison of the implied overall effective safety factors realized in different construction types (BSSC IT6 2012).

The most significant design issue related to diaphragms may be item 1 above, the underestimation of diaphragm force. This condition, due primarily to higher mode effects (as discussed in *Section 5.4*), is essentially independent of construction material. Thus, a key consideration is why the potentially destructive effects of these overload forces have been witnessed primarily in precast floor diaphragms. Differences in structural configuration, floor mass, inherent redundancy, overstrength, plastic redistribution and deformation capacity are all considered factors. The reader is encouraged to consult BSSC IT6 (2012) when it is published.

Regardless of the approaches used for other construction techniques, it is the consensus of the creators of this design methodology that the conditions present often in precast concrete floor systems, namely long spans with relatively heavy floor masses, discrete force transfers, concentrated deformation demand, complex floor configurations and limited opportunity for plastic redistribution, require realistic assessment of the actual inertial forces that may develop in the floor system during DBE and MCE events, and provide the diaphragm reinforcement a combination of sufficient strength and inelastic deformation capacity, or overstrength, to maintain structural integrity during these seismic events.

Intent of Code Provisions

Elastic response has traditionally been the preferred behavior for diaphragms (ACI 1992). The preference originates from the recognition of the relationship between efficient diaphragm action and in-plane stiffness of the floor slab (Chopra 1995). However, for seismic design, the need for elastic diaphragms stems primarily from a desire to avoid non-ductile failure in the floor system, since this region of the structure is not typically provided with special detailing (fib 2003). Clearly, designs in which the diaphragm acts as the structure's weak link compromise the intent of the code provisions (Nakaki 2000) since the force reduction (R) factors used in seismic design are based on the expected ductility and energy dissipation of the LFRS and thus such design conditions are to be avoided (Wood et al 2000). This particular topic has recently received renewed attention, both in the recognition that certain structural systems have configurations that inherently produce controlling mechanism in the diaphragm, for instance box-type structures with wood diaphragms (Pathak and Charney 2008), as well as structural systems where the feasibility of an intentional diaphragm-controlled mechanism is worthy of investigation, for instance one-story metal deck diaphragms (Rogers and Tremblay 2010).

Prescriptive elastic diaphragm behavior, therefore, would seem an essential part of any seismic design code. However, seismic code provisions, while implying elastic diaphragm behavior, have not clearly accomplished this goal (Nakaki 2000). Consider the seismic design of reinforced concrete diaphragms (Moehle et al. 2010). Diaphragm strength is based on the *ultimate* limit state, as is typical practice with concrete flexural members (ACI 318 2008), and not on an *elastic* limit. Furthermore, design codes have traditionally used the same strength reduction ($\phi = 0.9$) for the diaphragm as for other elements of the LFRS (ICBO 1994). The inconsistency between code intent and realization brings into doubt the supposition that design provisions have historically produced elastic behavior for the DBE.

Despite this inconsistency, current codes do not provide much guidance on the required deformation capacity of the diaphragm. Codes do include structural integrity requirements for diaphragms compatible displacement demands (ACI 318 2008) (IBC 2003), however with little guidance on how to meet these requirements. As a result, most designers consider diaphragms to be elastic force-based elements and considerations of deformation capacity are not part of the design.

The consequences of unintended inelastic action in diaphragms not detailed for ductility may be severe, for instance as evidenced in the collapses of several parking structures during the Northridge earthquake (EERI 1994) (Iverson and Hawkins 1994). These structures did not have sufficient connections between the precast units and used (brittle) mesh for shear reinforcement. Investigations of these failures indicated that a combination of insufficient diaphragm strength (Wood et al. 1995) and diaphragm stiffness (Fleischman et al. 1996) likely led to the collapses. In light of the role that inelastic response was perceived to have played in the poor structural performance, practitioners advocated modifications to current codes to produce prescriptive elastic diaphragm designs (Ghosh 1999). These modifications are discussed next.

Recent Code Modifications

Immediately following the 1994 Northridge earthquake, a task group investigating parking structure performance proposed two code changes for precast diaphragms, later adopted by the 1997 Uniform Building Code (ICBO 1997): (1) minimum spacing, cover and transverse reinforcing for chords and collectors {UBC 1921.6.7.3}; and (2) a strength reduction factor of 0.6 {UBC 1909.3.4.2}. These changes, perhaps in recognition that the code did not provide a prescriptive elastic design, contain provisions intended to increase the precast diaphragm strength and ensure the existence of some ductility capacity in precast diaphragm chords and collectors. An additional code change pertaining to precast diaphragms was to limit the span-to-depth ratio of diaphragms that contain precast gravity systems to no more than 3:1 {UBC 1921.2.1.7}. This prescriptive requirement was intended to minimize excessive diaphragm deformations under the Design Basis Earthquake (Ghosh et al 1997).

The 1997 UBC also introduced the following modifications for diaphragms in general: (1) diaphragms with high compressive stress must possess confined collectors {UBC 1921.6.2.3}; and (2) the system overstrength factor (Ω_o) is to be applied to collector reinforcement transferring the diaphragm reaction to the primary LFRS elements (ICBO 1997). Since collectors for lateral load in one direction often serve as chords in the orthogonal direction, this requirement often produces confined chords as well.

Though not based on any conclusive results, the objectives of the code changes collectively were to improve the strength and toughness of chords and collectors in diaphragms and attempt to ensure that these elements to not yield in tension (SEAOC 1994). Clearly, the writers of these codes sections were concerned that diaphragms, especially precast concrete diaphragms, could be the weak link in a structure if not properly designed and detailed (Nakaki 2000).

Of the code changes listed above, the minimum spacing, cover and transverse reinforcing for collectors {ACI 318 § 21.11.7.6} and confined collectors for diaphragm with high compressive stress {ACI 318 § 21.11.7.5} have been carried over to the current code for reinforced/precast concrete diaphragms (ACI 318 2008). Additionally, the overstrength factor for collector elements {ASCE 7 2005 12.10.2.1} has been carried over to the current code for general construction (ASCE 7 2005).

The minimum spacing, cover and transverse reinforcing requirements do not apply to the chords in ACI 318-08. However, since the required length of diaphragm chords is typically longer than those commonly available for reinforcing steel, splices in chords are commonplace. Thus, ACI 318 § 21.11.7.6 often results in tied chords. With regard to diaphragm flexibility, rather than limiting the span-to-depth ratio, current code requires the deflection of the diaphragm to not exceed the permissible deflection of the attached elements (ASCE 7 2005).

The use of ϕ=0.6 for precast diaphragm reinforcement is not included in ACI 318 (2008). A general requirement that the diaphragm not employ a greater strength reduction factor than the LFRS {ACI 318 § 9.3.4} can produce a ϕ=0.6 for diaphragms in structures with shear-controlled LFRS. The 2000 and 2003 NEHRP Recommended Provisions Appendix A to Chapter 9 for Untopped Precast Diaphragms did propose a factor that combined the system overstrength factor Ω_o with the redundancy factor ρ. These provisions, like those previous, are an attempt to avoid building designs where the diaphragm is weaker than the LFRS.

ACI 318-08 permits accounting for shear reinforcement in the calculation of flexural strength {ACI 318 § 21.11.8} though this practice may not be widely adopted in practice (BSSC IT6 2012). ACI 318-08 also limits the shear strength for diaphragms with topping slabs based on a shear friction calculation, considering a pre-cracked topping slab at the diaphragm joints {ACI 318 § 21.11.9.3}.

The code provision requiring application of the LFRS overstrength factor Ω_o to collector elements has carried over to current code (ASCE 7 2005). However, this factor is not applied to the diaphragm flexure or shear reinforcement. Some design guidelines have suggested applying the Ω_o factor to all precast diaphragm reinforcement (PCI Design Handbook 2004) (Cleland and Ghosh 2007).

In the absence of a rational elastic design, the measures described above are important, but may not necessarily assure good performance (Nakaki 2000). The potential for elastic diaphragm design is considered next.

Elastic Diaphragm Design

Prescriptive elastic design has been promoted for diaphragms (Ghosh 1999) (Nakaki 2000), largely in recognition of the significant detrimental effects of inelastic behavior on the performance of floor systems (e.g., the 1994 Northridge parking structure collapses), given that this region of the structure is not typically detailed for such response.

A capacity design approach seems the most appropriate way to achieve a rational elastic diaphragm design (Nakaki 2000). The intent of a capacity design is to prevent nonductile behavior by designing a brittle component, not to an expected force, but instead relative to the strength of another portion of the structure that has been specially detailed for ductility (Pauley and Priestley 1992). One could imagine using the equivalent lateral force (ELF) pattern to design the diaphragm stronger than the primary vertical elements of the LFRS, thus relying on yielding of the specially-detailed walls or frames to limit the system responses, and hence the forces that occur in the diaphragm. Certain codes (NZCS 2004) have attempted to apply principles of capacity design to estimate the magnitude of lateral forces.

However a poorly understood aspect of building response is the relationship of the inertial forces that can develop at individual floor levels at a given instant during an earthquake (See *Sec. 5.4*). It has been demonstrated by several researchers that the maximum inertial forces that develop in a building structures during an actual earthquake can be significantly larger than those suggested by current code diaphragm forces (Rodriguez et al. 2002) (Fleischman et al. 2002) (Lee and Kuchma 2007). This behavior, due to higher mode effects, is described in detail in *Section 5.4: Seismic Design Forces*. The measures described in the previous section, based on first mode concepts, miss this important behavior.

While significantly larger diaphragm forces can make the resulting design uneconomical, it is not enough in of itself to disqualify a capacity design approach. However, the larger forces are due to higher modes, thus rendering the approach described above using the ELF pattern ineffectual, given that the ELF pattern is based on the first (fundamental) mode. Further, the large diaphragm forces can be driven by modifications in the structure's dynamic properties *after* yielding of the primary elements of the LFRS (Fleischman et al. 2002; Eberhard and Sozen 1993). As a result, even a capacity design approach for diaphragms that successfully initiates yielding in the LFRS while the diaphragm is still elastic, is no guarantee of sustained elastic diaphragm behavior throughout the seismic event. Because of these issues, it may be difficult to relate the relationship of different elements (i.e. LFRS and diaphragms) in the structure, and achieving a reliable capacity design is not as straightforward as it might appear. A prescriptive elastic diaphragm design, therefore, may be difficult to achieve reliably, without adding additional factors of safety to render it uneconomical.

Design guidelines have attempted to approximate a capacity design for the diaphragm through the use of the system overstrength factor Ω_o. In this approach, the Ω_o factor is applied to all the diaphragm reinforcement (PCI Design Handbook 2004) (Cleland and Ghosh 2007), not just the collector system. Likewise, in the aforementioned New Zealand procedure (NZCS 2004) the effects of system overstrength are included in a meaningful capacity design diaphragm force for frames using the product of the design lateral force at a level F_i and the system overstrength factor Ω_o. The conservatism in the selection of these lateral forces was justified because of the potential for exceptionally large inertia forces at a particular level due to higher mode effects (Bull 1997). For typical structural systems, the use of the overstrength factor roughly translates into diaphragm forces two to three times the magnitude of the design lateral force at a given level. Clearly, this level of force increase is impactful on the design economy, and without a rational basis, is still no guarantee of elastic behavior.

An important further consideration regarding the potential for a reliable and cost-effective elastic diaphragm design is the ability to reliably relate the diaphragm seismic force to diaphragm internal force. Clearly, the yielding of the diaphragm occurs locally, when the internal forces at a diaphragm section may exceed the elastic capacity of the diaphragm reinforcement at that section. Due to the complexity of floor systems, the transformation of the diaphragm global forces to internal forces may also not be as straightforward as implied by the horizontal beam approach used in current practice (See *Sec. 5.4: Diaphragm Internal Forces*). This added level of complexity needs to be considered in a viable prescriptive elastic diaphragm design.

Thus, an alternative to elastic design would be to provide a measure of deformation capacity to the diaphragm reinforcement. Such an approach may be attractive if an elastic design is either too difficult or too costly to produce reliably. In this approach, a viable seismic design for precast diaphragms should consider diaphragm inelastic deformation, both in terms of the required deformation capacity for diaphragm reinforcement, and the connectors capable of providing this deformation.

It is important to recognize that this approach is not a "ductile" diaphragm design in which the diaphragm serves as the structure's controlling element, i.e. the primary energy dissipating source, as has been proposed for other systems (Rogers and Tremblay 2010). It was considered impractical to attempt to develop the structure's inelastic dissipating mechanisms in a precast floor system represented practical, reliable or economical approaches to the design of precast diaphragms.

Precast Diaphragm Detailing Considerations

Based on the discussions in previous sections, current code may not prevent inelastic diaphragm response and economical reliable elastic diaphragm designs may be difficult to create. In the absence of any detailing requirements, the diaphragm may possess limited plastic redistribution qualities and could undergo a nonductile failure in a significant seismic event. Thus, the role of diaphragm detailing in a precast diaphragm design must be considered.

Precast diaphragm reinforcement details are often standard industry hardware, proprietary connectors, or other reinforcement elements designed primarily for serviceability (volume change, tolerances, erection, leveling) and nominal loads due to gravity or impact. Thus, precast diaphragm reinforcement has traditionally been designed without inelastic deformation capacity in mind. Many precast connectors do consider accommodation of deformation for volume change due to temperature or shrinkage, typically through elastic compliance or adjustment. However, the tension strength of these connectors is typically quite low, and thus the typical details that serve as chord elements are stiffer, thereby reaching their yield strength at modest joint openings (approximately $0.05''$).

Inelastic deformation demand on diaphragm reinforcement not designed for ductility is undesirable due to the potential for non-ductile diaphragm failure. This effect is exacerbated in precast floor systems where inelastic deformations concentrate between the precast panels, whether untopped or topped, thereby amplifying local ductility demands for a given global diaphragm inelastic deformation. Secondary elements, e.g. spandrels, may protect certain joints at the expense of others, e.g. column line joints, further concentrating inelastic deformation demand at localized areas (Wan et al. 2011). For these reasons, deformation capacity needs to be built into the precast floor system (Lee et al. 2007).

Care must be taken in developing reliable precast diaphragm designs that involve inelastic deformation in the reinforcement. A realistic relationship is required between the global diaphragm response and the local demands at the joint. These demands can be complicated to determine. Complex internal force paths are inherent in floor systems, including the effect of openings for stairwells, elevators and traffic ramps. It is unclear whether designs based on simple horizontal beam representations can avoid localized inelastic deformation demands for all situations, even if the actual diaphragm forces likely in large ground shaking events are accounted. Thus, the complex force paths that produce force combinations in the elastic range, produce similarly complex *deformation* patterns in the inelastic range.

Further, a design approach that builds a measure of deformation capacity into the diaphragm must ensure that the deformation demands are occurring in the intended regions and not in an alternate unanticipated load path. This is particularly important for precast concrete diaphragms because the precast floor system is an assemblage of several types of precast elements including the aforementioned "secondary" elements (spandrels, inverted tee beams, lite walls) that are not formally included in the diaphragm design but nevertheless may participate in the diaphragm action. The connections for these secondary elements are often industry standard hardware rather than elements designed for a seismic force. These elements do not usually possess sufficient strength or deformation capacity for plastic redistribution. Thus, if a section along the force path cannot accommodate the forces or displacements, a non-ductile failure may occur there.

B-11

Assurance of an Appropriate Limit State

For a diaphragm design that does not fully enforce elastic diaphragm response, the nature of the inelastic action must be considered. For a precast diaphragm using non-ductile elements throughout, the failure in the system might be anticipated in the chord reinforcement (e.g. a non-ductile chord connector) at the critical flexure joint, or at the anchorage to the LFRS (the diaphragm-to-LFRS connection). If the chord reinforcing is ductile (for instance, continuous bars in a pour strip) while the shear reinforcement is not, given a similar factor of safety for shear and flexure reinforcement, the diaphragm will likely undergo a nonductile shear failure prior to developing a full flexure mechanism since the chord bars will strain-harden (Refer to Fig. C1-a). Further, the precast diaphragm may lose its shear carrying capacity prematurely through force combinations acting on the shear reinforcement or strain-compatibility deformation demands on the joint from flexural demands (Farrow and Fleischman 2003).

Accordingly, it may be desirable to consider once again the use of capacity design principles, this time in terms of the relative strength of different reinforcement groups within the diaphragm (whereas earlier, these principles were discussed as they pertain to the global diaphragm strength relative to the LFRS). Approaches have promoted flexural limit states over shear limit states (Fleischman PCI 2005), through the use of overstrength factors for the shear reinforcement. This choice is based on assumption that a shear limit state is brittle, consistent with concepts from reinforced concrete (ACI 318 2008). It should be recognized, however, that given their jointed nature, the diagonal cracking shear mechanisms associated with reinforced concrete are not appropriate for precast diaphragms (Wood et al 2000). For this reason, the possibility exists for developing a ductile shear mechanism in the diaphragm, or a combined ductile shear/flexure mechanism. These alternative approaches were not pursued in the DSDM research, which instead focused exclusively on designs that promote flexural limit states over shear limit states.

It is noted that the overstrength factors used in the design methodology to protect the diaphragm shear reinforcement relative to the flexural reinforcement are not termed capacity design factors. Capacity designs work well for well-defined force patterns (consider shear in columns, which is easily bounded by $V_n > 2M_p/h$). Such simple relationships between shear and moment are not always readily available in the diaphragm, particularly for more complicated floor systems. Thus, not unlike the challenges that exist for a capacity design for elastic diaphragm behavior (due to uncertainty and complexity in the lateral load pattern, i.e. the actual seismic inertia forces not matching the ELF), similar challenges exist for protecting the shear reinforcement relative to the flexural reinforcement (because internal forces do not always match the moment and shear diagrams from the horizontal beam method). Thus, while the Ω factor has been calibrated in the analytical research to provide elastic shear response of the diaphragm in the MCE, care must be taken in ensuring the anticipated *M/V* ratio occurs in the diaphragm (See *Sec 5.4: Diaphragm Controlling Mechanism* and *Background -Appendix Sec. A2.4.4*).

Evolution of Design Concepts during DSDM Project

As an alternative to a prescriptive elastic design, the PCI Design Handbook (2004) suggested a performance-based design with two performance criteria: (1) the achievement of the diaphragm's elastic limit at life-safety and (2) the exhaustion of the diaphragm's available ductility at collapse-prevention. This proposed approach, introduced at the outset of the DSDM project, was driven by the idea that non-ductile precast diaphragms would fail in an MCE event (e.g. Northridge earthquake), even if designed elastically in a DBE event. It was recognized that to achieve this approach the diaphragm design forces would need to be increased over the values currently used in the code (Restrepo 2007).

During the early stages of the DSDM project, it was recognized that a more versatile design method could be achieved by providing the designer a selection of performance targets, driven by the deformation capabilities of the diaphragm reinforcement (Fleischman et al 2005a). This approach would allow a designer the flexibility to use diaphragm details of their choosing, with the understanding that a higher design force is associated with less ductile details. This is analogous to the seismic force reduction "*R*" factors used in the design of the LFRS, where higher *R* factors are justified for more ductile systems.

An early conceptual framework for this approach was proposed by Maffei (2005), in which the amplified diaphragm force is given by:

$$F_{px} = \frac{w_{dia} \Psi_{vert}}{\mu_{dia}} F_x \qquad\qquad (Eqn.\ B\text{-}1)$$

where F_x is the story seismic force; w_{dia} is the dynamic amplification of diaphragm (depends on story); Ψ_{vert} is the overstrength of vertical LFRS; and μ_{dia} is the ductility capacity of the diaphragm as a whole, which depends on connections used. For a fully elastic diaphragm design, $\mu_{dia} = 1.0$.

This is essentially the approach adopted in the DSDM design methodology, though the effects of w_{dia} and Ψ_{vert} are combined into one factor, the diaphragm force amplification factor Ψ (See *Commentary Step 3*), and the effect of the term μ_{dia} is realized through different equations for different design options (Elastic, Basic and Reduced), each corresponding to a different level of ductility in the diaphragm.

It should be noted that a force amplification approach defined relative to the current code value may not be fully rational, since the current code diaphragm design force is proportional to the seismic force reduction factor R, and the actual diaphragm inertial force is due from a combination of modes, of which only the fundamental mode has this direct relationship to the R factor (Rodriguez et al. 2002). A more rationally-based method for predicting the diaphragm inertial force, the First Mode Reduced (FMR) method, has been proposed for the seismic code (Restrepo 2007). The FMR expressions are aligned to required elastic diaphragm strength for the DBE, and thus are equivalent to Ψ_D used for the BDO (Eqn. 4, Step 5). Because there is no analog currently in the procedure for Ψ_E for Ψ_R, these methods cannot be directly introduced into the design methodology at this time. However, the FMR method could easily be adopted into the design methodology through an approach similar to that proposed by Maffei (2005), in which the FMR method controls the terms w_{dia} and Ψ_{vert} and different μ_{dia} values are provided for each design option (Elastic, Basic and Reduced). This step would require aligning the diaphragm performance targets with the design force values from the FMR method. A description of the FMR method and a comparison of FMR values with the DSDM force amplification factors Ψ_D, Ψ_E, Ψ_R is found in *Section 5.4*.

At about the midpoint of the project, the consensus of the DSDM research team on the needed design approach was detailed in a white paper that eventually was published in Part III of the NEHRP Recommended Seismic Provisions (BSSC 2009). According to this document, the following are necessary features of a viable diaphragm design methodology:

1. Accurate diaphragm design force magnitudes and appropriate design force patterns.
2. An accurate yet simple method for determining diaphragm internal forces including the likely force combinations on individual reinforcement or reinforcement groups, and recognition of alternate load paths. The following aspects should be reflected in this method:
   – Precast diaphragm reinforcement designed for force combinations when appropriate.
   – More rational load paths used to distribute forces to the primary LFRS elements.
   – Alternate load paths through secondary elements should be accounted for or mitigated, including preclusion of non-ductile failure modes in secondary elements.
3. Detailing provisions including:
   – Capacity design factors to protect non-ductile diaphragm reinforcing elements;
   – Estimate of the expected inelastic deformation demands for the remaining diaphragm details for a given set of design parameters; and
   – Demonstration of reliable deformation capacity for the diaphragm details in question.
4. A diaphragm elastic stiffness calculation procedure that can be used to properly estimate seismic design forces and check drift limits.

In essence, the DSDM Project performed the experimental and analytical research to put numbers to the concepts listed above. These activities are described in *Background Appendices A and B*.

Design Concept Modifications post-NEHRP Part III

Certain modifications or further enhancements were made to the approach described in the NEHRP white paper based on the results of the research. Principal among these were:

(1) <u>Introduction of Diaphragm Seismic Demand Levels</u>: In the earlier conceptual descriptions, the idea of EDO, BDO and RDO designs using LDE,MDE and HDE reinforcement were introduced, but there was no clear guidance on when these designs could or should be used. For this reason the Diaphragm Seismic Demand Levels were introduced which set boundaries for the use of these design options based on SDC, # of stories, diaphragm length and aspect ratio.

(2) <u>Introduction of a Diaphragm Force Vertical Distribution Factor (α_x)</u>: A constant diaphragm force vertical distributions proposed in earlier work (Fleischman et al. 1998) (Fleischman and Farrow 2001). The earlier research on which this recommendation was based involved analytical models that did not include the contribution to lateral resistance of the gravity system columns. This contribution, which was included in the DSDM research, turned out to have a non-negligible effect on the response of flexible diaphragms. A constant diaphragm force vertical distribution can still be used, but in many cases it will be overly conservative on many floors. Thus, the α_x factor was introduced to create more economical designs.

(3) <u>Diaphragm properties based on single load component testing</u>: The diaphragm reinforcement characteristics are obtained based on simple tests of the diaphragm connectors under single load components (e.g. cyclic shear and cyclic tension), and these values are introduced into the interaction formula to account for the combined effects of their simultaneous actions. The use of an interaction equation accounts for combined forces on the diaphragm reinforcement rather than relying on testing protocols involving combined axial and shear loading in the diaphragm reinforcement qualification.

This decision was made based on the challenges faced in attempting to create consistent testing protocols during the DSDM project to evaluate diaphragm reinforcement characteristics. There are many different parameters that can be controlled (shear-to-axial force ratio, shear-to-axial displacement ratio, proportional vs. constant amplitude loading trajectories) and it was difficult to find consistent test results among these protocols that provided the needed information. Further, it takes a significant level of testing expertise to conduct these tests properly. Therefore, it was considered impractical to require combined load testing as part of the qualification protocols. It is noted that the designs were verified in analyses of precast prototype structures using models that capture the non-proportional cyclic force combinations acting on the diaphragm.

(4) <u>Diaphragm reinforcement design based on the collective strength at each joint</u>: This decision was made in recognition of the force combinations (N,V,M) present at many diaphragm joints, and due to the desire to include the contribution of shear reinforcement to the flexural strength, as well as the need in cases to include the contribution of the chord reinforcement to the shear strength. Thus, the interaction formula is applied along the joint, rather than on a connector by connector basis.

(5) <u>Elimination of the Ω_a factor</u>: Originally, separate factors, Ω_v and Ω_a, were planned for the diaphragm shear reinforcement and the diaphragm anchorage (e.g. collectors and diaphragm-to-LFRS connection) respectively. When the decision was made to design the diaphragm force at the joint level, Thus, it was decided that there was no reason to distinguish between the design of a shear critical joint and the design of the diaphragm-to-LFRS connection. Thus, the diaphragm shear overstrength factor (Ω) is applied to the required shear strength in the interaction formula, regardless of whether a joint within the diaphragm or the connection to the LFRS.

(6) <u>Discontinuing use of the term "capacity design"</u>: The terminology regarding the overstrength factor Ω was modified to eliminate the terminology "capacity design factor", since based on the complex internal patterns observed in the analyses (See *Background -Appendix A2*), a rigorous capacity design cannot be assured.

Final DSDM Design Approach

The approach adopted in the final design methodology is described in *Section 5.2*. The procedure appears in PART 1, with appropriate force values provided by the DSDM Research (See the *Background Appendices*). The design approach was arrived through industry consensus through the DSDM TG.

5.4 Background on Diaphragm Seismic Behavior

In this section, background on the seismic behavior of precast concrete diaphragms is presented, including: (1) Diaphragm Seismic Forces; (2) Diaphragm Internal Force Paths; (3) Diaphragm Deformation Capacity; and (4) Diaphragm Flexibility.

Diaphragm Seismic Forces

An aspect of diaphragm behavior not elucidated in the codes and thus possibly not clearly understood is the relationship of the design forces used in equivalent lateral force (ELF) procedures to the inertial forces that may actually occur in floor diaphragms during a seismic event. It has been traditionally considered that inertia forces in diaphragms are related to the magnitude and distribution of the lateral forces for designing the lateral force resisting system. However, evidence exists to show that this assumption is not necessarily true, and instead, the seismic design code values may in cases significantly underestimate diaphragm inertial forces. Such observations have been deduced from accelerations measured during earthquakes (Hall 1995) and in shake table tests (Kao 1998). For instance, recorded maximum floor accelerations for 25 multistory buildings during the Northridge earthquake reached 4.6 times the peak ground accelerations (Hall 1995).

The primary contributor to the large inertial forces in diaphragms is higher mode effects in the building system (Rodriguez et al. 2002). The effect was first described as it relates to high seismic shear forces occurring in shear wall (Blakeley et al. 1975), leading to seismic design recommendations for shear walls (Kabeyasawa 1988). Eberhart and Sozen (1993) first formalized the basis of the effect, again as it pertains to seismic shear force in shear walls, by highlighting the similarity of the first mode with the base moment influence vector, including its direct equivalence to the mode shape of a base-hinged shear wall, and used the concept of mode orthogonality to elucidate the postulation that higher modes contribute primarily to the base shear, and only to the base shear for shear wall structures undergoing a base hinge.

Fleischman and Farrow (2001) extended this concept to the diaphragm forces that develop in shear wall structures, and compared the forces that develop in structures with different diaphragm characteristics. Figure B-2 reproduces a figure from the paper showing center of force scatter plots for three-story shear wall structures. Note that a lower instantaneous center of force implies a higher base shear for a given base moment strength, and hence the potential for a higher diaphragm force at one or more floor levels in the structure. The scatter plots show the center of force for all base shear values above a certain threshold force. Figure B-2a shows the ELF representing the equivalent lateral force (ELF) pattern used to design the LFRS, and extends a dashed line at the centroid of this force pattern. The scatter plots in Figure B-2 include: (b) an elastic rigid diaphragm structure; (c) an elastic flexible diaphragm structure; (d) an inelastic shear wall rigid diaphragm structure; (e) an inelastic shear wall structure with flexible elastic diaphragms; and (f) an inelastic shear wall structure with flexible inelastic diaphragms. A high diaphragm flexibility is used for the analyses of Figs. B-2c,e,f, roughly equivalent to what would occur in a perimeter wall parking structure.

As seen in Fig. B-2b, the center of force for a three story elastic structure is essentially clustered around the centroid implied by the ELF pattern. This can be explained by the lessened importance of higher modes in a three story structure (due to less mass participation and similarity of spectral acceleration in higher modes for short period structures). Figure B-2c shows that diaphragm flexibility will tend to increase the forces in the structure; this occurs because the flexible diaphragm produces higher modes that can vibrate semi-independently, and whose effects are less dependent on height from the base. However, compare this with the results shown in Figs. B-2-d-f, which pertain to the more expected case of an inelastic shear wall. In this case, the higher mode effects become more significant as the effective fundamental period lengthens and the effective mode shape is exactly aligned with the base moment influence vector (Eberhart and Sozen 1993). In this case, highly diaphragm flexibility actually raises the centroid, as the flexible diaphragm modes now uncouples more of the mass from the behavior exhibited in Figure B-2d. The conclusion drawn from these plots is that the primary driver of high diaphragm force is the dynamics of the LFRS, as modified by diaphragm flexibility.
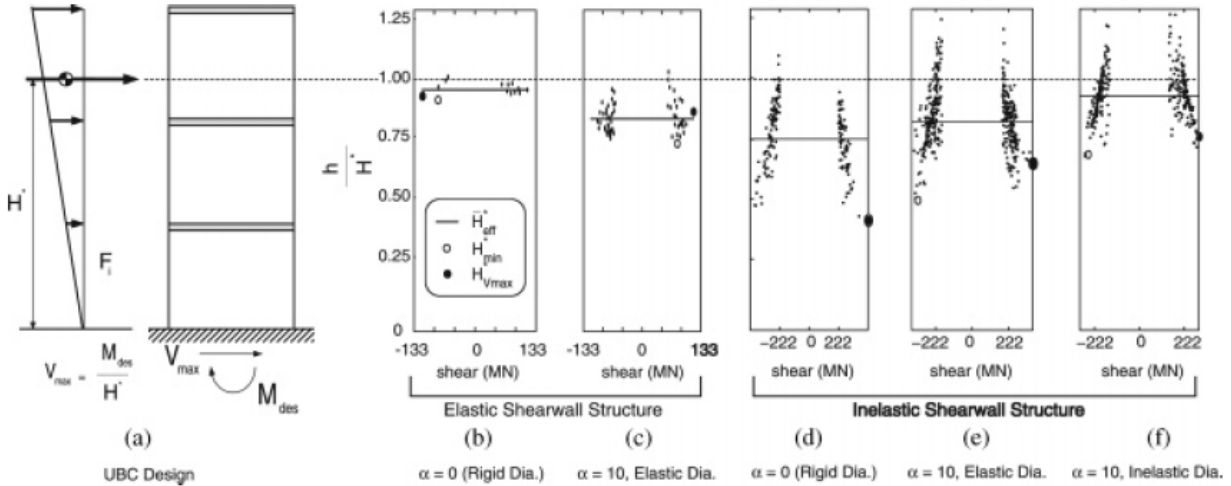
Figure B-2. Center of Force for different diaphragm conditions (Fleischman and Farrow, 2001).

In follow-up work, Fleischman et al (2002) showed that moderate to high diaphragm flexibility can add deformation to existing mode shapes, thereby amplifying inertial forces, while extremely high diaphragm flexibility (for instance that shown in Fig. B-2) tends to isolate the diaphragm into its own modes, thereby reducing inertial forces. This research also examined moment frame structures and determined that the effect was not as pronounced for this LFRS.

An important concept involved in the higher mode effect is that the response is driven by the dynamic characteristics of the *yielded* (LFRS) structure (e.g. compare Figs. B-2b and d). Thus, it is important to understand that elastic concepts (e.g. modal superposition may not properly capture these behaviors. Consider Figure B-3a, which shows floor accelerations for shear wall structures (the average of maximums from analyses of ten SDC D MCE events) of different stories and R factors. The plot clearly shows a reduction in maximum acceleration as R is increased, as may be expected. However, when scaling these results with the inelastic response spectrum (i.e., the structure design force that includes the R factor) as is done in Figure B-3b, it is clear that the diaphragm force amplification grows with increased inelastic action of the shear wall. Figure B-3c shows that this behavior also occurs in moment frame structures, though the amplification is less.
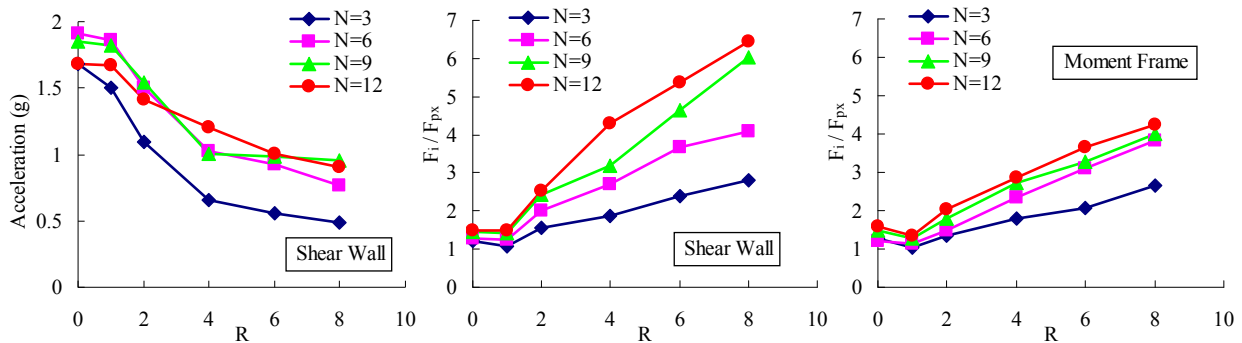
Figure B-3. Diaphragm Force vs. R factor (Zhang 2012): (a) Acceleration SW; Amplification for: (b) SW; (c) MF.

In parallel work demonstrating that the design code ELF values may in cases significantly underestimate floor inertial forces, Rodriguez et al (2002) were the first to clearly relate the higher mode effects to floor diaphragm inertial force. A key conceptual advance for diaphragm design provided in this work was the recognition that the seismic force reduction (*R*) factor is based on first mode response and does not therefore apply to the higher modes that drive maximum floor inertial forces.

To rationalize their research findings, Rodriguez et al (2002) proposed the First-mode reduced method (FMR) for evaluating inertia forces for the design of diaphragms. In this method, the absolute acceleration of the uppermost floor A_n is obtained from a modal combination rule in which only the spectral acceleration corresponding to the first mode of vibration S_{a1} is reduced by the R factor. The following equation was proposed for estimating A_n :

$$A_n = \sqrt{\left[\Gamma_1 \phi_n^1 \frac{S_{a1}}{R_1}\right]^2 + \sum_{q=2}^{r}\left[\Gamma_q \phi_n^q S_{aq}\right]^2} \qquad (Eqn.\ B\text{-}2)$$

in which Γ_q is the participation factor of mode q, ϕ_n^q is the amplitude of mode q at level n. S_{aq} is the spectral acceleration corresponding to translational mode q. The R factor, given by the coefficient R_1, accounts for the effect of ductility in the first mode of response. R_1 is also modified to account for the overstrength of the LFRS.

For routine design practice, Rodriguez et al (2002) provided a simplified version of the FMR expression for estimating A_n by removing the need to perform a modal response spectrum analysis through the use of an upper bound (Eqn. B-3a) and a lower bound (Eqn. B-3b) approximation for the modal response terms:

$$\text{Upper bound: } A_n / g = \sqrt{\left[\eta_1 \frac{C_h(T_1,1)}{R_1}\right]^2 + 1.75\ln(n)C_{ho}^2} \qquad (Eqn.\ B\text{-}3a)$$

$$\text{Lower bound: } A_n / g = \sqrt{\left[\eta_1 \frac{C_h(T_1,1)}{R_1}\right]^2 + 0.625\ln(n)C_{ho}^2} \qquad (Eqn.\ B\text{-}3b)$$

in which η_1 is a first mode contribution coefficient conservatively taken as 1.0 for single-story, and 1.6 (upper bound) and 1.2 (lower bound) for multi-story buildings. $C_h(T_1,1)$ is the 5% damped spectral acceleration normalized by the acceleration of gravity at the building's fundamental period, T_1. C_{ho} is the peak ground acceleration normalized by the acceleration of gravity. Further experimental research (Rodriguez et al 2007) and analytical studies (Schoettler 2010) showed that the estimated diaphragm acceleration using the simplified FMR upper bound equation (*Eqn. B-3a*) conservatively predicts the earthquake acceleration demands in DBE level at each floor diaphragm.

Later, by introducing the current code seismic design parameters into the simplified FMR upper bound equation, Restrepo and Rodriguez (2007) proposed a new equation to replace the current diaphragm seismic design force in current code (ASCE 7 2005). The roof diaphragm design force, F_{pn}, is determined using follow equation:

$$F_{pn} = w_{pn}\sqrt{\left[\eta_1 \Omega_o C_s\right]^2 + 0.28\ln(n)(IS_{DS})^2} \qquad (Eqn.\ B\text{-}4)$$

in which w_{pn} is the weight tributary to the diaphragm at level n. η_1 is 1.0 for single-story and 8/5 for multiple story buildings. Ω_o is the system overstrength factor, C_s is the seismic response coefficient, S_{DS} is design spectral response acceleration parameter at short periods and I is the important factor as specified in current code (ASCE 7 2005). For other floors, the diaphragm design force is calculated using:

$$F_{pi} = 0.4w_{pi}\Psi_i S_{DS}I \qquad (Eqn.\ B\text{-}5)$$

where Ψ_i is the diaphragm design force magnification factor defined as:

$$\Psi_i = \frac{F_{pn}}{0.4w_{pn}S_{DS}I} \qquad \text{for floors located between } 0.2 < h_i / h_n \leq 1.0$$

and

$$\Psi_i = 5\left(\frac{h_i}{h_n}\right)\left(\frac{F_{pn}}{0.4w_{pn}S_{DS}I} - 1\right) + 1 \qquad \text{for floors located between } 0 < h_i / h_n \leq 0.2$$

Note that the diaphragm design force magnification factor Ψ_i in the Restrepo and Rodriguez (2007) ASCE-7 code change proposal is equivalent in concept with the diaphragm vertical force distribution factor, α_x in this design methodology (and should therefore not be confused with the Ψ factors used as diaphragm amplification factors in PART 1). The need for vertical distribution factors for diaphragm force has been recognized in more recent research (Zhang 2010) (Schoettler 2010) incorporating the gravity system columns in the analytical models, which has produced different vertical force distributions.

Most recently, Schoettler (2010) proposed a diaphragm acceleration design equation modified from the simplified upper bound equation (*Eqn. B-3a*) from Rodriguez et al (2002):

$$A_n / g = \sqrt{\left[\eta_1 \frac{\lambda C_h(T_1,1)}{R}\right]^2 + \eta_k C_{ho}^2} \qquad (Eqn. \ B-6)$$

where R is the response modification factor in current code (ASCE 7 2005). $\eta_l = 1$ for one story structures and 1.5 for multi-story structures. and $\eta_k = \min\left(1.4\sqrt{n-1}, \ 5\right)$. λ is an overstrength factor recommended as 1.75. It is noted that the effect of diaphragm geometry, e.g. floor span as it impacts diaphragm flexibility, on diaphragm force was examined in the research, and its effect was considered secondary to the higher mode effects in the structure (Schoettler 2010).

It is noted that recently the higher mode phenomenon was seen in precast cantilever column structures, leading to similar design expressions as the FMR (SAFECAST 2012).

Comparison of FMR method with DSDM Ψ Factors

It will be instructive to compare the diaphragm forces produced by the FMR method to the diaphragm amplification factors in the DSDM design procedure (PART 1: *Eqns. 3-5*). The most recent FMR expressions (*Eqns. B-3a, B-3b, and B-6*) are selected for this purpose. The comparison is performed across a number of sites with seismic design parameters shown in Table B-1.

Table. B-1. Seismic design parameters

Compare cases	SDC	Site	Site class	S_{DS}	S_1	R	Ω_o
1	E	Berkeley (BE)	C	1.39	0.80	6	2.5
2	D	Seattle (SE)	C	1.05	0.48	6	2.5
3	D	Charleston (CH)	F	0.87	0.73	6	2.5
4	C	Knoxville (KN)	C	0.45	0.16	5	2.5

The value will be compared based on the diaphragm design accelerations at top floor. This value is directly obtained through the FMR approach; however the design methodology force equation (PART 1: *Eqn. 9*) must be converted to diaphragm acceleration by normalizing the design force with floor mass at top floor ($A_n = \Psi F_{Dn}/w_n$) to produce equivalent values to compare the two methods. The DSDM diaphragm force amplification expressions (PART 1: *Eqns. 3-5*) are also a function diaphragm length and span, unlike the FMR expressions, which are based only of number of stories. Therefore, the DSDM diaphragm force values will be presented over a range of diaphragm geometries.

The normalized diaphragm force comparisons between the FMR and the DSDM are shown in Figure B-20. The values are plotted versus number of stories. The range of FMR expressions are shown as a gray shaded area, with the blue boundary lines representing the upper bound (*Eqn. B-4 or B-3a*) and lower bound equations (*Eqn. B-3b*). The black line running inside the gray shaded region represents the modified FMR equation proposed by Schoettler (*Eqn. B-6*).

The vertically hashed regions represent the range of values for the DSDM Diaphragm Force Amplification Factor Equations: the upper hashed region (in purple) for Ψ_E; the middle hashed region (in green) for Ψ_D; and the lower hashed region (in light blue) for Ψ_R. The upper extent of each range represents the higher diaphragm forces produced by longer diaphragm geometries (span=300ft, AR=3

for EDO and BDO; span=270ft, AR=2.5 for RDO); the lower extent represents the shorter diaphragm geometries (span=60ft, AR=1.0 for all design options). Note that the only direct comparison can be made between the FMR and the BDO (i.e. Ψ_D from PART 1: *Eqn. 4*), since it aligns performance targets of elastic diaphragm behavior in the DBE.

As seen in Fig. B-4, the FMR lower bound equation on average will produce similar diaphragm design force as the DSDM equations for the BDO design values, indicating reasonable correlation between the methods. The FMR upper bound equation will tend to produce higher diaphragm design forces than the DSDM equations, even for most EDO design, and thus on the basis of the extensive DSDM analytical research (See *Background Appendices A1, A2*), may be too conservative. The FMR lower bound equation is in many design regimes similar to the DSDM equations, and thus could serve as a viable generic construction diaphragm force amplification factor, e.g. for ASCE-7, to use in conjunction with the diaphragm design methodology.
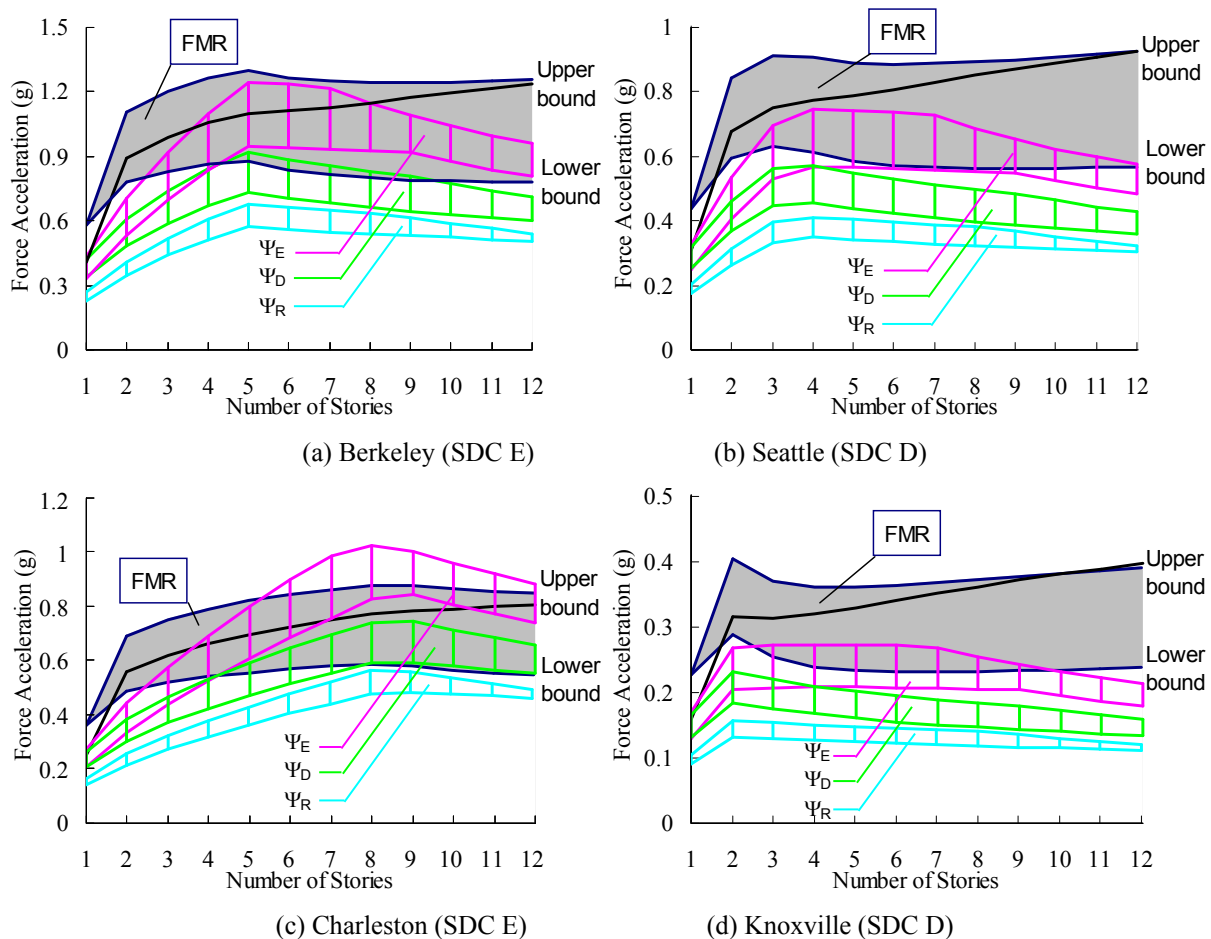
Figure B-4. Diaphragm design acceleration comparisons between DSDM and FMR expressions.

A similar comparison can be made between the DSDM force distribution factor, α_x (PART 1: *Eqn. 2*) and the FMR diaphragm design force magnification factor Ψ_i in the Restrepo and Rodriguez (2007) ASCE-7 code change proposal. Figure B-5 shows this comparison for three different height structures. As seen, the DSDM α_x factor attempts to provide more economical designs by reducing the diaphragm forces in the middle stories where higher mode effects are not as pronounced. This lower force region is due in part to the contribution of the gravity system, whose inherent stiffness reduces the magnitude of the high diaphragm demands seen to occur in the lower floors of the structure with earlier simpler models that did not include the gravity system columns (Fleischman et al. 2002).
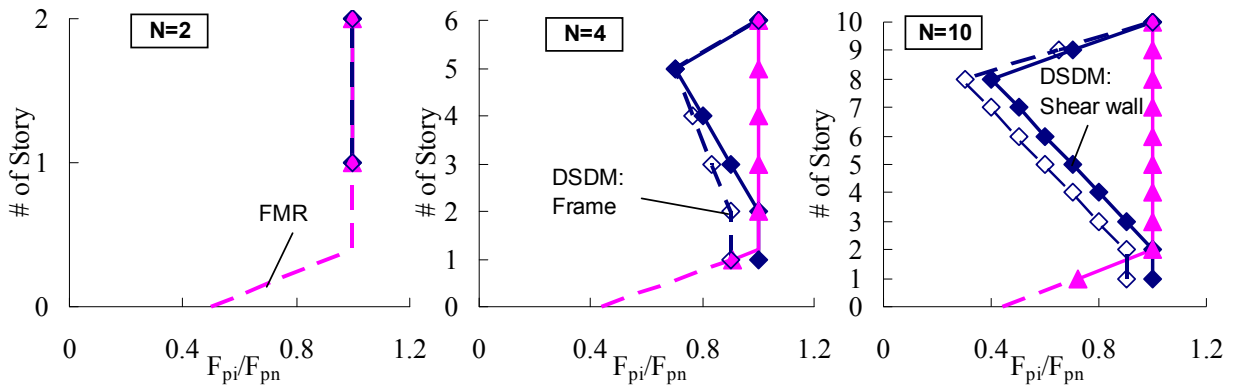
Figure B-5. Diaphragm design force distribution comparisons between DSDM and FMR expressions.

Note that the FMR method, though based on elastic modal superposition, includes inelastic effects in the design equations by employing the inelastic design spectrum on the first mode (i.e., the R factor is only associated with the first mode). For this reason, the FMR method captures well the effects of inelastic response (i.e. the trends indicated in Fig. B-3), as shown in Fig. B-6 for the upper bound FMR expression. Also, it should be noted that the DSDM diaphragm design force amplification factors, Ψ, were developed based on analyses of 2, 4 and 6 story evaluation structures, and verified with a limited number of structures (4-story shear wall parking structures and 8-story shear wall and 8-story moment frame office buildings. Thus, the accuracy of the Ψ factors for taller structures has not been fully established. This is seen in the underestimating of shear wall elastic force for the 12 story structure (See Fig B-6b). Thus it may be prudent to use a more conservative expression for Ψ for taller structures, for instance the alternative linear Ψ equation. However, it is noted that the results shown in Figure B-6 represent a substantially simpler model than the prototype structure models evaluated to verify the Ψ factors, and thus it is unclear if the DSDM equations are indeed not appropriate for taller structures. Likewise, it is seen that both the DSDM and FMR expressions do not currently fully capture the differences between shear wall and frame structures. Further work may be required on the difference between elastic and inelastic LFRS response, and between shear walls and frames, some of which is occurring within the auspices of BSSC IT6 (2012).
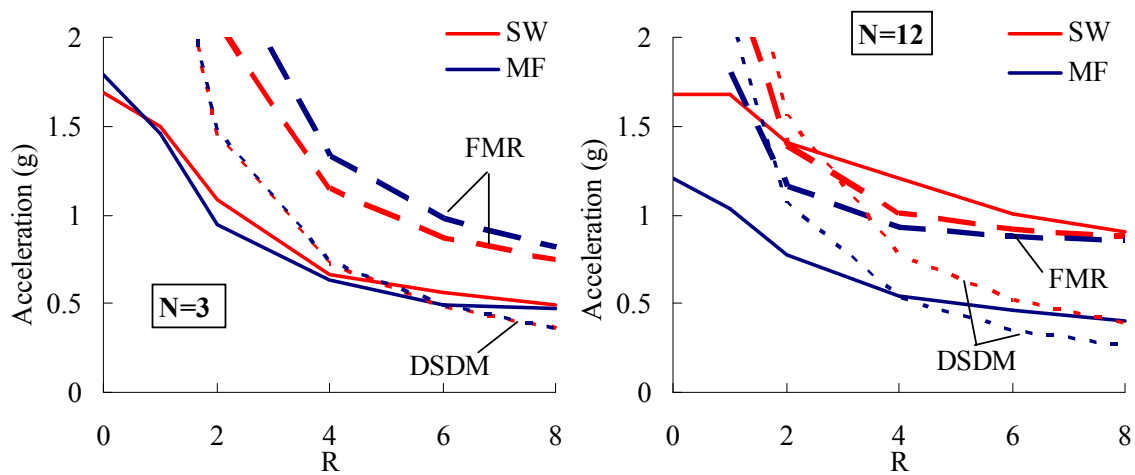
Figure B-6. Comparisons between DSDM and FMR expressions as a function of R and # of stories.

Diaphragm Internal Forces

The underestimation of diaphragm inertial forces (as described in the previous section) is a key issue in current diaphragm design. However, current design methods may also inadequately describe the internal forces that develop in the diaphragm. This step, the transformation of the story-level diaphragm force into internal forces within the diaphragm, is a key step in diaphragm design (Clough 1982).

Current practice (PCI Design Handbook 2004) uses a horizontal beam analogy (Gates 1981) to determine the internal forces due to F_{px}. In this approach, the diaphragm is treated as a simple beam (Bockemohle 1981) in order to calculate a maximum moment, shear and beam reactions (See Fig. B-23). Chord reinforcement is then designed for the tension component of the couple due to in-plane diaphragm moment; shear reinforcement across panel joints parallel to the seismic force is designed to carry the in-plane shear; and collectors bring these forces to the LFRS, whether in the topping slab or in the precast unit. The following observations are made with respect to this approach:

1. the internal force distribution assumed in the horizontal beam analogy implicitly relies upon elements in the precast joint with plastic redistribution qualities, without enforcing this characteristic.
2. the horizontal beam analogy is unable to capture complex force paths that can exist in the precast floor system, including force combinations involving simultaneous shear, moment, and thrust coinciding at a diaphragm section.
3. Alternate load paths can occur through secondary members.
4. The 90-degree paths associated with collectors do not provide a fully rational load path to the primary (vertical plane) LFRS elements. Likewise transfer conditions are not addressed.
5. the horizontal beam analogy does not produce an accurate force path for squat diaphragms, in which the internal forces more closely resemble that of a deep beam..
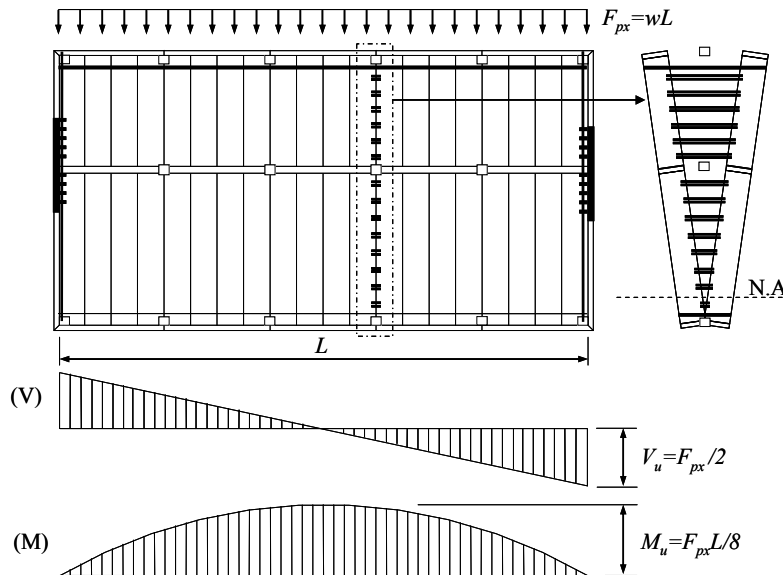
Figure B-7. Typical diaphragm layout.

Thus designs using the horizontal beam method may not be sufficiently accurate to lead to an adequate design. These issues are each discussed in more detail in the following:

1. Joint internal force distribution: First, the internal force distribution assumed in the horizontal beam method implicitly relies upon elements with plastic redistribution qualities. This is an important consideration that may have been overlooked in the past. Essentially, designing the chord reinforcement using the expression $A_s f_y = T = M_u/d$, requires that the diaphragm can undergo a deformation such that the chord reinforcement can reach its yield strain (See Fig. B-7). This condition is not assured in precast diaphragms because the shear reinforcement that exists in the joint is not currently subjected to any

(tension) deformation requirements. Recent codes (ACI 318-08) permit the contribution of shear reinforcement to flexural strength, but do not provide deformation requirements. Wood et al (2000) indicated that such strain compatibility should be considered in the design of shear reinforcement.

Such a requirement seems necessary. The precast diaphragm joint is essentially an extremely lightly-reinforced section with a neutral axis near the compression chord (see *Section 3.3, PART 3*). For a cross-section of significant depth, equivalent to the length of the precast unit, the shear reinforcement will undergo large opening compatible displacements in developing the strength of the joint. Note that while in many design cases this is a largely theoretical exercise, e.g. reinforcement ratio limits relative to ρ_b for reinforced concrete beams in gravity systems (ACI 318 2008), yielding is expected to occur for precast diaphragms designed using current codes in the design earthquake (Zhang et al. 2011). Since the tension failure deformation of some connectors used for shear reinforcement (Naito et al. 2006) is of similar magnitude as the chord yield displacement (Nakaki 2000), failure of the shear reinforcement could occur in the absence of strain compatibility provisions. This outcome not only has ramifications for the diaphragm shear strength, but also for the diaphragm flexural strength: Fleischman and Wan (2007) showed that the loss of nonductile shear reinforcement in a critical flexural joint due to compatible tension deformation will tend to concentrate the inelastic deformation in that joint, rather than allow the inelastic deformation demand to spread out among many joints.

2. Complex force paths: For the horizontal beam method, the maximum moment occurs at diaphragm midspan, maximum shear at diaphragm end, and axial thrust is relegated to the end collector reaction brought to the primary elements of the LFRS (e.g. Fig. B-7). This approach where the diaphragm is designed for a single moment value in one region and a single shear value in another region oversimplifies the actual force demands acting in the diaphragm. It has long been recognized that complex force paths exist in the precast floor system (Wood et al. 2000). The internal forces that develop in precast floor joints during earthquakes involve force combinations (Lee and Kuchma 2008), i.e., in plane thrust, shear and bending acting simultaneously (Farrow and Fleischman 2003). These situations occur due to the complexity in floor plans, including openings or other irregularities in the floor system, restraint including our-of-plane restraint of LFRS elements, or simultaneous action of flexure actions in one orthogonal direction with collector actions in the other direction.

Force combinations can include high shear and moment, high shear and tension, and in cases, non-negligible values of axial force, in-plane shear and moment. Several examples of force combinations are found in the results shown in *Background -Appendix A2*: Fig. A2-5 shows joints with high combined moment-axial and axial-shear demand; Fig. A2-23 shows joints with high shear and moment demand.

3. Alternate Load Paths. Alternate load paths may occur in the precast floor system through secondary elements such as spandrel beams, internal beam connections outside the chord lines that are not governed by tributary shear requirements, lite-walls in their out of plane direction, gravity columns, etc. These paths are unanticipated by the horizontal beam model. These effects should be accounted for in the determination of the internal force path. Essentially, there are four possible approaches to secondary element participation in the floor diaphragm (Wan et al. 2012): (1) Strong (elastic) connections; (2) Compliant (elastic) connections; (3) ductile (inelastic) connections; or (4) brittle (inelastic) connections. As an example, the European Union designers are considering the merits of these approaches for the attachment of precast wall panels to flexible cantilever column precast structures (SAFECAST 2012). In the first case, *strong* connections, the alternate load path is accepted and used in the resistance. This approach can be effective if the secondary system is stiff and well-behaved, for example St. George's Hospital Carpark, which performed well in the 2012 New Zealand earthquake through the participation of stiff perimeter precast lite-wall elements interacting with spandrel units, thereby protection the hollowcore floor system (PCI 2011). It is unclear if such an approach translates to the U.S. systems, where the secondary elements often have compliance for temperature change. Further, a well-defined secondary load path is required. The second case, a *compliant* connector, may be the best option. Examples of this are the use of a flexible angle between lite-walls and the ramp elements in precast

parking structures, while more rigidly tying in the flat parking regions to the opposite face of the lite wall (Cleland 2011). The use of this detail is in recognition of the difficulty in achieving good performance for rigidly-connected floor diaphragms on either side of the lite-walls, offset by short distances in elevation acting out of the plane of the lite wall. The third case, a *ductile* connection, is what was assumed in the research. Thus, the diaphragm analyses used to develop the design factors are estimating the force paths present with current details; however these details are assumed to have some deformation capacity. Thus, the impact of the actual current connections, which may not have the full deformation capacity assumed (e.g. case 4), must be considered. This issue is considered below in *Deformation Capacity*, since while these conditions do represent a diaphragm internal force issue in the elastic range, the major effect of these alternate load paths pertain to deformation patterns and the relationship of local to global deformation capacity.

3. Collector load paths: The 90-degree paths associated with collectors do not provide a fully rational load path to the primary (vertical plane) LFRS elements. Shear strength design equations based on inclined cracking are not consistent with the observed behavior for topped precast concrete diaphragms (Wood et al. 2000). The designer should use rational methods to bring the load path to the LFRS elements. The internal force conditions discussed do not include transfer conditions. These conditions have been shown to be failure critical in recent earthquakes (EERI 2011) (See *Commentary Step 5*).

4. Squat diaphragm force paths: The horizontal beam method will not create accurate force path for squat diaphragms, in which the internal forces more closely resemble that of a deep beam. Several methods exist for determining diaphragm internal load paths that are alternates to the horizontal beam approach. For example, strut and tie methods are used outside the United States (Fédération Internationale du Béton 2003). These methods were described in the Commentary for Step 8.

Diaphragm Controlling Mechanism
A flexural limit state is promoted in the design methodology over a shear limit state (Fleischman PCI 2005). This outcome is achieved in the design methodology through the use of overstrength factors for the shear reinforcement. However, these overstrength factors are not capacity design factors purpose, given that the moment and shear diagrams in diaphragms are not always clearly defined. Thus care must be taken in applying the factors in design for complicated floor systems. Two examples from the analyses of the prototype structures (See *Background -Appendix A2*) are used here to illustrate this point.

Before covering these examples, it is noted that the choice of a flexural controlling limit state is based on assumption that a shear limit state is brittle, consistent with concepts from reinforced concrete (ACI 318 2008). It should be recognized, however, that since the shear limit states will not occur in the concrete given the jointed nature of the floor system (Wood et al 2000), the possibility exists for developing a ductile shear mechanism in the diaphragm, or a combined ductile shear/flexure mechanism. These alternative approaches were not pursued in the DSDM research, which instead focused exclusively on designs that promote flexural limit states over shear limit states. However, this approach may be desirable for: (1) squat diaphragms where it is difficult to develop a flexural mechanism; (2) complex diaphragms where a capacity design based on flexure may be difficult to accomplish. The design factors and classifications developed here do not apply to this alternate approach. In this case, diaphragm connectors would require *shear* deformation capacity.

(1) Parking Structure with Perimeter Longitudinal Walls at Diaphragm Midspan
The first structure considered is a 4-story parking structure with longitudinal shear walls at the midspan region of the diaphragm when acting in the transverse direction. Figure B-8 shows typical floor plan for this case, designed with RDO option for the design factor verification stage (See *Background - Appendix A2*). In longitudinal direction, the two perimeter shear walls are located at diaphragm midspan. These perimeter longitudinal shear walls "cover" several joints close to the diaphragm midspan and provide restraint that prevents these joints from opening. This protection changes the relationship between

maximum moment and maximum shear based on a moment diagram (see north sub-diaphragm in Fig. B-8) results in flexural overstrength at joints close to midspan and a short shear span for the diaphragm which imply the shear overstrength using RDO option might not enough to prevent brittle shear failure.
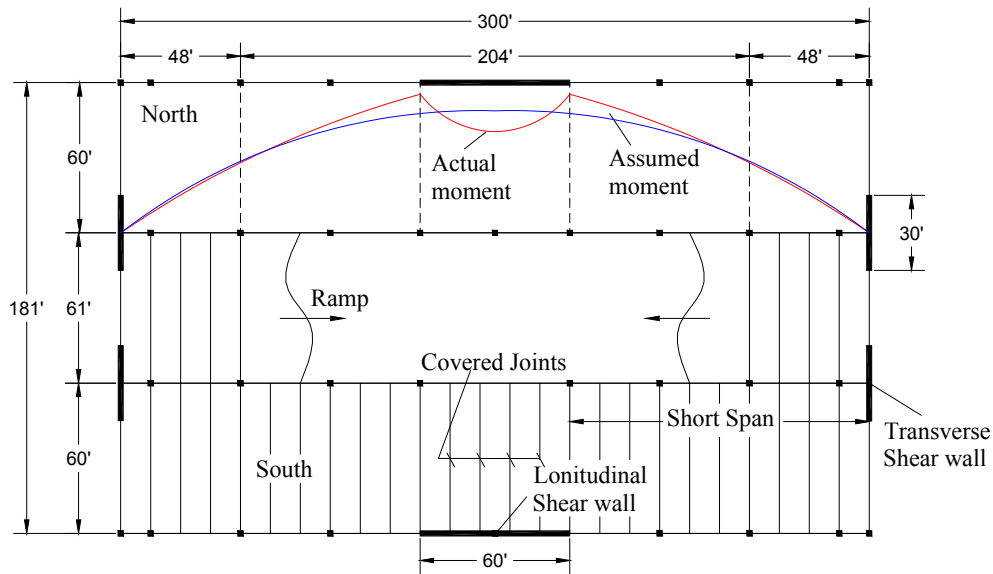
Figure B-8. Plan for a 4-story parking garage with perimeter shear walls.

Figure B-9 shows the maximum diaphragm opening and sliding demand under MCE for the 4-story parking garage with perimeter shear walls. As seen in Fig. B-9, diaphragm opening demand at covered joints is very small due the protection of longitudinal shear wall. Significant inelastic opening is concentrated at the first non-covered joint with a highest value of 1″ which is larger than the typical HDE capacity (0.6″). As seen in Fig. B-9b, diaphragm sliding demand exceeds yield sliding at multiple joints due to the flexural overstrength and short shear span which indicates brittle shear failure in the diaphragm.
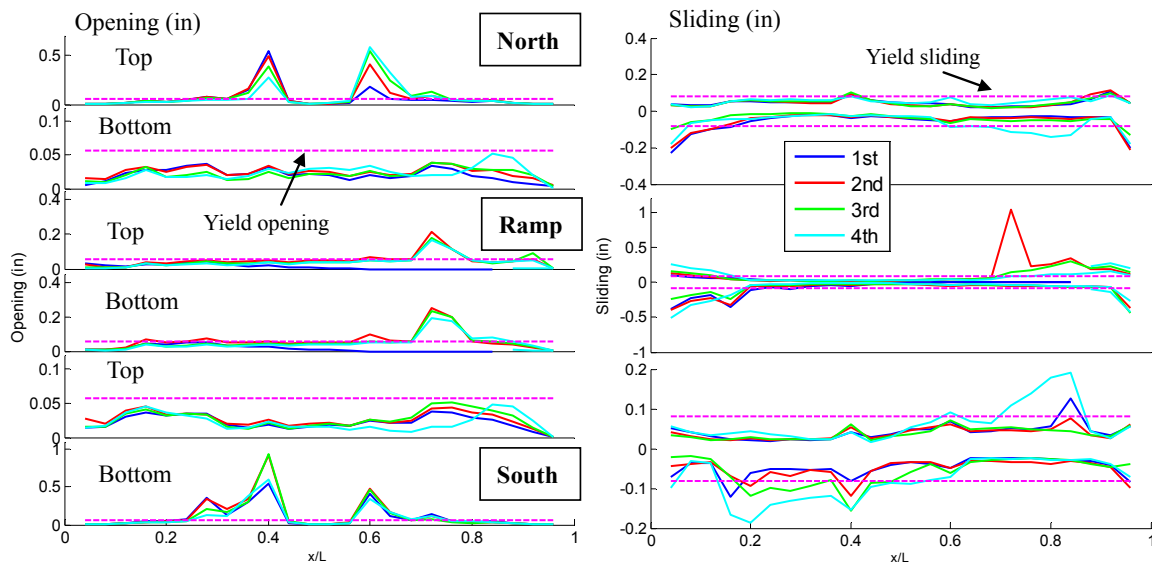
Figure B-9. Diaphragm joint max deformation demand under MCE: (a) Opening; (b) Sliding.

(2) Office Structure with Perimeter Longitudinal Walls at Diaphragm Quarter Span

The second structure considered is an 8-story office building with perimeter shear. Figure B-10 shows a typical floor plan, designed with RDO option for the design factor verification stage (See *Background - Appendix A2*). In longitudinal direction, four perimeter shear walls are placed at diaphragm quarter span. These perimeter longitudinal shear walls will provide restraint when the diaphragm deforms under transverse load (See Fig. B-10b). The resulting shearing forces will reduce the moment demand for the diaphragm from the perimeter shear wall to midspan which creates three critical flexural joints: one at midspan and the other two at the joints close to the longitudinal perimeter walls (See moment diagram in Fig. B-10b).
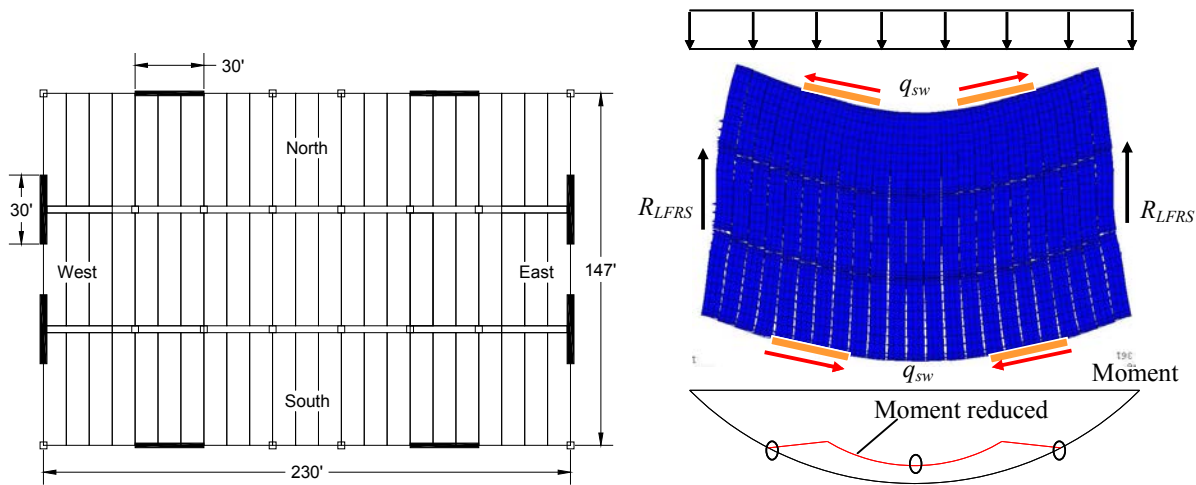
Figure B-10. 8-story parking garage with perimeter shear walls: (a) Plan; (b) FBD.

Figure B-11 shows the diaphragm internal force diagram for the 8-story office building with RDO design at 2nd floor under MCE. The red line represents the design force assumption. The light blue line represents the actual strength. The dark blue line represents the seismic demand from analysis results.

As seen in Fig. B-11, the joints close to the longitudinal perimeter walls has a significant flexural overstength in order to satisfy high shear demand at these joints. In the earthquake simulation, after the diaphragm yield in flexure at midspan, the moment demand of these joints can significantly increase due to its flexural overstrength without significant increase of midspan moment due to perimeter wall shear constraints (see dark blue line the Fig. B-11a). The increase of moment at the joints close to perimeter walls results in a significant larger shear demand compared to the design assumption (see Fig. Fig. B-11b). This in turn causes a brittle shear failure at multiple diaphragm joints as seen in Fig. A2-46.
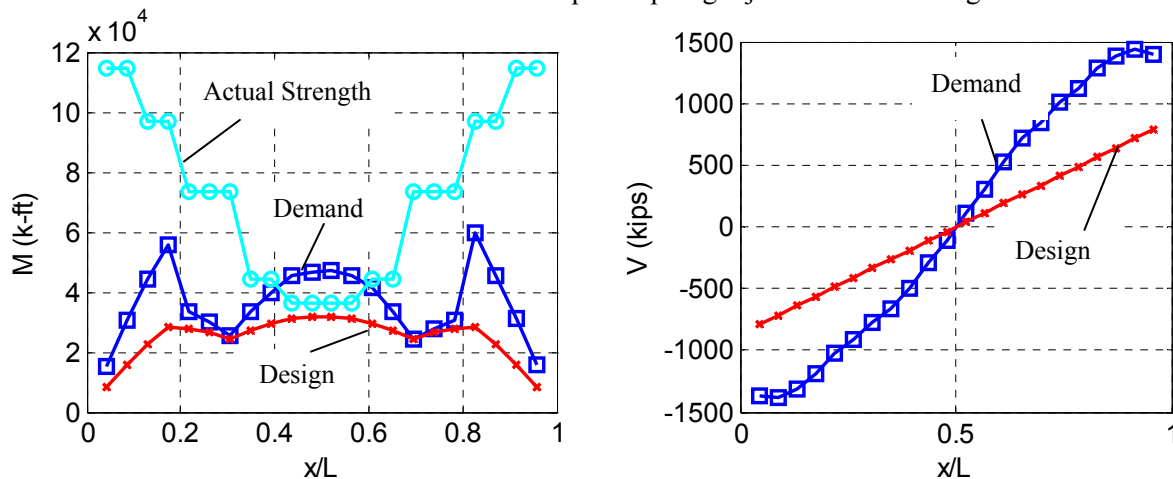
Figure B-11. Diaphragm internal force diagram at 2nd floor: (a) Moment; (b) Shear.

B-25

Diaphragm Deformation Capacity

The critical diaphragm cross-sections occur at the joints between the precast floor units. This condition occurs for untopped and topped precast concrete diaphragms alike, because cracking in the topping slab along the joints between precast units doe not ensure monolithic diaphragm action for topped diaphragms (Wood et al. 2000). In the elastic range, a non-negligible portion of overall diaphragm deformation is associated with deformation of the panel (flange) itself (Ware 2012). However after the diaphragm yields, inelastic deformation will tend to concentrate primarily at the joints.

Analytical research (Fleischman and Wan 2007) has indicated that precast diaphragms with shear reinforcement with limited *tension* deformation capacity tend to have inelastic deformation concentrate at a single joint rather than be spread out among the diaphragm joints. In other words, the initial joint to lose a portion of its shear reinforcement due to tension deformation demands created by flexural action will limit the peak value of further moments, thereby serving as a fuse in the diaphragm, protecting surrounding joints, and thus incurring the total inelastic deformation locally at the single joint. As a result, even though the tension strength of the shear reinforcement contributing to flexural strength is included in the design procedure (*See Commentary Step 5*), the tensile deformation capacity of shear reinforcement may be a more important characteristic in the design. For this reason non-ductile shear reinforcement, e.g. the shear friction contribution of cold-drawn welded wire fabric crossing joints in the precast diaphragm, should not be included unless elastic diaphragm response is assured (fib 2003).

An important component of the structural integrity measures is also the treatment of secondary members such as spandrels (see Figure B-12 where the spandrel is SP).

(a) Diaphragm high shear region   (b) Diaphragm high flexure region
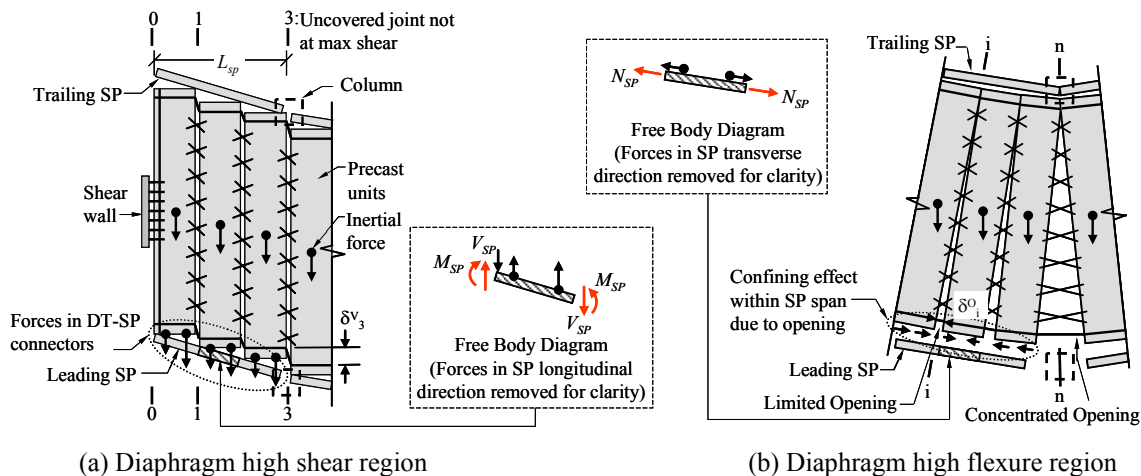
Figure B-12. Schematics of interaction between spandrels and precast floor units after (Wan et al. 2012).

The effect of the spandrel (See Fig. B-13) has been quantified in the analyses. Analyses (Wan et al. 2012) have indicated that demands on the secondary connections are less closely correlated to the diaphragm force than to diaphragm deformation demand, i.e. the forces that develop in these connections under earthquake loading is due to the imposed displacement compatibility of the floor system.

For this reason, secondary connections may be expected to have larger demands for diaphragms expected to undergo larger global inelastic response (e.g. the RDO). In the prototype structure analyses, inelastic demand is observed in these connections even for a structure with EDO diaphragm designs (See *Commentary Step 6*). Therefore, recommended deformation capacity of diaphragm secondary connection are provided (See *Comm-Appendix A2* Table B-4) to avoid unseating after possible connection failure. The impact of the loss of the secondary connections requires further consideration, e.g. the ramifications of loss of these connections with regard to load path, seating requirements, etc. (See *Sec. 5.5*).
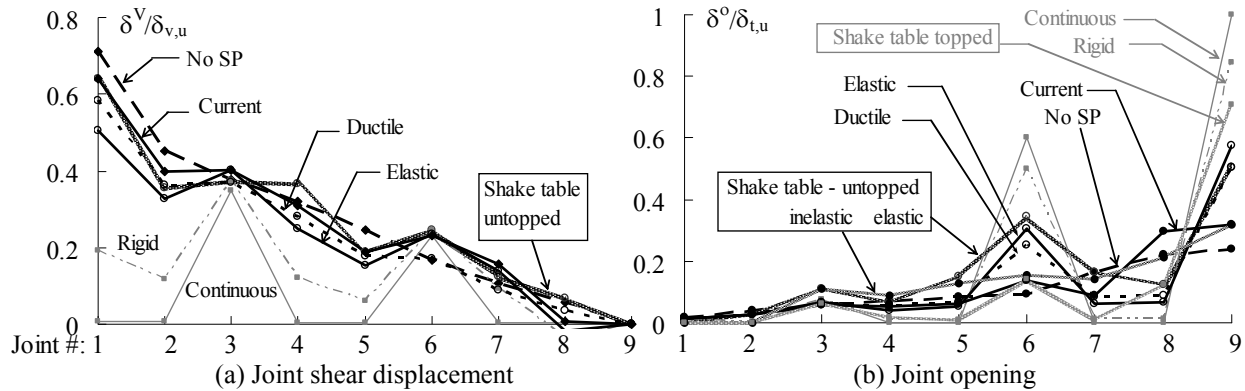
Figure B-13. Joint deformation profiles (Δ_{dia}=3.15cm) after (Wan et al. 2012).

It is important that the precast diaphragm maintain structural integrity. In addition to the classification system provided for the primary diaphragm reinforcement, requirements must include:

1. Adequate anchorage of diaphragms to the primary LFRS elements, including the carrying of superimposed gravity loads and accommodating imposed rotations from walls (Menegotto 2000);
2. Maintenance of seating for the precast units (Mejia-McMaster and Park 1994);
3. Provision of minimum ductility requirements for joint reinforcing details.

Diaphragm Flexibility

Precast concrete construction is commonly and effectively used for building systems with long floor spans. In these structures, distances between the primary LFRS elements can produce a diaphragm that is relatively flexible. The diaphragm flexibility is further increased by the inherent flexibility of a jointed system in comparison to a monolithic system. For these flexible diaphragms, the floor system and connected gravity force-resisting columns in regions removed from the primary LFRS elements can undergo amplified drift demands (Ju and Lin 1999; Tena-Colunga and Abrams 1992). These drift demands can be significant for long span precast concrete structures in a MCE (Lee and Kuchma 2007; Fleischman et al. 2002).

Several methods have been proposed for calculating the stiffness of a precast concrete diaphragm (Zheng and Oliva 2005; Farrow and Fleischman 2003; Nakaki, 2000). The methodology uses the analytical based spreadsheet-compatible method (See *Sec 3.3 of Design Methodology PART 3*), developed by Wan and Fleischman (2012), which has similarities to the prior approaches.

The analytical based method is used to calculate the elastic stiffness of the precast diaphragm in terms of equivalent elastic modulus and shear modulus and the flexural yield strength of the precast diaphragm including any contributions from the shear reinforcement to that strength. The calculation is based on a rational method and is used in the proposed design methodology to either manually determine the diaphragm deflection or conveniently model the floors in design software.

The method is calibrated by comparisons to finite element analyses of diaphragms with differing geometries and reinforcing details (See Fig. B-14). Figure B-14a compares the stiffness calculated by this method with that determined from FEM analyses (Wan and Fleischman 2012). Figure B-14b shows the same comparison for yield strength. The method shows reasonable agreement with FEM results. In addition, the methods are being calibrated using experimental results from the hybrid panel tests and will be further validated in the in the half-scale shake table.
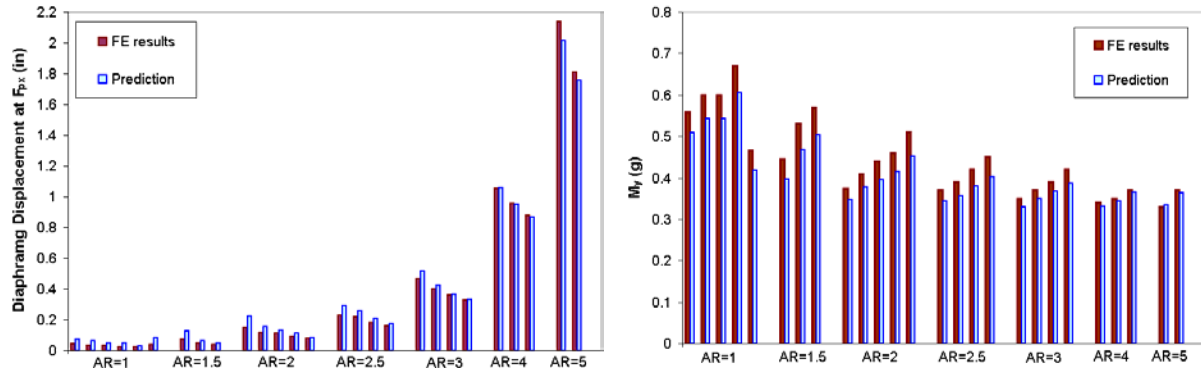
Figure B-14. Comparison with FE analysis: (a) Diaphragm displacement at F_{px}; (b) Yield strength.

5.5 Comments on DSDM Research Scope

The design procedure presented in PART 1 was produced through the efforts of a large 5+ year research project involving full-scale diaphragm connector testing, large scale laboratory tests on critical diaphragm joints, a half-scale shake table test of a diaphragm sensitive structure, and several hundreds of earthquake simulations using models developed through the testing program. This effort added significantly to the knowledge base on precast concrete diaphragms. Nevertheless, given the broad project objective, i.e. an industry-endorsed seismic design methodology for precast diaphragm structures nationwide, certain decisions had to be made in selecting scope. These decisions involved the type of diaphragm construction and connector types evaluated, the number of tests, and the key behaviors to include in the studies. Accordingly, the assumptions and limitations in the research, unresolved issues and next research steps are listed in this section. These items are presented as follows:

1. Limitations, including:
   – topics outside the project scope
   – aspects that received a secondary focus
   – behaviors examined only with limited data
2. Assumptions, including those made in:
   – the analytical portion of the research
   – the experimental portion of the research work
   – in the diaphragm design procedure
3. Impact of the Assumptions and Limitations:
   – unresolved or difficult to describe behaviors that require further research
   – suggested future work

Scope Limitations of the Research Program

Work Outside Project Scope

The following are the limitations in scope in the research performed in the DSDM project as it pertained to the development of the design methodology.

No evaluations of performance were made for:
1. Designs in SDCs A and B.
2. Untopped Hollowcore
3. Topped Noncomposite Double Tee Floor Systems
4. Transfer diaphragms, for instance over podiums or in dual systems.
5. Structures with vertical irregularity (e.g. change in diaphragm spans at different levels).

No physical testing was including in the experimental program for:
1. Diaphragm-to-LFRS connections and anchorages
2. Flat-plate Chord connections
3. Bar-plate shear connections [e.g. similar to those tested by Pincheira et al. (1998)].
4. Secondary connections in the floor system, including connections to spandrels, internal beams, and columns.

Topics of Secondary Focus

The following are topics that while examined in the research, were not the primary focus of the research performed during the DSDM project:

1. *Diaphragm-to-LFRS connections, anchorages and collector systems*: The research program focused on the design of chord reinforcement and shear reinforcement. Thus, the diaphragm-to-LFRS connections, anchorages and collector systems were not included in the component testing program. Further, to accommodate displacement compatibility in the shake table test due to biased (compressed) directional similitude in the precast structure, special vertically slotted (PSA

Connectors[1]) connections were used for the shake table diaphragm-to-shear wall connections. Additionally, the shake table specimen longitudinal span was such that collectors were not required. Thus, while force and deformation demands were tracked on the diaphragm-to-LFRS connections in the analytical program, the connection properties were estimated using one-sided bar-plate connectors tested by Pincheira et al. (1998). Further, in the analytical modeling the precast units (and topping slab above the units if applicable) are modeled as elastic elements. Thus, collector forces at the end of the floor are carried through the units in the analytical model, regardless of the collector detail.

2. *Diaphragm design at interior beam lines*: The research program focused on the design of chord reinforcement and shear reinforcement. In certain configurations, the forces across internal beam lines must also be considered, usually with tributary (*VQ/I*) shear calculations. The connections across these joints were included in the analytical models; however, these details were not tested, and thus only estimated of the nominal connector properties were used. Recommendations for the deformation capacity of interior beam connections are provided, however not based on any in-depth examination of possible details or design approaches that could be applied to these joints.

3. *Indeterminate LFRS Systems:* The structures examined in the analytical research (and the shake table testing) almost exclusively involved LFRS systems with pairs of vertical elements (shear walls or moment frames) along two symmetric lines of the structure in each direction (e.g. building perimeter, or first interior column line). For these structures, the diaphragm seismic load nominally splits between these lines. For structures with more redundancy in the LFRS layout (for instance both perimeter and interior LFRS elements), the distribution of the story shear (i.e., the diaphragm reactions) to these elements depends on the relative stiffness of these elements and the flexibility of the diaphragm. This topic was not included in the primary focus of the research. See PCI Seismic Design Manual (Cleland and Ghosh 2007) for more information on this topic.

4. *Topped Hollowcore, and Topped Double Tee Systems*: The research used pretopped double tee floor construction as the "workhorse" system to examine most general diaphragm behaviors. Thus the research focused primarily on this system, and performed a smaller set of analyses and experiments with other systems, including topped hollowcore and topped double-tees:
   – Trial design factors were developed using the pretopped diaphragm (though the factors were verified using both pretopped and topped systems).
   – The isolated connector testing program was fairly evenly divided among topped and untopped details; however, the hybrid tests of critical shear and critical flexure joints were limited to pretopped double tees.
   – The shake table test involved one floor each for topped double tees, pretopped double tees, and topped hollowcore. However, the topped systems were placed in the lower floors. Thus, by virtue of its location, the pretopped system was subjected to the highest seismic demands.

5. *Distributed reinforcement systems, high tension-stiffness and/or strong shear connectors*: The research focused primarily on shear connectors with lower tension strength and stiffness, due in part to the need in many precast floor systems to accommodate serviceability requirements related to volume change. The "workhorse" system used in the analyses to determine trial design factors, for instance, employed a pretopped double tee floor system with the JVI Vector as the shear reinforcement. For these systems, assumed to be typical precast construction, the ratio of total flexural strength at a joint provided by the shear reinforcement (relative to that provided by the chord reinforcement) is quite small. For this reason, these systems have limited redistribution qualities. Thus, if the chord reinforcement fails, the diaphragm is likely to lose load-carrying ability. "Distributed" reinforcement systems, on the other hand, may possess joints with improved

---

[1] JVI Inc, Lincolnwood IL 60712

redundancy. Likewise, these systems have a different relationship between yield and ultimate moment, with ramifications on nominal moment strength (*See Commentary on Step 6*). While some analyses were performed with shear connections with high tension stiffness or strength (e.g. topped diaphragms with the ductile ladder mesh, as was examined for two of the prototype structure design methodology verification analyses in *Background -Appendix A2*), further examination of these distributed reinforcement systems may provide benefit, including the possibility that such systems could translate into lower design force factors.

6. *Bond between topping and precast units*: Concrete toppings required to resist seismic forces should be well bonded to adequately roughened precast elements (Menegotto, 2002). The lower two floors of the shake table test involved a topping slab over precast units. For the double tees, a rough broom finish was called for in production to maximize the composite action for the double-tees, while no special measures were taken for the surface of the hollow core units (Schoettler et al. 2009). The second floor (topped hollowcore) was subjected to high demands, while the first floor (topped double tees) was subjected to moderate demand (See Fig B-15). No sign of debonding was observed over the 16 ground motions to which the test specimen was subjected. Thus, for this small sample size of floors under inertial force from ground motion excitation, the bond between topping and precast units was sufficient without any special surface preparation.

7. *Seating of precast units*: The U.S. practice uses fairly substantial seating dimensions (PCI Handbook 2004), in contrast to some precast construction (e.g. New Zealand, where 50mm existing construction and 75mm new construction is common). Thus the research did not focus directly on the seating performance except directly in the performance of the shake table test. It is noted that the ultimate failure of the shake table test specimen did involve an unseating failure at one end of the 3rd floor pretopped diaphragm (See *Background Appendix B.4)*. However, this was the 16th strong ground motion, and at this point the seating in this region of the structure was 2 7/8″ (down from an original 5″) due to "walking out" of the gravity frame during loss of shear wall post-tensioning in early shake tests.

Evaluations Involving Limited Data

The design factors were developed through extensive analytical work. However, certain aspects of the design methodology could only be examined through a limited set of analyses or experiments, and thus could benefit from a more comprehensive parameter study or testing program than that performed during the DSDM project. These aspects include:

1. *Diaphragm force vertical distribution factor α_x* (Design Procedure Step 1): This factor was determined using a simple evaluation structure for only 3 different story heights, and verified through a limited number of analyses of prototype structures of constant number of stories (4-story parking garages and 8 story office buildings (See *Background* -Appendix A2). Re-examination of data generated by the UCSD MDOF studies (Schoettler 2010) or a careful parameter study focusing on refinement of this factor would be beneficial.

2. *15% penalty factor* (Design Procedure Step 3): This penalty factor is enforced when "undermatching" the diaphragm design option for a given diaphragm seismic demand level (See *Commentary Step 2*). The value of this penalty, 15%, is an initial estimate based on a limited number of analyses (See Fig. B-3), and could benefit from further analytical data.

3. *Statistically Significance of Connector Test Data*: The decision was made at the outset of the project to examine a large number of diaphragm connectors. The need for characteristics under different load components (tension, shear, shear/compression, shear/ tension) meant that several tests were required to completely characterize a single connector. For this reason, the number of test results for a specific load characteristic of a given connector is not large. The confidence levels for the connectors could benefit from a more statistically significant set of data. In fact, no connectors tested strictly comply with the prequalification test quantity requirements of PART 2.

4. *Interior LFRS Layouts*: The primary layout investigated in the parameter studies involved perimeter LFRS layouts. One prototype parking structure layout and one prototype office building structure employed interior LFRS layouts. Thus, a more detailed investigation of interior LFRS layouts would allow refining of the diaphragm internal force patterns.

5. *LFRS overstrength*: The diaphragm design factors were calibrated for structures with nominal strengths close to the required strength. Further research examining the effect of LFRS overstrength would be useful in refining the factors.

6. *Moment Frames*: Most of the analyses involved shear wall structures. A small subset of the simple evaluation structure parameter studies involved frame structures. One prototype office building structure employed moment frames. Thus the data used to obtain the diaphragm amplification factors for frame structures was limited. Since these results are slightly different than those previously obtained with simpler models (Fleischman et al. 2002), it would be of interest to more closely examine the response of diaphragms in moment frames.

7. *Seismic Design Category*: The analyses of evaluation structures used to determine the trial design factors were primarily performed for SDC E (Berkeley, CA), with a small amount performed for SDC C (Knoxville, SC). The prototype structure verification analyses were performed for both SDC C (Knoxville, SC) and SDC D (Seattle, WA). In the shake table test program, the structure had accumulated damage to the LFRS and gravity system due to unexpected failures (See *Background Appendix B.4*).

8. *Different column density, spandrel length, precast panel width*: A constant spandrel length (30′) was used leading to a fairly even gravity system column density. Additionally, most analyses used a precast floor unit width of 10′, except that the studied parking garage structures have a precast floor unit width of 12′. Thus, research examining the effect of different column density, spandrel length and precast panel width would be useful in refining design factors.

9. *Gravity System Stability*: Most of the earthquake simulations performed were first order analyses, for ease of computation time and convergence. However, it was recognized that accounting for second order (P-Δ) effects could be important for taller structures (e.g. the 8-story office building) or highly flexible diaphragms where the gravity columns might undergo large drifts. Second order effects were included in these analyses, and from examining the difference between the first order and second order analyses, the C_Δ factor has been introduced into the design methodology (See PART 1: Step 12). However, this factor is based on a small number of analyses, and the drift capacity of the gravity system is estimated. In general, the topic of gravity system stability could use more attention as a research area unto itself.
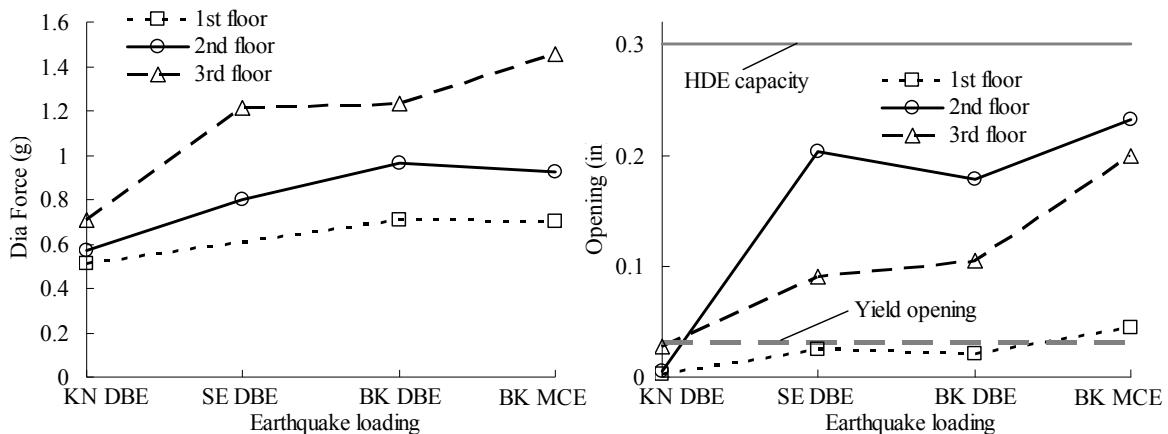
Figure B-15. Shake table test results: (a) Maximum diaphragm force; (b) Maximum joint opening.

Assumptions of the Research

<u>Assumptions of the Analytical Research</u>

The DSDM design methodology is based on nonlinear monotonic "pushover" analyses of isolated precast diaphragms and nonlinear transient dynamic analyses, e.g. earthquake simulations, of three-dimensional models of precast structures. For these analyses, a precast diaphragm model developed in the research, termed the "discrete" precast diaphragm model, was used. In the discrete model, the precast diaphragm connectors are modeled directly as elements in the analytical model.

The following are assumptions involved in the diaphragm discrete analytical models, used to determine the diaphragm design factors:

1. In the modeling, all inelastic deformation in the diaphragm is assumed to occur in the joint between the precast units:

   – *Primary Diaphragm Reinforcement*: The modeling parameters (strength, stiffness and post-yield behavior) for these elements are developed based on cyclic testing of individual diaphragm connectors performed at Lehigh University (Naito et al. 2006)(Naito et al. 2007). The hysteretic models for these elements include pinching, cyclic stiffness degradation in tension, cyclic strength degradation in shear, and tension-shear coupling (See *Background Appendix B.2*), as observed in the testing.

   – *Secondary Diaphragm Reinforcement*: The secondary connections in the floor system, diaphragm to internal beam connections, diaphragm to spandrel connections etc., were estimated as no testing of these elements was performed in the research program. The connector characteristics are assumed to be equivalent to a one-sided version of the bar-plate shear connector tested by Pincheira et al. (1998), i.e. with the same strength, but twice the stiffness and half the deformation capacity. One-side connectors are modeled with the same strength, doubled stiffness and half of deformation capacity as the two-side connections (e.g. connections between two precast floor units). The hysteretic model for the one-side connection includes effects of pinching and tension-shear coupling without cyclic stiffness or strength degradation.

   – *Diaphragm-to-LFRS Connections*: The diaphragm-to-LFRS connections were modeled using the same one-side connector model as the diaphragm secondary connections. This approach is an approximation since the actual connectors used for diaphragm-to-LFRS connections are typically straight bar welded connectors in lower seismic hazard and dowels in the topping slab in higher seismic hazard. Since none of these details were tested it was assumed sufficiently accurate to use the angled bar connector test results (Pincheira et al. 1998), adjusted for one side in recognition of the nearly rigid response of headed stud anchor plates in the wall/frame. The diaphragm-to-LFRS connector models are provided with unlimited deformation capacity in the model in order to determine required deformation capacity.

   – *Further notes on Connections*:
     a. The modeling was based on a limited set of diaphragm connector properties. Early analyses (Wan and Fleischman 2012) (Ren and Naito 2011) on the effect of connector stiffness, strength, indicated that the fluctuation of diaphragm demands due to the range from the most flexible to the most stiff connector details is not large compared to the overall diaphragm flexibility due to span. In this way, the results (primarily connector inelastic deformation demands) based on a generic set of connector properties can be applied to all different connector details based on the diaphragm reinforcement classification system (See *Background Step 4*).
     b. The evaluation structure and the prototype parking structure contained chord reinforcement with the JVI Vector, and the prototype office building structure

contained chord reinforcement, hairpin connections and a ductile mesh in the topping at the joint.

c. The chord reinforcement is based on a hysteretic model developed from the pour strip chord cyclic test, due to limitations in test data for other of chord types: difficulties in testing of the dry chord connector that led to unreliable or inconclusive data, no testing of the dry chord flat plate connector.

d. It is assumed that the secondary connectors are able to deform without strength reduction after yield, with tension and shear responses are coupled in the model.

e. The spandrel-to-column connection is modeled to allow free separation between spandrel and column in the direction perpendicular to the precast floor unit joints.

2. *Precast Units*:
   – The precast units are modeled as elastic elements using the flange/slab cross-section.
   – The structural models include the secondary elements in the floor system: spandrels, internal beams. These elements are assumed to respond elastically using gross section properties (due to the presence of prestress).
   – The gravity columns are modeled as elastic elements with pinned bases pinned at the foundation and pinned connections to floor systems (at the spandrels).

3. *Out-of-Plane Action*: The out-of-plane of the floor (vertical) actions, due to uplift or rotation of the LFRS elements, are ignored.

4. *Gravity Load Effects*: The effect of gravity load on diaphragm connector behavior was not included in the analytical modeling.

5. *Seating:* Except for a limited number of models of the shake table specimen, the seating of floor units was not modeled. Thus, relative movement of the spandrel and floor units is measured directly at the deck level.

6. *Uncertainty*: The models are based on deterministic nominal values, without consideration of uncertainty. No overstrength is considered in the design of elements, either for the diaphragm or the LFRS. The LFRS strength is assigned the nominal value, with no overstrength assigned to the actual yield strength of the LFRS system.

7. *Asymmetry*: No accidental asymmetry or variation in parameters is assumed.

8. *LFRS Nonlinear Response*: Shear walls are modeled as base-hinging elements; Moment frames are modeled as beam end hinging elements (strong column/weak beam).

9. *Vertical Elements*: The confining effect to the floor joints due to the out-of-plane stiffness of vertical elements (shear walls, moment frames and lite walls) is included in the models.

The design factors are determined using the analytical studies described in Appendix A. Trial design factors were first developed as described in *Background* -Appdx. A1 and verified in the study described in *Background* -Appdx. A2. The detailed list of assumptions and limitations for each analytical research stage are listed at the beginning of the corresponding *Background* Appendix (*See Sections A1.0, A2.0*).

Assumptions of the Experimental Research
   Connector Testing Program:
   1. The testing program was targeted specifically for diaphragm flange-to-flange connectors.
   2. The connector testing program is limited to assessing the in-plane strength, stiffness, and deformation capacity of precast concrete diaphragm connectors.

3. The testing method determines the shear and tension performance of connections independently. Alternative procedures are provided for determining shear-tension coupled behavior.
4. The testing program examined individual connector performance, i.e. one isolated connector per test specimen.
5. The connector joined two 4′ x 2′ precast pieces intended to represent the tributary portion of the floor unit flange. These pieces were non-prestressed and contained 6x6 W2.9xW2.9 welded wire reinforcement.
6. Both dry chord connectors and chord bars in the pour strip were back-end anchored using a faceplate at the far end of the panel, 2′ from the joint being tested. It was assumed that this was sufficiently beyond the development length not to have a significant effect on the results.
7. Best construction practices were used with regard to alignment, ambient welding conditions, etc.
8. Vertical movement of the precast test specimen was restricted.
9. Tests were conducted under quasi-static displacement control at a rate less than 0.05in/sec.
10. The cyclic loading protocol involves 3 repeated cycles at given amplitude of applied displacement. The connector performance is assessed using a backbone approximation in accordance with the procedure outlined in ASCE/SEI 41-06.
11. For the testing of critical diaphragm joints, the precast floor units were securely attached to fixturing, one panel width away from the joint being tested.

Shake Table Testing:
1. The connections and elements were created in half-scale (also for the critical joint tests):
    a. For chord reinforcement, #6 bars were scaled by using #3 bars.
    b. Special half-scale Vector connections were made by JVI for the testing. These half-scale connectors were tested in isolated fashion to confirm verisimilitude.
2. Vertically-slotted diaphragm-to-LFRS connections were used (JVI PSA connectors).
3. The structural system incurred damage prior to the full testing program including:
    a. Failure of the 3rd floor (pretopped) chord in the first Seattle DBE, causing:
        – the 2nd floor (topped HC) underwent large demands during the failure.
    b. Failure of the Rocking Wall PT anchors during the first Berkeley MCE, causing:
        – "Walking" of the gravity system such that spandrel connections had to be replaced and available seating magnitudes were reduced.
        – Undetected damage to Diaphragm-to-LFRS (PSA) connections
    c. Subsequent failures of the PSA connections during Berkeley DBEs
    d. Failures of the outrigger sliders
    e. Final failure due to unseating of the 3rd floor region with the lower available seating in a Berkeley MCE.
4. As a result of the aforementioned failures, some tests or data have to be interpreted carefully, and other data cannot be directly used in calibration.
5. The topped DT floor was not tested to MCE levels due to its location on the first floor.

A detailed description of the shake table testing and related model calibration activities appears in Appendices C and B.

Assumptions in the Design Methodology
The diaphragm design procedure (PART 1) contains the following assumptions:
1. The diaphragm joints are designed using an interaction expression (Eqn. 10). The interaction expression, involving direct addition of axial and moment, and vector addition of the shear force, is not based on any theoretical derivation involving precast concrete joints. However, the expression has been empirically verified using the results of the seismic simulations of the prototype structures. It should be noted however, that the analytical models themselves possess connector elements that are based on an approximate coupling of shear and axial response (See

Background Appendix B.1) based on individual load component testing and limited combined loading of isolated connectors (See *Background Appendix B.2*). Note that the axial component in the interaction equation is signed, so axial compression is beneficial as it will act again the moment demand. This benefit has been witnessed in isolated connector testing (Naito et al. 2006) and hybrid testing of a critical shear joint (See *Background Appendix B.3.1*).

2. The use of the interaction expression also eliminates the need for including tests under combined loading (for instance simultaneous shear and tension, or simultaneous shear and compression) in the diaphragm connector qualification protocol. Such tests are difficult to perform straightforwardly without special equipment, and it is unclear what best represents an effective diaphragm connector load history (cyclic shear in the presence of constant axial force; cyclic shear force with a proportional axial force; cyclic shear displacement with a proportional axial displacement; and if one of the latter two, what that proportion should be). Thus the decision was made to require component testing (cyclic shear, cyclic tension) and combine the effects of tension and shear using the interaction equation. It is important to note that the verification of the interaction equation is performed using nonlinear dynamic earthquake simulation that does indeed reproduce the complex set of load histories on individual connectors, and using models whose connector elements are based on the testing of isolated connectors in the experimental program, including under combined forces.

3. The diaphragm design factors were developed using an evaluation structure with a simple rectangular diaphragm layout and loaded in a single (transverse) direction. The verification is based on limited analyses of prototype structures.

4. The design factors equations are based on a curve fit using a 90% confidence interval for the mean value of data points over the 5 earthquakes of maximum response data.

5. The development of trial design factors occurred directly after the research phase, which included the shake table testing. For this reason, a fully-calibrated model was not available at this time. Model calibration using the shake table results occurred in parallel in the later (design procedure development) phase, prior to the establishment of the final diaphragm design factors. See Appendix B for full details of the calibration.

6. The effect of gravity load on diaphragm connector performance was considered secondary (as most connectors are located between floor units acting as one-way slab elements, and thus vertical force components are not expected to be significant), and thus was not considered in the experimental or analytical research, nor included in the design procedures. However, these actions should be considered in cases where important.

Impact of Limitations and Assumptions:

The following are aspects of the diaphragm behavior that are unresolved, or that of have been identified as difficult to accurately describe, and thus would benefit from further research:

1. *Chord deformation distribution*: The distribution of concentrated joint opening vs. strain penetration in the precast unit at the chord, as observed in hybrid and shake table testing.

2. *Joint Opening Profiles*: The spread of inelastic deformation demand in different joints, due to-variability in strength among the joints.

3. *Diaphragm bending spans:* Some diaphragm layouts, such as perimeter walls with longitudinal walls along the span may create short diaphragm spans with a *potential for* shear failure.

4. *Diaphragm End Conditions*: Choices exist in design regarding end fixity and shear transfer along internal joints based on the details provided in these locations.

5. *Diaphragm force amplification for Moment Frames* vs. wall systems – role of inelastic response on this value. Role of diaphragm flexibility on the R factor.

6. *Coupling of Axial and Shear Actions in Connectors*: The connector testing program attempted to develop these relationships, but they turned out to be quite difficult to describe.

7. *Lack of a reliable dry chord connector*: The connectors tested thus far result in LDE behavior.

Further, the impact on the design methodology of topics that were not a major focus include should be considered, including:

1. *Collector systems*: Wood et al (2000) showed that shear strength design equations based on inclined cracking are inconsistent for precast diaphragms due to the absence of monolithic action in the topping slab. No detailed examination of precast collectors was performed in DSDM.

2. *Distributed reinforcement systems, high tension-stiffness and/or strong shear connectors*: Stiff vs flexible web connectors: "Distributed" reinforcement systems may possess joints with improved redundancy. Establish better the relationship between yield and ultimate moment toward determining nominal moment strength. Further examination of these distributed reinforcement systems may provide benefit, including the possibility that such systems could translate into lower design force factors.

Suggested Future Research:

1. Calibrate/verify the design procedure for a larger set of realistic diaphragm layouts, including:
   – Evaluate the overstrength factor for different diaphragm layouts to improve confidence in capacity designs to prevent non-ductile shear failure.
   – This analytical research could first use pushover analyses of isolated diaphragms, but requires NLDTA of the entire structure under two-directional components of ground motion.

2. Provide certain design factors with a more statistically robust set of analytical data including:
   – the diaphragm vertical force distribution factor α_x.
   – the 15%force penalty for using a lower design option than recommended
   – the C_Δ factor used for determining diaphragm-induced drifts

3. Better quantify the inertial force demands on moment frames and the role of LFRS ductility demand on diaphragm forces. What are the factors that make this behavior, presumably occurring in all structures, more critical in precast diaphragms than other construction?

4. Further study on the impact of different diaphragm reinforcement characteristics, including impact of overstrength in the floor system, strain hardening ratio; flexible vs. stiff web connector.

5. Quantify the effect of LFRS overstrength on diaphragm demand.

6. The impact of the loss of secondary connections requires further consideration. Current connections will not likely survive a seismic event. What is the ramifications of loss of these connections with respect to seating?

7. Expand the physical testing database on diaphragm reinforcing details including:
   – Diaphragm-to-LFRS connections and anchorages (including out-of-plane loading)
   – Flat-plate Chord connections
   – Stiff shear connections, e.g. similar to those tested by Pincheira et al. (1998)
   – Secondary connections in the floor system, including connections to spandrels, internal beams, and columns.

8. Develop a fully satisfactory loading protocol to characterize coupled connector response, including tests that provide insight on the effect of force combinations on diaphragm response, for example shear performance in a region that undergoes high collector (tension) action.

9. Better understanding of the distribution of concentrated joint opening vs. strain penetration in the precast unit at the chord, as observed in hybrid and shake table testing, through further testing.

10. Quantification of the effect of erection tolerances on the performance of pretopped connectors.

11. Certain configurations not included in the analytical research could be analyzed including:
    – structures with different LFRS layout along building height.
    – structures with precast units oriented in two orthogonal directions such as core structure
    – Redundant LFRS layouts, dual systems, etc.

12. Innovative precast connectors, including ductile shear connectors, etc.

5.6 References

ACI 318-05. (2005). Building Code Requirements for Structural Concrete (ACI 318-05) and Commentary (ACI 318-05), American Concrete Institution committee 318.

ACI (1992). "Use of concrete in buildings". ACI Manual of Standard Practice (ACI-ASCE 442), American Concrete Institution Farmington Hills, MI.

ASCE 7-05. "Minimum Design Loads for Buildings and Other Structures". American Society of Civil Engineering 2005.

Bull, D.K. (1997). "Diaphragms". Seismic Design of Reinforced Concrete Structures, Technical Report No.20, New Zealand Concrete Society.

Bockemohle, L.W. (1981). "A practical paper on design of topped concrete diaphragms and precast concrete structures". Proceedings, Workshop on Design of Prefabricated Concrete Buildings for Earthquake Loads, Applied Technology Council.

Building Seismic Safety Council, Committee TS-4. (2009). "Seismic design methodolgy for precast concrete floor diaphragms," Part III, 2009 NEHRP Recommended Sesimic Provisions, Federal Emergency Management Agency, Washington, D.C.

Building Seismic Safety Council, Issue Team 6. (2012). "Diaphragm issues". Resource Paper, Provision Update Committee. Editor: S.K. Ghosh. Scheduled for publication in October 2012.

Blakeley, R.W.G., Cooney, R..C., Megget, L.M. (1975). "Seismic shear loading at flexural capacity in cantilever wall structures". Bulletin of the New Zealand National Society for Earthquake Engineering, 8(4): 278-290.

Blaauwendraad, J. and Hoogenboom, P.C.J. (1996). "Stringer panel model for structural concrete design". ACI Structural Journal V93 (3): 295-305.

Chopra, A.K. (1995). "Dynamic of structures: theory and applications to earthquake engineering". Prentice Hall, Inc. Engelwood Cliffs, NJ.

Clough D.P. (1982). "Considerations in the design and construction of precast concrete diaphragms for earthquake loads". PCI Journal. March-April: 78-93.

Cleland N. (2011). DSDM TG Communication Blue Ridge Consulting. DSDM Denver Research Meeting.

Cleland N. and Ghosh S.K. (2007). "Seismic design of precast/prestressed concrete structures". PCI Seismic Design Manual, 1st Edition.

DSDM, (2006). Year 2 Report to National Science Foundation: GOALI Project "Development of a Precast Floor Diaphragm Seismic Design Methodology (DSDM), August 17.

EERI (1994). Northridge Earthquake, January 17, 1994. Preliminary Reconnaissance Report, Earthquake Engineering Research Institution, Oakland, CA.

EERI (2011). Learning from Earthquakes: The M 6.3 Christchurch, New Zealand, Earthquake of February 22, 2011. Special Earthquake Report, Earthquake Engineering Research Institute, K. Elwood, Editor, May.

Eberhard, M. O., and M. A. Sozen. (1993). "Behavior-Based Method to Determine Design Shear in Earthquake-Resistant Walls," American Society of Civil Engineers, Journal of Structural Engineering, 119(2): 619-640.

Fib. (2003). "Seismic design of precast concrete building structures". fib State-of-art report No.27.

Farrow, K. T. and Fleischman, R. B. (2003). "Effect of dimension and detail on the capacity of precast concrete parking structure diaphragms" PCI Journal 48(5): 46-61.

Fleischman, R. B., and Farrow, K. T. (2001) "Dynamic response of perimeter lateral-system structures with flexible diaphragms", Journal of Earthquake Engineering & Structural Dynamics, V.30, No. 5, May, pp. 745-763.

Fleischman, R.B. Farrow, K.T. Eastman, K. (2002) "Seismic response of perimeter lateral-system structures with highly flexible diaphragms" Earthquake Spectra, 18 (2) May: 251-286.

Fleischman, R. B., Naito C.J., Restrepo J., Sause R. and Ghosh S.K. (2005a). "Seismic design methodology for precast concrete diaphragms, Part 1: design framework", PCI journal, v 50, n 5, 68-83.

Fleischman, R.B., Naito C.J., Restrepo J., Sause R., Ghosh S.K., Wan G., Schoettler M., and Cao L. (2005b). "Seismic design methodology for precast concrete diaphragms, Part 2: research program." PCI Journal, 51(6), 2-19.

Fleischman, R.B., Sause, R., Pessiki, S., and Rhodes, A.B. (1998). "Seismic behavior of precast parking structure diaphragms." PCI Journal, 43 (1), Jan-Feb: 38-53.

Fleischman, R.B., Sause, R., Rhodes, A.B and Pessiki, S. (1996). "Seismic behavior of precast parking structure diaphragms". Proceedings, XIV ASCE Structures Congress, Edited by S.K. Ghosh, V2, Chicago, IL, April 15-18: 1139-1146.

Fleischman, R.B. and Wan, G. (2007). "Appropriate overstrength of shear reinforcement in precast concrete diaphragms", ASCE J. Structure Eng. 133(11), 1616-1626.

Gates W.E. (1981). "Seismic design considering for untopped precast concrete floor and roof diaphragm". Proceedings, Workshop on Design of Prefabricated Concrete Buildings for Earthquake Loads, Applied Technology Council.

Ghosh, S.K. (1999). Task Report, PCI Fast Team, April 11.

Ghosh, S.K., Nakaki, S.D. and Krishnan, K. (1997). "Precast structures in regions of high seismicity: 1997 UBC provisions". PCI Journal, Nov-Dec.

Hall, J.F, editor (1995). Northridge Earthquake of January 17, 1994 Reconnaissance Report V1, Earthquake Spectra, Supplement C to V11, Publication 95-03, p523.

ICBO (1994). Uniform Building Code, 1994 Edition. International Conference of Building Officials, Whittier, CA, May.

ICBO (1997). Uniform Building Code, 1997 Edition. International Conference of Building Officials, Whittier, CA, May.

Iverson, J.K., Hawkins, N.M. (1994) "Performance of precast/prestressed concrete building structures during northridge earthquake," PCI Journal: 39 (2): 38-55.

Ju, S.H., and M. C. Lin. (1999). "Comparison of Building Analyses Assuming Rigid or Flexible Floors," ASCE/SEI Journal of Structural Engineering, 125(25).

Kao, G. 1998. "Design and Shake-Table Tests of a Four-Storey Miniature Structure Built with Replaceable Plastic Hinges,"M.E. Thesis, Department. of Civil Engineering, University of Canterbury, Christchurch, New Zealand.

Kabeyasawa T. (1999). "Evaluation of column and wall actions in the ultimate-state design of reinforced concrete structure". Proceeding of 9th World Conference on Earthquake Engineering, August 2-9, Tokyo-Kyoto, Japan.

Lee, H. J., and D. A. Kuchma. (2007). "Seismic Overstrength of Shear Walls in Parking Structures with Flexible Diaphragms," Journal of Earthquake Engineering, 11(1): 86-109.

Lee, H.J., and Kuchma, D.A. (2008). "Seismic response of parking structures with precast concrete diaphragms." PCI Journal, 53(2), 71-94.

Lee, H. J., M. A. Aschheim, and D. Kuchma. (2007). "Interstory Drift Estimates for Low-Rise Flexible Diaphragm Structures," Engineering Structures, 29(7):1375-1397.

Maffei, J.R. (2005). DSDM Task Group Research Meeting #5, Napa CA, August.

McSaveney, L.G. (1997). "Precast concrete flooring system design and detailing for seismic purpose". Conference Technical Papers (TR19), New Zealand Concrete Society, August: 14-26.

Menegotto, M. (2000). "Precast floors under seismic action," in Proceedings, The Second International Symposium on Prefabrication, Helsinki, Finland, May 2000.

Menegotto, M. (2002). Fib WG 3/4 Correspondence, January.

Moehle, J.P., Hooper, J.D., Kelly, D.J. and Meyer, T.R. (2010) "Seismic Design of Cast-in-Place Concrete Diaphragms, Chords, and Collections" NEHRP Seismic Design Technical Brief No.3.

Mejia-McMaster, J. C., and R. Park. (1994). "Tests on Special Reinforcement for End Support of Hollow-Core Slabs," PCI Journal, 39(5): 90-105.

Nakaki, S. D. (2000) "Design guidelines for precast and cast-in-place concrete diaphragms" Technical Report, EERI Professional Fellowship, Earthquake Engineering Research Institute, April.

New Zealand Concrete Society (1994). "Revisions to the New Zealand Standard for the design of concrete structures: NZS 3101". Technical Report No. 15 (TR15), May.

Naito, C., Jones, C., Cullen T. and Ren, R. (2007). "Development of a seismic design methodology for precast diaphragms - phase 1b summary report". ATLSS Report. ATLSS Center, Lehigh University, PA.

Naito, C., Peter, W. and Cao, L. (2006). "Development of a seismic design methodology for precast diaphragms - phase 1 summary report". ATLSS Report No.06-01, ATLSS Center, Lehigh University, PA.

Naito, C.J. and Ren, R. (2011). "An evaluation method for precast concrete diaphragm connectors based on structural testing" PCI Journal. Submitted.

Otanl, S., Kabeyasawa, T., Shiohara, H., and Aoyama, H. (1984). "Analysis of the full scale seven story reinforced concrete test structure". ACI Structural Journal, Special Publication SP84-08:203-239.

Precast/Prestressed Concrete Institution. (2004). "PCI design handbook: precast and prestressed concrete." Sixth Edition, Chicago IL.

Precast/Prestressed Concrete Institution. (2011). "Summary of precast performance in Feb 22nd Christchurch New Zealand earthquake." Report to PCI, July.

Pathak, R. and Charney, F.A. (2008). "The effects of diaphragm flexibility on the seismic performance of light frame wood structures." Conference Proceeding, The 14th World Conference on Earthquake Engineering, Beijing China.

Pincheira, J. A., Oliva, M. G., and Kusumo-rahardjo, F. I. (1998). "Tests on double tee flange connectors subjected to monotonic and cyclic loading." PCI Journal, 43 (3): 82-96.

Paulay, T. and Priestley, M.J.N. (1992). "Seismic design of reinforced concrete and masonry buildings". John Wiley and Sons.

Restrepo, J.I. and Rodriguez, M. (2007) "Proposal to Revise the 2005 Edition of ASCE7". Task Committee Action on Proposal: Revise Section 12.10 of ASCE 7 Standard.

Rodriguez, M., Restrepo, JI, and Blandon, J.J. (2007) "Seismic design forces of rigid floor diaphragms in precast concrete building structures". ASCE Journal of Structural Engineering 133(11): 1604-1615.

Rodriguez, M., Restrepo, JI, and Carr, A.J. (2002) "Earthquake induced floor horizontal accelerations in buildings". Earthquake Eng. & Structural Dynamics, 31(3): 693-718.

Rhodes, A.B., Sause, R., Pessiki, S. and Fleischman, R.B. (1997). "Seismic performance of precast parking structures: transverse direction". Earthquake Engineering Research Report No. EQ-97-03, Department of Civil and Environmental Engineering, Lehigh University, Bethlehem, PA, 1997.

Rogers, C.A. and Tremblay, R., (2010). "Impact of diaphragm behavior on the seismic design of low-rise steel buildings." AISC Engineering Journal, 47(1), 21-36.

SAFECAST (2012). "European research on precast structures contributions of the SAFECAST project". High Council of Public Works of Italy, International Conference, Ministry of Infrastructures and Transports. Roma, Italy March 22.

SEAOC (1994). Committee Correspondence, Structural Engineers Association of California (SEAOC) AD Hoc Committee on Precast.

Schoettler, M.J. (2010) "Seismic demands in precast concrete diaphragms" Ph.D. Dissertation. University of California, San Diego, CA.

Schoettler, M.J., Belleri, A., Zhang, D., Restrepo, J., and Fleischman, R.B., (2009). "Preliminary results of the shake-table testing for development of a diaphragm seismic design methodology." PCI Journal, 54 (1), 100-124.

Schlaich, J. Schaefer, K. and Jennewein, M. (1987). "Towards a consistent design of structural concrete". PCI Journal V32 (3): 74-150.

Tena-Colunga, A., and D. P. Abrams. (1992). Response of an Unreinforced Masonry Building During the Loma Prieta Earthquake, Structural Research Series 576, Department of Civil Engineering, University of Illinois at Urbana-Champaign.

Wan, G., and R. B. Fleischman. (2012). "A Rational Method for Calculating the Service Stiffness and Yield Strength of Precast Floor Diaphragms," in preparation for submission to PCI Journal.

Wan, G., Fleischman, R.B. and Zhang, D. (2012). "Effect of spandrel beam to double tee connection characteristic of flexure-controlled precast diaphragms", J. of Structural Eng. ASCE. Scheduled published in Feb. 2012.

Wood, S. L., Stanton, J. F., and Hawkins, N. M. (1995), "Performance of precast parking garages during the 1994 Northridge earthquake", Proceedings, XIII ASCE Structures Congress, Restructuring: America and Beyond, **1**, New York, NY, pp. 563-566.

Wood S. L., Stanton J. F., Hawkins N. M. (2000). "New seismic design provisions for diaphragms in precast concrete parking structures", PCI Journal, 45 (1): 50-65.

Ware, A.R., Zhang, D., Fleischman, R.B. and Mielke M. (2012). "Calibration of Models for Topped Precast Diaphragm". Under preparation.

Zhang, D. and Fleischman, R.B. (2012a). "Establishment of Seismic Design Force Factors for Precast Concrete Diaphragms". under preparation.

Zhang, D. and Fleischman, R.B. (2012b). "Dynamic response of precast concrete parking garage under seismic loading". under preparation.

Zhang, D., Fleischman, R.B., Naito, C., and Ren, R. (2011). "Experimental evaluation of pretopped precast diaphragm critical flexure joint under seismic demands." J. Struct. Eng. ASCE, V137(10).

Zheng, W., and Oliva, M. G. (2005). "A Practical Method to Estimate Elastic Deformation of Precast Pretopped Double Tee Diaphragms," PCI Journal, 50(2): 44-55.

CHARLES PANKOW FOUNDATION

Building Innovation through Research

Seismic Design Methodology Document for Precast Concrete Diaphragms

PART 5: BACKGROUND APPENDICES

on the Precast Concrete Diaphragm Seismic Design Methodology

2/16/2014

TABLE OF CONTENTS

Introduction

        The design methodology was developed through research performed in the PCI[1]-CPF[2]-NSF[3] funded DSDM[4] project. The design procedure in PART 1 was established through analytical research performed in a *Design Procedure Development Phase* after the DSDM Project main research phase. These studies produced the numerical values for the design factors, equations, and classifications used in the design procedure, and are described in Appendix A. The analytical models used in the *Design Procedure Development Phase* were developed and calibrated on the basis of extensive test data, as described in Appendix B. The experimental work that produced the test data occurred during the primary phase of the DSDM Project (See Appendix C). A comprehensive list of the publications produced by the research appears in Appendix D.

---

[1] PCI – Precast/Prestressed Concrete Institute
[2] CPF – Charles Pankow Foundation
[3] NSF – National Science Foundation
[4] DSDM – Diaphragm Seismic Design Methodology

Appendix A. Design Procedure Calibration and Verification

The *Design Procedure Development Phase* involved two main analytical studies: (1) the development of *trial design factors* using a simple evaluation structure; and (2) the verification of the *diaphragm design procedure*, including the trial design factors, using realistic prototype structures. This research phase involved significant collaboration with the DSDM Task Group Design Development Team (*listed in Sec 5.1*) in order to evaluate and improve the usability of the design procedure.

Both analytical stages involved earthquake simulation using nonlinear transient dynamic analysis of three-dimensional models of precast structures. The structural models employ "discrete" diaphragm models, that is they include the diaphragm reinforcement directly through diaphragm connector elements located at discrete locations along the joint.

The first analytical stage is described in Appendix A.1. In this analytical stage, an extensive parameter analysis was performed using a simple evaluation structure with rectangular diaphragm geometry. This study was used to develop trial design factors for the diaphragm design procedure.

The second analytical stage is described in Appendix A.2. In this analytical stage, the design procedure, including the trial design factors developed in previous stage, was verified or appropriately modified based on a limited set of analyses of realistic structures. The structures were selected from a portfolio of prototype structures developed for the project.

Evaluation of design procedure usability occurred organically within the second analytical stage. The first step for each analysis in this stage was to use the design procedure to design the prototype structure in order to create the desired structural model. Thus, this step provided an opportunity for the DSDM Task Group Design Development Team to review the design process and suggest improvements. This step is also to provide the design examples in PART IV of the Design Methodology.

Appendix A.1   Trial Design Factor Parametric Study

In the first stage of the *Design Procedure Development Phase*, an analytical study is performed to establish values for the diaphragm design force factors and deformation capacity requirements over the range of expected design parameters. The analyses are performed on an evaluation structure using a three-dimensional finite element (3D-FE) model (Zhang et al. 2012) constructed using test data on isolated diaphragm connectors (Naito et al. 2009) (Cao et al. 2009) (Oliva 2000) (Shaikh and Feile 2004) (Pincheira et al. 1998) and verified on the basis of extensive parallel testing (Zhang et al. 2011) (Fleischman et al. 2012) (Schoettler 2009). The outcomes of this stage are trial design factors that are calibrated on realistic structures in the next stage (as described in Appendix A.2).

TABLE OF CONTENTS

A1.0 ASSUMPTIONS AND LIMITATIONS OF TRIAL DESIGN FACTOR STUDY

The following are the overall assumptions and limitations of the trial design factor parametric study:

1. The diaphragm design factors were developed using an evaluation structure with a simple rectangular diaphragm layout and loaded in a single (transverse) direction.
2. The geometry of the evaluation structure was limited to:
   – Three different heights: 2, 4 and 6 stories.
   – Aspect ratios between 1-4
   – Diaphragm lengths of 60-240 ft.
3. The structure was assumed to have a constant smeared floor weight of 115 psf, a constant floor-to-floor height of 10′, and a constant column spacing of 30′.
4. The precast floor units were limited to two geometries:, (1) a 60′ deep x 10′ wide unit with a 4″ thick flange, corresponding to a typical precast double tee (DT) geometry; and (2) a 32′ deep x 4′ wide unit with a 4″ thick flange, corresponding to a common precast hollowcore (HC) geometry.
5. A generic precast diaphragm detail was used for all the analyses: a pretopped diaphragm with JVI Vector flange-to-flange connectors and a pour strip with continuous chord reinforcement.
6. The Seismic Design Categories (SDCs) were limited to single sites in SDC C and SDC E.
7. The evaluation structure, other than the diaphragm, was designed using IBC 2006, which references ASCE 7-05 and ACI 318-05.
8. Lateral Force Resisting Systems (LFRS) were limited to perimeter shear walls or moment frames.
9. Most analyses involved SDC E shear wall structures with precast DTs (See Table A1-10).
10. The seismic excitation was limited to a suite of 5 spectrum compatible historic ground motions.
11. The data points used to determine the design factors are based on the mean value of maximum response data produced in the 5 earthquake simulations over the suite of ground motions.
12. The design equations are based on a curve fit using a 90% confidence interval for the mean data.
13. The trial design force amplification factors Ψ are developed relative to diaphragm nominal design strength, which in the evaluation structure is set to the diaphragm yield moment, $M_n = M_y$.
14. The LFRS strength is assigned the nominal value, with no overstrength assigned to the actual yield strength of the LFRS system.

Table A1-0. Analysis matrix for trial design factor parametric study.

SDC	LFRS	Floor depth ft	# of parameters for # of stories	for AR	# of design cases	# of seismic hazard levels	# of ground motions	# of Runs
E	Shear wall	60	3	4	3	2	5	360
E	Shear wall	32	3	2	2	1	5	60
E	Mom Frame	60	3	2	3	2	5	180
C	Shear wall	60	3	2	2	1	5	60
Total # of runs								660

Some comment is warranted for assumptions 5 and 13 above. Earlier analytical research during the project indicated that the key global demands (diaphragm force) used here to determine the trial design factors are not particularly sensitive to the diaphragm reinforcement stiffness (Schoettler 2010). Hence, the decision was made to determine the trial design factors using a single generic set of diaphragm reinforcement, and confirm the applicability to other diaphragm reinforcement sets during the evaluation of the prototype structures (See Appendix A2). For the reinforcement selected, involving JVI Vector connectors, the difference between the yield moment (M_y) and ultimate (plastic) moment (M_p) is quite small; thus diaphragms designs based on yield or ultimate are nearly identical. However, for diaphragm reinforcement schemes with larger overstrength, for instance a topped diaphragm with ductile mesh, this larger ratio of ultimate-to-yield strength (M_p/M_y) has an impact, and has to be accounted in the selection of nominal strength M_n (See Commentary Step 10). Background on this topic appears in Commentary Section 5.6 in Section: *Diaphragm Controlling Mechanism*.

The following are the modeling assumptions and limitations involved in the evaluation structure analyses:

1. The shear wall nonlinear response is assumed to occur entirely in a base plastic hinge of length corresponding to half the shear wall horizontal dimension.
2. The shear wall base plastic hinge nonlinear moment-curvature backbone is determined through a fiber analysis of the designed shear wall cross-section using nominal material properties.
3. The shear wall hinge flexural strength includes biaxial moment to include out-of-plane response.
4. The moment frame sway mechanism is based on a strong column-weak beam assumption. The beam plastic hinge nonlinear moment-curvature backbone is determined through a fiber analysis of the designed beam cross-section using nominal material properties.
5. The hysteretic model for the shear wall base plastic hinge employs a pinched hysteresis characteristic of unbonded post-tensioned precast walls.
6. The out-of-plane stiffness of vertical elements (shear walls, litewalls, moment frames) is included in the model, in order to capture restraining effects on the diaphragm deformation.
7. No foundation rotation in the out-of-plane direction of the shear wall is included.
8. The floor system is modeled as a two-dimensional (in the horizontal plane) system.
9. The precast floor units are modeled as elastic plane stress elements with appropriate mass but stiffness based only on the flange thickness.
10. Spandrels are modeled as line-type 2D elastic beam elements, deforming in the floor plane only.
11. Gravity columns are modeled as 3D elastic beam elements with a pinned base at the foundation and pinned connections at each floor level.
12. Gravity loads are not included directly in the analyses except for moment frame structures in order to obtain the proper end moments ($M_g + M_E$) in the frame. Gravity load effects are included indirectly in shear wall structures in the moment-curvature response of the shear wall base hinge.
13. The effect of gravity load and vertical actions on the diaphragm connection response is ignored
14. The connections are assumed to be pristine prior to the seismic loading.
15. P-Δ effects were ignored in the study. A limited set of follow-up analyses were performed to empirically calibrate a P-Δ multiplier, similar to the δ_s multiplier in the current code (ACI 318 2008), as part of the diaphragm contribution to gravity column inter-story drift.
16. The dynamic analyses employed 1% Rayleigh damping aligned with the first (fundamental) and last significant transverse vibrational modes (cumulative mass participation ratio $\geq$ 99%).

The following assumptions and limitations are involved in modeling of diaphragm connectors:

1. Key characteristics of the diaphragm reinforcement (strength, stiffness and post-yield behavior) are obtained from the cyclic tests of isolated diaphragm connectors (See PART 2).
2. Hysteretic models for the diaphragm reinforcement include the effects of pinching cyclic stiffness degradation in tension, and tension-shear coupling.
3. One-sided connections to embed plates (e.g. diaphragm-to-LFRS connections, diaphragm-to-inverted tee connections, diaphragm-to-spandrel connections) were not tested in the research program. The characteristics for these connections are obtained from the test data from two-sided connections by using the same strength, doubling the stiffness and halving the deformation capacity. In order to determine recommendations for the required deformation capacity of these "secondary" diaphragm connections, the element models for these connections are given unlimited deformation capacity with no cyclic degradation or post-yield secondary slope (but with tension-shear coupling).
4. The spandrel-to-column connections permit unrestrained relative movement between spandrel and column in the direction perpendicular to the precast floor unit joints (sliding along the column face). In the direction parallel to the precast floor unit joints, the spandrel and column are rigidly connected by coupling the DOF in this direction.

A1.1 DESCRIPTION OF STUDY

The analytical parameter study establishes trial values for: (1) the diaphragm force amplification factors Ψ_D, Ψ_E and Ψ_R; (2) the diaphragm shear overstrength factors Ω_v; and, (3) the required deformation capacity for the different diaphragm reinforcement classifications (LDE, MDE, and HDE). These values are established over a range of design parameters. The study is performed using nonlinear transient dynamic analysis (NLTDA) of a three-dimensional finite element (3D-FE) model of a simple evaluation structure under spectrum-compatible ground motions.

A1.1.1 Evaluation Structure

A simple precast structure with a rectangular floor plan (See Fig. A1-1) is used as the evaluation structure to establish trial design values for the design methodology. This structure permits straightforward assessment of diaphragm seismic demands over the expected range of design parameters. The structure has a 10′ floor to floor height and 115 psf smeared floor mass. The evaluation structure lateral force resisting system (LFRS) possesses a perimeter layout, and is considered only for the diaphragm transverse (critical) direction only. The seismic design of the lateral system elements is based on ASCE 7-05 (2005) and ACI 318-05 (2005). The seismic design coefficients for each distinct LFRS case are listed in Table A1.1.
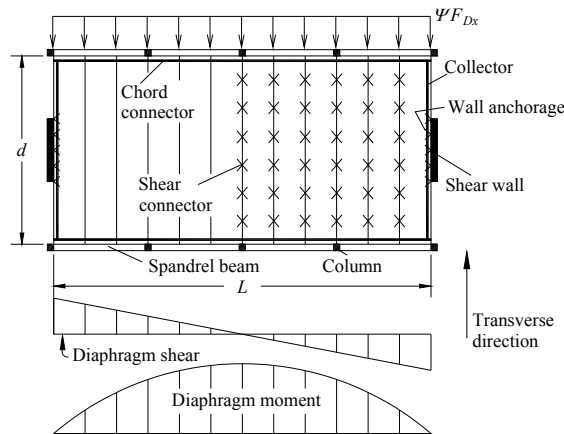
Fig.A1-1. Typical precast floor plan used for evaluation structure.

Table A1-1. IBC seismic design coefficients and factors.

Site	SDC	LFRS	IBC Category	R	Ω_o	C_d
Berkeley	E	Shear wall	Special RC shear walls	6	2.5	5
Berkeley	E	Frame	Special RC moment frame	8	3	5.5
Knoxville	C	Shear wall	Ordinary RC shear walls	5	2.5	4.5

A baseline diaphragm seismic design force (F_{Dx}) is first determined for each set of design parameters based on the maximum (top floor) F_{px} from ASCE 7-05 (2005). The term "baseline" refers to the diaphragm design forces prior to the application of amplification factors.

The required diaphragm design strength for the analyses is obtained by applying the diaphragm force amplification factor Ψ to F_{Dx}. For each baseline design, different diaphragm design strengths can be evaluated by applying different trial values of Ψ. For the study, the amplified diaphragm design force is applied using a constant vertical profile along the height of the structure in accordance with the original recommendations of the draft design methodology (BSSC TS-4 2009). *It is noted that on the basis of the analytical results from this research phase, a varying diaphragm force vertical profile (controlled by the α_x factor) is now included in the design procedure (See Section A.1.5.3).*

The amplified design force is applied to the diaphragm to determine internal forces. For the evaluation structure's simple layout, the diaphragm required design moment (M_u) and shear (V_u) can be determined using the horizontal beam method (PCI Design Handbook 2004), as shown by the diagrams in Figure A1-1. *More accurate methods for determining the internal forces are presented in PART 3 based on the results of the prototype structure analytical results* (See Appendix A2).

The nominal moment capacity (M_n) of the diaphragm is calculated using strain compatibility procedures developed in the project (BSSC TS-4 2009) and includes the shear reinforcement contribution to flexure (ACI 318 2005). The nominal shear strength (V_n) includes the chord reinforcement dowel action contribution to the shear reinforcement based on cyclic shear test (Cao et al. 2009). The design strength values used for the individual diaphragm reinforcement are obtained from the database of diaphragm connector properties obtained in testing (Ren and Naito 2011) and reproduced in PART 2.

A sample design for one design case of the evaluation structure is shown in Table A1-2: SDC E 6-story shear wall structure with a 240′ by 60′ floor plan.

Table A1-2. Evaluation structure sample design: SDC E, shear wall, 240′x60′.

Seismic design	Weight	Coefficient	Base shear		Base moment	Top floor
	w (kips)	C_s	V_b (kips)		M_b (k-ft)	F_{Dx} (kips)
	9936	0.231	2296		100279	670
Shear wall design	Length	Width	Boundary	Web	M_u [k-ft]	ϕM_n	$\phi M_n/M_u$
	L_w (ft)	t_w (in)	area steel	steel	Per wall	[k-ft]	
	30	14	14 # 14	2#4@11"	50140	51993	1.04
Diaphragm design	Ψ_D	$\Psi_D F_{Dx}$	M_u	ϕM_n (ϕ=0.9)	V_u	V_n	Ω_v
		(kips)	(k-in)	(k-in)	(kips)	(kips)	V_n/V_u
	2.12	1420	42613	42932	710	837	1.18

A1.1.2 Design Parameters

The trial design factors are determined across a set of design parameters related to building geometry, construction type and seismic hazard level. These parameters cover the range of design values considered typical for precast diaphragm construction (See Table A1-3). The design parameters related to building geometry include: (1) diaphragm length, L; (2) diaphragm aspect ratio, AR; (3) number of stories, N; and, (4) diaphragm depth, d (representing common dimensions of double tee and hollowcore precast units). Two LFRS types are evaluated, both with perimeter layouts: shear wall and frame. Seismic design categories include SDC E (high) for Berkeley (BK) CA and C (moderate) for Knoxville (KN) TN. These sites were selected as evaluation sites for the DSDM project (Fleischman et al. 2005).

Table A1-3. Design parameters evaluated.

Length (ft)	240	180	120	60
Aspect Ratio (AR)	4	3	2	1
# of story (N)	6	4		2
Depth (ft)	60		32	
LFRS Type	Shear wall		Frame	
SDC	E		C	

It should be noted that varying the diaphragm geometry modifies the relationship between several key factors including: (1) the diaphragm moment-to-shear ratios; (2) the ratio of diaphragm-to-LFRS stiffness (Fleischman and Farrow 2001); and, (3) the relationship between diaphragm local and global

C-A-8

deformation demands. Note also that increasing diaphragm length has a disproportional effect on the diaphragm-to-LFRS stiffness ratio (See Fig. A1-2a), since not only does the diaphragm flexibility increase, but the LFRS stiffness will tend to increase due to the higher required lateral force from more mass tributary to the LFRS element. Likewise, as a diaphragm gets longer, the diaphragm flexibility lengthens the structural period (See Fig. A1-2b).
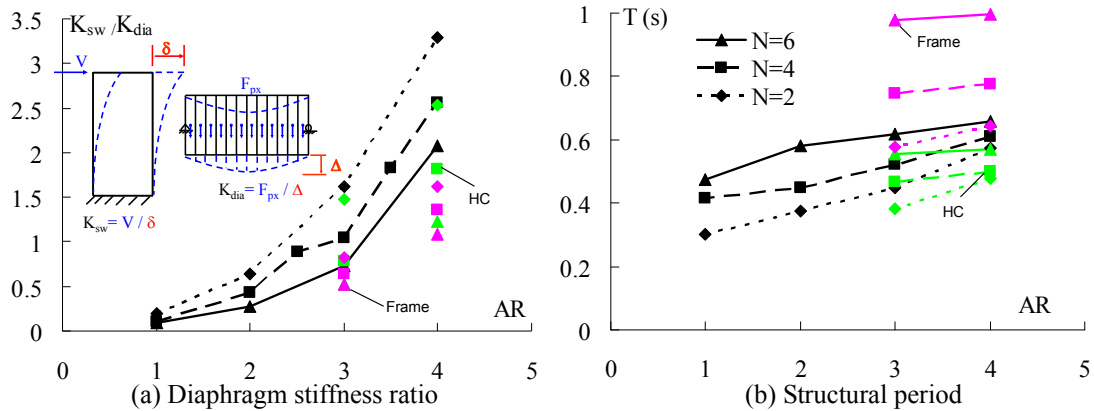
Fig. A1-2. Structural characteristics for shear wall structures (BDO).

A1.1.3 Ground Motions

A suite of five earthquake strong ground motions are used in the parametric study for each SDC (See Table A1-4). The earthquakes represent anticipated seismic hazard for the sites in Table A1-1. The suite of motions is scaled such that their mean response spectrum reasonably matches the design spectrum for the design basis earthquake (DBE), as shown in Fig. A1-3. The individual motions are scaled by 1.5 for the MCE analyses. The motions are applied as a uni-directional transverse component. For reference, the evaluation structure periods (shown previously in Fig. A1-2b) are indicated on the response spectra.

Table A1-4. Information of ground motions used in the parametric study

Label	Earthquake	Magnitude	Scale factor	d_t (s)	Duration (s)	PGA (g)
KN1	Kocaeli, Turkey	7.4	1.295	0.005	25.3	0.283
KN2	Landers	7.3	0.845	0.02	44.0	0.128
KN3	Nahanni, Canada	6.8	0.325	0.005	20.6	0.356
KN4	Nahanni, Canada	6.8	0.701	0.005	20.0	0.343
KN5	Tabas, Iran	7.4	0.549	0.02	23.8	0.223
BK1	Erzincan, Turkey	6.7	1.380	0.005	20.8	0.684
BK2	Loma Prieta	7.0	0.723	0.005	25.0	0.407
BK3	Loma Prieta	7.0	2.140	0.005	40.0	0.694
BK4	Northridge	6.7	1.057	0.005	15.0	0.500
BK5	Superstition Hills	6.7	1.764	0.01	22.4	0.666
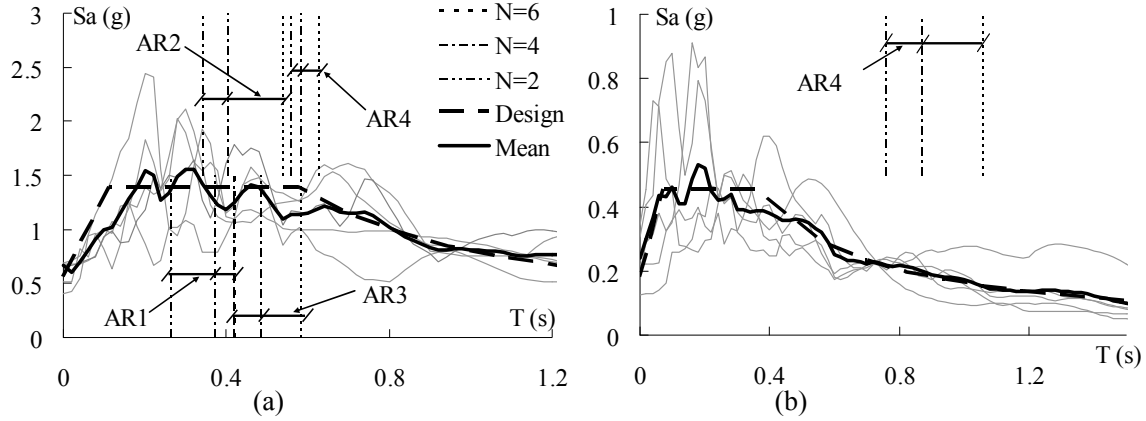
Fig. A1-3. Response spectra (DBE): (a) SDC E; (b) SDC C.

A1.1.4 Parametric Study Procedure

The design factors are calibrated to force and deformation targets for each design option as summarized in Table A1-5.

Table A1-5. Design Options and Performance Targets

Design Option	Performance Target	Force Ampl. Factor	Target Metric in Analysis	MCE Defo. Target	Shear Ovrstr. Factor	Target Metric in MCE Analysis	Drift Metric in MCE
EDO	Elastic diaphragm response in MCE	Ψ_E	$T^{MCE}_{chrd} = A_sF_y$	—	Ω_E	None ($\underline{\Omega_E} = 1.0$)	θ_{dia}
BDO	Elastic diaphragm response in DBE / MDE allowable opening in MCE	Ψ_D	$T^{DBE}_{chrd} = A_sF_y$	$\delta_{chrd} \leq \delta^{ALL}_{MDE}$	Ω_B	$V_{max,FE} / V_u$ where $V_u = \underline{\Psi_D} F_{px}/2$	θ_{dia}
RDO	HDE allowable opening in MCE	Ψ_R	—	$\delta_{chrd} \leq \delta^{ALL}_{HDE}$	Ω_R	$V_{max,FE} / V_u$ where $V_u = \underline{\Psi_R} F_{px}/2$	θ_{dia}

The calibration of design force factors for the seismic design methodology is a trial-and-error process since the nonlinear analysis results to be aligned with performance objectives are dependent on the diaphragm design strengths initially selected. An approach used with simpler multi-degree of freedom (MDOF) mass-spring models in previous research involved gradually incrementing the diaphragm strength from the current code design strength levels until the desired performance targets were met (Fleischman and Farrow 2002). Such an approach is not feasible here, where, even for the simpler evaluation structure, time intensive NLTDA of large DOF finite element models are being performed. Hence, the following analysis sequence was introduced for each parameter set in the design space to minimize the overall time of the analytical study:

1. Determine Ψ_D for BDO

In the first step of the sequence, the factor Ψ_D is sought. Given the BDO performance target of elastic DBE response, this step can be performed using an analytical model with elastic diaphragms. This model is subjected to DBE-level hazard and the maximum elastic force registered by the diaphragm during the analysis is used to determine the trial factor for Ψ_D. Note that the LFRS must still be represented by an inelastic model (and designed accurately in terms of an appropriate R factor) in order to arrive at the proper Ψ_D factor. Furthermore, as precast diaphragm reinforcing strength and stiffness are not unrelated (Naito et al. 2009) (Cao et al. 2009), and diaphragm seismic force demands are sensitive to

diaphragm flexibility (Fleischman and Farrow 2001), an estimate of Ψ_D must be made a priori in order to provide the elastic diaphragm model with reasonable diaphragm stiffness. Accordingly, if the resulting analytically measured Ψ_D is not within a tolerance (15%) of the a priori estimate, the analysis is repeated with an improved stiffness estimate.

2. Determine Ψ_E for EDO

The same process is repeated to determine the Ψ_E factor for the EDO. The elastic diaphragm model is again used since Ψ_E is also associated with elastic diaphragm response. However: (1) the model is subjected to MCE-level hazard to align Ψ_E with the appropriate performance target (See Table A1-5); and (2) the model possesses a higher initial diaphragm stiffness based on the diaphragm reinforcement required for the estimated Ψ_E. The maximum gravity column drift is measured (*See Step 3c below*).

3. Determine Ω_v and Diaphragm Reinforcement Classification for BDO

Once Ψ_D is established from the DBE-level analyses in step 1, the expected MCE performance for this same design can be determined. For this step, the diaphragm model is extended to inelastic response, based on a diaphragm designed with the Ψ_D identified in Step 1. This model is subjected to MCE-level hazard to determine: (a) the inelastic deformation demand on key diaphragm reinforcement elements; (b) the required overstrength of diaphragm-to-LFRS connection and shear reinforcement (Ω_v) to keep these elements elastic; and, (c) the diaphragm-induced gravity column drift demands.

(a) The BDO is to be paired with moderate deformability elements (MDE). Thus the maximum diaphragm reinforcement deformation demands in the MCE (measured in terms of opening across the joint between precast units) are to be maintained within the allowable deformation of the MDE reinforcement. At the outset of the trial factor parameter study, the allowable deformation limits for the diaphragm reinforcement classification system was not yet established. Thus, the results of this step, interpreted with respect to the range of feasible deformation capacities exhibited in the testing of common diaphragm connectors (Ren and Naito 2011), established the allowable deformation limits for MDE reinforcement as 0.2″.

(b) To obtain Ω_v, the diaphragm-to-LFRS connection reinforcement and the shear resistance of shear reinforcement in critical shear regions are modeled elastically. The *tension* resistance of shear reinforcement in critical flexure regions is modeled inelastically to produce accurate flexural strength. It should be noted that this simplification for the shear reinforcement model is only possible for the simple evaluation structure, which possesses well-defined critical shear and flexure regions. Thus, a major objective of the verification studies on realistic diaphragms that followed (Appendix A2) was to verify or further calibrate to Ω_v factors for cases where the effects of combined shear and tension play an important role on the shear reinforcement response.

(c) In this step, as with all MCE analyses, the maximum gravity column drift demand is measured and compared to the maximum LFRS drift to determine the amplification of gravity system drift (θ_{dia}) due to diaphragm flexibility. The value is compared to the drift increment based on an elastic diaphragm calculation in order to calibrate: (i) a reduction factor C_r to convert maximum diaphragm deformation to the diaphragm induced gravity column drift; (ii) an inelastic diaphragm deformation factor, C_{dia} needed to convert the elastic design calculation to an accurate estimate of the inelastic diaphragm deformation, similar in concept to the δ_s factor used for the LFRS (ACI 318 2008); and (iii) a C_Δ factor to account for P-Δ effects on the gravity system column for flexible diaphragms (this factor is based on the comparison of a smaller subset of runs with second order effects included).

4. Determine Ψ_R, Ω_v and Diaphragm Reinforcement Classification for RDO.

The RDO performance target involves limiting the maximum diaphragm joint opening demands in the MCE to within the HDE allowable deformation. Thus, the determination of Ψ_R requires calibration

using structural models with inelastic diaphragms subjected to MCE level hazard. The HDE allowable deformation was established relative to the maximum reliable cyclic opening capacity produced by the best performing existing diaphragm reinforcement. Based on the testing, the HDE qualification opening deformation was established as 0.6″ (Naito et al. 2009), and by applying a 2/3 factor of safety suggested by the DSDM TG, produced the allowable deformation of 0.4″ for HDE reinforcement.

An estimate for Ψ_R must be made in order to generate a trial design. The initial estimate for Ψ_R was obtained by interpolating between Ψ_D and unity, which in the analyses tends to produces a maximum opening deformation greater than the HDE allowable limit. A second analytical iteration is performed with a sufficiently higher Ψ_R (based on the maximum opening of the initial analysis) to produce a maximum opening deformation lower than the HDE allowable limit. To limit the number of iterations in this step, the design factor Ψ_R is established after the second analyses by interpolating (or extrapolating) between the results of the deformation ratio $\delta_{max}/\delta_{ALL}$ for the two estimates.

Note finally that the due to the higher diaphragm overstrength potential in the MCE for the RDO, a higher Ω_v is typically obtained for the RDO than for the BDO. For a comprehensive description of RDO diaphragm performance, the DBE response is also evaluated analytically using the Ψ_R value obtained.

Using this sequence, a minimum of six NLDTA 3D-FE analyses are performed per ground motion for each unique parameter set in the design space to completely characterize its design factors (See Table A1-6). Each 12 analyses take about one week including pre-process, run time and post-process.

Table A1-6. Parametric study sequence

Study	EQ level	# of EQ	Diaphragm design	Objective determine	Parameter combinations	Number of runs
1	DBE	5	Est Ψ_D	Ψ_D	30	150
2	MCE	5	Est Ψ_E	Ψ_E	30	150
3	MCE	5	Ψ_D	$\delta_{max}, \Omega_{vB}$	18	90
4	MCE (2) & DBE	5	Est Ψ_R	Ψ_r, Ω_{vR}	18	270
Total number of Runs						660

A1.2 ANALYTICAL MODELING

The analytical work is performed using a three-dimensional finite element (3D-FE) model of the precast evaluation structure. The 3D-FE models uses "discrete" diaphragm models in which the diaphragm reinforcement is modeled directly through connector elements placed at discrete locations along the diaphragm joint. The connector elements are developed based on test data from the Lehigh testing program. The detailed description of the diaphragm model used in this study is discussed in Appendix B1 and B2 Calibration of the models appears in Appendix B3 and B4.

A1.2.1 Evaluation Structure Model

The three-dimensional finite element (3D-FE) model of the evaluation structure is shown in Fig. A1-4. The model, created using the general-purpose FE program ANSYS[5], employs discrete connector elements to represent the diaphragm (Wan et al. 2012a). This approach permits examination of local demands by explicitly modeling the diaphragm reinforcement elements. The model is based on a planar diaphragm model developed for nonlinear static "pushover" analysis (Fleischman and Wan 2007), modified to include gravity-system elements present in the floor system such as precast spandrel beams (Wan et al. 2012b), and extended for NLTDA (Zhang et al. 2012). The evaluation structure is modeled in half-symmetry for run time and disk space efficiency.

---

[5] ANSYS version 10, Inc., Canonsburg, PA
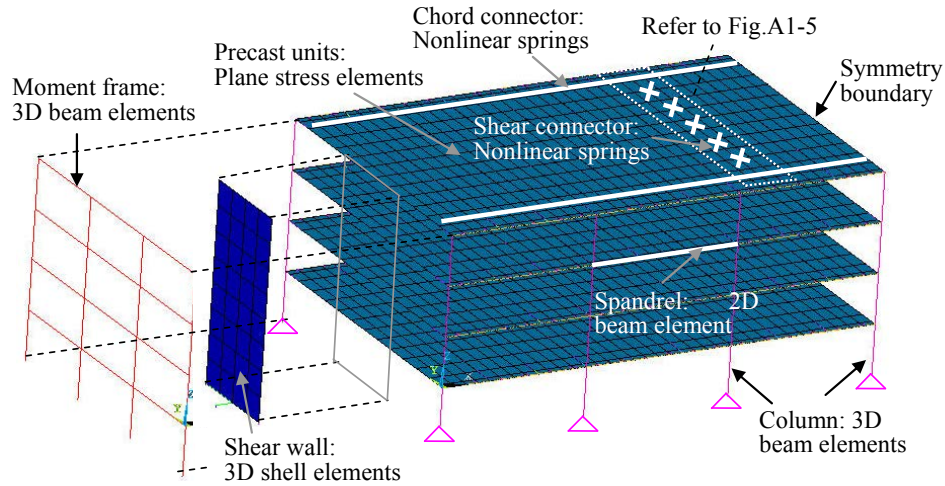
Fig. A1-4. 3D-FE half-symmetry model of evaluation structure.

The shear wall is modeled with 3D elastic shell elements with nonlinear coupled springs at the ground to capture wall base biaxial hinge response as described in (Zhang 2010). The moment frame is modeled as 3D elastic beam elements with concentrated plastic hinge spring elements at the beam ends and the column base (Zhang 2010). The hinge properties for shear wall and frame are developed using section analysis software XTRACT[6] with a bilinear steel model (1.2 strain hardening ratio) and a Mander model for concrete. The plastic hinge length for shear wall is set as minimum of half of shear wall depth and story height. The plastic hinge length for frame member is set as the frame member depth.

The precast floor units are modeled as elastic plane stress elements with an input flange thickness and an effective smeared mass to including the weight of DT stem. The perimeter spandrel beams and columns are modeled as elastic beam elements.
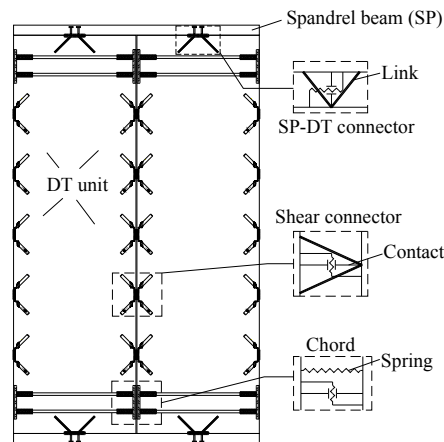
Fig. A1-5 Diaphragm joint model detail.

The precast diaphragm connections are represented by assemblages of coupled nonlinear cycle-degrading springs and contact elements (see Fig. A1-5), as described in PART B1 and B2. The properties for the springs are derived from tests of isolated reinforcement under different combinations of shear and tension load (Naito et al. 2009) (Cao et al. 2009). The tension response for chord model and shear connector model includes the pinching and stiffness degradation effects observed in the test. The shear response of chord model and shear connector model is modeled elastically in order to directly determine

---

[6] XTRACT Imbsen commercial software, Inc. Rancho Cordova, CA.

C-A-13

the required shear overstrength. The tension-shear coupling effect is not included in the chord reinforcement and shear connector models because the evaluation structure has a well defined critical shear demand region (both ends of diaphragm) and critical flexural demand region (midspan). The hysteretic model for the SP-DT connector includes pinching and tension-shear coupling, but without cyclic stiffness or strength degradation.

Key aspects of the model as they pertain to this study include: (1) Shear connectors in high flexural regions of the floor diaphragm participate in carrying a portion of in-plane moment; (2) Chord connectors in high shear regions of the floor diaphragm participate in transferring a portion of in-plane shear through dowel action. (3) The contribution of the spandrel beams, as limited by their connections to the precast double tees, are included and provide a secondary path for a small portion of diaphragm shear and flexure; (4) The diaphragm-to-LFRS connection is modeled as a rigid connection (via coupling of the appropriate DOFs of LFRS elements to diaphragm plane stress elements); (5) The gravity columns are modeled as 3D beam elements with a pinned base and pinned connections to the diaphragm at each level, and therefore participate in transferring a small portion of base shear and thus reduce diaphragm flexibility (Ware et al. 2012).

A1.2.2 Dynamic Analysis Parameters

In the trial factor study, an equivalent damping value of 1% aligned with the first (fundamental) and last significant transverse vibrational modes (cumulative mass participation ratio ≥ 99%) was used, based on recent findings on the amount of viscous damping present in nonlinear systems (Panagiotou et al. 2006). It is noted that this value is conservative relative to that used to produce the design spectra (ASCE 7 2005). The discrete diaphragm model cannot be used effectively for modal analysis due to the uncertain initial status of the contact elements (open, sliding, stuck). Thus, the Rayleigh damping parameters are determined through modal analyses performed on 3D elastic models with monolithic diaphragms. The diaphragm stiffness is estimated through effective moduli (Wan and Fleischman 2012).

A1.3 GENERAL ANALYTICAL RESULTS

Selected results from the evaluation structure study are first presented to provide an overview of the general seismic response of the evaluation structure, including the diaphragm behavior, prior to presenting parametric results for the trial design factors.

A1.3.1 General Seismic Response

It will be useful to show the seismic demands on the evaluation structure LFRS in order to benchmark the diaphragm demands to follow. Further, it is important to recognize the trial design factors are developed with analyses employing 1% critical damping, and include MCE level hazard, whereas the design codes are based on a 5% damped spectrum at the design basis earthquake (DBE). Accordingly, Figure A1-6a shows the shear wall maximum base rotation (scale shown on left-hand axis) and the diaphragm maximum chord opening deformation (scale shown on right-hand axis) for the evaluation structure design case (AR1-N6-SDC E-BDO) at different levels of damping. Analyses are performed under DBE and MCE level hazard Motion BK5 (see Table A1-4), for critical damping ratios ranging from 1% to 5%. As seen for the 5% damping DBE case, which allows direct comparison to anticipated code demands, the maximum LFRS base rotation is within 2%, as would be expected in the design basis earthquake. The influence of lower critical damping on the LFRS and diaphragm demands can be seen in Fig. A1-6a. Figure A1-6b shows a scatter plot of maximum LFRS demands for each case in the parameter study, with DBE level shown as solid markers and MCE level as hollow markers (frames are indicated in gray). As seen, the combination of MCE level hazard and a conservative value of 1% critical damping used in the analyses leads to higher demands. However, all cases are within anticipated DBE drifts (2% according to ASCE-7 2005), except those for the 2-story shear wall structures. Note, however, that this case was shown to be code compliant for the 5% design spectrum in Figure A1-6a.
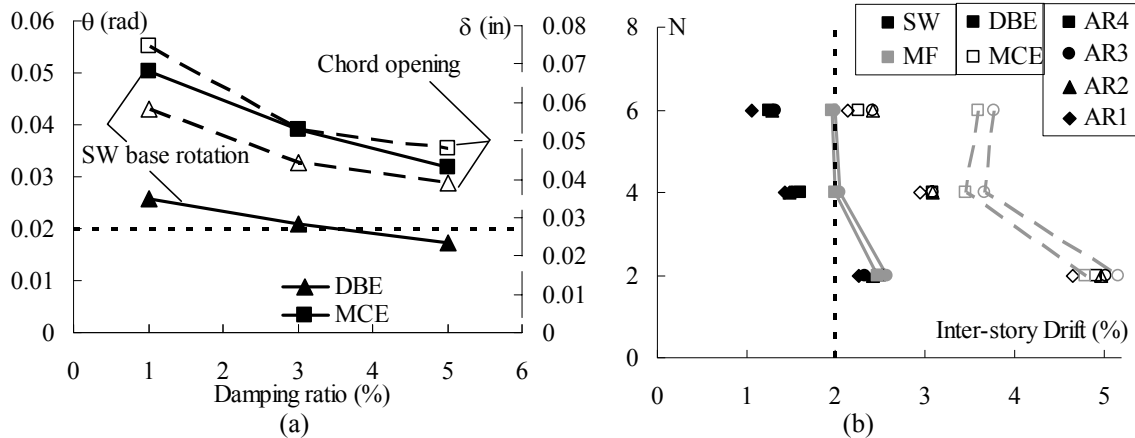
Fig. A1-6. Evaluation LFRS response: (a) SW base rotation; (b) Maximum inter-story drift.

Figure A1-7 shows the diaphragm response in a MCE event (BK2 in Table A1-4) for the evaluation structure case (n=6, AR= 4, SW, SDE E) for trial design factors equivalent to the each of the three diaphragm design cases (EDO, BDO, RDO). Figure A1-7a shows the global diaphragm demands, expressed as the top floor inertial forces vs. diaphragm midspan deformation (Refer to insert in Fig. A1-7b). As seen, though dissipating more energy, the difference between the global hysteresis between the three curves is not stark, underlining the intent that the diaphragm is not intended to serve as the primary energy dissipation mechanism, even in the RDO; rather this is reserved for the LFRS (e.g. as shown in Fig. A1-6a). However, the marked difference in *local* diaphragm demand for the different designs is observed in Figure A1-7b, which shows the chord force vs. joint opening (Refer to insert in Fig. A1-7b) at midspan of the top floor. As seen, the EDO chord remains elastic while the BDO and RDO designs endure inelastic chord opening cycles. Note that also indicated in the plot is the allowable deformation limit for the LDE, MDE and HDE reinforcement, showing the adequacy of these designs with respect to the diaphragm reinforcement classifications.
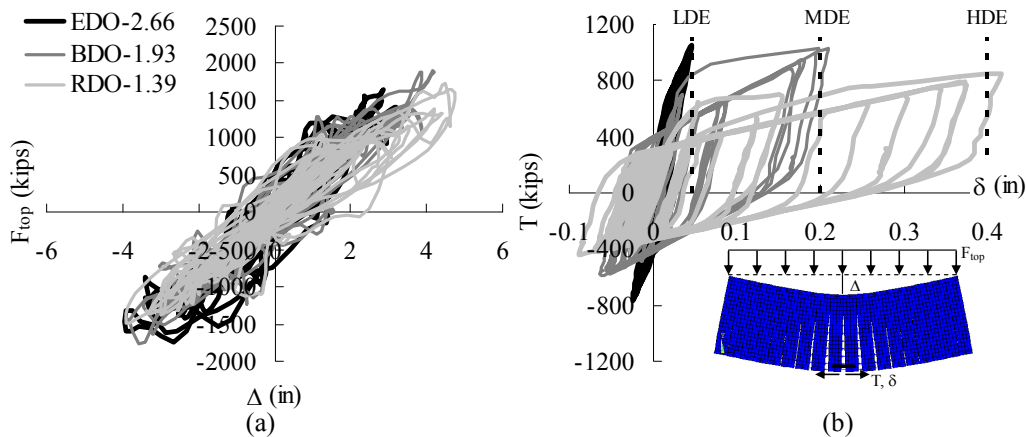
Fig. A1-7. Diaphragm demands for AR4-N6 under MCE: (a) Global and (b) Local.

A1.3.2 Diaphragm Seismic Demand Profiles

The majority of parametric results used to determine trial design factors are shown as maximums for the diaphragm anywhere in the building. It will be useful, however, to examine diaphragm demand profiles along the height of the structure, and along the length of the diaphragm. Figure A1-8 shows two profiles along the height of the building: (a) diaphragm maximum inertial force, normalized by the maximum value on any floor; and (b) maximum chord opening (at midspan) at each floor level. The

C-A-15

results are for MCE hazard for SDC E shear wall structure; the former for an elastic diaphragm model (EDO design) ; the latter for an inelastic diaphragm model (RDO level design). Note that in either case, the maximum values used to determine design factors occurs only at one floor level, with others lower.

The force profiles shown in Figure A1-8a are typical of taller structures in that: (a) the maximum diaphragm demand usually occurs at the top floor; (b) upper regions of the structure have lower forces; (c) lower stories have increased forces relative to upper stories but typically not as large as the top level force. In shorter structures, the increase in lower stories is not as pronounced. The distribution of diaphragm force along building height is seen to be dissimilar than the inverted triangular form used in current design. As seen in Figure A1-8b, the force demands are transformed into chord opening demands of a similar profile when the diaphragm design does not remain elastic.
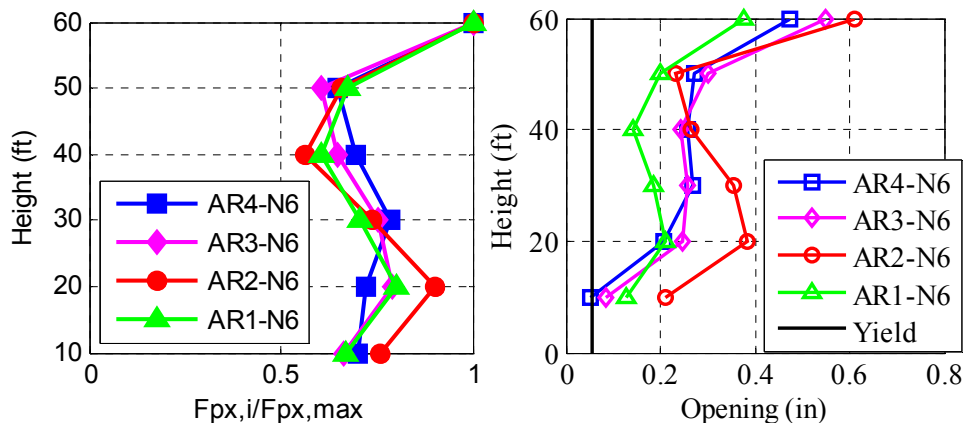
Fig. A1-8. Normalized diaphragm response profile under MCE: (a) Force; (b) Chord opening.

It is important to note that these models included the gravity system columns (Refer to Fig. A1-4), and thus maximum demands at the lowest level of the structure, as was observed in previous work using models that do not include the gravity system (Fleischman et al. 2002), did not occur with gravity system included (Ware et al. 2012). For this reason, rather than advocating a constant diaphragm force profile, a vertical force distribution factor (α_x) is included in the current diaphragm design (See PART 1, Appendix I). The analytical results that produce the α_x factor are described later in Section A1.5.3.

(a) AR4 structure   (b) AR2 structure
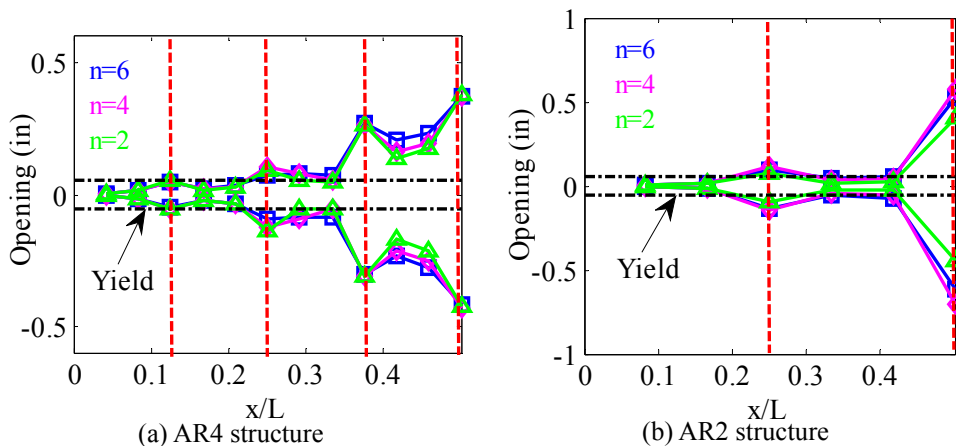
Fig. A1-9. Chord max opening demand along diaphragm length under MCE.

Figure A1-9 shows the diaphragm maximum chord opening profile at top floor for the SDC E shear wall structure designed with the trial RDO. Column line joints, where the spandrel terminates, are indicated as red dashed line. The chord yield opening is indicated on the plot. As seen, chord opening demands concentrate at the column joints because adjacent joints are protected by the spandrel beams

(Wan et al, 2012). The longer span diaphragm (AR4) has more distributed inelastic opening than the shorter span diaphragm (AR2), due to more joints under high flexure. Thus, a larger concentration of inelastic opening demand occurs at critical flexural joint for the shorter span.

A1.4 PARAMETETIC RESULTS

The trial design factors and parametric results reported in this paper are based on mean results (of maximum values) from the suite of five earthquake simulations, instead of suite of seven earthquake simulations as required by ASCE 7 procedure (ASCE 7 2005). This decision was based on time considerations for the analytical program (see Table A1-6), and considered appropriate given the trial nature of the factors (see below). The maximum values (diaphragm force, shear force, chord deformation demand, etc.) for a given motion can occur anywhere in the structure but the statistical mean used to determine design factors is based on combinations at *coincident locations* for response across the individual ground motions.

The values reported here are referred to as "trial" design factors because a subsequent step exists prior to their incorporation in the design methodology. In this step, a set of realistic precast structures from a portfolio of prototype structures developed for the project (Fleischman et al. 2005) were designed using the trial values developed here and evaluated for the purposes of calibrating the design factors. The realistic structures possess more complicated configurations than the evaluation structure, including floor systems with multiple floor bays, plan irregularity, and openings (such as parking structures), and, were subjected to orthogonal components of ground motions (Zhang and Fleischman 2012). Such evaluations would not be appropriate for developing the basic relationships for the design factors, nor would they be manageable for the trial-and-error process described, but are suitable for verification purposes. The *maximum response* of three earthquake simulations is used in the verification study, in accordance with ASCE 7 procedures (2005).

A1.4.1 Diaphragm Pushover Curve

The results presented in this study are maximum *dynamic* demands. However, it would be useful to view these demands in terms of the diaphragm *capacity*. Accordingly, the parametric results produced by NLDTA will be presented on diaphragm capacity curves, created by nonlinear static "pushover" analyses. The pushover curves were constructed using nonlinear static analysis by applying an increasing body force to the discrete model of the isolated diaphragm (removed from the structure). The isolated diaphragm model uses simple support conditions for the perimeter LFRS and ignores the contribution of columns. Figure A-10 shows the pushover curves for two design cases, each with the hysteretic response at top floor of three selected earthquakes superimposed. The mean responses of five ground motions are shown as markers on the pushover curve. For clarity, subsequent plots leave off the hysteretic curve but include the markers.
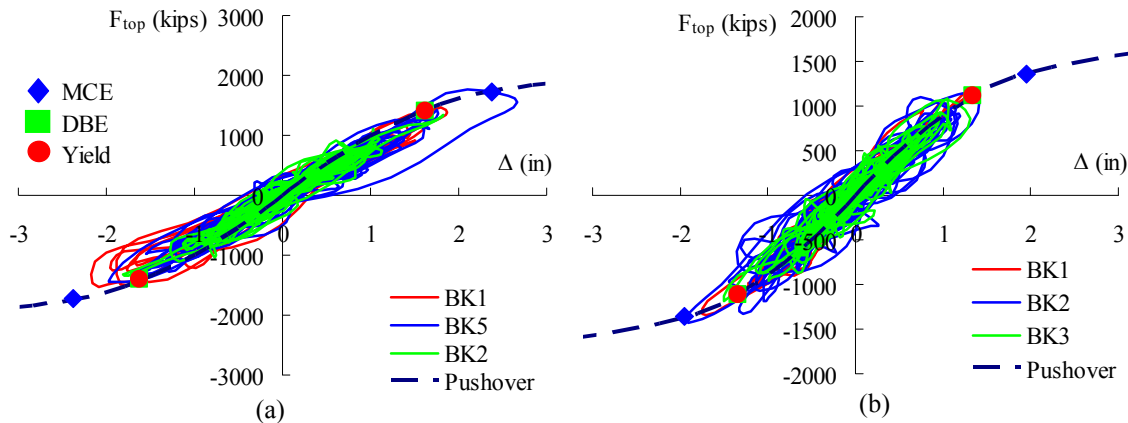
Fig. A1-10. Diaphragm force vs. deformation response: (a) AR3-N6; (b) AR3-N4

Figure A1-11 shows diaphragm seismic response from the dynamic analyses. The left hand column shows diaphragm global demands (diaphragm force vs. maximum deformation) indicated as points on diaphragm pushover curve schematics. The right hand column shows the corresponding local demands, expressed as maximum chord axial force vs. joint opening at midspan, superimposed on connector load-vs.-deformation backbone curves established in the testing protocols (REF). Note that the dynamic (earthquake) and static (pushover) results do not exactly coincide (refer to Fig. A1-10), due to dynamic loading patterns. Thus, points on the pushover curves (left hand plots) are approximate dynamic maxima, referenced directly to the local design target (right-hand plots) achieved in the dynamic analysis.

Fig. A1-11. Maximum seismic demands shown on pushover curves for selected runs.
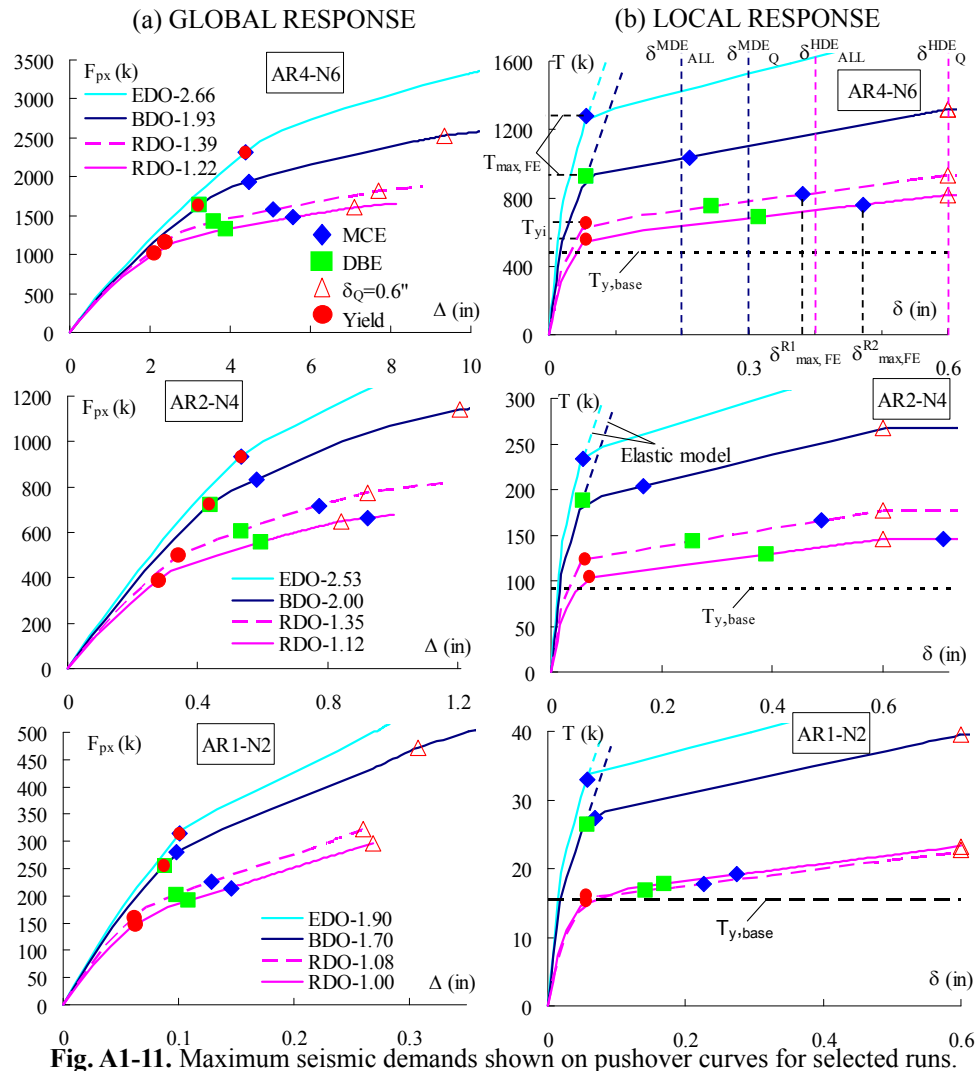
Each row shows the results from three distinct SDC E shear wall designs: (1) AR4-N6; (2) AR2-N4; and, (3) AR1-N2. Each plot shows the characteristic curve of, from top to bottom: the EDO, the BDO, and the two trial RDO designs. The (green) square is DBE demand and the (blue) diamond is MCE demand. These markers represent the mean of maximum results from the NLTDA. The (red) circle in the plots represents the yielding of the chord in the pushover, and the (hollow) triangle represents the achieving of the HDE qualification deformation (0.6″). These markers represent target demands (maximum HDE deformation capacity) obtained in the pushover analysis.

The amplification factor for each curve is listed in the legend. As these are not known a priori, the pushover curves are constructed after the sequence of analyses described in Section A1.1.4. The

performance targets for each design option are identifiable: (1) EDO: elastic MCE response; (2) BDO: elastic DBE response and MDE allowable deformation in the MCE; and (3) RDO: HDE allowable deformation in the MCE. Figure A1-11 also shows that diaphragm stiffness changes with design strength.

A1.4.2 Design Factor Determination

The MCE performance target for the EDO and the DBE performance target for the BDO are elastic diaphragm response. As indicated in Table A1-5, the diaphragm force amplification factors in these cases, Ψ_E and Ψ_D respectively, are obtained using a strict definition of elastic response, i.e., the diaphragm force at which the chord steel reaches its expected yield force (Naito et al. 2009). The reason for defining this target locally, rather than using the achievement of the yield moment M_y (in accordance with the moment diagram in Figure A1-1), is that in more realistic floor diaphragms, axial and shear force combinations, as well as longitudinal inertial effects, limit the usefulness of the simple beam calculations.

The expression used to determine diaphragm force amplification factors for the EDO and BDO is:

$$\Psi = T_{\max,FE} / T_{y,base}$$

where $T_{\max,FE}$ is the maximum chord force demand measured in the (elastic diaphragm) analyses. These points are shown in Fig. A1-11b as blue diamonds (EDO) and green squares (BDO). $T_{y,base}$ is the chord yield strength calculated using the diaphragm baseline design force (F_{Dx}):

$$T_{y,base} = F_{Dx} L / 8 d_{chord}$$

where d_{chord} is the equivalent moment arm determined using strain compatibility procedures developed in the project (BSSC TS-4 2009) to include the shear reinforcement contribution to flexure (ACI 318 2005). $T_{y,base}$ is shown as a dotted line in Fig. A1-11b.

The RDO performance target is satisfied when the maximum chord opening demand measured in a MCE level analysis ($\delta_{\max,FE}$) is within the allowable HDE opening (δ^{HDE}_{ALL}), as indicated in Table A1-5. The corresponding strength of the diaphragm is used to determine the required force amplification factor, Ψ_R. As the diaphragm strength is therefore not know a priori, the method described in A1.1.4 is used to interpolate a solution through two trial RDO analyses, noted as R1 and R2 (dashed and solid pink lines respectively in Fig. A1-11). The maximum chord opening demands ($\delta^{R1}_{\max}$ and $\delta^{R2}_{\max}$ shown as blue diamonds in Fig. A1-11b) obtained from the MCE simulations for each case are measured and used for interpolation (or rarely extrapolation) of the Ψ_R factor as follows:

$$\Psi_R = \Psi_{R1} + (\Psi_{R2} - \Psi_{R1})(\delta^{HDE}_{ALL} - \delta^{R1}_{\max,FE})/(\delta^{R2}_{\max,FE} - \delta^{R1}_{\max,FE})$$

where Ψ_{R1} and Ψ_{R2} are the trial diaphragm force amplification factor for RDO design determined using the following expression:

$$\Psi_{Ri} = T_{yi} / T_{y,base}, \text{ i= 1 or 2.}$$

where T_{yi} is the chord yield strength of the analytical model, as indicated as red circle in Fig. A1-11b.

Also indicated in Table A1-5, the shear overstrength factor Ω_v is determined using the ratio between the maximum diaphragm shear force demand measured in the MCE analysis ($V_{\max,FE}$), located at the diaphragm ends for the simple evaluation structure layout (see Fig. A1-12), and diaphragm design shear force calculated with the diaphragm force amplification factor ($V_u = \Psi F_{Dx}/2$):

$$\Omega_V = 2V_{\max,FE} / \Psi F_{Dx}$$

where Ψ is the corresponding diaphragm force amplification trial design factor, Ψ_D or Ψ_R, as calculated using the method described above (note for the EDO that $\Omega_v = 1.0$). Note that the maximum demand measured in the analysis is based on the absolute value of shear force (refer to Fig. A1-12).
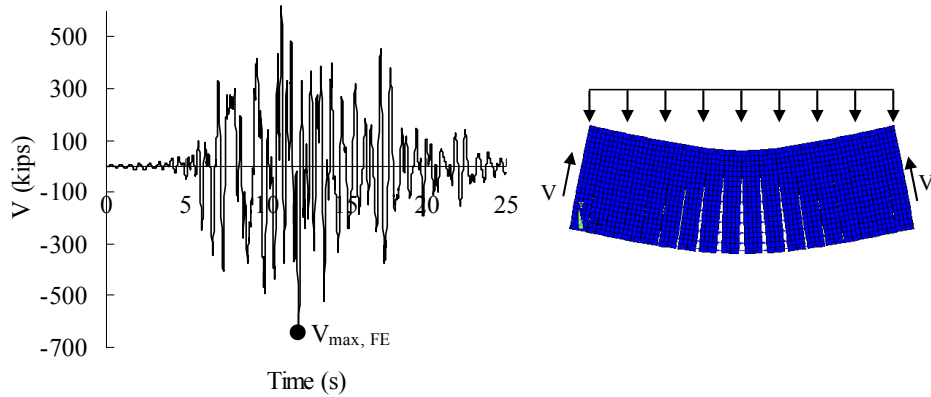
Fig. A1-12. Diaphragm shear time history (SDC E-AR3-N6-MCE-BK5).

A1.4.3 Diaphragm Design Force Amplification Factor

This trial factors produced for the different design options (EDO, BDO and RDO), shown for selected designs in Fig. A1-11, are gathered for all analyses in parametric plots in Figure A1-13 to 17.

(a) Number of story parameters;   (b) Diaphragm AR parameters.
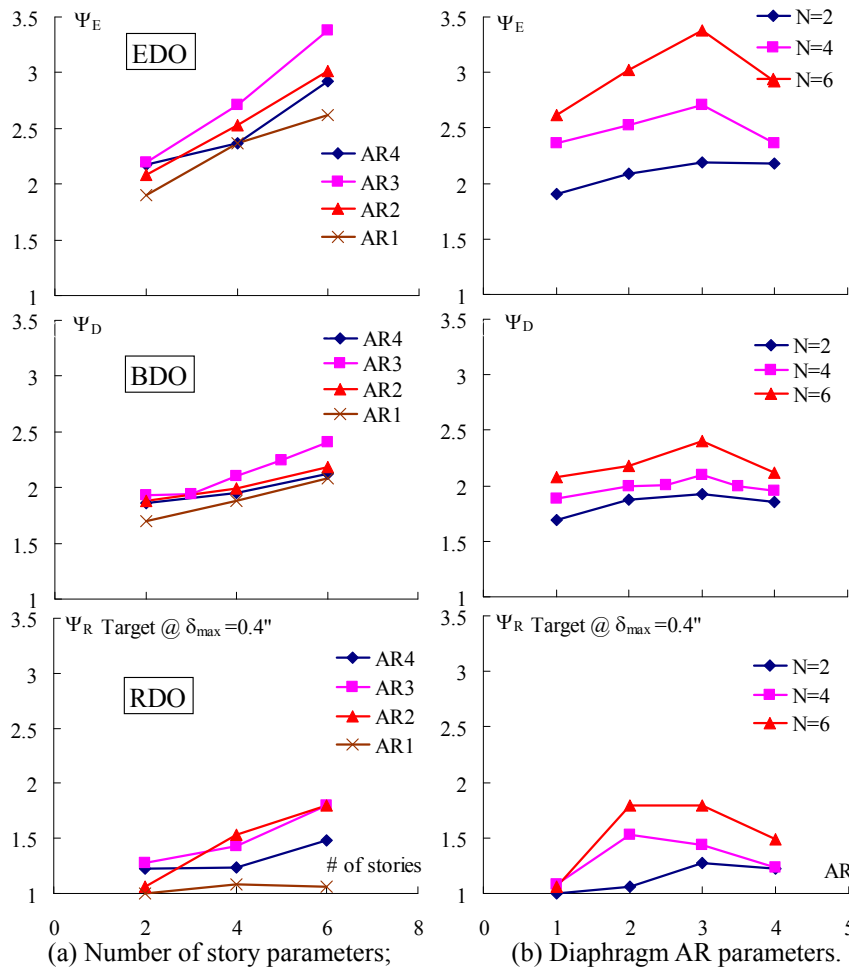
Fig. A1-13. Diaphragm force amplification factors for different building geometries.

Figure A1-13 shows SDC E shear wall designs and the same results are shown versus: (a) number of stories; and (b) diaphragm aspect ratio. Note that, as expected, Ψ values decrease when moving from Ψ_E to Ψ_D to Ψ_R. The following trends are further identified for the different building geometries in Fig.

C-A-20

A1-13: (1) maximum diaphragm force typically increases with number of stories; (2) diaphragm force will increase with aspect ratio to a point after which the effects of diaphragm flexibility actually lower diaphragm force. This effect is more noticeable in taller structures; and, (3) the effect of number of stories is more significant than the effect of diaphragm aspect ratio. This latter point indicates that higher mode effects (see Sec. 5.6), are more significant than the effect of diaphragm flexibility.

Fig. A1-14 plots the effect of diaphragm length on the diaphragm force amplification for the structure with the same AR. The solid lines in Fig.A1-14 represent the structures with AR=4 and the dashed lines in Fig. A1-14 represent the structures with AR=3. The triangle, square and diamond markers in Fig. A1-14 represent 6-story, 4-story and 2-story structures respectively. Generally the required diaphragm force amplification factor increases with increase in diaphragm length due to diaphragm flexibility.
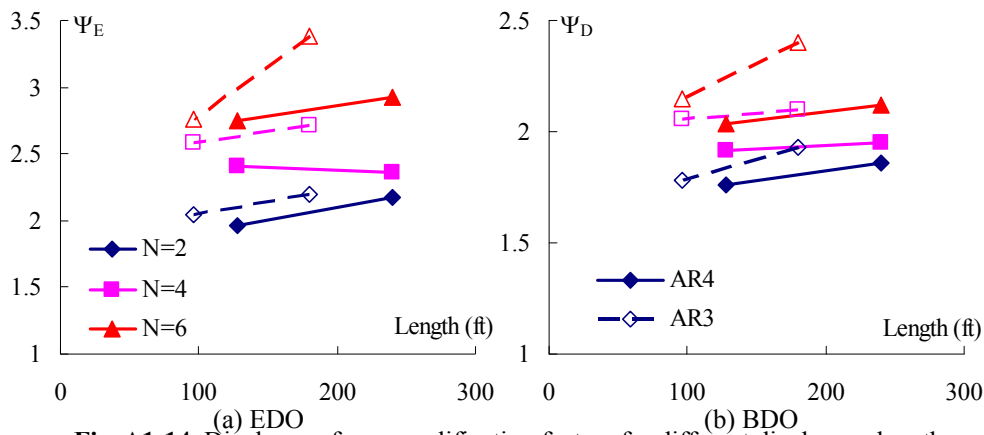
Fig. A1-14. Diaphragm force amplification factors for different diaphragm length.

Next, the required diaphragm design forces among different LFRS types are compared for SDC E. Because the shear wall (SW) and moment frame (MF) structure designs utilize different R factors (refer to Table A1-1), Figure A1-15 first shows required diaphragm design forces translated into required floor acceleration. Each plot in Figure A1-15 shows the floor acceleration required to meet the design target for each diaphragm design option: (a) EDO; (b) BDO; (c) RDO. As seen, the shear wall structure requires higher diaphragm design acceleration than the moment frame structure, and the difference grows as the structure becomes taller. These results imply that higher mode effects may have a larger effect on the shear wall structure than the moment frame structure.
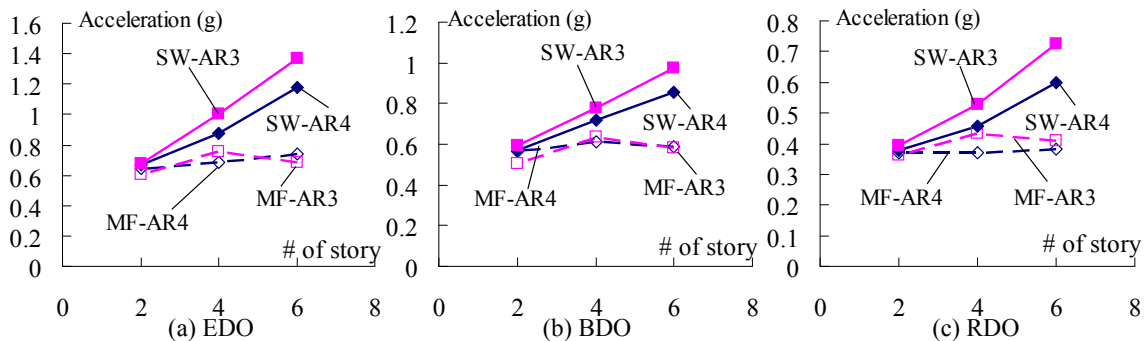
Fig. A1-15. Floor acceleration for different LFRS types required to meet the design targets.

As mentioned above, the code prescribed R factor for the shear wall structure (R=6) and the moment frame structure (R=8) are different, which results in a lower diaphragm baseline design force for the moment frame structure. Thus, the comparison of trial diaphragm force amplification factors shown in Fig. A1-16 is different than the floor acceleration plots in Fig. A1-15. As seen, except for the tallest

structure evaluated (N=6), the trial amplification factors implied in the analyses for the shear wall structure are slightly lower than the moment frame structure. For the 6-story structure, where higher mode effects are more prominent, the shear wall Ψ factors are considerably larger than the moment frame Ψ factors. Given the similarity of low-rise structures, and the conservative nature for taller structures, the Ψ factor design equations (See Section A1-5.1) proposed in the design procedure do not directly include a parameter considering different types of LFRS. However, the proposed equations bound the data points shown in Fig. A1-16, including both shear wall and moment frame structures.
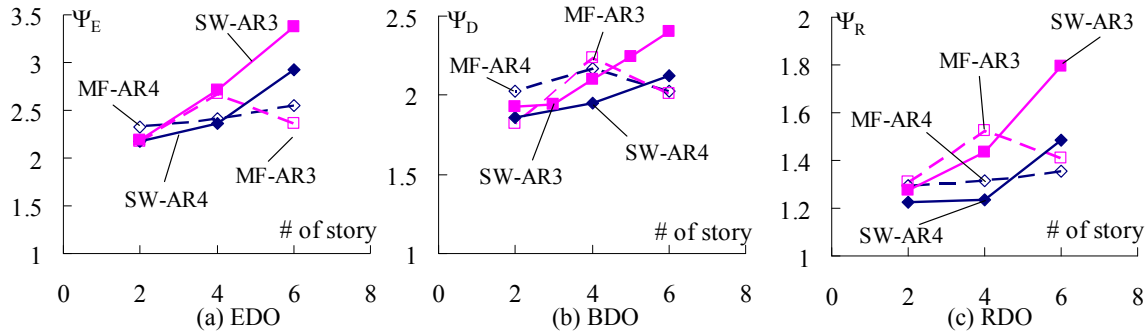
Fig. A1-16. Diaphragm force amplification factors for different LFRS types.

Figure A1-17 compares the diaphragm design force amplification factors for SDC E and SDC C. The comparison is made using shear wall structures with AR=4 and AR=2 for EDO and BDO diaphragm designs. As seen, trial diaphragm force amplification factors implied by the analytical results are typically lower for SDC C designs when compared to the analogous SDC E design case. The differences become more significant in shorter structures. This difference can be attributed to two reasons: (1) one is that the code prescribed R factor for the SDC C structure (R=5) and the SDC E structure (R=6) are different (see Table A1-1); (2) the other is the relationship between the design structural period, calculated as maximum allowable design period according to Section 12.8.2 in ASCE-7 (2005), and the (estimated actual) fundamental period provided by the analytical model. Figure A1-17c shows the design response spectrum with the design structural periods and estimated actual fundamental periods for the AR=4structure. As seen in Fig. A1-17c, for a shorter structure (N=2), the difference in the design spectrum acceleration corresponding to the design and estimated actual structural periods is much larger for the SDC C structure than for the SDC E structure. For taller structures (e.g., N=6), this difference is less pronounced between the SDC C and SDC E structures.

Given the similarity of the response for the high-rise structures, and the conservatism built into the expression for shorter structures, the Ψ factor design equations (See Section A1-5.1) proposed in the design procedure do not directly include a parameter considering different SDC. As with LFRS, the proposed design equations include all data points in Fig. A1-17, including those from SDC C and SDC E.
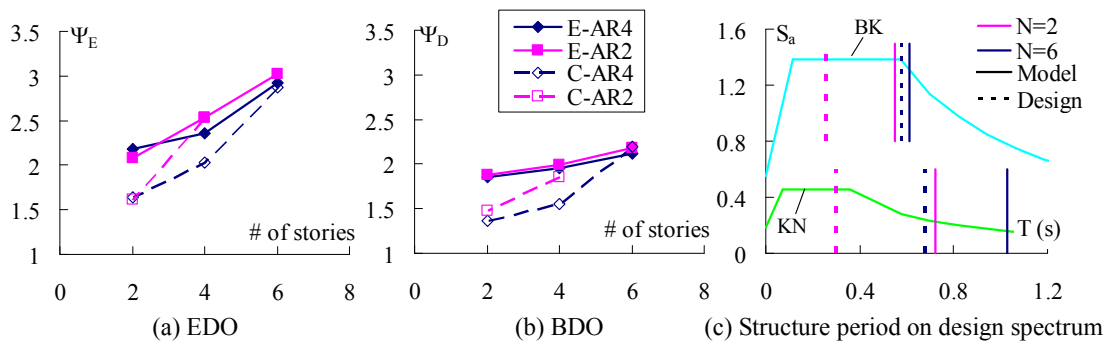
Fig. A1-17. Diaphragm force amplification factors for different SDC.

A1.4.3 Diaphragm Shear Overstrength Factor

Figure A1-18 shows the diaphragm shear overstrength factor (Ω_V) parametric plots. As mentioned previously, the diaphragm overstrength factor is measured relative to the amplified diaphragm force (i.e. Ω is stacked onto Ψ). Using this approach, the Ω_v factors for BDO and RDO design options are plotted with diaphragm aspect ratio in Fig A1-18. These factors were calculated using the expression provided in Section A1.4.2. According to the elastic design target for EDO, no diaphragm overstrength factor is required ($\Omega_{vE} = 1.0$).

It is noticed in Fig. A1-18 that (a) the BDO design requires less shear overstrength than the RDO design because it incurs less inelastic flexural demand and strain hardening than the RDO; (2) The required diaphragm shear overstrength typically increases with the decease of diaphragm AR; (3) The required diaphragm shear overstrength is similar in shear wall and frame structures.
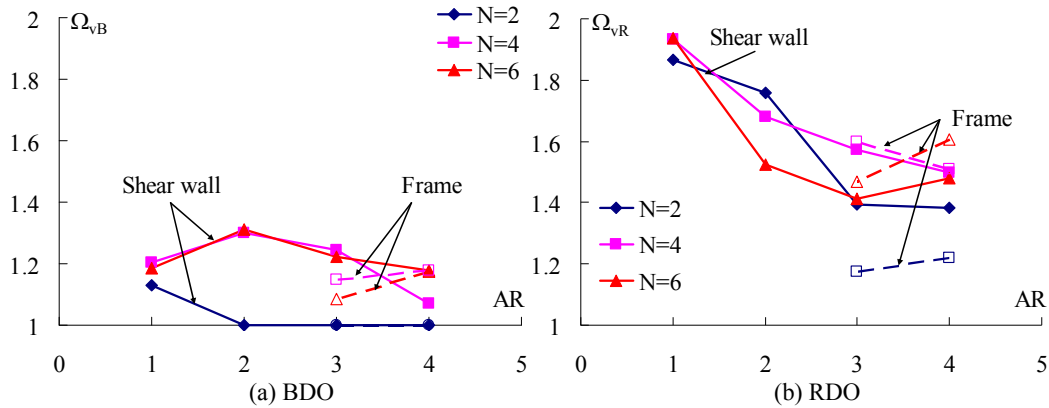
Fig. A1-18. Diaphragm shear overstrength factors

A1.5 DESIGN EQUATIONS

Based on the parametric results shown in section A1.4, a set of design equations are developed for the diaphragm design factors.

A1.5.1 Design Equations for Diaphragm Force Amplification Factor (Ψ)

The diaphragm force amplification factor is influenced by the following design parameters: structure geometry (diaphragm length, diaphragm AR and number of story), LFRS types and SDC as discussed in section A1.4.1. Among these parameters, structure geometry has the most significant effect on the diaphragm force amplification factor. Therefore the diaphragm design factor equations are set as the function of diaphragm aspect ratio (AR), number of story (n) and diaphragm span (L). These equations are developed using curve-fits for the results data presented in section A 1.5.1 with a confidence interval of 90% (i.e. 90% of data point is below the design equations). The curve-fits are combinations of power equation for n, polynomial equation for AR and exponential equation for L, which are shown as solid line in Fig. A1-19.
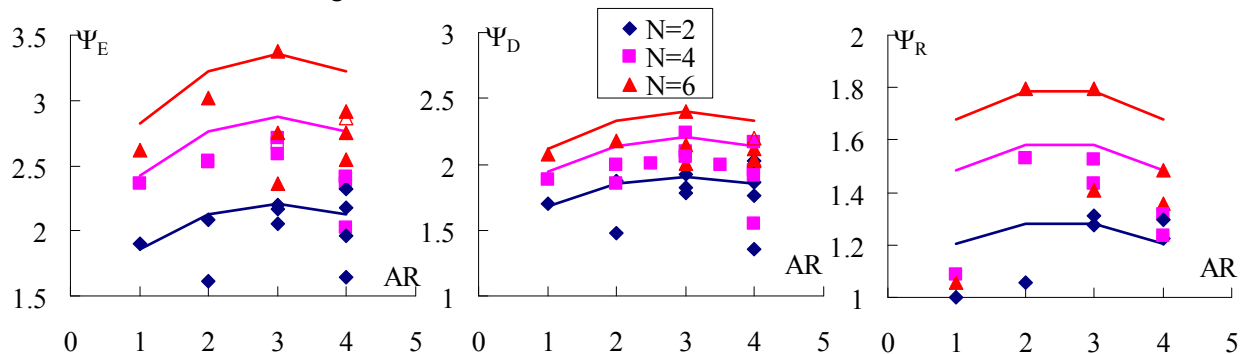
Fig. A1-19. Diaphragm force amplification factor equations: (a) EDO; (b) BDO; (c) RDO.

The design equations shown in Fig. A1-19 are expressed as below:

EDO: $1.0 \leq \Psi_E = 1.7n^{0.38}[1 - 0.04(3 - AR)^2]1.05^{(L/60-AR)} \leq 3.9$ Eqn. A1-1a

BDO: $1.0 \leq \Psi_D = 1.65n^{0.21}[1 - 0.03(3 - AR)^2]1.05^{(L/60-AR)} \leq 2.9$ Eqn. A1-1b

RDO: $1.0 \leq \Psi_R = 1.05n^{0.3}[1 - 0.03(2.5 - AR)^2]1.05^{(L/60-AR)} \leq 2.2$ Eqn. A1-1c

In each case, AR is limited between 0.25 to 4 and (L /60-AR) is limited between -2 to +2.

Alternatively, simpler expressions can be used. These include linear (blue solid line in Fig. A1-20) or power curve fits (black solid line in Fig. A1-20). These expressions are functions of the number of stories only. These simpler and more conservative values can be used in lieu of the expressions given earlier in equations A1-1a-c.
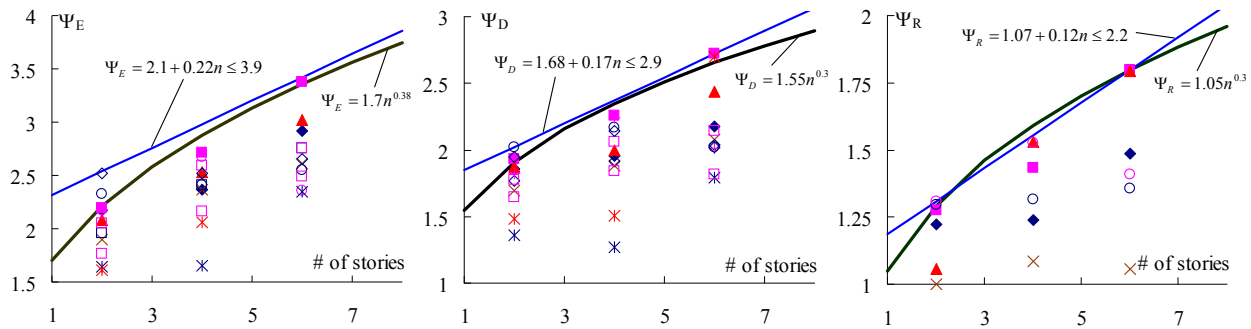
Fig. A1-20. Simplified diaphragm force amplification factor equations: (a) EDO; (b) BDO; (c) RDO.

A1.5.2 Diaphragm Shear Overstrength Factor (Ω_v)

The diaphragm shear overstrength equations are created as a function of diaphragm aspect ratio (AR). The analytical results of Figure A1-18 are shown as markers in Fig. A1-21, plotted with respect to aspect ratio (AR). The Ω_v design equations are indicated as black line in Fig. A1-21: Ω_{vE} for the EDO in Fig. A1-21a; Ω_{vR} for the RDO in Fig. A1-21b. The design equations are power curve-fits with a confidence interval of 90% (i.e. 90% of data points are below the design equation), as follows:

EDO: $\Omega_{vE} = 1.0$ Eqn. A1-2a

BDO: $\Omega_{vB} = 1.42 AR^{-0.13} \leq 1.7$, where the AR is limited between 0.25 to 4   Eqn. A1-2b

RDO: $\Omega_{vR} = 1.92 AR^{-0.18} \leq 2.46$, where the AR is limited between 0.25 to 4   Eqn. A1-2c
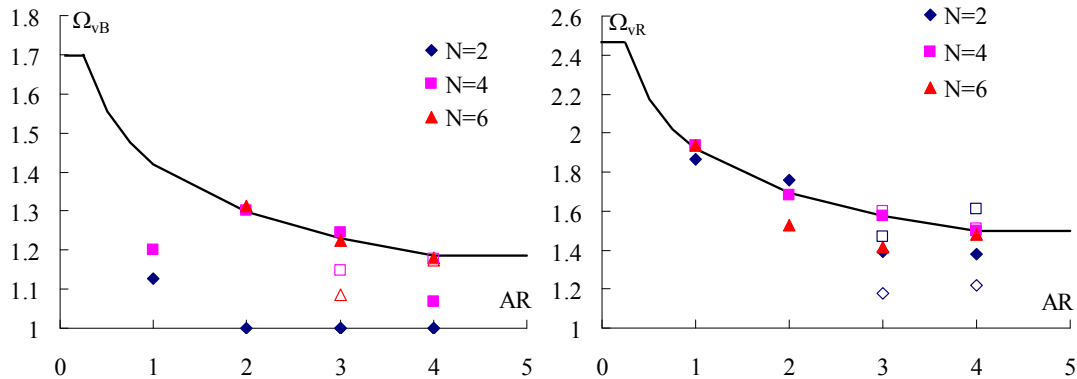
Fig. A1-21. Diaphragm shear overstrength factor: (a) BDO; (b) RDO.

A1.5.3 Diaphragm Design Force Vertical Distribution (α factor)

In past research (Fleischman and Farrow 2001), a constant diaphragm force pattern was proposed for along the height of the building. However, the diaphragm vertical force profiles has become more clarified as analytical models for precast structures have advanced, including models developed in the DSDM research that include the effect of the gravity system columns (Ware et al. 2012). The more recent analyses indicate a tendency for the maximums to occur only at a single level of a given structure. For this reason, the diaphragm design force magnitudes can be provided a distribution along building height to create a more economical design.

Accordingly, a diaphragm design force vertical distribution factor (α_x) is introduced into the design methodology. The α_x factors are developed based on the mean of maximum analytical results from the suite of ground motions in the parametric study. Figure A1-22 shows these results and the proposed α_x distributions, shown as a red dashed line. Also shown is the constant distribution (black dotted line) which can be used as a simpler but more conservative alternative. Note that neither of the vertical force distributions proposed match the inverted pattern F_{px} provided in current seismic code provisions.
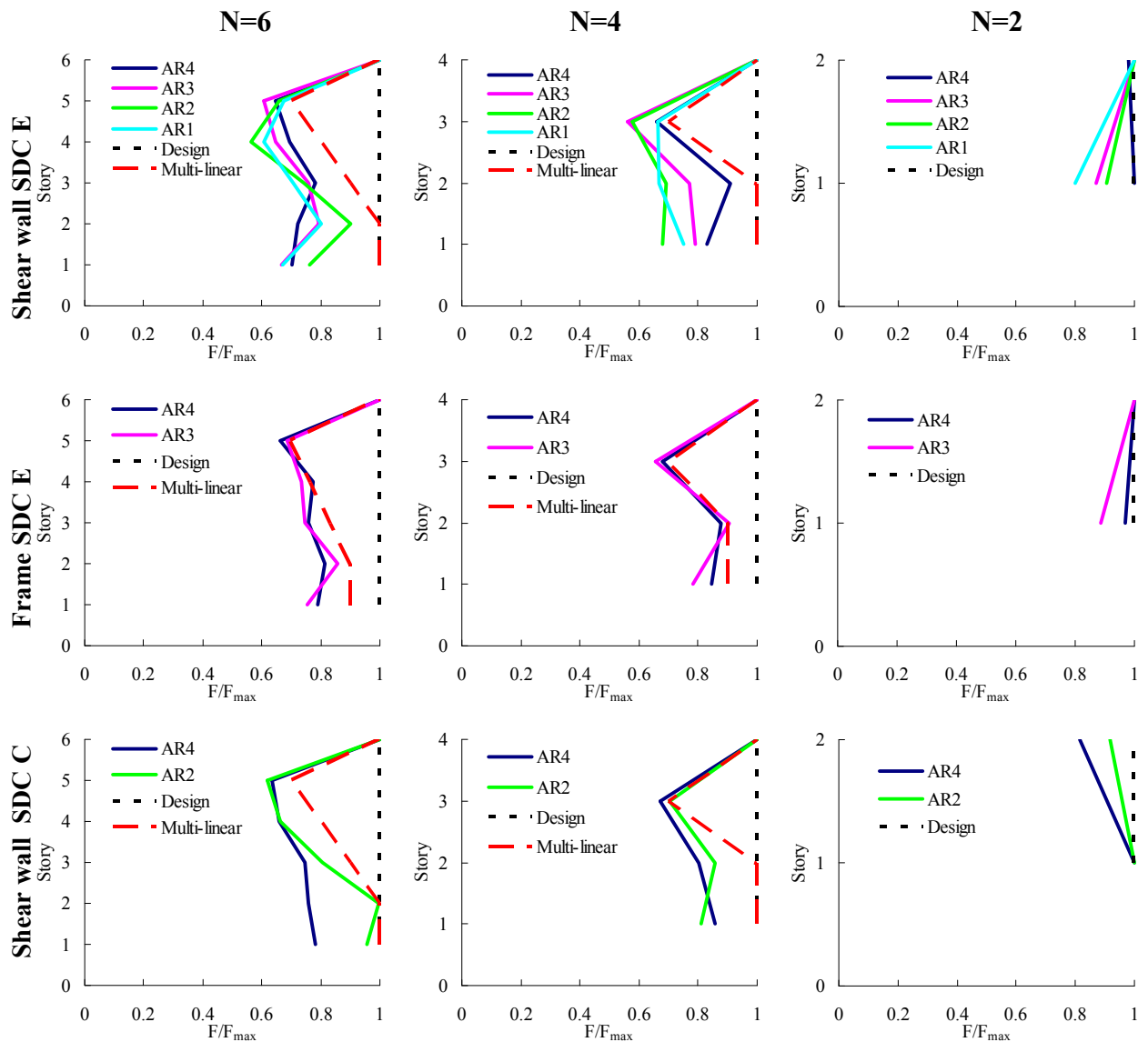
Fig. A1-22. Max diaphragm force distribution.

The diaphragm design force vertical distribution factor (α_x) can be determined using the following equations, described below for shear wall and moment frame structures, and calculated for different number of stories in Table A1-7a and A1-7b. Note that the α_x factor is different for parking structures (See Fig. C-2 in PART 5).

$n \leq 3$: $\qquad \alpha_x = 1.0$ for all floors

$3 < n \leq 6$:

    For shear wall structure:

$\qquad \alpha_x = 1.0$ for top and 1st floor

$\qquad \alpha_x = 0.7 + 0.3(n-1-x)/(n-3)$ for other floors (i.e. x=n-1, n-2, …. 2)

    For moment frame structure:

$\qquad \alpha_x = 1.0$ for top floor

$\qquad \alpha_x = 0.9$ for 1st floor

$\qquad \alpha_x = 0.7 + 0.2(n-1-x)/(n-3)$ for other floors (i.e. x=n-1, n-2, …. 2)

$6 < n$:

    For shear wall structure:

$\qquad \alpha_x = 1.0$ for top and 1st floor

$\qquad \alpha_x = 1 - 0.3(n-x)$ for two lower floors next to the top floor (i.e. x=n-1 and n-2)

$\qquad \alpha_x = 0.4 + 0.6(n-2-x)/(n-4)$ for other floors (i.e. x=n-3, n-4, …. 2)

    For moment frame structure:

$\qquad \alpha_x = 1.0$ for top floor

$\qquad \alpha_x = 0.9$ for 1st floor

$\qquad \alpha_x = 1 - 0.35(n-x)$ for two lower floors below the top floor (i.e. x=n-1 and n-2)

$\qquad \alpha_x = 0.3 + 0.6(n-2-x)/(n-4)$ for other floors (i.e. x=n-3, n-4, …. 2)

where is n the total number of story, x is the story number and α_x is the design force distribution factor.

Table A1-7a. Diaphragm design force vertical distribution factor (α_x) for shear wall structure

Story Number	Total Number of Story									
	1	2	3	4	5	6	7	8	9	10
1	1.00	1.00	1.00	1.00	1.00	1.00	1.00	1.00	1.00	1.00
2		1.00	1.00	1.00	1.00	1.00	1.00	1.00	1.00	1.00
3			1.00	0.70	0.85	0.90	0.80	0.85	0.88	0.90
4				1.00	0.70	0.80	0.60	0.70	0.76	0.80
5					1.00	0.70	0.40	0.55	0.64	0.70
6						1.00	0.70	0.40	0.52	0.60
7							1.00	0.70	0.40	0.50
8								1.00	0.70	0.40
9									1.00	0.70
10										1.00

C-A-26

Table A1-7b. Diaphragm design force vertical distribution factor (α_x) for moment frame structure

Story Number	Total Number of Story									
	1	2	3	4	5	6	7	8	9	10
1	1.00	1.00	1.00	0.90	0.90	0.90	0.90	0.90	0.90	0.90
2		1.00	1.00	0.90	0.90	0.90	0.90	0.90	0.90	0.90
3			1.00	0.70	0.80	0.83	0.70	0.75	0.78	0.80
4				1.00	0.70	0.77	0.50	0.60	0.66	0.70
5					1.00	0.70	0.30	0.45	0.54	0.60
6						1.00	0.65	0.30	0.42	0.50
7							1.00	0.65	0.30	0.40
8								1.00	0.65	0.30
9									1.00	0.65
10										1.00

A1.5.4 Diaphragm Reinforcement Classification.

In the proposed procedure, diaphragm reinforcement classification is divided into low deformability (LDE), moderate deformability (MDE) and high deformability (HDE) elements according to the reliable deformation capacity exhibited in full-scale isolated connector tests following a qualification protocol (found in PART 2 of the Design Methodology). The required deformation capacity in the tests for each diaphragm reinforcement classification, namely greater than 0.6″ for HDE; between 0.3″ and 0.6″ for MDE; and less than 0.3″ for LDE, were selected by considering: (1) the range of the tension deformation capacities exhibited by the various precast diaphragm connectors in cyclic tests in the experimental program (Naito et al. 2006) (Naito et al. 2007); and (2) with an approximate understanding of the ranges of maximum joint opening required in the seismic response of precast floor diaphragms relative to the design parameters and the design force levels.

As the analyses in this study were performed, the relationship between diaphragm design parameters, design force and the required maximum joint opening were quantified. On the basis of these analyses, it was confirmed that allowable deformations of 0.2″ for MDE and 0.4″ for HDE provide feasible ranges of deformation capacity to be used with the diaphragm force amplification factors. Note that this diaphragm reinforcement allowable deformation implicitly creates a design factor of safety of 2/3 against connection deformation capacity.

The recommended reinforcement classification for the BDO is MDE. However, as the calibration of Ψ_D for the BDO is based on a design target of elastic diaphragm response in the DBE, no a priori assurance for the adequacy of MDE reinforcement is obtained in the selection of Ψ_D. Accordingly the inelastic demands (joint opening) in the MCE level analyses for the BDO diaphragm designs were evaluated with respect to the MDE reinforcement allowable deformation (See Fig. A1-23a). The results of these analyses led to the recognition that BDO diaphragm designs are maintained within the MDE allowable deformation limit of 0.2″ except for design cases involving the combination of long span diaphragms and taller structures. This observation led to the establishment of Diaphragm Seismic Demand Levels, based on diaphragm geometry, building height and SDC (See Step 1 in PART 1). The boundary between moderate and high Diaphragm Seismic Demand Levels was selected as the design geometries that produce demands on either side of the allowable MDE deformation. Subsequent additional analyses at incremental diaphragm strength increases indicated that increasing the diaphragm design force by 15% for the high seismic demand cases adequately lower the maximum MCE opening demands to less than the allowable deformation limit of 0.2″ (See open markers in Figure A1-23a).
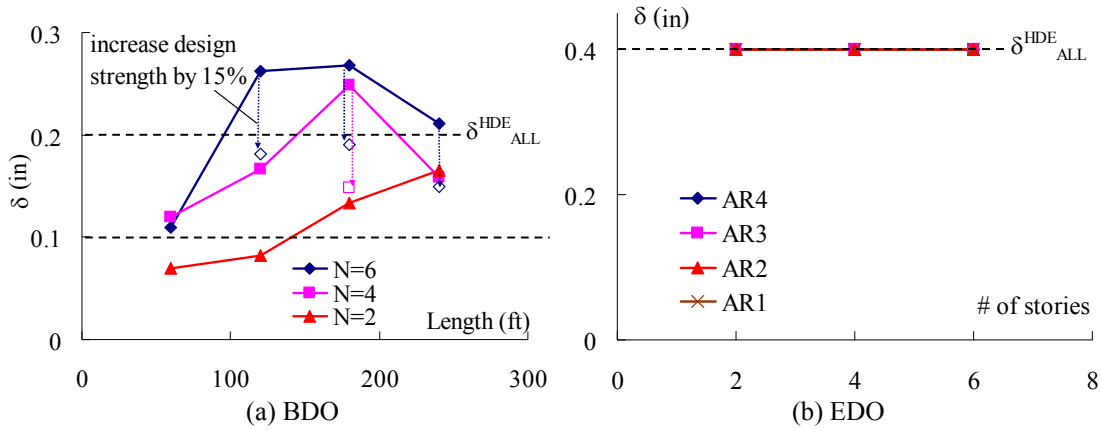
Fig. A1-23. Diaphragm maximum chord opening under MCE.

The RDO design target is the HDE allowable deformation in the MCE, i.e. a maximum chord opening of 0.4″. Since this target is enforced in the analytical program (See Sec. A1.4.2), this target is met for all design parameter combinations since the diaphragm force amplification factors for RDO targets at 0.4″ maximum chord opening (See Fig. A1-23b).

For connectors which meet the required maximum deformation capacity, the required cumulative inelastic deformation capacity is also met. This is evidenced in Fig. A1-24, which shows the diaphragm *cumulative* joint opening demand under MCE analysis corresponding to the design factors that produced the *maximum* allowable joint opening demand shown in Fig. A1-23. As seen, the cumulative demands are significantly lower than the cumulative deformation capacity achieved in the cyclic tension tests indicated by the horizontal trend line (Naito et al. 2006) for both the BDO and RDO.
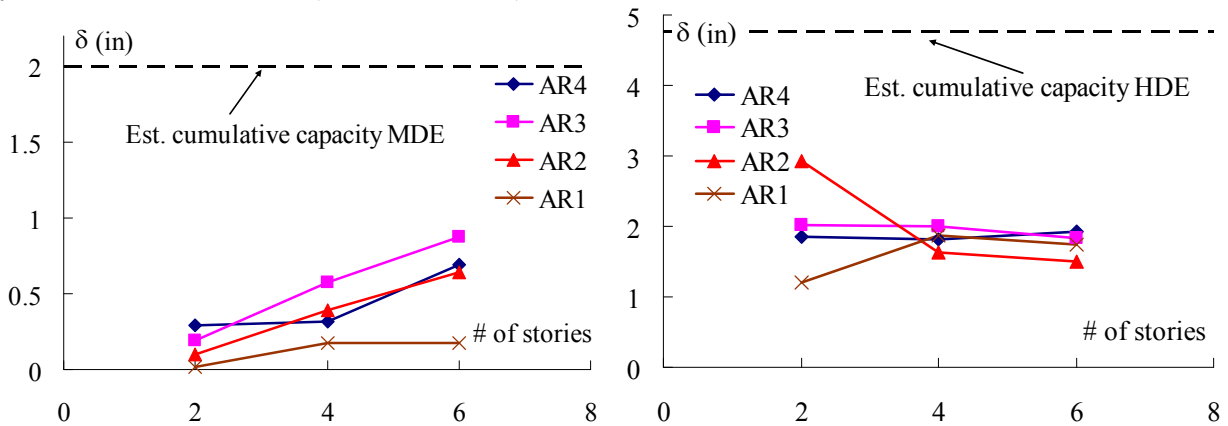
Figure A1-24**.** Diaphragm cumulative joint opening demand, MCE analysis: (a) BDO design; (b) RDO design.

A1.5.5 Design Factors for Diaphragm Induced Gravity Column Inter-story Drift Calculation.

Figure A1-25a shows the plan of the structure at level i, and defines LFRS $\Delta_{LFRS, i}$ and diaphragm displacement $\Delta_{dia, i}$, as well as diaphragm deformation $\delta_{dia, i}$. Figure A1-25b shows an elevation of the structure showing the LFRS inter-story drift $\theta_{LFRS, i}$ at level i, as well as the inter-story drift of a gravity system column attached to the diaphragm at level i, $\theta_{col, i}$. The diaphragm induced gravity column inter-story drift is expressed as the difference between the gravity column inter-story drift and LFRS inter-story drift ($\theta_{dia, i} = \theta_{col, i} - \theta_{LFRS, i}$ at each level i).

(a) Plan   (b) Elevation
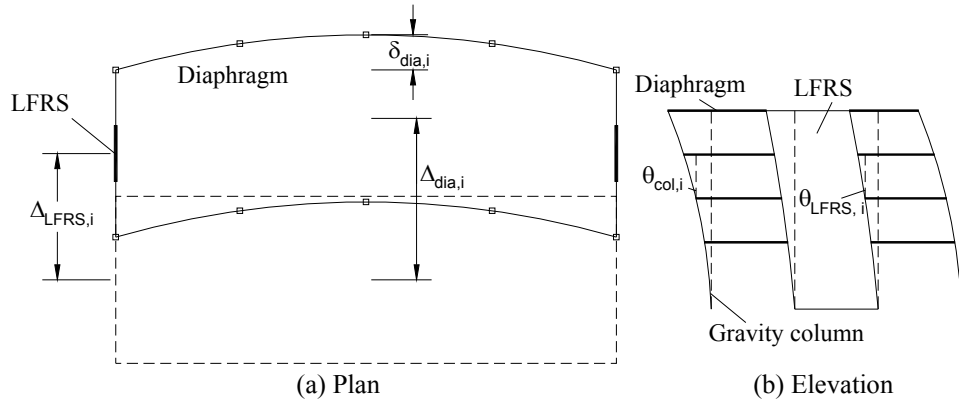
Fig. A1-25. Diaphragm induced gravity column inter-story drift.

The maximum diaphragm induced gravity column drift ($\theta_{dia,\,Max}$) under MCE of SDC E shear wall structure is shown in Fig. A1-26a, b, and c for EDO, BDO and RDO design respectively. It can be noticed that the diaphragm induced gravity column drift increases (a) with the diaphragm length, (b) with number of story and (c) from EDO to RDO as diaphragm yields more.
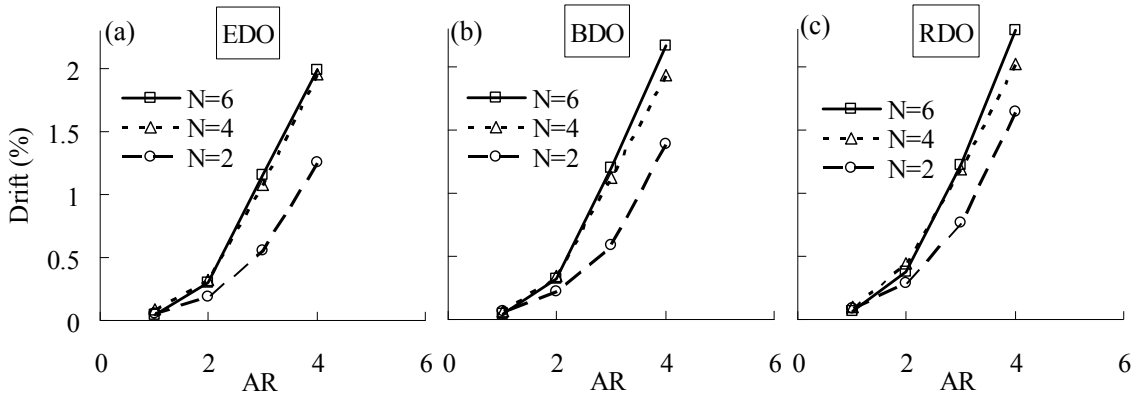
Fig. A1-26. Max diaphragm induced gravity column drift demand under MCE

Diaphragm induced gravity column inter-story drift discussed is to be calculated for diaphragm design purpose based on the elastic diaphragm deformation using two subsequent procedures with two design factors: (1) diaphragm inelastic deformation amplification factor $C_{d,dia}$ and (2) diaphragm drift reduction factor $C_{r,dia}$.

The first procedure is to transform the elastic diaphragm deformation into inelastic deformation. The following equation is used to transform the elastic diaphragm deformation into inelastic deformation:

$$\delta_{dia} = C_{d,dia}\, \delta_{dia,\,el}$$

where diaphragm inelastic deformation amplification factor $C_{d,dia}$ has two parts. One is the ratio between the maximum diaphragm MCE deformation demand divided by the elastic diaphragm deformation (See Fig.A1-27). Figure A1-28 shows the parametric data for the 1st part of $C_{d,dia}$ factor using the analytical results from this parametric study.
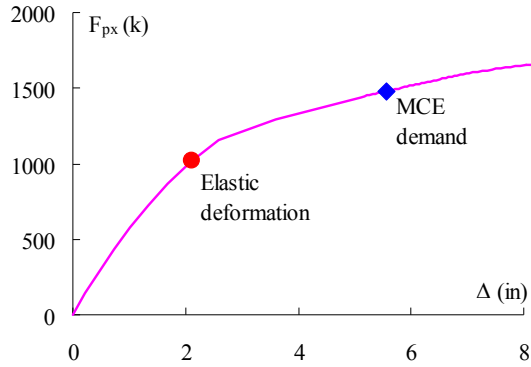
Fig. A1-27. Diaphragm deformation demands on push-over curve.

The $C_{d,dia}$ also involves another part, a C_{Δ} factor, which is a P-Δ multiplier for the gravity columns due to diaphragm-amplified drift, $C_{\Delta} = 1 + C_1 (L/240)(AR/4)$ where C_1 is 0.06 for EDO, 0.08 for BDO and 0.1 for RDO. Raw data for the C_{Δ} multiplier is shown in Fig. A1-29.

Based on Figure A1-28 and A1-29, $C_{d,dia}$ factor is proposed for the EDO, BDO and RDO design as: EDO: $C_{d,dia} = 1.0 C_{\Delta}$; BDO: $C_{d,dia} = 1.5 C_{\Delta}$; RDO: $C_{d,dia} = 2.9 C_{\Delta}$.
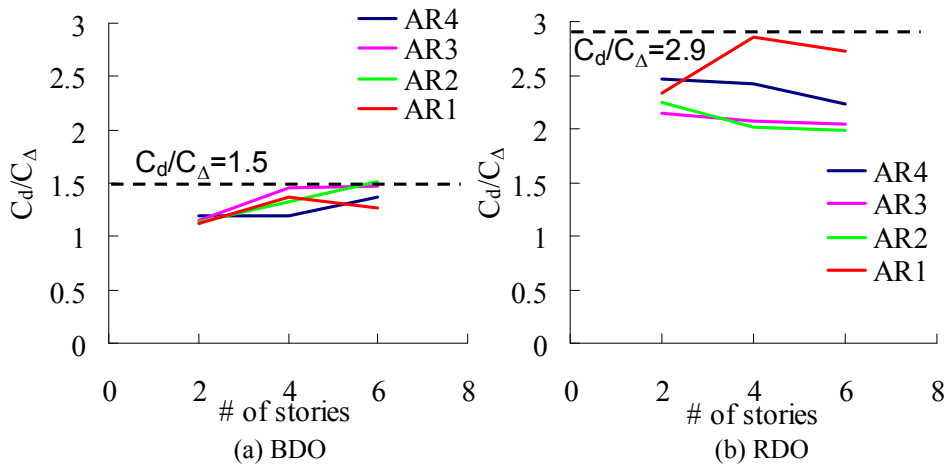
Fig. A1-28. Diaphragm inelastic deformation amplification factor.

Figure A1-29. P-Δ multiplier for the gravity columns: (a) EDO; (b) BDO; and (c) RDO.

C-A-30
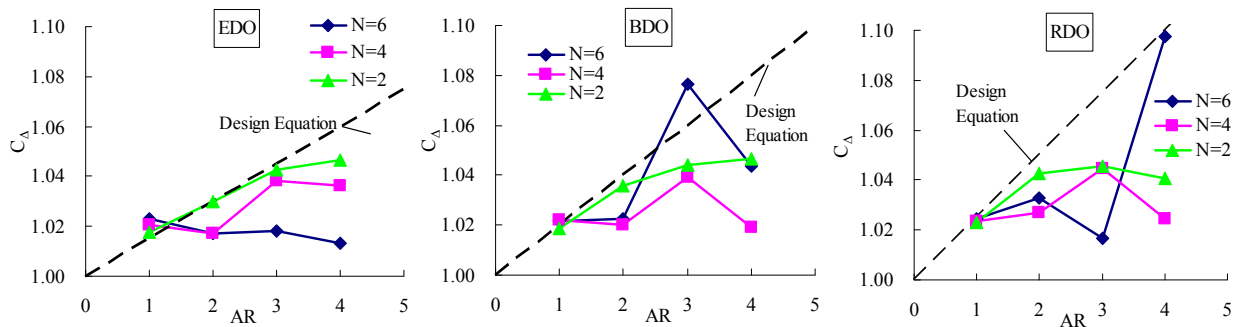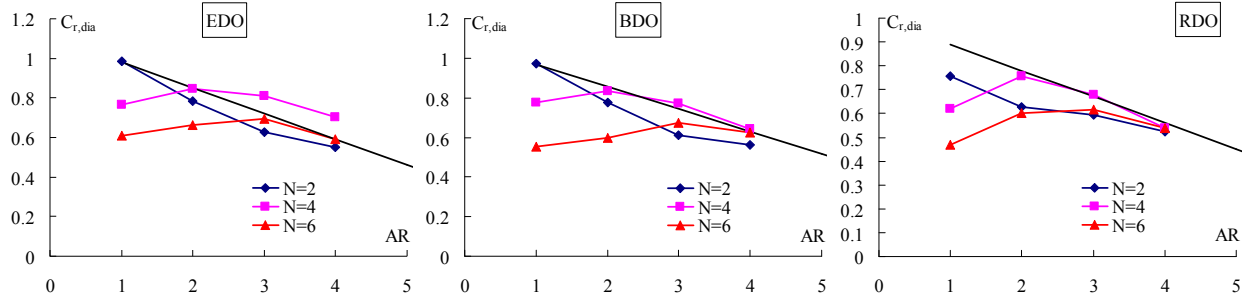
Fig. A1-30. Diaphragm drift reduction factor.

The second procedure is to related the diaphragm deformation to diaphragm induced gravity column induced drift. The following equation is used to relating the diaphragm deformation to diaphragm induced drift:

$$\theta_{dia} = \delta_{dia} C_{r,dia} / h$$

where $C_{r,dia}$ is the diaphragm drift reduction factor which is established based on the maximum diaphragm deformation ($\delta_{dia, max}$) and maximum diaphragm induced drift [$\theta_{dia,max} = (\delta_{dia, i} - \delta_{dia, i-1})/h$] (See Fig. A1-25) under MCE earthquake with following equation:

$$C_{r,dia} = \theta_{dia,max} \, h / \delta_{dia,max}$$

Figure A1-30 shows the parametric data for $C_{r,dia}$ factor using the analytical results from this study. The linear cure-fit equation is shown as black solid line in the Fig. A1-30 as well.

Based on the linear curve-fit in Fig. A1-30, design equation for diaphragm drift reduction factor is proposed as:

$$\text{For EDO: } 0.4 \le C_{r,dia} = 1.11 - 0.13AR \le 1.0$$

$$\text{For BDO: } 0.4 \le C_{r,dia} = 1.08 - 0.11AR \le 1.0$$

$$\text{For RDO: } 0.4 \le C_{r,dia} = 1.00 - 0.11AR \le 1.0$$

A1.6 CONCLUSIONS

The parametric study of calibrating trial design factors for the emerging diaphragm seismic design methodology through NLTDA is presented in this chapter. A range of key diaphragm design parameters were examined. The following design quantities are identified in the parametric study.

(1) Trial diaphragm force amplification factors are proposed with equations.
  – The values for the EDO (Ψ_e) are determined using Eq. 1a.
  – The values for the BDO (Ψ_d) are determined using Eq. 1b.
  – The values for the RDO (Ψ_r) are determined using Eq. 1c.
(2) Trial diaphragm reinforcement overstrength factors are proposed.
  – The values for shear/anchorage reinforcement are determined using Eq. 2.
(3) The ranges of deformation capacity associated with different Diaphragm Reinforcement Classifications (DRCs) are proposed:
  – The values for MDE are shown in Figure A1-23a.
  – The values for HDE are shown in Figure A1-23b.
The above listed factors reflect the following findings based on the parametric results:

(1) The required diaphragm design force will increase with the increase of number of structure story. Diaphragm force amplification factors typically increase with AR to a point after which the effects of diaphragm flexibility actually lower required diaphragm forces.

(2) The frame structure typically requires less diaphragm amplification factors compared to shear wall structure. The structure design in SDC C typically requires less diaphragm amplification factors than that design in SDC E.

(3) Diaphragm shear/anchorage overstrength factor typically increase with the decrease of diaphragm AR. The frame structure requires higher diaphragm shear/anchorage overstrength than the shear wall structure.

The following conclusions on diaphragm behavior are made based on the parametric study using the 3D NLTDA model:
(1) A constant distribution of diaphragm design force along building height is reasonable. Peak diaphragm inelastic demand typically occurs in top floor and the 2nd floor usually has large inelastic demand in multi-story building.
(2) The inelastic diaphragm joint opening demand typically concentrates at the joint where the spandrel beam discontinues. The concentration is higher in lower aspect ratio diaphragms and is higher for diaphragms designed for low seismic hazard.

A1.7 REFERENCES

ACI 318-05. Building Code Requirements for Structural Concrete (ACI 318-05) and Commentary (ACI 318-05), *ACI committee 318* 2005.

ASCE 7-05. Minimum Design Loads for Buildings and Other Structures. *ASCE* 2005.

Building Seismic Safety Council, Committee TS-4. Seismic design methodology for precast concrete floor diaphragms. Part III, *NEHRP Recommended Seismic Provisions* 2009 Federal Emergency Management Agency, Washington, D.C.

Cao L., Naito C. Precast double-tee floor connectors part II: shear performance. *PCI Journal* 2009; 54(2): 97-115.

Fleischman R. B., Farrow K. T. Dynamic Response of Perimeter Lateral-System Structures with Flexible Diaphragms. *Earthquake Engineering & Structural Dynamics* 2001; 30(5): 745-763.

Fleischman R. B., Naito C.J., Restrepo J., Sause R., Ghosh S.K. Seismic Design Methodology for Precast Concrete Diaphragms, Part 2: Research Program. *PCI journal* 2005; 51(6): 2-19.

Fleischman R.B., Wan G. Appropriate overstrength of shear reinforcement in precast concrete diaphragms. *ASCE Journal of Structure Engineering* 2007; 133(11): 1616-1626.

Fleischman R.B., Zhang D., Ren R, and Naito C. Experimental evaluation of precast diaphragm critical shear joint under seismic demands. Under preparation 2012.

Naito C.J., Cao L., Peter W. Precast Double-Tee Floor Connectors Part I: Tension Performance. *PCI Journal* 2009; 54(1): 49-66.

Oliva M.G. Testing of the JVI flange connector for precast concrete double-Tee system. *Structures and Materials Test Laboratory Report* 2000, College of Engineering, University of Wisconsim, Madison, WI.

Precast/Prestressed Concrete Institution. PCI design handbook: precast and prestressed concrete. Sixth Edition 2004, Chicago IL.

Zhang D., Fleischman R.B., Wan G. and Naito C.J. Development of Hysteretic Models for Precast Concrete Diaphragm Connectors for Use in Three-Dimensional Nonlinear Dynamic Analysis. Under

preparation, 2012.

Pincheira J. A., Oliva M. G., Kusumo-rahardjo F. I. Tests on double tee flange connectors subjected to monotonic and cyclic loading. *PCI Journal* 1998; 43 (3): 82-96.

Panagiotou M., Restrepo J., Conte J.P., Englekirk R.E. Shake Table Response of a Full Scale Reinforced Concrete Wall Building Slice. *Structural Engineering Association of California Convention* 2006: 285-300.

Shaikh A.F., Feile E.P. Load Testing of a Precast Concrete Double-Tee Flange Connector. *PCI Journal* 2004; 49(3): 84-95.

Ren R. and Naito C.J. Precast Concrete Diaphragm Connector Performance Database and Response Estimation Modeling Approach. *ASCE Journal of Structure Engineering.* Submitted 2011

Schoettler M.J., Belleri A., Zhang D., Restrepo J., Fleischman R.B. Preliminary Results of the Shake-table Testing for Development of A Diaphragm Seismic Design Mythology. *PCI Journal* 2009; 54 (1): 100-124.

Wan G. and Fleischman R.B. A Rational Method for Calculating the Service Stiffness and Yield Strength of Precast Floor Diaphragms. In preparation for submission to the *PCI Journal* 2012.

Wan, G., Fleischman, R.B. and Zhang, D. Effect of spandrel beam to double tee connection characteristic of flexure-controlled precast diaphragms, J. of Structural Eng. ASCE 2012b. Scheduled published in Feb. 2012.

Wan G., Fleischman R.B., Zhang D., Naito C.J. Development of Connector Models for Nonlinear Pushover Analysis of Precast Concrete Diaphragms. Under preparation, 2012a.

Ware A., Fleischman R.B., Zhang, D. Effect of Gravity System Columns on the Seismic Response of Precast Concrete Diaphragms. Under preparation, 2012.

Zhang, D. Examination of Precast Concrete Diaphragm Seismic Response by Three-Dimensional Nonlinear Dynamic Transient Analyses. Ph.D. Dissertation. University of Arizona, Tucson, AZ 2010.

Zhang D. and Fleischman R.B., Calibration of Diaphragm Design Factors on Realistic Precast Structures. Under preparation, 2012.

Zhang, D., Fleischman, R.B., Naito, C., and Ren, R. Experimental evaluation of pretopped precast diaphragm critical flexure joint under seismic demands. J. Struct. Eng. ASCE 2011, V137(10).

Appendix A.2   Design Procedure Evaluation: Prototype Structures

In the second analytical stage of the *Design Procedure Development Phase*, the design procedure, including the trial design factors determined in the first stage (See Appendix A.1), is evaluated using realistic structure configurations. The realistic structures are selected from a portfolio of prototype structures developed for the project (Fleischman et al. 2005), and also serve as the precast structures used in the examples provide in PART 4 of the *Design Methodology*. The evaluation is performed through nonlinear transient dynamic analysis of 3D FE models of the prototype structures, using discrete diaphragm models enhanced from stage 1 (Appendix 1A) through further calibration to test data. In this appendix, the prototype structure analytical results are compared to the intended design outcomes in order to evaluate the efficacy of the design methodology.

TABLE OF CONTENTS

A2.0 ASSUMPTIONS AND LIMITATIONS OF PROTOTYPE STRUCTURE ANALYSES

The following overall assumptions and limitations are applied to the design procedure evaluation/trial design factor calibration studies:

1. The study was limited to a small number of analyses of realistic structure layouts as follows:
    a. Two primary structure types were evaluated:
        i. a 4-story central ramp parking garage with a 300′x180′ footprint;
        ii. an 8 story office building with a 230′x147′ footprint.
    b. Two LFRS layouts were evaluated for each structure:
        i. Parking garage: Perimeter and interior transverse shear wall layout was evaluated, both possessing litewalls along the ramp.
        ii. Office building: LFRS layout was limited to two cases: Perimeter shear wall and interior moment frame LFRS were evaluated (both directions).
    c. These structures were selected from a portfolio of prototype structures developed for the project by the DSDM Industry TG.
2. Floor Systems:
    Each structure type employed distinct floor system construction:
    a. <u>Parking garage</u>: pretopped double tee diaphragms using the JVI Vector connector for shear reinforcement, and various chord reinforcement depending on the diaphragm design option selected: dry chord connector for EDO; flat plate connector for BDO and continuous bars in a pour strip for the RDO.
    b. <u>Office building</u>: topped double tee diaphragms involving hairpin connections between the precast units acting compositely with a ductile ladder mesh in the topping slab for shear reinforcement, and continuous bars in the topping slab for chord reinforcement.
3. Two Seismic Design Categories (SDCs) were evaluated, selected from a set of geographically-based hazard sites established by the DSDM Industry TG at the outset of the project:
    a. SDC C (Charleston, SC)
    b. SDC D (Seattle, WA).
4. The prototype structures were designed using IBC 2009, which references ACI 318 (2005) and ASCE 7 (2005). The diaphragms in the structures were designed using the new seismic design methodology.
5. The evaluation was based on the response to three (3) spectrum compatible historic ground motions. Due to time considerations, certain structures were evaluated using only one of the 3 ground motions. The ground motion selected for these cases was the one with the highest spectral response at the structure fundamental period.
6. The analyses employed 2.5% Rayleigh damping aligned with the first (fundamental) and last significant transverse vibrational modes (cumulative mass participation ratio $\geq$ 99%). The structure periods are determined based on modal analysis for a 3D elastic structure model with monolithic diaphragm using effective moduli.
7. In accordance with ASCE-7 guidelines in Chapter 16 for assessments using 3 ground motions, the designs are evaluated using the maximum response values over the earthquake simulations.

The following are the assumptions and limitations applied in the modeling of the prototype structures:

1. The shear wall nonlinear response is assumed to occur entirely in a base plastic hinge of length corresponding to half the shear wall horizontal dimension.
2. The shear wall hysteretic model employs a stiffness degrading hysteresis characteristic of reinforced concrete walls.
3. The shear wall base plastic hinge nonlinear moment-curvature backbone is determined through a fiber analysis of the designed shear wall cross-section using nominal material properties, including axial load due to self weight.

4. The shear wall hinge flexural strength includes biaxial moment to include out-of-plane response. No foundation rotation in the out-of-plane direction of the shear wall is included.
5. The moment frame sway mechanism is based on a strong column-weak beam assumption. The beam plastic hinge nonlinear moment-curvature backbone is determined through a fiber analysis of the designed beam cross-section using nominal material properties.
6. The out-of-plane stiffness of vertical elements (shear walls, litewalls, moment frames) is included in the model, in order to capture restraining effects on the diaphragm deformation.
7. The floor system is modeled as a two-dimensional (in the horizontal plane) system except floor units on ramp which is modeled as elastic shell elements.
8. The precast floor units are modeled as elastic plane stress elements with appropriate mass but stiffness based only on the flange thickness.
9. Spandrels and internal beams are modeled as 2D elastic beam elements (in the floor plane).
10. Gravity columns are modeled as 3D elastic beam elements with pinned base at the foundation and pinned connections at each floor level.
11. Gravity loads are not included directly in the analyses except for moment frame structures in order to obtain the proper end moments ($M_g + M_E$) in the frame. Gravity load effects are included indirectly in shear wall structures in the moment-curvature response of the shear wall base hinge.
12. The effect of gravity load and vertical actions on the diaphragm connection response is ignored
13. The connections are assumed to be pristine prior to the seismic loading..
14. P-Δ effects are included for the analyses of the eight story office building, but are ignored in the analyses of the four story parking structure.

The following assumptions and limitations are involved in the modeling of the diaphragm connectors:
1. The modeling parameters (strength, stiffness and post-yield behavior) for all the reinforcement are calibrated based on the cyclic tests on the individual diaphragm connection between two precast floor units.
2. A hysteretic model developed from a pour strip chord cyclic test is used for all types of chord modeling including: dry chord, dry chord with flat plate and pour strip chord.
3. The hysteretic model for chord and shear reinforcement includes effects of pinching, cyclic stiffness degradation in tension, cyclic strength degradation in shear, and tension-shear coupling.
4. One-side connections, e.g. diaphragm to LFRS connections, diaphragm to internal beam connections, diaphragm to spandrel connections etc, are modeled with the same strength, doubled stiffness and half of deformation capacity as the two-side connections (e.g. connections between two precast floor units). These connections are given ultimately deformation capacity without strain hardening.
5. The hysteretic model for the one-side connection includes effects of pinching and tension-shear coupling without cyclic stiffness or strength degradation.
6. The spandrel to column connection is modeled to allow free separation between spandrel and column in the direction perpendicular to the precast floor unit joints. In the direction parallel to the precast floor unit joints, the connection of spandrel and column are modeled as ductile nonlinear springs representing the tension strength and stiffness of typical coil rod connection.

Some comment is required on the transition from the analysis of the evaluation structure for determining the trial design factors to the analyses of prototype structures used here in the evaluation of the design procedure:

First, the 3D-FE discrete diaphragm model had advanced between the analytical stages due to further calibration of the connector models based on the large scale diaphragm joint tests at Lehigh University (Zhang et al. 2011), and calibration of the overall model with the UCSD shake table tests (Ware et al. 2012).

Secondly, certain aspects of the analyses were different, most notably damping and the shear wall LFRS model. In the trial design factor studies, a damping value of 1% had been selected in an attempt to

provide conservative values. This value was upwardly adjusted to 2.5% in the verification studies, in an attempt to more accurately represent the amount of damping present. The establishment of trial design factors using low damping in the evaluation structure can be justified by the fact that these conservative values will somewhat offset the effects of force interactions in the more complex diaphragms of the prototype structures. Similarly, the original model, which had been developed and calibrated to the shake table specimen, a total precast structure with unbonded post-tensioned rocking walls, was adjusted to reinforcement concrete shear wall behavior to better match typical construction practices. The difference in response between these LFRS systems as it impacts diaphragm response is not overly significant.

Thirdly, the trial design factors were developed using a generic pretopped diaphragm with JVI Vector shear connectors. Such diaphragms have limited overstrength, i.e., a M_p/M_y ratio near unity. In the prototype structure analyses, the desire existed to evaluate precast floor diaphragms with different properties. As such, an office building prototype structure was included, whose typical construction involves a topped diaphragm. For these structures, a topped composite diaphragm with a thin topping and the ductile ladder mesh connector was used. This system possesses different stiffness and properties than the pretopped double tee, including most significantly a flexural strength contribution from the shear (web) reinforcement that produces an ultimate strength M_p that is approximately 50% greater than its yield strength M_y. This significant diaphragm overstrength has to be accounted in design, in particular with regard to preserving the intended capacity design. On the basis of the analyses, it was determined that diaphragm design factors calibrated on the basis of the pretopped diaphragm are still valid for topped diaphragms provided the relationship between yield and ultimate moment strength (M_p/M_y) is accounted when determining the nominal moment strength M_n. These nominal strength values have to be considered differently for the EDO, for instance, where the performance target should be aligned with first yield, than for the RDO, where the diaphragm performance target is aligned with ultimate strength. Accordingly, M_n design expressions that both recognize the different performance target and included the effect of different diaphragm overstrength (M_p/M_y) are provided in the commentary (Eqns. 34 in PART 3). These expressions were verified through the prototype structure analyses as described in Section A2.3.7)

Finally, it should be noted that while the prototype structures possessed realistic floor systems, none of the structures evaluated possessed redundant LFRS in which the flexibility of the diaphragm impacts the distribution to the LFRS elements. These structures could benefit from further evaluation.

A2. 1 DESCRIPTION OF STUDY

This analytical stage is used to evaluate the design procedure, including calibration of the trial design factors established in the earlier analytic stage. This objective is accomplished by comparing the seismic response of realistic structures designed using the design methodology to their intended seismic performance. Note that this procedure involves the evaluation of maximum considered earthquake (MCE) level hazard, since the success of each design option is determined through performance requirements at the MCE level (elastic diaphragm response in the EDO, within MDE allowable deformation in the BDO; within HDE allowable deformation in the RDO). This section provides the details of the study.

A2.1.1 Evaluation Structure
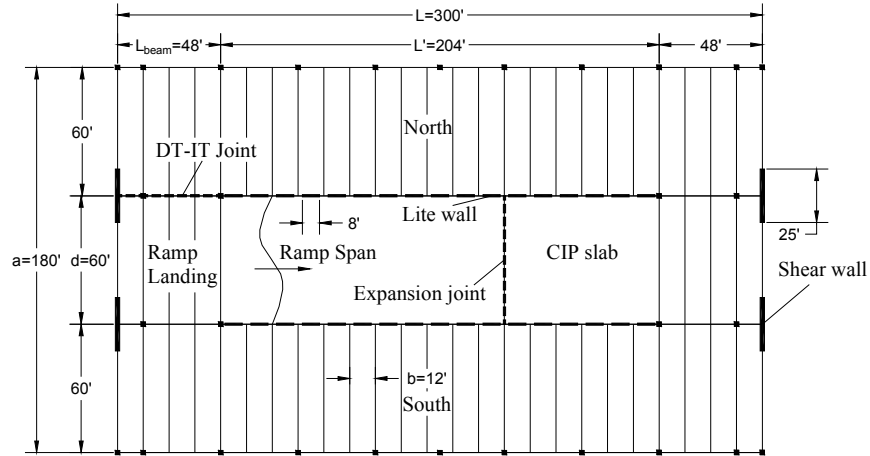
(a) 4-story exterior wall parking garage at 1st floor, SDC C (Example 1 in PART4)
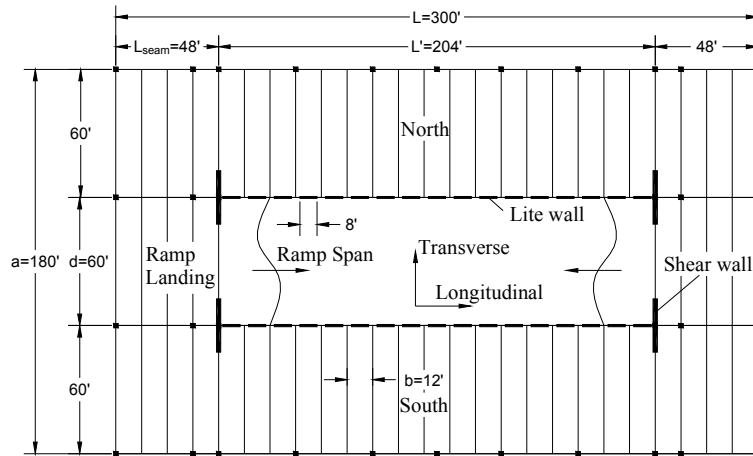
(b) 4-story interior wall parking garage, SDC C and D (Example 2 in PART4)

(c) 8-story moment frame office, SDC C (Ex. 3A) (d) 8-story moment frame office, SDC D (Ex. 3B)

(e) 8-story perimeter wall office, SDC C (Ex. 4A) (f) 8-story perimeter wall office, SDC D (Ex. 4B)
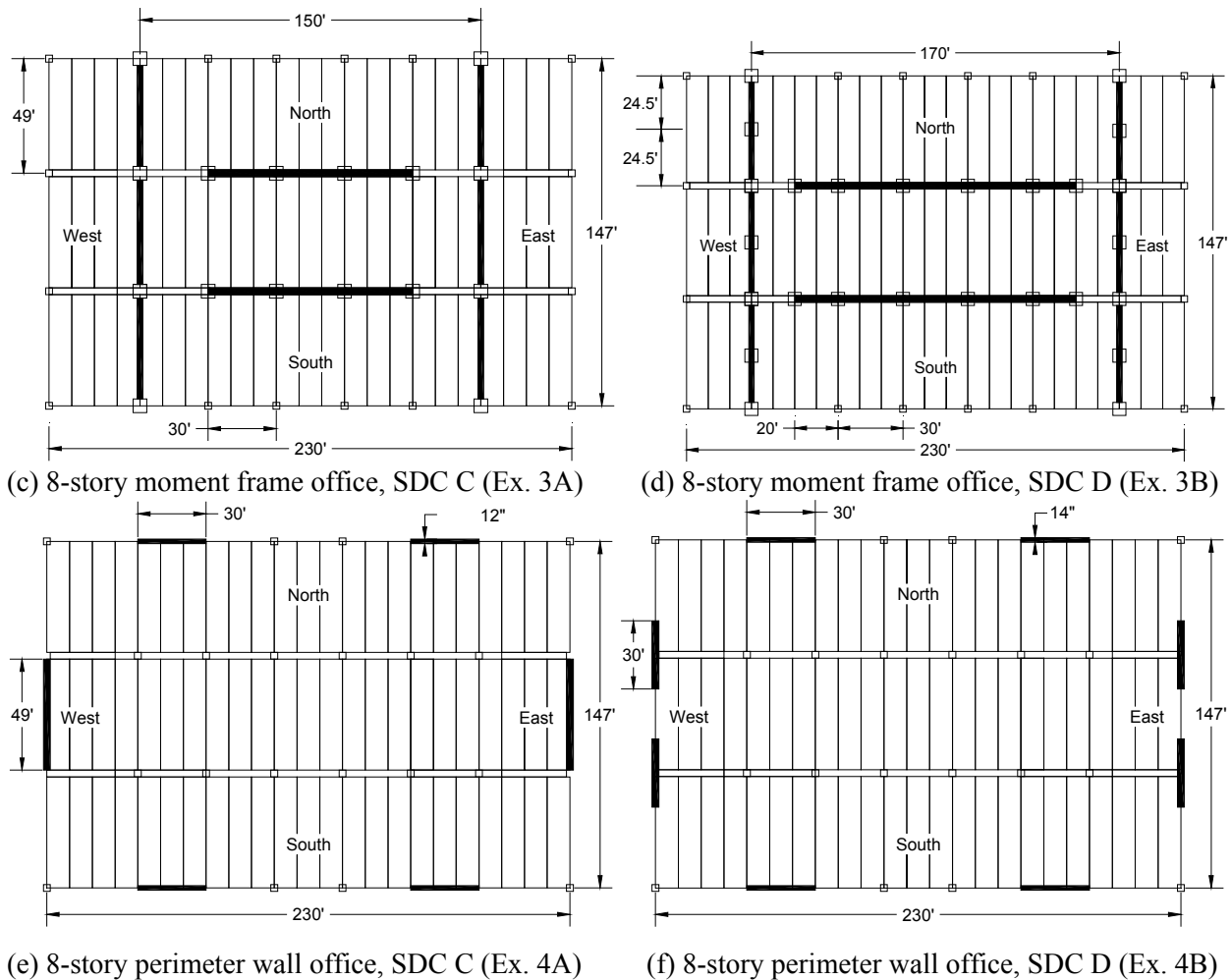
Fig. A2-1. Plans for prototype structures evaluated in the study.

Two precast structures are used in the evaluations: a 4-story parking garage and an 8-story office building. Two LFRS layouts are considered for the 4-story parking garage: (a) exterior shear walls with litewalls along the ramp (See Fig. A2-1a); and, (b) interior shear walls with litewalls along the ramp (See Fig. A2-1b). A 1″ construction expansion joint is placed between the 1st floor ramp and CIP slab (see Fig. A2-1a). Two basic LFRS layouts are also considered for the 8-story office building, however each involving slight modifications in the layout depending on the SDC: (a) interior moment frames, with different layouts for SDC C and D (See Fig. A2-1c,d); and, (b) perimeter shear walls, with different layouts for SDC C and D (See Fig. A2-1e,f).

The prototype structures shown in plan views of Figure A2-1 are each representative of a different SDC as indicated in the figure captions. Each prototype structure is designed using IBC 2009, and is evaluated for different diaphragm design options as listed in the next section. The full details of the prototype structure designs each appear as a design example in PART 4, as also indicated in the caption.

A2.1.2 Study Matrix

The design methodology evaluation covers the following parameters: (1) structure configuration (parking garage and office building); (2) LFRS layout (interior and exterior); (3) LFRS type (shear wall and moment frame); (4) SDCs C (Knoxville TN) and D (Seattle WA); and, (5) diaphragm design option (EDO, BDO and RDO). The detailed study matrix is shown in Table A2-1.

Table A2-1. Study Matrix

Run #	Structure	LFRS layout	Site	SDC	Design option	EQ	Design Example[1]
1			Knoxville	C	EDO	All three	1A
2	Parking garage	Exterior wall	Knoxville	C	BDO	KN2	1B
3			Knoxville	C	RDO	KN2	1C
4	Parking garage	Interior wall	Knoxville	C	EDO	SE8	2A
5			Seattle	D	RDO	All three	2B
6	Office building	Moment frame	Knoxville	C	EDO	KN2	3A
7			Seattle	D	RDO	SE8	3B
8	Office building	Perimeter wall	Knoxville	C	EDO	KN2	4A
9			Seattle	D	RDO	SE08	4B

[1]Design Examples are found in PART 4 of the Diaphragm Seismic Design Methodology.

A2.1.3 Evaluation Methodology

The prototype structure analytical models are subjected to bi-directional earthquake inputs. Three historical ground motion pairs are selected for each site as shown in Table A2-2. The scaling of the ground motion pairs follows the ASCE 7 (Section 16.1.3.2) procedure: *The average of the SRSS 5% damping spectra does not fall below 1.3 times the corresponding ordinate of the design response spectrum by more than 10% for each period between 0.2T and 1.5T, where T is the fundamental period of structure.* The SRSS response spectra of scaled ground motion pairs are shown in Fig. A2-2. As seen, the average of the SRSS response spectra meets the ASCE7 requirement within the period range 0.2-1.5 sec, representing the minimum and maximum fundamental period among the prototype structure designs. Between the two ground motion pairs, the stronger component is applied in the structure transverse direction and the other component is applied in longitudinal direction.

Table A2-2a. EQ information for SDC C, Knoxville

EQ # *	Earthquake	Magnitude	Scale factor	Scaled PGA at DBE level (g)	
				Trans. (y)	Long. (x)
KN2	Landers	7.3	**0.6**	0.147	0.091
KN3	Nahanni, Canada	6.8	**0.35**	0.352	0.394
KN5	Tabas, Iran	7.4	**0.575**	0.234	0.189

Table A2-2b. EQ information for SDC D, Seattle

EQ# *	Earthquake	Magnitude	Scale factor	PGA (g)	
				Trans. (y)	Long. (x)
SE1	Cape Mendocino	7.1	**0.58**	0.868	0.603
SE8	Northridge	6.7	**0.6**	0.506	0.363
SE10	Western Washington	7.1	**2.0**	0.560	0.329

* Selected from the suite of EQs developed by Schoettler (2005) for the DSDM project and rescaled (scale factor indicated relative to original motion).

According to ASCE 7 analysis procedures, the *maximum* demand from the three earthquake analyses is used to evaluate the structure performance. However because each earthquake simulation requires extensive computer space and run time, only two design cases are evaluated using all three earthquake (See Table A2-1). The other cases were evaluated using simulation of a single earthquake record pair. The record chosen for the single record analysis is the one that produces the highest spectral response in the period range (0.72 to 2.66 sec) of the prototype structures evaluated (See black dashed line in Fig. A2-2). Thus, though the analyses with the other ground motions could be performed in the

future, given the ASCE-7 procedure maximum demand requirement, it is likely that the results of the single earthquake analysis also represent the final statistical result. Recall again that due to the controlling performance targets, the ground motions shown in Table A2-2 and Fig. A2-2 were scaled to the MCE level with a scaling factor of 1.5 before using for the earthquake simulations.
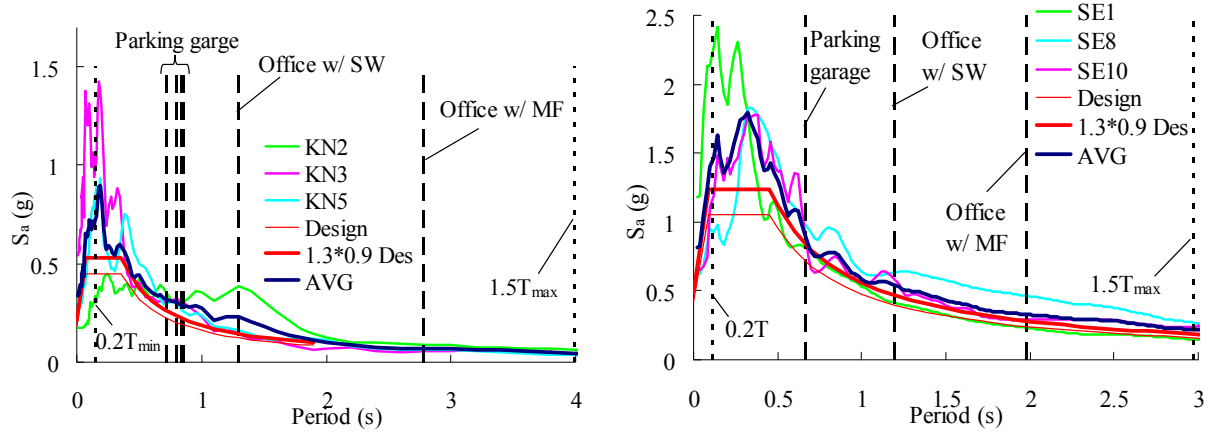
(a) SDC C, Knoxville　　　　　　　　　　(b) SDC D, Seattle
Fig. A2-2. SRSS response spectrum for selected EQs at DBE level.

A2.2 ANALYTICAL MODEL

The prototype structures are evaluated using nonlinear transient dynamic analysis of three dimensional finite element (3D-FE) models. The analytical model used in this stage is an improved version of the model used in the trial design factor stage (Stage 1), as further calibration to the experimental work performed in the main research phase occurred in parallel.

3D-FE models for the 4-story precast parking garage and the 8-story office building are shown in Fig.A2-3. The model is created using the commercial general purpose finite element software ANSYS[7]. The detail of modeling technique is summarized as following:

1. The model includes the following elastic elements:
   (a) 2D discrete plane stress elements for precast floor units
   (b) 3D discrete shell elements for precast units in the ramps
   (c) 2D beam elements for the spandrels and IT beams
   (d) 3D shell elements for shear walls and litewalls
   (e) 3D beam elements for the moment frame members and gravity columns
2. The nonlinearity of LFRS is modeled as:
   (a) Base plastic hinges for the shear wall (biaxial shoot-through model representing a regular reinforced concrete wall response) and the litewall (uniaxial slip-catch model representing a typical litewall response) using a set of nonlinear springs and contact elements.
   (b) Plastic hinges at beam member ends for the moment frame (uniaxial shoot-through model representing a regular reinforced concrete beam response) using a set of nonlinear springs and contact elements.
   (c) The hinge properties for shear wall, litewall and frame beam are developed using section analysis software XTRACT[8] with a bilinear steel model (1.2 strain hardening ratio) and Mander model for concrete. The plastic hinge length for shear wall and litewall is set as minimum of half of shear wall depth and story height. The plastic hinge length for frame member is set as the frame member depth.
   (d) Gravity loads are not included directly in the analyses except for moment frame structures in order to obtain the proper end moments ($Mg + ME$) in the frame. Gravity load effects are included indirectly in shear wall structures in the moment-curvature response of the shear wall base hinge.
3. The diaphragm reinforcement is modeled as assemblages of nonlinear link, spring and contact elements (see PART B1 and B2) with the following characteristics:
   (a) Chord reinforcement model includes pinching effect, cyclic stiffness degradation for tension, cyclic slip-catch for shear, strength degradation for shear and tension-shear coupling effect.
   (b) Shear reinforcement model includes pinching effect, cyclic stiffness degradation for tension, cyclic strength degradation for shear and tension-shear coupling effect.
   (c) Secondary reinforcement model (including LFRS-diaphragm connector, internal beam to diaphragm connector and spandrel to diaphragm connector) includes pinching effect and tension-shear coupling effect without cyclic strength degradation.
4. The gravity column is modeled with pinned connection at base. At each floor level, the connection between column and spandrel/internal beam is modeled as:
   (a) The spandrel/internal beam to column connection are modeled to allow free separation between spandrel/internal beam and column in the direction perpendicular to the precast floor unit joints.
   (b) In the direction parallel to the precast floor unit joints, the connection of spandrel/internal beam and column are modeled as ductile nonlinear springs

---

[7] ANSYS, Inc. (version 11), Canonsburg, PA
[8] XTRACT Imbsen commercial software, Inc. Rancho Cordova, CA.

representing the tension strength and stiffness of typical coil rod connection.
5. The interface of construction expansion joint in parking structure is modeled as a series of point to point contact elements along the diaphragm joint.

(a) 4-story parking garage   (b) 8-story office building
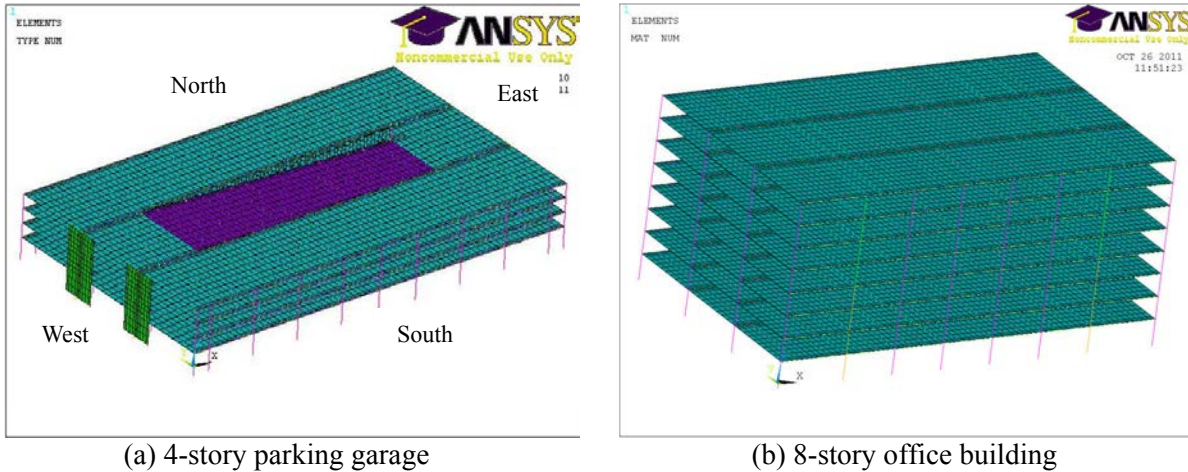
Fig. A2-3. 3D-FE models of the prototype structures

An equivalent damping value of 2.5% aligned with the first (fundamental) and last significant transverse vibrational modes (cumulative mass participation ratio ≥ 99%) was used. The discrete diaphragm model cannot be used effectively for modal analysis due to the uncertain initial status of the contact elements (open, sliding, stuck). Thus, the Rayleigh damping parameters are determined through modal analyses performed on 3D elastic models with monolithic diaphragms. The diaphragm stiffness is estimated through effective moduli (Wan and Fleischman 2012).

A2. 3 PERFORMANCE EVALUATION OF PROTOTYPE STRUCTURE DESIGNS

The efficacy of the design procedure and the suitability of the of the trial design factors are evaluated through comparisons of expected performance and anticipated design levels to the demands incurred in the earthquake simulations. Table A2-3 shows the comparisons performed to evaluate the design methodology. The structures are designed using the different design options as indicated in Table A2-1. The results presented are grouped by prototype structure design. Results are shown for the most critical earthquake for each design site. Recall that all the earthquakes are scaled to the MCE level.

Section A2.3 has nine subsections, one to present the earthquake simulation results for each of the designs listed in Table A2-1. It is noted that the analytical results are presented in great detail for the first prototype structure design in Section A2.3.1, a 4-story SDC C EDO parking structure. In subsequent sections, the results are presented in less detail, focusing on results with major design implications or results that are different from the previous structures presented. Significant design issues raised in the analyses of the prototype structures are discussed in Section A2.4.

Table A2-3. Evaluation of the design methodology.

Design Option	EDO	BDO	RDO
Analysis	Diaphragm designed with trial Ψ_E, Ω_{vE}, and LDE reinforcement	Diaphragm designed with trial Ψ_D, Ω_{vB}, and MDE reinforcement	Diaphragm designed with trial Ψ_R, Ω_{vR}, and HDE reinforcement
Seismic Hazard Level	MCE	MCE	MCE
MCE Design Target	Elastic Response	Within MDE allowable deformation	Within HDE allowable deformation
Diaphragm Design Option Specific Design Evaluation	Are diaphragms elastic?	Are maximum MDE allowable opening deformations exceeded?	Are maximum HDE allowable opening deformations exceeded?
General Design Evaluation	Are the diaphragms under-designed by a small or large amount? Are the diaphragms overdesigned by a small or large amount? Do diaphragms respond similarly at all levels? Do diaphragms respond similarly relative to design at all locations? Are non-conforming regions localized or widespread? What are the key behaviors that impact the design?		

A2.3.1 Four-story parking garage w/exterior shear wall: SDC C EDO (Example 1A)

The first prototype structure diaphragm design evaluation involves a SDC C EDO diaphragm design option for a 4-story parking garage with exterior shear walls. The earthquake simulation is performed through nonlinear transient dynamic analysis (NLTDA) under bi-directional components of a MCE-level ground motion. The diaphragm design of the prototype structure is based on the design procedure in PART 1. The design of this particular structure is described in Example 1A (PART 4).

The final diaphragm design produced in Example 1A, PART 4 is shown in Figure A2-4. The chord reinforcement shown in right part and shear reinforcement shown in left part (since the diaphragm design is symmetric across the diaphragm span). The diaphragm reinforcement indicated in Fig. A2-4 is for the top floor; the design for the other floors is indicated in parentheses if different from the top floor. The pretopped diaphragm is detailed with low deformability element or LDE reinforcement (dry chord connectors and JVI Vector flange-to-flange connectors respectively for flexure and shear reinforcement). The diaphragm design factors are $\Psi_E = 2.9$ and $\Omega_{vE} = 1.0$. The diaphragm design force profile is determined using the diaphragm force vertical distribution factor α_x.

The diaphragm-to-LFRS connection is angle bar connectors designed for the tributary shear at each shear wall. The diaphragm to litewall connection on the parking flats is the angle bar connector designed for tributary shear and axial force. The litewall-to-ramp connection is ½" steel angles with slotted holes for compliance. The spandrel-to-DT connection and IT to-DT connection is also angle bar connectors. . The IT-to DT connections are designed for the tributary shear and a portion of diaphragm inertia force from the outer (flat) sub-diaphragms to the shear wall, These reinforcement details are also shown in Fig. A2-4 and discussed in detail in design example 1A of PART 4.
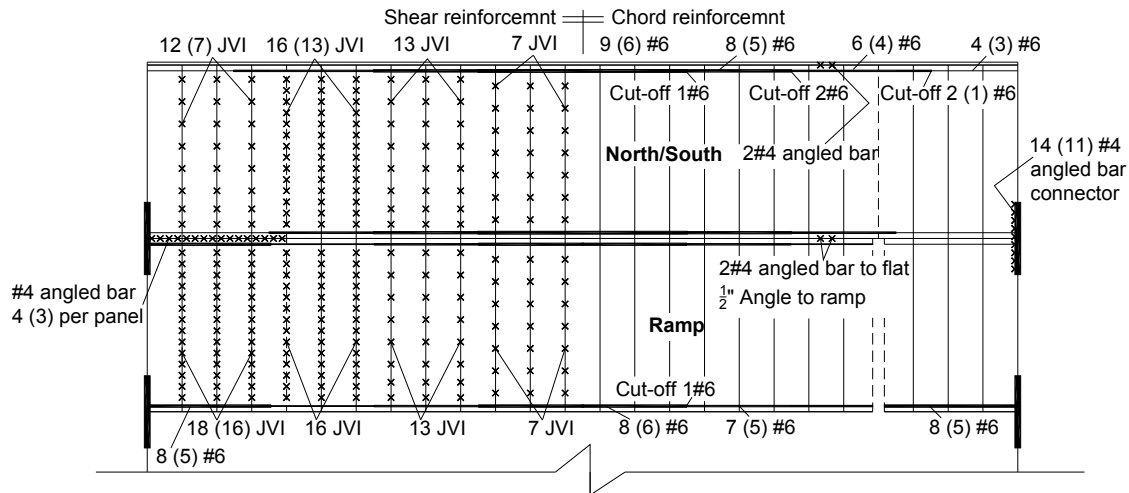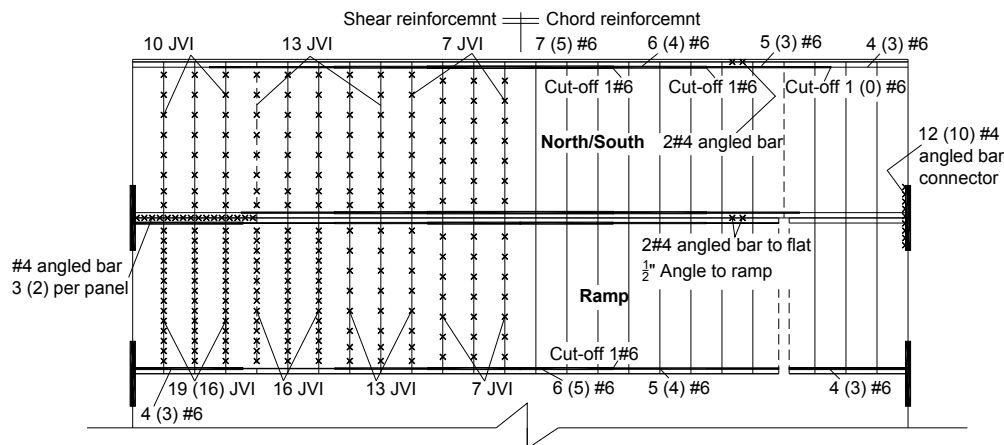

Fig. A2-4. Diaphragm reinforcement design for design example 1A.

Figure A2-5 and A2-6 shows the maximum diaphragm inertial force profile along the building height in the structure transverse (N/S) direction and the structure longitudinal direction respectively. Figure A2-5a and A2-6a shows the force profiles for total inertial forces at a floor level and three different profiles are indicated: (1) the design profile, $\alpha_x\Psi_E F_{px}$, where α_x is the diaphragm force vertical distribution factor (α_x=1.0 at top floor and α_x =0.68 at other floors, see PART 1); (2) the envelope of maximums occurring at any time during the earthquake; and (3) the instantaneous profile at the time of the maximum diaphragm force occurring anywhere in the structure. Figure A2-5b and A2-6b shows the maximum envelope force profile for each sub-diaphragm with the design force profile tributary to each sub-diaphragm shown as green dashed line.

As seen in Fig. A2-5 and Fig. A2-6, the diaphragm design force overestimates the diaphragm total inertia force demand at each floor level in both transverse and longitudinal directions. However, the

maximum north and south sub-diaphragm force demand is well represented by the diaphragm design force tributary to each sub-diaphragm because of the uneven distribution of diaphragm inertia force demand among each sub-diaphragm. As seen in Fig. A2-4b and 2-5b, typically ramp has less inertia force demand than the north and south flats.
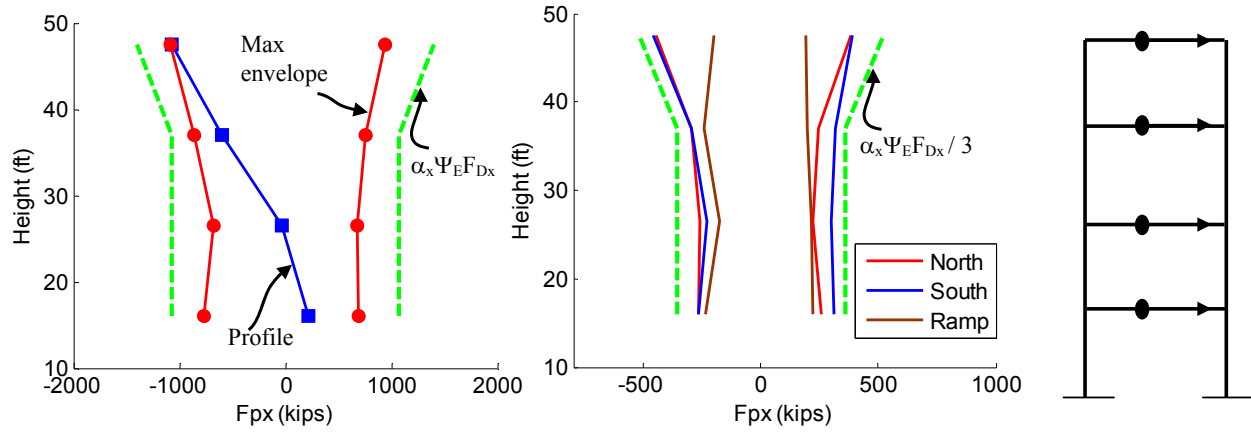
Fig. A2-5. Diaphragm inertia force in transverse direction: (a) floor total; (b) sub-diaphragm.
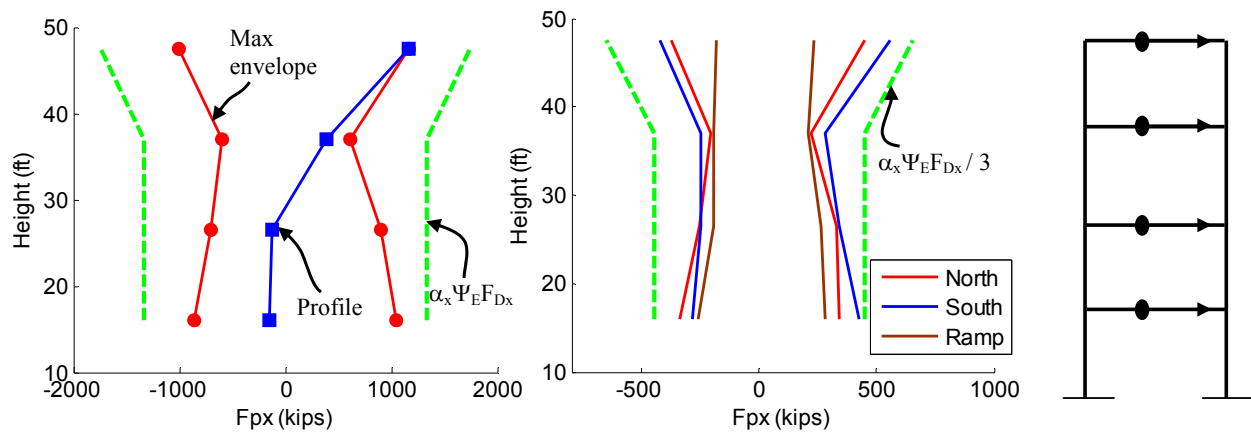
Fig. A2-6. Diaphragm inertia force in longitudinal direction: (a) floor total; (b) sub-diaphragm.

Figure A2-7 shows the diaphragm internal forces time history at a critical joint which is defined as the joint with maximum force interaction demand (M-N-V). This joint is located close to the midspan of top floor north sub-diaphragm (See schematic in Fig. A2-7). The force interaction demand is calculated with an expression consistent with the design interaction equation in PART 1, as follows:

$$M - N - V = \sqrt{\left(\frac{M_{FE}}{M_n} + \frac{N_{FE}}{N_n}\right)^2 + \left(\frac{V_{FE}}{V_n}\right)^2} \qquad \text{(Eqn. A2-1)}$$

where M_{FE}, N_{FE} and V_{FE} are the moment, axial and shear force demand obtained in the earthquake simulation. M_n, N_n and V_n are the joint nominal moment, axial and shear strength (See Section 3.3B in PART 3). The individual diaphragm internal force components are also shown in Fig. A2-7, normalized by the nominal strength. Maximum and minimum forces in the time history are indicated with circular markers in Fig. A2-7.

As seen in Fig. A2-7, although the diaphragm individual internal force demands are considerably lower than the nominal strength, the combined effect of the diaphragm internal forces brings the joint close to its design strength (M-N-V reaching unity), though not repeatedly, during the earthquake.
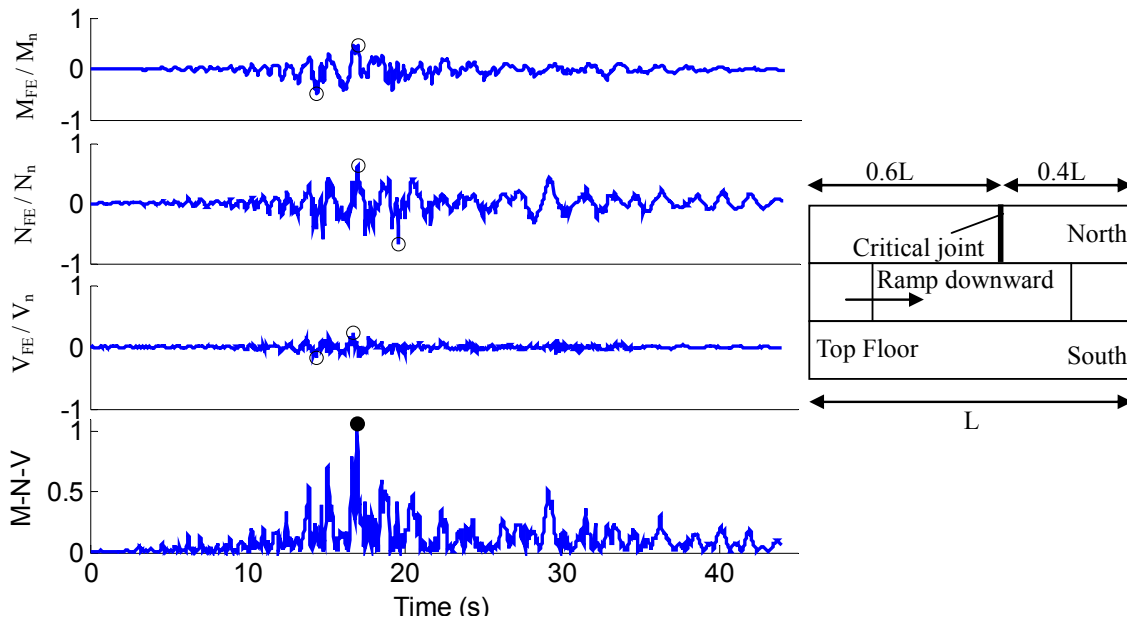
Fig. A2-7. Diaphragm joint internal force time history at critical joint of top floor.

Figure A2-8 shows the diaphragm internal force diagrams (moment, axial and shear) for the top floor north sub-diaphragm under the ground motion: transverse component only; longitudinal component only; and, bi-directional components. The south sub-diaphragm has similar, lower force demand and thus is not shown here; the ramp is discussed later. Each plot shows: (a) the envelopes of maximum positive and negative force response at any time during the earthquake; (b) the force profiles at t=19.69s, the instant of maximum force under the transverse earthquake component; (c) the force profiles at t=17.08s, the instant of maximum axial force under the longitudinal earthquake component; and, (d) the design diagrams for required diaphragm strength using the FBD method from the design methodology. The design diagrams are calculated in Design Example 1 of PART 4. The bi-axial plot design curves are the most critical diagram from transverse and longitudinal loading in accordance with the design methodology. An adequate design should be demonstrated under the bi-axial earthquake, however the discussion begins with the individual components to better understand behavior as it effects design.

Under transverse earthquake loading, the moment, axial and shear demands at the time of critical transverse loading (t=16.96s) are reasonably estimated by the design diagrams. The moment demand diagram is skewed slightly to the up-ramp side of the parking flat. This skew is caused by the shift of center of mass tributary to the top level toward the down-ramp side due to the presence of a single ramp at the top level. The shift causes moment demand to be higher than the design diagram in the half span (0.5<x/L<1.0). However in this same half span, the design axial force diagram *overestimates* axial force demand, also due to the mass center shift, thereby compensating for the underestimated design moment.

Next considering longitudinal earthquake loading, the moment, axial and shear demand diagrams at the time of critical longitudinal loading (t=17.08s) are reasonably estimated by the design diagrams. The axial force demand is seen to be underestimated by the design axial force diagram, due to a non-uniform distribution of the reactions at the litewall in the earthquake simulation, as opposed to the uniform distribution assumed in the FBD method (See Sec. 3.2.B in PART 3). This condition is compensated by a lower moment demand than the design moment diagram, also due to the non-uniform distribution of wall reactions.

For the bi-axial earthquake loading, the critical diaphragm internal force demand occurs at t=16.96s when the transverse loading effect is maximum. The combined effects from the bi-directional ground motion components increase the axial force demand. The diaphragm design procedure, on the other hand, does not combine the effects of the two loading directions, instead basing the design on the most critical loading case. For this reason, the design diagram underestimates axial force demand in the

diaphragm span 0.2<x/L<0.6. However, the combined loading tends also to decrease moment demand to levels below the design moment diagram in the span 0.2<x/L<0.5, thereby somewhat compensating for the underestimation of axial force. The actual diaphragm strength in the model is slightly higher than the required strength in the design diagram because of the use of strength reduction factors (ϕ_f= 0.9 for axial and flexure and ϕ_v=0.85 for shear, See PART 4). Therefore the diaphragm design is sufficient in keeping the chord and shear reinforcement elastic under the bi-axial MCE earthquake (e.g., Fig. A2-11).
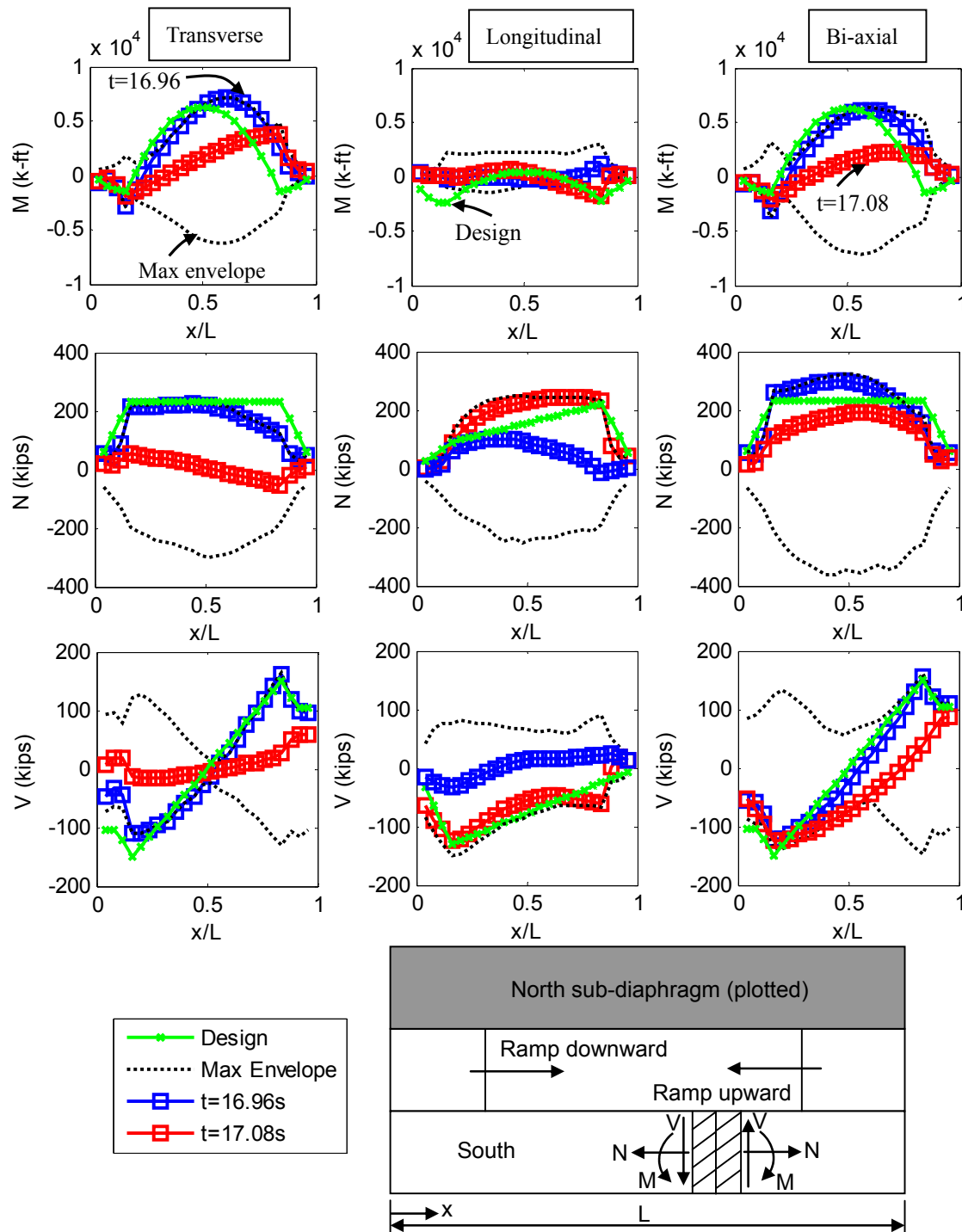
Fig. A2-8. Diaphragm joint internal force diagram at north sub-diaphragm of top floor.

These compensating actions suggest a comparison between the more involved FBD method promoted in the design methodology and the horizontal beam method used in current design. Accordingly, Figure A2-9, compares the analytical results for diaphragm internal force demand (M_{FE}, N_{FE}, V_{FE}) profile under transverse loading, shown as blue lines in Fig. A2-9, to three design approaches: (1) the design provided by the diaphragm seismic design methodology using the amplified diaphragm forces and the internal forces provided by the FBD method (green line Figs. A2-8, A2-9); (2) a design considering the amplified diaphragm forces, but using the current horizontal beam method (red line in Fig. A2-9); and, (3) current design, in which no amplification factor is applied and the horizontal beam method is used to determine the diaphragm design (black line in Fig. A2-9). As seen in Fig. A2-9, the FBD method using the proposed amplified diaphragm forces in the design methodology provides the most accurate prediction for the diaphragm internal force demand under the earthquake simulation. A comparison of designs using the FBD method and the horizontal beam is found in Section A2.4.
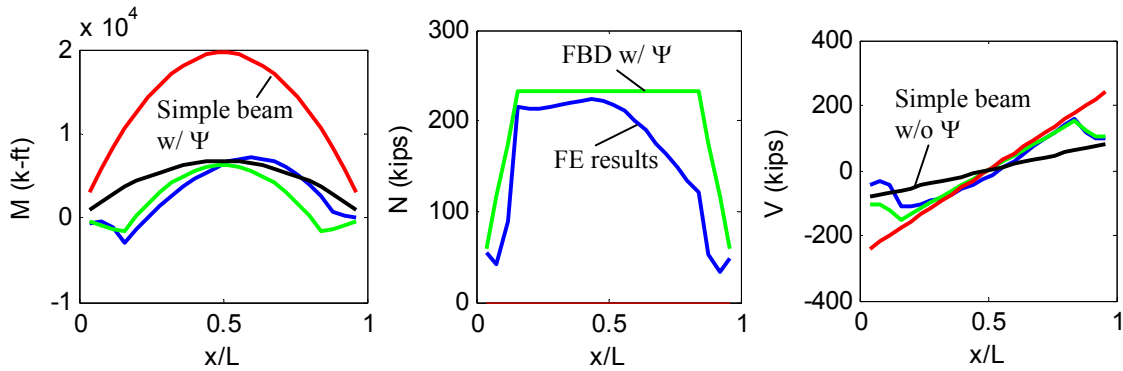
Fig. A2-9. Diaphragm joint internal force comparison: (a) moment; (b) axial and (c) shear.

Figure A2-10 shows the diaphragm internal force diagrams (moment, axial and shear) for the top floor ramp sub-diaphragm under the bi-axial earthquake loading. On each plot is shown: (a) the envelopes of maximum positive and negative force response at any time during the earthquake; (b) the force profile at the instant of maximum axial force; and, (c) the design diagrams for required strength using the FBD method from the design methodology. The required diaphragm design strengths shown in the design diagrams are calculated in Design Example 1, PART 4 for both transverse (*Tr*) seismic and longitudinal (*Lg*) seismic loading. The calculated values are listed in tables in Page 8 of PART 4. These tables indicate that the diaphragm design is controlled in the ramp landing region by transverse seismic loading and controlled in the ramp span by longitudinal seismic loading.

As seen in Fig. A2-10b, a higher axial force demand from longitudinal loading occurs in the ramp span than in the flat spans (e.g. Fig. A2-8). The FBD method design axial force diagram for longitudinal loading is seen to match this maximum axial load demand well. The FBD method design shear force and moment diagrams, both based on transverse loading, are shown to match the large shear force demand in the ramp landing region (Fig. A2-10c) and the moderate moment in the ramp (Fig. A2-10a).
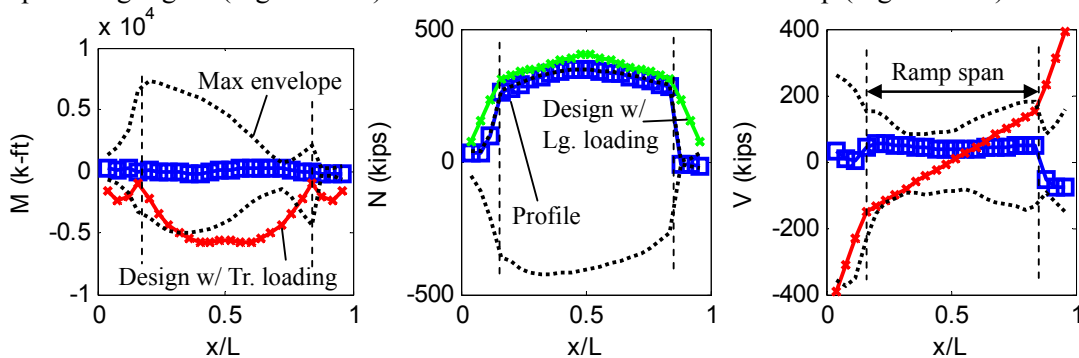
Fig. A2-10. Diaphragm internal force demand at ramp of top floor: (a) moment; (b) axial and (c) shear.

Figure A2-11 shows the maximum diaphragm internal force interaction demand (M-N-V) calculated using Eqn. A2-1 at each diaphragm joint in the entire parking structure. The design M-N-V interaction (refer to Eqn. 10 in PART 1) is shown as black dashed line calculated using Eqn. A2-2:

$$(M - N - V)_{DES} = \sqrt{\left(\frac{M_u}{\phi_f M_n} + \frac{N_u}{\phi_f N_n}\right)^2 + \left(\frac{V_u}{\phi_v V_n}\right)^2} \qquad \text{(Eqn. A2-2)}$$

where M_u, N_u and V_u are the required diaphragm design moment, axial and shear force demand obtained from required diaphragm design strength tables in PART 4. M_n, N_n and V_n are the joint nominal moment, axial and shear strength (See Section 3.3B in PART 3). Design strength reduction factors are specified in the design methodology as: $\phi_f = 0.9$ for axial and flexure and $\phi_v = 0.85$ for shear.

The interaction demand are seen to be below unity for most joints as would be required in an EDO design, indicating adequacy with respect to the design interaction equation. The interaction demand slightly exceeds unity, however, at a handful of joints. The high M-N-V demands are driven by combined moment and axial force in the midspan region of the flat (north/south) sub-diaphragms, by combined moment, axial and shear in the ramp landing region of the flats, and by axial force alone in the ramp span. Since the M-N-V interaction is an approximate expression, further investigation on the diaphragm local reinforcement demands is warranted to determine if the design meets the EDO design target.
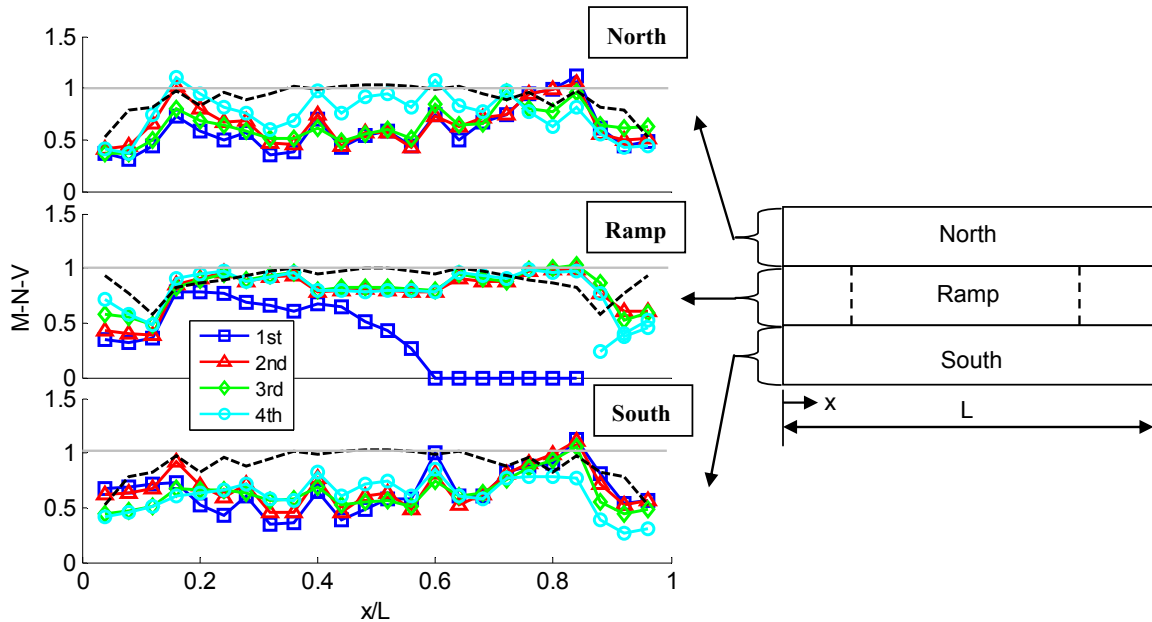
Fig. A2-11. Diaphragm joint demand ratio (M-N-V).

Examination of the interaction values relative to unity is useful in evaluating the efficacy of the design procedure. However, since the M-N-V interaction is an approximate expression, it is important to also examine local behavior (chord and shear reinforcement demands) to determine if the design is producing the desired elastic behavior. The measure used to evaluate diaphragm elastic behavior is yield *deformation*: joint *opening* and joint *sliding* (relative transverse motion of units flanking the joint). Yield deformation is chosen for several reasons: (1) it is rather insensitive to combined actions (simultaneous shear and tension), as opposed to yield strength which changes significantly depending on the combined forces; (2) it provides a clear indication of by how much the target is exceeded for non-conforming regions (unlike plotting force that will remain with a similar magnitude after yielding); and, (3) it provides ease of comparison for design options (e.g. RDO) with deformation-based performance targets.

Figure A2-12 shows maximum demands at every joint for: (a) chord opening at top and bottom of each sub-diaphragm, and (b) shear connector sliding at center of each sub-diaphragm. As seen in Fig. A2-

12a, the chords remain elastic at nearly every joint, as desired in an EDO design. The exception is the perimeter chord on the 1st floor flat co-linear with the (up-) ramp end (see blue dots on right-hand side of the plot). This minor exceeding of chord yield deformation (0.0056″) was considered acceptable.
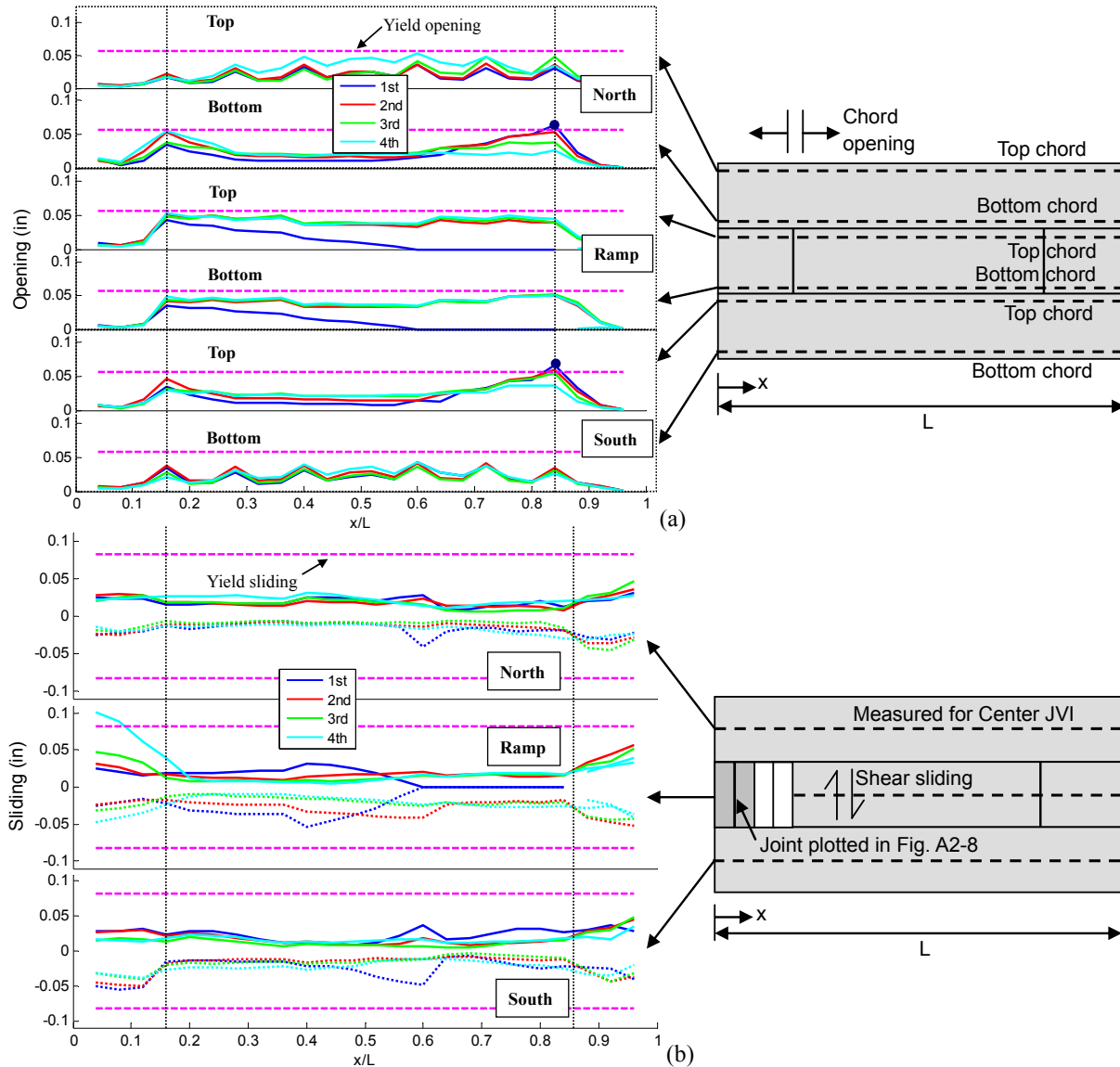
Fig. A2-12. Diaphragm reinforcement deformation demands: (a) chord opening; (b) shear sliding.

The shear connectors exhibit elastic sliding response except a single joint in the top floor ramp landing region with minor inelastic deformation 0.1″ (light blue dot in Fig. A2-12b). This inelastic demand is caused by a non-uniform distribution of sliding demand along the joint as shown in Fig. A2-8a. As seen, four connectors near the center of joint yield in shear, while the other connectors remain elastic. Figure A2-13b shows the shear-sliding hysteretic response of the highest loaded connector. This connector is modeled both with cyclic degradation and shear-tension coupling (refer to *Sec. A2-2*).

The results in A2-13b indicate only minor strength degradation, rather than complete connector failure. Thus, the inelastic shear sliding response of the JVI Vector connectors is sufficiently accommodated. It is noted that other shear connectors may not have this level of plastic redistribution, and could instead "unzip". Given the localized nature and modest values of the inelastic demand, this

behavior was considered acceptable. The shear performance of connectors under high tension (e.g. due to collector actions) is an important aspect, as covered later in Appendix A2 (See Section A2.4.7)
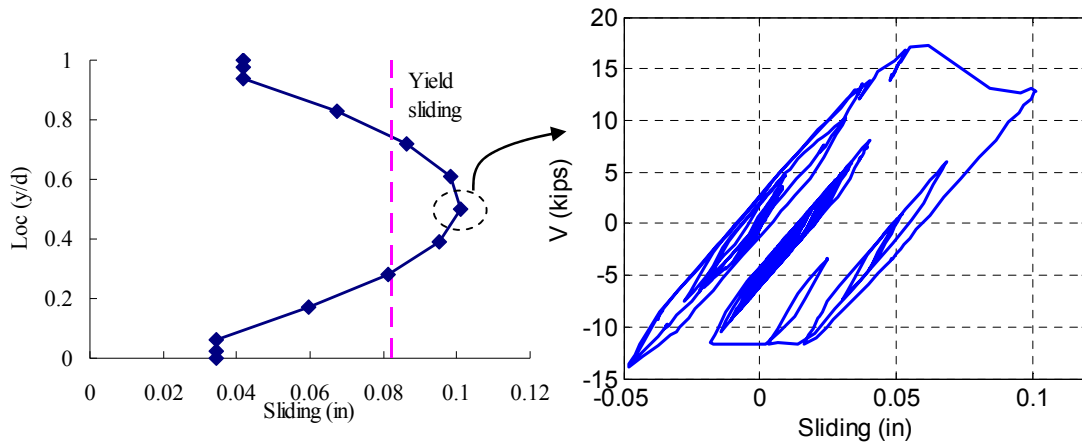
Fig. A2-13. Joint sliding demand: (a) profile at ramp landing of 4th floor; (b) Hysteresis.

An expansion joint between the 1st floor ramp and foundation permits relative displacement of the precast units to the cast-in-place ramp stub. Figure A2-14 shows displacement time histories at the expansion joint. Maximum displacement demands at the expansion joint are significant (1.3″ opening, 1.1″ sliding), and must be accounted to avoid failure elsewhere in the diaphragm.
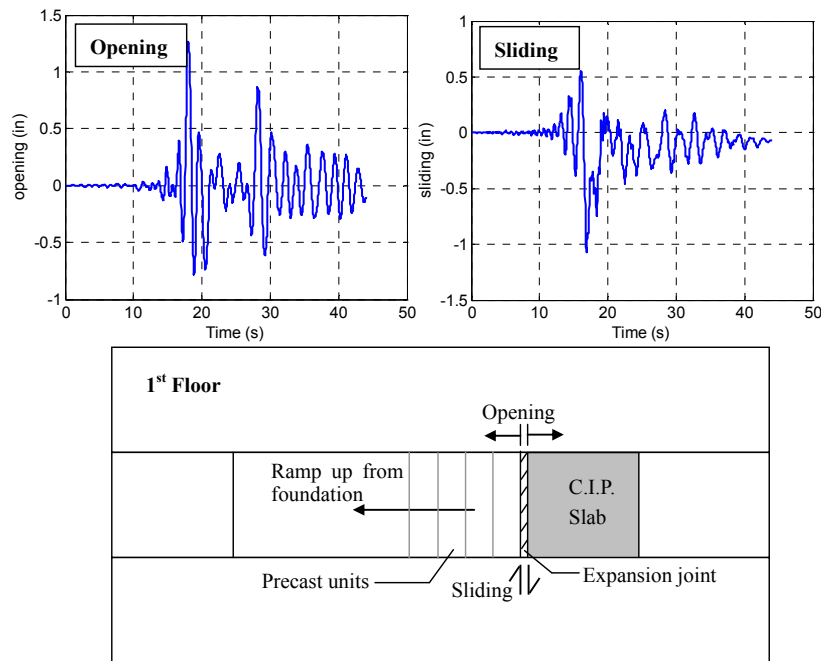
Fig. A2-14. Expansion joint response: (a) opening; (b) sliding

Next, the connection demands on the interior beams lines are considered. The beam lines include three distinct connections: (1) diaphragm-to-internal beam connections (angled bar-plate connectors between the DT units and the IT beam flanking the ramp landing); (2) diaphragm-to-litewall connections on the parking flat side (angled bar-plate connectors between the litewall and DT); and, (3) diaphragm-to-litewall connections on the parking ramp side (slotted hole steel angle connectors).

C-A-52
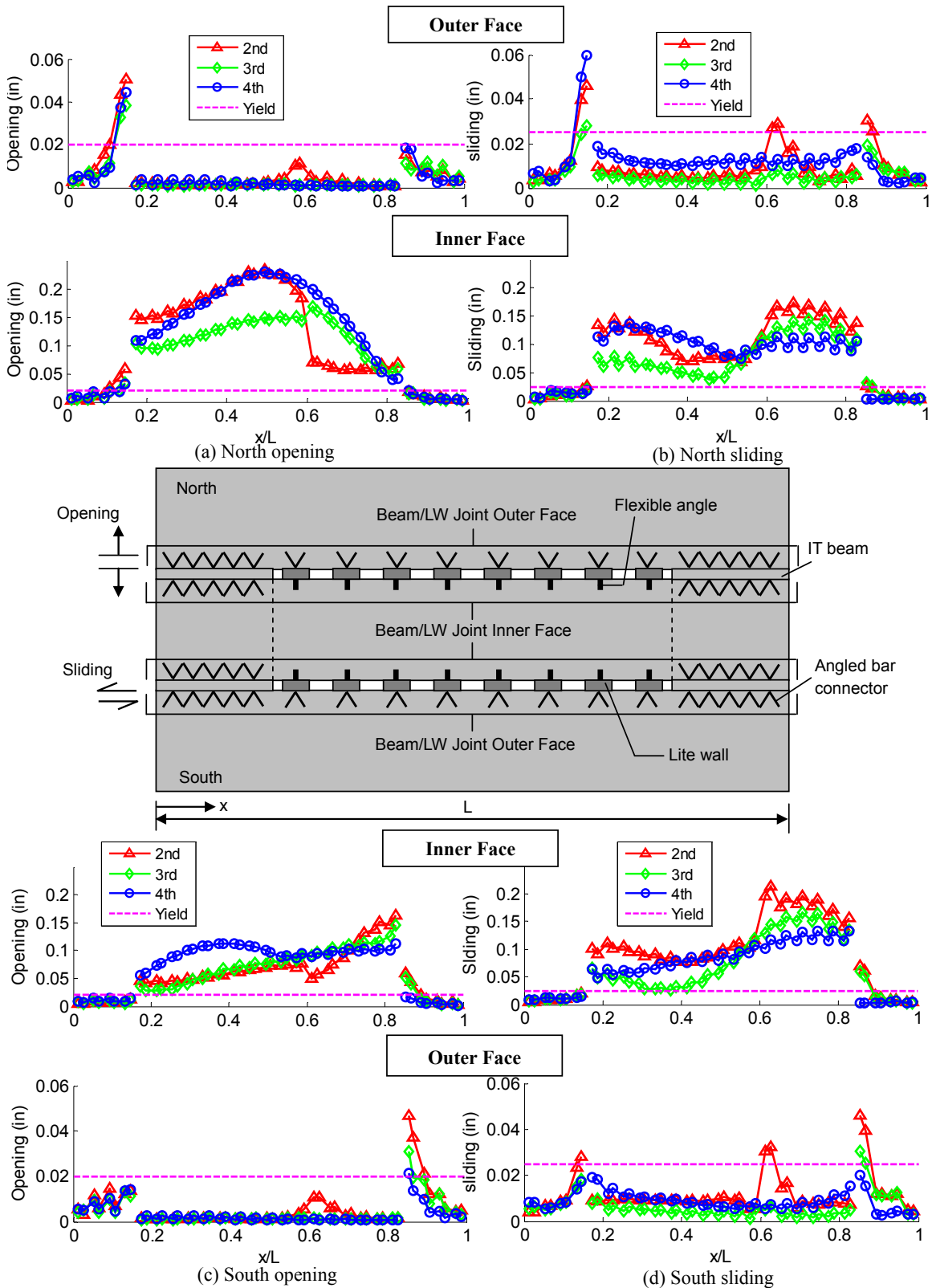
Fig. A2-15. Internal beam/litewall connector maximum deformation demands.

The first set of connections are designed for tributary shear VQ/I with the Ω_V factor and the axial/moment reactions (See PART 4, Example 1A). The second set of connections are designed as the

diaphragm-to-LFRS connections in the longitudinal direction, and are therefore designed for the diaphragm shear reaction including the Ω_V factor (See PART 4, Example 1A). The final set of connections are compliant connectors (see Sec. A2.4.5) that permit relative sliding due to the slotted holes and opening deformation due to the flexible angle connection, thereby mitigating the potential for incompatible displacements of the ramps and the flats subjecting the litewalls to severe internal forces.

Figure A2-15 shows the maximum deformation demands for connections along the interior beam lines of the parking structure. The plots show: opening of the beam line joint (left-hand plots), and sliding along the beam line joint (right-hand plots), for both the north (upper plots) and south (lower plots) beam lines. Each plot group shows the joint opening on either side of the beam line (inner and outer faces). . Each plot shows the results for floors 2-4. The connector demands at the beam lines on the 1st floor are amplified because of the aforementioned expansion joint (discussed in *Section A2.4.5*).

First, the connections on either face of the litewalls can be examined by focusing on the values between *x/L* =0.2 and 0.8 in the Fig. A2-15a plots. As seen, the compliance of the connections on the ramp side (lower of the two plots in Fig. A2-15a) provides the intended outcome of reducing the demands on the connections to the parking flat side (upper of the two plots in Fig. A2-15a). These compliant connections are seen to require approximately ¼″ of both sliding and opening deformation capacity to accommodate the relative movement anticipated in a MCE event.

By examining the upper of the two plots in both Fig. A2-15a,b, it is seen that almost all the load-carrying diaphragm-to-litewall LFRS connections are all well within their elastic range, showing the general efficacy of the diaphragm-to-LFRS design approach (See Sec. 3.2.B in PART 3). However, it is noted that one connector on each litewall at the 2nd floor undergoes localized yielding due to sliding. This result is due to a twisting effect under longitudinal loading, However, given the highly localized nature of the inelastic action, and the modest inelastic demands, it is assumed that the litewall connectors can redistribute these forces and the overall diaphragm-to-LFRS connection will be able to transfer the loads.

Next, the diaphragm to IT beam connectors can be examined by focusing on the values outside of *x/L* =0.2 to 0.8 in the Fig. A2-15a,b plots. These results indicate that both the opening and sliding demands grow for connectors as one moves inward along the IT beam (small demands at the IT beam end at the perimeter shear wall; large demands at the IT beam inner end at the ramp termination). The reason for this trend is the nature of the end moment and shear flow actions across the IT joint (termed "seam") due to the bending of the north flat sub-diaphragm, as has been described previously in (Fleischman et al. 1998). As seen in Fig. A2-15a,b, both the opening and sliding demands at the beam inner regions yield, slightly on the up-ramp (right hand) side, but significantly on the down-ramp (left hand) side.

It is important to consider the capacity of the IT beam connectors to accommodate these demands locally, the ramifications of a local failure, including the impact on the global performance of the diaphragm as presented in Figs. A2-5 to A2-17. These connectors were provided the characteristics of the angle bar-plate connector, but unlimited inelastic deformation capacity. Based on the testing on this connection (Pinchiera et al. 1998), it is unclear if the current angle bar-plate connector can accommodate these demands (maximum opening of 0.05″ and sliding of 0.06″ at a coincident location, occurring on each side of the IT beam). An improved connector or a pour strip along the IT beam with dowels will provide this performance. Design recommendations for these connectors are discussed in Section A2.4.2.

In comparing the north (plots a,b) and south beam lines (plots c,d), it is seen that while demands are similar, maximum demands occur on the down-ramp side in the north but on the up-ramp side for the south, indicating a torsional response mode, due in part to the bi-directional ground motion components.

Next consider the demands on the diaphragm-to-LFRS connections for the transverse shear walls. Figure A2-16 shows the maximum diaphragm-to-LFRS connector deformation demands for all four walls (refer to Fig. A2-1a). The value plotted is the largest opening and sliding demand on any single connector of the group of 14 connectors that comprise the diaphragm-to-LFRS connection at a single wall. First note in Fig. A2-16a that the opening demands indicate all connectors are well within the elastic range due to (longitudinal) axial forces in the diaphragm and the in-plane moment acting on the wall. This implies that the litewalls successfully limit the orthogonal force demands on the wall, and that the out-of-plane flexibility of the shear wall is sufficient to limit the opening demands on the connector. Now moving to

Fig. A2-16b, it is seen that the sliding deformation demands are within the elastic range at every location except for the SW wall at the 4th floor (adjacent to the roof level down-ramp landing). This slight yielding is due to a non-uniform distribution in sliding. Thus, the efficacy of the design of the diaphragm-to-LFRS connections (including both Ψ_E and Ω) seems given the localized and limited magnitude of the inelastic deformation demands. The diaphragm-to-LFRS connector responses are shown and design recommendations are discussed in Section A2.4.1.
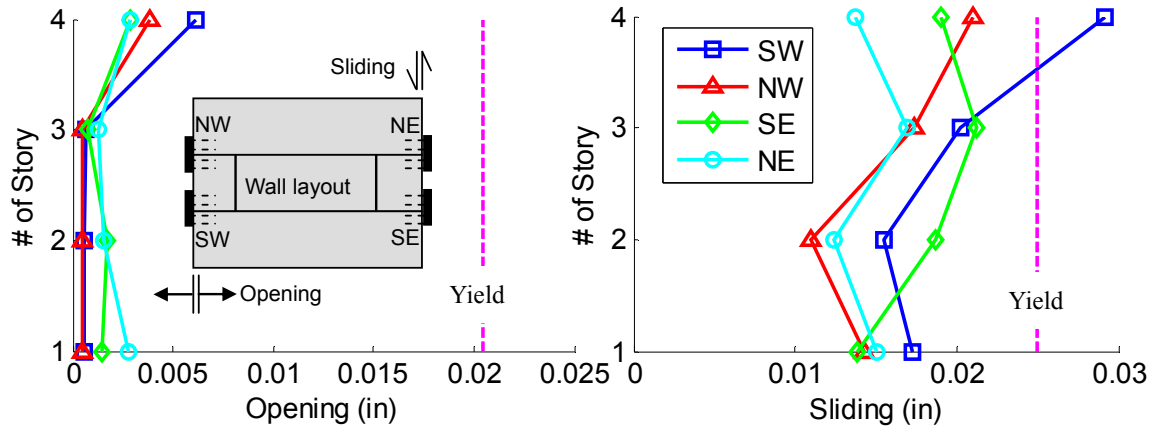
Fig. A2-16. Diaphragm-to-LFRS connector demand: (a) opening; (b) sliding.

Finally, consider the secondary diaphragm connections, i.e. the connections between the precast floor units and the perimeter spandrel beams. These connections are not explicitly part of the diaphragm design, but their participation in response has an effect on diaphragm response (and therefore were included in the shake table testing and the analytical modeling), and the ramifications of these connections failing during an earthquake must be considered.

Figure A2-17 shows the spandrel to diaphragm connector deformation demand at every floor. These connectors are also modeled using the properties of the angled bar-plate connector. As seen, the large majority of these connectors remain well within the elastic range in terms of opening deformation (corresponding to sliding of the precast DT joints), while have widespread and significant yielding in terms of sliding deformation (corresponding to opening of the precast DT joints). The relationship between DT-SP deformation and DT-DT joint deformation is clearly illustrated in Fig. C-28 (See Sec. 5.6 in PART 5). As expected the largest DT-SP connector opening demands occur at the sub-diaphragm ends, while the largest DT-SP connector sliding demands occur at the sub-diaphragm mid-span. As indicated in the plot, maximum DT-SP sliding demands occur at the spandrel ends (indicated as column lines in Fig. 2-17). The maximum inelastic deformation demands observed in these connectors are an opening demand of 0.023″ and sliding demand of 0.09″. Further discussion of DT-SP connector response and design ramifications appears in Section A2.4.1.

The design ramifications of these inelastic demands are considered secondary since the design procedure does not count for any force transferring through the spandrel. However, a sufficient deformation ductility capacity of DT-SP connector has to be provided to avoid potential unseating after the fracture of this connector. The recommended deformation ductility capacity has been made based on the analytical study results discussed in this section (PART 5 appendix A2) and is shown in Sec. A2.4.2.
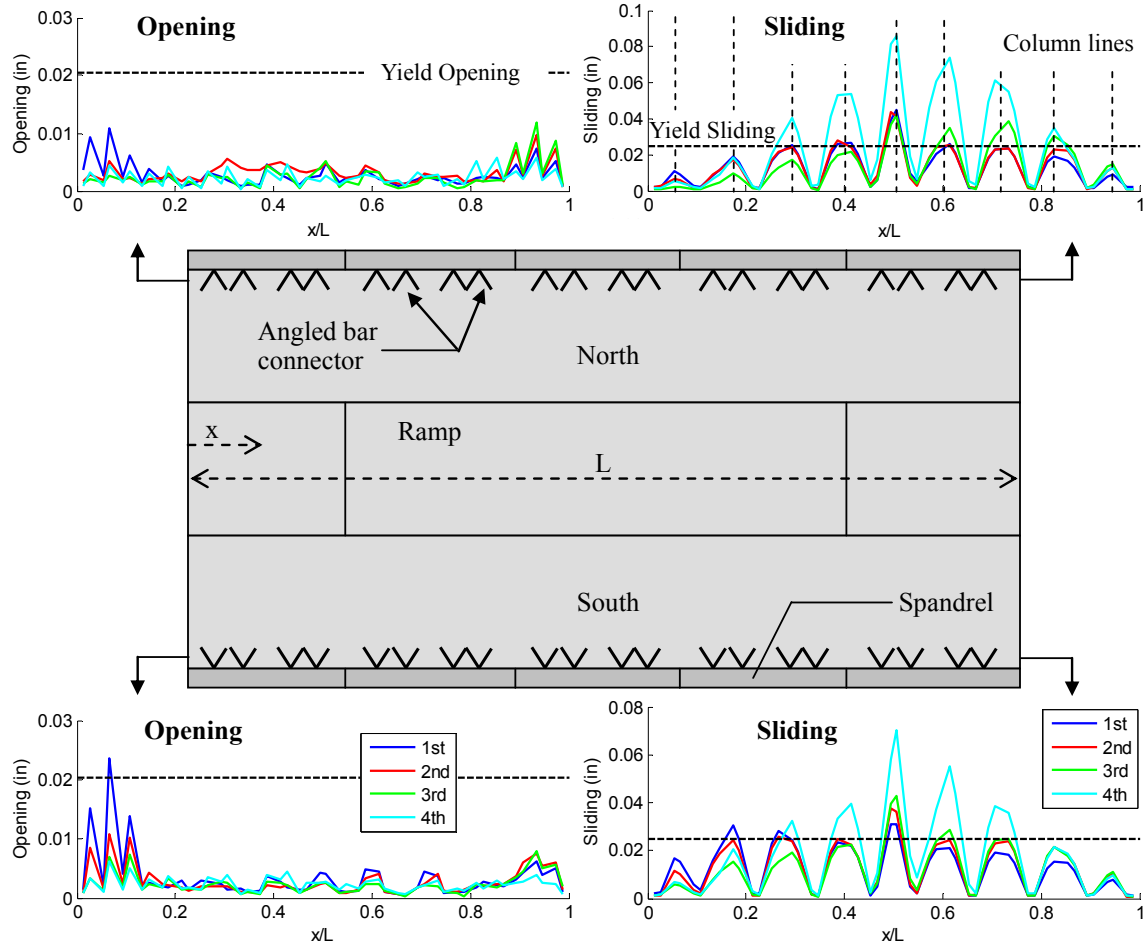
Fig. A2-17. Spandrel to diaphragm connector deformation demand: (a) opening; (b) sliding

The following conclusions are made based on the analytical results for the 4-story exterior wall parking garage SDC C EDO design (Design found in Example 1A of PART4) under a bi-directional MCE hazard level ground motion:

(1) The total floor inertial force demands at each level are conservatively predicted by the EDO design force $\Psi_E F_{Dx}$. When these forces are considered on the individual sub-diaphragms, the inertial forces are more closely and still conservatively predicted,by $\Psi_E F_{Dx}$. These conclusions apply to both the transverse and longitudinal direction.

   DESIGN CONCLUSION: The EDO design force $\Psi_E F_{Dx}$ is appropriate for this design case.

(2) The vertical profile of maximum diaphragm inertial forces are reasonably predicted by the α_x pattern for low-rise parking structures, i.e. maximum at the top level and a constant lower value at the remaining floors.

   DESIGN CONCLUSION: The diaphragm force vertical distribution factor α_x is appropriate for this design case.

(3) The diaphragm design internal forces using the FBD method (See Sec 3.2.B in PART 3) show good agreement with the dynamic analysis results.

DESIGN CONCLUSION: For this design example, the FBD method provides more accurate force patterns and more economical designs than the horizontal beam method.

(4) The moment, axial and shear interaction demand reasonably follows the expected design interaction equation (Eqn. 10 of PART 1).

    DESIGN CONCLUSION: The interaction equation seems adequate for design.

(5) Diaphragm reinforcement demands are within the design target (elastic behavior in the MCE) at most diaphragm joints. The localized, minor inelastic demands at a handful of joints were considered acceptable.

    DESIGN CONCLUSION: The elastic diaphragm design target was met for this EDO design using Ψ_E and Ω_{vE}.

(6) Large deformation demands are observed at the expansion joint and at the flexible angle connectors between the litewall and the ramp diaphragm.

(7) Significant inelastic deformation demand is observed at the diaphragm-to-litewall connectors near the expansion joint.

(8) Diaphragm-to-LFRS connection remains elastic at most locations except a minor localized sliding yield at one location (south west wall at top floor).

    DESIGN CONCLUSION: The LFRS design using Ψ_E and Ω_{vE} is deemed acceptable.

(9) Yield deformation occurs in the internal beam and the spandrel beam to diaphragm connections. Recommendations are provided in sec. A2.4.2.

A2.3.2 Four-story parking garage w/exterior shear wall: SDC C BDO (Example 1B)

The second prototype structure diaphragm design evaluation involves a SDC C BDO diaphragm design option for the same 4-story exterior shear wall parking garage from the previous section. The earthquake simulation is NLTDA under bi-directional components of a MCE-level ground motion. The prototype structure diaphragms are designed using the PART 1 design procedure, as described in Example 1B of PART 4.

The diaphragm design produced in Example 1B, PART 4 is shown in Figure A2-18. The chord reinforcement shown in right part and shear reinforcement shown in left part (since the diaphragm design is symmetric across the diaphragm span). The diaphragm reinforcement indicated in Fig. A2-18 is for the top floor; the design for the other floors is indicated in parentheses if different from the top floor. The pretopped diaphragm is detailed with moderate deformability element or MDE reinforcement (flat plate chord connectors and JVI Vector flange-to-flange connectors respectively for flexure and shear reinforcement). The diaphragm design factors are Ψ_D =2.25 and Ω_{vB} =1.19. The diaphragm design force profile is determined using the diaphragm force vertical distribution factor α_x.

The diaphragm-to-LFRS connection is angle bar connectors designed for the tributary shear at each shear wall. The diaphragm to litewall connection on the parking flats is the angle bar connector designed for tributary shear and axial force. The litewall-to-ramp connection is ½" steel angles with slotted holes for compliance. The spandrel-to-DT connection and IT to-DT connection is also angle bar connectors. . The IT-toDT connections are designed for the tributary shear and a portion of diaphragm inertia force from the outer (flat) sub-diaphragms to the shear wall, These reinforcement details are also shown in Fig. A2-18 and discussed in detail in design example 1B of PART 4.
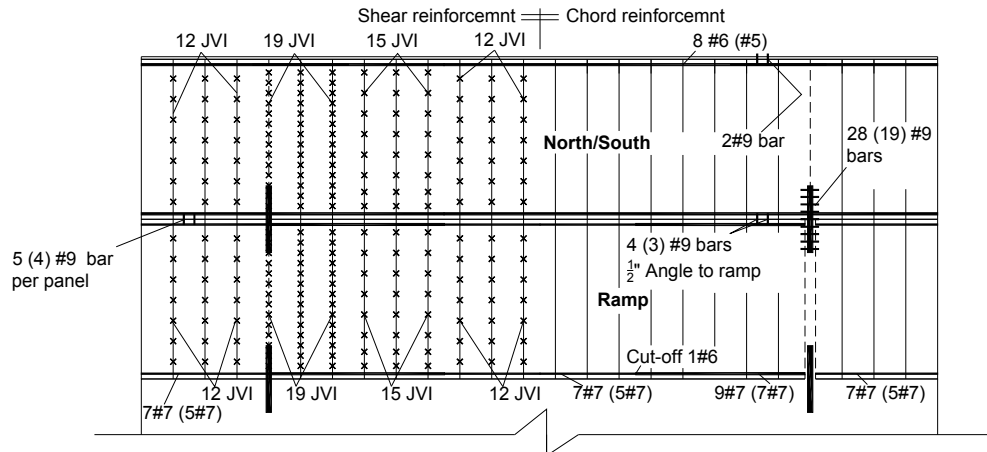

Fig. A2-18. Diaphragm reinforcement design for design example 1B.

The BDO design target is inelastic deformation demands in the MCE within the MDE allowable deformation of 0.2″. As such, it is not extremely useful to plot the vertical force profiles or the M-V-N internal force interaction plots in the MCE for the BDO design since the diaphragms are intended to reach their inelastic regime, and thus these forces are limited by the diaphragm design strength. Instead, the pertinent measure for determining the adequacy of the design are deformation demands: (1) chord opening demands, which can be compared to the MDE allowable values; and (2) joint sliding deformations (relative transverse motion of units flanking the joint), that can be compared to the joint *sliding* yield *deformation*.
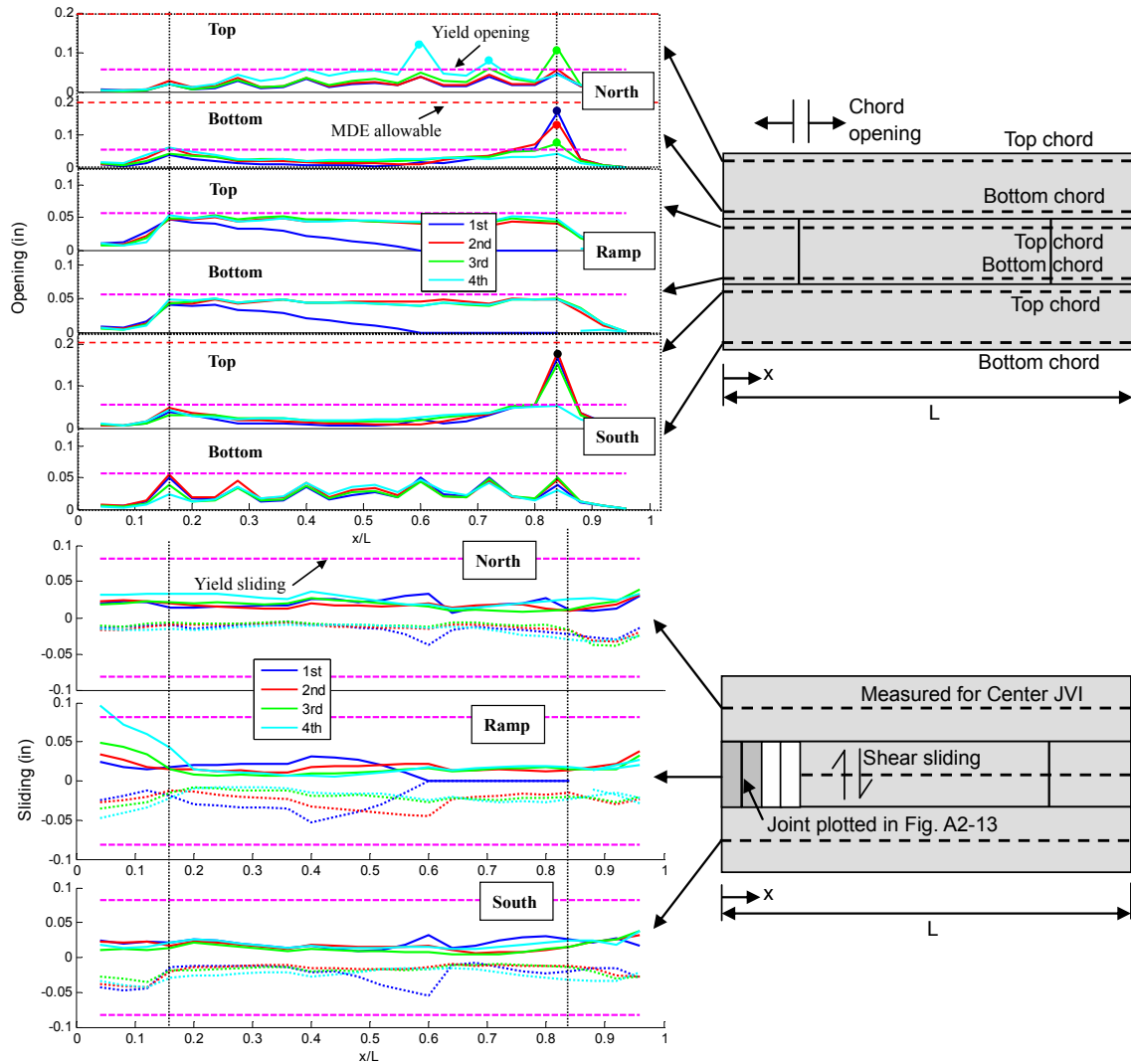
Fig. A2-19. Diaphragm reinforcement deformation demands: (a) chord opening; (b) shear sliding.

Figure A2-19 shows the maximum demands at every diaphragm joint in the structure for: (a) the chord opening at the top and bottom of each sub-diaphragm, and (b) the shear connector sliding at the center of each joint. Indicated in plot (a) is the yield opening deformation (purple large dashed line) for the flat plate chord connector and the MDE allowable deformation (red small dashed line) used to evaluate the adequacy of the trial Ψ_D value used in the design. Indicated in plot (b) is the yield sliding deformation for the JVI Vector connector used to evaluate the adequacy of the trial Ω_{vB} factor.

As seen in Fig. A2-19a, the flat plate chord connectors yield at multiple joints in the diaphragm, all at column lines where the spandrels terminate, including: (1) the top floor north flat sub-diaphragm perimeter chord at joints past mid-span on the up-ramp side (see light blue dots); (2) at the upper floors of the north flat at the joint collinear with the end of the ramp or ramp cavity on the up-ramp side (see green dots); (3) the lower floors of the north flat at the joint collinear with the end of the ramp on the up-ramp side (see red and dark blue dot); and (4) all floors of the south flat at the joint collinear with the end of the ramp on the up-ramp side (see black dot) Additionally, many joints possess connectors at or near their yield point as evidenced from response curves near the purple dashed line. The skewing of higher demands to the up-ramp site at the top floor is due to C.O.M. offset as described in the previous section. Of all yielded joints, only case 3 above is near the MDE allowable deformation, and in all places below this value. These results show the adequacy of the trial Ψ_D factor in meeting the BDO design target.

C-A-59

Now examining Fig. A2-19b, the shear connectors are within their elastic range for sliding deformation demands at all joints except a single location. This location is the end joint of the ramp landing area at the top floor. This joint is subjected to an inelastic sliding deformation of approximately 0.1″. This yielding is caused by a non-uniform distribution of the sliding demand along the joint (similar to that shown previously in Fig. A2-13a for Example 1A).

Figure A2-20 shows the force vs. deformation for the most critical loaded: (a) flat plate chord connector and (b) JVI Vector shear connector. The inelastic shear sliding response exhibited is considered sufficiently localized and small in magnitude to be accommodated by the limited shear plastic redistribution qualities of the JVI Vector connector or similar. Thus the adequacy of Ω_{VB} is considered demonstrated by the results.
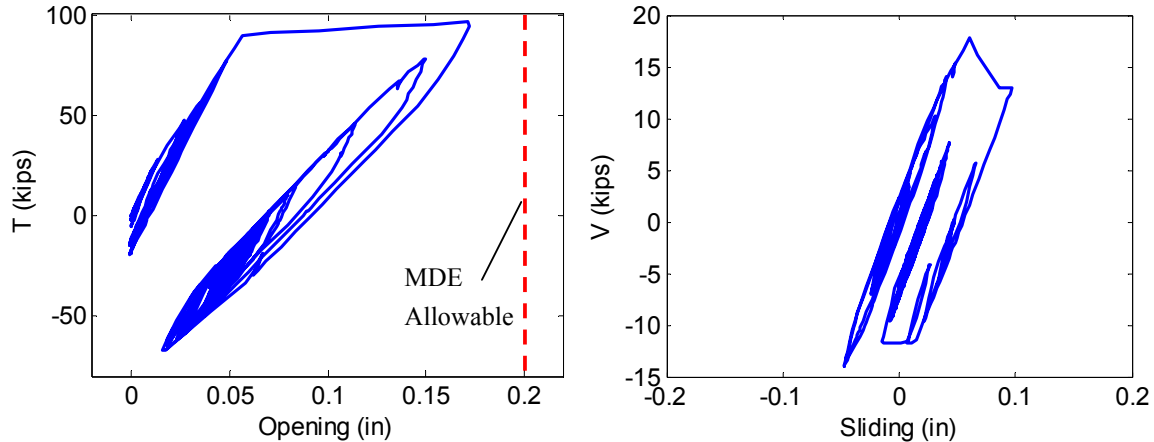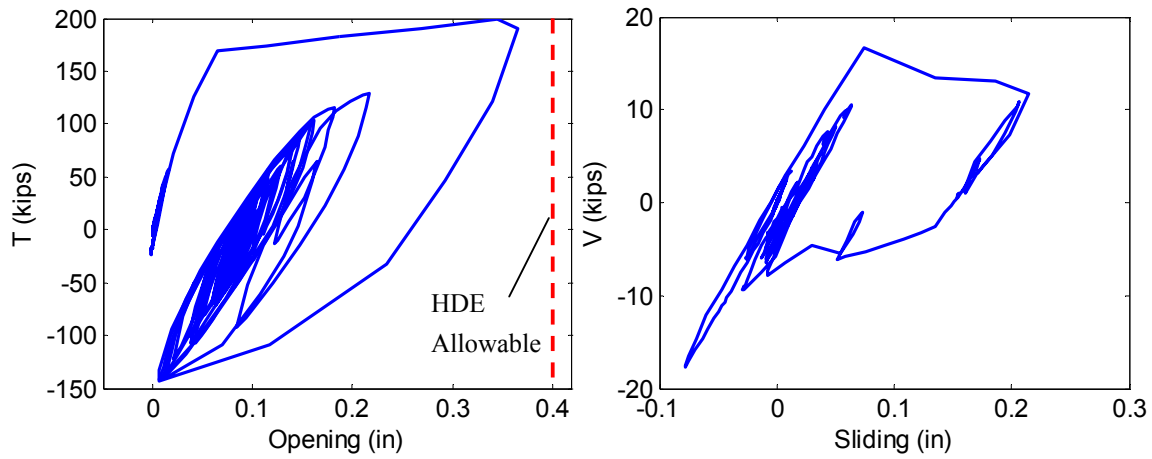

Fig. A2-20. Force vs. deformation response for: (a) chord connector in tension; (b) JVI in shear.

Similar demands to that presented for Example 1A in Section 2.3.1 are observed for the diaphragm-to-LFRS connection (See Sec A.2.4.1), the diaphragm secondary connection including internal beam connection and spandrel beam connection (See Sec A2.4.2), and the expansion joint (See Sec A.2.4.5). These demands are discussed in Section 2.4 in the section noted above.

Based on the analytical results for the BDO diaphragm design 4-story exterior shear wall parking structure (Design found in Example 1B in PART4) under a bi-directional MCE hazard level ground motion, the following conclusions are made:

(1) The diaphragm chord reinforcement inelastic deformation demands meet the design target for MCE level hazard: inelastic opening within the MDE allowable of 0.2″ for the flat plate chord connector.

DESIGN CONCLUSION: The BDO diaphragm design force $\Psi_D F_{Dx}$ is appropriate for this design case.

(2) The diaphragm shear reinforcement response meets the design target for MCE level hazard: elastic shear response), at all diaphragm joints except one. The yield sliding demand is caused by the non-uniform distribution of sliding along diaphragm joint.

DESIGN CONCLUSION: The BDO diaphragm design shear force overstrength factor Ω_{VB} is appropriate for this design case.

Similar to the conclusions for Example 1A:

(3) Significant opening and sliding deformation occurs at the expansion joint and at the flexible angle connector between the litewall and ramp. .

(4) Significant inelastic deformation demand is observed at the diaphragm to litewall connectors near the expansion joint.

(5) Diaphragm-to-LFRS connections remain elastic at most locations except localized minor yielding at two locations (south west wall and north west wall at top floor).

(6) Yielding occurs in the internal beam and spandrel beam to diaphragm connectors.

A2.3.3 Four-story parking garage w/exterior shear wall: SDC C RDO (Example 1C)

The third prototype structure diaphragm design evaluation involves a SDC C RDO diaphragm design option for the same 4-story exterior shear wall parking garage from the previous two sections. The earthquake simulation is NLTDA under bi-directional components of a MCE-level ground motion. The prototype structure diaphragms are designed using the PART 1 design procedure, as described in Example 1C of PART 4.

The diaphragm design produced in Example 1C, PART 4 is shown in Figure A2-21. The chord reinforcement shown in right part and shear reinforcement shown in left part (since the diaphragm design is symmetric across the diaphragm span). The diaphragm reinforcement indicated in Fig. A2-21 is for the top floor; the design for the other floors is indicated in parentheses if different from the top floor. The pretopped diaphragm is detailed with high deformability element or HDE reinforcement (continuous chord reinforcement in a pour strip and JVI Vector flange-to-flange connectors respectively for flexure and shear reinforcement). The diaphragm design factors are $\Psi_R = 1.56$ and $\Omega_{vR} = 1.5$. The diaphragm design force profile is determined using the diaphragm force vertical distribution factor α_x.

The diaphragm-to-LFRS connection is steel reinforcing dowel bars extending into a pour strip, and designed for the tributary shear at each shear wall. The diaphragm to litewall connection on the parking flats is steel reinforcing dowel bars extending into a pour strip designed for tributary shear and axial force. The litewall-to-ramp connection is ½" steel angles with slotted holes for compliance. The spandrel-to-DT connection is the angle bar connectors. The IT to-DT connection is steel reinforcing dowel bars extending into a pour strip designed for the tributary shear and the axial/moment sub-diaphragm reactions at the IT beam. The IT-to-DT connections are designed for the tributary shear and a portion of diaphragm inertia force from the outer (flat) sub-diaphragms to the shear wall, These reinforcement details are also shown in Fig. A2-21 and discussed in detail in design example 1C of PART 4.
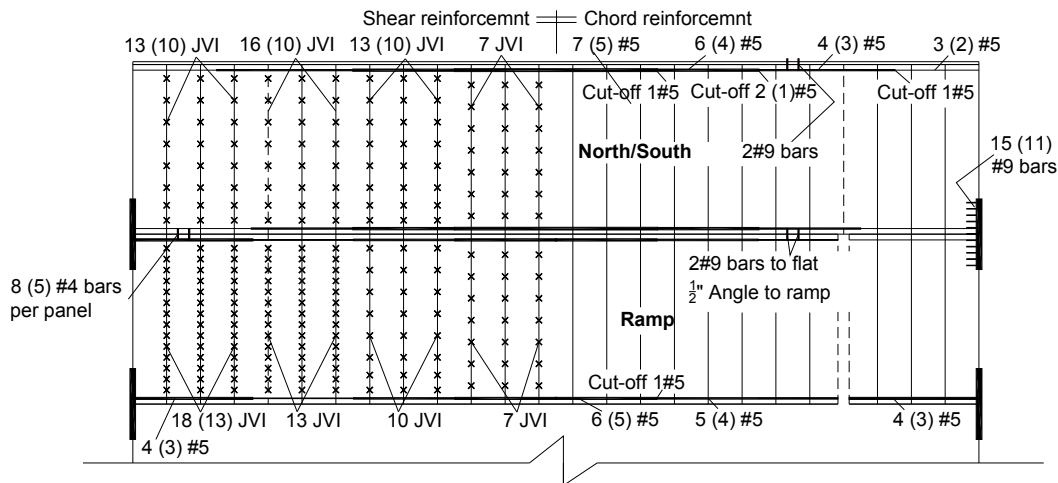
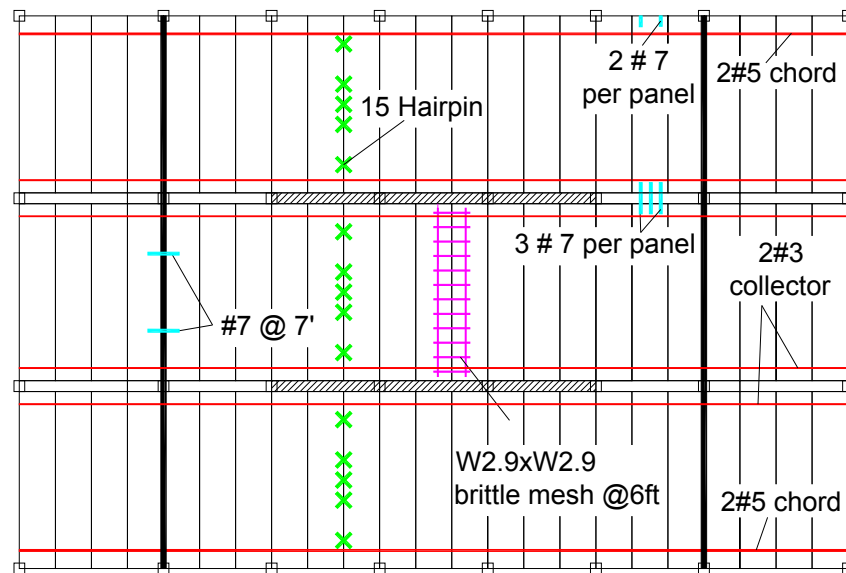**Fig. A2-21.** Diaphragm reinforcement design for design example 1C.

The RDO design target is inelastic deformation demands in the MCE within the HDE allowable deformation of 0.4″. As such, the pertinent measure for determining the adequacy of the design are deformation demands: (1) chord opening demands, which can be compared to the HDE allowable values; and (2) joint sliding deformations (relative transverse motion of units flanking the joint), that can be compared to the joint *sliding* yield *deformation*.
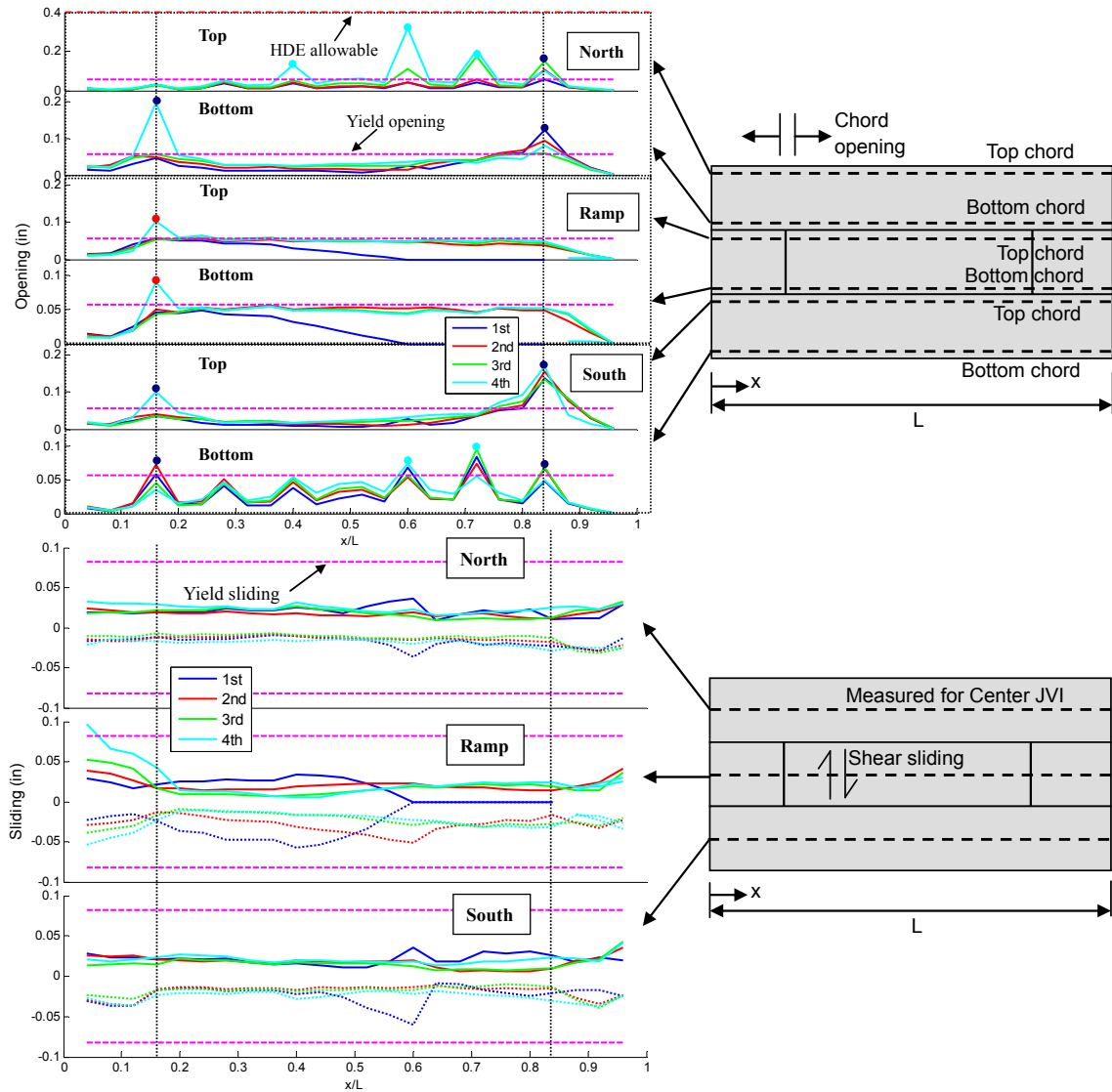
Fig. A2-22. Diaphragm reinforcement deformation demands: (a) chord opening; (b) shear sliding.

Figure A2-22 shows the maximum diaphragm reinforcement demand at every diaphragm joint in the structure for: (a) the chord opening at the top and bottom of each sub-diaphragm, and (b) the shear connector sliding at the center of each joint. Indicated in plot (a) is the yield opening deformation (purple large dashed line) for the chord reinforcement and the HDE allowable deformation (red small dashed line) used to evaluate the adequacy of the trial Ψ_R value used in the design. Indicated in plot (b) is the yield sliding deformation (purple large dashed line) for the JVI Vector connector used to evaluate the adequacy of the trial Ω_{vR} factor.

As seen in Fig. A2-22a, the chord reinforcement yields at multiple joints in the diaphragm, all at column lines where the spandrels terminate, including: (1) on multiple floors at the north and south flat sub-diaphragms perimeter chords at joints past mid-span on the up-ramp side (see light blue dots); (2) on multiple floors of the north and south flat at the joint collinear with the end of the ramp on both the up-ramp and down-ramp side (see dark blue dots); and (3) the top floor ramp end joint on the down-ramp side (see red dots). Additionally, many joints possess connectors at or near their yield point as evidenced from response curves near the purple dashed line. The skewing of higher demands to the up-ramp site at the top floor is due to the C.O.M. offset as described previously. Of all yielded joints, none exceed the

C-A-62

HDE allowable deformation. These results show the adequacy of the trial Ψ_R factor in meeting the RDO design target.

Now examining Fig. A2-22b, the shear connectors are within their elastic range for sliding deformation demands at all joints except the same single location identified in Example 1B.

Figure A2-23 shows the force vs. deformation for the most critical loaded: (a) chord reinforcement and (b) JVI Vector shear connector. The inelastic shear sliding response exhibited is considered sufficiently localized and small in magnitude to be accommodated by the limited shear plastic redistribution qualities of the JVI Vector connector or similar. Thus the adequacy of Ω_{VR} is considered demonstrated by the results.
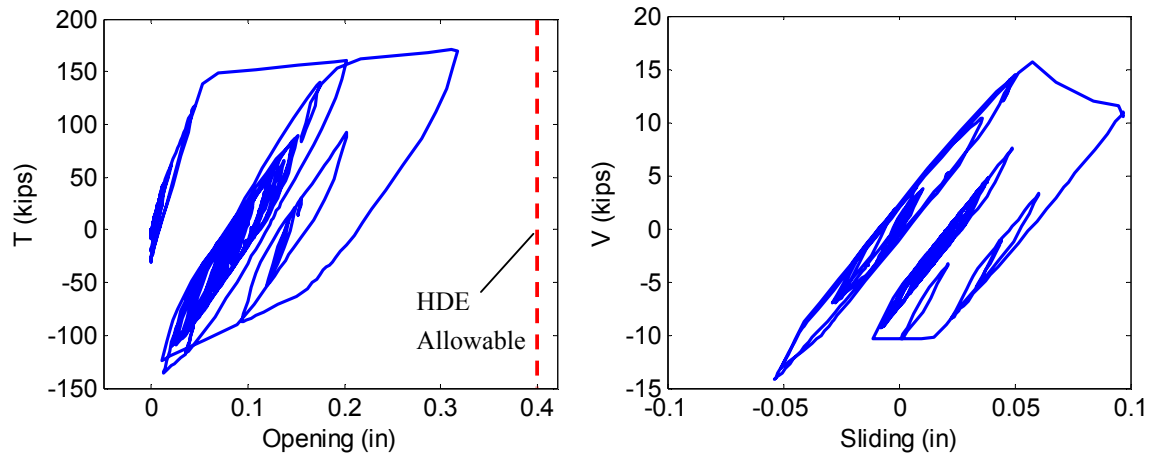
Fig. A2-23. Force vs. deformation response for: (a) chord connector in tension; (b) JVI in shear.

Figure A2-24 shows the maximum inter-story drift profile at the most critical sub-diaphragm (north of top floor) including: (1) gravity column drift at midspan (solid blue line); (2) LFRS drift (solid pink line); and (3) drift induced by diaphragm deformation (solid green). Also plotted in the Fig. A2-24 is the current code gravity column MCE limit (ASCE 7 2005) and the diaphragm induced drift limit based on the design procedure (See step 12 in PART 1). As seen, the gravity column drift is less than the current code limit and the diaphragm induced drift is less than the limit specified in the design procedure.
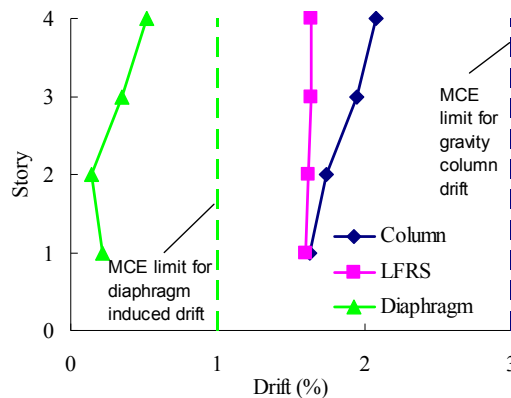
Fig. A2-24. Maximum inter-story drift profile at north sub-diaphragm of top floor.

Similar demands to that presented for Examples 1A,B in Sections 2.3.1 and 2.3.2 are observed in the diaphragm-to-LFRS connection (See Sec A.2.4.1), diaphragm secondary connection including internal beam connection and spandrel beam connection (See Sec A2.4.2), and expansion joint (See Sec A.2.4.5) as observed in Example 1A. These demands are discussed in Section 2.4 in the section noted above.

Based on the analytical results for the RDO diaphragm design 4-story exterior shear wall parking structure (Design found in Example 1C in PART4) under a bi-directional MCE hazard level ground motion, the following conclusions are made:

(1)   The diaphragm chord reinforcement inelastic deformation demands meet the design target for MCE level hazard: inelastic opening within the HDE allowable of 0.4″ for the chord reinforcement,
     DESIGN CONCLUSION: The RDO diaphragm design force $\Psi_R F_{Dx}$ is appropriate for this design case.

(2)   The diaphragm shear reinforcement response meets the design target for MCE level hazard (elastic shear response), at all diaphragm joints except one. The yield sliding demand is caused by the non-uniform distribution of sliding along diaphragm joint.
     DESIGN CONCLUSION: The RDO diaphragm design shear force overstrength factor Ω_{VR} is appropriate for this design case.

(3)   The diaphragm induced gravity column drift meets the design limit.
     DESIGN CONCLUSION: The diaphragm induced gravity column drift check in the design procedure is sufficient.

Similar to the conclusions for Example 1A:

(1)   Significant opening and sliding deformation occurs at the expansion joint and at the flexible angle connector between the litewall and ramp..
(2)   Significant inelastic deformation demand is observed at the diaphragm to litewall connectors near the expansion joint.
(3)   Diaphragm-to-LFRS connections remain elastic at most locations except localized minor yielding at two locations (south west wall and north west wall at top floor).
(4)   Yielding occurs in the internal beam and spandrel beam to diaphragm connectors.

A2.3.4 Four-story parking garage w/interior shear wall: SDC C EDO (Example 2A)

The fourth prototype structure diaphragm design evaluation involves a SDC C EDO diaphragm design option for a 4-story *interior* shear wall parking garage. The earthquake simulation is NLTDA under bi-directional components of a MCE-level ground motion. The prototype structure diaphragms are designed using the PART 1 design procedure, as described in Example 2A of PART 4.

The diaphragm design produced in Example 2A, PART 4 is shown in Figure A2-25. The chord reinforcement shown in right part and shear reinforcement shown in left part (since the diaphragm design is symmetric across the diaphragm span). The diaphragm reinforcement indicated in Fig. A2-25 is for the top floor; the design for the other floors is indicated in parentheses if different from the top floor. The pretopped diaphragm is detailed with low deformability element or LDE reinforcement (dry chord connector and JVI Vector flange-to-flange connectors respectively for flexure and shear reinforcement). The diaphragm design factors are $\Psi_E = 2.86$ and $\Omega_{vE} = 1.0$. The diaphragm design force profile is determined using the diaphragm force vertical distribution factor α_x.

The diaphragm-to-LFRS connection is angle bar connectors designed for the tributary shear and negative moment at each shear wall. The diaphragm to litewall connection on the parking flats is the angle bar connector designed for tributary shear and axial force. The litewall-to-ramp connection is ½" steel angles with C-shape welding for tension compliance. The spandrel-to-DT connection and IT to-DT connection is also angle bar connectors. The IT-to DT connections are designed for the tributary shear and a portion of diaphragm inertia force from the outer (flat) sub-diaphragms to the shear wall. These reinforcement details are also shown in Fig. A2-25 and discussed in detail in design example 2A of PART 4.
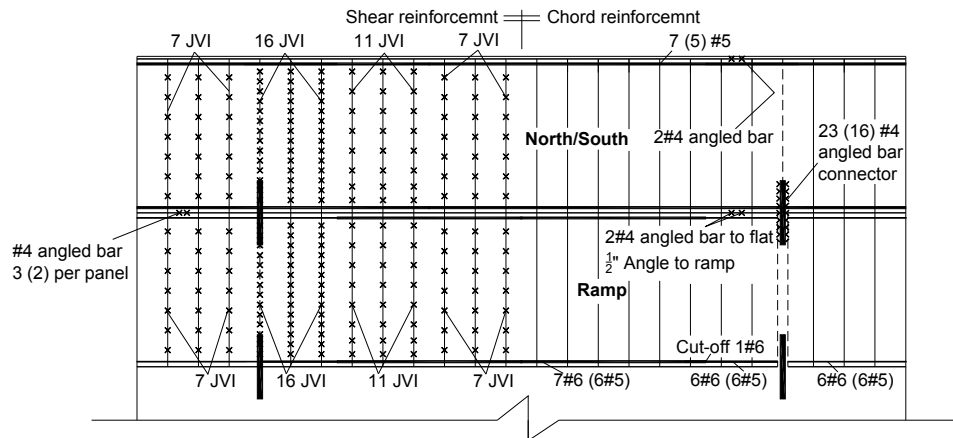
Fig. A2-25. Diaphragm reinforcement design for design example 2A.
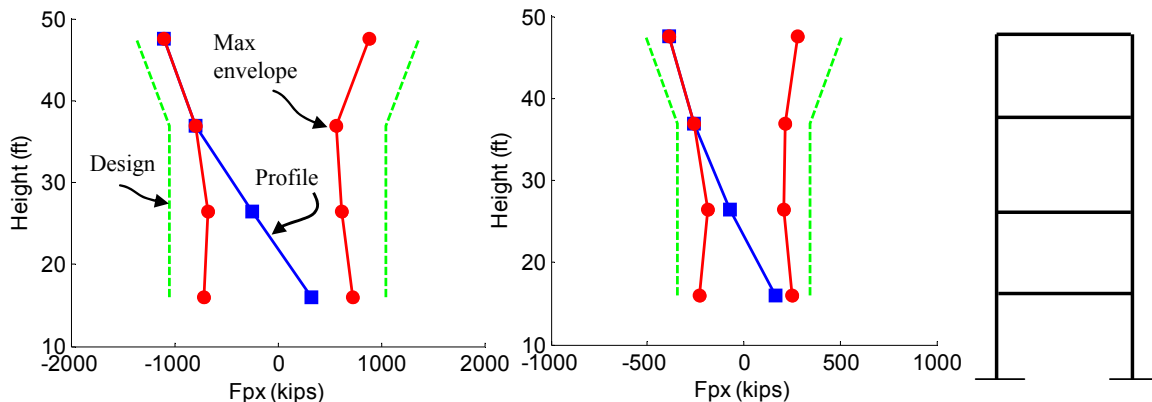
Fig. A2-26. Diaphragm inertia force in transverse direction: (a) floor total; (b) north sub-diaphragm

Figure A2-26 shows the maximum diaphragm inertial force profile along the building height in the structure transverse (N/S) direction for: (a) total inertial force at a floor level and (b) tributary inertia force at north sub-diaphragm. Three different profiles are indicated: (1) the design profile, $\alpha_x \Psi_E F_{Dx}$, where α_x is the diaphragm force vertical distribution factor (α_x=1.0 at top floor and α_x =0.68 at other floors, see PART 1); (2) the envelope of maximums occurring at any time during the earthquake; and (3) the instantaneous profile at the time of the maximum diaphragm force occurring anywhere in the structure.

As seen in Fig. A2-26, the diaphragm design force overestimates the diaphragm total inertia force demand at each floor level. However, the north sub-diaphragm force demand is well represented by the diaphragm design force tributary to each sub-diaphragm because of the uneven distribution of diaphragm inertia force demand among each sub-diaphragm similar as the Example 1A.

Figure A2-27 shows maximum demands at every joint for: (a) chord opening at top and bottom of each sub-diaphragm, and (b) shear connector sliding at center of each sub-diaphragm. As seen in Fig. A2-27a, the chords remain elastic at nearly every joint, as desired in an EDO design. The exception is the chord on the 1st floor ramp span (see blue dots). This minor exceeding of chord yield deformation (0.0056″) was considered acceptable.
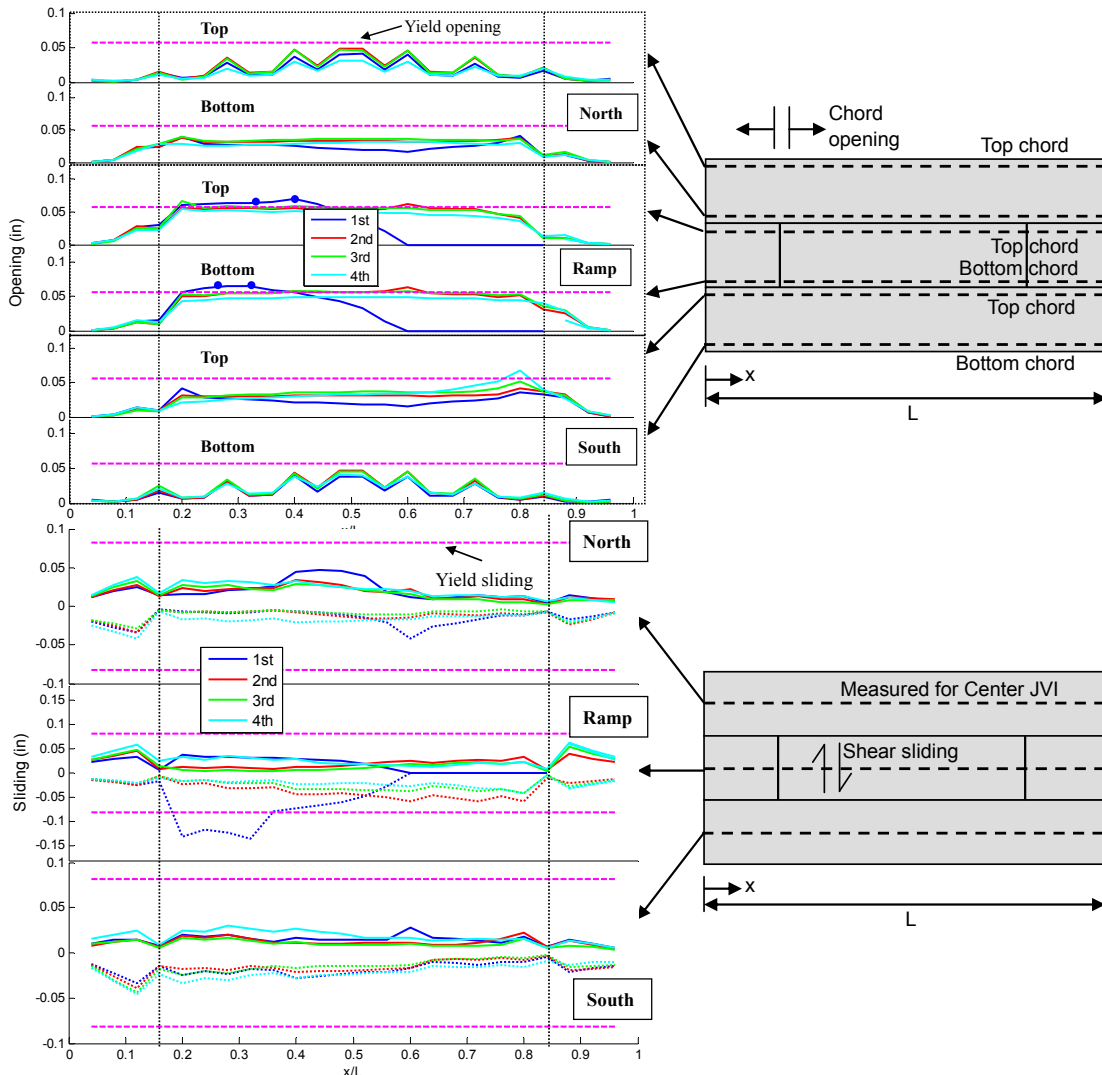
Fig. A2-27. Diaphragm reinforcement deformation demands: (a) chord opening; (b) shear sliding.

Now examining Fig. A2-27b, the shear connectors are within their elastic range for sliding deformation demands at all joints except several joints at 1st floor ramp span. This joint is subjected to an inelastic sliding deformation of approximately 0.15″. This yielding is caused by a non-uniform distribution of the sliding demand along the joint (similar to that shown previously in Fig. A2-13a for Example 1A).

Next consider the demands on the diaphragm-to-LFRS connections for the transverse shear walls. Figure A2-28 shows the maximum diaphragm-to-LFRS connector deformation demands for all four walls (refer to Fig. A2-1b). The value plotted is the largest opening and sliding demand on any single connector of the group of 23 connectors that comprise the diaphragm-to-LFRS connection at a single wall. First note in Fig. A2-28a that the opening demands indicate some connectors are slightly yield in South East and North West wall due to (longitudinal) axial forces in the diaphragm and the in-plane moment acting on the wall. Now moving to Fig. A2-28b, it is seen that the sliding deformation demands are within the elastic range at every location. Thus, the efficacy of the design of the diaphragm-to-LFRS connections (including both Ψ_E and Ω) seems given the localized and limited magnitude of the inelastic deformation demands. The design ramifications of diaphragm-to-LFRS connector responses and design recommendations are discussed in Section A2.4.1.
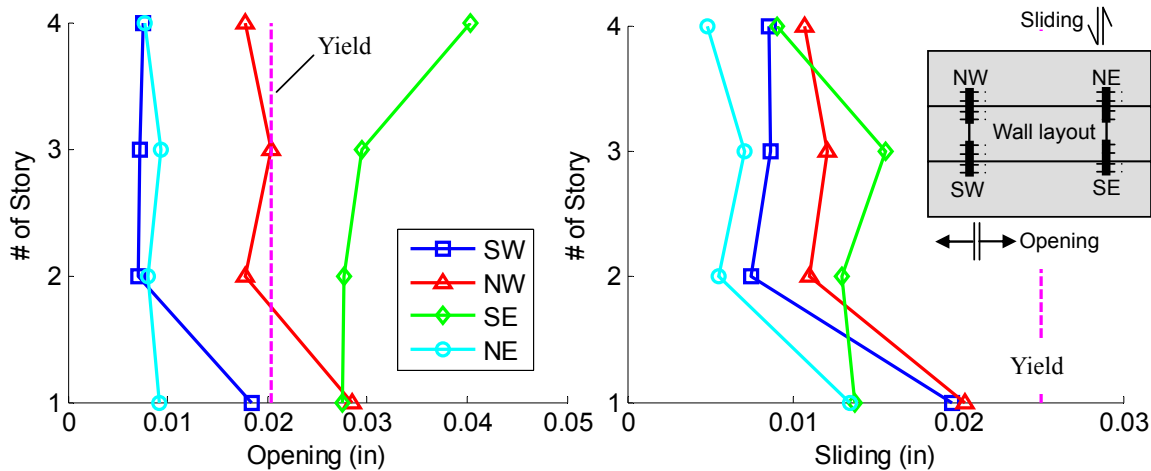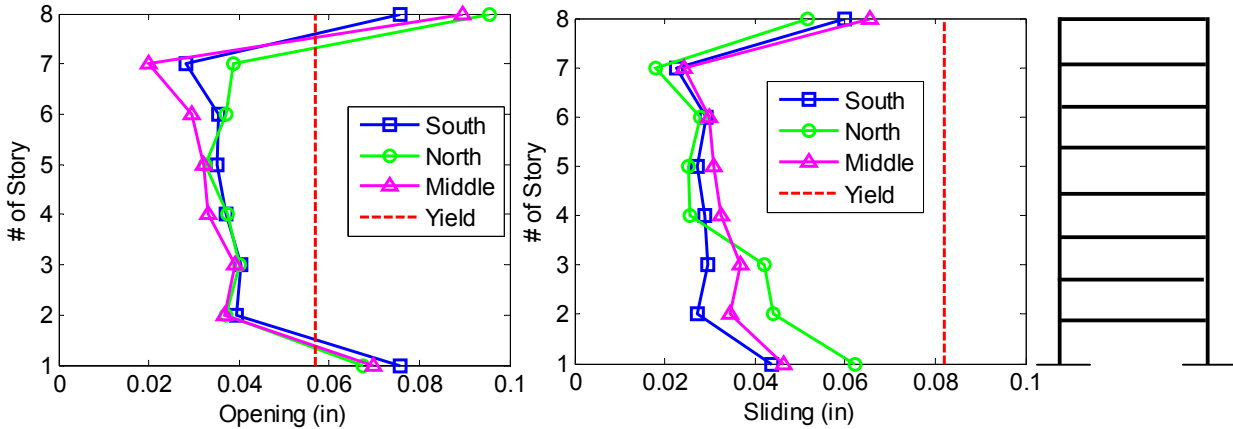

Fig. A2-28. Diaphragm-to-LFRS connection demand: (a) opening; (b) sliding.

Next, the connection demands on the interior beams lines are considered. The beam lines include three distinct connections: (1) diaphragm-to-internal beam connections (angled bar-plate connectors between the DT units and the IT beam flanking the ramp landing); (2) diaphragm-to-litewall connections on the parking flat side (angled bar-plate connectors between the litewall and DT); and, (3) diaphragm-to-litewall connections on the parking ramp side (steel angle connectors with C-shape welding).

The first set of connections is designed for tributary shear VQ/I with the Ω_V factor (See PART 4, Example 2A). The second set of connections is designed as the diaphragm-to-LFRS connections in the longitudinal direction, and are therefore designed for the diaphragm shear reaction including the Ω_V factor (See PART 4, Example 1A). The final set of connections are tension compliant connectors (see Sec. A2.4.5) that permit relative opening deformation due to the flexible angle connection, thereby mitigating the potential for incompatible displacements of the ramps and the flats subjecting the litewalls to severe internal forces.

Figure A2-29 shows the maximum deformation demands for connections along the interior beam lines of the parking structure. The plots show: opening of the beam line joint (left-hand plots), and sliding along the beam line joint (right-hand plots), for both the north (upper plots) and south (lower plots) beam lines. Each plot group shows the joint opening on either side of the beam line (inner and outer faces). Each plot shows the results for floors 2-4. The connector demands at the beam lines on the 1st floor are amplified because of the aforementioned expansion joint (discussed in *Section A2.4.5*).
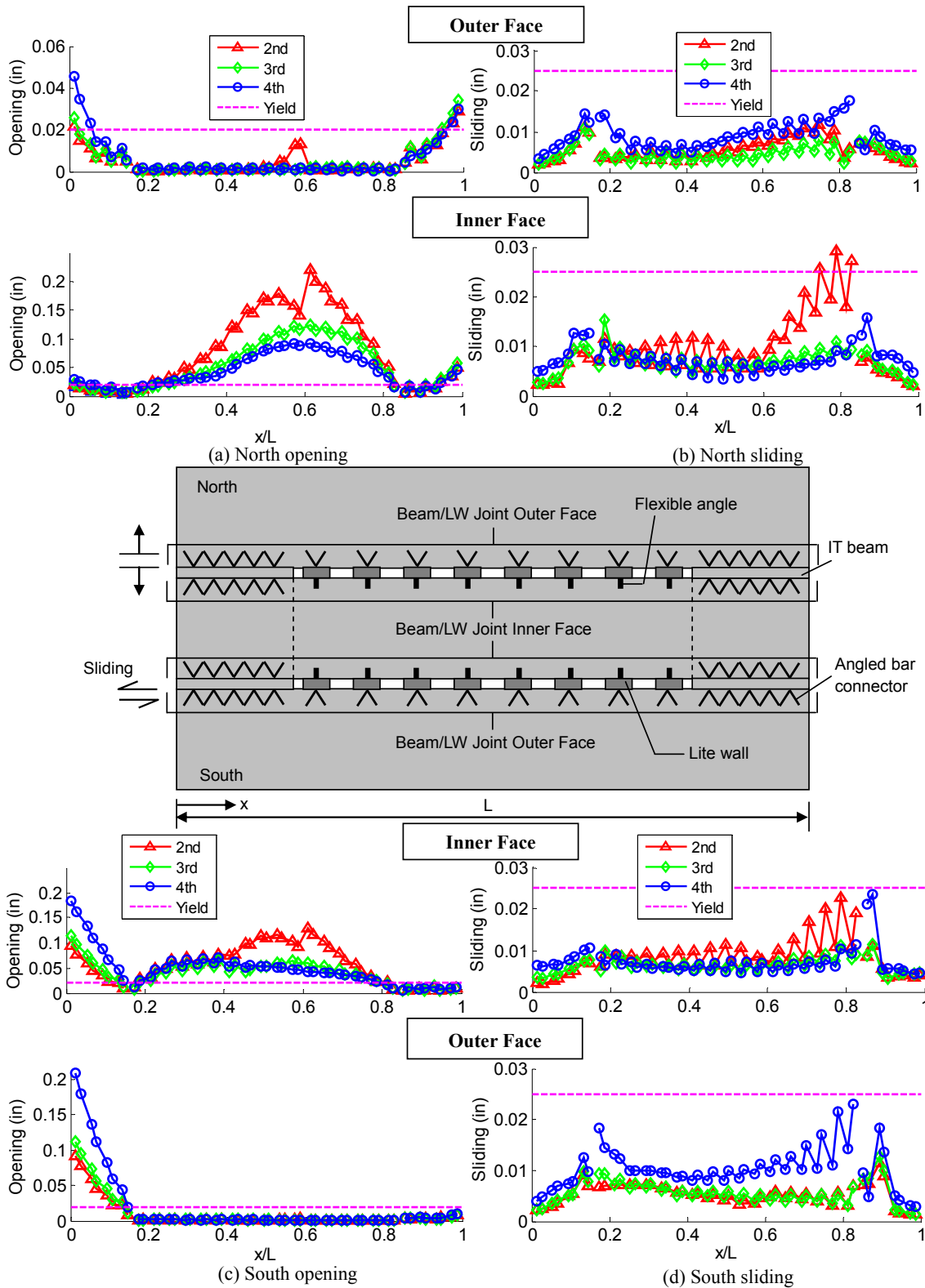
Fig. A2-29. Internal beam/litewall connector max demand: (a) opening; (b) sliding.

First, the connections on either face of the litewalls can be examined by focusing on the values between *x/L* =0.2 and 0.8 in the Fig. A2-29a plots. As seen, the compliance of the connections on the

ramp side (lower of the two plots in Fig. A2-29a) provides the intended outcome of reducing the demands on the connections to the parking flat side (upper of the two plots in Fig. A2-29a). These compliant connections are seen to require approximately ¼″ of opening deformation capacity to accommodate the relative movement anticipated in a MCE event.

By examining the upper of the two plots in both Fig. A2-29a,b, it is seen that all the load-carrying diaphragm-to-litewall LFRS connections are all well within their elastic range, showing the general efficacy of the diaphragm-to-LFRS design approach (See Sec. 3.2.B in PART 3).

Next, the diaphragm to IT beam connectors can be examined by focusing on the values outside of *x/L* =0.2 to 0.8 in the Fig. A2-29a, b plots. These results indicate that the sliding demands are within elastic range while the opening demands grow for connectors as one moves outward along the IT beam (small demands at the IT beam end at the interior shear wall; large demands at the IT beam outer end). The reason for this trend is the nature of the end moment actions across the IT joint (termed "seam") due to the bending of the flat sub-diaphragm, as has been described previously in (Fleischman et al. 1998). It is necessary to consider the deformation capacity of the IT beam connectors to accommodate these inelastic demands locally. The recommendation of the deformation capacity is discussed in Sec. A2.4.2

Similar demand and response are observed in the spandrel beam connection (See Sec A2.4.2), and expansion joint (See Sec A.2.4.5) as observed in Example 1. The demand levels of these joints are summarized in Sec. A.2.4.

The following conclusions are made based on the analytical results for the 4-story interior wall parking garage SDC C EDO design (Design found in Example 2A of PART4) under a bi-directional MCE hazard level ground motion:

(1) The total floor inertial force demands at each level are conservatively predicted by the EDO design force $\Psi_E F_{Dx}$. When these forces are considered on the individual sub-diaphragms, the inertial forces are more closely and still conservatively predicted, by $\Psi_E F_{Dx}$. These conclusions apply to both the transverse and longitudinal direction.
    DESIGN CONCLUSION: The EDO design force $\Psi_E F_{Dx}$ is appropriate for this design case.

(2) The vertical profile of maximum diaphragm inertial forces are reasonably predicted by the α_x pattern for low-rise parking structures, i.e. maximum at the top level and a constant lower value at the remaining floors.
    DESIGN CONCLUSION: The diaphragm force vertical distribution factor α_x is appropriate for this design case.

(3) Diaphragm reinforcement demands are within the design target (elastic behavior in the MCE) at most diaphragm joints. The localized, minor inelastic demands at a handful of joints were considered acceptable.
    DESIGN CONCLUSION: The elastic diaphragm design target was met for this EDO design using Ψ_E and Ω_{vE}.

(4) Diaphragm-to-LFRS connection remains elastic at most locations except a minor localized opening yield at several locations (in south east and north west wall).
    DESIGN CONCLUSION: The LFRS design using Ψ_E and Ω_{vE} is deemed acceptable.

(5) Large deformation demands are observed at the expansion joint and at the flexible angle connectors between the litewall and the ramp diaphragm.
(6) Significant inelastic deformation demand is observed at the diaphragm-to-litewall connectors near the expansion joint.
(7) Yield deformation occurs in the internal beam and the spandrel beam to diaphragm connections. Recommendations are provided in sec. A2.4.2.

A2.3.5 Four-story parking garage w/interior shear wall: SDC D RDO (Example 2B)

The fifth prototype structure diaphragm design evaluation involves a SDC D RDO diaphragm design option for the same 4-story interior shear wall parking garage from the previous section. The earthquake simulation is NLTDA under bi-directional components of a MCE-level ground motion. The prototype structure diaphragms are designed using the PART 1 design procedure, as described in Example 2B of PART 4.

The diaphragm design produced in Example 2A, PART 4 is shown in Figure A2-30. The chord reinforcement shown in right part and shear reinforcement shown in left part (since the diaphragm design is symmetric across the diaphragm span). The diaphragm reinforcement indicated in Fig. A2-30 is for the top floor; the design for the other floors is indicated in parentheses if different from the top floor. The pretopped diaphragm is detailed with high deformability element or HDE reinforcement (continuous chord reinforcement in a pour strip and JVI Vector flange-to-flange connectors respectively for flexure and shear reinforcement). The diaphragm design factors are $\Psi_R = 1.55$ and $\Omega_{vR} = 1.54$. The diaphragm design force profile is determined using the diaphragm force vertical distribution factor α_x.

The diaphragm-to-LFRS connection is steel reinforcing dowel bars extending into a pour strip, and designed for the tributary shear and negative moment at each shear wall. The diaphragm to litewall connection on the parking flats is steel reinforcing dowel bars extending into a pour strip designed for tributary shear and axial force. The litewall-to-ramp connection is ½" steel angles with C-shape welding for tension compliance. The spandrel-to-DT connection and IT to-DT connection is also steel reinforcing dowel bars extending into a pour strip. The IT-to DT connections are designed for the tributary shear and a portion of diaphragm inertia force from the outer (flat) sub-diaphragms to the shear wall. These reinforcement details are also shown in Fig. A2-30 and discussed in detail in design example 2B of PART 4.

Fig. A2-30. Diaphragm reinforcement design for design example 2B.

The RDO design target is inelastic deformation demands in the MCE within the HDE allowable deformation of 0.4″. As such, the pertinent measure for determining the adequacy of the design are deformation demands: (1) chord opening demands, which can be compared to the HDE allowable values; and (2) joint sliding deformations (relative transverse motion of units flanking the joint), that can be compared to the joint *sliding* yield *deformation*.

Figure A2-31 shows the maximum diaphragm reinforcement demand at every diaphragm joint in the structure for: (a) the chord opening at the top and bottom of each sub-diaphragm, and (b) the shear connector sliding at the center of each joint. Indicated in plot (a) is the yield opening deformation (purple large dashed line) for the chord reinforcement and the HDE allowable deformation (red small dashed line) used to evaluate the adequacy of the trial Ψ_R value used in the design. Indicated in plot (b) is the yield

sliding deformation (purple large dashed line) for the JVI Vector connector used to evaluate the adequacy of the trial Ω_{vR} factor.
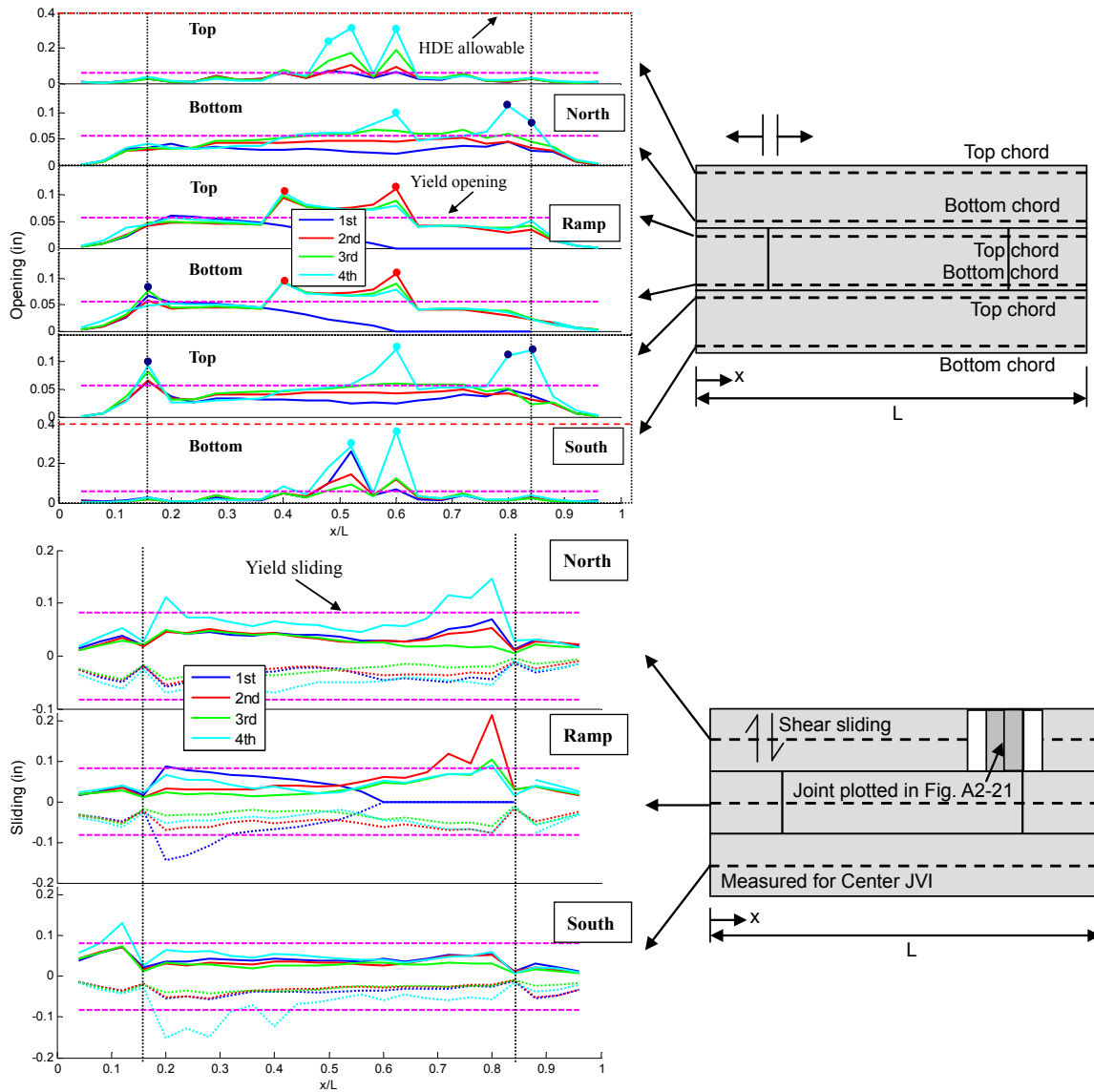
Fig. A2-31. Diaphragm reinforcement deformation demands: (a) chord opening; (b) JVI sliding.

As seen in Fig. A2-31a, the chord reinforcement yields at multiple joints in the diaphragm, all at column lines where the spandrels terminate, including: (1) on multiple floors at the north and south flat sub-diaphragms perimeter chords at joints past mid-span on the up-ramp side (see light blue dots); (2) on multiple floors of the joints near the interior wall; and (3) Joint near the mid-span of ramp on multiple floors (see red dots). Additionally, many joints possess connectors at or near their yield point as evidenced from response curves near the purple dashed line. Of all yielded joints, none exceed the HDE allowable deformation. These results show the adequacy of the trial Ψ_R factor in meeting the RDO design target.

Now examining Fig. A2-31b, the shear connectors are within their elastic range for sliding deformation demands at all joints except the joints near interior walls (see dark dots). These joints have moderate inelastic sliding demand (maximum at ~0.2″) for two reasons: (1) the non-uniform distribution across the joint similar as the Example 1; and (2) the flexural overstrength as discussed in Sec. A2.4.4.

The results in A2-32b indicate only minor strength degradation, rather than complete connector failure. Thus, the inelastic shear sliding response of the JVI Vector connectors is sufficiently accommodated. It is noted that other shear connectors may not have this level of plastic redistribution, and could instead "unzip". Given the localized nature and modest values of the inelastic demand, this behavior was considered acceptable. The shear performance of connectors under high tension (e.g. due to collector actions) is an important aspect, as covered later in Appendix A2 (See Section A2.4.7)

Figure A2-32 shows the force vs. deformation for the most critical loaded: (a) chord reinforcement and (b) JVI Vector shear connector. The inelastic shear sliding response exhibited is considered sufficiently localized and small in magnitude to be accommodated by the limited shear plastic redistribution qualities of the JVI Vector connector or similar. Thus the adequacy of Ω_{VR} is considered demonstrated by the results.

Fig. A2-32. Force vs. deformation response for: (a) chord connector in tension; (b) JVI in shear.

Similar demands to that presented for Example 2A in Sections 2.3.4 are observed in the diaphragm-to-LFRS connection (See Sec A.2.4.1), diaphragm secondary connection including internal beam connection and spandrel beam connection (See Sec A2.4.2), and expansion joint (See Sec A.2.4.5) as observed in Example 2A. These demands are discussed in Section 2.4 in the section noted above.

Based on the analytical results for the RDO diaphragm design 4-story interior shear wall parking structure (Design found in Example 2B in PART4) under a bi-directional MCE hazard level ground motion, the following conclusions are made:

(1) The diaphragm chord reinforcement inelastic deformation demands meet the design target for MCE level hazard: inelastic opening within the HDE allowable of 0.4″ for the chord reinforcement,

> **DESIGN CONCLUSION**: The RDO diaphragm design force $\Psi_R F_{Dx}$ is appropriate for this design case.

(2) The diaphragm shear reinforcement response meets the design target for MCE level hazard (elastic shear response), at all diaphragm joints except joints near the interior wall. The yield sliding demand is caused by the non-uniform distribution of sliding along diaphragm joint and the flexural overstrength.

> **DESIGN CONCLUSION**: The RDO diaphragm design shear force overstrength factor Ω_{VR} is appropriate for this design case.

Similar to the conclusions for Example 2A:

(3) Significant opening and sliding deformation occurs at the expansion joint and at the flexible angle connector between the litewall and ramp..

(4) Significant inelastic deformation demand is observed at the diaphragm to litewall connectors near the expansion joint.

(5) Diaphragm-to-LFRS connections remain elastic at most locations except a minor localized opening yield at several locations (in south east and north west wall).

(6) Yielding occurs in the internal beam and spandrel beam to diaphragm connectors.

A2.3.6   Eight-story office building w/moment frame: SDC C EDO (Example 3A)
        The sixth prototype structure diaphragm design evaluation involves a SDC C EDO diaphragm design option for an 8-story office building with moment frames. The earthquake simulation is performed through nonlinear transient dynamic analysis (NLTDA) under bi-directional components of a MCE-level ground motion. The diaphragm design of the prototype structure is based on the design procedure in PART 1. The design of this particular structure is described in Example 3A (PART 4).
        The final diaphragm design produced in Example 3A, PART 4 is shown in Figure A2-33. The diaphragm reinforcement indicated in Fig. A2-33 is for all floors. The topped diaphragm is detailed with LDE or above reinforcement (topped chord connectors and brittle mesh/topped hairpin flange-to-flange connectors respectively for flexure and shear reinforcement). The diaphragm design factors are $\Psi_E = 3.4$ and $\Omega_{vE} = 1.0$. A conservative constant profile is used for the diaphragm design force along building height.
        The diaphragm-to-LFRS connection in transverse and longitudinal directions is steel reinforcing dowel bars extending into the topping slab, and designed for the tributary shear and negative moment at each moment frame. The spandrel-to-DT connection and IT to-DT connection is also steel reinforcing dowel bars extending into the topping slab. The IT-to DT connections are designed for the tributary shear VQ/I. These reinforcement details are also shown in Fig. A2-33 and discussed in detail in design example 3A of PART 4.

Fig. A2-33. Diaphragm reinforcement design for design example 3A.

        Figure A2-34 shows the maximum diaphragm inertial force profile along the building height in the structure transverse (N/S) direction and the structure longitudinal direction. Three different profiles are indicated: (1) the design profile, $\Psi_E F_{Dx}$; (2) the envelope of maximums occurring at any time during the earthquake; and (3) the instantaneous profile at the time of the maximum diaphragm force occurring anywhere in the structure.
        As seen in Fig. A2-34, the diaphragm design force represents the maximum diaphragm inertia force demand at top floor in both transverse and longitudinal directions. However, in other floors, the diaphragm design force overestimates the diaphragm inertia force demand because a conservatively constant design profile is used. Based on the results shown in Fig. A2-34, a more economical design profile has been developed for the design procedure (See Appendix 1 in PART 1).
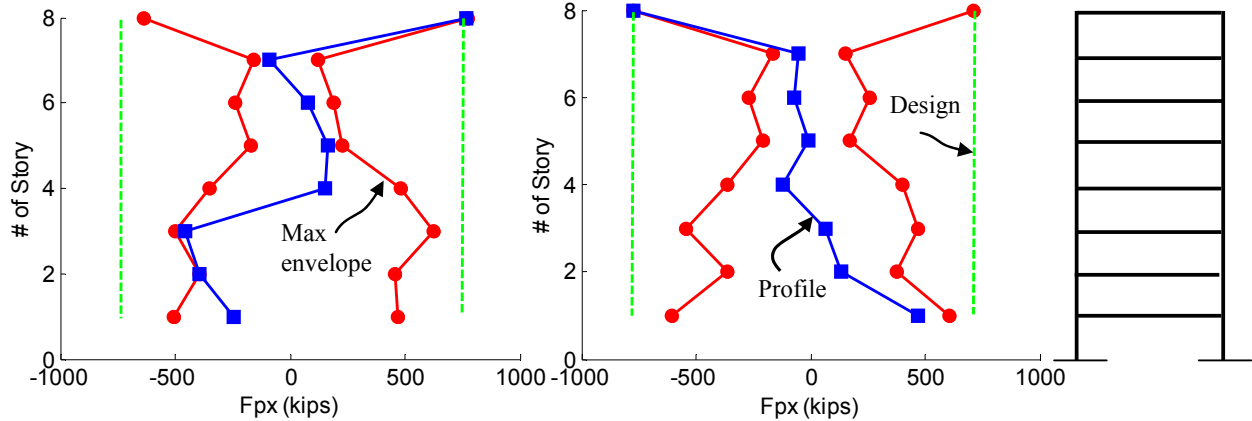
Fig. A2-34. Diaphragm inertia force: (a) transverse; (b) longitudinal

Figure A2-35 shows the diaphragm internal force diagrams (moment, axial and shear) for the top floor under the bi-directional ground motions. Each plot shows: (a) the envelopes of maximum positive and negative force response at any time during the earthquake; (b) the force profiles of the instant of maximum moment; and, (c) the design diagrams for required diaphragm strength using the FBD method from the design methodology. The design diagrams are calculated in Design Example 3 of PART 4.

As seen, the diaphragm internal force design diagrams (indicated as green line in Fig. A2-35) using FBD method in PART3 well represent the diaphragm internal force demand obtained from earthquake simulation.
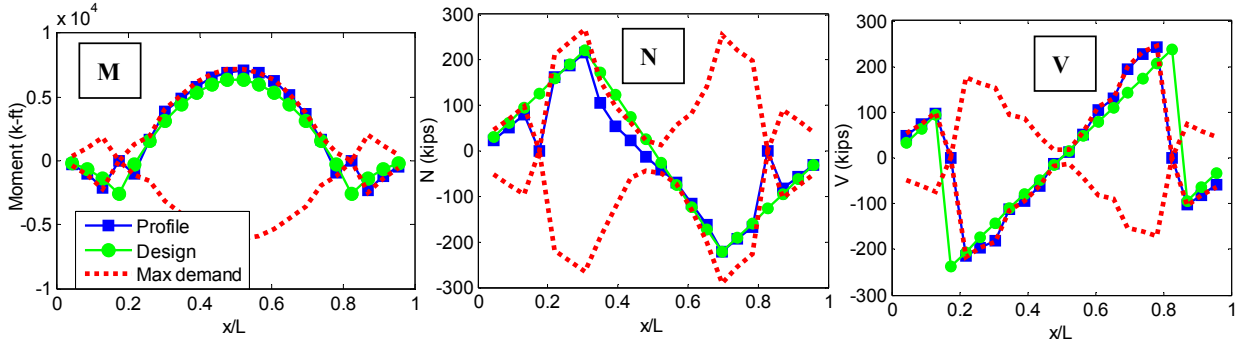
Fig. A2-35. Diaphragm internal force at top floor: (a) moment; (b) axial; (c) shear.
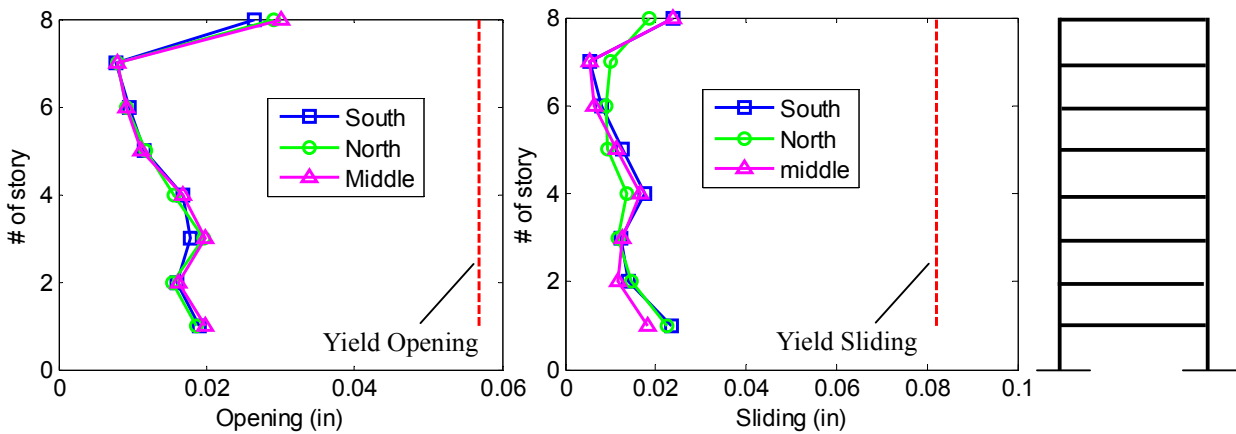
Fig. A2-36. Diaphragm reinforcement deformation demands: (a) Opening; (b) Sliding.

Figure A2-36 shows the diaphragm maximum joint deformation demand along building height in each sub-diaphragm for: (a) opening and (b) sliding. As seen, all the diaphragm joints remain elastic and the deformation demand is significantly less than the yield deformation. This is because the diaphragm reinforcement is sized using a commonly used minimum reinforcement rather than the calculated required diaphragm internal force demand (See Example 3A in PART 4).

Next consider the demands on the diaphragm-to-LFRS connections for the transverse moment frame. Figure A2-37 shows the maximum diaphragm-to-LFRS connector deformation demands. The value plotted is the largest opening and sliding demand on any single connector of the group all the connector across the joint between transverse moment frame and diaphragm. First note in Fig. A2-37a that slightly opening yield demand is observed at top and bottom floor due to the negative bending moment. Also note in Fig. A2-37b that minor inelastic opening demand occurs at top and bottom floor. This yielding in shear response is due to non-uniform distribution. Thus, the efficacy of the design of the diaphragm-to-LFRS connections (including both Ψ_E and Ω) seems given the localized and limited magnitude of the inelastic deformation demands. The diaphragm-to-LFRS connector responses are shown and design recommendations are discussed in Section A2.4.1.
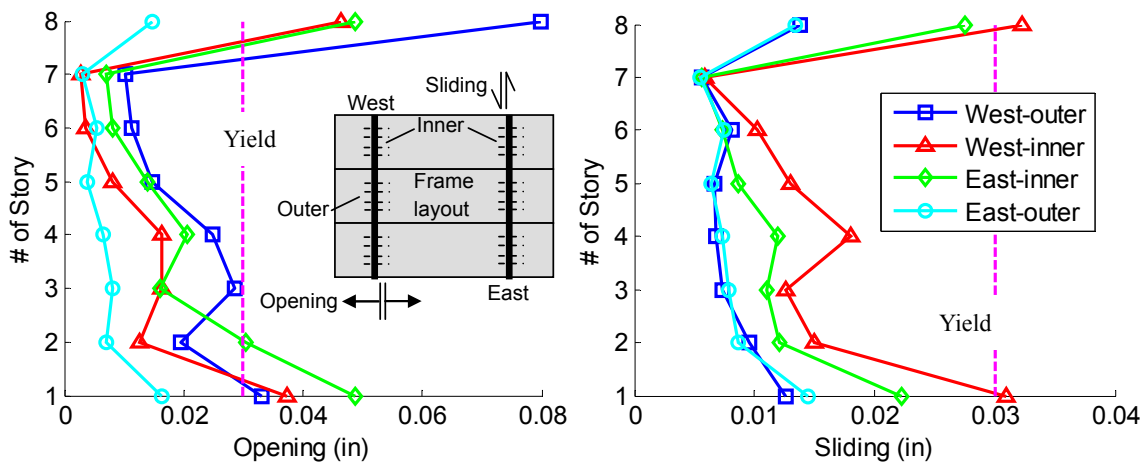
Fig. A2-37. Diaphragm-to-LFRS connection demand: (a) opening; (b) sliding.

Next, the connection demands on the interior beams lines are considered. Figure A2-38 shows the maximum deformation demand of diaphragm to internal beam/longitudinal frame beam connectors on the both north and south sides at each floor.

As seen in Fig. A2-38, these connectors remain elastic in both opening and sliding. This elastic response implies that the connectors in the interior beam lines designed with the tributary shear force can sufficiently transfer the seismic load.

Finally, consider the secondary diaphragm connections, i.e. the connections between the precast floor units and the perimeter spandrel beams. Figure A2-39 shows the maximum deformation demand of diaphragm to spandrel beam connectors on the both north and south sides at each floor. As seen, these connectors remain elastic in shear sliding. However slightly inelastic opening demand is observed in these connector.
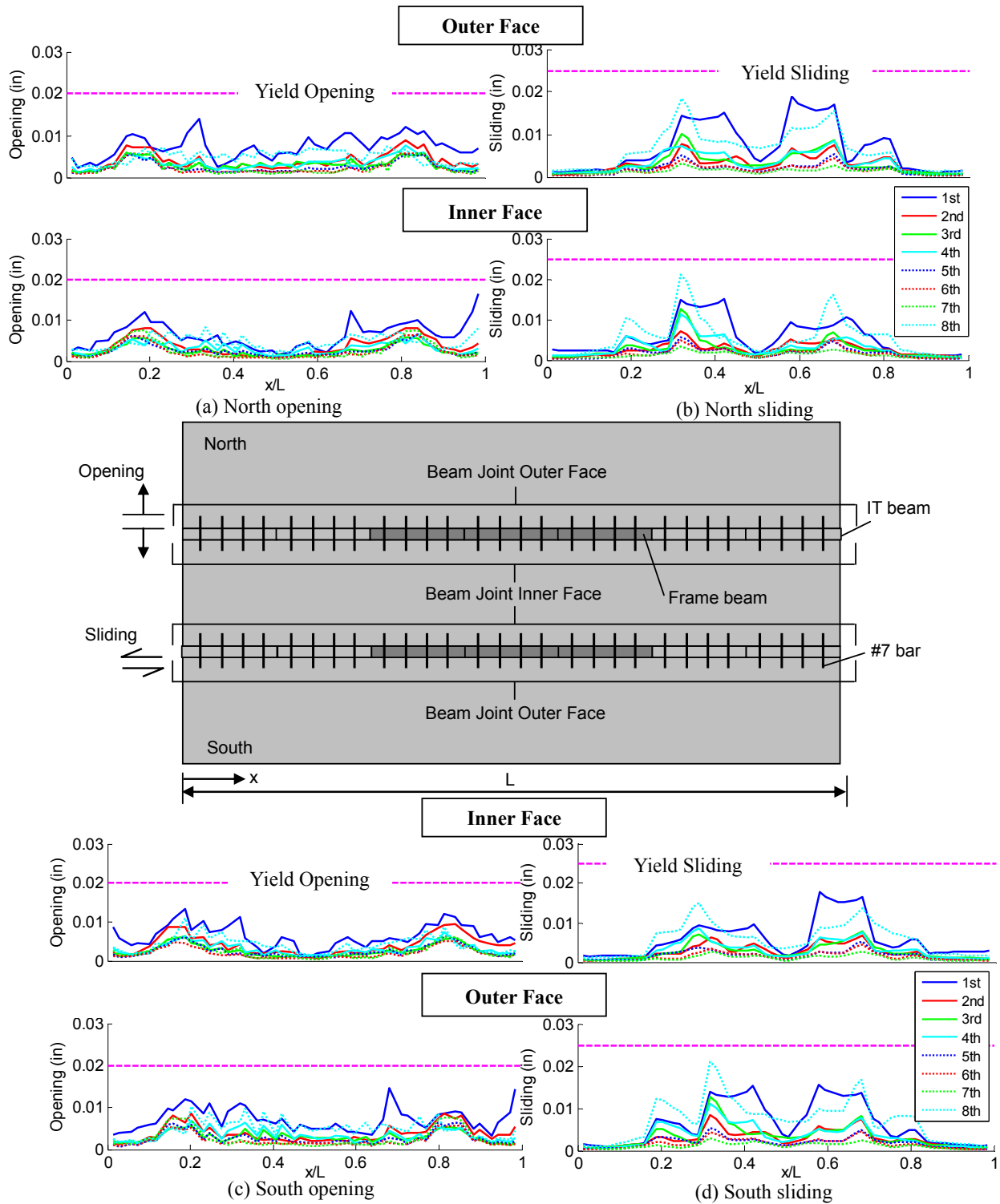
Fig. A2-38. Diaphragm internal beam joint deformation demand.

The following conclusions are made based on the analytical results for the 8-story moment frame office building SDC C EDO design (Design found in Example 3A of PART4) under a bi-directional MCE hazard level ground motion:

(1) The total floor inertial force demands at each level are conservatively predicted by the EDO design force $\Psi_E F_{Dx}$. The maximum inertial forces are closely predicted by $\Psi_E F_{Dx}$ at top floor. These conclusions apply to both the transverse and longitudinal direction.

> **DESIGN CONCLUSION**: The EDO design force $\Psi_E F_{Dx}$ is appropriate for this design case.

(2) The diaphragm design internal forces using the FBD method (See Sec 3.2.B in PART 3) show good agreement with the dynamic analysis results.

> **DESIGN CONCLUSION**: For this design example, the FBD method provides accurate force patterns.

(3) Diaphragm reinforcement demands are within the design target (elastic behavior in the MCE) at most diaphragm joints.

> **DESIGN CONCLUSION**: The elastic diaphragm design target was met for this EDO design using Ψ_E and Ω_{vE}.

(4) Diaphragm-to-LFRS connection remains elastic at most locations except a minor localized sliding and opening yield at top and bottom floor.

> **DESIGN CONCLUSION**: The LFRS design using Ψ_E and Ω_{vE} is deemed acceptable.

(5) Yield deformation occurs in the spandrel beam to diaphragm connections. Recommendations are provided in sec. A2.4.2.

Fig. A2-39. Spandrel to diaphragm connector deformation demand: (a) opening; (b) sliding.

A2.3.7 Eight-story office building w/moment frame: SDC D RDO (Example 3A)

The seventh prototype structure diaphragm design evaluation involves a SDC D RDO diaphragm design option for an 8-story office building with moment frames. The earthquake simulation is performed through nonlinear transient dynamic analysis (NLTDA) under bi-directional components of a MCE-level ground motion. The diaphragm design of the prototype structure is based on the design procedure in PART 1. The design of this particular structure is described in Example 3B (PART 4).

The final diaphragm design produced in Example 3B, PART 4 is shown in Figure A2-40. The topped hairpin connector shown in left part and ductile mesh reinforcement shown in left part (since the diaphragm design is symmetric across the diaphragm span). The diaphragm reinforcement indicated in Fig. A2-40 is for all floors. The topped diaphragm is detailed with HDE reinforcement (topped chord connectors and ductile mesh/topped hairpin flange-to-flange connectors respectively for flexure and shear reinforcement). The diaphragm design factors are $\Psi_E = 2.01$ and $\Omega_{vE} = 1.87$. A conservative constant profile is used for the diaphragm design force along building height.

The diaphragm-to-LFRS connection in transverse and longitudinal directions is steel reinforcing dowel bars extending into the topping slab, and designed for the tributary shear and negative moment at each moment frame. The spandrel-to-DT connection and IT to-DT connection is also steel reinforcing dowel bars extending into the topping slab. The IT-to DT connections are designed for the tributary shear VQ/I. These reinforcement details are also shown in Fig. A2-40 and discussed in detail in design example 3B of PART 4.

Also note in Fig. A2-40 that the chord reinforcement is selected as 4 #5. This design value is slightly larger than the design presented in PART 4 for Example 3B (3#5 is used). This difference is due to the different consideration for the design moment strength (M_n). In this section, the design moment strength is taken as $0.5M_y + 0.5M_p$, where M_y and M_p is the yield and plastic moment (See Sec. 3.3.B in PART 3). However in the design example shown in PART 4, the design moment strength has been modified to $1.0\ M_p$ based on the findings discussed in this section.
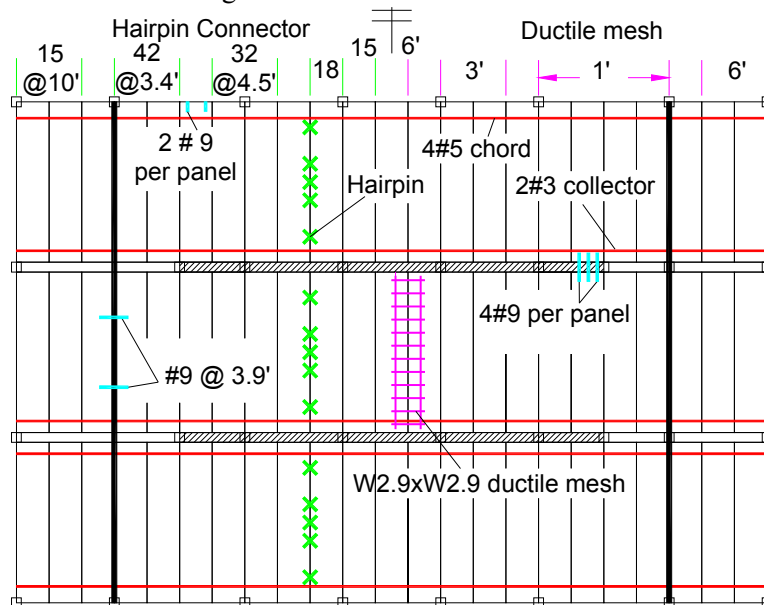
Fig. A2-40. Diaphragm reinforcement design for design example 3B.

The RDO design target is inelastic deformation demands in the MCE within the HDE allowable deformation of 0.4″. As such, the pertinent measure for determining the adequacy of the design are deformation demands: (1) chord opening demands, which can be compared to the HDE allowable values; and (2) joint sliding deformations (relative transverse motion of units flanking the joint), that can be compared to the joint *sliding* yield *deformation*.

Figure A2-41 shows the diaphragm maximum joint deformation demand along building height in each sub-diaphragm for: (a) opening and (b) sliding. As seen in Fig. A2-41b, all the diaphragm joints remain elastic in shear sliding which meet the elastic shear design tarter. Inelastic opening demand is observed in the diaphragm joints at top and bottom floors but the magnitude is conservatively lower than the HDE allowable opening demand (0.4″). This conservatively inelastic joint opening demand is caused by a large strain hardening in the diaphragm moment response after the perimeter chord reinforcement. This large strain hardening is due to a significant contribution of stiff web reinforcement (ductile mesh and topped hairpin). Thus for the design example shown in PART 3, the diaphragm moment nominal strength has been reduced to the M_p rather than $0.5(M_y+M_p)$ used in this evaluation.

Fig. A2-41. Diaphragm reinforcement deformation demands: (a) opening; (b) sliding.

Next, the connection demands on the interior beams lines are considered. Figure A2-42 shows the maximum deformation demand of diaphragm to internal/moment frame beam connectors on the both north and south sides at each floor. As seen in Fig. A2-42, these connectors remain elastic in shear sliding. Slightly inelastic opening demand is observed in the diaphragm to internal beam connectors at top and bottom floors.

Similar demands to that presented for Example 3A in Sections 2.3.6 are observed in the diaphragm-to-LFRS connection (See Sec A.2.4.1) and diaphragm secondary connection including spandrel beam connection (See Sec A2.4.2). These demands are discussed in Section 2.4 in the section noted above.

The following conclusions are made based on the analytical results for the 8-story moment frame office building SDC D RDO design (Design found in Example 3B of PART4) under a bi-directional MCE hazard level ground motion:

(1) The diaphragm chord reinforcement inelastic deformation demands conservatively lower than the design target for MCE level hazard: inelastic opening within the HDE allowable of 0.4″ for the chord reinforcement.
    DESIGN CONCLUSION: The RDO diaphragm design force $\Psi_R F_{Dx}$ is appropriate for this design case.

(2) The diaphragm shear reinforcement response meets the design target for MCE level hazard (elastic shear response).
    DESIGN CONCLUSION: The RDO diaphragm design shear force overstrength factor Ω_{VR} is appropriate for this design case.

(3) The connectors between diaphragm internal beam joint remain elastic at most location except slightly sliding yield at 1st floor and top floors

Similar to the conclusions for Example 3A:

(4) Diaphragm-to-LFRS connection remains elastic at most locations except a minor localized sliding and opening yield at top and bottom floor.

   DESIGN CONCLUSION: The LFRS design using Ψ_E and Ω_{vE} is deemed acceptable.

(5) Yield deformation occurs in the spandrel beam to diaphragm connections. Recommendations are provided in sec. A2.4.2.
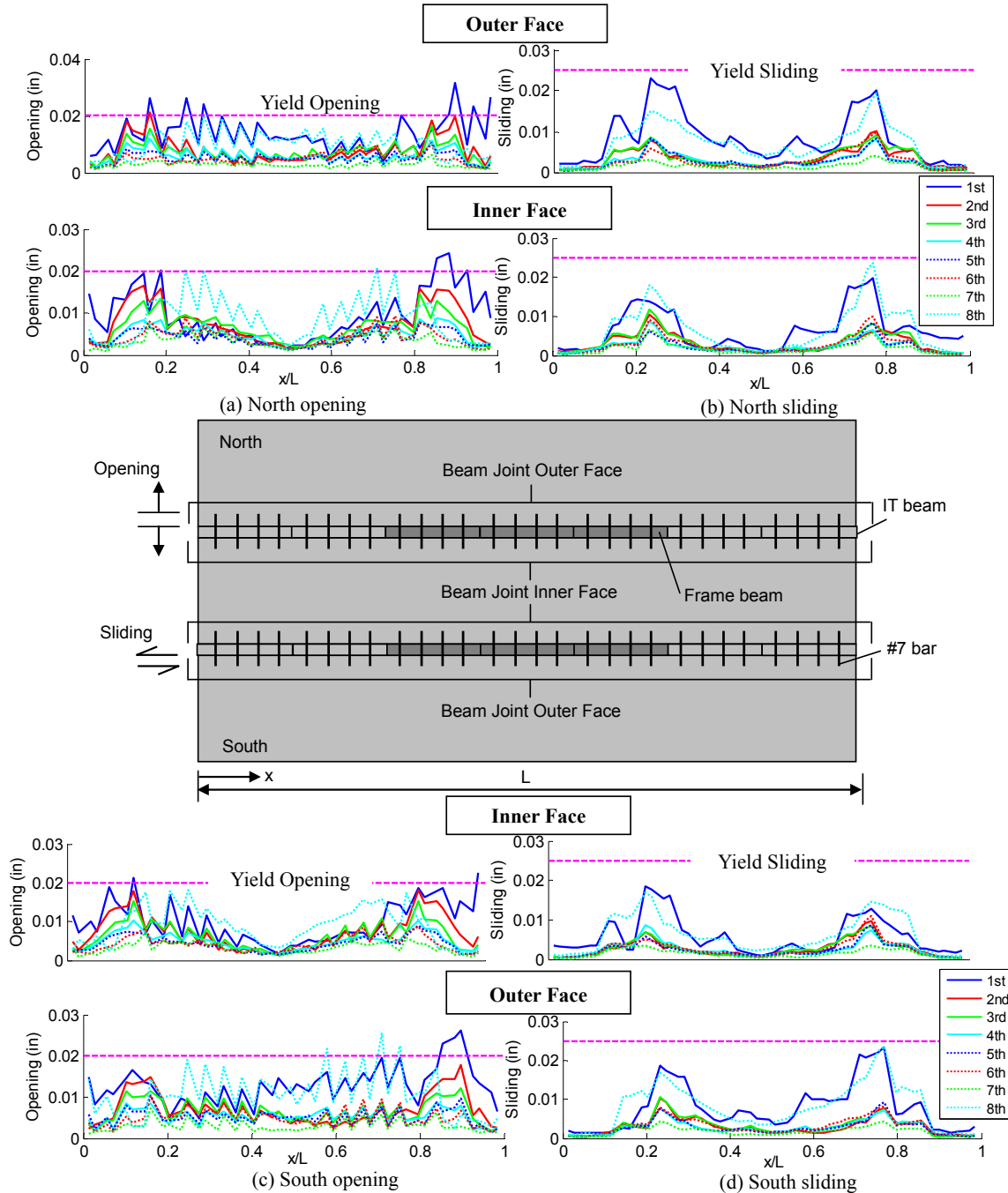
Fig. A2-42. Diaphragm internal/frame beam joint demand.

A2.3.8 Eight-story office building w/ perimeter shear walls: SDC C EDO (Example 4A)

The eighth prototype structure diaphragm design evaluation involves a SDC C EDO diaphragm design option for an 8-story office building with perimeter shear walls. The earthquake simulation is performed through nonlinear transient dynamic analysis (NLTDA) under bi-directional components of a MCE-level ground motion. The diaphragm design of the prototype structure is based on the design procedure in PART 1. The design of this particular structure is described in Example 4A (PART 4).

The final diaphragm design produced in Example 4A, PART 4 is shown in Figure A2-43. The diaphragm reinforcement indicated in Fig. A2-43 is for all floors. The topped diaphragm is detailed with LDE or above reinforcement (topped chord connectors and brittle mesh/topped hairpin flange-to-flange connectors respectively for flexure and shear reinforcement). The diaphragm design factors are $\Psi_E = 3.79$ and $\Omega_{vE} = 1.0$. A conservative constant profile is used for the diaphragm design force along building height.

The diaphragm-to-LFRS connection in transverse and longitudinal directions is steel reinforcing dowel bars extending into the topping slab, and designed for the tributary shear at each wall. The spandrel-to-DT connection and IT to-DT connection is also steel reinforcing dowel bars extending into the topping slab. The IT-to DT connections are designed for the tributary shear VQ/I. These reinforcement details are also shown in Fig. A2-43 and discussed in detail in design example 4A of PART 4.
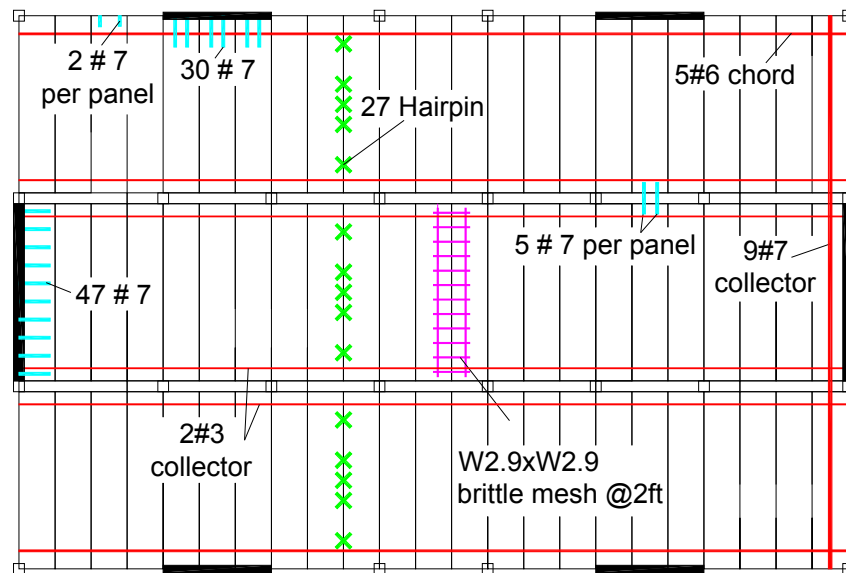
Fig. A2-43. Diaphragm reinforcement design for design example 4A.

Figure A2-44 shows the maximum diaphragm inertial force profile along the building height in the structure transverse (N/S) direction and the structure longitudinal direction. Three different profiles are indicated: (1) the design profile, $\Psi_E F_{Dx}$; (2) the envelope of maximums occurring at any time during the earthquake; and (3) the instantaneous profile at the time of the maximum diaphragm force occurring anywhere in the structure.

As seen in Fig. A2-44a, the diaphragm design force represents the maximum diaphragm inertia force demand at top and 1st floors in transverse direction. However, in other floors, the diaphragm design force overestimates the diaphragm inertia force demand because a conservatively constant design profile is used. Based on the results shown in Fig. A2-44a, a more economical design profile has been developed for the design procedure (See Appendix 1 in PART 1). As seen in Fig. A2-44b, the diaphragm design force slightly overestimates the maximum diaphragm inertia force demand at all floors in longitudinal direction.
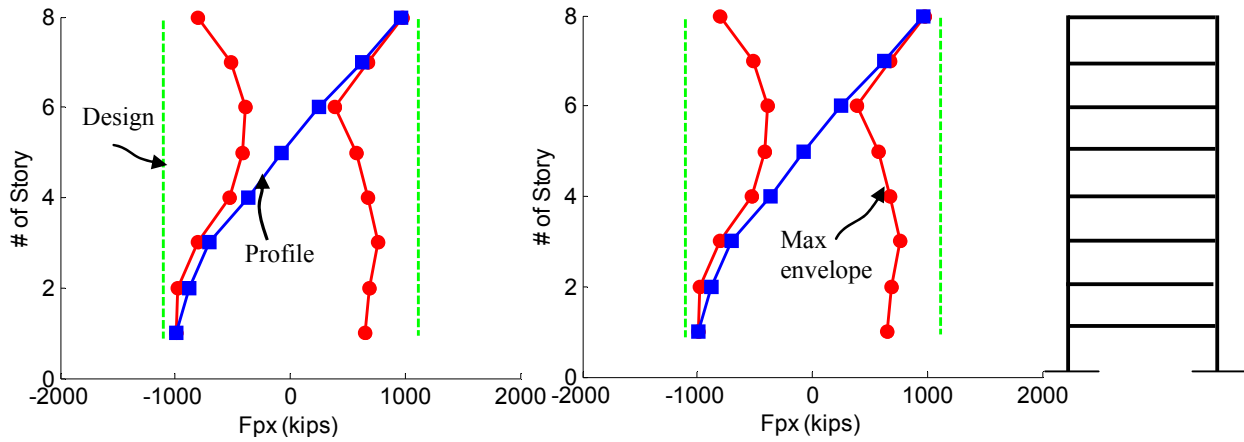
Fig. A2-44. Diaphragm inertia force: (a) transverse; (b) longitudinal

Figure A2-45 shows the diaphragm internal force diagrams (moment, axial and shear) for the top floor under the bi-directional ground motions. Each plot shows: (a) the envelopes of maximum positive and negative force response at any time during the earthquake; (b) the force profiles of the instant of maximum moment; and, (c) the design diagrams for required diaphragm strength using the FBD method from the design methodology. The design diagrams are calculated in Design Example 4 of PART 4.

As seen in Fig. A2-45, the diaphragm internal force design diagrams using FBD method in PART3 well represent the diaphragm internal force demand obtained from earthquake simulation.
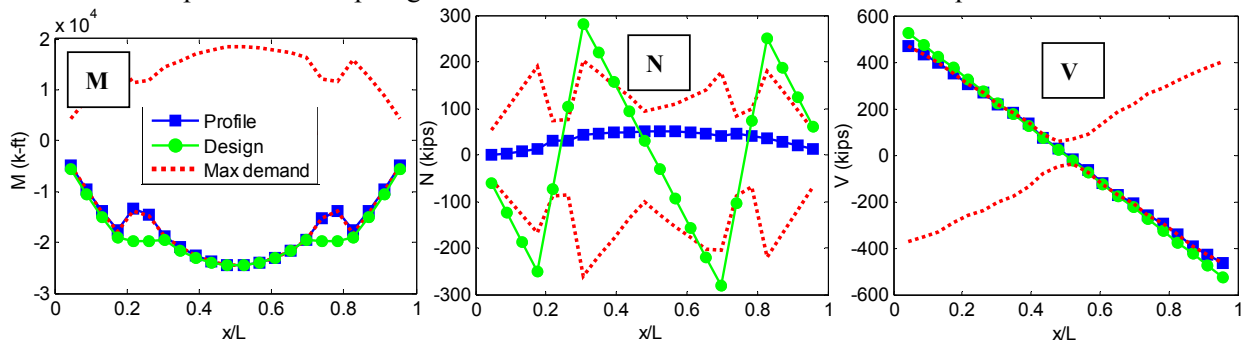
Fig. A2-45. Diaphragm internal force at top floor: (a) moment; (b) axial; (c) shear.

Figure A2-46 shows the diaphragm maximum joint deformation demand along building height in each sub-diaphragm for: (a) opening and (b) sliding. As seen, all the diaphragm joints remain elastic in both opening and sliding. Therefore the EDO design target is met.
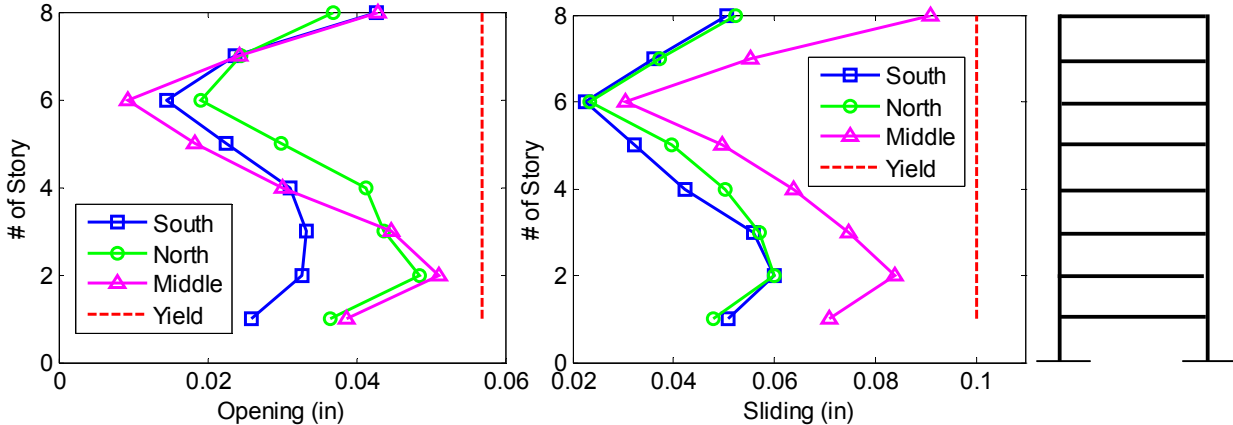
Fig. A2-45. Diaphragm reinforcement deformation demands: (a) chord opening; (b) JVI sliding.

Next consider the demands on the diaphragm-to-LFRS connections for the transverse and longitudinal walls. Figure A2-46 shows the maximum diaphragm-to-LFRS connector deformation demands. The value plotted is the largest opening and sliding demand on any single connector of the group all the connector across the joint between LFRS-to-diaphragm. As seen in Fig. A2-46a,d, the connectors in transverse walls remain elastic in opening and the connector in longitudinal walls remain elastic in shear sliding. As seen in Fig. A2-46b,c, inelastic sliding demand is observed in the connector of transverse walls at lower floors and inelastic opening demand is observed in the connector of longitudinal walls at lower floors. The efficacy of the design of the diaphragm-to-LFRS connections (including both Ψ_E and Ω) seems given the localized and limited magnitude of the inelastic deformation demands. The diaphragm-to-LFRS connector responses are shown and design recommendations are discussed in Section A2.4.1.
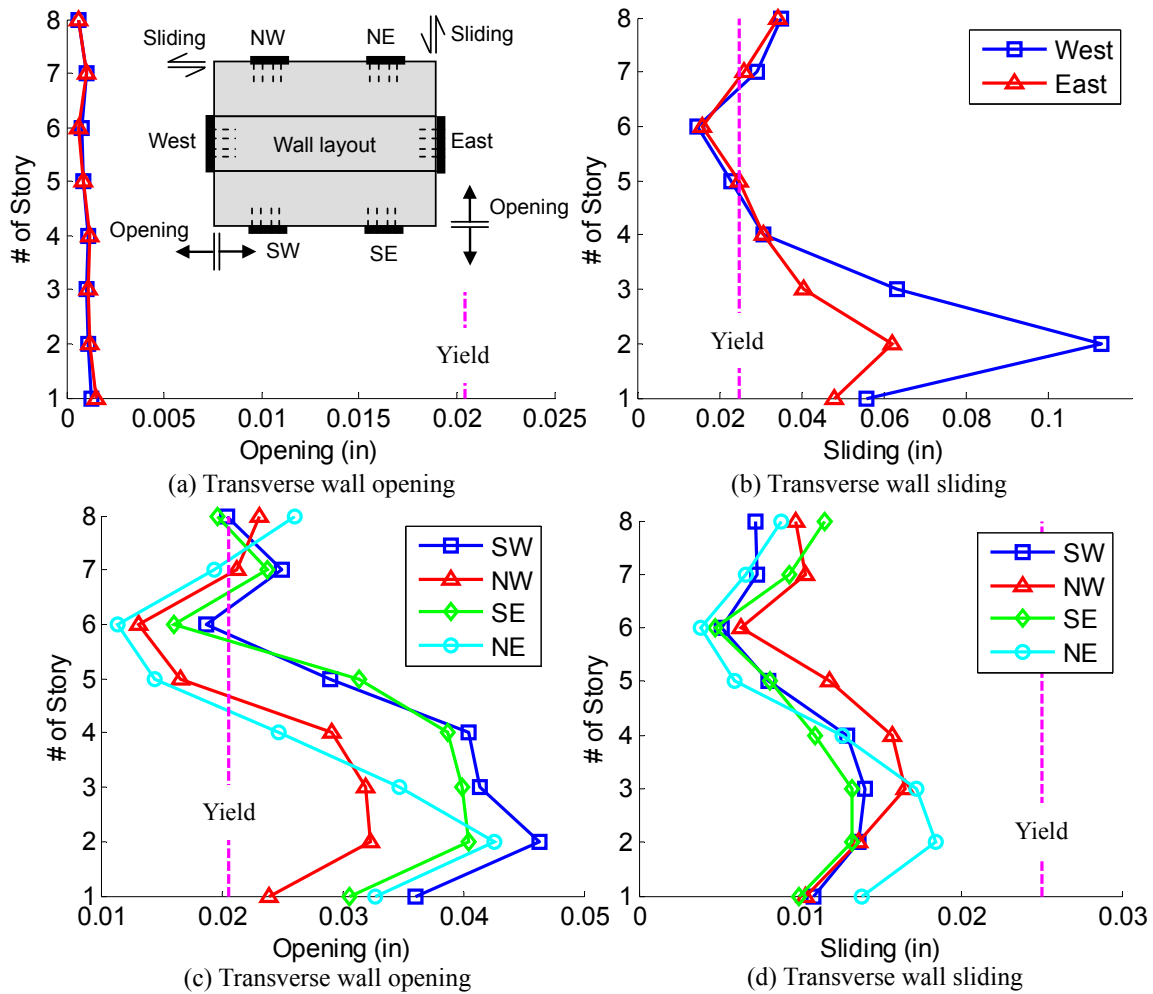
Fig. A2-46. Diaphragm-to-LFRS connection deformation demand.

Next, the connection demands on the interior beams lines are considered. This set of connections is designed for tributary shear VQ/I with the Ω_V factor (See PART 4, Example 4A). Figure A2-47 shows the maximum deformation demands for connections along the interior beam lines. The plots show: opening of the beam line joint (left-hand plots), and sliding along the beam line joint (right-hand plots), for both the north (upper plots) and south (lower plots) beam lines. Each plot group shows the joint opening on either side of the beam line (inner and outer faces).

As seen in Fig. A2-46, these connectors have slightly inelastic shear sliding demand at couple locations. Fairly large (~0.25″) inelastic opening demand is observed in these connectors near the end of diaphragm span. This inelastic opening demand is caused by the fact that the transverse shear walls placed at the middle sub-diaphragm do not cover and protect the internal beam joint. Significant opening deformation reduction might be expected if the transverse walls are placed across the internal beam joints.
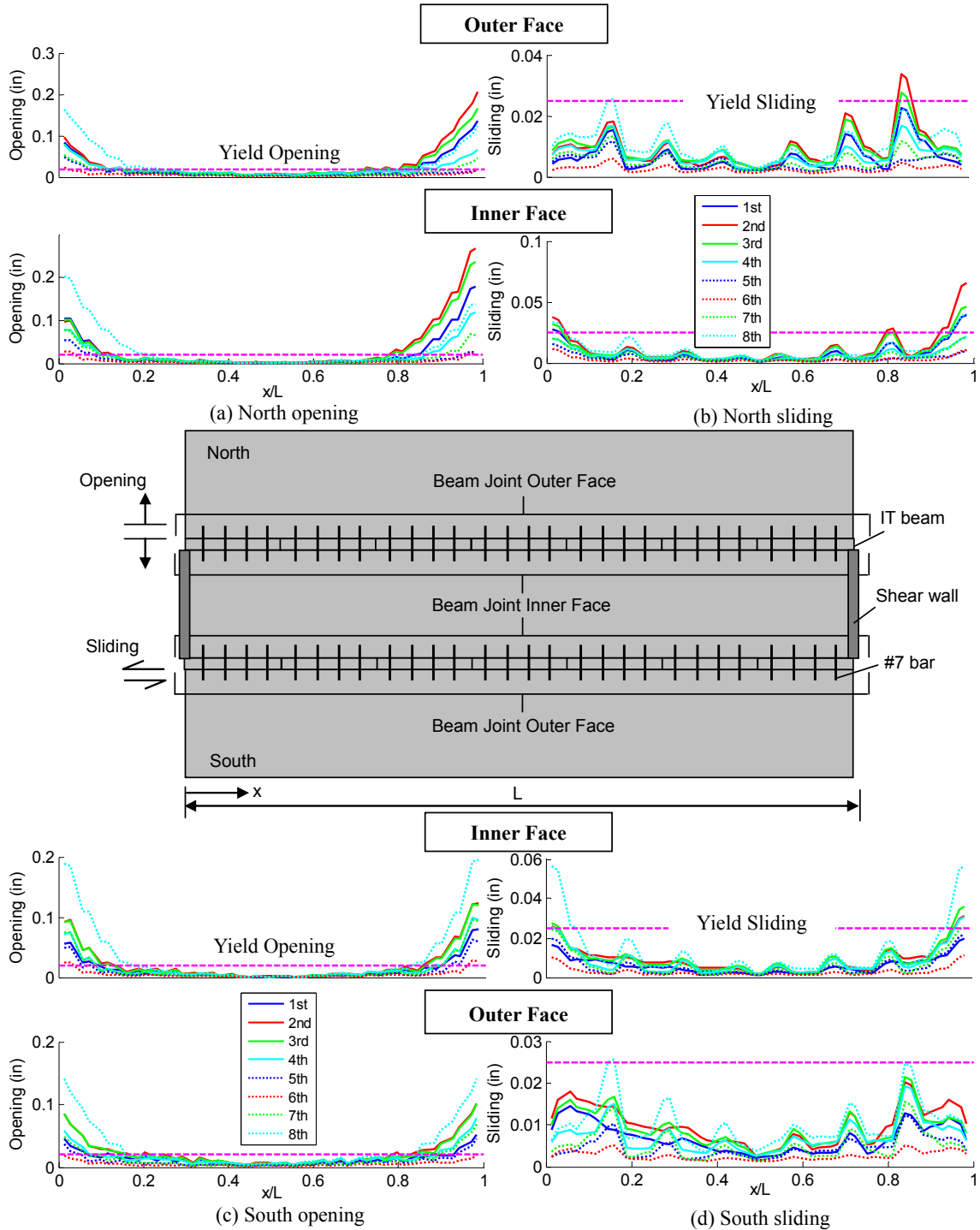
Fig. A2-46. Diaphragm internal beam joint demand: (a) opening; (b) sliding.

Similar demands to that presented for Example 3B in Sections 2.3.7 are observed in diaphragm secondary connection including spandrel beam connection (See Sec A2.4.2). These demands are discussed in Section 2.4 in the section noted above.

The following conclusions are made based on the analytical results for the 8-story perimeter wall office building SDC C EDO design (Design found in Example 4A of PART4) under a bi-directional MCE hazard level ground motion:

(1) The total floor inertial force demands at each level are conservatively predicted by the EDO design force $\Psi_E F_{Dx}$. The maximum inertial forces are closely predicted by $\Psi_E F_{Dx}$ at top floor. These conclusions apply to both the transverse and longitudinal direction.

DESIGN CONCLUSION: The EDO design force $\Psi_E F_{Dx}$ is appropriate for this design case.

(2) The diaphragm design internal forces using the FBD method (See Sec 3.2.B in PART 3) show good agreement with the dynamic analysis results.

DESIGN CONCLUSION: For this design example, the FBD method provides accurate force patterns.

(3) Diaphragm reinforcement demands are within the design target (elastic behavior in the MCE) at most diaphragm joints.

DESIGN CONCLUSION: The elastic diaphragm design target was met for this EDO design using Ψ_E and Ω_{vE}.

(4) Diaphragm-to-LFRS connection remains elastic at most locations except a minor localized sliding and opening yield at top and bottom floor.

DESIGN CONCLUSION: The LFRS design using Ψ_E and Ω_{vE} is deemed acceptable.

(5) Yield deformation occurs in the secondary connectors including internal beam to diaphragm and spandrel beam to diaphragm connections. Recommendations are provided in sec. A2.4.2.

A2.3.9 Eight-story office building w/ perimeter shear walls: SDC D RDO (Example 4B)

The ninth prototype structure diaphragm design evaluation involves a SDC D RDO diaphragm design option for an 8-story office building with perimeter shear walls. The earthquake simulation is performed through nonlinear transient dynamic analysis (NLTDA) under bi-directional components of a MCE-level ground motion. The diaphragm design of the prototype structure is based on the design procedure in PART 1. The design of this particular structure is described in Example 4B (PART 4).

The final diaphragm design produced in Example 4B, PART 4 is shown in Figure A2-47. The diaphragm reinforcement indicated in Fig. A2-47 is for all floors. The topped diaphragm is detailed with HDE reinforcement (topped chord connectors and ductile mesh/topped hairpin flange-to-flange connectors respectively for flexure and shear reinforcement). The diaphragm design factors are $\Psi_E = 2.1$ and $\Omega_{vE} = 1.77$. A conservative constant profile is used for the diaphragm design force along building height.

The diaphragm-to-LFRS connection in transverse and longitudinal directions is steel reinforcing dowel bars extending into the topping slab, and designed for the tributary shear at each wall. The spandrel-to-DT connection and IT to-DT connection is also steel reinforcing dowel bars extending into the topping slab. The IT-to DT connections are designed for the tributary shear VQ/I. These reinforcement details are also shown in Fig. A2-47 and discussed in detail in design example 4B of PART 4.
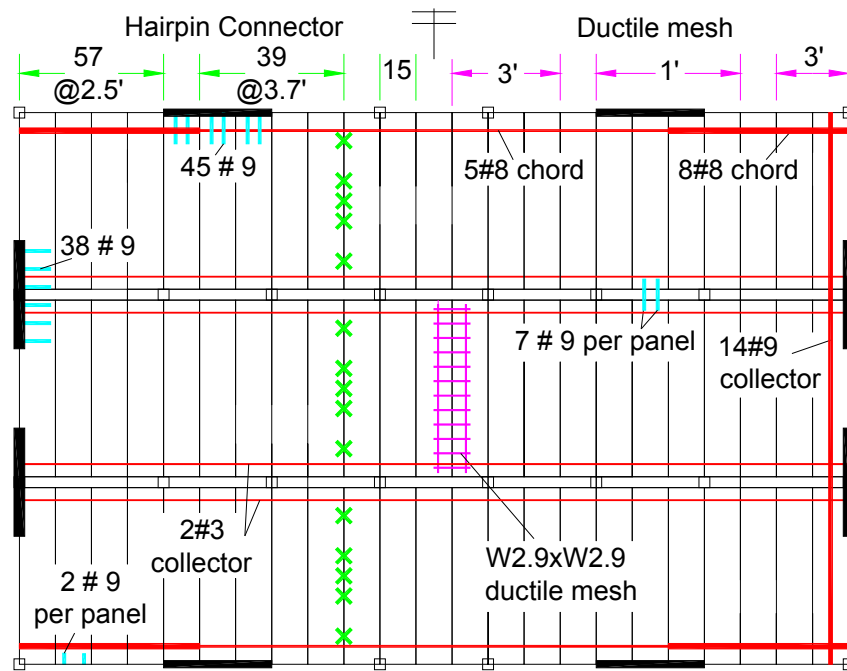
Fig. A2-47. Diaphragm reinforcement design for design example 4A.

The dynamic analysis for this structure does NOT success due to the non-convergence results from EQ simulation after excessive inelastic shear sliding demand (see Fig.A2-47b) and corresponding strength shear strength reduction under cyclic load. This large inelastic shear sliding demand at multiple diaphragm joints is observed because the layout of this structure has potential brittle shear failure issue as described in Sec. A2.4.3. Therefore an inelastic design is not recommended for a perimeter wall structure.
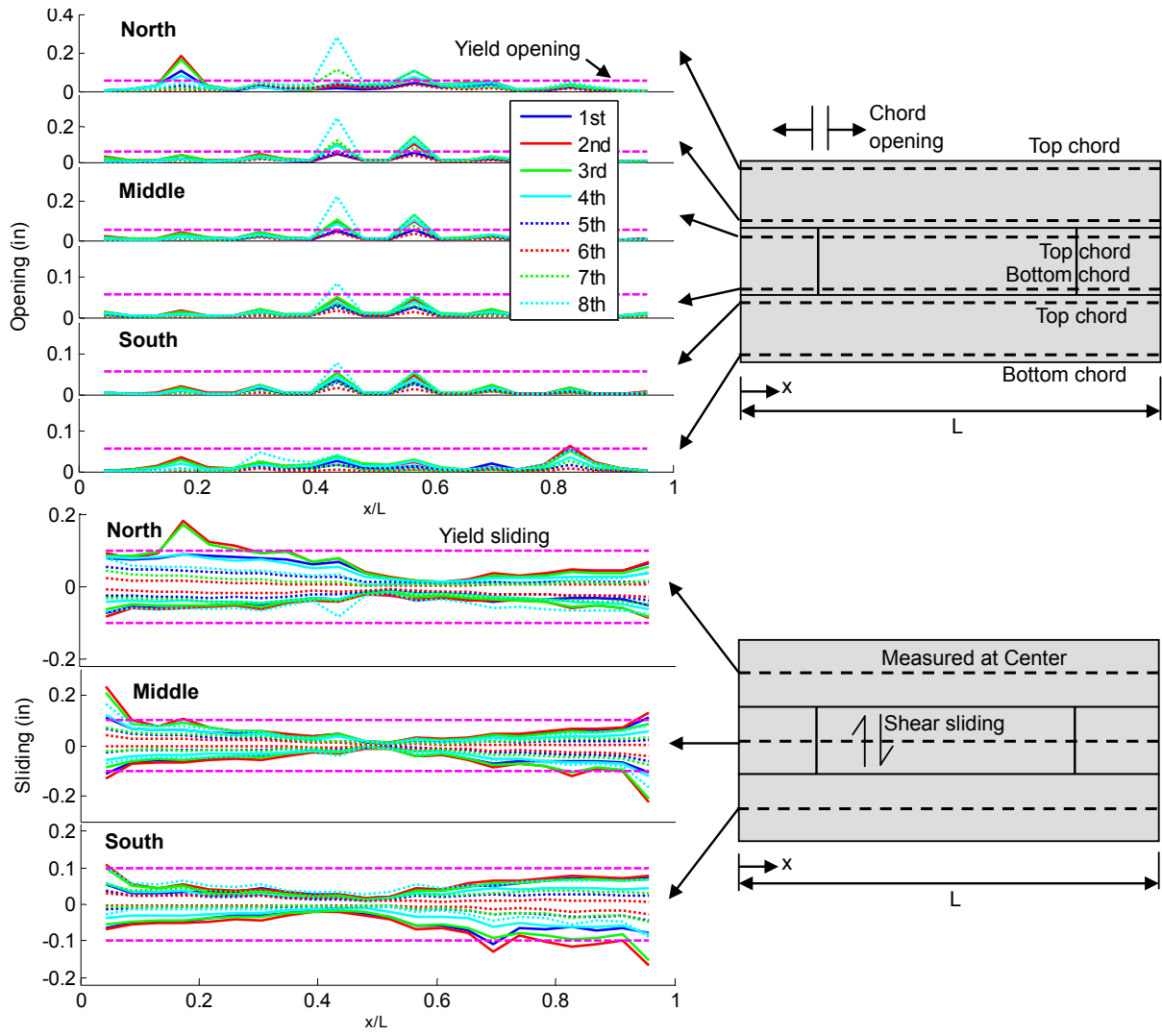
Fig. A2-47. Diaphragm reinforcement deformation demands: (a) chord opening; (b) JVI sliding.

A2.4 FURTHER KEY RESULTS IMPACTING DESIGN

In Section 2.4, the key general results and findings with design implications are summarized from the results observed in the analyses of the prototype structures described in Section 2.3.

A2.4.1 Deformation Demand: Diaphragm-to-LFRS connection

In the design methodology, the diaphragm-to-LFRS connection strength is established using both the diaphragm force amplification factor Ψ and the shear overstrength factor Ω_v, the latter being significant since the diaphragm reaction at the LFRS is dominated by shear. This approach, as also lower-bounded by the system overstrength factor Ω_o, was found to provide sufficient strength to nominally meet the LFRS force demands. However, as indicated in Section A2.3, certain connectors of the diaphragm-to-LFRS connection undergo yielding due to localized deformation demands due to uneven force distributions, restraint or local secondary actions such as twisting of the LFRS. The localized yielding of the connector can be manifested in tension (opening deformation demands) or shear (sliding deformation demands), and can occur at several locations along the walls at different floor levels in the structure. In this section provides: (a) the inelastic deformation demand for the diaphragm-to-LFRS connectors for different layouts and designs; and, (b) provides design recommendations on the required deformation capacity for these connectors.

Figure A2-48 shows the force-deformation response for the diaphragm-to-LFRS connectors under the largest deformation demands, including the most critical: (a) tension response (from interior wall connector at top floor); (b) shear response (from lite wall connector at top floor). These critical cases (Example 2B 4-story interior wall parking garage: SDC D RDO) are identified from among all the connectors at each LFRS connection in all prototype structures analyzed. Recall that in the analyses, these connectors are given the characteristics of an angled bar connector (Pincheira et al. 1998), but provided with unlimited deformation capacity in order to determine deformation capacity requirements. The angled bar connector test cyclic backbones (Pincheira et al. 1998) are indicated as dashed pink lines in the plots, and are used to evaluate the performance.

As noted in the figure, the most critical diaphragm-to-LFRS connector in tension approaches the failure tension deformation of the common welded bar connector (See Fig. A2-48a), while the most critical diaphragm-to-LFRS connector in shear exceeds the failure shear deformation of the common welded bar connector (See Fig. A2-48b). Though only representing the response to one ground motion, the connectors are seen to be subjected to approximately three major cycles of inelastic action. Based on this result it is assumed that maximum, and not cumulative deformation demand, is the key measure. It is important, therefore, to track the inelastic deformation demand on the individual diaphragm-to-LFRS connectors in the analyses of different structures.
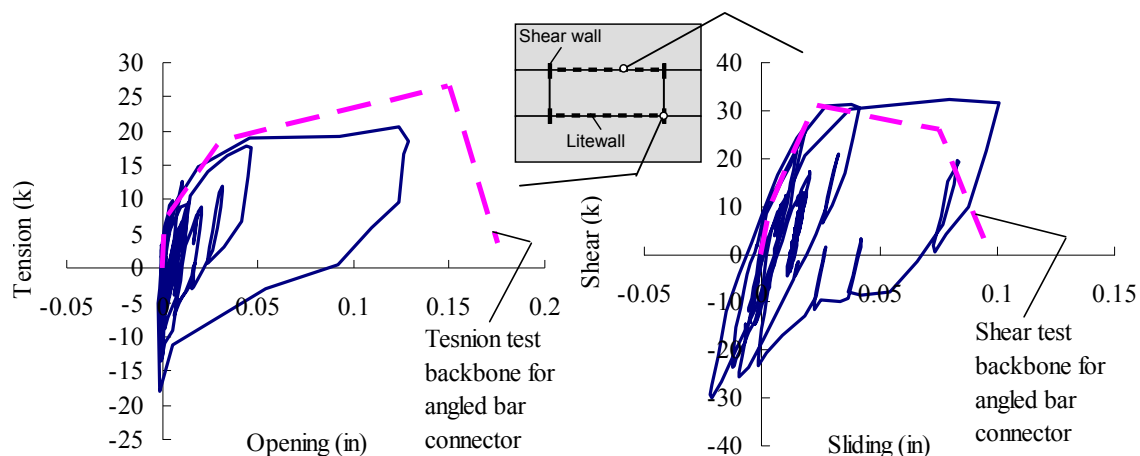
Fig. A2-48. Diaphragm-to-LFRS connector hysteresis response: (a) Opening; (b) Sliding.

Figure A2-49 summarizes the maximum opening and sliding demand incurred by any diaphragm-to-LFRS connector in the 4-story parking structure earthquake simulations for each diaphragm design case (Refer to Figs. A2-1a, b).

Considering first the exterior wall layout, the localized maximum opening demands are in the elastic range for all designs (See Fig. A2-49a); the localized maximum shear sliding demands are in the inelastic range for all design cases, but are below the failure deformation (See Fig. A2-49b).

Next consider the diaphragm-to-LFRS connector demands for the interior wall layout. In this case, opposite to what was observed for the exterior wall, the localized maximum sliding deformation demands are within the elastic range (See Fig. A2-49b), but the localized maximum opening demands are in the inelastic range, and are below the failure deformation (See Fig. A2-49a).

Finally for diaphragm-to-LFRS connector demands on the litewall, the maximum opening demand is in the elastic range for EDO and BDO designs, and slightly exceeds the yield opening for RDO design (See Fig. A2-49a). The maximum sliding demand exceeds the yield sliding deformation for all cases, and increases as the design moves from EDO to RDO designs, with the demand exceeding the connector sliding failure deformation for the latter (See Fig. A2-49b).

It can be inferred from these findings that: (1) exterior walls incur localized shear yielding due to their position on the structure perimeter, where shear and flexure actions tend to translate the precast units along the wall; (2) interior walls are subjected to localized tension yielding due to in-plane flexure, analogous to negative moments at interior supports in continuous beams; and (3) the lite walls incur localized shear yielding due to displacement compatibility with flexural opening actions of the primary joints acting in the precast diaphragm
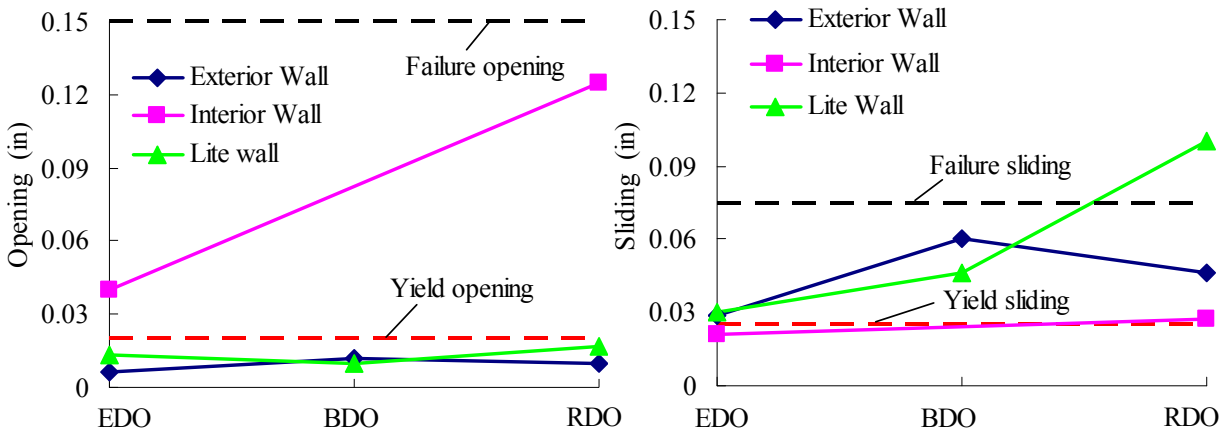
Fig. A2-49. Diaphragm-to-LFRS deformation demand in the parking garage: (a) Opening; (b) Sliding.

Consider now the distributions of the diaphragm-to-LFRS maximum localized connector demands along the height of the building, as shown in Fig. A2-50a and Fig. A51a. Figure A2-50a shows the maximum localized *opening* deformation demand for diaphragm-to-LFRS connectors along the height of the parking structure, Figure A2-51a shows the maximum localized *sliding* deformation demand. The former is for the *interior* shear wall case; the latter is for the *exterior* shear wall case, as was explained previously.

As seen in Figure A2-50a for *opening* demand: (1) diaphragm-to-LFRS connector yielding is observed at every floor level; (2) the maximum opening demand is at the top level; and (3) the maximum opening demand is larger in a RDO design than for the EDO design.

As seen in Figure A2-51a for *sliding* demand: (1) diaphragm-to-LFRS connector yielding is observed at upper floor levels; (2) the maximum sliding demand is at the top level; and (3) the maximum opening demand is largest in the BDO design.
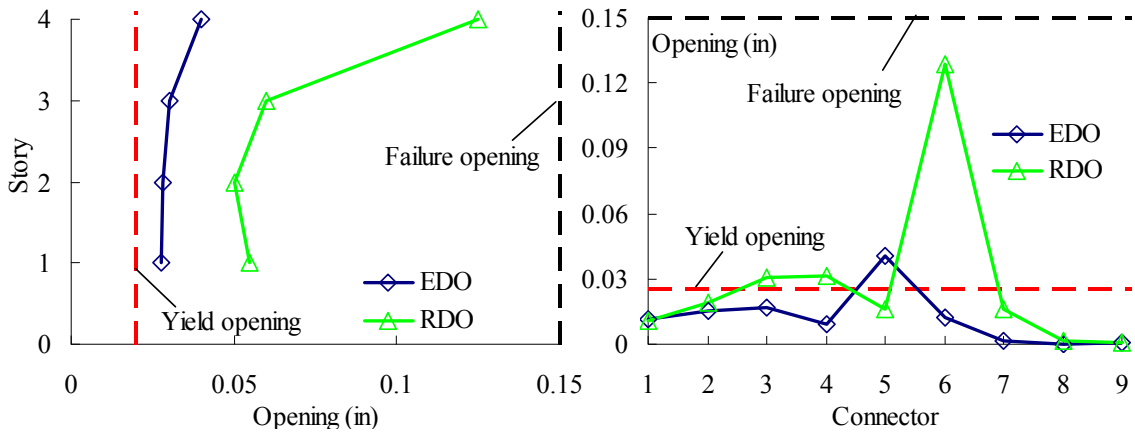
Fig. A2-50. Diaphragm-to-LFRS opening profiles for interior wall: (a) along floor; (b) along the joint at top floor.

Considering next the distribution *along* the joint, Figure A2-50b and A2-51b shows the maximum localized diaphragm-to-LFRS connector demands along the face of the shear wall: (a) opening for the top floor interior wall (i.e., story 4 in Fig. A2-50a); and, (b) sliding for the top floor exterior shear wall (i.e., story 4 in Fig. A2-51b). As seen, the large demands on the top floor are caused by a non-uniform distribution of demands across the joint (See Fig. A2-51b).
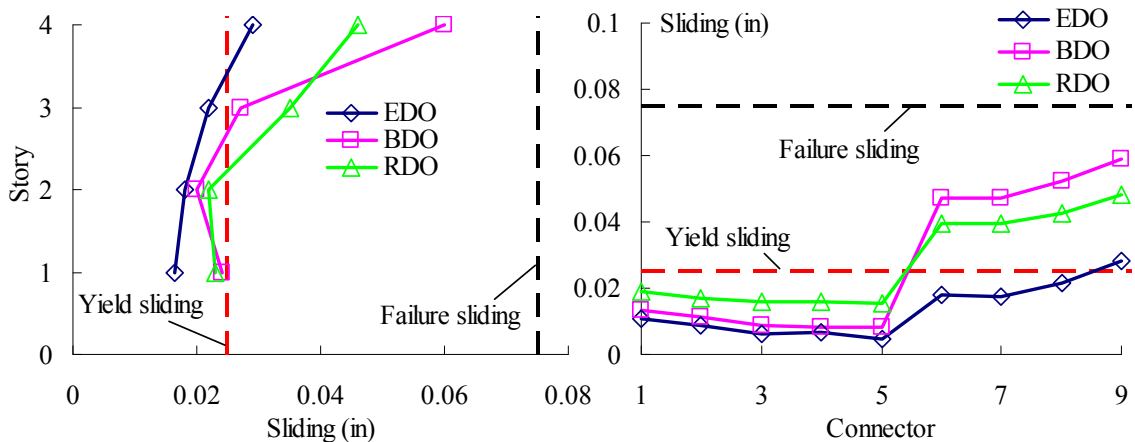
Fig. A2-51. Diaphragm-to-LFRS sliding profiles for exterior wall: (a) along floor; (b) along the joint at top floor.

Now considering diaphragms in precast office buildings, Figure A2-52 shows the maximum localized opening and sliding demand of the diaphragm-to-LFRS connector in the 8-story office building for different design cases. The design cases include different diaphragm design options (EDO and RDO), and different LFRS types. Note that the shear wall (SW) office buildings employ a perimeter wall LFRS layout (Refer to Figs. A2-1e,f), while the moment frame (MF) office buildings employ an interior frame LFRS layouts (Refer to Figs. A2-1c,d)

Consistent with the results of the parking structure analyses, Fig. A2-52 indicates that the diaphragm-to-LFRS connectors for LFRS elements at the perimeter of the floor plan (in this case perimeter shear walls for the office building) undergo more critical sliding deformation than opening deformation. Likewise, the diaphragm-to-LFRS connectors for LFRS elements at the interior of the floor plan (in this case internal moment frames for the office building) undergo more critical opening deformation than sliding deformation.

As also seen in Fig. A2-52, the transverse perimeter walls (refer to Fig. A2-1e,f) undergo larger sliding demands than the longitudinal perimeter walls. The sliding demands exceed the failure opening, even for the EDO diaphragm design option. Conversely, the longitudinal shear wall possesses larger maximum opening demand than sliding demand. Similarly, the diaphragm-to-LFRS connectors for the transverse moment frames are in the inelastic range for both opening and sliding; while those for the longitudinal moment frames are within the elastic range for both opening and sliding or the interior moment frame structure, except for opening in the RDO diaphragm design.
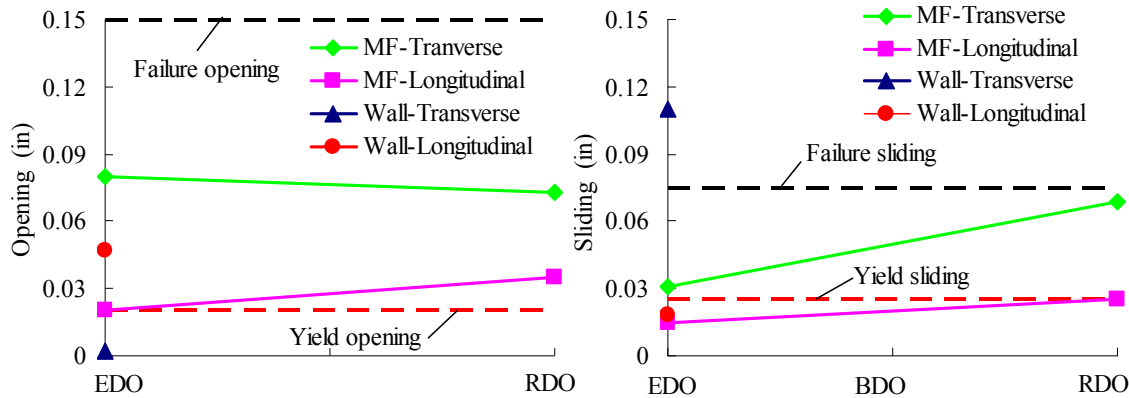
Fig. A2-52. Diaphragm-to-LFRS deformation demand in the office building: (a) Opening; (b) Sliding.

Based on the deformation demands observed in the prototype structure analyses for the diaphragm-to-LFRS connection, the following conclusions and recommendations are made: (1) the strength provided to the diaphragm-to-LFRS connection by the diaphragm factors Ψ and Ω_v, and lower-bounded by Ω_o, seems appropriate as all diaphragm-to-LFRS connections analyzed were subjected to nominal forces less than the strength provided; (2) it is difficult, however, to keep all the connectors elastic in a diaphragm-to-LFRS connection due to localized actions. It is important to note that the 3D-FE discrete analytical models developed in the DSDM project (See Appendix B) provide one of the first real opportunities to examine these localized demands; (3) perimeter elements and litewalls are dominated by shear sliding demands; (4) interior elements are dominated by tension opening deformations; and, (5) though there is not a strong direct proportionality between the diaphragm-to-LFRS connector demands and the diaphragm design option, as exists for the diaphragm primary reinforcement, the demands do tend to increase as the design moves from EDO to BDO to RDO.

As a result of these findings, in addition to the diaphragm design factors intended to keep the diaphragm-to-LFRS connection nominally elastic, a deformation requirement is added to the design methodology for connectors used in the diaphragm-to-LFRS connection. This deformation requirement is not the same as the diaphragm reinforcement classification used for the primary diaphragm reinforcement; but instead is intended to permit the diaphragm-to-LFRS connection sufficient plastic redistribution capabilities to prevent "unzipping" of the diaphragm-to-LFRS connection.

Diaphragm-to-LFRS deformation requirements are shown in Table A2-3. The deformation capacity requirements are developed based on the estimated maximum localized the deformation demands observed in the prototype structure analyses. Additional refinement of these requirements has been made to include influence of the diaphragm design option on the deformation demands (See Appendix 2 of PART1).

Table A2-3. Deformation requirements for the diaphragm-to-LFRS connectors.

	Exterior wall	Interior wall	Litewall	Moment frame
Opening	0.05"	0.15"	0.05"	0.1"
Sliding	0.1"	0.05"	0.15"	0.1"

A2.4.2 Deformation Demands: Diaphragm-to-Beam Connections

There are two primary diaphragm to beam connections in the precast floor system: (1) Connections between precast floor units and internal beams in the floor interior, typically Inverted Tee (IT) beams; and (2) Connections between precast floor units and spandrel beams (SP) at the floor perimeter. The term diaphragm secondary connection has been coined to refer to connections in the floor system that are not explicitly part of the diaphragm design. Diaphragm-to-spandrel connections typically fall into this category, regardless of whether the spandrels are load bearing or non-load-bearing. Diaphragm-to-internal beam connections, on the other hand, may be included explicitly in the diaphragm design using tributary shear (VQ/I) calculations. In other cases, these connections are simply provided by standard industry hardware and the floor portions on either side of the beam are treated as independent sub-diaphragms.

Figure A2-48 shows the load-deformation response for the diaphragm-to-LFRS connectors under the largest deformation demands, including the most critical: (a) tension response; (b) shear response. These critical cases (exterior wall parking structure for tension critical case and interior wall parking structure for shear critical case) are identified from among all the connectors at each LFRS connection in all prototype structures analyzed. Recall that in the analyses, these connectors are given the characteristics of an angled bar connector (Pincheira et al. 1998), but provided with unlimited deformation capacity in order to determine deformation capacity requirements. The angled bar connector test cyclic backbones (Pincheira et al. 1998) are indicated as dashed pink lines in the plots, and are used to evaluate the performance.

Figure A2-53 shows that the most highly loaded diaphragm-to-beam connectors undergo significant inelastic deformation demands, including multiple cycles of significant inelastic action. The maximum demands shown in Figure A2-53a indicate that the most critical case in tension exceeds the angled-bar failure opening deformation. Likewise, Figure A2-53b indicates that the most critical case in shear exceeds the angled-bar failure sliding deformation. is modeled with ultimate deformation capacity, the shear and tension failure would be expected if the angle bar connector is used in the structure. It is important, therefore, to track the inelastic deformation demand on the individual diaphragm-to-beam connectors, both in IT tributary shear connections and SP secondary connections, in the analyses of different structures.
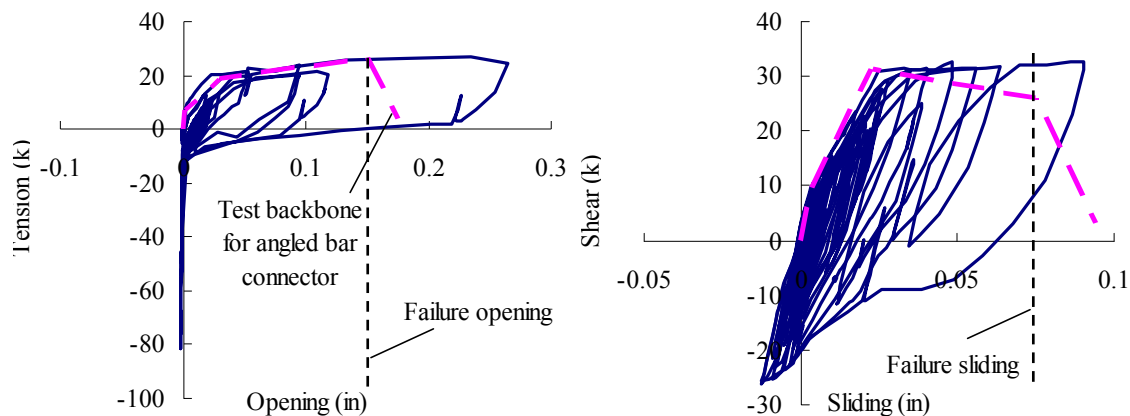
Fig. A2-53. Diaphragm-to-beam connector response: (a) Opening; (b) Sliding.

Figure A2-54 summarizes the maximum localized deformation demand for connectors between the internal beam (IT) and the precast floors unit for different prototype structures and design options. As seen in Fig. A2-54a, the IT connector opening maximum localized demand exceeds the yield opening for all design options, with a maximum value of approximately 0.25″. As seen in Fig. A2-54b, the IT connector maximum localized sliding demand exceeds the yield sliding for all design options, with a maximum value of approximately 0.12″.
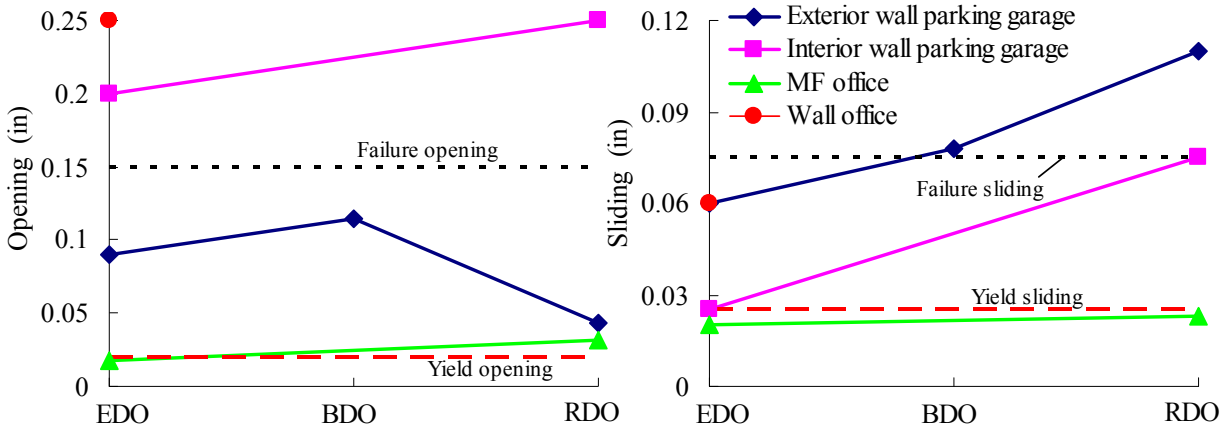
Fig. A2-54. Maximum demand in the internal beam to precast unit connector: (a) opening; (b) Sliding.

Figure A2-55 shows the maximum deformation demand in the connectors between the spandrel beam (SP) and precast floor unit for different structures and design options. As seen in Fig. A2-55a, the SP connector opening maximum localized demand exceeds the yield opening for all design options, with a maximum value of approximately 0.12″. As seen in Fig. A2-55b, the SP connector sliding maximum localized demand exceeds the yield sliding for all design options, with a maximum value of approximately 0.1″.
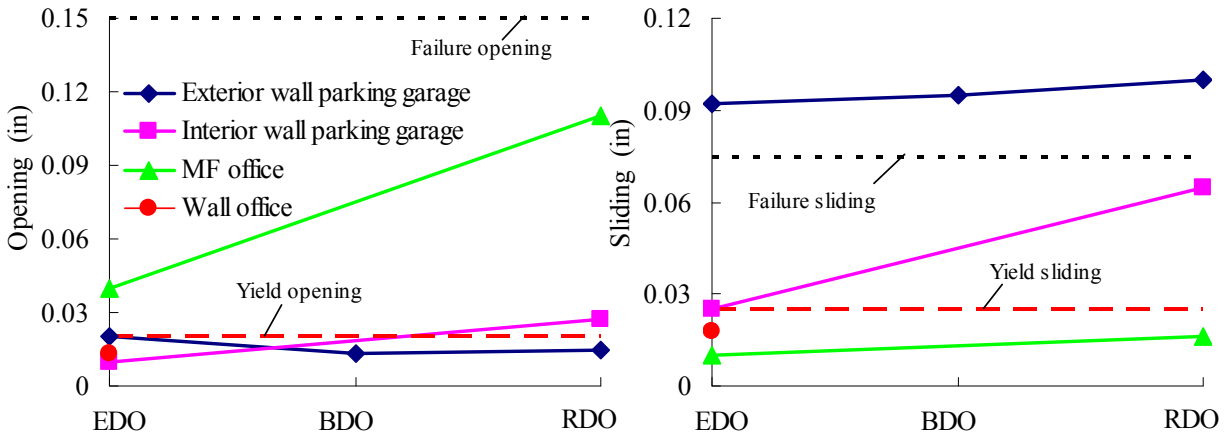
Fig. A2-55. Maximum demand in connector between spandrel and precast unit: (a) opening; (b) sliding.

Table A2-4 provides the deformation capacity requirement for diaphragm to beam connectors. The values are based on the deformation demand observed in the prototype structure analyses.

Table A2-4. Deformation requirement for the diaphragm secondary connection.

Deformation	Parking Structure		Regular building	
	Internal beam	Spandrel	Internal beam	Spandrel
Opening	0.25"	0.1"	0.25"	0.15"
Sliding	0.15"	0.15"	0.1"	0.1"

C-A-94

A2.4.3 Diaphragm Layouts with Potential Failure Issues

This section summarizes two prototype structure layouts analyzed that indicate the potential for diaphragm failure when the structure is designed using inelastic diaphragm design options that target inelastic diaphragm response under the MCE hazard (e.g. the BDO and RDO).

(1) Structures with Perimeter Longitudinal Walls at Diaphragm Midspan

Figure A2-56 shows a typical floor plan for a 4-story parking garage structure. In the longitudinal direction, two perimeter shear walls are placed at the mid-length of the floor plan. The longitudinal shear walls are not considered in the design of the transverse LFRS because of their small out-of-plane stiffness in the direction perpendicular to the wall axis. However, these walls "cover" several floor joints close to the diaphragm midspan, thereby restraining opening in these diaphragm joints.

In an EDO diaphragm design, this condition simply translates into added strength. However for an RDO design, this restraint can: (1) cause a redistribution in the patterns of inelastic deformation demands, including the potential for concentrated inelastic demands; and (2) change the relationship between maximum moment and shear in the diaphragm by changing the bending span, in this case shortening the span by the length of the wall. The former can lead to reduced ductility in the diaphragm; the latter can compromise the intended capacity design of the diaphragm provided by the shear overstrength factor Ω_v since $V_{max} = 2M_{max}/L$, analogous to the failure witnessed in short columns. Either or a combination of these conditions could lead to a non-ductile diaphragm failure. These ideas are pursued using the findings from some prototype structure analysis results. It is noted that analyses that indicated a propensity for failure were not included in the results section (A2.3) and the design examples of PART 4. Enhancements to the design methodology were made on the basis of these findings.
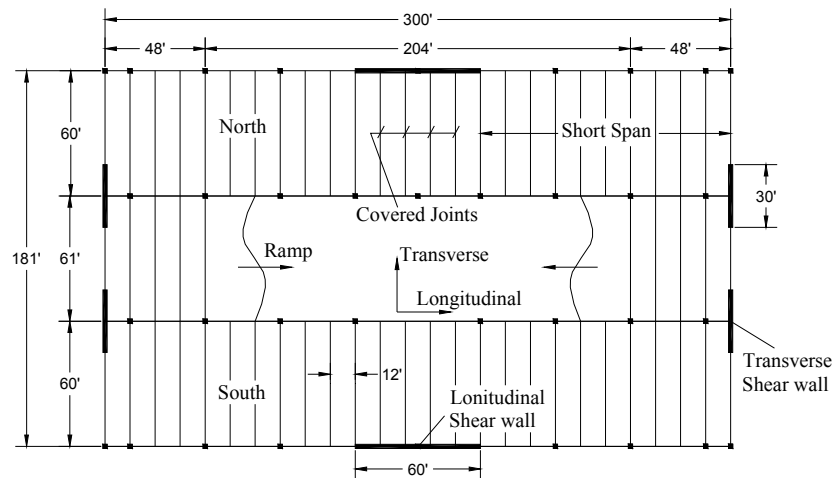
Fig. A2-56. Plan for a 4-story parking garage with perimeter shear walls.

Figure A2-57 shows the maximum diaphragm opening and sliding demand under the MCE for the 4-story perimeter shear walls parking structure with an RDO diaphragm design. As seen in Fig. A2-57a, diaphragm joint opening demands at the joints covered by the longitudinal shear walls is very small due the restraint provided by the wall. Significant inelastic opening is concentrated at the first joint on either side of the longitudinal shear wall, with a maximum value of 1″. This demand is significantly larger than the allowable HDE deformation (0.4″) and even the demonstrated HDE capacity (0.6″). Furthermore, as observed in Fig. A2-57b, the diaphragm sliding deformation demands exceed the yield sliding deformation at multiple joints in the diaphragm. This outcome is due to an increased diaphragm flexural overstrength relative to the diaphragm shear strength provided by Ω_v, created by the shorter actual shear span caused by the presence of the longitudinal wall. Thus the capacity design intent of the diaphragm design provided by the shear overstrength factor Ω_v is not sufficient. Thus, the analytical results indicate that this design would undergo both diaphragm shear failure and flexural failure.

C-A-95
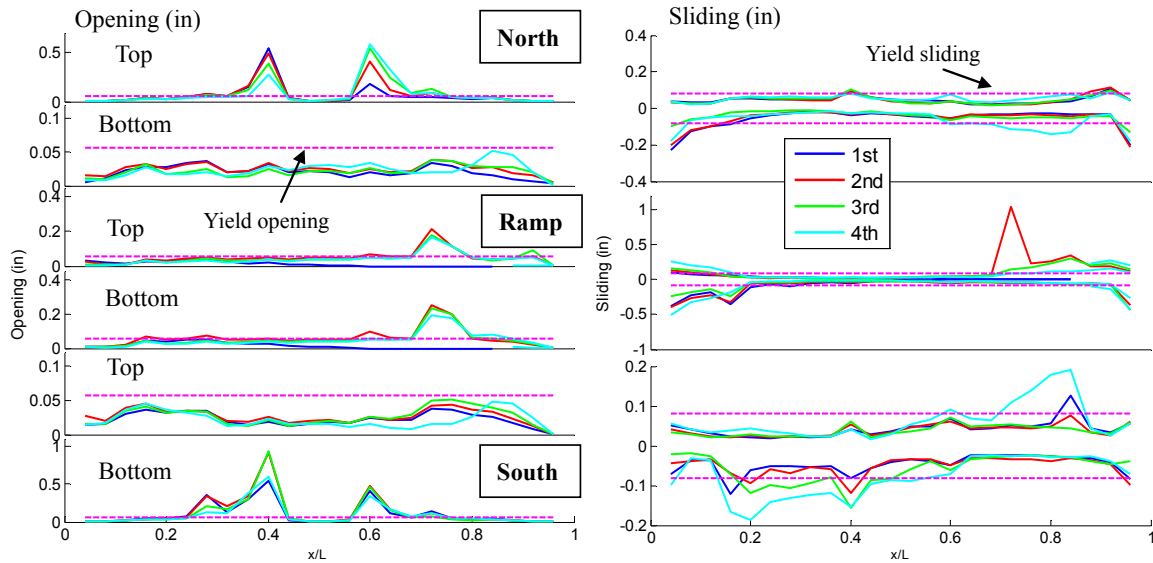
Fig. A2-57. Diaphragm joint max deformation demand under MCE: (a) Opening; (b) Sliding.

(2) Structures with Perimeter Longitudinal Walls at Diaphragm Quarter Span

Figure A2-58a shows a typical floor plan for the 8-story office building with perimeter shear walls. The case considered is for the structure with diaphragms designed with the RDO option (Example Analysis 4B in Sec. A2.3.9). In the longitudinal direction, four perimeter shear walls are placed, one each at the diaphragm quarter span at the north and south face of the structure. These shear walls will restrain the diaphragm as it attempts to deform under transverse load. In response to the diaphragms flexure response, these walls will develop shear reaction forces q_{sw} (See Fig. A2-58b). These shear reaction forces will tend to reduce the diaphragm moment demand from the quarter span to midspan (See moment diagram in Fig. A2-58b). This condition produces three critical flexural joints in the diaphragm: one at midspan, and the others at the joints adjacent to the outer end of the longitudinal perimeter walls (See circles on moment diagram in Fig. A2-58b). This concept is pursued further using the findings from results from some of the prototype structure analyses.
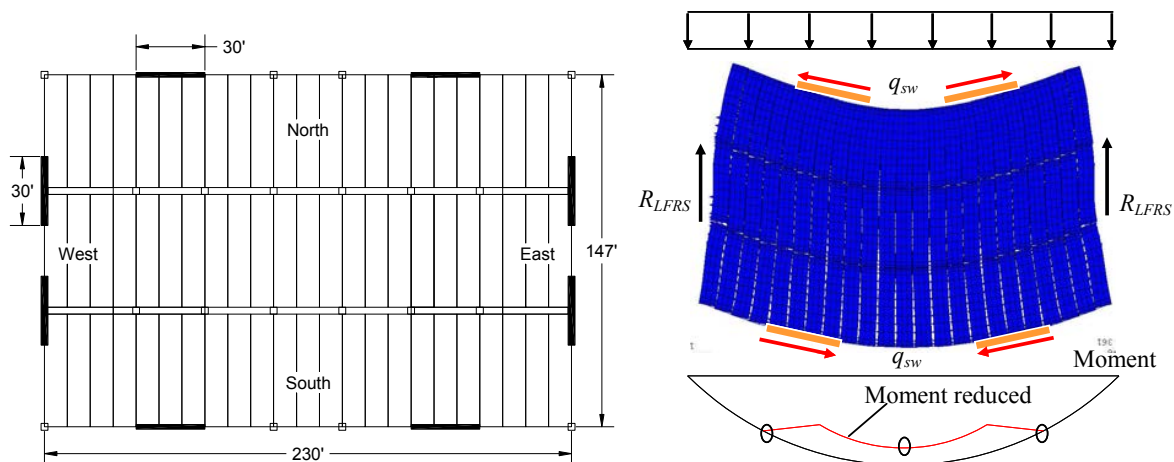
Fig. A2-58. 8-story parking garage with perimeter shear walls: (a) Plan; (b) FBD.

Figure A2-59 shows the diaphragm internal force diagram for the 2nd floor of the 8-story office building with the RDO diaphragm design under MCE level hazard. The red line (with crosses) represents the required strength provided by the diaphragm design forces using the factors from the design

C-A-96

methodology and the FBD method (See Example 4B in PART 4). The light blue line (with circles) represents the actual strength provided in the design. The reason for the significant difference between the required and actual strength is due to placing of excessive (in terms of required flexural strength) chord reinforcement in the joints in order to satisfy high shear demand. The dark blue line (with squares) represents the seismic demands profile when the shear force demand at end diaphragm reaches maximum observed in the MCE analysis.

As seen in Fig. A2-59a, the joints close to the longitudinal perimeter walls have a significant flexural overstength in order to satisfy high shear demand at these joints. In the earthquake simulation, after the diaphragms yield in flexure at midspan (as implied by the dark blue square line exceeding the light blue circle line at x/L=0.5), the moment demand of these joints can significantly increase due to its flexural overstrength without significant increase of midspan moment due to the restraint of the longitudinal wall shear . The increase of moment at the joints adjacent to outer edge of the longiudinal shear walls (as indicated by the peaks in the dark blue line the Fig. A2-59a), translates into significantly larger shear force demands compared to the values anticipated in the design (see Fig. A2-59b). These high shear forces due to the flexural overstrength causes yielding of shear connector at multiple diaphragm joints, as shown in Fig. A2-60.
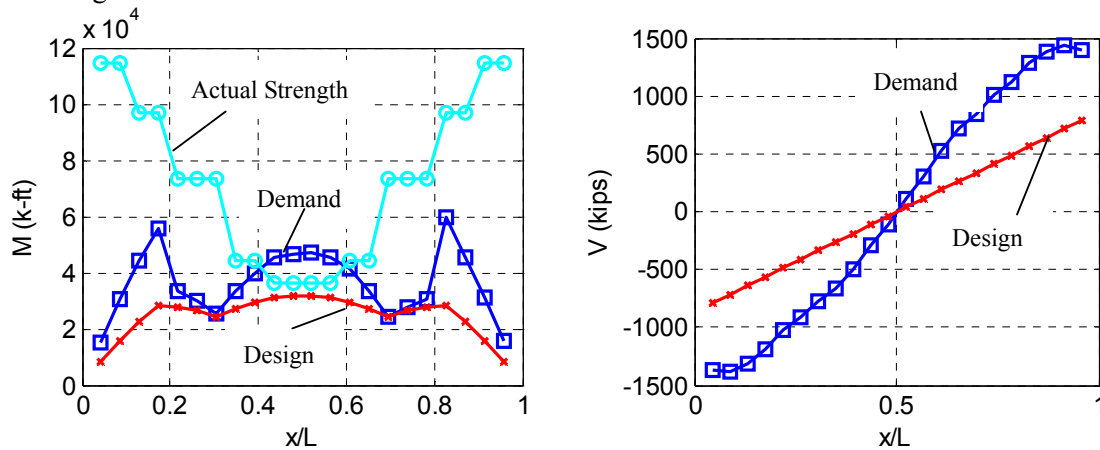
Fig. A2-59. Diaphragm internal force diagram at 2nd floor: (a) Moment; (b) Shear.
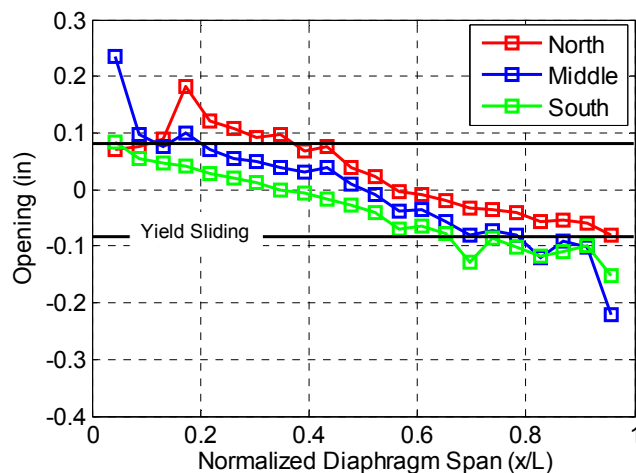
Fig. A2-60. Diaphragm maximum sliding profile at 2nd floor

Based on analytical results for the two structures with potential failure, it is realized that overstrength factors proposed in the design procedure are not capacity design factors purpose, given that the moment and shear diagrams in diaphragms are not always clearly defined. Thus care must be taken in applying the factors in design for complicated floor systems.

A2.4.4 Assuring Capacity Design Intent

The capacity design intent embodied in the diaphragm design methodology is to avoid the potential for non-ductile shear failure by promoting a ductile flexural mechanism in the diaphragm. This intent is realized through the use of the shear overstrength factor Ω_v. In the previous section, a layout was shown that compromised this capacity design intent. This concept is pursued further in this section.

For a structure with interior shear walls, the diaphragm shear force demand after the diaphragm yields at critical flexural joints at midspan and the interior walls (shown as supports in Fig A2-61) can be calculated as $V = 4(M_n^+ + M_n^-)/L'$, as illustrated in the FBD of Fig. A2-61. Therefore, any condition that leads to diaphragm flexural overstrength at either midspan or at the wall will tend to increase the diaphragm shear demand in the diaphragm post-yield regime.
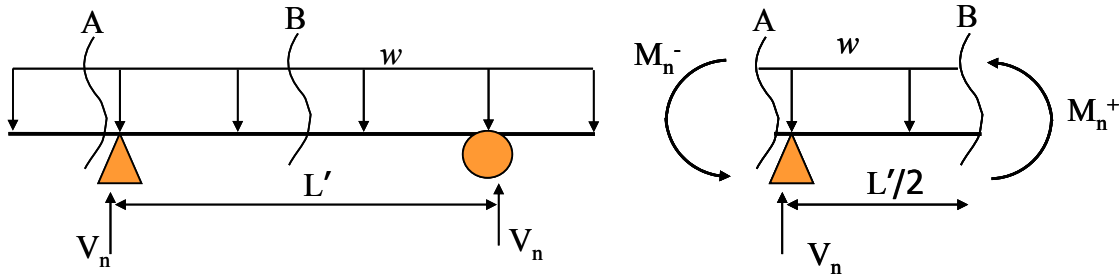
Fig. A2-61. FBD for a diaphragm with interior support.

Figure A2-62 shows the diaphragm internal force diagrams for the 4-story interior wall parking structure with an RDO diaphragm design. The results are for the top floor diaphragm under the MCE level analysis (Example 2B in Sec. A2.3.5). The red line (with crosses) represents the required design strength provided by the design methodology using the design factors and the FBD method (See Example 2B in PART). The light blue line (with diamonds) represents the actual strength provided in the diaphragm design and included in the analytical model. The dark blue line (with squares) represents the seismic demand from analysis results when the shear force demand at supports reaches maximum.

The design provided by the design methodology does not provide significant flexural overstrength at diaphragm midspan (as implied by the close proximity of the lines at $x/L=0.5$ in A2-62a. However, as seen in A2-62a, at the interior wall supports, significant flexural overstrength is seen. This condition occurs because in order to develop the required diaphragm shear strength, chord reinforcement was added in these locations to provide dowel action (adding more shear connectors was not practical due to minimum spacing requirements). The significant flexural overstrength resulting from these added chord bars in turn leads to higher diaphragm shear demand than anticipated in the design (as seen in A2-62b).
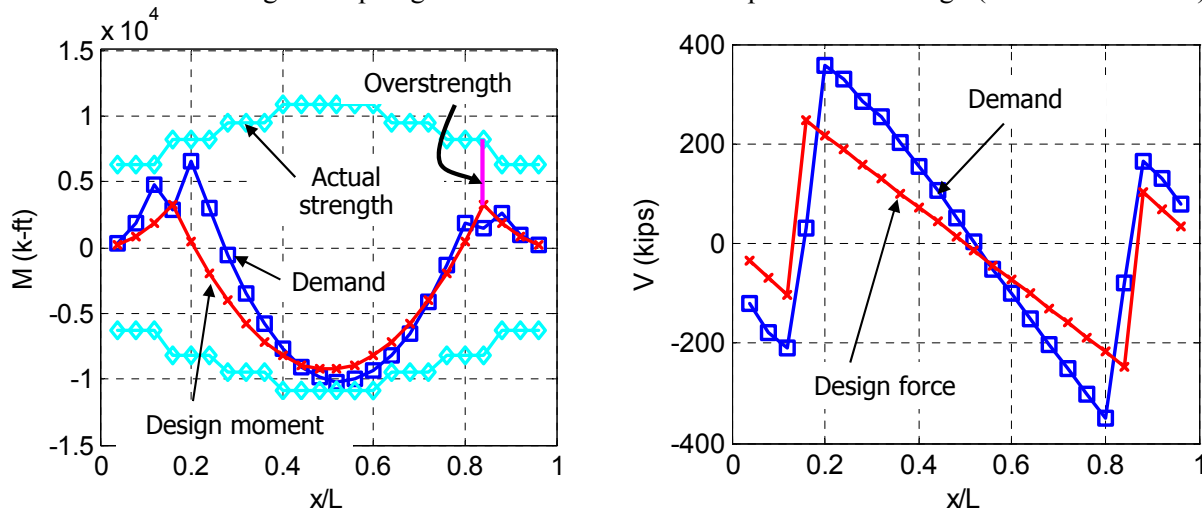
Fig. A2-62. Diaphragm internal force diagram: (a) Moment; (b) Shear.

Thus, these conditions could lead to non-ductile shear failures in a MCE event. To avoid such failures, it is recommended in the design methodology that the diaphragm flexural overstrength be limited. The diaphragm shear strength (V_n) should not be less than $4\beta(M_n^+ + M_n^-)/L'$, where β is a strain hardening coefficient, to be set equal to 1.2. Diaphragm flexural overstrength may not be able to be avoided using typical details. One concept is to provide the needed shear response through a new tension compliant high shear strength connector, or by providing dowel action with a chord connector at the cenroid of the diaphragm joint (see Fig. A2-63).
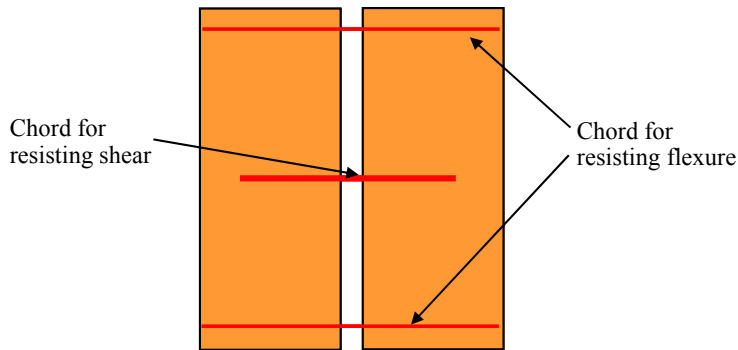
Fig. A2-63. Illustration for moving shear resistant chord into center of diaphragm.

A2.4.5 Considerations for Parking Structures

The analyses of parking structures indicated sensitivity of diaphragm response to a number of details. As an example, Figure A2-64 shows a parking structure plan, indicating an expansion joint, typically placed between the 1st floor ramp precast units and the c.i.p slab integral with the foundation. The expansion joint allows free movement of the 1st floor ramp relative to the foundation. The precast diaphragm seismic demands in the lower levels of the structure were found to be sensitive to this detail.
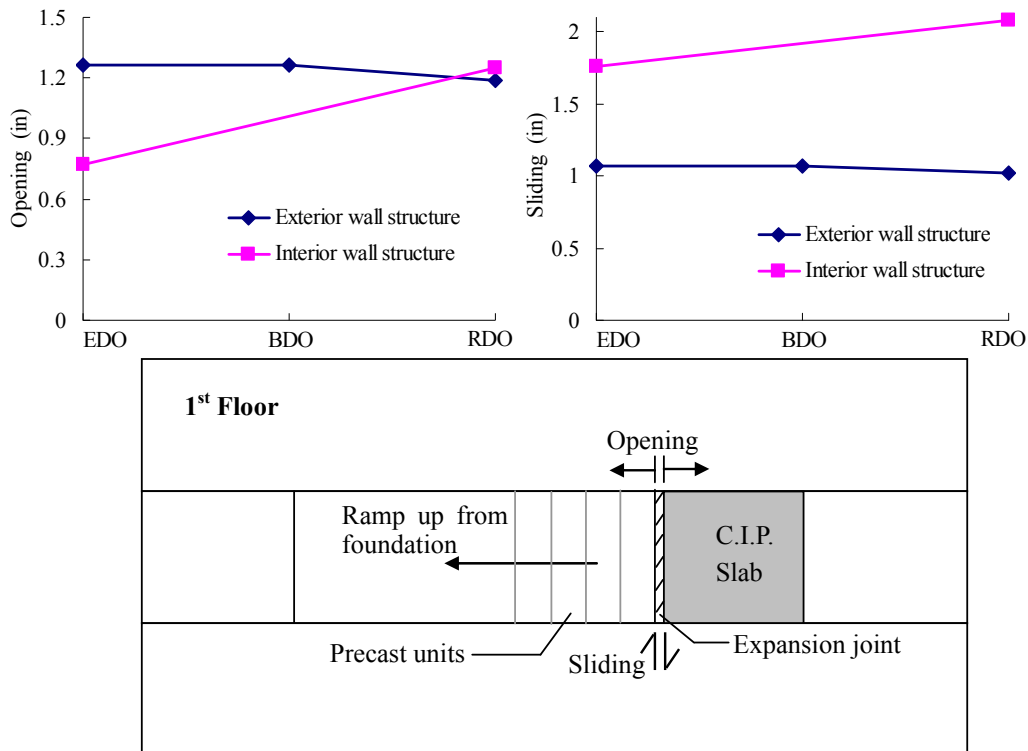
Fig. A2-64. Maximum deformation demand in expansion joint.

Figure A2-65 shows the maximum diaphragm deformation demands within the 1st floor ramp. The plots compare the response of a parking structure with and without the expansion joint. As seen, the expansion joint significantly reduces the joint deformation demands in the 1st floor ramp, both for joint opening and sliding. This reduction occurs because the opening and sliding deformations are relocated to the expansion joint. Without the expansion joint, the diaphragm ramp at the lower level yields at multiple joints in tension and shear, and has demands that are quite significant (approaching the MDE allowable limit for opening deformation, and in the degrading regime of diaphragm sliding demands).
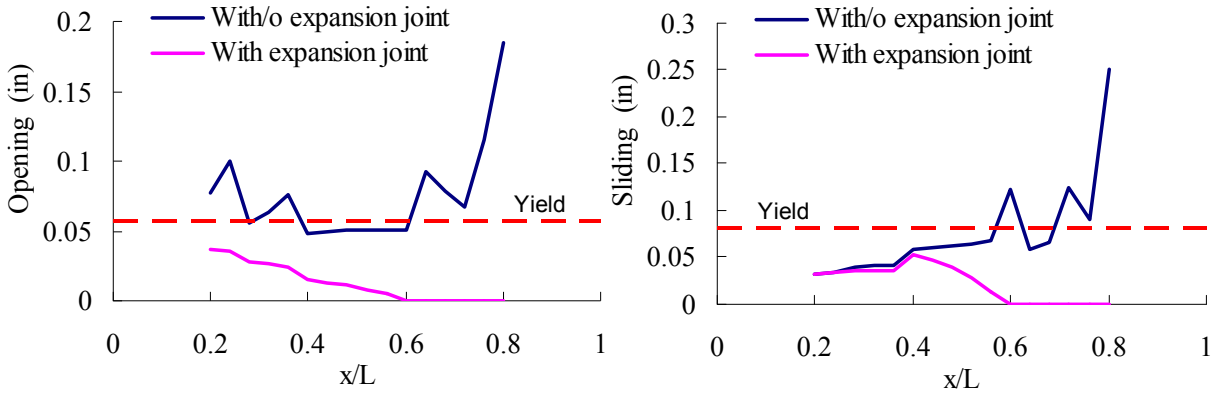
Fig. A2-65 Maximum deformation demand in ramp joint at 1st floor: (a) opening; (b) sliding.

Conversely, the expansion joint significantly increases the litewall-to-DT connector deformation demand at connection directly above the expansion joint (See Figure A2-66).
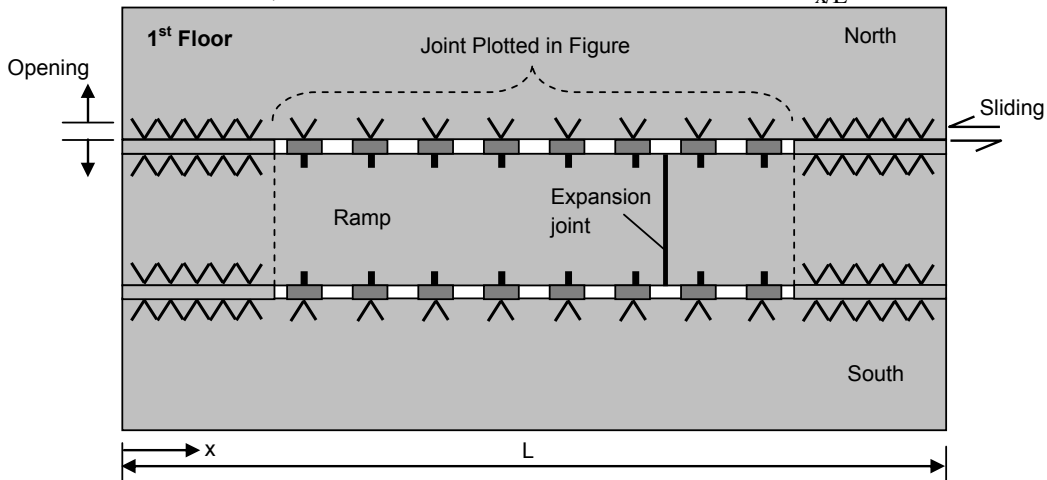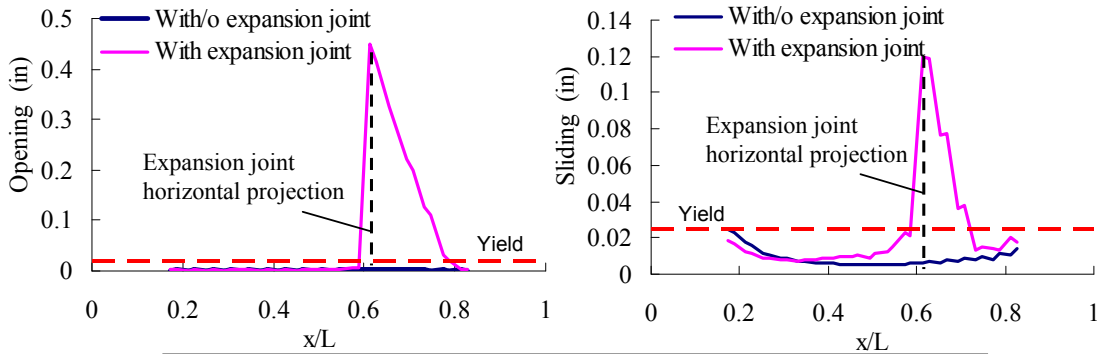
Fig. A2-66 Max demand profile in litewall to DT connector at 1st floor: (a) opening; (b) sliding.

The maximum litewall-to-DT connector deformation demand directly above the expansion joint is shown in Fig. A2-67. As seen, large inelastic deformation demands in opening and sliding are observed for all design cases, especially for the exterior wall structures. Therefore special detailing has to be applied to these connectors to provide large deformation capacity (0.5″ in opening and 0.2″ in sliding).
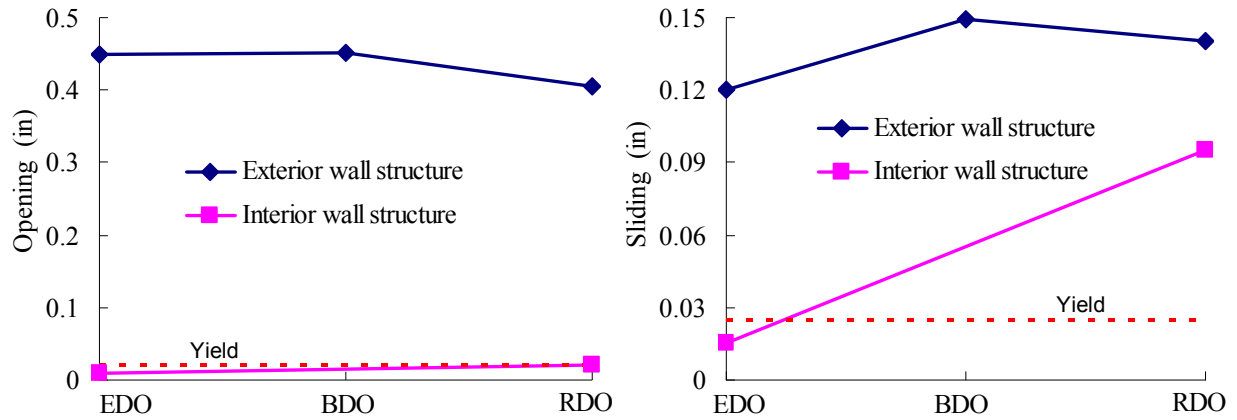
Fig. A2-67 Max demand in litewall to DT connector at 1st floor: (a) opening; (b) sliding.

To avoid a "capured column" effect for the litewall, flexible angle connectors are used on the litewall on the ramp side. Two flexible angles configurations are used in the analyses: (1) an angle with a slotted hole in the vertical leg and C-shaped fillet weld in the horizontal leg (See Fig. A2-68); and, (2) an angle with a C-shaped fillet weld (See Fig. A2-69).
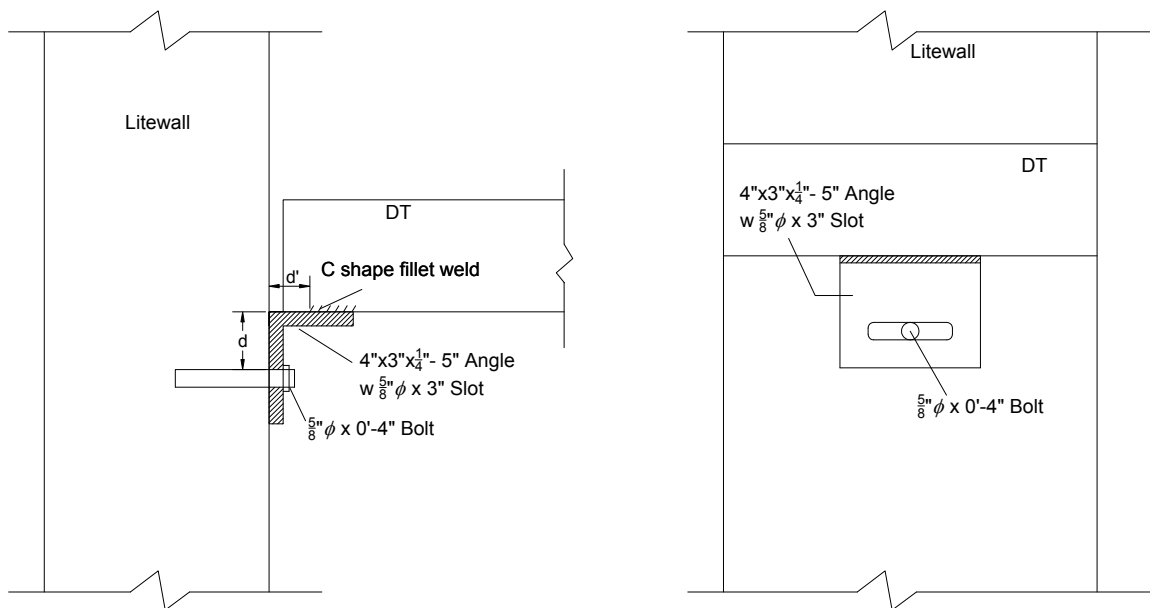
Fig. A2-68 Flexible angle with slotted hole.
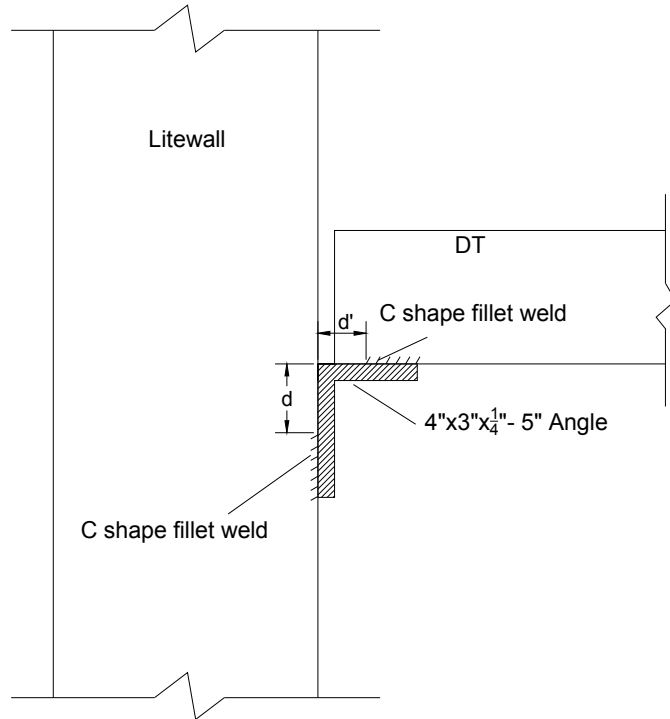
Fig. A2-69 Flexible angle with C-shape welding.

The first flexible angle configuration (with the slotted hole) is designed to be flexible in both tension and shear, and was used in analyses of the exterior wall parking structures. The second flexible angle configuration with the C-shaped weld is designed to be flexible in tension only, and stiff in shear. This configuration was used in analyses of the interior wall parking structures. The maximum deformation demands on the flexible connectors are shown in Fig. A2-70.
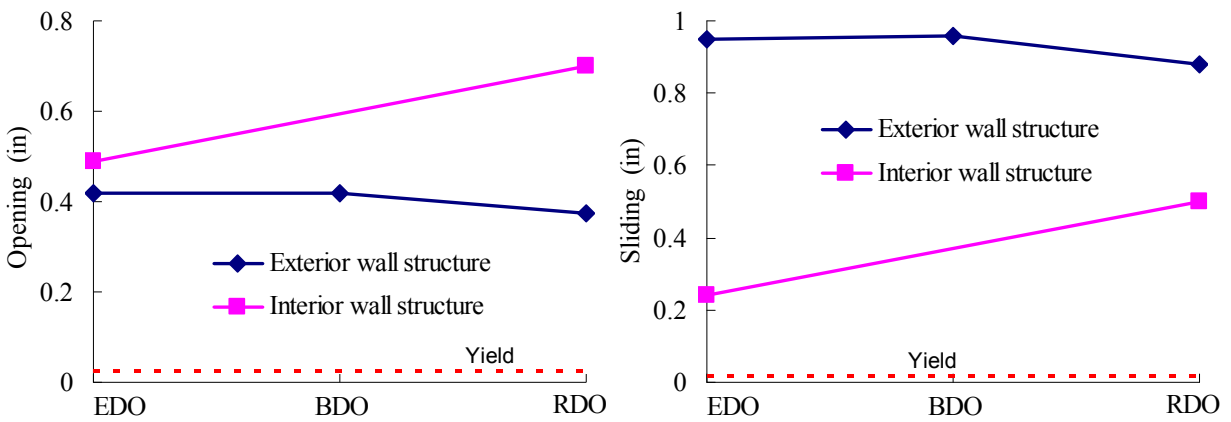
Fig. A2-70 Max demand in litewall to ramp flexible angle: (a) opening; (b) sliding.

A2.4.6 Sensitivity to Diaphragm Effective Stiffness

The design procedure in Part 1 involves the calculation of effective stiffness. , A diaphragm effective stiffness calculation is provided based on the diaphragm reinforcement provided. As diaphragms may be designed with different reinforcement at different joints, the values of E_{eff} and G_{eff} can vary along precast floor.

There are three options for calculating the E_{eff} and G_{eff} in diaphragm design:

    a)   Use varying (discrete) values for each precast floor joint/panel
    b)   Use the minimum values calculated among all the precast floor joint/panels
    c)   Use the average value calculated from all the precast floor joint/panels

This section investigates the sensitivity on the diaphragm design of calculating E_{eff} and G_{eff} in these different ways.

1.   Diaphragm Internal Force Calculation:

The diaphragm internal force calculation involves input of the E_{eff} and G_{eff} in a monolithic diaphragm computer analysis if the computer structural analysis option is used. To study the effect of E_{eff} and G_{eff}, a 2D monolithic diaphragm model for a parking structure (see Fig. A2-71) is created with the three aforementioned ways of calculating E_{eff} and G_{eff}. As a control case, a analysis is performed for the 2D model with the gross section properties. These static analyses are performed with the diaphragm design force applied as a uniform body force.

Fig. A2-71. 2D monolithic diaphragm model.

The diaphragm internal force diagrams for the south sub-diaphragm are shown in Fig. A2-72. For comparison purposes, the diagrams created using the FBD method (See Sec. 3.2.B in Part 3) is also shown in the Fig. A2-72. As seen, calculating E_{eff} and G_{eff} in different ways has little effect on the diaphragm internal force diagrams. Both the FBD method and the computer analysis methods produce similar diaphragm internal forces.
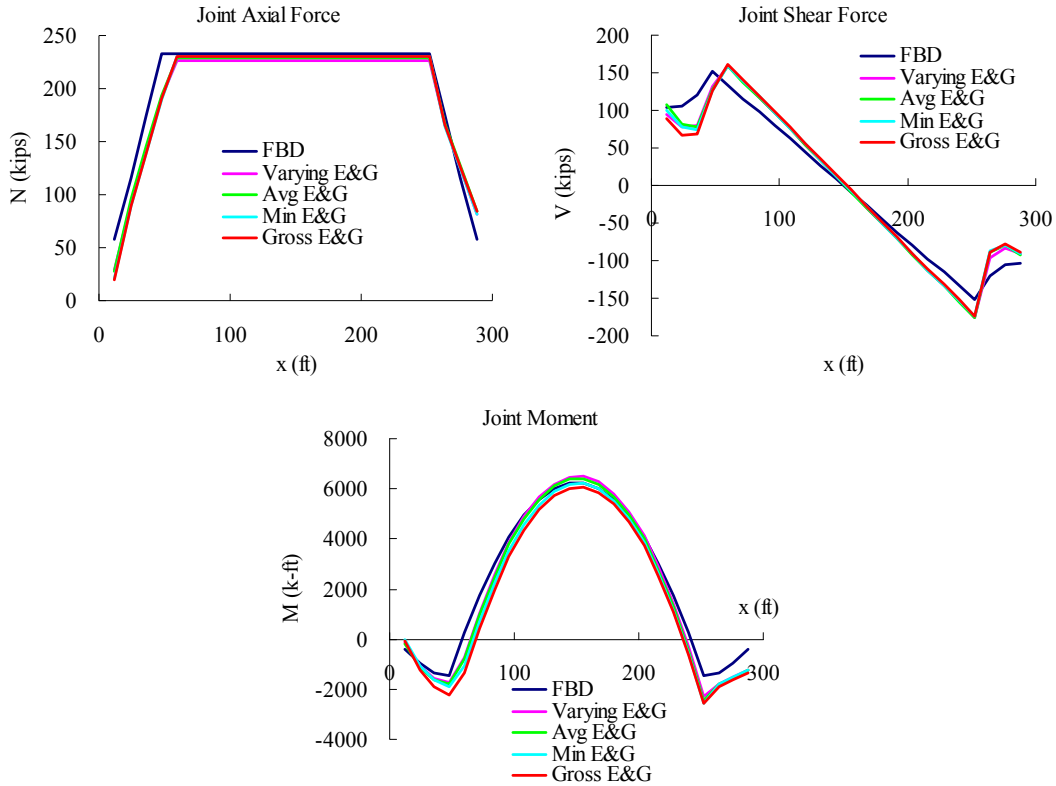
Fig. A2-72. Diaphragm internal force diagrams for the south sub-diaphragm.

2. Diaphragm Maximum (Midspan) Deformation

The diaphragm deformation calculation in the design methodology uses E_{eff} and G_{eff}. Figure A2-73 shows the calculated diaphragm midspan deformation using the integration method and static computer analysis method (See Sec. 3.3.C in Part 3) with E_{eff} and G_{eff} calculated in three aforementioned ways. As seen, calculating E_{eff} and G_{eff} in the different ways has a noticeable effect on the diaphragm deformation. As seen, the diaphragm deformation using the average value of E_{eff} and G_{eff} is similar to that using the discrete value of E_{eff} and G_{eff}. The integration method produces similar but slightly conservative diaphragm deformation values in comparison to the static computer analysis method.
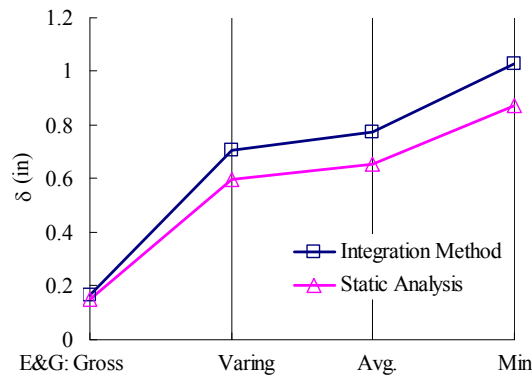
Fig. A2-73. Diaphragm midspan deformation.

C-A-104

A2.4.7 Tension-shear Coupling Effect

It has been observed from the individual diaphragm reinforcement tests that the tension and shear strength of the diaphragm reinforcement will be reduced under combined tension and shear loading. The analytical model used for the evaluation includes a tension-shear coupling feature (See Appendix B1 and B2) to capture the possible shear yielding in presence of tension load or tension yielding in presence of shear load. In this section, this approach is examined.

Figure A2-74 shows the force-deformation response for diaphragm reinforcement (chord and shear reinforcement) at the joint near the interior shear wall at the top floor of the 4-story interior wall parking garage designed with SDC D RDO diaphragms (refer to Example 2B). The pushover backbone under tension loading only and shear loading only is shown as the red dotted line in Fig. A2-74. As seen, for the chord and shear reinforcement, the tension and shear yield strength reduces due to the tension-shear coupling effect. The shear yield strength reduction in the presence of tension forces leads to large inelastic shear sliding deformation at a shear loading level which is less than its design yield strength. This result indicates that the analyses are successful of indentifying shear critical conditions due to the presence of tension, for shear loading levels lower than shear failure levels.
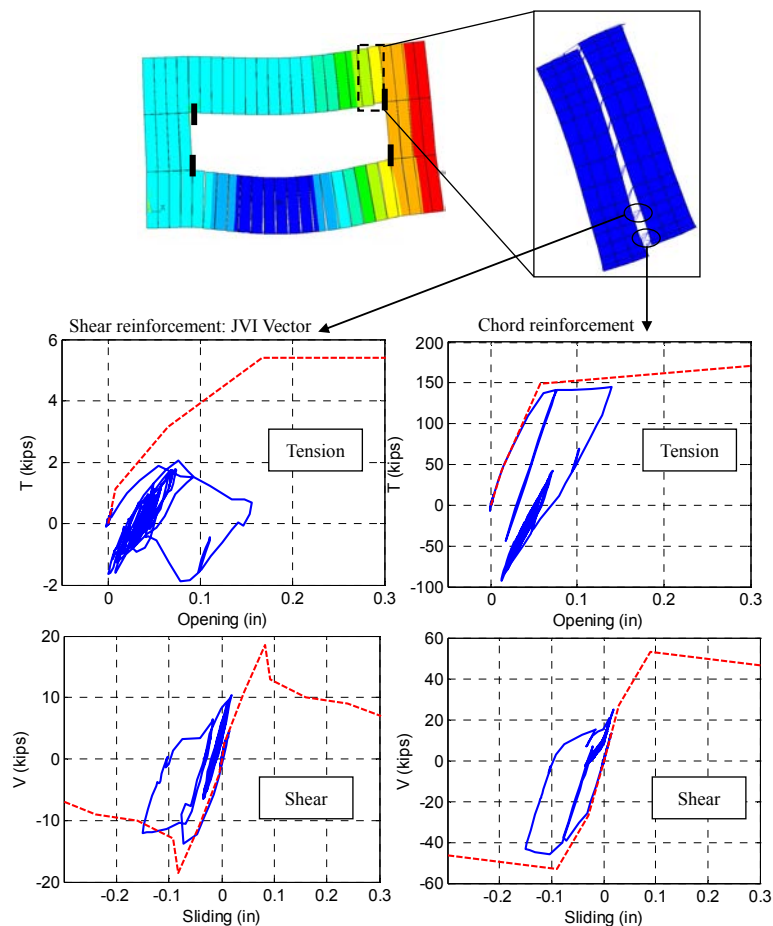
Fig. A2-74. Diaphragm reinforcement hysteresis response.

A2.4.8 Design Comparison: FBD Method vs. Horizontal Beam Method

Figure A2-9a and A2-9c indicate that the diaphragm internal moment and shear using the horizontal beam method are considerably larger than that from the FBD method proposed in the design methodology. However also note in Figure A2-9b that the simple beam method has zero required axial force while the FBD method produces a significant design axial force. Thus it is unclear which method will produce a more economical design under the combination of moment, axial and shear loading effects.

In this section, the two methods are compared in terms of design economy for a selected structure, the 4-story parking garage structure with exterior shear walls (Example 1A). To do so, the diaphragm joint design force (moment, axial and shear) obtained from the two methods is converted to an M-N-V interaction ratio using the following equation:

$$M - N - V = \sqrt{\left(\frac{M_u}{M_n} + \frac{N_u}{N_n}\right)^2 + \left(\frac{V_u}{V_n}\right)^2}$$

where M_u, N_u and V_u are the required diaphragm joint strength calculated using: (1) the FBD method, and (2) the horizontal beam method. M_n, N_n and V_n are the nominal diaphragm joint strength for design example 1A (See Design Example 1A in PART 4). These values are fixed for the two methods. Thus the method which produces a smaller M-N-V interaction ratio will produce a more economical design in comparison to the other method.

Figure A2-75 shows the M-N-V ratio at every joint in the north sub-diaphragm of the top floor for horizontal beam method and the FBD method. As seen, at every joint, the horizontal beam method requires a higher M-N-V ratio than the FBD method. This higher M-N-V ratio in the horizontal beam method implies that it will produce a less economical design compared to the FBD method. Given the fairly large amplified diaphragm design force proposed in the design methodology, it may be desirable to use the FBD method in determining the diaphragm design internal forces in order to keep the design economical and competitive.
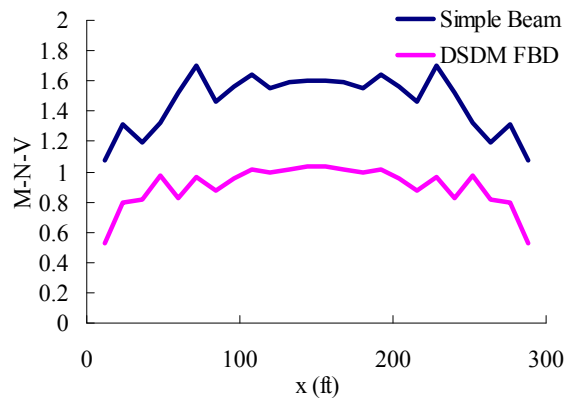
Fig. A2-75. M-N-V comparison for simple beam and FBD methods.

A2.5 REFERENCES

ACI 318-05. (2005). Building Code Requirements for Structural Concrete (ACI 318-05) and Commentary (ACI 318-05), American Concrete Insitution committee 318.

ASCE 7-05. "Minimum Design Loads for Buildings and Other Structures". American Society of Civil Engineering 2005.

Fleischman, R.B., Naito C.J., Restrepo J., Sause R., Ghosh S.K., Wan G., Schoettler M., and Cao L. (2005). "Seismic design methodology for precast concrete diaphragms, Part 2: research program." PCI Journal, 51(6), 2-19.

Fleischman, R.B., Sause, R., Pessiki, S., and Rhodes, A.B. (1998). "Seismic behavior of precast parking structure diaphragms." PCI Journal, 43 (1), Jan-Feb: 38-53.

Pincheira, J. A., Oliva, M. G., and Kusumo-rahardjo, F. I. (1998). "Tests on double tee flange connectors subjected to monotonic and cyclic loading." PCI Journal, 43 (3): 82-96.

Ware A., Fleischman R.B., and Zhang, D. "Calibration of 3D finite element model using shake table test results". Under preparation, 2012.

Zhang, D., Fleischman, R.B., Naito, C., and Ren, R. (2011). "Experimental evaluation of pretopped precast diaphragm critical flexure joint under seismic demands." J. Struct. Eng. ASCE, V137(10).

Appendix B. Development and Calibration of Analytical Models

The analytical research performed to develop the PART 1 design procedure was conducted using models developed, verified and calibrated on the basis of extensive parallel experimental work. These analytical models, intended for precast diaphragm *research* and not design, are finite element (FE) based[9], and involve both two-dimensional (2D) and three-dimensional (3D) representations. The key aspect of these models is that the precast diaphragm connectors are discretely modeled directly as nonlinear elements whose properties and characteristics are developed based on the monotonic and cyclic tests of individual precast diaphragm connector. Such models have been termed "discrete" precast diaphragm models. Thus, the analytical models will be identified as *2D-FE* and *3D-FE discrete models*.

The analytical model development involved two primary activities: (1) development of connector elements using the results of tests on isolated precast diaphragm connectors; and, (2) precast diaphragm and structure model calibration using the results from tests of critical precast diaphragm joints and a half-scale shake table test of a diaphragm-sensitive precast structure.

In the connector development stage, two levels of models were developed: (a) a 2D-FE discrete precast *diaphragm* model employing monotonic shear-tension coupled connector elements used for nonlinear pushover analyses of isolated diaphragms; and (b) a 3D-FE discrete diaphragm precast *structure* model employing cyclic degrading connector elements used for nonlinear transient dynamic analyses. The former determined the capacity and limit state sequence of the precast diaphragms. The latter provides the seismic demands on precast diaphragms and its reinforcement under simulated earthquakes. **Appendix B.1** describes the creation of the connector elements for the 2D-FE discrete model; **Appendix B.2** describes the creation of the connector elements for the 3D-FE discrete model.

In the model calibration stage, the 3D-FE discrete precast diaphragm structure model was calibrated through large-scale testing. First, half-scale tests of precast diaphragm joints in critical flexure and shear regions were performed to evaluate the accuracy of modeling precast diaphragm local behavior. These tests were also used to demonstrate performance and map diaphragm damage to seismic hazard levels. These tests indicated that the cyclic model for precast diaphragm reinforcement developed based on isloated connector tests, was able to reasonably reproduce the response of groups of precast diaphragm connectors that comprise the flexure-critical and shear-critical joints level within the precast diaphragm. The second test is a half-scale shake table test of a 3-story precast structure. Using the shake table test results, the 3D precast diaphragm model has been verified and calibrated. **Appendix B.3** describes the model calibration associated with the diaphragm joint testing; **Appendix B.4** describes the model calibration associated with the diaphragm shake table testing.

BACKGROUND

Precast diaphragm seismic behavior is difficult to capture using the commonly used monolithic diaphragm models available in typical design office structural analysis packages. Thus, while structural analysis software can be used in the *design* procedure (See Sec. 3.1 PART 3), finite element models of precast floor systems with *discrete* representations of the connector elements were developed for the *research* underlying the design methodology (BSSC TS4 2009):

Floor diaphragms are often treated as rigid and sufficiently strong in the analysis and design of building structures in response to seismic excitation. This assumption cannot always be made for precast concrete construction in which the floor system is composed of series of individual flooring units. A critical feature of these diaphragms is the nature of the force transfer across the joints between the flooring units. The units are joined by connectors alone or in concert with a thin reinforced topping slab. Thus, unlike the distributed force transfer in monolithic floor slabs that serve as diaphragms in steel composite and reinforced concrete structures, forces in precast diaphragms are transferred at discrete connector locations. The floor joints serve as critical sections in the precast diaphragm, and thus precast diaphragm behavior is highly dependent on the characteristics of the connectors.

---

[9] Using the general purpose finite element software program ANSYS.

Since the collapses of several precast concrete structures due to failures of the floor systems in the 1994 Northridge earthquake (Iverson and Hawkins 1994), steady progress has been made on understanding the behavior of precast floor diaphragms for the purposes of improving their seismic design. These advances in knowledge have been driven largely through analytical research.

Diaphragm analytical models used in research, like those used in the design practice, originally involved monolithic models, including Bernoulli beam formulations (Nakaki 2000), fiber element and smeared crack models (Fleischman et al. 1998), and elastic plane stress finite elements (Tena Colunga and Abrams 1996) (Ju and Lin 1999) (Lee and Kuchma 2008). However, recognizing the limitations associated with modeling precast diaphragms using monolithic models, precast diaphragm models with *discrete* representations of the connectors were developed.

The discrete diaphragm models have been used extensively in research on precast concrete floor diaphragms in the DSDM research. These models employ diaphragm connector elements based on the extensive connector tests performed in the DSDM research. Among other advantages, these models offer the ability to map individual connector demand directly to global diaphragm response and simulate the localized mechanisms that can lead to global non-ductile failure modes.

In these models (see schematic in Fig. B-1), the precast concrete floor units are modeled as elastic plane stress elements. In the joints between the precast units, the precast connectors are modeled as assemblages of nonlinear springs, links and contact elements to capture the actions between the precast units. Initial versions of the discrete models were used for two-dimensional (2D) nonlinear static monotonic "pushover" analyses of isolated diaphragms (Farrow and Fleischman 2003) (Fleischman and Wan 2007). The formulation of these elements is covered in *Appendix B1*. The two-dimensional models were extended to three-dimensional precast structure models for dynamic analyses (earthquake simulations). The connector elements for the three-dimensional precast structure models possess the cyclic characteristics of diaphragm reinforcement. These models were used to develop and calibrate the design factors for the precast concrete design methodology. The development of the connector elements for the three-dimensional analysis is covered in *Appendix B2*.
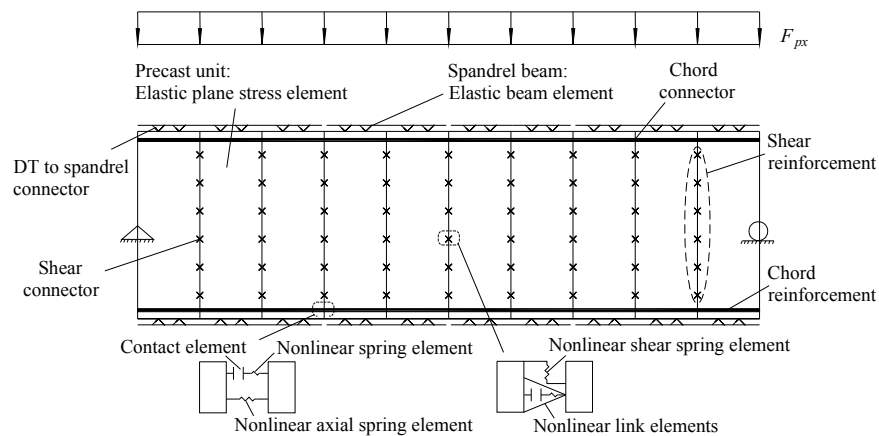
Fig. B-1. Discrete diaphragm model

Appendix B1. Connector Elements for 2D Diaphragm Pushover Models

Appendix B.1 describes the formulation of the general connector element developed for use in the 2D-FE discrete model for pushover analyses of precast concrete diaphragms. The connector elements are nonlinear, coupled for shear and tension interaction, enable friction mechanisms, and possess descending branch behavior. The properties of the connector elements are aligned to match results from tests of isolated precast connectors. These elements were used for diaphragm pushover analyses (Fleischman and Wan 2007), and are the basis for the connector elements in 3D-FE dynamic models (*See Appendix B.2*).

The 2D-FE discrete diaphragm model includes monolithic diaphragm connector elements discretely modeled within two-dimensional finite-element representations of an isolated floor diaphragm. The capabilities of the 2D-FE discrete models have evolved from diaphragm flexure response only (Fleischman et al. 1998), to uncoupled flexure and shear response (Farrow and Fleischman 2003), to coupled flexure and shear response (Fleischman and Wan 2007) during the DSDM research project.

The 2D-FE discrete models have been primarily used in nonlinear static analyses of isolated diaphragms under increasing monotonic in-plane inertial forces, to determine the precast diaphragm characteristics, limit states and capacity. Such analyses are similar to so-called "pushover" analysis (FEMA 365 2000) used to evaluate the capacity of the lateral force resisting system (LFRS) e.g. shear walls, moment frames, and this same terminology is adopted here.

Connector characteristics impact the global characteristics (Ren and Naito 2011) and local failure modes (Wood et al. 2000) (Farrow and Fleischman 2003) in the floor diaphragm. Thus, the connector elements in the 2D-FE discrete model must possess accurate representation of the connector stiffness, strength and deformation capacity. These values are needed for both shear and axial response, and must be coupled as diaphragm connectors are often subjected to simultaneous actions (Naito and Ren 2011).

TABLE OF CONTENTS

B1.1 INTRODUCTION

Precast Diaphragm Connectors

A variety of connectors are used in practice to provide precast diaphragm reinforcement, including industry standard hardware and proprietary connections (Naito et al. 2006). The creation of the 2D-FE connector models centered around a set of commonly-used flange-to-flange connectors that can be used as the complete set of reinforcement for a precast floor diaphragm (See Figure B1-1): (a) the JVI Vector[10] for shear reinforcement; (b) a dry chord connector for flexure reinforcement; and (c) an angled bar-plate connector, often used to connect precast floor units to beams and walls. These connectors, like others, transfer force through anchorage mechanisms created by bars extending into the precast unit, and employ field-welds to complete the connection between panels. These particular connectors have been extensively tested, and are used here to demonstrate the connector element construction.
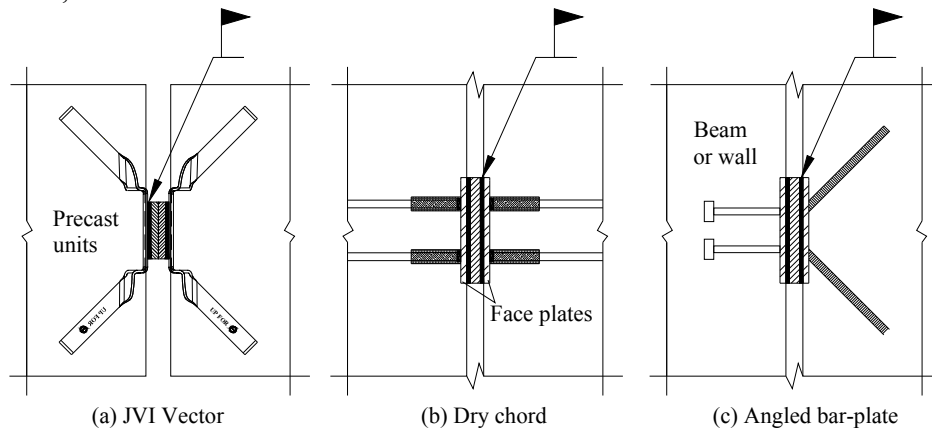
Fig. B1-1: Precast diaphragm connectors.

Diaphragm Connector Force Demands

Consider Figure B1-2(a), a schematic of a simple precast diaphragm under lateral load. Note that the neutral axis is not at the centroid (Zhang et al. 2010). Indicated on the schematic are the different internal force conditions that can develop at various discrete transfer points within the diaphragm. The following conditions approximate the forces to which connectors are subjected at any one instant: (1) tension alone; (2) compression alone; (3) shear in the presence of tension; (4) shear in the presence of compression; and (5) pure shear.
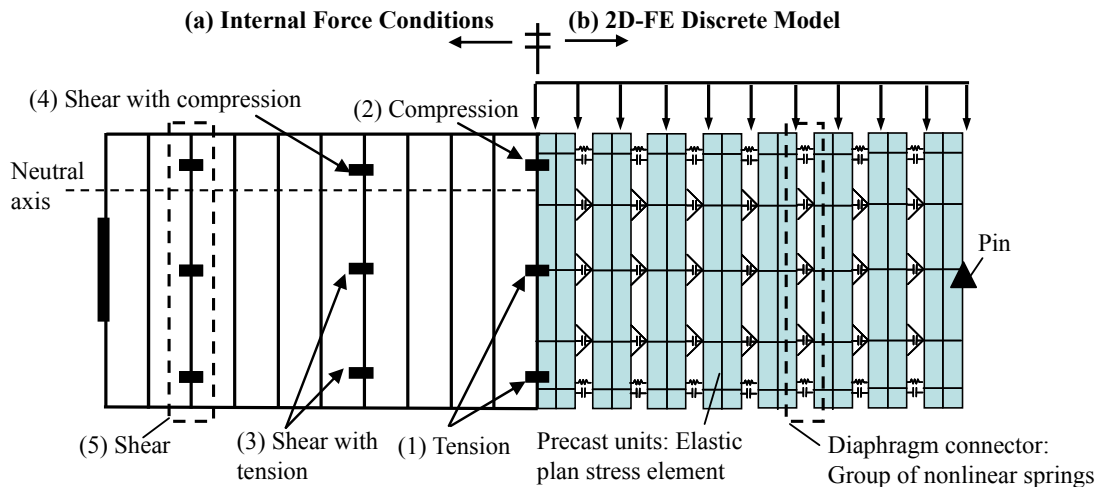
Fig. B1-2. Precast diaphragm schematic showing: (a) connector loading cases; (b) 2D-FE discrete model.

---

[10] JVI, Inc. Lincolnwood, IL 60712

Connector Response to Force Combinations

The Figure B1-2(a) schematic implies two conditions must be considered in modeling: (1) Connector response under combined tension and shear; and, (2) Connector shear response in the presence of axial compression. Consider first connector response under combined tension and shear. As seen in the monotonic connector tests results (Pinchiera et al. 1998) of Figure B1-3(a), precast connectors exhibit strength and deformation reductions under combined tension and shear loading relative to the connector subjected to only tension or only shear load.
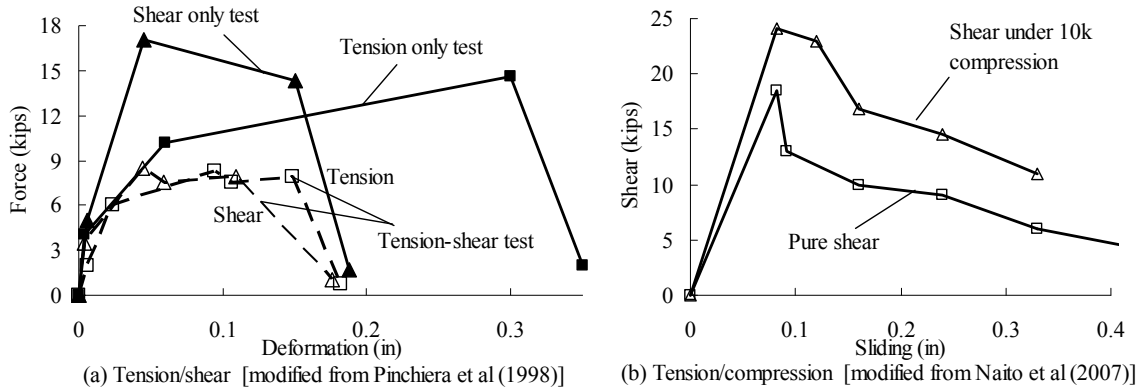
Fig. B1-3. Coupled connector response.

Next consider the shear response under axial compression (Naito et al. 2007) shown in Fig. B1-3(b). As seen, precast connectors exhibit shear stiffness and strength increases when axial compression is present. Note that this can be shear-friction (Mattock and Hawkins 1972) in a topped-precast diaphragm, or simply direct friction behind the face plate (refer to Fig. B1-1) in an untopped diaphragm (Naito et al. 2007).

B1.2 2D-FE DISCRETE MODEL

In the 2D-FE discrete model (See Fig. B1-2b), diaphragm precast units are modeled as elastic plane stress elements. The connectors between precast units are modeled as assemblages of nonlinear springs and contact elements.

Connectors in a realistic floor diaphragm, with more complexity/irregularity in both the floor system and LFRS layout (frames or walls), and subjected to a ground motion of uncertain attack angle, producing bi-directional components, will be under simultaneous and varying non-proportional combinations of tension/compression and shear (Zhang et al. 2010).The 2D-FE discrete model has the ability to provide a realistic representation of the precast floor global boundary conditions (confinement perpendicular to the joint due to the other structural elements) and local deformation patterns (e.g. joint opening not conforming to Bernoulli beam assumptions) as the diaphragm responds to seismic loading.

Thus, this modeling technique has the ability to more accurately capture the local demands on individual precast connectors or key diaphragm joints in an earthquake, provided the connector element model can replicate key behaviors.

The presence of simultaneous shear and axial force in the diaphragm connector loading (Fig. B1-2a), including in key regions of the diaphragm under earthquake loading (Zhang et al. 2010), in conjunction with the reduced strength exhibited in precast connectors in tension (Fig. B1-3a), and the increased strength and stiffness in compression (Fig. B1-3b), underscores the importance of capturing both the tension-shear coupling effect and the friction mechanism associated with compression in the precast diaphragm connector element model.

Three steps are needed to accomplish this goal: (1) An experimental program that establishes the needed characteristics of a given connector; (2) The creation of an element that can distinguish and

respond to the conditions described above; and (3) The derivation of algorithms that convert the test data into model input. These steps are described in this paper.

B1.3 CONNECTOR TESTING PROGRAM

The connector elements were developed in conjunction with a comprehensive testing program on common precast diaphragm connectors (Naito et al. 2006) (Naito et al. 2007), and also make use of results from previous testing (Pinchiera et al. 1998) (Oliva 2000) (Shaikh and Feile 2004). A distinction is drawn between those test required for connector qualification in a new design methodology (BSSC TS4 2009), and supplemental tests performed to improve analytical models.

Connector Qualification Testing

The testing program (Refer to Fig. B2-2, *Section B2.1*) produced a set of qualification protocols for precast connectors (Naito and Ren 2011). Figure B1-4 shows the connector qualification backbone for tension and shear response based on FEMA-356 (2000) curve typology. The curves are constructed from the cyclic test envelope and express the key characteristics of the connector in tension and shear: initial stiffness (K_{iT}, K_{iV}), yield strength (T_Y, V_Y), secondary stiffness (K_{2T}, K_{2V}), and deformation capacity (Δ_{uT}, Δ_{uV}). It is noted that for precast connectors, shear response is typically associated with Type 3 curve (force-controlled non-ductile behavior), while tension response is typically associated with Type 1 or 2 curve (deformation-controlled ductile behavior). Note also that the deformation capacity definition for the Type 2 and Type 3 curves is slightly different. The dashed line represents response beyond the range of expected demand in precast diaphragms.
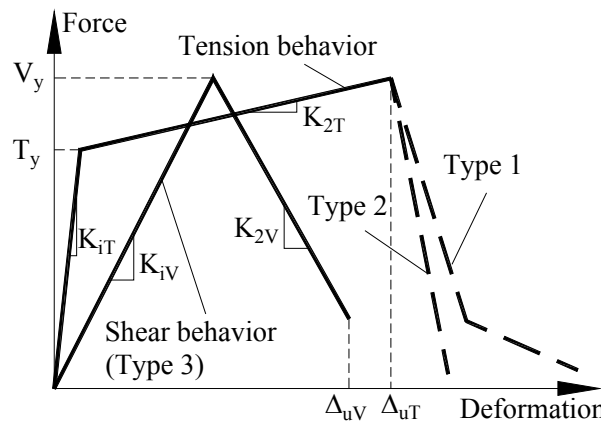
Fig. B1-4. Connector qualification backbone [modified from Naito and Ren (2011)].

Table B1-1. Characteristics measured in isolated connector tests

Test Series	Load Protocol	Characteristic			
		Initial Stiffness	Yield Strength	Secondary Stiffness	Deformation Capacity
Qualification Protocol	Tension Load Only	K_{iT}	T_Y	K_{2T}	Δ_{uT}
	Shear Load Only	K_{iV}	V_Y	K_{2V}	Δ_{uV}
Connector Element Model	Shear w/compression	-	$V_Y{}^C$	-	-
	Shear w/tension	-	$V_Y{}^{VT}$, $T_Y{}^{VT}$	-	-

The upper part of Table B1-1 lists the tests used to populate the characteristics of the qualification backbone curves. These tests are performed on isolated connectors: (1) a cyclic tension test

with zero applied shear force; and (2) a cyclic shear test with zero applied tension force. These tests are performed to qualify connectors within the framework of a new design methodology (BSSC TS4 2009). However, the data produced also serves as the basic data to create connector element models.
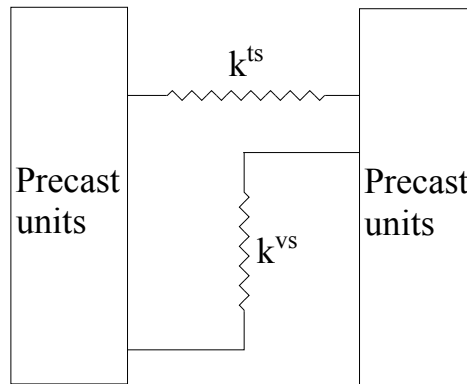
Fig. B1-5. Simple uncoupled spring model (Farrow and Fleischman 2003).

Figure B1-5 shows an uncoupled connector element that could be constructed with the eight Qualification Protocol data entries in Table B1-1. Such an approach was used in the past (Farrow and Fleischman 2003). The four parameters that describe the uncoupled tension characteristic $\{K_{iT} \ T_Y \ K_{2T} \ \varDelta_{uT}\}$ are obtained directly from the tension load only test. The four parameters that describe the uncoupled shear characteristic $\{K_{iV} \ V_Y \ K_{2V} \ \varDelta_{uV}\}$ are obtained from the shear load only test. These parameters can be considered as a basic set of characteristic values that can be used to build a more advanced model for the DSDM research, as described in this Appendix.

Supplemental Testing
A set of supplemental tests was performed in the research program. These tests, external to the qualification procedure, were used to develop more reliable connector elements for the 2D-FE discrete model (See Table 1, lower portion). These tests subjected isolated connectors to: (1) shear in the presence of constant axial compression (Naito and Ren 2011); and (2) a combination of tension and shear loading. The former is used to determine coefficient of friction used in the connector model; the latter is used to calibrate the tension-shear coupling within the connector element.

Two important ratios are identified for connector response to combined shear and tension: (1) the tension-to-shear force ratio α, $\alpha = T/V$; and (2) the tension-to-shear deformation ratio λ, $(\lambda = \varDelta_T/\varDelta_V)$. These values do not typically coincide in response due to differences in tension and shear stiffness. Thus, one of these ratios is enforced in testing, either α for force control (Pinchiera et al. 1998), or λ for deformation control (Naito et al. 2006), and the other ratio measured through instrumentation.

B1.4 PRECAST CONNECTOR ELEMENT MODEL CONSTRUCTION
The precast connector element for the 2D-FE discrete model is a nonlinear shear-tension coupled friction element. The connector element must be feasible for insertion into precast diaphragms models with dozens to hundreds of these connectors. The element configuration is selected to match observed behavior in these tests, and the properties are selected to match the characteristic values obtained in the testing.

Figure B1-6(a) shows the basic components of the precast diaphragm connector element. The connector element is constructed from an assemblage of three groups of finite element components: (1) inelastic "inclined" links in order to capture the coupled tension and shear behavior; (2) inelastic tension and shear springs in parallel with the link elements to partially uncouple the response as observed in the testing; and, (3) a contact and an inelastic compression spring in series for modeling the compression and friction behavior.

(a) Model   (b) Characteristic backbone
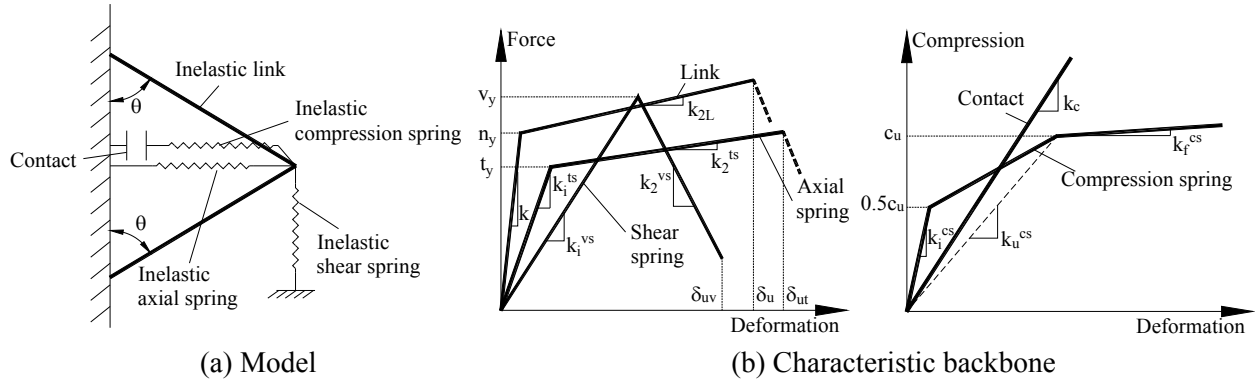
Fig. B1-6. Precast diaphragm connector model.

Key features of the element include: (1) capturing of the interaction of components of load (tension-shear coupling) through the inclined links; (2) mobilizing the effect of applied compression on shear resistance through use of a contact with friction capabilities; and (3) including compression limit states (softening/crushing) of the surrounding concrete through a nonlinear spring in series with the contact.

The characteristic backbone for each component is shown in Fig. B1-6b. The required properties for these components are derived in this section. The derivation uses the following notation: small letters indicate the local response of individual components of the connector element; capital letters indicate the global degrees of freedom (DOFs) of the overall connector element; and, bold capital letters indicate the experimental data derived from tests on isolated connectors (e.g. Table B1-1).

The mathematical formulation of the coupled link is described in supplemental section B1-10 found in this appendix, located after the Reference Section, and summarized here. A partially coupled formulation is selected. Section B1-10 first derives relationships for a fully coupled link assemblage (See Fig. B1-7). The fully coupled link is then shown to not be fully adequate to describe most precast diaphragm connectors due to differences in shear and tension response quantities, but serves as the basis for the partially-coupled formulation.

(a) Kinematics   (b) Shear transformation   (c) Tension transformation
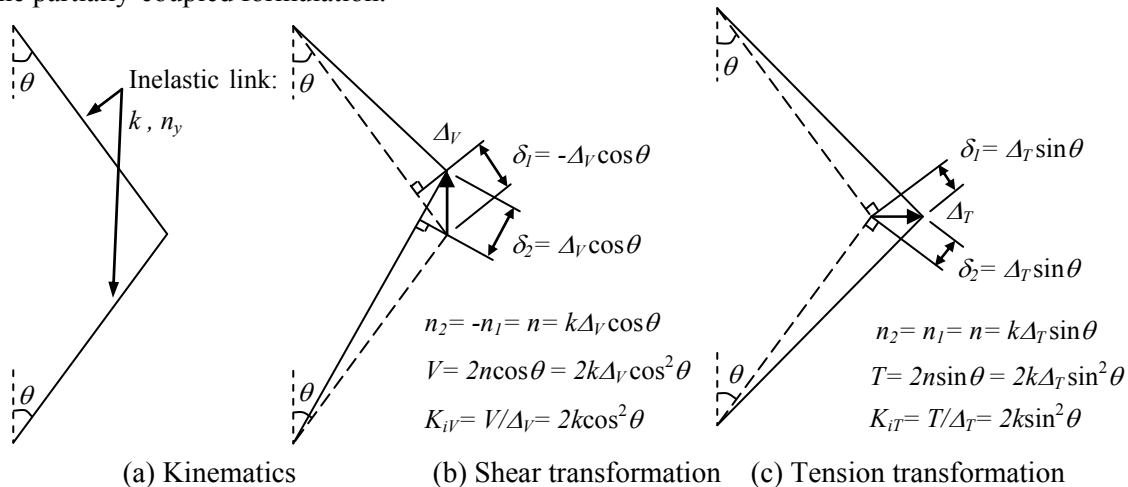
Fig. B1-7. Fully-coupled link formulation.

The partially coupled formation is achieved through the addition of uncoupled inelastic shear and axial tension springs to the coupled link elements (Refer to Fig. B1-6). This partially-coupled formulation is effective in describing most precast diaphragm connectors, as shown later in Section B1-10.

The key aspects of the connector model include:

(1) Nonlinear connector elements with properties [initial stiffness (k), yield strength (n_y), secondary stiffness (k_{2L}) and deformation capacity (δ_u)] and an orientation of angle θ

(2) Nonlinear shear and tension springs with properties [initial stiffness (k_i^{vs}, k_i^{ts}), yield strength (v_y, t_y), secondary stiffness (k_2^{vs}, k_2^{ts}) and deformation capacity (δ_{uv}, δ_{ut})].

The key aspects of the connector formulation described in Section B1-10 are summarized here:

(1) A connector element link orientation angle θ aligned to ratio of the tension and shear yielding deformations of the uncoupled springs to that of the link elements. This angle is calculated using Equation 5 from the supplemental section, reproduced here:

$$\theta = \tan^{-1}[(V_Y K_{i,T} / T_Y K_{i,V})] \qquad \textit{(Eqn. 5)}$$

(2) An uncoupled tension (ω_t) and shear (ω_v) strength factor, defined as the ratio of strength of the coupled vs. uncoupled portions of the connector element

$$\omega_t = t_y / T_Y$$
$$\omega_v = v_y / V_Y$$

Trial ω_t and ω_v factors can be found using the strength reduction charts (Fig. B1-9), based on data from tension-shear proportional loading test (See Section B1.6).

(3) The final factors ω_t and ω_v are selected to match the strength reductions under combined tension and shear loading observed testing (See Sec. B1.6) or an assumed level of coupling in the absence of supplemental testing. Compare the connector response between model and test under tension-shear proportional loading and modify the selected trail uncoupled tension (ω_t) or shear (ω_v) strength factor if necessary. To produce an accurate total strength between the coupled and uncoupled components, the ratio of ω_t and ω_v has to meet Eqn. 6 from the supplemental section, reproduced below:

$$(1-\omega_v)/(1-\omega_t) = T_Y \cos\theta / V_Y \sin\theta \qquad \textbf{(Eqn. 6)}$$

(4) Finally, the other model properties for the link, inelastic shear springs and inelastic tension springs (if necessary) are calculated using Eqn. 7 to 9 from the supplemental section.

B1.5 RESPONSE UNDER COMPRESSION

The response to axial force perpendicular to the joint is highly asymmetric. In tension, the elements of the connector are free to deform (as covered in the previous section), while in compression these elements bear directly on the surrounding concrete. This characteristic must be included for the model to provide an accurate neutral axis, thereby impacting both local (opening) deformation demand as well as global diaphragm response.

Contact Element Formulation: Compression

The asymmetric response is accomplished in the model through the use of contact pseudo-elements (refer to Fig. B1-6a). These elements use a penalty function formulation to limit incompatible penetration of the precast units (ANSYS 2007). The contact elements are linear and the surrounding precast panels in the 2D-FE discrete model are represented with elastic plane stress elements (refer to Fig. B1-2). Thus, an inelastic compression spring is introduced in series with the contact element (refer to Fig. B1-6a) to capture the softening and eventual limiting compressive strength due to concrete crushing, thereby preventing artificially high compression forces from developing in the floor system.

The compression spring properties are obtained through a theory-based calculation for two precast concrete half-panels acting over a total gage length b (center-to-center panel distance) and effective compression width d_{eff} (width of face plate for untopped connector or center-to-center spacing for topped connector) (refer to Fig. B1-8a). Initial uncracked compression stiffness (K_i), secant compression stiffness (K_u) at peak concrete compressive stress, and compression force (C_u) at peak concrete compressive stress are determined using the following expressions:

$$K_i = E_c d_{eff} t / b \qquad (Eqn. B1-1a)$$

$$K_u = E_{cu}\, d_{eff}\, t\, /\, b \qquad\qquad \text{(Eqn. B1-1b)}$$
$$C_u = f_c{}'\, d_{eff}\, t \qquad\qquad \text{(Eqn. B1-1c)}$$

where E_c is the elastic modulus of concrete; E_{cu} is the secant modulus of concrete for a peak compressive stress $f_c{}'$ and strain ε_0 ($E_{cu} = f_c{}' / \varepsilon_0$); and t is the precast panel thickness. Note from Fig. B1-8b that K_u is calculated by assuming the concrete starts to soften at $0.5f_c{}'$. For numeric stability in the model, the post-crushing response is provided a slight positive slope, with tangent compression stiffness (K_f) taken as 1% of K_u, rather than the actually concrete degrading behavior (refer to Fig. B1-8b). This assumption has only a minor effect on the response of the precast diaphragm, since for a typical precast diaphragm with large depth, the compression force that can be sustained is limited by the tensile strength of the connector at the other end of the joint. For high axial collector cases, error occurs in a high axial compressive force, and a limit on that force through "ductile" crushing eliminates that artifact. Thus, the approximation for post-peak concrete compression response was deemed acceptable.

The stiffness of the three components in series (elastic panels and contact, and inelastic compression spring) in the model is aligned to match the theory-based values in the above expressions. The elastic panel stiffness in the model (k_e) is equal to the theoretical initial uncracked stiffness (Eqn. B1-2a) by assigning the elastic modulus of concrete (E_c) to the plan stress elements. The contact stiffness (k_c) and initial inelastic compression spring stiffness (k_i^{cs}) are set as a high order values ($k_c = 20k_e$ and $k_i^{cs} = 200k_e$) to make the initial stiffness in the model close to the theoretical initial stiffness (Eqn. B1-2b).

The secant stiffness (k_u^{cs}) and tangent stiffness (k_f^{cs}) of inelastic compression spring are solved using Eqn B1-2c and Eqn. B1-2d by equaling the combined stiffness of three components to the theoretical stiffness.

$$k_e = K_i \qquad\qquad \text{(Eqn. B1-2a)}$$
$$(1/ k_e + 1/ k_c + 1/ k_i^{cs})^{-1} \approx K_i \qquad\qquad \text{(Eqn. B1-2b)}$$
$$(1/ k_e + 1/ k_c + 1/ k_u^{cs})^{-1} = K_u \qquad\qquad \text{(Eqn. B1-2c)}$$
$$(1/ k_e + 1/ k_c + 1/ k_f^{cs})^{-1} = K_f \qquad\qquad \text{(Eqn. B1-2d)}$$
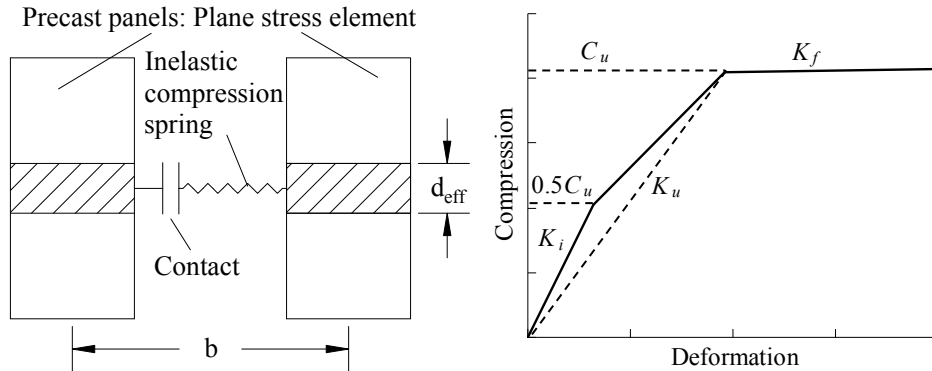
Fig. B1-8. Modeling of contact effect: (a) model; (b) theoretical stiffness.

Contact Element Formulation: Friction

Compression across the joint also affects the shear response through friction between precast units and the diaphragm connector under compression. A coefficient of friction (μ_s) is assigned to the contact element to account for this friction effect. The coefficient of friction (μ_s) is calibrated from the results of isolated connector shear tests (Naito et al. 2007) with and without the presence of axial compression:

$$\mu_s = (V_Y{}^C - V_Y) / C \qquad\qquad \text{(Eqn. B1-3)}$$

where $V_Y{}^C$ is the peak shear strength under constant axial compression force (C) obtained from a cyclic shear test with constant axial compression force.

B1.6 IMPLEMENTATION OF CONNECTOR ELEMENT

Model Construction

The implementation of the diaphragm connector element uses the partially-coupled formulation as described in section B1-4 and contact element formulation as described in section B1-5. This section will focus on the procedure for construct tension-shear coupled model while the contact model can be straightly constructed using Eqn. B1-1 to B1-3. The step-by-step coupled model construction procedure for the connector element is summarized as follows:

(1) Calculate the connector element link orientation angle θ using Equation 5 from the supplemental section.
(2) Read a trial uncoupled tension (ω_t) and shear (ω_v) strength factor using the strength reduction charts (Fig. B1-9), based on data from tension-shear proportional loading test. Average value can be used if multiple tension-shear proportional loading tests are available.
(3) Adjust the strength factors to meet Eqn. 6 from the supplemental section.
(4) Calculate the model properties for link, inelastic shear and tension springs using Eqn. 7 to 9 from the supplemental section.
(5) Compare the connector response between model and test under tension-shear proportional loading and modify the selected trial ω_t or ω_v factor if necessary.

(a) JVI Vector   (b) 2#5 chord   (c) #3 Angled bar-plate
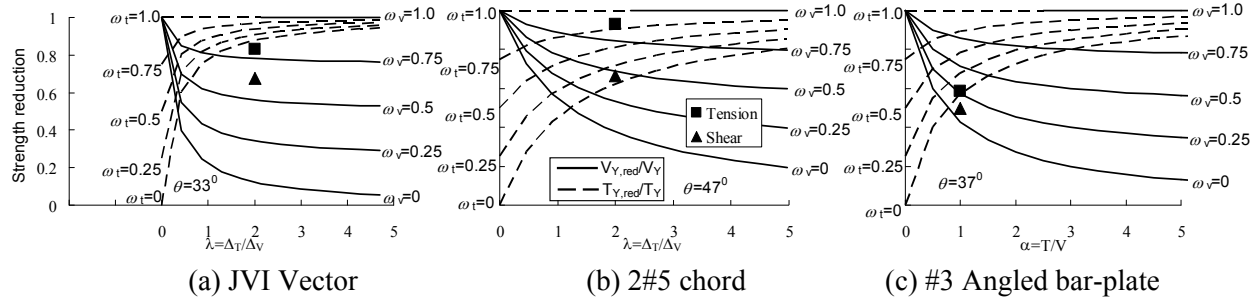
Fig. B1-9. Strength reduction chart with test data mapping

Model Construction Example

Table B1-2 shows the connector characteristics based on the qualification backbone of isolated tension and shear tests for the JVI Vector (Naito et al. 2006), a 2#5 chord connector (Naito et al. 2007) and a #3 angled bar-plate (Pinchiera et al. 1998). Following the procedure described above, the model parameters (θ, ω_t and ω_v) are given in Table B1-3 and calculated as follows:

(1) The orientation of link element is calculated using Eqn.5.
(2) The uncoupled strength parameters are selected based on the strength reduction charts with the tension-shear proportional tests results mapping on (see the black square and triangle in Fig. B1-13). It is noted that the selected uncoupled strength parameters have to meet Eqn.6.
(3) The model properties for the link element, inelastic tension and shear springs are calculated from Table B1-1 and Table B1-2 using Eqns. 7 to 9.
(4) The resulting connector element properties are shown in Table B1-4.

Table B1-2. Connector characteristics measured in qualification tests.

Characteristic	JVI Vector		2#5 Chord connector		#3 Angled bar-plate	
	Tension	Shear	Tension	Shear	Tension	Shear
Initial stiffness (k/in)	38	226	524	176	170	380
Yield strength (k)	4.8	18.1	42	15	10.22	17.1
Secondary stiffness (k/in)	5.4	-38	14.1	-12	18	-75
Deformation capacity (in)	0.498	0.490	0.607	0.736	0.300	0.250

Table B1-3. Model parameters for partially-coupled formulation.

Model parameters	θ	ω_t	ω_v
JVI Vector	33^0	0	0.6
2# 5 Chord connector	47^0	0.83	0.55
#3 Angled bar-plate	37^0	0	0.2

Table B1-4. Connector model properties.

Element Properties		JVI Vector	2#5 Chord connector	#3 Angled bar-plate
link	n_y (kips)	4.4	4.9	8.5
	k (k/in)	63.9	84.5	236.6
	k_2 (k/in)	4.9	2.3	25.3
	δ_u (in)	0.438	0.438	0.18
Tension spring	k_i^{ts} (k/in)	-	434.3	-
	t_y (kips)	-	34.7	-
	k_2^{ts} (k/in)	-	11.65	-
	δ_{ut} (in)	-	0.601	-
Shear spring	k_i^{vs} (k/in)	136.0	97.1	77.1
	v_y (kips)	11.2	8.3	3.5
	k_2^{vs} (k/in)	-44.9	-14.4	-107.4
	δ_{uv} (in)	0.49	0.657	0.25
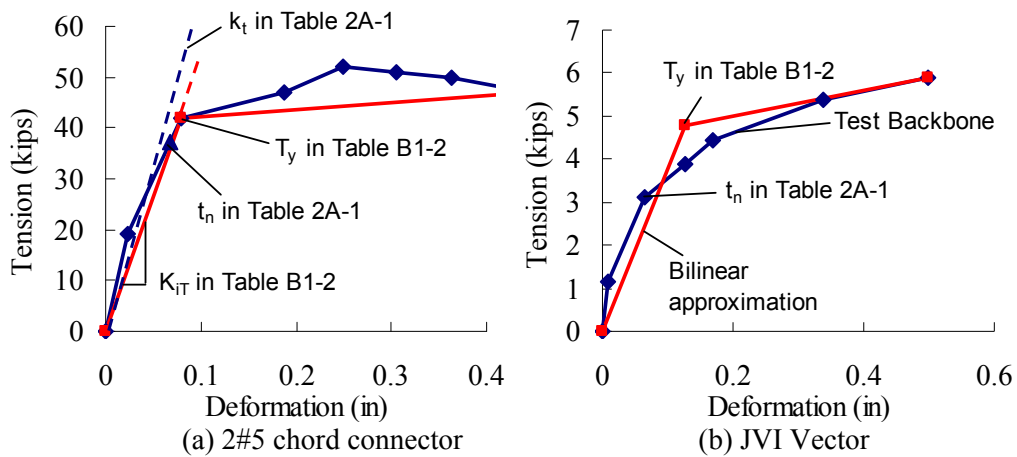
Fig. B1-10. Bilinear approximation for tension test backbone.

  (a) 2#5 chord connector   (b) JVI Vector

It should be noted at the time of the connector model being developed, PART 2 was not created. Thus there are some differences for the values in Table B1-2 and the values in Table 2A-1 in PART 2. These differences are:

(1) The model formulation uses a bilinear model. So the initial stiffness listed in Table B1-2 is secant stiffness at connector yield. However the initial stiffness in Table 2A-1 of PART 2 is taken as the secant stiffness at $0.75T_y$ or $0.75V_y$ (See Fig. B1-10a).

(2) The chord tension yield strength listed in Table 2A-1 of PART2 uses nominal strength (60ksi) of Gr.60 steel. However the chord tension yield strength shown in Table B1-2 is the actual yield strength observed in the test (See Fig. B1-10a)..

(3) The JVI Vector tension test does not show a well-define yield point (See Fig. B1-10b). In the Table 2A-1 of PART 2, a conservative low value is used for JVI yield tension strength. However in the model development a bilinear approximation is used for the test backbone and then the JVI yield strength listed in Table B1-2 is from this bilinear approximation.

Comparison to Tests

Figure B1-11 to B1-13 show the comparison of connector response obtained with push-over analysis of the individual connector model and the test results under tension load only, shear load only and tension-shear proportional load for the connectors using a displacement ratio λ=2.0 for JVI Vector and 2#5 chord and a force ratio a=1.0 for #3 angled bar-plates. As seen in the figures, the connector model produces response closely matches the individual component loading, and that reasonably matches the response obtained in the connector tests under combined loading, including similar strength reduction, stiffness reduction, and descending branch behavior. This result implies that the connector models can be used effectively in the 2D-FE discrete analyses, where complex loading on the connector element will translate into softened behavior relative to the response under simple individual force components.
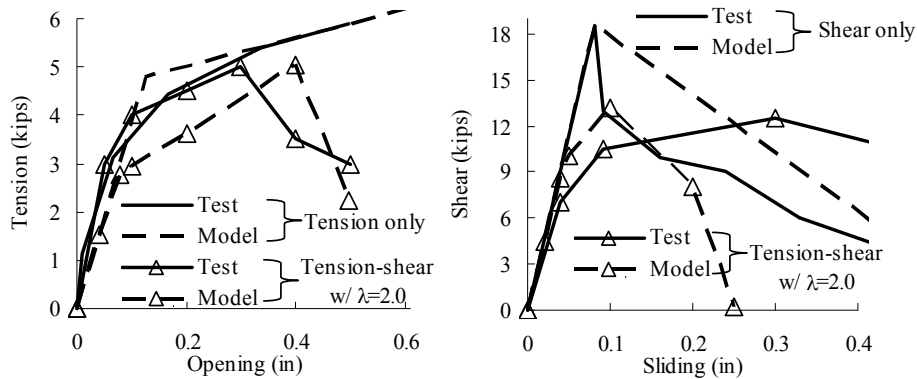
Fig. B1-11. Comparison between model and test for JVI Vector: (a) tension; (b) shear.
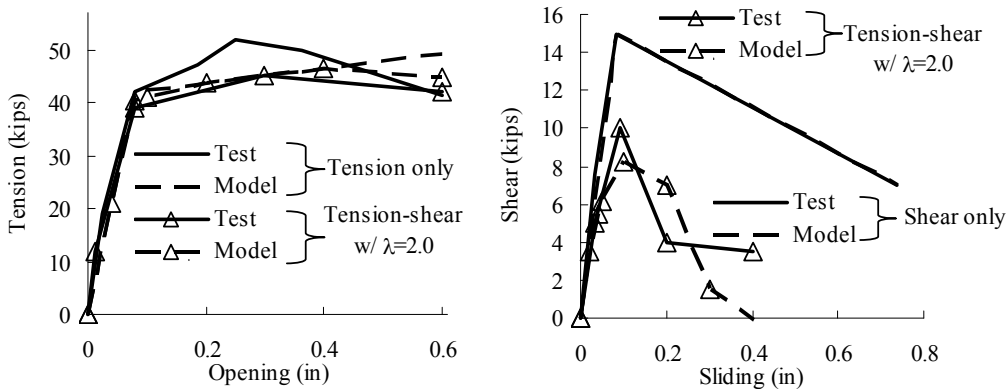
Fig. B1-12. Comparison between model and test for 2#5 chord: (a) tension; (b) shear.

C-A-120
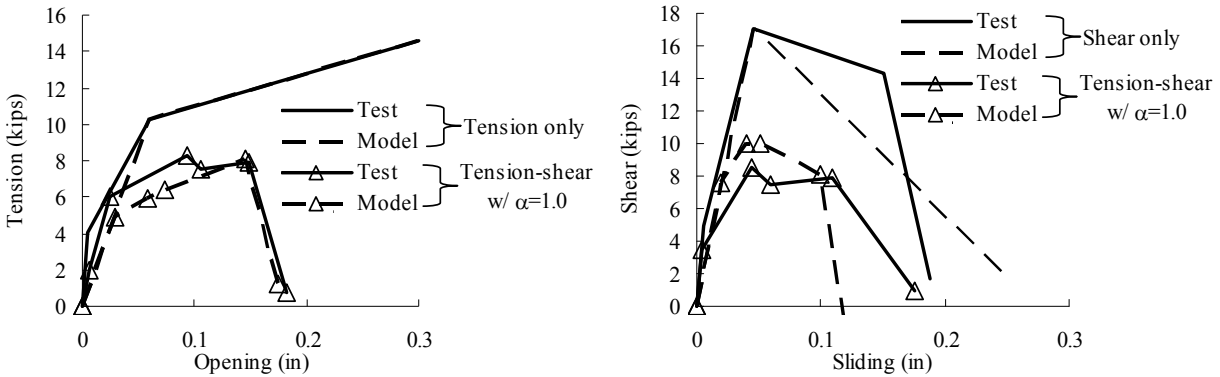
Fig. B1-13. Comparison between model and test for #3 angled bar-plate: (a) tension; (b) shear.

B1.7 SUMMARY AND CONCLUSIONS

Discrete connector elements have been developed for use in two-dimensional finite element models for nonlinear static monotonic "pushover" analysis. These connector elements were constructed on the basis of data from cyclic tests of isolated connector elements under individual loading components, i.e. tension/compression and reversing shear. Tests of isolated connectors under combined loading indicated modified behavior. Shear and tension loading tests indicate tension-shear coupled response (strength and stiffness reductions); shear in the presence of compression indicated higher stiffness and strength. A partially-coupled element formulation was shown to be effective in capturing the tension-shear interactions; contact pseudo elements were able to produce the compression effects. A procedure is presented that permits construction of the connector element from test data of individual load component tests, and calibrated on the basis of a small set of combined loading tests. The connector elements produce response that closely matches the individual component loading, and that reasonably match the response obtained in the connector tests under combined loading. The connector elements successfully reproduces key behaviors exhibited in the tests including tension-shear coupling behavior, high stiffness contact, concrete compression softening behavior, and friction under compression. This result implies that the connector models can be used effectively in the 2D-FE discrete analyses, where complex loading on the connector element will translate into softened behavior relative to the response under simple individual force components. These analyses have been successfully performed in support of developing the capacity of precast diaphragms, a first step in developing the design methodology contained in these documents.

B1.8 NOTATION

k, k_{2L} = initial, secondary stiffness of link;

$k_{1,2}$ = stiffness in the link element;

$\underline{k}_{1,2}$ = instant stiffness in the link element;

$k_2{}^{ts}$, $k_2{}^{vs}$ = secondary tension, shear stiffness of uncoupled spring;

$k_i{}^{ts}$, $k_i{}^{vs}$ = initial tension, shear stiffness of uncoupled spring;

$n_{1,2}$ = force in one of link element;

n_y = yield strength of link element;

T = tension force;

T_Y = connector tension yield strength;

t_y = tension yield strength of uncoupled spring;

V = shear force;

V_Y = connector shear yield strength;

$V_Y{}^C$ = connector shear yield strength under compression;

v_y = shear yield strength of uncoupled spring;

Δ_T, Δ_V = tension, shear deformation;

Δ_{uT}, Δ_{uV} = connector ultimate tension, shear deformation;

$\Delta_{uT,red}$, $\Delta_{uV,red}$ = reduced ultimate tension, shear deformation;

$\delta_{1,2}$ = deformation in one of link;

δ_u = ultimate deformation of link;

δ_{ut}, δ_{uv} = ultimate tension, shear deformation of uncoupled spring;

θ = orientation angle of line element.

B1.9 REFERENCES

ANSYS version 11. (2007). "Elements (00853) and theory reference (00855)" SAS Inc.

Building Seismic Safety Council, Committee TS-4. "Seismic design methodolgy for precast concrete floor diaphragms." Part III, NEHRP Recommended Sesimic Provisions 2009 Federal Emergency Management Agency, Washington, D.C.

Federal Emergency Management Agency (2000). "Prestandard and commentary for the Seismic Rehabilitation of Buildings" FEMA 356, Washington, DC.

Farrow, K. T. and Fleischman, R. B. (2003). "Effect of dimension and detail on the capacity of precast concrete parking structure diaphragms" PCI Journal 48(5): 46-61.

Fleischman, R.B., Sause, R., Pessiki, S. and Rhodes, A.B. (1998). "Seismic behavior of precast parking structure diaphragms" PCI Journal, 43 (1) Jan-Feb: 38-53.

Fleischman, R.B. and Wan, G. (2007). "Appropriate overstrength of shear reinforcement in precast concrete diaphragms", ASCE Journal of Structure Engineering 133(11): 1616-1626.

Iverson, J.K. and Hawkins, N.M. (1994). "Performance of precast/prestressed concrete building structures during northridge earthquake" *PCI Journal*: 39 (2): 38-55.

Ju, S.H. and Lin, M.C. (1999). "Comparison of building analyses assuming rigid or flexible floors" ASCE Journal of Structural Engineering 125(1):25-31.

Lee, H.J. and Kuchma, D.A. (2008). "Seismic response of parking structures with precast concrete diaphragms" PCI Journal 53(2): 71-94.

Mattock, A.H. and Hawkins, N.M. (1972). "Research on shear transfer in reinforced concrete" PCI Journal 17(2): 55-75.

Nakaki, S. D. (2000). "Design guidelines for precast and cast-in-place concrete diaphragms" Technical Report, *EERI Professional Fellowship*, Earthquake Engineering Research Institute.

Naito, C., Jones, C., Cullen T. and Ren, R. (2007). "Development of a seismic design methodology for precast diaphragms - phase 1b summary report". ATLSS Report. ATLSS Center, Lehigh University, PA.

Naito, C., Peter, W. and Cao, L. (2006). "Development of a seismic design methodology for precast diaphragms - phase 1 summary report". ATLSS Report No.06-01, ATLSS Center, Lehigh University, PA.

Naito, C.J. and Ren, R. (2011). "An evaluation method for precast concrete diaphragm connectors based on structural testing" PCI Journal. Submitted.

Oliva, M.G., (2000). "Testing of the JVI flange connector for precast concrete double-Tee system", Structures and Materials Test Laboratory, College of Engineering, University of Wisconsim, Madison, WI.

Pincheira, J. A., Oliva, M. G., and Kusumo-rahardjo, F. I. (1998). "Tests on double tee flange connectors subjected to monotonic and cyclic loading." PCI Journal, 43 (3): 82-96.

Ren, R. and Naito, C.J. (2011). "Precast concrete diaphragm connector performance database and response estimation modeling approach" ASCE Journal of Structural Engineering, Submitted.

Shaikh, A.F. and Feile, E.P., (2004). "Load Testing of a Precast Concrete Double-Tee Flange Connector", PCI Journal, May-June: 85-94.

Tena-Colunga, A and Abrams, DP. (1996). "Seismic behavior of structures with flexible diaphragms" ASCE Journal of Structural Engineering 122 (4): 439-445.

Wood S. L., Stanton J. F. and Hawkins N. M. (2000). "New seismic design provisions for diaphragms in precast concrete parking structures", PCI Journal, 45 (1): 50-65.

Zhang, D., Fleischman, R.B., Naito, C., and Ren, R. (2010). "Experimental Evaluation of Pretopped Precast Diaphragm Critical Flexure Joint under Seismic Demands." J. Struct. Eng. ASCE, Accepted in Dec.

Zhang, D., Fleischman, R.B., Wan G. and Naito, C.J. (2011) "Development of Hysteretic Models for Precast Concrete Diaphragm Connectors for Use in Three-Dimensional Nonlinear Dynamic Analysis" Under preparation.

B1.10 PRECAST CONNECTOR ELEMENT MODEL FORMULATION

Coupled Link Formulation

The coupled behavior is modeled through the inclined link components. It will be instructive to consider first a pair of angled links acting alone, with geometry as shown in Fig B1-8(a). The relationships are derived here for single displacement components as would be applied in the Qualification Protocol tests listed in Table B1-1.

The relationship between the connector global stiffness and strength characteristics $\{K_{iT}\ K_{iV}\ T_Y\ V_Y\}$ and the properties of the individual links (axial stiffness k, strength n_y, and deformation capacity δ) are obtained through contragradient laws [see Fig. B1-8(b) and B1-8(c)]:

$$K_{iT} = 2k\sin^2\theta \qquad T_Y = 2\,n_y\sin\theta \qquad \Delta_{uT} = \delta_u/\sin\theta \qquad \textbf{(Eqn. 1a,b,c)}$$
$$K_{iV} = 2k\cos^2\theta \qquad V_Y = 2\,n_y\cos\theta \qquad \Delta_{uV} = \delta_u/\cos\theta \qquad \textbf{(Eqn. 2a,b,c)}$$

Note that symmetry dictates that $k_1=k_2=k$; etc. Parameters θ and k, needed to establish the elastic properties of the coupled link element, can be obtained by combining Eqns. 1a and 2a, and setting the connector characteristics to the corresponding measured values in the Qualification Protocol tests described in Table 1:

$$\theta = tan^{-1}\,[(\boldsymbol{K_{iT}}\,/\,\boldsymbol{K_{iV}})^{1/2}] \qquad \textbf{(Eqn. 3a)}$$
$$k = \boldsymbol{K_{iT}}\,/2sin^2\theta \qquad \textbf{(Eqn. 3b)}$$

In this way, a single value of k in the links will produce the desired connector shear and tension stiffness via the parameter θ, an approach that is adequate for elastic models. However an over-constrained solution exists for nonlinear connector models regarding strength (Eqn. 1b, 2b) and ductility (Eqn. 1c, 2c), since there is no certainty that the θ selected will also fulfill:

$$\theta = tan^{-1}\,[(\boldsymbol{T_Y}\,/\,\boldsymbol{V_Y})] \qquad \textbf{(Eqn. 4a)}$$
$$\theta = tan^{-1}\,[(\boldsymbol{\Delta_{uV}}\,/\,\boldsymbol{\Delta_{uT}})] \qquad \textbf{(Eqn. 4b)}$$

Many precast connectors resemble the two link assemblage shown in Fig. B1-8(a) (e.g refer to Fig. B1-1), and thus it might be first thought that the strength and deformation capacity of the connector may be well approximated by Eqn. 4. However, the precast connector tension and shear response can be quite different because the presence of the surrounding concrete creates boundary conditions due to bearing, local concrete crushing, debonding etc., that produces quite dissimilar gage lengths for tension

and shear, and these conditions can differ in the elastic, yielded and near ultimate state (Naito et al. 2006). Thus, for a θ determined using Eqn. 3a, parameters n_y and δ can typically only accurately specify an element strength and deformation capacity for one of the two force components (e.g., tension), and will produce inaccurate measures for the other (e.g., shear). Alternately, θ can be determined using Eqn. 4a instead of Eqn. 3a thereby enforcing an accurate connector strength, at the expense of accurate initial connector stiffness. These limitations render a directly proportional coupled precast connector element as not practical for the pushover analyses. A partially-coupled formulation is instead adopted.

Partially-Coupled Formulation

The partially coupled formation is achieved through the addition of uncoupled inelastic shear and axial tension springs to the coupled link elements as shown in Fig. B1-6. In this approach, three parameters are available to be adjusted to match the individual tension and shear test results: (1) the angle θ; (2) a tension strength ratio for the uncoupled tension spring ($ω_t = t_y / T_Y$); and (3) a shear strength ratio for the uncoupled shear spring ($ω_v = v_y / V_Y$).

The orientation of the links can be selected to match stiffness, strength or yield deformation capacity. For the precast elements, the latter was found to be most straightforward and produced sufficiently accurate results for use in the modeling (See Sec. B1.7). The derivation that follows is for bilinear uncoupled springs with yield deformation aligned to the yield point of inclined links. Multi-linear springs have been used to improve the accuracy (Fleischman and Wan 2007) (Zhang et al. 2011).

The angle θ is determined by aligning the tension and shear yield deformation of the bilinear springs to that of the link element:

$$θ = tan^{-1} [(V_Y K_{i,T} / T_Y K_{i,V})] \hspace{3cm} \textbf{(Eqn. 5)}$$

The parameters $ω_t$ and $ω_v$ are selected to match the strength reductions under tension-shear coupling load observed in the supplemental tests (See Sec. B1.7) or an assumed level of coupling in the absence of supplemental testing. To produce an accurate total strength between the coupled and uncoupled components, the ratio of $ω_t$ and $ω_v$ has to meet:

$$(1-ω_v)/ (1-ω_t) = T_Y cos θ / V_Y sin θ \hspace{2.5cm} \textbf{(Eqn. 6)}$$

Then the input properties of the coupled link element (yield strength n_y and elastic stiffness k) can be determined:

$$n_y =(1-ω_t) T_Y / 2sin θ \hspace{0.5cm} = (1-ω_v) V_Y / 2cos θ \hspace{2cm} \textbf{(Eqn. 7a)}$$
$$k = (1-ω_t)K_{iT} / 2sin^2 θ \hspace{0.5cm} =(1-ω_v) K_{iV} / 2cos^2 θ \hspace{1.3cm} \textbf{(Eqn. 7b)}$$

The input properties of the uncoupled springs are straightforwardly calculated as:

$$t_y = ω_t T_Y \hspace{3cm} k_i^{ts} = ω_t K_{iT} \hspace{2cm} \textbf{(Eqn. 8a, b)}$$
$$v_y = ω_v V_Y \hspace{3cm} k_i^{vs} = ω_v K_{iV} \hspace{2cm} \textbf{(Eqn. 8c, d)}$$

For the typical diaphragm connector response (refer to Fig. B1-12), the post-yield tension response exhibits strain hardening behavior while the post-yield shear response typical involves strength degradation (negative stiffness). For this reason, the secondary stiffness and deformation capacity of link element was selected to mimic the tension response (Eqn. 9a and 9b), and the descending branch behavior was captured in the uncoupled shear spring (Eqn. 9d):

$$k_{2L} =(1-ω_t) K_{2T} / 2sin^2 θ \hspace{4cm} \textbf{(Eqn. 9a)}$$
$$δ_u =Δ_{uT} /sin θ \hspace{5cm} \textbf{(Eqn. 9b)}$$
$$k_2^{ts} = ω_t K_{2T} \hspace{5.5cm} \textbf{(Eqn. 9c)}$$
$$k_2^{vs} = K_{2V} - 2k_{2L} cos^2 θ \hspace{4cm} \textbf{(Eqn. 9d)}$$
$$δ_{ut} =Δ_{uT} \hspace{6cm} \textbf{(Eqn. 9e)}$$
$$δ_{uv} =Δ_{uV} \hspace{6cm} \textbf{(Eqn. 9f)}$$

Note that for the condition shown in Fig. B1-4, K_{2V} is negative and Eqn. 9a produces a positive k_{2L}, thus Eqn. 9d returns negative stiffness.

B1.11 COUPLED LINK RESPONSE TO GENERAL LOAD TRAJECTORIES
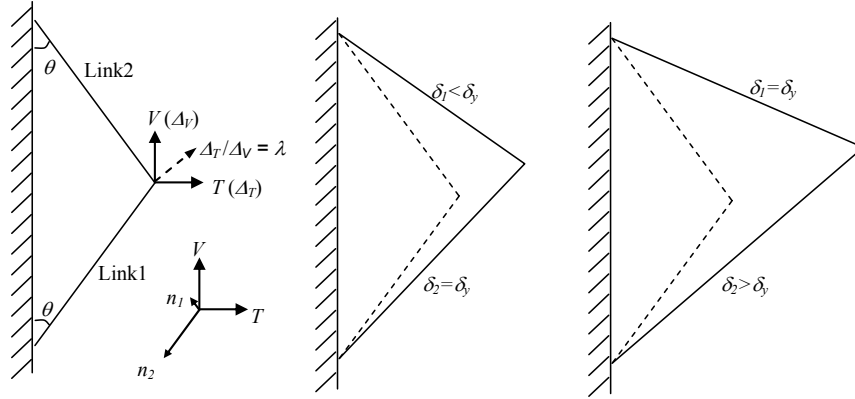
Fig. B1-14. Combined tension and shear: (a) layout; (b) yield of link 1; (c) yield of both links.

The connector element response to combined loading is derived. This response can be used to calibrate the model. Consider the mechanics of the inclined links alone subjected to a trajectory of combined shear and tension (see Fig. B1-14a).

Equations 10-12 express the equilibrium, constitutive and kinematic transformation relationships under small deformation for the individual link elements with respect to the global connector DOFs. Note the forces in the link elements are no longer equal and are designated n_1 and n_2.

Equilibrium:

$$(-n_1 + n_2) \cos\theta = V \quad\quad\quad \textbf{(Eqn. 10a)}$$
$$(n_1 + n_2) \sin\theta = T \quad\quad\quad \textbf{(Eqn. 10b)}$$

Constitutive:

$$n_1 = k_1\, \delta_1 = k\, \delta_1 \quad\quad\quad \textbf{(Eqn. 11a)}$$
$$n_2 = k_2\, \delta_2 = k\, \delta_2 \quad\quad\quad \textbf{(Eqn. 11b)}$$

Kinematic:

$$\delta_1 = \Delta_T \sin\theta - \Delta_V \cos\theta \quad\quad\quad \textbf{(Eqn. 12a)}$$
$$\delta_2 = \Delta_T \sin\theta + \Delta_V \cos\theta \quad\quad\quad \textbf{(Eqn. 12b)}$$

Strength Reduction

The derivation of response under combined loads first focuses on strength reduction. Note classical virtual work solutions imply no reduction in elastic stiffness due to combined loading, an assumption supported by experimental evidence (Naito et al. 2006). Considering first the force interaction, solving Eqn. 10a and 10b for n_1 and n_2 provides:

$$n_1 = \tfrac{1}{2}\, T/\sin\theta - \tfrac{1}{2}\, V/\cos\theta \quad\quad\quad \textbf{(Eqn. 13a)}$$
$$n_2 = \tfrac{1}{2}\, T/\sin\theta + \tfrac{1}{2}\, V/\cos\theta \quad\quad\quad \textbf{(Eqn. 13b)}$$

Equation 13 indicates that for positive values of both force components ($V > 0$, $T > 0$) link 2 will yield first. Accordingly, substituting the tension-to-shear force ratio α into Eqn. 13b and rearranging provides the relationship between global and local force:

$$V = 2n_2\, [(\sin\theta \cos\theta)/(\alpha \cos\theta + \sin\theta)] \quad\quad\quad \textbf{(Eqn. 14)}$$

Introducing the constant $C_\alpha = 1/(\alpha \cos\theta + \sin\theta)$, substituting $n_2 = n_y$ ($n_1 < n_y$), based on the yielding of link 2, and finally normalizing by the direct (unreduced) yield loads (Eqn. 1b and 2b) provides the reduced tension and shear strength ratios:

$$V_{Y,red} / V_Y = C_\alpha \sin\theta \qquad \text{(Eqn. 15a)}$$
$$T_{Y,red} / T_Y = \alpha C_\alpha \cos\theta \qquad \text{(Eqn. 15b)}$$

The resulting strength reduction is shown in Fig. B1-15(a) for different connector element link angles. Note that this plot indicates that a steeper angle can be used for connectors whose response exhibits a higher reduction in tension strength due to the presence of shear load and a shallower angle for those whose response exhibits a higher reduction in shear strength due to the presence of tension load.

The relationship in Fig. B1-15 can be adjusted relative to α by the introduction of the uncoupled shear and axial springs. For this case, Eqns. 15a and 15b become:

$$V_{Y,red} / V_Y = (1-\omega_v) C_\alpha \sin\theta + \omega_v \qquad \text{(Eqn. 15c)}$$
$$T_{Y,red} / T_Y = (1-\omega_t)\alpha C_\alpha \cos\theta + \omega_t \qquad \text{(Eqn. 15d)}$$
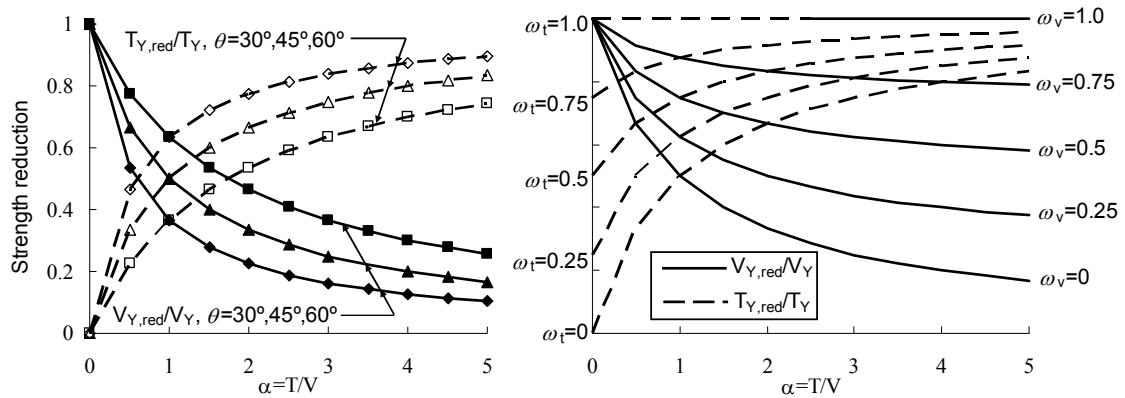
Fig. B1-15. *Strength reduction: (a) for θ with $\omega_v = \omega_t = 0$; (b) for ω_v and ω_t with θ=45°.*

Figure B1-15b shows these relationships for θ = 45° with ω_v and ω_t varying from 0 (fully coupled) to 1 (fully uncoupled). As seen, the relative strength reduction in shear and tension can be adjusted using ω_v and ω_t.

Post Yield Behavior

In the post-yield regime, where characteristics such as yield deformation and secondary stiffness are of interest, it is more useful to define the coupled response in terms of the displacement ratio λ. Note that for any trajectory other than outside of the bounding cases of pure shear (λ=0) or tension (λ=∞) where the link elements yield simultaneously, one link will yield prior to the other, thus a distinction is made between a "softening" state [one link yielded, refer to Fig. B1-14(b)] and the fully yielded state [both links yielded, refer to Fig. B1-14(c)]. For the fully coupled case shown in Fig. B1-14(a) with positive deformation component values ($\Delta_V > 0$, $\Delta_T > 0$), Eqns. 11 and 12 indicate that link 2 will yield first. Inserting Eqn. 11b into Eqn. 12b, setting $n_2=n_Y$, and substituting the trajectory parameter λ, provides the following "softening" deformations which have been normalized by the unreduced yield deformations ($\Delta_{VY} = V_Y / K_{iV}$ and $\Delta_{TY} = T_Y / K_{iT}$):

$$\Delta_{VYs} / \Delta_{VY} = \cos\theta / (\lambda \sin\theta + \cos\theta) \qquad \text{(Eqn. 16a)}$$
$$\Delta_{TYs} / \Delta_{TY} = \lambda \sin\theta / (\lambda \sin\theta + \cos\theta) \qquad \text{(Eqn. 16b)}$$

The same process used to create Eqn. 16 can be repeated for link 1 by instead using Eqn. 11a and 12a, thereby providing the normalized "fully" yielded condition:

$$\Delta_{VYf} / \Delta_{VY} = \cos\theta / (\lambda \sin\theta - \cos\theta) \qquad \text{(Eqn.17a)}$$
$$\Delta_{TYf} / \Delta_{TY} = \lambda \sin\theta / (\lambda \sin\theta - \cos\theta) \qquad \text{(Eqn.17b)}$$

The normalized softening and fully-yielded deformations of Eqn. 16 and 17 are shown in Fig. B1-16a for θ=45°. It is seen that the shear softening deformation decreases and tension softening deformation increases with λ, and both are less than the unreduced yield deformations. The total resultant yield deformation $\Delta_{y,TOT} = \sqrt{\Delta_V^2 + \Delta_T^2}$ is seen to be reduced slightly for trajectories with similar tension and shear components.

The region between the softening and fully-yielded deformation is characterized by a secondary (reduced) stiffness, even for link elements provided with elastic-perfectly plastic material response. Relationships are written in incremental form to determine the secondary slope. Consider a positive increment of deformation components ($\partial\Delta_V > 0$, $\partial\Delta_T > 0$), with a perfectly plastic link 2 yielding first, producing the state ($k_1 = k$; $k_2 = 0$):

<u>*Equilibrium*</u>:

$(-\partial n_1 + \partial n_2)\cos\theta = \partial V$ **(Eqn. 18a)**

$(\partial n_1 + \partial n_2)\sin\theta = \partial T$ **(Eqn. 18b)**

<u>*Constitutive:*</u>

$\partial n_1 = \underline{k_1}\,\partial\delta_1 = k\,\partial\delta_1$ **(Eqn. 19a)**

$\partial n_2 = \underline{k_2}\,\partial\delta_2 = 0$ **(Eqn. 19b)**

<u>*Kinematic:*</u>

$\partial\delta_1 = \partial\Delta_T\sin\theta - \partial\Delta_V\cos\theta$ **(Eqn. 20a)**

$\partial\delta_2 = \partial\Delta_T\sin\theta + \partial\Delta_V\cos\theta$ **(Eqn. 20b)**

Substituting the values in Eqn. 19 into Eqn. 18, and in turn combining with Eqn. 20 provides the secondary stiffness of the connector element:

$K_{2V} = \partial V / \partial\Delta_V = -k\,(\lambda\sin\theta\cos\theta - \cos^2\theta)$ **(Eqn. 21a)**

$K_{2T} = \partial T / \partial\Delta_T = k\,(\sin^2\theta - \sin\theta\cos\theta / \lambda)$ **(Eqn. 21b)**

Normalizing these values by the original elastic stiffness provided by the links (Eqn. 1a and 2a) provides the softening stiffness ratios κ_v, κ_t, as plotted in Fig. B1-16b:

$\kappa_v = K_{2V} / K_{iV} = -(\lambda\tan\theta - 1) / 2$ **(Eqn. 22a)**

$\kappa_t = K_{2T} / K_{iT} = (1 - \cot\theta / \lambda) / 2$ **(Eqn. 22b)**

The ratio between the fully-yielded and softening deformations ($\mu = \Delta_{VYs} / \Delta_{VYf}$) is also shown in Fig. B1-16b. It is noted that deformation trajectory exists ($\lambda = \tan\theta$) in which a "fully" yielded condition is not reached ($\lambda = 1.0$ in Fig. B1-16), but this coincides with the trajectory in which the secondary softening slope possesses a zero value, thus not creating a performance issue for the connector element.
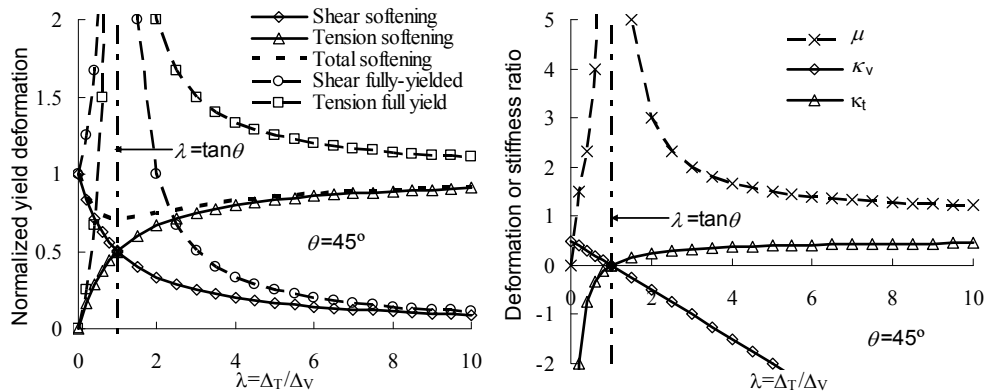
Fig. B1-16. *Staged yielding condition: (a) normalized yield deformation; (b) softening stiffness.*

For a trajectory with non-zero shear and tension deformation components, link 2 will reach ultimate deformation prior to the link 1 similar as the yield deformation discussed above. Defining the ultimate deformation state of the connector element as one of link reaches its ultimate deformation, the ultimate tension and shear deformation will be reduced following the same trend as the "softening" deformation. Replacing the δ_y by δ_u in Eqn. 16 obtain:

$$\Delta_{uV,red} = \delta_u / (\lambda \sin\theta + \cos\theta) \qquad \textbf{\textit{(Eqn. 23a)}}$$
$$\Delta_{uT,red} = \lambda\, \delta_u / (\lambda \sin\theta + \cos\theta) \qquad \textbf{\textit{(Eqn. 23b)}}$$

Appendix B2. Connector Elements for 3D Nonlinear Dynamic Structure Models

Appendix B.2 describes the development of cyclic connector elements for 3D-FE discrete precast structure models used for nonlinear transient dynamic analysis (NLDTA). These connector elements are based on the monotonic connector elements developed for the 2D-FE discrete model used in pushover analyses of precast concrete diaphragms, as described in *Appendix B.1*. For use in 3D-FE NLDTA analysis, the connector elements are extended to capture several important cyclic responses including hysteretic pinching, stiffness degradation, strength degradation, and slip mechanisms. Results from cyclic load tests on isolated precast connectors were used to calibrate the hysteretic characteristics. The connector models are appropriate for insertion into large degree-of-freedom 3D-FE NLDTA models.

TABLE OF CONTENTS

B2.1 INTRODUCTION

The design factors for the precast diaphragm seismic design methodology are indexed to diaphragm performance targets related to the deformation capacity of the precast diaphragm reinforcement. These design factors were calibrated through nonlinear dynamic transient analysis (NLDTA) of three dimensional finite element models (3D-FE) of diaphragm-sensitive precast concrete structures (Zhang et al. 2011), as described in *Appendices A1* and *A2*. The diaphragm response is highly dependent on the characteristics of the diaphragm connectors. Thus, a key feature of the modeling was accurate hysteretic models of the precast diaphragm connectors. These connector models are described in this appendix.

The 3D diaphragm connector models are developed using the results of full-scale physical testing of isolated precast diaphragm connectors (Naito et al. 2007). Cyclic loading protocols were imposed that are intended to resemble the demands incurred during seismic action, including combinations of reversing compression and tension in the presence of cyclic shear force. The connectors tested exhibited several important hysteretic responses including hysteretic pinching, stiffness degradation, strength degradation, and slip mechanisms.

The 3D-FE precast structural models possess thousands of degrees-of-freedom (DOFs) and earthquake time steps, and thus rely on the strong user interfaces for preprocessing, graphical interfaces, and post-processing available in commercial finite element (FE) software[11]. Thus, it is preferable to use assemblages of existing elements in the software package, rather than writing custom-made elements.

Thus, appropriate connector models must be: (1) able to capture the key behaviors described above; (2) capable of representing precast diaphragm behavior with sufficient accuracy to produce effective design procedures; and (3) appropriate for insertion into large degree-of-freedom 3D-FE NLDTA models.

The 3D diaphragm connector model used for 3D NLTDA is extended from the 2D discrete connector model. The 3D connector model includes the key features of the 2D discrete model including: (1) the interaction of components of load (tension-shear coupling) through use of "inclined" link elements; (2) high stiffness contact between precast panel with the compression limit states (softening/crushing) of the surrounding concrete through a nonlinear spring element in series with the contact element; and (3) mobilizing the effect of applied compression on shear resistance through use of a contact element with friction capabilities (assigning a coefficient of friction μ to contact element). The 3D diaphragm connector model has been extended to include the hysteretic effects exhibited in the individual connector cyclic tests (Naito et al. 2007) have to be captured in the 3D connector model. This appendix presents the detail calibration of the 3D diaphragm connector model to include the hysteretic effects.

Appendix B.2 presents the details of the construction of the 3D connector hysteretic models using the test data. Large-scale tests of key precast diaphragm joints (Zhang et al. 2010) (Fleischman et al. 2011) are used to experimentally verify the models. These models successfully predicted the response of shake table test for a three-story half-scale precast structure (Schoettler et al. 2009), and were used in 3D-FE NLDTA to calibrate precast diaphragm seismic design factors (Zhang et al. 2011).

(a)   (b)
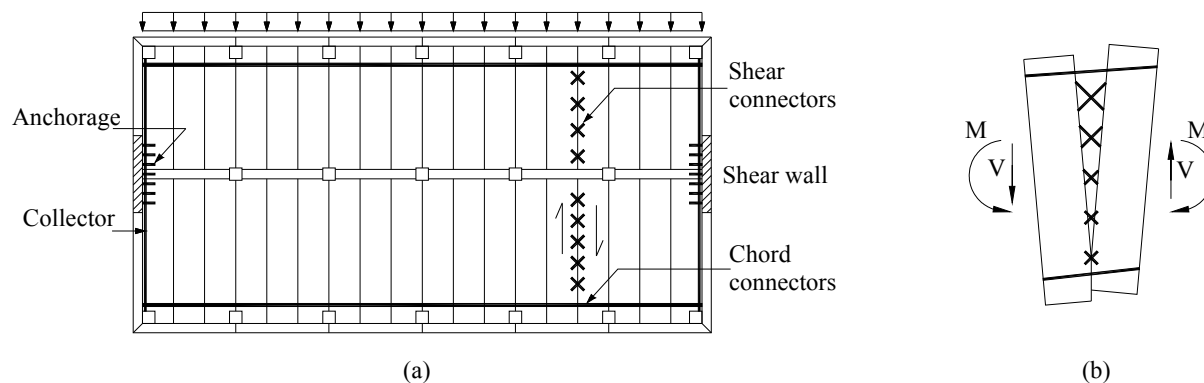
Fig. B2-1. Typical precast diaphragm: (a) plan; (b) combined forces on precast units.

---

[11] ANSYS version 10, Inc., Canonsburg, PA

B2.2 PRECAST CONNECTOR CHARACTERISTICS UNDER CYCLIC LOADING

Precast Diaphragm Connector Test Program

A set of common diaphragm connectors were tested under cyclic loading to determine their characteristics. A multi-directional test fixture was developed to allow for the simultaneous control of in-plane shear, axial, and bending deformations at the panel joint. The fixture employs three actuators, two that apply axial displacement to the connector or joint and one that applies a shear displacement (See Fig. B2-2a). Combined shear, axial, and bending loading is used in the verification testing (See *Sec. B2-4*). Full details of the specimen are found in (Zhang et al. 2010).
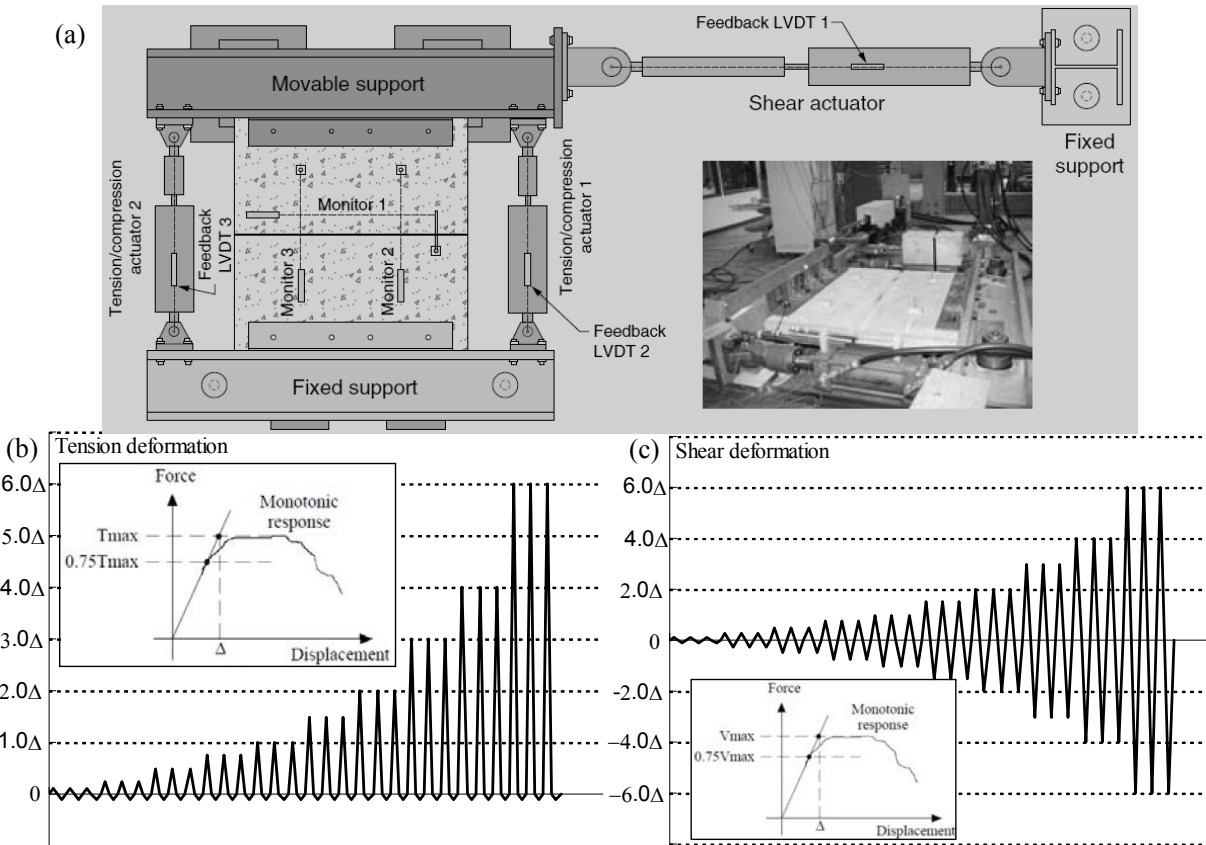
Fig. B2-2. Diaphragm connector cycle test: (a) test setup; (b) tension test protocol; (c) shear test protocol.

The connector characteristics were providing through loading protocols for cyclic tension/compression and shear, as shown in Fig. B2-2(b) and Fig. B2-2(c) respectively. The cyclic protocol consisted of three cycles of tension/compression or shear at increasing levels of tension (opening) or shear (sliding) deformation. For the cyclic tension/compression tests, the shear actuator provided compensation displacement to generate a constant shear force. For the cyclic shear tests, the two axial actuators provided compensation displacement to generate a constant axial force. Baseline characteristics were determined with the constant secondary force held to zero.

Precast Diaphragm Connector Test Results

Figure B2-3 shows the cyclic test results and backbone curve for three typical diaphragm connectors: (a) a dry chord connector (2#5) under cyclic tension with zero shear force; (b) an untopped flange to flange shear connector (JVI) under cyclic shear with zero axial force; and, (c) a topped shear connector (ductile mesh connector) under cyclic shear with zero axial force.
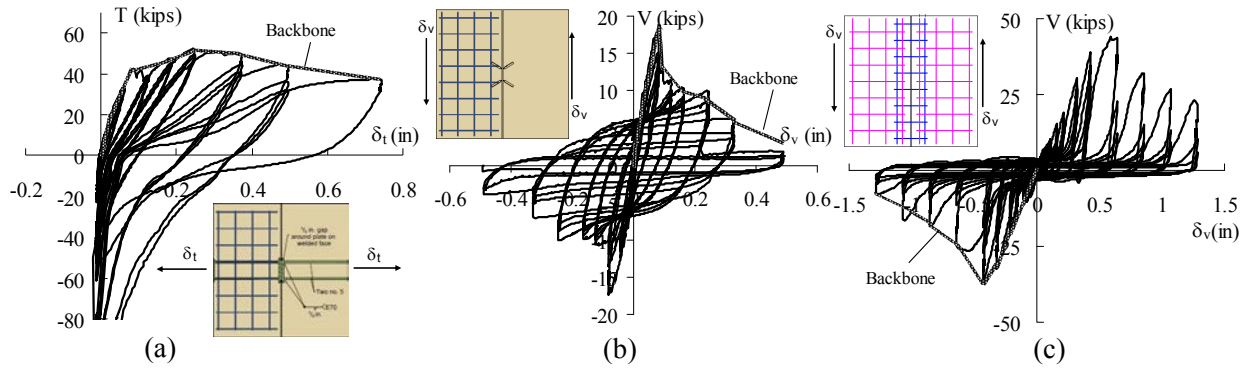
Fig. B2-3. Connector cyclic tests: (a) chord; (b) JVI; (c) ductile mesh.

Observed Hysteretic Behaviors

As observed in Fig. B2-3, four basic hysteretic effects were observed in the response of the typical diaphragm connectors (shown schematically in Fig. B2-4), sometimes in combination (Naito et al. 2007):
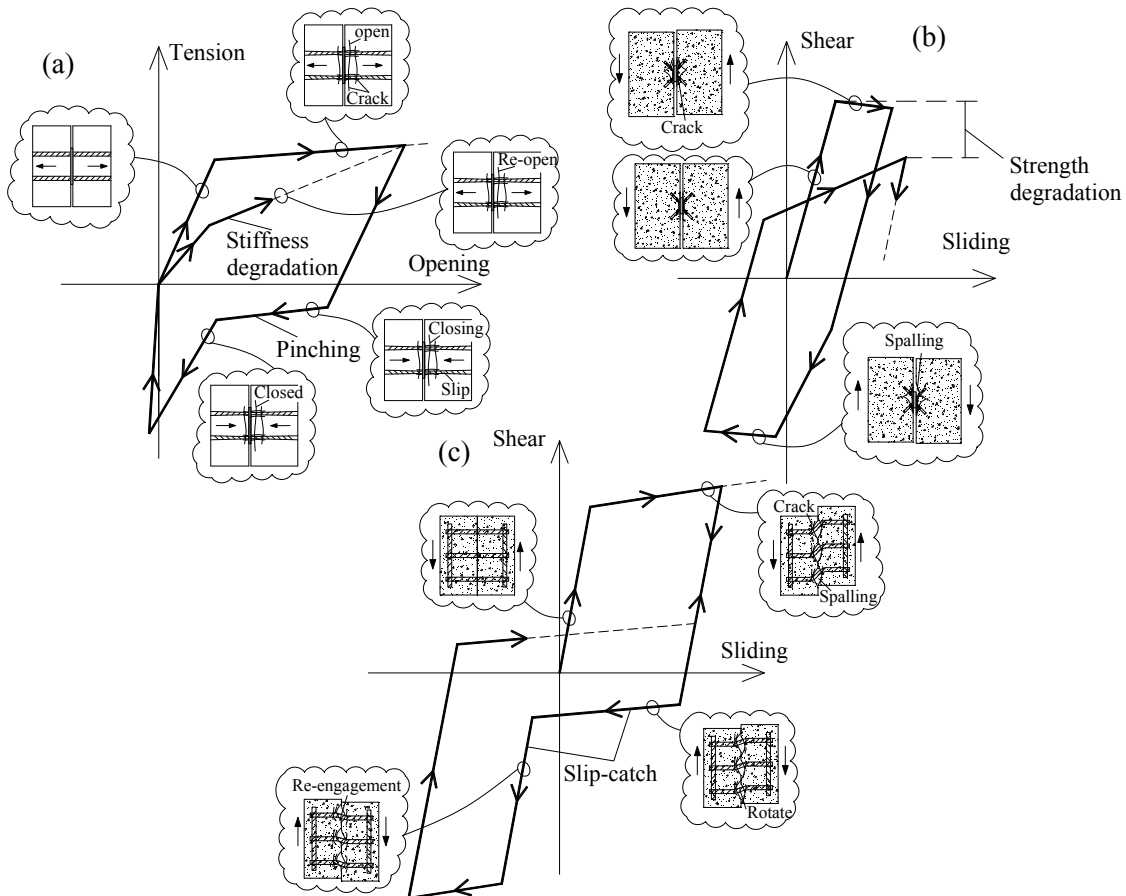
Fig. B2-4. Basic hysteretic effect of diaphragm reinforcement: (a) pinching & stiffness degradation; (b) strength degradation; (c) slip-catch.

(1) A pinching effect due to bond slip. This effect is generated by the loss of bond and subsequent slip of the reinforcement in the concrete during reversal loading. This effect occurs after large joint

inelastic opening that causes cracking in the surrounding concrete, but prior to compression transfer associated with joint closing (Naito et al. 2007).

(2) A stiffness degradation effect due to cracking of the surrounding concrete. This effect is observed during the reloading cycle following a large inelastic tension deformation cycle that caused the concrete surrounding the steel elements region crack (Naito et al. 2007). Instead of following the initial elastic loading stiffness, the reloading path in this case will "shoot through" at a lower stiffness, until the maximum opening point of the previous cycle is reached. This effect was also observed in half-scale testing of diaphragm critical flexure joints (See Section B3.1).

(3) A strength degradation effect due to loss of surrounding concrete. This effect is observed during the reloading cycle following a large inelastic shear deformation cycle that caused local spalling of concrete surrounding the connection region (Naito et al. 2007).

(4) A slip-catch effect due to slip and re-engagement of the steel element anchorages. This phenomenon is exhibited during large shear deformation after a major cyclic shear load event sufficient to fully degrade the dowel action through cracking and spalling of the concrete surrounding the steel element(s). A region of near-zero stiffness (slip) through the +/- sliding displacement range occurs in subsequent cycles where the reinforcement bars can rotate prior to the re-engaging due to catenary ("kinking") action.

B2.3 HYSTERETIC MODEL FOR DIAPHRAGM REINFORCEMENT

The connector model used in the 2D discrete diaphragm model (See *Appendix B1*) is modified for use in NLTDA earthquake simulations of 3D precast structures. Due to the cyclic nature of the response to earthquakes, the properties of the nonlinear connector sub-assemblage elements are extended to incorporate hysteretic rules.

The hysteretic model for the diaphragm connector is calibrated to match cyclic tests of the isolated diaphragm reinforcement (Naito et al. 2007). The four basic hysteretic effects discussed in background section have been modeled using the following modeling techniques in ANSYS[12]. The use of the commercial software package ANSYS facilitates the handling of multi-step iterative solutions of large degree-of-freedom structural models, but necessitates the use of available elements within the element library to create the desired behavior. The behaviors exhibited by the connections are different from that produced by standard elastic-plastic kinematic or isotropic hardening models available in the software (ANSYS 2007). Thus, the 3D NLDTA connector elements are created through assemblages of multiple elements in series and/or parallel with different properties or unloading rules, to create the desired structural response features. This approach is in contrast to the procedure available with certain research software where user-defined elements can be created to model certain behaviors directly (OpenSees 2011). Since the elements are calibrated to match test response, and are used create engineering solutions, the assemblage approach was deemed acceptable.

Modeling of Pinching Effect

To capture the pinching effect, the connector subassemblage includes two nonlinear axial springs in parallel (See Fig. B2-5a) with different unloading protocols available in the software (ANSYS 2007): an elastic-plastic spring that unloads with its initial stiffness; and a nonlinear elastic spring that unloads along its loading path (See,Fig. B2-5b).

The effect of pinching can be adjusted by a factor α, which is defined as the portion of the total strength assigned to elastic-plastic spring. As seen in Fig. B2-5(b), when $\alpha=1.0$, no pinching effect is observed in the model under unloading. When $\alpha=0$, fully pinching effect is observed in the model under unloading. The strength characteristics for the springs are biased toward compression (See,Fig.B2-5b) rather than provided with symmetric strength since the pinching effect is manifested after tension unloading in the compression region (see Fig. B2-3a). The bias is achieved by assigning a low tension strength to the spring elements.

---

[12] ANSYS, Inc. (version 11), Canonsburg, PA

(a) Pinching model　　　　　　　(b) Material input of springs
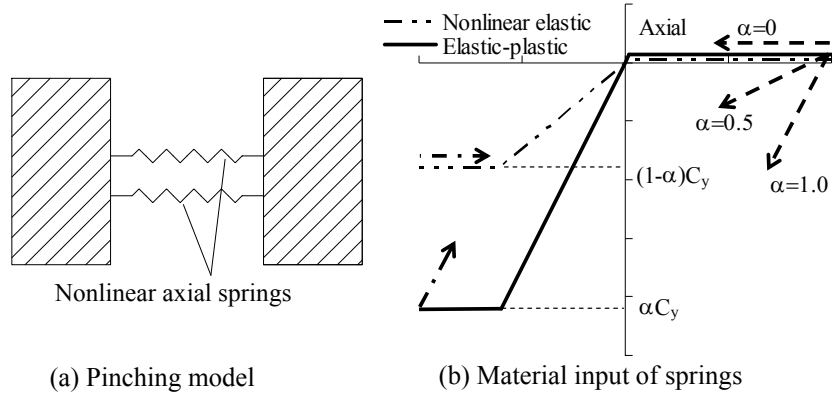
Fig. B2-5. Modeling of pinching effect.

Modeling of Stiffness Degradation

A connector subassemblage consisting a group of nonlinear link elements in parallel has been used to model the stiffness degradation effect. The connector subassemblage (See Fig.B2-6a) is produced through a series of N links with an isotropic strain hardening rule in conjunction with one link element with a kinematic strain hardening rule (ANSYS 2007). The sum of initial stiffness of the N+1 links is set to the connector initial stiffness. The stiffness degradation is realized by assigning each isotropic link a strength (F_{ti}) and elastic limit deformation (δ_{ti}). The strength of each isotropic link will degrade to a pre-assigned residual strength R at deformation of $\delta_{t(i+1)}$ after passing its elastic limit deformation. Note that each link has a successively increasing elastic limit deformation and decreasing strength (See Fig.B2-6b). The kinematic strain hardening nonlinear link element with a strength of F_{N+1} and yield deformation of δ_{N+1} is required in the subassemblage to keep the strength from degradation with the increasing inelastic deformation as observed in the test (See Fig.B2-3a).

The material model inputs for the N+1 link elements are determined based on N+1 control points on a backbone curve (See Fig.B2-6b) from the cyclic tension/compression test. Each control point is corresponding to a force T_i and a deformation δ_{ti}. The control points should at least consist the following four points: (1) elastic deformation point (e.g. 0.3 δ_{ty}); (2) yield deformation point (δ_{ty}); (3) ultimate deformation point (δ_{tu}); (4) after yielding point [e.g. ($\delta_{tu} + \delta_{ty}$)/2]. To match the stiffness degradation pattern in the test, more after yielding points can be used. The strength (F_{ti}) of each link element is calculated by solving the following N+1 linear equations, (where i ranges from *1* to *N+1*):

$$T_i = \delta_{ti} \sum_{j=i}^{N+1} {F_{tj}} \Big/ {\delta_{tj}} + (i-1)R \qquad \text{(Eqn. 1)}$$

(a) Model　　　　　　　　(b) Material inputs
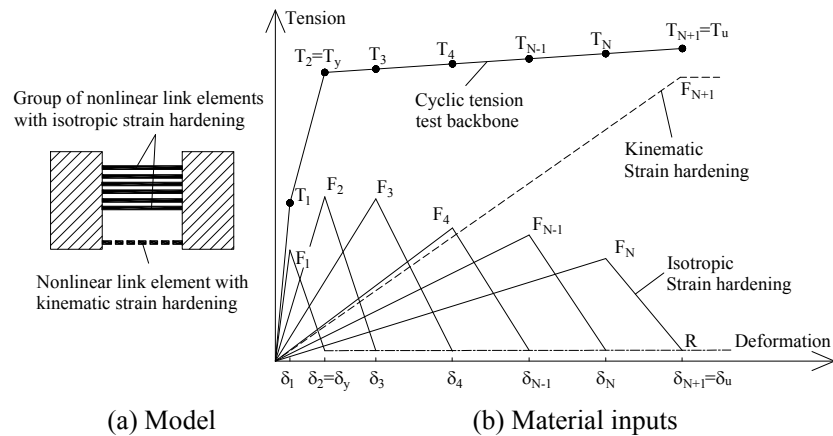
Fig. 2B-6. Modeling of stiffness degradation effect.

Modeling of Strength Degradation

The strength degradation effect has been modeled using a nonlinear degrading link element with the multilinear isotropic strain hardening rule which can produce the yield surface/strength reduction based on accumulative plastic strain (ANSYS 2007). The material inputs [force (F_{vi}) and deformation (δ_{vi})] for the link element are determined based on control points on the cyclic shear test backbone curve (See Fig.B2-7a). Each control point is corresponding to an absolute shear deformation (δ_{vai}) and a shear force (V_i). The control points before the peak load (V_y) can be directly assigned to the material inputs for the link element. However the control points after peak load (V_y) cannot be directly assigned to the material inputs because the strength degradation is based on the cumulative plastic deformation (δ_{vcpi}) rather than absolute plastic deformation (δ_{vpi}). Therefore, the absolute plastic deformation (δ_{vpi}) has been modified into the cumulative plastic deformation (δ_{vcpi}) with the following equation:
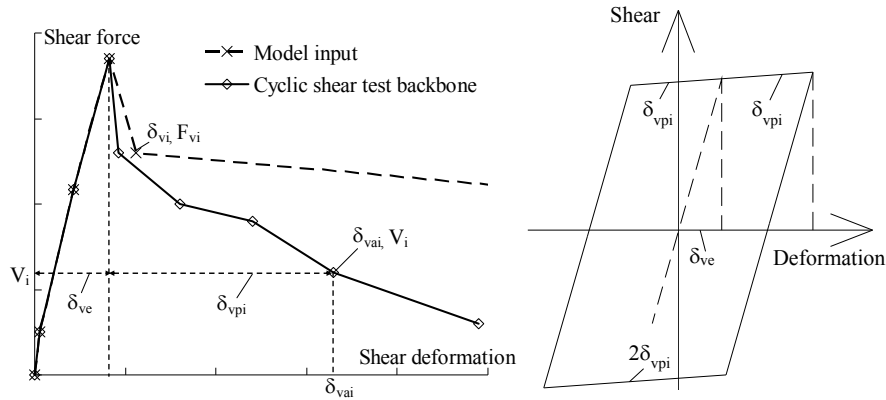
(a) Material input (b) Plastic deformation for one typical cycle

Fig. 2B-7. Modeling of strength degradation effect.

$$\delta_{vcpi} = 3n_1\delta_{vap1} + \sum_{j=2}^{i} 4n_j\delta_{vcpj} \qquad \text{(Eqn. 2)}$$

where n_i is the number of repeated cycles at i-th loading amplitude. For each loading cycle, the cumulative plastic strain is considered as 4 times of the absolute plastic strain except 3 times for the 1st inelastic cycle as indicated in Fig. 2B-7b. Then the material inputs for the link element can be calculated using the following equations:

$$F_{vi} = V_i \qquad \text{(Eqn. 3)}$$

$$\delta_{vi} = \delta_{vai} \qquad \text{for the points before the peak load} \qquad \text{(Eqn. 4)}$$

$$\delta_{vi} = \delta_{ve} + \delta_{vcpi} \quad \text{for the points after the peak load} \qquad \text{(Eqn. 5)}$$

where δ_{ve} is the absolute elastic shear deformation.

This approach produces a hysteretic strength degradation that will match the loading history of the test, and thus will produce slight differences for other loading histories. Comparison of this model to large-scale testing of precast diaphragm joints under expected seismic histories demonstrated the adequacy of this assumption.

Modeling Slip-catch Response

A "hook" mechanism (See Fig.B2-8a) is used to capture the slip-catch hysteretic effect. This modeling technique connects two precast panels with two symmetrical groups of elements including a nonlinear spring and a contact element connecting in series with a rigid link element. Each nonlinear shear spring, whose unloading path is parallel to its initial loading path, provides a stiffness contribution

only when its associated contact element is closed. Therefore only one group of element will be activated when the shear loading is applied in one direction for the two panels.

In a shear loading cycle, as the two precast panels slide relative to each other in one direction, only one of nonlinear spring will provide stiffness contribution and will yield with increasing of shear loading. When this nonlinear spring unloads to a loading reversal point, its associated contact element serves as a "hook", possessing memory of the location of this point (See Fig.B2-8b) and starting to open. Thus the nonlinear spring has no stiffness contribution after passing the loading reversal point. In the next shear loading cycle, the nonlinear spring can develop stiffness again only after the reloading displacement reaches the loading reversal point from the previous cycle and the contact element closes [dotted line in Fig. 2B-8b].

(a) Model (b) Response of one nonlinear spring
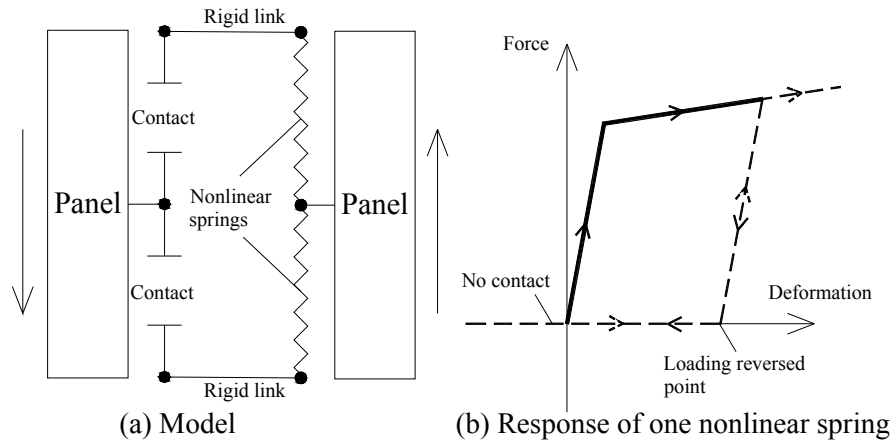
Fig. 2B-8. Modeling of slip-catch effect.

B2.4 COMPARISON OF CONNECTOR MODELS TO TEST RESULTS

The response of the connector elements constructed using the rules in the previous section is now compared to: (1) cyclic increasing amplitude tests of full-scale isolated connectors; and (2) simulation-driven large scale testing of critical precast diaphragm joints under expected seismic loading histories.

The cyclic response of diaphragm reinforcement usually exhibits one or more hysteretic effect discussed in above sections. In this section, the cyclic response of representative diaphragm reinforcement will be presented by comparison between test results and analytical model response.

Diaphragm Dry Chord Connector

As seen in Fig.B2-3a, the cyclic tension/compression test results for 2#5 dry chord connector exhibit the following effects: (1) pinching; (2) stiffness degradation and (3) high stiffness contact in compression. As shown in Fig. B2-9a, the connector model for 2#5 dry chord combines the modeling techniques discussed in previous sections for these three effects.

Table B2-1. Material inputs of the link elements for the 2#5 dry chord connector model

Control force	T_1	$T_2=T_y$	T_3	T_4	T_5	T_6	$T_7=T_u$
(kips)	19	42	47	52	50	45	38
Control opening	δ_{t1}	$\delta_{t2}=\delta_{ty}$	δ_{t3}	δ_{t4}	δ_{t5}	δ_{t6}	$\delta_{t7}=\delta_{tu}$
(in)	0.023	0.08	0.187	0.249	0.363	0.479	0.738
Solved force	F_1	F_2	F_3	F_4	F_5	F_6	F_7
(kips)	7.2	21.0	8.0	17.3	16.2	19.1	31.6

For the pinching effect model (described in *Sec B2.3.1*), the α factor and C_y are set as 0.5 and 75% tensile yield strength (T_y) respectively which results in a good match for the unloading response between model and test (See Fig.B2-9b). The low tension strength is assigned as 1kips.

For the stiffness degradation effect model (described in section *Sec B2.3.2*), seven control points (N=6) on the test backbone curve are used to calculate the material inputs of the link elements (see Table B2-1). The residual strength is set as 1kips. Using the Eqn. 8, the strength of each link element is solved and shown in the last row of Table B2-1.

For the high stiffness contact effect, the model input for contact and nonlinear spring is based on the theoretical compression stiffness of two precast panel and is described in (Wan et al. 2011).

As shown in Fig. B2-9b, the dry chord connector model results exhibits good agreement with the cyclic tension/compression test results. The stiffness degradation effect, pinching effect and high stiffness contact effect observed in the test results are successful captured by the dry chord connector model.
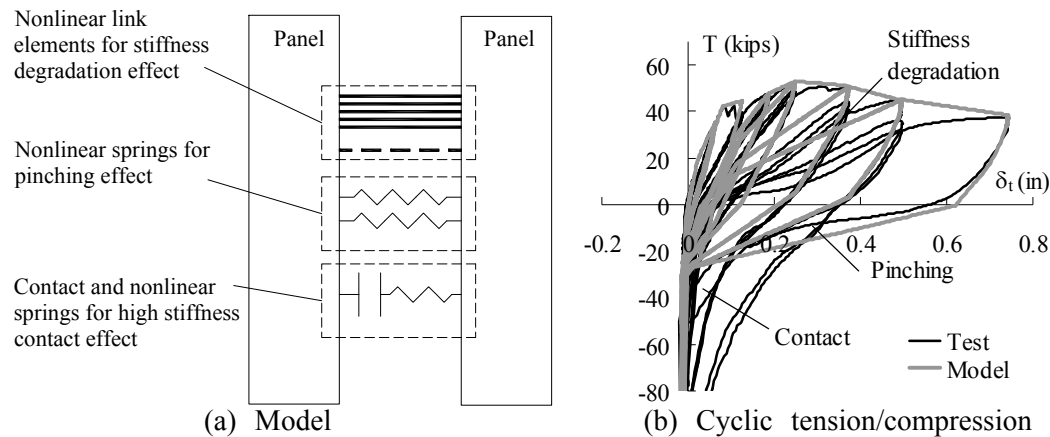
Fig. B2-9. Comparison of test results and model for 2#5 dry chord connector.

Untopped Diaphragm Shear Connector

As seen in Fig. B2-3a, the typical untoped flange-to-flange shear connector (JVI) exhibits strength degradation effect under cyclic shear loading as well as the tension-shear coupling effect (Wan et al. 2011). These two effects are isolated because the strength degradation is due to the damage of surrounding concrete (see *Sec B2.2.3*) while the tension-shear coupling effect is due to the yielding of connector (Wan et al. 2011). To accomplish these two isolated effect, the connector subassemblage model is composed of two groups of elements connected in series (see Fig. B2-10): (1) one group is for modeling strength degradation effect (see *Sec B2.3.3*) and (2) the other group is for modeling tension-shear coupling effect (Wan et al. 2011). In addition a group of contact elements is placed in parallel (see Fig. B2-10) to model the friction effect under compression (Wan et al. 2011).
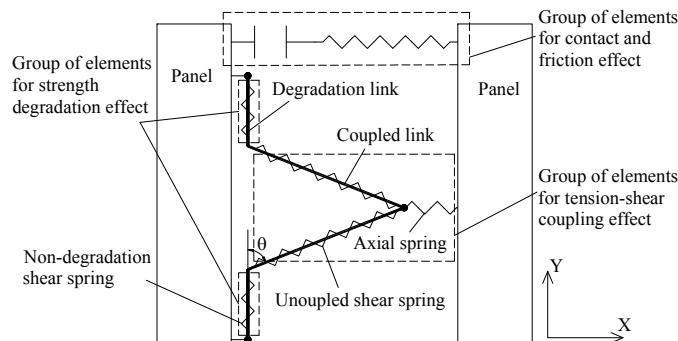
Fig. B2-10. Model for JVI connector.

C-A-137

Table B2-2. Material inputs of the strength degradation group elements for the JVI connector model

Test backbone		Cumulative deformation			Deg. element		Non-Deg.	
δ_v	V	δ_{vap}	n	δ_{vcp}	δ_{vap}	V_{deg}	δ_v	$V_{non-deg}$
(in)	(kips)	(in)		(in)	(in)	(kips)	(in)	(kips)
0.005	2.5	-	-	-	0.005	2.46	0.005	0.03
0.042	10.8	-	-	-	0.042	10.59	0.042	0.26
0.082	18.1	-	-	-	0.082	18.00	0.082	0.50
0.092	13	0.01	1	0.03	0.112	12.44	0.092	0.56
0.16	10	0.078	2	0.654	0.736	9.02	0.16	0.98
0.24	9	0.158	2	1.918	2	7.53	0.24	1.47
0.33	6	0.248	1.5	3.406	3.488	3.98	0.33	2.02
0.49	3	0.408	1.5	5.854	5.936	0.00	0.49	3.00
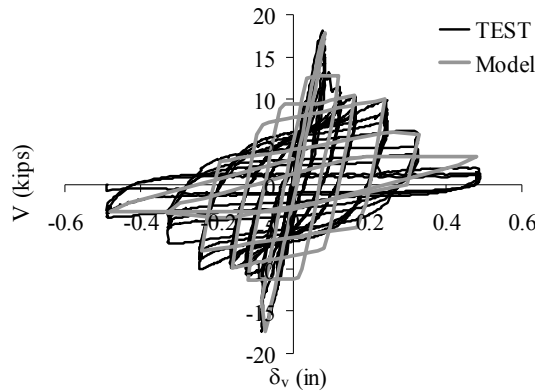
Fig. B2-11. Comparison of test and model for JVI.

The modeling technique discussed in Sec.B2.3.3 has been used for the strength degradation group of element in the JVI connector model. The material inputs for the nonlinear degradation link element are calculated from Eqn. 2 to 5 based on the cyclic shear test backbone (See Fig.B2-3b) as shown in Table B2-2. A non-degradation shear spring with a low strength and stiffness is added for modeling stability and avoiding zero stiffness after the degradation link element loses its strength completely. Fig.B2-11 compares the cyclic shear test results to the model prediction. A good agreement is observed between test and model for the JVI connector.

The modeling technique discussed in (Wan et al. 2011) has been used for the tension-shear coupling group of element in the JVI connector model. For the JVI connector model, the angle θ of "inclined" link element has been calibrated as 33 degrees.

The dynamic response (shear and tension) of one JVI connector model obtained from an earthquake simulation of a precast structure model is shown in Fig. B2-12 with the pushover response (pure shear and pure tension) marked as dash line. The JVI model separately shows the shear strength reduction before yielding due to tension-shear coupling effect and exhibits shear strength degradation effect after the peak load. The tension strength of JVI model reduces as well due to the coupling effect.
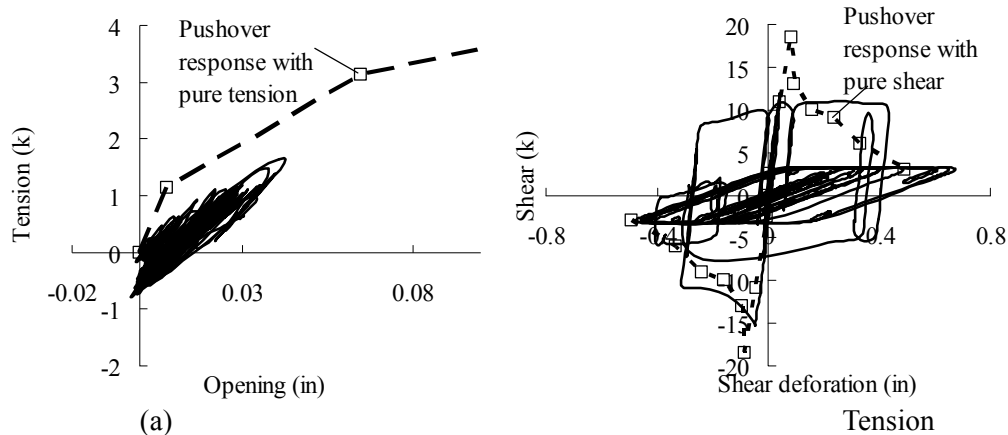
Fig. 2B-12. Dynamic response of JVI connector model.

For the modeling of contact friction in the JVI connector model, the friction coefficient μ for the contact element has been calibrated from a cyclic shear test under constant 10k compression load perpendicular to the joint (see Fig B2-13). As seen in Fig. B2-13(b), the model with a coefficient of friction (μ) of 0.55 shows good match between test results and model prediction.
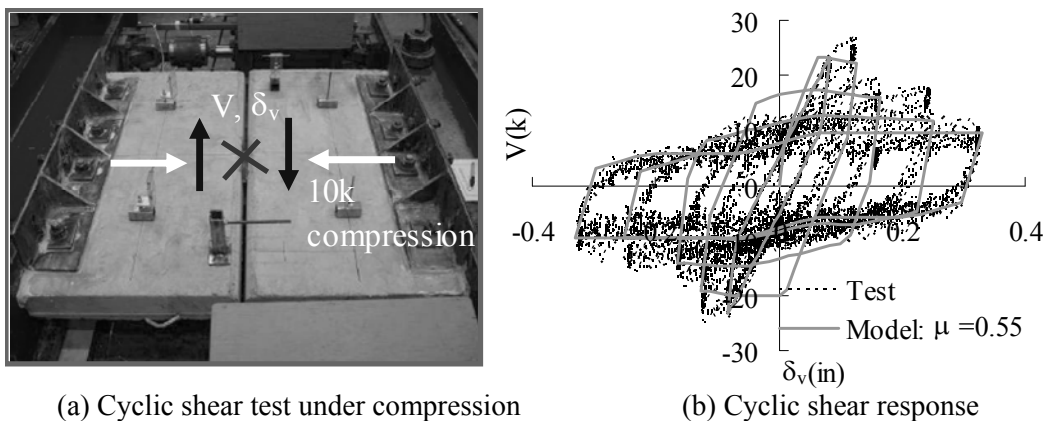
(a) Cyclic shear test under compression   (b) Cyclic shear response

Fig. B2-13. Calibration of friction coefficient for JVI model.

Topped Diaphragm Shear Connector

As seen in Fig. B2-3c, the cyclic shear test results of topped shear connector (ductile mesh) shows the following effects: (1) slip-catch effect; and (2) strength degradation effect. The modeling techniques discussed in *Sec. B2.3.4* and *Sec. B2.3.3* have been used to model the slip-catch and strength degradation effect respectively. The strength degradation effect has been built into the "hook" mechanism by replacing the nonlinear springs shown in Fig. B2-8a with the nonlinear link element using isotropic strain hardening rule as discussed in Sec B2.3.3. The material input for the nonlinear link element has been determined using Eqn. 2 to 5 based on the cyclic test backbone curve See Fig.B2-4c. Good agreement is observed between the test and model prediction (see Fig. B2-14).
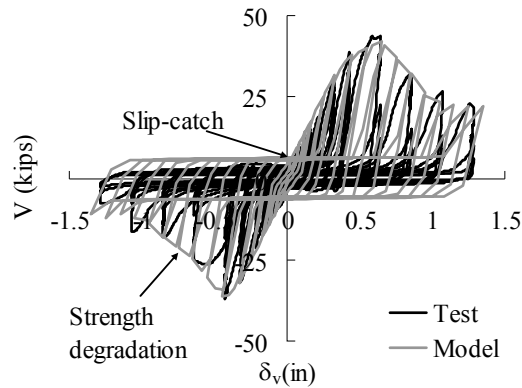
Fig. B2-14. Comparison of test and model for ductile mesh.

B2.5 CONCLUSIONS

The hysteretic models for precast connector diaphragm connector have been developed in this paper which will be used in the large DOF structure model for the 3D NLTDA. These hysteretic connector models have been calibrated to match the isolated connector cyclic tests. The following characteristics of the diaphragm connectors observed in the tests have been captured by the models:

    (1) Pinching effect under reverse loading in the cyclic tension test.
    (2) Stiffness degradation with increase of inelastic opening in the cyclic tension test.
    (3) Strength degradation with increase of inelastic shear deformation in the cyclic shear test
    (4) Slip-catch effect under reverse loading in the cyclic shear test.
    (5) Tension-shear coupling effect under combined loading.
    (6) High stiffness contact and friction effect under compression.

These elements are used in the calibration of the design factors (See *Appendix A2*).

B2.6 REFERENCES

ANSYS version 11. (2007). "Elements (00853) and theory reference (00855)" SAS IP, Inc.

Building Seismic Safety Council, Committee TS-4. "Seismic design methodolgy for precast concrete floor diaphragms." Part III, *NEHRP Recommended Sesimic Provisions* 2009 Federal Emergency Management Agency, Washington, D.C.

Farrow, K. T. and Fleischman, R. B. (2003). "Effect of dimension and detail on the capacity of precast concrete parking structure diaphragms" PCI Journal 48(5): 46-61.

Fleischman, R.B. and Wan, G. (2007). "Appropriate overstrength of shear reinforcement in precast concrete diaphragms", ASCE Journal of Structure Engineering 133(11): 1616-1626.

Fleischman, R.B., Zhang, D., Ren, R, and Naito, C., (2010). "Experimental evaluation of precast diaphragm critical shear joint under seismic demands." under preparation.

Naito, C.J., Peter, W., and Cao, L., (2006). "Development of a seismic design methodology for precast diaphragms - phase 1 summary report." ATLSS Report No.06-03, ATLSS Center, Lehigh University, PA.

Naito, C.J., Ren, R., Jones, C. and Cullen T. (2007). "Development of a seismic design methodology for precast diaphragms - phase 1b summary report." ATLSS Report 07-04. ATLSS Center, Lehigh University, PA.

OpenSees Version 2.2.2 (2011). "OpenSees Comand Language Manual." University of California at Berkeley, CA.

Schoettler, M.J., Belleri, A., Zhang, D., Restrepo, J., and Fleischman, R.B. (2009). "Preliminary results of the shake-table testing for development of a diaphragm seismic design methodology." PCI Journal, 54 (1), 100-124.

Wan, G., Fleischman, R.B., Naito, C.J., Zhang, D. (2011). "Development of Connector Models for Nonlinear Pushover Analysis of Precast Concrete Diaphragms". Under preparing.

Wan, G., Fleischman, R.B. and Zhang, D. (2011). "Effect of spandrel beam to double tee connection characteristic of flexure-controlled precast diaphragms", J. of Structural Eng. ASCE. Accepted in Apr. 2011.

Wan, G. (2007). "Analytical Development of Capacity Design Factors for A Precast Concete Diaphragm Seismic Design Methodology", Ph.D dissertation, the University of Arizona, Tucson, AZ.

Zhang, D. and Fleischman, R.B. (2011). " Establishment of Seismic Design Force Factors for Precast Concrete Diaphragms". Under preparation.

Zhang, D., Fleischman, R.B., Naito, C., and Ren, R. (2010). "Experimental Evaluation of Pretopped Precast Diaphragm Critical Flexure Joint under Seismic Demands." J. Struct. Eng. ASCE, Accepted in Dec 2010.

B2.7 NOTATION

C_y = compression strength of pinching model;
F = tension force inputs of stiffness degradation model;
F_v = shear force inputs of strength degradation model;
M = Moment;
N = number of control points for stiffness degradation model;
n = number of repeated cycles at the same loading amplitude;
R = residual strength of link element in stiffness degradation model;
T = chord tension force;
T_y T_u = chord tension yield, ultimate force;
t = the thickness of diaphragm.
V = shear force of the shear connector;
V_y = peak shear force of the shear connector;
α = ratio of elastic-plastic spring strength over total strength;
Δ = deformation corresponding to the peak load;
δ_t = chord deformation (opening);
δ_{ty} δ_{tu} = chord yield, ultimate deformation (opening);
δ_v = shear connector deformation (sliding);
δ_{va} = absolute sliding of shear connector;
δ_{vap} = absolute plastic sliding of shear connector;
δ_{vcp} = cumulative plastic sliding of shear connector;
δ_{ve} = elastic sliding of shear connector;
δ_{vap} = absolute plastic sliding of shear connector;
ε_0 = concrete stain at peak compression strength;
μ = coefficient friction;
θ = angle of inclined element in the tension-shear coupling model;
θ' = joint rotation.

Appendix B3. Diaphragm Model Calibration using Precast Joint Tests

The 3D-FE discrete diaphragm model described in Appendix B2 was used in analysis-driven testing of critical regions of the precast floor diaphragm. These tests allowed: (1) evaluation of the seismic behavior of key regions in the precast diaphragm; and (2) verification or further calibration of the connection models used in the 3D-FE discrete models.

This portion of the research, analysis-driven integrated physical tests, was a collaboration between DSDM researchers at the University of Arizona (UA) and Lehigh University (LU), and was performed at the LU testing facilities. The testing procedure integrated analytical components (model-based structure simulation at UA) with experimental components (physical test substructure at LU). The load applied to the LU test specimens was controlled by output from nonlinear transient dynamic analyses (NLTDA) of the three-dimensional finite element (3D-FE) analytical models of precast structures. The analytical models use discrete representations of the reinforcement in the precast diaphragm through the inclusion of cyclic connector elements in the model (See Appendices B1, B2). For brevity, these models are herein termed as *3D NLTDA* models throughout the Appendix.

Two separate testing programs are performed: (a) The evaluation of a diaphragm critical flexure joint under predetermined displacement histories derived from NLDTA; and, (b) The evaluation of a diaphragm critical shear joint using hybrid (adaptive) testing techniques, in which the NLTDA and experiment are performed simultaneously, with the physical test specimen acting as a substructure of the analytical model superstructure. Both tests are performed at half-scale using a special testing fixture developed at Lehigh University. The test fixture accepts a pair of precast floor panels and is capable of simultaneously providing shear, axial and moment to the joint between the panels.

Section B3.1 describes the predetermined displacement history (PDH) testing of a diaphragm critical flexure joint. Section B3.2 describes the hybrid testing of a diaphragm critical shear joint.

TABLE OF CONTENTS

B3.1 PDH TEST OF DIAPHRAGM CRITICAL FLEXURE JOINT

In this testing program, analysis-driven integrated physical testing is first used to examine the seismic performance of a critical flexure joint in a pretopped precast concrete diaphragm. Critical flexure joint refers to the floor joint undergoing the highest in-plane flexural demands in the diaphragm. A 3-story precast parking garage is used as the evaluation structure (See Fig. B3-1). A 3D NLTDA model of this structure is created as described in Appendix B2. Simulation of this structure is used to control the loading of a test specimen, which represents the diaphragm high flexure region in the structure (shaded region in Fig B3-1).
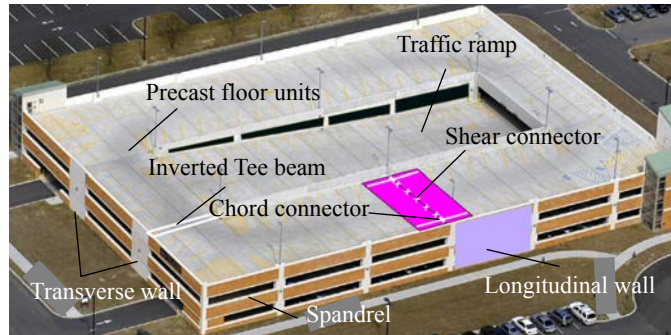
Fig. B3-1: PDH evaluation structure: 3 story parking structure.

The seismic loading is applied as predetermined displacement histories (PDHs), representing the interface degrees-of-freedom (DOF) between the analytical superstructure and physical substructure. The PDHs subject the critical flexural joint to the sliding and opening histories experienced in the analytical superstructure during the earthquake simulations.

The evaluation structure is designed with trial factors from the design methodology. The diaphragm joint is detailed with HDE reinforcement. Thus, the testing program intends to examine the joint under anticipated seismic demands, including those that extend response into the inelastic regime.

The analytical model of the evaluation structure is shown in Figure B3-2a. The experimental substructure is a portion of the floor diaphragm in the high flexure region (see solid panels Figure B3-2a). The test specimen replicates this region, composed of the two pretopped precast DT units surrounding the critical flexure joint (Figure B3-2b). The units are connected by diaphragm reinforcing elements designed for seismic performance. The experiment is conducted at half-scale. Seismic demands are introduced to the specimen through interface displacements between the analytical superstructure and the experimental substructure (white arrows in Figure B3-2a) which are generated from NLTDA. This loading condition is realized through a test fixture (Figure B3-2b) capable of simultaneously statically providing shear, axial and moment to the joint (Naito et al. 2007).
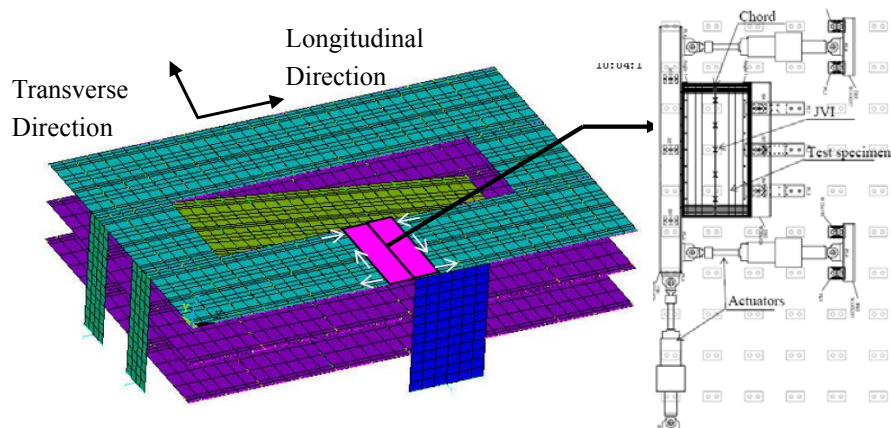
(a) Analytical superstructure;   (b) Experimental substructure.
Fig. B3-2: PDH test program.

The objectives of the PDH testing program are to:

(1) Examine the seismic performance of a flexure critical pretopped precast concrete diaphragm joint including: (a) the flexural strength and stiffness under progressive damage; (b) the rotational deformation capacity under realistic cyclic loading; and (c) the failure modes including mapping damage levels to seismic hazard.

(2) Calibrate the 3D NLTDA model, developed using test results of isolated diaphragm reinforcing.

(3) Determine the system behavior of individual reinforcing elements acting together under combinations of internal shear, axial force and flexure.

(4) Demonstrate the performance of pretopped diaphragm HDE details in achieving expected seismic demands.

(5) Predict the critical flexure joint performance of a shake table test specimen of identical detail in a parallel thrust of the research (See Appendix B4).

The following aspects of the testing program are described in the sections that follow: (1) Evaluation structure; (2) Analytical program; (3) Experimental program; and (4) Experimental results and analytical comparison; and (5) Conclusions.

B3.1.1 PDH Prototype Structure
Selection of Prototype Structure

The selection of the PDH structure was driven by two competing requirements: (1) the need to subject the test specimen to a realistic and demanding set of displacement histories expected of a diaphragm critical flexure joint; and (2) the desire to use this test to predict performance in an upcoming shake table test (Schoettler et al. 2009).

To meet the first criteria, the PDH structure configuration was selected from a portfolio of precast prototype structures developed for the project (Fleischman et al. 2005b). The configuration selected, termed PS#1, is a 4 story 3-bay side-by-side parking structure with perimeter shear walls. The PDH structure is then created by modifying the PS#1 dimensions such that the critical flexure joint design matches that of the shake table structure (STS).

Table B3-1 compares the PS#1, STS and PDH structures. Floor plan dimension notation is indicated in Figure B3-3; the STS floor plan is rectangular (L x d). As seen in the table, the following modifications were made to PS#1 to meet the design constraints:

(1) The short dimension in plan (a) is modified to allow each subdiaphragm, i.e. diaphragm parking flat (dimension d) to match the STS floor depth 32ft.

(2) The DT width (b) is modified to match the STS DT width 8ft.

(3) The long dimension (L), aspect ratio (L/d), number of stories (n), floor-to-floor height (h), floor mass (w) and SDC are all modified such that the PDH and STS maximum diaphragm design moment essentially match (~4000k-ft).

Table B3-1: Comparison of PS#1, STS and PDH structures.

Structure	Seismic Location	SDC	h ft	L ft	a ft	d ft	b ft	w psf	F_{px} kips	Ψ_d	M_u k-ft
PS#1	Knoxville	E	10	300	180	60	12	143	585	1.0	7320
STS	Berkeley	D	13	112	32	32	8	150	190	1.5	3980
PDH	Charleston	C	13	144	96	32	8	150	450	1.5	4050

The resulting PDH structure floor plan is shown in Figure B3-3. Also identified in Figure B3-3 for later discussion are the PDH structure diaphragm reinforcement and key diaphragm joints.

The shear walls are on the structure perimeter (Figure B3-3): a pair of 12ft transverse walls and single 24ft longitudinal wall at each end of the floor. The symmetric longitudinal walls of PS#1 are offset about the symmetry line in the PDH structure. This layout, not uncommon in parking structures, is

adopted here to eliminate the confining effect of the longitudinal wall on the critical flexure joint, while also introducing longitudinal wall collector forces to this joint, thereby creating a highly demanding condition.
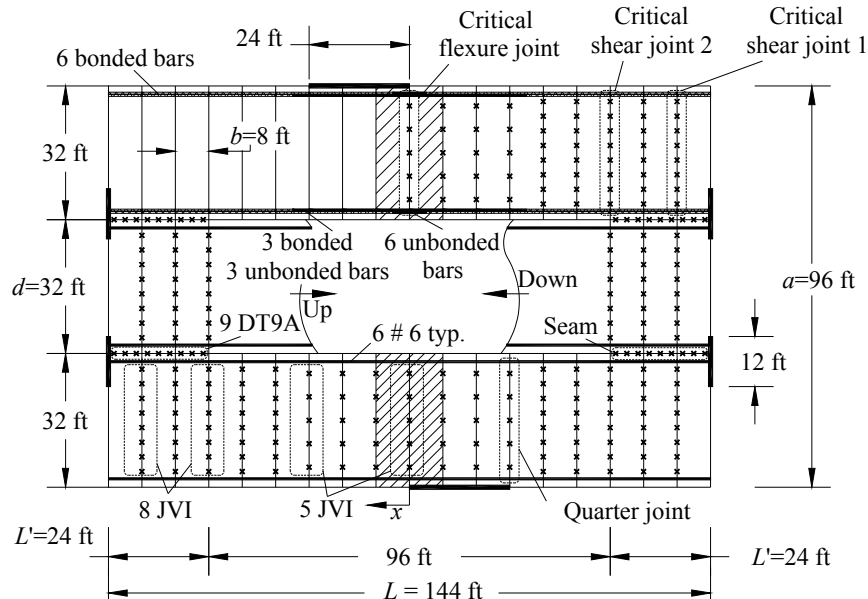
Fig. B3-3: Plan of PDH structure.

PDH Structure LFRS Design

The PDH structure seismic design is based on existing code (IBC 2003), with the adoption of certain aspects of the emerging methodology for diaphragm design. The site is Charleston (SC), SDC D, soil class F (Ss=1.39, S1=0.4). The seismic-resistant system is special reinforced concrete (RC) shear wall (R=6, Ω_o=2.5, Cd=5); The Equivalent Lateral Force (ELF) procedure (Cs=0.145, T=0.44 sec) appears in Table B3-2.

Table B3-2: ELF design for PDH structure.

Floor	h_x	w_x	$w_x h_x^{k}$	c_{vx}	F_x	Shear	Moment
	ft	kips			kips	kips	k-ft
3	39	2068	80644	0.50	450	0	0
2	26	2068	53763	0.33	300	450	5854
1	13	2068	26881	0.17	150	750	15610
Sum:		6203	161289	1.00	901	901	27318

Table B3-3: Shear wall design for PDH structure.

Shear Wall	Base Shear (kips)	Moment (k-ft)	Chord bars	Web Reinforcing	$\phi_f M_n$ (k-ft)
Transverse	225	6785	12 # 9	2 # 4 @ 18ft	7065
Longitudinal	450	13569	10 # 9	2 # 4 @ 18ft	14131

Table B3-3 provides the shear wall design. Inelastic action is assumed to be limited to the base. Figure B3-4a shows the base detail for each shear wall: chord bars in boundary elements and web reinforcement at maximum allowable spacing produce the required flexural capacity as per ACI 318

(2005). Figure B3-4b shows the moment-curvature response at the shear wall bases: The solid line is produced from fiber model analysis; the dotted line is the backbone curve used in the 3D NLTDA model.

(a) Detailing;   (b) Pushover response at base.
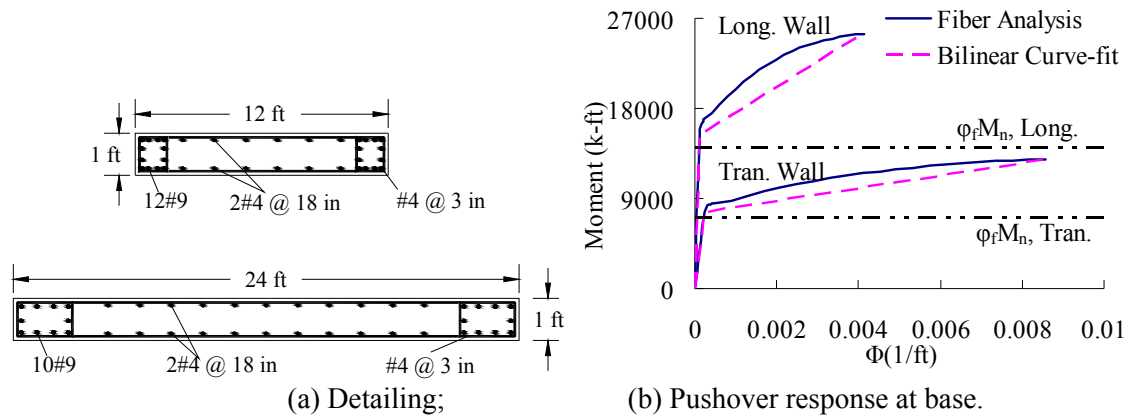
Fig. B3-4: Shear wall in PDH structure.

PDH Structure Diaphragm Design

The diaphragm design of PDH structure is based on the design methodology in PART 1. A constant diaphragm design force profile assigned the current maximum diaphragm force, 450k (from Table B3-1) is used in accordance with the emerging design methodology. Reduced design option (RDO) is adopted for designing the PDH structure. According to RDO, a diaphragm force amplification factor Ψ_r will be applied to the diaphragm design force. The value of Ψ_r is assigned as 1.5 based on the NLTDA analyses for designing the diaphragm of shake table test specimen. It is noticed that the PDH structure is designed for Charleston site. This amplified diaphragm design force is approximately equal to the current diaphragm design force per (IBC 2003) for Berkeley site. Therefore it allows checking the performance of diaphragm flexural joint under both new design and current design method by imposing earthquakes ground motion equivalent to Charleston site and Berkeley site respectively.

Key diaphragm joints are shown in Figure B3-3 and include: (1) critical flexure (CF) joints (shaded region on each side of the floor); (2) critical shear (CS) joints at the diaphragm ends; (3) the internal beam joint at the ramp landing, termed "seam"; and, (4) the joint at diaphragm quarter span (QT). Note that while the CF joint must be explicitly designed to create the test specimen, other regions of the diaphragm must also be designed accurately so that the analytical model produces the proper NLDTA results.

The design forces at these joints are given in Table B3-4. Some comment is required on the procedure to calculate these internal forces. The diaphragm force path in parking structures is complex (Wood et al. 2000) and the force distribution changes depending on the condition of the seam (Fleischman et al. 1998), analogous to a fixed-ended beam while the seam remains intact, and a simple beam afterward. For conservatism, the simple beam assumption is used to calculate the midspan diaphragm moment. This approach results in the following expression for $M_u(x)$, based on the load tributary to one subdiaphragm ($\Psi_r F_{px} d/a$=225k) per PCI Handbook (2004):

$$M_u(x) = \Psi_r \left\{ (d/a)(F_{px})(L/2-x)/2 - (d/a)(F_{px})(L/2-x)^2/2L \right\} \quad \text{(Eq. 1)}$$

The shear design accounts for both an intact seam (CS2) and a "failed" seam condition (CS1) case. The expression for the required design shear is:

$$V_u(x) = (d/a)(\Psi_r F_{px})x/L \quad\quad\quad\quad \text{(Eq. 2)}$$

The intact seam condition is used to determine the maximum (negative) moment at CS2 (analogous to a fixed end moment):

$$M_u = \Psi_r \{(d/a)(F_{px})(L - 2L')/12\}$$ (Eq. 3)

The seam is designed for tributary shear flow (V_rQ/I) as per PCI Handbook (2004).

$$V_u = L'V_rQ/I = (a/d)\,6L'V_r(a-d)d/a^3$$ (Eq. 4)

Table B3-4: Diaphragm design forces for PDH structure.

Location	x	V_u		M_u	
	ft	kips	Eq.	k-ft	Eq.
Critical flexure joint (CF)	0	0	4.2	4050	4.1
Quarter joint (QT)	24	38	4.2	3600	4.1
Critical shear joint 1 (CS1)	72	112	4.2	850	4.1
Critical shear joint 2 (CS2)	48	75	4.2	1800	4.3
Seam	NA	94	4.4	900	4.5

The seam is also subjected to axial force and flexure. Since there is no accepted method for accounting for these forces in current practice, the seam was designed by estimating the forces as a designer might with an elastic analysis of the floor plate. The resulting forces (N=48k; V=98k=1.05V_u; M=561k-ft=0.62Mu) under diaphragm design force (Ψ_rF_{px}) is used to set a design moment at the seam of half the value in Eq. 3, ignoring axial force. The resulting seam design moment is:

$$M_u = \Psi_r \{(d/a)(F_{px})(L - 2L')/24\}$$ (Eq. 45)

The unbonded dry chord, bonded dry chord and JVI Vector (Figure B3-3) are specified for primary diaphragm reinforcement throughout the PDH structure. The unbonded chord detail eliminates shear transfer within the range of expected joint sliding (Naito et al. 2007) for better controlled (HDE) flexure response. Standard flange-to-flange angled bar connectors (termed as DT9A in Figure B3-2) (Pincheira et al. 1998) possessing higher strength than the JVI Vector, and endowed here with HDE characteristics, are provided for the seam reinforcement.

Table B3-5: Diaphragm shear design for PDH structure.

Joint	V_u	Shear connector			Bonded chord			V_n	Ω_v
		$v_n{}^1$	# of	$V_{n,con}$	$v_n{}^2$	# of	$V_{n,ch}$		
	kips	kips	conn.	kips	kips	bars	kips	kips	V_u/V_n
CF	0	13	5	65	5.4	0	0	65	-
QT	38	13	5	65	5.4	6	32	98	2.6
CS1	112	13	8	104	5.4	12	65	169	1.5
CS2	75	13	8	104	5.4	12	65	169	2.23
Seam	94	17	9	154	-	0	-	154	1.64

[1] JVI Vector shear strength from (Naito et al. 2007), angled bar shear strength from (Pincheira et al. 1998)
[2] Bonded dry chord shear strength from (Naito et al. 2006)

Table B3-5 provides the diaphragm shear design. Shear strengths for the bonded chord, JVI Vector, and angled bar are based on the testing indicated. A shear overstrength factor $\Omega_v \geq 1.5$ is enforced to prevent non-ductile shear limit states according to the RDO design procedure in the emerging design

methodology (section 2.4). The shear overstrength factor is pre-selected through a pushover parametric study finding (Fleischman and Wan 2007) and is checked through a series of trial dynamic analyses. The needed shear strength in diaphragm high shear regions is achieved by activating dowel action in fully bonded chord reinforcement. This transition is performed in stages (without bar cut-offs) as shown in Figure B3-2.

Table B3-6 provides the diaphragm flexure design. The flexural strength includes the tension contribution of shear reinforcement as per ACI 318 (2005) and is calculated using an analytically-based procedure (Wan 2007). The procedure estimates the neutral axis by assuming: (1) the chord reinforcement has yielded in tension; (2) a triangular stress distribution exists in the concrete in compression; (3) the contribution of the compression reinforcement is ignored.

Table B3-6: Diaphragm flexure design for PDH structure.

Joint	M_u	Shear connector			Chord #6			$\varphi_f M_n$
		t_n[1]	# of	$M_{n,\,conn}$[2]	t_n[3]	# of	$M_{n,\,ch}$[2]	
	k-ft	kips	conn.	k-ft	kips	bars	k-ft	k-ft
CF	4050	3.1	5	277	26.4	6	4408	4217
QT	3600	3.1	5	277	26.4	6	4408	4217
CS1	850	3.1	8	349	26.4	6	4405	4278
CS2	1800	3.1	8	349	26.4	6	4405	4278
Seam[4]	900	10.3	9	993	-	0	-	893

[1] JVI Vector tension strength and stiffness from (Naito et al. 2007)
[2] Flexure strength from analytical-based procedure (Wan 2007)
[3] Dry chord tension strength, t_n,chord = $A_s f_y$
[4] Angled bar tension strength from (Pincheira et al. 1998).

B3.1.2 NLTDA for PDH Structure

Dynamic Analysis Procedure

3D NLTDA Model Description

The three-dimensional finite element analytical model (3D NLTDA) using discrete diaphragm models, in which the diaphragm connectors are directly modeled (refer to *Appendix B2*) is used for the dynamic analysis of the PDH structure. To save the computer time and storage, full discrete model only applies to critical seismic demand floor which identified as top floor by trail dynamic analyses. Other non-critical floors are modeled as reduced discrete model (Figure B3-2). The shear wall is modeled as elastic shell element with base plastic hinge springs. The chord reinforcement is modeled with pinched hysteretic effect and the shear reinforcement is modeled with strength degradation hysteretic effect. The "pushover" curves for the models of chord and shear reinforcement are shown as dash line in Figure B3-10. The secondary reinforcements such as DT-spandrel and DT-internal beam connections are modeled with pinched hysteretic effect.

The physical test is performed at half-scale. Though the option exists to analyze the full-scale structure and scale the outputs to create the PDH, the approach adopted is to scale the structure and use the outputs directly.

The PDH structure is reduced to half-scale in the analytical model via the following scale rules: (1) Structural dimensions are reduced by the scale factor; (2) Deformation capacity is reduced by the scale factor; (3) Force and moment strengths are reduced by the square and cubic of the scale factor, respectively. The similitude of the scaled model was verified through comparison of scaled results from a full-scale model.

Selection of Ground Motion

Five ground motions are selected for the PDH test sequence. The first three motions represent seismic hazard for Charleston SC corresponding to levels of increasing intensity: service (SVC), Design Basis Earthquake (DBE), and Maximum Considered Earthquake (MCE). The fourth motion is a bi-directional motion corresponding to the Charleston DBE level. This motion is intended to subject the critical joint to the combined effects of flexure due to the transverse component in conjunction with in-plane twisting and collector forces due to the longitudinal component. The final ground motion corresponds to a Berkeley MCE level.

(a) Time history;   (b) Response spectrum.
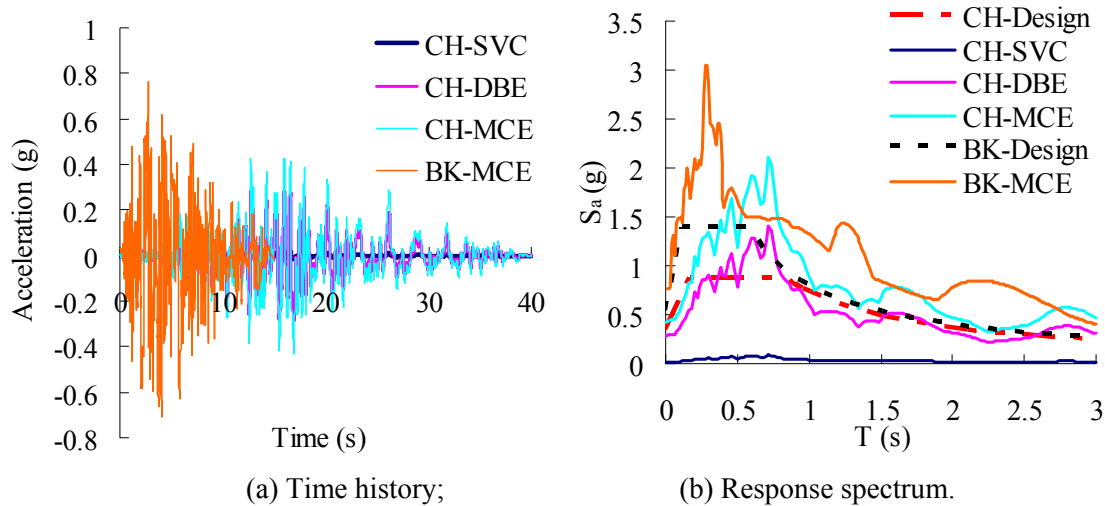
Fig. B3-5: Ground motions used for NLTDA of PDH structure.

It is noted that the PDH structure Charleston design, which incorporated design factors from the emerging design methodology (Ψ_r, Ω_v), corresponds roughly to a current diaphragm design for the Berkeley SDC. Thus this last test is not only intended to examine "overload" conditions, but also to make references on current design.

The Charleston motions are developed from the 1986 Taiwan earthquake, scaled to match the Charleston SC design spectrum. The Berkeley motion was developed from the 1994 Northridge earthquake, scaled to match the Berkeley CA design spectrum (Schoettler 2005). The time history and response spectra of the Charleston and Berkeley MCE are shown in Figure B3-5.

Dynamic Analysis Parameters

The dynamic analysis is conducted using time steps of 0.05 sec for Charleston and 0.025 sec for Berkeley (time-compressed records). The time-stepping technique is the Newmark integration method with two substeps per time step. The convergence technique is a modified Newton-Raphson iteration method with force tolerance error of 0.5% (ANSYS 2007).

A conservative value of 0% equivalent damping is used except for two earthquake runs, the bi-directional Charleston DBE and Berkeley MCE, requiring 2% equivalent damping to converge.

Sequence of Loading

The NLTDA is performed for the PDH structure model subjecting a set of increasing amplitude ground motions (Table B3-7). Each ground motion is applied to the PDH structure model in a pristine status. The seismic response of precast concrete diaphragms in parking structures is somewhat complex (Lee and Kuchma 2008) (Fleischman et al. 1998). If the seams successfully transfer the tributary shear, the outer parking flats are subjected to flexure combined with axial force. The leading flat is under bending and tension; the trailing flat under bending and compression (Figure B3-6).
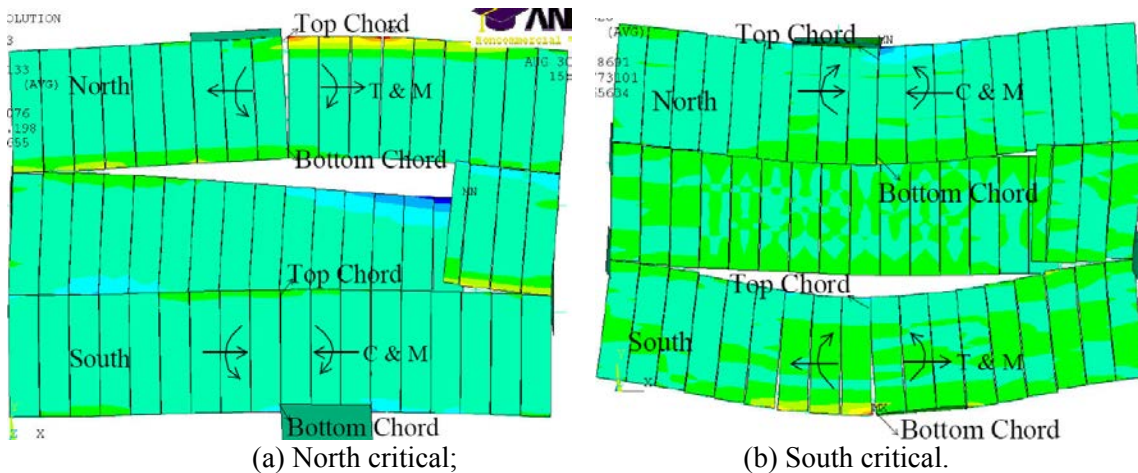
(a) North critical;   (b) South critical.
Fig. B3-6: Diaphragm deformation shape.

This creates a situation in which the outer chord of each flat is critical (tension component of bending adding to axial tension) for either direction of vibration: north flat top chord when the diaphragm deforms to the north (Figure B3-6a) and south flat bottom chord when the diaphragm deforms to the south (Figure B3-6b). If all PDHs are produced from either north CF joint or south CF joint, only top chord or bottom chord will incur large loading demand. Therefore, the opportunity exists to impose large opening demand for both ends of chord in a single specimen by successively alternating the experimental substructure from north to south CF joint for different earthquake loading, essentially flipping the critical chord from top to bottom in the test loading sequence (Table B3-7).

Table B3-7: Loading sequence.

Analysis	Earthquake	Intensity	Direction	Panel used for test
PDH 1	Charleston (CH)	SVC	Transverse	South
PDH 2	Charleston (CH)	DBE	Transverse	North
PDH 3	Charleston (CH)	MCE	Transverse	South
PDH 4	Charleston (CH)	DBE	Bi-direction (Bi-Dir)	North
PDH 5	Berkeley (BK)	MCE	Transverse	South

Dynamic Analysis Results
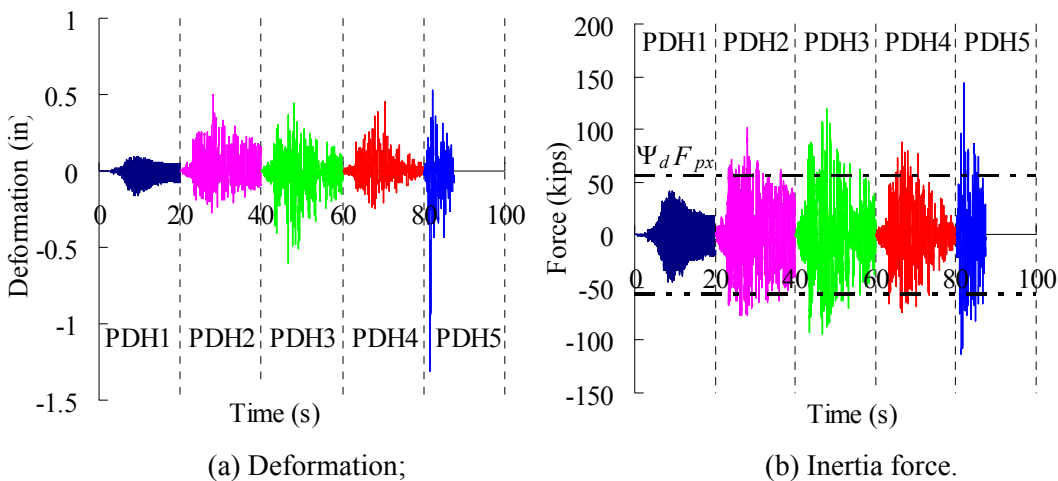
(a) Deformation;   (b) Inertia force.
Fig. B3-7: Diaphragm response at critical floor (3rd).

Results are presented here in half-scale since the NLTDA is performed at half-scale. For the full scale response, the force and moment need to be scaled by four and eight respectively; deformation and time need to be doubled.
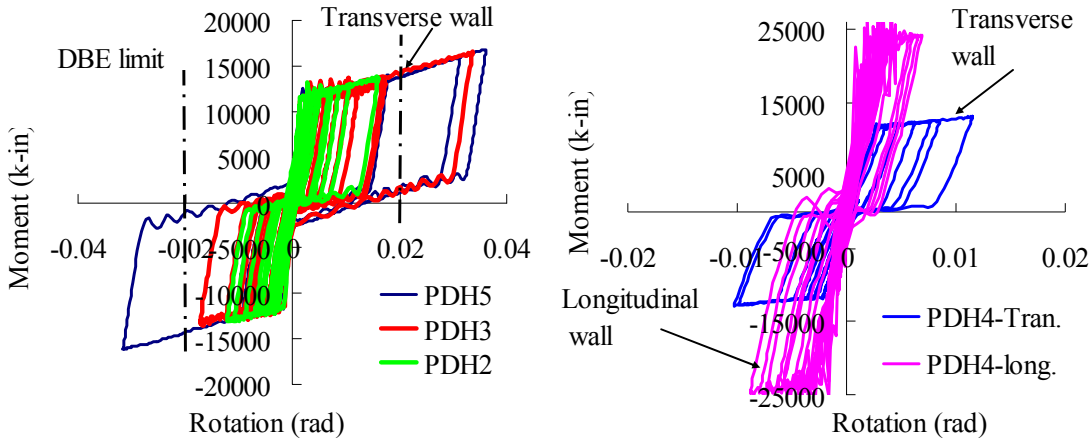
(a) PDH2, PDH3 and PDH5; (b) PDH4.

Fig. B3-8: Shear wall base moment rotation response.

Global Response
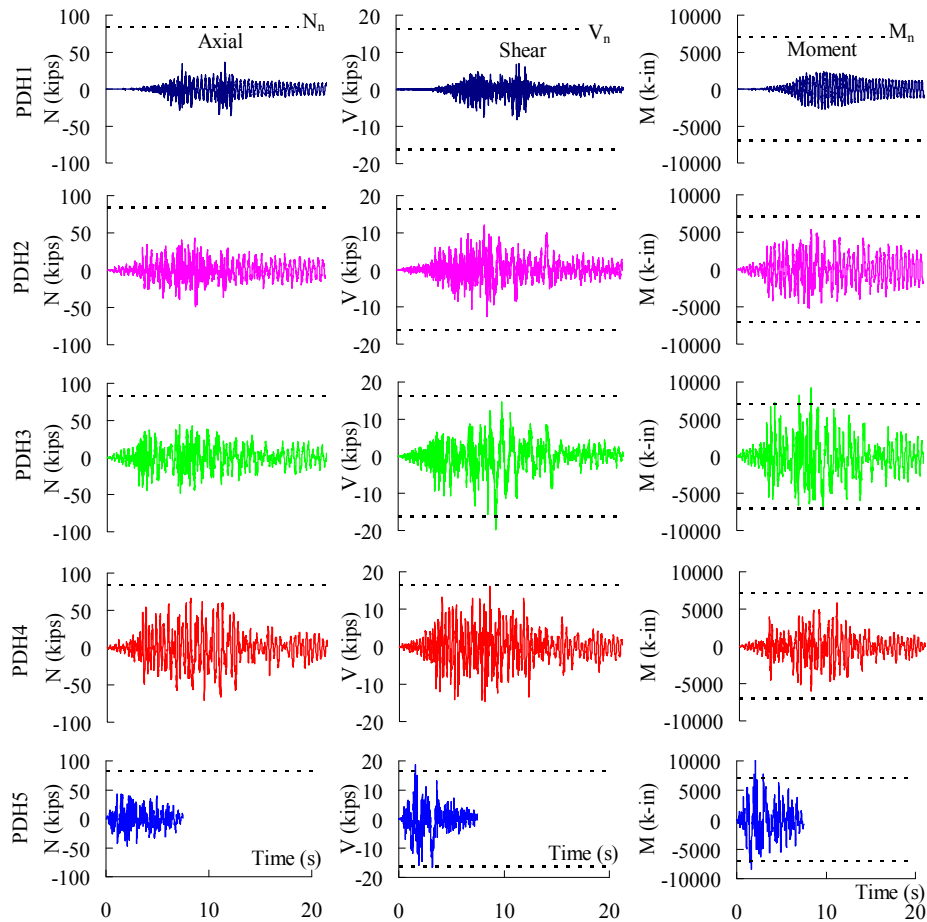
(a) Axial; (b) Shear; (c) Moment.

Fig. B3-9: Critical flexure joint internal forces.

C-A-151

The global response of the PDH Structure is shown in Figure B3-7 and Figure B3-8. Figure B3-7 shows the critical (3rd) floor diaphragm deformation (which is defined as the difference between diaphragm midspan displacement and the average of diaphragm two ends displacement) and inertial force time histories across the earthquake motions. The design force is indicated on the force plot. The shear wall moment-rotation is shown in Figure B3-8 for selected motions: Figure B3-8a indicates CH DBE (PDH2) shear wall rotational demands are within DBE design target per IBC (2003). Figure B3-8b shows that the longitudinal wall participates significantly in the bi-directional motion.

Local Response: Critical Flexure Joint

Figure B3-9 shows the internal force time histories for the CF joint: (a) axial force; (b) shear force; and (c) moment. In each case, the nominal design strengths are indicated. Though individual internal force components rarely reach design values, their combined effects consistently yield the diaphragm reinforcement as shown next.
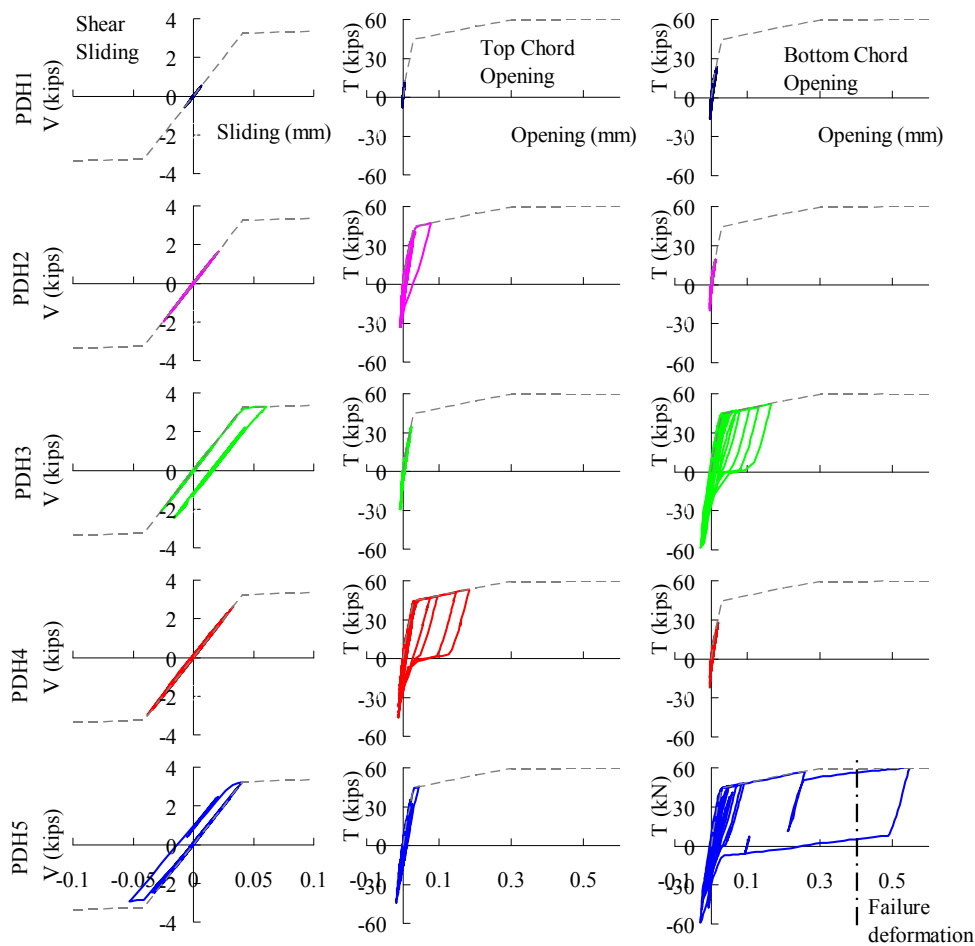
(a) JVI Vector shear;   (b) Top chord tension; (c) Bottom chord tension.
Fig. B3-10: Diaphragm reinforcement hysteretic responses.

Force-deformation responses at the CF joint are shown in Figure B3-10 for the center JVI Vector connector (shear-sliding) and the chords (axial force-opening). The dotted lines represent pushover response for individual connector. Recall that for each earthquake motion, the critical chord switches from top to bottom. The following is observed: the critical joint force-deformation response for CH SVC (PDH1) is essentially elastic. For CH DBE (PDH2), the top chord yields while the shear force-

deformation response remains elastic. In CH MCE (PDH3), the shear response also enters the inelastic regime. The maximum inelastic chord opening deformation increases with each successive ground motion with a maximum of approximately 0.55″ in half-scale for the BK MCE. For reference, the chord connector failure deformation capacity from isolated connector test (Naito et al. 2007) is shown, indicating the likelihood of failure during the BK MCE motion. It is noticed that in CH MCE the chord inelastic opening deformation demand is less than the chord failure deformation while it is larger than the chord failure deformation in BK MCE. This implies the proposed diaphragm design will survive MCE level earthquake while the current diaphragm design can not survive MCE level earthquake.

PDH Generation

The PDHs are generated from the NLTDA as three critical flexure joint interface displacements: joint sliding, joint opening at top chord and joint opening at bottom chord. As discussed above, the PDHs will successful put the critical flexure joint from elastic flexural demand into inelastic flexural demand, and further into close failure demand under overload ground motion with non-trivial joint shear demand. The PDHs is shown in sequence in Figure B3-11.

| (a) Opening at top; | (b) Opening at bottom; | (c) Sliding. |
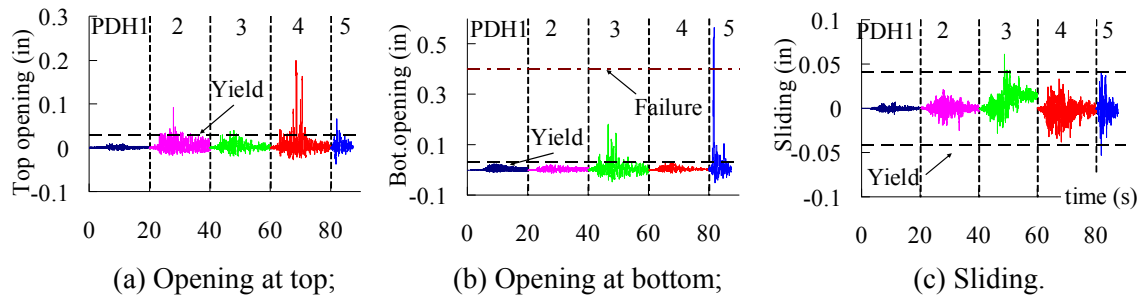
Fig. B3-11: PDHs from NLTDA.

B3.1.3 Experimental Program

The physical portion of the PDH test is conducted at LU. The LU researchers designed and produced the test specimen, set up the test fixtures, and conducted the test with the PDHs input generated from NLTDA at UA. The experimental program is briefly discussed in this section.

Specimen Detail
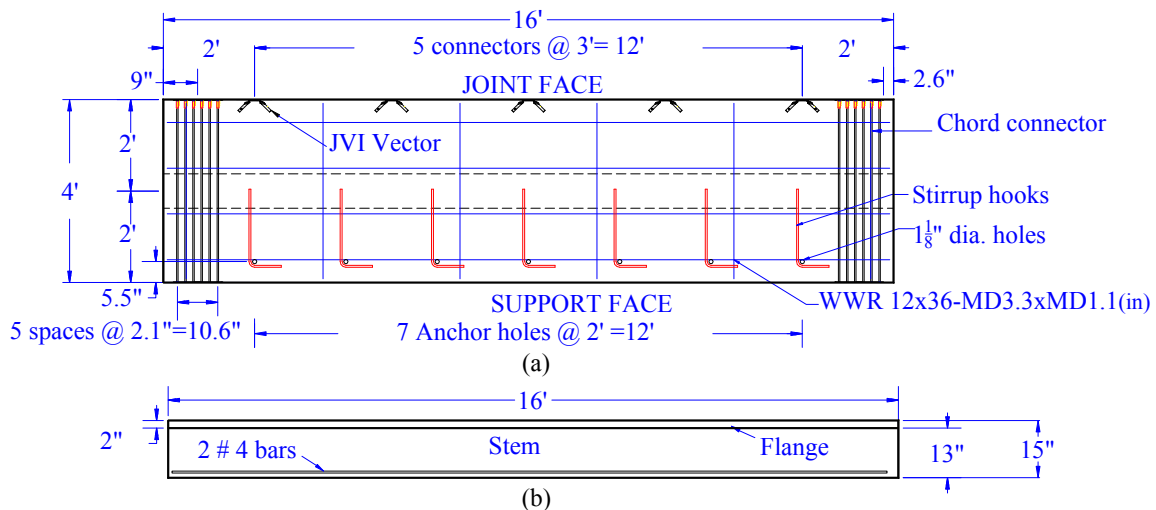
Fig. B3-12: Specimen detail: (a) plan; (b) side elevation (one panel of two).

The resulting specimen reinforcement layout is shown in Figure B3-12. In addition to primary reinforcement, each precast panel contains WWR for temperature and shrinkage reinforcement (ACI 2005). Conventional reinforcing bars (2 #4 bars @ 1.75″) are placed at the bottom of the stem in lieu of prestressing (Figure B3-12b). Anchor holes, reinforced with L-shaped #4 bars, are provided at the fixture supports.

Test Fixture

The test specimen is placed in a multi-degree-of-freedom (MDOF) loading fixture developed specially for the test program (Figure B3-13). The fixture provides simultaneous control of three DOFs in the plane of the specimen through three 281k actuators attached to a movable support beam: Actuators 1 (ACT1) and 2 (ACT2) control displacement perpendicular to the joint at the specimen top/north and bottom/south (producing opening/closing of the joint); Actuator 3 (ACT3) controls displacement parallel to the joint (producing joint sliding displacement). Independent control of these actuators allows for application of the interface displacements determined in the analytical simulations, thereby subjecting the specimen to the non-proportional combinations of in-plane shear, axial and bending actions exhibited at the panel joint during the earthquake simulations.
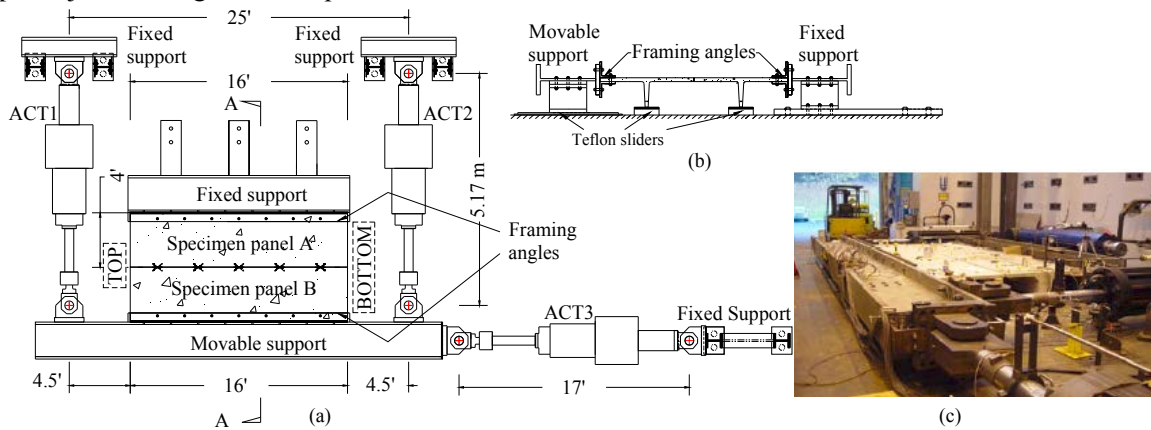
Fig. B3-13: Test fixture: (a) plan; (b) section; (c) photo.

Instrumentation
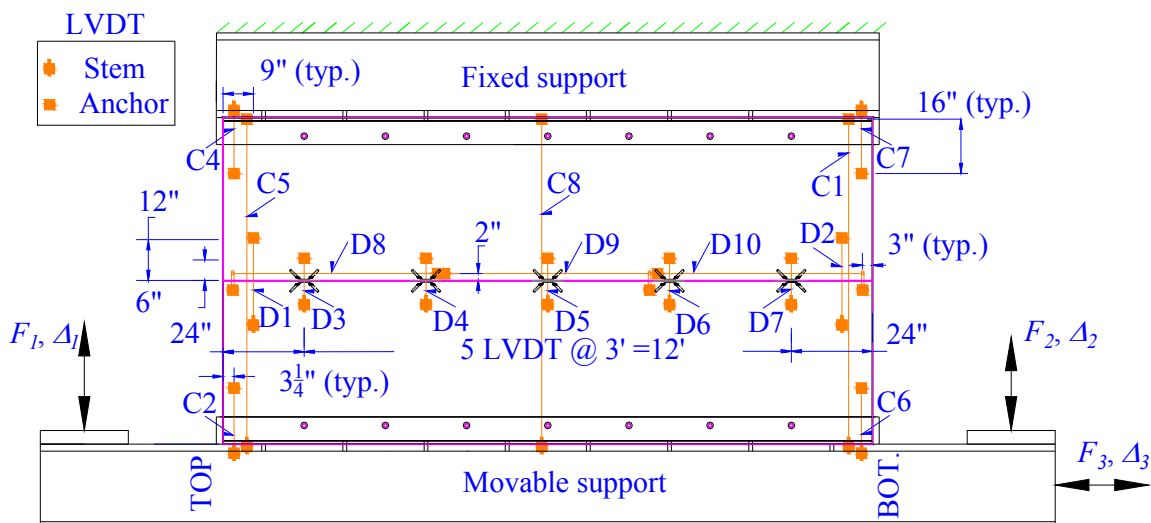
Fig. B3-14: Instrumentation layout.

Seventeen relative displacements are measured on the specimen (Figure B3-14) by LVDTs: Joint opening displacement across each connector (D1-D7); sliding displacement along the joint at three equal gages of 2.5′ (D8-D10); total panel deformation between supports at chord (C5, C1) and panel centerline (C8); movement of the panel relative to the supports at each chord back end (C2, C4, C6, C7). Actuator displacements, Δ_1, Δ_2, and Δ_3 and restoring forces (F_1, F_2, F_3) are measured by internal LVDTs and external load cells, respectively.

Test Loading Protocol

Control Algorithm

The interface PDHs are applied to the specimen using the same time discretization as the NLTDA. Due to the test specimen high elastic stiffness, displacement commands associated with low force levels are of the same order of magnitude as play in the actuator clevise. For this reason, actuator displacement commands (Δ_1, Δ_2, Δ_3) were controlled through a multiple loop architecture using external LVDTs C5, C1 and D9. Each outer loop displacement step (one PDH step) is divided into smaller substeps (actuator command increment of 0.006″; changed to 0.002″ after PDH2) at approximately the actuator resolution (0.004″). In the inner loop, each substep is applied through actuator displacement control until displacement targets are achieved at C5, C1 and D9. The substeps are repeated, with actuators not achieving the target within a tolerance (originally 0.002″; changed to 0.003″ after PDH1) slightly extended or retracted, until the outer loop full step is achieved on all feedback channels.

Transformations of PDH

Force and displacement components are shown in Figure B3-15 for: (a) the FE model; (b) the test specimen; and, (c) at the joint. The FE model interface DOFs are transformed to LVDT test control DOFs using Eq. 6; likewise, the LVDT control DOFs are transformed into actuator command DOFs (Eq. 7) and calculated global displacements (Eq. 8).

$$C5 = PDH_{xt} = U_{x2} - U_{x1} \tag{Eq. 6a}$$

$$C1 = PDH_{xb} = U_{x4} - U_{x3} \tag{Eq. 6b}$$

$$D9 = PDH_{y} = U_{y6} - U_{y5} \tag{Eq. 6c}$$

$$\Delta_1 = C5 + \theta \cdot (c + d_1) \tag{Eq. 7a}$$

$$\Delta_2 = C1 - \theta \cdot (c + d_1) \tag{Eq. 7b}$$

$$\Delta_3 = D9 - \theta \cdot (b + e) \tag{Eq. 7c}$$

$$\theta = (C5 - C1)/d \tag{Eq. 8a}$$

$$\Delta_a = (C5 + C1)/2 \tag{Eq. 8b}$$

$$\Delta_v = D9 \tag{Eq. 8c}$$

(a) FE model;   (b) Test specimen;   (c) Deformed shape;   (d) FBD.
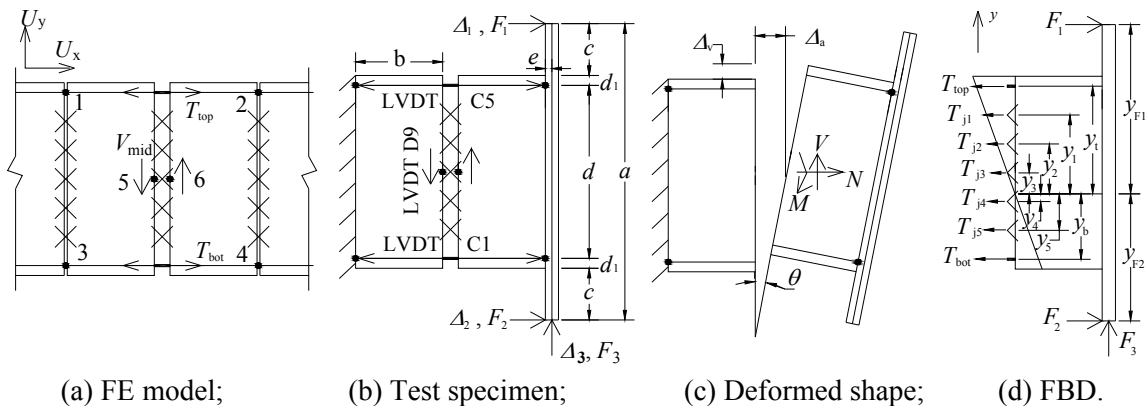
Fig. B3-15: PDH transformation.

Similarly, the actuator forces are transformed to panel forces (Eq. 9) and internal forces (Eq. 10 and Eq. 11), based on free body diagram (FBD) shown in Figure B3-15d.

$$M = (F_1 - F_2)(c + d_1 + d/2) - F_3(b + e) \qquad \text{(Eq. 9a)}$$

$$N = F_1 + F_2 \qquad \text{(Eq. 9b)}$$

$$V = F_3 \qquad \text{(Eq. 9c)}$$

$$T_{top} y_t + \sum_{i=1}^{5} T_{ji} y_i + T_{bot} y_b = \sum_{i=1}^{2} F_i y_{Fi} - F_3(b + e) \qquad \text{(Eq. 10a)}$$

$$T_{top} + \sum_{i=1}^{5} T_{ji} + T_{bot} = \sum_{i=1}^{2} F_i \qquad \text{(Eq. 10b)}$$

$$V_{mid} = F_3 \qquad \text{(Eq. 10c)}$$

$$T_{ji} = \alpha_{t,c} (y_i / y_{t,b}) T_{top,bot} \qquad \text{(Eq. 11)}$$

where α is the chord to shear connector stiffness ratio in tension (α_t=19.1) or compression (α_c=5.2) as determined from testing (Natio and Ren 2008).

PDH Test Input
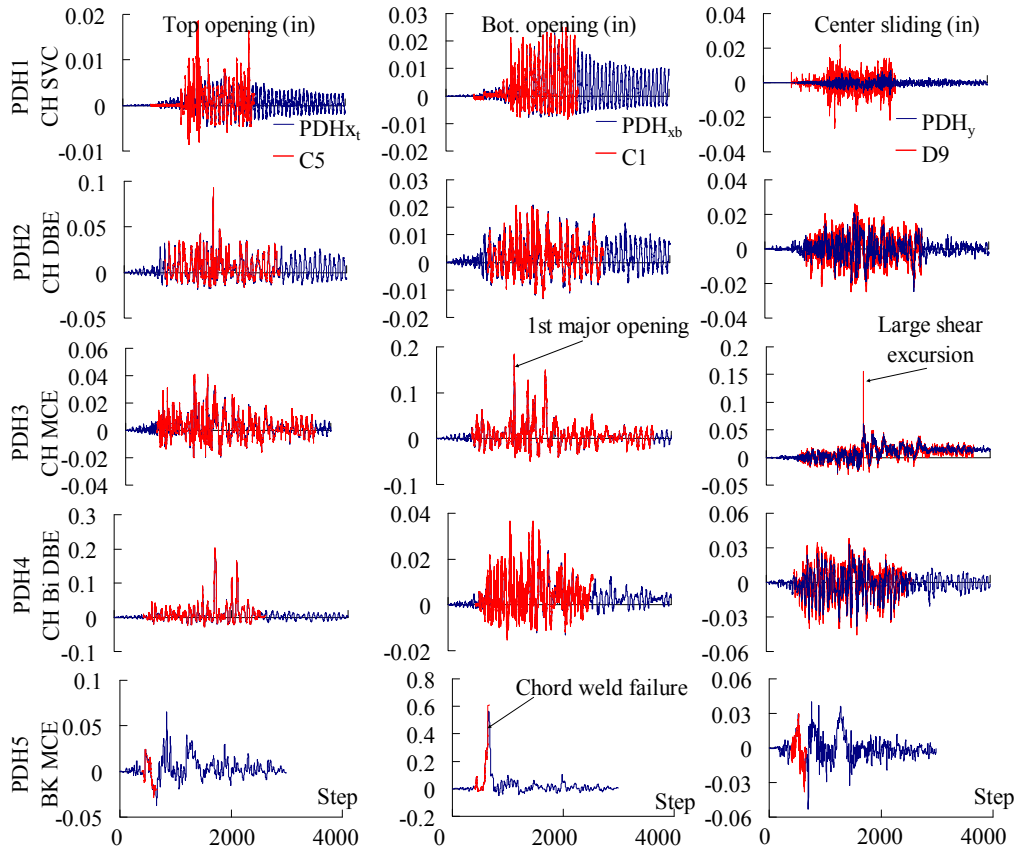
(a) Top opening;   (b) Bottom opening;   (c) Sliding.
Fig. B3-16: PDH and test control time history.

The PDH test is conducted as a quasi-static test with a displacement command speed of 0.001 in/sec. The actual test control histories (Eq. 6) are shown in Figure B3-16 superimposed on the analytically-

derived PDHs. Three differences are noted: (1) due to the time-intensive nature of the testing control convergence protocol, the test input data (red lines) is truncated to include only the major response regions of each earthquake motion; (2) control of sliding displacements in early tests was poor, resulting in signal error, and resolved as discussed in *Control Algorithm* (see Figure B3-16c); (3) during the Charleston MCE (roughly midpoint of testing), a large shear excursion occurred (Figure B3-16c, PDH3). Though unplanned, it permits the examination of the effect of shear degradation on flexural response.

PDH Test Prediction

The PDHs are derived from NLTDA which is performed individually for each ground motion loading with pristine model status. Further, the critical flexure joint used for the test reverses from north to south for each successive earthquake loading. So the determination of cumulative damage at each chord region over the entire test sequence is not possible using the structure model with NLTDA. Thus, the PDH test sequence itself is simulated using a static nonlinear FE model representing the test specimen and loading frame (Figure B3-15b) through a "restart" feature. This approach also creates reasonable file sizes and run times for the full sequence.

The predicted joint hysteretic response (Figure B3-15c) is shown in Figure B3-17. Nominal design strengths are indicated in Figure 4.17 as well. An *M-V-N* interaction expression used later is:

$$\sqrt{(\left|M/M_n\right| + N/N_n)^2 + (V/V_n)^2} \qquad\qquad \text{(Eq. 12)}$$

(a) Moment; (b) Axial; (c) Shear.
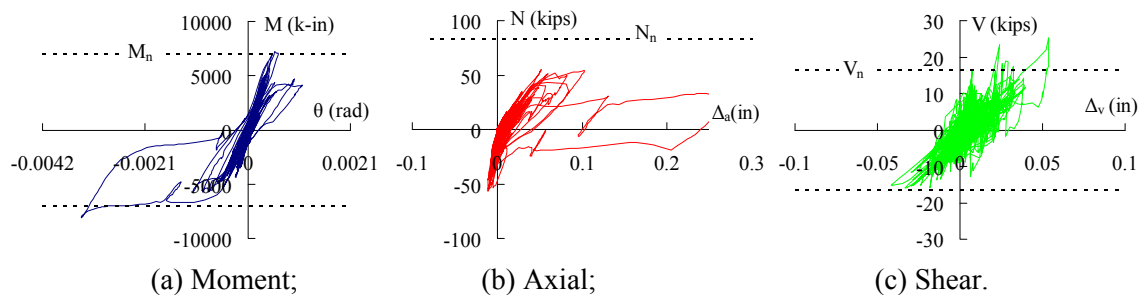
Fig. B3-17: Joint response from static analyses.

B3.1.4 Experimental Results

Experimental results are processed, interpreted and compared to analytical predictions in the following categories: (1) joint force response; (2) joint reinforcement response; (3) joint opening profile; and (4) stiffness degradation.

Joint Force Response

Figure B3-18 shows the measured force response histories (Eq. 9) and interaction expression (Eq. 12) compared to analytical predictions. The analytical predictions are seen to be reasonably accurate throughout. Figure B3-18d indicates elastic diaphragm response during CH SVC and inelastic response in succeeding earthquakes. The failure event, weld fracture on the chord, is noted as the abrupt termination of the test curve at a large combined force event during the BK MCE. As discussed in section B3.1.1, the diaphragm of PDH structure is designed for Charleston site with new design methodology and is equivalent to the current diaphragm design for Berkeley site. As seen in Figure B3-18, the specimen successfully survives the CH MCE but fails in the BK MCE which implies that the diaphragm under proposed design will survive the MCE level earthquake while the diaphragm under current design cannot.

(a) Axial;   (b) Shear;   (c) Moment;   (d) M-N-V.
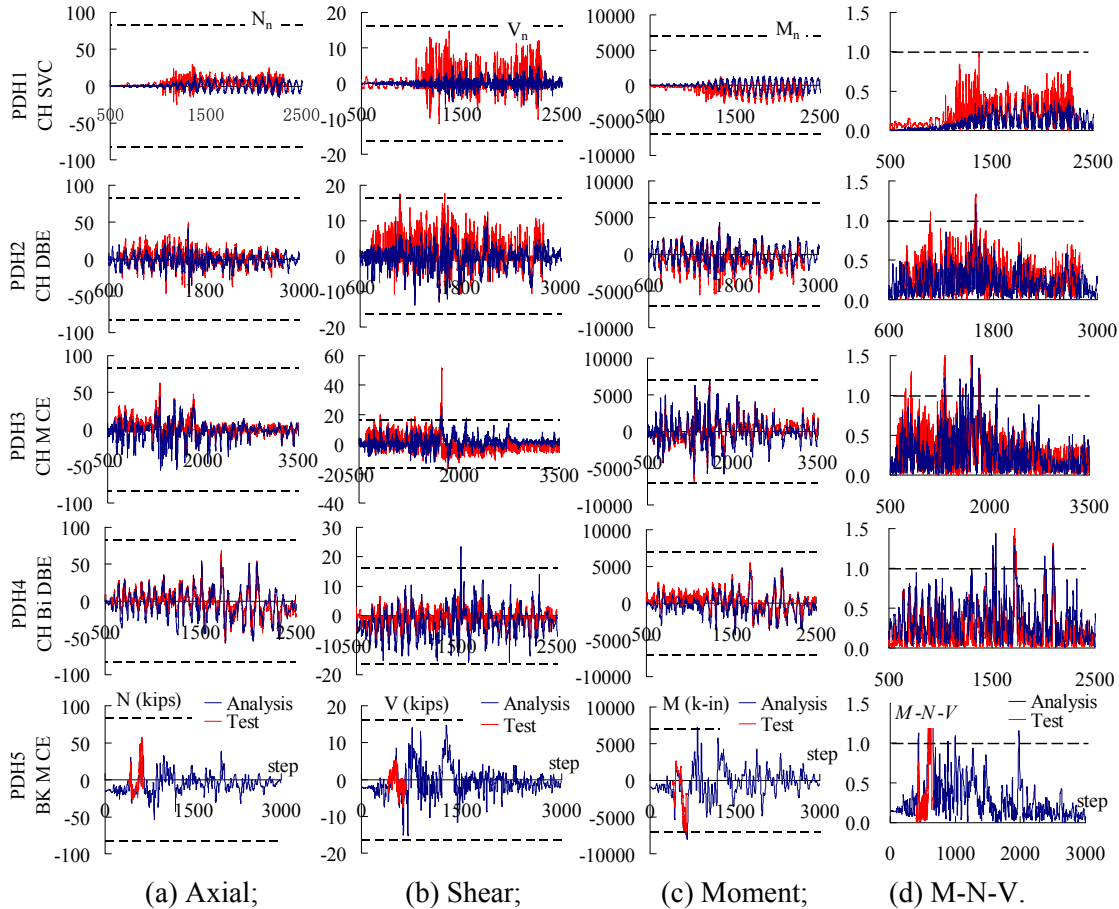
Fig. B3-18: Joint force history responses.

(a) PDH2;   (b) PDH4.
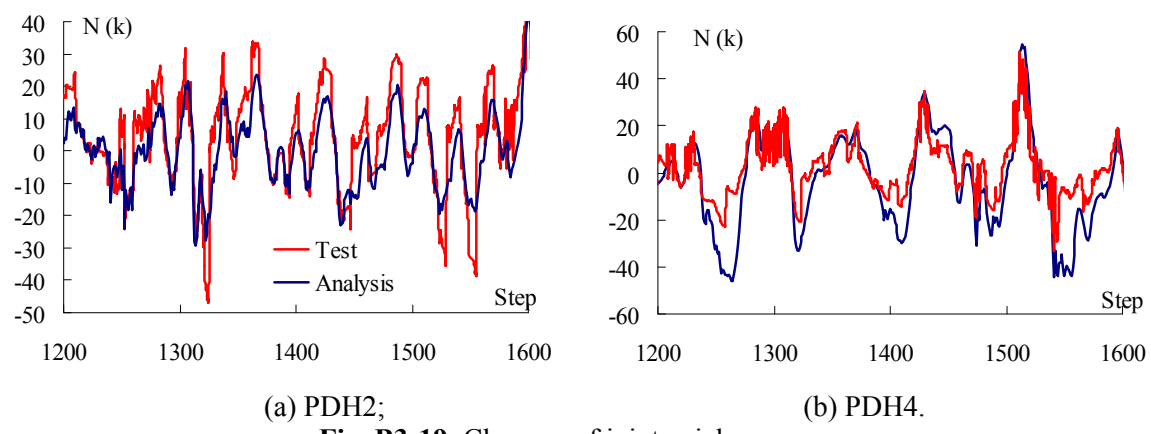
Fig. B3-19: Close up of joint axial response.

A close-up of data from Figure B3-18a indicates that the FE model underestimates axial forces in early tests Figure B3-19a but overestimates peak compression forces in later tests Figure B3-19b. Thus, the actual test specimen possesses higher initial stiffness and more concrete crushing degradation than the analytical model.

(a) SVC; (b) CH DBE; (c) CH MCE;

(d) Bi-directional DBE; (e) BK MCE;

Fig. B3-20: Moment vs. joint rotation response.

(a) Top photo; (b) Top response; (c) Bottom response; (d) Bottom photo.
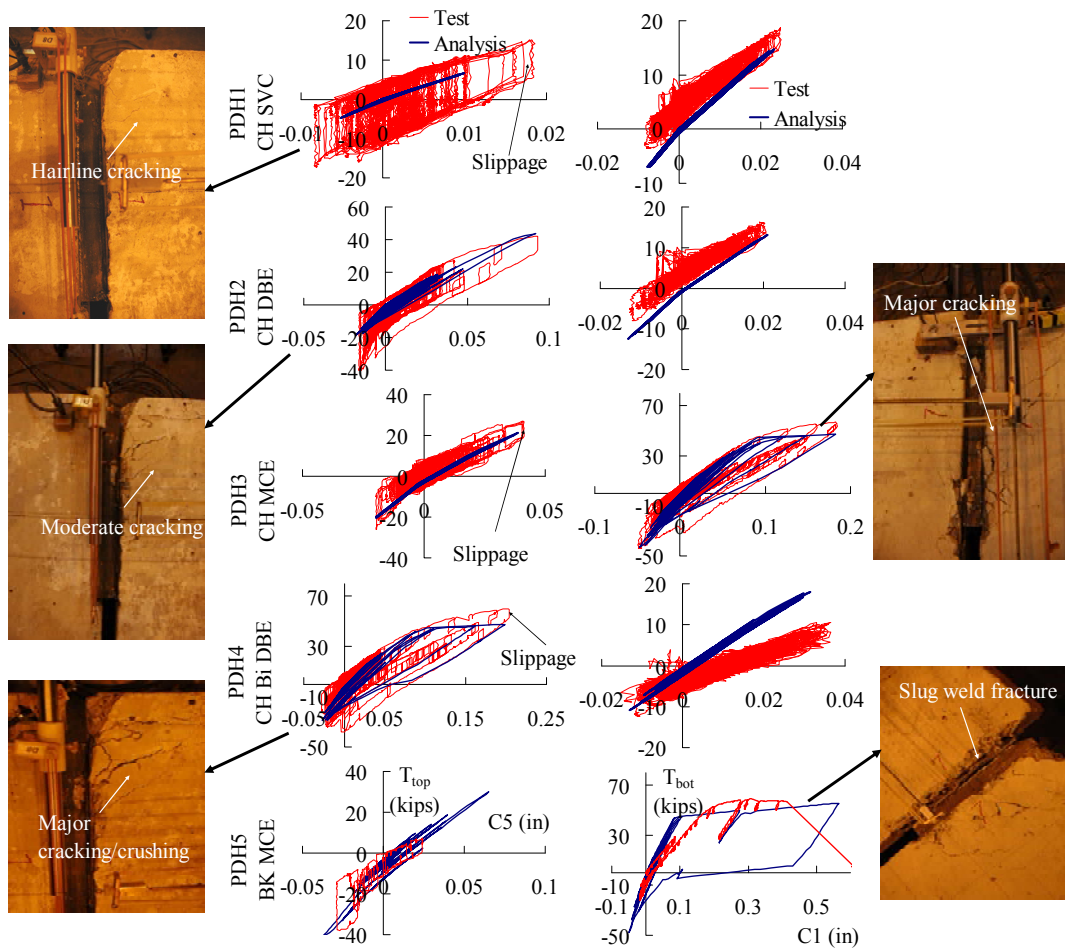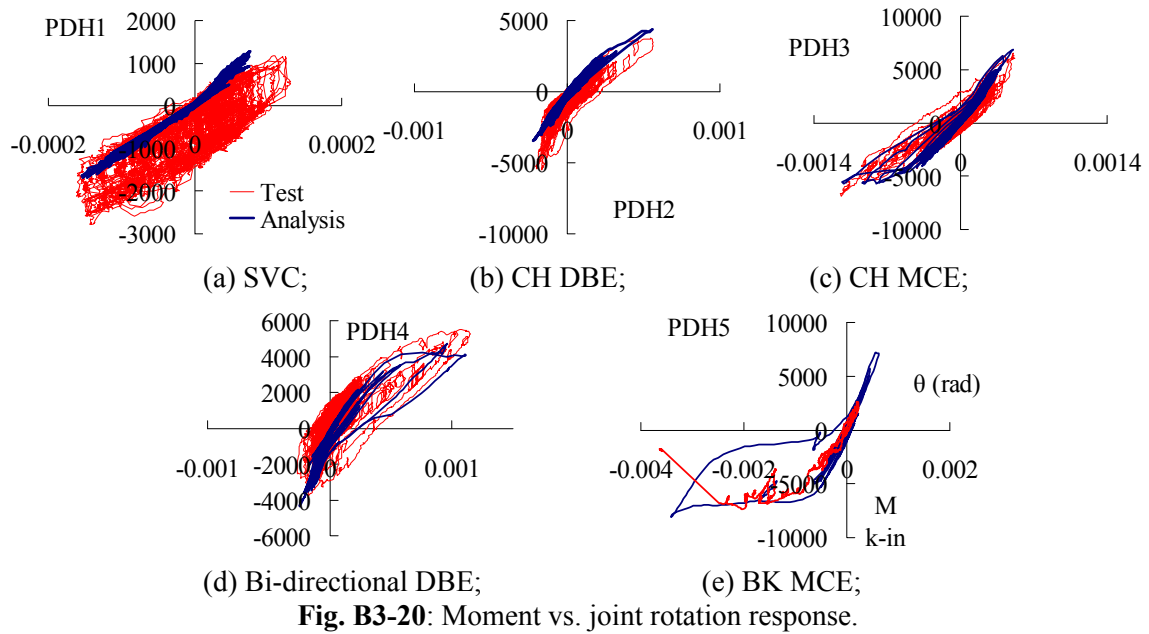
Fig. B3-21: Chord connection responses.

C-A-159

The joint moment-rotation response is shown in Figure B3-20. The analytical model shows excellent agreement except that the model underestimates the energy dissipation in early test due to the slippage of actuator clevise system. It is noted that the slight difference in axial force exhibited in Figure B3-19 has an impact on moment prediction in the presence of non-negligible axial force (Figure B3-20b): underestimated compression force leads to an underestimated moment; underestimated tension force to overestimated moment. Figure B3-20e indicates a maximum rotation capacity for the joint of approximately 0.0025 rad.

Joint Reinforcement Response
Chord Connector
The chord connector hysteretic response (Eq. 10 vs. Eq. 6) is shown in Figure B3-21 and compared to the analytical predictions. The progression of damage in the chords is as follows (Figure B3-21a and Figure B3-21d): (1) hairline cracks appear in the chord region during the essentially elastic response to the SVC earthquake; (2) the top chord forms moderate cracks in the DBE earthquake, where chord strength is reached but no large inelastic deformation demand is incurred; (3) major cracking is evidenced in the bottom chord in the MCE where the chord incurs significant inelastic opening deformation; (4) major cracking/crushing is exhibited in the top chord for the Bi-Dir DBE, in which inelastic opening occurs in combination with significant compression cycles; and, finally, (5) fracture of the slug of the bottom chord connector at a maximum deformation capacity of 0.4″.

The analytical results show good agreement with the chord response. However the following observed discrepancies are identified. First, the analytical results show lower energy dissipation than the test results shows especially during the early test because the slippage of actuator clevise system makes the hysteresis response of test "squaring". The influence of system slippage is obvious in the early test (Figure B3-21b PDH1) but is trivial in the later test with large inelastic opening (Figure B3-21b PDH4). The other difference is that the analytical predictions fail to capture the stiffness degradation after large inelastic opening in the test (Figure B3-21c PDH4). This is because the analysis prediction uses the spring model with pinching hysteretic behavior (refer to Appendix B2) for chord connector without stiffness degrading capability. The enhanced chord model with combined stiffness degradation and pinching hysteretic behavior (refer to Appendix B2) is developed based on the stiffness degrading observed in the test. The stiffness degradation prediction of the enhanced chord model in the test sequence is shown as dashed-line in Figure B4-25a. The last difference is that the test results have more strain hardening ratio than the analytical predictions have.

JVI Vector
The hysteretic response, damage development and axial-shear interaction response for JVI Vector j5 near the bottom chord (Figure B3-15d) is shown in Figure B3-22. Cracking begins during the DBE; the surrounding concrete starts spalling during the MCE after 0.15″ shear displacement. The connector fractures under tension with significant shear during the BK MCE at approximately 0.35″ opening.

The analytical results generally show good agreement with the JVI Vector response. However, several differences between the test and analytical model are seen in the Figure B3-22: (1) the sliding loading in PDH1 is much higher in the test than the model due to the poor loading control described in *PDH test input* of section B3.1.3; (2) The shear stiffness of test after unplanned overloading in PDH3 is lower than the model prediction due to the analytical model does not subject to unplanned shear overloading. (3) The strain hardening in tension is higher in the test than the analytical prediction.

(a) Axial;　　　(b) Shear;　　　(c) *N-V*;　　　(d) Photo.
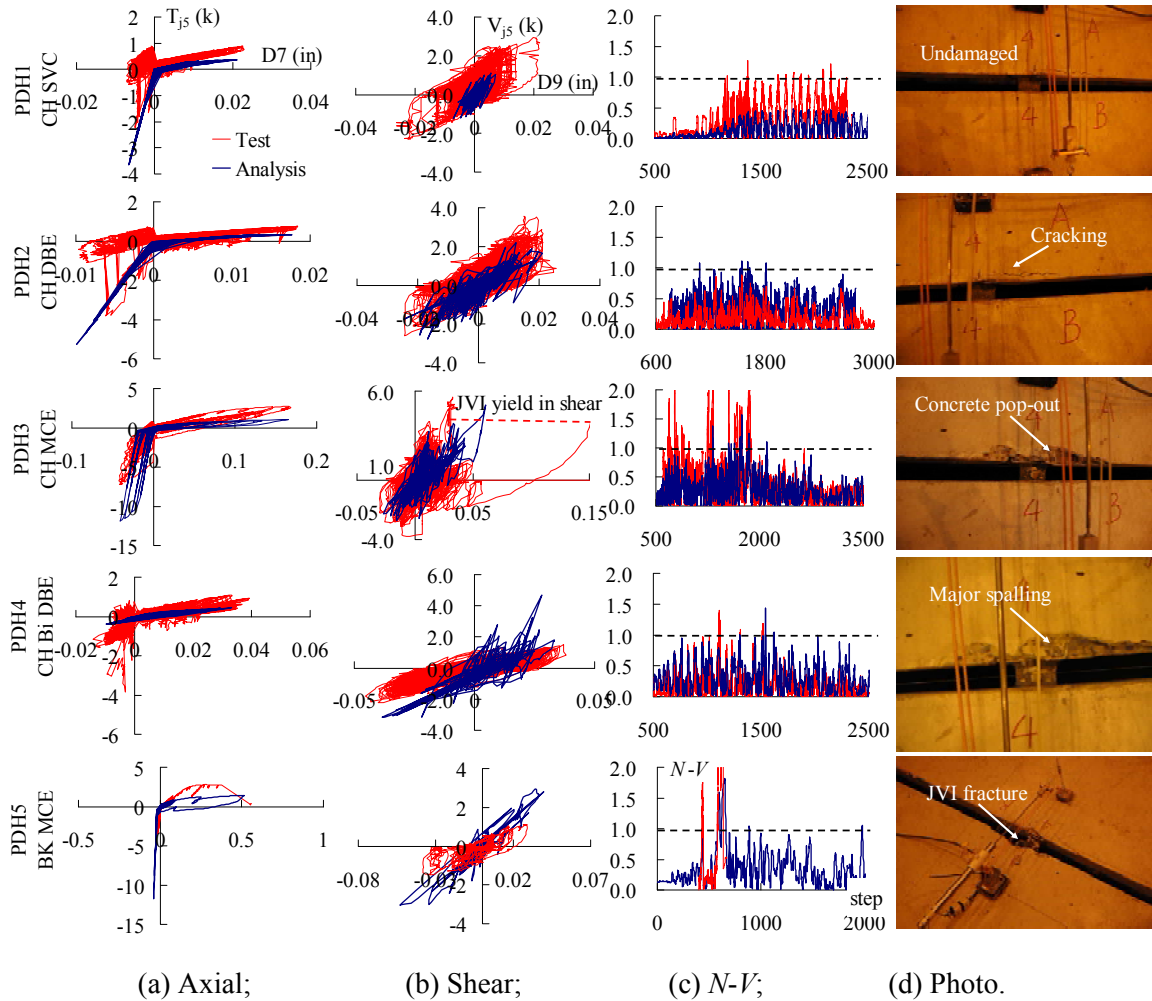
Fig. B3-22: JVI Vector responses.

Joint Opening Profile
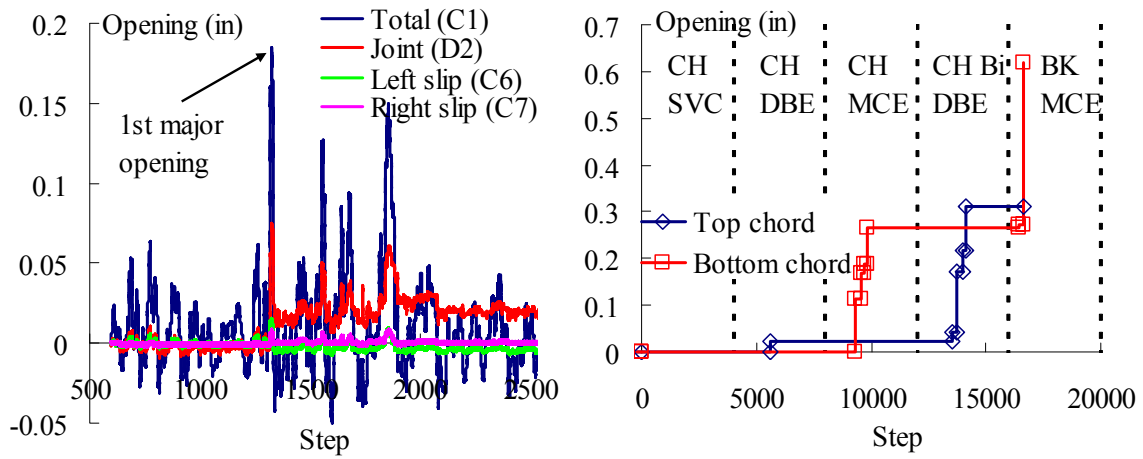
(a) Distribution for CH MCE;　　　(b) Plastic cumulative.

Fig. B3-23: Chord opening response.

C-A-161

Figure B3-23a shows the distribution of panel opening at the chord along the total width of the specimen during the CH MCE. The response shown on either side of the first major opening excursion (indicated) is typical for response prior to and following that point during the entire sequence. First, note that the slip on the back-end on the specimen is negligible. Prior to the excursion, the experimental substructure opening is accommodated almost entirely within the panel (strain penetration due to panel cracking) as inferred by the difference between C1 and the sum of D2, C6, C7. Following the excursion, opening does concentrate at the joint but the panel contribution is still significant. Finally, the joint does not close at the chord following the major opening excursion. Figure B3-23b shows the cumulative chord opening through the test sequence.

Figure B3-24 shows the profile along the specimen (at maximum opening) for: (a) total opening across the panels; and (b) joint opening. Note that while plane sections are enforced for the total opening, the joint itself forms a bowed shape. This distribution occurs because the deformation demand at the chord is distributed (via cracking) along the entire panel width, while the inherent tension flexibility of JVI Vector allows relaxation of the concrete panels (Figure B3-24c).
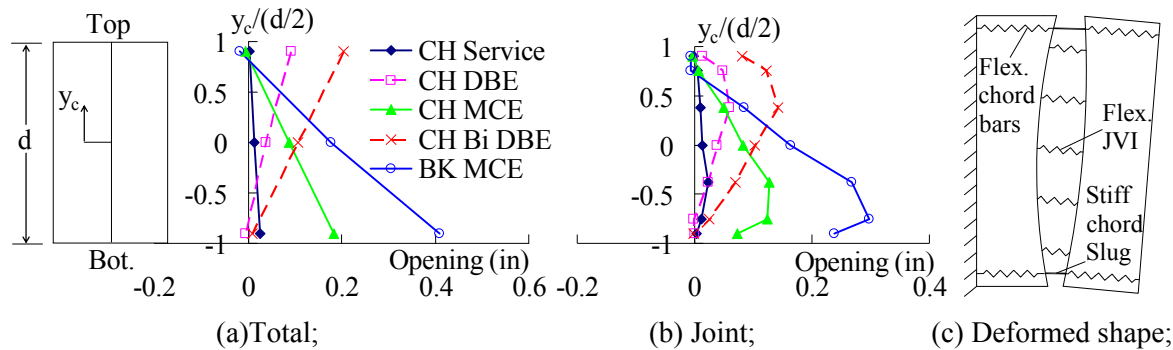
Fig. B3-24: Opening profile at maximum demand.

Stiffness Degradation
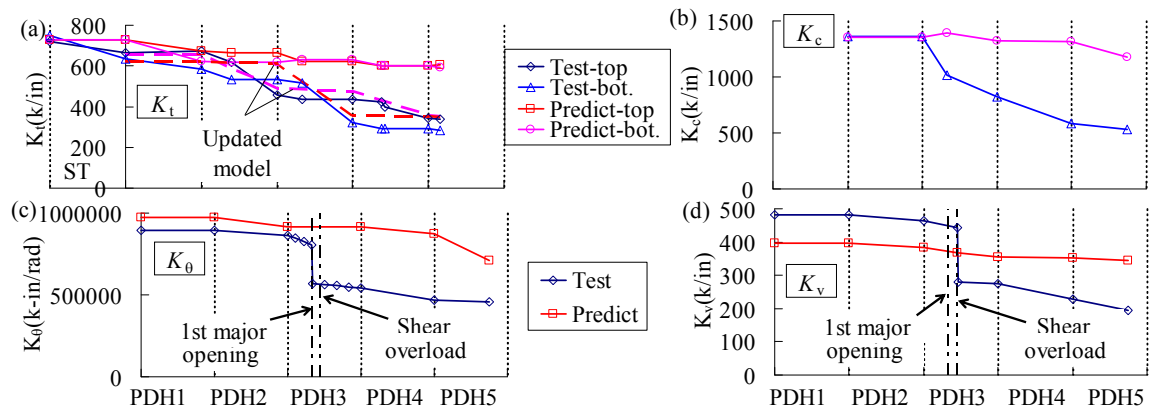
Fig. B3-25: Stiffness: (a) chord tension; (b) compression; (c) rotation; (d) shear.

Stiffness degradation through the test sequence is shown in Figure B3-25 including: (a) chord tension (K_t); (b) chord compression (K_c); (c) rotation (K_θ) and (d) shear (K_v). As seen, the tension, compression and rotation stiffness degrades as the specimen accumulates damage. The model does a reasonable job of predicting diaphragm joint stiffness but: (1) does not degrade sufficiently due to a lack of adequate stiffness degradation model for the chord connector in the original model (the prediction for the enhanced stiffness degradation model (refer to Appendix B2), indicated by the dashed-line in Figure B3-25a, exhibits good agreement with the test chord stiffness degradation results); and (2) underestimates

the shear stiffness because a conservative model is used for shear connector by ignoring the stiff initial shear response prior to "popping out" of surrounding concrete. A close-up of K_θ near the shear overload excursion indicates that the major chord tension stiffness reduction is due to the first major opening excursion (Fig. B3-25c), while the shear overload event only affects the shear stiffness (Fig. B3-25d).

Figure B3-26 shows the effect of axial forces on specimen shear stiffness, indicating significantly higher values under axial compression and slightly lower values under axial tension.
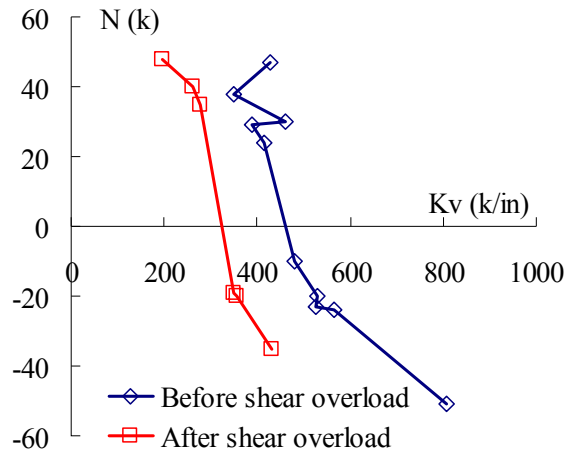
Fig. B3-26: Shear stiffness under axial force.

B3.1.5 Conclusions from PDH Test

The critical flexure joint in a pretopped concrete diaphragm was tested at half-scale under displacement histories from NLDTA. The following conclusions are made:

(1) Using the design methodology proposed by DSDM research group, the critical flexural joint survived its designated MCE earthquake. Under current design, the joint will likely fail during its designated MCE earthquake.

(2) The test demonstrates that the unbonded dry chord connector exhibited good inelastic tensile deformation capacity corresponding to a joint rotation of 0.0025 rad (0.4″ opening in half-scale). It is noted however, that this same connector exhibited brittle failure during a shake table test (Schoettler et al. 2009). This event indicates the importance of construction tolerance and sensitivity of this connector to misalignment, as well as the potential for fracture under high strain rate.

(3) The JVI Vector connector exhibited good inelastic tension compliance, achieving 0.35″ opening (half-scale) before pulling out from the surrounding concrete.

(4) The joint rotational stiffness degrades to approximately half its original values at flexure critical joint under expected earthquake loading.

(5) The 3D NLTDA model shows good agreement with the joint flexure response, including reasonable predictions of local responses. However the stiffness degradation under cyclic tension for the chord connector observed in the testing was not captured by the chord connector model used in the PDH analytical prediction (see Fig. B3-25a). Based on this test finding, the cyclic stiffness degradation model for the chord reinforcement introduced in Sec. B2. 3 was developed.

B3.2 HYBRID TESTING OF DIAPHRAGM CRITICAL SHEAR JOINT

In this testing program. analysis-driven integrated physical testing is used to examine the seismic performance of a critical shear joint in a pretopped precast concrete diaphragm. In this case, hybrid (adaptive) testing techniques are used to simulate the anticipated seismic demands on the diaphragm critical shear joint. The experiment is conducted at half-scale. The simulation structure is a three-story precast concrete shear wall building structure with a single diaphragm bay. The experimental (physical) substructure consists of the floor units surrounding the shear critical joint (similar in dimension to the PDH test specimen described in Sec. B3.1). The analytical superstructure is the entire structure, less the portion which is physically modeled by the experimental substructure. The test uses nonlinear transient dynamic analyses (NLTDA), i.e., earthquake simulation of the simulation structure, to drive the test. The analytical superstructure is modeled by a reduced degree-of-freedom (RDOF) model. The RDOF model is used instead of the three-dimensional discrete diaphragm (3D NLTDA) model described in *Section B3.1* due to time and computer memory limitations of the MATLAB program used for hybrid algorithm (See Sec. B3.2.2). The reduced MDOF was validated using the 3D NLTDA model as discussed in Sec. B3.2.2.

The objectives of the hybrid testing program are to:

(1) Examine the shear strength and stiffness of a pretopped precast concrete diaphragm joint under progressive cyclic damage.

(2) Examine the inelastic shear deformation capacity of a pretopped precast concrete diaphragm joint under progressive cyclic damage. For this purpose, the shear critical joint is intentionally designed with smaller shear overstrength than prescribed in the design methodology, thereby allowing inelastic shear response to occur at the joint.

(3) Examine the combined behavior of individual reinforcing elements acting together in a joint under force combinations of internal shear, axial and flexure.

(4) Verify or further calibrate the 3D NLTDA models and the diaphragm connector elements developed on the basis of tests of isolated diaphragm reinforcing details.

(5) Predict the critical shear joint performance of a shake table test specimen of identical detail in a parallel thrust of the research (See B4).

The sections that follow describe: (1) the simulation structure; (2) the RDOF model; (3) the hybrid testing procedure; (4) the experimental program; (5) experimental results; and, (6) conclusions.

B3.2.1 Simulation Structure

The structure being modeled in the hybrid experiment, termed the simulation structure, is a three story precast building matching the prototype for a shake table test structure from a parallel thrust in the research (Schoettler et al. 2009). In comparison to the shake table test prototype structure (refer to Appendix B4), the following differences are noted in the hybrid simulation structure: (1) all three floors in the simulation structure are pretopped construction while the shake table test structure had different construction at each floor; (2) the shear wall in the simulation structure was originally designed as a RC wall, however when an unbonded post-tensioned wall was selected for the shake table test structure for repeatability purposes, the hysteresis response was modified to that typical of a rocking wall; and, (3) the critical shear joint in the simulation structure is purposely given a lower shear strength than required in the design methodology (and provided in the shake table test structure) in order to study failure modes.

As shown in Figure B3-27, the simulation structure has a 112′ x 32′ footprint. The precast double tee (DT) units are 8′ wide and 32′ deep. The lateral force resisting system (LFRS) is 16′ x 1′ reinforced concrete (RC) shear walls oriented in the transverse direction at each end of the structure. The simulation structure is assumed to be stable in the longitudinal direction. The floor to floor height is 13′.

Diaphragm reinforcement is adopted as follows: (1) an unbonded dry chord connector is used for diaphragm flexure reinforcement. The unbonded dry chord connector (see Table 2A-3 in PART 2 for the detail drawing) provides both a longer gage length for inelastic deformation capacity, and mitigates a potential complex stress state due to shear by eliminating dowel action. This detail is used in the high flexure regions of the diaphragm (Refer to Fig. B3-27a), and contributes to the diaphragm flexural design strength but not to the diaphragm shear strength; (2) a bonded dry chord connector is used for the flexure

reinforcement in high shear regions. The bonded dry chord connector (see Table 2A-3 in PART 2 for the detail drawing) provides dowel action that contributes to the shear transfer and is accounted in the diaphragm shear design. As seen in Fig. B3-27a, the transition between the bonded and unbonded chord detail is gradual, with an intermediate region between the high flexure and high shear regions in which the chord detail is half unbonded and half bonded dry chord connectors; (3) the JVI Vector connector, a popular flange-to-flange connector (see Table 2A-3 in PART 2 for detail drawing), is used for the diaphragm shear reinforcement; (4) an angled bar-plate connector (See Fig. B1-1 for detail drawing) is used for secondary connections in the floor system, including the connectors between the spandrels/L-beams and the precast floor units; (5) the connection between LFRS and diaphragm is assumed to be rigid and possess sufficient strength.
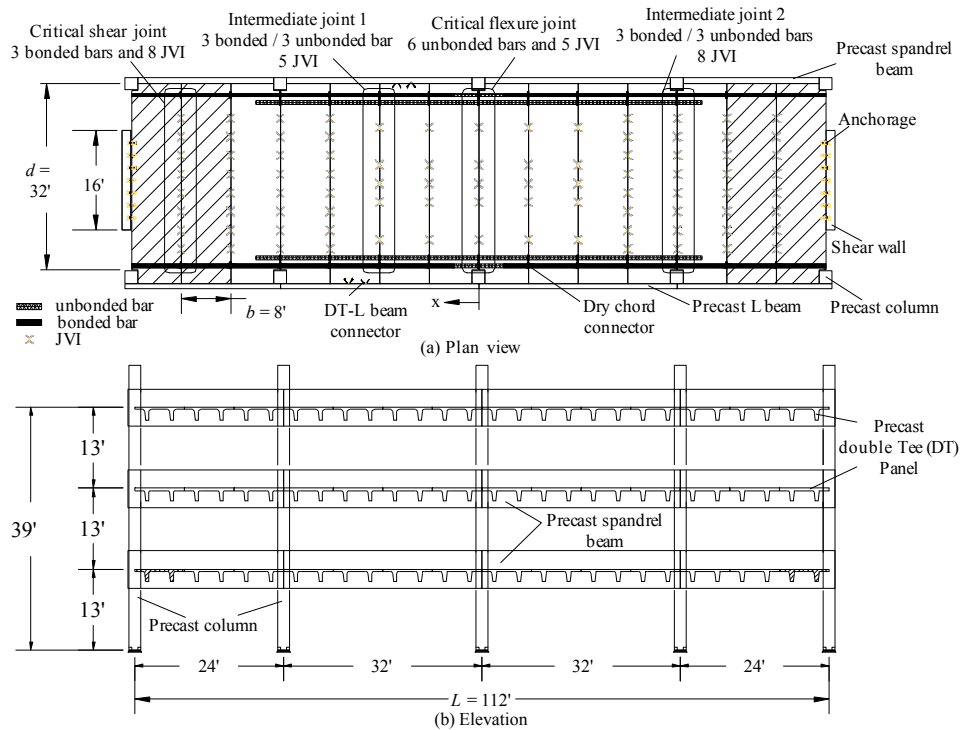
Fig. B3-27: Simulation structure for hybrid test.

Hybrid Simulation Structure LFRS Design

The seismic design of LFRS in the simulation structure was based on the current code (IBC 2003) at the time of the test. The structure is designed for a SDC E site, Berkeley CA (S_s= 2.08, S_1= 1.92) for soil class C. The seismic resistant LFRS is special RC shear walls (R= 6, Ω_o= 2.5 C_d = 5). The Equivalent Lateral Force (ELF) procedure values (for design parameters C_s = 0.231, T = 0.44 sec) appear in Table B3-8. The simulation structure design provided below is for a full-scale structure. Note however that the hybrid test and shake table test are performed at half-scale. Thus, all aspects of the hybrid testing, including the physical test specimen, analytical superstructure and experimental substructure, and the stand-alone dynamic analyses that are used for comparisons are presented in half-scale (See Sec. B3.2.2).

The design forces tributary to each shear wall is shown in Table B3-9. Only the base cross-section detail is considered since shear wall inelastic action is assumed to be limited to this region. Figure B3-28a shows the detail at base: (1) chord reinforcing bars in boundary elements; and, (2) web reinforcement at maximum allowable spacing. These reinforcement groups combine to produce the required flexural capacity as per ACI 318 (2005).

Table B3-8: LFRS design for simulation structure.

Floor	h_x	w_x	$w_x h_x^{\ k}$	c_{vx}	F_x	Story Shear	Moment
	ft	kips			kips	kips	k-ft
3	39	538	20982	0.50	187	0	0
2	26	538	13988	0.33	124	187	2425
1	13	538	6994	0.17	62	311	6466
Sum:		1614	41964	1.00	373	373	11315

Figure B3-28b shows the moment-curvature response at the shear wall base which is used for develop the shear base hinge model: the solid line is produced from fiber model analysis using section analysis software XTRACT[13] with a bilinear steel model (1.5 strain hardening ratio) and Mander model for concrete; the dotted line is the backbone bilinear curve used in the 3D NLTDA model.
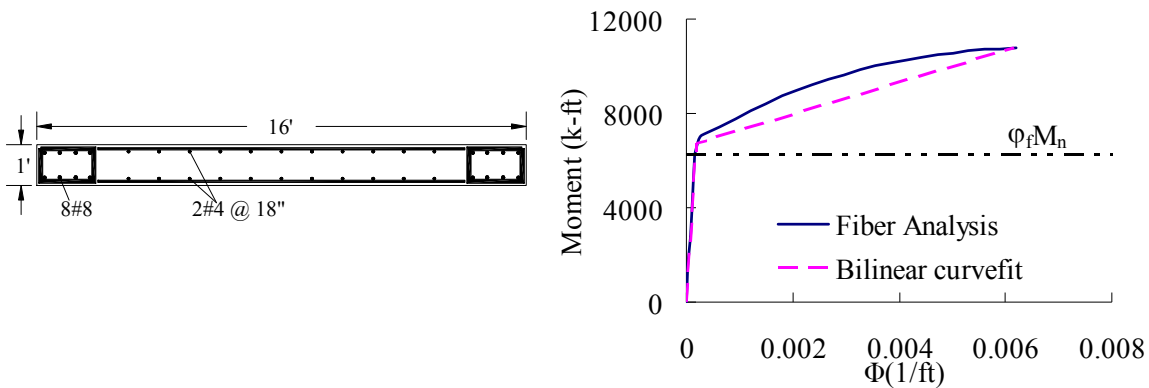
(a) Wall Base Detailing;   (b) Moment-curvature response.
Fig. B3-28: Simulation Structure Shear wall.

Table B3-9: Shear wall design for simulation structure.

Shear wall Design	Base Shear (kips)	Moment (k-ft)	Chord bars	Web Reinforcing	$\phi_f M_n$ (k-ft)
RC wall	187	5657	8 # 8	2 # 4 @ 18"	6257

Simulation Structure Diaphragm Design

The simulation structure diaphragm design uses the same concepts as the proposed design methodology. A constant diaphragm design force profile assigned the current maximum diaphragm force, 187k (from Table B3-8) is used in accordance with the emerging design methodology. The reduced design option (RDO) is adopted for designing the diaphragms in the simulation structure (See Sec. 5.4 in PART 5). According to the RDO, a diaphragm force amplification factor Ψ_R is applied to the diaphragm design force. The value of Ψ_R is assigned as 1.5 based on the NLTDA analyses used for preliminary designs of the the shake table test specimen. As it turned out, the final design of the shake table test specimen used $\Psi_R = 1.38$ as the shake table structure possess more weight than the simulation structure (refer to B4.2.2) and the current design procedure in PART 1 would produce a $\Psi_R = 1.35$.

Key diaphragm joints requiring design are shown in Figure B3-27a. These joints include: (1) the critical flexure joint at midspan; (2) the critical shear joints at the diaphragm ends (the end diaphragm

---

[13] XTRACT Imbsen commercial software, Inc. Rancho Cordova, CA.

joint is one panel in from the shear wall at the floor perimeter); (3) intermediate joints, at locations 1 and 2 as indicated in the figure.

The design forces at these joints are given in Table B3-10. Diaphragm design moment and shear are determined using a simply-supported beam model, i.e. the horizontal beam method (PCI Design Handbook 2004) under uniform distributed force (Eq. 13 and Eq. 14).

$$M_u(x) = \Psi_R \left\{ (F_{px})(L/2 - x)/2 - (F_{px})(L/2 - x)^2 / 2L \right\} \qquad \text{(Eq. 13)}$$

$$V_u(x) = \Psi_R F_{px} x / L \qquad \text{(Eq. 14)}$$

It is noted that the horizontal beam method is viable for the simple simulation structure; detailed free body methods are proposed for more complicated floor plans (See Sec 3.2 in PART 3).

Table B3-10: Diaphragm design force for simulation structure.

Location	x ft	V_u kips	Eq.	M_u k-ft	Eq.
Critical flexure joint (CF)	0	0	4.14	3917	4.13
Intermediate joint 1 (IM1)	16	40	4.14	3597	4.13
Intermediate joint 2 (IM2)	32	80	4.14	2638	4.13
Critical shear joint (CS)	48	120	4.14	1039	4.13

Table B3-11 provides the diaphragm shear design. Shear strengths for the bonded chord and JVI Vector connector are provided by the testing indicated in the table notes. A smaller shear overstrength factor (Ω_v =1.13) is assigned to the simulation structure than required for the RDO in the design procedure (Ω_{vR} =1.53 for this diaphragm geometry). It should also be noted that the shake table test was designed using a calibrated value for the RDO diaphragm design of shake table test of 1.38. A smaller shear overstrength factor than required in the design methodology is intentionally used in the simulation structure to place the shear response of test joint into the inelastic region, which allows the study of the post-yield behavior of the critical shear joint. This design translates into about half the bonded chord reinforcement at diaphragm end in the simulation structure as in the shake table test structure.

Table B3-11: Diaphragm shear design for the simulation structure.

Joint	V_u kips	Shear connector $v_n{}^1$ kips	#	$V_{n,con}$ kips	Bonded chord $v_n{}^2$ kips	# of bars	$V_{n,ch}$ kips	V_n kips	Ω_v V_u/V_n
CF	0	13	5	65	5.4	0	0	65	-
IM1	40	13	5	65	5.4	6	32	97	2.44
IM2	80	13	8	104	5.4	6	32	136	1.71
CS	120	13	8	104	5.4	6	32	136	1.13

[1] JVI Vector shear strength from (Naito et al. 2007).
[2] Bonded dry chord shear strength from (Naito et al. 2006).

Table B3-12 provides the diaphragm flexure design. The flexural strength includes the tension contribution of shear reinforcement as per ACI 318 (2005) and is calculated using the analytically-based procedure (Wan 2007) contained in Sec. 3.3 PART 3.

Table B3-12: Diaphragm flexure design for the simulation structure.

| Joint | M_u | Shear connector | | | Chord #6 | | | $\varphi_f\, M_n$ |
| | | t_n [1] | # of | $M_{n,\ conn}$ [2] | t_n [3] | # of | $M_{n,\ ch}$ [2] | |
	k-ft	kips	conn.	k-ft	kips	bars	k-ft	k-ft
CF	3917	3.1	5	276	26.4	6	4409	4217
IM1	3597	3.1	5	276	26.4	6	4409	4217
IM2	2638	3.1	8	349	26.4	6	4405	4278
CS	1039	3.1	8	215	26.4	3	2254	2222

[1] JVI Vector tension strength and stiffness from (Naito et al. 2007)
[2] Flexure strength from analytical-based procedure (Wan 2007)
[3] Dry chord tension strength, t_n,chord $= A_s f_y$

Connectors between main precast units and gravity beams (see Figure B3-27a) are selected as two #3 angled bar-plate connectors per panel.

Shear Transfer Mechanism

It will be useful to briefly describe the shear transfer mechanism across the critical shear joint (see Figure B3-29). The shear transfer can be divided into primary and secondary shear transfer mechanisms. The primary shear transfer mechanism is provided by elements that are explicitly part of the diaphragm shear design, in this case: (1) the shear reinforcement (V_{sh}) provided by the JVI Vector connector; the dowel action of the bonded dry chord (V_{chd}), included in the diaphragm design as was shown in Table B3-11. The secondary shear transfer is provided through mechanisms and elements not explicitly included in the design, but nevertheless present in the floor system: the friction that develops in joint compression zone (V_f), and the transverse restraint provided across the joint by the spandrel beam (V_{sp}). The former is due to the confining effects of the transverse walls and the presence of a small diaphragm moment at the location of the first joint. The latter is limited by the strength and stiffness of the spandrel to double-tee (SP-DT) connections, as described in Wan et al (2012).
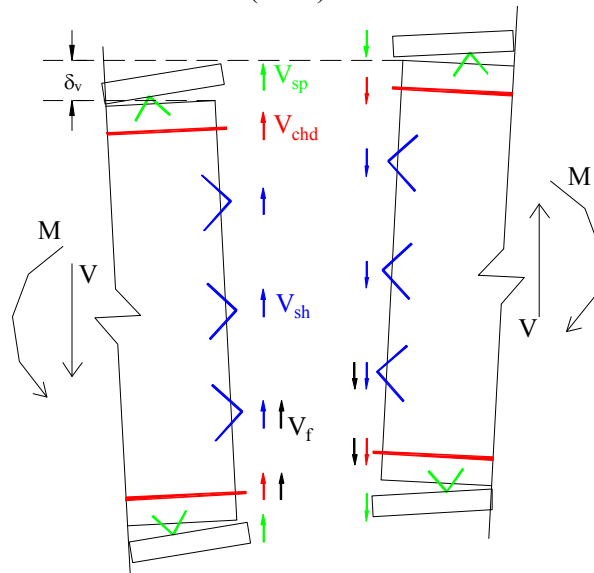
Fig. B3-29: Shear transfer mechanism across critical shear joint.

B3.2.2 Modeling of Simulation Structure

The primary analytical model used in the DSDM research is a 3D NLTDA model. The 3D NLTDA (symmetry) model of the simulation structure is shown in Figure B3-30a. The full 3D NLTDA model

cannot be used directly in the hybrid testing because of the matrix size limitations in the Matlab program used to perform the hybrid algorithm. The 3D NLTDA simulation structure symmetry model shown possesses approximately 6500 degrees-of-freedom (DOF), resulting in a 6500 x 6500 matrix requirement for the hybrid algorithm, which produces an "out of memory" error in Matlab. The simulation structure model used in the hybrid testing, therefore, was a simplified version of the 3D NLTDA model termed a reduced degree-of-freedom (RDOF) model (See Figure B3-30b). Note that both the 3D NLDTA and RDOF models are half-symmetry models of the full simulation structure, and are created with the general purpose finite element program ANSYS[14].

The process of inverting a large matrix in Matlab is highly time-consuming, even for DOF numbers within the Matlab size limitations of a 12450x12450 matrix. Thus, in order to keep the hybrid test duration (involving 2900 time steps) within a reasonable time, the simulation structure model DOFs were minimized. A reduction in DOFs from the 3D NLTDA model is possible here because the focus of nonlinear behavior occurs at one location (the critical shear joint on one floor), and a properly characterized simpler model can approximate global demands reasonably. In order to determine the minimum number of DOFs for an acceptable model, a sensitivity study was performed between the RDOF model and the 3D NLDTA model. The sensitivity study produced a RDOF model consisting of 134 DOF for the hybrid testing.
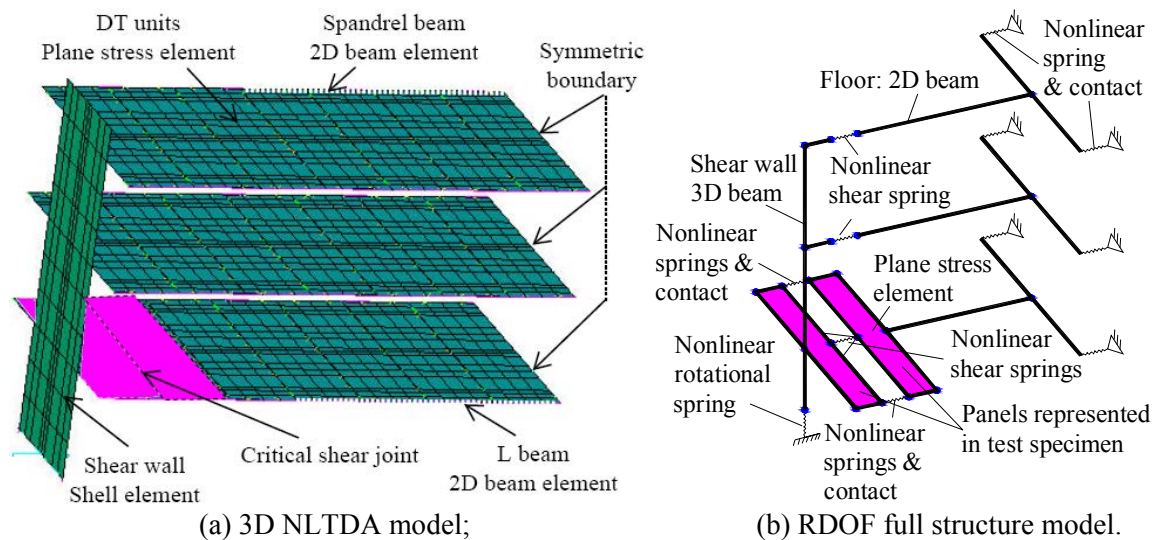
(a) 3D NLTDA model;   (b) RDOF full structure model.
Fig. B3-30: Modeling of simulation structure.

A distinction is made between RDOF *full structure* and RDOF *superstructure* models. The former, shown in Figure B3-30b, is used in stand-alone computer earthquake simulations to calibrate the RDOF model with the 3D NLDTA. The latter, shown in Figure B3-38a, is used in the actual hybrid test. The difference in these models is that the 1st floor critical shear joint is included in the RDOF *full structure* model; it is removed from the RDOF *superstructure* model, and is instead directly represented as a *physical substructure* in the LU testing laboratory.

As mentioned in above section, the hybrid test is conducted on a half-scale test specimen, whose precast units are identical in dimension to the half-scale shake table test (See Appendix B4). Thus both the 3D NLTDA model and the RDOF models are created in half-scale (relative to the full-scale simulation structure design described in *Section B3.2.1*). The scaling rules are the same as described for the PDH test (*See Section B3.1.2*).

---

[14] ANSYS version 10, Inc., Canonsburg, PA

3D NLTDA Model

The 3D NLTDA model of the simulation structure used to validate the RDOF model is described here. Full details of this model appear in (Zhang 2010). The shear wall is modeled with 3D elastic shell elements with nonlinear coupled springs at the ground to capture wall base biaxial hinge response. The hinge properties for shear wall are developed using section analysis software XTRACT[15] with a bilinear steel model (1.5 strain hardening ratio) and Mander model for concrete. The plastic hinge length for shear wall is set as minimum of half of shear wall depth and story height, which is 4′ in half-scale.
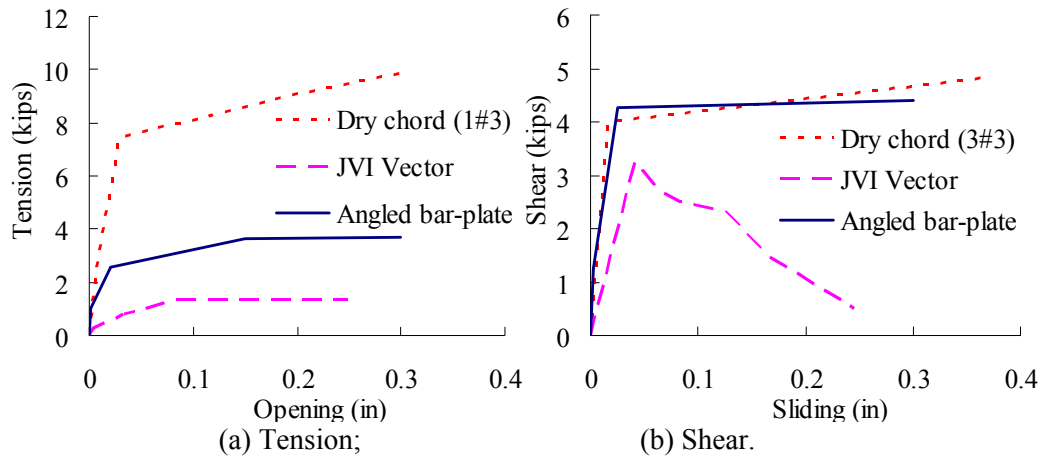
(a) Tension;   (b) Shear.
Fig B3-31: Response backbone for diaphragm reinforcement model.

The diaphragm in the 3D NLTDA model is modeled as group of nonlinear spring. Link and contact element using the discrete modeling approach described in Appendix B2. The tension and shear response of dry chord connector and angled bar-plate connector and tension response of JVI Vector are modeled with a pinched hysteretic effect (See Sec. B2.3.1) with unlimited ductility capacity. The shear response of the JVI Vector is modeled with a strength degrading hysteretic effect (See Sec. B2.3.2). The high stiffness contact and its associated friction between the precast units are modeled as contact element with coefficient of friction in series with a nonlinear compression spring (See Sec. B1.6). The response backbones of the diaphragm reinforcement models used in the 3D NLTDA model are shown Figure B3-31.

The test specimen occupies the region surrounding the critical shear joint in the simulation structure. This joint is selected as the one with the maximum sliding demand measured in the 3D NLDTA simulation. The critical shear joint was identified as the end joint on the 1st floor. It is noted that at the time of the testing, the contributions of the gravity system to diaphragm response was not fully understood. In later simulations that included the gravity system columns, the critical shear joint was found to be the end joint on the top (third) floor. Based on this finding, the pretopped diaphragm was placed on the top floor of the shake table test structure; the 1st floor of the shake table specimen was instead a topped diaphragm (See *Appendix B4*). Accordingly, while the hybrid test ended up not to directly represent the shake table test 1st floor joint, it did reasonably reproduce the demands on the top floor (pretopped) diaphragm end joint.

Creation of Reduced MDOF Model

The RDOF model is created by introducing the following simplifications into the 3D NLTDA model:

(1) The number of diaphragm joints explicitly modeled is reduced (from every panel joint in the 3D NLTDA model) to two joints per floor: the critical shear joint at floor end and the critical flexural joint at midspan. The diaphragm region between these joints is modeled monolithically (using continuous 2D

---

[15] XTRACT Imbsen commercial software, Inc. Rancho Cordova, CA.

C-A-170

beam elements) and is provided with effective elastic moduli (E_{eff} and G_{eff}) in order to account for the added flexibility missing in the RDOF model due to the removed joints. The effective moduli are determined using procedures from PART 3 of the design methodology (See Sec. 3.3.A in PART 3).

(2) The critical flexure joint model at all floors is changed from elastic plane stress elements with discrete nonlinear group of springs, links and contacts (See Fig. B3-32a) into a rigid beam with nonlinear axial springs and contact element pairs at the top and bottom chord regions (see Fig. B3-32b). The chord region springs include the combined contributions to flexural resistance of the chord and shear reinforcement, using a plane section transformation for the tension characteristics based on an assumption that the compression centriod is at center of chord region. The effective tension strength in the axial spring (T_{eff}) can be calculated as $T_{eff} = (T_{chord}d_{chd} + \sum_i T^i_{JVI}d^i_{JVI})/d_{chd}$. Thus, the RDOF model critical flexure joints are simplified versions of the 3D NLDTA discrete reinforcement joint models.
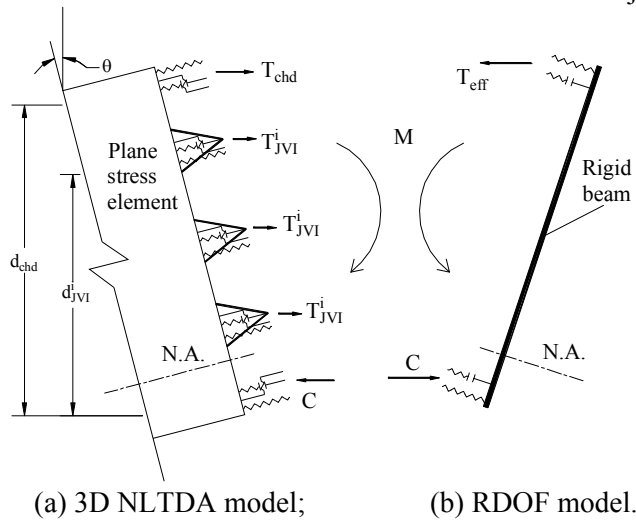
(a) 3D NLTDA model;   (b) RDOF model.
Fig. B3-32: Modeling of flexural critical joint.
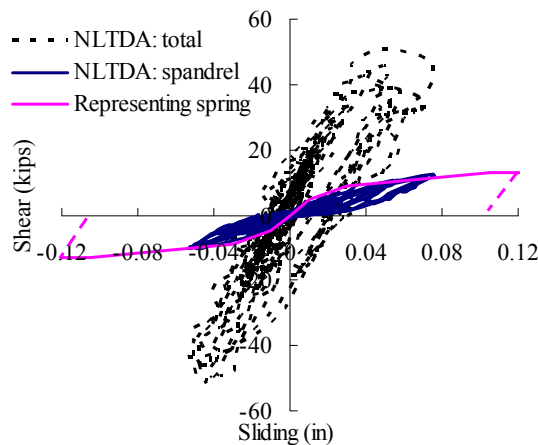
Fig. B3-33: Property calibration for representing nonlinear spring for spandrel beam.

(3) The critical shear joint at the floors 2nd and 3rd floor is modeled as three nonlinear shear springs in parallel to include the shear strength contributions from: (a) sum of all JVI Vector; (b) sum of all chord dowel action; and (c) spandrel beam shear resistance. The representing shear spring property for the spandrel beam contribution is approximately determined based on analysis using the 3D NLTDA model (see Fig. B3-33). The stiffness and strength of all the JVI Vector has been increased by 15% in the

representing nonlinear shear spring to account for the contribution from friction. The NLTDA results to follow show these estimations are reasonable (e.g. Figure B3-37b).

(4) The critical shear joint at the 1st floor in the RDOF model is still modeled as plane stress elements representing two full precast panels adjacent to the joint (see Fig. B3-34). In the RDOF *full structure* model, instead of using full discrete group of elements across the joint as the 3D NLTDA model (See Fig. B3-34a), the joint reinforcement is modeled as four groups of nonlinear elements (see Fig. B3-34b): (a) nonlinear tension spring and contact element in parallel at top and bottom chord location to model the tension/compression and friction response; (b) nonlinear shear spring and links in parallel at mid-depth to model the shear response of all JVI Vectors; (c) nonlinear shear spring at mid-depth to model the shear response of all bonded chord reinforcement; (d) nonlinear shear spring at mid-depth to model the shear response from the spandrel beam contribution. In the RDOF superstructure model, all the nonlinear elements are removed except for the nonlinear shear spring representing the contribution from the spandrel beam (See Fig. 34c).
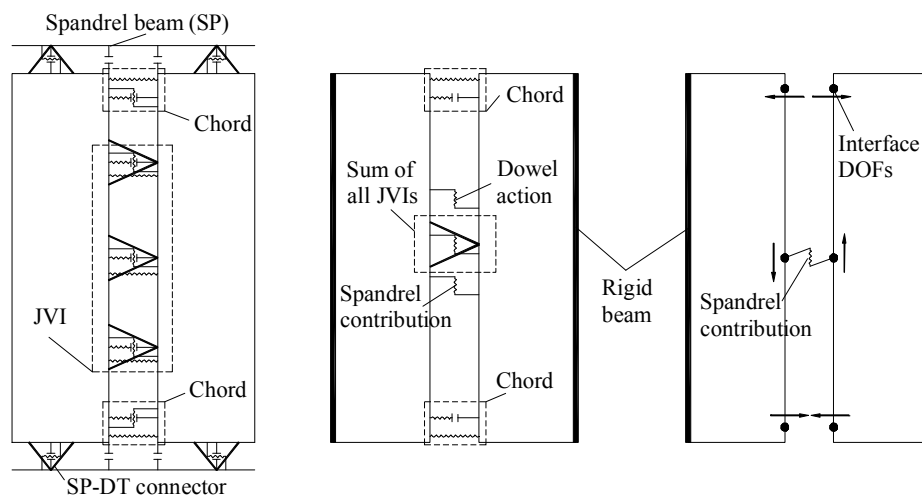
(a) 3D NLTDA model; (b) RDOF full structure model; (c) RDOF superstructure model.
Fig. B3-34: Modeling of shear critical joint at 1st floor.

(5) The shear wall is modeled as a 3D beam element with an inelastic rotational spring at the base (as opposed to 3D shell element with offset inelastic axial springs for the 3D NLDTA model). The RDOF shear wall rotational springs provide the same pinched hysteretic response (based on the precast rocking wall used in the shake table test structure) as produced by the base axial springs.

Dynamic Analysis Procedure for Analytical Simulations
The time-stepping technique of nonlinear dynamic analysis of simulation structure is the Newmark integration method. The nonlinear convergence technique is a modified Newton-Raphson iteration method with force tolerance error of 0.5% (ANSYS 2007). Based on simulations of the RDOF model, an undamped analysis (0% equivalent damping) is selected. Low values of damping, relative to the design spectrum damping value of 5%, were used in dynamic analyses throughout the DSDM project based on research findings (Panagiotou et al. 2006). This conservative approach is adopted to assure evaluation of the shear critical joint under substantial damage, as investigating the degrading nature of the joint is a primary objective.

The ground motion used in the hybrid test and the associated simulations is a historical ground motion from the 1994 Northridge earthquake, scaled to match the SDC E the design spectrum for Berkeley CA for the DSDM project (Schoettler 2005). The ground motion is scaled to MCE hazard for the hybrid test. The MCE time history and response spectra at full scale are shown in Figure B3-5. The ground motion is scaled to half-scale for the earthquake simulations using the following procedure: (1)

the amplitude of ground acceleration is amplified by the scale factor; and (2) the time is compressed by the scale factor (see Fig. B3-35).
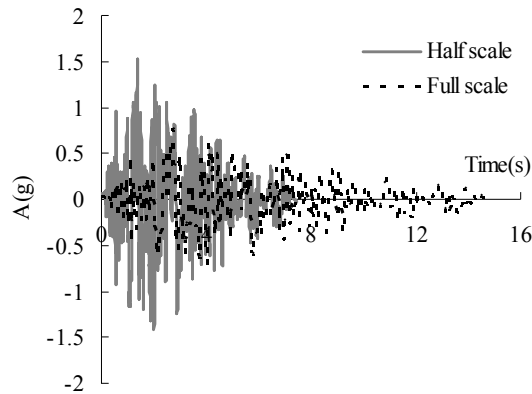
Fig. B3-35: Ground motion used for hybrid test.

RDOF Model Calibration

The RDOF model needed for the hybrid testing is calibrated by aligning its response with the 3D NLTDA model. The NLTDA results are presented in half-scale. Both global and local response is compared.

Global Response

The global responses of the RDOF (*full structure*) and 3D NLDTA analytical models are compared in Figure B3-36. The shear wall base moment vs. rotation is shown in Figure B3-36a. This plot indicates a maximum rotational demand in the MCE of 0.03rad. Figures B3-36b-d shows the diaphragm inertial force (F_i) vs. diaphragm midspan deformation for each floor level of the simulation structure. The global responses of the RDOF model (134 DOFs) is seen to reasonable match the 3D NLDTA model (6500 DOFs) global response, though in general the RDOF has less global demand than the 3D NLTDA model.

(a) Shear wall base;

(b) 1st floor;

(c) 2nd floor;   (d) 3rd floor;
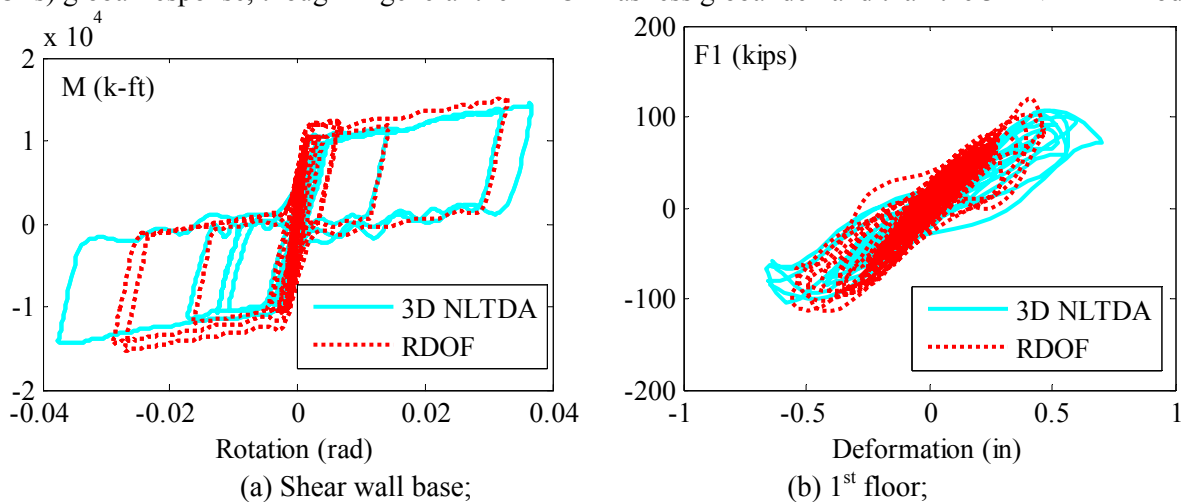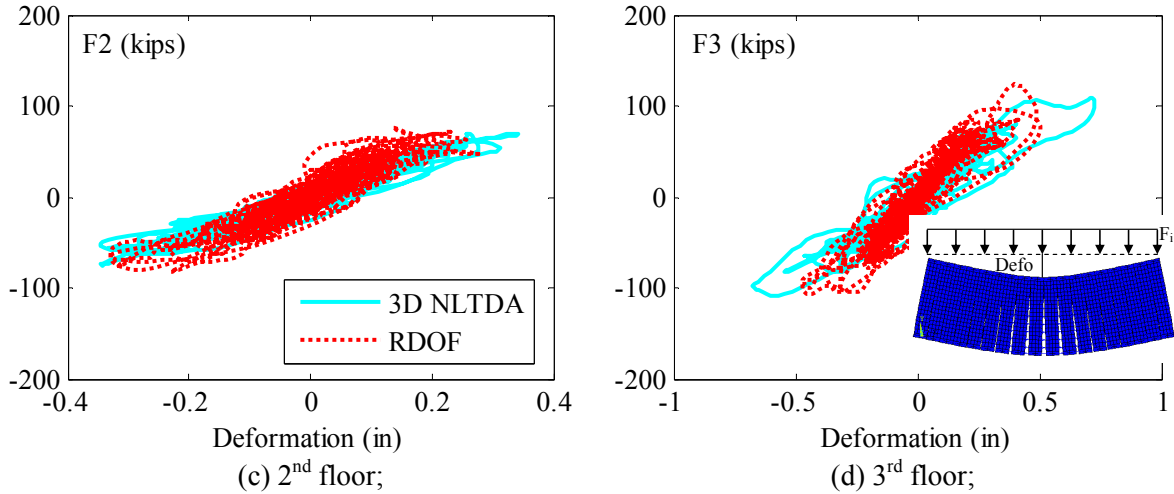
Fig. B3-36: RDOF and 3D NLTDA Comparison: Global response.

Local Response

Figure B3-37 compares the RDOF and 3D NLDTA model diaphragm critical flexural (midspan) joint response. Moment-rotation is plotted for these joints for the 1st and 3rd floors; the 2nd floor with lower response is omitted from the plot. The simulation structure diaphragm is seen to undergo significant inelastic flexural response (0.018rad) under MCE.

(a) 1st floor;   (b) 3rd floor.
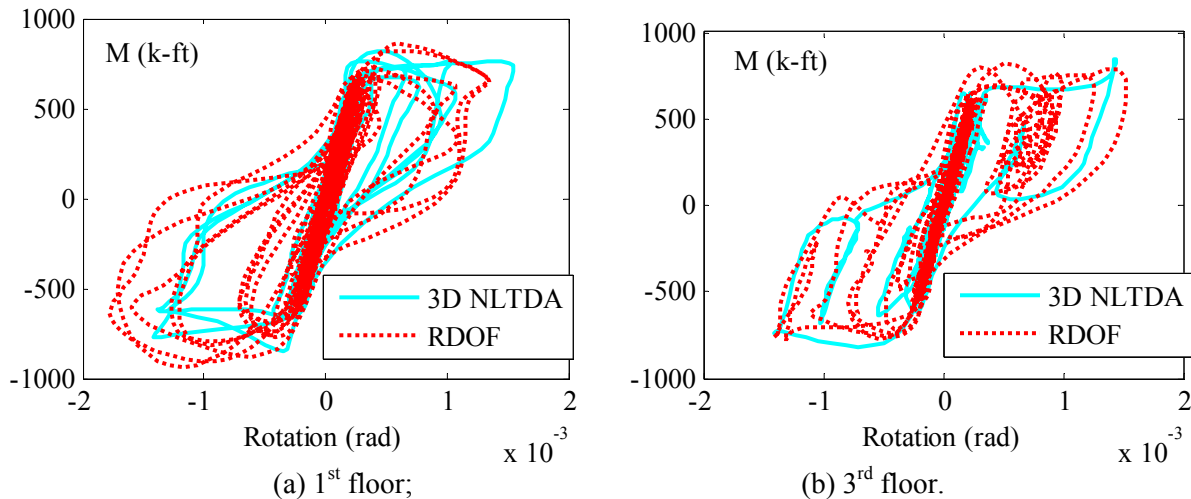
Fig. B3-37: RDOF and 3D NLTDA Comparison: Critical Flexure Joint.

The RDOF and 3D NLDTA model diaphragm shear joint response are now compared in Figure B3-38. Shear-force vs. sliding deformation response is plotted for the 1st and 3rd floor diaphragm end (critical shear) joint. It is noted that the maximum shear sliding deformation occurs at the 1st floor. The joint is seen to undergo inelastic shear deformation. The maximum shear force and shear sliding deformation for the RDOF model (134 DOF) is seen to reasonably approximate the critical shear response of the 3D NLDTA model (6500 DOF). Thus, the RDOF model at X DOF is selected for the hybrid test, and the as the 1st floor end (critical shear) joint is selected as the physical substructure for the hybrid test.

C-A-174
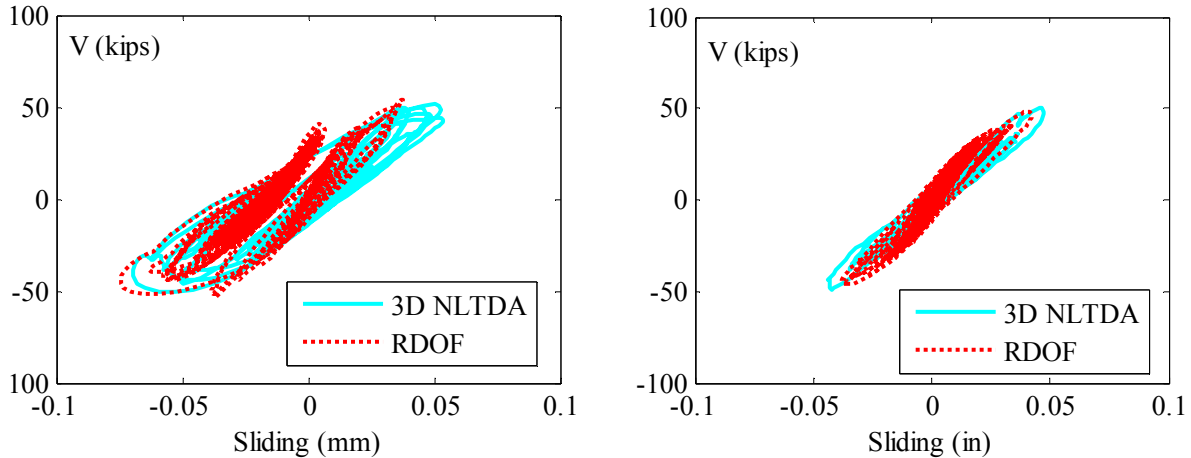
(a) 1st floor (solid panels in Figure B3-30a);   (b) 3rd floor;

Fig. B3-38: RDOF and 3D NLTDA Comparison: Critical Shear Joint.

Time history responses of the internal force components (in-plane axial, shear and moment) at the diaphragm (1st floor) critical shear joint at are presented in Figure B3-39. In each plot, the nominal design strengths are indicated as dashed lines. As expected, the shear force demand in seen to exceed the nominal design shear strength. The overstrength in the shear force relative to the nominal strength is due to the secondary shear transfer mechanisms. Although the critical shear joint axial force and moment do not reach their nominal strength values, these force components are not negligible. The RDOF model and the 3D NLTDA models produce similar force responses.
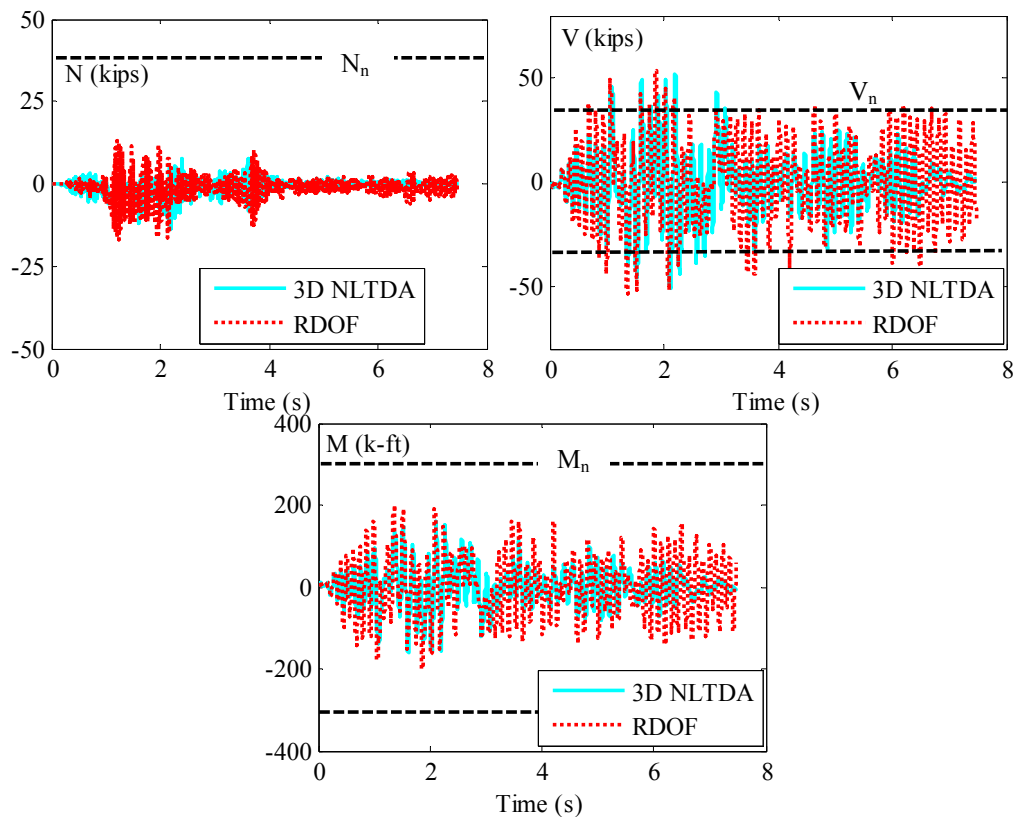
Fig. B3-39: RDOF Critical shear joint Force Comparison: (a) Axial; (b) Shear; (c) Moment.

B3.2.3 Hybrid Testing Procedure
Hybrid Algorithm

  The Newmark implicit time integration method used in the fully-simulated earthquake analyses requires iterations to determine unknowns (displacement, velocity and acceleration) at the current step. In order to perform the iterations in hybrid simulation using analytical superstructure and physical testing, data exchanges between superstructure dynamic analysis and physical testing is required during these iterations. This process cannot be realized through the commercial finite element program ANSYS used for the fully-simulated earthquake analyses since it is not possible to update the feedback from physical testing while the ANSYS program is in processing of iterations. For this reason, an independent unconditionally stable integration algorithm, Alpha method with a fixed number of iterations (Mercan and Richle 2005), is used for the hybrid testing. This algorithm is written based on MATLAB script computer language and is in charge of dynamic time step integration while the RDOF superstructure model created in ANSYS is served as a static restoring force determinator as illustrated in Fig. B3-40.

(a)ANSYS program;   (b) MATLAB program;   (c) Physical test;
Fig. B3-40: Hybrid test.
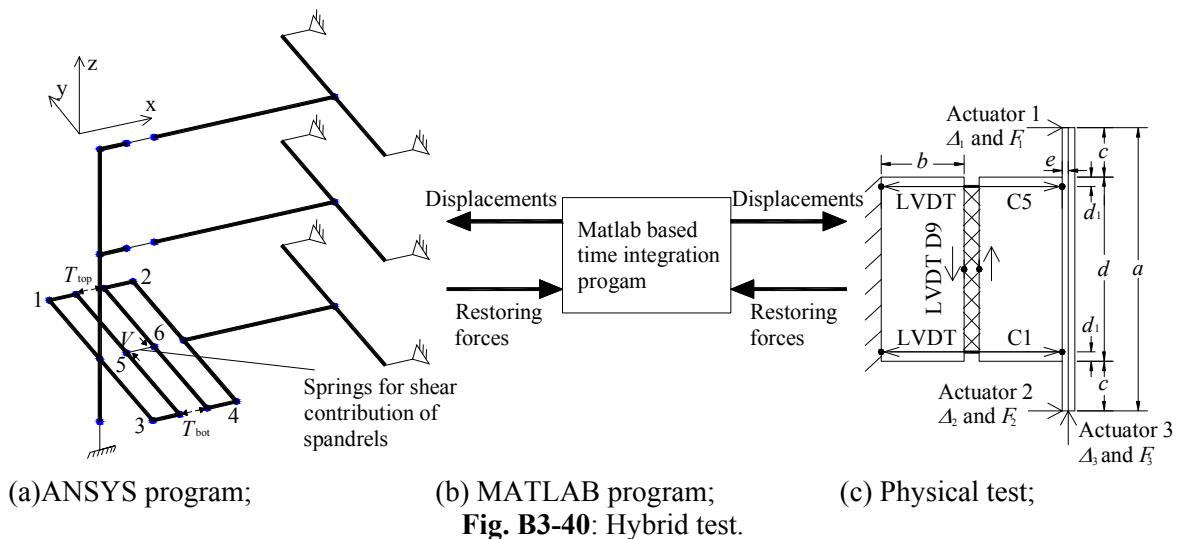
  As seen in Fig. B3-40, the MATLAB based time integration program using the Alpha time integration method (see Mercan and Richle 2005 for the full description of integration algorithm) generates a displacement vector at a given iteration of a given time step. These displacements are applied to the RDOF *superstructure* model and to the physical test. The *static* restoring forces from the RDOF model and the physical test are returned to the MATLAB program to check the error and calculate the displacement vectors for the next iteration. After the required iterations have been reached (two fixed iterations are used in each step for hybrid simulation), the MATLBA program will save the displacement, velocity and acceleration at current step and move on to the next step.

  The RDOF *superstructure* model used for the hybrid test has interface DOFs U_{xi} and U_{yi}, $i=1\text{-}6$, whose relative displacements are applied to the physical test substructure (Figure B3-40c) as three absolute displacements imposed in the physical testing: opening at the top of the joint ($U_{x2} - U_{x1}$), opening at the bottom of the joint ($U_{x4} - U_{x3}$) and sliding along the joint ($U_{y6} - U_{y5}$). These displacements are controlled by linear variable displacement transducers (LVDTs) C5, C1, and D9, respectively. The instrumentation is shown in Figure B3-40c, where each LVDT acts between the black dots in the schematic. Similar as the PDH test, the loading control algorithm involves two loops. Each outer loop displacement obtained from the MATLAB program is divided into smaller substeps (actuator command increment of 0.002) at approximately the actuator resolution (0.004″). In the inner loop, each substep is applied through actuator displacement control until displacement targets are achieved at C5, C1 and D9. The substeps are repeated, with actuators not achieving the target within a tolerance (0.003″)

slightly extended or retracted, until the outer loop full step is achieved on all feedback channels.. Three restoring forces of physical test [axial force at top (T_{top}), axial force at bottom (T_{bot}) and shear force of the joint (V)] are calculated from the actuator cells forces with following equations:

$$T_{top} = \left[F_1(c + d - d_1) - F_2(c + d_1) - F_3(b + e)\right]/(d - d_1) \qquad \text{(Eq. 15a)}$$

$$T_{bot} = \left[F_2(c + d - d_1) - F_1(c + d_1) + F_3(b + e)\right]/(d - d_1) \qquad \text{(Eq. 15b)}$$

$$V = F_3 \qquad \text{(Eq. 15c)}$$

Hybrid Test Simulation

Prior to the actual physical test, the hybrid test is first simulated. This simulation is accomplished by representing the physical substructure (Fig. B3-40c) as a two-dimensional (2D) nonlinear static finite element model. The test substructure model, like analytical superstructure, is model using ANSYS. The precast panel is modeled as elastic plane stress elements with fixed boundary condition at outer side of left panel and a rigid beam is attached to the outer side of right panel (refer to Fig. B3-40c). The diaphragm reinforcement across the joint is modeled as full discrete nonlinear group of spring, link and contact elements. The time integration also is conducted in MATLAB using the Alpha method (refer to Fig. B3-40a) and the restoring forces of other DOFs are also determined using the RDOF superstructure model (refer to Fig. B3-40b). The simulation of the physical hybrid experiment , indicated as "hybrid simulation" in plot legends for brevity, permitted troubleshooting and fine-tuning of the hybrid algorithms, actuator convergence schemes, force and displacement transformations, interface compatibility and communication protocols without the possibility of premature damage to the test specimen, fixtures or equipment. The global and local responses of the hybrid test simulation are compared to the RDOF *full structure* simulations as discussed next.

Global Response

Figure B3-41 compares the global response of the hybrid test simulation and the RDOF analysis including: (a) shear wall base moment vs. rotation; (b-d) diaphragm inertial force vs. midspan deformation at the 1st, 2nd and 3rd floor respectively. Good global agreement is observed between the hybrid test simulation and the RDOF analysis.

(a) Shear wall base;   (b) 1st floor;

(c) 2nd floor;   (d) 3rd floor;
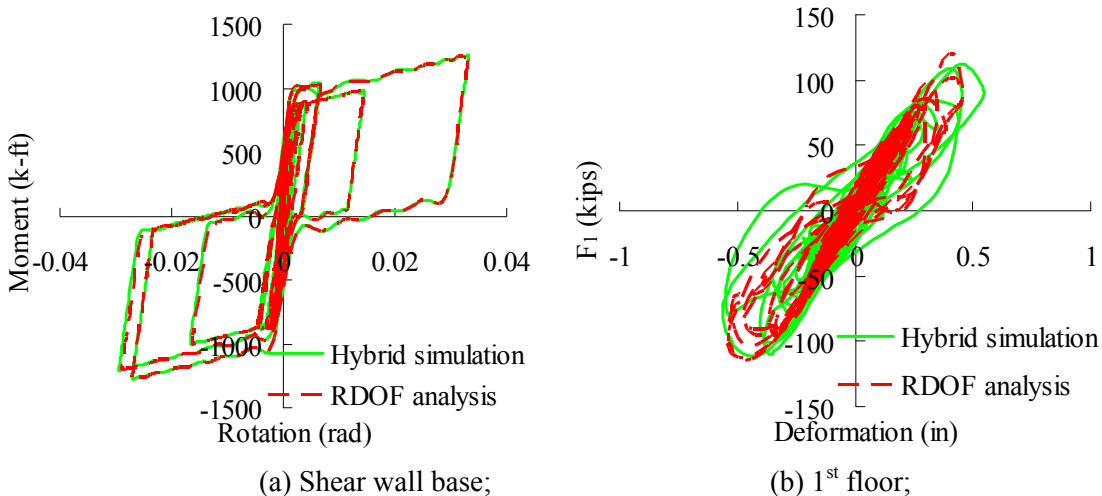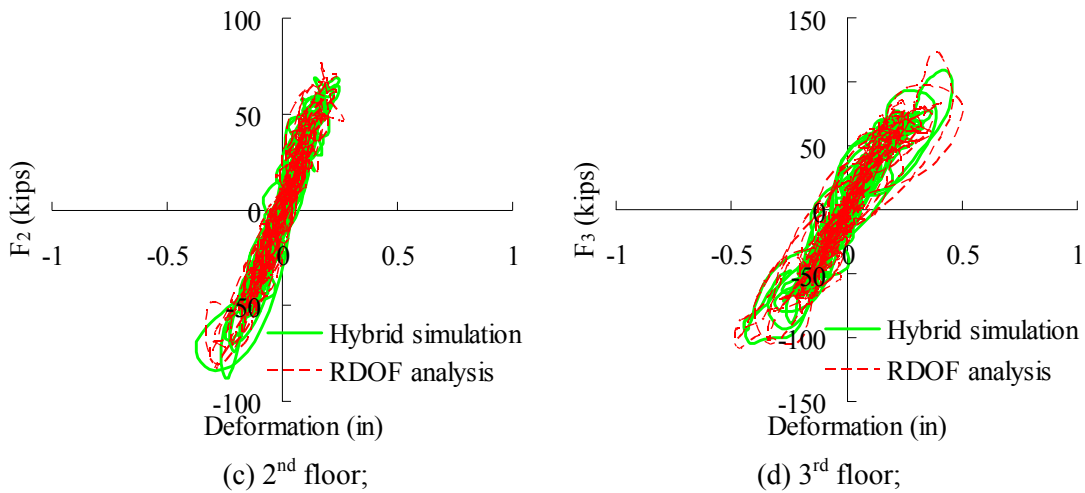
Fig. B3-41: Hybrid test simulation vs. RDOF Analysis: Global responses.

Local Response

The response of the diaphragm critical joints are now compared for the hybrid test simulation and the RDOF analysis. Results are shown for the 1st and 3rd floors. Figure B3-42 shows the critical flexure (midspan) joint moment-rotation response. . Figure B3-43 shows the critical shear joint shear force vs. sliding deformation. The following is noted: (1) excellent agreement is observed between the hybrid test simulation and the RDOF analysis results for critical joints on the 3rd floor ; (2) the hybrid simulation exhibits lower moment and rotation demand at the 1st floor critical flexure joint relative to the RDOF analysis results; and, (3) the hybrid simulation exhibits higher shear sliding deformation demand at the 1st floor critical flexure joint relative to the RDOF analysis results, including significant shear strength degradation, even though the joint did not undergo a larger shear force. It may be inferred from the results that the lower demand at the 1st floor critical flexure joint for the hybrid simulation is due to the more extensive yielding of the 1st floor critical shear joint in this analysis. This action both limits the magnitude of the moment possible at midspan (due to limiting the shear transfer to the shear wall), and reduces the required inelastic rotations at midspan to achieve an overall diaphragm inelastic deformation demand due to greater inelastic sliding deformation at the diaphragm ends. Thus, the focus on the discrepancy between the hybrid test simulation and the full dynamic analyses focused on the response of the critical shear joint.

(a) 1st floor;   (b) 3rd floor;
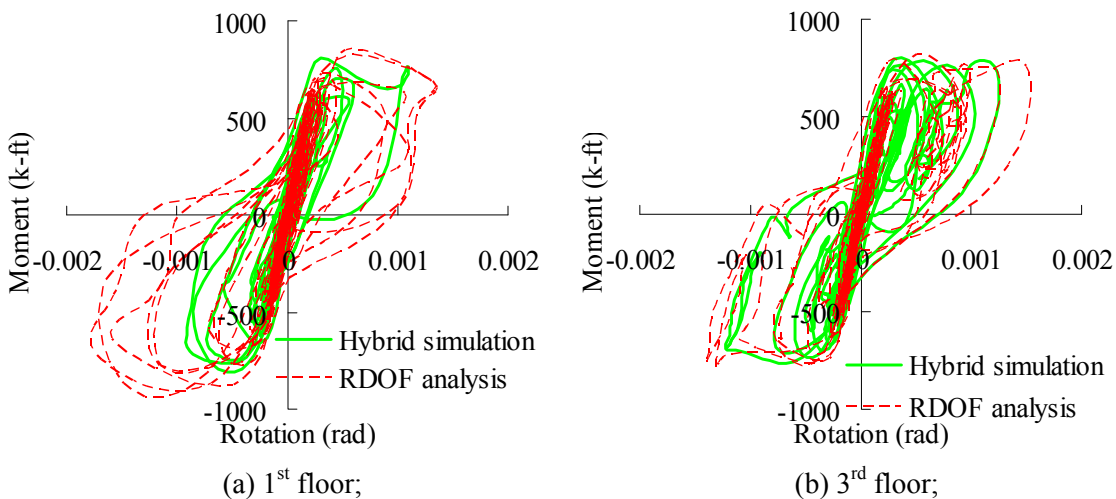
Fig. B3-42: Hybrid test simulation vs. RDOF Analysis: critical flexure joint.

(a) 1st floor;   (b) 3rd floor;
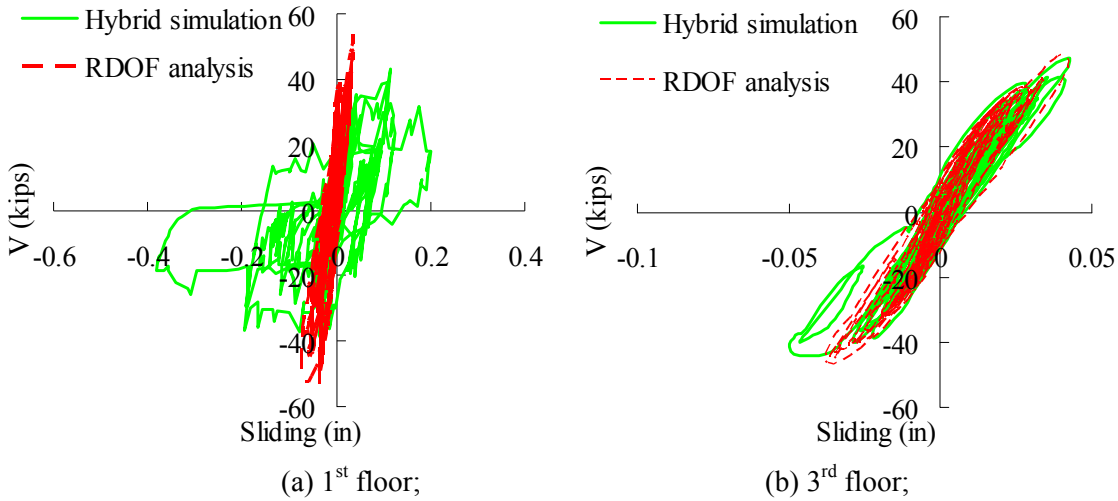
Fig. B3-43: Hybrid test simulation vs. RDOF Analysis: critical shear joint.

Troubleshooting

The hybrid test simulation permitted troubleshooting of the interface between the ANSYS models and the Matlab hybrid algorithm. However, the difference in the 1st floor critical shear joint shear response between the hybrid test simulation and the dynamic analysis NLTDA required a closer examination of the algorithm and analytical components of the hybrid test to determine the source of the discrepancy. After a detailed examination of the different components that comprise the hybrid testing elements, it was hypothesized that the difference in the hybrid simulation and the dynamic analysis stemmed from the inability for the hybrid algorithm to adequately treat the contact condition. This phenomenon has recently been identified as an important unresolved issue in hybrid testing, particularly in how it applies to dynamic impact.

(a) Opening/closing at top of joint;   (b) Axial force;
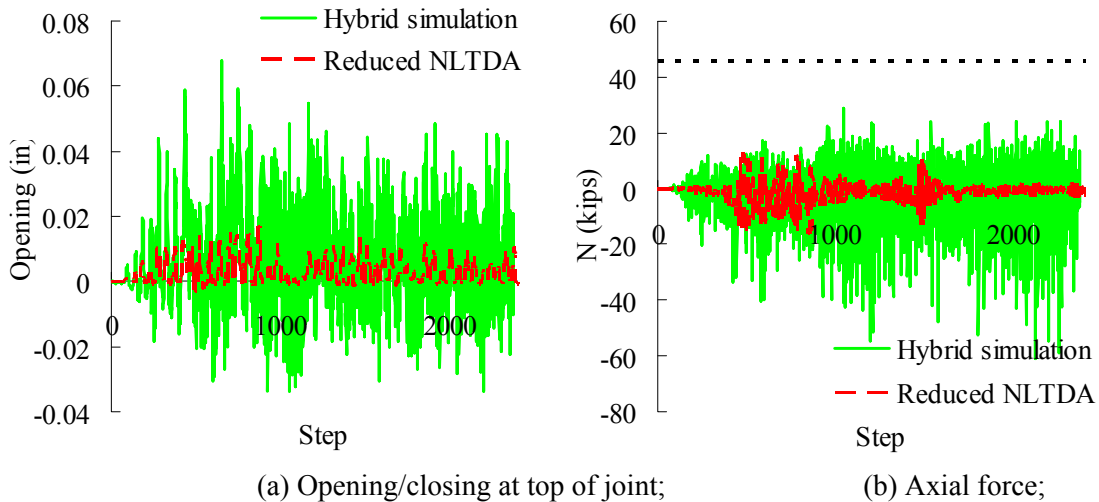
Fig. B3-44: Time histoy response at critical shear joint

The RDOF full structure models, like the 3D NLTDA, uses contact pseudo-elements available in ANSYS to model the joint coming into contact under axial compression or in the compression zone in flexure. The contact elements employ a penalty function formulation (ANSYS 2007). The hybrid integration algorithm, on the other hand, has no capability of considering the contact algorithm. In the hybrid simulation, no contact algorithm means high panel penetration might occur and introduce high

C-A-179

panel opening/closing and high joint axial forces (Figure B3-44). These high joint axial forces will have a significant influence on the joint shear response since it can change the contribution of friction and reduce the connector shear strength. Figure B3-45 shows the time history responses close-up from step 428 to 429 where the difference in the joint sliding demand start to occurs between RDOF analysis and hybrid simulation. As seen, during these steps, the top of joint is open for both RDOF analysis and hybrid simulation while the bottom of joint is close for the RDOF analysis but undergoes a open/closing cycle for the hybrid simulation due to lack of contact algorithm. As a consequence of this observation, the joint is in compression for RDOF analysis but undergoes a tension/compression cycle for the hybrid simulation during these steps. In the steps (429 and 430) when the joint is in tension in hybrid simulation, the shear sliding demand starts exceed the demand obtained in RDOF analysis and entering inelastic response domain because the shear strength of a joint with compression force is larger than that with tension force. In hybrid simulation, as the joint yield in sliding, the joint shear strength will start to degrade and thus the sliding demand keep increasing even in a later step (step 431) where a compression force is observed.
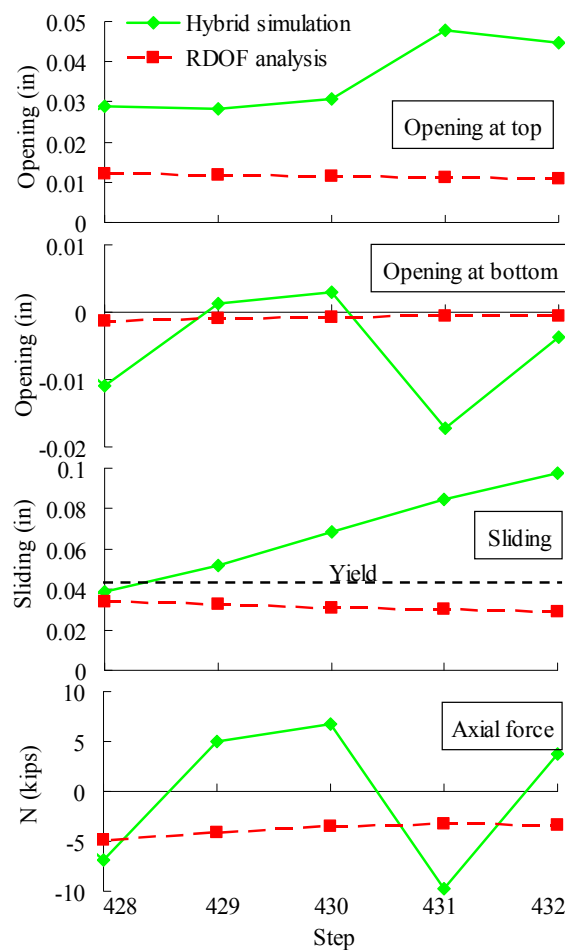
Fig. B3-45: Time history response close-up at critical shear joint.

To verify the difference is caused by the fact that hybrid integration algorithm fails to capture contact algorithm, the contact elements at critical shear joint are removed from both the RDOF full structure model in RDOF analysis and the 2D test substructure model in hybrid simulation. The comparison for the models without contact elements between hybrid simulation and NLTDA is shown in Figure B3-46. The good agreement for the shear-sliding response at critical shear joint is found.
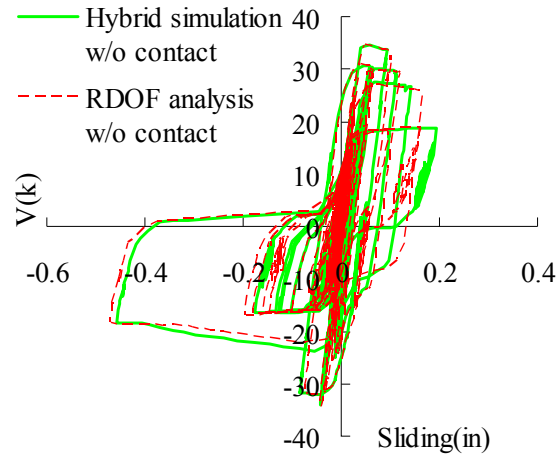
Fig. B3-46: Critical shear-sliding response of hybrid simulation without contact.

Although the hybrid algorithm does not capture the shear response at critical shear joint observed in RDOF analysis, it introduces more inelastic shear demand to the joint which can serve the purpose of testing the post-yield behavior of diaphragm shear critical joint. At the same time, it is difficult to develop a new hybrid algorithm considering the time constraint on the schedule of test utilities. Therefore, the hybrid algorithm discussed above is still used for the test.

B3.2.4 Experimental Program
The physical test part of hybrid test is conducted at LU. The LU research group of DSDM project designs the test specimen, produces the test specimen, set up the test fixture and conducts the test. The experimental program is similar as the PDH test discussed in section B3.1.3. The same test fixtures and instrumentations are used for both PDH and hybrid test. The only difference is that the hybrid specimen employs diaphragm reinforcing details shown in Figure B3.27a at the critical shear joint.

B3.2.5 Experimental Results Discussion
Hybrid test results are processed, interpreted and compared to hybrid simulation predictions in the following categories: (1) joint displacement time history; (2) joint force time history; (3) joint hysteresis response; and (4) joint shear stiffness.

Joint Displacement Time History
Three interface displacements: opening at top chord (C5), opening at bottom chord (C1) and sliding at center (D9) are shown in Figure B3-47. The ground motion is discretized into 2990 time steps but the test stops at step 1600 due to a shear failure (Figure 4.47c). A good agreement is found between hybrid test and hybrid simulation in the early stage of test (0 to 1000 steps). However the sliding demand in the later stage of hybrid test is much larger than that of hybrid simulation. This lager shear sliding demand causes concrete adjacent to the joint to crush which in turn results in a high panel penetration (Figure 4.47b).

(a) Opening at top; (b) Opening at bottom;
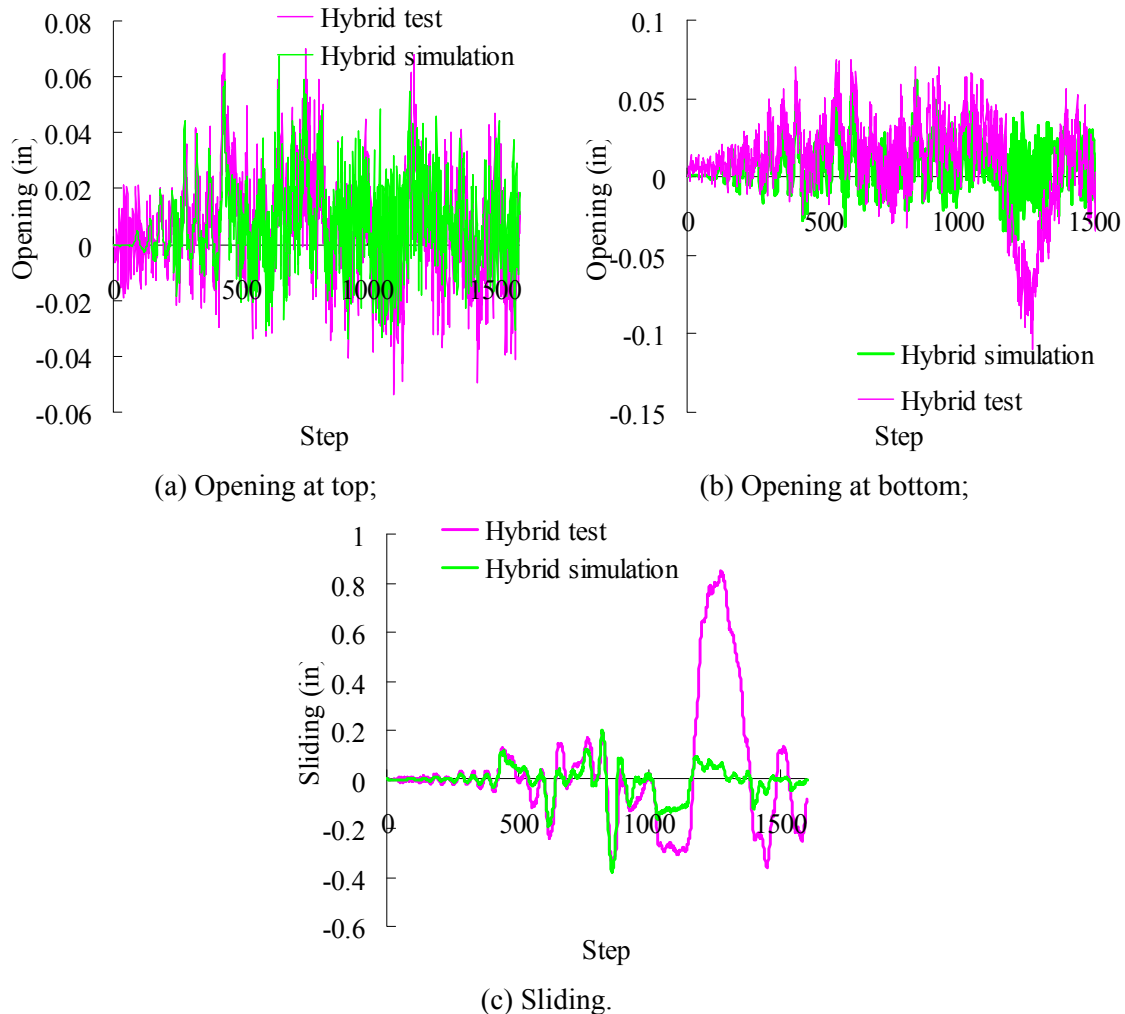
(c) Sliding.

Fig. B3-47: Joint displacement time history of hybrid test.

The higher shear sliding demand of hybrid test compared to hybrid simulation is due to the overloading caused by the loading control iteration algorithm in hybrid test. As described in section B3.1.3, the three interface displacements are coupled in the test system and have to follow the displacement compatibility. So an iteration algorithm is used to make the three displacements converged at target value through an inner loop which divides the displacement inputs into substeps as described in B3.2.3. This iteration process means before the displacements meet the target displacement values (termed actuator command in Figure B3-48) generated from the MATLAB time integration program, the joints will undergo a set of trial displacements (termed actuator input in Figure B3-48). The overloading is originated from this iteration process. Figure B3-48 shows a close-up of joint sliding and shear force time history. At step 428, the actuator command requires a 0.06″ sliding for the test joint (Figure B3-48a). However during the actual test, the joint undergoes a set of trial displacements (Blue line in Figure B3-48a) before reaching the target displacement values. A shear sliding overloading is seen in the iteration process and in turn a shear force overloading is generated (Figure B3-48b). Because the shear sliding demand at this step is larger than the JVI Vector yield strength, strength degradation is observed at end of step 428 which in turn causes the high sliding demand obtained from MATLAB time integration at next step 429 compared to the hybrid simulation. This shear sliding overloading accumulates in the whole test and results in the high shear sliding demand and consequently large shear strength degradation in the rest

of test. Thus a better loading algorithm for the precast diaphragm joint test is required when considering the flexure and shear coupled loading.
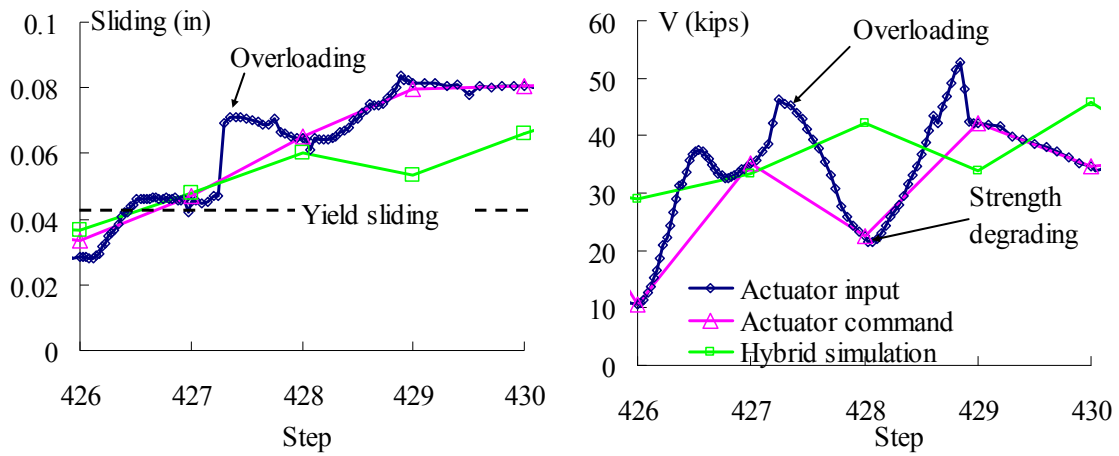
(a) Sliding; (b) Shear force;
Fig. B3-48: Close-up of joint sliding demand for hybrid test.
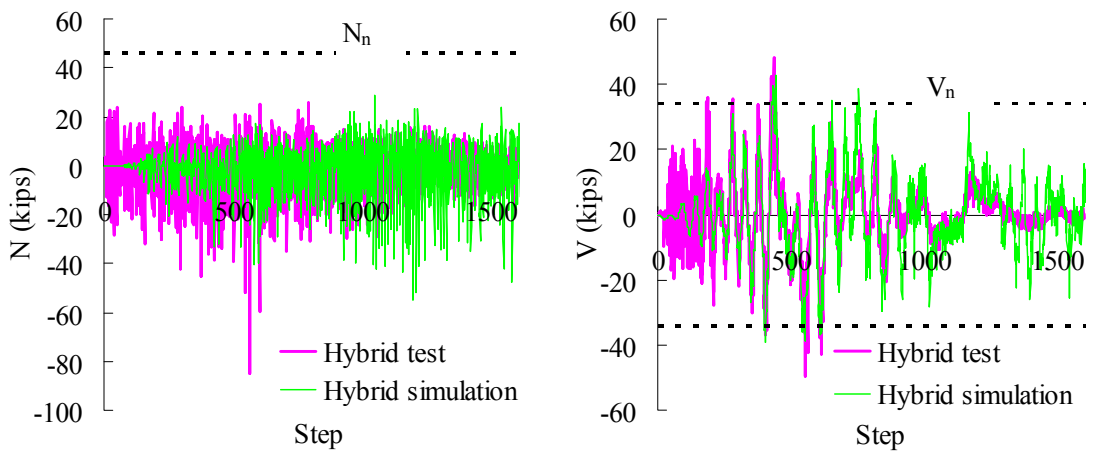
(a) Axial; (b) Shear;
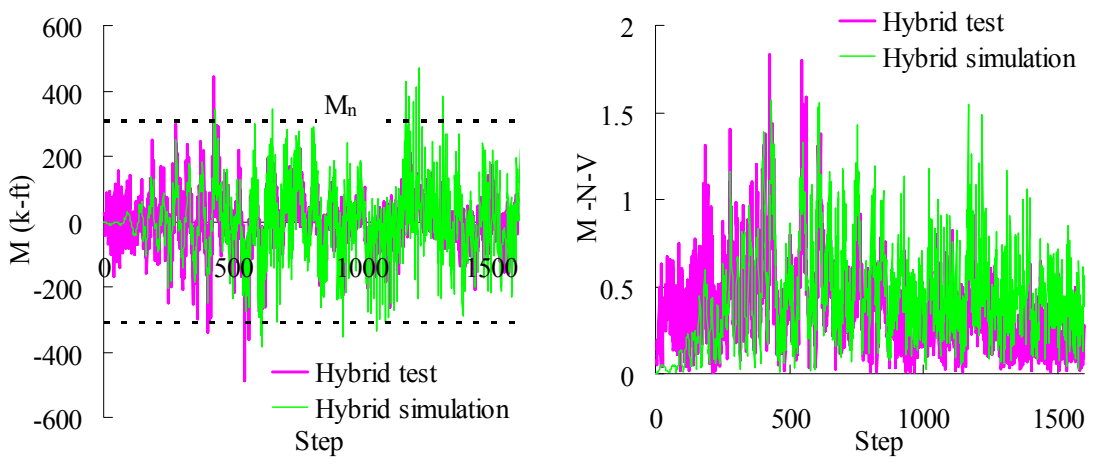
(c) Moment; (d) *M-N-V*.
Fig. B3-49: Joint force time history of hybrid test.

Joint Force Time History

Figure B3-49 shows joint forces time history responses: (a) joint axial force; (b) joint shear force; (c) joint moment; and (d) M-N-V iteration from Eq. 12. The nominal design strengths are indicated as well. A good agreement between hybrid test and hybrid simulation is found except that: (1) in the late stage of test more shear strength degradation is shown in the hybrid test (Figure B3-49b) for the reason described in above section; (2) in the beginning of test, the forces responses of hybrid test has a high frequency oscillation with non-trivial magnitude though not yield because the displacements command is very small and falls into the actuator resolution.

Joint Hysteresis Response

(a) Axial;　　　(b) Shear;　　　(c) Moment;　　(d) Photo.
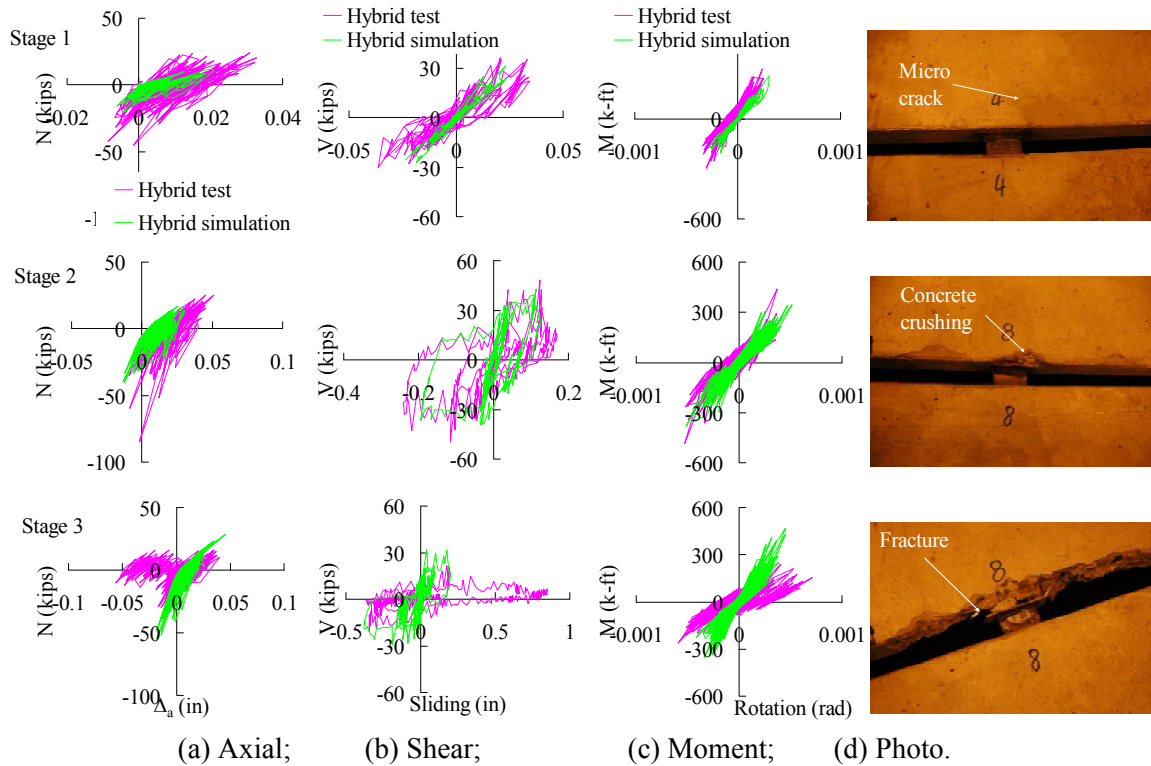
Fig. B3-50: Joint hysteretic responses of hybrid test.

Joint hysteresis response is shown in Figure B3-50 which divides the whole test into three stages: stage 1 (1 to 400 steps), stage 2 (401 to 800 steps) and stage 3 (801 to 1600 steps).

In stage 1, the joint is in elastic condition and only micro cracks are observed (Figure B3-50d). In stage 2, the shear reinforcements start to yield. Large shear sliding demand and shear strength degradation occur followed with the local concrete crushing (Figure B3-50d). Good agreement between the test and simulation is seen in the first two stages. In stage 3, the shear overloading results in high sliding demand and large shear strength degradation in the test. Figure B3-50d shows the fracture of shear reinforcements and crushing of surrounding concrete which in turn causes the softening of axial and flexure strength (Figure B3-50a and B3-50c).

Shear Stiffness

Figure B3-51 shows the shear stiffness of the joint. The degradation of the shear stiffness during the test is more than that in hybrid simulation (Figure B3-51a) due to the overloading in the test. The axial compression force increases the shear stiffness while tension force decreases the shear stiffness as expected (Figure B3-51b).
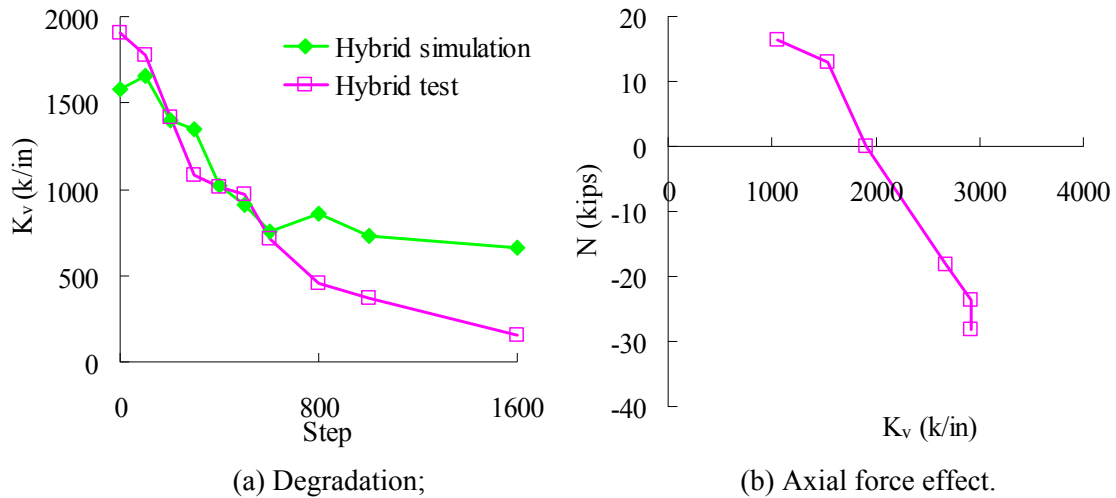
(a) Degradation;   (b) Axial force effect.
Fig. B3-51: Joint shear stiffness of hybrid test.

B3.2.6 Conclusions from Hybrid Test

The critical shear joint in a pretopped concrete diaphragm was tested at half-scale under hybrid "adaptive" algorithm. The following conclusions are made:

(1) The shear reinforcement (JVI Vector) shows strength and stiffness degradation with increasing inelastic shear sliding loading.

(2) The critical shear joint designed with shear overstrength factor of 1.1 will likely fail in the expected earthquake after the significant shear strength loss. Thus higher shear overstrength factor is required for the diaphragm shear design to prevent non-ductile shear failure.

(3) The analytical model shows good agreement with joint shear response, including reasonable predictions of local responses. The strength degradation model of JVI Vector can capture the stiffness and strength degrading effect observed in the test.

(4) The shear stiffness is influenced by joint axial force. The compression force generally increases the joint shear stiffness. On the other hand tension force decreases the joint shear stiffness.

(5) An improved hybrid time integration method is needed to include the contact effect for the precast concrete diaphragm test.

A better loading control algorithm is needed for applying tension, shear and moment coupling loads to precast concrete panel joint to avoid overloading.

B3.3 REFERENCES

ACI 318-05. (2005). Building Code Requirements for Structural Concrete (ACI 318-05) and Commentary (ACI 318-05), ACI committee 318.

ANSYS version 11. (2007). "Elements (00853) and theory reference (00855)" SAS IP, Inc.

Fleischman, R.B., Naito C.J., Restrepo J., Sause R., Ghosh S.K., Wan G., Schoettler M., and Cao L. (2005). "Seismic design methodology for precast concrete diaphragms, Part 2: research program." PCI Journal, 51(6), 2-19.

Fleischman, R.B., Sause, R., Pessiki, S., and Rhodes, A.B. (1998). "Seismic behavior of precast parking structure diaphragms." PCI Journal, 43 (1), Jan-Feb: 38-53.

Fleischman, R.B. and Wan, G. (2007). "Appropriate overstrength of shear reinforcement in precast concrete diaphragms", ASCE Journal of Structure Engineering 133(11): 1616-1626.

IBC (2003). International Building Code, 2003 Edition, International Code Council, Inc., Falls Church, VA.

Lee, H.J., and Kuchma, D.A. (2008). "Seismic response of parking structures with precast concrete diaphragms." PCI Journal, 53(2), 71-94.

Mercan, O. and Ricles, J.M. (2005). "Evaluation of real time pseudodynamic testing algorithms for seismic testing of structural assemblages." ATLSS Report No. 05-06. Bethlehem, PA

Naito, C., Jones, C., Cullen T. and Ren, R. (2007). "Development of a seismic design methodology for precast diaphragms - phase 1b summary report". ATLSS Report. ATLSS Center, Lehigh University, PA.

Naito, C., Peter, W. and Cao, L. (2006). "Development of a seismic design methodology for precast diaphragms - phase 1 summar report". ATLSS Report No.06-01, ATLSS Center, Lehigh University, PA.

Naito, C. and Ren, R., (2008). "Development of a seismic design methodology for precast diaphragms - phase 1c half scale". ATLSS Report #08-09. ATLSS Center, Lehigh University, PA.

Precast/Prestressed Concrete Institution. (2004). "PCI design handbook: precast and prestressed concrete." Sixth Edition, Chicago IL.

Pincheira, J. A., Oliva, M. G., and Kusumo-rahardjo, F. I. (1998). "Tests on double tee flange connectors subjected to monotonic and cyclic loading." PCI Journal, 43 (3): 82-96.

Schoettler, M.J. (2005). "Selection of ground motion." DSDM project internal document.

Schoettler, M.J., Belleri, A., Zhang, D., Restrepo, J., and Fleischman, R.B. (2009). "Preliminary results of the shake-table testing for development of a diaphragm seismic design methology." PCI Journal, 54 (1), 100-124.

Wood S. L., Stanton J. F., Hawkins N. M. (2000). "New seismic design provisions for diaphragms in precast concrete parking structures", PCI Journal, 45 (1): 50-65.

Wan, G. (2007). "Analytical Development of Capacity Design Factors for A Precast Concete Diaphragm Seismic Design Methodology", Ph.D dissertation, the University of Arizona, Tucson, AZ.

Appendix B4. Model Verification Using Shake Table Test

A three-story diaphragm sensitive structure was tested on the NEES@UCSD shake table (Schoettler et al. 2009) (Schoettler 2010). The primary objectives of the shake table test program were to: (1) demonstrate the seismic performance of different untopped and topped precast diaphragm designs; and, (2) verify or further calibrate the 3D-FE discrete NLDTA model described in Appendix B2 and B3.

TABLE OF CONTENTS

B4.1 SHAKE TABLE TEST PROGRAM DESCRIPTION

The specific objectives of the shake table test program include to: (1) demonstrate the performance of precast diaphragms and the efficacy of the design methodology; (2) prequalify certain diaphragm designs at a given level of performance; (3) provide information for use in calibrating analytical models, and (4) provide new knowledge on the behavior of precast diaphragms.

B4.1.1 Shake Table Test Specimen

Figure B4-1 shows a photograph of the half-scale shake table test specimen. This three story test specimen consisted of precast concrete elements with the completed structure weighing 302-kip. A single 56-ft by 16-ft bay created a rectangular floor plan with an aspect ratio of 3.5, see Figure B4-2. The simplified building with an open configuration resembled a parking garage, yet contained three unique floor systems. Floor-to-floor heights were 6.5-ft with walls and columns extending 23-ft above the foundation level.

Fig. B4-1. Shake table testing specimen (Modified from Schoettler et al. 2009).

As shown in Fig. B4-2, the structure has three floor levels with a different floor construction technique used for each level: (1) a composite topped double tee system on the 1st floor with topped chord reinforcement and ductile mesh plus topped hairpin connector in the web; (2) a non-composite topped hollow core system on the 2nd floor with topped chord reinforcement and ductile mesh in the web; and (3) an untopped double tee system on the 3rd floor with dry chord reinforcement and half-scale JVI Vector in the web. The diaphragm reinforcement detailing is shown in Fig. B4-3. Each of the floor diaphragms was designed with concepts from the design methodology.
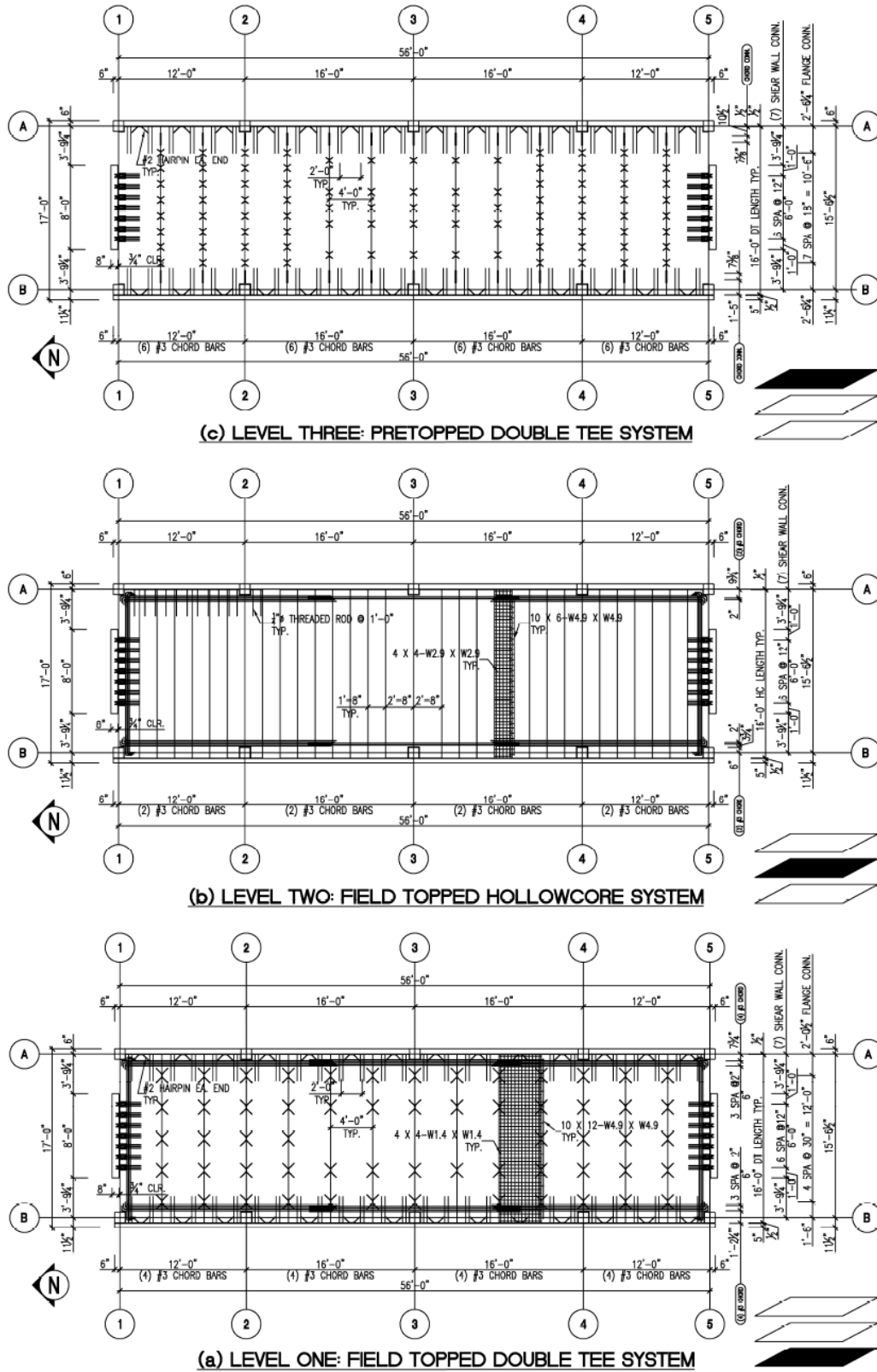
Fig. B4-2. Floor diaphragm plan for shake table testing specimen (after Schoettler et al. 2009).
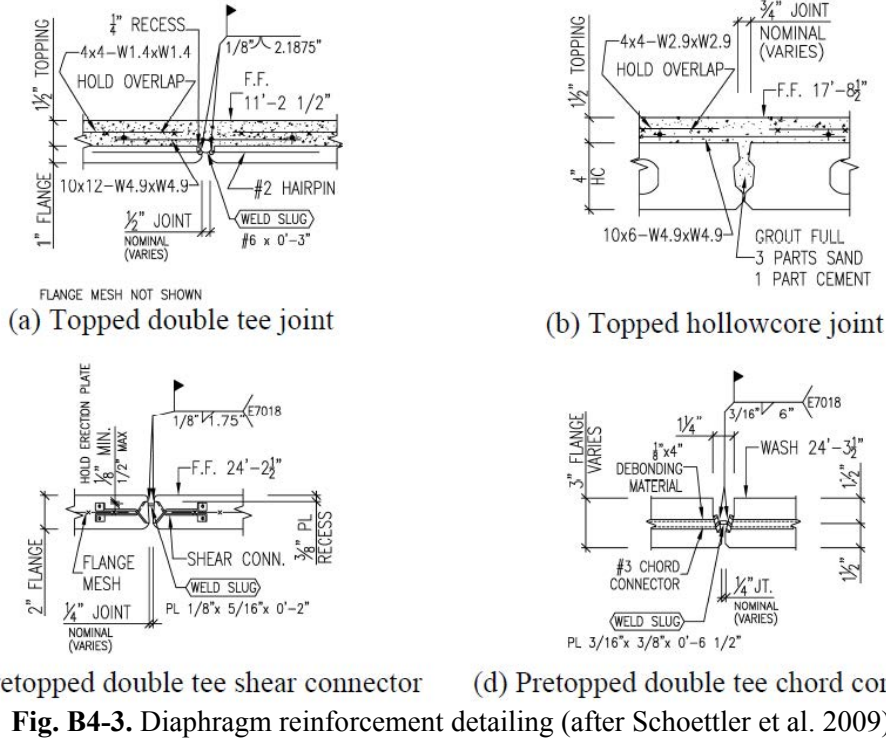
Fig. B4-3. Diaphragm reinforcement detailing (after Schoettler et al. 2009).
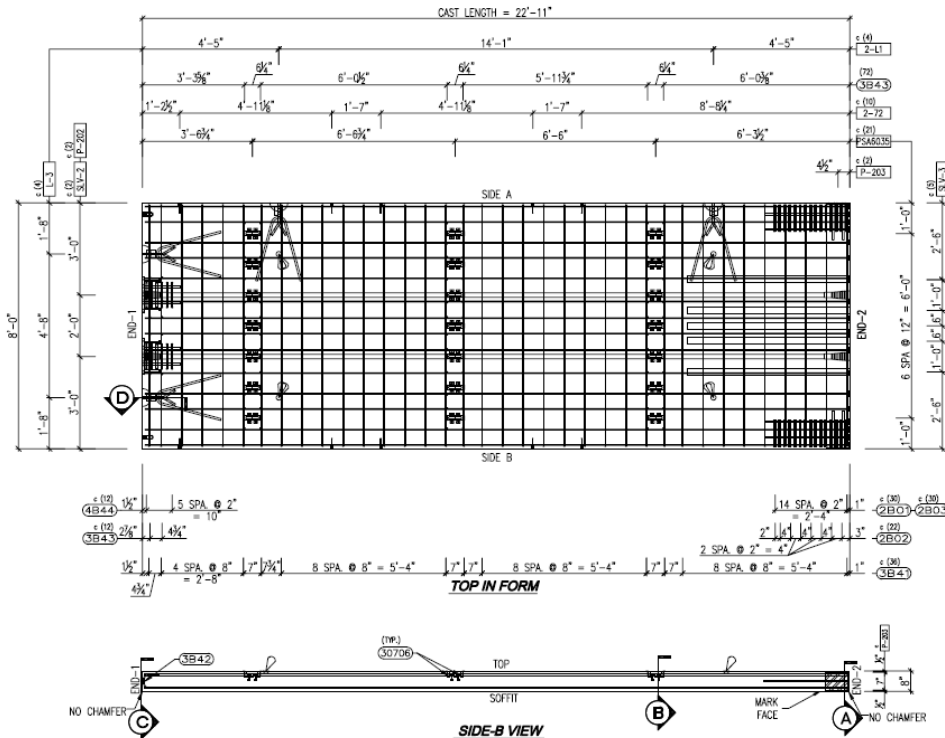
Fig. B4-4. Unbonded post-tensioned precast rocking wall.

The structure lateral force resisting system (LFRS) was unbonded post-tensioned (PT) precast rocking walls, oriented in the transverse (loading) direction, located at each end of the structure. The use of the PT rocking walls permitted repeatability in the earthquake testing of the structure without incurring

C-A-190

significant damage or degradation to the shear walls. The PT rocking wall detail is shown in Fig. B4-4 and includes: (1) a pair of unbonded post-tensioning tendons (5 0.5″ G270) offset from the center which is passed through the wall and ducts in the outrigger beam and were anchored by wedge anchor plates beneath the beams and were mounted on 100-ton hollow core plunger jacks that were positioned above the wall ducts.; (2) a pair of mild reinforcement energy dissipation (ED) #7 bars in the grout duct which is extended 6′ from the wall base into the wall for development length purpose (Although five ducts are shown at bottom, only two of them will be grout for each test. Other bars in other ducts are leaving as ungrouted and served as replacement when the current grouted bars fatigue after multiple cycle of loading). The diaphragm-to-LFRS connection is provided by JVI PSA connectors (See Fig. B4-5), that provide in-plane shear transfer, but allow the vertical motion associated with the precast walls rocking. The structure was braced with cables in the longitudinal (non-loading) direction.
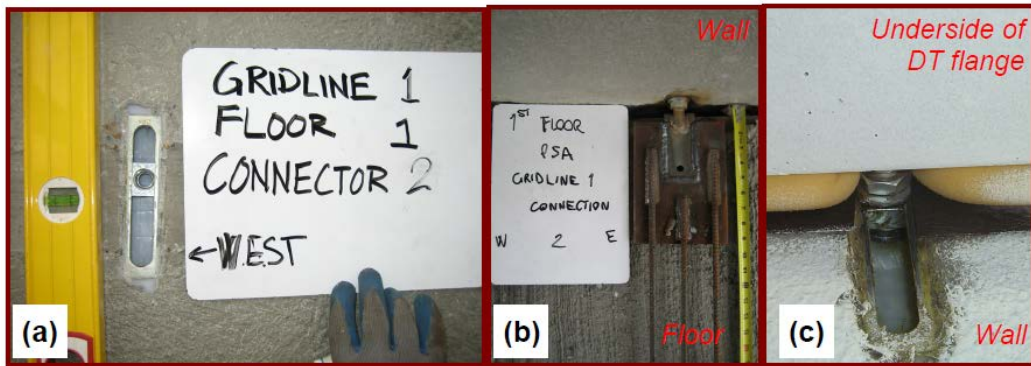
Fig. B4-5. Shake table test setup – wall-to-floor connection (after Schoettler 2010): (a) vertical slot in wall, (b) insert tab welded to floor embed plate, and (c) underside view of slotted connection.

The structure includes the precast gravity system columns, spaced at 16 feet in the longer span and 12 feet in shorter span (See Fig. B4-6). These columns support spandrel beams on one face (See Fig. B4-6), representing a perimeter structure face, and L-beams on the other face (See Fig. B4-7), to represent an interior beam line. The columns are connected to the foundation beam using 4 3/8″ nuts (See Fig. B4-8) and use a ferrule rod connection between the column and beams (See inserts in Fig. B4-6 and Fig. B4-7). These latter connections provide the ability for free relative (sliding) displacements of the beams along the column face.
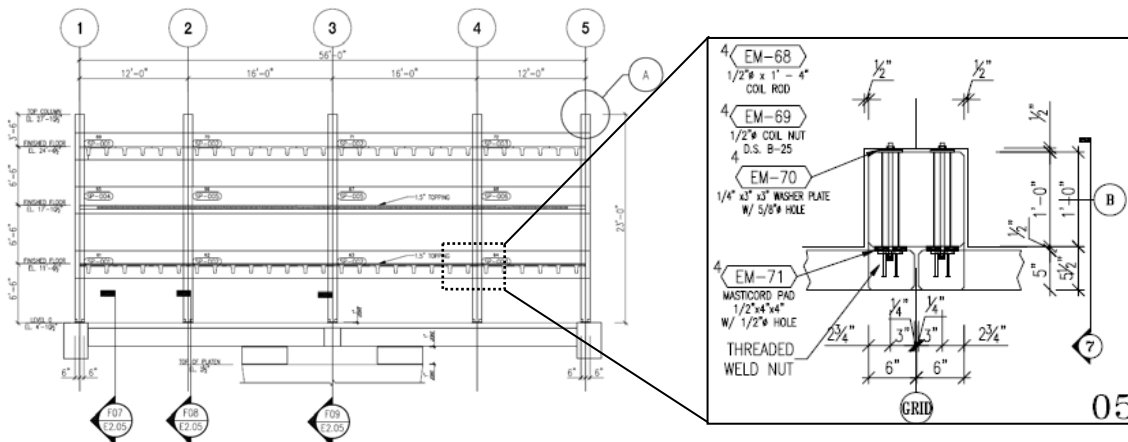
Fig. B4-6. Elevation in spandrel side.
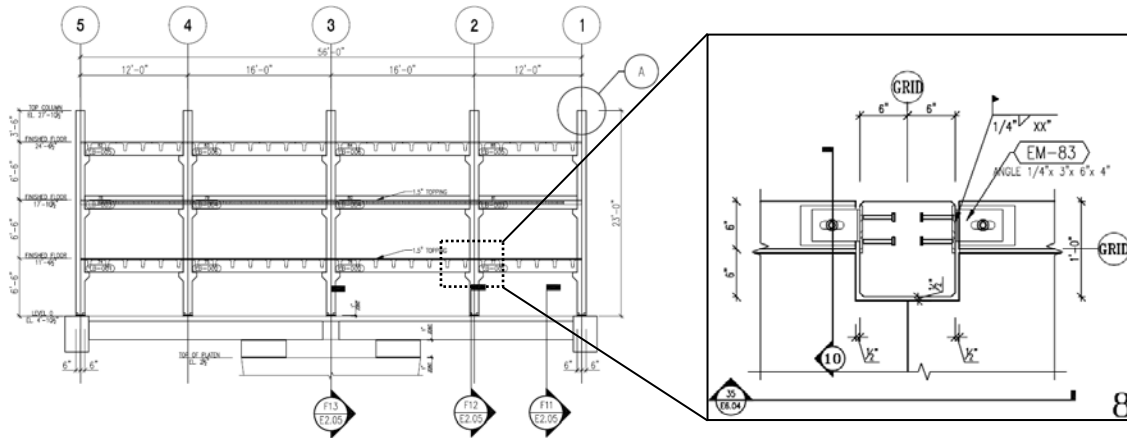
Fig. B4-7. Elevation in L beam side.
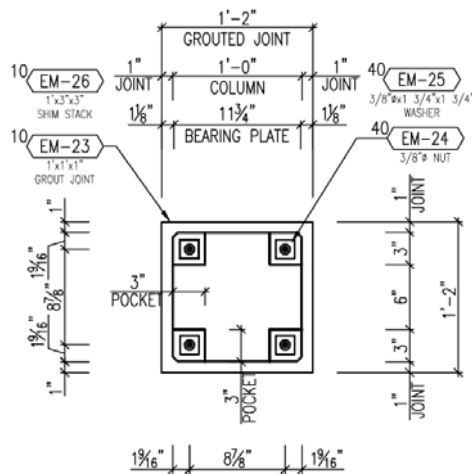
Fig. B4-8. Column base detail.

B4.1.2 NEES@UCSD Shake Table

The use of the NEES@UCSD shake table was an important aspect of the testing program due to the size of its platen (25′ x 40′). The large size of the shake table permits the testing of a structure with reasonably sized and realistically configured precast units and precast connectors. This situation is desirable for adequately demonstrating the performance of the precast diaphragm systems, as opposed to a small scale test structure with simple precast units and idealized connectors that would be required on most other existing shake table tests. Such "toy" structures would not directly reproduce the configurations, anchorages, or construction tolerances of actual precast concrete structures. The NEES@UCSD shake table is the largest shake table in the U.S. Nevertheless: (1) the test structure still had to be scaled (to half-scale); and (2) the half-scale test structure still did not fit on the table. The reason the structure did not fit is that to study diaphragm action, a large dimension is required *transverse* to the direction of loading. Most shake table testing requires a significant dimension in the direction of loading (e.g. a moment frame), and thus the larger platen dimension is in this direction. Accordingly, a special two-way post-tensioned outrigger foundation on special sliders was designed and constructed (See Fig. B4-9). The foundation components totaled 536-kip and included precast outrigger beams, support beams upon which a 7-in. thick cast-in-place topping was placed, and spacer blocks that sat directly on the shake table. Post-tensioning bars provided much of the interconnection between precast components and locked the foundation to the table by clamping the foundation structure to the table with 7.2 million pounds of initial post-tensioning force. The 7-in. cast-in-place topping created a very stiff and strong diaphragm that

C-A-192

was designed to remain uncracked under the large in-plane inertia forces, thus ensuring consistent boundary conditions for the building throughout testing. Hydrostatic slider bearings, with a friction coefficient below 1% were employed to isolate the outrigger beam from the ground surrounding the shake table. The bearings slid on mirrored-finish stainless steel plates, see Figure insert in Fig. B4-9. The low friction minimized the effect of perturbing the input energy by introducing undesirable rectangular lateral force-displacement hysteresis. Decompression of the slider bearing was undesirable because the pressure of the oil film between the slider and stainless steel sliding surface would be lost and the detrimental effects of impact after uplift. Therefore, a minimum operating pressure was identified and ensured before testing via low profile 400-kip capacity hydraulic jacks that were sandwiched between the slider and the underside of the beam. The pressure of each jack and, for redundancy, each bearing was monitored separately.
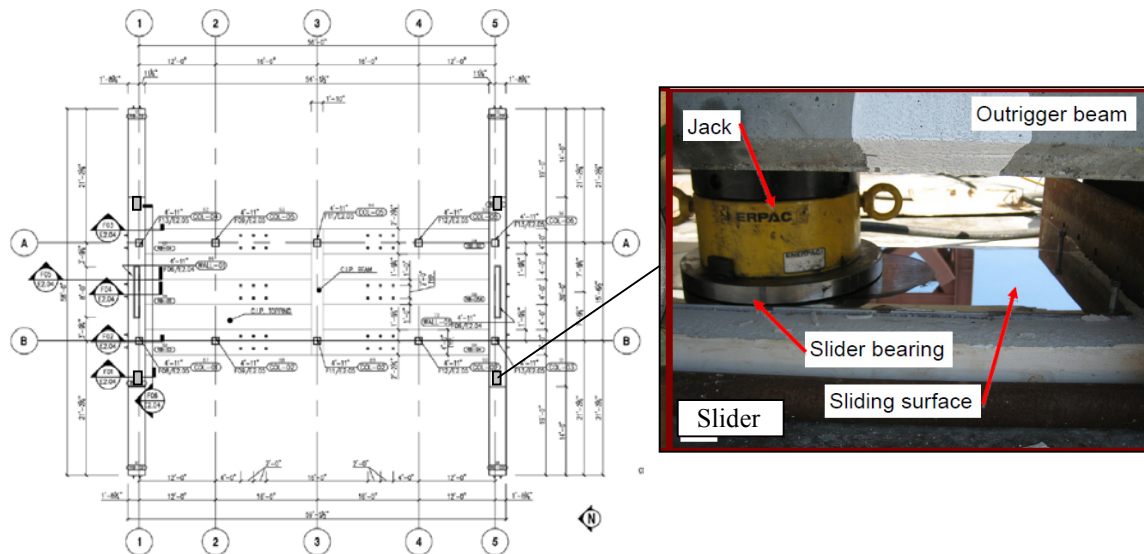
Fig. B4-9. Foundation detail (modified from Schoettler 2010).

B4.1.3 Ground Motions

Ground motions were selected for three sites with low, moderate, and high seismic hazard. Knoxville, TN, Seattle, WA, and Berkeley, CA were deemed representative of low, moderate, and high hazards, respectively. The Berkeley site's seismic setting included a possible rupture on the Hayward fault resulting in near-fault ground motions. A test protocol of increasingly more demanding ground motions was used. Increasing demands as testing progressed ensured that a large number of tests could be completed, allowing sufficient data sets to be gathered for computer model validation. Different ground intensities were applied by ordering the ground motions for the sites according to increasing seismic hazard.

The test sequence called for a design basis earthquake (DBE) for the Knoxville site, followed by a DBE for Seattle, a DBE for Berkeley, and a maximum considered earthquake (MCE) for the Berkeley site. The representative ground motions selected for those events came from the 1979 Imperial Valley and 1989 Loma Prieta earthquakes. The acceleration time histories were scaled to match target response spectra at 5% damping for the representative site (See Fig.B4-10). Table B4-1 identifies the historic ground motions used and applicable scaling factor.
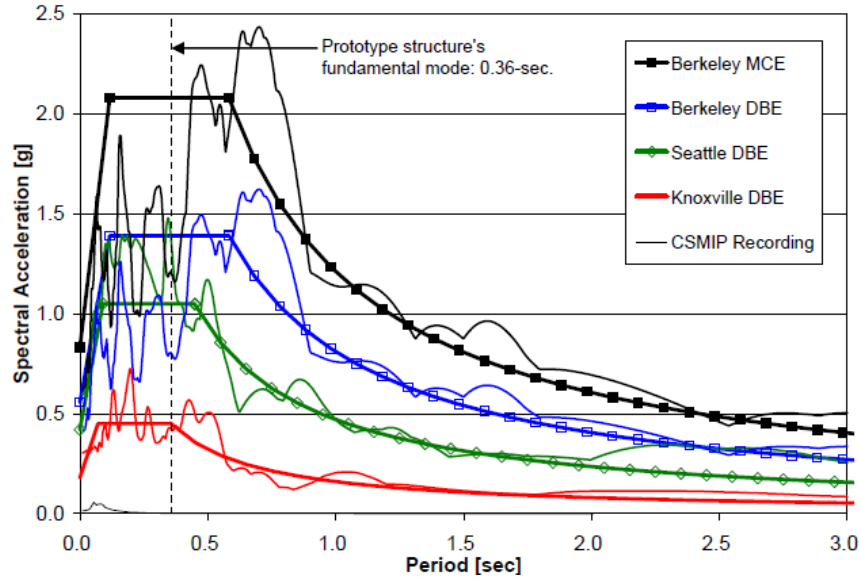
Fig. B4-10. Acceleration response spetrum (after Schoettler et al. 2009).

Table B4-1. Test program matrix

Test #	SDC	Site	Target Level	Historic earthquake	Scaled PGA (g)
1	C	Knoxville (KN)	DBE	1979 Imperial Valley	0.30
2	D	Seattle (SE)	DBE	1979 Imperial Valley	0.59
3	E	Berkeley (BK)	DBE	1989 Loma Prieta	0.41
4	E	Berkeley (BK)	MCE	1989 Loma Prieta	0.61

B4.1.4 Instrumentation

Six hundred and fifty one sensors were installed on the building to capture its response. Six types of sensors were mounted on the structure to monitor accelerations, displacements or deformations, strains, and pressures. These 651 sensors are separate from the control data that added another 64 channels of comparison data. A complete list of all types of sensors is shown in Table B4-2.

Table B4-2. Instrumentation list

Sensor Types	Accelerometer	Pressure Transducer	LVDT	String potentiometers	Strain Gauge	GPS
Number	194	12	250	63	128	4

Five separate data acquisition (DAQ) systems were used to record the data including 85 channels in a mobile DAQ system from NEES at UCLA. Sampling rates for the five systems varied, but the results were post processed and resampled to a common 240 samples per second. Ten sensors came from the California Strong Motion Implementation Program (CSMIP) and recorded their response on their own automatically triggering DAQ system. A 128 channel strain gauge system from 79 UCSD's Powell's Structural Engineering Laboratory was utilized to monitor critical regions of the structure expected to undergo plastic deformation. Four channels of GPS data were recorded on a separate dedicated DAQ system, and the remaining sensors were routed to the shake table's DAQ system operated by NEES at UCSD.

A majority of accelerometers were mounted in the direction of shaking, but some were also oriented transverse to the direction of excitation or vertically. Global displacements were measured from four GPS antennas mounted on the structure with two additional antennas acting as reference receivers.

Relative deformations were captured by string potentiometers, linear voltage displacement transducers (LVDT) - see Figure B4-11a, and linear potentiometers. Critical reinforcing bars were strain gauged to monitor their deformation history through tests. These included the chord reinforcement, ductile mesh, and wall energy dissipation bars. Concrete strain gauges were deployed on the toes of one wall to capture compressive strains as the walls rocked. Strain gauge DAQ settings corresponded to saturation at 0.05 strain.

(a) Displacement transducers across a double tee joint

(b) Pressure transducer measuring PT force in a wall jack

(c) Photo documentation of joint layout
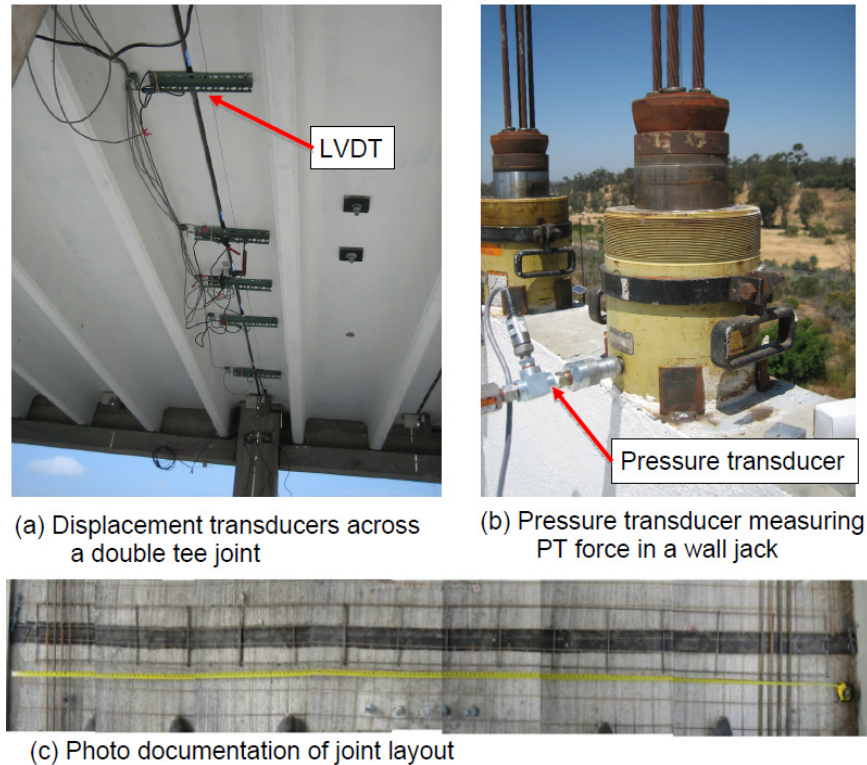
Fig. B4-11. Shake table test instrumentation examples (after Schoettler 2010).

Pressure transducers were installed on the four slider bearings and four 200-ton jacks under the outrigger beams. These provided the dynamic response of the pressure change in the bearings during testing and allowed the computation of overturning moment. An additional four pressure transducers were installed on the jacks on the walls, see Figure B4-11b. These measured the force in the post-tensioning tendons during the tests.

Fourteen cameras recorded shaking during the earthquake simulations. Eleven cameras were mounted on the structure to help with visualization and interpretation of data. They captured crack opening and movement in the structure. Three additional 80 cameras recorded the overall structural response. Extensive photo documentation provided as-built construction details - see Figure B4-11c, instrumentation orientation, crack propagation, and damage.

Three dimensional sensor coordinates were essential for results analysis. Prior to testing, the sensors' locations were measured and mapped in painstaking detail. These were transformed into tabulated data and the graphical representation for each test. A sample of mapped locations for the sensors on top floor is shown in Fig. B4-12.
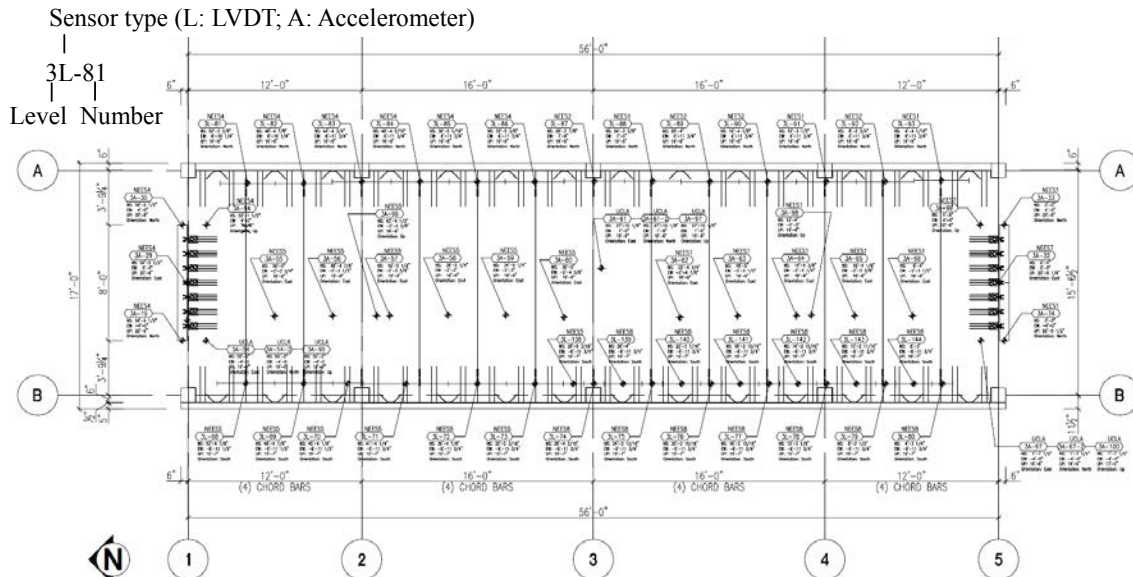
Fig. B4-12. Instrumentation map for top floor (modified from Schoettler 2010).

B4.2 TEST STRUCTURE DESIGN

The design procedure involved an assumed prototype structure with typical precast units and standard connection details whose dimensions depended on limitations set by the scale factor and test setup. Based on test site restrictions, the longitudinal diaphragm dimension of the test structure was set to 54-ft. With a diaphragm aspect ratio of 3.5, the test structure was developed with a scale factor 0.5 standard precast geometries were used in the design of this test structure. The test structure is designed for a SDC E site, Berkeley CA (S_s= 2.08, S_1= 1.92) for soil class C. The seismic design parameters for post-tensioning wall adopt the values (R= 6, Ω_o= 2.5 C_d = 5) for the special RC shear walls. The structure design period (T=0.44s) is determined as the upper limit period according to Sec. 12.8.2 of ASCE-7 (2005).

B4.2.1 LFRS Design

The displacement based design procedure for the hybrid rocking wall was reported by Belleri (2009). System design strengths based on ASCE-7 (2005) requirements were met in this procedure. Overturning moment capacity accounted for contributions from the walls only as the column bases were modeled as pinned. Design shear forces were checked and adjusted according to nonlinear dynamic time history analyses.

Table B4-3. Average initial post-tensing force in the wall (after Schoettler 2010).

Test	Axial force on the wall	Axial stress on the wall	Tendon stress
	[kips]	[ksi]	f_{si}/ f_{pu}
Knoxville (KN) DBE	50	0.13	24%
Seattle (SE) DBE	76	0.2	37%
Berkeley (BK) DBE	74	0.19	36%

The primary performance based objectives were to achieve a maximum base rotation at two performance levels and ensure gap closure. Maximum base rotation at the Berkeley MCE event was established as 0.0274 rad. A maximum base rotation of 0.018 rad was targeted for the Berkeley DBE. With mild steel reinforcement used to increase energy dissipation, gap closure can only be assured if the

initial posttensioning force can overcome the mild steel reinforcement's ultimate strength. This ensures no residual deformation at the base of the wall. These intertwined design considerations include the amount of mild steel reinforcement, the debonded length of this reinforcement for strain distribution, and quantity of post-tensioning steel for the wall selected wall configuration.

For the Knoxville test, the energy dissipating mild reinforcing bars at the base of the wall were omitted. A partial grouting of one bar in the South wall was performed, but the grout was flushed with water before setting. The levels of initial post-tensioning in the walls are provided in Table B4-3. The initial axial force in the Knoxville DBE test was lower than that for the other tests to account for the reduced demands at this site.

B4.2.2 Diaphragm Design

The diaphragm design follows the concept of the design methodology. A RDO design option is selected for the diaphragm design. The current code diaphragm design force (F_{px}) is determined based on ASCE-7 2005 as indicated in Table B4-4. The diaphragm baseline design force (F_{Dx}) is adopted as the maximum F_{px} at top floor and is applied to all the floors: $F_{Dx} = \max (F_{px}) = 51$ kips.

Table B4-4. Diaphragm design force according to ASCE-7 2005.

Floor	h_x [ft]	w_x [kips]	$w_x h_x^k$	c_{vx}	F_x [kips]	F_{px} [kips]
3	19.5	73	1429	0.479	51	**51**
2	13	80	1043	0.350	38	46
1	6.5	79	510	0.171	18	44
Sum:		232	2983	1.0	107	

Diaphragm force amplification factor $\Psi_R=1.38$ is used for the diaphragm design. At the time of the shake table test design, values for these factors did not exist and thus 3D nonlinear transient dynamic analysis was used to calibrate this design factor specifically for the shake table test structure. Since the design factors calibrated unique for shake table test structure, a larger chord deformation demand (0.5″) is selected as the RDO flexure design target (See Fig. B4-13 for maximum chord demand in DBE occurs at top floor and MCE occurs at 1st floor) instead of 0.4″ used in the design procedure (see PART 1). Furthermore, this would allow the examination of the flexure limit state of diaphragm reinforcement under earthquake.
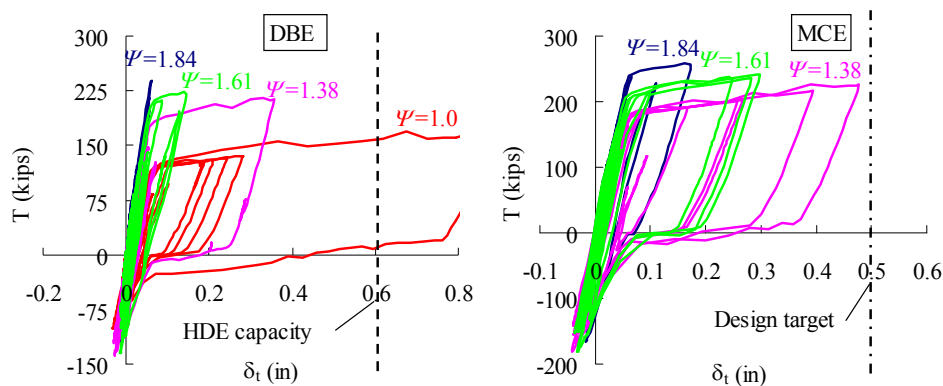
(a) Chord response at midspan of 3rd floor;   (b) Chord response at midspan of 1st floor.
Fig. B4-13. Diaphragm force amplification factor calibration for shake table test structure.

Diaphragm shear overstrength factor Ω_v=1.38 is used for the diaphragm design, which is calibrated to keep the diaphragm shear response remain elastic under MCE using the 3D nonlinear transient dynamic analysis as well. Figure B4-14 shows a parametric plot for the maximum diaphragm shear sliding demand with different design shear strength (combination of diaphragm force amplification factor and shear overstrength factor). As seen in Fig. B4-14, in order to keep the diaphragm in elastic under MCE, the mutilation of Ψ_R and Ω_v need to be around 1.8~2.1. As the Ψ_R has been determined as 1.38, the shear overstrength factor is selected as 1.38 to produce $\Psi_R * \Omega_v$ = 1.9.
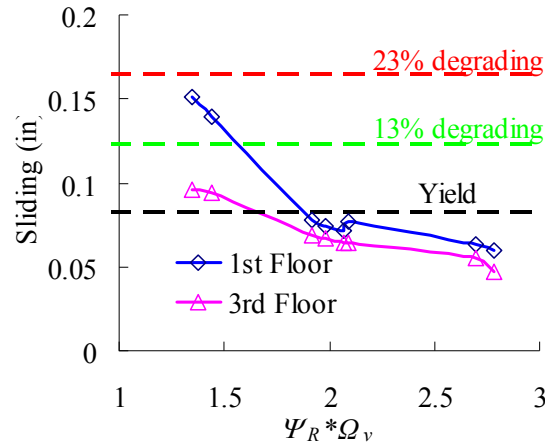
Fig. B4-14. Diaphragm shear overstrength factor calibration for shake table test structure.

The selected diaphragm force amplification factor and shear overstrength factor for the shake table test structure design are not identical to the values calculated from the design equations (Eqn. 5 and 8 in PART 1) proposed in the design procedure (See Table B4-5).

Table B4-5. Diaphragm design factors.

Case	Ψ_R	Ω_v
Shake table test structure	1.38	1.38
Design procedure	1.35	1.53

After amplified the diaphragm baseline design force by Ψ_R, the diaphragm internal forces (shear and moment) are calculated based on the simple supported beam given the simple layout nature of shake table test structure. Table B4-6 shows the diaphragm design forces for shear critical joint (1st diaphragm joint from the shear wall) and the flexural critical joint at midspan.

Table B4-6. Diaphragm design forces.

Floor	F_{Dx}	$\Psi_R F_{Dx}$	Shear critical joint		Flexural critical joint	
			V_u	M_u	V_u	M_u
	[kips]	[kips]	[kips]	[kip-ft]	[kips]	[kip-ft]
3	51.4	70.9	30.4	111.5	10.1	496.5
2	51.4	70.9	32.9	121.6	10.1	496.5
1	51.4	70.9	30.4	111.5	10.1	496.5

Table B4-7 shows the diaphragm reinforcement design for the shear critical joint. Table B4-8 shows the diaphragm reinforcement design for flexural critical joint. Also noticed, the diaphragm design

used for the shake table test structure does not use the interaction equation (Eqn. 10 in PART 1) rather it designs the diaphragm joint to resist the moment and shear independently. Chord reinforcement cut-off or the spacing varying of ductile mesh steel is not applied to the shake table test structure. The shear connector at top and 1st floor varies the spacing once at 5th joint (refer to Fig. B4-2).

Table B4-7. Diaphragm reinforcement design for the shear critical joint.

Floor	#3 chord *			Ductile mesh W4.9xW4.9 **			Shear connector ***			V_n	Ω_v	ϕM_n
	t_n/A (ksi)	v_n/A (ksi)	#	t_n/A (ksi)	v_n/A (ksi)	s (in)	t_n (k)	v_n (k)	#	[kips]		[kip-ft]
3	60	12	6	Not used			0.78	3.25	8	42.0	1.38	509
2	60	12	2	54	22	6	Not used			45.3	1.38	507
1	60	12	4	54	22	12	2.25	3.25	5	46.9	1.54	509

*Bonded chord is used for all three floors.

** Design strength is determined based on testing (Naito and Ren 2008).

*** Half-scale JVI Vector for top floor and #2 topped Hairpin for 1st floor. Design strength is determined based on testing (Naito and Ren 2008).

Table B4-8. Diaphragm reinforcement design for the flexural critical joint.

Floor	#3 chord *			Ductile mesh W4.9xW4.9 **			Shear connector ***			V_n	Ω_v	ϕM_n
	t_n/A (ksi)	v_n/A (ksi)	#	t_n/A (ksi)	v_n/A (ksi)	s (in)	t_n (k)	v_n (k)	#	[kips]		[kip-ft]
3	60	-	6	Not used			3.1	13	5	16.3	1.60	503
2	60	12	2	54	22	6	Not used			45.3	4.48	507
1	60	12	4	54	22	12	9	13	4	43.7	4.31	508

* Unbonded chord is used for top floor and bonded chord is used for other floors.

** Design strength is determined based on testing (Naito and Ren 2008).

** Half-scale JVI Vector for top floor and #2 topped Hairpin for 1st floor. Design strength is determined based on testing (Naito and Ren 2008).

Diaphragm-to-LFRS connector (PSA connector refer to Fig. B4-2) is designed to resist the amplified shear design force ($V_u = \Psi_R F_{Dx}/2 = 35.5 kisp$) using the following equation:

$$n = \frac{\Omega_v V_u}{\phi_v v_n} = \frac{1.38 \times 35.5}{0.75 \times 10} = 6.5 \approx 7$$

where v_n is the shear strength of PSA is determined from tests (Shaikh and Gehlhoff 2007).

Industry standard connector (#2 Hairpin) is placed at one per very panel to connect the diaphragm and spandrel/L beam (refer to Fig. B4-2).

The final selected diaphragm reinforcement is shown in Fig .B4-2 and the diaphragm reinformcent detailing is shown in Fig. B4-3.

B4.2.3 Gravity System Design

Five columns on each side of the structure created four bays of precast concrete beams. Spandrel beams were 3' high and 5" thick with a 6"n. ledge for the floor elements. A similar size ledge was present in the ledger beams which were 6" thick and 19.5" tall.

The pocket columns (Fig. 4B-6) in the side of spandrel beam measured 15.5" by 12" and the corbel column (Fig. 4B-7) in the side of L beam dimensions were 12" by 12". Well confined columns with #3 transverse hoops at 2.5" ensured the seismic integrity of the gravity system and eliminated a possible shear failure. A prestress force of 15-kip coupled with eight #5 bars for the longitudinal

reinforcement in the columns. The 0.5" 270ksi prestressing strand was stressed to $0.36f_{pu}$ which applied an average stress of 104psi on the 12" square concrete column. Column anchor bolts on the ten columns were specified as 3/8"diameter A36 threaded rod in an attempt to minimize the shear capacity of the gravity load system and maximize the floor flexibility (see Fig. 4B-8).

B4.3 TESTING SEQUENCE

The shake table test specimen has subjected to 16 strong motions in a sequence of increase of earthquake intensity. This test sequence is summarized in Table B4-9. Also noticed, two white noise and two small amplitude earthquake input tests have been performed before and after each test shown in Table B4-9 in order to track the structure characteristics before and after major tests.

As listed in the last column of Table B4-9, not all the test under strong motion is successful. Several failures are observed in the tests in which the following two failures have the most impacts to the shake table test: (1) dry chord fracture at 3rd floor midspan under SE DBE ground motion for test 4-6. (2) post-tensioning (PT) strand rupture under BK MCE ground motion for test 9.

Table B4-9. Shake Table test sequence and major event.

Test #	Test ID	EQ Intensity	PT Stress (ksi)	Major Event/Failure
1	**KN-DBE 1**	**KN-DBE**	**70.2**	-
2	KN-DBE 2	KN-DBE	70.2	-
3	KN-DBE 3	KN-DBE	70.2	-
4	SE-DBE 1	SE-DBE	94.5	Chord fracture at 3rd floor
5	SE-DBE 2	SE-DBE	94.5	Chord fracture at 3rd floor
6	SE-DBE 3	SE-DBE	94.5	Chord fracture at 3rd floor and chord buckling at 2nd floor
7	**SE-DBE 4**	**SE-DBE**	**94.5**	-
8	**BK-DBE 1**	**BK-DBE**	**94.5**	Partial PT failure in south wall
9	BK-MCE 1	BK-MCE	94.5	Rupture of PT strand in south wall, resulting in fracture of gravity system connections
10	BK-DBE 2	60% BK-DBE	135	Anchorage failure at 3rd floor
11	BK-DBE 3	60% BK-DBE	135	-
12	BK-MCE 2	BK-DBE	135	Crack in DT at 3rd floor wall connection
13	**BK-MCE 3**	**BK-DBE**	**135**	-
14	BK-DBE 4	60% BK-DBE	135	Anchorage failure at 2nd floor
15	BK-MCE 4	BK-DBE	135	-
16	BK-MC*	BK-MCE	135	Floor unseating leading to partial collapse of 3rd floor

▭ Indicates successful test

After the dry chord failure at top floor in three tests (test 4 to test 6), two curbs are placing at top and bottom of diaphragm. This changes the top floor chord reinforcement detailing from the dry chord to the pour strip chord (See Fig. B4-15).

After the PT strand rupture under BK MCE ground motion in test 9, the PT strand initial stress has increased from 94.5ksi to135ksi. This increase of PT initial stress results in a stiffer wall which in turn typically will increase the demand in diaphragm. Thus for the rest of tests (test 10 to test 15), scaled equivalent ground motions are used to achieve equivalent DBE and MCE level diaphragm demand. The scale factor is determined from the analytical earthquake simulations (Zhang 2010) and is applied to the

original BK DBE ground motion: 0.6 for obtaining equivalent DBE diaphragm demand and 1.0 for obtaining equivalent MCE diaphragm demand. A factor of 1.5 on top of the original BK DBE (1.0 on top of the original MCE) ground motion is used in the last test (test 16) in order to test the diaphragm in an overload condition.

Among all the successful tests, four representative test (see rows in Table B4-9 with bond font) results under an increasing sequence of earthquake intensity (KN DBE, SE DBE, BK DBE and BK MCE) are selected to report in the next section.
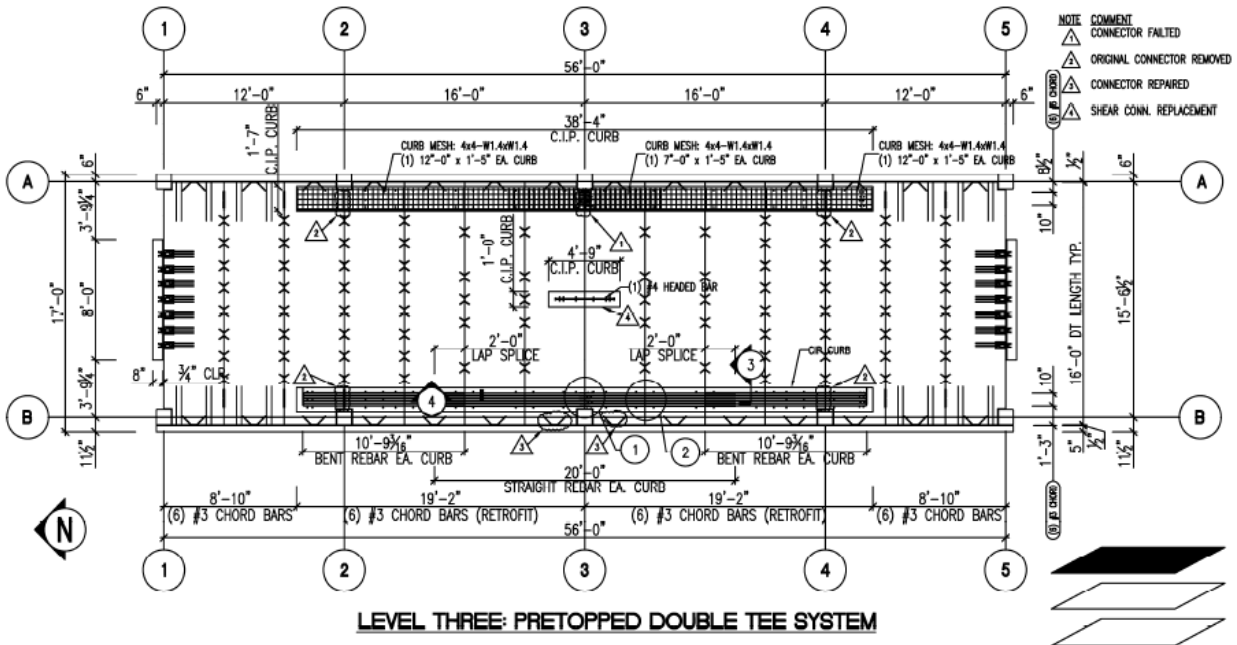
Fig. B4-15. Plan for top floor repairing after dry chord fracture in test 6.

B4.4 SHAKE TABLE TEST RESULTS

B4.4.1 Design Targets Check
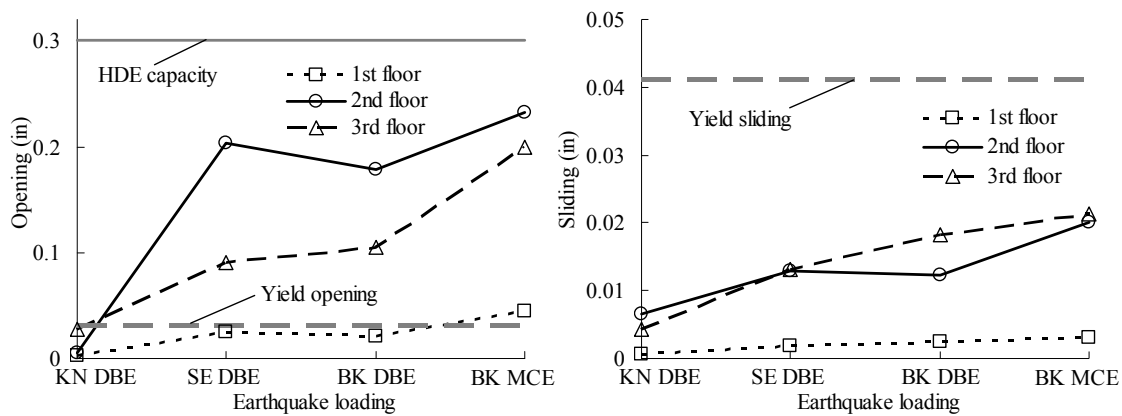
Fig. B4-16. Diaphragm joint maximum deformation demand: (a) opening (b) sliding.

Figure B4-16 show the maximum diaphragm joint deformation demand for all three floors: (a) opening and (b) sliding. This is to check if the shake table test specimen meets the design targets. As seen in Fig. B4-16a, with the increase in earthquake loading, the diaphragm joint opening increases progressively from elastic to inelastic but remained below the HDE deformation capacity of chord reinforcement. Also noticed in Fig. B4-16b, the maximum diaphragm joint sliding demand at all floors for all four level earthquake loadings safely remain elastic. These results indicate that the diaphragm design for shake table test structure meet the RDO design targets under MCE: (1) inelastic flexural response with the maximum joint opening demand less than the HDE capacity of chord reinforcement and (2) elastic shear response with the maximum joint sliding demand less than the shear reinforcement yield sliding.

B4.4.2 Post-tensioning Wall Response

In the PT walls, the most important measureable parameters are the in-plane rotation and the overturning moment at the base. The rotation of the wall is simply measured as the difference in vertical displacement at the two ends of the wall divided by the width of the wall.

$$\theta = (\delta_{end1} - \delta_{end2}) / L_{wall} \tag{Eq. 1}$$

The moment, however, is less simple to calculate. There are two methods that were considered. The first involves taking the total diaphragm force at each level and multiplying it by the respective height. However, it was decided that this is not accurate because it yields the total overturning moment of the entire structure, of which the columns have some overturning resistance (even though that resistance is neglected in design). To get the overturning moment in the wall alone, a free-body diagram (See Fig. B4-17) of the wall was cut and the forces in the ED bars (F_{ED}) and PT strands (F_{PT} calculated using the strain gauge and PT data), along with the weight of the wall, were used to calculate the overturning moment.
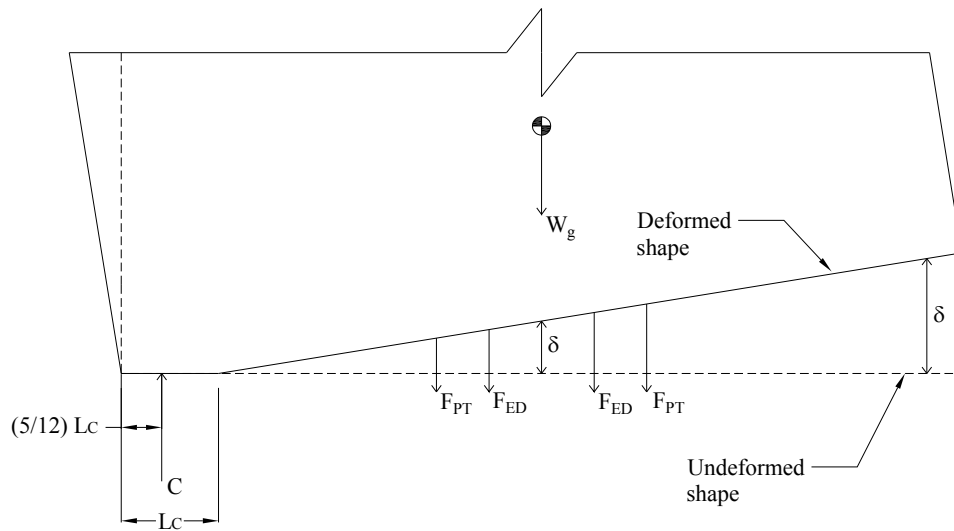
Fig. B4-16. Free-body diagram of the PT wall

The moment was taken about the point in which the compression force acted in the toe of the wall, giving the need to find the neutral axis of the wall when the rotation was at or near a peak value. To do this, displacements taken from LVDT data at the ends and at the centerline of the wall were used. It was assumed that the wall was rigid and made a straight line from the point of contact at the foundation to the end that was rocking. Therefore, the displacements at the lifted edge and the centerline LVDTs were extrapolated to the point in which the wall was touching the foundation. This point was considered the neutral axis. It was assumed that the negative displacement of the wall in the compression zone was negligible and was considered zero. Furthermore, the compression zone of the concrete was assumed to

be between an increasing linear distribution and a parabolic distribution. Thus, using the average of the centroid location of these two distributions, a location of 5/12 of the compression zone length was used for the compression force (See Fig. B4-16).

A problem that arose when using this method to calculate the overturning moment was that the data taken from the strain gages on the ED bars was often unusable. To alleviate this problem, the straight line assumption that was used to find the neutral axis location was also used to extrapolate the vertical displacement at any location along the wall; specifically, it was used to find the displacement at the location of the ED bars. This displacement was then converted to strain based on the unbonded length of the bars (18 in), which could then be converted to a force using stress-strain constitutive relationship of the bars together with the bar area (0.6 in^2 for #7 bar).

Figure B4-17 shows the wall base hysteresis response. It can be seen that the wall base rotation demand increases with the increase in earthquake intensity except that the rotation demand of the BK-MCE earthquake is lower than that of the BK-DBE because the wall has a higher initial PT stress in the BK MCE than the BK DBE as discussed in Sec. B4.3.
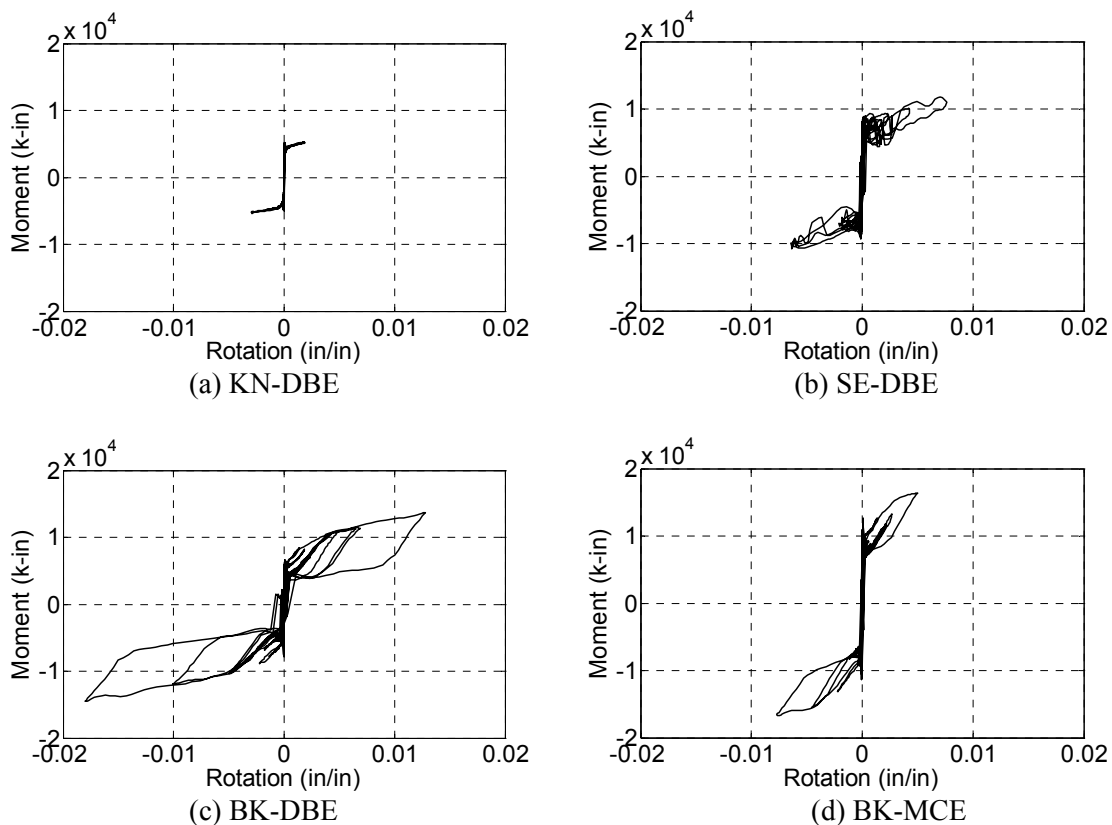
Fig. B4-17. Moment vs. rotation of PT wall.

B4.4.3 Diaphragm Response

As a main focus of the shake table test, this section will present the diaphragm response results including inertia force, internal shear and moment across the diaphragm length, deformation, inter-story drift, and joint opening.

B4.4.3.1 Diaphragm Inertia Force

Diaphragm inertia force has been calculated as the mutilation of accelerations taken from the accelerometers located at each panel in the floors (See Fig. B4-12) and the corresponding panel tributary mass including the panel, the portion of the spandrel/L beam within the panel projection, and for panels at

column lines, the gravity column tributary to each floor level. The total inertia force for each level was taken as the summation of the inertia force in each panel. Figure B4-18 shows the time histories of the diaphragm inertia force at each level truncated to include only the major shaking.
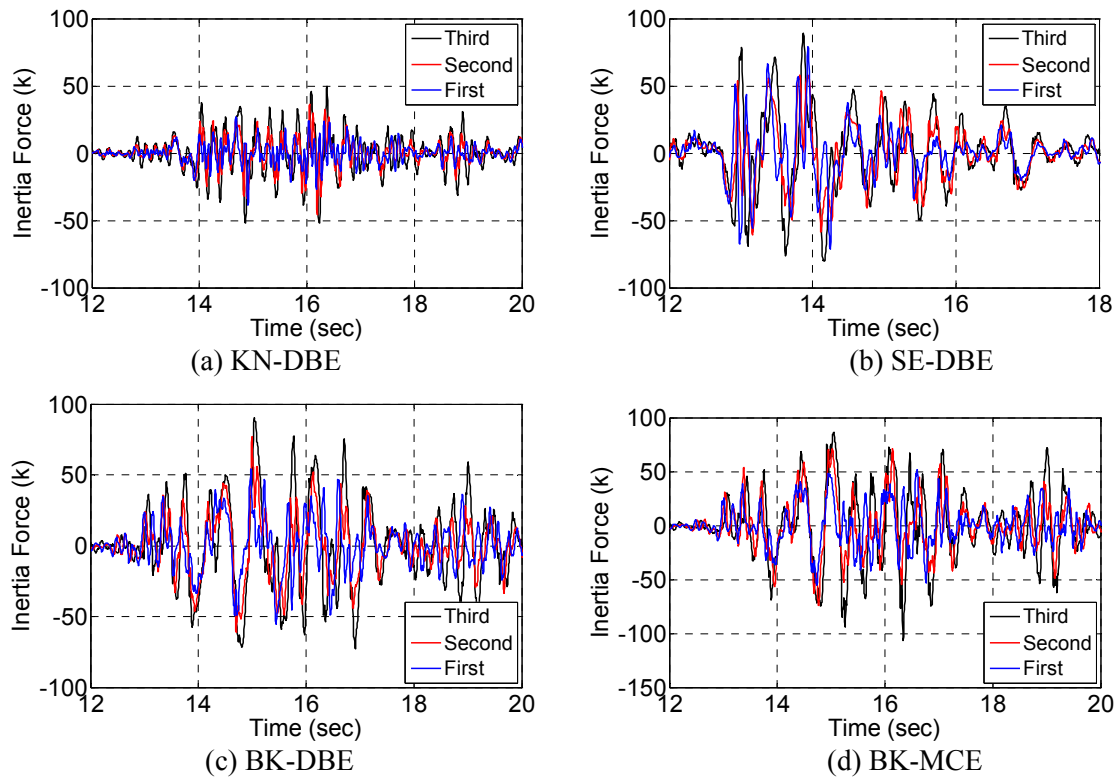
Fig. B4-18. Diaphragm inertia force time histories.

The maximum diaphragm inertia forces at each floor throughout the major earthquake tests are shown in Table **B4-10**. Generally, the force increases with floor height, with the exception being the SE-DBE, where the second floor has the lowest inertia force. Also, it should be noted that the forces seen in the SE-DBE are very similar to those of the BK-DBE.

Table B4-10. Maximum inertia force in each floor throughout tests

Floor	KN-DBE (k)	SE-DBE (k)	BK-DBE (k)	BK-MCE (k)
1	38.7	79.0	55.5	55.1
2	46.0	60.9	77.1	74.0
3	52.0	89.1	90.4	106.9

The diaphragm inertia force profile along the diaphragm span at the time of the maximum inertia force is shown in Fig. B4-19. It can be seen that the force profiles were not constantly distributed, as the design assumes. In fact, the force is considerably higher at the midspan than that at the ends due the diaphragm flexibility. This nonlinear inertia force distribution is more significant in the higher density earthquake (e.g. BK MCE) in which the diaphragm deformation is significant as well.
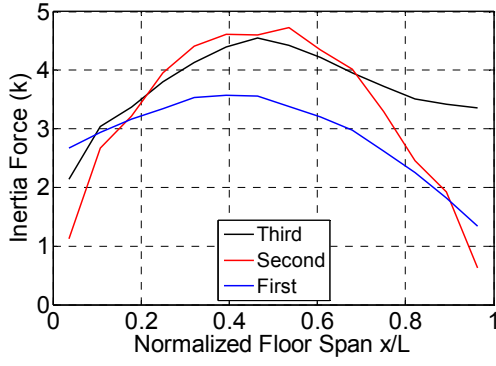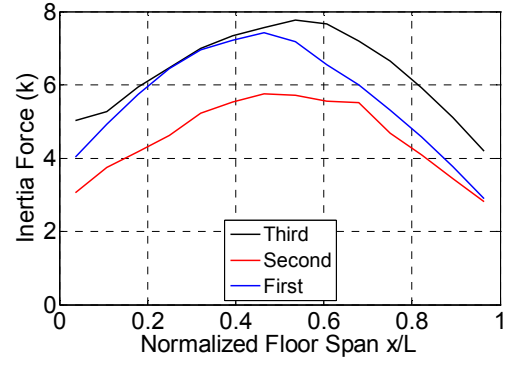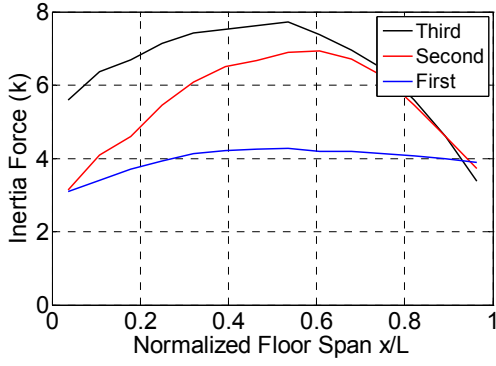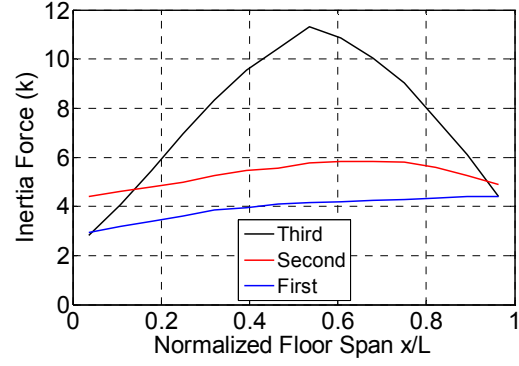
Fig. B4-19. Inertia force floor profiles for each floor.

(a) KN-DBE

(b) SE-DBE
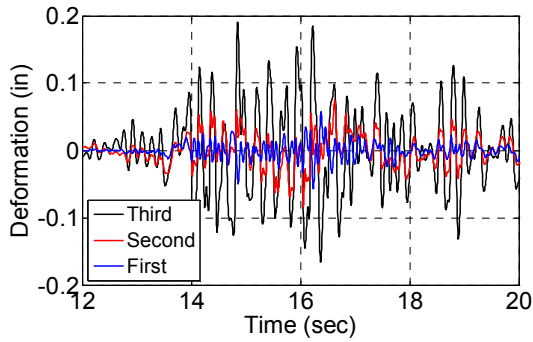
(c) BK-DBE

(d) BK-MCE

(a) KN-DBE
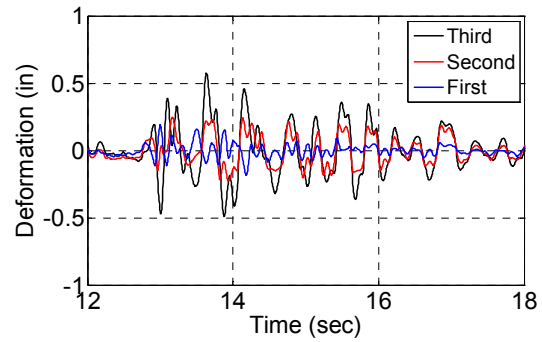
(b) SE-DBE
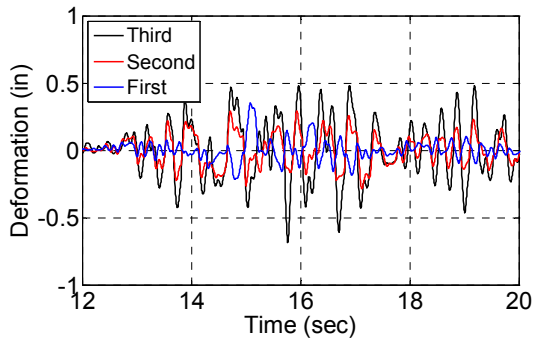
(c) BK-DBE
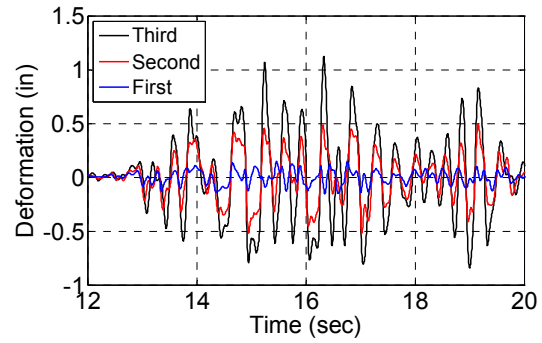
(d) BK-MCE

Fig. B4-20. Diaphram midspan deformation time histories.

B4.4.3.2 Diaphragm Deformation

Diaphragm displacements in each panel along the diaphragm span at each floor level is determined by the double integration of the accelerations taken from the accelerometers with respect to time using a constant baseline correction. The diaphragm midspan deformation is defined as the difference between the displacement at diaphragm midspan and the average displacement of two PT walls at the same floor level. Figure B4-20 show the diaphragm midspan deformaiton time histories truncated to include only the major shaking. As seen, the diaphragm midspan deformation increases with the increase of the earthquake intensity. Typically the top floor has the largest diaphragm midspan deformation demand.

B4.4.3.3 Inter-story Drift at Diaphragm Midspan

The inter-story drift at diaphragm midspan is calculated as the difference in diaphragm midspan displacement between two adjacent floors normalized by the story height. Figure B4-21shows the inter-story drift at diaphragm midspan truncated to include only the major shaking..

(a) KN-DBE   (b) SE-DBE

(c) BK-DBE   (d) BK-MCE
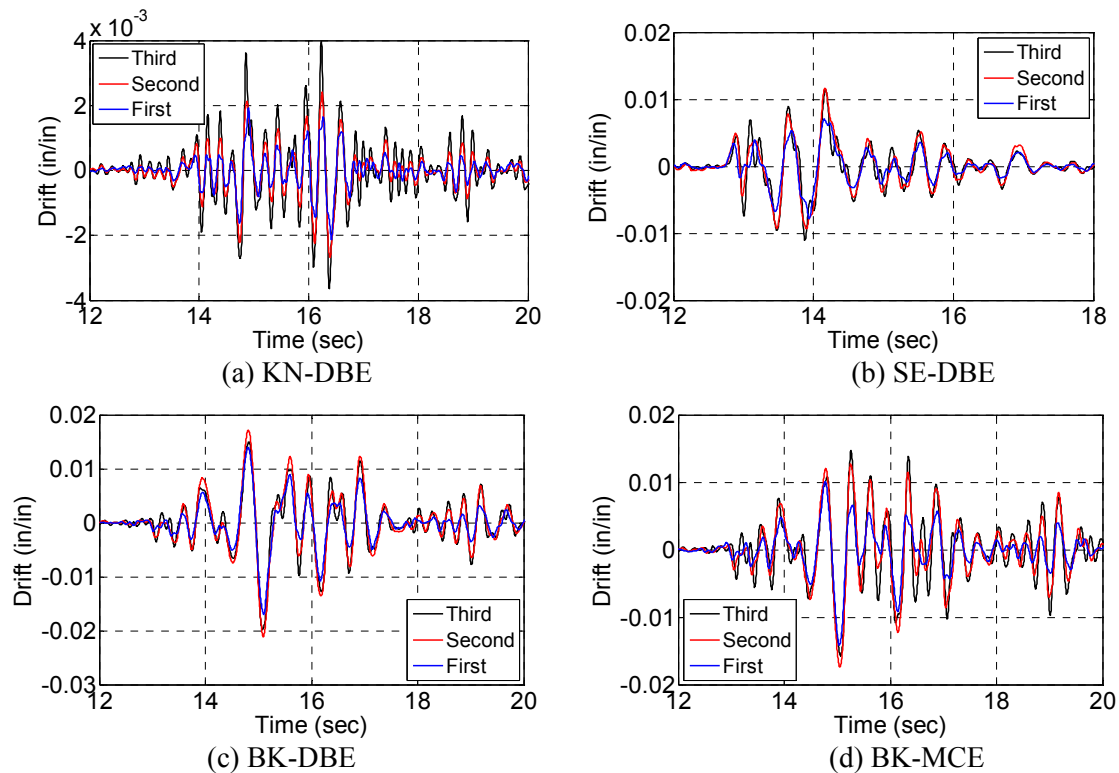
Fig. B4-21. Diaphram Mmdspan inter-story drift time histories.

B4.4.3.4 Diaphram Internal Forces

The diaphragm internal forces, shear and moment, were found using the inertia forces outlined in section B4.4.3.1. The force at each panel was divided by the panel tributary width to get a non-uniform distributed force along the entire diaphragm. This distributed force was then integrated to get the shear and moment diagram at a given time during the earthquake history. Figure B4-22 and Figure B4-23 shows the diaphragm shear force and moment diagram for each floor at time of the shear force at diaphragm end reaching maximum and at time of the moment at midspan reaching maximum respectively. As seen, diaphragm internal force increases with the increase of earthquake intensity. However the increase rate is lower between higher intensity earthquakes (from BK DBE to BK MCE) while this rate is higher between lower intensity earthquakes (from KN DBE to SE DBE) due to the yielding of diaphragm in the higher intensity earthquakes.
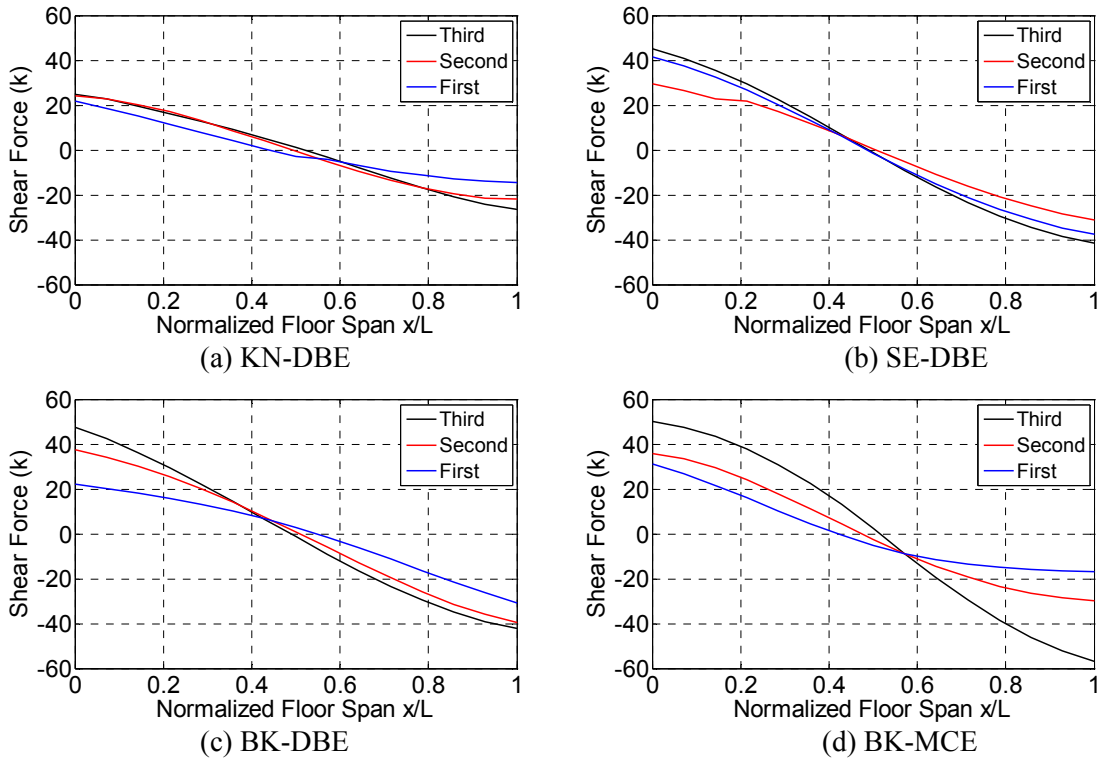
Fig. B4-22. Diaphragm shear diagrams for each floor.

(a) KN-DBE

(b) SE-DBE

(c) BK-DBE

(d) BK-MCE
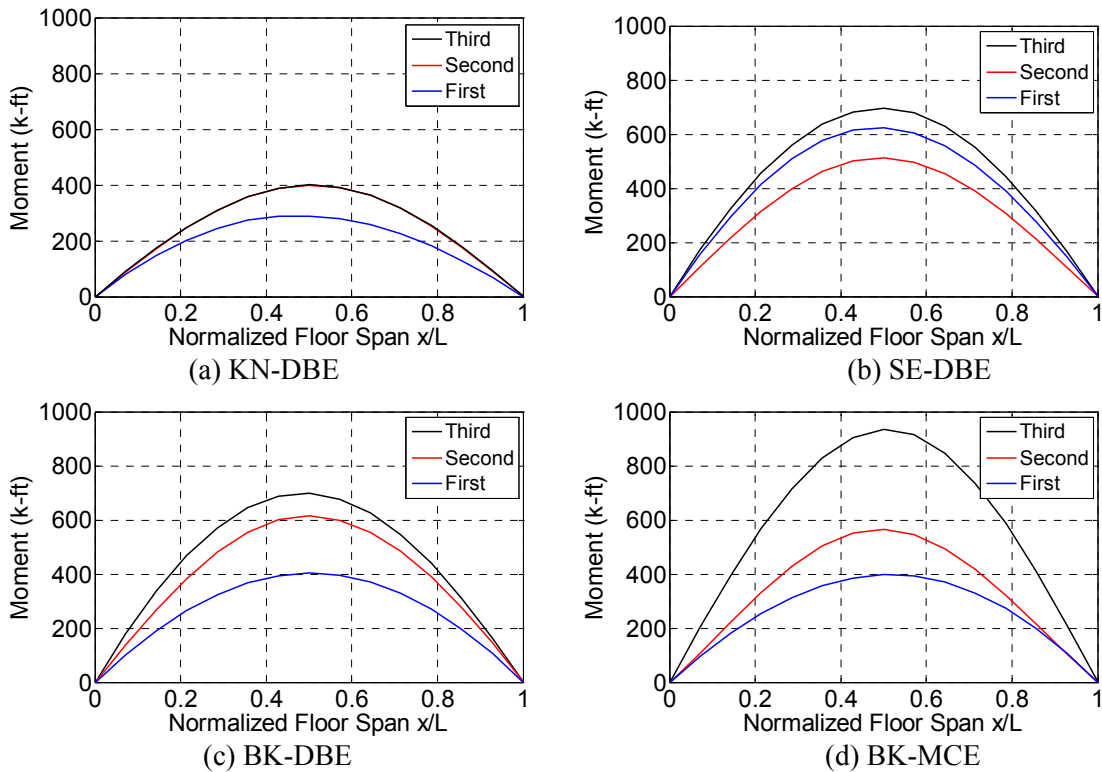
Fig. B4-23. Diaphragm moment diagrams for each floor.

(a) KN-DBE

(b) SE-DBE

(c) BK-DBE

(d) BK-MCE

B4.4.3.5 Diaphragm Joint Opening

The diaprhagn joint opening at top and bottom of chord reinforcement is taken from a measurement of the relative displacement between two adjacent panels. This relative displacement was measured directly using LVDTs (refer to Fig. B4-12). The joint opening at top and bottom chord reinforcement is also used to find the precast panel joint rotation which is taking as the difference in opening at top and bottom chord reinforcement and dividing by the distance between the centriod of top and bottom chord. Figure B4-24 shows the joint opening time history at top chord of the diaphragm midspan. The yield opening of 0.028" is shown as the dashed pink line in Fig. B4-24. As seen, diaphragm joint opening demand increases with the increase of the earthquake intensity which bring the diaphragm from elastic response region into inelastic response region.

(a) KN-DBE   (b) SE-DBE

(c) BK-DBE   (d) BK-MCE
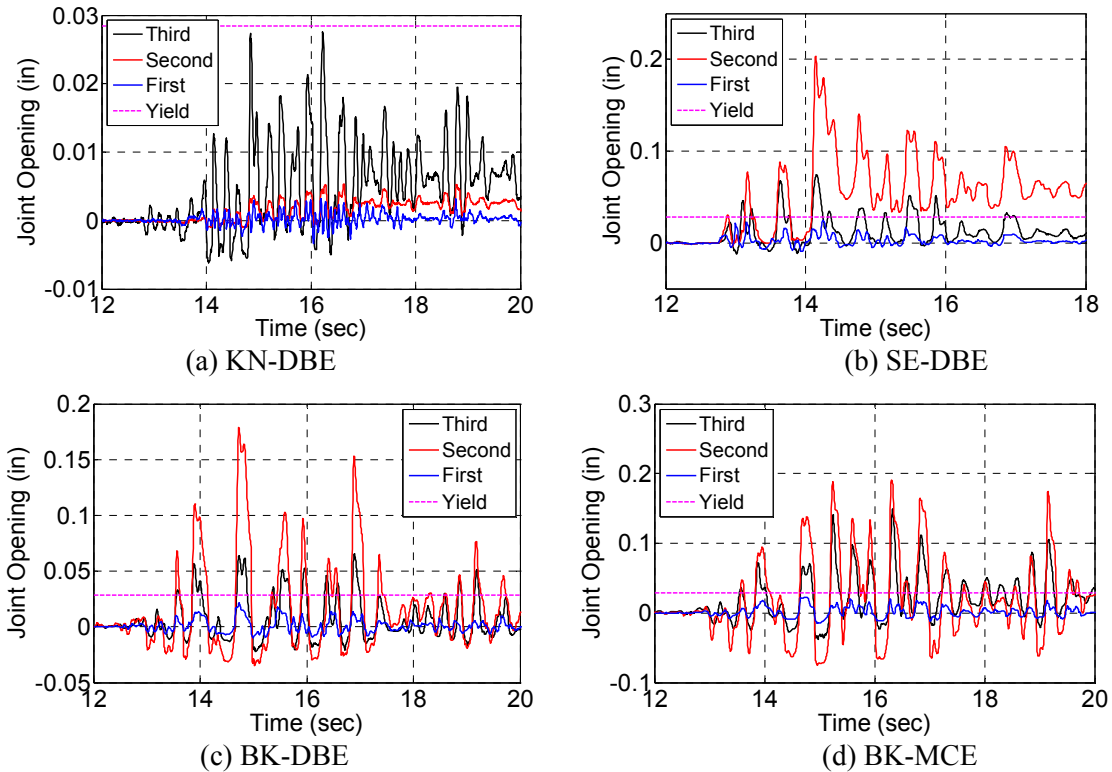
Fig. B4-24. Diaphragm joint opening time histories for each floor.

(a) elastic behavior (KN-DBE)   (b) inelastic behavior (BK-DBE)
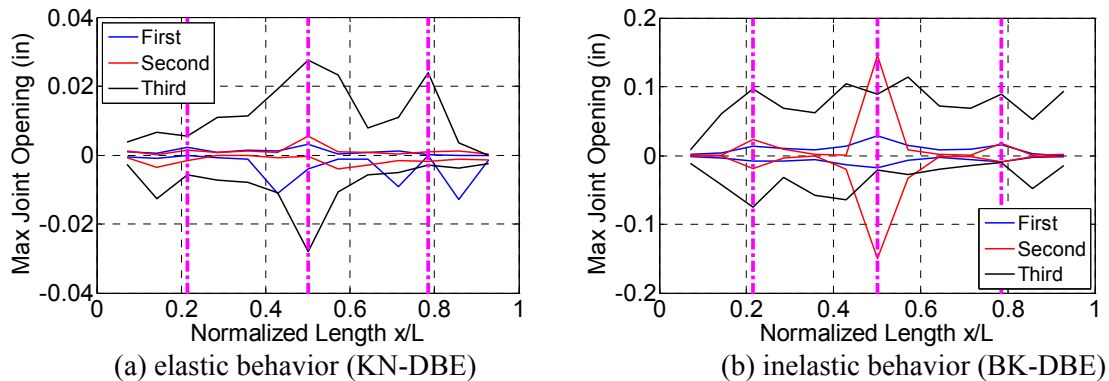
Fig. B4-25. Maximum joint opening profiles for each floor.

Figure B4-25 shows the diaphragm maximum joint opening profile at top (shown as positive value) and bottom (shown at negative value) chord reinforcement with column line indicated as dashed

pink line. As seen, due to the protection of spandrel/L beam, the diaphragm joint deformation is concentrated at the column lines where the spandrel/L beam discontinues.

B4.4.3.6 Diaphragm Hysteresis Response

Figure B4-26 shows the total diaphragm inertia force vs. midspan deformation hysteretic response. As seen, the pretopped diaphragm (top floor) has the lowest stiffness while the composite topped diaphragm (1st floor) has highest stiffness among the three floors. The stiffness of the non-composite topped diaphragm is less than the composite topped diaphragm but higher than the pretopped diaphragm.

(a) KN-DBE

(b) SE-DBE

(c) BK-DBE

(d) BK-MCE
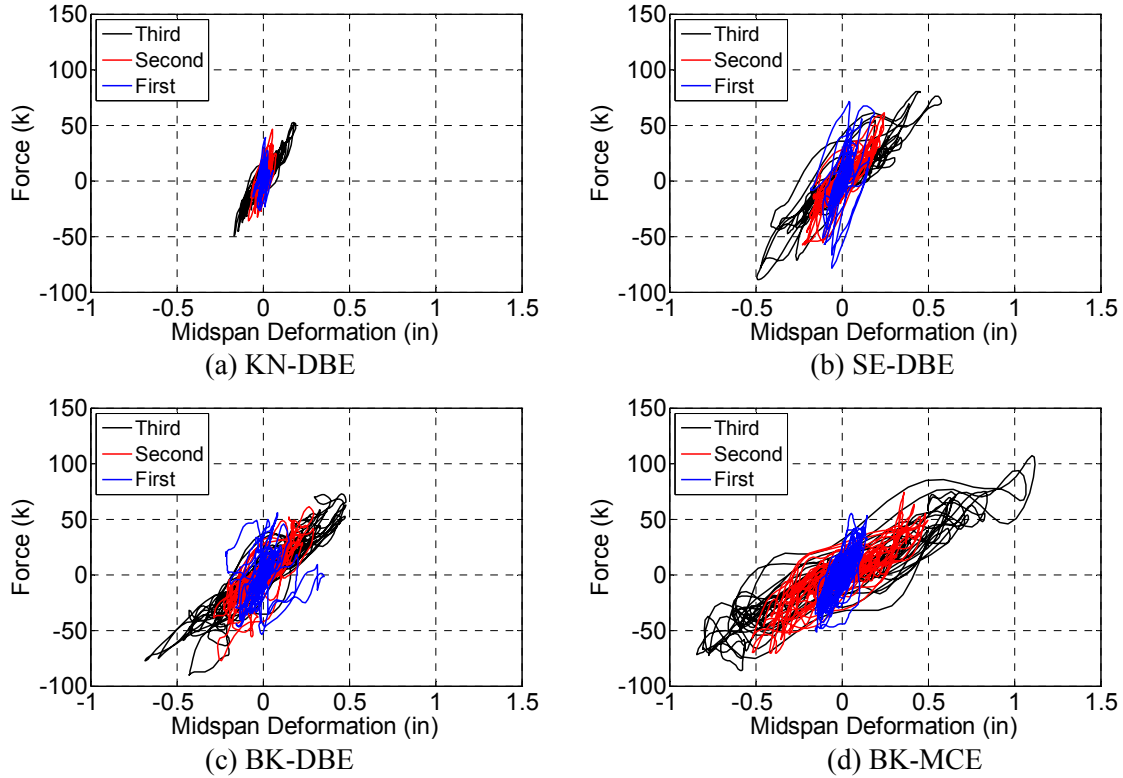
Fig. B4-26. Force vs. deformation hysteresis for each floor/

Fig. B4-27. Diaprhagm stiffness degradation throughout test sequence.

C-A-209
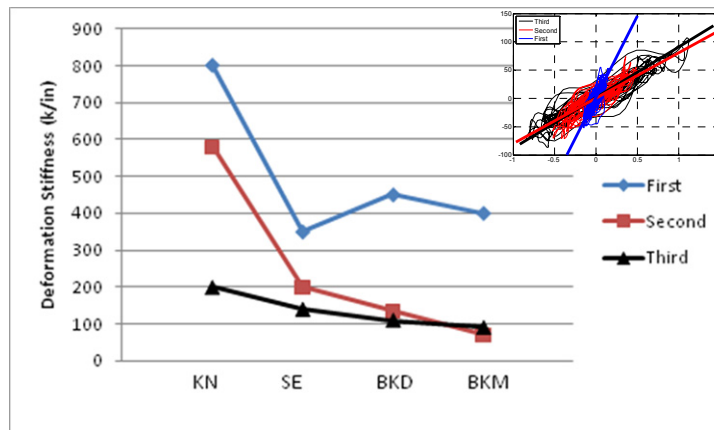
Figure B4-27 shows the diaphragm stiffness degradation throughout test sequence. It is detemined using the diaphragm hysteresis response shown in Fig. B4-26 as illustrated in insert of Fig. B4-27. The significant diaphragm stiffness in KN DBE at 1st and 2nd floor can be attributed to the cracking of the topping slab that occurred during the KN DBE test. The gradually stiffness degradation at top floor through the test sequence and at 2nd floor from SE DBE to BK MCE can be attributed to the yielding of diaphragm reinforcement and local concrete cracking in the precast panel. After the first significant stiffness degradation, the diaphragm stiffness at 1st floor almost remain unchanged which implies there is little damage and yielding in the 1st floor.

Figure B4-28 shows the diaphragm moment vs. joint rotation at the flexural critical joint (midspan). It is observed that a significant strength and stiffness degradation occurs at the 2nd floor after KN-DBE. This degradation is initiated in three tests with dry chord failure at top floor between the successful KN-DBE and SE DBE tests. The failure of dry chord at top floor changes the lateral force transfer path and imposes more demand in the 2nd floor which causes the significant yielding/fracture in the chord and ductile mesh reinforcement in the 2nd floor at diaphragm midspan joint. This yielding and fracture of diaphragm reinforcement at 2nd floor midspan results in the flexural strength and stiffness degradation at this joint.
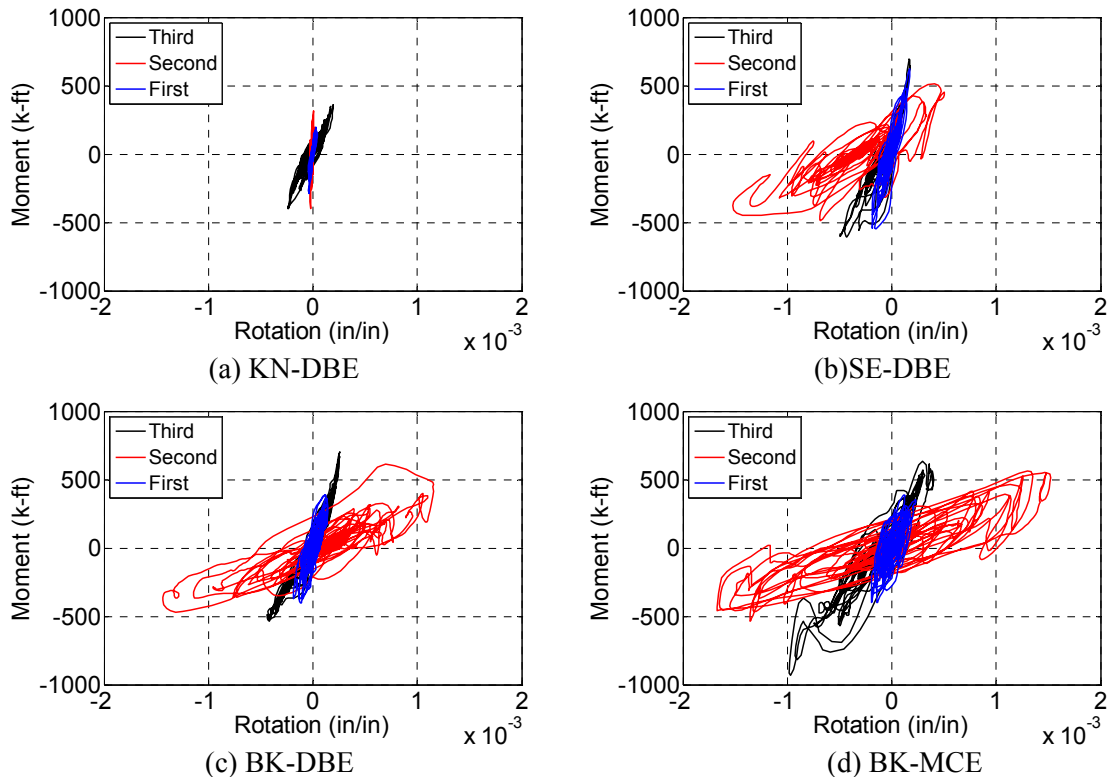
Fig. B4-28. Moment vs. rotation hysteresis at midspan for each floor.

B4.5 ANALYTICAL MODEL

Two 3D models of the half-scale precast shake table test specimen were created for shake table test analytical simulations. The first model is the 3D NLTDA model which has been used for the analytical simulation of hybrid test (refer to B3). The other mode is a 3D floor profile model which is extended from 3D NLTDA model with the modeling of realistic 3D floor profile and gravity take-down. The 3D floor profile model contains more DOFs than the 3D NLTDA and requires more extensive run time and post-processing time. Thus 3D floor profile model is used only for the purpose of predicting shake table tests results and 3D NLTDA model is calibrated using the shake table test results and is used for parametric studies to determine/verify diaphragm design factors (See A1 and A2).

B4.5.1 3D NLTDA Model

As seen in Fig. B4-29, the 3D NLTDA model is a half symmetric model and replicates dimensions of the shake table test specimen. The precast floor units are modeled as elastic plane stress element with input of flange thickness. Though the double Tee stem stiffness is ignored, its mass is smeared into the plane stress element. The precast beams are model as 2D elastic beam element. The precast columns are modeled as 3D elastic beam element with pin-connection at base and each floor level.

Diaphragm at all three levels is modeled as full discrete panels which represents a pre-crack condition at precast diaphragm joints for 1st and 2nd floor topping slab. All the diaphragm reinforcment across the precast joints between precast units and diaphragm-to-spandrel in the test specimen are modeled as group of nonlinear spring, link and contact elements which represents their hysteretic effects including pinching, stiffness degradation, strength degradation, slip-catch and tension-shear coupling observed in the isolated connector tests (refer to Appendix B1 and B2). The connection between diaphragm and PT wall is modeled as rigid through the continuity between the diaphragm plane stress elements and PT wall shell elements.

The unbonded post-tension (PT) wall is modeled as 3D elastic shell element and the unbonded post-tension strand is modeled as nonlinear link element with initial stress. The energy dissipation bars at wall base is modeled as nonlinear spring. The interface between the wall and foundation is modeled with contact elements.
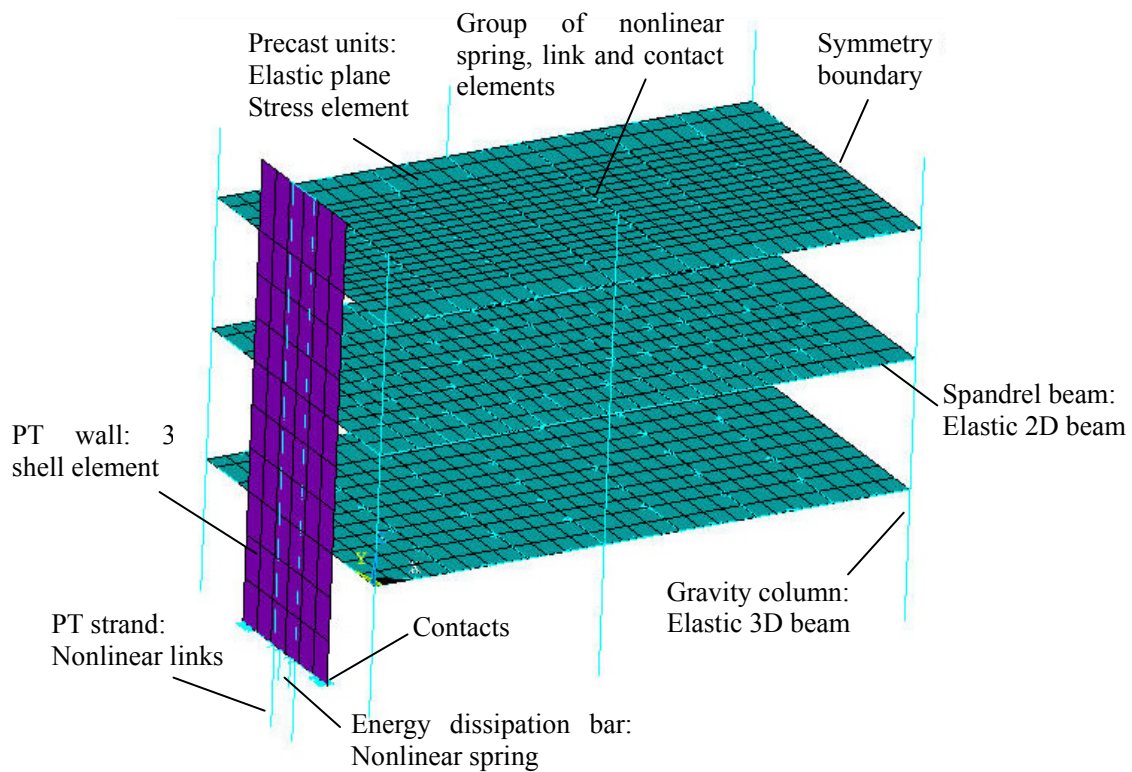
Fig. B4-29. Shake table test model.

B4.5.2 3D Floor Profile Model

The 3D floor profile model is extended from the 3D NLTDA model. The modeling of diaphragm reinforcement in the diaphragm joint remain unchanged in the 3D floor profile model. As seen in Figure B4-30, 3D floor profile model has realistic profiles of diaphragm precast units (double Tee or hollow core) and secondary elements (spandrel, L beam and column) by modeling them as elastic shell element which is capable of modeling the gravity load in addition to seismic load. This 3D floor profile model is able to

check the demand in the secondary elements (spandrel, L beam and column) and and 3D displacement compatibility among the diaphragm, spandrel/L beam and column.
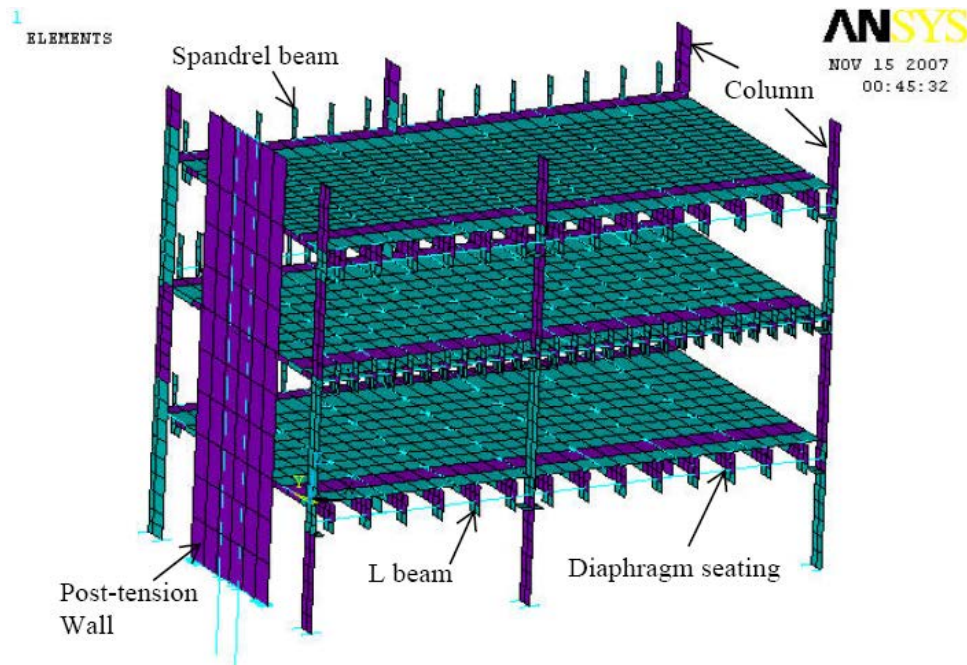
Fig. B4-30. Enhanced 3D NLTDA model for shake table test prediction.

The 3D floor profile model has been used to (1) study the effect of PT initial stress level on diaphragm demand; (2) check the demand in secondary elements and their connections (e.g. spandrel, L beam and column); and (3) calibrate the scale factor of ground motion for the tests after PT rupture as discussed in Sec. B4.3. These studies are fully described in Zhang (2010).

B4.6 MODEL CALIBRATION
As one of major objective of the shake table test, the 3D NLTDA model described in Sec. B4.5.1 is verified and calibrated using the shake table test results. The model verification and calibration is carried out by a direct comparison between the test results and the analytical earthquake simulation results. The comparison is performed at two levels: shear wall response and diaphragm response and at three earthquake intensities: Knoxville (KN) DBE, Seattle (SE) DBE and Berkeley (BK) MCE.

B4.6.1 Calibration of PT Wall Model
The calibration of the PT wall model was an important first step in the calibration process due to the dependence of the diaphragm response on the wall response. If the wall was not calibrated properly, it would be impossible to tell if any unmatched diaphragm response from the analytical model were a result of the diaphragm model itself or the wall model. Thus, a great deal of time went into getting the wall modeled correctly before the diaphragm model was even looked at. There were several changes to the wall model that did not yield positive results and subsequently were not used further. These results are not shown in this section, which instead focuses on the changes to the wall model that showed improvement.

Since the test structure accumulated damage and required repairs throughout the test sequence, especially in the wall, it became more and more dissimilar to the structure that was modeled. Because of this, the wall was calibrated using only the KN-DBE and SE-DBE earthquakes, which still represent the structure in both an elastic and inelastic state before it accrued much damage beyond the chord failure.

The first step was to investigate the original model and identify what worked and what did not. From there, it could be decided how to alter the model in a way that would improve the inaccurate response characteristics. Figure B4-31 shows the Moment vs. Rotation hysteretic plots of the original model and the north wall in the test. The hysteretic plot for the south wall could not be shown due to unreliable PT strand data.

(a) KN DBE   (b) SE DBE
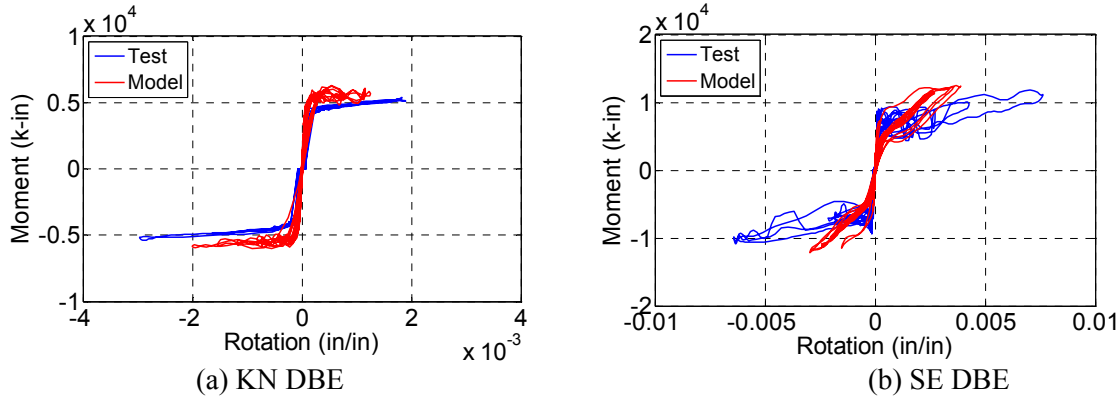
Fig. B4-31. Model comparison of moment vs. rotation of PT wall.

It can be seen that in both earthquake simulations the PT wall model shows a higher stiffness and strength than the test results. This in turn results in underestimation of the seismic demand in the analytical model. It has been found out that the higher stiffness and strength in the analytical model is caused by the underestimation of the height of compression zone. To fix this, the contact element arrangement and stiffness at the bottom of the wall were changed (see Fig B4-32). The contact element spacing was increased and contact stiffness was reduced in order to increase the compression zone of the wall model.

(a) original model   (b) updated model
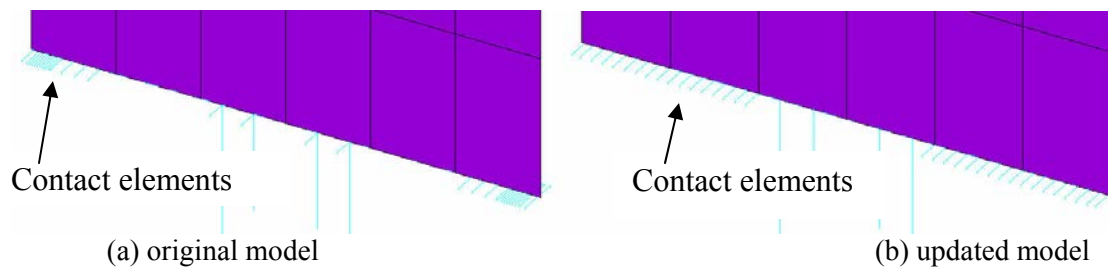
Fig. B4-32. Arrangement of contact elements.

(a)   (b)
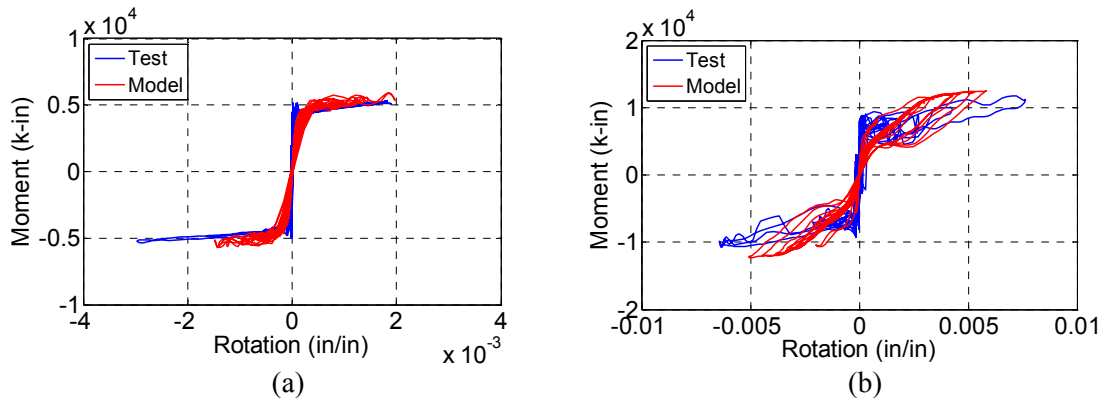
Fig. B4-33. Updated model comparison of moment vs. rotation of PT wall for (a) KN-DBE; (b) SE-DBE.

There was a marked improvement in both tests in both strength and stiffness of PT wall (see Fig. B4-33). For the KN-DBE test, the PT wall strength and stiffness are matched between analytical model and test although the rotation demand in the model is lower than the test results. This unmatched rotation demand is caused by the asymmetry wall responses in the test. Figure B4-34 shows the base rotation time history comparison for KN-DBE. As seen, the north wall incurs larger demand than the south wall. This asymmetry wall response in the test is due to uneven grouting of the energy dissipation bars in the two walls. When comparing the tests results to the model which has an assumed symmetry at peak response, it can be seen that the PT wall response predicted by the model was in between the two walls from the test.
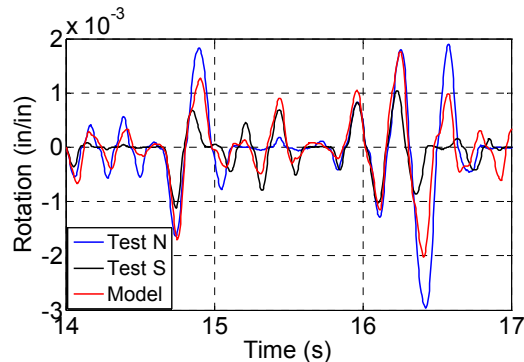
Fig. B4-34. Rotation time history in KN-DBE.

For the SE-DBE test, the PT wall strength and stiffness in the model is still slightly higher than the test results. This discrepancy has been found is because the analytical model did not include the concrete softening at bottom of the wall as a group of contact elements was used while for a larger intensity test (SE-DBE), the concrete at bottom of wall might incur softening and localized crushing. To considering the concrete softening, a nonlinear spring is added in series between the contact element and the wall shell element similarly as the softening spring added between the precast diaphragm units in the precast diaphragm model (refer to Appendix B1).

Figure B4-35 shows the PT wall response results comparison with softening spring in the analytical model. Good agreement is observed for the PT wall response in both tests between the analytical model and test results as seen in Fig. B4-35.

(a)   (b)
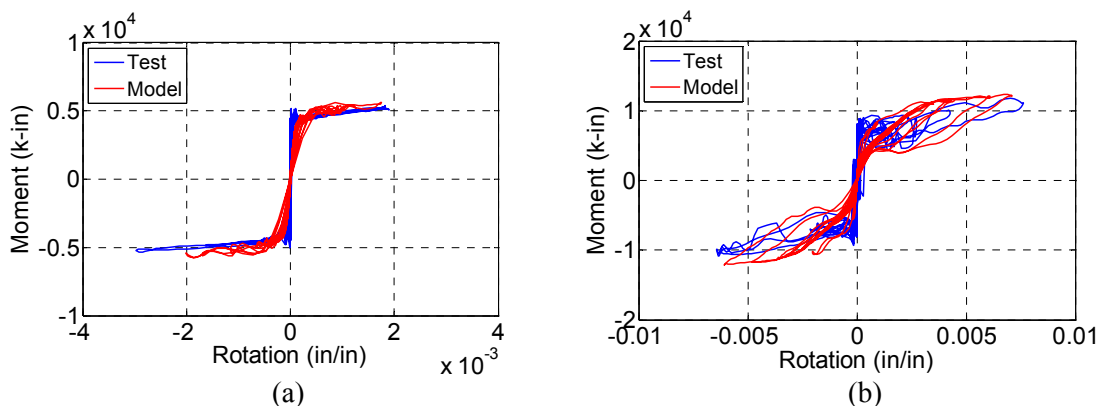
Fig. B4-35. Comparison of PT wall response with softening spring for (a) KN-DBE; (b) SE-DBE.

B4.6.2 Calibration of Precast Diaphragm Model

The calibration of precast diaphragm model is carried out at two earthquake intensities: (1) KN-DBE which represents a low intensity compared to the strength of shake table specimen; and (2) SE-DBE which represents a moderate intensity. It is very difficult to calibrate the model using the high earthquake

intensity tests (e.g. Berkeley DBE and MCE) because the specimen has undergo several damages and repairs (e.g. dry chord and PT wall strands etc.) before the tests. Therefore the calibration of the model for Berkeley ground motion is limited and will be discussed in Sec. B4.6.3.

B4.6.2.1 Model Calibration for KN DBE Earthquake

The first shake table test at KN-DBE level was selected for calibration due to the fact that it allowed the model to be compared to a pristine test structure with no major damage to the structure during the ground motion test. The primary focus of this section is the calibration of topped precast concrete diaphragms, due to the fact that the topping slab remained uncracked at several joints and only partially cracked at others while the 3D precast diaphragm structure model assume a fully cracked condition at the joints; attributable to the low intensity of the ground motion. Consequently, most of the research calibrations presented will focus on the topped precast concrete floor diaphragms (the first and second levels). The third floor, being an untopped precast concrete diaphragm, will be discussed separately at the end of this section.

Topped Diaphragm Calibration (1st and 2nd floor)

As described in the beginning of section B4.5.1, the discrete model which assumes a fully cracked condition of topping slab at diaphragm joints (see Fig. B4-36a) has been used for the shake table test specimen earthquake simulation. This fully cracked discrete model is appropriate for the high intensity earthquake loading under which the topping slab will crack in the early cycles. However for the low intensity ground motion (e.g. KN-DBE) might not strong enough to crack the topping slab on the first and second floors completely. For this reason, other two precast diaphragm models have been developed for calibrating a proper model of topping slab under low intensity earthquake. The first model is a completely uncracked model (see Fig. B4-36b) where it was assumed that the slab will not crack at all before and after the low intensity KN-DBE earthquake and the second model is a self cracking model where the concrete is initially uncracked and is allowed to crack along the joint when the concrete cracking force is reached during the earthquake simulation (see Fig. B4-36b).

(a) Fully Cracked Model   (b) Uncracked Model

(c) Self Cracking Model
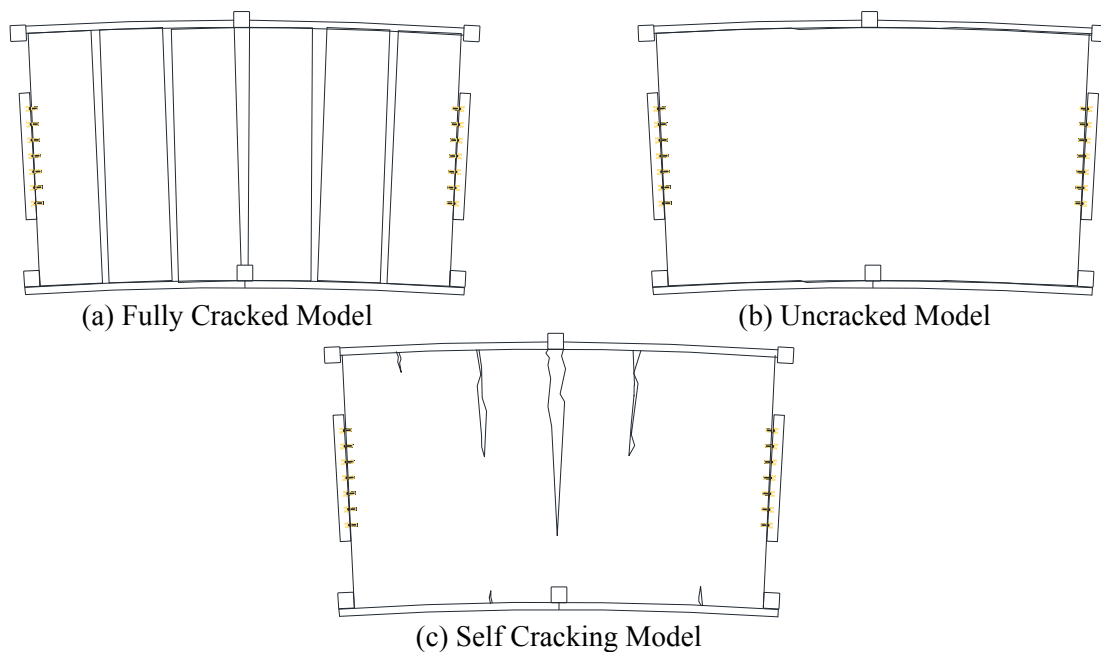
Fig. B4-36. Precast diaphragm models used for Calibration of KN-DBE earthquake.

Figure B4-37 shows the diaphragm inertia force vs. midspan deformation hysteresis response at 1st and 2nd floor for the fully cracked discrete model and test results. As seen, the fully cracked model

underestimates the diaphragm stiffness and in turn overestimates the diaphragm deformation demand. Figure B4-38 shows the maximum diaphragm joint opening profile comparison between the fully cracked discrete model and test results. As seen, the model has a significant larger joint opening demand than the test results. Therefore the fully cracked diaphragm model cannot represent the behavior of topping slab under a low level earthquake loading.

(a) First Floor   (b) Second Floor
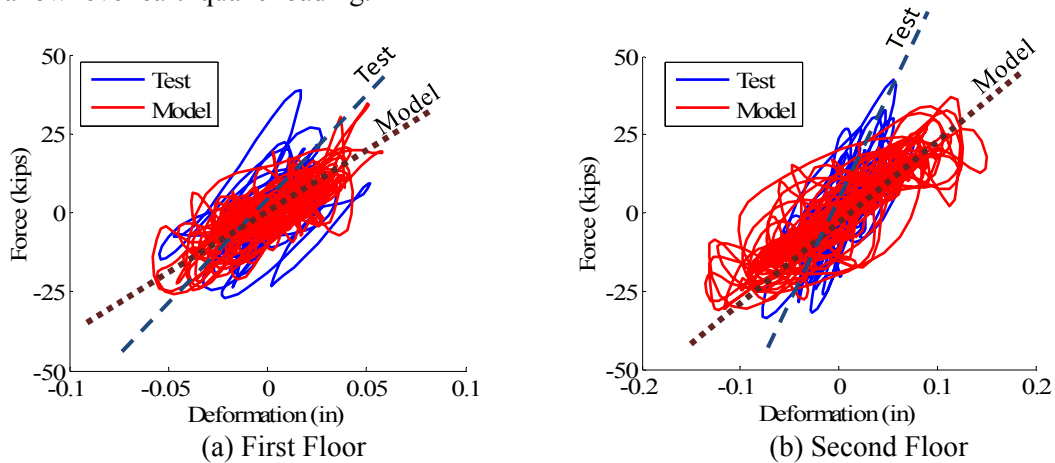
Fig. B4-37. Fully cracked model - Inertia force vs. Midspan deformation.

(a) First Floor   (b) Second Floor
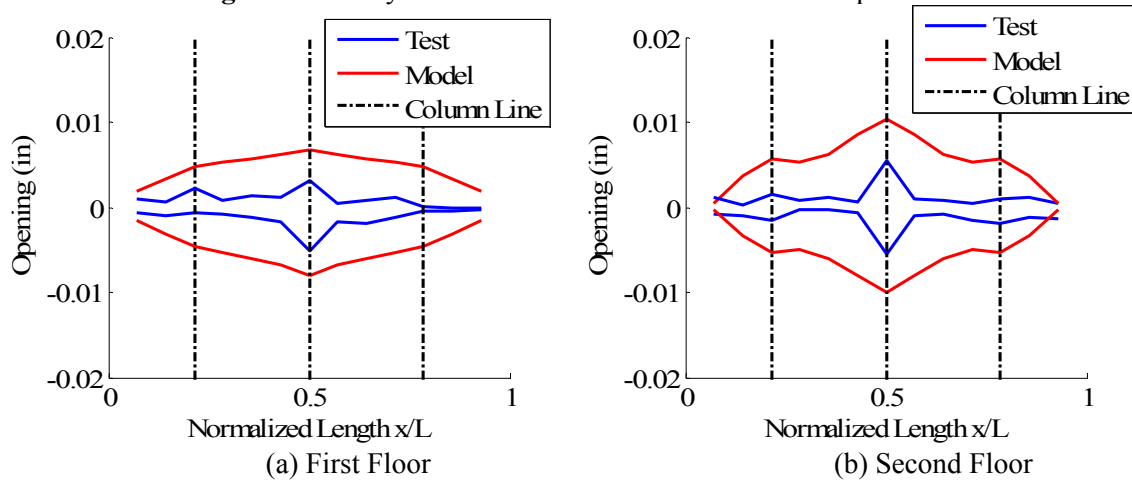
Fig. B4-38. Fully cracked model - Maximum joint opening along the diaphragm.

(a) First Floor   (b) Second Floor
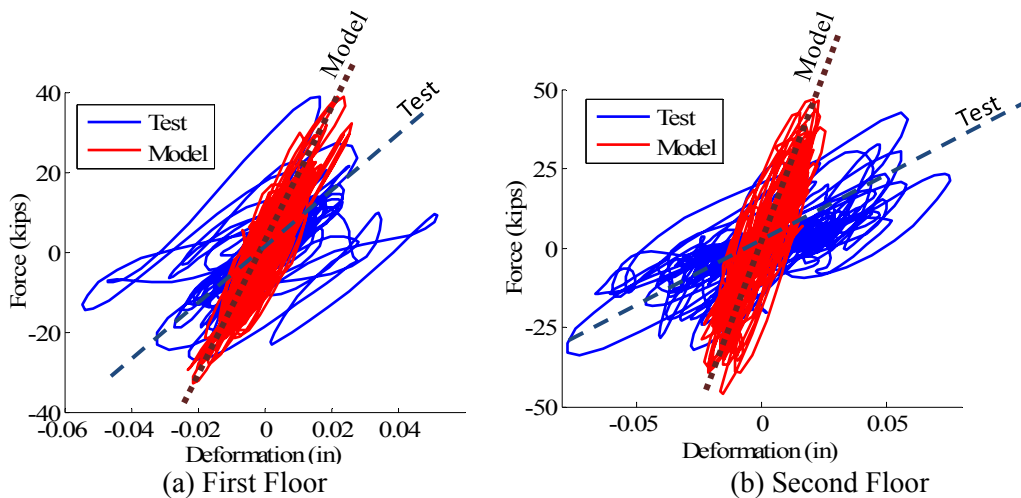
Fig. 4B-39. Uncracked model - Inertia force vs. Midspan deformation.

(a) First Floor   (b) Second Floor
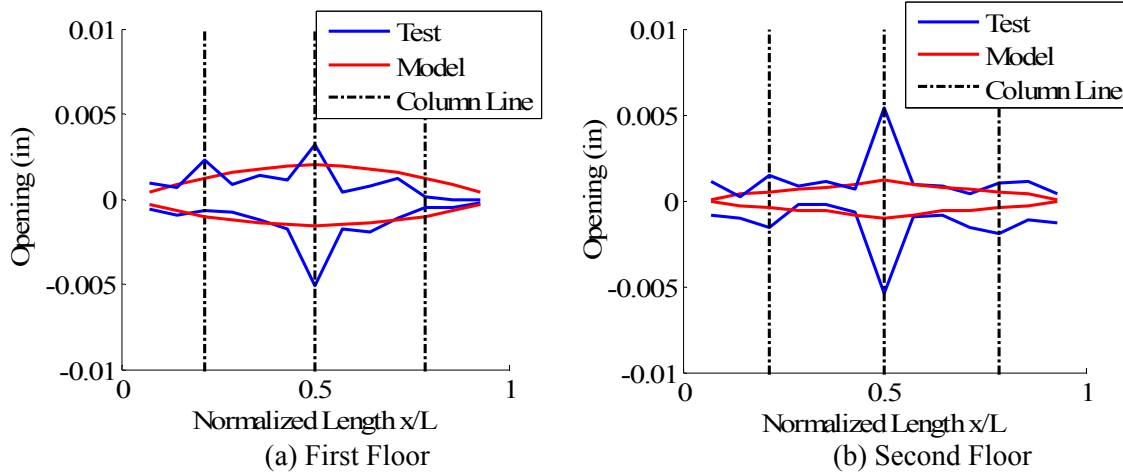
Fig. B4-40. Uncracked model - Maximum joint opening along the diaphragm.

       As a first step of model calibration, an uncracked precast diaphragm model is created. The precast panel and topping slab is modeled as 2D monolithic elastic elements with gross section properties and the diaphragm reinforcement stiffness is ignored in this model (refer to Fig. B4-36). Figure 4B-39 shows the diaphragm inertia force vs. midspan deformation hysteresis response at 1st and 2nd floor for the uncracked model and test results. As seen, the uncracked model overestimates the diaphragm stiffness and in turn underestimates the diaphragm deformation demand. Figure B4-40 shows the maximum diaphragm joint opening profile comparison between the uncracked model and test results. As seen, the uncracked model has a significant lower joint opening demand at midspan than the test results. However the diaphragm joint opening in some other joints shows good agreement between uncracked model and test results which indicates during the test the diaphragm only cracked in some joints. Therefore it will be appropriate to model the cracking of concrete in this lower level earthquake loading.

       The self cracking floor slab model is developed using tension only link elements across the joints instead of smear crack model which might cause convergence issue after cracking. The link element is placed between elastic precast panels in parallel with the group of nonlinear elements for diaphragm connector (see Fig. B4-41). This link element is initially rigid with a 50 times of elastic topping slab stiffness over a panel center-to-center gauge length and is "killed" (the stiffness contribution of the link element will be set as zero) during the analysis once the force demand in the element reached the concrete cracking force.
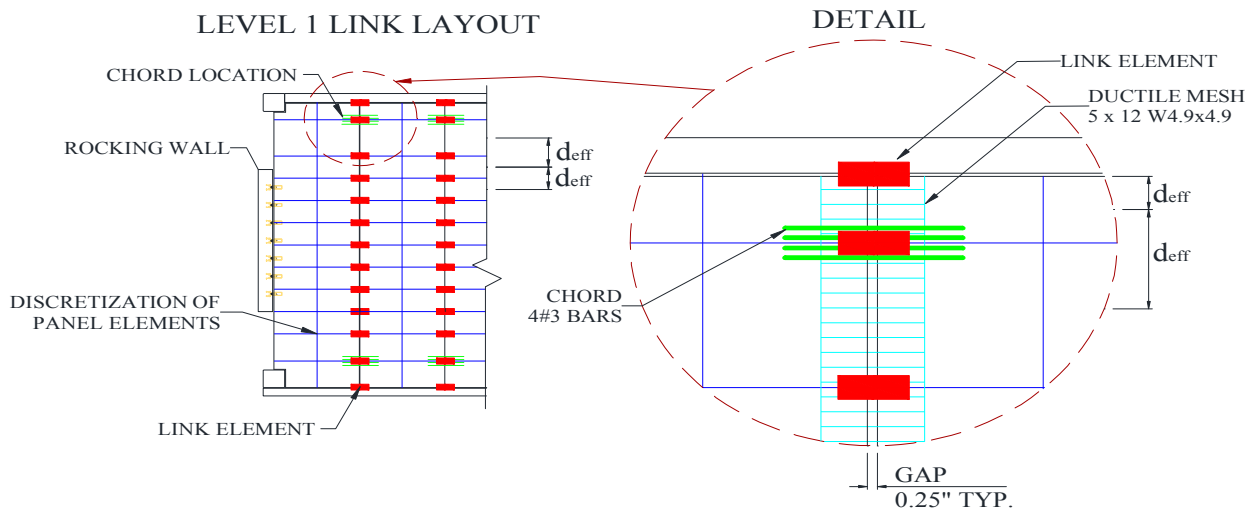
Fig. B4-41. Link layout and detail of link around top chord area.

The concrete cracking force calculated for the link elements is based on the details (see Fig. 4B-42) and concrete compressive stress of first and second floor topping slab. The concrete compressive stress of topping slab as well as the grout in the 2nd floor hollow key (see Fig. 4B-42) is obtained from the material tests (see Table 4B-11). The concrete cracking force calculation is calculated based on the concrete fracture stress (f_r) and the tributary concrete area (A_{trib}) of the link element representing (refer to Fig. B4-14) using the following equations:

$$f_r = 7.5\sqrt{f_c^{'}}$$ (Eq. 2)

$$f_{crack} = f_r A_{trib}$$ (Eq. 3)

The concrete tributary area (A_{trib}) is calculated as product of the effective thickness (t_{slab}) of the topping slab and the effective distance (d_{eff}) between each link excluding the area of the ductile mesh steel (A_{mesh}) and the chord steel ($A_{chord\ steel}$):

$$A_{trib} = t_{slab} d_{eff} - A_{chordsteel} - A_{mesh}$$ (Eq. 4)

For the second floor, the tension strength of the grout (taken as 1/10 of the grout compressive strength) between each joint is also considered and the effective grouting thickness is taken as 1.5″:

$$f_{crack} = f_r A_{trib} + f_{grout} t_{grout} d_{eff} / 10$$ (Eq. 5)
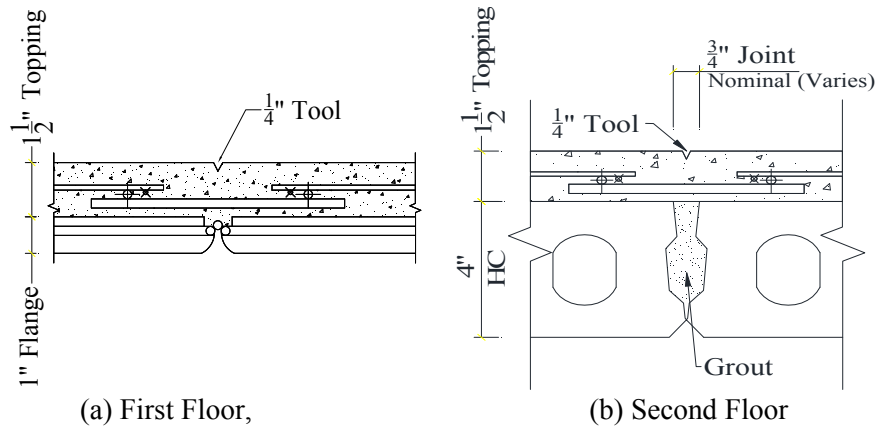
(a) First Floor,   (b) Second Floor
Fig. B4-42. Topping detail at precast diaphragm joints.

Table B4-11. Material properties for topping slab.

Floor	$f_c^{'}$ (ksi)	f_{grout} (ksi)
1st	5.1	-
2nd	5.1	3.1

The topping slab thickness is 1.5″ as indicated in Fig. B4-42. Also noticed, on the first floor, a 1/4 inch tooled "v" notch was made at each joint along the diaphragm in order to control the location of cracking due to shrinkage and temperature in the concrete topping at the joints. The second floor was notched with a 1/4 inch "v" notch at every three joints due to the smaller width of the HC panels. Therefore a reduced effect thickness is used and adjusted by comparing the analytical results to test results. The final calibrated effect thickness and link cracking forces are listed in Table B4-12.

Table B4-12. Concrete cracking force summation

Location of Link	Effective height	1st Floor		2nd Floor		
		"v" notch		"v" notch		no "v" notch
Link Elements	d_{eff} (in)	t_{slab} (in)	F_{crack} (k)	t_{slab} (in)	F_{crack} (k)	F_{crack} (k)
Top Link	5.8	0.78	2.79	0.75	5.48	7.35
Top Chord Link	18	0.90	8.58	0.90	16.94	22.72
3rd Link from Top	19.7	0.90	9.45	0.90	18.56	24.89
Middle Links	15	0.90	7.20	0.90	14.14	18.96
3rd Link from Bot.	16.7	0.90	8.01	0.90	15.73	21.09
Bottom Chord Link	18	0.90	8.58	0.90	16.94	22.72
Bottom Link	8.8	0.90	4.23	0.75	8.31	11.14

Figure 4B-43 shows the diaphragm inertia force vs. midspan deformation hysteresis response at 1st and 2nd floor for the final calibrated self-cracking model and test results. Figure 4B-44 shows the maximum diaphragm joint opening profile comparison between the final calibrated self-cracking model and test results. As seen, good agreement between analytical model and test results is observed.
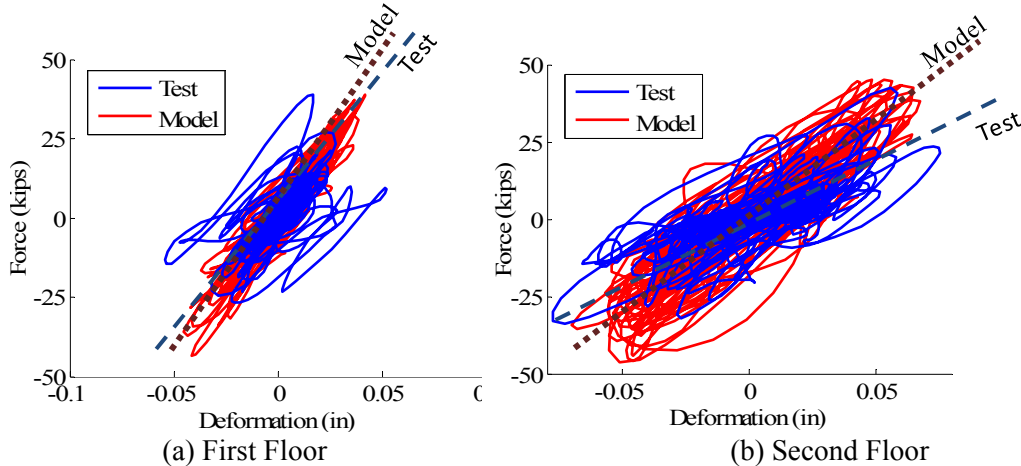
(a) First Floor   (b) Second Floor
Fig. B4-43. Self-cracking model - Inertia force vs. Midspan deformation.
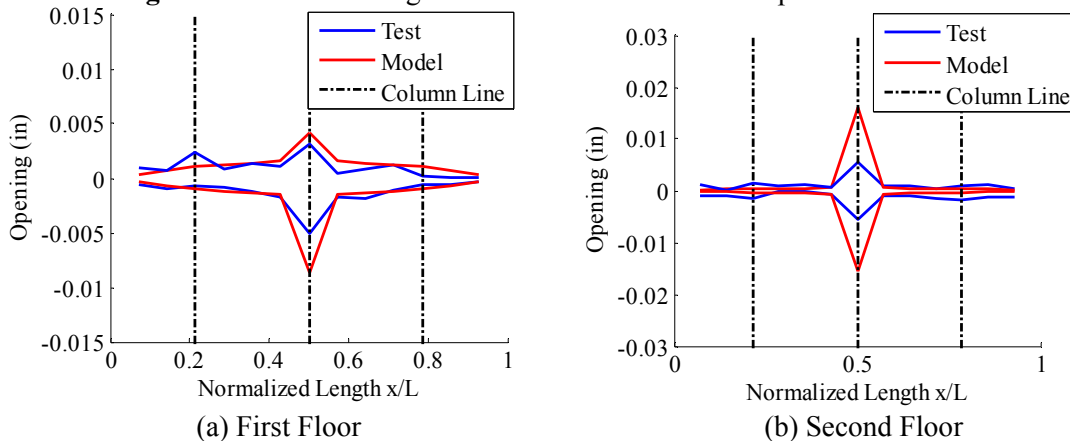
(a) First Floor   (b) Second Floor
Fig. B4-44. Self-cracking model - Maximum joint opening along the diaphragm.

Figure B4-45 shows the crack pattern (link status) after the earthquake simulation. This analytical crack pattern is also verified by the photo evidence after test as indicated in the Fig. B4-45.
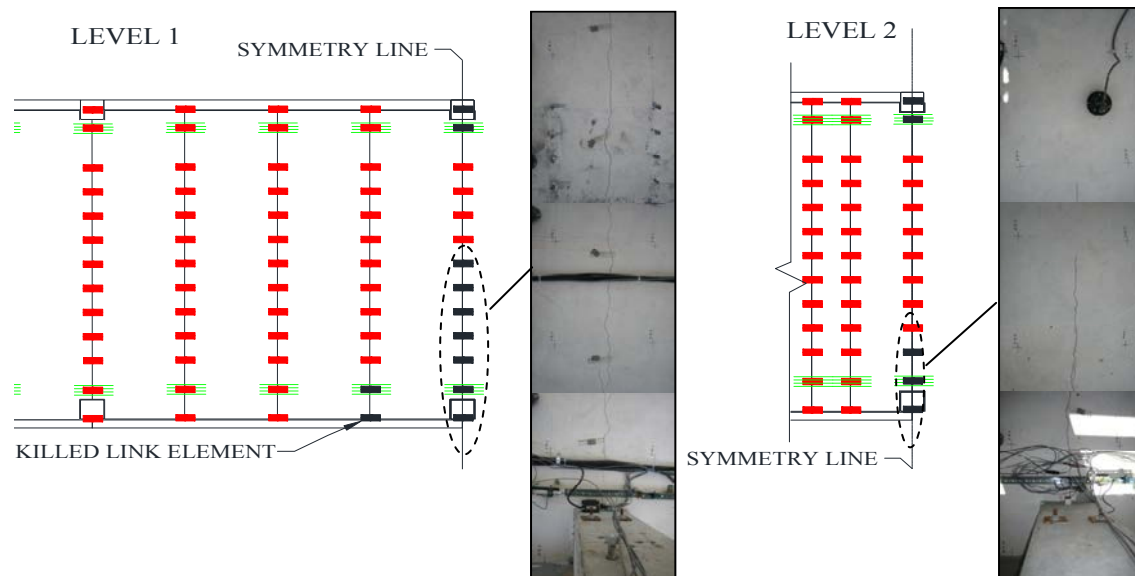
Fig. B4-45. Link element status after simulation and test photo evidence.

Untopped Diaphragm Model Verification (3rd floor)

Fully discrete model is used at top floor. Figure 4B-46 shows the diaphragm inertia force vs. midpsan deformation hysteresis response and maximum diaphragm joint opening demand for analytical model and test results. As seen, good agreement between the analytical model and the test results is observed in the uptopped diaphragm response at 3rd floor.
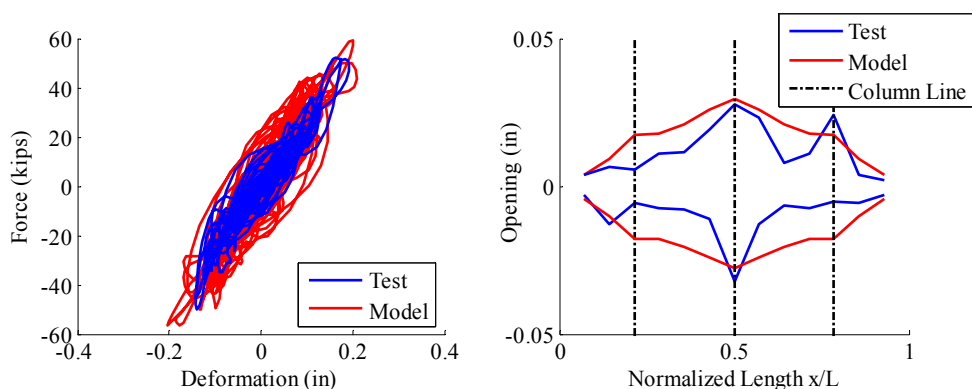
(a) Diaphragm hysteresis   (b) Diaphragm joint opening.
Fig. B4-46. Fully discrete model at 3rd floor for KN-DBE.

B4.2.6.2 Model Calibration for SE DBE Earthquake

The last SE-DBE shake table test, SE-DBE 4, was selected for calibration because it was the only SE-DBE test run without a major failure. The selection of this test also allowed for the model calibration of damage in the structure which occurred during the first three SE-DBE tests when the third floor chord failure caused damage on the third and second floor. Two significant modifications are made to the calibrated model from KN-DBE earthquake simulation. The first model modification is that the crack pattern is modified from the KN-DBE self-cracking model to represent the initial cracking status of topping slab before SE-DBE 4 test. The second model modification is to adjust the 2nd floor diaphragm connector model to match damage at the second floor symmetry line. Also the diaphragm response at untopped 3rd floor from analytical model is verified.
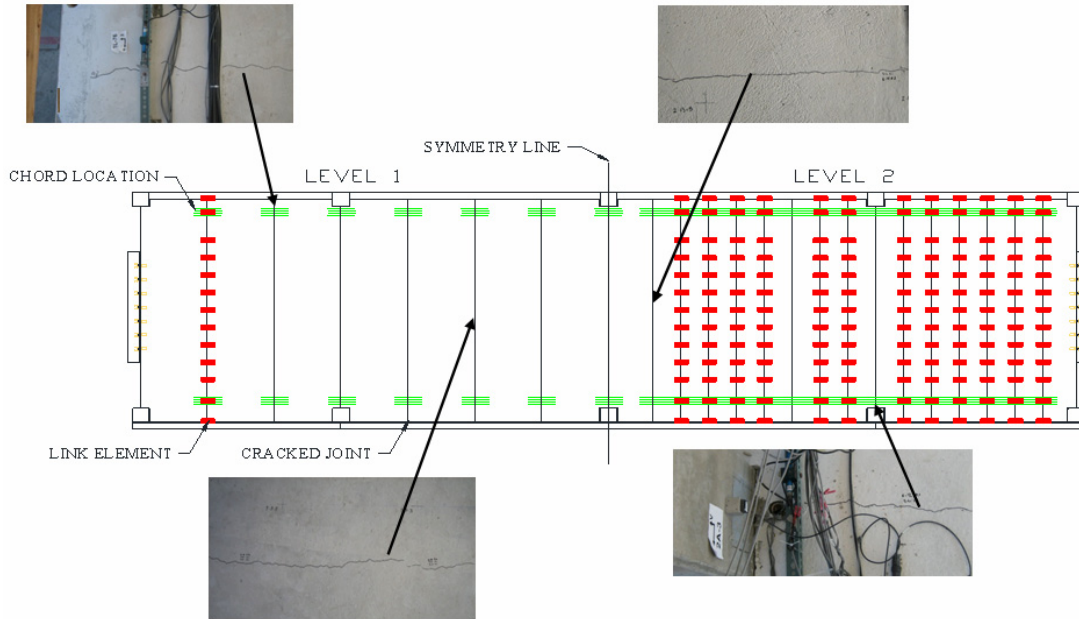
Fig. B4-47. SE-DBE initial cracked status and link element locations in analytical model.

The self-cracking model calibrated from the KN-DBE is used in the calibration of the SE-DBE 4 shake table test. The model is modified l to represent the initial status of the test structure before the SE-DBE 4 test. The cracked status of the structure is based on photo evidence at the end of SE-DBE 3. The self cracking link elements are adjusted to match the damaged structure by placing link elements only at joints that have not cracked. Figure B4-47 shows the location of the links for the SE-DBE 4 model.

Figure B4-48 shows the maximum diaphragm joint opening profile at 1st and 2nd floor for analytical model and test results. As seen in Fig. Fig.B4-48a, the diaphragm joint opening demand obtained in analytical model reasonably matches the demand observed in the test at 1st floor. However as seen in Fig. B4-48b, the analytical model highly underestimates the diaphragm joint opening demand at midspan joint of 2nd floor. This significant discrepancy is caused by the fact that the 2nd floor ductile mesh reinforcement along the midspan joint has been heavy damaged during the previous three SE-DBE tests as mentioned above. The damage of ductile mesh reinforcement results in a weaker diaphragm midspan joint at 2nd floor than the analytical model.

(a) First Floor   (b) Second Floor
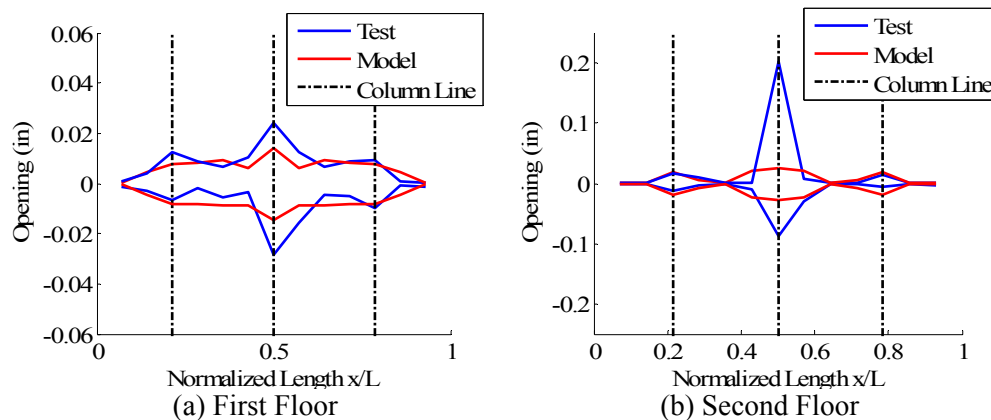
Fig. B4-48. Self-cracking model - Maximum joint opening along the diaphragm under SE-DBE.

The damage of ductile mesh reinforcement is shown in the strain gauge data from the SE-DBE 3 test (see Fig. B4-49). As seen, the ductile mesh on one side (L beam side) of the structure has shown a

larger strain at 17 sec which might be buckled after the succeed compression cycle while on the other side (spandrel beam side) the fairly small ductile mesh strain demand is observed. Although curbs had been added for repairing the chord, the ductile mesh reinforcement was unable to be repaired. Therefore, it is appropriate to modify the analytical model at 2nd floor midpsan to remove the failed ductile mesh from the model.

(a) Ledger Beam Side   (b) Spandrel Side
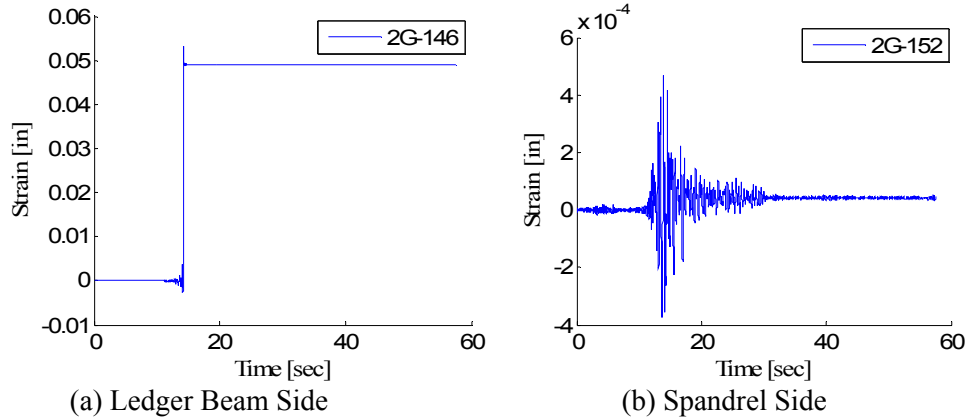
Fig. B4-49. Ductile mesh strain gauge time history SE-DBE 3 Shake Table Test.

According to the previous test data evidence, ductile mesh reinforcement in the model is removed from the top half of the structure. Only one ductile mesh reinforcement element is left at the midspan which is shown in Fig. B4-50.
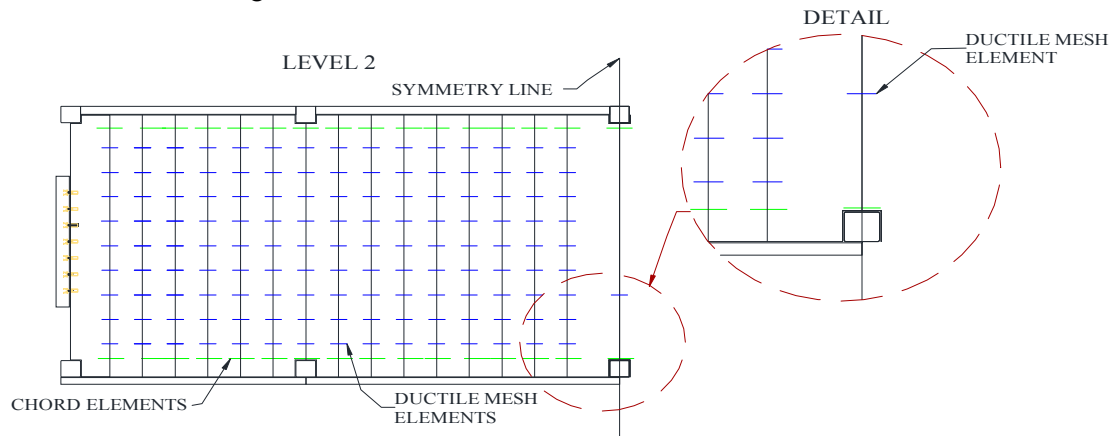
Fig. B4-50. Ductile mesh reinforcement element layout in second floor.

(a) First Floor   (b) Second Floor
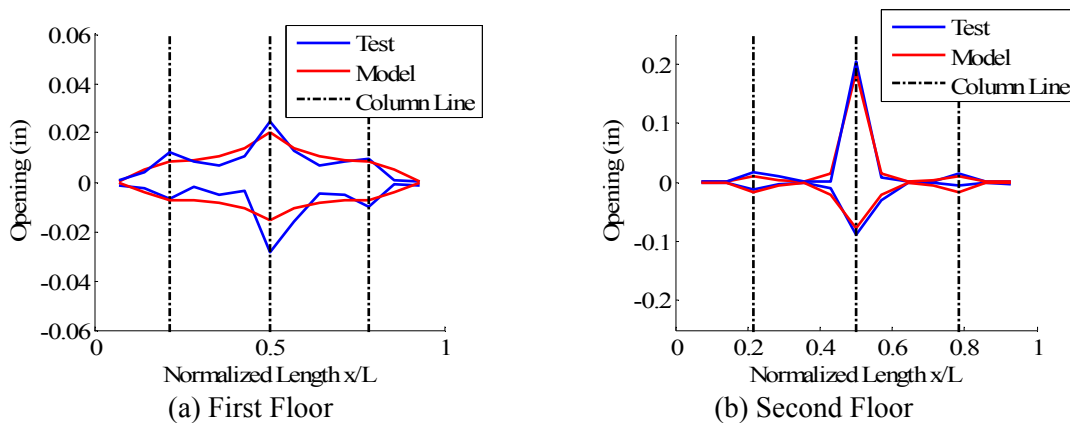
Fig. 4B -51. SE-DBE modified model - Maximum joint opening along the diaphragm.

C-A-222

Figure B4-51 shows the maximum diaphragm joint opening profile between the modified analytical model and the test results. As seen, the maximum diaphragm joint opening demand obtained from the analytical model reasonably matches the demand observed in the test. Also good agreement between the analytical model and test is observed in the diaphragm force-deformation hysteresis response as shown in Figure B4-52.

(a) First Floor   (b) Second Floor
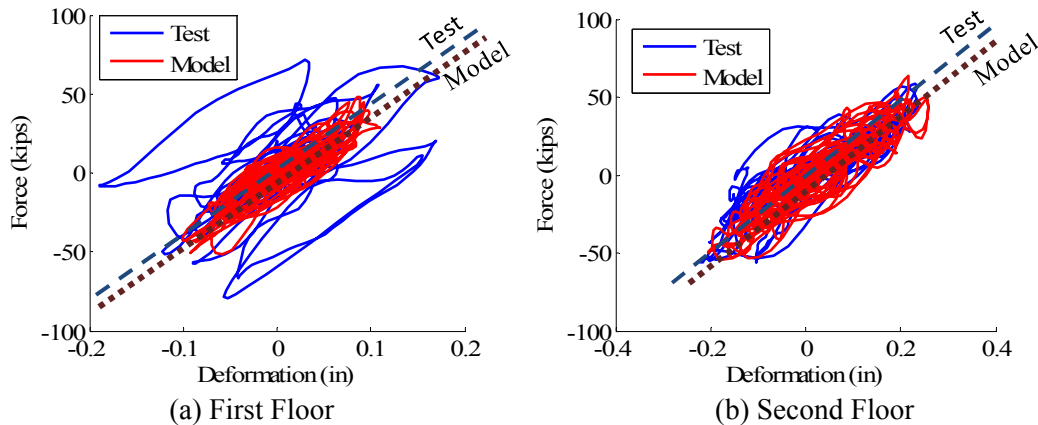
Fig. B4-52. SE-DBE modified model - Inertia force vs. midspan deformation.

Figure 4B-53 shows the diaphragm inertia force vs. midpsan deformation hysteresis response and maximum diaphragm joint opening demand for analytical model and test results at top floor in SE-DBE 4. As seen, good agreement between the analytical model and the test results is observed in the uptopped diaphragm response at 3rd floor.

(a) Diaphragm hysteresis   (b) Diaphragm joint opening
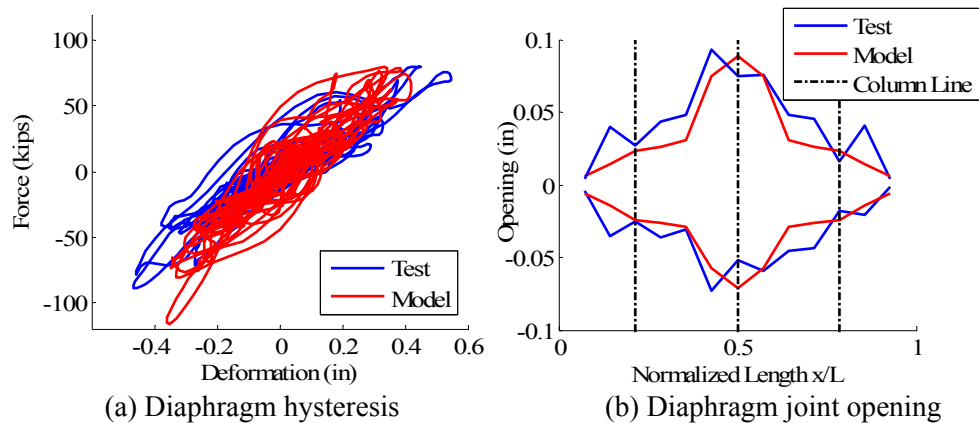
Fig. B4-53. Fully discrete model at 3rd floor for SE-DBE.

B4.6.3 Model Calibration for BK MCE Earthquake

The shake table test specimen has subjected to a lot of repairing and modification before a successful BK MCE test (test 13) due to the unexpected local failures as discussed in Sec. B4.3. It is very difficult to calibrate the 3D NLTDA model since characteristic of shake table test has been changed due to the repairing and modifications. Thus the calibration of the 3D NLTDA model is limited to the most important diaphragm local response (maximum joint opening at chord reinforcement locations).

A pristine model fully cracked half-symmetry model which has been calibrated for SE-DBE 4 is used for simulations under BK MCE ground motion. Figure B4-54 shows the diaphragm maximum joint opening comparison for all three floors. As seen, in general, the 3D NLTDA model significantly overestimates the diaphragm joint opening demand as compared to the test results.

(a) 1st floor   (b) 2nd floor   (c) 3rd floor
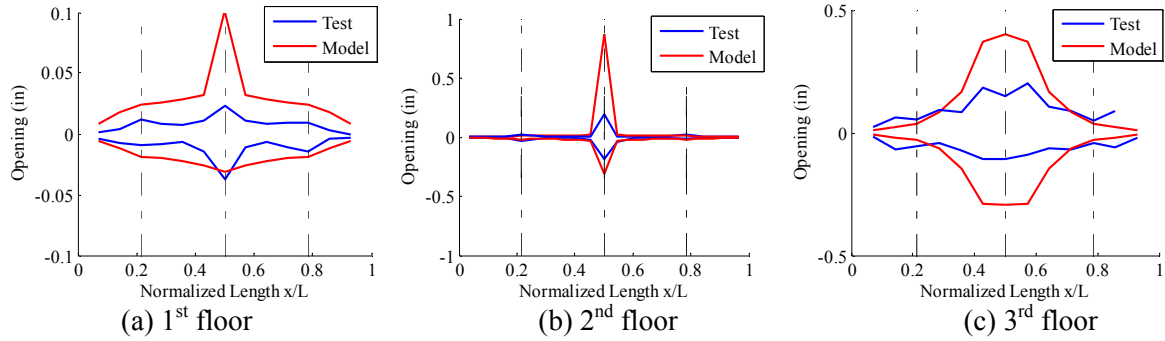
Fig. B4-53. BK-MCE half symmetry model - maximum joint opening along the diaphragm.

After investigating the global response of the structure it was found that the shear walls had an unsymmetrical response in the test results which cannot be captured by the half symmetry model. Figure B4-54 shows the base hysteresis response of the north and south wall of the shake table test compared to response obtained in the analytical simulation using half symmetry model. As seen, an asymmetric response of the two walls in the test is observed as the south wall has a much larger base rotation demand than the north wall. Also noticed, the PT wall in the model has a similar strength as the north wall but has a fairly higher strength than the south wall. The higher base moment strength of the PT wall in the model compared to the south wall in the test can cause a higher diaphragm inertia force in the model and a higher diaphragm joint opening demand in the model as observed in Fig. B4-53. Thus the half symmetry calibrated wall model would not be sufficient for predicting the diaphragm response results in BK MCE test. A full model with two different strength of walls is necessary.

(a) North wall   (b) South Wall
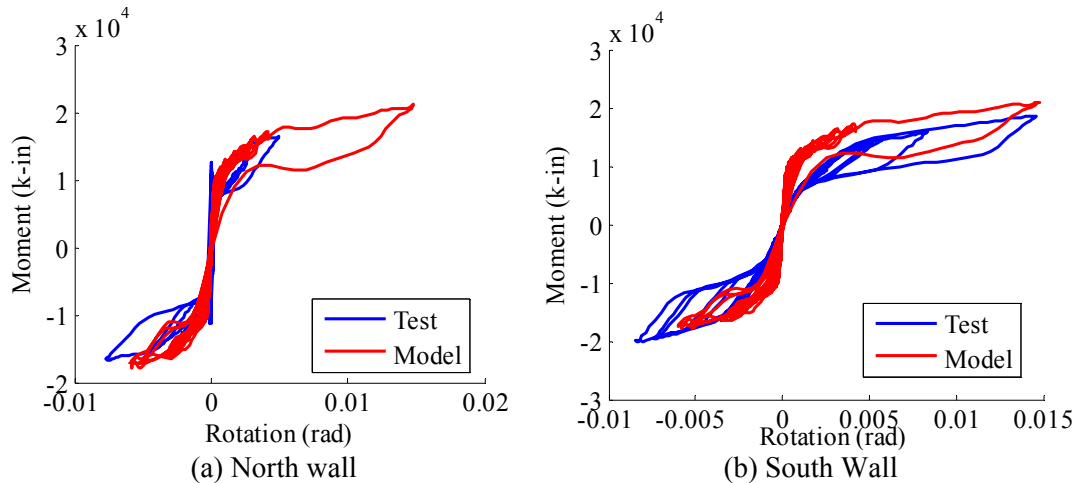
Fig. B4-54. BK-MCE half symmetry model wall response – Base moment vs. Rotation.

The full model is extended from the half symmetry 3D NLTDA model by weakening the south wall to match the test results. Figure B4-55 shows the wall base response comparison. As seen, a good agreement in the PT wall base responses (in terms of stiffness, strength and base rotation demand) in both south and north walls between the 3D NLTDA full model and shake table test results.

Figure B4-56 shows the diaphragm maximum opening demand comparison between the 3D NLTDA full model and shake table test results. As seen, the diaphragm opening demand at 1st floor in the model matches well the test results. Also the diaphragm opening demand at 2nd and 3rd floor obtained from the 3D NLTD full model reasonably and conservatively represents the test results.

C-A-224

(a) North wall (b) South Wall
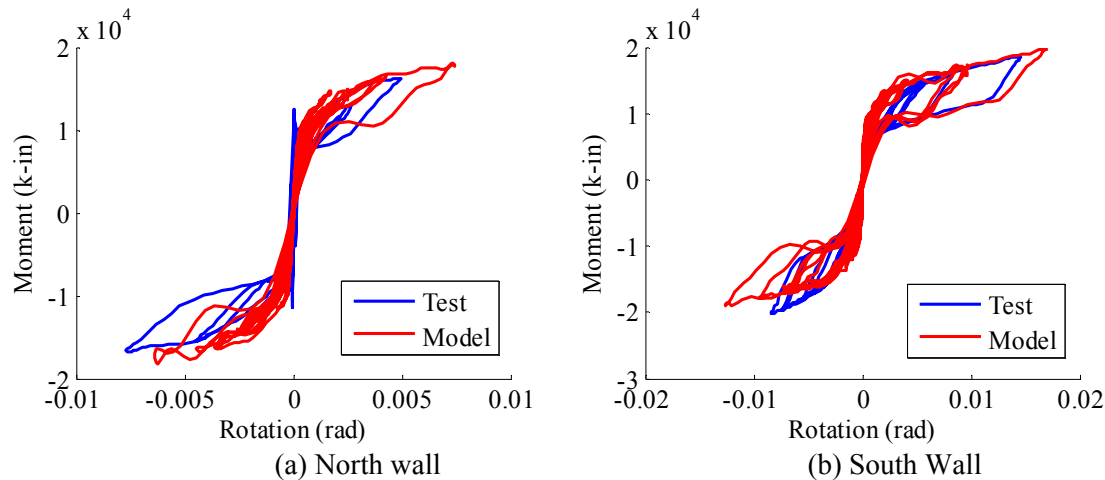
Fig. B4-55. BK-MCE full model wall response – Base moment vs. Rotation.

(a) 1st floor (b) 2nd floor (c) 3rd floor
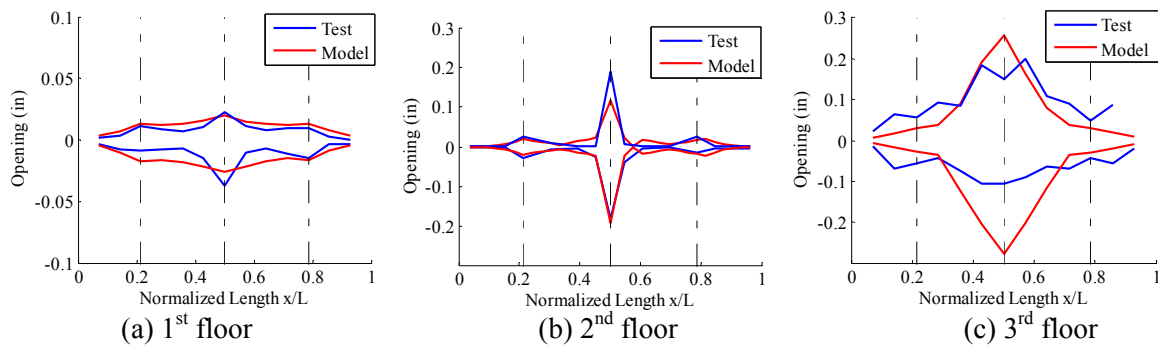
Fig. B4-56. BK-MCE full symmetry model - maximum joint opening along the diaphragm.

B4.7 COLUMN EFFECTS

As observed in the early analytical study (Zhang 2010), the gravity column can generate non-negligible lateral restraint forces. This lateral restraint forces provided by the gravity column may:

1) change the force patterns along the diaphragm, thereby effecting the shear and moment diagrams.
2) change the diaphragm force and deformation patterns along the height of the building.
3) change the magnitude of deformation demands in the diaphragm, particularly for precast diaphragms under strong motions that may concentrate inelasticity in the joints between precast units.
4) change the diaphragm stiffness.

These effects caused by the gravity column are verified by comparing the 3D NLTD model with and without gravity column to the shake table test results. The successful SE DBE test (test 7) is selected to demonstrate the column effect.

B4.7.1 Force Patterns along the Diaphragm

Figure B4-57 shows the free body diagrams of diaphragm in first floor for the two models with and without columns at the similar peak responses of diaphragm total inertia froce. For the model without column, all the inertia forces will transfer to the shear wall while for the model with column, part of the inertia forces will be balanced by the columns restraint forces which is higher at the middle of span.
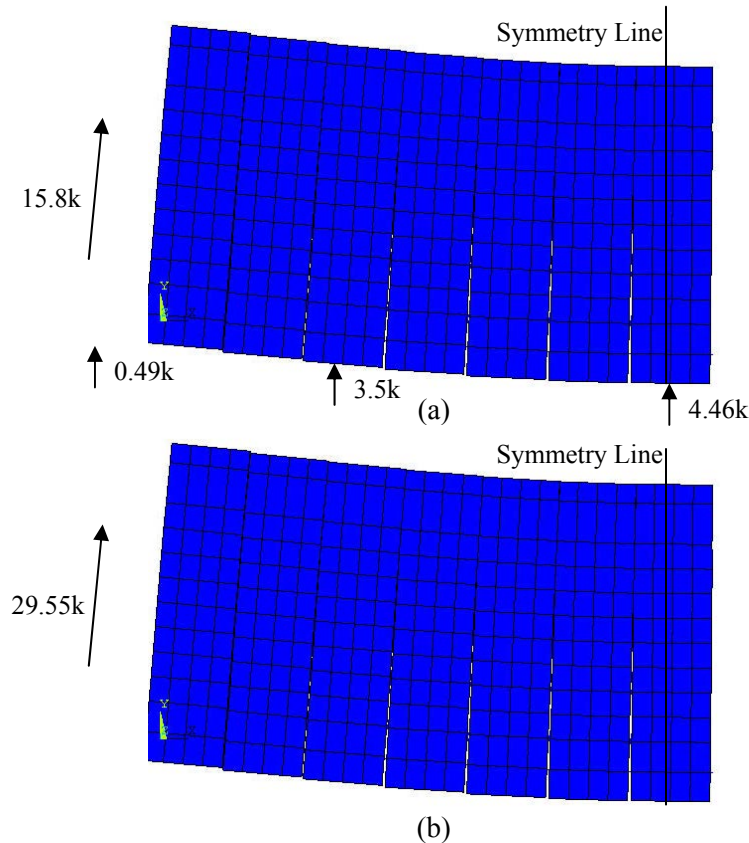
Fig. B4-57. 1st Floor Diaphragm FBD for Models: a) with columns; b) without columns

Figure B4-58 shows the diaphragm internal forces (moment and shear) diagram for two models with and without gravity column. As seen, the moment and shear along the diaphragm are lower in the model with columns compared to the one without column, as an expected effect of column restraint forces in the diaphragm.
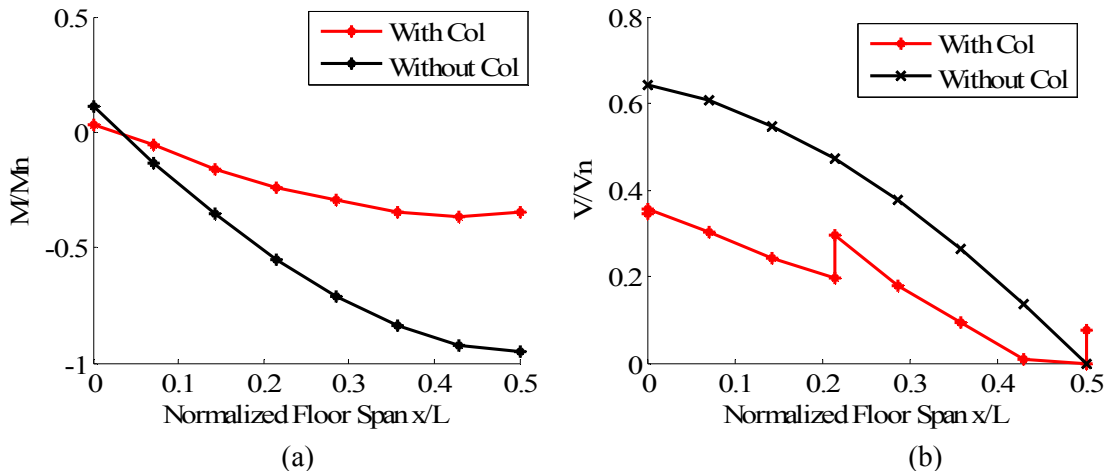
Fig. B4-57. 1st Floor Diaphragm Internal Forces Snapshot: a) Moment; b) shear

B4.7.2 Diaphragm Inertia Force Demand Pattern along the Building Height

Figure B4-58 shows the diaphragm maximum inertia force distribution along the building height. As seen, due to the column restrain effect, the diaphragm total inertia froce distribution has difference between the model with and without column. Also noticed, the model with column matches the test

C-A-226

results better than the model without column. The model without column overestimates the diparhgam inertia force at bottom floor but underestimates the diaphragm inertia force at top floor as compared to shake table test results. The column restaint forces is higher in lower floor than that in top floor as observed from the analysis using the model with column.
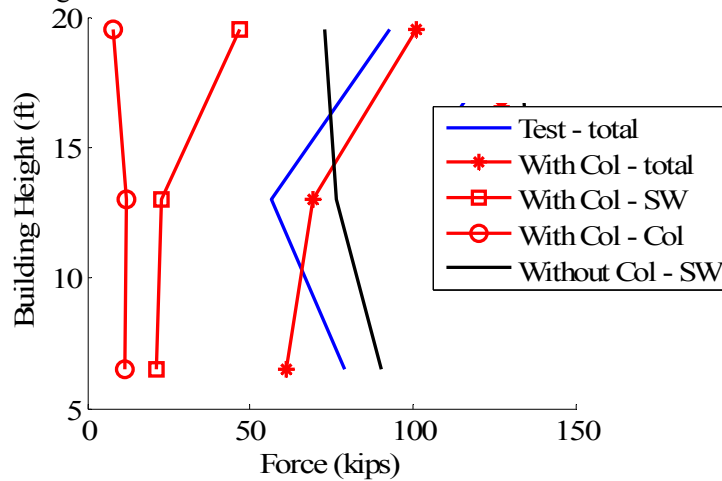
Fig. B4-58. Diaphragm Max Inertia Forces along the Building Height

B4.7.3 Diaphragm Deformation Demand Pattern along the Building Height

Figure B4-59 shows the diaphragm maximum deformation demand distribution along the building height. As shown in Fig. B4-59, the diaphragm maximum deformation in the model with column matches the test results better thant that in the model without column. The model without column sigifincatly overestimate the daiphagm maximum deformation demand in the lower floor as compared to the test results.
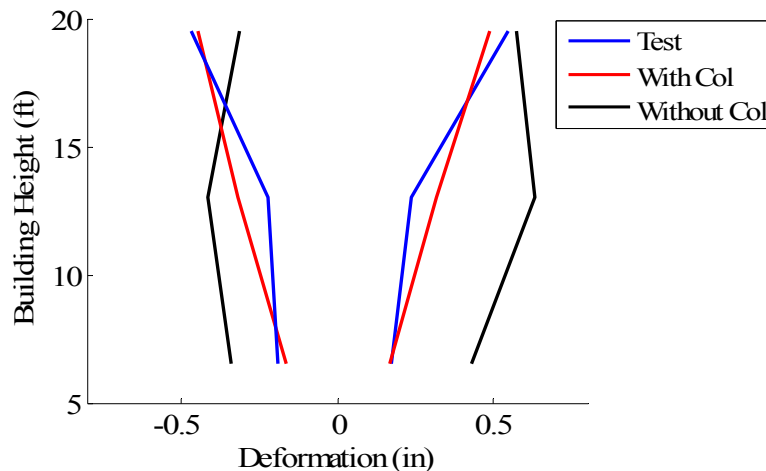
Fig. B4-59. Diaphragm Max and Min Deformation along the Building Height

B4.7.4 Diaphragm Joint Opening Profile Along Diaphragm Span

Figure B4-60 shows the maximum dipahragm joint opening profile along the diaphragm span. As seen, the diaphrgam joint opening demand obtained from the model with column mathes the shake table test results well. The model without column overestimates the diaphragm joint opening demand as compared to the test results. This higher demand in the model without column is significant in the first floor.

C-A-227
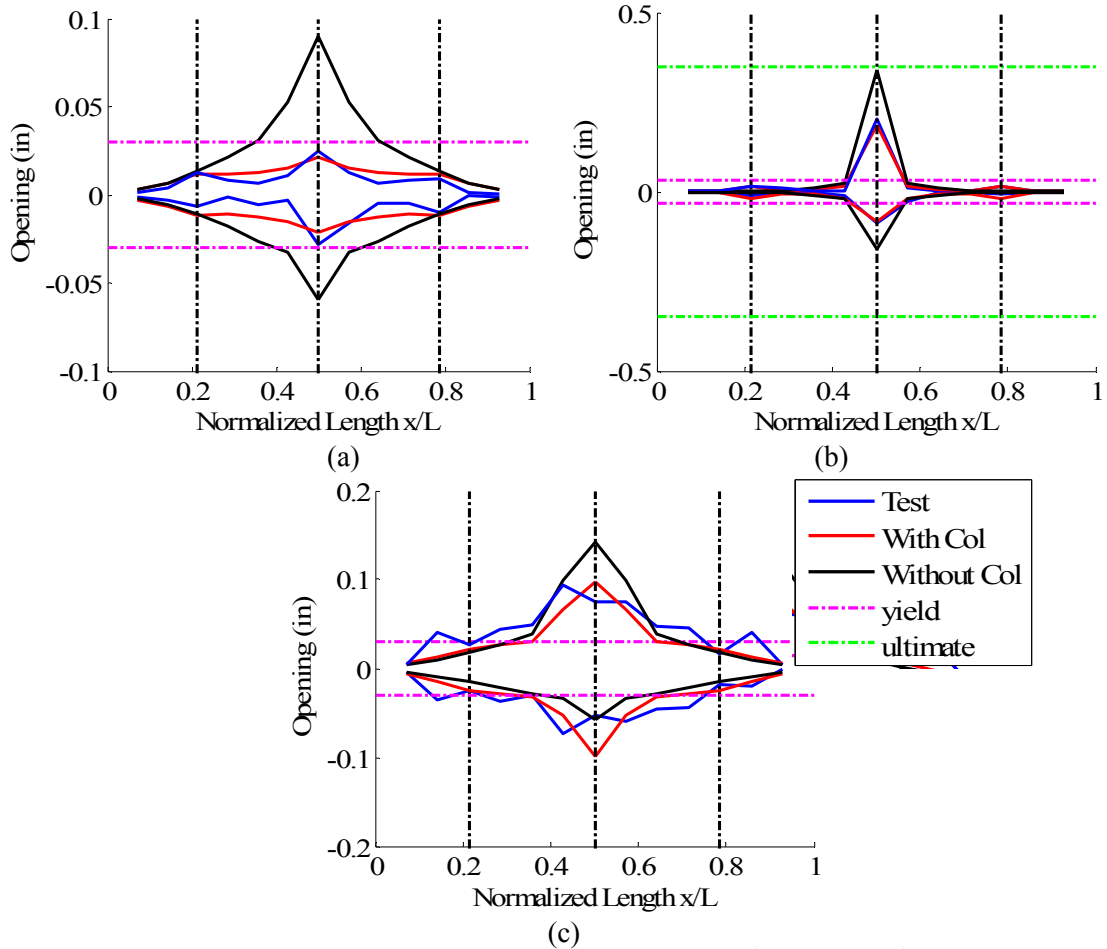
Fig. B4-60. Max Joint Opening: (a) 1st Floor (b) 2nd Floor (c) 3rd Floor

B4.7.5 Diaphragm Stiffness

Figure B4-61 shows the diaphragm mhysteresis response (diaphragm inertia force vs. diaphragm midspan deformation) at all three floor. As seen, the model with column has a better match to the test results than the model without column. The model without column has lower diaphragm stiffness than the model with column and test results, especially in the lower floor.

(c)
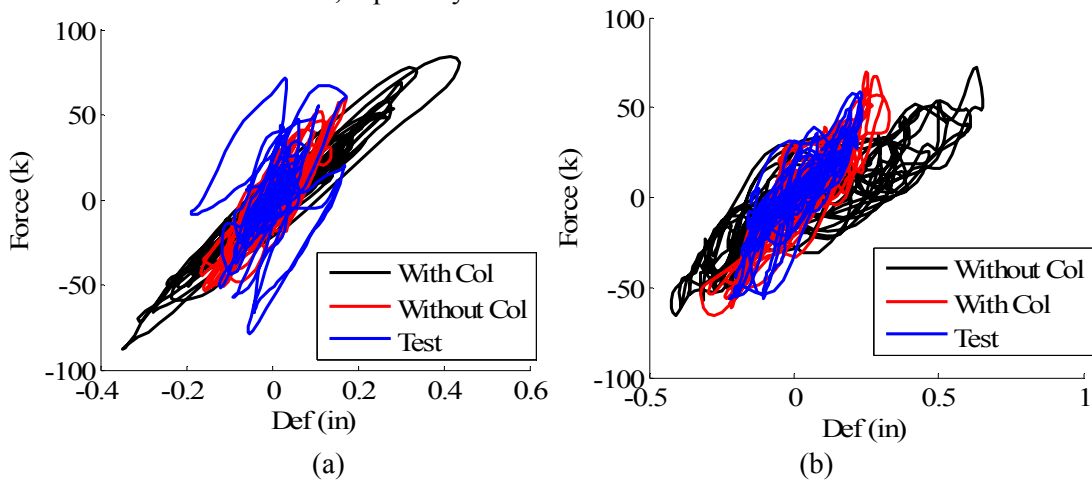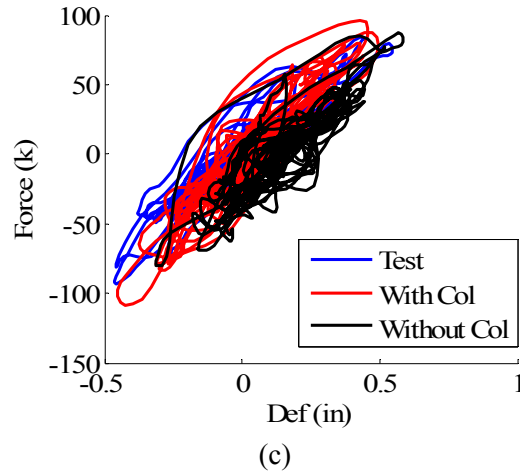
Fig. B4-61. Diaphragm Force vs. Deformation: (a) 1st Floor (b) 2nd Floor (c) 3rd Floor

B4.8 CONCLUSIONS

The shake table test specimen which represents a half-scale three story precast concrete structure has been subjected a sequence of 16 strong motions with increasing earthquake intensity. The diaphragm design of the shake table test specimen follows the concepts in the design methodology and uses a RDO design option. The test results has indicated the shake table test specimen meet the diaphragm design targets under MCE including: (1) the maximum chord opening demand is less than the HDE capacity and (2) the maximum joint sliding demand is less than the yield sliding of shear reinforcement.

Further, the shake table test results have been used to calibrate/verify the 3D NLTDA model. This calibrated model is used for the parametric studies in developing the diaphragm design factors in the design methodology. The following conclusions are made based on the calibration of the 3D NLTDA model using shake table tests:

(1) The response obtained from the modified PT wall model reasonably matches the observed wall response characteristics and seismic demand in low and moderate seismic demand from the shake table test.

(2) The 3D NLTDA model used for the untopped floor reasonably predicts the diaphragm global (force vs. deformation) and local (joint opening) demand as observed in the shake table tests at low and moderate earthquake intensity level.

(3) For low level earthquake intensity, the initial uncracked status and possible cracking in the topping slab during the earthquake influence the diaphragm response and are necessarily included in the analytical model.

(4) The self-cracking model with added tension only link element to the 3D NLTDA model reasonably catches the concrete topping cracking pattern observed in the shake table test and reasonably predicts the diaphragm demand observed in the shake table test.

(5) Due to substantial damage and modification of the shake table specimen before the high intensity earthquake tests (Berkeley DBE and MCE), it is not feasible to fully calibrate the analytical model based on these tests. Based on the limited calibration, the 3D NLTDA model reasonably and conservatively reproduces the diaphragm local flexural demand observed in the test.

(6) The gravity column has non-negligible effects on the diaphragm seismic response. This effect is more significant in the lower floor where the column restrain forces are more significant than the higher floor.

B4.9 REFERENCES

ASCE 7-05. Minimum Design Loads for Buildings and Other Structures. *ASCE* 2005.

Belleri, A. (2007). "Displacement based design for precast concrete structures". Ph.D. Dissertation. Starrylink Editrice Brescia, Italy.

Naito, C. and Ren, R., (2008). "Development of a seismic design methodology for precast diaphragms - phase 1c half scale". ATLSS Report #08-09. ATLSS Center, Lehigh University, PA.

Schoettler, M.J. (2010) "Seismic demands in precast concrete diaphragms" Ph.D. Dissertation. University of California, San Diego, CA.

Schoettler, M.J., Belleri, A., Zhang, D., Restrepo, J., and Fleischman, R.B. (2009). "Preliminary results of the shake-table testing for development of a diaphragm seismic design methology." PCI Journal, 54 (1), 100-124.

Shaikh, A.F. and Gehlhoff, J. (2007). "Load tests on new JVI PSA slotted inserts anchored in concrete slabs". Report on Test Results, Structural Engineering Laboratories at College of Engineering and Applied Science. University of Wisconsin Milwaukee.

Appendix C. Summary of DSDM Main Research Phases

TABLE OF CONTENTS

Appendix C. Summary of DSDM Main Research Phases

C1. INTRODUCTION

In 2003, the Prestressed/Precast Concrete Institute (PCI) issued a Request for Proposal (RFP) for a university consortium to develop an industry-endorsed seismic design methodology for precast concrete floor diaphragms. The impetus for the RFP was the failure of precast concrete diaphragms in recent earthquakes, most notably the 1994 Northridge earthquake (Iverson and Hawkins 1994). Several code changes (ACI 318 2005) and subsequent research (Wood et al. 2000) were enacted in reaction to the earthquake. However, there was consensus that a comprehensive design methodology was required to create reliable precast diaphragm designs. This in turn would open up markets for precast construction in regions of significant seismic hazard. The consortium team that was awarded the RFP, and a subsequent National Science Foundation (NSF) award under the Grant Opportunities for Academia Liaison with Industry (GOALI) program, recognized that knowledge required to create an effective design methodology did not currently exist, in large part due to the inability of past research to fully describe the complex behavior of precast concrete diaphragms. Thus, the imminent commissioning by NSF of the George E. Brown Network for Earthquake Engineering Simulation (NEES) was viewed as a unique opportunity to create this knowledge. Accordingly, a supplement was awarded to upgrade the project to use NEES equipment sites at Lehigh University and the University of California San Diego (UCSD). This paper provides a comprehensive summary of this NEES project, including descriptions of the research approach, activities and outcomes. Detailed information on the specific activities and findings of each research component appears in several publications produced by the project.

C2. PRECAST DIAPHRAGMS

Precast prestressed concrete is an economical and durable construction system. However, the vulnerability of precast floor systems during diaphragm action under earthquake loading limits efficient use of these systems in regions of high seismicity.

Precast Diaphragm Design

Diaphragms are reinforced to carry in-plane shear, flexure and anchorage forces (Moehle et al. 2010). In precast diaphragms, these forces must be carried across joints between the precast floor units. Mechanical connectors in an untopped precast diaphragm or reinforcing steel in the cast-in-place topping slab in a topped precast diaphragm are designed to carry these forces. Figure C-1a shows a simple diaphragm schematic, indicating internal force diagrams and the connectors intended to transfer: (a) in-plane shear force between the units; (b) chord forces associated with in-plane flexure; and (c) collector/anchorage forces to walls and frames. Figure 1b shows typical welded connector details used for precast diaphragm reinforcement.
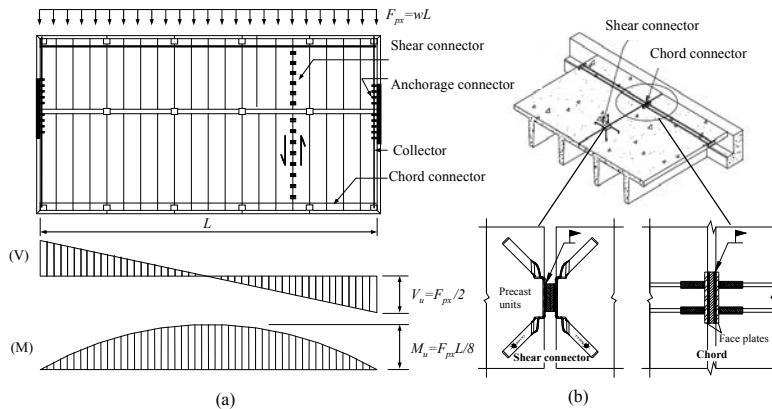

Fig. C-1: Precast diaphragm design: (a) Plan with internal forces (modified from Fleischman and Wan 2007); (b) Typical reinforcement details.

Precast Diaphragm Earthquake Performance

Precast concrete floor diaphragms have exhibited poor performance during major earthquakes. Figure C-2 shows one of the nine precast parking garage that collapsed in the 1994 Northridge earthquake (Iverson and Hawkins 1994). As an outcome of these failures and subsequent research (Wood et al. 2000), several code changes were enacted (ACI 318 2005). As a result, neither untopped precast diaphragms (using mechanical connectors only) nor topped composite diaphragms (using mechanical connectors in conjunction with a thin topping with mesh or light bars) are permitted in regions of high seismic hazard. Instead a non-composite topping slab (typically a thick topping with heavy two-way reinforcement) is required, and the precast floor units serve only as gravity load-resisting elements, thereby limiting the economic effectiveness of the precast construction. Should these systems be proven reliable under seismic loading when properly designed and detailed, the stringent restrictions could be reassessed. Thus, a viable precast diaphragm seismic design methodology would not only make precast structures safer, but would also enable cost-effective precast construction solutions in regions of high seismic hazard.

Fig. C-2: Precast parking structure collapse, 1994 Northridge Earthquake (Courtesy: *Los Angeles Times*).

Precast Diaphragm Behavior

The behavior of precast concrete diaphragms is complex: (1) floor diaphragms in general can undergo large instantaneous inertial forces (Rodriguez et al. 2002), even after yielding of the lateral force resisting system (LFRS) (Fleischman et al. 2002); (2) force paths within the diaphragm can be complicated (Wood et al. 2000); (3) most precast diaphragm reinforcement is under non-proportional combinations of cycling axial and shear force (Lee and Kuchma 2008) (Farrow and Fleischman 2003); and (4) precast concrete is often used in long floor systems where diaphragm flexibility can amplify inter-story drifts (Fleischman et al. 1998) (Fleischman and Farrow 2001). The combinations of these factors lead to conditions where current design practice cannot assure elastic diaphragm action. For precast floor systems, inelastic diaphragm deformations will concentrate in critical joints between the precast units (Fleischman and Wan 2007). Precast diaphragm reinforcement is of various types, including proprietary connectors and standard industry connections, which do not necessarily provide significant deformation capacity.

In summary, the development of an effective precast concrete diaphragm design methodology is challenging, in that complex nonlinear diaphragm behavior and structural system dynamics must be understood and accurately described for various precast diaphragm configurations. Precast diaphragms must satisfy tight economic, constructability and serviceability constraints, under conditions where inaccuracy in understanding the behavior can lead to structural failure.

C3. RESEARCH APPROACH

The features of the industry-endorsed seismic design methodology as described in the RFP included: (1) the forces to which the precast diaphragm is to be designed; (1) the deformations to which

the precast diaphragm should be designed; and (3) the precast concrete diaphragm reinforcement details that can provide this performance. The challenges in developing such a methodology (as described in the previous section) necessitates a research program with the following features: (1) a clear and effective design framework to guide the research; (2) integrated analytical and experimental research to enable numerous design parameters and large complex systems to be evaluated by computer simulations with confidence that these simulation models are based on physical reality through experimental verification/calibration; and, (3) strong industry oversight to ensure that the research involves practical applications and produces meaningful and useful results.

Design Philosophy

The precast diaphragm seismic design methodology (BSSC TS-4 2009) developed for the project adopts an approach where diaphragm force factors and diaphragm reinforcing details are aligned with performance targets. This approach is taken in recognition of the behavior anticipated for precast concrete diaphragms relative to the economic constraints.

The design methodology has the following primary features:

1. Diaphragm force amplification factors (Ψ) calibrated to performance targets.
2. Diaphragm reinforcement overstrength factors (Ω) that provide a capacity design by enforcing a higher design force for critical and potentially non-ductile reinforcement groups (shear reinforcement, collectors, anchorages) .
3. A diaphragm reinforcement classification system based on deformation capacity (Low, Moderate and High Deformability Elements or LDE, MDE and HDE) that align to the performance targets.
4. Diaphragm flexibility limits to avoid large diaphragm-induced inter-story drifts

Figure C-3 shows schematic diaphragm pushover curves used to illustrate the design approach. The designer has the following options: (1) a Basic Design, in which the diaphragm amplification factor (Ψ_D) targets elastic behavior for the design basis earthquake (DBE), and requires MDE diaphragm reinforcement, which possesses sufficient inelastic deformation capacity for the maximum considered earthquake (MCE); (2) an Elastic Design, in which a larger diaphragm amplification factor (Ψ_E) is enforced to target elastic behavior for the MCE, allowing diaphragm reinforcement without any special detailing requirements (LDE); and (3) a Reduced Design, in which a lower diaphragm amplification factor (Ψ_R) is used so that yielding under the DBE is permitted, and provides sufficient inelastic deformation capacity to the diaphragm for the MCE by specifying HDE diaphragm reinforcement.
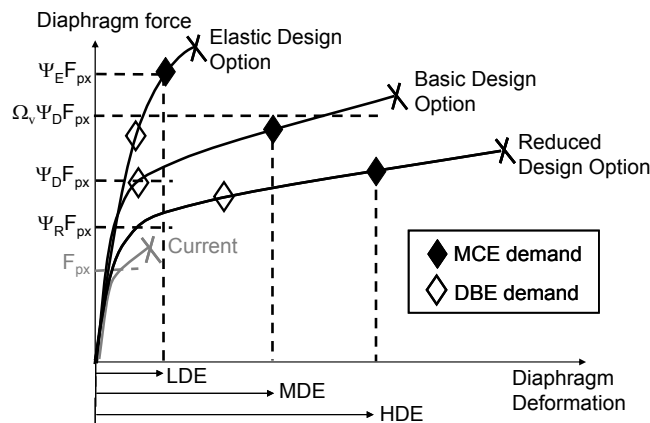

Fig. C-3: Diaphragm pushover schematic: precast diaphragm design approach.

Research Plan

Significant knowledge of the characteristics and behavior of precast diaphragms is required to determine the diaphragm design factors and reinforcement classifications described in the previous

section. This knowledge includes information at three distinct levels: (1) the reinforcing detail level (connector characteristics); (2) the diaphragm level (force paths, deformation demands); and, (3) the structural system level (diaphragm inertial forces, diaphragm deformation induced inter-story drifts). Further, information gathered at one level is needed to determine behavior at other levels.

Research by each university team focused on one level: (1) experimental and analytical research on reinforcement details and critical diaphragm joint response using the NEES@Lehigh facility; (2) experimental and analytical research on system response using the NEES@UCSD facility, and (3) analytical research at the University of Arizona to bridge the experimental work at the NEES Sites. The research was performed in three phases with the second phase relying most heavily on the NEES Equipment Sites. A key aspect of this research approach was the availability of telepresence tools for NEES research, which facilitated integration of the activities at each university.
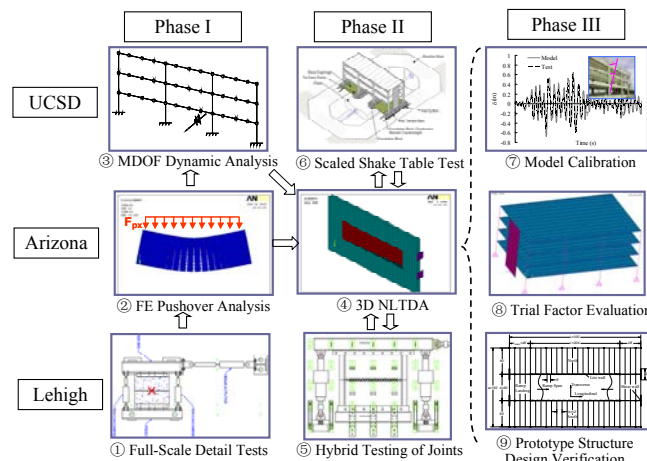
Fig. C-4: Project research flow.

Figure C-4 shows the research flow for the project. Each row refers to the activities at a university site. Each column represents the activities of one of the research phases. Each box represents a research step focused on developing knowledge about diaphragm capacity (1,2,5,7) or diaphragm demands (3,4,6,8,9). The research steps are as follows:

In Step 1, diaphragm connectors were tested in isolated fashion under cyclic loading protocols. Connector properties and classifications were determined.

In Step 2, the test results from Step 1 were used to build connector elements for two-dimensional (2D) analytical models of precast diaphragms. These models were used in nonlinear static "pushover" analyses of isolated diaphragms.

In Step 3, the diaphragm properties determined in Step 2 were used to create simple multi-degree-of-freedom (MDOF) models. These models were used to perform extensive parametric studies on the effect of structure configuration, diaphragm flexibility and seismic hazard intensity on floor inertial forces.

In Step 4, the information gathered in total from Phase 1 were used to create three-dimensional (3D) analytical models of precast concrete structures for use in nonlinear transient dynamic analysis (NLDTA).

In Step 5, the 3D NLDTA models were used to perform simulation-driven physical testing at NEES@Lehigh including hybrid simulation of earthquake response.

In Step 6, the performance of diaphragms under earthquake excitation was examined through a half-scale shake table test at NEES@UCSD.

In Step 7, the test results of Steps 5 and 6 were used to calibrate the 3D NLDTA model.

In Step 8, the calibrated analytical model was used to determine trial design factors for the diaphragm based on NLDTA of a simple evaluation structure.

In Step 9, realistic prototype structures designed with the trial factors was evaluated through NLDTA to calibrate final design factors. This step was also used to improve the usability of the design procedure, evaluate the economic competitiveness of the new designs, and to create design examples for dissemination of the research.

Industry Participation

A key aspect of the research was the close industry oversight in each stage of the project. At the outset, the industry group worked with the researchers to establish the physical scope of the project including: (1) a portfolio of prototype structures for use in the research and in developing design examples; (2) a set of seismic design sites ranging from low to high seismic hazard for developing baseline designs of the prototype structures and suites of spectrum-compatible ground motions for the research; and, (3) representative diaphragm reinforcement details for use in test specimens for the experimental program. During the research stages, the industry team had regular face-to-face meeting or teleconferencing with the research team.

C4. PHASES I, II: NEES RESEARCH ACTIVITIES

This section summarizes the experimental and analytical research activities of the project during Phase I and Phase II, highlighting key knowledge obtained in each step.

Step 1: Diaphragm Connector Testing

Isolated connector tests (Naito et al. 2009) (Cao and Naito 2009) were performed on the existing diaphragm connectors selected as representative details using a test fixture specially developed for the project. The test fixture (See Fig. C-5) can simultaneously apply nonproportional components of axial and shear force or displacement (Naito et al. 2006).

A testing protocol (Naito and Ren 2011) was established to determine the connector characteristics under cyclic tension and shear. Using the protocol, each connector type was prequalified for the design procedure as follows: (1) the connector is assigned a classification, i.e. LDE, MDE or HDE, based on the deformation capacity exhibited in the testing; and, (2) the connector characteristics (e.g. elastic stiffness, yield strength, secondary stiffness) in shear and tension are determined using a qualification backbone based on FEMA 356 (2000) and entered into a connector property database for use in the design procedure (Ren and Naito 2011).
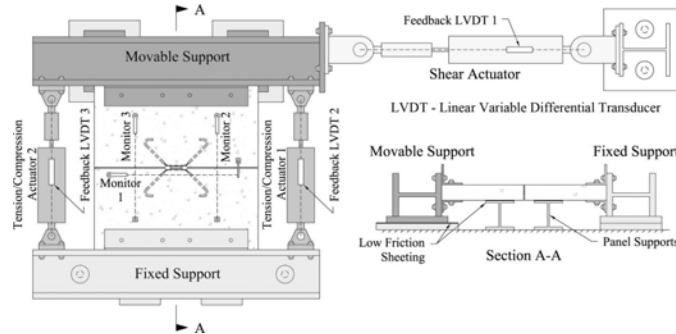

Fig. C-5: Isolated connector testing setup (after Naito and Ren 2011).

The test results for the representative details (see, for example, test results shown subsequently in Figure C-9b) showed that few existing precast diaphragm connectors are in the HDE classification. Accordingly, new connector details were developed including a ductile dry chord connector (Cao and Naito 2007) and a ductile ladder mesh (Naito et al. 2007) for shear reinforcement. Figure C-6 shows highlights from these activities including: (a) analytical modeling created in DIANA[16] used to develop the

---

[16]DIANA, Delft, Netherlands

ductile dry chord; (b) the ductile ladder mesh detail; and (c) ductile ladder cyclic shear results showing high inelastic shear deformation capacity.
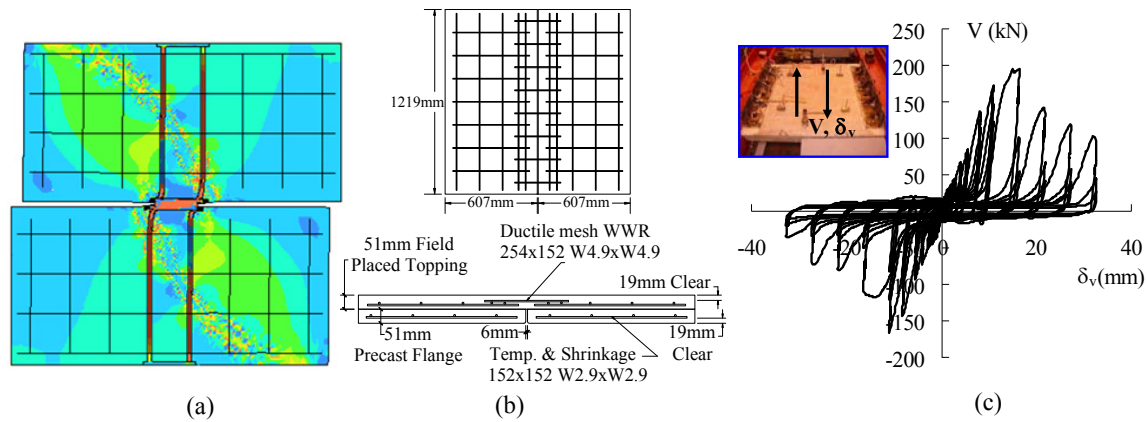

(a)

(b)

(c)

Fig. 6: Connector Research: (a) Dry chord modeling (after Cao and Naito 2007); (b) Ductile ladder detail (after Naito et al. 2007), (c) Response.

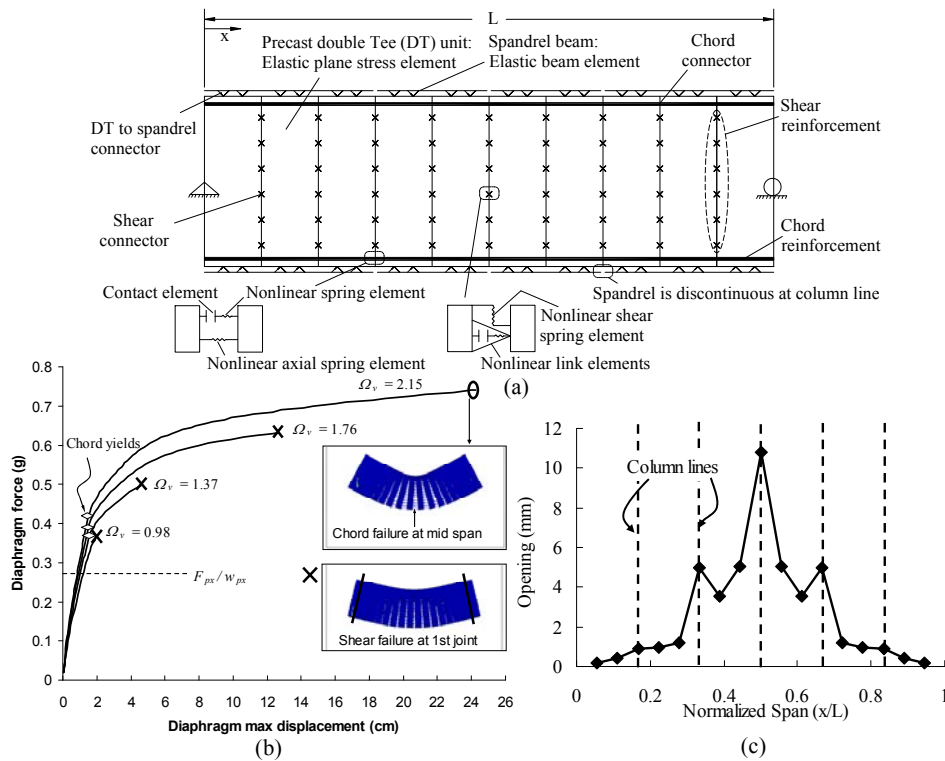## Step 2: Diaphragm Analytical Modeling and Analysis

(a)

(b)

(c)

Fig. C-7: Diaphragm Analysis: (a) 2D-FE model; (b) Pushover curve (after Fleischman and Wan 2007); (c) Deformation profile.

Two-dimensional (2D) finite element (FE) models of the precast diaphragm were developed. A key feature of these models is the explicit modeling of the precast diaphragm connectors. Such an approach permits direct evaluation of: (1) the force paths in the diaphragm, which involves discrete force transfers across the joints between the precast floor units; (2) non-Bernoulli deformation patterns that

C-A-237

occur in the floor system; and (3) the local demands acting on connectors including combined forces and inelastic deformation demands.

Test results from Step 1 were used to build the connector element models for the FE models (Wan 2007). A critical requirement for these elements is the need to produce accurate shear response in the presence of axial tension, where coupled response occurs (Pinchiera et al. 1998), and in the presence of axial compression, where friction mechanisms are mobilized (Naito et al. 2006). Thus in addition to the aforementioned connector qualification testing in Step 1, supplemental tests of connectors under cyclic shear in the presence of tension and compression were performed.

The 2D-FE model (See Fig. C-7a) was used for nonlinear static "pushover" analyses of isolated diaphragms (Fleischman and Wan 2007). These analyses were used to determine diaphragm characteristics, such as global stiffness, strength, deformation capacity, and to examine load paths and deformation patterns, including concentrated deformation demands created by the variation of diaphragm reinforcement characteristics between joints, by non-ductile shear reinforcement, or by the protection of certain joints by gravity beams in the floor system (Wan et al. 2012). As an example, Fig. C-7b shows the sensitivity of diaphragm strength and deformation capacity to the shear reinforcement overstrength factor Ω_v, while Fig. 7c shows the joint opening profile, indicating a concentration of inelastic deformation demand for joints at the column lines where the precast spandrel beams are discontinuous. Thus the major findings from this step pertain to the global characteristics of the diaphragm and the relationship between diaphragm global and local deformation demands
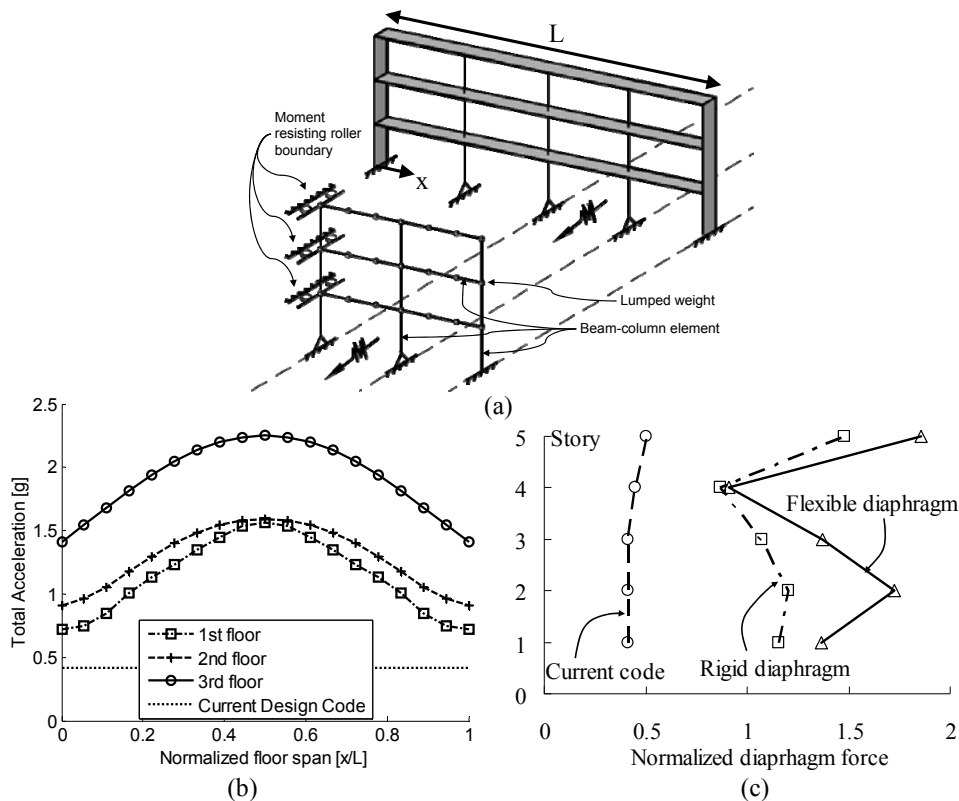
Step 3: Structure MDOF Modeling

Fig. C-8: MDOF study: (a) Model (after Schoettler 2010); (b) Floor accelerations; (c) Trial design forces for elastic response.

C-A-238

The diaphragm properties determined in Step 2 were used to create simple multi-degree-of-freedom (MDOF) models of diaphragm-sensitive structures (See Fig. C-8a). These simple models were used to perform extensive parametric studies (Schoettler 2010) on the relationship between structure configuration, diaphragm flexibility and seismic hazard intensity. Figure 8a shows the MDOF model, where the diaphragm is modeled using beam elements with effective shear and flexural properties based on the pushover analyses from Step 2. The models are subjected to the suites of spectrum-compatible ground motions developed for different sites, as described earlier. As an example of results produced in this step, Figure C-8 shows maximum floor inertial force results for seismic design category (SDC) E under the DBE, including: horizontal profiles across the diaphragm showing a non-uniform distribution in contrast to the uniform diaphragm force design distribution used in codes (Fig C-8b); and, vertical profiles showing the trial design forces determined for elastic response (Fig. C-8c).

Step 4: Structure NLDTA Modeling

More detailed models of the precast concrete structures were developed for use in nonlinear transient dynamic analysis (NLTDA). These three-dimensional finite element (3D-FE) models (See Fig. C-9a) incorporate the discrete diaphragm connector models used in the 2D-FE model described in Step 2, extended for cyclic loading. The key step in extending the model is modifying the connector elements to capture the characteristics observed in the isolated connector cyclic loading tests, including the hysteretic behavior, strength degradation, stiffness degradation, slip, and cyclic ductility (Zhang 2010). Figure C-9b compares a cyclic shear test result from Step 1 with the results from connector element under cyclic loading.

The finite element model treats the three-dimensional behavior of the structure, including the nonlinear behavior of the primary vertical elements of the LFRS, confinement of the floor joint opening by the out-of-plane stiffness of shear walls and moment frames, and the restraint provided by the gravity columns. Realistic treatment of the confinement perpendicular to the diaphragm joints and the supplemental interstory stiffness provided by gravity columns was shown to have a significant effect on precast diaphragm response (Zhang 2010).
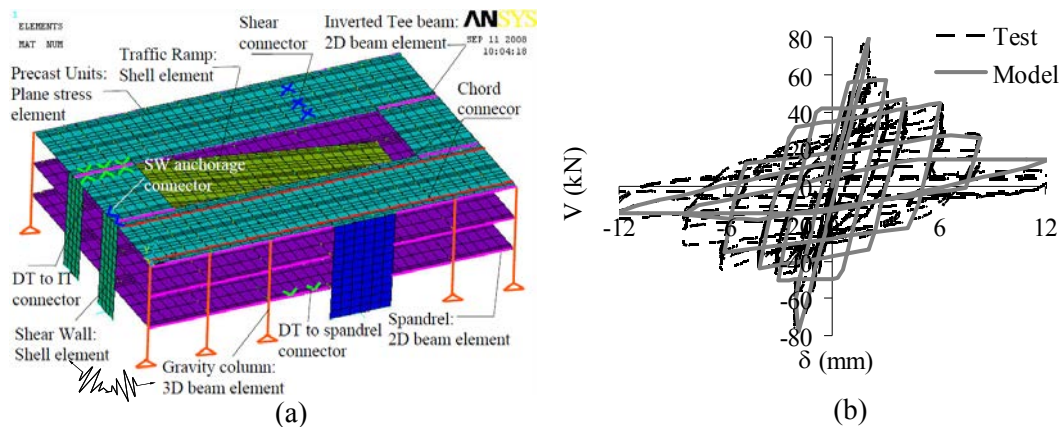

Fig. C-9: NLDTA modeling: (a) 3D model of parking structure; (b) Connector cyclic response.

The 3D-FE model was the production model for the subsequent research steps including: (1) analyses to determine diaphragm-sensitive precast structure seismic behavior; (2) serving as analytical superstructure for the hybrid simulations; and (3) for calibrating diaphragm design factors for the design methodology (Zhang 2010).

Step 5: Simulation-driven Physical Testing

Key diaphragm joints were examined through simulation driven physical tests performed using the 3D-FE NLTDA models: (1) a critical flexure joint from a precast parking structure diaphragm (Zhang

et al. 2011); and (2) a critical shear joint taken from a diaphragm of the test structure designed for the subsequent shake table test (Zhang 2010).
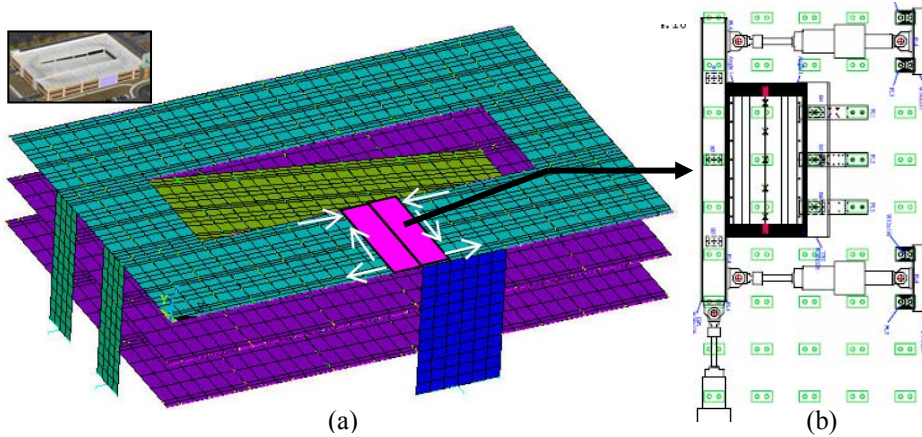

(a)   (b)

Fig. C-10: Simulation driven test, critical flexure joint: (a) analytical superstructure (modified from Zhang et al. 2011); (b) experimental substructure.

In the first set of tests, NLDTA of the parking structure model under single and bi-directional ground motions (See Fig. C-10a) was used to create a predetermined displacement history for the 3 degrees of freedom (DOFs) of a half-scale experimental substructure (See Fig. C-10b). The substructure contains a joint that is under simultaneous flexure, shear and axial cyclic loading due to the combined effects of transverse diaphragm bending, in-plane twisting due to the ramp cavity and collector forces transferred to the longitudinal shear wall.
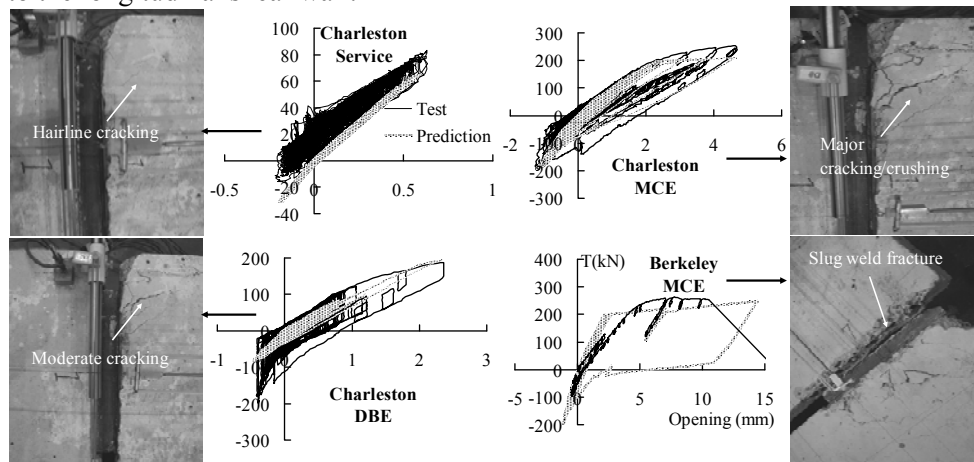
Fig. C-11. Chord responses of Simulation driven test (Modified from Zhang et al. 2011).

The flexural strength, stiffness, rotational deformation capacity and progressive damage of the critical flexural joint were examined under a sequence of increasing intensity earthquakes. Figure C-11 shows the critical chord tension response in and damage mapping with increasing earthquake loading intensity. The prediction from the NLTDA is shown on top of the test results. The major findings from this test are: (1) using the new design methodology, the critical flexural joint survived its designated MCE earthquake; (2) the unbonded dry chord connector and shear (JVI Vector) connector exhibited good inelastic deformation capacity; and (3) the analytical model shows good agreement with the joint deformation response, including reasonable predictions of local response.
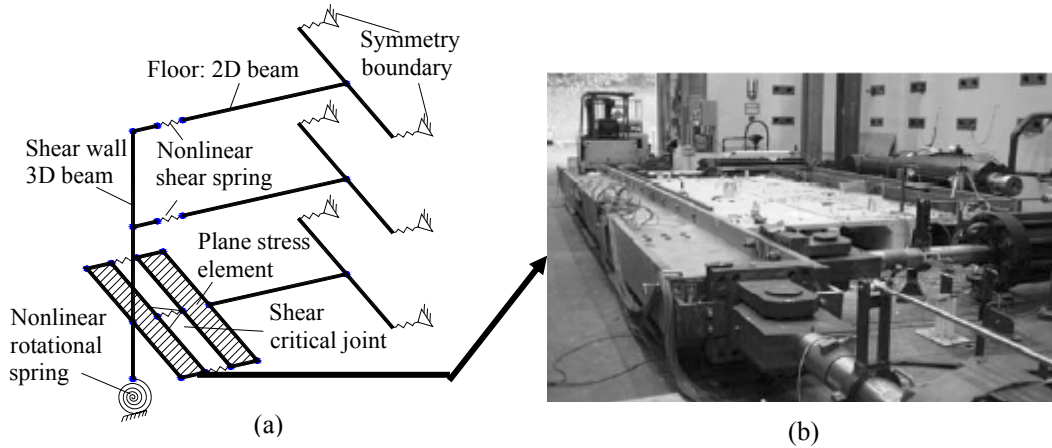
C-A-240

Fig. C-12: Hybrid test, shear joint: (a) analytical superstructure (modified from Zhang 2010); (b) experimental substructure.

In the second set of tests, the critical shear joint from a diaphragm of the shake table test structure was evaluated using hybrid simulation. A half-scale specimen of the critical shear joint (See Fig. C-12) was the experimental substructure. The use of hybrid simulation for this evaluation is crucial since the shear response of a precast diaphragm joint can be extremely sensitive to axial force perpendicular to the joint, either tension or compression, and the moment acting on the joint. In isolated connector tests, simplified assumptions of restraint perpendicular to the joint are typically made. In this test, the cyclic axial and flexural actions that occur simultaneously with the cyclic shear, including non-proportional loading due to the interaction of the softening experimental substructure with the analytical superstructure are captured.

The hybrid simulation applied the anticipated seismic demands to the critical shear joint. The shear strength and stiffness of a pretopped precast concrete diaphragm joint were examined under progressive cyclic loading damage. Figure C-13a shows the hysteretic response (at half scale) of joint shear vs. joint sliding from the hybrid simulation with the NLTDA model prediction on top. Figure C-13b shows the shear stiffness (at half scale) degradation under the progressive cyclic loading damage. The major findings from this test are: (1) the shear (JVI Vector) connectors show strength and stiffness degradation with increasing sliding deformation; (2) a shear overstrength factor is required for the seismic design to prevent a non-ductile shear failure; and, (3) the analytical results and hybrid simulation results are in good agreement.
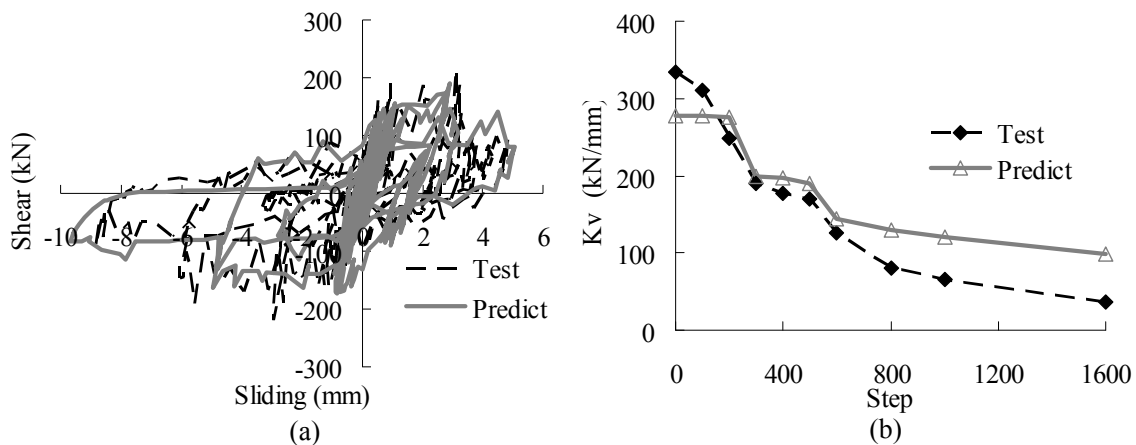

Fig. C-13. Shear responses of hybrid test: (a) Hysteresis (b) Stiffness degradation.

C-A-241

Step 6: Shake Table Testing

A three-story diaphragm sensitive structure was tested on the NEES@UCSD shake table (Schoettler et al. 2009). Figure C-14a shows the half-scale shake table test specimen. The structure has three floor levels with a different construction technique used for each level: (1) a topped double tee system; (2) a topped hollow core system; and (3) an untopped double tee system (See Fig. C-14b). Each of the floors was designed with concepts from the design methodology. The structure possessed unbonded post-tensioned precast rocking walls which permitted repeated testing of the structure without significant damage to the walls.
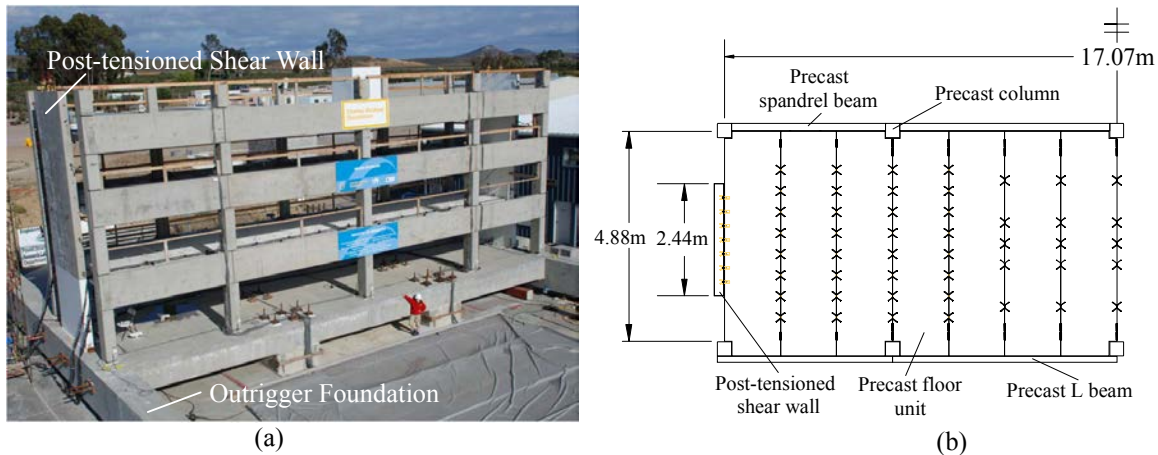

Fig. C-14: Shake table testing specimen (modified from Schoettler et al. 2009): (a) Specimen photo; (b) Plan of 3rd floor

The use of the NEES@UCSD shake table was essential to demonstrate the performance of the diaphragm design concepts at large scale as it is difficult to produce small scale precast units and connectors. Most other existing shake table tests would require an idealized "toy" test structure that would not directly reproduce the configurations, anchorages, or construction tolerances of actual precast concrete structures. Even though the NEES@UCSD shake table is large, the half-scale test structure did not fit on the table, and a special outrigger foundation on special sliders (shown in Fig. 14a) was needed.

The objectives of the shake table test program include: (1) to demonstrate the performance of precast diaphragms and the efficacy of the design methodology; (2) to prequalify certain diaphragm designs at a given level of performance; (3) to provide information for use in calibrating the analytical models, and (4) to provide new knowledge of the behavior of diaphragm sensitive precast structures. To do so, the test structure was designed for Berkeley (SDC E) using the RDO design option and it was put through a suite of increasing intensity earthquakes, from a SDC C DBE to a SDC E MCE (see Table C-1). The data acquisition at NEES@UCSD was supplemented by the NEES@UCLA mobile truck to include over 600 channels of data. A NEES payload project on equipment isolation was conducted on the shake table specimen (Cassidy and Gavin 2008).

Table C-1. Test program matrix

Test #	SDC	Site	Target Level	Historic earthquake	Scaled PGA (g)
1	C	Knoxville (KN)	DBE	1979 Imperial Valley	0.30
2	D	Seattle (SE)	DBE	1979 Imperial Valley	0.59
3	E	Berkeley (BK)	DBE	1989 Loma Prieta	0.41
4	E	Berkeley (BK)	MCE	1989 Loma Prieta	0.61

Figure C-15 highlights results from the shake table test program. Figure C-15a shows the diaphragm inertia force profile along the floor span at the 3rd floor. As expected for a RDO design, the diaphragm yields under both DBE and MCE. Note that the force profiles were not uniformly distributed along the diaphragm, as current design practice assumes. Figure C-15b shows the maximum diaphragm joint opening demand. As seen, with the increase in earthquake loading, the diaphragm joint opening increases progressively from elastic to inelastic but remained below the target failure opening. This result indicates that the diaphragm joint inelastic deformation demand met the RDO design target.
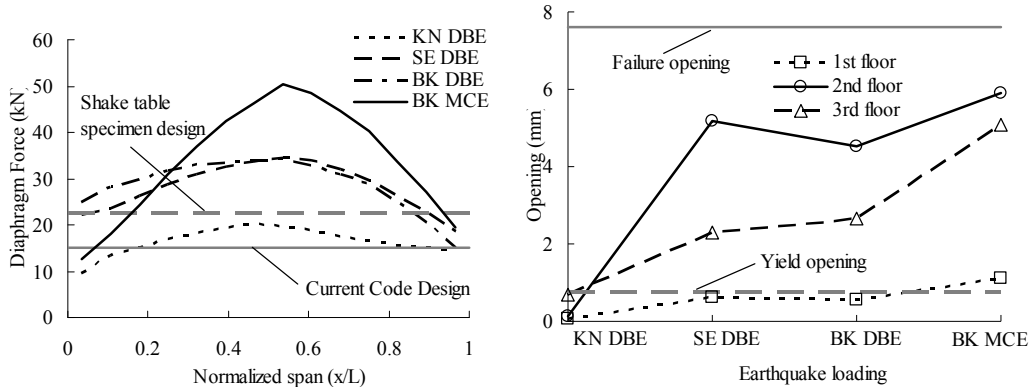

Fig. C-15. Shake table test results: (a) Diaphragm force profile, 3rd floor (b) Maximum joint opening.

C5. PHASE III: DESIGN METHODOLOGY DEVELOPMENT

The NEES research activities described in the previous section provided new knowledge on the characteristics of precast diaphragm reinforcement, the behavior of precast diaphragms and the seismic demands on diaphragm-sensitive precast structures. A major objective of these research activities was to develop analytical models for calibration of diaphragm design factors over a wide range of structural conditions. This step occurs in Phase III.

Step 7: Analytical Model Calibration

Model calibration involved comparing analytical response to the global and local response from the shake table tests (Zhang 2010) and the simulation-driven tests (Zhang et al. 2011). Global experimental responses include: (1) diaphragm force; (2) diaphragm deformation; (3) LFRS drift demand; (4) interstory drift; and (5) structure period. Local responses include: (1) deformation profiles along the length of the diaphragm; (2) individual diaphragm connector deformation demands; and (3) failure modes.
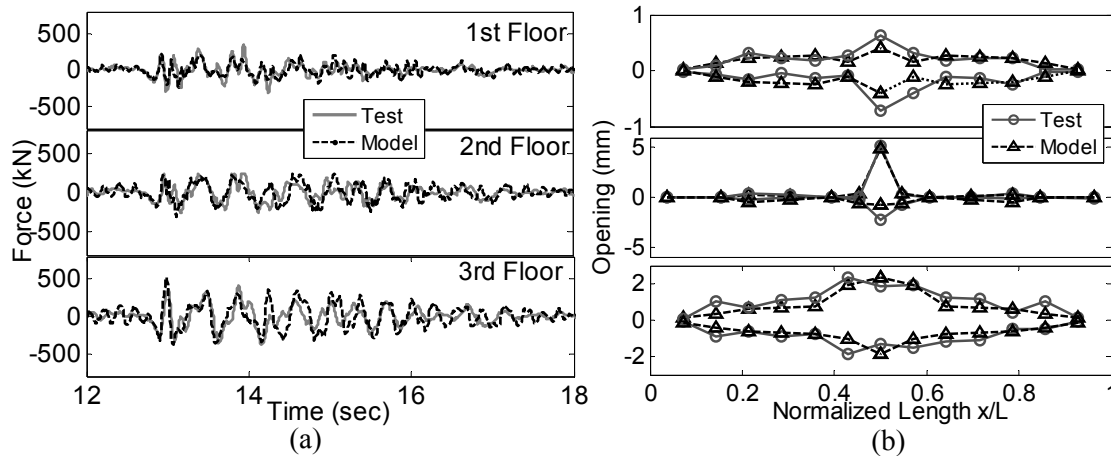

Fig. C-16. Diaphragm response model-test comparison: (a) Inertia force (b) Maximum opening.

Figure C-16 compares the diaphragm response from a shake table test and the calibrated analytical model. Results are shown for diaphragm inertia force and maximum diaphragm joint opening under the Seattle DBE earthquake. Good agreement is seen between test and calibrated model results. Such agreement permits the use of the 3D-FE model for developing diaphragm design factors.

Step 8: Trial Design Factor Parameter Study

The calibrated analytical model was used to perform a parameter study to determine trial design factors (Zhang 2010). A simple evaluation structure (see Fig. C-17a) was used for this study, to permit easily varying the diaphragm geometry (length and aspect ratio), number of stories, SDC (C, D and E), and layout and type of LFRS (shear walls and moment frames). The objective of this study was to determine trial values of the diaphragm design factors (Ψ, Ω) described earlier. To accomplish this objective, the diaphragm design strength is increased in the analysis until the associated diaphragm performance target (See Fig. C-3) is met. This process was guided by preliminary findings on diaphragm inertial force obtained in Step 3.
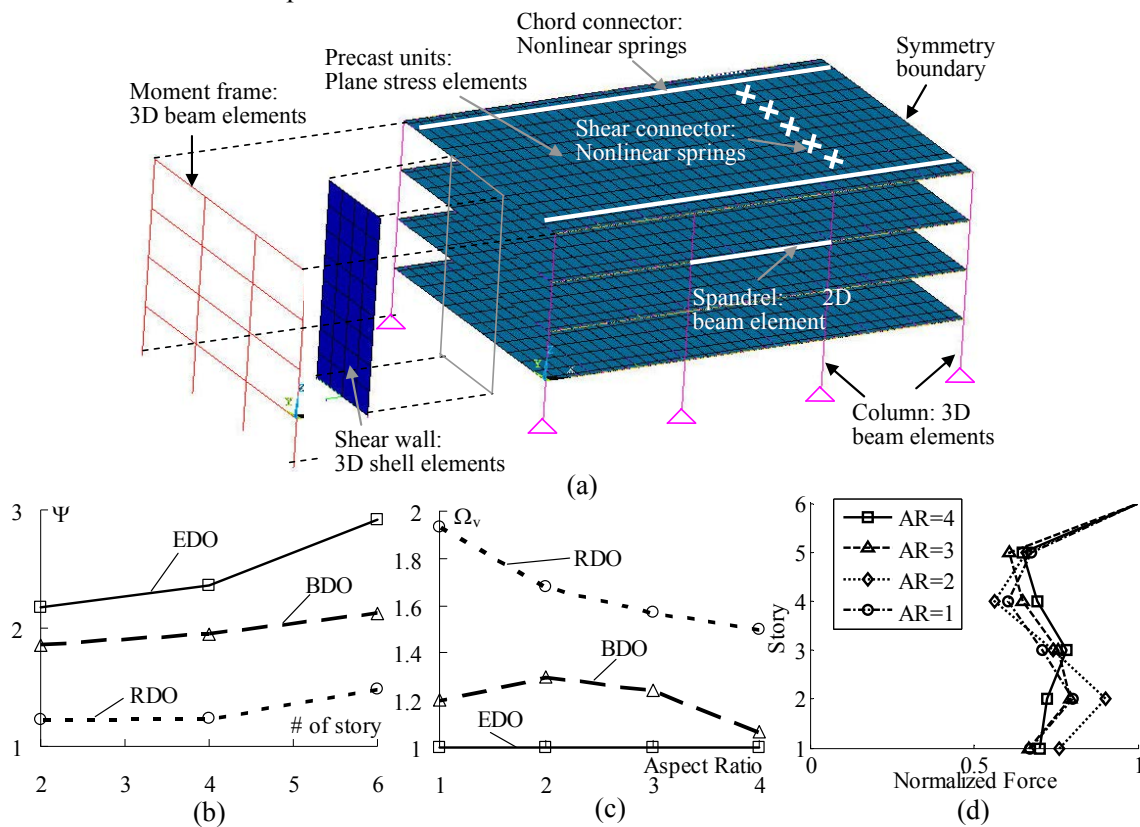

Fig. C-17. Parametric study: (a) Evaluation structure (b) Ψ factors; (c) Ω factors; (d) Diaphragm force profile.

Figure C-17b shows the diaphragm force amplification factors meeting the design targets for structures with a diaphragm aspect ratio of 4. Figure C-17c shows the diaphragm shear overstrength factors determined for 4-story structures. It is seen that Ψ typically increases with number of stories and Ω typically decreases with the diaphragm aspect ratio. Figure C-17d shows the normalized diaphragm inertia force under the MCE indicating that the maximum diaphragm force typically occurs at the top floor.

This step established the trial values of the diaphragm design factors (Ψ, Ω). These factors have been used in the proposed diaphragm design methodology. The prototype structures designed with these factors are evaluated in step 9

Step 9: Final Design Factor Calibration

The final research step is the calibration of the design factors (Zhang 2010). In this step, the prototype structures selected at the outset of the project are designed using the design methodology with the trial design factors determined in the previous step. During this process, analytical models created to design the prototype structures were used by research team, in close collaboration with the industry advisory team, to: (1) evaluate the "usability" of the design procedure and improve it as needed; (2) examine the economics of the new designs relative to current designs and suggest modifications; and (3) create design examples for use in handbooks.

As an example of this final calibration, Figure C-18 shows the results of prototype parking structure designed for SDC C under bi-directional MCE loading. Figure 18a shows a typical floor plan and photo of the structure. Figure C-18b shows the diaphragm inertia force profile vs. story. Figure C-18c shows the diaphragm moment diagram. In each case, the proposed design force values are included in the plot. It is seen that the design values estimate well and bound the diaphragm force demands under the earthquake loading in most cases. Figure C-18d shows the diaphragm maximum joint opening profile for different design options. This figure indicates that the diaphragm opening demand for each design option has met the design performance targets (elastic behavior for the EDO; deformation within MDE allowable deformation for the BDO, and deformation within HDE allowable deformation for the RDO).
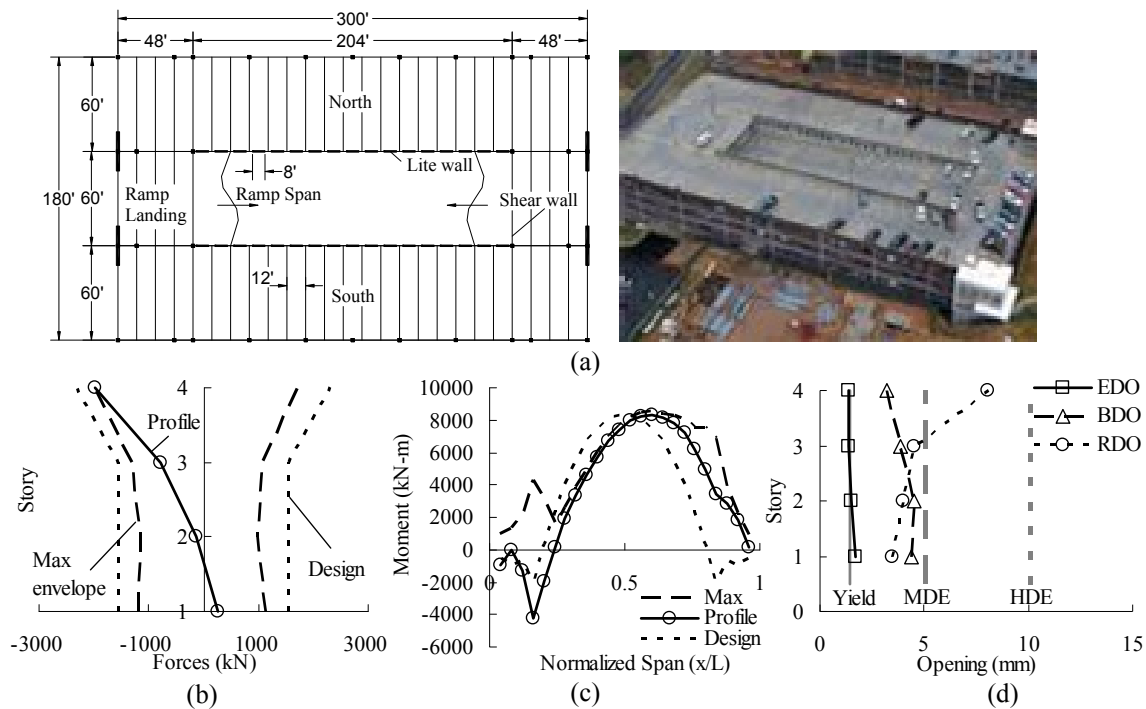

Fig. C-18. Prototype parking structure: (a) Floor plan and isotropic view (b) Diaphragm inertia; (b) North sub-diaphragm moment; (c) Diaphragm joint opening.

Codification Activities

In parallel with the research activities summarized herein, the industry advisory team worked closely with the researchers to create a usable design methodology and to initiate mechanisms to transfer the products of the research into practice. These ongoing activities include: (1) a draft design methodology (Fleischman 2009); (2) a white paper accepted to Part 3 of the 2009 NEHRP Recommended Provisions for Seismic Design for New Buildings (BSSC TS4 2009); and (3) active participation of industry advisory team members on ACI 550 sub-committees and BSSC PUC IT task groups pertaining to diaphragm design.

C6. CONCLUSIONS

A multi-university team has successfully used the equipment, methods and collaborative research tools provided by NEES to develop a new design methodology for precast concrete diaphragms. The project used research facilities at the NEES Equipment Sites to develop new knowledge and calibrate analytical models pertaining to precast concrete floor diaphragms. This knowledge has informed a new design methodology, and the calibrated analytical models have been used to quantify design factors required in the diaphragm design procedure. The project's industry advisory team is currently working with code-writing bodies to move the results of the project into the design codes.

C7. REFERENCES

ACI 318-05 (2005). Building Code Requirements for Structural Concrete (ACI 318-05) and Commentary (ACI 318-05), ACI committee 318.

Building Seismic Safety Council, Committee TS-4. (2009) "Seismic design methodology for precast concrete floor diaphragms." Part III, NEHRP Recommended Seismic Provisions Federal Emergency Management Agency, Washington, D.C.

Cassidy I. and Gavin H.P. (2008) "Modeling of a half-scale pre-cast pre-stressed reinforced concrete building" Internal report, Department of Civil and Environmental Engineering, Duke University.

Cao L., and Naito C. (2007) "Design of precast diaphragm chord connections for in-plane tension demands." ASCE Journal of Structure Engineering 133(11): 1627-1635.

Cao L., and Naito C. (2009) "Precast double-tee floor connectors part II: shear performance." PCI Journal; 54(2): 97-115.

Federal Emergency Management Agency (2000). "Prestandard and commentary for the seismic rehabilitation of buildings" FEMA 356, Washington, DC.

Fleischman R.B. (2009). "Development and design of untopped precast concrete diaphragm system for high seismic zones" Charles Pankow Foundation, <http://www.pankowfoundation.org/grants.cfm?research=1>

Farrow, K. T. and Fleischman, R. B. (2003). "Effect of dimension and detail on the capacity of precast concrete parking structure diaphragms" PCI Journal 48(5): 46-61.

Fleischman, R. B., and Farrow, K. T. (2001) "Dynamic response of perimeter lateral-system structures with flexible diaphragms", Journal of Earthquake Engineering & Structural Dynamics, V.30, No. 5, May, pp. 745-763.

Fleischman, R.B. Farrow, K.T. Eastman, K. (2002) "Seismic response of perimeter lateral-system structures with highly flexible diaphragms," Earthquake Spectra, 18 (2) May: 251-286.

Fleischman, R.B., Sause, R., Pessiki, S., and Rhodes, A.B., "Seismic Behavior of Precast Parking Structure Diaphragms, PCI Journal, 43 (1), January/February, pp. 38-53, 1998.

Fleischman, R.B. and Wan, G. (2007). "Appropriate overstrength of shear reinforcement in precast concrete diaphragms", ASCE Journal of Structure Engineering 133(11): 1616-1626.

Iverson, J.K. and Hawkins, N.M. (1994). "Performance of precast/prestressed concrete building structures during Northridge earthquake" *PCI Journal*: 39 (2): 38-55.

Lee, H.J. and Kuchma, D.A. (2008). "Seismic response of parking structures with precast concrete

diaphragms" PCI Journal 53(2): 71-94.

Moehle, J.P., Hooper, J.D., Kelly, D.J. and Meyer, T.R. (2010) "Seismic Design of Cast-in-Place Concrete Diaphragms, Chords, and Collections" NEHRP Seismic Design Technical Brief No.3.

Naito, C.J., Cao, L., and Peter, W. (2009). "Precast double-tee floor connectors part I: tension performance." PCI Journal, 54(1), 49-66.

Naito, C., Peter, W. and Cao, L. (2006). "Development of a seismic design methodology for precast diaphragms - phase 1 summary report". ATLSS Report No.06-03, ATLSS Center, Lehigh University, PA.

Naito, C., Ren, R., Jones, C., and Cullen T. (2007). "Development of a seismic design methodology for precast diaphragms - phase 1b summary report". ATLSS Report 07-04. ATLSS Center, Lehigh University, PA.

Naito, C.J. and Ren, R. (2011). "An evaluation method for precast concrete diaphragm connectors based on structural testing" PCI Journal. Submitted.

Ren, R. and Naito, C.J. (2011). "Precast concrete diaphragm connector performance database and response estimation modeling approach" ASCE Journal. Submitted.

Rodriguez, M., Restrepo, JI, and Carr, A.J. (2002) "Earthquake induced floor horizontal accelerations in buildings". Journal of Earthquake Engineering & Structural Dynamics, v 31, n 3, March, 693-718.

Schoettler, M.J. (2010) "Seismic demands in precast concrete diaphragms" Ph.D. Dissertation. University of California, San Diego, CA.

Schoettler, M.J., Belleri, A., Zhang, D., Restrepo, J., and Fleischman, R.B., (2009). "Preliminary results of the shake-table testing for development of a diaphragm seismic design methodology." PCI Journal, 54 (1), 100-124.

Wan, G. (2007). "Analytical development of capacity design factors for a precast concete diaphragm seismic design methodology", Ph.D dissertation, the University of Arizona, Tucson, AZ.

Wan, G., Fleischman, R.B. and Zhang, D. (2012). "Effect of spandrel beam to double tee connection characteristic of flexure-controlled precast diaphragms", J. of Structural Eng. ASCE. Scheduled published in Feb. 2012.

Wood S. L., Stanton J. F. and Hawkins N. M. (2000). "New seismic design provisions for diaphragms in precast concrete parking structures", PCI Journal, 45 (1): 50-65.

Zhang, D. (2010) "Examination of precast concrete diaphragm seismic response by three-dimensional nonlinear transient dynamic analyses." Ph.D. Dissertation. University of Arizona, Tucson, AZ.

Zhang, D., Fleischman, R.B., Naito, C., and Ren, R. (2011). "Experimental evaluation of pretopped precast diaphragm critical flexure joint under seismic demands." J. Struct. Eng. ASCE, V137(10).

C8. NOTATION
F_{px} = diaphragm design force in current code;
K_V = diaphragm joint shear stiffness;
L = diaphragm span;

M_u, V_u = diaphragm design moment and shear;
V = diaphragm joint shear force;
T = diaphragm connector tension force;
x   = distance to diaphragm end;
δ_v = connector shear deformation.

Appendix D. DSDM Project Publications and Reports

TABLE OF CONTENTS

Appendix D. DSDM Project Publications and Reports

D1. JOURNAL ARTICLES

Published
Cao L., and Naito C. (2007) "Design of precast diaphragm chord connections for in-plane tension demands." J. of Structural Eng. ASCE, 133(11): 1627-1635.

Cao L., and Naito C. (2009) "Precast double-tee floor connectors part II: shear performance." PCI Journal, 54(2): 97-115.

Fleischman, R. B., Naito C.J., Restrepo J., Sause R. and Ghosh S.K. (2005a). "Seismic design methodology for precast concrete diaphragms, Part 1: design framework", PCI Journal, 50(5): 68-83.

Fleischman, R.B., Naito C.J., Restrepo J., Sause R., Ghosh S.K., Wan G., Schoettler M., and Cao L. (2005b). "Seismic design methodology for precast concrete diaphragms, Part 2: research program." PCI Journal, 51(6):2-19.

Fleischman, R.B. and Wan, G. (2007). "Appropriate overstrength of shear reinforcement in precast concrete diaphragms", ASCE J. Structure Eng. 133(11), 1616-1626.

Naito, C.J., Cao, L., and Peter, W. (2009). "Precast double-tee floor connectors part I: tension performance." PCI Journal, 54(1), 49-66.

Schoettler, M.J., Belleri, A., Zhang, D., Restrepo, J., and Fleischman, R.B., (2009). "Preliminary results of the shake-table testing for development of a diaphragm seismic design methodology." PCI Journal, 54 (1), 100-124.

Wan, G., Fleischman, R.B. and Zhang, D. (2012). "Effect of spandrel beam to double tee connection characteristic of flexure-controlled precast diaphragms", J. of Structural Eng. ASCE, 138 (2): 247-258.

Zhang, D., Fleischman, R.B., Naito, C., and Ren, R. (2011). "Experimental evaluation of pretopped precast diaphragm critical flexure joint under seismic demands." J. of Structural Eng. ASCE, V137(10): 1063-1074.

Submitted:
Fleischman R.B., Restrepo J.I, Naito C.J., Sause R., Zhang D. and Schoettler M. (2011). "Integrated Analytical and Experimental Research to Develop a New Seismic Design Methodology for Precast Concrete Diaphragms" Special Issue of the ASCE Journal of Structural Engineering on NEES: Advances in Earthquake Engineering, Submitted.

Naito, C.J. and Ren, R. (2011). "An evaluation method for precast concrete diaphragm connectors based on structural testing" PCI Journal, Submitted.

Ren, R. and Naito, C.J. (2011). "Precast concrete diaphragm connector performance database and response estimation modeling approach" J. of Structural Eng. ASCE, Submitted.

In Preparation
Fleischman R.B., Zhang D., Naito C.J. and Ren, R. (2012). "Experimental Evaluation of Precast Diaphragm Critical Shear Joint under Seismic Demands" In preparation for submission to PCI Journal.

Wan, G., and R. B. Fleischman. (2012). "A Rational Method for Calculating the Service Stiffness and Yield Strength of Precast Floor Diaphragms," In preparation for submission to PCI Journal.

Wan G., Fleischman R.B., Zhang D. and Naito C.J. (2012). "Development of Connector Models for Nonlinear Pushover Analysis of Precast Diaphragms" In preparation for submission to Computer and Structures.

Ware, A.R., Zhang, D., Fleischman, R.B. and Mielke M. (2012). "Calibration of Models for Topped Precast Diaphragm". In preparation.

Zhang D. and Fleischman R.B. (2012a). "Establishment of Seismic Design Force Factors for Precast Concrete Diaphragms" In preparation for submission to Earthquake Engineering and Structural Dynamics.

Zhang, D. and Fleischman, R.B. (2012b). "Dynamic response of precast concrete parking garage under seismic loading". In preparation.

Zhang D., Fleischman R.B., Wan G. and Naito C.J. (2012). "Development of Hysteretic Models for Precast Concrete Diaphragm Connectors for Use in Three-Dimensional Nonlinear Dynamic Analysis" In preparation for submission to ACI Structural Journal.

D2. REPORTS

Building Seismic Safety Council, Committee TS-4. (2009). "Seismic design methodolgy for precast concrete floor diaphragms," Part III, 2009 NEHRP Recommended Sesimic Provisions, Federal Emergency Management Agency, Washington, D.C.

Naito, C., Peter, W., Cao, L. (2006). "Development of a Seismic Design Methodology for Precast Diaphragms - PHASE 1 SUMMARY REPORT," ATLSS Report No. 06-03, ATLSS Center, Lehigh University.

Naito, C., Ren, R., Jones, C., Cullen, T. (2007). "Development of a Seismic Design Methodology for Precast Diaphragms - PHASE 1B SUMMARY REPORT", ATLSS Report No.07-04, ATLSS Center, Lehigh University.

Naito, C., Ren, R. (2008). "Development of a Seismic Design Methodology for Precast Diaphragms – PHASE 1C SUMMARY REPORT", ATLSS Report No.08-09, ATLSS Center, Lehigh University.

Fleischman R.B. (2009). "Development and design of untopped precast concrete diaphragm system for high seismic zones" Charles Pankow Foundation. <http://www.pankowfoundation.org/grants.cfm?research=1>

Naito, C., Peter W., Creek J. (2006a). "T.C.S. Twister Connector Universal Form Clamp Company In-plane Performance", *ATLSS Report* No. 06-08, ATLSS Center, Lehigh University.

Naito, C., Peter W., Creek J. (2006b). "T.C.H.D. Twister Connector Universal Form Clamp Company In-plane Performance", *ATLSS Report* No. 06-09, ATLSS Center, Lehigh University.

Naito, C. (2007). "Erector Connector Meadow Burke Company In-plane Performance", *ATLSS Report* No. 06-22, ATLSS Center, Lehigh University.

Hodgson I, Naito, C., Stokes F., Bowman C. (2007). "Erector Connector Meadow Burke Company In-

plane and out-of-plane Performance", *ATLSS Report* No. 07-12, ATLSS Center, Lehigh University.

Naito, C., Hendricks R. (2008). "In-plane and Out-of-plane Performance of the MC Flange Connector", *ATLSSReport* No. 08-08, ATLSS Center, Lehigh University.

Naito, C. (2008). "Universal Form Clamp Company Next Generation Twister Connector Performance", *ATLSS,Report* No. 08-14, ATLSS Center, Lehigh University.

Naito, C., Ren, R. (2009a). "In-plane and Out-of-plane Performance of Building Products Edge Connector System," *ATLSS Report* No. 09-02, ATLSS Center, Lehigh University.

Naito, C., Ren, R. (2009b). "In-plane and Out-of-plane Performance of the Mini-MC Flange Connector", *ATLSS Report* No. 09-05, ATLSS Center, Lehigh University.

Ren, R., Naito, C. (2010). "In-plane and Out-of-plane Performance of MC Flange Connector." *ATLSS Report* No. 10-02, ATLSS Center, Lehigh University.

D3. PHD DISSERTATION AND MS THESIS

PhD Dissertation

Cao L. (2006). "Effective design of precast concrete diaphragm connections subjected to in-plane demands." Ph.D. Dissertation. Lehigh University, Bethlehem, PA.

Ren, R. (2011). "Seismic Performance Evaluation and Effective Design of Precast Concrete Diaphragm." Ph.D. Dissertation. Lehigh University, Bethlehem, PA.

Schoettler, M.J. (2010) "Seismic demands in precast concrete diaphragms" Ph.D. Dissertation. University of California, San Diego, CA.

Wan, G. (2007). "Analytical development of capacity design factors for a precast concete diaphragm seismic design methodology", Ph.D Dissertation, University of Arizona, Tucson, AZ.

Zhang, D. (2010) "Examination of precast concrete diaphragm seismic response by three-dimensional nonlinear transient dynamic analyses." Ph.D. Dissertation. University of Arizona, Tucson, AZ.

MS Thesis

Mielke, M. (2011) "Data analysis and model calibration for shake table test of three-story diaphragm-sensitive precast concrete structure." MS. Thesis. University of Arizona, Tucson, AZ.

Ware, A.R. (2012) "Precast sensitive diaphragm calibration and column participation study using shake table test data." MS. Thesis. University of Arizona, Tucson, AZ.